Lengthscale Effects in the Damage and Failure of Composites

by

Jeffrey Thomas Chambers

B.S. Mechanical Engineering
University of California (2004)

S.M. Aeronautical and Astronautical Engineering
Massachusetts Institute of Technology (2006)

Submitted to the Department of Aeronautics and Astronautics
in partial fulfillment of the requirements for the degree of

Doctor of Philosophy in Aeronautics and Astronautics

at the

MASSACHUSETTS INSTITUTE OF TECHNOLOGY

June 2014

Author .....
Department of Aeronautics and Astronautics
May 12, 2014

Certified by .....
Paul A. Lagacé
Professor of Aeronautics and Astronautics and Engineering Systems
Chair, Thesis Committee

Certified by .....
John W. Hutchinson
Abbott and James Lawrence Research Professor of Engineering, Harvard University
Thesis Committee

Certified by .....
John Dugundji
Professor of Aeronautics and Astronautics Emeritus
Thesis Committee

Accepted by .....
Paulo C. Lozano
Associate Professor of Aeronautics and Astronautics
Chair, Graduate Program Committee

[THIS PAGE INTENTIONALLY LEFT BLANK]

Lengthscale Effects in the Damage and Failure of Composites

by

Jeffrey Thomas Chambers

Submitted to the Department of Aeronautics and Astronautics
on May 12, 2014, in partial fulfillment of the
requirements for the degree of
Doctor of Philosophy in Aeronautics and Astronautics

Abstract

The primary objective of this work is to investigate and identify lengthscale effects associated with damage in composite materials and their structures, and to determine how these lengthscales vary across levels of composites and can be used in assessing the overall response of composite structures. This is an advancement in a much larger pursuit towards developing a new methodology that utilizes composite failure and material data collected across all levels in order to predict the occurrence of damage and its effects at any operative level of composite structures. Documentation procedures are developed to capture qualitative and quantitative information on damage within experimental specimens, and computed microtomography provides additional information on the damage process. Specimens containing structural details are investigated postmortem to identify lengthscales associated with damage modes. Finite element models are developed in order to investigate the interaction of lengthscales associated with structural details with those associated with the basic damage modes. Based on these experimental and numerical results, lengthscales associated with five basic damage modes, as identified from previous studies, and the four structural details included in this investigation are identified and discussed, as are their interactions and importance. It is found that it is important to recognize two damage regimes, initiation and propagation, in characterizing lengthscales associated with damage modes. Identifying key lengthscales within each regime allows investigation of how the critical lengthscale(s) controlling the damage mode(s) change(s) across regimes. The concept of the "observable lengthscale" is identified as an important consideration when investigating lengthscales in experimental specimens and structures in that the observable lengthscale sets the ability to resolve damage and interactions of such. In a manner analogous to the "observable lengthscale," key lengthscales of basic damage modes and of structural details need to be used when choosing the scale of finite element models so that models have a resolution at least as fine as the key lengthscale of the mode under investigation. The results of the work show that the concept of lengthscales is a viable tool to characterize the overall response of composite structures, particularly involving damage initiation, damage propagation, and overall failure. The determination of how these lengthscales

vary across levels in composites provides an important tool that can be used to assess this overall response of composite structures. Particular conclusions considering each damage mode are offered. In addition, a new damage type, called "transverse zigzag," is identified and studied, resulting in a finding that loads can "bypass" and "carry-through" regions of damage, depending on the geometry and laminate. Recommendations for further investigations are proposed based on the understanding of the role of lengthscales in the damage and failure of composites acquired from this work, and the needs identified to further this understanding.

Thesis Supervisor: Paul A. Lagacé
Title: Professor of Aeronautics and Astronautics and Engineering Systems, Massachusetts Institute of Technology

Acknowledgments

There are many people I would like to thank for contributing and helping me complete this research. First, to my advisor, Prof. Paul Lagacé, for the support, help, and guidance he has given me during the course of this research. Prof. Lagacé's high expectations have made me a stronger engineer and scientist, giving me skills that I will utilize throughout my career. Second, to my committee members, Prof. Hutchinson and Prof. Dugundji, for their support and guidance over the course of the thesis. Dr. Michopoulos for facilitating the experimental investigation and providing the opportunity to spend a summer at the Naval Research Laboratory. To all the people who have helped with this research: John Kane, Dave Robertson, and all my friends in TELAMS for providing a fun and productive workspace. There were many late nights spent in the office or lab, and I am thankful for your support: Namiko Y., Roberto G., Alberto G., Holly J., Sunny W., Miso K., Chris B., and Rich L. A special thanks Josh K. and Fabio F. for their support and encouragement throughout the qualifiers, general exams, and the normal ups and downs of the process. In addition, I would like to thank Prof. Willcox and Beth Marois for their support from the department and Dean Staton for helping along the way.

Finally, I would like to thank my wife, Maureen, for her unrelenting support, encouragement, and patience, and for introducing Lily, the strangest little creature (supposedly a dog), into my life. My parents for always loving and supporting me in all of my endeavors, including my academic journey.

[THIS PAGE INTENTIONALLY LEFT BLANK]

Foreword

This work was performed in the Technology Laboratory for Advanced Materials and Structures (TELAMS) of the Department of Aeronautics and Astronautics at the Massachusetts Institute of Technology. This work was sponsored by the Office of Naval Research under award number N00014-07-1-0614, and by the Naval Research Laboratory under award number 019606-001.

[THIS PAGE INTENTIONALLY LEFT BLANK]

Table of Contents

[THIS PAGE INTENTIONALLY LEFT BLANK]

List of Figures

List of Tables

Nomenclature

$\boldsymbol{A}$	-	extensional stiffness matrix
A_{ij}	-	terms of extensional stiffness matrix, relating in-plane loads to in-plane strains
$\boldsymbol{B}$	-	coupling stiffness matrix
B_{ij}	-	terms of coupling stiffness matrix, relating in-plane loads to curvatures and moments to in-plane strains
C_1	-	constant related to X-ray machine
C_2	-	constant related to X-ray machine
D	-	hole diameter
$\boldsymbol{D}$	-	bending stiffness matrix
D_{ij}	-	terms of bending stiffness matrix, relating moments to curvatures
E_L	-	longitudinal modulus
E_T	-	transverse modulus
E_Z	-	modulus in the z-direction
G	-	strain energy release rate
G_{LT}	-	in-plane shear modulus
G_{LZ}	-	transverse (L-Z plane) shear modulus
G_{TZ}	-	transverse (T-Z plane) shear modulus
h	-	height of specimen to be X-rayed
$l_{characteristic}$	-	characteristic length
l_5	-	characteristic length for strain to return to within 5% of far-field strain

l_{10} - characteristic length for strain to return to within 10% of far-field strain

L - specimen length

L_g - grip length

L_{GAGE} - specimen gage length

n - number of radii away from edge of structural feature

$\widehat{n}$ - effective number of plies

N - total number of plies within laminate

$\overline{Q}_{ij}$ - transformed reduced stiffnesses

r - radial distance in polar coordinate system

r' - radial distance in offset polar coordinate system

r_o - radius of structural feature

R_x - rotation about the x-direction in experimental tests

R_y - rotation about the y-direction in experimental tests

R_z - rotation about the z-direction in experimental tests

S - axis aligned with the positive θ direction

$\widehat{S}$ - axis aligned with the negative θ direction

t - specimen thickness

t_k - thickness of ply k

$\mathbf{U}$ - displacement path in experimental tests

u_x - in-plane translation in the x-direction in experimental tests

u_y - in-plane translation in the y-direction in experimental tests

u_z - out-of-plane translation in the z-direction in experimental tests

w - specimen width

X - sublaminate

X_D - dropped sublaminate

x - coordinate aligned with length of specimen (also represented by subscript '1')

$\widehat{\mathbf{x}}$ - unit vector in x-direction in experimental tests

x'	-	curvilinear coordinate defining rotation about x-axis in experimental tests
$\widehat{\mathbf{x}}'$	-	unit vector in x'-direction in experimental tests
y	-	coordinate aligned with width of specimen (also represented by subscript '2')
$\widehat{\mathbf{y}}$	-	unit vector in y-direction in experimental tests
y'	-	curvilinear coordinate defining rotation about y-axis in experimental tests
$\widehat{\mathbf{y}}'$	-	unit vector in y'-direction in experimental tests
z	-	coordinate aligned with thickness of specimen (also represented by subscript '3')
$\widehat{\mathbf{z}}$	-	unit vector in z-direction in experimental tests
z'	-	curvilinear coordinate defining rotation about z-axis in experimental tests
$\bar{z}_k$	-	through-thickness distance from midplane to centroid of ply k
$\widehat{\mathbf{z}}'$	-	unit vector in z'-direction in experimental tests
α	-	angle along the z'-direction in experimental tests
Δ	-	applied boundary displacement
$\Delta\epsilon$	-	change in strain
$\Delta\sigma$	-	change in stress
ϵ^o	-	midplane strain
ϵ_{ij}	-	strain (i, j indicates direction)
ϵ_C	-	minimum strain
ϵ_{C^*}	-	minimum global strain
ϵ_S	-	maximum magnitude of shear strain
ϵ_T	-	maximum strain
ϵ_{T^*}	-	maximum global strain
$\eta_{XY,X}\ (\equiv \eta_{16})$	-	coefficient of mutual influence (shearing in x-y plane due to extension in x)

$\eta_{XZ,X}\,(\equiv \eta_{15})$	-	coefficient of mutual influence (shearing in x-z plane due to extension in x)
$\eta_{YZ,X}\,(\equiv \eta_{14})$	-	coefficient of mutual influence (shearing in y-z plane due to extension in x)
θ	-	ply fiber angle
$\nu_{LT}\,(\equiv \nu_{XY})$	-	Poisson's ratio (L-T plane)
$\nu_{LZ}\,(\equiv \nu_{XZ})$	-	Poisson's ratio (L-Z plane)
ν_{TZ}	-	Poisson's ratio (T-Z plane)
σ_{ij}	-	stress (i, j indicates direction)
ϕ	-	angle measure in polar coordinate system
ψ	-	angle measure in offset polar coordinate system
#	-	wildcard character within specimen identification representing a single digit
?	-	wildcard character within specimen identification representing a single letter

Chapter 1

Introduction

Composite materials are finding applications in an expanding number of fields, from aerospace to sporting goods, as designers take advantage of their efficiencies. Composite materials offer several advantages, including high specific strength and specific stiffness, corrosion and fatigue resistance, and the ability to tailor properties to meet specific design requirements. The aerospace industry has led the way in incorporating composite materials into structures, motivated by the weight savings offered by these materials. Moreover, as better characterization of composite behavior continues to be achieved, designers are making greater use of composites. For example, in the most recently designed Boeing commercial aircraft, the Boeing 787, a large portion ($\sim$50%) of the airframe and primary structure are made of composites as opposed to the Boeing 777 (aircraft designed prior to the 787) where only 12% of the structure was composite [1]. Other industries, such as automotive, marine, and civil infrastructure, are also slowly incorporating composites into their designs. These other industries are typically less motivated by the weight saving advantages and are slower to implement composites into designs due to the complex material behavior. In particular, there is still a lack of a firm understanding of the damage behavior of composite structures. Until such an understanding of the damage behavior is reached, designers will shy away from composites (use traditional materials such as aluminum and steel) or be forced to use sub-optimally efficient designs (i.e., over-designed structures to compensate for unknown damage behavior).

The study of composite damage behavior has received great attention during the past 50 years. Many researchers have done in-depth studies to first identify and then attempt to characterize the behavior of the basic damage modes that can become present within composite structures [e.g., 2–6]. To date, five basic damage modes have been identified at the constituent and ply levels: fiber fracture, matrix cracking, fiber microbuckling, interfacial debonding, and ply delamination. Much of the previous works investigate a single damage mode, focusing on characterizing the behavior of solely one of these basic damage modes. These works typically tested specimens at a specific level (i.e., test the same size coupons) and identified mechanisms which influenced the single mode. Although these works have established lengthscales associated with each basic damage mode, the behavior of these modes are still not fully characterized. An understanding of how these basic damage modes as well as interactions among the modes (described later), including the mechanisms/lengthscales influencing the modes, change as the level of testing is varied is still uncertain.

The uncertainties in the understanding of these basic modes directly affects the ability to predict failure. Results from the recent World-Wide Failure Exercise for composites, organized and coordinated by Mike Hinton and colleagues [7], show just how far the overall composites community and industry are from being able to predict general failure behavior of relatively simple composite configurations (i.e., coupon specimens under various loading conditions). In particular, the coordinators note that even in predicting the initial strength (i.e., at onset of first failure/damage) of multidirectional laminates, "the level of agreement between theoretical predictions and the available experimental results was generally not very good." Furthermore, it is noted that in progressing to the prediction of final strength (i.e., ultimate failure), "the 'exercise' has shown that the current theories are not sufficiently robust" [7]. There is, therefore, much to be accomplished in order to be able to properly and fully characterize and predict composite behavior, even at the ply and laminate levels.

From the point of understanding at these fundamental levels, much needs to be accomplished to be able to use such an understanding in an ability to predict the behavior and failure through the levels up to full-scale structures. A key item that

is lacking is the ability to effectively utilize data and observations made at length-scales associated with laboratory-sized specimens in predicting the actual behavior manifested in full-scale structures [8]. As one moves through various levels, greater complexity is added due to the variety of structural details and the geometry of the basic structural configuration, structural response and phenomena with different lengthscales, and the occurrence of damage and the lengthscales associated with such. This is further complicated by the interaction of these items and the stress fields associated with that. At a recent conference organized by Peter Beaumont on "Advances in Multi-Scale Modelling of Composite Material Systems of Components" [9], the invited participants all made the point and agreed that there is much to be accomplished in order to work fully across the multiple lengthscales in the mechanical behavior of composite structures, particularly with regard to failure, when considering a real-life operative environment including the presence of damage. This, furthermore, has yet to progress to fully addressing long-term behavior including damage propagation.

Beyond the understanding of the basic damage modes, another complexity arises in composite structures when addressing interactions between levels. In composite structures, where the operable lengthscales increase, damage mechanisms and modes can interact between levels involving multiple lengthscales. To understand these interactions, the mechanisms controlling damage must be identified as well as the lengthscales at which these mechanisms act. It is possible that the lengthscales at which some of these mechanisms act are not currently defined and may require the definition of a new lengthscale. For example, a strain-field gradient due to a structural detail (e.g., hole, ply-drop) influences the initiation and growth of damage near the detail. However, a generic definition to describe strain-field gradients does not exist at present. A primary objective of this work is to identify, and define as necessary, the associated lengthscales influencing each damage mechanism, including lengthscales associated with geometric features (e.g., holes, stiffeners), and investigate if and how the associated lengthscales change as the modes interact and the testing levels change.

The "state-of-the-art" approach used to relate changes in composite behavior as the operable level increases is the use of material allowables and knockdown fac-

tors. This approach accounts for changes in the behavior of composites as the level is changed by defining an "allowable" strength for a composite at a lower level and then "knocking down" (decreasing) this allowable as the levels are increased [10, 11]. This is done to account for unknown changes in the manifestations of the primary damage mechanisms as the levels are increased. In large part due to this lack of understanding, composite structures are currently designed and certified/validated for safe operation by using a primarily empirically-based methodology known as the "Building Block Approach" (BBA). This approach provides a method for producing safe structures (structures designed not to fail for intended loads), but it does not provide designers knowledge of the level of safety, only that the structure will not fail under the intended loads. The BBA is fundamentally based on demonstrating behavior via experiments and preforming assessment using probabilistic approaches, often as a simple determination of "performance values" via assumed statistical models for a large database of behavior characterization. Such behavior is first documented at the most basic operative level of composites – the material ply. Greater structural complexity is then progressively addressed as experiments are conducted on specimens at higher levels – subelements, elements, subcomponents, components, and full-scale structures. While structural complexity and the various lengthscales involved increase at each step along the building block, the number of tests conducted at each step decrease. Nevertheless, the approach relies heavily on experimentation and therefore is costly. This approach is described in more detail in Section 2.3, where the BBA is discussed. However, the BBA has many limitations. Using a system of allowables and knockdown factors conceals information about the damage process from the designers, making it difficult (if not impossible) to understand which mechanisms may be driving the overall damage leading to structural failure. If this information were available, the designers might be able to identify factors limiting their designs, and thereby make changes to produce more efficient structures. There are also points along the approach where it can be necessary to return to a previous step as what was manifested at a lower level of the building block was not seen in a specimen of greater complexity. The lack of understanding also results in the use of "knockdown

factors." This causes a smaller fraction of the full capability of the basic material to be employed in the final structure.

To date, the composites community has defined operable levels and associated lengthscales corresponding with convenient manufacturing, assembly, and testing techniques. The BBA clearly defines these levels from the coupon up to the full-scale component. However, the currently defined levels do not necessarily capture the lengthscales associated with the mechanisms controlling damage in composites. For example, the design of composite structures evolves from the material constituents up to the final component (as is illustrated in Figure 1.1), with new lengthscales being introduced at each level. But the defined levels do not necessarily capture the lengthscales associated with the mechanisms that influence the behavior of composites. These mechanisms act over the continuum of the composite, not at the pre-defined levels. Therefore, consideration to define new levels and lengthscales corresponding to these mechanisms must be taken to better characterize the behavior of composites.

Clearly, an important issue when analyzing composites is choosing the lengthscale at which to perform the analysis. While a virtual continuum exists from the atomic scale to the full-scale structure, composite engineers must choose a scale that is practical and useful for their need. This choice of scale determines applicable models and valid assumptions for the analysis. For example, in Classical Laminated Plate Theory, the laminate plies are assumed to be transversely isotropic, homogeneous materials. This model does not account for individual fibers and matrix, but instead assumes averaged or "smeared" elastic properties across the individual plies. Assumptions used in models are typically implicit to a particular scale and create boundaries between lengthscales [12]. The choice of scale can also determine how the composite behaves. As an example, after studying the effects of ply thickness and neighboring ply angles on the strength of a laminate, Flaggs and Kural [2] suggest the transverse strength should not be considered as an intrinsic ply property. Instead, they found that the same ply produced varying transverse strengths depending on laminate ply thicknesses and ply angles. Many studies in the literature on composites can be re-analyzed to show the importance in choice of the appropriate lengthscale(s)

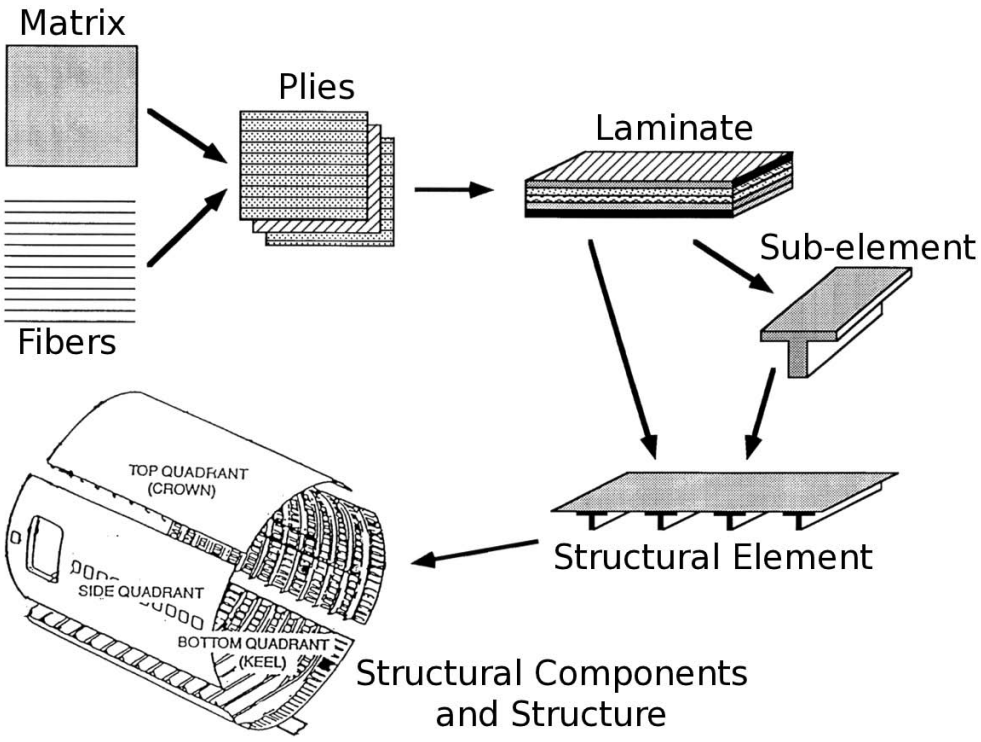

Figure 1.1 Examples of possible levels in composite structural engineering.

for analysis considerations, and to have a good understanding of lengthscale effects.

The primary objective of this work is to investigate and identify lengthscale effects associated with damage in composite materials and their structures, and to determine how these lengthscales vary across levels of composites and can be used in assessing the overall response of composite structures. Many lengthscales are present and (currently) play unknown roles in the composite damage process. This thesis work is meant to further the understanding of damage in composites by identifying the key/critical lengthscales involved in the basic damage modes, investigating and identifying if and how the lengthscales of the individual damage modes change as multiple modes interact, and presenting a method that can be used to investigate lengthscale effects up through full-scale structural behavior. The outcomes of this work are also intended to expand the understanding of damage, and to enable composite engineers to design more efficient structures without sacrificing safety. Such a methodology will guide and optimize the overall composite design process, thereby reducing the number of experiments needed to certify/validate components, thus, substantially reducing the cost and overall risk in structural development, as well as lead to fuller utilization of basic material capability.

This thesis work is organized as follows. A summary of the previous work accomplished on this topic is presented in Chapter 2. In that chapter, research on the basic composite damage modes and mode interactions is assessed, the current capabilities to predict damage in composites are evaluated, and the presence of lengthscales within these works are discussed. This is followed in Chapter 3 by a full articulation of the thesis objectives and the associated approach used in this work to accomplish such objectives. Details of the specimens considered during this work are presented in Chapter 4. The development of a novel procedure to document and record damage in composite specimens is presented in Chapter 5, including a nondestructive technique to investigate damage within specimens. In Chapter 6, the results from applying the procedures to tested composite specimens in order to document and characterize damage are presented. Models to determine stress/strain field gradients for the various specimen configurations are investigated in Chapter 7, and lengthscales associated

with these fields are identified. Findings from the results are discussed in Chapter 8, including a discussion of the role of lengthscales in composite damage. Finally, in Chapter 9, conclusions and recommendations for future work based on the results of the current work are presented.

Chapter 2

Previous Work

A review of the literature on composite damage and failure, and on the current predictive capabilities for damage and failure of the composites community is presented. As previously noted, damage and failure within composites has been of great interest to composite engineers and designers, with significant research being done on these topics with the goal of achieving an understanding of the damage and failure processes. While the selected literature spans a variety of topics, from basic damage modes to failure prediction, the primary focus of this review is to identify the underlying lengthscale effects which, although not directly addressed by the authors, were intrinsically affecting the results presented in the works. The review is broken into six sections: basic composite damage/failure modes, mode interaction, design approach, prediction of damage and failure, lengthscales in composites, and a summary.

2.1 Basic Composite Damage/Failure Modes

An understanding of the basic damage and failure modes in composites is required before considering more complex damage, such as interacting damage modes. Significant research has been done on these topics with the goal of achieving such an understanding. Basic composite damage modes can be categorized into two types: in-plane and out-of-plane. In-plane damage modes involve the constituents and include fiber fracture, matrix cracking, fiber microbuckling, and interfacial debonding

(also known as pull-out or push-out) [2–5], while the one out-of-plane damage mode, occurring at the laminate level, is ply delamination [6]. The basic mechanics of each damage mode and the analytical and experimental procedures that historically have been used to study these modes are subsequently presented. In the ensuing section, Section 2.2, the situation where two or more of these basic damage modes interact is discussed.

2.1.1 Fiber Fracture

Fiber fracture occurs in composites when loading on the laminate causes a fiber to break basically perpendicular to its length. Typically, this happens when loading on the composite results in a tensile longitudinal load/stress in a lamina resulting in the strength of a fiber being exceeded. Once the loading causes the stress in a fiber to exceed the critical strength of the fiber, the fiber fractures and the loading redistributes locally to the regions surrounding the failed fiber [13]. An illustration of a fiber fractured in a unidirectional lamina due to longitudinal tension is shown in Figure 2.1. Catastrophic failure (all fibers fracturing at once) typically does not occur at the load causing initial fiber fracture due to the variation of individual fiber strength [14, 15]. The variation of fiber strength can be attributed to manufacturing variations (e.g., distribution of flaws within fibers, variation in fiber geometries, and variations in fiber material properties). These variations in fiber strength are often modeled by probabilistic distributions (e.g., Weibull distributions) of fiber strength [5, 16–18]. Continued loading past the initial fiber fracture causes adjacent fibers to reach their critical strength and fracture, increasing the density of fractured fibers within the lamina. The load continues to redistribute until the remaining fibers cannot support the load, and catastrophic failure occurs.

Fiber fracture may also occur under certain conditions when a lamina experiences longitudinal compression. Under such loading, the matrix provides support of the fibers and the fibers may microbuckle (discussed in Section 2.1.3). If microbuckling occurs, the fibers bend and may eventually fracture due to bending [19]. However,

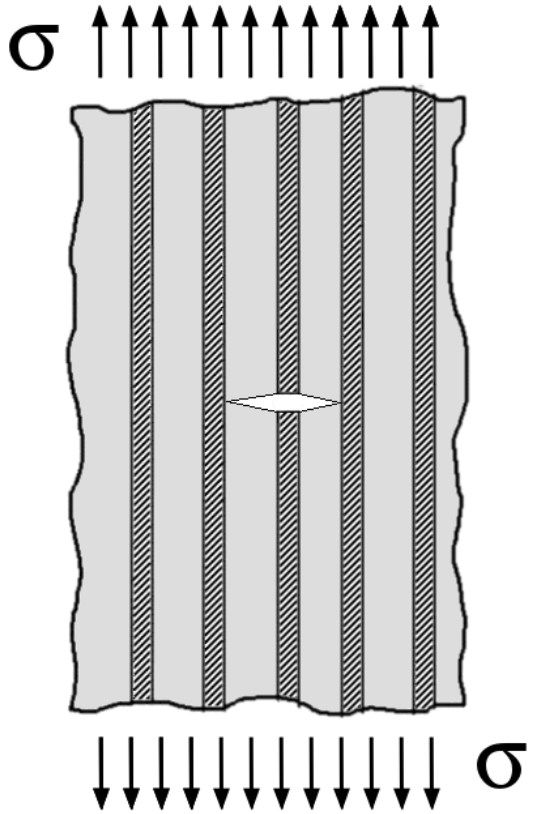

Figure 2.1 Illustration of a single fiber fracture in a unidirectional lamina under longitudinal tension.

although this damage results in a fractured fiber, it is not typically referred to as fiber fracture, but is encompassed in the microbuckling damage mode.

Mechanistic models are used to understand and predict fiber fracture in composites. In the strength of materials approach, composite fibers are modeled as simple cylindrical, transversely isotropic solids. The model also assumes the fibers to be loaded longitudinally (along the cylindrical axis) and the geometry to be constant throughout. More complex models incorporate additional parameters, such as flaws within the fiber (to account for defects inherent in the manufacturing process) or transverse loading on the fiber (to account for the interaction with the matrix), in order to more accurately capture the response of fibers [20].

In addition to studying fiber fracture with models, this damage mode is commonly observed in experimental tests of composite laminates. There is good agreement between the strength of materials model and the experimental mean fiber strengths. In experiments on composite laminates, fiber fracture is observed as the dominant failure mode in cross-ply laminates and also in laminates with angle plies containing a large number of 0° and 90° plies [21, 22]. The effects of fiber diameter on fiber strength have also been studied in experiments. In such studies, the strength of fibers increases as the fiber diameter is decreased. This increase in strength is attributed to the probability of fewer flaws being present in fibers of smaller diameter. Researchers found that as the fiber diameter was decreased, the presence of larger flaws (on the order of the fiber diameter) caused the fibers to break during manufacturing. Therefore, the fibers of smaller diameter precluded the presence of larger flaws, resulting in inherently stronger fibers [5, 18, 23].

2.1.2 Matrix Cracking

Matrix cracking is a common damage mode observed in composites structures. The mode initiates as microcracks within the matrix. These microcracks typically begin at singularities (e.g., voids, flaws, material discontinuities) within the material [24], but can also begin at points in the matrix where the stress field exceeds the matrix strength. As the microcracks grow, they interconnect, thereby creating a

main crack that will typically grow normal to the loading direction. An illustration of matrix cracking in a unidirectional lamina is provided in Figure 2.2. As loading is increased and if matrix cracking is the only damage mode present in a laminate, a uniform density of matrix cracks form within the damaged laminate layer until the loading exceeds a critical point. This causes the cracks to propagate into neighboring layers or initiate other failure modes (e.g., delamination) [6, 25].

Mechanistic models are used to understand and predict matrix cracking in composites. These models range from simple strength of materials models to damage-dependent constitutive models. The simple models typically predict the initiation of matrix cracks, while the more complex damage-dependent models capture the effects of matrix cracking on laminate strength [26]. This cracking reduces the strength of the laminate [6]. Another approach to predicting the initiation and growth of matrix cracking uses concepts from linear elastic fracture mechanics [2].

The parameters influencing matrix cracking have been studied by analytical models, such as those previously mentioned, and in experimental tests. Flaggs and Kural [2] observed that the formation and growth of matrix cracks depend strongly on laminae thickness and also on the orientation of adjacent plies. These variables have been found to influence the matrix crack spacing (distance between cracks) within a laminate. In other works, transverse cracking was observed to initiate in the cross (90°) plies of laminates (of many different layups) under longitudinal tensile loading (loading along the 0° axis) [2, 27–29]. These transverse cracks would grow through the ply within which they initiated until reaching an adjacent ply. If the cracks met an adjacent ply at the same orientation, the crack would continue to propagate through the adjacent ply. If the crack met an adjacent ply of another angle, the crack would typically arrest (not continue into the adjacent ply), and may act as the initiation point for local (internal) delamination [26, 30].

2.1.3 Fiber Microbuckling

Microbuckling is the dominant damage mode observed in composite laminates loaded in compression [31]. Microbuckling has been studied since the 1950's and

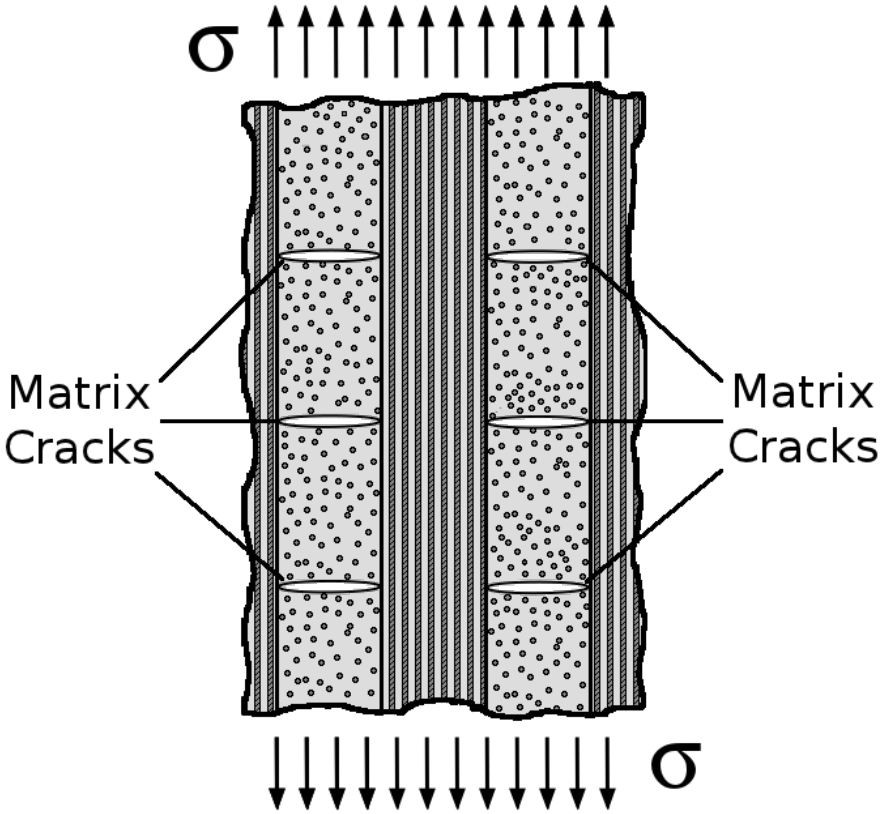

Figure 2.2 Illustration of matrix cracking in a cross-ply laminate under tensile loading.

two different theories on the mode have emerged [32]. The first group of theories assumes the fibers and matrix behave elastically, while the second group assumes a plastic response. For the elastic microbuckling case, compressive loading causes the continuous fibers to locally buckle (i.e., buckling occurring at the fiber level as opposed to structural (Euler) buckling, which involves buckling of the entire composite specimen). This results in either an extensional or shear mode of fiber buckling [3, 19, 33]. In the extensional mode, the fibers buckle out of phase, and create regions of compressive and tensile loading in the matrix between the fibers. In the shear mode, the fibers buckle in phase, and create a shear loading in the matrix between the fibers [13, 33]. The two types of elastic microbuckling are illustrated in Figures 2.3 and 2.4. If the magnitude of the buckling becomes large enough, the extensional or shear stress (depending on the elastic buckling mode) exceeds the matrix strength, causing matrix failure. As mentioned in Section 2.1.1, the fibers continue to locally buckle until the amplitude of buckling causes fiber fracture due to bending. In both modes of elastic microbuckling, the matrix behaves in a linear elastic manner. For the plastic microbuckling case, which has been found to be more common than elastic microbuckling [32, 34, 35], the compressive loading causes a nonlinear (plastic) response in the matrix. In this type of microbuckling, a localized group of relatively misaligned fibers "kink" when the compressive load is applied, forming a "kink band" as shown in Figure 2.5. This failure begins with the kinking of a few misaligned fibers, which then changes the local fields of stress and strain and creates instabilities in neighboring fibers [19]. These neighboring fibers eventually also kink and the result is a kink band. During this process, the matrix around the kinked fibers behaves in a nonlinear fashion.

Many models have been proposed to capture the mechanisms of microbuckling [e.g., 3, 19, 32, 36–38]. The various models were developed due to the varying theories of the dominant compressive failure mechanisms. In the 1960's, Rosen [3] was one of the first to model elastic microbuckling. His model assumed elastic bending of the fibers, elastic shear of the matrix, and perfect fiber alignment. The Rosen model has served as the basis for many subsequent models developed. In the 1990's, Budiansky

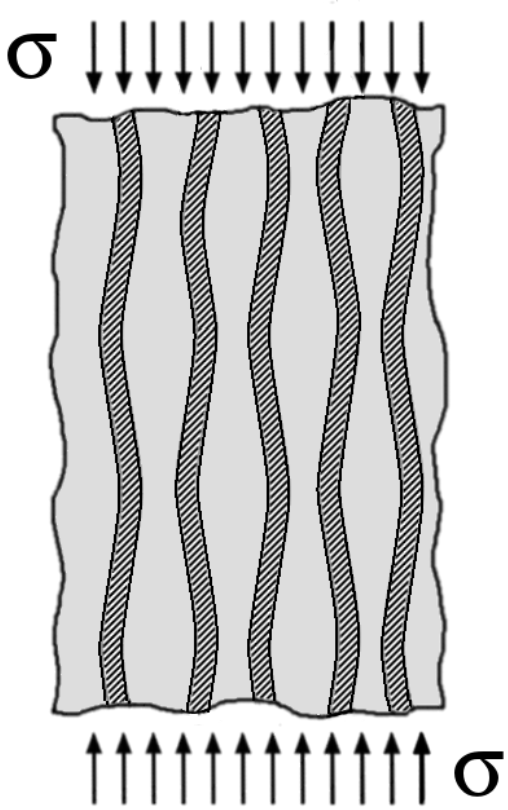

Figure 2.3 Illustration of out-of-phase elastic microbuckling in a unidirectional composite under longitudinal compressive loading.

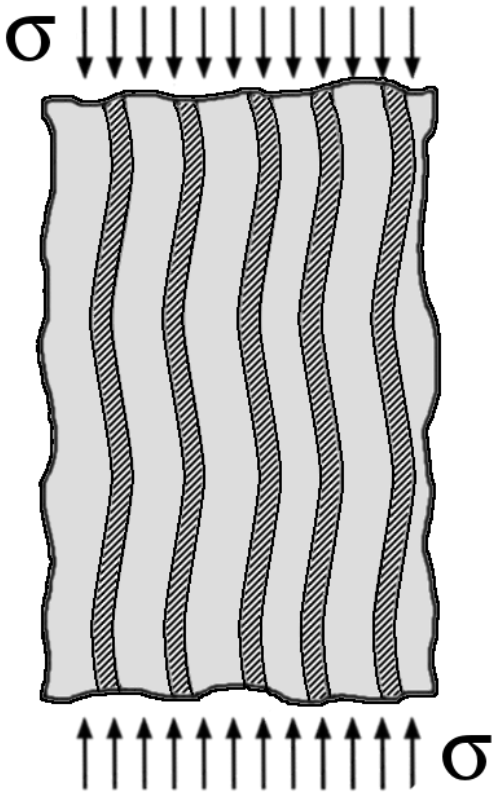

Figure 2.4 Illustration of in-phase elastic microbuckling in a unidirectional laminate under longitudinal compressive loading.

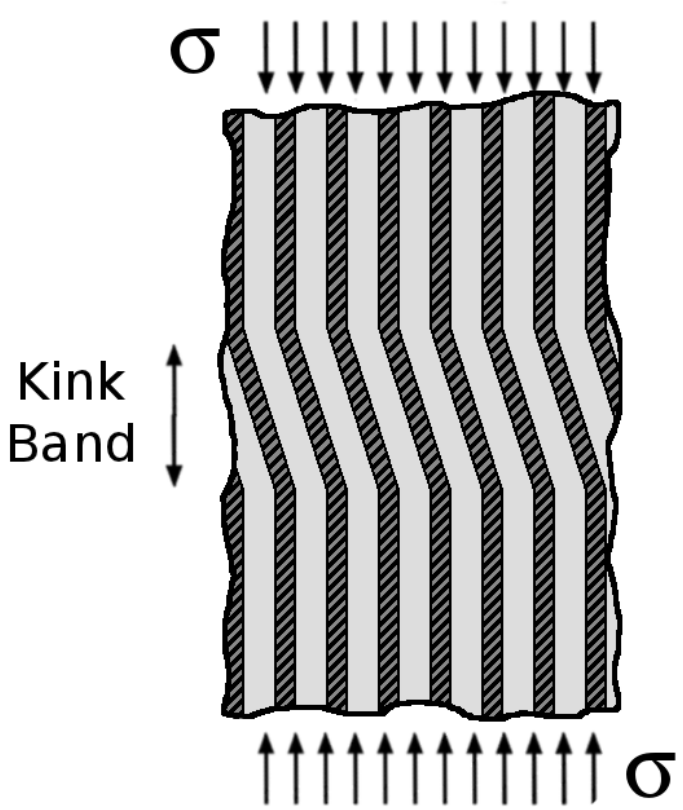

Figure 2.5 Illustration of plastic microbuckling and the resulting "kink band" region in a unidirectional laminate under longitudinal compressive loading.

and Fleck [35, 37] developed one of the first models for plastic microbuckling. Their model assumed an initial fiber misalignment that, when loaded in compression, lead to nonlinear behavior of the matrix and the formation of a kink band. The predictions from the Budiansky-Fleck [32] model have good agreement with the limited amount of experimental kinking results.

Many experimental investigations on microbuckling can be found in the literature. Jelf and Fleck [32] were able to achieve elastic microbuckling using non-traditional composites (one made of glass fibers and the other of wheat flour/spaghetti fibers, both in a silicone matrix). They found that the matrix must behave in a linear elastic fashion up to high strains in order to observe elastic microbuckling. When the matrix met this requirement, Jelf and Fleck had good agreement with the predictions of the Rosen model. However, they note that the majority of matrices used in commercially available composites do not exhibit this behavior. The more common experimentally observed form of this damage mode is plastic microbuckling. Berg and Salama [39] were among the earliest to observe plastic microbuckling in graphite/epoxy composites followed by more extensive studies by Weaver and Williams [40]. Many experimental studies have followed since, and typically find plastic microbuckling to occur in plies aligned with the loading direction when a multidirectional laminate is loaded in compression [19, 31, 32, 36, 39–42]. Experimental observations from these studies have found the kink bands (area of plastic microbuckling) to be nearly parallel and to scale with fiber diameter [31, 36].

2.1.4 Interfacial Debonding

Interfacial debonding, or fiber pull-out/push-out, is a damage mode in composite laminates loaded in tension or compression where the embedded fiber debonds from the matrix, allowing the fiber to slide past the matrix. Interfacial debonding has two main steps: the first is the debonding between the fiber and matrix, and the second is the extraction (sliding) of the fiber from the matrix [43–45]. These mechanisms are both governed by the interfacial shear stresses. An illustration of interfacial debonding

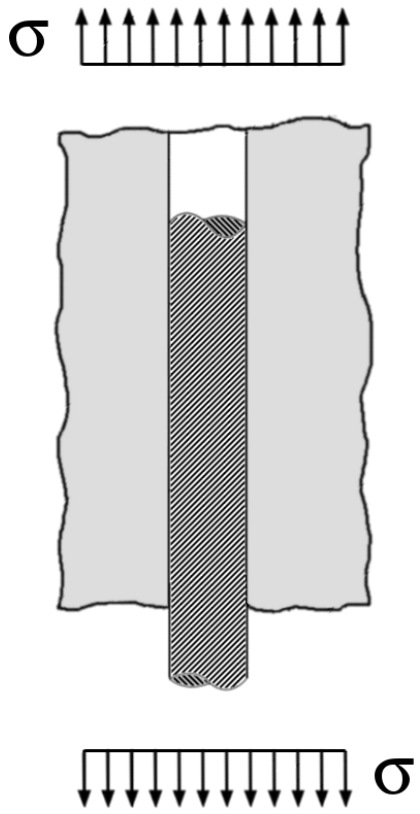

Figure 2.6 Illustration of interfacial debonding of a fiber from the matrix for a composite in tension.

is shown in Figure 2.6.

Analytical models of interfacial debonding have been proposed [e.g., 43–49]. Many of the models represent the fiber and matrix as a single cylindrical fiber embedded in a cylindrical block of matrix. The fiber is then either pulled or pushed out of the matrix. Each model uses different assumptions about the mechanisms at work during the interfacial debonding process, according to the underlying theory of the model. In shear lag theory, the axial stress in the fiber is assumed to be entirely transfered to the matrix through shear stress at the fiber-matrix interface, the residual radial stress to be uniform, and the debonding to initiate from the top surface. Other theories incorporate friction effects, relax some of the assumptions used in the shear lag theory, and/or use finite element methods to analyze the process [e.g., 44–46]. The advantage to the shear lag theory is that it provides a closed-form solution, allowing the effects of the model parameters to be efficiently analyzed. These parameters include the elastic mismatch between the fiber and matrix, fiber radius, bonded fiber length, and residual stress.

Experiments have been conducted to study the parameters of interfacial debonding. Kelly and Tyson [50] were some of the earliest researchers, in 1965, to investigate the pull-out phenomenon by testing metal-metal composites. Continued experimental work found direct relationships between the extraction load, required to pull out an embedded wire from a matrix, and the embedded length and diameter of the wire [43]. Another parameter found to be important in the pull-out process is friction. Studies found that the compressive stress between the matrix and fiber had a significant effect on the friction stress, and therefore on the load required to extract fibers [44, 51]. Beaumont and Phillips [52] observed pull-out during their research on the tensile strength of notched composites. In their work, fibers were surface-treated and the mean fiber pull-out lengths were recorded. They found the mean fiber pull-out lengths ranged from 2 to 30 fiber diameters for carbon fibers in a polymer matrix with various fiber surface treatments [52]. In other studies, fiber pull-out was observed to be the dominant failure mode in angle-ply tensile specimens with a central hole when the ply angles were small (less than 30°) [53]. This finding shows that interlaminar

effects influence interfacial debonding. It was also observed that changing the constitutive properties (e.g., changing the fiber or matrix type) affects the stress state and hence the interfacial debonding damage mode [24, 48].

2.1.5 Ply Delamination

Delamination is an out-of-plane damage mode in composite laminates where plies separate from neighboring plies. Delamination initiates due to interlaminar stresses developed from in-plane loading (e.g., gradient stress fields due to structural details, flaws, the presence of other damage modes, ply drops, free-edge effects) and/or out-of-plane loading (e.g., impact) of laminates, resulting in a separation between two laminate layers [4, 6, 30, 54, 55]. This separation causes the internal stresses/loads to redistribute around the delamination [56, 57]. Delamination itself does not typically coincide with final failure, but the redistribution of stresses/loads due to the delamination generally results in an in-plane failure mode causing final failure [58]. For in-plane loading, delamination typically initiates at points where large stress gradients are present, such as at ply drops and free edges. For out-of-plane loading, such as low velocity impact, delamination can typically initiate anywhere within the laminate (through the thickness) near the point of transverse loading [56]. An illustration of a free-edge delamination and an internal delamination is shown in Figure 2.7.

Two basic approaches have been used to model delamination in composites. In the mechanics of materials approach, the prediction of interlaminar stresses is used and compared with the interlaminar strength of the composite [58, 59]. This method relies on an accurate prediction of the interlaminar stresses and determination of the interlaminar strength. Various methods, such as the semi-analytical approach, have been suggested to predict the interlaminar stresses [58–62]. After obtaining the interlaminar stresses, the methods predict delamination to initiate once this stress has exceeded the interlaminar strength over a characteristic length. Kim and Soni [59] take this length to be a ply thickness. The other approach to predicting delamination is a fracture mechanics approach. This approach treats the delamination as a crack

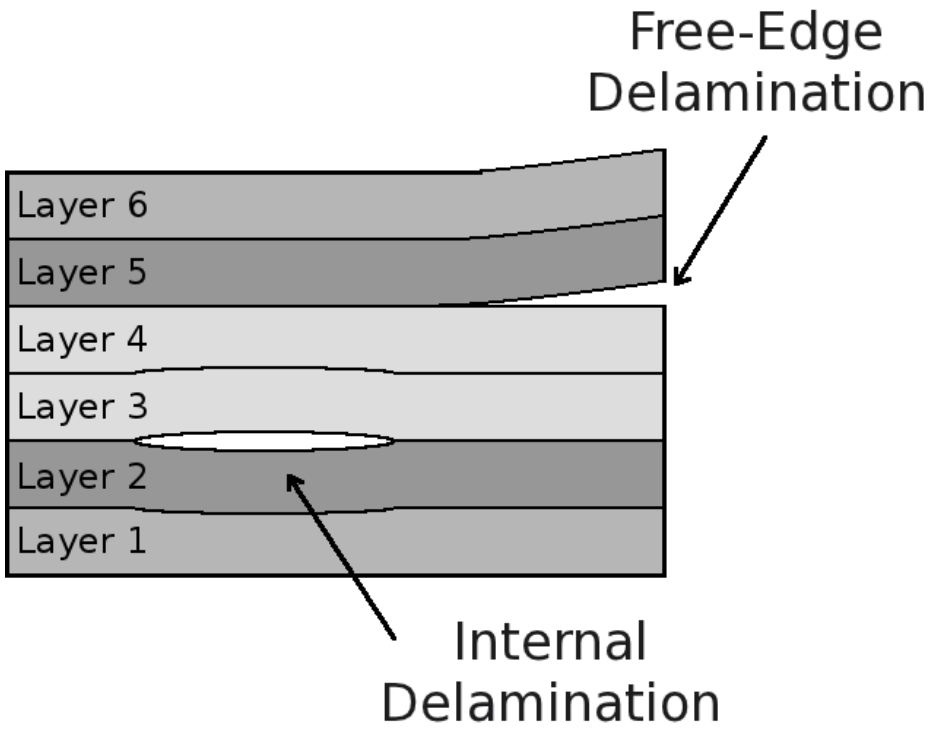

Figure 2.7 Illustration of a free-edge delamination and an internal delamination in a composite laminate.

propagating between two layers. The approach typically defines a critical strain energy release rate to determine crack propagation [6, 56, 63, 64]. Limitations of this method include the necessity of defining a crack initiation point and a propagation path before the analysis.

Much work has also been done experimentally to reach a better understanding of the delamination process in composites [e.g., 30, 56, 57, 59, 64]. Many of the studies revealed the thickness of laminates, in particular the relative thickness of plies, to be an important parameter. Pagano and Pipes [4] found the stress required for the onset of delamination to be dependent on the composite material, and that the developed stress fields were dependent on the laminate thickness and stacking sequence. O'Brien [55] studied the effect of the stress-free edge on the growth of internal delamination and found the thickness of the laminate to control whether edge delamination or internal delamination initiated. Studies were also conducted on the effect of ply thicknesses on delamination in $[\pm 25/90_n]_S$ laminates [30]. It was found that edge delaminations formed at the $-25/90$ interfaces when n was less than or equal to 3. However, when n was greater than 3, internal delaminations formed in the 90° plies. The papers on delamination all found the ply thickness to be a critical parameter in the stress fields affecting the delamination process. Others also investigated the effect of interlaminar stresses on delamination. As previously mentioned, Pagano and Pipes [4] found the stacking sequence of a laminate to affect delamination initiation. They found that the angle between neighboring plies affects the interlaminar stresses. Other work applied a quadratic delamination criterion to experimental tests and showed the interlaminar stresses and an averaging dimension (defined for each laminate) to be directly proportional to the effective ply thickness [58]. From this criterion, the interlaminar strength parameters were found to be material constants, but their averaging dimension had to be determined experimentally. In further work, delamination was able to be suppressed by altering the interlaminar stresses in a laminate with the addition of interlayers [65]. These interlayers were found to delay delamination initiation by providing a reduction of interlaminar stresses.

2.2 Mode Interaction

A knowledge of the basic damage modes, as discussed in Section 2.1, is necessary to understand damage and failure of composites. However, in actual test specimens and structures, the damage process usually involves more than one active damage mode. Each damage type present affects the stress distribution in the composite and therefore causes interactions (even if indirect) between the modes. An example of a commonly observed interaction is between matrix cracks and delaminations. Flaggs and Kural [2] observed this interaction, noting that matrix cracking was present in all their tested T300/934 composite specimens (with various stacking sequences) before interlaminar delamination occurred. While a large fraction of research has historically focused on understanding of the individual damage modes, it is essential to also understand how the modes interact.

Studies investigating mode interactions are relatively limited. Of these, the interaction of matrix cracking and delaminations has received the most focus. Some studies have shown the modes to interact in ways to resist further damage. For example, experiments found matrix microcracks to interact with delaminations resulting in a resistance behavior to delamination growth [66]. In other experiments, matrix cracking was observed in all test specimens that exhibited ply delamination [59, 67], suggesting a strong interaction between the two modes. Another observed interaction between matrix cracks and delaminations, termed "delamination shifting," was where a delamination growing along one interface comes to a transverse matrix crack and the delamination face switches to a new interface [6]. This interaction requires both modes to be present in order to occur. For the case of a $[0_2/\pm\theta_2]_S$ graphite/epoxy laminate under tension-tension fatigue loading, matrix cracking in the $-\theta$ plies always preceded the onset of internal delamination at the $\theta/-\theta$ interface [63]. The presence of matrix cracks was found to alter the stress state at the free edges which effect the initiation of edge delaminations [67]. Studies on the interactions between other modes are even more limited. One such study observed matrix cracking in the wake of interfacial debonding, and proposed that the interaction between modes determines the direction of damage propagation [68].

The influence of interlaminar effects on damage modes also contributes to mode interaction. These interlaminar effects include stacking sequence, ply thicknesses, holes and details of components, free edges, ply drops, and fiber bridging. Pagano and Pipes [4] were among the first to investigate the influence of the stacking sequence on the strength of laminates. They and others demonstrated that interlaminar stresses (responsible for delamination) could be controlled by changing the stacking sequence of a composite [4, 69]. The stacking sequence has also been found to change the mode of failure within laminates [70, 71]. For example, the stacking sequence of laminates influences the mechanisms (i.e., stress fields) controlling damage, which determines the damage mode(s) that initiate, and in some cases, the path that the mode grows [e.g., 21].

An interlaminar effect that has received much attention in the literature is the effect of specimen size on material characterization and damage. Changing the in-plane (width and length) and out-of-plane (thickness) dimensions results in a change of specimen strength and in some cases a change in failure mode [72–74]. Similar work has investigated the effects of scaling specimens. Scaling composites in the thickness direction presented challenges since composites are a layered material. To increase the through-thickness dimension of specimens, two methods are common: ply-level scaling and sublaminate-level scaling [75]. Ply-level scaling increases the thickness of each ply for a given stacking sequence, while sublaminate-level scaling repeats stacking of a basic sublaminate to form thicker laminates. The strength and toughness of angle-ply laminates increases significantly when using a sublaminate-level scaling compared to using the ply-level method [74]. This increase in strength and toughness is related to the effect of the ply thickness on interlaminar stresses. These observations are due to the influence of ply orientations (and location through the thickness) on the interlaminar stress in the laminate. The effect of grouping plies of the same angle (the ply-level method) can be viewed as equivalent to having an "effective" single ply with a thickness equal to the combined thicknesses of the combined plies [76]. Testing of scaled rectangular specimens in flexure found that cross-ply laminates exhibited a transition in failure mode with specimen size [77].

The smaller scaled specimens were observed to fail by fiber fracture while the larger scaled specimens failed by delamination. These works show that lengthscales do not simply scale with geometric lengths and that an interaction between the loading (and hence the present fields of stress and strain) and the mechanisms controlling the initiation of damage modes changes as the specimen size changes. An example of this phenomenon is the strength of a laminate. Some researchers claim that the strength is influenced by the material volume without considering the individual dimensions [78]. However, other research has shown that the in-plane dimensions (width and length) have little effect on the strength of a laminate and that the out-of-plane dimension (thickness) and location of plies through the thickness are the items that are directly (generally through the effect on interlaminar stresses) related to the strength of a laminate [73, 76, 79].

Fiber bridging is another interlaminar effect observed in composites. It occurs when a delamination runs through a ply, resulting in fibers bridging the two surfaces created by the delamination [66]. This damage exposes multiple lengthscales that must be considered, such as the length of the bridging fiber, the fiber diameter, and the distance of the delamination opening at the bridge. Fiber bridging causes artificially high values of the measured strain energy release rate, G [80], when using fracture mechanics to describe delamination. Therefore, this bridging effect must be considered when developing and using damage models in order to accurately capture the composite behavior.

Another interlaminar interaction observed experimentally is referred to as "stitch cracking." Stitch cracks are a form of high density matrix microcracks that develop in layers above or below a traditional matrix crack. Some of the earliest researchers to observe this mode were Jamison et al. [81]. The breakthrough for discovering these small matrix cracks was due to the development of a higher resolution X-ray technique. Before the high resolution technique, these cracks were not resolved in X-ray images. However, Jamison et al. only noted the observation of small matrix cracks crossing over larger matrix cracks and did not investigate them any further. Further study did not occur until Lavoie and Adolfsson [82] observed these small

cracks while investigating matrix cracking using computed microtomography (CμT). Their work utilized the newly available CμT nondestructive evaluation technique to investigate damage of composites in three dimensions. They recognized that small cracks were forming in the neighboring layers around traditional matrix cracks, and observed that these cracks appeared to be 'stitching' the traditional matrix crack and thus referred to this phenomenon as "stitch cracks." An image from this work showing stitch cracks is shown in Figure 2.8. These stitch cracks formed within the -45° plies, aligned with the fiber direction, and repeated along the path of the major (traditional) matrix cracks in the 90° plies. It was found that the difference in angle between neighboring plies determined whether stitch cracking or delamination initiated from these traditional matrix cracks.

2.3 Design Approach

The general intent of studies on composite failure is to gain the knowledge necessary to design safe composite structures. The current approach to designing safe (i.e., avoiding damage or maintaining damage tolerance) composite structures is the building block approach (BBA). This approach was first demonstrated by Whitehead and Deo [11] when they discussed the necessity of an approach for certification of composite structures in aircraft. The building block approach defines experimental tests along the levels leading up to the final, full-scale component. As part of this process, the need for verification tests starting at lower levels (i.e., coupons) and leading up to a full-scale test is emphasized. The verification tests at lower levels allow designers to reach an understanding of the behavior of structural features individually. Reaching the same understanding through full-scale testing is cost prohibitive due to the number of tests required and the expenses in producing and instrumenting the full-scale, more complex components [83].

The building block methodology has become the accepted approach for certifying composite structures [10, 84, 85]. It has been proven to produce successful and safe structures [8, 84]. As described in Composite Materials Handbook 17 [10], the method

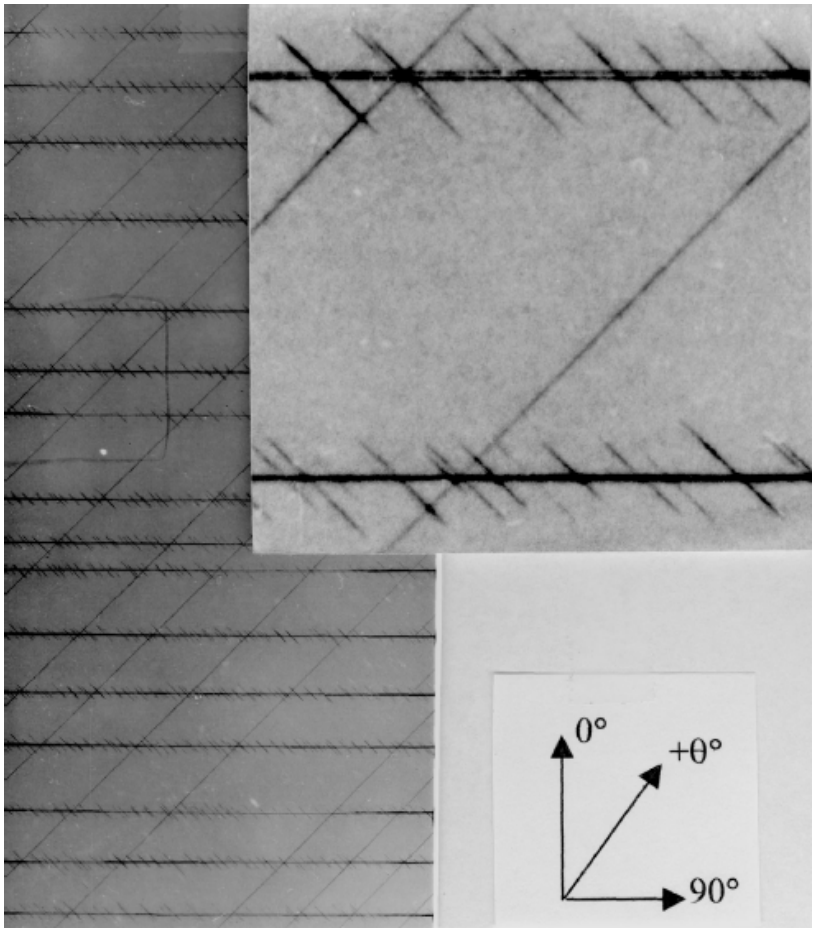

Figure 2.8 X-radiograph illustrating stitch cracks (along the $-45°$ direction) formed along major (traditional) matrix cracks (along the $90°$ direction) in a $[+45_4/-45_4/90_8]_S$ laminate [82]. (Note: Scale of image and enlarged image (upper right) not included in [82])

provides a systematic way of treating composite materials to obtain material "allowables." These allowables are determined through extensive experimental testing at the basic coupon level. The allowables are then utilized at higher structural levels by incorporating "knockdown" factors to account for changes in material response. The building block approach splits the levels into three main groups [10], as shown in Figure 2.9, with each group building off the lower one.

The base group of the BBA, group A shown in Figure 2.9, begins with collecting material data on candidate materials and making a decision on which material(s) will be selected for a given project. Numerous experimental tests are conducted on coupons to gather statistically significant material data for the selected material(s). The next higher level in this group assumes the preliminary material and processing data have been collected. The objective of this level is to study the effects of process variables on the material behavior. The third level in this group establishes "firm" material allowables to be used in the design of composite structures using such a material [10, 85]. These allowables take into account environmental effects (e.g., hygrothermal), lamination effects (e.g., ply orientations, stacking sequence, laminate thickness), and effects of defects and variability during manufacturing. Once the testing of group A is completed, details of the material system are fully established. These details are then passed upward to the next group of testing.

The second group of the BBA, group B, begins introducing structural details that are often specific to the project. The first level of this group tests structural details that are found within the structure being designed (e.g., joints, bolt or rivet holes, stiffeners). The data collected from these tests are frequently used to support analytical techniques. Testing at this level becomes more time consuming and costly than the base level because of the increased complexity of the specimen (compared to the coupon specimens). Therefore, fewer and fewer tests are run at the higher levels (a trend throughout the entire BBA) [10, 85]. In the second level of group B, data on subcomponents is collected. The subcomponents combine multiple structural details into one specimen to permit assessment of load redistribution due to local damage.

The final group of the BBA, group C, is the final stage of testing. At this point, the

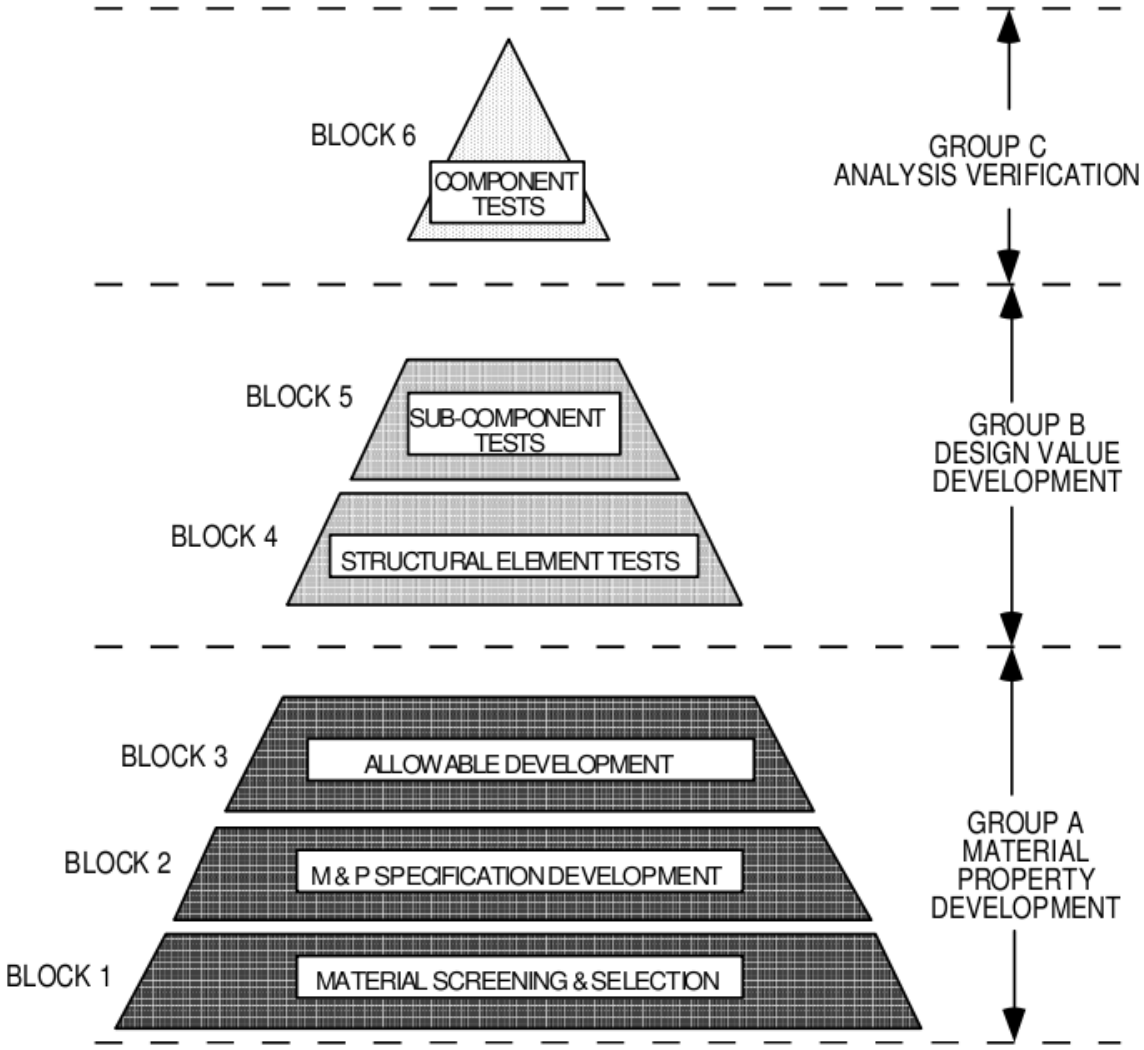

Figure 2.9 The levels of composite design as defined in the Building Block Approach [10].

material specifics are well-established and damage resulting from structural details has been well studied. The final test required by the BBA is a single test of the designed component [10]. This one test is used to verify model predictions, such as strains and deflections, and is the final stage in the certification process.

While the building block approach has provided a methodology for certifying safe composite structures, the approach has limitations and does not allow full utilization of the advantages and efficiencies offered by composites. After material allowables are determined at a lower level, they are passed to higher levels by using knockdown factors. These knockdown factors decrease the material allowables to account for changes, often unknown, in material response (i.e., strength and/or stress field variabilities) as more structural complexities are included. However, to establish valid knockdown factors, the damage type present in the lower level test is required to remain the same throughout higher level testing. As an example, if a stiffener buckles at the sub-component level but buckling was not observed at the element level, additional testing would need to be done at the element level to determine the buckling behavior of the stiffener. Any variation in the damage type (e.g., an additional damage mode, not present in the lower level test, initiating during the higher level test) or interaction of damage types nullifies the establishment of a valid knockdown factor. This is a considerable limitation of the building block approach, resulting in a virtually one-way process relying heavily on empirical and semi-empirical approaches. Any new observations made at higher levels indicating the necessity of changes at lower levels result in restarting the process from a previous level, or in some cases restarting from the beginning. Otherwise, the designer proceeds with a sub-efficient design [8].

The other key limitation to the building block approach is its inability to allow researchers and designers to investigate lengthscale effects. Without knowledge of how damage mechanisms change across levels, the design process is very inefficient. Preliminary designs of structures are made without knowledge of how damage will affect the performance/strength of the structure. Testing then must be done, following the BBA, to decide if the preliminarily designed structure will meet performance

criteria. If the preliminary design does not meet the criteria, a redesign is necessary and testing must be repeated from the early stages of the BBA. Even if the preliminary design meets the performance criteria set for the component, there is no guarantee that the most efficient design has been reached, only that the design is adequate. This is due to the underlying methodology of the BBA which produces components designed not to fail. However, the BBA provides no insight into when failure occurs. Designing not to fail is acceptable in some applications, but others, such as designing automotive crumple zones, require a precise knowledge of failure initiation. Spearing, Lagacé, and McManus [8] identify these drawbacks and offer a more efficient philosophy for the process that makes greater use of mechanism-based models in the certification process. Using such models allows the mechanisms controlling damage, as well as how these mechanisms change across lengthscales, to be better understood. This enhanced understanding allows a two-way design process to be achieved, permitting information gathered at each level to be shared across levels, resulting in a more efficient design process. However, this process relies on an ability to predict the effects of damage on the structure.

2.4 Prediction of Damage and Failure

In order to use composites to their full potential as structural materials, it is important to have the capability to predict the conditions under which the composites fail. Failure criteria use models, often with implicitly associated lengthscales and occasionally with explicitly associated lengthscales, to attempt to capture the behavior of composites. Many of the models were developed before the importance of lengthscale effects were recognized. Therefore, these lengthscale effects were not explicitly worked into these models. The ultimate goal of these criteria is to accurately predict when damage/failure will occur. The numerous criteria proposed can be grouped into two general categories: non-mechanistic and mechanistic. The non-mechanistic-based criteria predict failure in a general sense (without predicting the damage mode(s) responsible for failure) while the mechanistic-based criteria predict

the particular damage mode(s) causing damage/failure. The development of failure criteria has been the focus of many researchers around the world [86, 87].

In the 1990's, concerns about the general problems faced when designing with composites led to an 'experts meeting' held in the United Kingdom [86]. Composites experts from around the world were invited to discuss failure and failure criteria. There were two outcomes from the meeting: one, there was no universal definition of 'failure' in composites, and two, there was a lack of confidence in the universal applicability of the failure criteria [86]. From these results and the discussions at this meeting, two researchers, Hinton and Soden, began organizing the World-Wide Failure Exercise.

The World-Wide Failure Exercise (WWFE) was developed to 'test' current failure criteria through a series of round robin studies. The exercise began in 1998 and was concluded in 2004. The goals of the exercise were to provide an unbiased comparison between the various criteria, to offer a summary of the strengths and shortcomings of each criterion, and to establish the current level of maturity of composite failure prediction. Originally, eleven groups decided to participate, with other groups later joining the exercise [86, 88]. The exercise was broken into two parts. The first part required participants to predict failure for a series of test cases from data made available to all participants. The participants were provided with the test geometry, laminate arrangements, laminate material properties, and loadings. However, the participants were kept 'blind' by not being provided with the experimental failure data during the first part of the exercise. The 'blind' failure predictions were collected from the participants by the organizers and compared for each of the test cases (14 in total). The second part of the exercise provided the participants with the detailed experimental procedures and failure results from the test cases. The participants were then asked to compare their original predictions to these results and discuss any refinements made to their predictions after receiving the failure data. The organizers again collected papers from the participants and compared the refined theories [86].

The results from the WWFE showed that the current predictive criteria were unable to fully capture failure in composites [89]. Criteria could typically predict

failure for certain load cases (e.g., a specific in-plane biaxial load) reasonably well, but would break down for other loadings (e.g., changing the regime of biaxial loading). The WWFE also showed that many of the criteria are empirically dominated. Empirically based criteria rely on experimental data collected from laminates to set failure envelops. However, these criteria are unable to adjust for changes in laminates (such as simply changing the order of the layup) without requiring additional experimental data to be collected. Failure predictions were made via the criteria involved in the WWFE given the supplied data for the six laminate layups tested, but a few of the criteria were designed for unique laminates and had limitations allowing them to make predictions only for a subset of the tests. A detailed summary with comparisons between the performance and capabilities of the criteria from the WWFE is found in several publications [7, 90, 91].

While literature has traditionally classified failure criteria (such as those to participate in the WWFE) as either based on strength of materials or based on fracture mechanics, it is more useful to understand the lengthscales involved in failure criteria by classifying the criteria as mechanistic-based or non-mechanistic-based. Mechanistic-based methods have the advantage that they allow researchers to gain knowledge of the parameters influencing damage and failure in composites. The mechanistic-based methods [e.g., 92] help identify critical lengthscales, and allow the effects of changing laminate properties (e.g., fiber and matrix constituents, laminate layups) to be observed without the need for extensive testing. However, non-mechanistic methods [e.g., 93–96] are based on empirical fitting, and do not offer insight on the lengthscales involved in the damage/failure process. In the following subsections, some of the current non-mechanistic and mechanistic criteria are presented and discussed.

2.4.1 Non-Mechanistic-Based Methods

The majority of failure criteria, to date, are non-mechanistic and rely on empirical data to predict the conditions for failure of composites at the constituent and ply levels. The simplest, and some of the first, criteria offered to predict failure in

composites are the maximum-stress and maximum-strain criteria. These criteria descended from metallic failure criteria, with the basic idea that there exists a critical level of stress, or strain, that once exceeded, will cause failure in the material. One of the earliest researchers to apply a maximum-strain criterion to composites was Waddoups [97–100]. The maximum-strain criterion considers in-plane strains and is a non-interactive model, requiring five empirically-determined critical values to predict failure. The critical values necessary for the criterion are the maximum strains for a ply. These include the tensile and compressive values along the fiber direction, the tensile and compressive values along the transverse direction, and the shear value. The damage type occurring in the composite is usually inferred by the critical value exceeded. For example, when the critical value along the fiber direction is exceeded, fiber fracture (for tension) or microbuckling (for compression) is assumed. However, the model does not explicitly give the failure mode. Bogetti developed a variation of the maximum-strain criterion which allows nonlinear shear behavior and includes a simple progressive failure method [93, 101]. As with the maximum-strain criterion, the maximum-stress criterion considers only in-plane stresses and is a non-interactive model, requiring five empirically-determined strength values. One of the earliest researchers to apply a maximum-stress criterion to composites was Jenkins [99, 102]. For the maximum-stress criterion, the strength values determined are critical stress values. Zinoviev developed a maximum-stress criterion which assumes linear-elastic material behavior up to initial failure and includes continuous correction factors for the effects of the change in fiber orientation [94, 103]. Bogetti and Zinoviev both submitted their criteria to the World-Wide Failure Exercise (WWFE) and were ranked highly (performed well) compared to the other participating criteria. The implicit lengthscale associated with the maximum-strain and maximum-stress based criteria is on the order of a ply thickness. This is due to the method used in calculating the ply-level strains or stresses. This is traditionally done by using the classical laminated plate theory (CLPT).

The Tsai-Wu [95] criterion is another criterion involved in the WWFE and also ranked highly. In its general form, the criterion includes terms representing a full

three-dimensional state of stress as well as stress interaction terms, resulting in a quadratic failure surface for anisotropic materials. When applied to orthotropic materials, material symmetries reduce the criterion to be dependent on a two-dimensional state of stress (including interaction terms). The criterion requires empirically-determined material strengths to define critical tensile, compressive, and shear stresses. To determine the interaction terms, combined stress testing (such as biaxial stresses in appropriate planes) is required. While the Tsai-Wu criterion does define different strengths for tensile and compressive loading, it does not differentiate between matrix-controlled and fiber-controlled damage/failure. As with the maximum-stress and maximum-strain criteria, ply level stresses are determined via CLPT, and, therefore, the implicit lengthscale associated with the Tsai-Wu criterion is on the order of a ply thickness.

The criterion developed by Puck and Schürmann uses a phenomenological model which incorporates nonlinearities due to microdamage, matrix cracking, and changes in fiber angle [96, 104]. The criterion uses two fracture criteria to differentiate between two damage modes: fiber fracture and matrix cracking. The model also identifies uncertainty in damage/failure prediction when different laminates are analyzed by considering stress concentration factors and the effects of stiff neighboring plies on cracks. In their work, Puck and Schürmann used CLPT to determine strains and stresses in each layer, and, as with the previously discussed criteria, the implicitly associated lengthscale is the ply thickness. However, unlike the Tsai-Wu criterion, Puck and Schürmann's criterion also have some explicitly associated lengthscales included in their phenomenological model, such as the change in fiber angle within a ply. Puck and Schürmann's criterion and the Cuntze criterion (discussed in Section 2.4.2) were the top two ranking criteria to participate in the WWFE [91], although even these criteria only marginally handled all the cases tested in the WWFE. For example, the envelops predicted by Puck and Schürmann's criterion captured the shape of the experimental envelops in 3 of the 14 test cases [7]. In the other cases, there were either slight or major variations.

2.4.2 Mechanistic-Based Methods

Very few failure criteria are based on mechanistic principles. The advantage to mechanistic-based methods is that they use physical parameters to model the failure process, allowing the mechanisms involved in damage to be better understood. Thus, mechanistic-based methods offer true (i.e., capturing the actual physical damage process) predictive capabilities. While a purely mechanistic-based method would be desirable, composites are too complex with many parameters that at best can be modeled by probabilistic distributions. However, the move away from criteria that rely on empirical curve-fitting allows researchers to better understand the mechanisms critical to the damage process. Mechanistic-based methods also require fewer experimental tests to obtain necessary variables for failure criteria and will therefore save time and money.

One of the earliest researchers to develop a mechanistic-based criterion for composites was Chamis [92]. His criterion is semi-empirical, using constitutive properties to predict uniaxial strengths of laminae. The model used to predict these strengths considers many parameters of the composite: volume fractions, fiber size and distribution, and elastic and strength properties of the fiber and matrix. Chamis realized that not every variable affecting the properties of composites could be accounted for directly, so he introduced "theory-experimental correlation factors." These factors indirectly account for variables introduced during the fabrication process (e.g., void size, void distribution, fiber misalignment, interfacial bond strength, residual stresses) into the criterion. Chamis used the constitutive properties and the correlation factors to create governing equations for the strengths of the laminate. These strengths are used to define a combined-stress strength criterion based on a distortion energy principle [92]. Because the Chamis criterion uses a mechanistic approach, there are multiple associated lengthscales: e.g., fiber diameter, fiber spacing, and the ply thickness. Chamis [105, 106] participated in the WWFE, with his criterion performing adequately compared to the other participating theories. As noted by Hinton et al. [7], when comparing the performance of the participating theories, Chamis' criterion

typically produced a failure envelop that was slightly conservative (under predicting strength) for most test cases, but his theory had a few significant and fundamental weaknesses, such as a lack of robustness and maturity in the approach taken for post-initial failure modeling.

The criterion developed by Cuntze is another mechanistic-based criterion [107]. It uses nonlinear analysis to predict progressive failure. The criterion considers in-ply failure mechanisms in terms of three-dimensional stresses and includes interactions between failure modes due to probabilistic effects. The main idea of the criterion by Cuntze is the formation of five independent damage models: two for fiber failure and three for matrix failure. These include the fiber fracture, fiber microbuckling, and matrix cracking modes as discussed in Section 2.1. Delamination and interfacial debonding are not modeled in this criterion. For each of the five damage modes considered, a single strength and modulus are used to characterize the damage mode [107]. Unlike the criterion of Chamis, that of Cuntze relies more heavily on empirical data. However, that latter criterion investigates the mechanisms of damage in greater detail and also includes parameters for mode interaction [108]. The lengthscales associated with the criterion include the ply thickness, the void or nucleation size responsible for the initiation of microcracks, and the fiber diameter. The criterion of Cuntze was in the top two criteria ranked that participated in the WWFE [91].

2.5 Lengthscales in Composites

Many lengthscales associated with composite materials can be identified throughout the literature, although very few authors actually refer directly to the lengthscales in their manuscripts. One of the earliest papers addressing the role of lengthscales in composites was published in 1998 by Spearing, Lagacé, and McManus [8]. Relatively few papers directly addressing lengthscales in composites have since appeared. However, consideration of the many previous works on composite damage reveals investigations of the damage modes and mechanisms controlling damage at specific lengthscales. For example, the investigations on fiber fracture find the critical length-

scale of that damage mode to be a fiber diameter. While one can look through the literature on composite damage and extract information associated with lengthscales for each of the damage modes, no specific studies investigating the lengthscale effects have been found. Although the community has observed changes in damage characteristics as the scale of testing changes, there has been no explicit recognition or call out of these changes as lengthscale effects. To capture these changes in the composite structure certification process, the community developed multiple levels of testing. Before addressing lengthscale effects explicitly, it is therefore important to understand the levels commonly used for testing composites and how these are tied to manufacturing and assembly of such structures.

The current levels identified in the literature and used in design are the sub-ply, ply, laminate, sub-element, element, sub-component, and component [8, 10, 11]. Examples of these levels used in composite engineering are shown in Figure 2.10. Beginning at the sub-ply level, the mechanical properties of the composite constituents (matrix and fiber) are individually determined. Moving up a level to the ply level, the constituents are combined into a composite ply. Simple loading cases are typically tested to determine the properties of this ply [10]. Varying the constituents (from the sub-ply level) results in changed properties at the ply level. Proceeding to the next level, plies are stacked at various angles to form laminates. These laminates are produced by stacking plies and/or fabric layers to form unidirectional, cross-ply, angle-ply, quasi-isotropic, or other laminates. The laminate level is traditionally where most coupon testing is conducted [10, 11, 84, 85]. At the next level, that of the sub-element, structural details (e.g., holes, ply-drops, stiffeners) begin to be included. At the sub-element level and higher, structural features and configurations introduce lengthscale effects different from the material effects that dominate the lower levels. Sub-elements and laminates are combined at the element level to comprise structural details (e.g., sandwich structures, stiffened panels) that are repeated within the structure [10]. The sub-component level is again more complex than the lower element level, typically being sections of the full component, such as a wing box. The final level is the designed component. An example could be a composite wing formed of

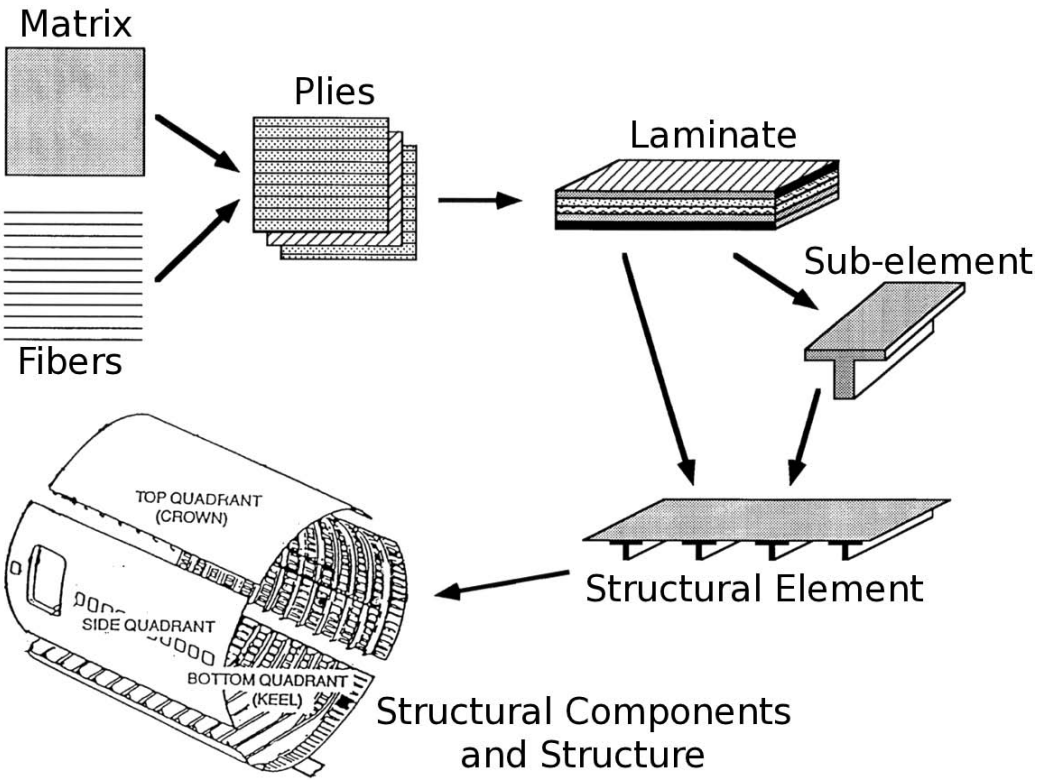

Figure 2.10 Examples of possible levels in composite structural engineering.

various laminates, stiffeners, holes, and other structural details that are all of smaller lengthscales.

As discussed in Section 2.3, these levels are utilized throughout the Building Block Approach. The lower levels (i.e., sub-ply, ply, and laminate) are based on convenient test sample sizes, related to testing procedures, while the higher levels (i.e., sub-element, element, sub-component, and component) are based on manufacturing and assembly techniques and issues. These specific levels are therefore not based on particular damage behavior observed, but rather on convenient lengths associated with manufacturing and production aspects. In the Building Block Approach, each level builds upon the previous lower level, with structural complexity increasing across the levels.

2.5.1 Lengthscales of the Basic Composite Damage Modes

Lengthscales associated with each of the basic composite damage modes (those discussed in Section 2.1) have been collected from the literature. These lengthscales have been identified by previous researchers as influencing the individual damage modes (although very few authors actually refer directly to the lengthscales). These are summarized herein.

The lengthscales found in the literature associated with fiber fracture are the fiber length, fiber diameter, and inter-fiber spacing [5, 13, 15, 17, 18, 20]. From the analytical and experimental studies in the literature, the key parameter identified for fiber fracture is the fiber diameter. This lengthscale has been shown to affect the fiber strength and the probability of flaws being present in the fiber. Therefore, the fiber diameter is the critical lengthscale for the fiber fracture damage mode.

The lengthscales associated with matrix cracking include the void or nucleation size responsible for the initiation of microcracks, the ply thickness, the spacing between cracks, and the length of the matrix crack [2, 6, 24–26, 30, 109]. It is also noted that the angle between plies plays an important role. However, there is no "length" defined to measure the angle between plies. Therefore a length associated with this measure needs to be defined. From the literature, a single critical lengthscale for the

matrix cracking damage mode has not been identified. Rather, multiple lengthscales contribute to the behavior of matrix cracking.

The lengthscales associated with microbuckling include the fiber diameter, buckling wavelength, and fiber misalignment [3, 13, 19, 31–37, 39–42]. The elastic and plastic microbuckling each have their own critical lengthscales since the mechanisms controlling each mode change. For elastic microbuckling, the critical lengthscales are on the order of a fiber diameter or smaller [3]. For plastic microbuckling, the critical lengthscales are on the order of 10-20 fiber diameters [19, 31, 33, 35, 36, 42].

The lengthscales associated with interfacial debonding include the fiber diameter, the bonded fiber length, and the sizing thickness [24, 43–49, 51–53]. Other factors, such as the stress state acting at the interface of the fiber and matrix, affect the mechanisms controlling interfacial debonding. The lengthscales associated with these factors have not been identified in the literature. The critical lengthscale for interfacial debonding, identified in the experimental and analytical studies, is on the order of tens of fiber diameters.

The lengthscales associated with delamination include the ply thickness, the length of the delamination crack, the interply region thickness, and the characteristic length of the interlaminar stress-field [4, 6, 30, 55–65]. The characteristic length has two typical definitions in models of delamination. The first defines the length as the distance over which the stress must exceed the strength of the material. The second defines the length as the distance away from a stress-concentrator that the stress has to exceed a critical value before delamination will initiate. As with matrix cracking, the angle between plies also plays an important role in delamination and a length associated with this measure needs to be defined. The literature has identified the laminate thickness as a critical lengthscale for delamination. The thickness of the laminate was found analytically to dominate the effects of interlaminar stresses and was found experimentally to determine the type of delamination to initiate. The literature also identifies the effect of the stacking sequence on the associated lengthscales.

A summary of the lengthscales associated with each of the basic damage/failure modes is shown in Table 2.1. These lengthscales were collected over the course of

Table 2.1 Lengthscales associated with the basic damage modes

Damage Mode	**Associated Lengthscales**
Fiber Fracture	Fiber diameter, fiber length, inter-fiber spacing
Matrix Cracking	Void/Nucleation size, ply thickness, angle between plies*, crack length, crack spacing
Microbuckling	Fiber diameter, buckling wavelength, fiber misalignment
Interfacial Debonding	Fiber diameter, bonded fiber length, sizing thickness
Delamination	Ply thickness, crack length, angle between plies*, interply region thickness, characteristic interfacial stress length

*A length measure associated with the angle between plies must be defined.

the literature review and have been identified by previous researchers as having influence on the individual damage modes. While these researchers may not have explicitly referred to these lengthscales, upon reexamination of their works, the associated lengthscales were identified. Other lengthscales may exist that influence the individual damage modes, but they were not identifiable from the previous works.

2.5.2 Other Issues in Lengthscales

Beyond the lengthscales of the basic damage modes, other issues in lengthscales were identified during the literature review. There was relatively little or no literature directly addressing these issues. However, from the collected literature, important considerations to be investigated were identified. The first issue was that of the observable lengthscale. In order to investigate and understand mechanisms driving damage, researchers must be able to observe the mechanisms to first realize their existence, and then to further study such. The second issue was that of choosing appropriate lengthscales to allow information to be passed across levels. Up to now, the choice of lengthscale for investigations, such as investigating a composite component using finite elements, has typically been driven by component size without consideration of the lengthscales associated with damage. However, after reviewing the literature, the need for a methodology to pass material properties across the levels of engineering while maintaining consideration of the lengthscales associated with mechanisms driving damage was identified.

An important consideration when investigating lengthscales in experimental studies of composite specimens and structures is the observable lengthscale of inspection techniques. In order to observe and study damage in composites, the damage must be resolvable via the inspection technique. An example is the observation of stitch cracks (described in Section 2.2), which had previously been undetected. Prior to the higher resolution X-ray technique, researchers had not been able to observe this damage type. Since composite inspection methods continue to improve, damage modes previously unknown are being (and may continue to be) identified. Bossi [110, 111] was one

of the first to apply computed tomography to composites in order to preform failure analysis. Since then, others have used the technique to investigate internal damage of composites. Schilling et al. [112] did further studies on stitch cracking as well as looking at the more general geometry of internal flaws and damage. Wright, Sinclair, and Spearing [113] have pushed the observable lengthscale even smaller using synchrotron X-ray tomography. The synchrotron X-ray tomography offers three-dimensional resolution down to a fraction of a fiber diameter. With an observable lengthscale down to that level, interactions occurring at levels smaller than a fiber diameter can be studied. As inspection techniques continue to improve, lengthscales not yet identified may be discovered. The new inspection techniques also allow the currently identified damage modes and mode interactions to be studied with greater resolution.

The other important issue identified over the course of the literature review was the ability to move information across levels. An important component of designing with and utilizing composites as structural materials is the capability to transfer material properties across the multiple levels used. As discussed in Section 2.3, the BBA is the currently used method for passing material allowables up through the levels of testing and design. However, the BBA has considerable limitations that result in partial utilization of the full potential of composites. Using a lengthscale approach will enable scientists and engineers to better their understanding of the mechanisms influencing damage and hence material properties as the structural lengthscales change.

Many studies in the literature on composites can be reanalyzed to show the importance in choice of the appropriate lengthscale(s) for damage modes to have a good understanding of lengthscale effects. Lengthscale effects can then be used to help researchers better understand how damage behavior changes as the level of testing changes, permitting a more efficient procedure for transferring material properties across the many levels of testing. Lengthscales also permit a new approach to studying damage mode interactions, allowing investigation into how the critical lengthscale for an individual mode changes (if it does) as it interacts with other modes. A lengthscale approach also allows the interactions of stress-field gradients on damage modes to be investigated in a new way.

2.6 Summary

Identifying the lengthscales involved in composites is an important step to advancing the understanding of damage and failure of composites. A review of the literature has extracted many composite lengthscales from physical, experimental, and analytical studies. While the majority of studies did not specifically address lengthscales, through their investigations to understand composite behavior, associated lengthscales have been determined. Each basic composite damage mode is presented in Section 2.1 and mechanisms influencing these damage modes are identified. Interactions between damage modes are then discussed in Section 2.2, bringing up questions on how the lengthscales from the basic damage modes are affected or changed by interactions with other modes (and hence, other lengthscales). The review found little work (relative to the studies of basic damage modes) investigating interactions of modes, making it difficult to identify effects of interactions on lengthscales. The current failure criteria used to predict damage in composites are discussed in Section 2.4. While the majority of failure criteria are non-mechanistic, a few criteria exist based on mechanistic methods and incorporate lengthscales into the prediction models. The concept of lengthscales associated with composites is presented in Section 2.5. The lengthscales associated with the basic damage modes, mode interactions, design, and failure criteria are summarized in this section.

The next steps to reaching a better understanding of composite failure are to determine whether the existing lengthscales are sufficient to describe the governing mechanisms of damage/failure and to identify the critical lengthscale (or possibly lengthscales) controlling the damage process across the multiple scales of composite structures.

[THIS PAGE INTENTIONALLY LEFT BLANK]

Chapter 3

Objectives and Approach

The primary objective of this work is to investigate and identify lengthscale effects associated with damage in composite materials and their structures, and to determine how these lengthscales vary across levels of composites and can be used in assessing the overall response of composite structures. This is an advancement in a much larger pursuit towards developing a new methodology that utilizes composite failure and material data collected across all levels to predict the occurrence of damage and its effects at any operative level of composite structures. As discussed in Chapter 2, the current approach, the Building Block Approach (BBA), is a one-way process only capable of transferring data to higher levels. Data is transferred via the BBA by defining material "allowables" at one level, and then applying "knockdown factors" in order to pass the data to the next higher level. These knockdown factors are necessary to account for changes in material and structural response that the BBA does not capture at lower levels of the approach as well as to capture probabilistic issues. However, a process that maintains knowledge of the mechanisms controlling the material and failure response of a composite across levels would allow the knockdown factors to be replaced with factors based on physical mechanisms, thereby permitting a two-way transfer of data across the levels. Developing a new methodology using the lengthscale approach can enable researchers and designers to have a better understanding of the changes in damage mechanisms as the levels change, and to more fully realize the efficiencies offered by composites.

In this chapter, an approach to accomplish the primary objective is discussed in detail. The sub-objectives associated with this objective are articulated and an overview of the approach to address these items is given in the first section. The questions needing to be answered in order to accomplish the sub-objectives are segmented via a question tree in the next section. In the third section, the need for a procedure to document, characterize, and archive damage in composite specimens is discussed.

3.1 General Overview

In working towards accomplishing the primary objective, several sub-objectives were defined. These are:

1. To formulate an improved process to document and describe damage in composites;

2. To establish a framework for, and implement an initial base of, data to enable investigation of lengthscales effects; and

3. To further develop the idea of lengthscales associated with damage mechanisms and structural details, and to investigate how these lengthscales change and interact at different structural levels.

Efforts associated with these sub-objectives are meant to be key contributions from this work. In the case of a formulation of a procedure to better document and describe damage in composites, such would enable researchers to describe damage in a consistent manner, thereby allowing damage trends to be identified across multiple projects/sites. This is a capability that currently is not possible. In the case of establishing the framework for and then the initial implementation of a comparison database, such would allow composite damage trends to be investigated across specimens (of the same or different levels) in order to identify lengthscale effects. In the case of further developing the idea of lengthscales and investigating how these lengthscales change at different levels, such would provide researchers a new approach

for investigating damage mechanisms and how these mechanisms change across the many levels of composites, thereby allowing a better understanding of the factors influencing composite damage to be reached.

In the pursuit of this effort, the necessity of recognizing two damage regimes was identified. The first regime involves the initiation of damage along with the mechanisms and lengthscales associated with such. The second regime involves damage propagation and the interaction of damage modes along with the mechanisms and lengthscales associated with such. Lengthscales associated with individual damage modes are identified for both regimes, and lengthscales associated with the propagation of damage are identified for the second regime, thereby allowing investigation of how the critical lengthscale(s) controlling the damage mode(s) change(s) (if they do) across regimes. This concept of key lengthscales also allows investigation into the manner by which different damage modes interact, and ultimately a better understanding of the damage progression process from initiation to final failure. An approach, employing lengthscales, is developed to allow differences in the two regimes to be identified, and to accomplish the objectives of the work.

The first step in this approach involved conducting a detailed literature review. The findings from this review are included in Chapter 2. From the reviewed literature, questions that needed to be answered in order to accomplish the primary objective were formed, and placed into and worked within a "question tree." The primary objective of the work is broken down into root questions in the tree. The sub-objectives emerged from the compilation of the question tree branches. The tree contains two main branches, one focusing on the physical mechanisms of damage, and the other focusing on predictive capabilities. The overall question and these first two level branches of the question tree are shown in Figure 3.1. The branches continue to be split into lower levels until root questions are reached. Those details are discussed in the next section. Work to answer questions are pursued starting at the root level and then working upward until the primary objectives of the work can be accomplished.

Once the question tree was formed, some of the literature was re-evaluated to see which questions could be answered, in part or in full, based on partial contributions

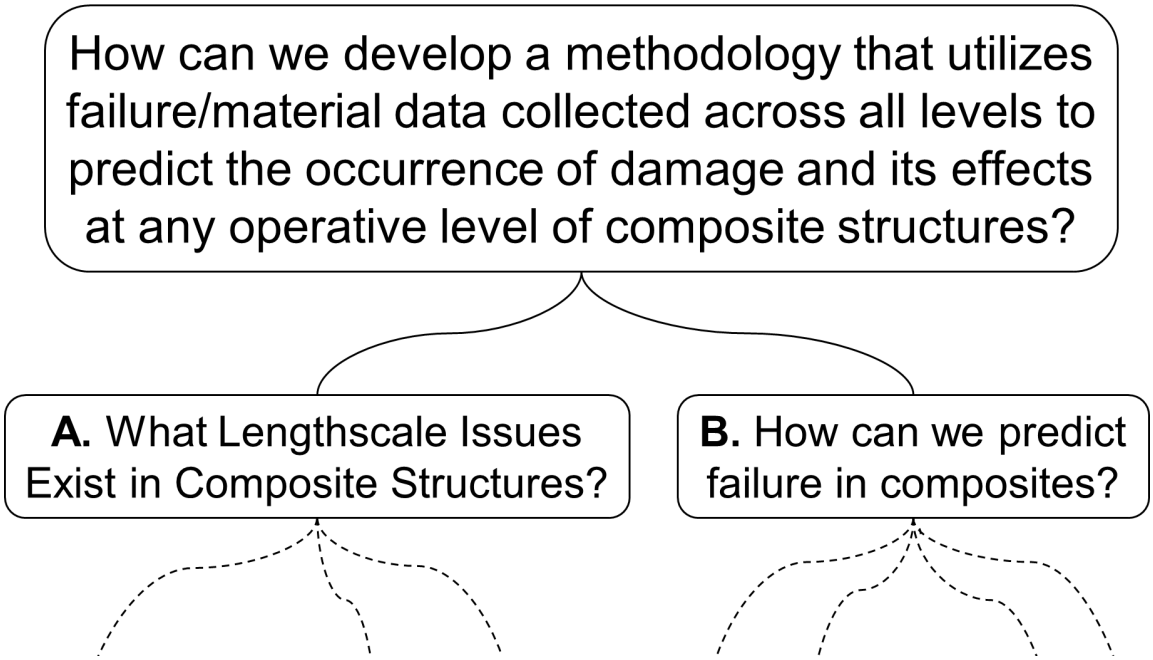

Figure 3.1 Primary question and two top-level splits of the Question Tree.

from existing works. The experimental testing conducted as part of an associated effort involving the U.S. Naval Research Laboratory (NRL) located in Washington D.C., U.S.A., and the Cooperative Research Centre for Advanced Composite Structures (CRC-ACS) located in Victoria, Australia, was designed in large part to help investigate questions remaining in the question tree that could not be answered from the literature review. These details are described in Chapter 4.

As part of this specific work, a documentation procedure is developed to investigate lengthscale effects present in experimental tests. This procedure aims to address a lack in the testing area of composites as identified during the literature review. It was obvious that each researcher generally used their own methods to describe damage, and that a commonly accepted methodology allowing direct comparison of damage didn't exist, even amongst specimens at the same testing level. In order to investigate changes in material response across the structural levels, a unifying procedure is needed. Such a procedure has the goal of documenting damage in specimens and providing both qualitative (enabling the active damage modes, damage paths, and mode interactions to be identified via damage sketches) and quantitative (enabling damage extent to be captured via damage grids) information, which can then be input into a "comparison database." The comparison database is to be unlike previous composites databases, which collected information primarily to establish material allowables, in that it is to enable investigation of lengthscale effects. The database is to push for trends in damage to be investigated by organizing the details on the material, geometry, and failure in a searchable and sortable database. The information to be included in this database is largely to be determined from answers to pieces of the question tree.

3.2 The Question Tree

As previously noted, the first step taken during this work was to investigate the background of topics related to the project and plan an approach to accomplish the objectives. The literature review that was conducted, as detailed in Chapter 2, was

used to pull together more recent and past literature dealing with the thesis topics. Using the information and knowledge determined from the literature review, a question tree was developed to help guide the process of accomplishing the primary thesis objective of investigating and identifying lengthscale effects associated with damage in composite materials and their structures, and determining how these lengthscales vary across the levels of composites. To aid in accomplishing the objective, the overall goal was broken into smaller, more manageable questions. This breakdown continued until "root" questions, those that had to first be answered before answering higher-level questions, were reached.

The high level, complex question dealing with the overarching pursuit of the development of a methodology that utilizes composite failure and material data collected across all levels to predict the occurrence of damage and its effects at any operative level of composite structures is broken down into two primary branches in the question tree. The lead question of Branch A asks "What lengthscale issues exist in composite structures?" Thus, the overall focus of Branch A deals with the manifestation of different damage mechanisms within a composite material, laminate, and structure, along with the lengthscales associated with such mechanisms. This branch is the main focus of this work. The lead question of Branch B asks "How can we predict failure in composites?" Thus, the overall focus of Branch B deals with the predictive capabilities to calculate stress states, to predict failure, and to assess overall structural behavior. This branch motivates the need for answers from Branch A in that a better understanding of the mechanisms controlling damage, and a knowledge of how these mechanisms change at the various levels of testing, is required before damage theories can incorporate further mechanistic models, thereby improving their predictive capabilities. Information has been acquired addressing the questions in Branch B, such as the strengths, weaknesses, and limitations of the existing theories. However, it is not the objective of this work to directly answer questions from Branch B.

From these two primary branches, further breakdowns are made into other sub-level branches. These overall breakdowns are captured in Appendix A. Answers

to such questions are needed in order to answer the questions at the higher levels. The entire A and B branches of the question tree are shown in Figures A.1 and A.2, with more detailed views of the sub-branches shown in Figures A.3-A.7 (all included in Appendix A). The questions in the tree that have been answered from the literature are indicated in the question tree as shaded branches, those questions that are partially answered are indicated with a hatched pattern, while the outstanding questions are left unshaded. Those questions answered from literature sources are discussed in this section, while answers coming out of this work are discussed in later chapters.

Lengthscales associated with the physical occurrences within a composite when damage initiates or grows is the focus of Branch A.1, shown in Figures A.3 and A.4. Due to the complex nature of composites and the structures of such, many different damage modes can occur. One of the first "root" questions reached deals with the need to establish two regimes of damage: initiation and growth. The question of "How do we differentiate between damage initiation and growth?" is posed in Branch A.1.1.2. As was found in the literature, the mechanisms driving damage initiation are often different from the mechanisms controlling damage propagation. The instigating factors, such as the stress field, can change upon damage initiation. For example, the initiation of delamination within a laminate causes loads to redistribute, and these redistributed loads may no longer provide the driving forces to propagate the delamination. Understanding how the critical lengthscale(s) change between the initiation and propagation regimes is necessary in order to develop a solid methodology and is investigated in this work.

In the other branch at this level, Branch A.1.1.1, the specifics of the individual damage modes are broken down. The literature review spanned from the specifics associated with studies of each damage mode in isolation, including studies at different testing levels, to interactions among damage modes. The review revealed that understandings of mode behavior under specific conditions and at specific levels can be reached, although typically using empirical methods. In some cases, these methods include implicit lengthscales. The review also revealed the need to identify the char-

acteristic lengthscale(s) of each mode, and showed that these are not well documented or understood, particularly as damage grows and mode interactions become present. Damage at the level of the ply to the laminate can be categorized into two areas: in-plane and out-of-plane. In-plane damage modes identified from the literature include fiber fracture, matrix cracking, fiber microbuckling, and interfacial debonding.

The out-of-plane damage mode is delamination and the interlaminar effects on the out-of-plane damage mode are specifically questioned. From the literature, interlaminar effects were identified including stacking sequence, ply thickness, structural details, free edges, and fiber bridging. The question dealing with the lengthscales at which these modes are observed or present is posed. This is the root question to Branches A.1.1.1.1 and A.1.1.1.2 that needs to be answered in order to begin answering questions at higher levels of the tree. An important consideration when investigating composite damage is to always keep in mind "unk-unks", or unknown unknowns. There is always a possibility that a previously unknown damage mode is discovered, and that it will be unknown how to address this mode. "Unk-unks" are not attached to the tree, but are included below the in-plane and out-of-plane damage modes, A.1.1.1.1 and A.1.1.1.2, as a reminder that unknown modes and issues may exist.

In addition to the damage and failure work considered, the implicit and explicit levels associated with testing of composites are addressed in Branch A.3 ("What lengthscales are currently identified in composites?"), shown in Figure A.5. The methodology of the Building Block Approach (BBA) was carefully reviewed and considered in order to better understand and characterize the current certification/validation procedure used in designing composite structures. As described in Section 2.3, the BBA provides the means to transfer information up structural levels in the overall design and certification process. Answers to Branch A.3 came primarily from consideration of the BBA, where the following levels are identified: sub-ply, ply, laminate, sub-element, element, sub-component, component, and structural detail. The levels implicitly introduced in this approach are linked to the particulars of manufacturing, assembly, testing techniques/issues, and structural details, as opposed to explicitly

defining levels based on the particulars of the damage lengthscales and their manifestations. The BBA method requires the identification and isolation of a specific damage mode, and the determination of material "allowables" associated with such. This allowable must be passed to the higher structural level(s) of testing, and only the isolated damage/failure modes accounted for at the lower levels of testing may be present in the higher level testing in order to successfully utilize the approach and the data. If other modes arise at a higher level, then considerations (e.g., redesign at that level) most be made to exclude these other modes, or the BBA process most be restarted with testing redesigned to include these other modes at the appropriate lower levels. The results between the two levels are compared to establish "knockdown factors" to use with the baseline data. These "knockdown factors" are used to establish statistical allowables that account for changes in material response introduced at higher structural levels including mechanisms controlling the damage that have changed in some way. The knockdown factor fails to identify what such mechanism(s) are and how changes have occurred.

The information gathered from the BBA, as well as other literature, establishes answers to the root questions of Branch A.3.1 where the question "How high/low should we investigate?" is posed. These answers are used in identifying experimental testing, including specimen geometries, loadings, as well as data to collect, that will allow investigation of lengthscales. The question of additional lengthscales, beyond those defined in the BBA, that may need to be identified and defined, are raised in Branch A.3.2. An answer to this root question is to come from this work. Answers to A.3.3 ("What are contributing factors at each level?") are of particular importance as this addresses the factors affecting composite damage and how these factors change across lengthscales. In particular, these factors are to be used when setting up the documentation procedures, described in Section 5.1, ensuring that all the contributing lengthscale factors effecting damage are documented so that key relations can be investigated. This work aims to provide answers to the remaining root questions of Branch A.3.

An important aspect of utilizing the full potential of composites as a structural

material is the ability to predict the conditions under which the structure will fail. Issues relating to predictive capabilities to calculate stress states, predict failure, and assess overall structural behavior are addressed in Branch B. The main purpose of this branch, as related to the current work, is in providing motivation to answering the questions from Branch A. The existing failure theories work to capture the response characteristics of composites. However, the majority of the failure theories are empirically dominated, most do not address damage type, and no one theory is able to fully capture all aspects contributing to failure in composites. These limitations serve as motivation to reach a better understanding of the damage process through the use of lengthscales, as such an understanding would enable improved predictive capabilities. The limitations were particularly shown in the World-Wide Failure Exercise [7, 86–91], discussed in Section 2.4.

In working this question tree, articles from the literature review addressing composite damage and failure theories played a key role. One of the focuses in reviewing the literature was on identifying lengthscale issues as encountered in previous works, as described in Section 2.5.1. While most previous works do not specifically identify lengthscale issues and effects, at times these lengthscales are implicitly included in the previous works and are often partially explored, allowing information to be garnered from what is reported. The questions that remain unanswered, after reviewing the literature, serve as a guide to fulfilling the objectives of this work. Answers needed to identify the importance of lengthscales in composite damage are provided by addressing these questions. The better categorization and documentation of damage in specimens is important in order to investigate the mechanisms influencing damage of composite materials.

3.3 Damage Documentation, Characterization, and Archiving

The formulation of procedures to document and characterize damage are critical in the investigation of lengthscale effects in composites. Due to the complex nature

of composites, the lengthscale effects may not be revealed without good procedures. Therefore, the development of documentation and characterization procedures is a key sub-objective of this work. These procedures are to be developed using the specific specimens (detailed in Chapter 4) investigated during this work, but are also intended, as developed, for application to more general composite damage testing.

The goal of the damage documentation procedures is to fill a void in the testing of composites by establish a unifying method for documenting and reporting damage in specimens. These procedures are to provide methods for comparing damage both qualitatively and quantitatively, and thereby allow lengthscale effects to be investigated across the levels of composite testing. The procedures are to allow damage mode interactions to be characterized, and lengthscales associated with such to be studied.

Factors influencing damage were determined during the literature review and are contained in the question tree. In order to completely investigate all factors that may be associated with lengthscale effects, it is important that the established procedures completely document these factors. For example, the effective ply thickness affects the damage developed in specimens. Therefore, it is important that this, and all other factors that may influence damage, be captured in the procedures. Once all the factors are documented and the damage characterized, the information from the procedures can be used in a comparison database, where researchers can investigate trends in damage across the many levels associated with composites.

A comparison database is established to allow investigation of lengthscale effects in composites across multiple specimen types (e.g., different geometries, different laminates, different loadings) and across the operative levels of composites. The database is to contain all the information gathered from the damage documentation procedures (damage extent, damage paths, damage modes, etc.) as well as specifics on the specimens (fiber and epoxy type, laminate layups, geometry, loading history, etc.). By organizing all this information into a sortable and searchable database, comparisons can be made to find trends and expose differences in damage as the level of testing is changed. For example, a researcher may be interested in the change in

damage extent caused by varying only the size of a structural feature (e.g., a hole). By establishing a comparison database, one can be enabled to fix particular parameters (e.g., material, laminate stacking sequence, etc.) while varying others (e.g. the size of a structural feature) in order to investigate the effects on damage. Investigation of multiple parameter interactions can also be made possible with the comparison database.

The advantage of such a comparison database is that it can represent a new focus, investigating lengthscale effects, whereas previous databases on composites are used principally in determining material allowables for specific laminates. Damage information is lacking from these previous databases, partially due to absence of damage documentation procedures, making it nearly impossible for researchers to use the contained information to study failure trends based on mechanisms of damage. This ultimately limits the ability to design the most efficient structures as previously discussed. The comparison database is to be developed and implemented using damage documentation data collected from experimental specimens of this study. This database is to provide researchers with a standard platform to investigate damage trends and lengthscale effects across multiple specimen types and levels while also allowing damage/failure data to be shared with one another.

Chapter 4

Specimens Evaluated

Composite specimens can be manufactured with an almost infinite number of combinations of geometry, material, and laminate configurations. Specimens are typically designed for specific projects, with testing objectives motivating the selection criteria for the geometries studied, the materials tested, the stacking sequences used, and the loadings applied. Selection of the specimen parameters is driven by the goals of the testing, such as the need to acquire material allowables, to verify a finite element code, or to certify a component. This leads to a wide range of composite specimens, with testing levels from the coupon level all the way up to the final component.

The damage documentation procedures developed during this work were considered in the context of the many variables involved in specimen design, with the intent of producing a generalized procedure capable of capturing lengthscale effects regardless of the specimen parameters. In order to develop these procedures and to begin investigating lengthscale effects, specimens from different levels and with different structural features are evaluated. The evaluated specimens include multiple testing levels, varying laminates, and various structural features to allow investigation of the lengthscales and mechanisms controlling damage across these specimens. Parameters (e.g., geometry, laminate) were selected for these specimens to allow investigation of lenghtscales and to address unanswered questions from the question tree (discussed in Section 3.2). For example, two effective ply thicknesses were used throughout the specimens (with the exception of the NRL single-edge-notched specimens) to allow

investigation of the influence of change in this critical lengthscale on damage mechanisms. The specifics of the experimental specimens directly considered in this work are presented in this chapter.

In total, four different experimental specimen types were directly considered during this work. These are referred to as single-edge-notched, double-edge-notched, open-hole tension, and ply-drop. These specimen types each incorporate different structural details, allowing investigation of lengthscale effects that arise as the levels of composite testing, as described in Section 2.3, are maneuvered. The single-edge-notched and double-edge-notched specimens provide a baseline characterization for the material used during this study. These specimens have relatively simple geometries. The higher levels of testing include the specimens with an open hole and the specimens with ply drop-offs. These specimens represent an increase in structural complexity from the baseline characterization tests and allow an investigation of how the mechanisms controlling damage are affected at an increased structural level. In particular, the inclusion of the structural details, the open hole and the ply drop-offs, change the stress-field gradients within the structure, and thus the material. These gradients can change the forcing lengthscale, and introduce the possibility of inducing damage mechanisms and interactions associated with different lengthscales. The geometric dimensions and structural detail of each specimen type are summarized in Table 4.1, with the specifics of the specimens further described in the sections of this chapter.

All specimens were manufactured and tested by collaborators at the NRL (Naval Research Laboratory) in Washington D.C., U.S.A., and the CRC-ACS (Cooperative Research Centre for Advanced Composite Structures) in Victoria, Australia. The specimens were all made of the same composite material, AS4/3501-6 carbon/epoxy, with the exception of a subset of the NRL single-edge-notched specimens (described in Section 4.1), which were made of AS1/3501-6 carbon/epoxy. The only difference between the AS4/3501-6 and AS1/3501-6 material is the fiber used to form the pre-impregnated unidirectional plies. The AS1 and AS4 fibers have almost identical mechanical properties (i.e., Young's modulus, fiber diameter, density), with the main

Table 4.1 Key geometric aspects of experimental specimens directly considered in work (all given in English units)

Specimen Type[a,b]	**Nominal Dimensions**[c]			**Geometric Feature**[a]
	Length [in]	**Width [in]**	**Thickness [in]**	
Single Edge-Notched	1.5	1.0	0.14	Single Notch
Double Edge-Notched	2.95	1.97	0.165	Double Notches
0" OHT	7.48/11.81[d]	0.98	0.126	0" Diameter Hole
0.5" OHT	7.48/11.81[d]	1.97	0.126	0.5" Diameter Hole
1" OHT	13.39/22.05[d]	3.94	0.126	1.0" Diameter Hole
Ply-Drop	7.87	1.50	0.187-0.125	Drop of 12 Plies

[a] " = inch.
[b] OHT = Open Hole Tension.
[c] All dimensions converted to English units.
[d] First round length/second round length (described in Section 4.3).

difference being that the AS4 fibers have a 40% increase in tensile strength over the AS1 fibers [114–116]. Dimensions listed in this chapter are nominal and are given in the system in which they were manufactured, except in Table 4.1 where all units are converted to English units to allow straightforward comparison of the specimen sizes. The single-edge-notched specimens were manufactured for a previous NRL study (as discussed in Section 5.1) using English units. All other specimens were manufactured using SI (International System) units. These are reported in each subsection where the individual specimens are described.

4.1 Single-Edge-Notched Specimens

The NRL single-edge-notched specimens were designed and tested for a previous study conducted in the 1990's [117]. The experimental data and postmortem specimens were readily available for inspection. These specimens are at the baseline testing level, and are of the same material used for the other specimen types. Therefore, they are included in this investigation. The specimens have a rectangular geometry with nominal in-plane dimensions of 1.5 inches in length and 1.0 inches in width. The thickness of these specimens is on the order of 0.14 inches, depending on the material (AS1 or AS4 as fiber) and the number of plies. In all specimens, there is a strain riser cut at the mid-length. This strain riser is 0.04 inches wide, 0.6 inches in length, ending with a semi-circular notch tip, and cut through the thickness using a bandsaw. The purpose of the strain riser is to create a region, away from the specimen edge, of high strain within the material, including a gradient of the strain field. By isolating the region from the influences of specimen boundaries and structural features, characterization of the response of the material and laminate configuration to controlled strain fields can be achieved. An illustration of the single-edge-notched specimen is shown in Figure 4.1.

Specimens of different materials (matrix and fiber combinations) and different stacking sequences had been included in the original NRL study. Each combination of material and stacking sequence is referred to as a particular item. Seven different

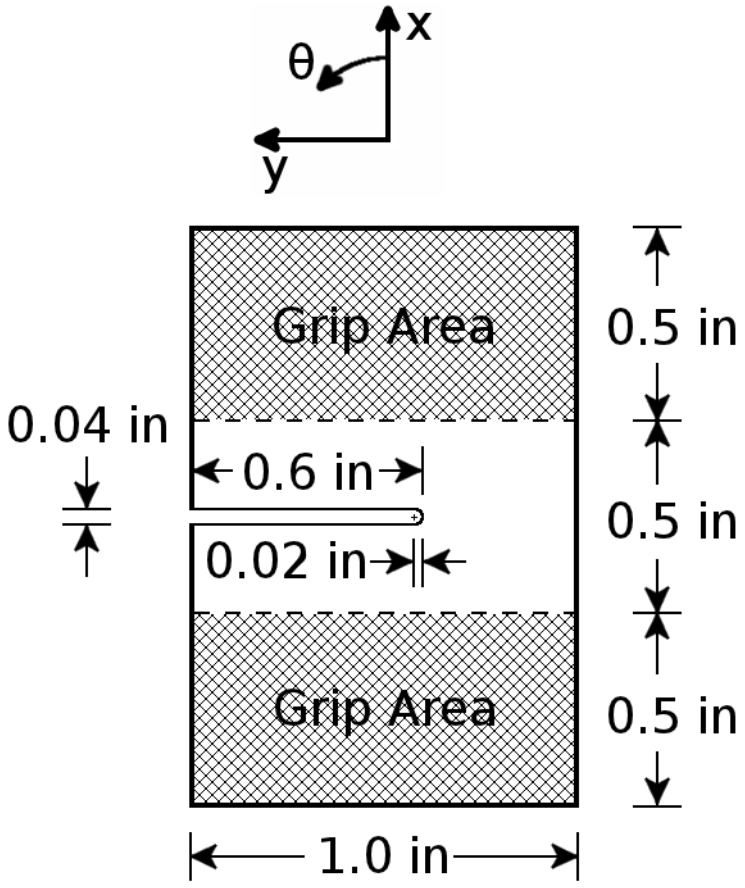

Figure 4.1 Planar illustration of the NRL single-edge-notched specimen.

items (four with AS1 fibers and three with AS4 fibers, all with 3501-6 matrix) were selected from the original study for investigation. These items have the same (or similar in the case of items with AS1 fibers) material, and similar stacking sequences used for the other specimen types considered in this work. In total, 210 single-edge-notched specimens were used. Some items had missing specimens (unaccounted for after 20 years), but all remaining specimens from these items were documented. The material specifics of these items are shown in Table 4.2. The specimen IDs in the table contain wildcard characters, where '#' represents a single number. The first three numbers of the specimen ID represent the NRL item number, while the two wildcard characters are used to assign a unique number to each specimen. Further details on the NRL single-edge-notched specimens can be found in [117].

One issue found while inspecting the specimens was the improper reporting of the laminate stacking sequences. It is important to have knowledge of the laminate layup in order to identify and investigate the effects of effective ply thicknesses. The layups for the items received were reported as $+/-\theta$, with the number of plies unspecified. However, inspection of the sides of the specimens under an optical microscope revealed that the laminates were not a simple layup of $+/-\theta$. Using a lighting technique, where a bright light is shined at an angle to the edge of the specimen, plies at different angles could be identified. A microscope image taken from a specimen from item 001, shown in Figure 4.2, shows alternating bright and dark plies, corresponding to plies at different angles. Also visible in the microscope image is the separation between individual plies. As is seen in the image, there is a single top ply followed by two plies at different angle, followed by three plies at the same (or nearly same) angle as the top ply (determined by the brightness of the ply), and so on.

In order to properly determine the ply angles and stacking sequence for each item, a matrix burn-off was conducted on one sample from each item. The burn-off was carried out using a propane torch, with a flame being hot enough to burn away (i.e., off) the matrix while leaving the carbon fibers intact. Once all the matrix burned away, a razor blade was used to separate the plies. A separation could only be made at interfaces between plies of varying fiber angles. Therefore, effective plies could be

Table 4.2 Material and layup characteristics of NRL Single Edge-Notched specimens [117]

Specimen ID[a]	**Fiber**	**Resin**	**Specimen Count**	**Reported Layup**	**Determined Stacking Sequence**[b]
001-##	AS1	3501-6	30	+/-15	$[\text{-}75/+75_2/\text{-}75_3/(\pm 75_2)_2/+75_3/(\mp 75_2)_2/\text{-}75]_T$
002-##	AS1	3501-6	19	+/-30	$[(\text{-}60/+60_2/\text{-}60_2/+60)_S]_S$
003-##	AS1	3501-6	36	+/-60	$[(\text{-}30/+30_2/\text{-}30_2/+30)_S]_S$
004-##	AS1	3501-6	35	+/-75	$[\text{-}15/+15_2/\text{-}15_3/(\pm 15_2)_2/+15_3/(\mp 15_2)_2/\text{-}15]_T$
005-##	AS4	3501-6	30	+/-15	$[(\text{-}75/+75_2/\text{-}75_2/+75)_S]_S$
007-##	AS4	3501-6	30	+/-60	$[(\text{-}30/+30_2/\text{-}30_2/+30)_S]_S$
008-##	AS4	3501-6	30	+/-75	$[(\text{-}15/+15_2/\text{-}15_2/+15)_S]_S$

[a] '#' is a wildcard character representing a single number.

[b] Coordinate transformation applied from that reported in [117] to maintain consistent coordinate definition among the specimens of this work.

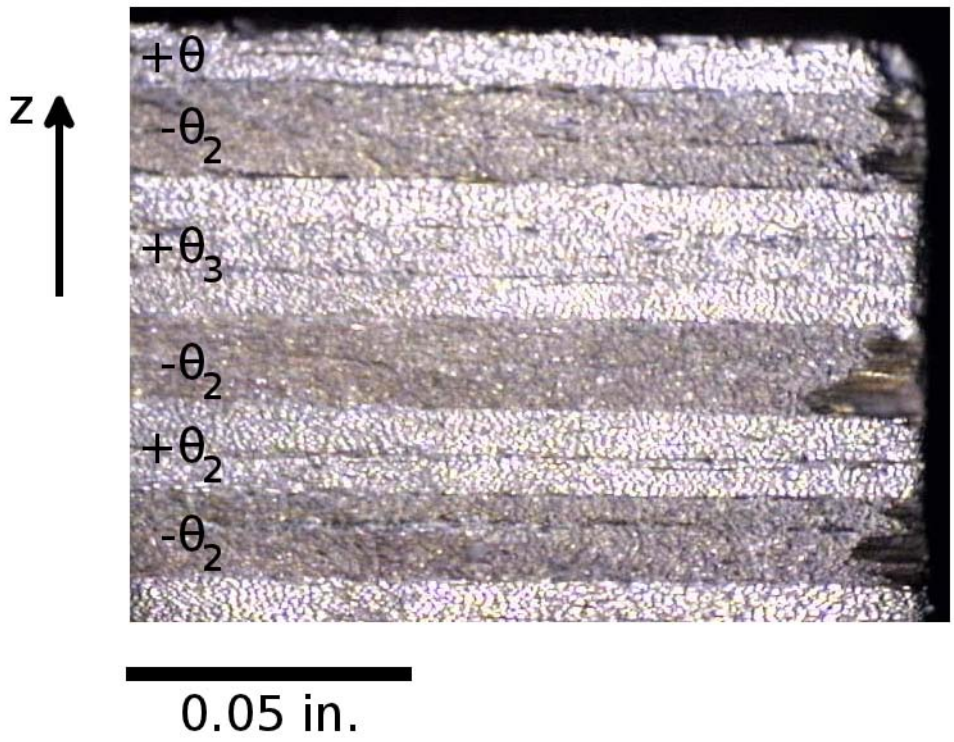

Figure 4.2 Microscope image showing a portion of the side (through-the-thickness) of a NRL single-edge-notched specimen.

separated. The number of effective plies for each item agreed with the results from the optical inspection. The results from items 001 and 004 showed these specimens to have two extra plies, making these laminates unsymmetric. All the other items were determined to be balanced and symmetric laminates as indicated in [117]. The stacking sequences, as reported and as determined via this technique, are listed in the last columns of Table 4.2. The NRL researchers had defined the 0° ply direction along the length of the strain riser. In order to maintain consistency among specimens evaluated in this work, a coordinate transformation was applied to the angles reported in [117] to align the 0°-direction along the length of the specimen (x-axis).

The single-edge-notched specimens are subjected to 15 different possible load paths. The load paths are applied to specimens using the NRL In-Plane Loader System (IPLS). This is a custom-made, fully automated, displacement-controlled, three degree-of-freedom testing machine [117]. This machine has a fixed lower grip and a movable upper grip. Hydraulic actuators control the three planar degrees-of-freedom (DoF) of the upper grip. These DoF are referred to as compression/tension (u_x, in-plane translation in the x-/0°-direction), shear (u_y, in-plane translation in the y-/90°-direction), and in-plane rotation (R_z, rotation about the z-axis, which is through the thickness). Individual load paths are defined by displacement vectors with components in the three-dimensional displacement space. Unit vectors for each path are defined with components, u_x, u_y, and R_z, associated with each degree of freedom. Each displacement path of the upper grip can therefore be represented by:

$$\boldsymbol{U} = r(u_x\widehat{\mathbf{x}} + u_y\widehat{\mathbf{y}} + R_z\widehat{\mathbf{z}'}), \tag{4.1}$$

where r is a proportional scalar increasing from 0 to 0.05 inches for each load path such that the change in each degree of freedom is proportional during the loading. The items $\widehat{\mathbf{x}}$, $\widehat{\mathbf{y}}$, and $\widehat{\mathbf{z}'}$ are unit vectors along the x, y, and z' directions, respectively, where z' refers to a curvilinear coordinate defined along the path traced by the endpoint of a radius, one inch in length, with origin corresponding to the x-y coordinate system origin, rotated in the clockwise direction. Instead of specifying the in-plane rotation

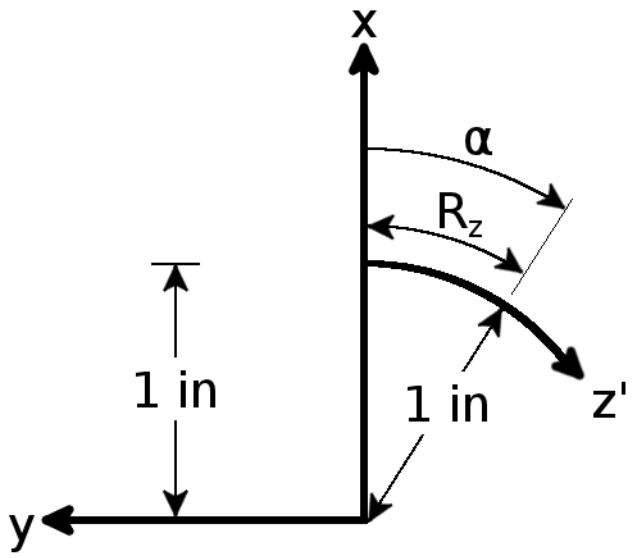

Figure 4.3 Illustration of the degree of freedom referred to as R_z, defined as the arc length scribed by a one inch radius rotated through an angle α along the z' direction.

in radians, the magnitude of this rotation, R_z, is defined as the length of the arc traveled along the z' coordinate as the radius travels over an angle of α [117]. An illustration of this definition is shown in Figure 4.3. This definition allows the three DoF to all be measured in units of length.

The unit magnitudes of these components for the different load paths are shown in Table 4.3. For example, load path 5, with u_x and u_y equal to -0.707 and R_z equal to 0.000, has the upper grip moving from (0 in, 0 in, 0 in) to a final displacement of (-0.035 in, -0.035 in, 0 in). Refer to [117, 118] for further details on the load paths used with the single-edge-notched specimens and the choice thereof. Note that the coordinate transformation applied to the original coordinate definition changes the component labels listed in Table 4.3 from those reported in [117, 118]. The compression/tension component along the length of the specimen, u_x is equivalent to a_1 in [117, 118], the shear component, u_y is equivalent to -a_0 in [117, 118], and the in-plane rotation component, R_z is equivalent to a_2 in [117, 118]. These definitions allow consistent coordinates to be used throughout the specimens of this work.

4.2 Double-Edge-Notched Specimens

The double-edge-notched specimens were designed and tested for the current work. They are at the baseline testing level. The specimen geometry is largely based on that of the single-edge-notched specimens, with the double-edge-notched specimens being slightly larger in size, and incorporating a second notch. The second notch was added to achieve a symmetric geometry, and allows a region of high strain to develop within the material and away from the specimen edges, including a gradient of the strain field. As with the single-edge-notched specimens, by isolating the region from the influences of specimen boundaries and structural features, characterization of the material's response to controlled strain fields can be achieved. The specimens have a rectangular geometry with nominal dimensions of 75 mm by 50 mm and a thickness of 4.2 mm. Notches, with a width of 2.8 mm, are cut at the mid-length on both sides of the specimen. The notches are cut into the specimen 12 mm from

Table 4.3 Load path unit displacement magnitudes[a] for the Single Edge-Notched specimens with terminology used herein [117, 118]

Load Path ID	$\boldsymbol{u}_x$	$\boldsymbol{u}_y$	$\boldsymbol{R}_z$	**Loading Description**
1	-0.707	0.000	-0.707	Compression, in-plane rotation
2	-1.000	0.000	0.000	Compression
3	-0.707	0.000	0.707	Compression, in-plane rotation
4	-0.500	-0.500	-0.707	Compression, shear, in-plane rotation
5	-0.707	-0.707	0.000	Compression, shear
6	-0.500	-0.500	0.707	Compression, shear, in-plane rotation
7	0.000	-0.707	-0.707	Shear, in-plane rotation
8	0.000	-1.000	0.000	Shear
9	0.000	-0.707	0.707	Shear, in-plane rotation
10	0.500	-0.500	-0.707	Tension, shear, in-plane rotation
11	0.707	-0.707	0.000	Tension, shear
12	0.500	-0.500	0.707	Tension, shear, in-plane rotation
13	0.707	0.000	-0.707	Tension, in-plane rotation
14	1.000	0.000	0.000	Tension
15	0.707	0.000	0.707	Tension, in-plane rotation

[a] As defined in [117, 118].

the edge, ending with a semi-circular notch tip. A water jet is used to cut out the individual specimens, including the notches, from a large plate. An illustration of the double-edge-notched specimen is shown in Figure 4.4.

All the double-edge-notched specimens are made of AS4/3501-6 carbon/epoxy composite material. These specimens are made with eight different stacking sequences: $[+\theta/\text{-}\theta]_{16T}$ or $[+\theta_4/\text{-}\theta_4]_{4T}$ where θ is equal to 15°, 30°, 60°, or 75°. The material and layup specifics of the NRL double-edge-notched specimens are shown in Table 4.4. Each specimen is assigned a unique ID number. These specimen ID numbers contain information on the stacking sequence as well as manufacturing information, specifically the location on the cured composite plate where the specimen was cut. The letters 'CH' indicate the double-edge-notched specimen geometry. The next letter indicates the composite plate from which the specimens were manufactured and cut. The following two numbers indicate the layup angle, θ, of the plies. The third number indicates the stacking sequence of the specimen, where '1' indicates the laminate has single-ply effective ply stacking ($[+\theta/\text{-}\theta]_{16T}$) and '4' indicates the laminate has four-ply effective ply stacking ($[+\theta_4/\text{-}\theta_4]_{4T}$). The following entries of '#' are wildcard characters, where each '#' indicates a single number ranging from 0 to 9. The first pair of numbers indicate the row (starting at 01) and the second pair of numbers indicate the column (starting at 01) of the full composite plate where the specimen was cut out. Thus, each specimen has a unique identifier. For statistical purposes, two specimens are tested for each combination of stacking sequence and loading case. The repeated specimens are manufactured and cut from a different plate (i.e., each specimen has a "twin" specimen cut from another plate, both with the same laminate and both undergoing the same load path).

The double-notched specimens are tested at the NRL using a custom-built six degree-of-freedom loader system (6DLS). The 6DLS is based on the NRL IPLS, with the addition of three out-of-plane degrees-of-freedom. As with the IPLS, the 6DLS is fully automated, is displacement-controlled, and has a fixed lower grip and a movable upper grip. Hydraulic actuators control the displacements of the upper grip. Refer to [119] for details on the 6DLS. The six DoF of the 6DLS permit three translations and

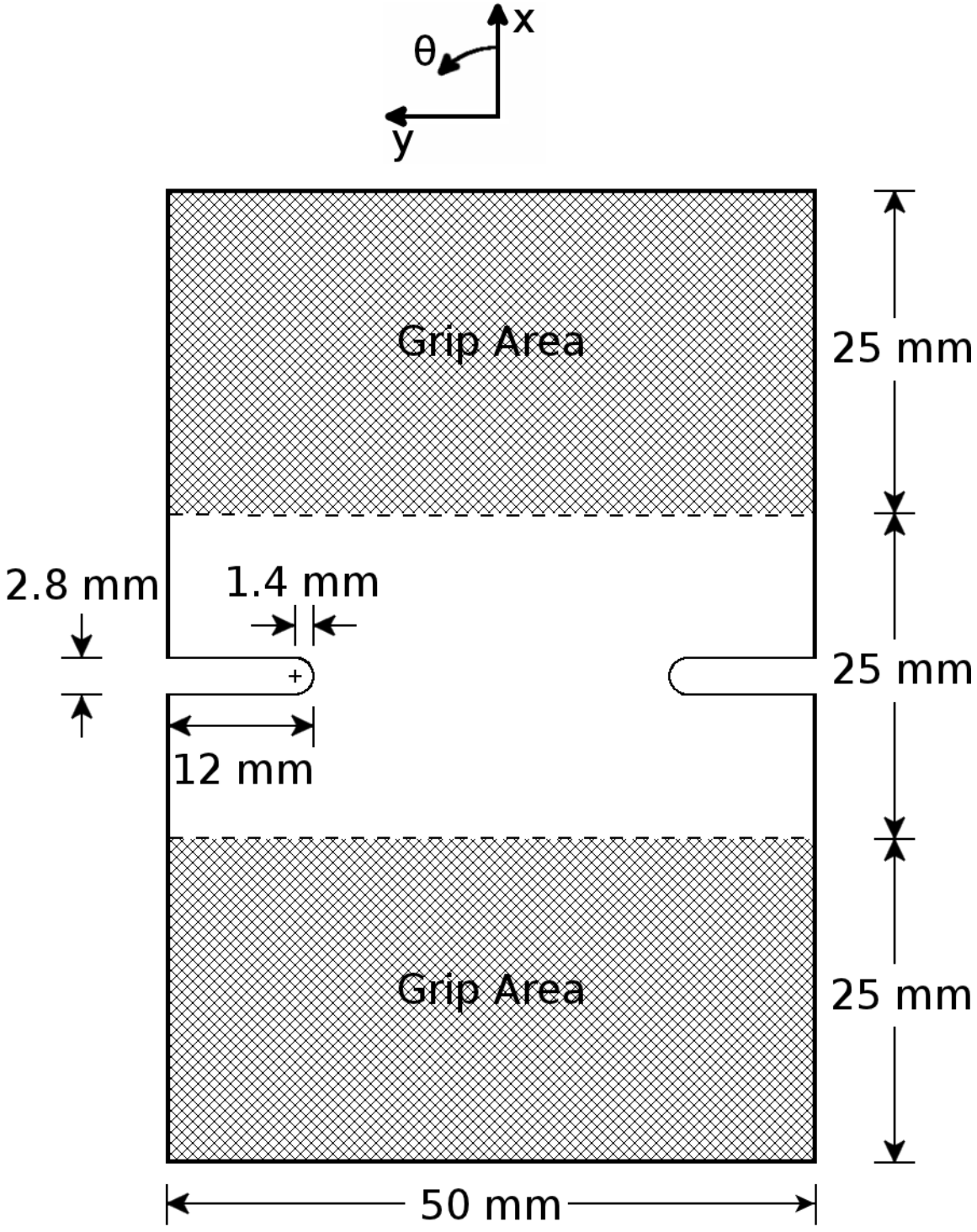

Figure 4.4 Planar illustration of the NRL double-edge-notched specimen.

Table 4.4 Material and layup characteristics of NRL Double Edge-Notched specimens

Specimen ID[a]	**Fiber**	**Resin**	**Specimen Count**	**Stacking Sequence**
CH-A301-####	AS4	3501-6	72	$[+30/\text{-}30]_{16T}$
CH-B601-####	AS4	3501-6	72	$[+60/\text{-}60]_{16T}$
CH-C601-####	AS4	3501-6	72	$[+60/\text{-}60]_{16T}$
CH-D301-####	AS4	3501-6	72	$[+30/\text{-}30]_{16T}$
CH-E151-####	AS4	3501-6	72	$[+15/\text{-}15]_{16T}$
CH-F151-####	AS4	3501-6	72	$[+15/\text{-}15]_{16T}$
CH-G751-####	AS4	3501-6	72	$[+75/\text{-}75]_{16T}$
CH-H751-####	AS4	3501-6	72	$[+75/\text{-}75]_{16T}$
CH-I304-####	AS4	3501-6	72	$[+30_4/\text{-}30_4]_{4T}$
CH-J304-####	AS4	3501-6	72	$[+30_4/\text{-}30_4]_{4T}$
CH-K604-####	AS4	3501-6	72	$[+60_4/\text{-}60_4]_{4T}$
CH-L604-####	AS4	3501-6	72	$[+60_4/\text{-}60_4]_{4T}$
CH-M154-####	AS4	3501-6	72	$[+15_4/\text{-}15_4]_{4T}$
CH-N154-####	AS4	3501-6	72	$[+15_4/\text{-}15_4]_{4T}$
CH-O754-####	AS4	3501-6	72	$[+75_4/\text{-}75_4]_{4T}$
CH-P754-####	AS4	3501-6	72	$[+75_4/\text{-}75_4]_{4T}$

[a] '#' is a wildcard character representing a single number.

three rotations: compression/tension (u_x, in-plane translation in the x-/0°-direction), shear (u_y, in-plane translation in the y-/90°-direction), out-of-plane shear (u_z, displacement in the z-/out-of-plane direction), twist (R_x, out-of-plane rotation about the x-axis), bend (R_y, out-of-plane rotation about the y-axis), and in-plane rotation (R_z, rotation about the z-axis which is in the through-the-thickness direction). Load paths are defined by combinations of these DoF.

In total, 72 different possible loading cases are defined for the current investigation. These defined paths do not utilize the shear translations, with u_y and u_z being zero for all 72 paths. A detailed explanation of these load paths is provided in [119]. The displacement components of the load paths are shown in Tables 4.5 and 4.6. These components have a similar definition as the load path components from the IPLS machine (discussed in Section 4.1), with each displacement path represented by:

$$\boldsymbol{U} = r(u_x\widehat{\mathbf{x}} + u_y\widehat{\mathbf{y}} + u_z\widehat{\mathbf{z}} + R_x\widehat{\mathbf{x}'} + R_y\widehat{\mathbf{y}'} + R_z\widehat{\mathbf{z}'}). \tag{4.2}$$

where r is a proportional scalar for each load path such that the change in each degree of freedom is proportional during the loading. The items $\widehat{\mathbf{x}}$, $\widehat{\mathbf{y}}$, and $\widehat{\mathbf{z}}$ are unit vectors along the x, y, and z directions, respectively. The items $\widehat{\mathbf{x}'}$, $\widehat{\mathbf{y}'}$, and $\widehat{\mathbf{z}'}$ are defined in a similar manner as the $\widehat{\mathbf{z}'}$ unit vector that is described in Section 4.1. Each is a unit vector along a curvilinear path, similar to that shown in Figure 4.3, that allows rotation about the subscripted axis to be measured in units of length. Therefore, $\widehat{\mathbf{x}'}$ lies in the y-z plane, $\widehat{\mathbf{y}'}$ lies in the x-z plane, and $\widehat{\mathbf{z}'}$ lies in the x-y plane. Note that the load path IDs do not correspond to the load path IDs from the single-edge-notch testing.

Along with recording the force and displacement data from the 6DLS, the strain fields on the front and back faces of the specimens were recorded using an optical strain mapping technique. The technique required a pattern to be printed on the faces of the specimen and pictures of the patterns to be taken during testing. These photographs were post-processed to determine the strain fields on these faces. In total, 1152 double-notched specimens were tested at the NRL and were subsequently inspected in this work.

Table 4.5 Load path displacement magnitudes[a] for the Double Edge-Notched specimens for load paths 1-36

Load Path ID	$\boldsymbol{u}_x$	$\boldsymbol{u}_y$	$\boldsymbol{u}_z$	$\boldsymbol{R}_x$	$\boldsymbol{R}_y$	$\boldsymbol{R}_z$	**Loading Description**
1	-1	0	0	0	0	0	compression
2	0	0	0	-6.6	0	0	twist
3	0	0	0	6.6	0	0	twist
4	1	0	0	0	0	0	tension
5	-0.5	0	0	-3.3	-10.6	0	compression, bend, twist
6	-0.5	0	0	-3.3	10.6	0	compression, bend, twist
7	-0.5	0	0	-3.3	0	-1.4	compression, rotation, twist
8	-0.5	0	0	-3.3	0	1.4	compression, rotation, twist
9	-0.5	0	0	0	-10.6	-1	compression, bend, rotation
10	-0.5	0	0	0	10.6	-1	compression, bend, rotation
11	-0.5	0	0	0	-10.6	1	compression, bend, rotation
12	-0.5	0	0	0	10.6	1	compression, bend, rotation
13	-0.5	0	0	3.3	-10.6	0	compression, bend, twist
14	-0.5	0	0	3.3	10.6	0	compression, bend, twist
15	-0.5	0	0	3.3	0	-1.4	compression, rotation, twist
16	-0.5	0	0	3.3	0	1.4	compression, rotation, twist
17	0	0	0	-3.3	-10.6	-1	bend, rotation, twist
18	0	0	0	-3.3	10.6	-1	bend, rotation, twist
19	0	0	0	-3.3	-10.6	1	bend, rotation, twist
20	0	0	0	-3.3	10.6	1	bend, rotation, twist
21	0	0	0	3.3	-10.6	-1	bend, rotation, twist
22	0	0	0	3.3	10.6	-1	bend, rotation, twist
23	0	0	0	3.3	-10.6	1	bend, rotation, twist
24	0	0	0	3.3	10.6	1	bend, rotation, twist
25	0	0	0	-4.7	-10.6	0	bend, twist
26	0	0	0	-4.7	10.6	0	bend, twist
27	0	0	0	-4.7	0	-1.4	rotation, twist
28	0	0	0	-4.7	0	1.4	rotation, twist
29	0	0	0	4.7	-10.6	0	bend, twist
30	0	0	0	4.7	10.6	0	bend, twist
31	0	0	0	4.7	0	-1.4	rotation, twist
32	0	0	0	4.7	0	1.4	rotation, twist
33	0.5	0	0	-3.3	-10.6	0	tension, bend, twist
34	0.5	0	0	-3.3	10.6	0	tension, bend, twist
35	0.5	0	0	-3.3	0	-1.4	tension, rotation, twist
36	0.5	0	0	-3.3	0	1.4	tension, rotation, twist

[a] See equation 4.2.

Table 4.6 Load path displacement magnitudes[a] for the Double Edge-Notched specimens for load paths 37-72

Load Path ID	$\boldsymbol{u}_x$	$\boldsymbol{u}_y$	$\boldsymbol{u}_z$	$\boldsymbol{R}_x$	$\boldsymbol{R}_y$	$\boldsymbol{R}_z$	**Loading Description**
37	0.5	0	0	0	-10.6	-1	tension, bend, rotation
38	0.5	0	0	0	10.6	-1	tension, bend, rotation
39	0.5	0	0	0	-10.6	1	tension, bend, rotation
40	0.5	0	0	0	10.6	1	tension, bend, rotation
41	0.5	0	0	3.3	-10.6	0	tension, bend, twist
42	0.5	0	0	3.3	10.6	0	tension, bend, twist
43	0.5	0	0	3.3	0	-1.4	tension, rotation, twist
44	0.5	0	0	3.3	0	1.4	tension, rotation, twist
45	-0.7	0	0	0	-10.6	0	compression, bend
46	-0.7	0	0	0	10.6	0	compression, bend
47	-0.7	0	0	0	0	-1.4	compression, rotation
48	-0.7	0	0	0	0	1.4	compression, rotation
49	-0.7	0	0	-4.7	0	0	compression, twist
50	-0.7	0	0	4.7	0	0	compression, twist
51	-0.4	0	0	-2.3	-10.6	-1	compression, bend, rotation, twist
52	-0.4	0	0	-2.3	10.6	-1	compression, bend, rotation, twist
53	-0.4	0	0	-2.3	-10.6	1	compression, bend, rotation, twist
54	-0.4	0	0	-2.3	10.6	1	compression, bend, rotation, twist
55	-0.4	0	0	2.3	-10.6	-1	compression, bend, rotation, twist
56	-0.4	0	0	2.3	10.6	-1	compression, bend, rotation, twist
57	-0.4	0	0	2.3	-10.6	1	compression, bend, rotation, twist
58	-0.4	0	0	2.3	10.6	1	compression, bend, rotation, twist
59	0.4	0	0	-2.3	-10.6	-1	tension, bend, rotation, twist
60	0.4	0	0	-2.3	10.6	-1	tension, bend, rotation, twist
61	0.4	0	0	-2.3	-10.6	1	tension, bend, rotation, twist
62	0.4	0	0	-2.3	10.6	1	tension, bend, rotation, twist
63	0.4	0	0	2.3	-10.6	-1	tension, bend, rotation, twist
64	0.4	0	0	2.3	10.6	-1	tension, bend, rotation, twist
65	0.4	0	0	2.3	-10.6	1	tension, bend, rotation, twist
66	0.4	0	0	2.3	10.6	1	tension, bend, rotation, twist
67	0.7	0	0	0	-10.6	0	tension, bend
68	0.7	0	0	0	10.6	0	tension, bend
69	0.7	0	0	0	0	-1.4	tension, rotation
70	0.7	0	0	0	0	1.4	tension, rotation
71	0.7	0	0	-4.7	0	0	tension, twist
72	0.7	0	0	4.7	0	0	tension, twist

[a] See equation 4.2.

4.3 Open-Hole Tension Specimens

The open-hole tension specimens represent an increase in structural complexity from the base-level characterization tests, and are designed to investigate the effect of an increased structural level on the mechanisms controlling damage. In particular, the inclusion of a structural detail, the open hole, changes the stress-field gradients within the structure, and thus the material. These gradients can change the forcing lengthscale, and thereby introduce the possibility of inducing damage mechanisms and interactions associated with different lengthscales.

The open-hole tension (OHT) specimens are made with six different geometries and two different laminate stacking sequences. These specimens were tested in two rounds. The first round contains three geometries: a specimen with nominal dimensions of 190 mm in length by 25 mm in width by 3.2 mm in thickness containing no hole (referred to as a hole diameter of 0.0 inches), a specimen with nominal dimensions of 190 mm in length by 50 mm in width by 3.2 mm in thickness containing a hole with a diameter of 0.5 inches (the hole saws used to produce the holes in all OHT specimens are of English units), and a specimen with nominal dimensions of 340 mm in length by 100 mm in width by 3.2 mm in thickness containing a hole with a diameter of 1.0 inches. During the second round, the lengths of the specimens were increased to enable a better measurement of the far-field strain and to distance the effects of the boundaries on the strains around the hole. The other dimensions remained the same. The three geometries of the second round are a specimen with nominal dimensions of 300 mm in length by 25 mm in width by 3.2 mm in thickness containing no hole (referred to as a hole diameter of 0.0 inches), a specimen with nominal dimensions of 300 mm in length by 50 mm in width by 3.2 mm in thickness containing a hole with a diameter of 0.5 inches, and a specimen with nominal dimensions of 560 mm in length by 100 mm in width by 3.2 mm in thickness containing a hole with a diameter of 1.0 inches. The hole in each specimen is through the thickness and centered on the length and width.

An illustrations of the basic geometry of the OHT specimen is shown in Figure 4.5,

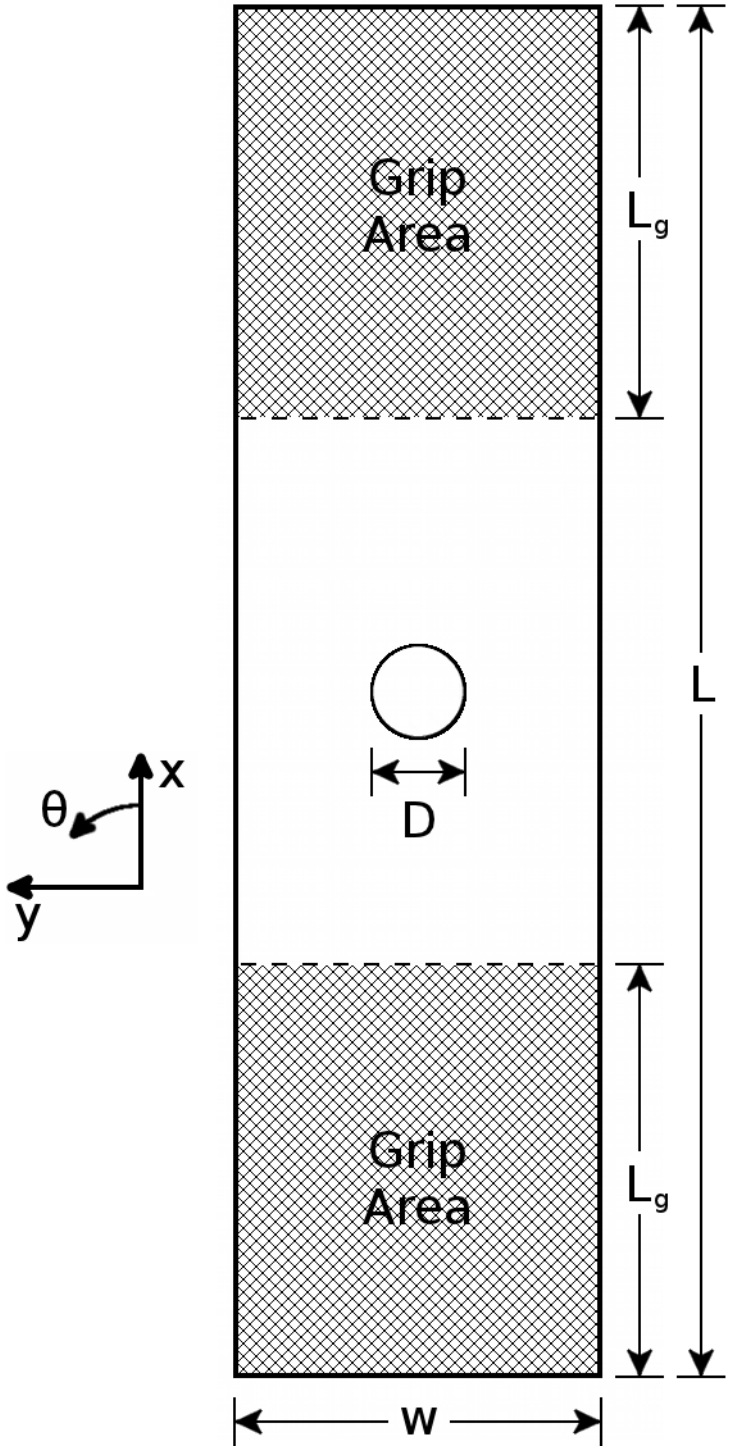

Figure 4.5 Planar illustration of the generic CRC-ACS OHT specimen geometry with length L, width w, grip length L_g, and hole of diameter D (including no hole: D=0).

where L indicates the specimen length, w indicates the specimen width, D indicates the hole diameter (including no hole: D=0), and L_g indicates the length gripped by the testing machine. Specimens of widths 25 mm and 50 mm have a gripped length of 65 mm, and specimens with a width of 100 mm have a gripped length of 95 mm. These six different OHT geometries were selected to allow investigation on the influences due to scaling. One of the unanswered questions from the question tree (Section 3.2) addresses the manner in which the critical lengthscale(s) are influenced by geometric scaling. The OHT specimens allow changes in lengthscale effects, including interactions of lengthscales, to be investigated as the specimen is scaled to different sizes, and thereby the results from these specimens address this question.

All the OHT specimens are made of AS4/3501-6 carbon/epoxy composite material. The two laminate stacking sequences used in these specimens are $[+45/0/\text{-}45]_{4S}$ and $[+45_4/0_4/\text{-}45_4]_S$. These two stacking sequences are selected in order to investigate the influence of effective ply thickness. As in the case of the double-edge-notched specimens, the first laminate has a single-ply effective ply thickness, and the second laminate has a four-ply effective thickness. The combinations of geometries and laminate of the OHT specimens are listed in Table 4.7. The specimen IDs listed in the table contain information on the specimen geometry and laminate as well as the specimen number. The specimen IDs in the table contain wildcard characters, where '?' represents a single letter and '#' represents a single number. These wildcards are used to assign unique IDs to each specimen. The parameter '?' ranges from A to F, indicating the plate from which the specimen was cut, and '#' is assigned sequentially, starting at 1, for each group (letter). The two numbers following the '?' wildcard indicate the hole diameter of the specimen, where '00' indicates a 0.0 mm hole (referred to as a 0-inch hole), '05' indicates a 12.5 mm hole (referred to as a 0.5-inch hole), and '10' indicates a 25 mm hole (referred to as a 1.0-inch hole). The third number following the '?' wildcard indicates the laminate of the specimen, where '1' indicates the $[+45/0/\text{-}45]_{4S}$ laminate and '4' indicates the $[+45_4/0_4/\text{-}45_4]_S$ laminate.

The OHT specimens were tested at CRC-ACS using several servohydraulic testing machines. All specimens are loaded along the 0°-direction in uniaxial tension at con-

Table 4.7 Material and layup characteristics of CRC-ACS Open-Hole Tension specimens

Specimen ID[a,b]	**Fiber**	**Resin**	**Specimen Count**	**Hole Diameter**[c] **[in]**	**Stacking Sequence**
OH-?001-0#	AS4	3501-6	8	0.0	$[+45/0/\text{-}45]_{4S}$
OH-?051-0#	AS4	3501-6	9	0.5	$[+45/0/\text{-}45]_{4S}$
OH-?101-0#	AS4	3501-6	9	1.0	$[+45/0/\text{-}45]_{4S}$
OH-?004-0#	AS4	3501-6	8	0.0	$[+45_4/0_4/\text{-}45_4]_S$
OH-?054-0#	AS4	3501-6	8	0.5	$[+45_4/0_4/\text{-}45_4]_S$
OH-?104-0#	AS4	3501-6	9	1.0	$[+45_4/0_4/\text{-}45_4]_S$

[a] '?' is a wildcard character representing a single letter.
[b] '#' is a wildcard character representing a single number.
[c] Hole saws used to produce holes are of English units.

stant displacement rates between 0.10 and 0.45 millimeters per minute. The crosshead displacement and resulting tensile load are recorded during each test. Strain data are also recorded using strain gauges as well as an optical strain mapping technique. Two strain gauges are bonded on the front face of each specimen, one at the edge of the hole and one away from the hole to measure the far-field strain. A pattern for optical strain mapping is placed on the back face of the specimen. Pictures of the back face are captured throughout the test and are used by the strain mapping algorithm to determine the strain-field history.

4.4 Ply-Drop Specimens

The ply-drop specimens are another representation of an increase in structural complexity from the base-level characterization tests. A ply drop, another type of structural feature, changes the stress-field gradients within the structure. The stress-field gradients resulting from a ply drop differ from the stress-field gradients resulting from an open hole in a structure. By including specimens with different structural features, more lengthscale effects are able to be investigated.

The ply-drop (PD) specimens are all made with the same geometry, and with two different stacking sequences. The overall dimensions of the specimens are 200 mm in length by 38.1 mm in width, with thickness at one end of 4.75 mm ranging to 3.17 mm at the dropped end. The plies are dropped in a region of length 12 mm in the middle of the specimen in a manner subsequently described. There is a planing tab bonded onto the dropped end of the specimen to compensate in testing for thickness differential due to the dropped plies. The tab is necessary to properly align the specimen within the grips of the testing machine. Without the tab, improper orientation of the specimen within the grips would result in a misalignment of the applied force during testing and unintended bending in the specimen upon gripping. The planing tab has dimensions of 50 mm in length by 38.1 mm in width and a thickness of 1.18 mm. The tab is made of T300/914C carbon/epoxy and is bonded to the cured specimen using Henkel Hysol EA 9394 with a 0.4 mm thickness scrim cloth. The tab has a 45° cut through

the thickness (in the x-z plane) at the end nearest the dropped region. An illustration of the ply-drop specimen is shown in Figure 4.6.

The PD specimens are made with two different laminate stacking sequences, similar in nature to those used in the open-hole tension specimens. The overall laminate configuration is a layup of $[X, X_D, X]_T$ where 'X' is a sublaminate and the subscript 'D' indicates the dropped sublaminate. The technique used for dropping the center sublaminate, X_D, is to have each successive ply shorter in length by 1.0 mm within the ply drop region. This results in twelve 'steps' to go from the $[X, X_D, X]_T$ laminate to the $[X, X]_T$ laminate as illustrated in Figure 4.7. The two sublaminates used in the specimens are $[+45/0/-45]_{2S}$ and $[+45_2/0_2/-45_2]_S$. This selection of sublaminates allows the influence of effective ply thickness to be investigated at this higher level of structural complexity (as compared to the double-edge-notched specimens). However, unlike the double-edge-notched and open-hole tension specimens, which have single-ply and four-ply effective ply thicknesses, the PD specimens only have single-ply and double-ply effective ply thicknesses. Had a four-ply effective ply thickness sublaminate been used in the PD specimens, the dropped region would have had a drop of 24 plies. This is a large number of plies to drop within the length of a test specimen [120–122]. The double-ply effective ply thickness sublaminate permits a drop of a maximum of only 12 plies. The material specifics of the ply-drop specimens are shown in Table 4.8. The specimen IDs listed in the table contain the wildcard character '#' that represents a single number. Each specimen was assigned a unique ID with the '#' sequentially increased, starting at 1 for each group. The 'A1' in the specimen ID indicates the single-ply sublaminate while the 'B2' indicates the double-ply sublaminate. All ply-drop specimens are made from AS4/3501-6 carbon/epoxy composite material.

The PD specimens were tested at CRC-ACS using several servohydraulic testing machines. All specimens are loaded along the 0° direction in uniaxial tension at constant displacement rates between 0.12 and 0.30 millimeters per minute. As with the OHT specimens, the crosshead displacement, load-cell force, and strain data are recorded during each test. Two strain gauges are bonded on the front face of each

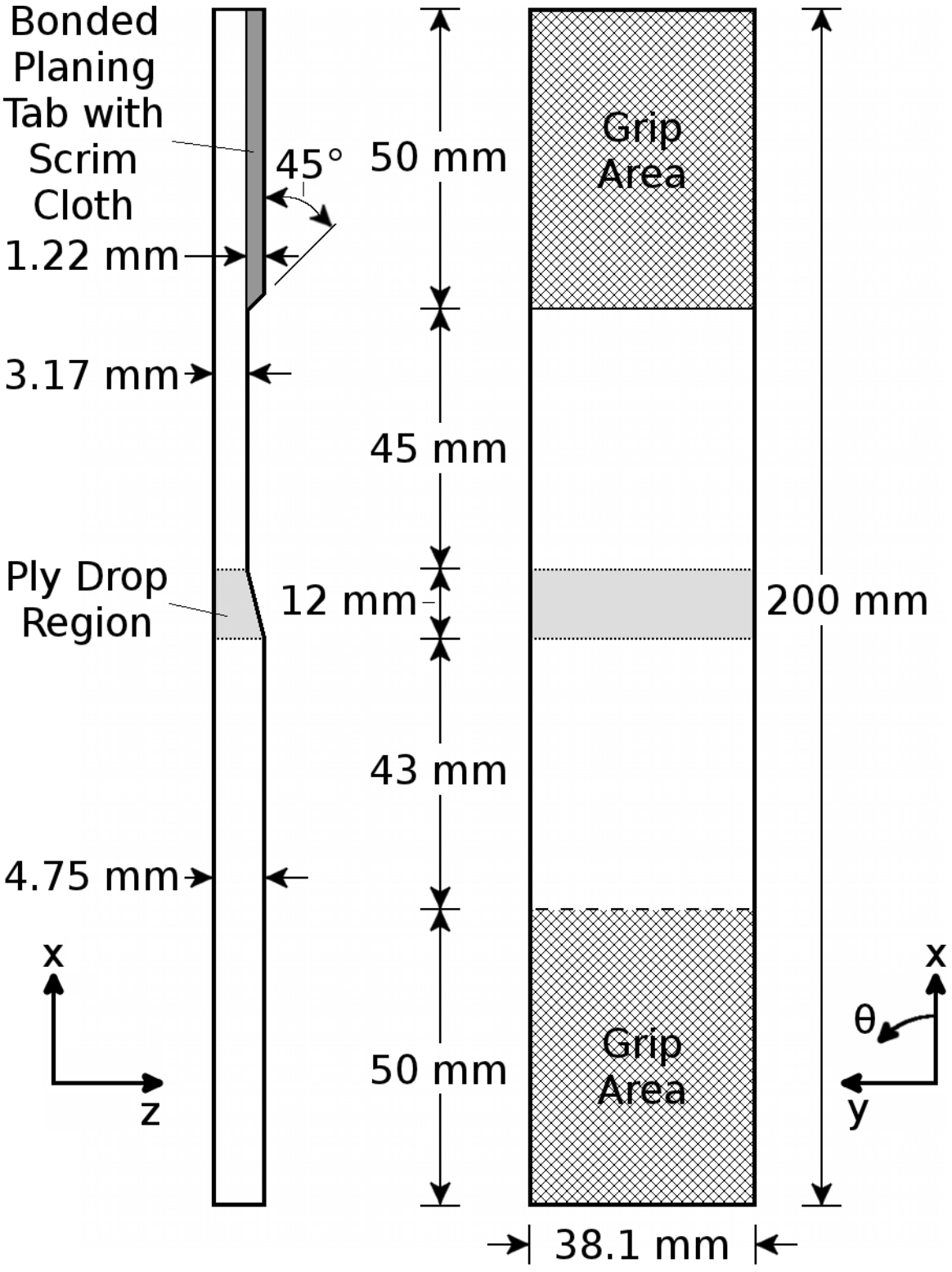

Figure 4.6 Illustration of the CRC-ACS ply-drop specimen showing, *(left)*, side view through-the-thickness, and, *(right)*, planar front view.

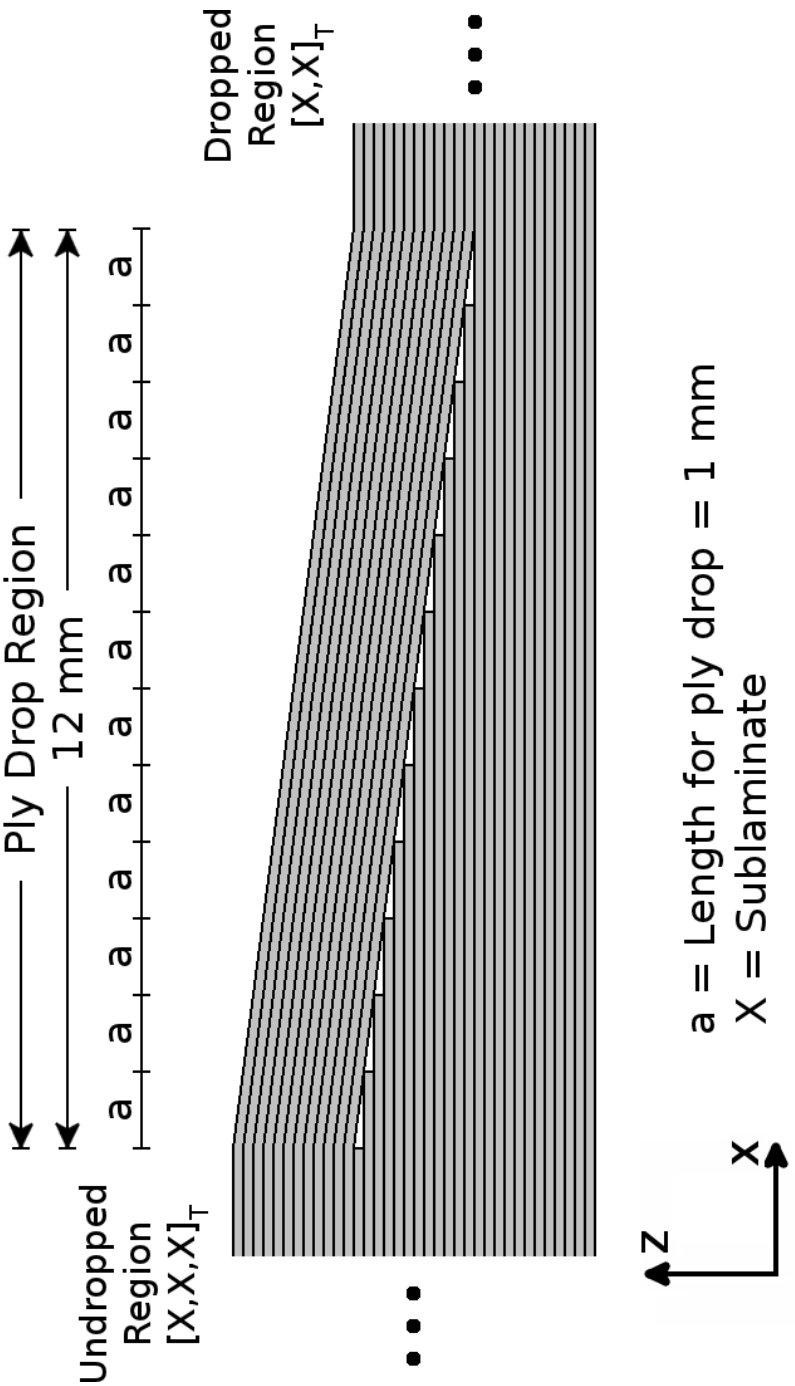

Figure 4.7 Illustration of ply drop region for $[X, X_D, X]_T$ configuration with X being sublaminate $[+45/0/-45]_{2S}$ or $[+45_2/0_2/-45_2]_S$.

Table 4.8 Material and layup characteristics of CRC-ACS Ply-Drop specimens

Specimen ID[a]	**Fiber**	**Resin**	**Specimen Count**	**Sublaminate, X**	**Stacking Sequence**[b]
PD-A1-0#	AS4	3501-6	5	$[+45/0/\text{-}45]_{2S}$	$[X, X_D, X]_T$
PD-B2-0#	AS4	3501-6	4	$[+45_2/0_2/\text{-}45_2]_S$	$[X, X_D, X]_T$

[a] '#' is a wildcard character representing a single letter.
[b] 'D' indicates dropped sublaminate.

specimen, one 3.54 inches from the top of the specimen and the other 2.85 inches from the top of the specimen, both centered on the width. A pattern for optical strain mapping is placed on the back face of each specimen. Pictures of the back face are captured throughout the tensile test and are used by the strain mapping algorithm to determine the strain-field history. Each test was stopped when ultimate failure (breaking into two pieces) of the specimen occurred or when a 10% drop from peak force was observed, whichever occurred first, with the exception of two specimens, PD-A1-06 and PD-B2-05, which were loaded until the first damage was detectable by the experimenter. This was equated to the first cracking noise being heard.

Chapter 5

Procedure for Documentation and Recording of Damage

The goal of the damage documentation procedure is to fill a void in the testing of composites by establishing a unifying method for documenting and reporting damage in specimens. The developed procedures offer ways to compare damage both qualitatively and quantitatively, and allow lengthscale effects to be better investigated across the levels of composite testing. A framework to enable investigation of lengthscale effects is established within these procedures by documenting factors that may influence damage mechanisms. The information from the procedures is used to initialize the comparison database, where researchers can investigate trends in damage across levels associated with composites. The development of this novel procedure to document and record damage in composite specimens, and the framework and initial implementation of a database enabling lengthscale investigations is presented in this chapter. A nondestructive technique, relatively newly applied to composite materials, used in investigating damage in specimens within this work is also described.

5.1 Damage Documentation Procedure

The procedure developed to document the factors of each test has a number of primary steps. The characterization portion of the procedure is used to investigate the 'active' damage modes, where an 'active' damage mode refers to a mode of dam-

age present ("turned on"/"at work") in the specimen. Answers from the question tree were used to identify the damage modes possible in composites, and also to distinguish the visual appearance of each of the modes. The goal of the set of characterization procedures is to provide a quantitative and qualitative description of the damage in the specimens. The extent of damage is compared across the specimens using the quantitative information. Active damage modes, mode interactions, and damage paths are identified and compared using the qualitative information. The procedures developed to document specimen testing for lengthscale investigation include taking digital photographs of the specimens and documenting the damage from these photographs by creating damage grids and damage sketches. While developing the procedures, it was important to realize that the goal of these procedures is to allow the gathered damage information to be placed into a comparison database, ultimately enabling lengthscale investigations. The development of a framework, and the initial implementation of such a database is discussed in Section 5.2. The details of each component of the procedures are further described in the following subsections.

Initial development of damage documentation procedures utilized the NRL single-edge-notched specimens described in Section 4.1. Further refinements to the procedures were made once the other experimental specimens were manufactured and tested. The decision to use specimens from a previous NRL study was made primarily because these tested specimens and the associated results were immediately available at the time the procedures were being initiated. In addition, the single-edge-notched specimens were made of the same (or similar, in the case of items with AS1 fibers) material, and were of similar stacking sequences used for the other specimen types. They were also at the baseline level being used in the work, and were of a similar geometry as the other specimens considered during this work. These specimens also exhibit multiple composite damage modes, thereby allowing diverse characterization.

The first step in developing the procedures involved identifying and considering the factors involved in composite damage. Answers to the question from the A.3.3 branch of the question tree ("What are the contributing factors of composite damage at each level?") were identified during the literature review. This helped to identify

factors involved with damage at various lengthscales. Examples of such factors are the influence of ply thickness on matrix cracks, the influence of neighboring ply angles on delamination, and effects of the level of specimen size [2, 4, 72]. In order to completely investigate all factors that could be associated with lengthscale effects, it is important that the documentation procedures be able to capture these factors. Factors such as the specifics of the fiber and matrix materials, laminate stacking sequences, specimen geometries and features (e.g., holes, ply drops, strain risers), and load histories of specimens were determined important to document. It is also desirable to document the damage initiation, progression, and final failure.

The developed damage documentation procedures capture these factors. The procedures begin by visually documenting the state of a specimen with a photograph. The photograph enables the information contained in a visual inspection of the specimen to be documented. Two images are then created, using the photograph, to document the quantitative and qualitative aspects of damage. The first image is the "damage grid," which is used to quantitatively document the extent of damage in the specimen. The second image is the "damage sketch," which captures the qualitative features of the damage. These components are combined into a single, "layered" image, with each component being a separate layer.

The final documentation image contains four different layers: layer 1 is the base documentation photograph layer, layer 2 is the damage grid layer, layer 3 is the damage sketch layer, and layer 4 is the axes layer. Each layer above the base documentation layer can be thought of as a transparency that can be placed on top of the base layer, as well as on top of other layers. An illustration of the layers used in the documentation procedures is shown in Figure 5.1. These layers are created and manipulated via an image-editing software. These layers have the advantage of being modified separately from the documentation photograph, thus preserving the documentation of the specimen. Additionally, each layer can be "turned on" or "turned off" to allow the different aspects of the documentation procedure to be investigated.

Details on each of these layers are provided in the following subsections. Note that the bottom layer in the image is the documentation photograph. Once the docu-

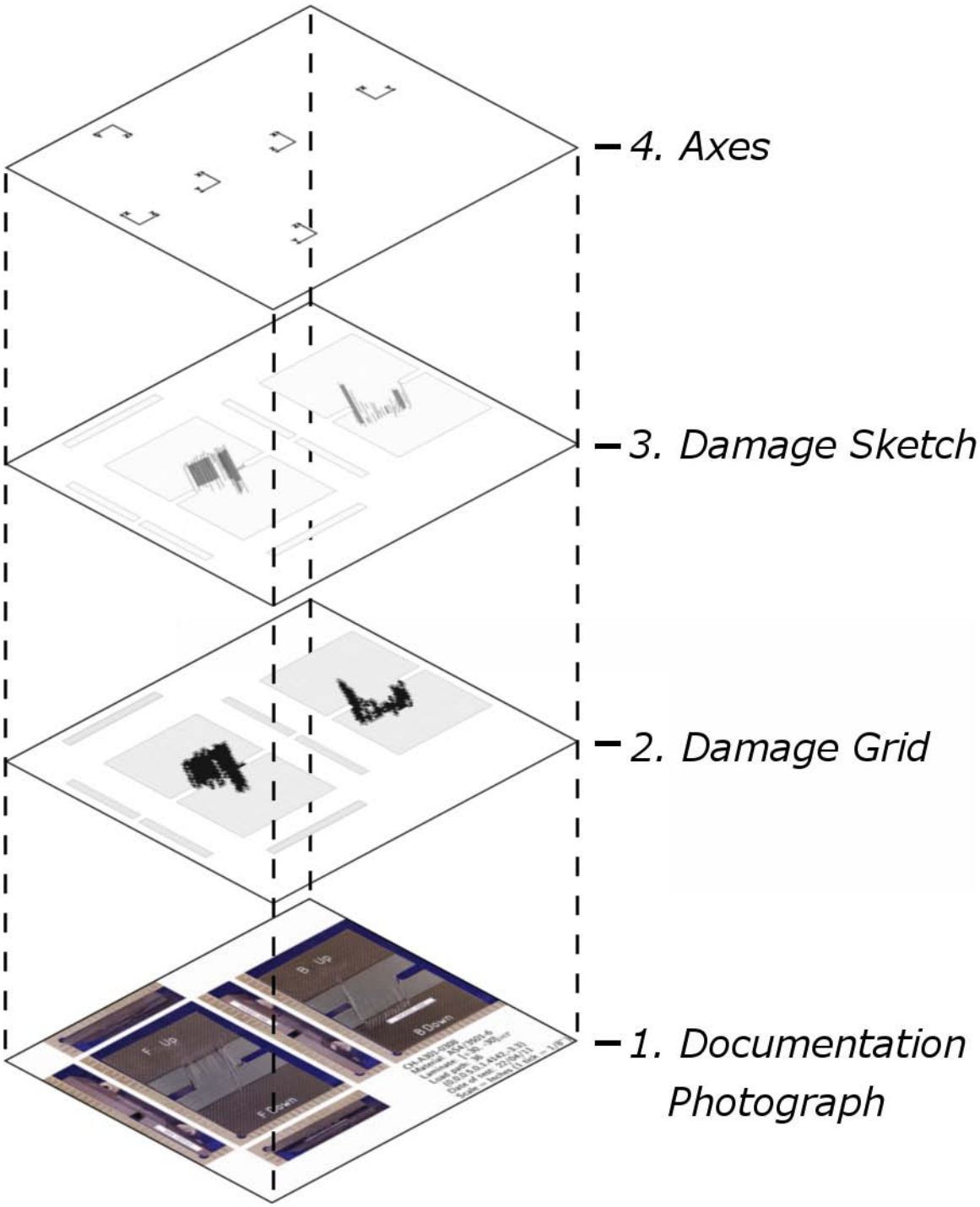

Figure 5.1 Illustration of the layers used in the documentation procedures.

mentation photograph layer is created, following the steps described in Section 5.1.1, this layer should not be edited in any way. Doing so would compromise the documentation.

5.1.1 Photograph Documentation

The first part of the documentation procedure involves photographing each of the surfaces of the tested specimen. Using digital photographs, instead of the physical specimens, to perform visual inspection has the key advantage of the ability to look at the specimens from any geographical location (shared electronically). This provides an easy means to discuss specimen damage details with researchers at other locations without having to send the specimens. Another advantage of using the digital photographs is the ability to manipulate the image for various reasons (e.g., to zoom in, up to the resolution limit when the image gets too pixilated, on areas of interest, such as areas showing possible damage) while the original state is unaltered and always available. In addition, the details are preserved and can be further examined even if destructive examination is done after documentation.

Several components are needed for a setup for such photographing. The first component is a camera. The key in choosing a camera is to look towards maximizing the resolution and, hence, detail of the specimen surface. One should look to provide a few pixels of resolution below the lengthscale of the damage to be encountered and/or of interest. In addition, specimen size, or size of structural detail of interest comes into consideration when setting focal length, and is a mix with the size of the specimen to be captured within one picture, and thus the numbers of pictures that must be taken in order to capture the full area(s) of interest. The number of pictures also relates to the amount of time needed, and the ease of the work.

A Nikon D60 DSLR camera with a NIKKOR DX AF-S 18-55 mm lens and a generic ultraviolet filter was used to photograph all the specimens of this work. The camera is placed in "Manual" mode to maintain consistent settings amongst the specimens. The camera settings are as follows: image quality set to fine, image size set to large, shutter speed set to 1/1.3, aperture set to F9, ISO sensitivity set to 100,

exposure and flash compensation both set to zero, and active D-lighting turned off.

The next component necessary in the documentation procedure is the lighting of the specimen. A direct light source, such as a flood light or a flash, can produce glare on the surface of the specimen, thereby interfering with the specimen documentation. Therefore, a diffuse light should be used, as this allows damage to be more easily and better seen in the photographs. In cases where the specimens are small in scale (as are the baseline specimens in this project), the specimen may be placed in a photographic light tent to produce diffuse lighting on the surfaces. For larger specimens, the use of a photography softbox can provide the necessary lighting. All specimens documented during this work fit within a 16-inch light tent, with two 50 Watt GU-10C halogen lights illuminating the tent walls. The tent and lights came as a generic kit available on Amazon.com (ASIN: B0027OUOVW). The tent opens to a cubic shape, with three sides made of a white, light-diffusing fabric. The base is made of a black fabric, and the top and front side open (no fabric). The open top permits the camera and tripod to be positioned over the specimens, and the open front side permits access to change the specimen to be photographed. The halogen lights are positioned outside the left and right sides of the tent. The resulting light intensity of this setup is 1160 lux measured at the center of the tent, at the height above the table that the specimen surface is photographed. A picture of the camera and light tent setup is shown in Figure 5.2.

The final component necessary for the setup of the camera is a fixed stand. By fixing the distance between the camera and the specimen for each specimen type, photographs of the same scale are produced. To capture the scale of the photographs, it is also important to provide a length reference in each photograph. This length reference will depend on the size of the specimens. If large numbers of specimens of the same geometry are being documented, using the same setup (e.g., camera settings, lighting) allows downstream processing of the photographs to be systematic. For this work, a Swanson (TS 157) 16 inch by 24 inch steel carpenter square is used to provide the scale, straight edge, and 90° corner. In addition to the camera setup, the specimen orientation must also be consistent. A reference to some angle pertinent to

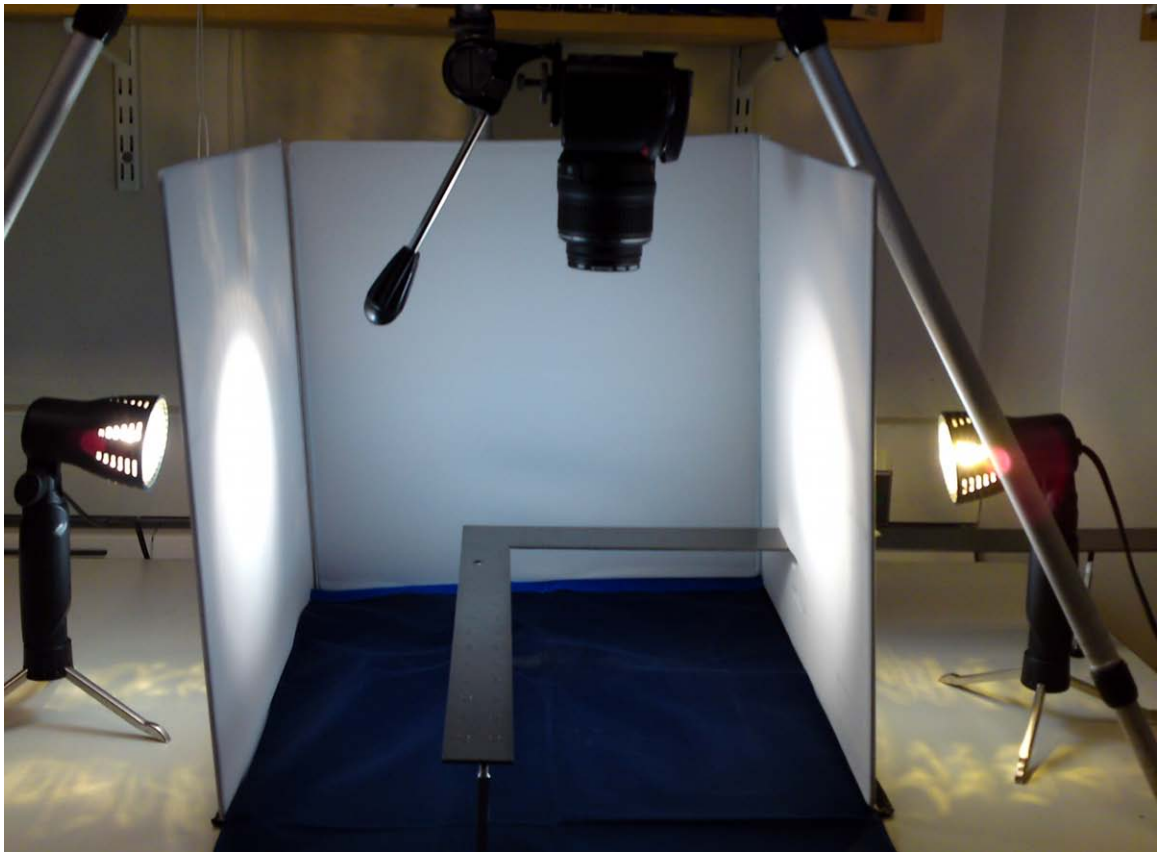

Figure 5.2 Photograph of camera and light tent setup for photographing experimental specimens.

the specimens must be established. This reference depends upon the type of specimens to be characterized. In general, it is suggested to be relative to ply angles and/or associated directions. For the specimens in this work, the 0° angle is defined along the x-axis, which corresponds to the length of the specimen, the y-direction is along the specimen width, and the z-direction is in the out-of-plane/through-thickness direction. The two edges of the square are aligned with the corresponding axes (depending on which specimen face is being photographed). All ply angles are defined relative to the 0° direction, which is clearly captured in photographs as one of the edges of the square, using a positive counter-clockwise convention.

Once the documentation via photographing is complete, the digital photographs are transferred from the camera to a computer. An image-editing software can be used to edit the digital photographs. GIMP (GNU Image Manipulation Program), a free image-editing software, is used throughout this work. The software allows simple manipulation of the stored photographic information. However, it is very important not to alter the documentation of the specimens while using the editing software. Editing actions should be limited to operations that do not change the appearance of the specimen. For example, it can be found that the documentation photographs have excess white space around the specimen faces. The image-editing software can be used to remove this irrelevant area by cropping the photographs to the size of the specimen face. Other such procedures can take place to process large batches of photographs automatically. A computer code can be developed that runs within the image-editing software. The specifics of the code are dependent on the details of the specimen.

Two sub-procedures exist as part of the photograph documentation in order to handle two classes of specimens; one, specimens that break into multiple pieces, and two, specimens that exhibit large planar deformations without breaking into multiple pieces. The sub-procedures are not applied to all specimens. These sub-procedures are developed in order to provide a consistent means to handle specimens that had failed into two or more pieces during testing, and to have a consistent manipulation of specimen images in order to return the planar dimensions to the virgin (untested) di-

mensions. These sub-procedures make the procedures more generally applicable, and thereby capable of being implemented across a wide range of composite specimens.

The first sub-procedure is a means to more consistently and clearly handle specimens that had failed and pulled apart into two or more pieces during testing. Following the photograph documentation procedure previously described, each individual specimen face is photographed. With failed specimens, additional surfaces below the original specimen surfaces are exposed due to the manner in which the laminated composite specimens fail (e.g., combination/interaction of the basic damage modes through the specimen thickness). Specimens can be separated into two, or more, pieces during failure. This separation can result in multiple ply surfaces being exposed. Such a case is shown in Figure 5.3. This is a CRC-ACS open-hole tension specimen, that had been loaded to ultimate failure, resulting in the specimen being broken into two pieces. The spotted pattern observed on the outer ply is an artifact from the optical strain mapping technique. As is visible in these photographs, due to the complex failure paths of composites, there are jagged edges at multiple layers. In order to set up the photos for implementation of the damage grids and damage sketches, discussed in Sections 5.1.2 and 5.1.3, it is necessary to recombine the broken pieces back into a "single" specimen.

Three basic methods for rejoining the specimens were considered. The first was to physically work to puzzle the broken specimen pieces back together. However, due to the extent of damage and deformation in individual layers of the composite, physically puzzling two (or more) specimen pieces back into one can be a difficult task, and would likely result in additional damage being introduced. The second idea was to modify the damage grid and damage sketch procedures to accommodate broken specimens. However, doing this would have resulted in inconsistencies (e.g., noncontinuous damage paths, possible overcounting/undercounting of damage grids) that would make comparison between unbroken and broken specimens misleading.

The third idea, which is included in the documentation procedure, involves "virtually joining" the individual pieces of the specimens. It begins with taking surface photographs of each of the broken specimen pieces, being sure to include consistent length

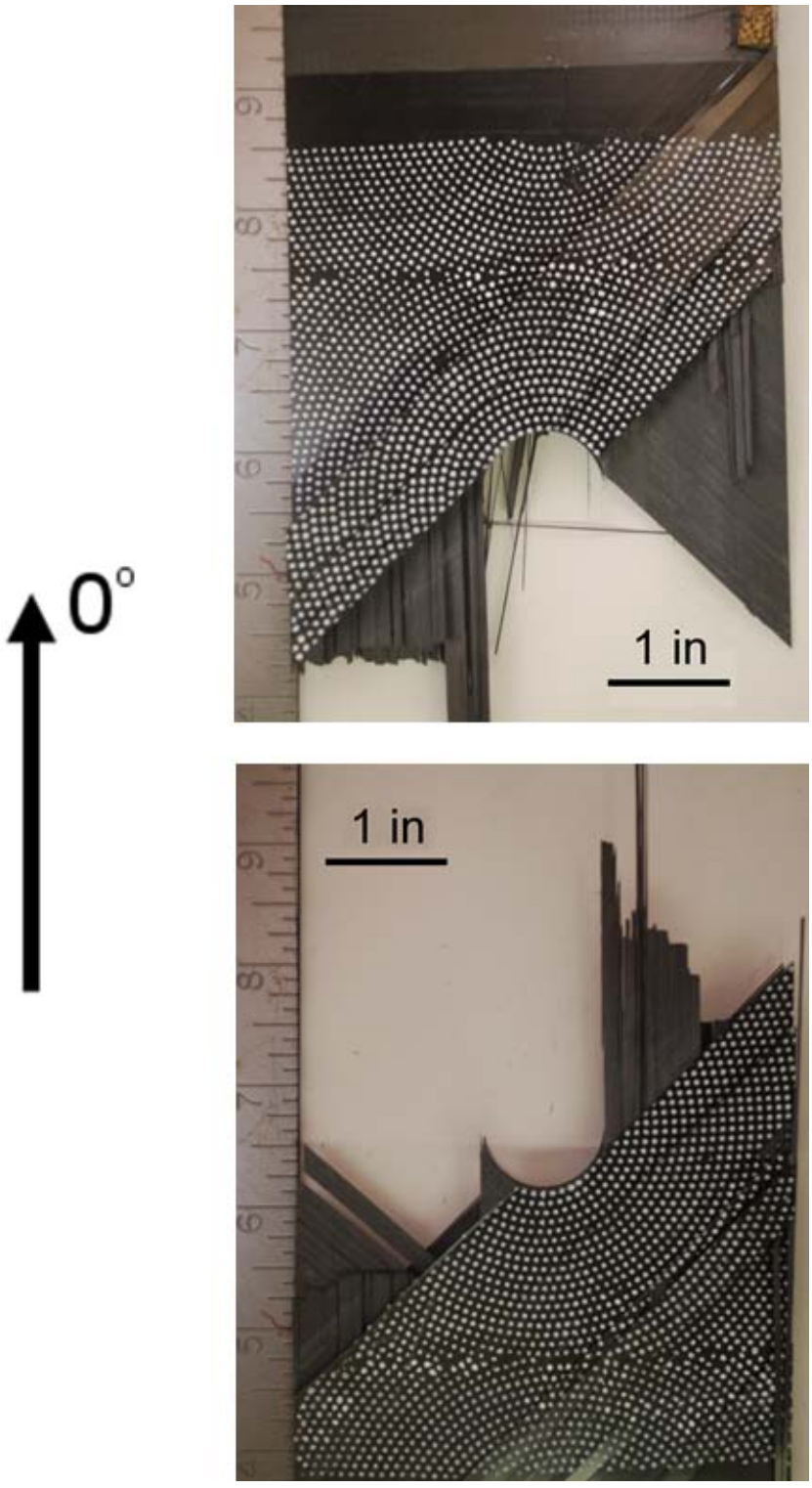

Figure 5.3 Photographs of a failed open-hole tension specimen (OH-B104-04), with hole diameter of 1.0-inches, showing *(upper)* actual back, upper-half face, and *(lower)* actual back, lower-half face.

references. The specimen pieces are then "digitally joined" using photo-editing software. This requires establishing a "joining template" to recombine the photographs of the broken surface. This joining template is established for the primary plane of the specimen using the dimensions of the virgin (original) specimen. It is desirable to use a width and length dimension based on preselected references on the specimen. The actual width of the specimen is used herein. However, since this procedure did not exist when these specimens were tested, a general length reference on the specimens did not exist. In the case of open-hole specimens, the hole can be used as a length reference in combination with a lengthwise edge of the specimen. The joining template for an open hole specimen using its back face and these references is illustrated in Figure 5.4. Dashed lines represent the template references.

The next step in the "virtual joining" procedure involves positioning the surface photographs from this perspective into the template. Each individual photograph is positioned within the template using the template references in relation to that dimension of the specimen in the photograph. A different "layer" within the photo-editing software is used for each photograph at this stage to allow for individual positioning.

The first photograph to be positioned is that of the piece containing the lengthwise edge that is used in referencing the position of the hole. The widthwise edge of the specimen is placed against a ruler with the lengthwise edge placed against a square at the point of "0" on the ruler. The joining template is moved relative to the photograph of the specimen so that the reference of the hole is placed against the hole edges visible in this photograph. This repositioning allows the location of the midpoint of the hole to be determined relative to the ruler in the photograph. This ruler is digitally placed along the width of specimen pieces in other photographs using the midpoint of the circle of the joining template as a reference relative to the ruler, and then positioning the specimen hole edges aligned with the circle of the joining template.

These individual layers are subsequently overlapped using the joining template as a guide. This results in overlaps of the surface photographs similar to overlapping

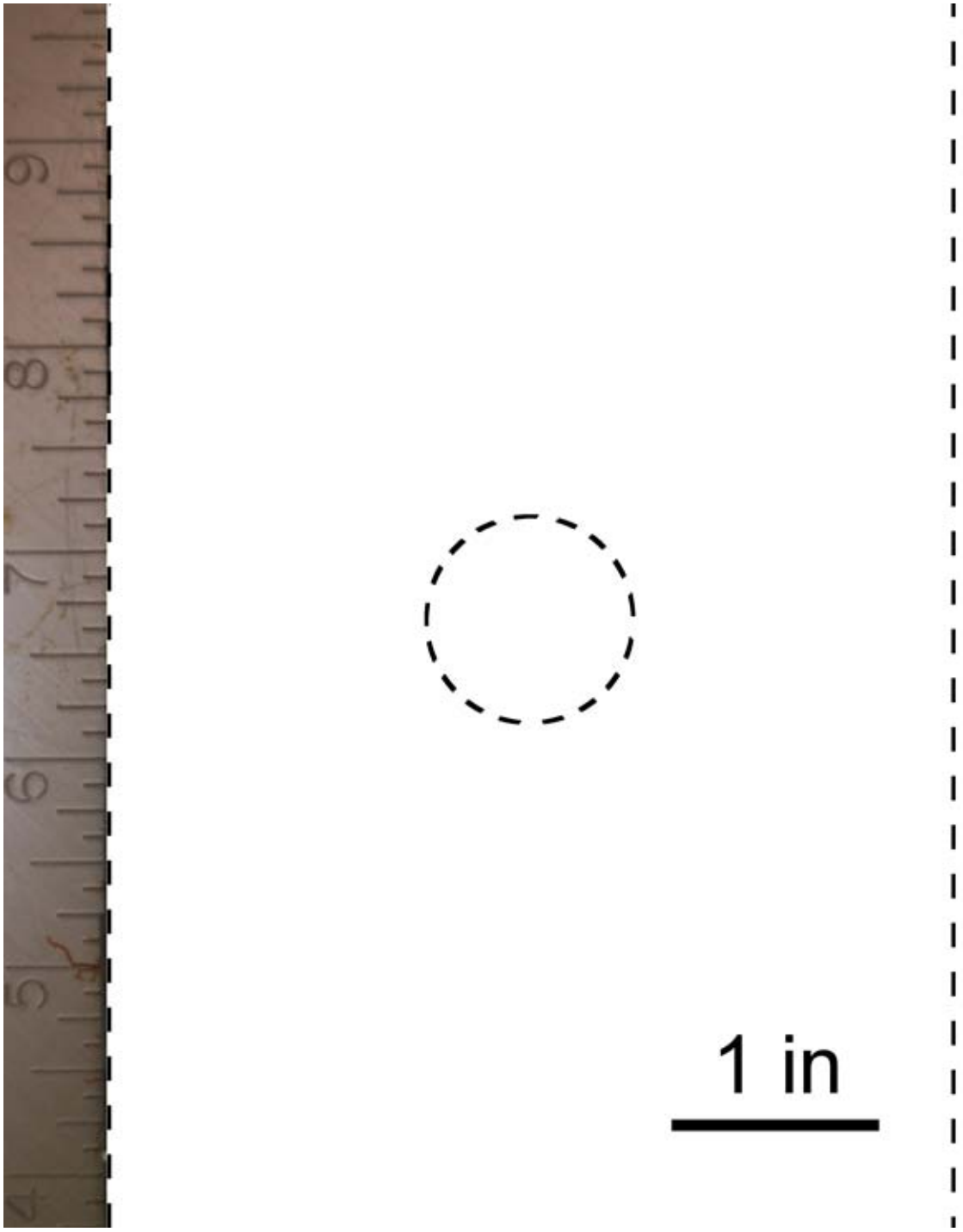

Figure 5.4 Illustration of "joining template" for open-hole specimen with hole diameter of 1.0-inches.

photographic slides, projecting light through them, and viewing that result. The measurement item (ruler in these cases) in the photographs is used to determine the distance that the individual photographs are moved in this process by comparing the ruler point that the midpoint of the circle intersects. This distance is then used to join the other photographs of the specimen surfaces. In the case of the open hole specimen, there are three other surfaces: front, left, and right.

However, since the purpose of this process is to document damage, the individual photographs are not brought together completely to their original length. A slight "offset" is required in order to clearly show damage for subsequent consideration. Completely returning the specimens to their original length could "mask" the damage, making it difficult to see the damage in the documentation photos. In setting this "offset," there needs to be a balance between clearly showing the damage that occurs, while properly representing the damage that would be visible. An offset of 0.01 inches is used for the specimens that are "virtually joined" during this work. This offset is in the 0° direction for all points along the specimen width. For cases requiring virtual joining, this offset achieved a balance in maintaining a visible damage path in the documentation photos while minimizing the "opening" of the specimen. A smaller offset results in cases where the damage "disappears," and is no longer visible within the photograph documentation. A section of the front face photograph documentation of a specimen that broke into two pieces and is virtually joined with and without an offset is shown in Figure 5.5. The photograph documentation in the upper figure has an offset while the lower figure completely closes (no offset) the opening. The visual damage on the front face of this specimen is a dominant matrix crack, which typically has a very straight damage path. Without using an offset, such damage paths becomes very difficult to visually identify.

The final step in the "virtual joining" procedure involves the determination of the surfaces that would be exposed based on their place in the specimen relative to the outer surface being considered. This process requires an objective judgment to determine which layers would be visible (determined by considering the stacking sequence and which layers are closer to the surface), and cropping out the material

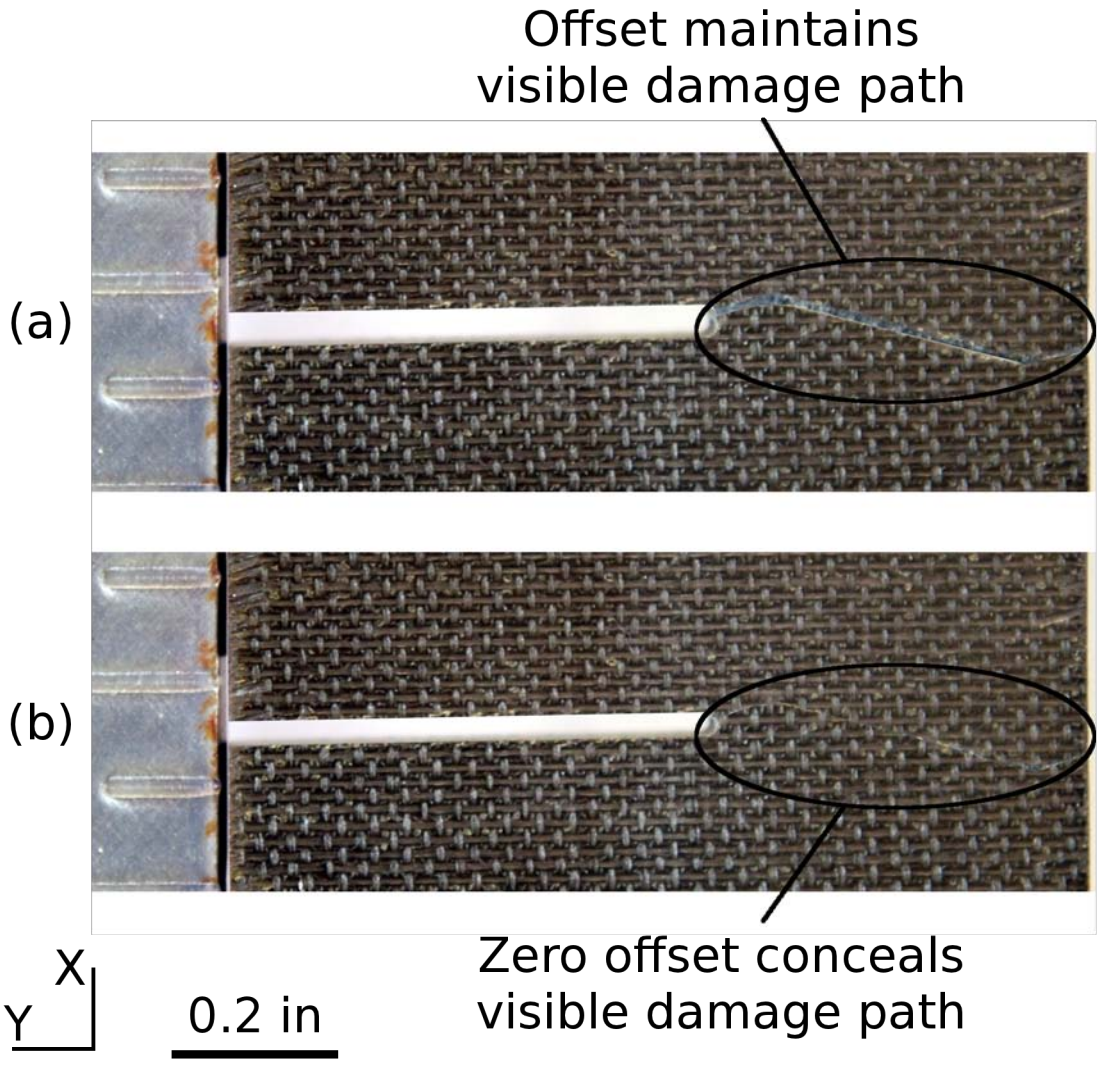

Figure 5.5 Photograph documentation of the front face of a specimen (single-edge-notched specimen 001-39), *(a)* with an offset of 0.01 inches, and *(b)* without an offset.

that would not be visible. Items determined to be below/under items are digitally deleted from the two images until only the item closest to the surface of consideration remains. This process results in one final view of that particular surface. Although this view is one integrated view, it is only integrated through the imaging of the software. The individual photographic pieces remain, and can later be consulted as needed.

An example of this "virtual joining" procedure is shown using the open-hole tension specimen (OH-B104-04), as tested at CRC-ACS, with a hole diameter of 1.0-inches. The original photographs of the two pieces of the back surface as failed are shown in Figure 5.3. The joining template, using the measured specimen width and the measured hole diameter as references, is shown in Figure 5.4. The individual layers as positioned within the joining template are shown in Figure 5.6. Portions of these layers are then digitally deleted until only outer layers that would have been visible can be seen. The resulting "virtually joined" back face of this specimen is shown in Figure 5.7.

With this virtual joining process, the damage documentation procedure can be applied to specimens that break during testing. This allows the damage data from such tests to be worked in order to be included in the comparison database with a consistent reference.

A second sub-procedure to the photograph documentation procedures is the normalization of the damage grid and damage sketch dimensions. In specimens containing damage paths through their entire thickness, changes in planar dimensions from the virgin (untested) dimensions can occur. This is, of course, also true in all specimens that separate into more than one piece upon failure. This change in dimensions can result in a change in the surface area being characterized by the damage grids and damage sketches. The change in area causes the extent of damage being compared across the same specimen type to be inconsistent. Consider the specimen shown in Figure 5.8 as an example. This is an open-hole tension specimen with a hole diameter of 0.5 inches. The hole in this failed specimen has become slightly elongated due to failure. This elongation can be ascertained by considering the photograph

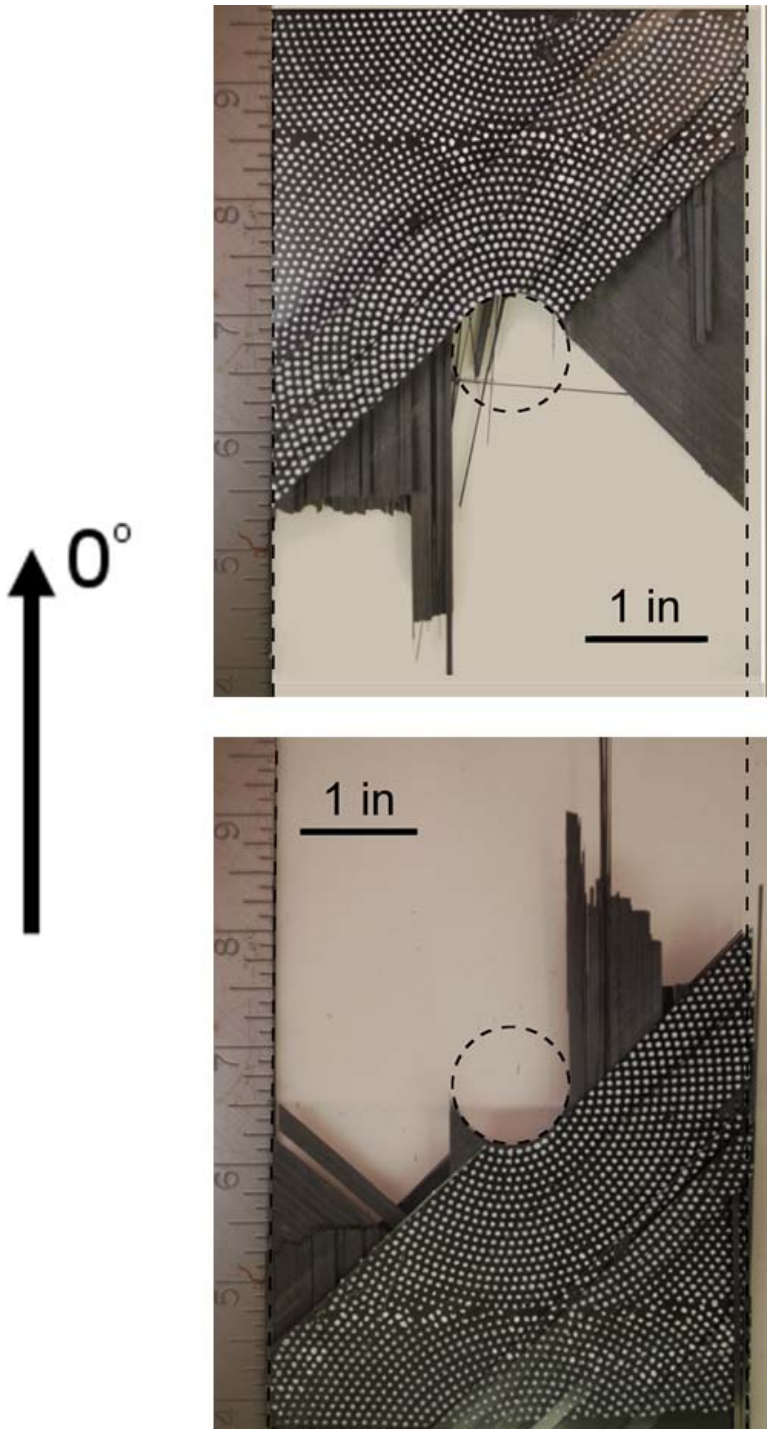

Figure 5.6 Photographs of a failed open-hole tension specimen (OH-B104-04), with hole diameter of 1.0 inches, positioned within the "joining template" showing *(upper)* actual back, upper-half face, and *(lower)* actual back, lower-half face.

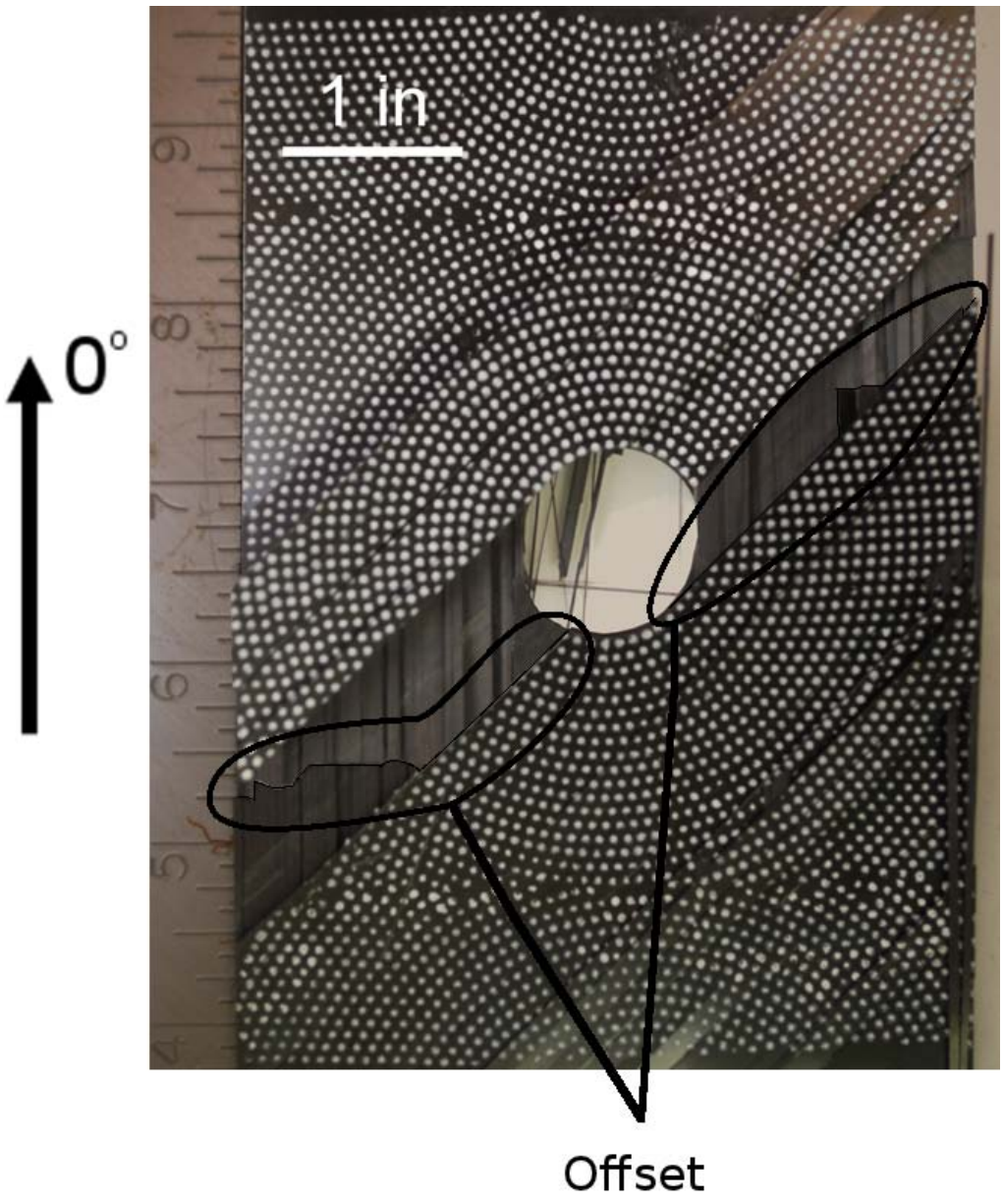

Figure 5.7 "Virtually joined" photograph of failed an open-hole tension specimen (OH-B104-04) with hole diameter of 1.0 inches using "offset" of 0.01 inches.

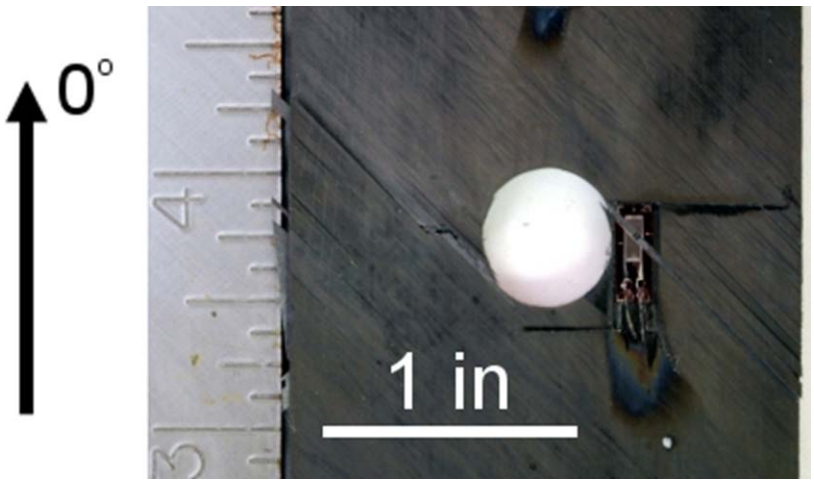

Figure 5.8 Photograph of a failed open-hole tension specimen (OH-A051-01), with hole diameter of 0.5 inches.

in Figure 5.9, where a black circle with the same diameter of 0.5 inches has been superposed on the original photograph.

In order to eliminate this inconsistency from the damage documentation procedure, another sub-procedure was added. This sub-procedure involves digitally editing the damage grids and damage sketches of the specimens back to virgin dimensions. This process is similar to the digital process of the first refinement of "virtual joining," with the change that grids and sketches of specimens that may still be in one piece may need to be "digitally cut" to return the specimen to the original (pre-tested) dimensions.

As described in Sections 5.1.2 and 5.1.3, the damage grid and damage sketch layers are superposed on the photograph documentation layer. The overall size of the grid and sketch, generally in the direction of loading, can be altered due to the failure process as the specimen has slightly changed size. The grids and sketches must therefore be digitally edited to return them to virgin dimensions. As is required in the "virtually joining" sub-procedure, virgin dimensions of the specimen are needed. In addition, the virgin dimensions of any structural details (e.g., open hole) can be an asset in the process. Using these references, the recordings of the post-tested specimen can be digitally returned to the virgin dimensions, thus allowing a consistent surface area comparison across specimens of the same geometries.

A key difficulty in this process is determining the locations at which to "digitally cut" the specimen to return the recordings back to the virgin dimensions. These locations generally needed to coincide with dominant damage as manifested at the multiple surfaces of the specimen. In the process, each surface of the specimen is considered individually as to location of cutting, although the distance that pieces are moved is consistent across all surfaces. For example, in some specimens, a dominant matrix crack ran along the surface plies of the specimen with a combination of damage (i.e., delaminations, matrix cracks, fiber fractures) occurring in plies below the surface. This combination of damage allowed the specimen to be "pulled apart," with two sections of the specimen opening along the dominant matrix crack. In such cases, the digital cut was to be made along the dominant matrix crack allowing the crack

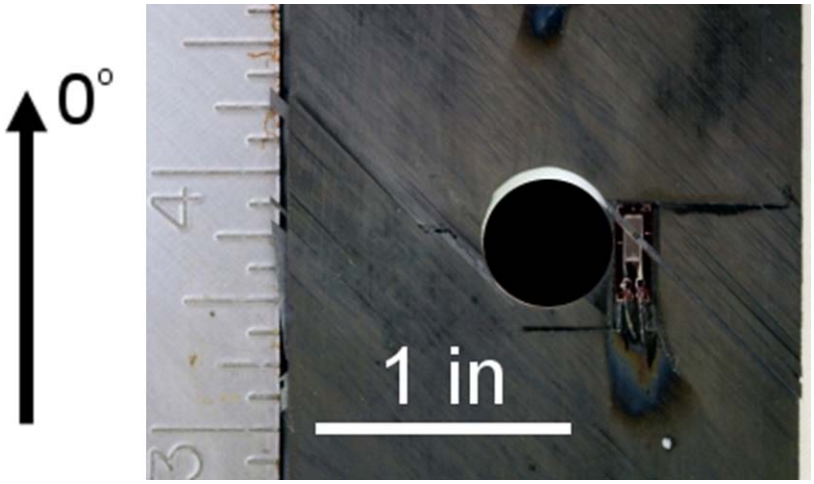

Figure 5.9 Photograph of a failed open-hole tension specimen (OH-A051-01), with hole diameter of 0.5 inches, including superposed black circle of diameter of 0.5 inches.

to be "closed," while maintaining the offset defined for the "virtual joining" sub-procedure. This thereby returns the specimen to its virgin dimensions compensated for the offset. In other specimens, there was no clear matrix crack on the surface, but rather a series of parallel matrix cracks that can "bend" to allow the surface ply to comply with the plies below the surface which "open." In these cases, a mapping procedure was developed to map the surface damage from the stretched specimen back to the virgin dimensions.

This overall mapping procedure is developed and used in specimens that exhibit such a failure. The specific length of the adjustment is one particular issue that was addressed during this work. In the case where the specimen requires the first refinement of "virtual joining," this adjustment length was defined by the offset length as previously discussed. When a structural detail exists in the specimen, the apparent change in this structural detail after failure can be used as the adjustment length. However, there are other situations, such as an unnotched specimen, that require a length reference to be placed on the specimen surface before testing. Such details need to be planned and worked into project specimens ahead of testing.

As an example of the mapping procedure, one of the OHT specimens exhibited a dominant matrix crack propagating from the hole to the outer edge on one side of the specimen, but had a series of parallel matrix cracks that "bent" to allow the specimen to "open" on the other side. The documentation of the specimen is shown in Figure 5.10. As can be seen on the front surface (indicated in the figure), there is a dominant matrix crack, propagating on the right side of the hole, with an "opening" where the specimen has been partially pulled apart. However, there is not a single dominant matrix crack to the left of the hole. Instead, a series of parallel matrix cracks have formed and allowed the top ply to "bend" in that vicinity. In order to maintain consistent damage grids and damage sketches, the mapping procedure maps this damage back to a "closed" specimen. Two enlarged photographs showing a section of the front surface of the specimen shown in Figure 5.10, concentrating on the dominant matrix crack to the right side of the hole, are shown in Figure 5.11. The upper image shows the "opening" of the specimen, and the lower image shows the

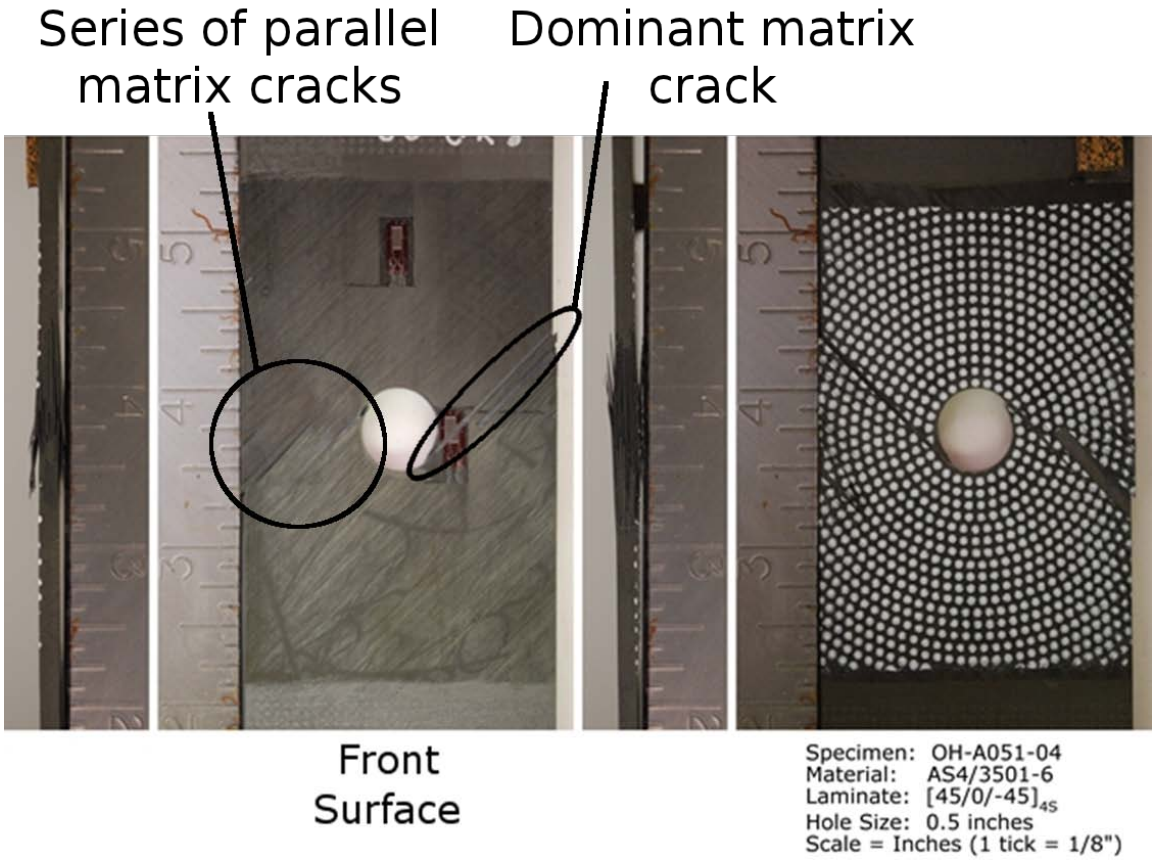

Figure 5.10 Photograph documentation of an open-hole tension specimen (OH-A051-04).

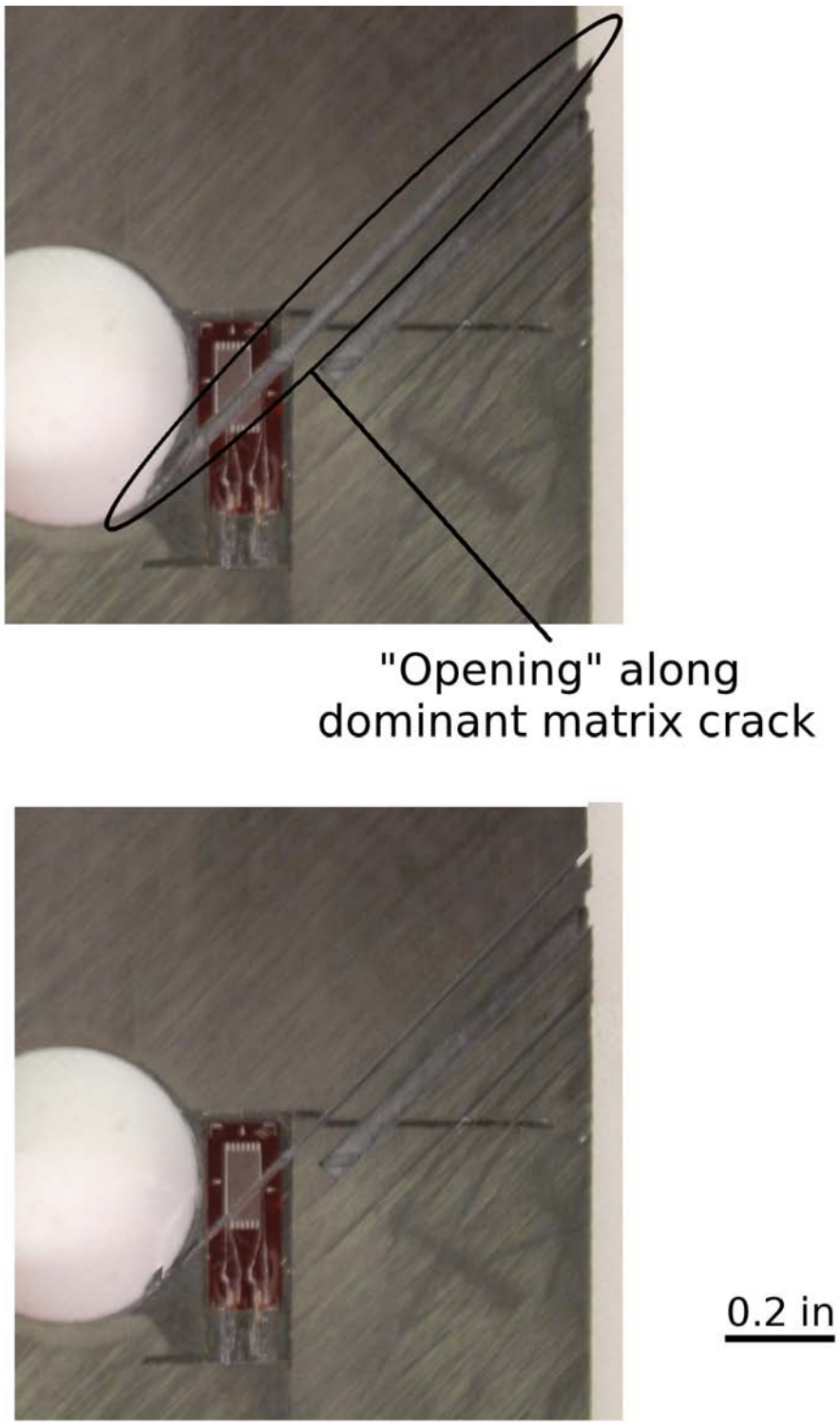

Figure 5.11 Enlarged view of a section of the front face of the OHT specimen shown in Figure 5.10, *(upper)* before mapping procedure, *(lower)* after mapping procedure has "closed" face back to virgin dimensions.

face after being mapped to the "closed" configuration (maintaining an offset to ensure a visible damage path). The damage sketch of this specimen, shown in Figure 5.12, is than completed using the "closed" configuration. This can be seen by observing the location of the dominant matrix crack, which, in the damage sketch, is now a single matrix crack (as opposed to the "opened" matrix crack observed in the documentation photograph of Figure 5.10). Also, the bent matrix cracks to the left of the hole have been mapped back to straight matrix cracks.

The two sub-procedures to the photograph documentation procedure are made to make the overall procedures for damage documentation more robust, and to enable the procedures to be implemented on a broader class of composites specimens. This includes specimens that break into multiple pieces during the testing, and specimens that are "stretched" during the loading. With the two sub-procedures in place, consistent photograph documentation is accomplished for specimens exhibiting dimensional changes, permitting the subsequent documentation procedures to be uniformly applied.

The layout for the documentation photographs is similar to an engineering drawing, showing an unfolded multiview projection. The image shown in Figure 5.13 is an example of the layout used for the photograph documentation. As in an engineering multiview projection drawing, each face is shown at the same scale. The individual faces are labeled in Figure 5.13. The bounding box of the figure captures the boundaries of the layer, where all information within the boundaries makes up the extent of the layer. Information outside the boundaries are not a component of the layer. The boundaries of the damage grid layer, the damage sketch layer, and the axes layer are determined by reference to the boundaries of the photograph documentation layer, which are established to surround the multiview photographs of the specimen faces. These bounding boxes are added to each layer shown in the remainder of this chapter to visualize the boundaries of each layer. These boundaries are used to orientate layers when superposing. The image shown in Figure 5.14 is an example of the final photograph documentation created for the specimens of this project. Specific specimen characteristics (specimen ID, material, laminate, loading,

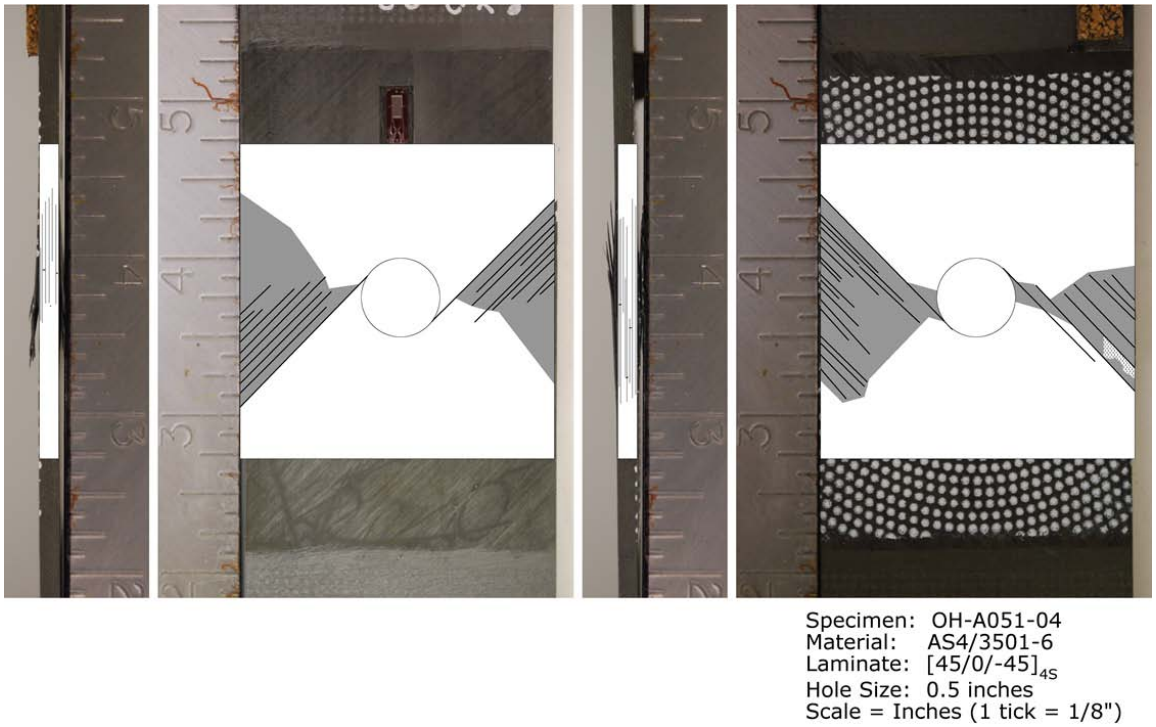

Figure 5.12 Damage sketch of the OHT specimen shown in Figure 5.10 with mapping procedure applied to damage sketch, resulting in specimen being "closed."

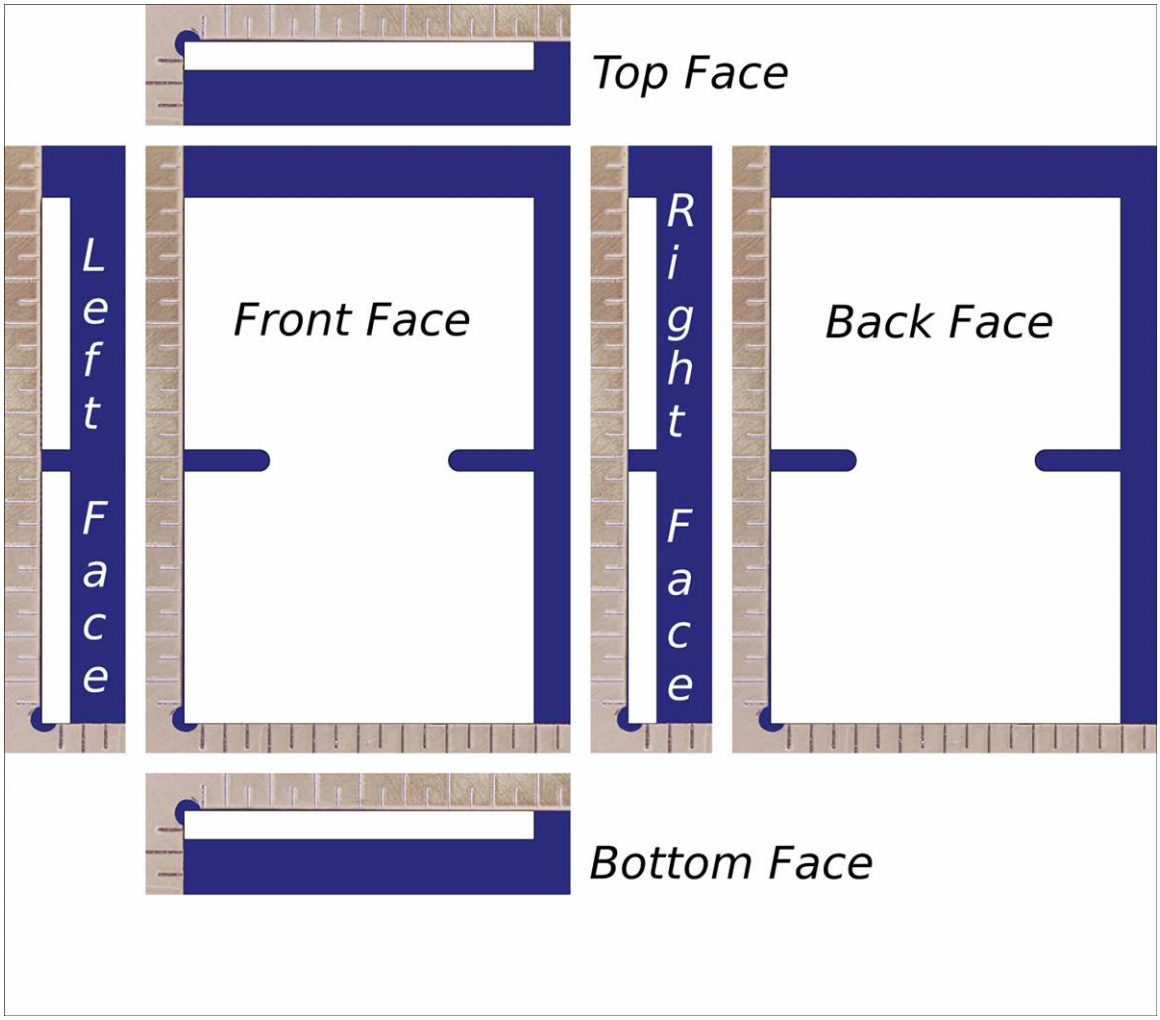

Figure 5.13 Example photograph documentation layout used for the NRL double-edge-notched specimens (outer box shows actual extent of layer).

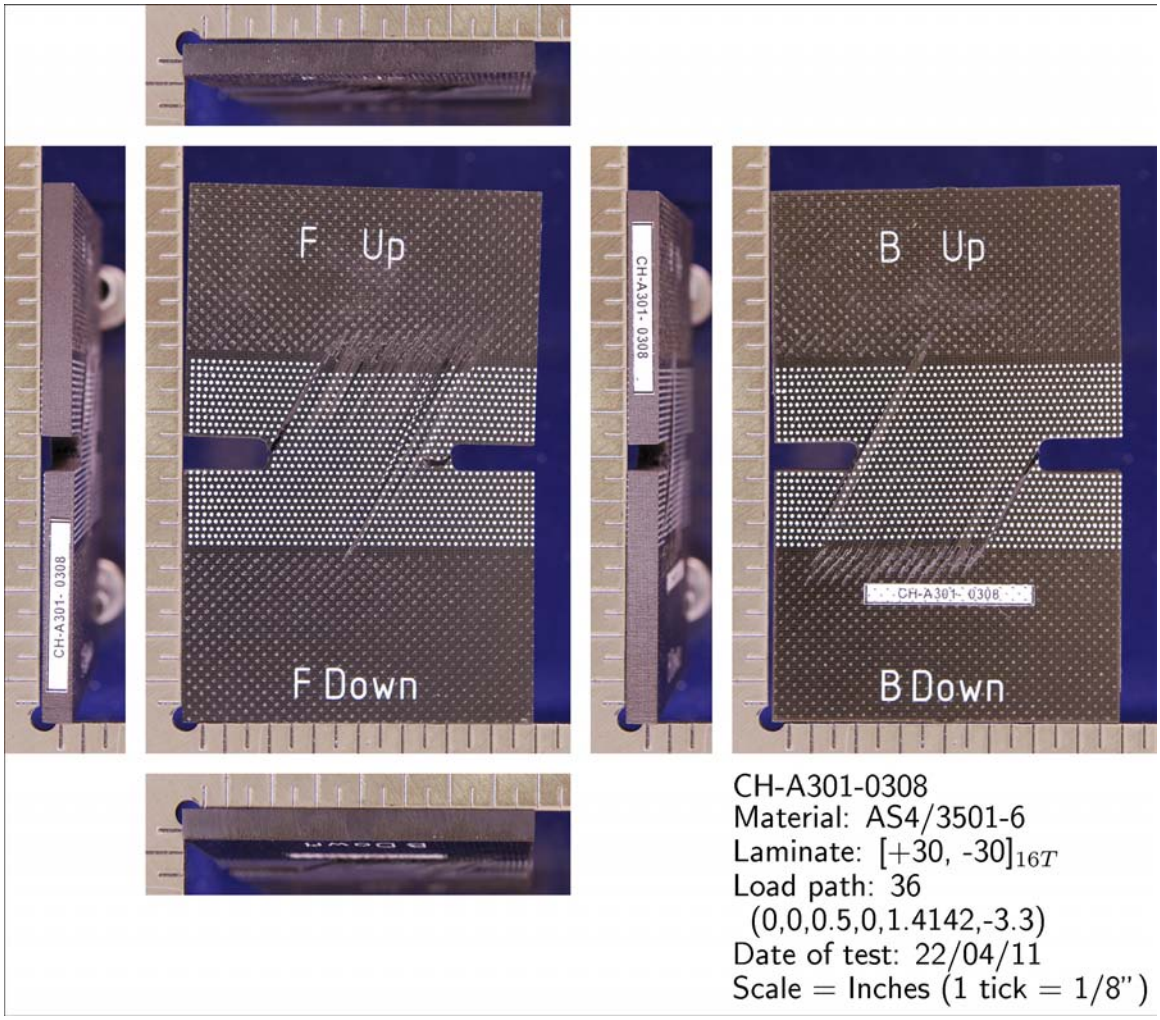

Figure 5.14 Photograph documentation of a typical NRL double-edge-notched specimen (outer box shows actual extent of layer).

test date, and photograph scale) are specified in the whitespace of the documentation photograph. Including this information in the documentation photograph ensures that these specimen characteristics are not separated from the visual documentation.

Once the base layer is established, the axes layer can be added using the base layer as reference. The axes layer contains a coordinate system, with the location of the axes placed manually on the layer at a defined reference location chosen for each specimen type, and for each of the faces displayed. The reference location for each of the specimens of this work is defined as follows. For the single-edge-notched specimens, the coordinate origin is located at the tip of the notch. For the double-edge-notched, open-hole tension, and ply-drop specimens, the coordinate origin is located at the geometric center of the specimen. For all specimens, the x-axis is oriented along the length of the specimen, the y-axis along the width of the specimen, and the z-axis in the thickness direction, as defined in Figures 4.1, 4.4, 4.5, and 4.6 for the specimens included in this work. The axes layer provides a visible coordinate system, providing the orientation of the different views, and allowing specifics of the specimen to be described, such as ply orientation and specimen geometry. An example of an axes layer is shown in Figure 5.15, where the axes are shown completely black to make them more visible. The axes used in the documentation procedures, as shown in Figure 5.17, are white, with a black outline, to make them visible against backgrounds that are either dark, such as the epoxy of the specimens, or light, such as the undamaged damage sketch. The axes locations shown in Figure 5.15 correspond to the example specimen used throughout the following subsections and shown in Figure 5.14. The bounding box, shown in this figure, illustrates the dimensions of the axes layer, and is used to orient the layer on top of the photograph documentation layer.

After completion of the photograph documentation, the photographs are used to begin characterization of damage. An objective approach is taken by first documenting the damage without considering the cause (e.g., type of loading, stacking sequence, material). The damage is determined by visual inspection of the photographs and

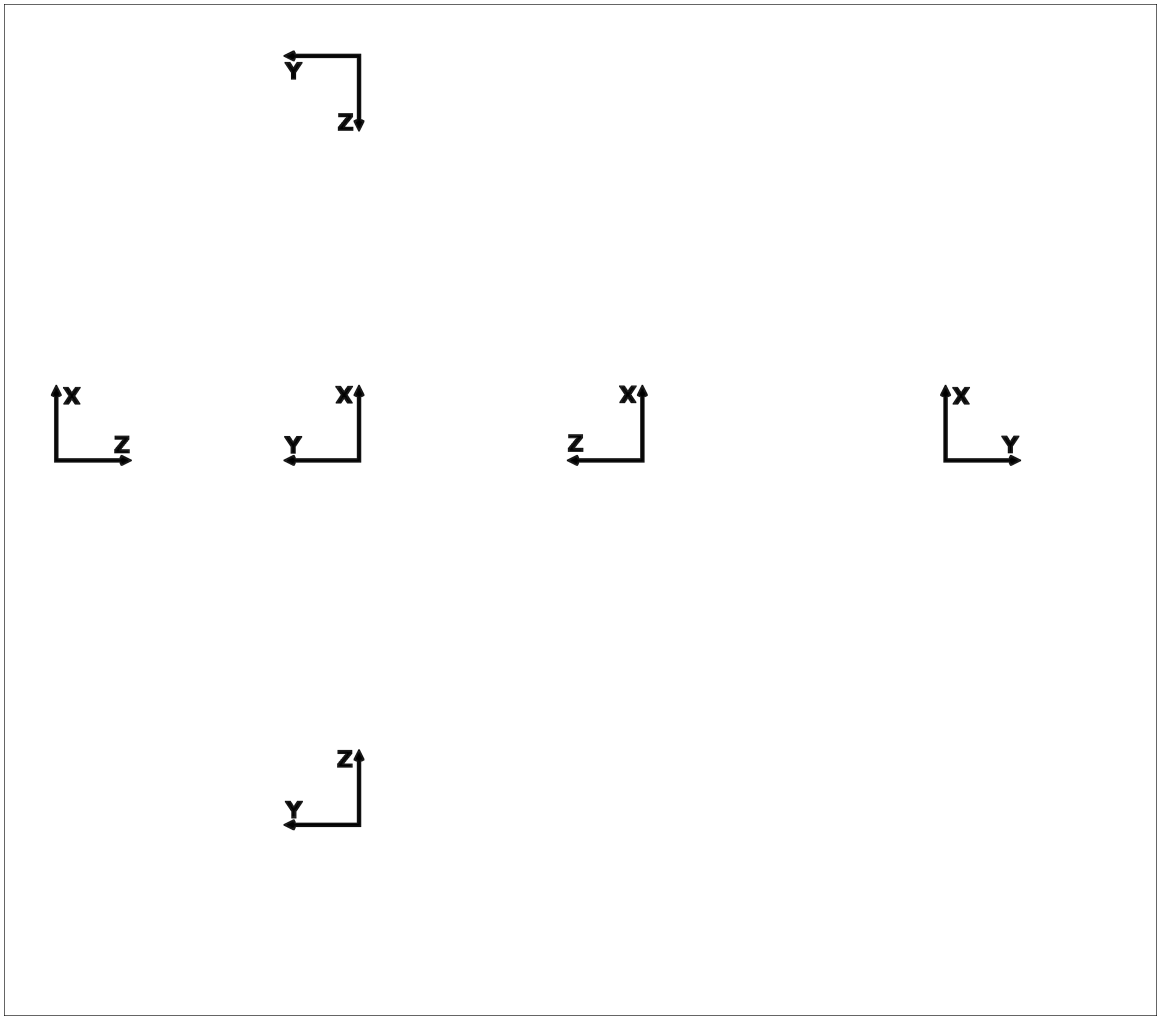

Figure 5.15 Example of an axes layer for a NRL double-edge-notched specimen (outer box shows actual extent of layer).

the specimens are inspected when clarification is needed. The damage modes that can be determined by visual inspection are limited by the lengthscale of the damage. This limits visual inspection to determining the following modes: matrix cracking, fiber fracture, and delamination. The inspector makes the determination of the type and extent of damage in the specimens. The goal of the damage characterization is to document the extent and paths of the 'active' damage modes to allow investigation of the lengthscale effects.

5.1.2 Damage Grid

The first means of documenting damage in the specimens is the use of damage grids. The damage grids provide the quantitative damage measure, allowing an objective comparison of the extent of damage across specimens via specific definitions of the amount of damage. This is done by use of the layers in the documentation procedure as described prior to Subsection 5.1.1. The damage grid layer is added above the documentation photograph layer and below the axes layer. The layer has the same dimensions as the photograph documentation and axes layers, and these dimensions, visualized by the bounding box, are used to align the superposed layers. The grid origin for each face is placed at the corresponding origin of the axes for that face. The grid spacing is selected based on the lengths associated with the damage types, not on the size of the specimen. It was learned from the work on the NRL single-edge-notched specimens that a finer grid spacing is necessary through the thickness of the specimens due to the lengthscales of the damage, and the geometric scale of the specimen on these surfaces. The through-thickness damage is typically interply (delamination) and/or intraply (matrix) cracks. These appear as line cracks along the side surfaces of the specimens during visual inspection. The finer grid spacing provides better quantification of the damage compared to using the coarser in-plane grid spacing. One can argue to go down to the level of ply thickness, but levels that small push the visible limits of unaided visual inspection, as well as the ability to determine the actual location of plies and the same z-location of a ply throughout a

specimen. For the damage grids in this work, the through-thickness grid spacing was half the in-plane grid spacing. This resulted in the through-thickness grid spacing to be approximately 4.9 times the ply thickness. This finer through-thickness grid spacing gave better damage grid resolution on the side faces, whereas if the same in-plane grid spacing had been used, there would have only been about three grid cells through the specimen thickness.

Once the grid is placed on the images, each grid square is characterized as being "undamaged," "partially damaged," or "completely damaged." The three levels are chosen to provide specific levels of quantification in characterizing the damage extent. In most cases where damage is present, the damage partially 'clips' the corner of the grid square. Because the damage grids are providing the quantification for damage extent, classifying a partially damaged square as "undamaged" would underestimate the extent, while classifying it as "damaged" would overestimate the extent. This provides the reasoning for a third classifier of "partially" or "completely" being used in addition to "damaged."

Initially, assigning the classifier to the grids was made by the inspector according to the following definitions in order to make the subjective (captured via the definitions) assignment an objective classification. The classification definitions give a set of rules for the inspector to follow, thereby classifying each grid square based on the facts (visible damage). This provides the objective classification after a subjective decision on damage type has been made. For a grid with damage, the determination between "partially damaged" or "completely damaged" is made based on the damage mode and the amount of the grid that is damaged. For delamination, the grid is assigned "partially damaged" if less than half the grid square is delaminated; otherwise, it is assigned "completely damaged." For matrix cracking and fiber fracture, damage paths are typically narrow and along a line. Thus, the grid is assigned "partially damaged" if the damage does not completely intercept opposite sides of the grid square. Other damage results in an assignment of "completely damaged." The "undamaged" classifier means there is no damage observed in the grid. From these damage grids, the extent of damage of each specimen is quantified.

After applying these rules to the single-edge-notched specimens, the process was automated to provide a faster and more efficient documentation process. This improvement better enables researchers to apply the documentation procedures to damaged specimens, one of the sub-objective (Section 3.1) of this work. A computer code was written to analyze each grid square, and then to use the rules to assign the damage classifier. This code requires a change in the procedural order, where the damage sketches, described in the next subsection, need to be filled in before running the code that completes the damage grids. A consequence of using the objective damage definitions applied to information from the subjective damage sketches is that the process of filling in the damage grids could be completely automated. The code determines the coordinates of the pixels within each grid square, and then analyzes the corresponding pixels from the damage sketch. As is described in Subsection 5.1.3, each damage mode has unique pixel colors assigned, allowing the code to determine the damage type and extent within each grid automatically. The rules defined for assigning a classifier to a grid square, defined in the previous paragraph, are used to set pixel-based thresholds to be used within the code. Take the thresholds defined for use with the delamination mode as an example. The "partially damaged" classifier is assigned to a grid square if delamination is indicated in at least one, and less than half, of the corresponding pixels. "Completely damaged" is assigned if half or more of the pixels in the corresponding grid coordinates indicate delamination. Similar threshold rules are used to assign the grid classifier for the other modes, and then the code fills the grid with the corresponding classifier color. The undamaged grids get filled with white, the partially damaged grids get filled with gray, and the completely damaged grids get filled with black. An example of a completed damage grid layer is shown in Figure 5.16, and an example of the damage grid with the axes layer and base documentation layer is shown in Figure 5.17.

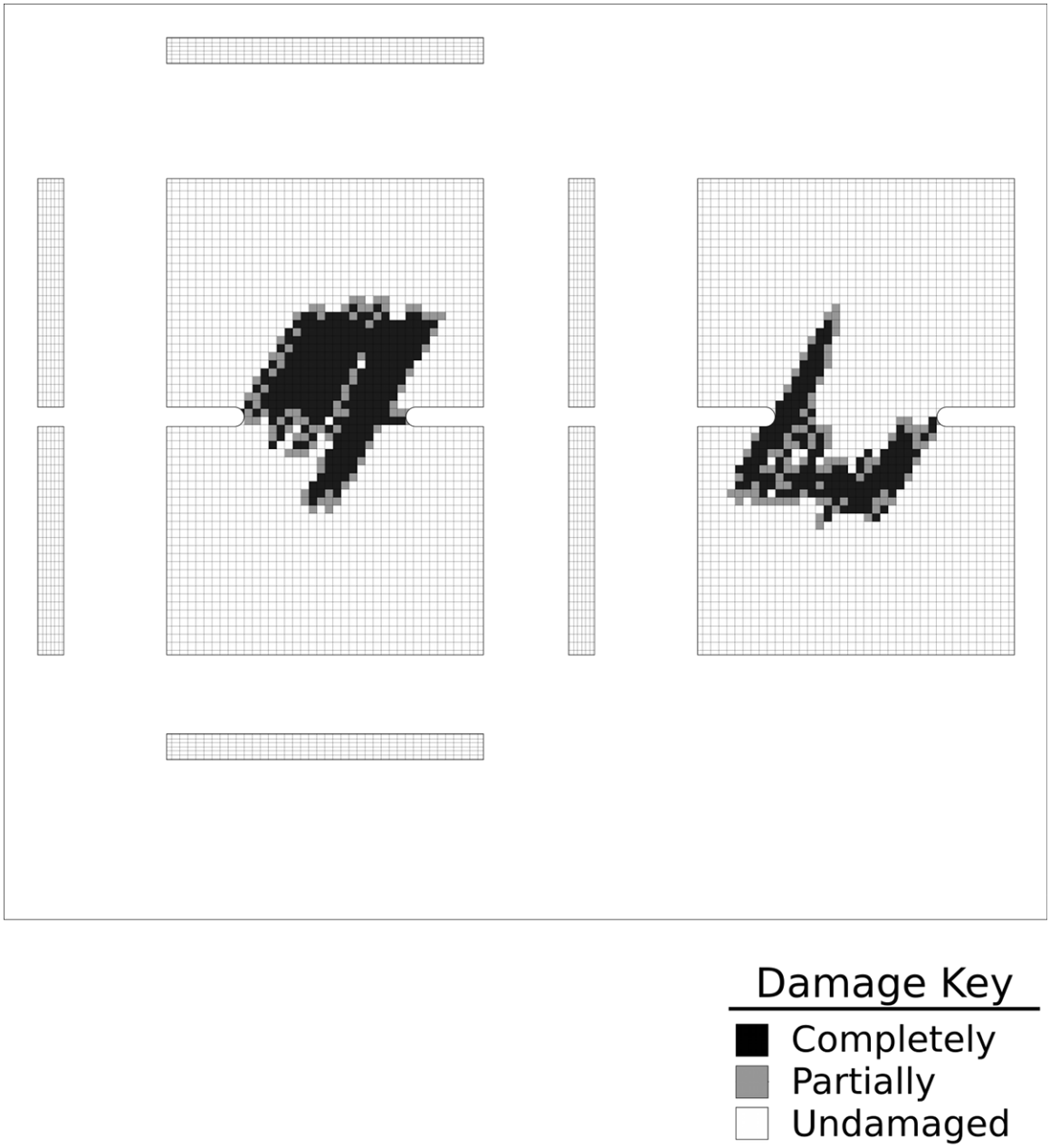

Figure 5.16 Example of a damage grid layer for a NRL double-edge-notched specimen (outer box shows actual extent of layer).

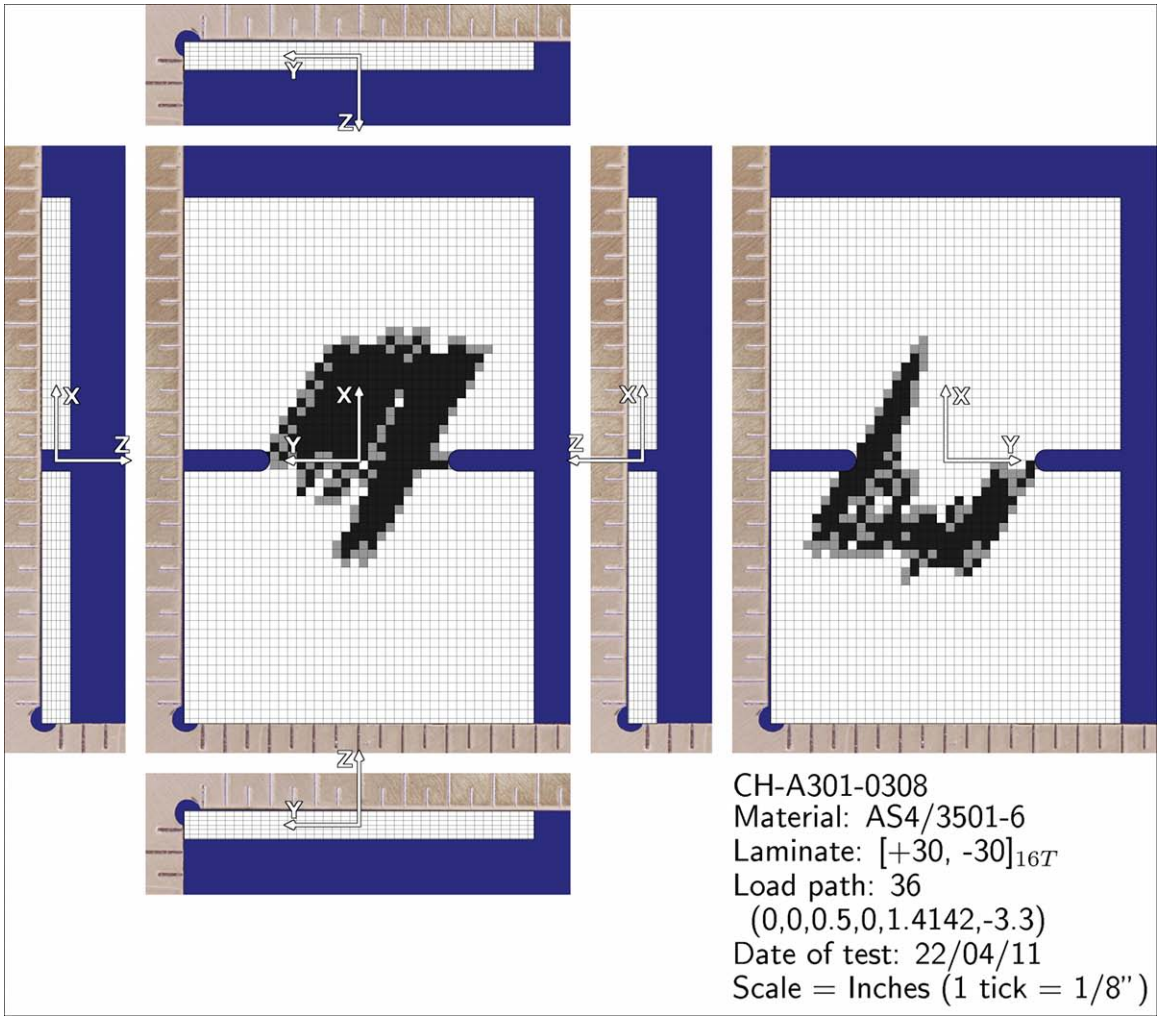

Figure 5.17 Example of a damage grid layer with axes layer and documentation photograph layer for a NRL double-edge-notched specimen (outer box shows actual extent of layer).

5.1.3 Damage Sketch

The damage sketch layer is added to the documentation image between the damage grid layer and the axes layer. Although the damage grids are used in quantification of damage, this characterization is not able to fully capture details of the damage type and damage shape. Therefore, another means of documenting damage was developed. This second means is the use of damage sketches. The damage sketches are developed to provide more information about the damage in a single image. The damage sketches are designed to capture the 'active' damage modes, the damage paths, the damage mode interactions, and the visual extent of damage, all in a single image. Classifiers for the damage modes are selected to convey the damage type. For the damage to be addressed as described in Subsection 5.1.2, matrix cracking is represented as a black line, delamination is a filled gray area, and fiber fracture is an area filled with a "divot" pattern (a specific hatch pattern), each having unique colors allowing implementation of the automated grid filling. The classifiers were selected to be similar to the damage modes. For example, matrix cracking usually occurs in a straight line, delamination occurs in an area when viewed in the plane of the ply and as a crack between plies when viewed from the side, and fiber fracture occurs in a jagged line creating an area of damage. With this classification scheme, the damage sketches can easily show the damage paths and lead to questions of mode interaction by displaying all 'active' damage modes in the same region.

The damage sketches are filled in by an investigator. Using an image-editing software, the damage sketch layer is "placed" on top of the documentation photograph and all other layers are turned off. Each face of the specimen is then inspected for damage and appropriately documented. Matrix cracks are indicated by drawing a black line along the path of the crack. Fiber fracture is indicated by filling the damaged region with a divot pattern. Delamination is indicated by selecting the affected region and filling it gray. An example of a completed damage sketch layer is shown in Figure 5.18, with a legend indicating the uniquely assigned colors for each damage mode, and the bounding box illustrating the layer boundaries. In this

damage sketch, the three damage modes are present. The damage sketch layer can then be combined with the other layers of the documentation image to investigate specifics of the specimen. An example of the axes layer, damage sketch layer, and base documentation photograph layer all superposed is shown in Figure 5.19, where the damage sketch layer obstructs the view of the specimen in the documentation photograph layer. The boundaries, visualized by the bounding boxes, of each layer are aligned when superposing. The documentation photograph layer can be seen in Figure 5.14.

5.2 Comparison Database

Another important component of the procedure to investigate lengthscale effects in composites is the use of a damage comparison database. One of the sub-objectives of this work was to establish a framework for, and implement an initial base of, data to enable investigation of lengthscales effects. The comparison database is established for this needed use in order to allow investigation of lengthscale effects in composites across multiple specimen types (e.g., different geometries, laminates, loadings). The database contains all the information gathered from the damage documentation procedures (damage extent from the damage grids, damage paths and damage modes from the damage sketches, etc.) as well as specifics about the specimens (fiber and epoxy type, laminate layup, loading history, etc.). By organizing all this information into a sortable and searchable database, comparisons can be made to find trends and expose differences in damage as the level of testing is changed. For example, a researcher may be interested in the change in damage extent caused by varying only the size of a structural feature (e.g., hole). From the comparison database, one can select the fixed parameters (e.g., material, laminate stacking sequence, etc.) and investigate how the damage extent varies as the size of the structural feature varies.

The advantage of this comparison database is that it represents a new focus, investigating lengthscale effects, whereas previous databases on composites were used in determining material allowables for specific laminates. Damage information was

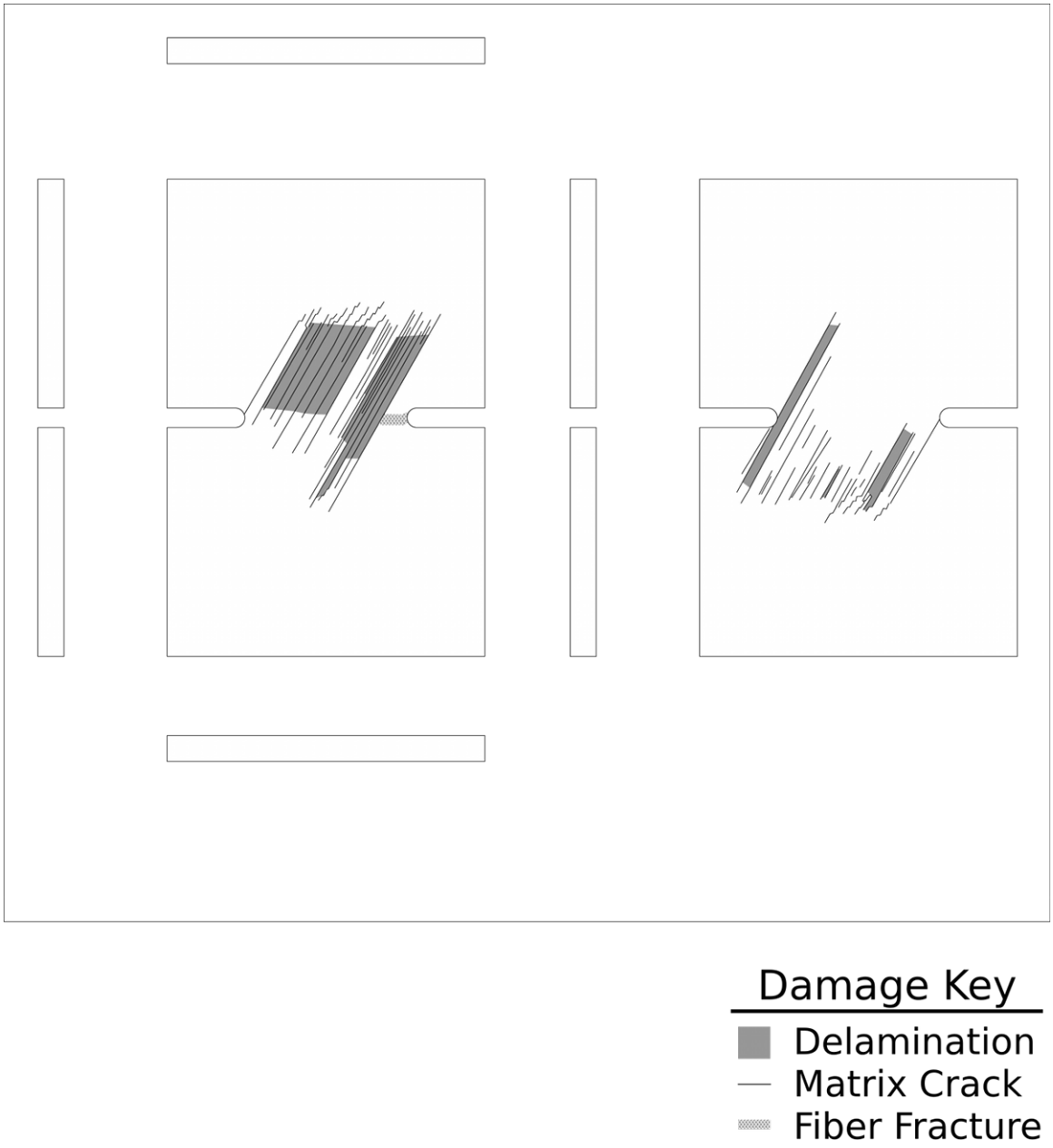

Figure 5.18 Example of a damage sketch layer for a NRL double-edge-notched specimen (outer box shows actual extent of layer).

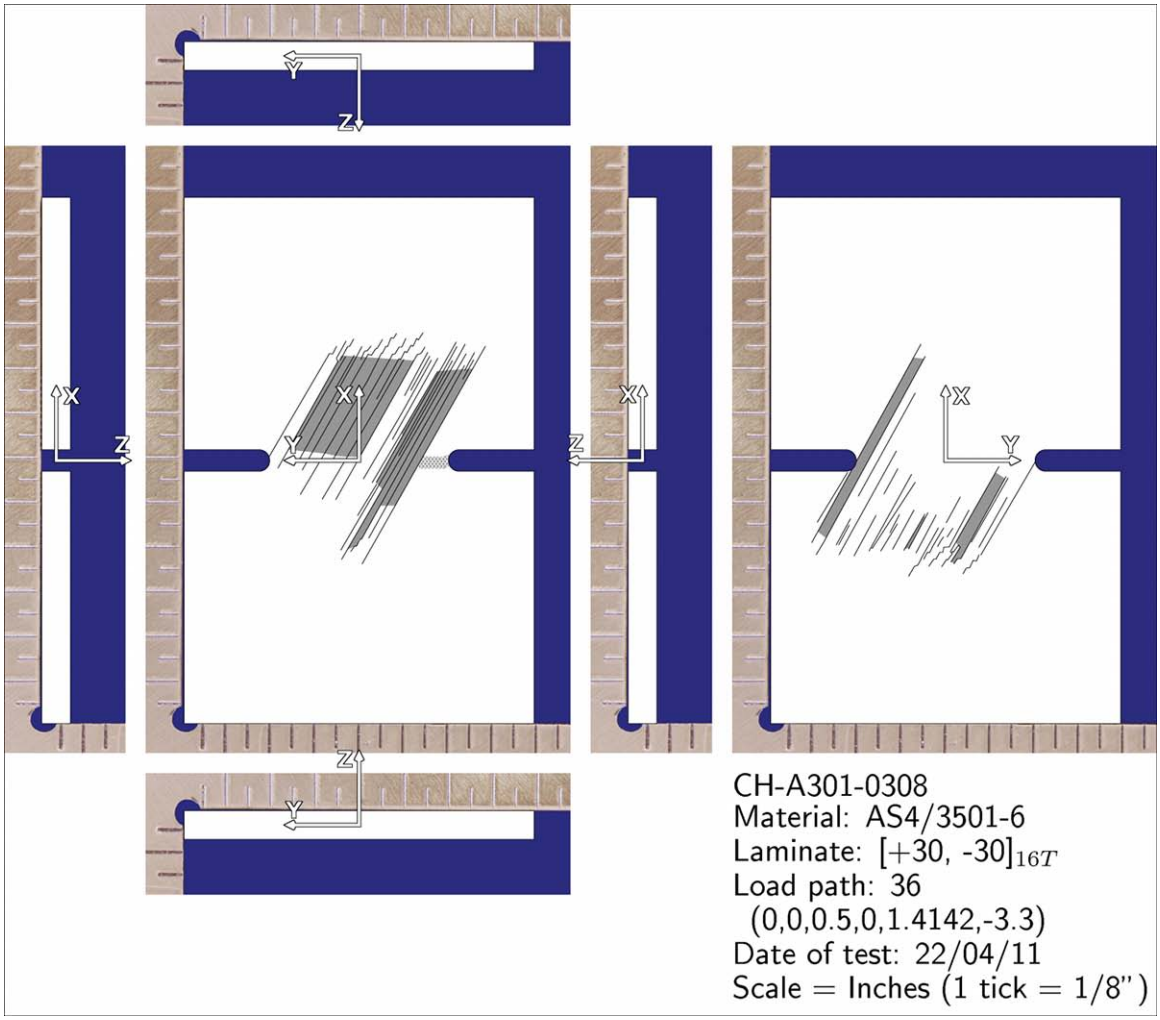

Figure 5.19 Example of a damage sketch layer with axes layer and documentation photograph layer for a NRL double-edge-notched specimen (outer box shows actual extent of layer).

lacking from these previous databases, partially due to absence of a damage documentation procedure and partially due to the lack of interest in the specific damage that occurred, as opposed to characterizing the stress at failure. This lack of information and usage makes it nearly impossible for researchers to use the information contained in such databases in order to study failure trends. This ultimately limits the ability to design the most efficient structures. The comparison database was developed and populated using the damage documentation data from the experimental specimens of the project. This database provides researchers with a standard platform to investigate damage trends and lengthscale effects across multiple specimen types while also allowing damage/failure data to be shared amongst researchers.

The database contains all the information gathered from the procedures as described. The test specifics (fiber and epoxy type, laminate layups, etc.) and damage specifics (extent, 'active' modes, paths, etc.) are all included in the database. A sample excerpt of the database is shown in Table 5.1. The first column gives the specimen identifier (specimen ID number). The next three columns capture the test inputs: material type (Matrl), stacking sequence (Stack), and load paths (Load Path). The material type is indicated by a classifier corresponding to the fiber and matrix (e.g., '1' corresponds to AS1/3501-6). The stacking sequence of the specimen laminate is indicated by a classifier assigned to each sequence. In a similar fashion, each load path is assigned a classifier. The following four columns capture the visually observed damage modes: delamination (Delam), matrix cracking (Matrix Cracking), fiber fracture (Fiber Fracture), and zigzags (Zig-Zags). The classifiers in these columns are binary, where a '1' indicates that the damage mode was visually observed, while a '0' indicates it was not. An exception is the "zigzags" column, where the number in that column represents the number of zigzag failures observed in the specimen.

It is noted that the "zigzag" failure mode is a mode identified during this work and is described in Section 6.1. The zigzag failure mode is an example of the manner in which additional failure characteristics can be added to the comparison database, in this case one which addresses Branch A.1.1.1.3 ("How do damage modes interact?") of the Question Tree (described in Section 3.2). Additional columns can be added to

Table 5.1 Example excerpt of the Damage Comparison Database

Specimen #	Test Parameters			Visually Observed Damage Modes				...
	Matrl	Stack	Load Path	Delam	Matrix Cracking	Fiber Fracture	Zig-Zags	...
001-33	1	1	1	1	0	0	0	...
001-34	1	1	2	1	1	0	0	...
001-36	1	1	4	1	0	0	0	...

...	Failure Summary			Damage Quantification	
...	Failure Present	# Active Modes	Zig-Zag Present	Partial	Complete
...	1	1	0	3%	1%
...	1	2	0	5%	8%
...	1	1	0	3%	1%

the database if other unique damage patterns are observed in future work. However, the damage characterizers should be kept to a minimum to allow data to be as widely applicable as possible. For example, incorporating project specific classifiers would begin to limit the usefulness of such a comparison database.

The next three columns in Table 5.1, labeled overall as "Failure Summary", capture the visual damage/failure observations. The "Failure Present" column indicates, via the binary value of '1' (yes) or '0' (no), whether damage (any mode) was visually observed in the specimen. The next column indicates the number of "active" damage modes, which is a summation of the cells from the "visually observed damage modes" columns. The "Zig-Zag Present" column indicates, via the binary value of '1' (yes) or '0' (no), whether zigzags were visually observed. The final two columns capture the damage quantification results from the damage grids. The damage is quantified as the percentage of the total number of grid squares in the specimen.

5.3 Supplemental Documentation: Computed Microtomography

In addition to the established documentation procedures, supplemental data giving further insights into the lengthscales involved in damage may be available by the use of other inspection techniques. While the purpose of the overall procedures was to establish a general characterization technique, easily applicable to a wide range of specimens, data from specialized techniques can supplement the characterization. The use of computed microtomography is an example of an experimental tool that can provide additional information on the damage process. Such supplemental data may allow investigation of lengthscales smaller than visual documentation permits, as well as beyond that available by observation of the surfaces of the specimen.

A major achievement during this work involved finding and utilizing the methodology of computed microtomography (CμT) in investigating damage in composite specimens. While computed tomography has been in use for many years in the medical field (CAT-scans), it is only recently that this technology has been applied to

composites [110–113]. There have been very limited studies using CμT to investigate damage in composites. However, the recent advances in this technology allow composite damage to be investigated as never before. Information can be gathered from specimens without any specimen preparation (e.g., use of dyes, access to interior damage). From the CμT scans, damage paths and the interaction of damage modes throughout the volume of the specimen can be investigated with greater detail than ever before.

Computed microtomography allows damage in composite specimens to be fully investigated in three dimensions without any specimen preparation and therefore requires no destructive sectioning, knowledge of damage location, coupling fluid for ultrasonic inspection, etc. This technique creates a digital representation of three-dimensional (3-D) volumes from scans of physical/experimental composite specimens. From the representations of these 3-D volumes, lengthscale effects associated with composite damage are studied in greater detail than ever before. The 3-D volumes are manipulated via a graphics software program. Thus, "virtual cuts" can be made through any plane of a specimen, and the damage on that plane can be examined with resolution down to the order of several microns. This allows visualization of damage paths and damage extent anywhere within the volume of the specimen, as well as observations of damage mode interactions throughout the volume of the specimen. Information, such as that from the CμT scans, can be included in the comparison database as additional, non-searchable, information. Providing such information in the database allows researchers more insight into the damage process.

Three-dimensional volume scans of specimens are conducted via a closed X-ray computed microtomography system. A specimen is mounted on a turntable in the X-ray cabinet, and then individual X-ray projections are captured as the specimen is rotated. An algorithm then uses these projections to recreate a virtual volume of the scanned specimen. The computed microtomography machine used during this work is located at Harvard University's Center for Nanoscale Systems (CNS) located in Cambridge, Massachusetts.

The machine is an X-Tek HMXST225 computed microtomography X-ray imaging

system. The system has an open source X-ray tube capable of a maximum resolution of 3 to 5 microns in reflection mode and 2 microns in transition mode. The achievable scan resolution is a function of specimen dimensions and decreases as specimen size increases (the geometric magnification used in the system results in the inverse relationship). Specifically, the resolution is proportional to the width, thickness, and height of the specimen as per:

$$Resolution \propto \frac{1}{C_1\sqrt{w^2+t^2}+C_2h} \tag{5.1}$$

where w, t, and h are the specimen width, thickness, and height, and C_1 and C_2 are constants dependent on the CμT machine. The machine can accommodate a specimen up to 6 inches in length by 6 inches in width by 6 inches in thickness with the limitation that X-rays must be able to fully penetrate the specimen (dependent on the X-ray attenuation of the specimen material). Targets of molybdenum (Mo), tungsten (W), silver (Ag), and copper (Cu) are available in order to optimize the X-ray spectrum for specimens of different materials. Each target produces a unique spectrum of X-ray wavelengths (and hence X-ray energy levels). The multiple targets allow a spectrum to be selected to optimize the attenuation of X-rays through a specimen. This attenuation is a function of the X-ray wavelength and the material. The CT algorithm calculates the attenuation from changes in intensity sensed at the X-ray detector (XRD). For example, a spectrum with short wavelength (high energy) X-rays will not have sufficient attenuation through a 'soft' (e.g., plastics) material to detect fine changes within the volume. However, a spectrum with long wavelength (low energy) X-rays will have too much attenuation through a 'hard' (e.g., metal) material and may result in zero intensity (X-rays not fully penetrating the material) at the X-ray detector. A Perkin Elmer X-ray detector 1621 X-ray panel provides 2000 by 2000 pixel (16 inch by 16 inch) field of view with 7.5 frames per second readout. The machine can be used to image a wide range of materials from organic materials to plastics, metals, and composites.

The CμT machine was utilized to further inspect damage modes and mode interac-

tions for a select group of project specimens. Applying the documentation procedures described in Section 5.1 and then interrogating the results, contained in the comparison database described in Section 5.2, allowed specimens exhibiting unique damage characteristics to be identified. These characteristics of interest include changes in damage mode due to different effective ply thickness, interactions of damage modes, and differences in damage paths. Utilizing CμT allows investigation of lengthscales within the specimen as well as investigation of lengthscales at smaller levels than permitted by visual inspection. Further details on the selection of specimens investigated using CμT is included in Section 6.3.

Chapter 6

Experimental Results

The results of the damage characterization of specimens investigated during this work are presented in this chapter. The documentation procedures presented in Chapter 5 have been applied to the experimental specimens detailed in Chapter 4. Overall, 1394 specimens are documented and characterized using the damage documentation procedures described in Section 5.1. In the first section of this chapter, details of the damage characterization from each specimen type are presented. This is followed by a presentation of results emerging from the comparison database, which enables trends across specimen types and specimen levels to be investigated. Finally, in the last section, results from applying computed microtomography, as described in Section 5.3, to a subset of specimens are presented.

6.1 Documentation of Damage

The experimental specimens investigated during this work include four different specimen types: single-edge-notched, double-edge-notched, open-hole tension, and ply-drop. In the following subsections, results and trends obtained from applying the damage documentation procedures are presented. The results presented are representative of the damage that occurs across all specimens. The details of all 1394 specimens are available in a laboratory report [123]. The resulting data from applying the procedures to every specimen of each type are collected and entered into the

comparison database. This is presented in Section 6.2.

6.1.1 Single Edge-Notched Specimens

The initial specimens documented and entered into the database are the NRL single-edge-notched specimens. These specimens are described in Section 4.1. Of the 210 single-edge-notched specimens documented, only 182 specimens were determined to have been tested (loaded) and 28 were virgin (untested/never loaded). This determination was based on the testing data received from the NRL, and was visually verified by the fact that the loaded specimens exhibited surface scarring of the epoxy in the region of the grip area (see Figure 4.1). Of the 182 specimens that had been loaded, only 106 show visual signs of damage, while the other 76 have visual signs only of the grip marks. Within the 106 specimens that show visual damage, some exhibit clearly visible damage, while others have barely visible damage that is only found after very close inspection with a trained eye.

Comparisons in the damage trends within these specimens were conducted. One finding is that fiber fracture only occurred in 23 of the specimens. A trend related to the fiber angle in specimens exhibiting fiber fracture is seen, with 17 of these 23 specimens having fiber angles of 15° or 75°, while the other 5 specimens had fiber angles of 30° or 60°. A second finding is that matrix cracking is the most common failure mode that is observed, as it occurs in 92 of the 106 specimens that show visual damage. This result is not surprising as matrix cracking is the most commonly observed damage mode reported in the literature. It is also noted that matrix cracking is present in all but 9 specimens that exhibit delamination (with a total of 43 specimens exhibiting delamination). However, matrix cracking did occur in 58 specimens where delamination is not observed.

One observation of mode interaction commonly found in these specimens is an interaction between matrix cracking and delamination occurring through the thickness. As documentation of such an interaction mode is not found in the literature, it is defined here to be "transverse zigzag" damage. This terminology is used due to the visual appearance of the damage. The zigzag pattern can be seen on the side

(through thickness) faces of specimens, with an example shown in Figure 6.1. The damage type is an interaction between matrix cracking and delamination, where matrix cracks occur between plies and are connected by small areas of delamination. Reviewing the literature, the most similar damage type found is referred to as delamination "switching," where a delamination propagates along a ply interface and a matrix crack through a ply allows the delamination to "switch" to a neighboring interface [e.g., 6, 124, 125]. The delamination continues propagating along its original direction, but at a "switched" interface. However, unlike delamination "switching," the transverse zigzag damage mode propagates in a back-and-forth manner through the laminate thickness, resulting in a narrow band, ranging from 2 to 7 ply thicknesses in width, of damage in the through-thickness direction. It should be noted that the small delaminations, typically no larger in length than 7 ply thicknesses and propagating along ply interfaces (visible in the x-z or y-z plane, depending on the face the transverse zigzag damage intercepts), associated with the transverse zigzag damage mode are not counted toward the number of specimens exhibiting general delamination as these particular ones have this special geometry.

This transverse zigzag pattern is observed in 52 of the specimens, with the damage initiating at the tip of the strain riser and progressing along the fiber angles to a side surface (surfaces defined in Figure 5.13). Almost half (24 specimens) of the specimens exhibiting this transverse zigzag pattern have a fiber angle of 75°, 10 specimens have a fiber angle of 60°, 11 specimens have a fiber angle of 30°, and the remaining 7 have a fiber angle of 15°. The surface to which the transverse zigzag propagates depends on the fiber angle of the laminate, as the propagation path starts at the tip of the strain riser and follows the fiber angle to the intercepting edge. Of those specimens exhibiting transverse zigzag, 10 specimens have multiple transverse zigzags present, while the other 42 specimens have only a single transverse zigzag. The damage paths in specimens with multiple transverse zigzags are always symmetric about the strain riser (i.e. the y-z plane). The example shown in Figure 6.2 has a transverse zigzag damage that is symmetric about the strain riser. In the enlarged portion of the figure, two distinct transverse zigzags are present (label as "clear zigzag"), and upon closer

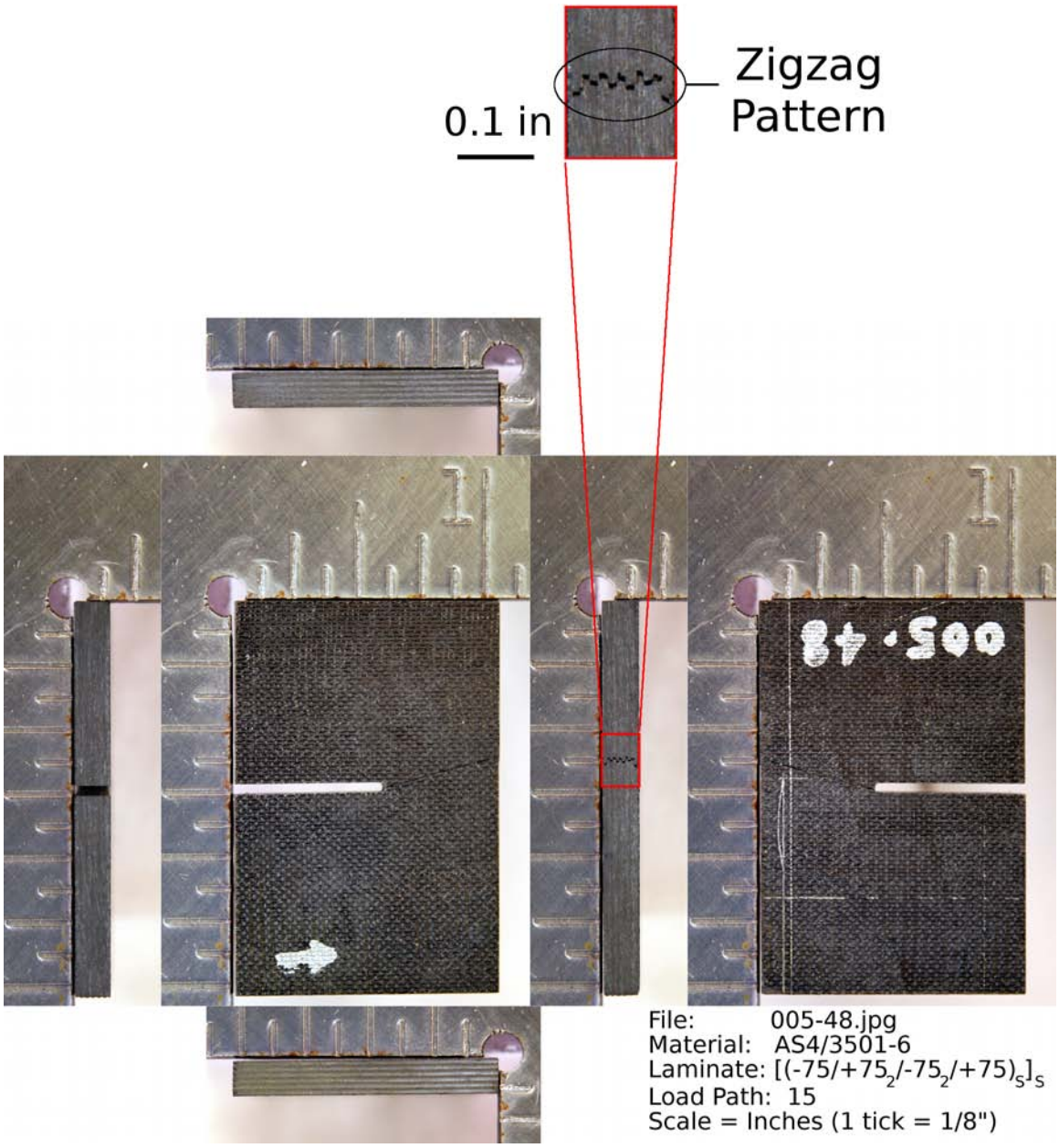

Figure 6.1 Documentation photograph layer for example of a NRL single-edge-notched specimen (005-48) with transverse zigzag damage, with an enlarged view of a section of the right face where the zigzag path intercepts the edge.

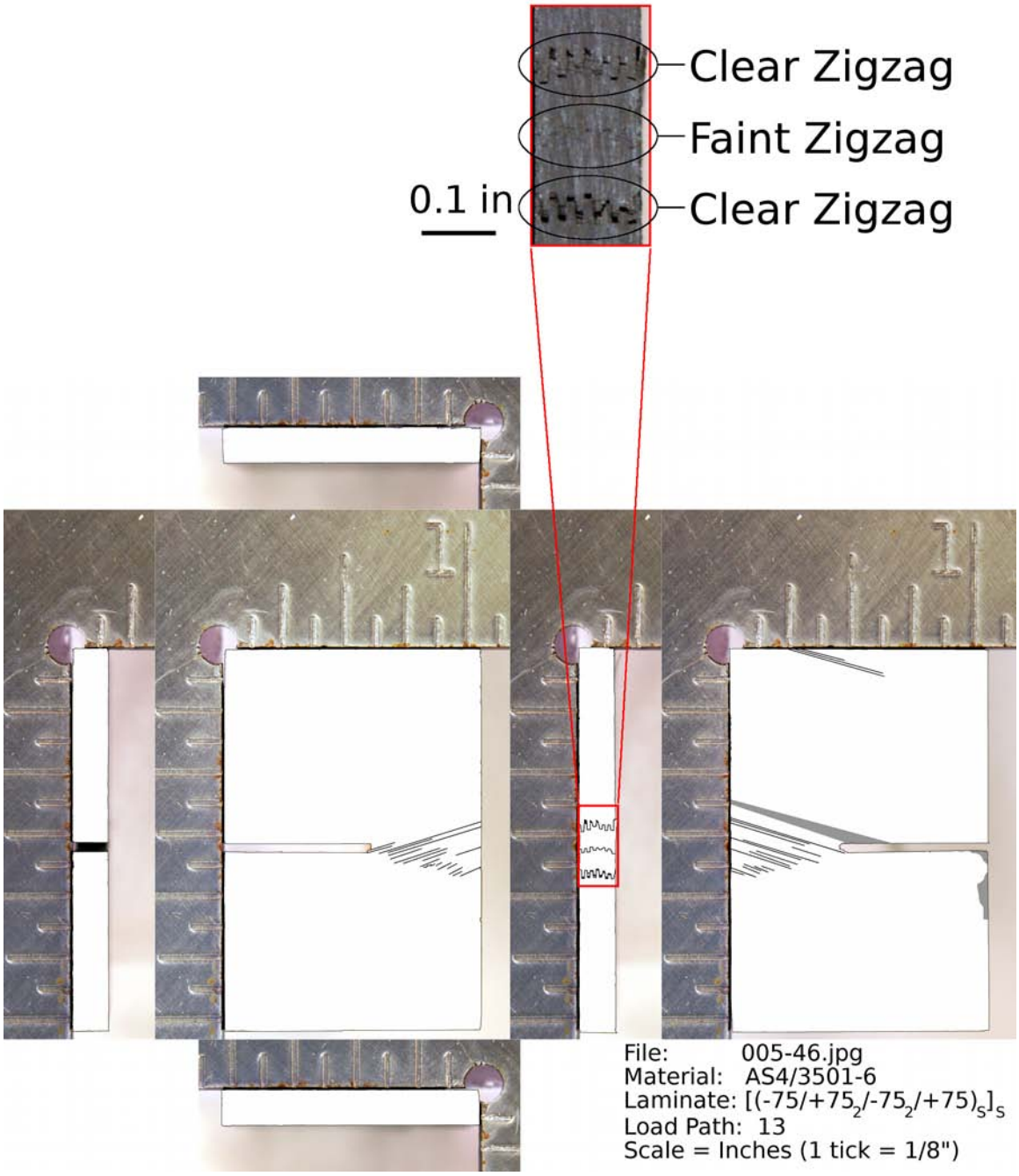

Figure 6.2 Damage sketch layer for example of a NRL single-edge-notched specimen (005-46) with multiple transverse zigzag damages, with an enlarged view of a section of the right face where the transverse zigzag paths intercept the edge.

inspection, a faint third transverse zigzag can be found (labeled as "faint zigzag").

An important lengthscale issue that is observed in the NRL single-edge-notched specimen testing is the influence of the boundaries (grips). Due to the combination of specimen geometry and laminate fiber angles, only specimens with fiber angles of 15° and 30° exhibit damage paths (generally initiating at the notch tip and propagating along the fiber angles) that intercept the grip boundaries. Damage paths in specimens with fiber angles of 60° and 75° generally intercept the right edge of the specimen before intercepting the boundaries. The one exception is a specimen (005-35) with fiber angles of 75° that exhibits primarily delamination, where the delamination propagates up to the grip boundary, and then the delamination runs along the boundary line. There are 22 specimens with fiber angles of 15° and 30° that have damage paths that intercept the grip boundaries. Of these 22 specimens, 16 damage paths appear to be unaffected by the boundary grips, and damage continues along its original path after arriving at the boundaries. This can be seen in Figure 6.3, where matrix cracking and fiber fracture originate from the notch tip, both propagate along fiber directions (although each goes along a separate direction), each intercepts the boundary (grip line), and then continues propagating along their original path direction until intercepting the specimen edge. In the other 6 cases, the damage appears to change direction right at the boundaries. This can be seen in Figure 6.4, where fiber fracture originates from the notch tip, propagates to the lower boundary (grip line), and then appears to reflect and the mode to change to matrix cracking. In Figure 6.4, it is also noticed that fiber fracture apparently initiates at the upper boundary, directly above the point where the first damage path reflects.

Another mode interaction observed in 11 specimens is the change of damage mode along the progression path. Of the 11 specimens exhibiting this change, 8 are made of the AS1-3501-6 material. Of these 8 specimens, 7 had fiber angles of either 60° or 75°. Of the 3 specimens of AS4-3501-6 that exhibited this interaction, two had fiber angles of 75° and one had fiber angles of 15°. As seen in Figure 6.5, matrix cracking and fiber fracture are observed on the front faces, while only matrix cracking is observed on the back face. The damage paths on both these faces are associated

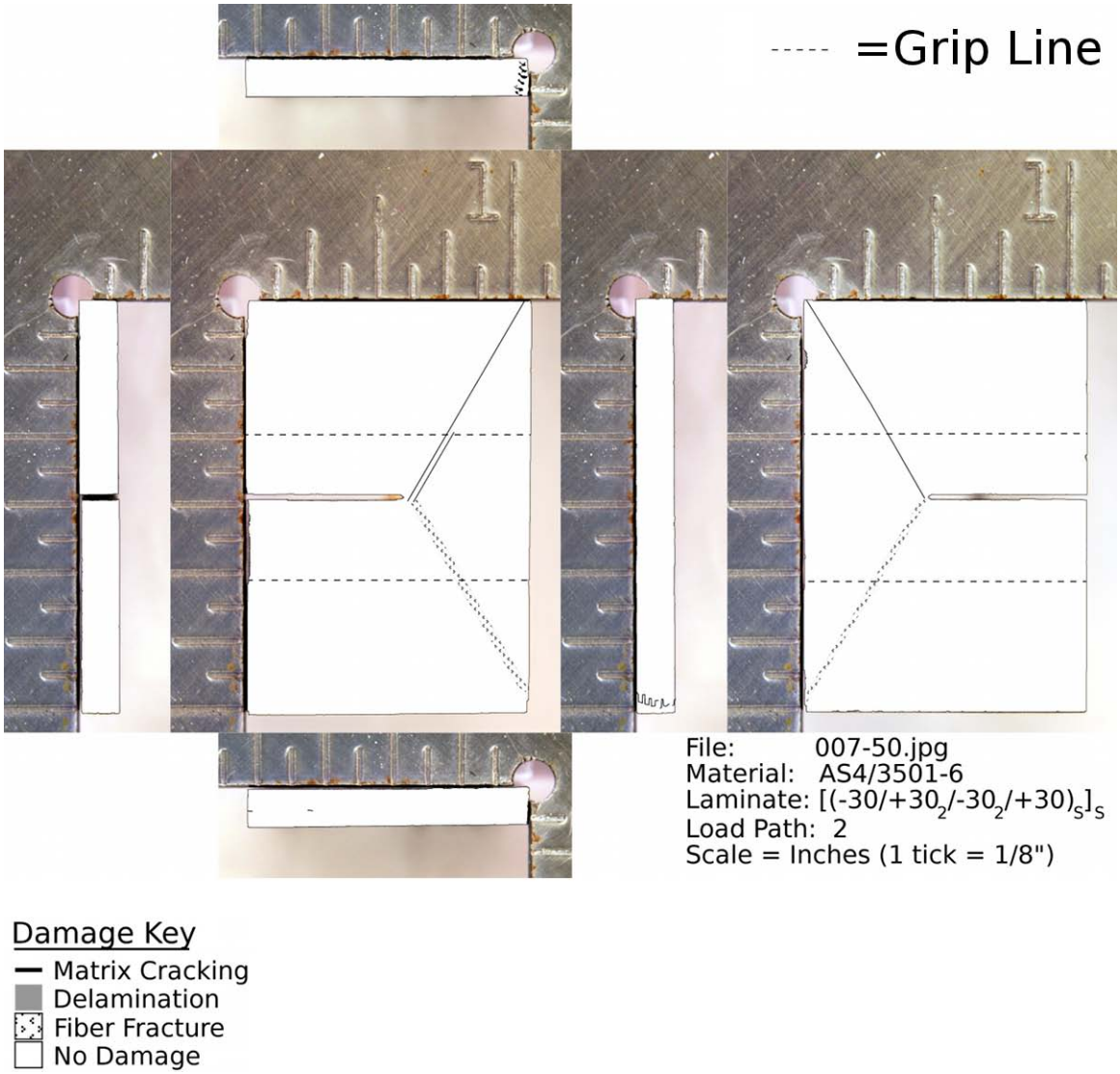

Figure 6.3 Damage sketch of a NRL single-edge-notch specimen (007-50) indicating a boundary (lengthscale) effect present in some specimens.

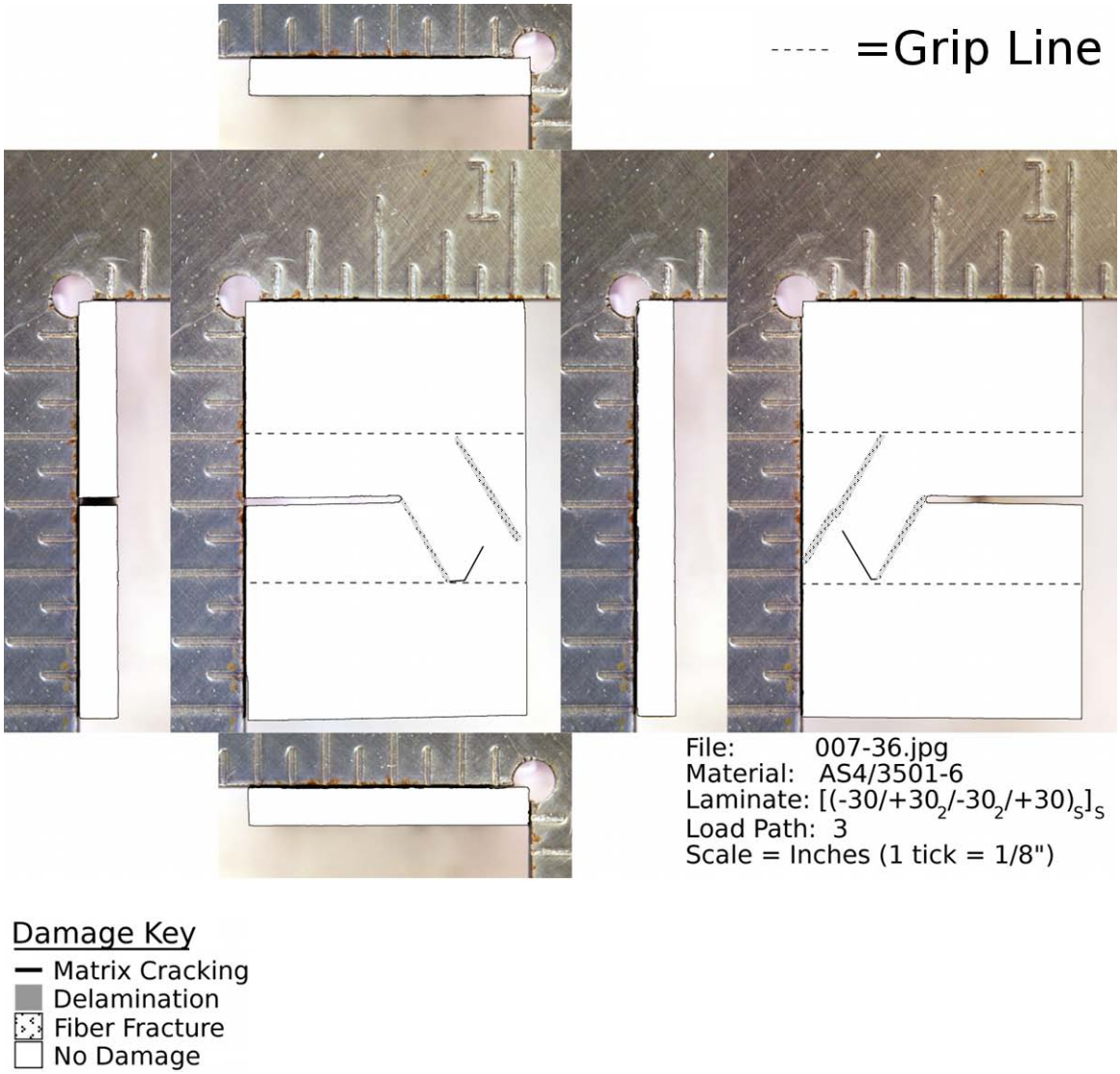

Figure 6.4 Damage sketch of a NRL single-edge-notch specimen (007-36) indicating a boundary (lengthscale) effect present in some specimens.

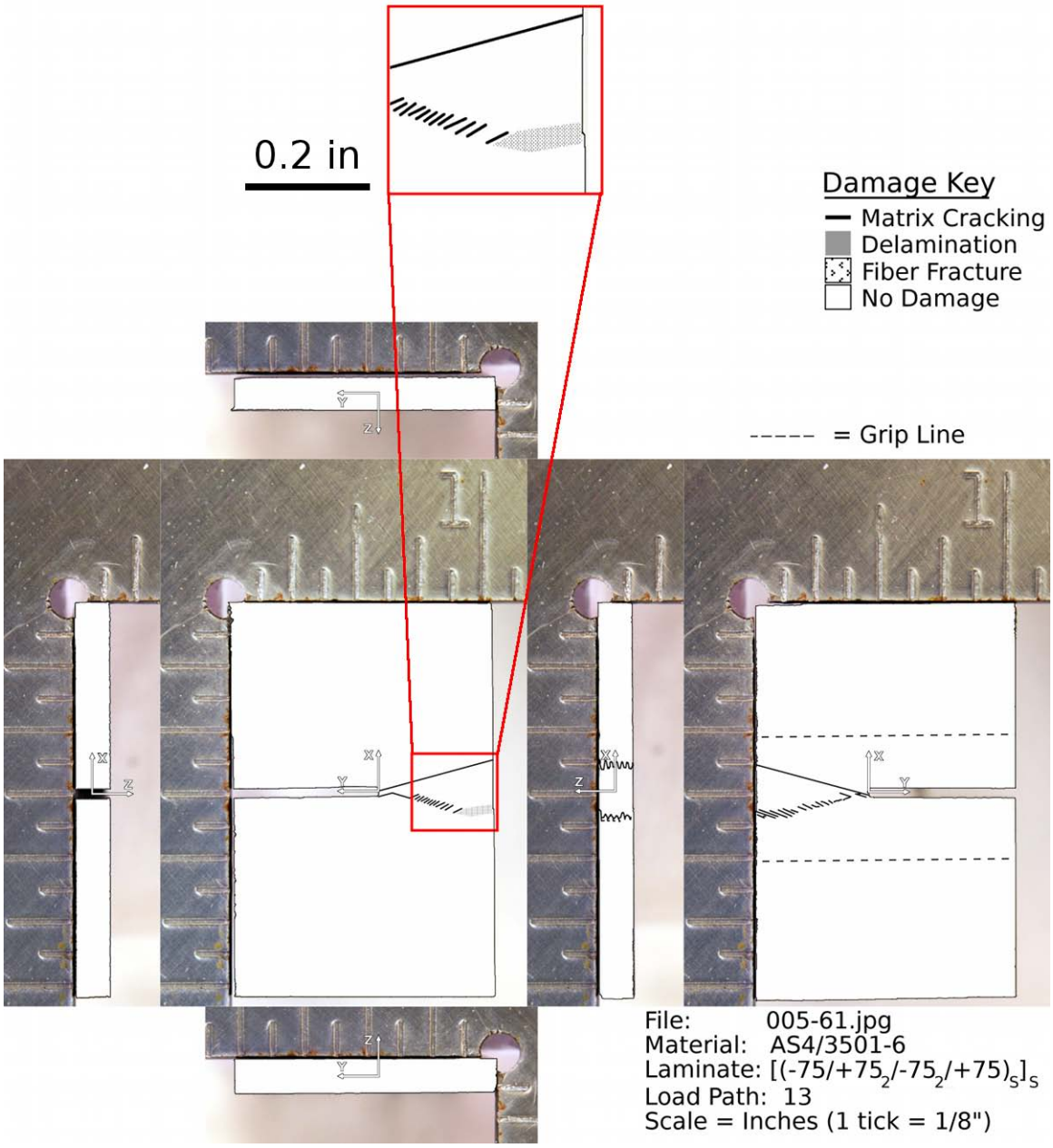

Figure 6.5 Damage sketch of a NRL single-edge-notched specimen (005-61) indicating a damage mode change along the damage progression path with an enlarged image of the particular damage.

with the fiber angles. As seen in the enlarged view of the front face damage sketch, a change in damage mode occurs along the damage path following the positive fiber angle. Short, nearly parallel, matrix cracks propagate from the notch tip to within a distance of approximately fifteen ply thicknesses of the specimen edge. At this point, the active mode switches to fiber fracture and the damage path slightly changes direction. This type of change is observed in 10 other specimens, with the location of the switch typically occurring in two ranges; either a distance equal to two to five ply thicknesses away from the specimen edge (in the y-direction), or a distance of thirty ply thicknesses away from the specimen edge (half-way between the notch and the right edge). The short, nearly parallel, matrix cracking along the path shown in Figure 6.5 is an example of "stitch cracking," which is described in the literature review (Section 2.2) [81, 82]. Further results dealing with stitch cracking are presented in Section 6.3.

6.1.2 Double Edge-Notched Specimens

The NRL double-edge-notched specimens were all documented using the damage documentation procedures. These specimens are described in Section 4.2. There are a total of 1152 specimens that were tested (loaded). Out of the 1152 specimens tested, 826 specimens show visual damage, while the other 326 have no signs of visual damage. All the specimens have clear grip marks in the grip regions, as detailed in Section 4.2. Within the 826 specimens showing visual damage, some exhibit clearly visible damage while others have barely visible damage only found after close inspection via a trained eye. One of the advantages of the damage documentation procedures, specifically the damage sketches and damage grids, is that damage within specimens, as documented, can be easily located via the sketches and/or grids by untrained researchers.

Comparisons in the damage trends within these specimens were conducted. As is the case in the single-edge-notched specimens, matrix cracking is the most common damage mode, being observed in 767 of the double-edge-notched specimens. Delamination is the next most frequent damage mode observed, occurring in 334 specimens.

Matrix cracking occurs in all but 9 of the specimens exhibiting delamination. Fiber fracture is observed in 315 specimens. There are 135 specimens with all three damage modes active, 320 specimens with only two active damage modes, and 371 specimens with only a single active damage mode.

Transverse zigzag damage similar to that seen in the single-edge-notched specimens is observed in the double-edge-notched specimens. A single transverse zigzag damage is observed in 171 of the specimens, while only 2 specimens exhibit a double transverse zigzag damage. The initiation point for transverse zigzag damage is always at the tip of one of the notches, with the damage progressing along the fiber angle until intercepting a specimen edge. Unlike in the single-edge-notched specimens, one of the two double transverse zigzag damage paths is not symmetric about the notch direction. The one specimen with unsymmetric (about the y-z plane) transverse zigzag damage has a single zigzag initiating from each notch tip. The damage sketch of this specimen is shown in Figure 6.6. The two damage paths progress along the fiber angles and cross at the centerline of the specimen. Minimal interaction between the two damage paths is apparent from the visual damage. Both paths appear to be unaffected by the other path, continuing along their original direction while crossing. Further investigation of the damage paths of this specimen was conducted using computed microtomography, described in Section 6.3. The other specimen with a double zigzag had both transverse zigzag damage paths originate at the same notch tip, similar to the transverse zigzag damage seen in the single-edge-notched specimens. The damage sketch of this specimen is shown in Figure 6.7. The paths both followed fiber directions, making the paths symmetric about the y-z plane (notch direction). In this sketch, it is observed that the transverse zigzag damage mode progressing toward the top of the specimen (positive x-direction) intercepts the top edge of the specimen while the path progressing toward the bottom of the specimen (negative x-direction) does not reach the bottom edge.

Unlike the single-edge-notched specimens, the double-edge-notched specimens did exhibit a strong influence due to the grip boundaries. Delaminations are observed to propagate up to the grip boundary and then run along the boundary. An example

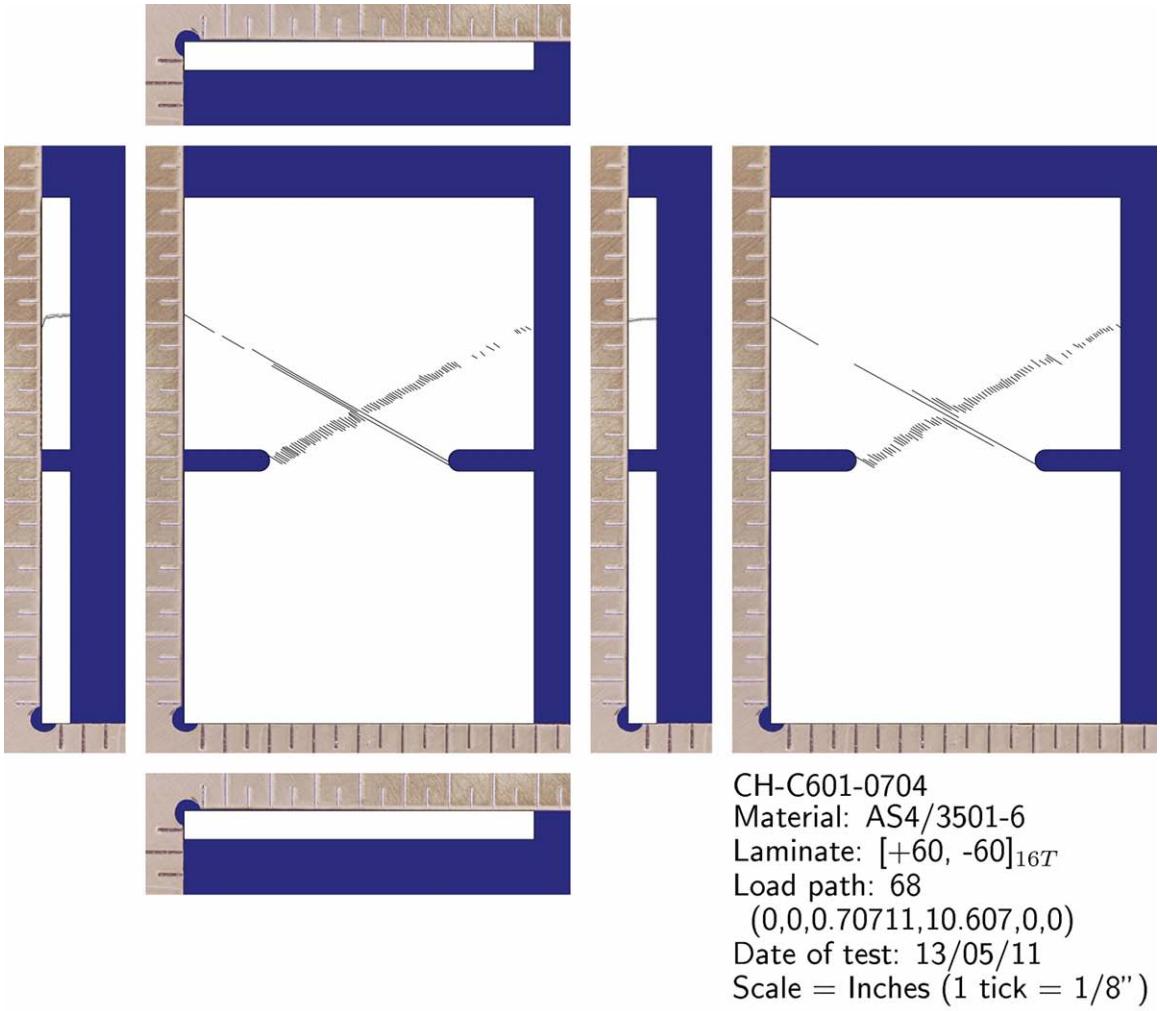

Figure 6.6 Damage sketch of a NRL double-edge-notched specimen (CH-C601-0704) exhibiting crossing transverse zigzag damage.

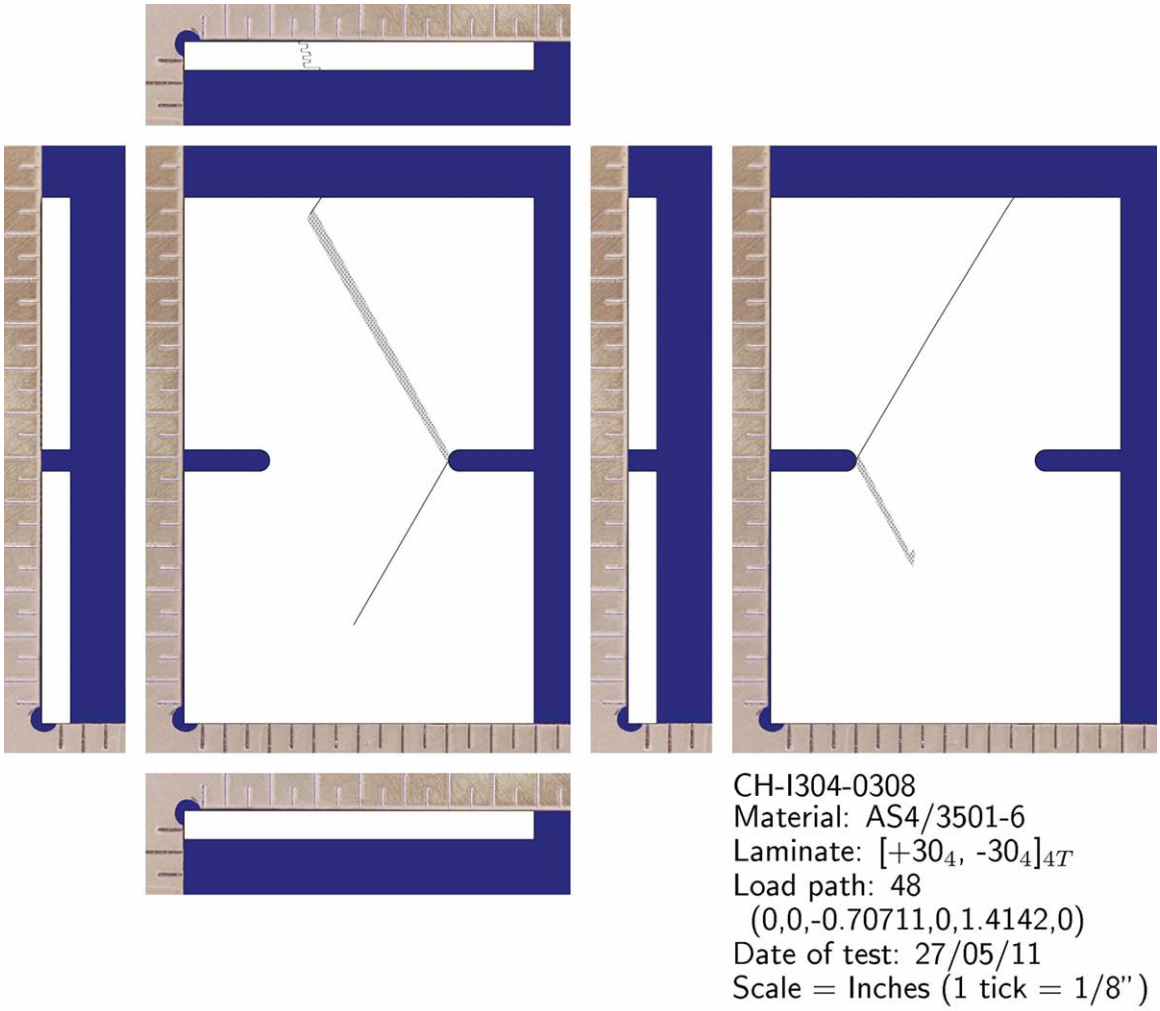

Figure 6.7 Damage sketch of a NRL double-edge-notched specimen (CH-I304-0308) exhibiting symmetric transverse zigzag damage.

of this is shown in Figure 6.8, where delamination on the front face is observed to propagate to the lower grip line and not beyond. Another boundary influence observed, similar to the single-edge-notched specimens, is where damage modes appear to reflect at the boundary. The damage sketch of one of the specimens with such a damage path is shown in Figure 6.9. However, this damage mode reflection was far less common in the double-edge-notched specimens, occurring only in twenty-four specimens. Most damage paths were observed to intercept the grip boundary and continue along their original path (along the fiber angle) without any apparent influence from the grip. As with the single-edge-notched specimens, the geometry and laminate combinations of the double-edge-notched specimens with ply angles of 75° generally resulted in the damage paths intercepting the left or right specimen edge before intercepting the grip boundary.

These specimens are designed to allow investigation of the effects of effective ply thickness. Two observations are made across the specimens with different effective ply thicknesses. The first deals with the length of the stitch cracks, which are described in the literature review (Section 2.2), observed on the front and/or rear faces of the specimens. Specimens with a single-ply effective ply thickness exhibit a nearly uniform stitch crack length, with lengths on the order of 6 to 20 ply thicknesses, and a nearly uniform stitch crack spacing, with spacing on the order of 2 ply thicknesses in length. A typical single-ply effective ply thickness specimen exhibiting stitch cracking is shown in Figure 6.10. As is seen in the figure, the stitch cracking has a fairly uniform spacing and each stitch crack is relatively the same length. This is not observed in the four-ply effective ply thickness specimens. In these specimens, the stitch cracking length is typically much longer, with lengths ranging between 13 and 130 ply thicknesses, and the spacing between stitch cracks is not uniform, with spacing ranging between 3 and 10 ply thicknesses. A typical four-ply effective ply thickness specimen exhibiting stitch cracking is shown in Figure 6.11.

As with the single-edge-notched specimens, a change of damage mode along a damage path is observed in the double-edge-notched specimens. This is most common among the single-ply effective ply thickness specimens with a fiber angle of 75°. Stitch

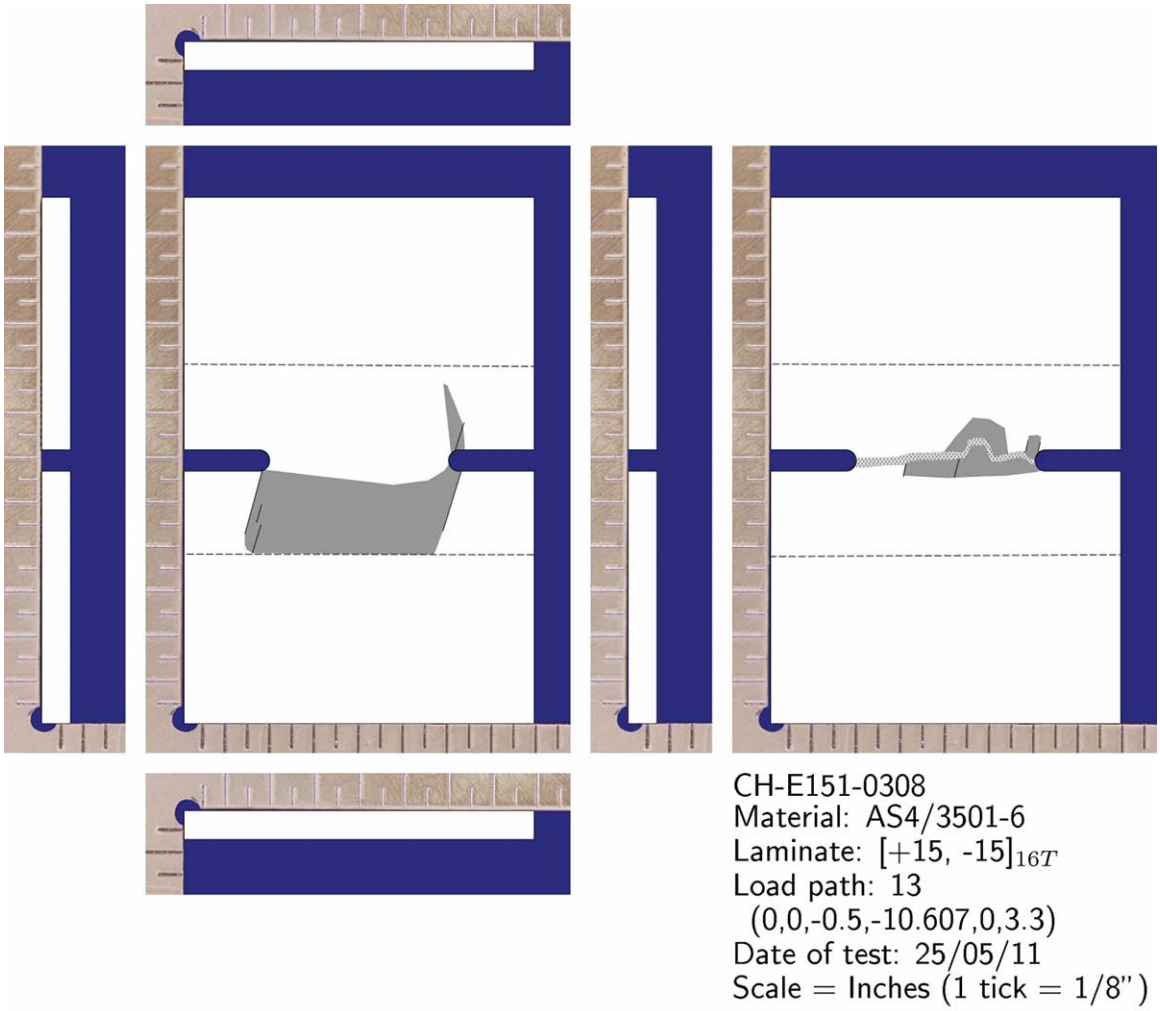

Figure 6.8 Damage sketch of a NRL double-edge-notched specimen (CH-E151-0308) exhibiting a boundary influence.

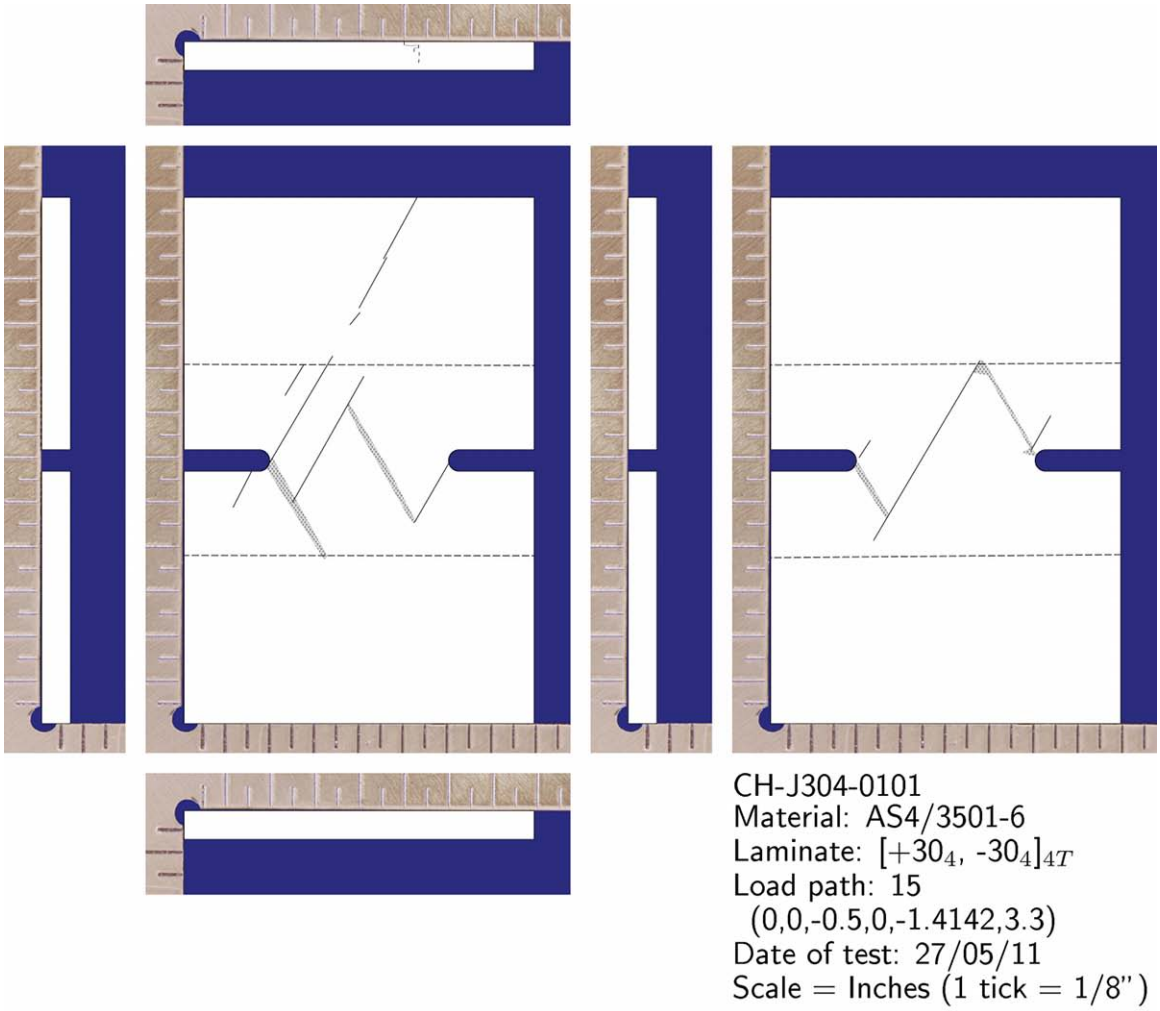

Figure 6.9 Damage sketch of a NRL double-edge-notched specimen (CH-J304-0101) exhibiting a boundary influence.

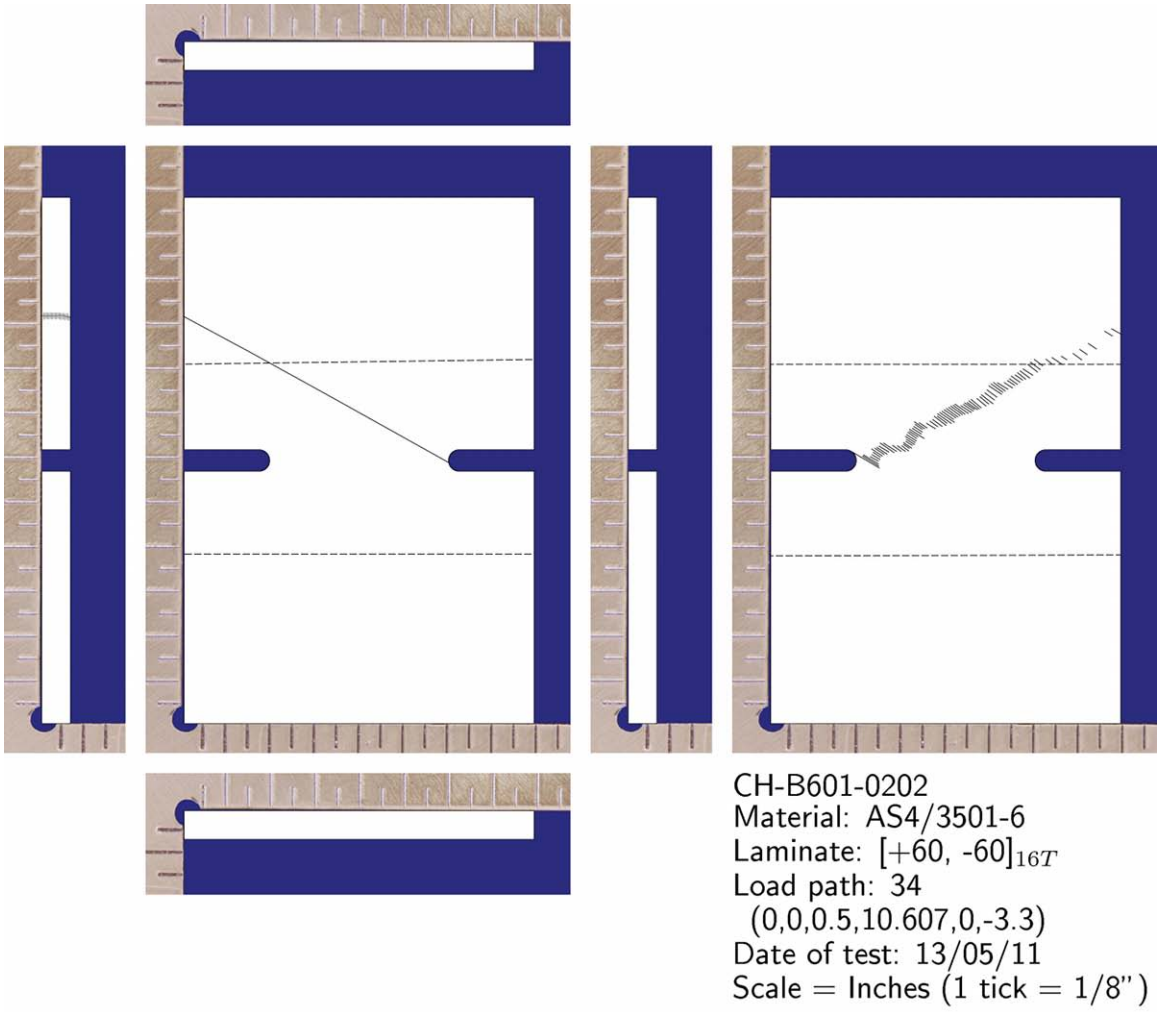

Figure 6.10 Damage sketch of a NRL double-edge-notched specimen (CH-B601-0202) with single-ply effective ply thickness laminate exhibiting stitch cracking.

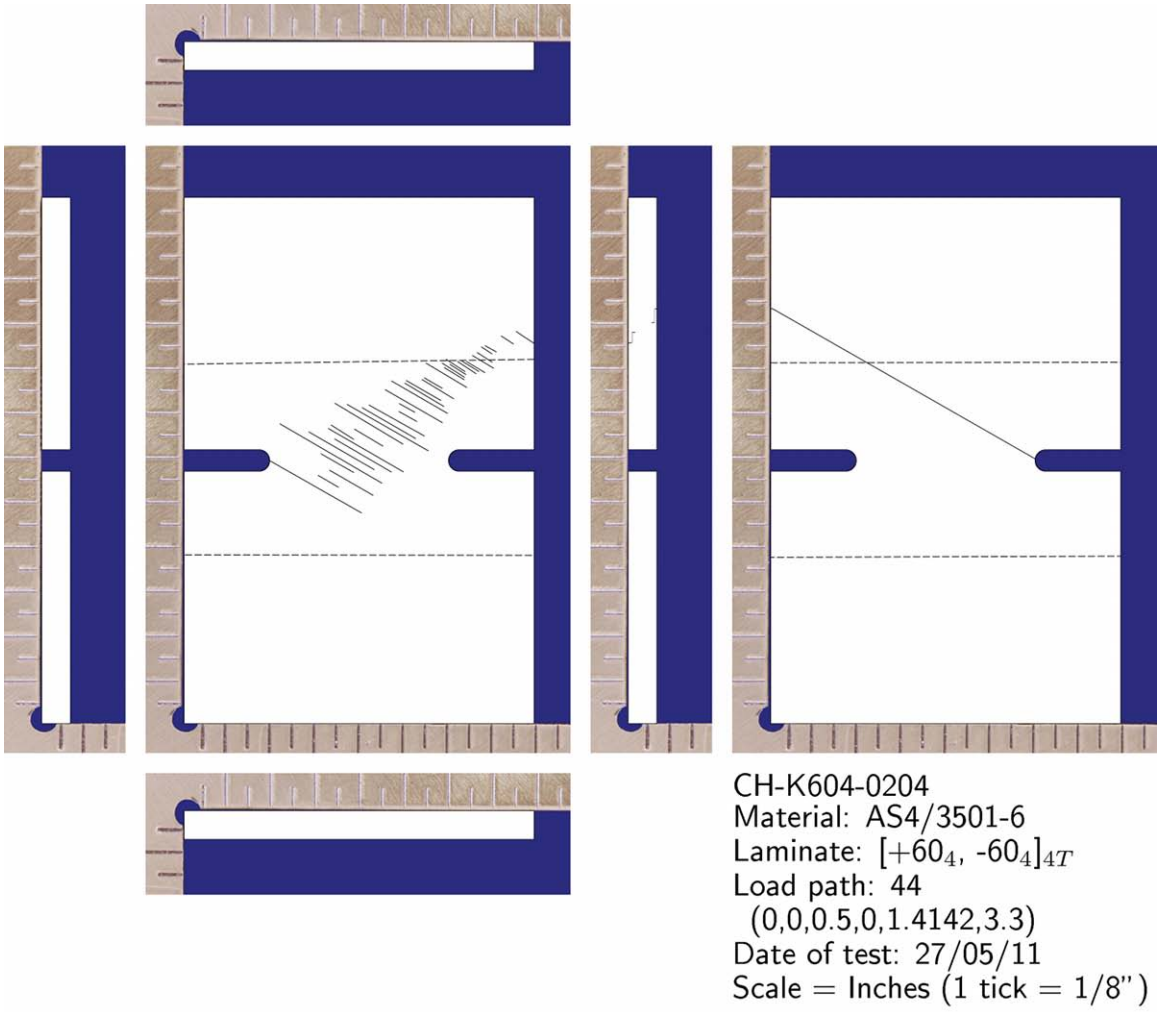

Figure 6.11 Damage sketch of a NRL double-edge-notched specimen (CH-K604-0204) with four-ply effective ply thickness laminate exhibiting stitch cracking.

cracking is observed in 21 of these specimens, and 10 of these exhibit a damage mode change along a damage path. A damage sketch of a specimen exhibiting a mode change is shown in Figure 6.12. As seen in the sketch, stitch cracking is present on the front face, propagating from the right notch tip towards the left edge along the $-75°$ fiber angle. A change from stitch cracking to fiber fracture occurs at the point almost directly below the left notch tip. An enlarged view of this section is shown in the figure.

6.1.3 Open-Hole Tension Specimens

The results from applying the damage documentation to the OHT (open-hole tension) specimens are presented in this subsection. These specimens are described in Section 4.3. In total, 51 specimens were documented during this work, with the data resulting from application of the documentation procedures being added to the comparison database. The OHT specimens were manufactured and tested in two rounds. The first round of specimens were manufactured from plates 'A' and 'B.' An improper drilling technique was used during the manufacturing of these specimens, resulting in damage, typically delamination, around the holes prior to testing. This damage was identified while investigating the specimens using computed microtomography, as is presented in Section 6.3. Not all specimens of the first round show visual damage due to the drilling technique. The second round of specimens were manufactured from plates 'C' through 'F,' and the hole drilling technique was corrected to minimize the chances of introducing damage during the manufacturing of these specimens. None of the specimens of the second round show damage due to drilling.

Upon receiving the batch of 21 OHT specimens of the first round, the damage documentation procedures were applied and trends were investigated. An initial trend found is the presence of matrix cracking in the outer layers of all specimens, with the cracks running along the outer-ply fiber angle. Delaminations are observed to form at interfaces between different ply angles. Another trend common across all OHT specimens of the first round is that a dominant surface matrix crack runs

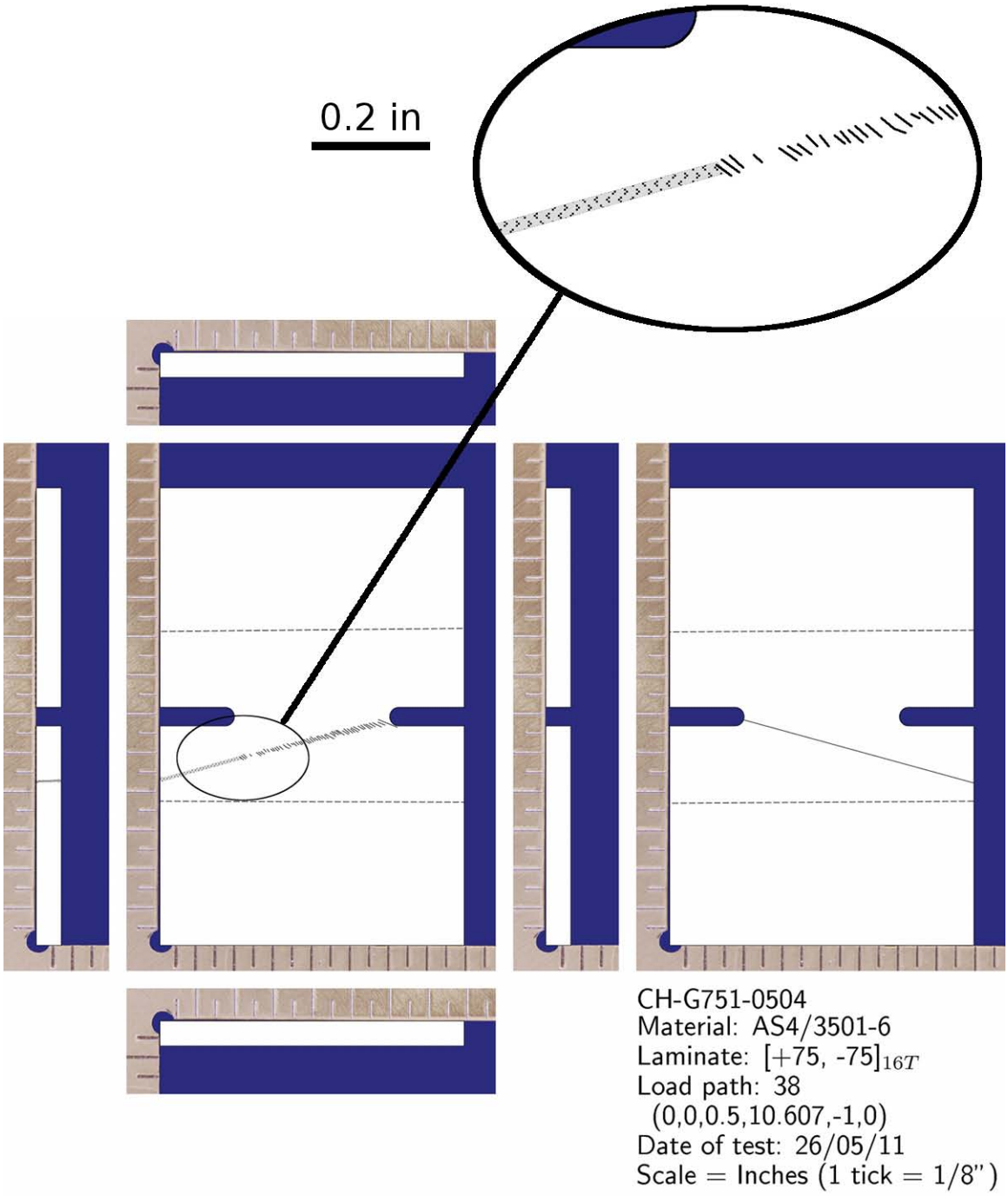

Figure 6.12 Damage sketch of a NRL double-edge-notched specimen (CH-G751-0504) exhibiting a damage mode change along a path.

tangent to the hole edge along the outer ply angle. This can clearly be seen in the damage captured in Figures 6.13 and 6.14. A third trend from these specimens is that the specimens with the four-ply effective ply thickness laminate, $[+45_4/0_4/-45_4]_S$, broke into two separate pieces at final failure, whereas those specimens with the single-ply effective ply thickness laminate, $[+45/0/-45]_{4S}$, did not. The photograph documentation, shown in Figure 6.15, is of a four-ply effective ply thickness specimen that broke into two separate pieces.

The specimens of the second round reveal similar trends as the specimens of the first round. In total, 30 of the OHT specimens of the second round were documented. Of these 30 specimens, 22 were tested (loaded) to ultimate failure, 4 were tested to loads below the ultimate load, and 4 remain virgin (untested). As with the specimens of the first round, matrix cracking and delamination are the dominant damage modes observed. Delamination and matrix are observed in every tested specimen, with the exception of two of the specimens (OH-D054-06 and OH-D104-05) that were not loaded to ultimate failure. Both of these specimens are made of the four-ply effective ply thickness laminate. Delamination and matrix cracking are observed in the other two specimens (OH-F051-05 and OH-F101-04), both of the single-ply effective ply thickness laminate, that were not loaded to ultimate failure. The criterion used for stopping the loading in the four cases not taken to ultimate failure is to load the specimen until the first audible damage is noted. Fiber fracture is observed in 17 of the specimens of the second round. The trend of a dominant surface matrix crack running tangent to the hole edge is observed in all OHT specimens of the second round that exhibit damage (excluding the OHT specimens with a 0-inch "hole").

Across all OHT specimens (both of the first and second rounds), a trend in damage propagation is observed. In all single-ply effective ply thickness specimens with a hole diameter greater than zero, damage is observed to form in two triangular regions of the front and back faces of the specimens. A damage gird illustrating the typical area over which damage occurs in these specimens is shown in Figure 6.16. These triangular regions occur on each side of the hole. A dominant matrix crack propagates along a line tangent to the hole and along the outer ply fiber angle (+45°). The damage along

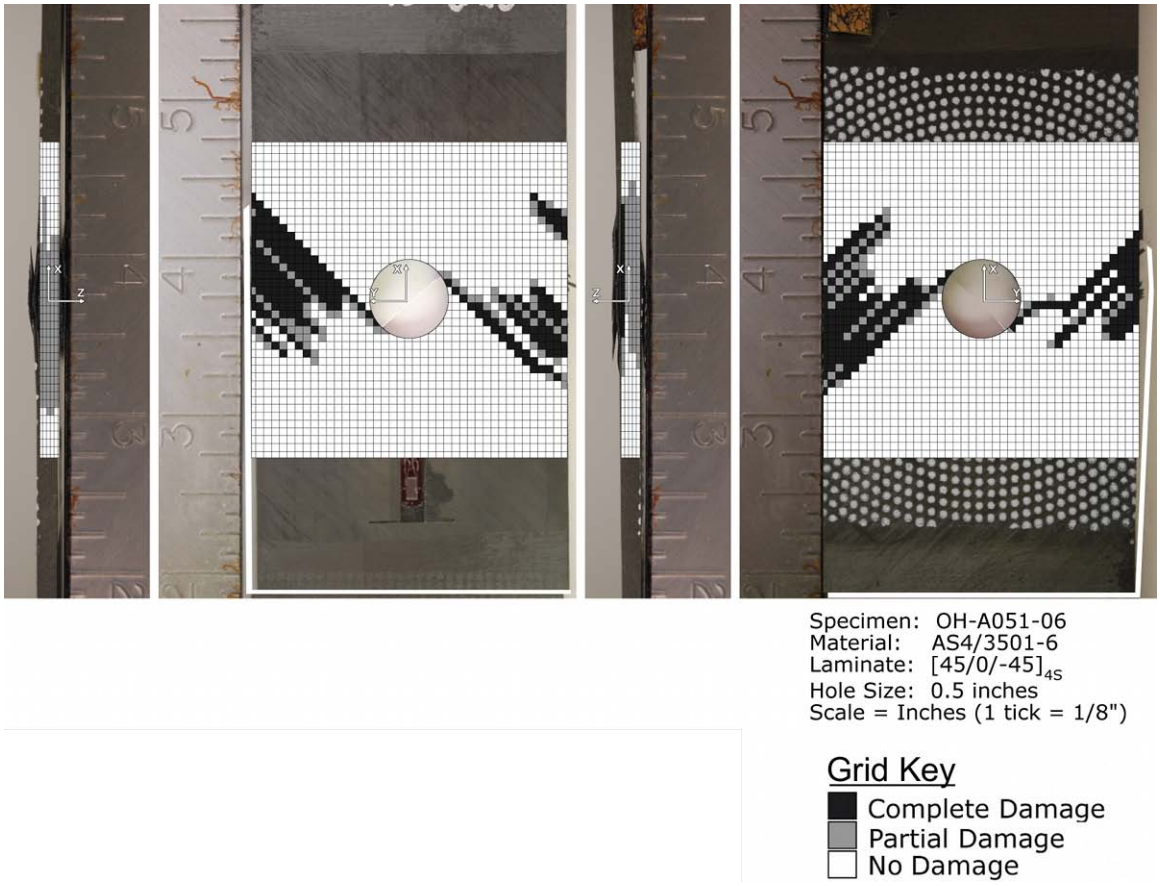

Figure 6.13 Damage grid of a failed OHT specimen (OH-A051-06), with hole diameter of 0.5 inches.

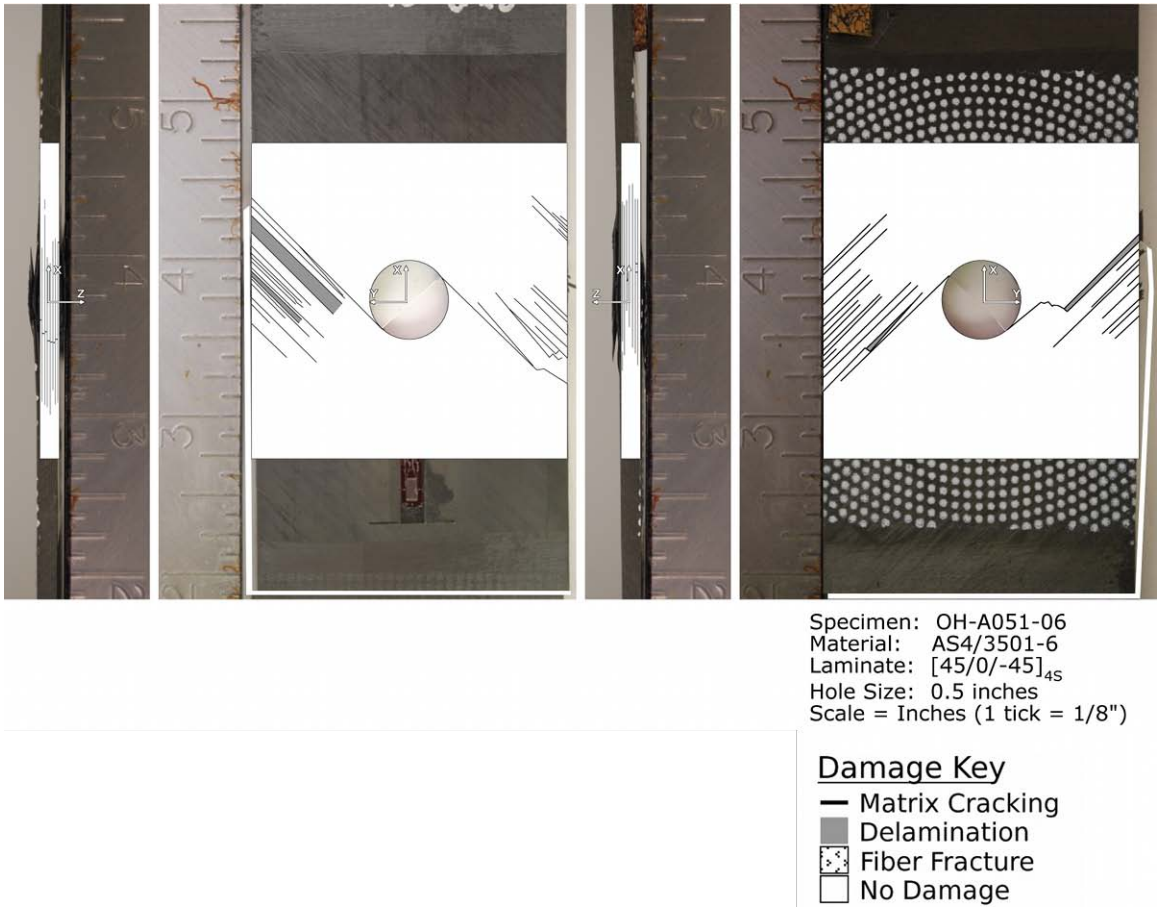

Figure 6.14 Damage sketch of a failed OHT specimen (OH-A051-06), with hole diameter of 0.5 inches.

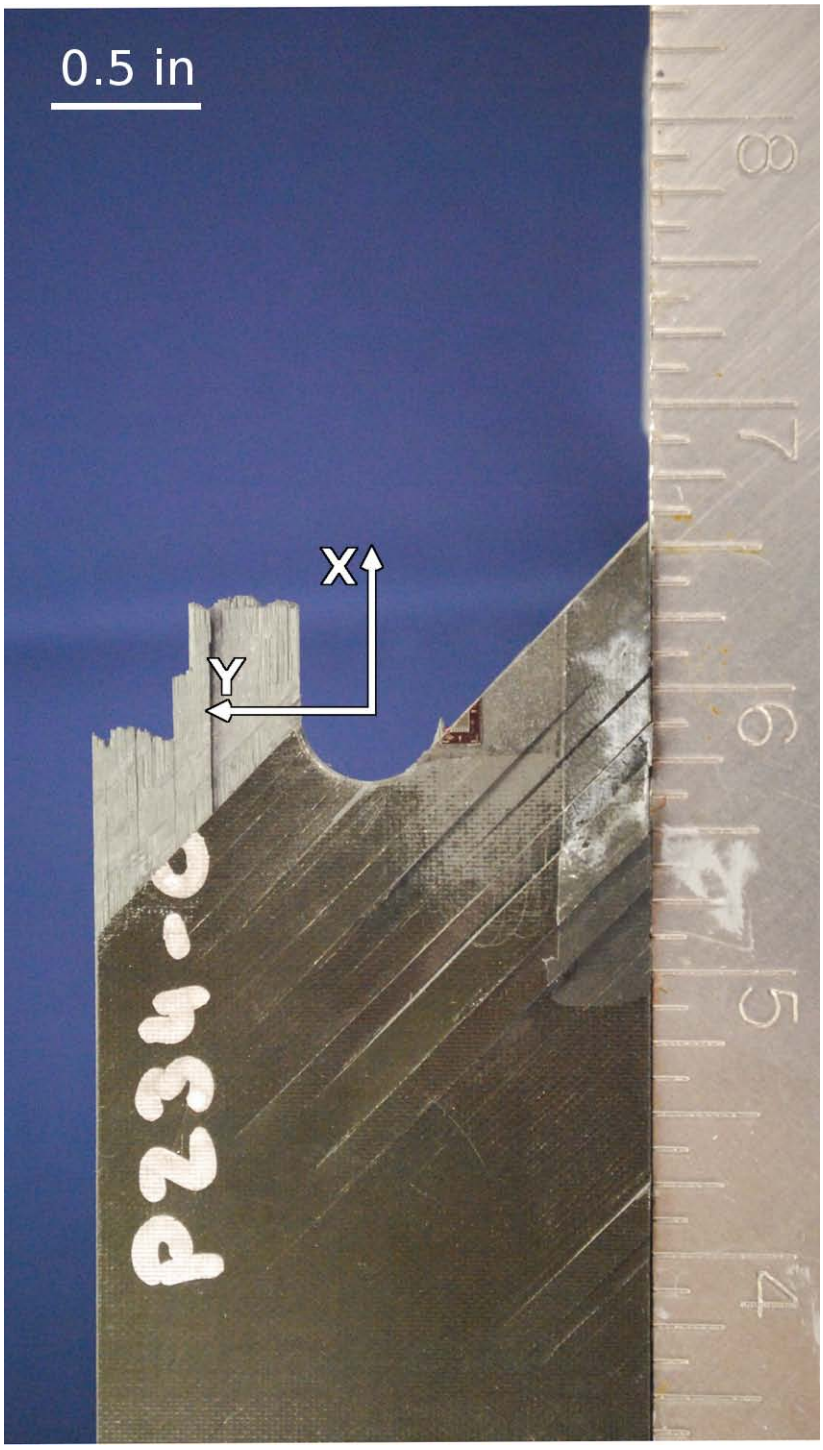

Figure 6.15 Photograph documentation of the front face of the top half of a failed OHT specimen (OH-C054-02), where final failure resulted in the specimen breaking into two parts.

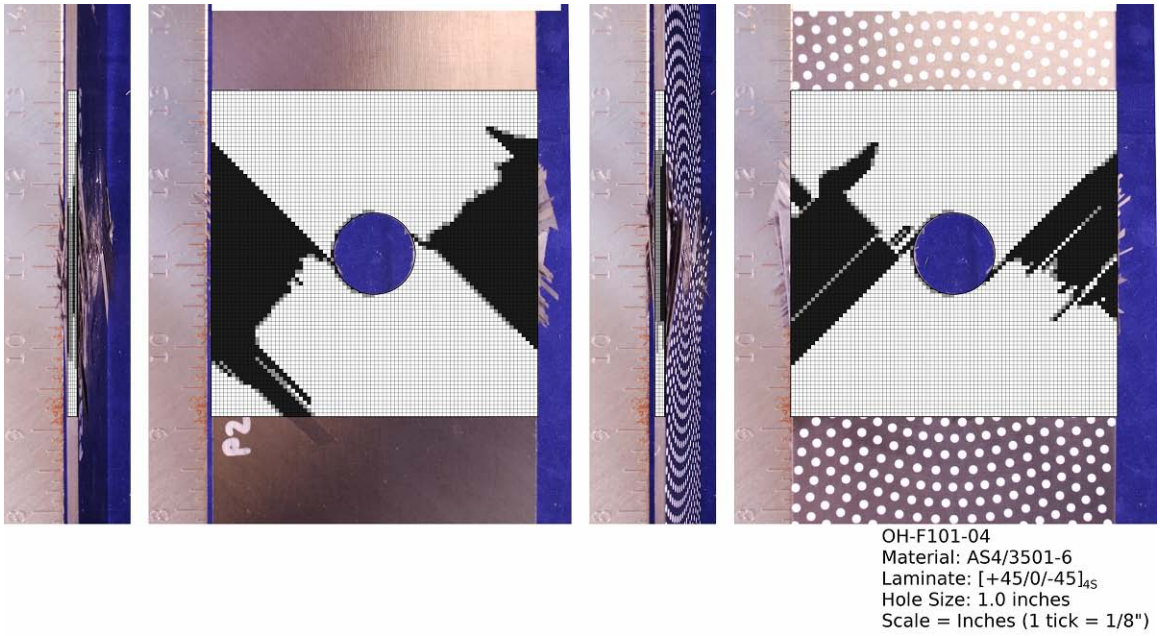

Figure 6.16 Damage grid of an OHT specimen (OH-F101-04) with single-ply effective ply thickness laminate showing typical triangular region within which damage occurs.

the $-45°$ direction appears to follow the inner ply fiber angle. However, this damage path requires fibers to break, resulting in a jagged damage path at the outer surface. The overall planar size of this region depends on the geometric size of the specimens. A different trend is observed in the four-ply effective ply thickness specimens. In these specimens, the majority of damage occurs along a diagonal region, aligned with the outer ply fiber angle, and tangent to the hole. A damage grid illustrating this is shown in Figure 6.17. The width of this region varies between half the hole diameter and three hole diameters. Additional damage occurs outside this primary damage region.

The transverse zigzag damage observed in the single- and double-edge-notched specimens is also observed in five of the OHT specimens. These are only specimens with the single-ply effective ply thickness laminate and with a 1.0-inch diameter hole. There are a total of 8 specimens tested with this laminate and hole size, with one of these not tested to ultimate failure. The transverse zigzag damage in the OHT specimens always occurs on one side of the specimen hole, and fiber fracture is always present along the transverse zigzag damage path, typically spanning from the hole edge to the specimen edge. An example of a damage sketch with this failure is shown in Figure 6.18. This path is always perpendicular to the loading direction, originating at the side of the hole and progressing to the specimen edge.

Overall, damage trends are similar among specimens with the same effective ply thickness, with the exception of the specimens without a hole. The specimens without a hole exhibit different damage characteristics and different damage initiation locations than those with a hole. Of specimens with a hole (of diameter greater than zero), damage typically initiates near the highest stress concentration points at the hole boundary. Specimens with single-ply effective ply thickness laminates exhibit matrix cracking and delamination in a triangular region defined by the ply angles of the laminate ($45°$ for the specimens tested here). Specimens with four-ply effective ply thickness laminates exhibit matrix cracking and delamination in the diagonal regions, along the outer ply angle, about the hole. The hole size influenced both damage regions, where the diameter of the hole was correlated to the planar dimension of the

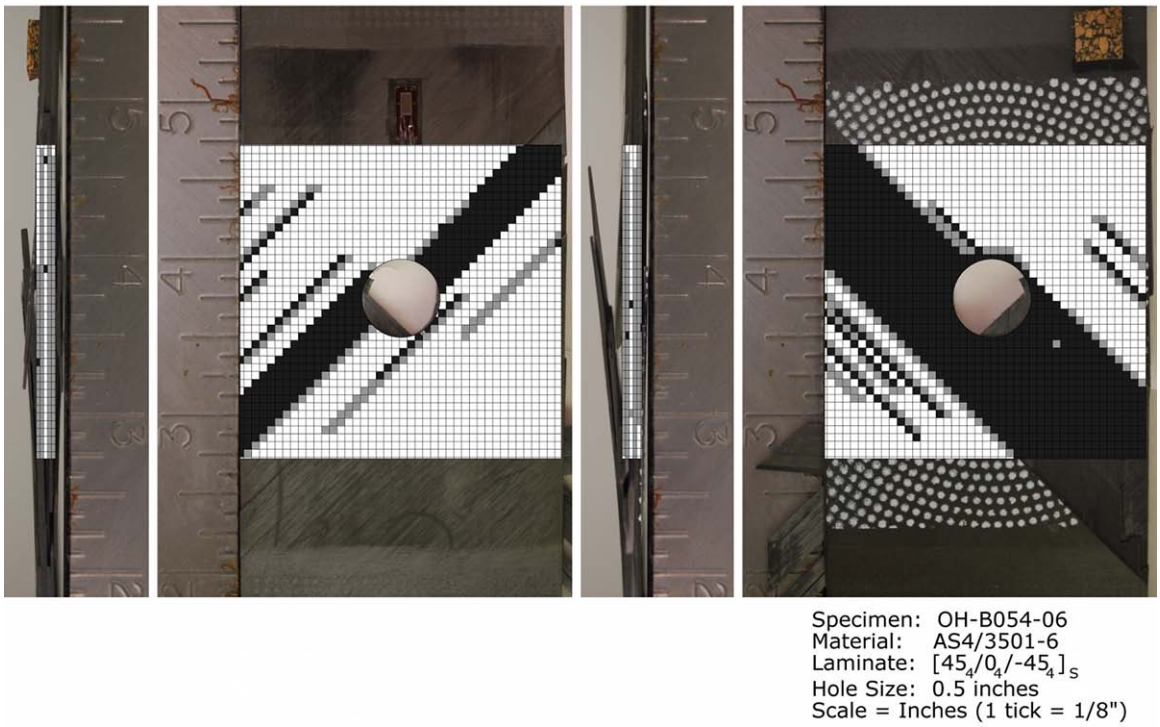

Figure 6.17 Damage grid of an OHT specimen (OH-B054-06) with four-ply effective ply thickness laminate showing typical diagonal region along which damage occurs.

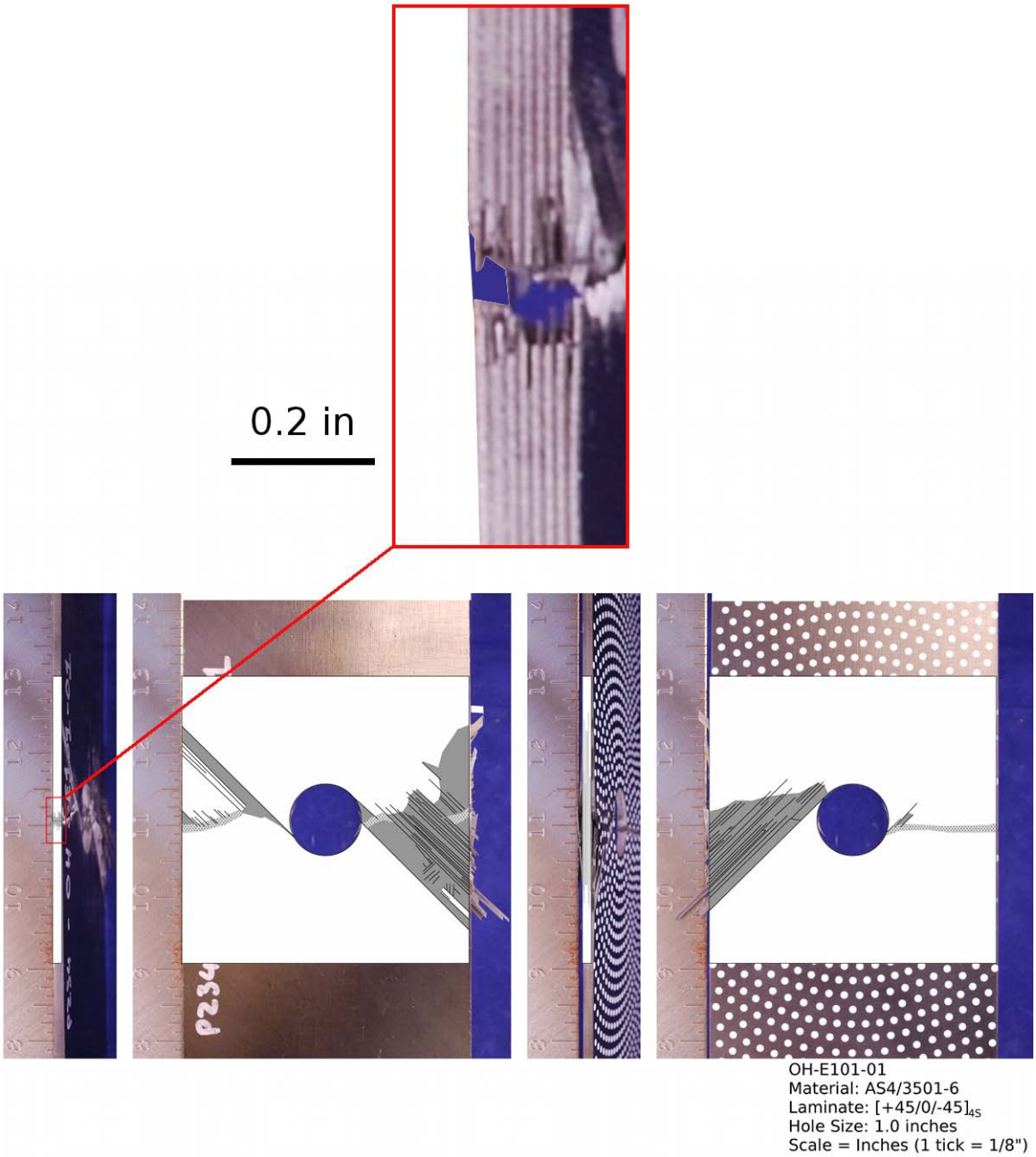

Figure 6.18 Damage sketch of an OHT specimen (OH-E101-01) exhibiting transverse zigzag damage, with enlarged photograph of the surface where the transverse zigzag pattern is visible.

region.

6.1.4 Ply-Drop Specimens

The ply-drop specimens were the final specimens to be documented as part of this work. These specimens are described in Section 4.4. There were a total of 9 ply-drop specimens tested (loaded), with 6 showing visual signs of damage. Damage in these specimens is dominated by matrix cracking and delamination. In the specimens exhibiting visual damage, matrix cracking and delamination is observed in all of these specimens, and fiber fracture is observed in 2 of these specimens. Transverse zigzag damage is not observed in any of the ply-drop specimens. The majority of visual damage observed occurs between the ply-drop region and the bonded planing tab (see Section 4.4 for details on specimen geometry).

Comparison of damage trends within these specimens reveal that delamination is typically observed in the region of the ply drop. Of the 5 specimens with the single-ply effective ply thickness laminate, 4 specimens show delamination occurring between plies in the region of the ply drop. In these four specimens, the delamination propagates along the interfaces of the dropped sublaminate (laminate details are presented in Section 4.4). An example of the typical delamination propagation paths, illustrated in a damage sketch, is shown in Figure 6.19, with an enlarged view of the right face damage sketch in the region of the dropped plies shown in Figure 6.20. From this view, it can be seen that the two delamination paths follow the interfaces between the dropped sublaminate and the continued sublaminates (where the continued sublaminates sandwich the dropped sublaminate). In the region beyond the dropped sublaminate, delamination occurs between at least 7 of the plies (as determined via visual inspection).

For specimens with the two-ply effective ply thickness laminate, 2 of the 4 specimens exhibit visual damage. These 2 specimens have delamination occurring between plies in the region of the ply drop. The damage sketches of these two specimens are shown in Figures 6.21 and 6.22. Of these specimens, only one had delamination paths following the interface of the dropped sublaminate. The other specimen exhibits additional delaminations within the plies of the sublaminates. This is more

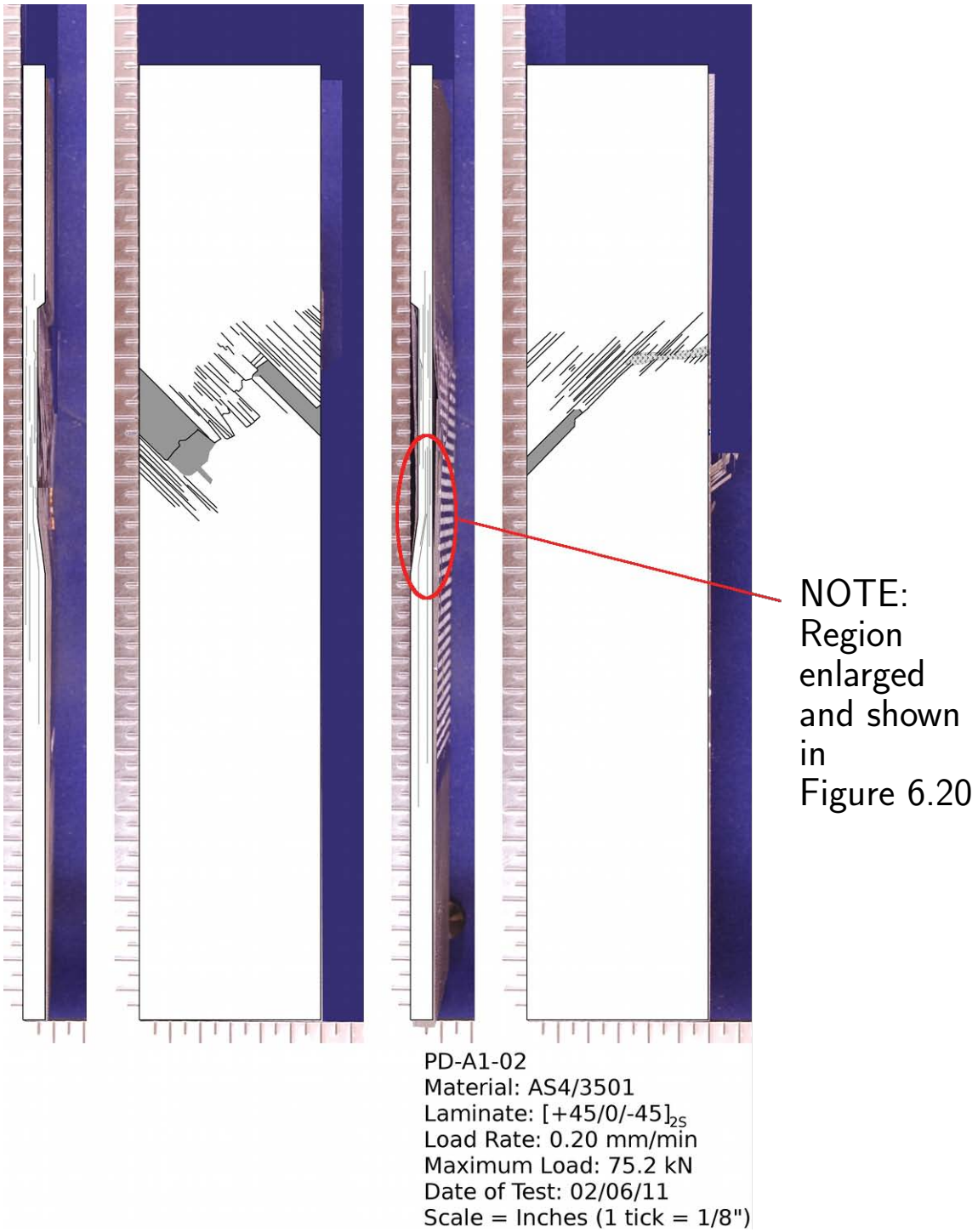

Figure 6.19 Damage sketch of a ply-drop specimen (PD-A1-02) with single-ply effective ply thickness laminate exhibiting delamination along sublaminate interfaces.

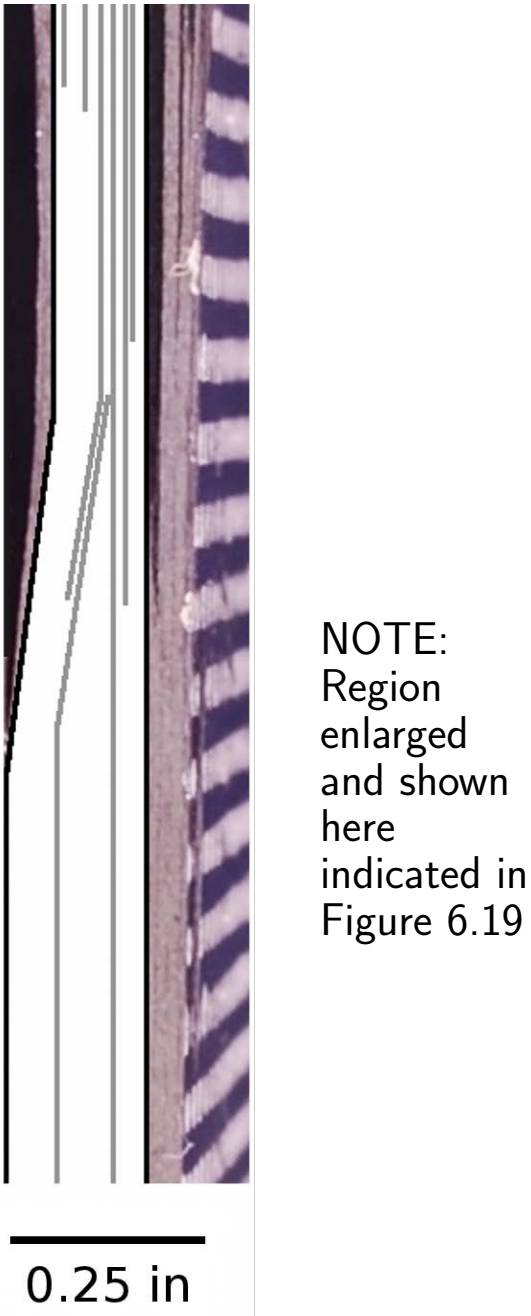

Figure 6.20 Enlarged view of the right face damage sketch in the region of the dropped plies of a ply-drop specimen (PD-A1-02) with single-ply effective ply thickness laminate exhibiting delamination along the sub-laminate interfaces.

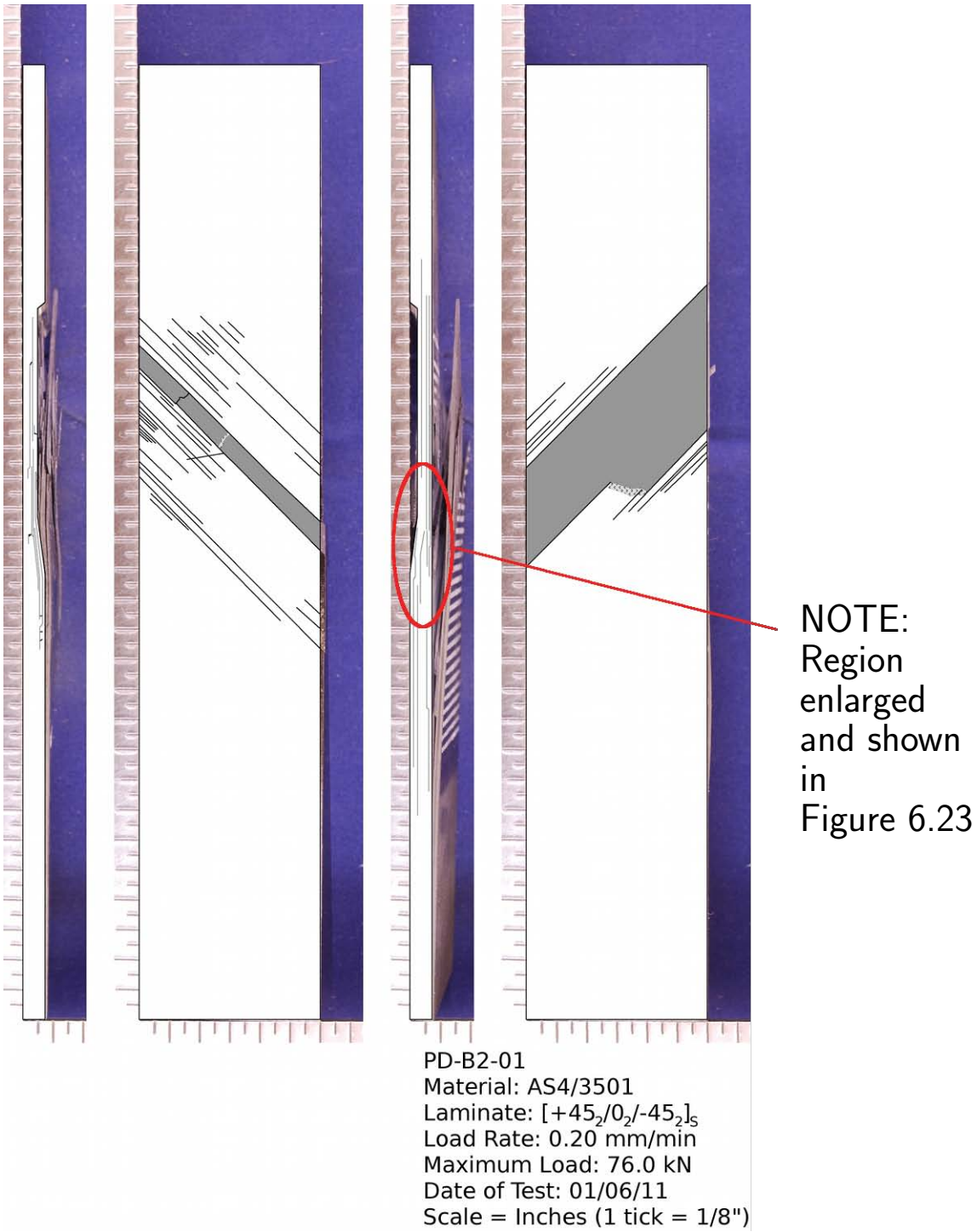

Figure 6.21 Damage sketch of a ply-drop specimen (PD-B2-01) with two-ply effective ply thickness laminate exhibiting delamination along the sublaminate interfaces and within the continued sublaminate layers.

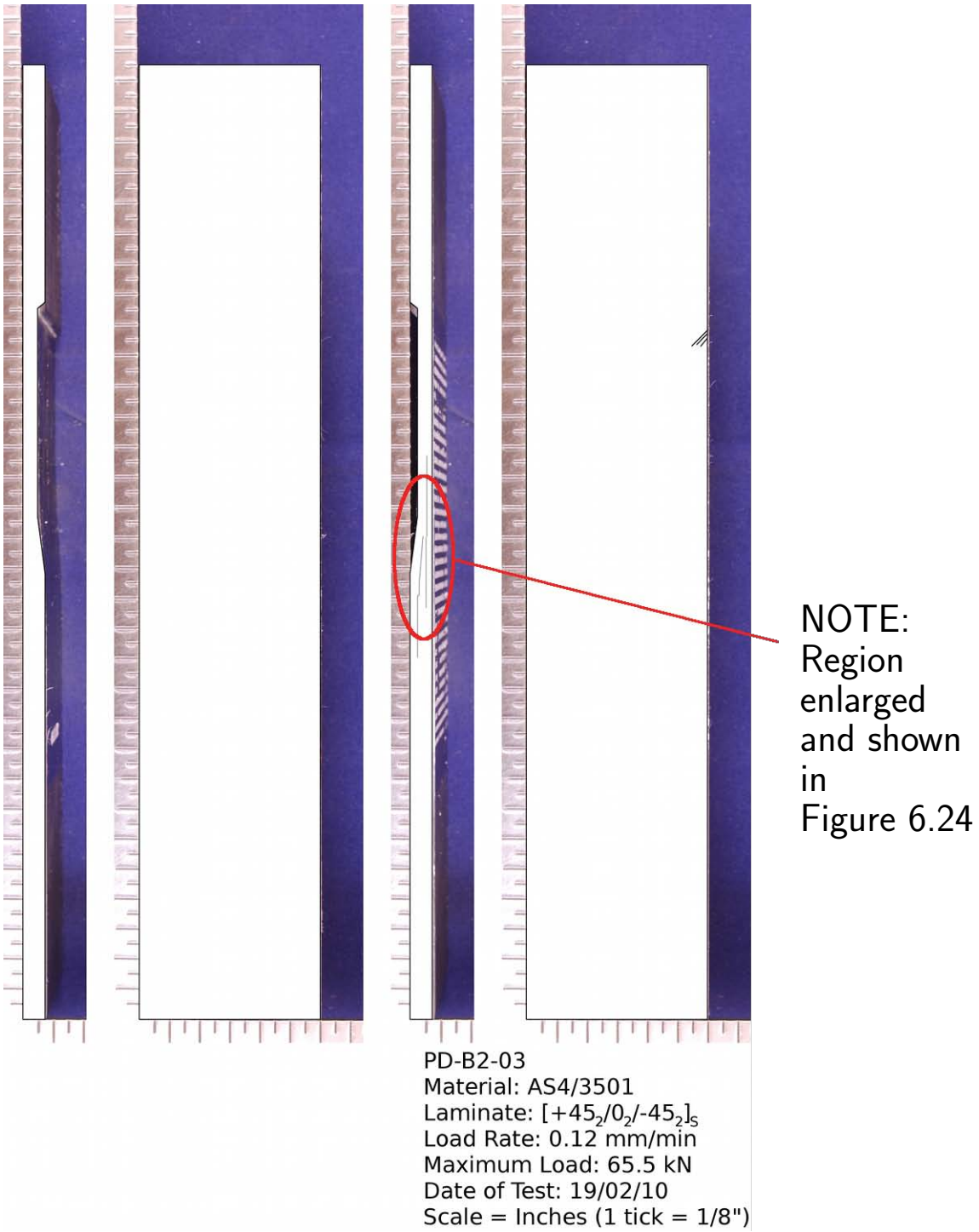

Figure 6.22 Damage sketch of a ply-drop specimen (PD-B2-03) with two-ply effective ply thickness laminate exhibiting delamination along sublaminate interfaces.

easily seen in the enlarged right face damage sketches shown in Figures 6.23 and 6.24. In the sketch illustrated in Figure 6.23, delaminations occur along the interface of the dropped sublaminate, but additional delaminations occur in the sublaminates surrounding the dropped sublaminate. This is not observed in the single-ply effective ply thickness specimens. The damage sketch illustrated in Figure 6.24 shows the same delamination characteristics as in the single-ply effective ply thickness specimens, where delamination propagates along each of the interfaces of the dropped sublaminate and the continued sublaminates. Note that specimen PD-B2-01 was loaded to higher tensile load than specimen PD-B2-03, and a greater damage extent is observed in the higher-loaded specimen. It is possible that additional delaminations would have initiated and propagated in the continued sublaminates of PD-B2-03 had the same level of loading been applied.

6.2 Comparison Database

The comparison database enables lengthscale effects in composites to be investigated. An initial damage comparison database was established via the implementation of the damage documentation procedures on the four specimen types investigated in this work. This database can continue to grow as the damage documentation procedures are applied to additional specimens of the same or different types. As results from the damage documentation of specimens of different geometries were added to the database, investigation of lengthscale effects across specimen types (e.g., different geometries, laminates, loadings) was conducted.

The database contains all the information gathered from the damage documentation procedures (damage extent from the damage grids, damage paths and damage modes from the damage sketches, etc.) as well as specifics concerning the specimens (fiber and epoxy type, laminate layups, loading history, etc.). At the end of this work, 1394 tested specimens had been entered into the database. This includes the 182 tested NRL single-edge-notched specimens, the 1152 NRL double-edge-notched specimens, the 51 CRC-ACS open hole tension specimens, and the 9 CRC-ACS ply-

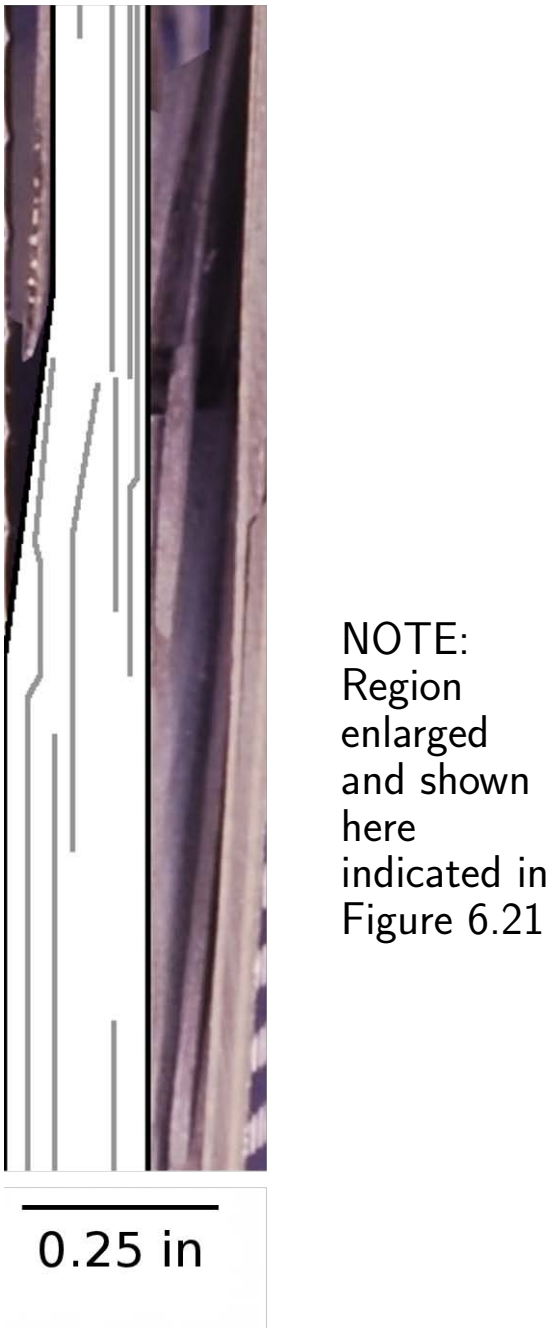

Figure 6.23 Enlarged view of the right face damage sketch in the region of the dropped plies of a ply-drop specimen (PD-B2-01) with two-ply effective ply thickness laminate exhibiting delamination along the sublaminate interfaces and within the continued sublaminate layers.

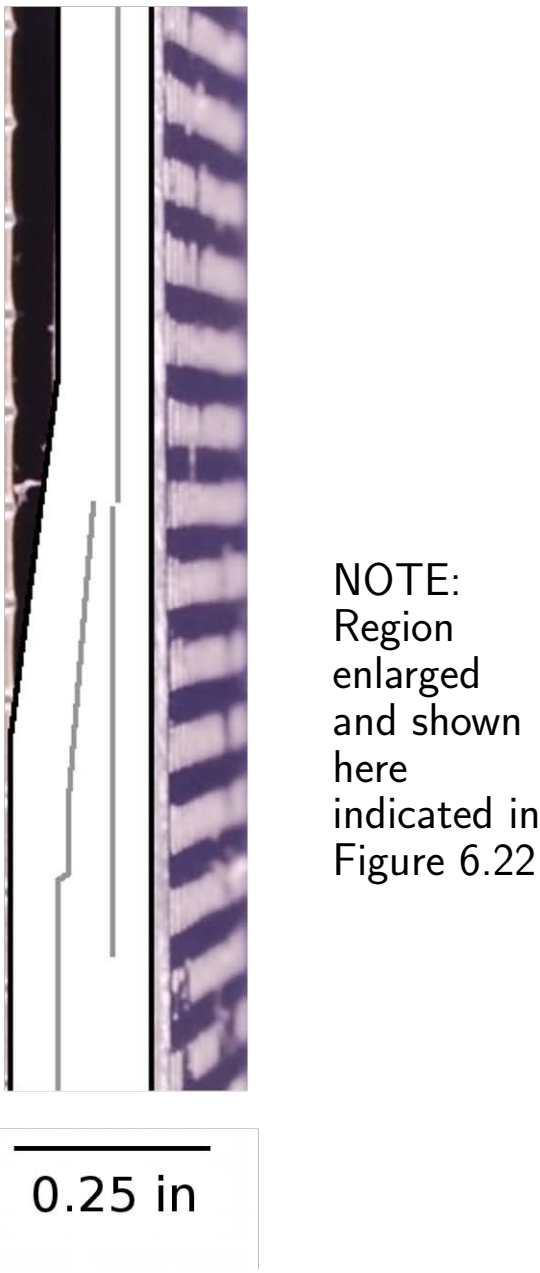

Figure 6.24 Enlarged view of the right face damage sketch in the region of the dropped plies of a ply-drop specimen (PD-B2-03) with two-ply effective ply thickness laminate exhibiting delamination along sublaminate interfaces.

drop specimens included in this work. By organizing all this information into a sortable and searchable database, comparisons were made to find trends and expose differences in damage as the laminate is changed within specimen type and as the level of testing is changed.

The findings from the database are discussed in Chapter 8. However, one example is presented here to demonstrate how the database enables lengthscale results to be compared across specimen types. An example of one possible utilization of the database reveals trends between the presence of transverse zigzag damage and the applied load in different specimen types. In the single-edge-notched specimens, there is a clear trend between the combination of load path and laminate that resulted in the 'activation' of transverse zigzag damage. The graph shown in Figure 6.25 illustrates the number of specimens that exhibit transverse zigzag damage for each of the load paths to which the specimens were exposed. A few load paths are found to never induce transverse zigzag damage among the specimens tested. The data in this graph can be further assessed by the laminate fiber angles. The four graphs shown in Figures 6.26 and 6.27 illustrate the number of specimens that exhibit transverse zigzag damage for each of the load paths, where each graph contains specimens of a specific fiber angle. A trend is identified from these graphs. Specimens with fiber angles of 15° and 30° always exhibit transverse zigzag damage when subjected to load paths 2 and 4 (with the exception of one 15° specimen subjected to load path 2). Load paths 3 and 12 also activate transverse zigzag damage within a few of the 30° specimens. Specimens with fiber angles 60° and 75° always exhibit transverse zigzag damage when subjected to load paths 7 and 10 through 15 (with the exception of one 75° specimen subjected to load path 10). One of the four 75° specimens subjected to load path 9 exhibited transverse zigzag damage. Referring to Table 4.3, where the components of each load path are listed, relations between the components of the loading (i.e., tension/compression, shear, and in-plane rotation components) can be investigated. One such observation is that load paths 10 through 15 all have a tension component. Relating this to the activation of transverse zigzag damage within specimens of fiber angles 60° and 75° suggests that a component of load perpendicular

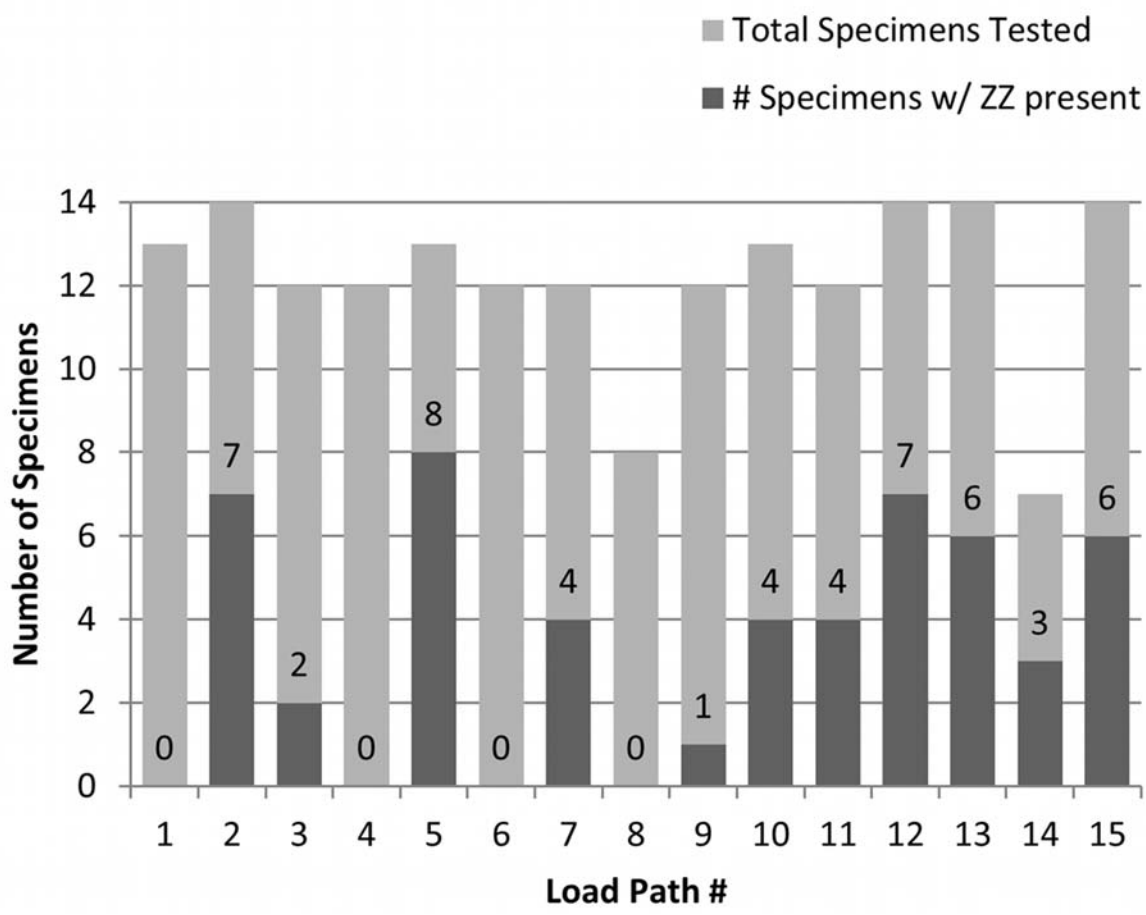

Figure 6.25 Graph of the single-edge-notched specimens with 'active' transverse zigzag damage and the corresponding load path.

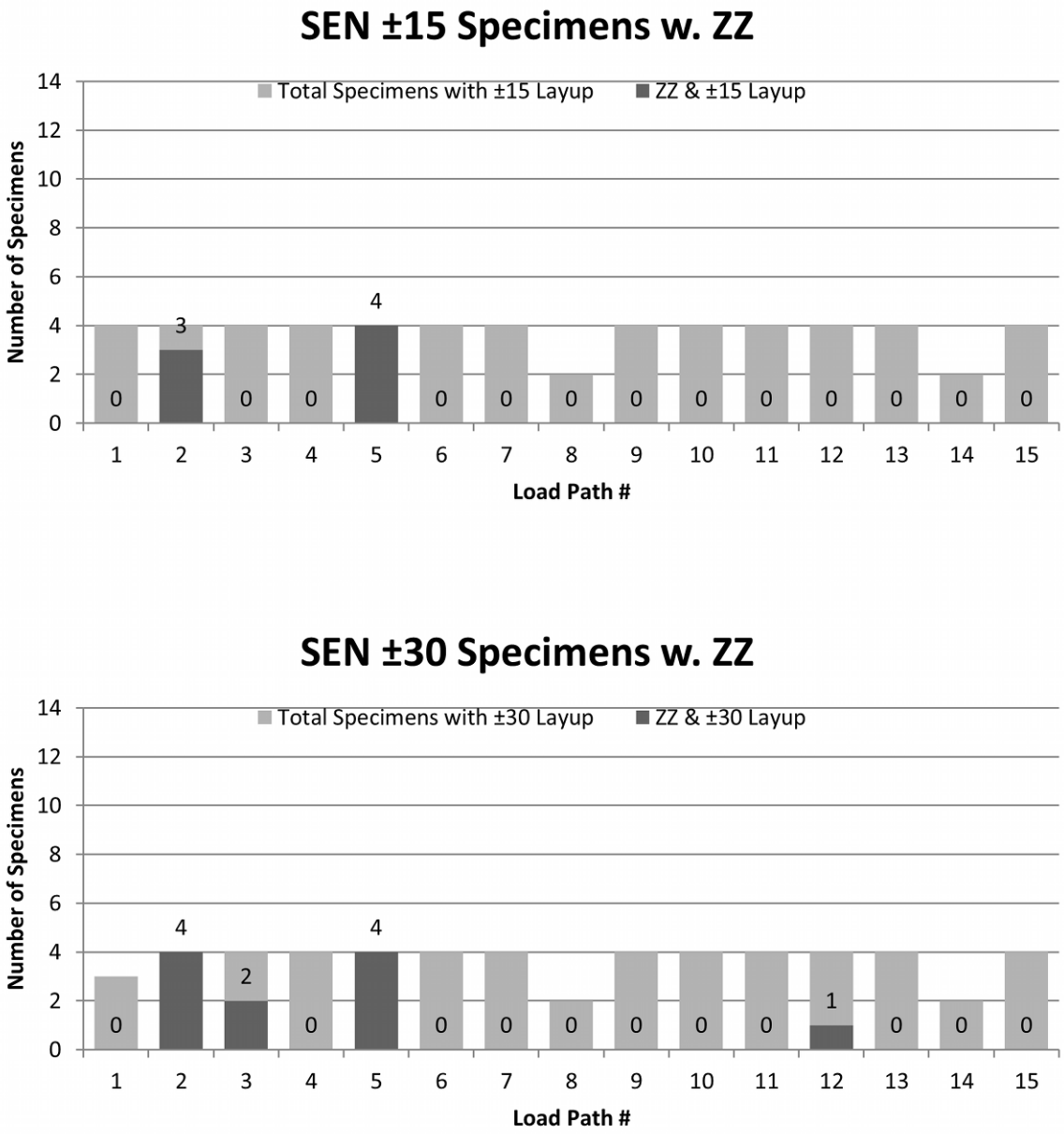

Figure 6.26 Graphs of the single-edge-notched specimens with 'active' transverse zigzag damage and the corresponding load path, broken down by laminate fiber angle: *(upper)* specimens with fiber angles of 15°, and *(lower)* specimens with fiber angles of 30°.

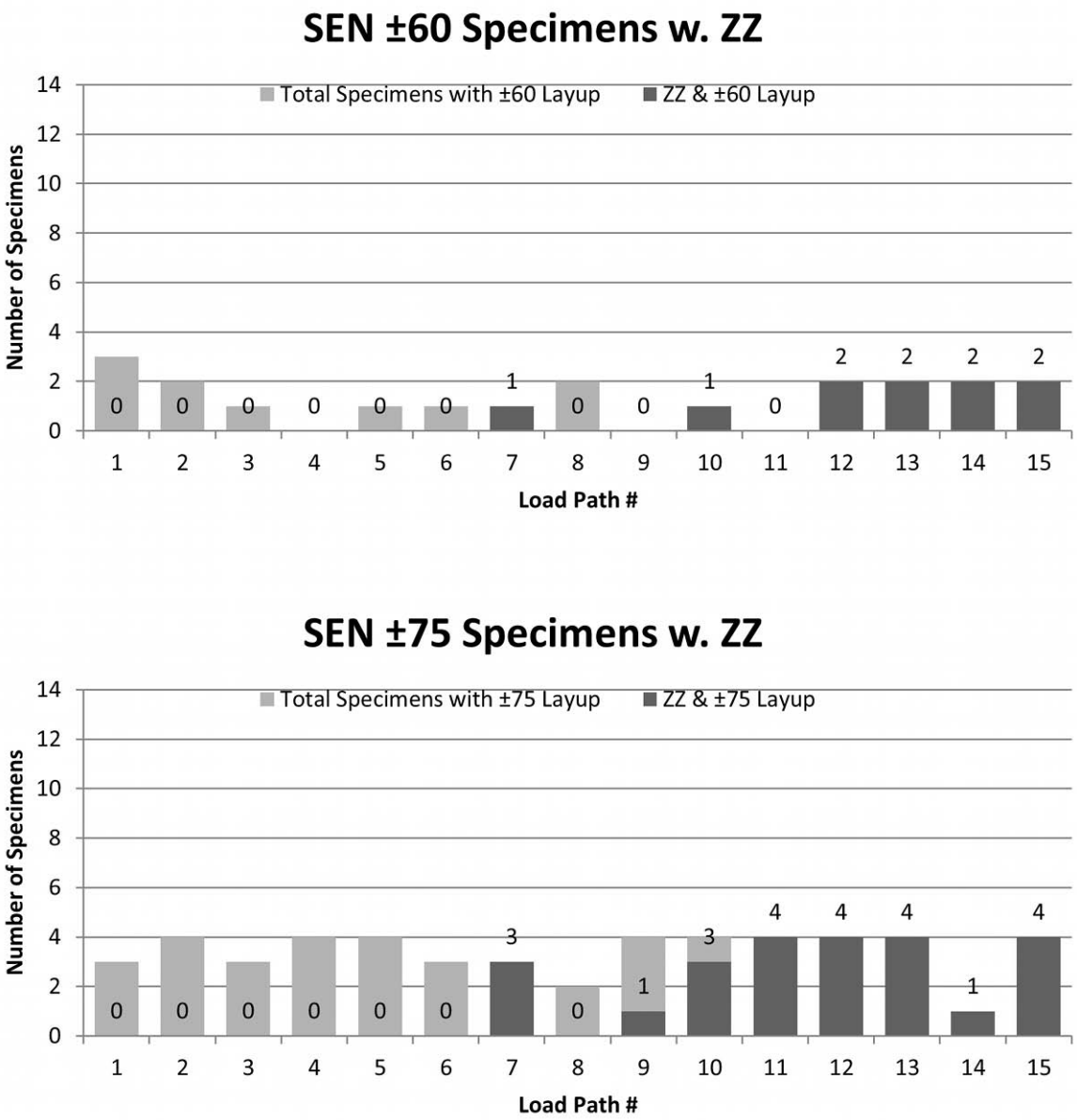

Figure 6.27 Graphs of the single-edge-notched specimens with 'active' transverse zigzag damage and the corresponding load path, broken down by laminate fiber angle: *(upper)* specimens with fiber angles of 60°, and *(lower)* specimens with fiber angles of 75°.

to the fibers is necessary to activate transverse zigzag damage. Further development on such relations are discussed in Chapter 8.

A similar investigation can be made of the double-edge-notched specimens. The graph shown in Figure 6.28 illustrates the number of double-edge-notched specimens exhibiting transverse zigzag damage and the associated load paths to which these specimens were subjected. Two 'groups' of load paths are identified. These are load paths 33 through 49 (excluding 46), and load paths 60 through 72. Again, investigating the database and assessing the specimens by laminate fiber angle identifies that the specimens with active transverse zigzag damage within these two groups correspond to laminate angles of 60° or 75°. As with the graphs shown for the single-edge-notched specimens, the results in the database of the double-edge-notched specimen can be used to investigated the influence of the laminate angle and effective ply thickness on the exhibited damage. For example, the graphs shown in Figures 6.29 through 6.36 illustrate the number of double-edge-notched specimens, grouped by laminate angle and effective ply thickness, exhibiting fiber fracture and the associated load paths to which these specimens were subjected. More details are discussed in Chapter 8.

Thus, the comparison database allows lengthscale effects in composite specimens to be investigated. Incorporating all the data from the damage documentation procedures, described in Chapter 5, enables these lengthscale effects to be identified. As the example above indicates, trends within experimental specimens, and across specimen types can be explored by utilizing the database.

6.3 Computed Microtomography

Over the course of this work, 57 specimens were scanned using computed microtomography (CμT). This included scans of 9 of the NRL single-edge-notched specimens, 28 of the NRL double-edge-notched specimens, 17 of the open-hole tension specimens, and 3 of the ply-drop specimens. A list of the specimens scanned and a brief reason that the specimen was selected to be scanned is given in Tables 6.1 through 6.4. Further dialog on the reasons these specimens were selected are included throughout this

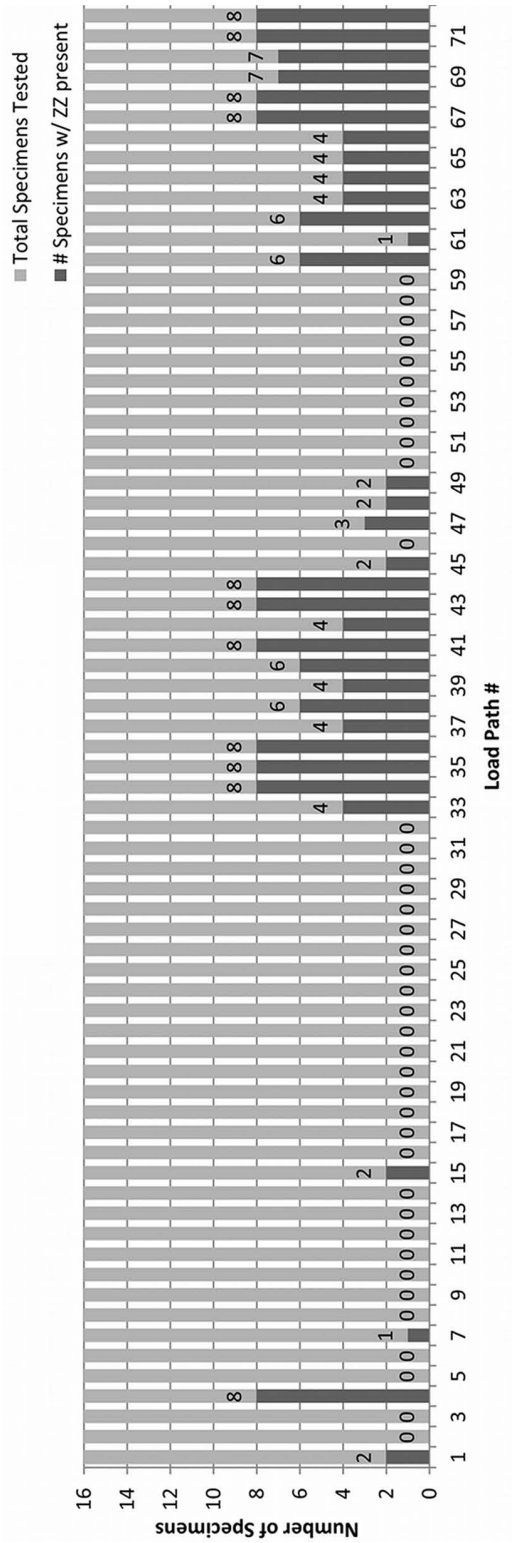

Figure 6.28 Graph of the double-edge-notched specimens with 'active' transverse zigzag damage and the corresponding load path.

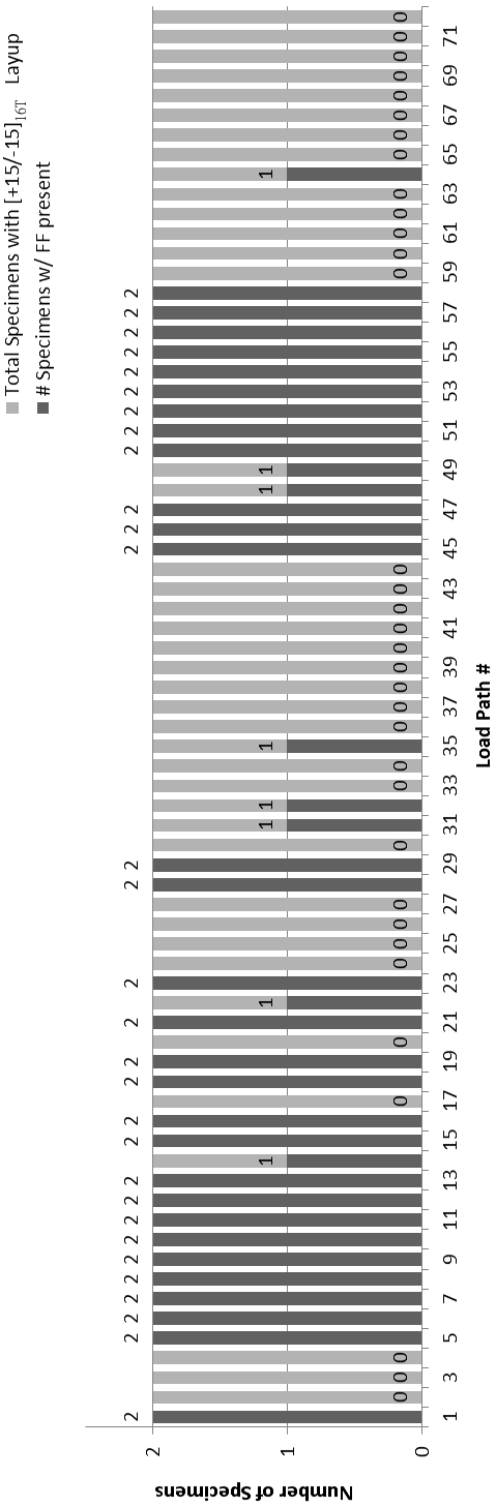

Figure 6.29 Graph of the double-edge-notched specimens with 'active' fiber fracture damage and the corresponding load path, for the single-ply effective ply thickness laminate with θ equal to 15°.

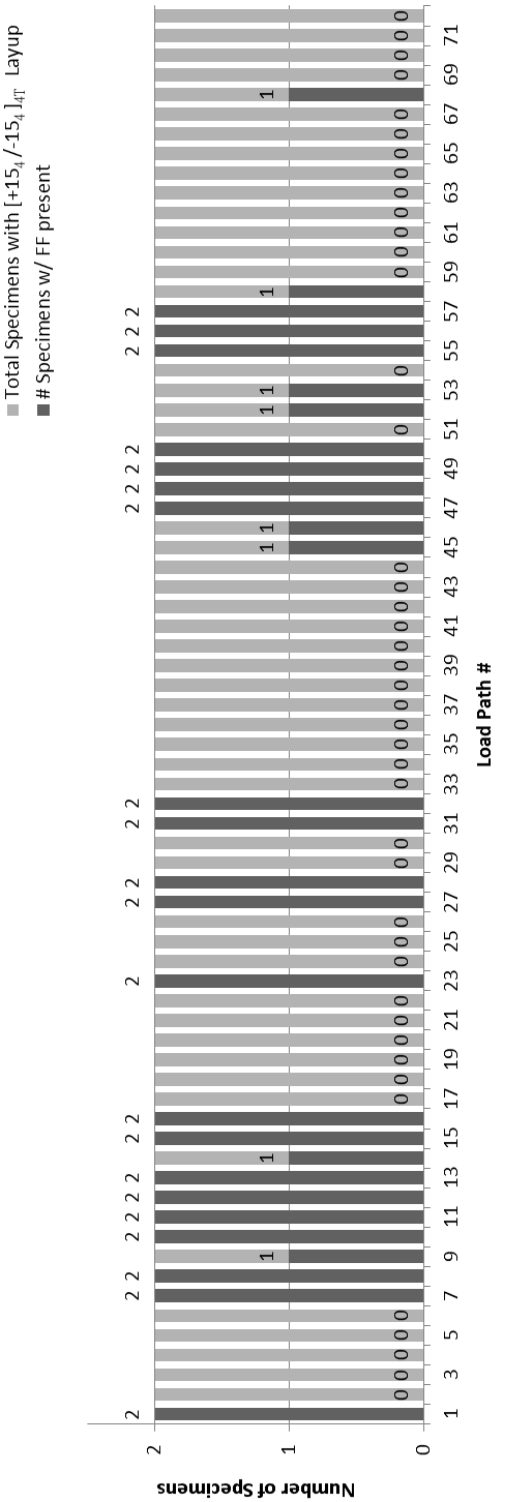

Figure 6.30 Graph of the double-edge-notched specimens with 'active' fiber fracture damage and the corresponding load path, for the four-ply effective ply thickness laminate with θ equal to 15°.

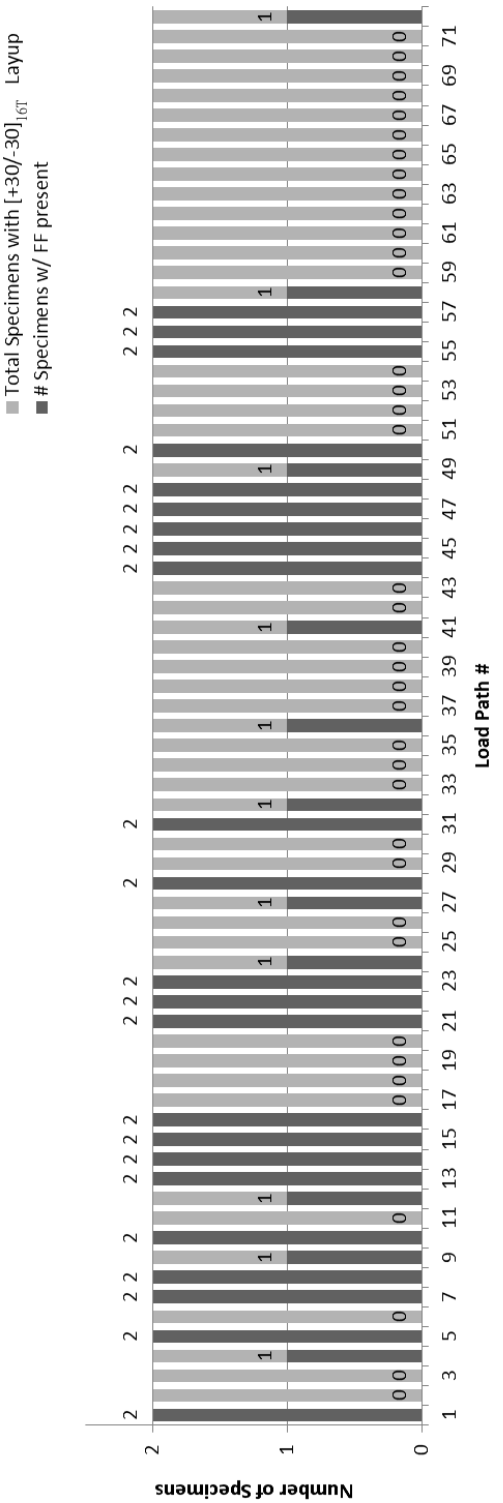

Figure 6.31 Graph of the double-edge-notched specimens with 'active' fiber fracture damage and the corresponding load path, for the single-ply effective ply thickness laminate with θ equal to 30°.

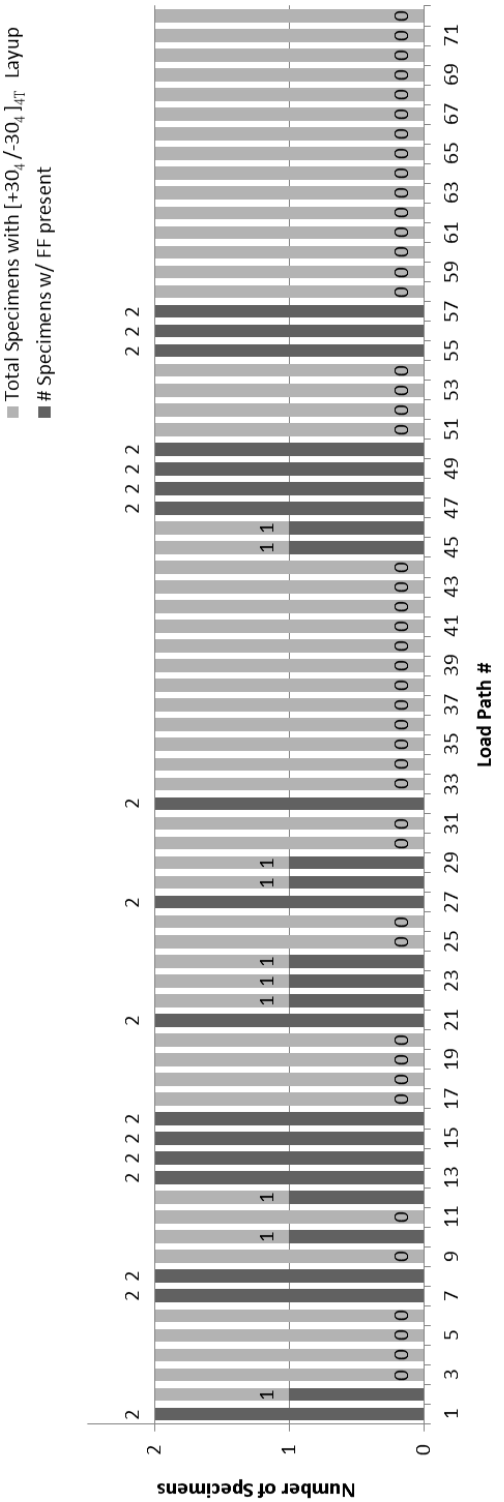

Figure 6.32 Graph of the double-edge-notched specimens with 'active' fiber fracture damage and the corresponding load path, for the four-ply effective ply thickness laminate with θ equal to 30°.

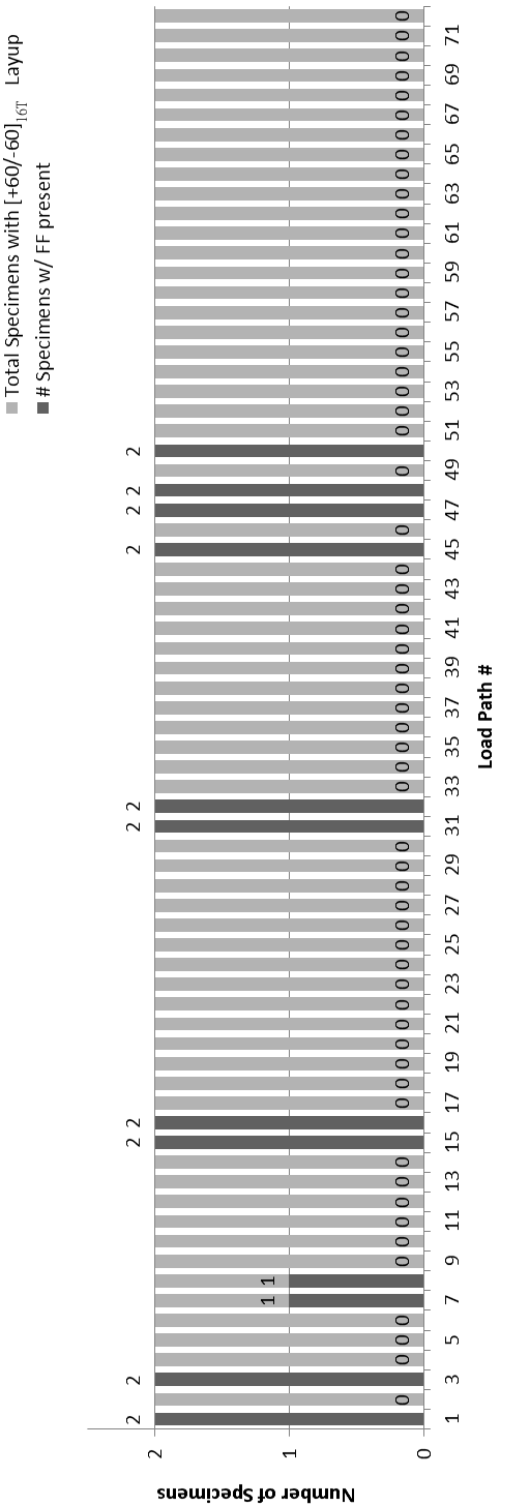

Figure 6.33 Graph of the double-edge-notched specimens with 'active' fiber fracture damage and the corresponding load path, for the single-ply effective ply thickness laminate with θ equal to 60°.

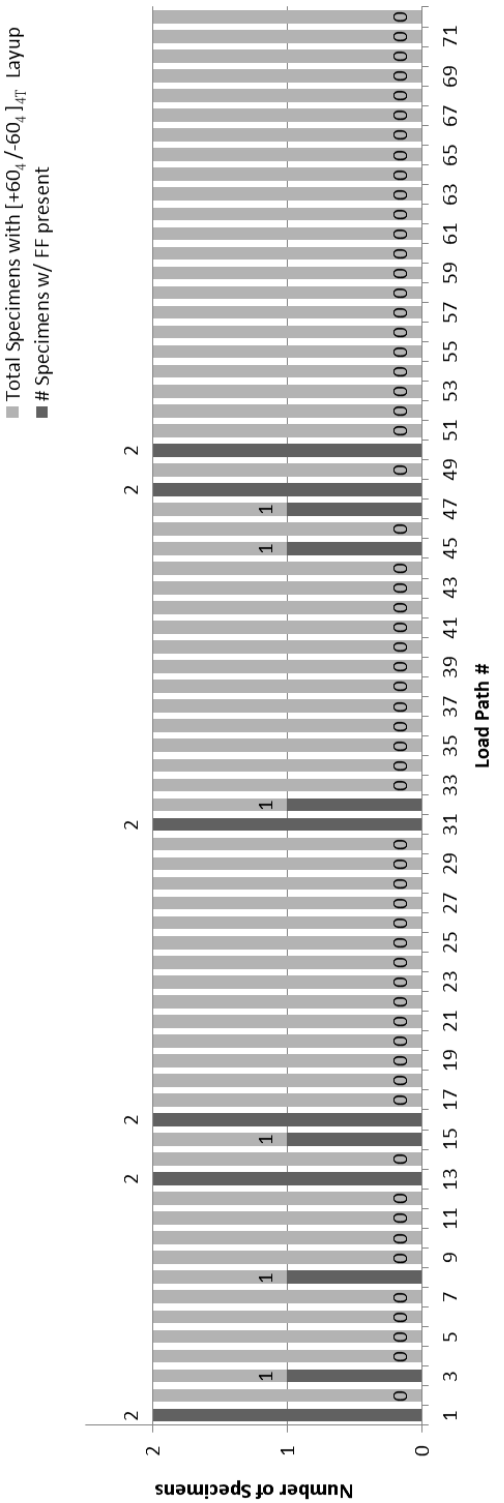

Figure 6.34 Graph of the double-edge-notched specimens with 'active' fiber fracture damage and the corresponding load path, for the four-ply effective ply thickness laminate with θ equal to 60°.

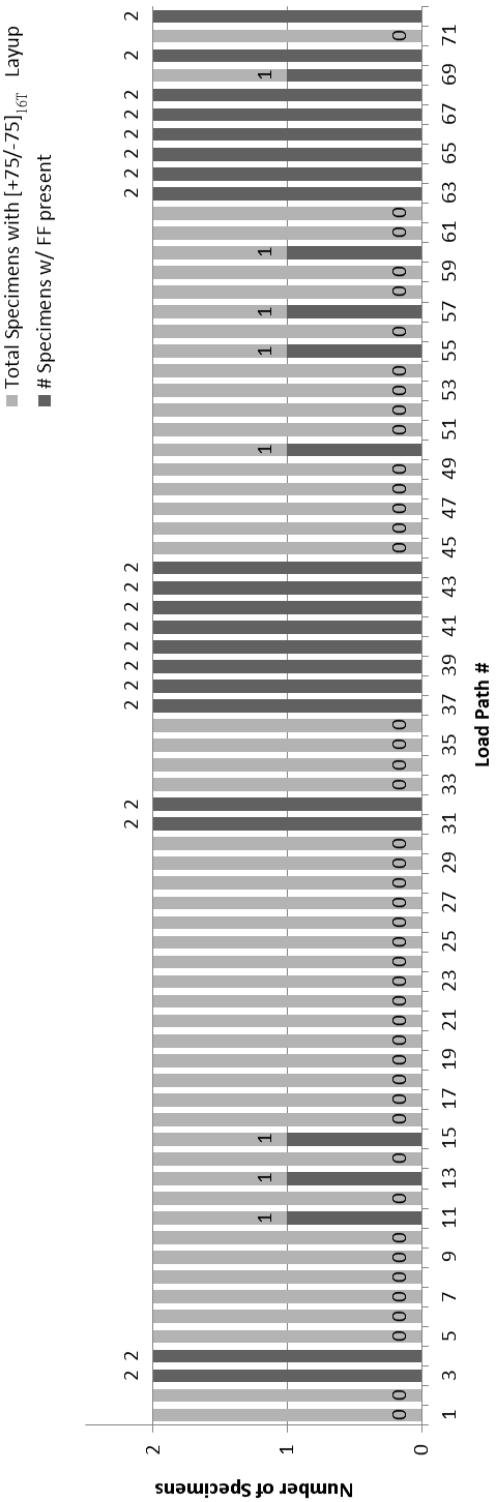

Figure 6.35 Graph of the double-edge-notched specimens with 'active' fiber fracture damage and the corresponding load path, for the single-ply effective ply thickness laminate with θ equal to 75°.

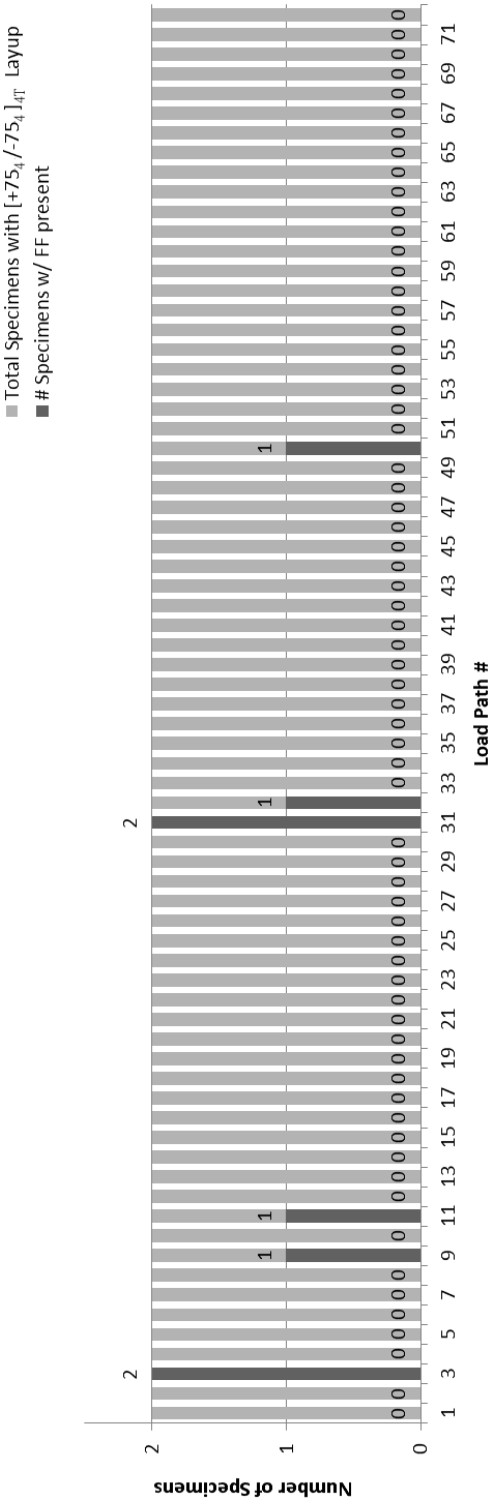

Figure 6.36 Graph of the double-edge-notched specimens with 'active' fiber fracture damage and the corresponding load path, for the four-ply effective ply thickness laminate with θ equal to 75°.

section. Many observations about damage, damage paths, and mode interaction are made from these scans. The specifics of the CμT scanning technique are described in Section 5.3. Each scan produces on the order of 20 gigabytes of data, including the individual X-ray projections (typically around 2000 projections per scan) and the recreated three-dimensional (3-D) volume. All scan data is stored on an external hard drive. A volume rendering software program is required to view the recreated specimen volumes. VGStudio Max (©Volume Graphics GmbH) was used throughout this work to investigate the volumes and to create the CμT images seen in this section.

From the scans of the single-edge-notched specimens, one of the most interesting damage characteristics investigated is the transverse zigzag damage mode. As first described in Section 6.1.1, this transverse zigzag damage consists of alternating through-thickness matrix cracks and short delaminations between plies, resulting in a transverse zigzag damage path as observed on one of the side faces. The face where the transverse zigzag is observed depends on the ply angles and the geometry of the specimen. This damage mode is observed in 52 of the 106 single-edge-notched specimens that exhibit visual damage. As indicated in Table 6.1, four specimens exhibiting different characteristics of transverse zigzag damage were selected for scanning. These specimens are representative of the transverse zigzag damage observed throughout the single-edge-notched specimens. The different characteristics of the transverse zigzag damage mode include a triple zigzag appearing on the face of the specimen, a single zigzag that exhibits a change in the damage mode observed on the front and back faces, a double zigzag that exhibits a change in the damage mode observed on only one face, and a single zigzag that propagates through the boundary of the grip without showing visual signs of being influenced by the boundary. From the CμT scans investigating transverse zigzag damage, it is observed that this mode initiates near the tip of the strain riser and propagates along the same angle as one of the plies (although the damage goes through multiple plies).

An example of a CμT scan and observed results for a single-edge-notched specimen, specimen 005-61, exhibiting transverse zigzag damage follows. This specimen is made of AS4/3501-6 with a stacking sequence of $[(-75/+75_2/-75_2/+75)_S]_S$. The

Table 6.1 NRL single-edge-notched specimens selected for computed microtomography scan

Specimen	**Reason Scanned**
005-46	Triple zigzag damage mode
005-53	Extensive delamination damage
005-60	Single zigzag with mode switching on two faces
005-61	Double zigzag with mode switching one one face
007-51	Boundary reflection and mode switch at boundary
008-34	Minimal matrix cracking only at notch tip
008-38	Single zigzag running through boundary
008-49	Minimal matrix cracking only at notch tip
008-58	No visible damage

Table 6.2 NRL double-edge-notched specimens selected for computed microtomography scan

Specimen	**Reason Scanned**
CH-A301-0403	Load Path 1 (Compression)
CH-A301-0507	Tension only loading
CH-B601-0103	Compression and twist loading
CH-B601-1104	Load Path 1 (Compression)
CH-C601-0704	Crossing double zigzag
CH-C601-1201	Load Path 1 (Compression)
CH-D301-0304	'W' Failure Path
CH-D301-0808	Load Path 1 (Compression)
CH-E151-0203	Load Path 1 (Compression)
CH-F151-0206	Load Path 1 (Compression)
CH-F151-0402	Compression, bend, and twist loading
CH-F151-0702	One-sided Damage
CH-G751-0803	Primarily Delamination
CH-H751-0701	Compression and twist loading
CH-I304-0108	Double zigzag with reflection
CH-I304-0204	'W' Failure Path
CH-I304-0606	Load Path 1 (Compression)
CH-J304-0308	'W' Failure Path
CH-J304-0802	Load Path 1 (Compression)
CH-K304-1104	Load Path 1 (Compression)
CH-L604-0805	Tension and twist loading
CH-L604-1102	Load Path 1 (Compression)
CH-M154-0507	Load Path 1 (Compression)
CH-N154-0404	Load Path 1 (Compression)
CH-N154-0406	Interaction of damage modes
CH-O754-0302	Tension and twist loading
CH-O754-0503	Load Path 1 (Compression)
CH-P754-0201	Load Path 1 (Compression)

Table 6.3 CRC-ACS open-hole tension specimens selected for computed microtomography scan

Specimen	**Reason Scanned**
OH-A001-02	Effect of effective ply thickness
OH-A001-03	Effect of effective ply thickness
OH-A001-06	Effect of effective ply thickness
OH-A051-02	Effect of effective ply thickness and hole drilling damage
OH-A101-02	Effect of effective ply thickness and hole drilling damage
OH-A101-05	Effect of effective ply thickness and hole drilling damage
OH-A101-06	Effect of effective ply thickness and hole drilling damage
OH-B004-02	Effect of effective ply thickness
OH-B004-03	Effect of effective ply thickness
OH-B004-06	Effect of effective ply thickness
OH-B054-01	Effect of effective ply thickness and hole drilling damage
OH-B054-02	Effect of effective ply thickness and hole drilling damage
OH-B054-06	Effect of effective ply thickness and hole drilling damage
OH-B104-01	Effect of effective ply thickness and hole drilling damage
OH-B104-03	Effect of effective ply thickness and hole drilling damage
OH-B104-04	Effect of effective ply thickness and hole drilling damage
OH-B104-05	Effect of effective ply thickness and hole drilling damage

Table 6.4 CRC-ACS ply-drop specimens selected for computed microtomography scan

Specimen	**Reason Scanned**
PD-A1-02	Delamination failure paths
PD-B2-01	Delamination failure paths
PD-B2-03	Delamination failure paths

0°-axis is defined as parallel to the length of the specimen, which is perpendicular to the strain-riser (described in Section 4.1). The specimen was subjected to load path 13 ($u_x = 0.707$, $u_y = 0.000$, $R_z = -0.707$), as defined in Section 4.1 and Table 4.3. This involves an extensional load along the length and an in-plane counterclockwise rotation about the specimen center. The documentation photographs of the faces of the failed specimen are shown in Figure 6.37.

Virtual images taken of the specimen and created via the CμT process are shown in Figures 6.38 and 6.39 as examples of such created 3-D volumes. The volume shown in Figure 6.38 represents the specimen material between the dashed lines of Figure 6.37. These dashed lines encompass the damaged region as determined from the damage grid of the specimen. This specimen exhibits multiple damage modes (fiber fracture, matrix cracking, and delamination), all of which are observable in the recreated 3-D volume. One of the most powerful features of this process is the ability to investigate damage within the specimen without sectioning (cutting) the specimen, but by "virtually cutting" the 3-D volume. An example of a virtual cut of the specimen is shown in Figure 6.39. The cutting plane (location of cut) is that shown in Figure 6.38 as a shaded plane intersecting the volume. This is the end of the piece shown in Figure 6.39 with the shaded plane still there to help in its identification. This is emphasized in a two-dimensional presentation of the cutting plane in Figure 6.40.

It is observed in this specimen that the damage on the outer right-face of the specimen consists of matrix cracks and short delaminations alternating through the thickness. This can be seen upon close observation of the photographs shown in Figure 6.37. As can be seen in Figures 6.39 and 6.40, this damage at the "virtually cut" face has the same pattern as on the outer right face (also more clearly seen in Figure 6.38 than in Figure 6.37). Taking additional virtual cuts, shown in Figures 6.41 and 6.42, it is found that the damage initiates at the strain riser and propagates along the positive and negative fiber directions until reaching the outer right face. As can be seen in these two figures, the damage alternates between the positive and negative oriented plies. In order to get this same information with traditional

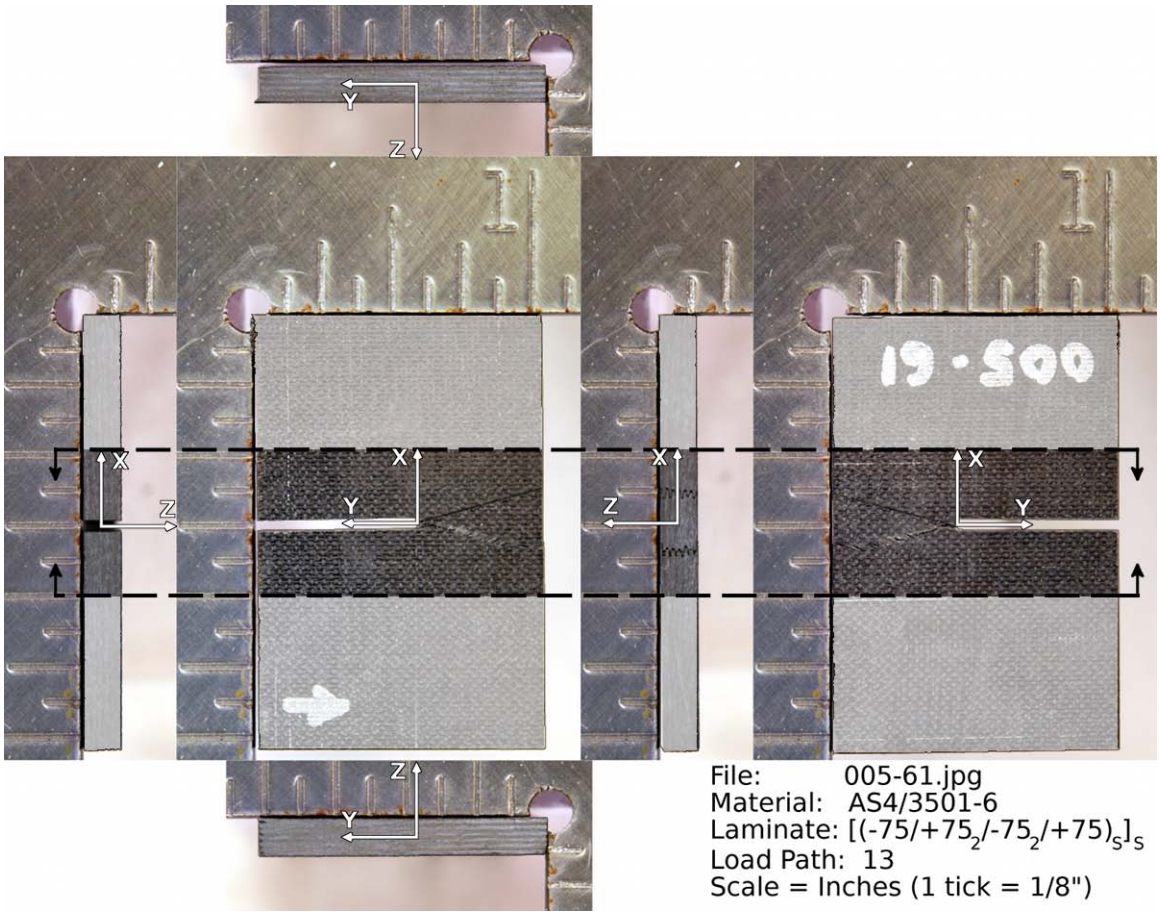

Figure 6.37 Optical documentation photographs of a NRL single-edge-notched specimen (005-61). (Note: Region between dashed lines represents material volume scanned and depicted in Figures 6.38 through 6.42.)

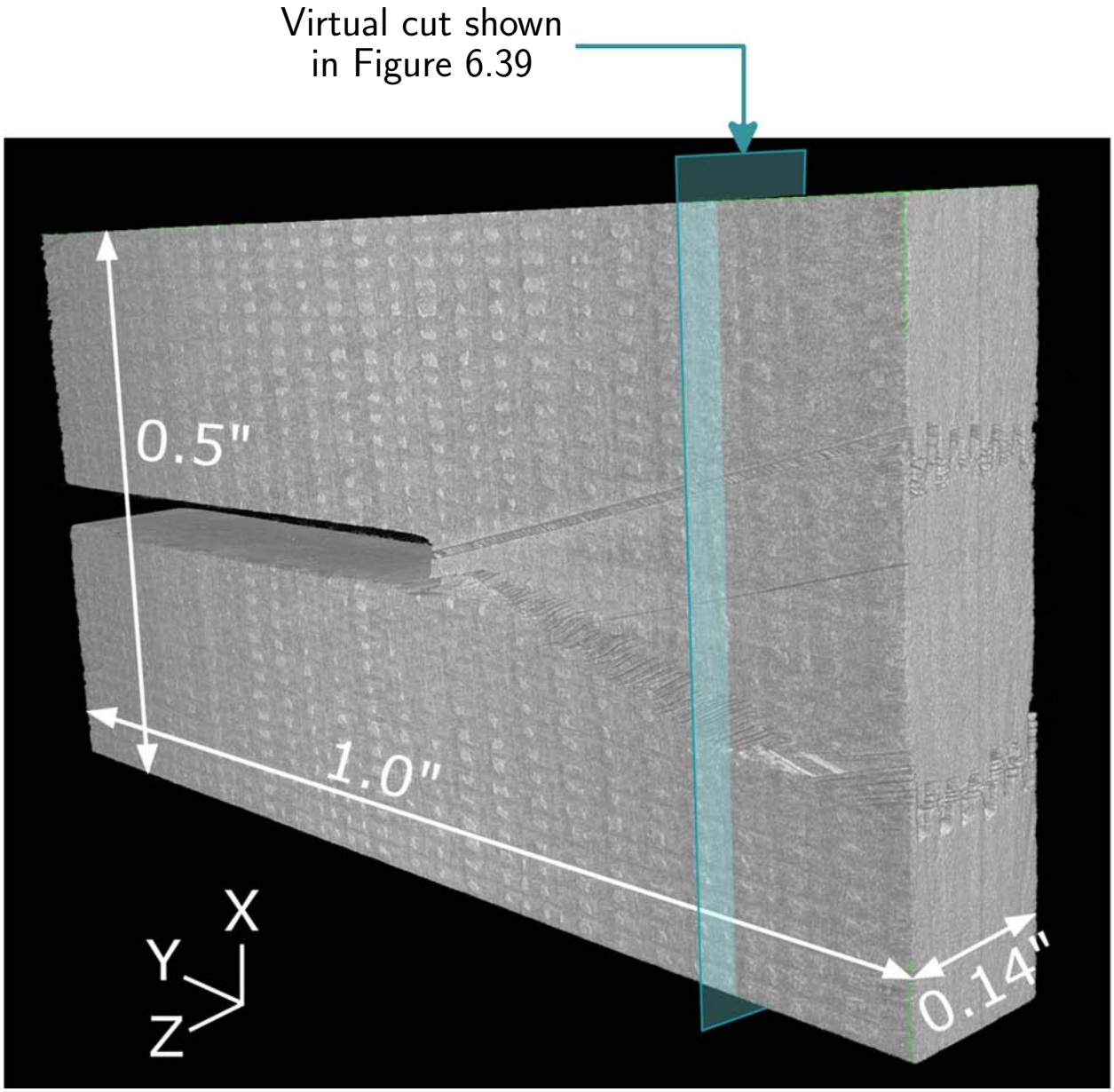

Figure 6.38 Virtual 3-D volume of a NRL single-edge-notched specimen (005-61), shown in Figure 6.37, with the material in the region between the dashed lines of Figure 6.37 virtually recreated by computer microtomography (CμT).

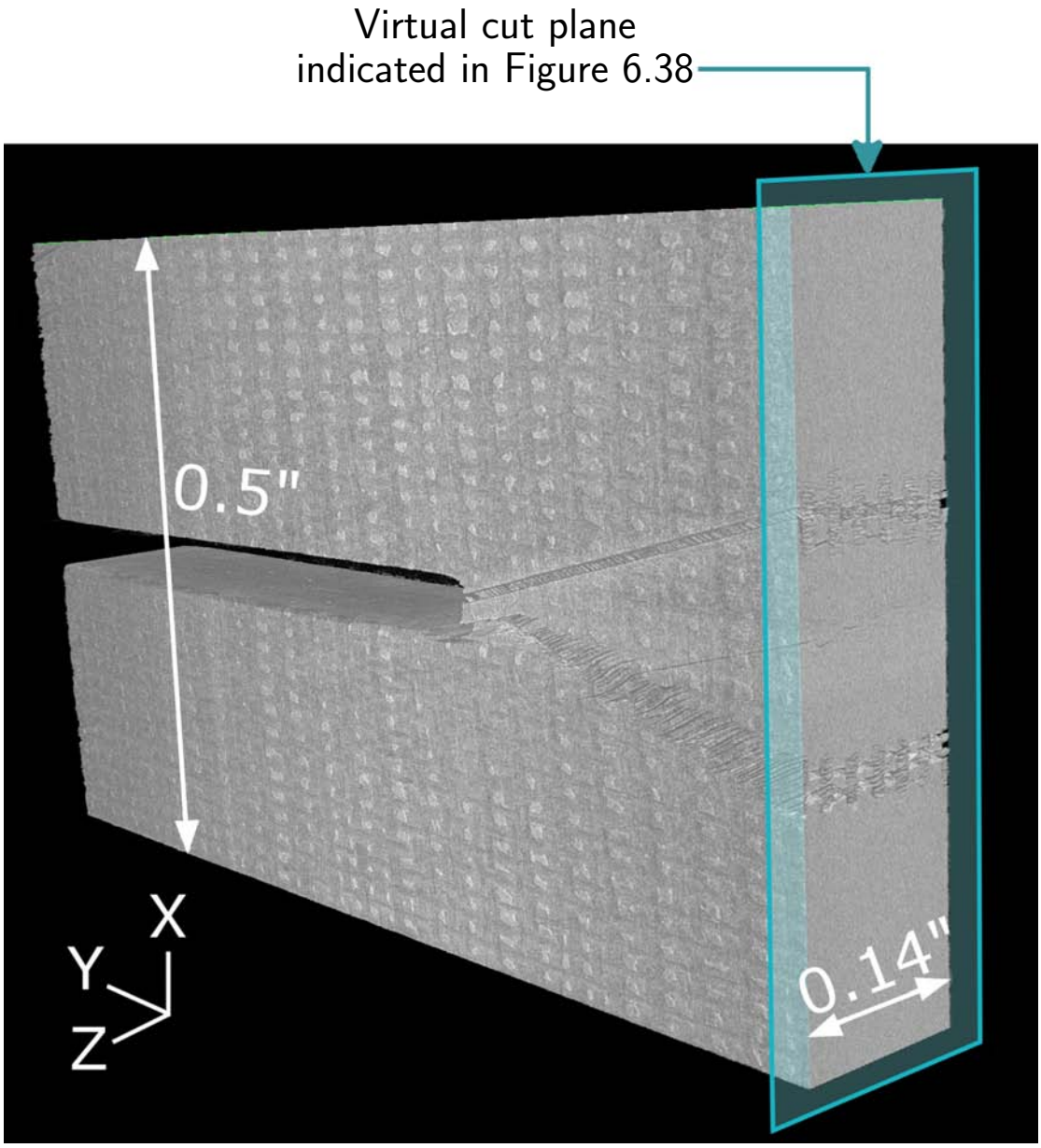

Figure 6.39 "Virtual cut" of a NRL single-edge-notched specimen (005-61), shown in Figure 6.37, with the end piece outlined by the shaded plane corresponding to the shaded plane intersecting the virtual 3-D volume of Figure 6.38.

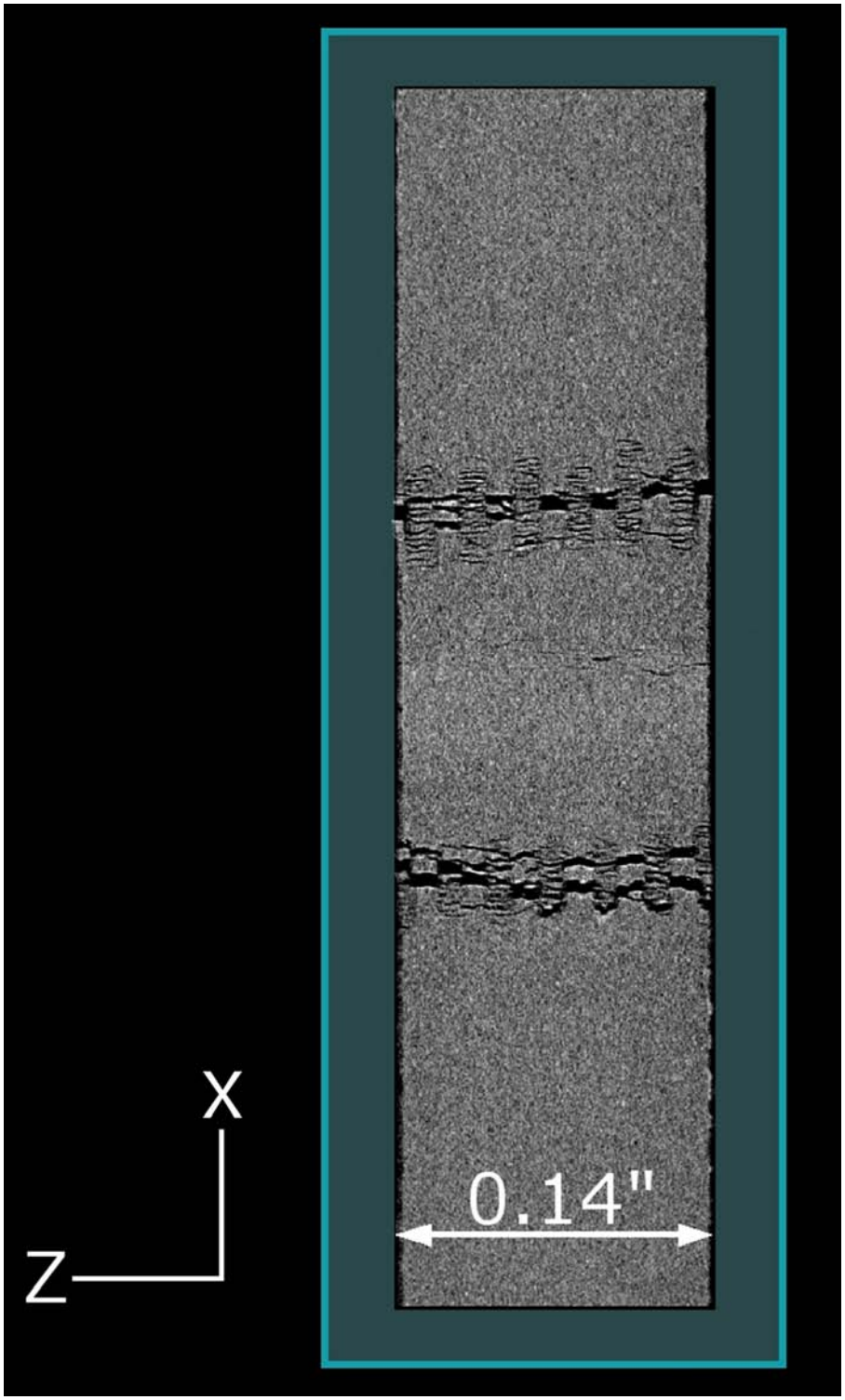

Figure 6.40 Planar presentation of the "virtual cut" of a NRL single-edge-notched specimen (005-61), shown in Figure 6.37, with the plane corresponding to the shaded plane intersecting the virtual 3-D volume of Figure 6.38 (and shown in Figure 6.37).

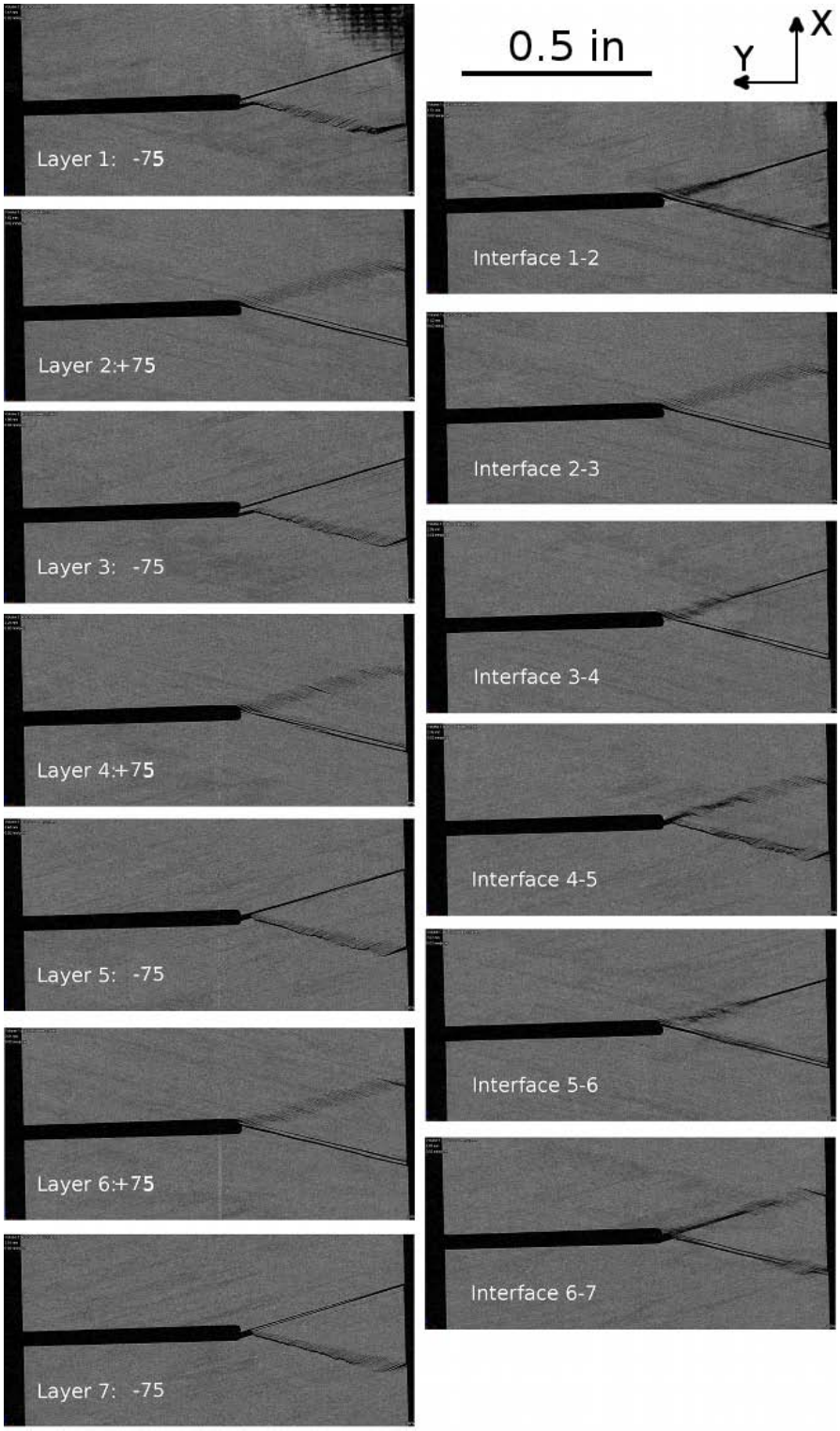

Figure 6.41 Multiple virtual cuts of a NRL single-edge-notched specimen (005-61), shown in Figure 6.37, with the views shown being from the 'front', with material virtually removed (sectioned) through the thickness from the first ply down to the seventh ply (continued in Figure 6.42).

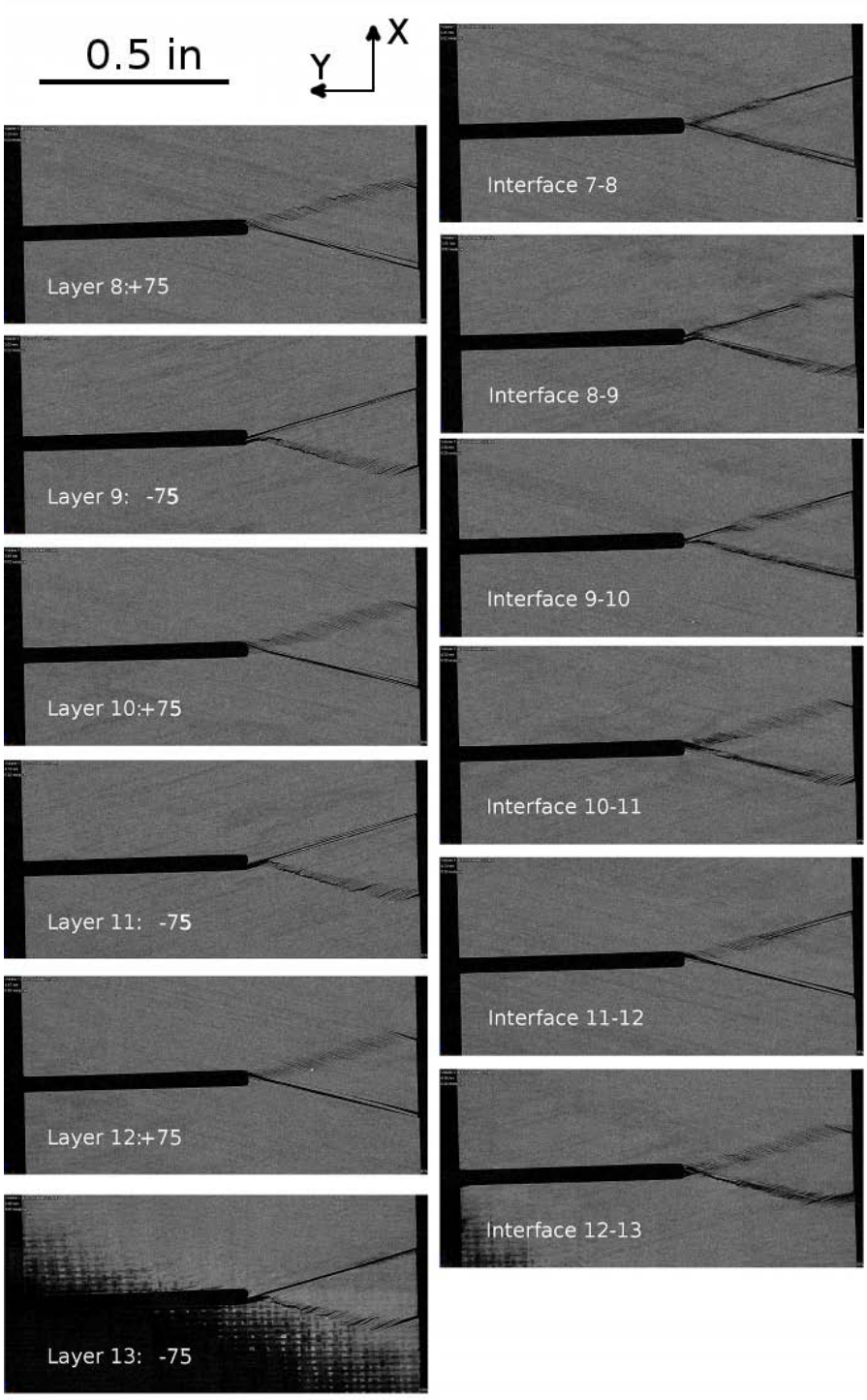

Figure 6.42 (Continuation of Figure 6.41) Multiple virtual cuts of a NRL single-edge-notched specimen (005-61), shown in Figure 6.37, with the views being from the 'front', with material virtually removed (sectioned) through the thickness from the eighth ply down to the thirteenth ply.

methods, multiple cuts of finite width would need to have been made, along with the analysis of each face exposed from this sectioning. This would have made it impossible to do further work/testing on that sectioned specimen, as well as destroying parts of the actual damage volume via the sectioning. With the virtual cutting, further work can be done quite easily, and no details are affected.

The double-edge-notched specimens were selected for CμT scans based on observations from the results of applying the documentation procedures. After reviewing the specimen documentation, it was identified that load path 1 (compression along the specimen length, $u_x < 0$, with all other components set to zero) produced surface damage across most of the specimen groups (i.e., the specimens with different ply orientations as well as stacking sequences with different effective ply thicknesses) that shows paths or mode interactions not previously seen in other project test specimens. Beyond looking at the differences in damage paths and damage modes caused by load path 1, other specimens with unique damage characteristics were selected, as indicated in Table 6.2. Three specimens were selected that exhibit a failure path resembling the letter 'W'. These specimens clearly show the surface damage being influenced by the grip boundaries. Another specimen exhibits a large amount of damage only on one face, whereas the majority of specimens exhibiting damage show a fairly equal amount of damage on the front and back faces. To allow further investigation into a damage mode first observed in the NRL single-edge-notched specimens, two specimens exhibiting the transverse zigzag damage mode were selected. However, the transverse zigzag damage in the two selected double-edge-notched specimens show changes in path characteristics compared to the single-edge-notched specimens exhibiting that mode. Another specimen selected primarily shows delamination on one face. This is unique within the double-edge-notched specimens, where delamination is usually a small portion of the observable damage (typically the dominating damage mode is matrix cracking). After selecting specimens based on damage characteristics, it was noticed that all but one of the specimens' load paths had a component of compression. Additional specimens were selected to investigate the internal damage caused by other load paths not containing compression.

An example of a virtual 3-D volume created of a double-edge-notched specimen is shown in Figure 6.43. The volume shown in this figure represents the specimen material between the dashed lines of Figure 6.44. This specimen was identified from the documentation procedures as exhibiting two transverse zigzag damages, one initiating from each notch tip. The failure paths follow the fiber angles and cross at the centerline of the specimen, as shown in Figures 6.45 through 6.48. Using CμT, the failure paths are able to be investigated layer by layer. As seen in the figures, the two transverse zigzag damage paths initiate from the two notch tips and progress along the positive and negative fiber angles. The damage along each damage path alternates layer to layer between a dominant matrix crack and a series of parallel stitch cracks. In layers with a positive ply angle, the damage originating from the right notch tip and propagating to the left edge is a dominant matrix crack while the damage originating from the left notch tip and propagating to the right edge is a series of parallel stitch cracks. In layers with a negative ply angle, this switches and the damage originating from the right notch tip is a series of parallel stitch cracks and the damage originating from the left notch tip is a dominant matrix crack. The spacing between the stitch cracks and the length of the stitch cracks are consistent in all the layers, including in the region where the two paths cross, suggesting that there is no interaction between the paths.

Scans of the open-hole tension specimens also reveal observations about the damage. The OHT specimens selected for CμT scans are listed in Table 6.3. Specimens with the three different hole diameters (including no hole, referred to as a 0.0-inch diameter hole) and with the two different laminates were selected. A majority of the specimens of the first round were scanned in order to investigate an unexpected damage initiation point. Specimens were also selected in order to investigate the characteristic damage regions identified via the documentation results, where the damage extent in single-ply effective ply thickness laminates is primarily contained in a triangular region next to the holes, while the damage extent in the four-ply effective ply thickness laminate is primarily contained in a diagonal region about the hole.

A unique and unexpected failure is found in a few of the specimens of the first

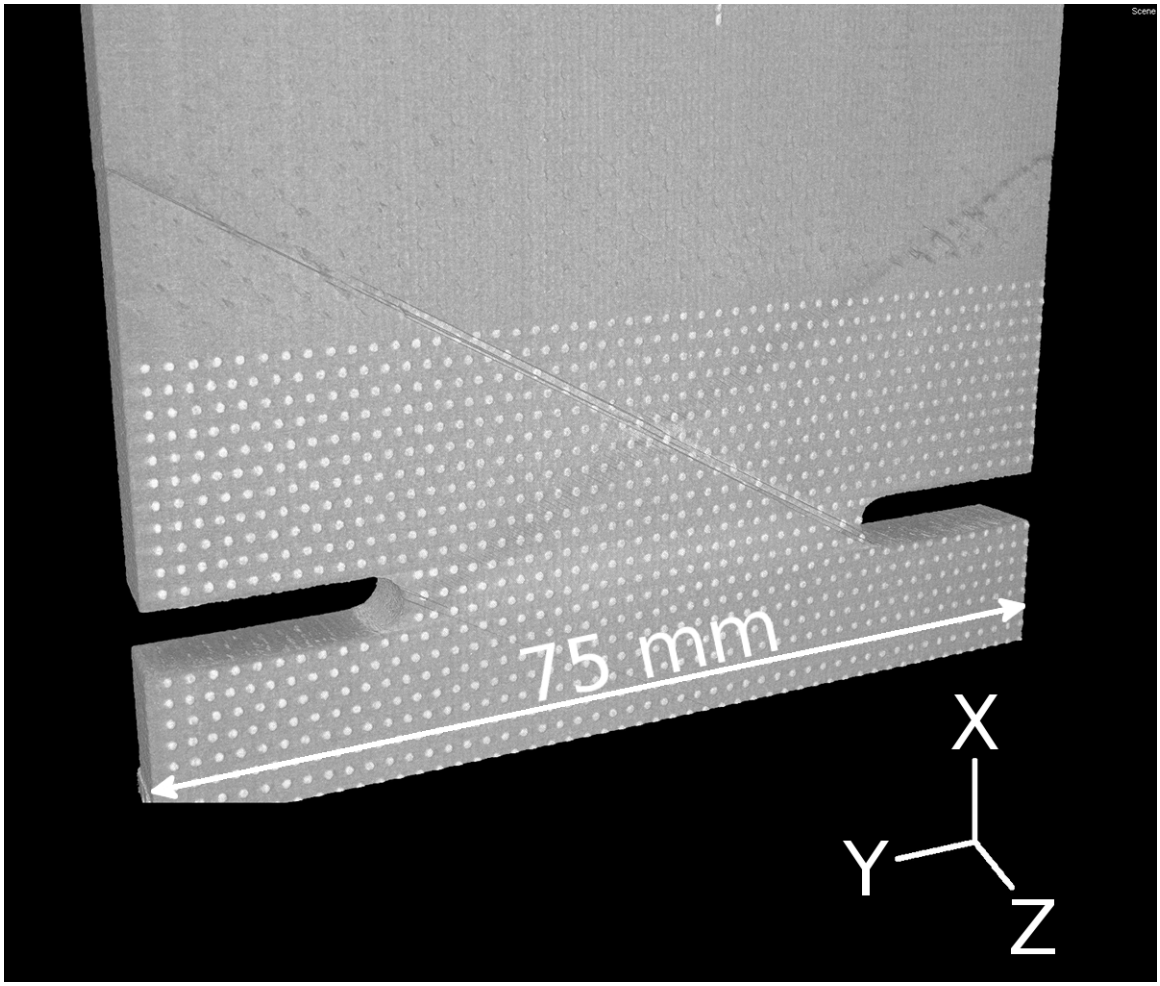

Figure 6.43 Virtual 3-D volume of a double-edge-notched specimen (CH-C601-0704), showing a view from the front surface, with the double, crossing transverse zigzag damage visible.

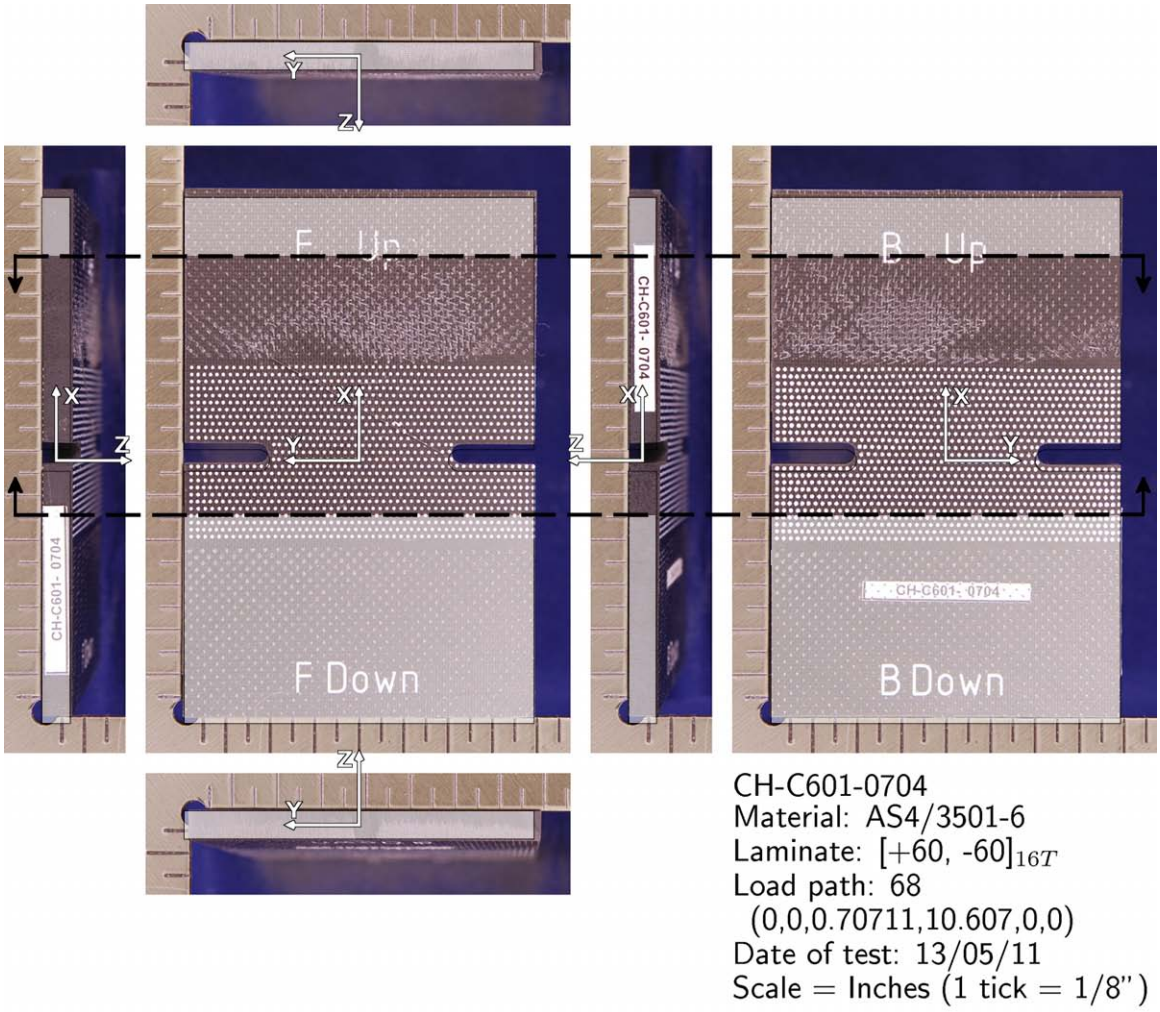

Figure 6.44 Optical documentation photographs of a double-edge-notched specimen (CH-C601-0704). (Note: Region between dashed lines represents material volume scanned and depicted in Figure 6.43.)

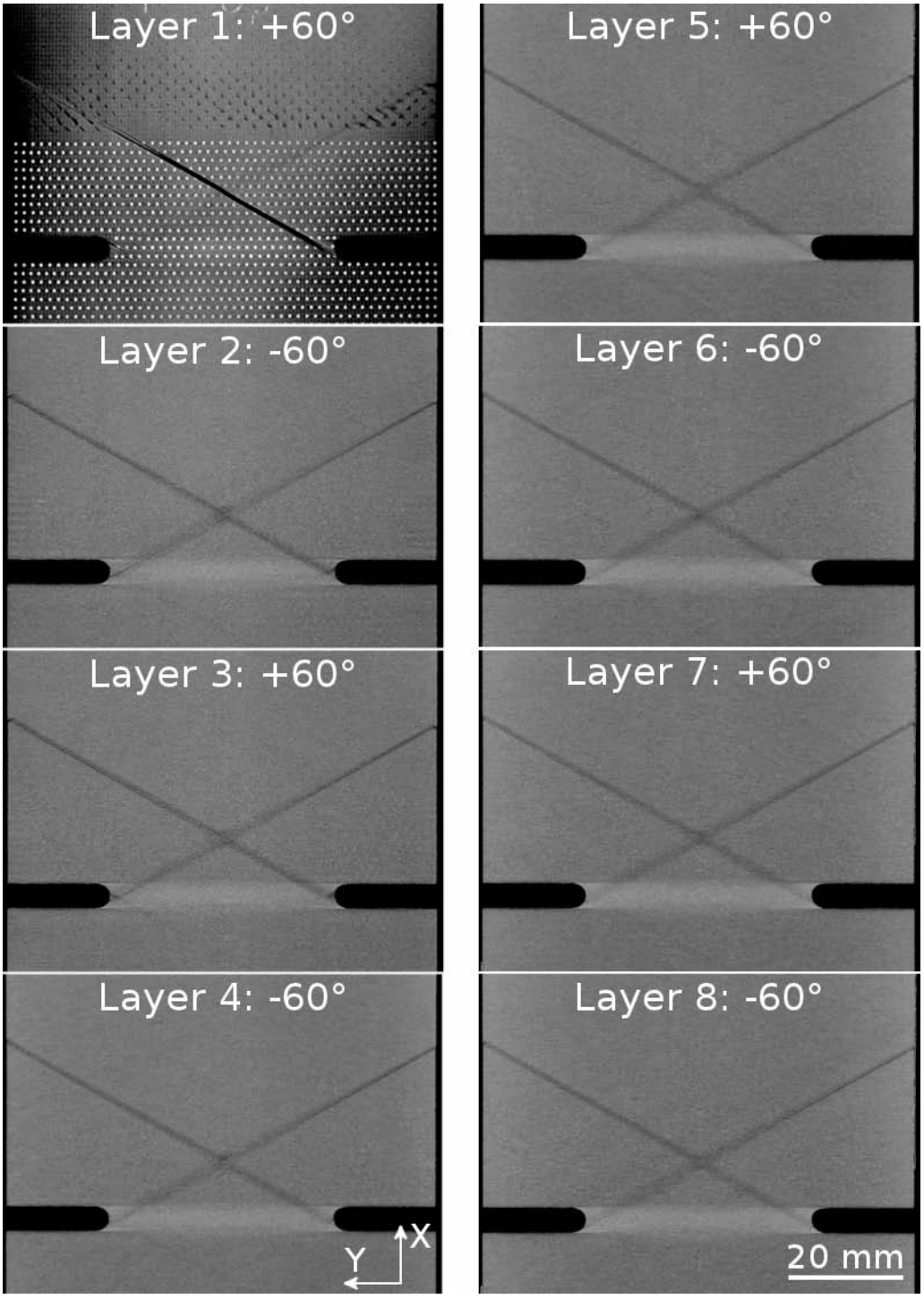

Figure 6.45 Multiple virtual cuts of a double-edge-notched specimen (CH-C601-0704) shown in Figure 6.43, showing 'front' views with virtually removed material (sectioned) from the first ply to the last ply (plies 1 through 8 shown here and continued in Figures 6.46 through 6.48).

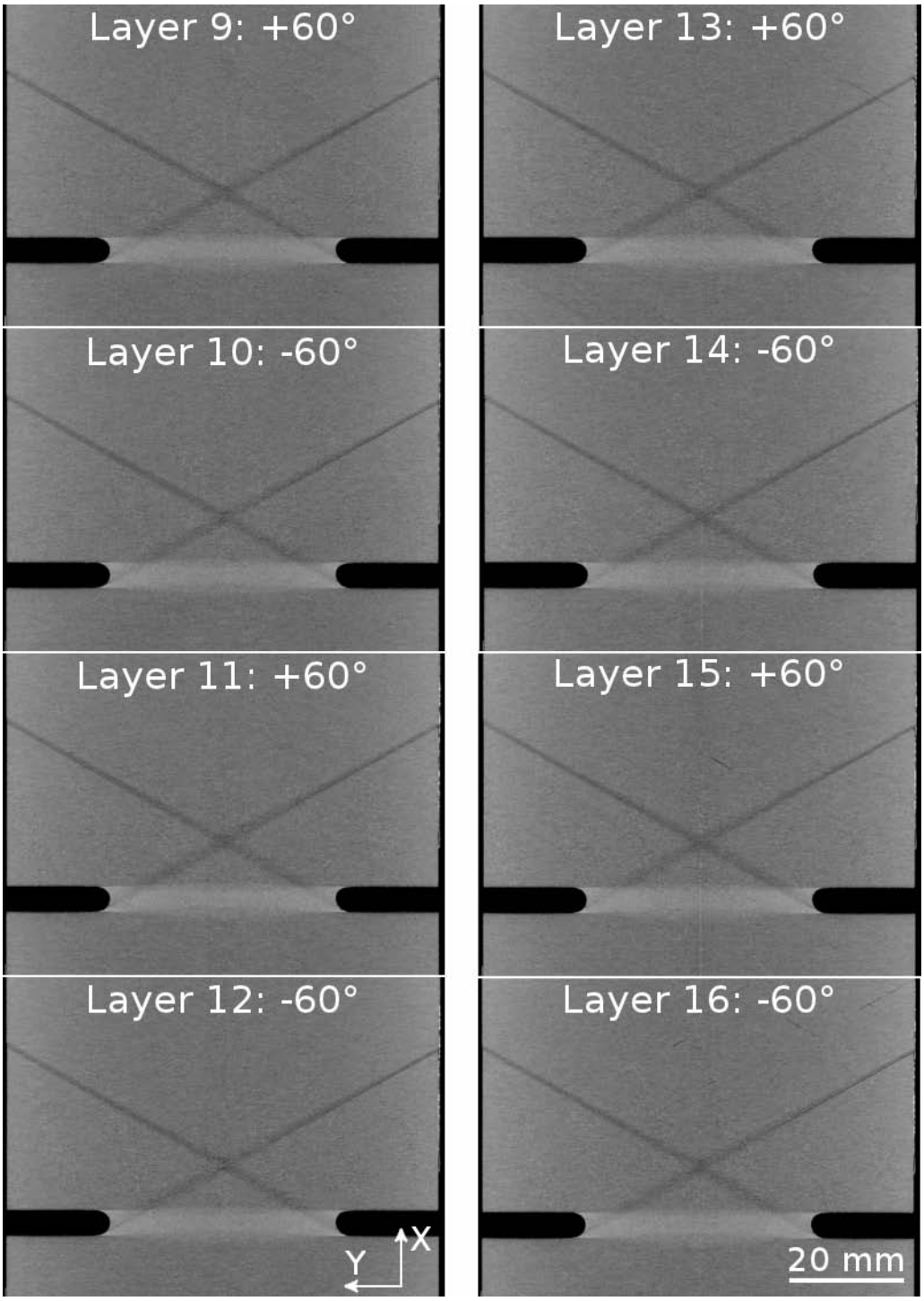

Figure 6.46 Multiple virtual cuts of a double-edge-notched specimen (CH-C601-0704) shown in Figure 6.43, showing 'front' views with virtually removed material (sectioned) from the first ply to the last ply (plies 9 through 16 shown here with previous plies in Figure 6.45 and other plies shown in Figures 6.47 through 6.48).

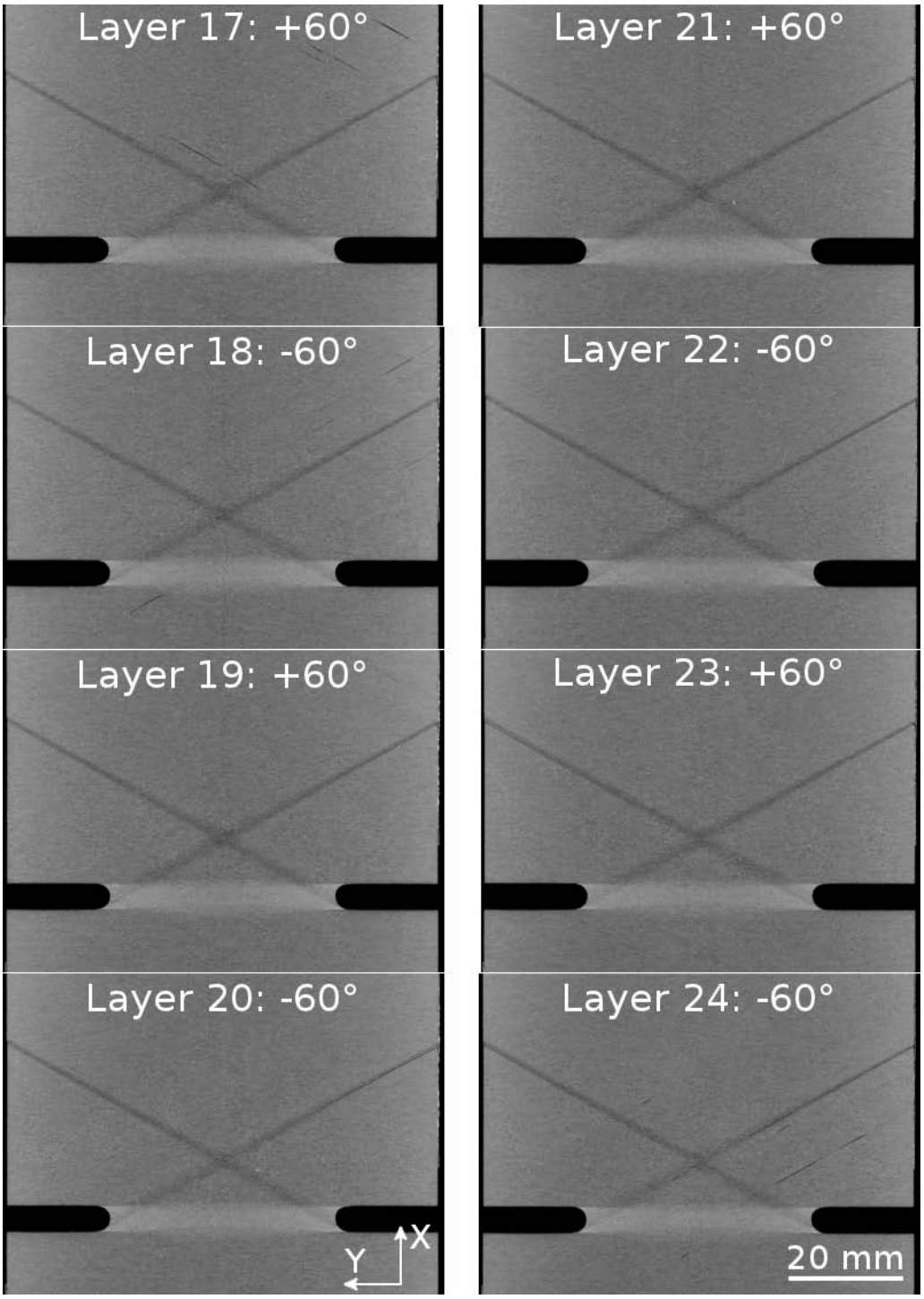

Figure 6.47 Multiple virtual cuts of a double-edge-notched specimen (CH-C601-0704) shown in Figure 6.43, showing 'front' views with virtually removed material (sectioned) from the first ply to the last ply (plies 17 through 24 shown here with previous plies shown in Figures 6.45 and 6.46 and other plies shown in Figure 6.48).

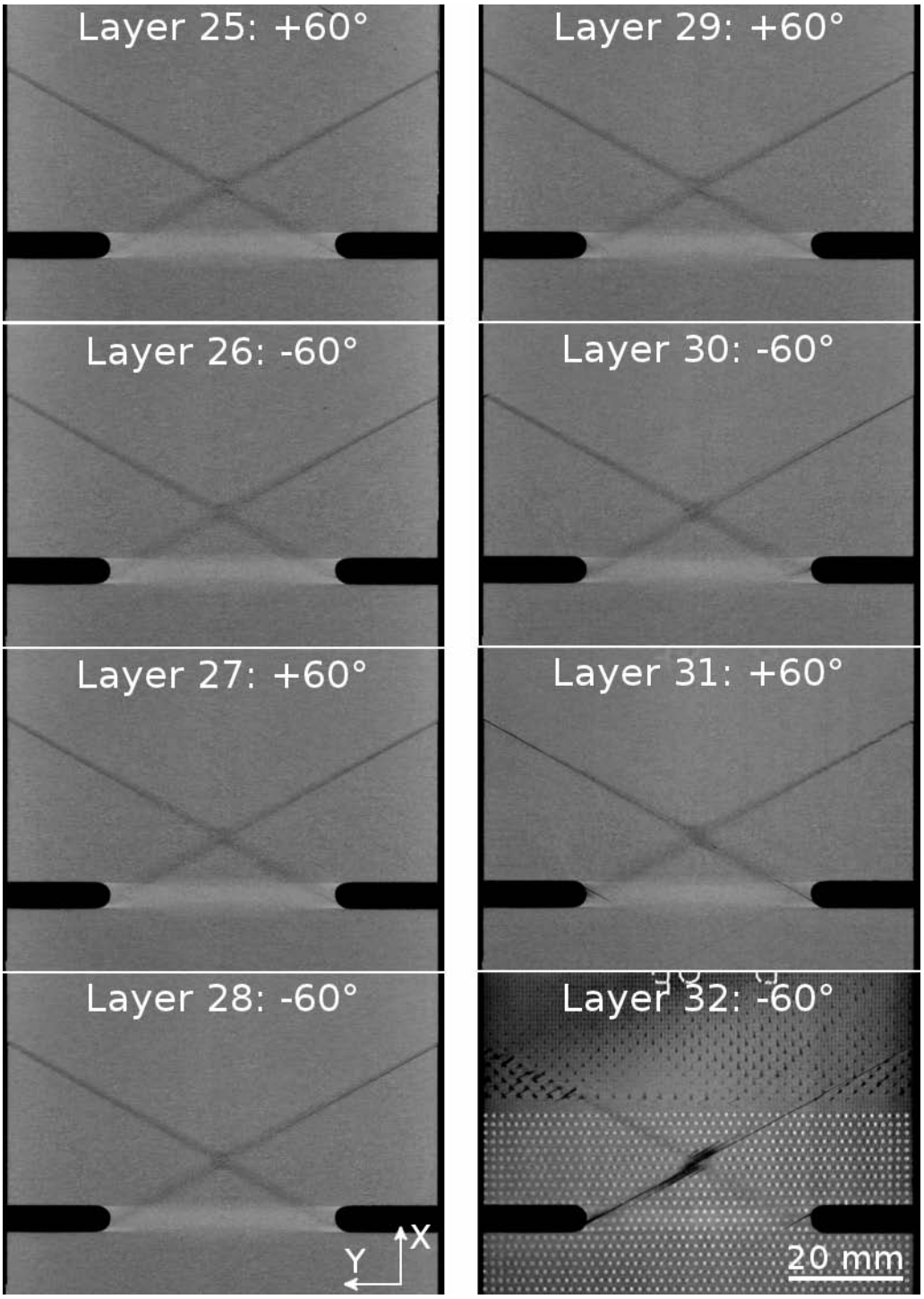

Figure 6.48 Multiple virtual cuts of a double-edge-notched specimen (CH-C601-0704) shown in Figure 6.43, showing 'front' views with virtually removed material (sectioned) from the first ply to the last ply (plies 25 through 32 shown here with previous plies shown in Figures 6.45 through 6.47).

round, where damage occurs at the top and bottom of the hole in addition to the expected damage location (at the maximum stress/strain concentration). This is shown in the following figures of this section. After investigating this unexpected failure location via CμT scans, it was determined that there was preexisting damage due to the specimen manufacturing procedure, specifically the drilling technique to produce the open hole, as previously noted. From these results, the drilling technique was corrected for the manufacturing of the specimens of the second round. The preexisting damage in the specimens of the first round can cause large stress concentrations and resulting stress gradients beyond those from the structural detail (hole), thereby creating multiple, unexpected initiation points for damage.

An example of a CμT scan and observed results of an OHT specimen follows. The specimen was loaded in tension until ultimate failure, resulting in the specimen breaking into two pieces. Optical photographs, from the documentation process, of the faces of the failed specimen are shown in Figure 6.49. Note that the entire length of the specimen is not shown in these photos. As described in Subsection 5.1.1, a lengthscale related to damage documentation is defined for each specimen type. This defines the "bounding area" for damage documentation, and this "bounding area" is defined such that the majority of the damage is documented. However, there are some cases where the specimens were loaded well past ultimate failure and damage propagated beyond this "bounding area." The virtual joining procedure, described in Subsection 5.1.1, was used during the documentation process to recombine the broken specimen pieces, as shown in Figure 6.49. The individual specimen pieces were scanned with the CμT resulting in two 3-D volumes. Virtual images, with an orientation normal to the back surfaces of the 3-D volumes, of these two pieces are shown in Figures 6.50 and 6.51. As can be seen in these figures, this specimen exhibits different damage modes (fiber fracture, fiber pull-out, matrix crack, and delamination) through the thickness of the specimen. The spotted pattern observed on the outer plies is an artifact from the optical strain mapping technique. The changes in damage mode and damage paths were investigated by "virtually cutting" (previously described for single-edge-notched specimen) material in a ply-by-ply manner.

Figure 6.49 Documentation photograph and axes layer of an OHT specimen (OH-B104-01) that broke into two pieces.

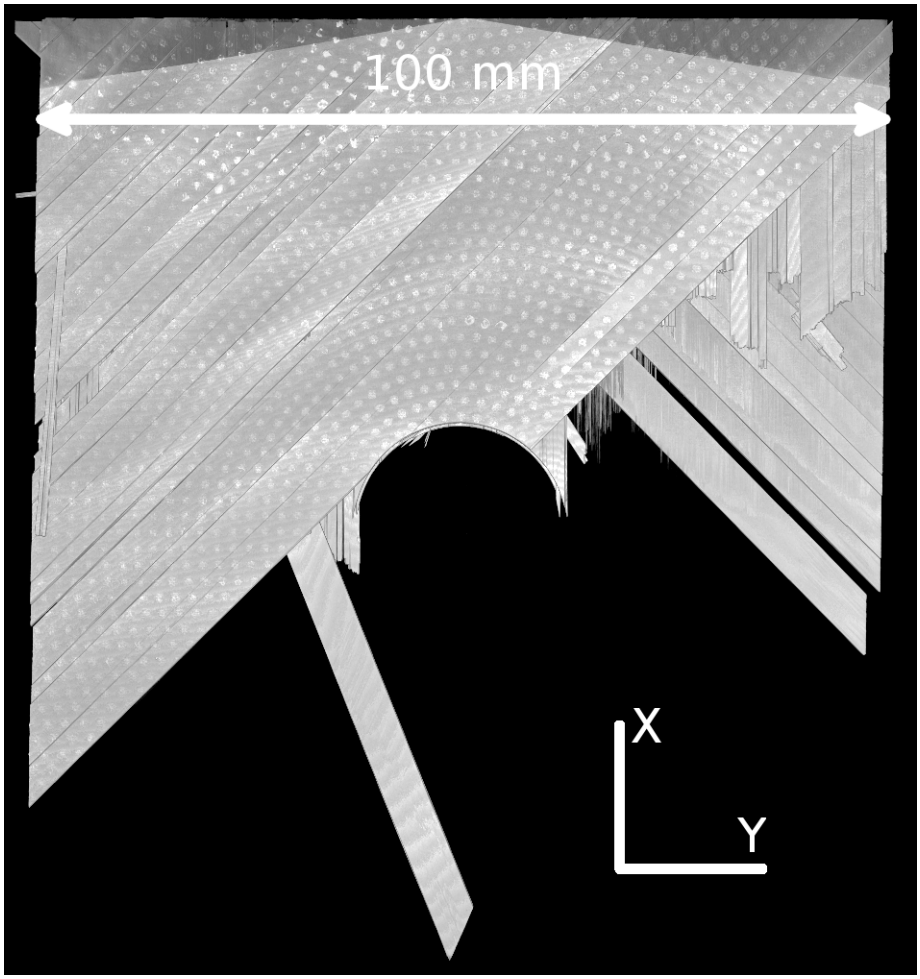

Figure 6.50 Virtual 3-D volume (back surface view) of the top half of a broken OHT specimen (OH-B104-01), shown in Figure 6.49.

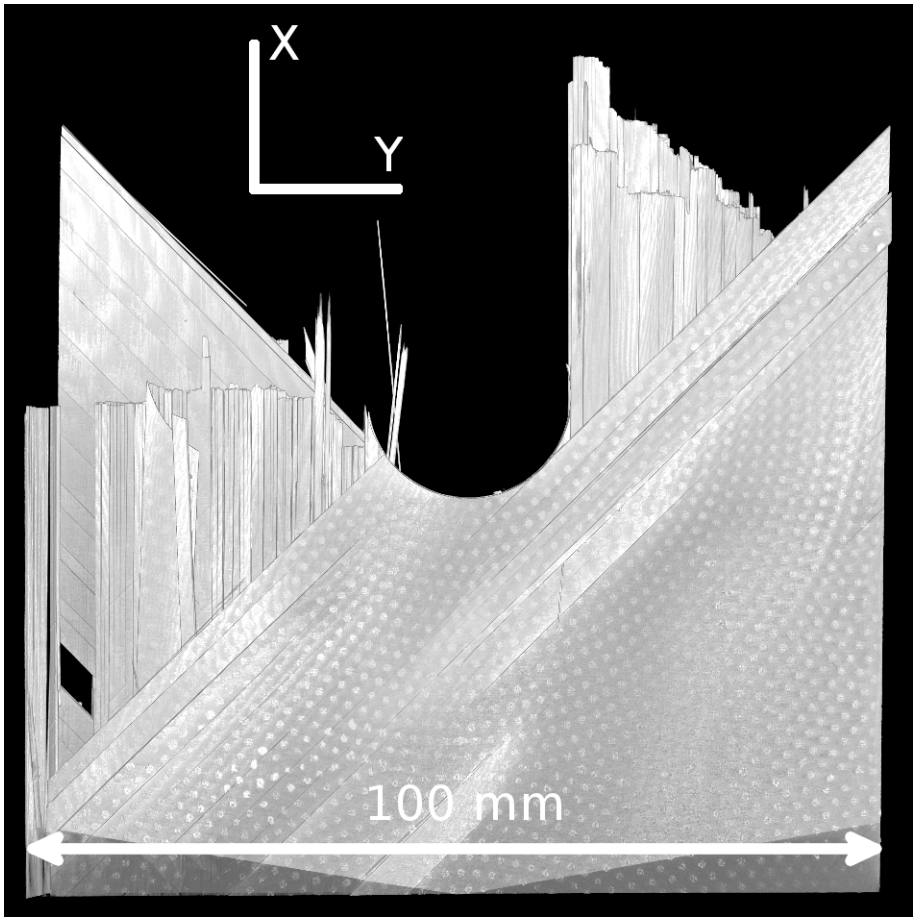

Figure 6.51 Virtual 3-D volume (back surface view) of the bottom half of a broken OHT specimen (OH-B104-01), shown in Figure 6.49.

The ply-by-ply virtual cuts of the top half of the specimen are shown in Figure 6.52. Similar damage trends are observed in virtual cuts of the bottom half of the specimen. A three-dimensional view of both specimen pieces combined into a single image, as shown in Figure 6.53, allows one to easily see the failure paths, on a ply-by-ply basis, that resulted in the specimen separating into two pieces. It is observed for this specimen that the dominant damage mode varies through the thickness of the laminate, with matrix cracking occurring in the $\pm 45^\circ$ plies, fiber fracture and matrix cracking occurring in the 0° plies, and delamination occurring at interfaces where the ply angle changes. Similar observations are seen in the other OHT specimens. Thus, there is a dependence on fiber orientation.

As identified by the documentation procedures, OHT specimens with four-ply effective ply thickness exhibit a much larger extent of damage than specimens with single-ply effective ply thickness. Each laminate has characteristic regions where damage occurred. Specimens of both laminate types were investigated via CμT. The photograph documentation of a specimen with single-ply effective ply thickness is shown in Figure 6.54. Note that the entire length of the specimen is not shown in these photos. A scan of this specimen is shown in Figure 6.55. As seen in this figure, the majority of damage is contained in two triangular regions to the left and right of the hole. Damage due to the technique used to drill of the hole, as described in Section 6.1.3, is seen at the top of the hole. The damage at the top and/or bottom of the hole was unexpected when first inspecting these specimens, as the damage is expected to initiate to the left and right sides of the hole. The triangular regions of damage are observed in all the single-ply effective ply thickness laminates, whereas the damage due to the hole drilling technique is observed only in a few of the specimens of the first round (from both the single- and four-ply effective ply thickness laminates). Virtually sectioned views of OHT specimen OH-A101-06 are shown in Figures 6.56 and 6.57. In these figures, the virtual cuts are taken at a distance away from the midplane of the specimen (views are in the x-y plane at a distance z from the midplane). The loading on the specimen and resulting damage caused the material above the hole to deform out of plane. Because of this, the cutting plane is referenced

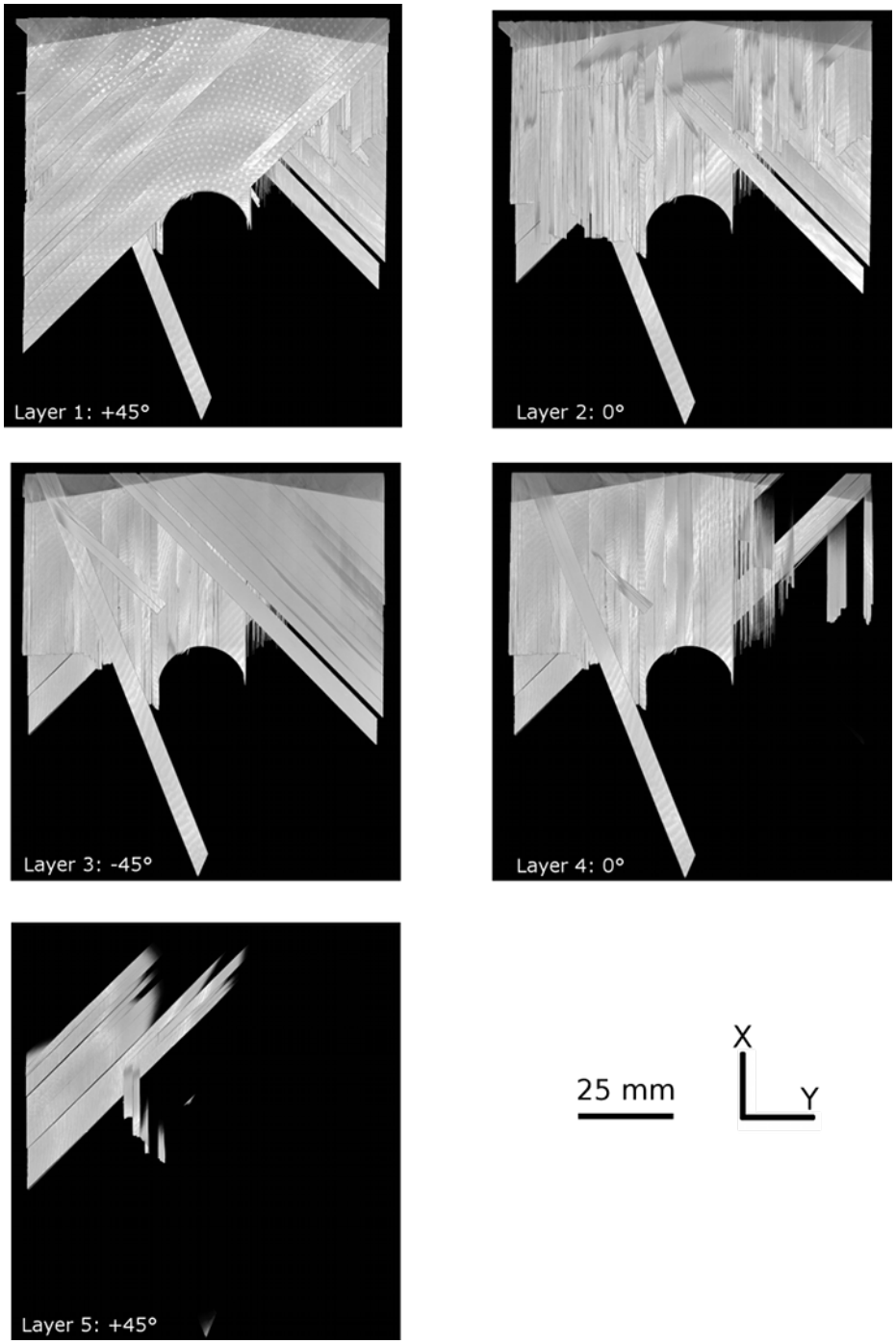

Figure 6.52 Virtually sectioned views of an OHT specimen (OH-B104-01), shown in Figure 6.50, with the views shown being from the 'back', with material virtually removed (sectioned) through the thickness from the outermost surface down.

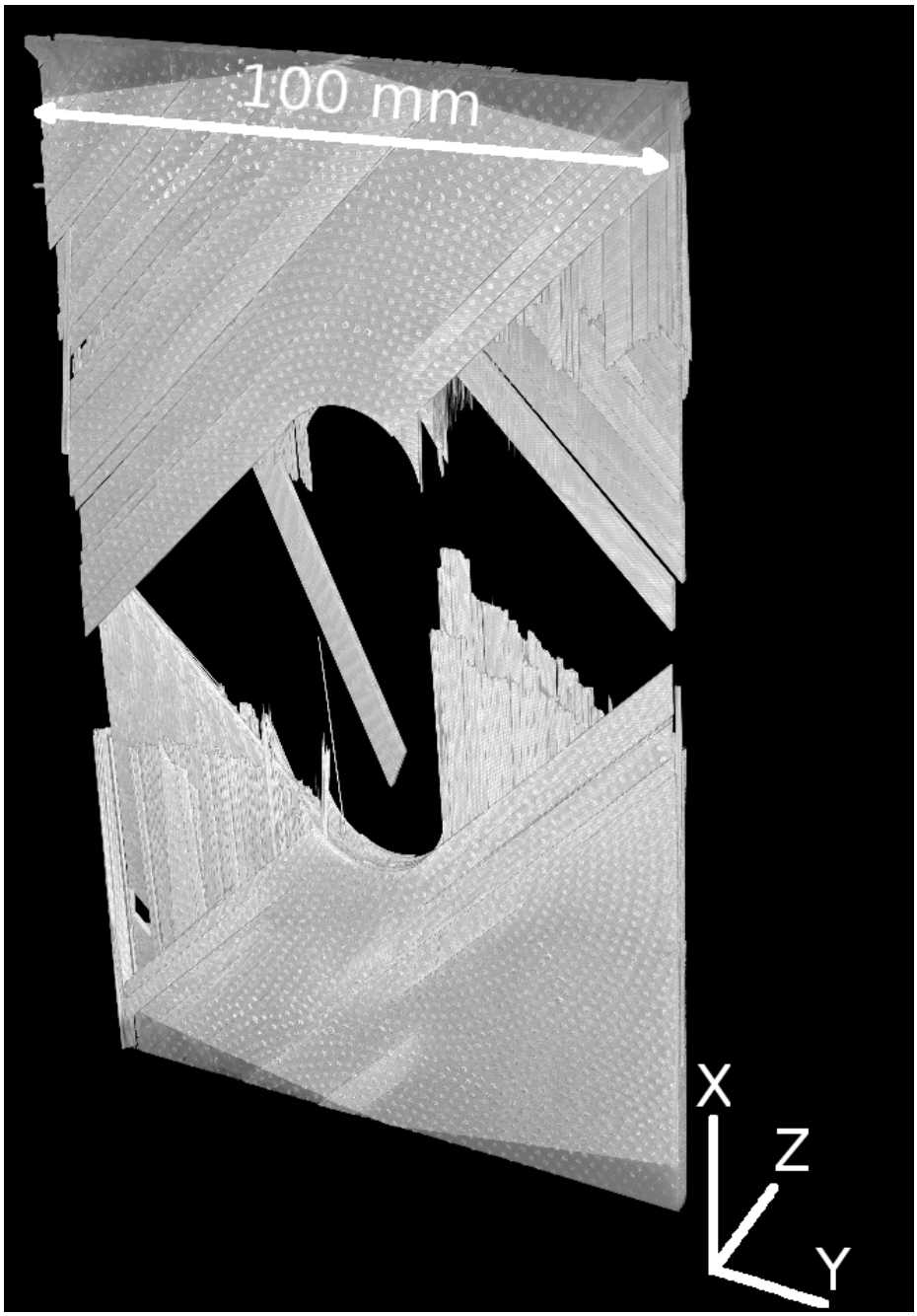

Figure 6.53 Three-dimensional view of OHT specimen (OH-B104-01) pieces from Figures 6.50 and 6.51.

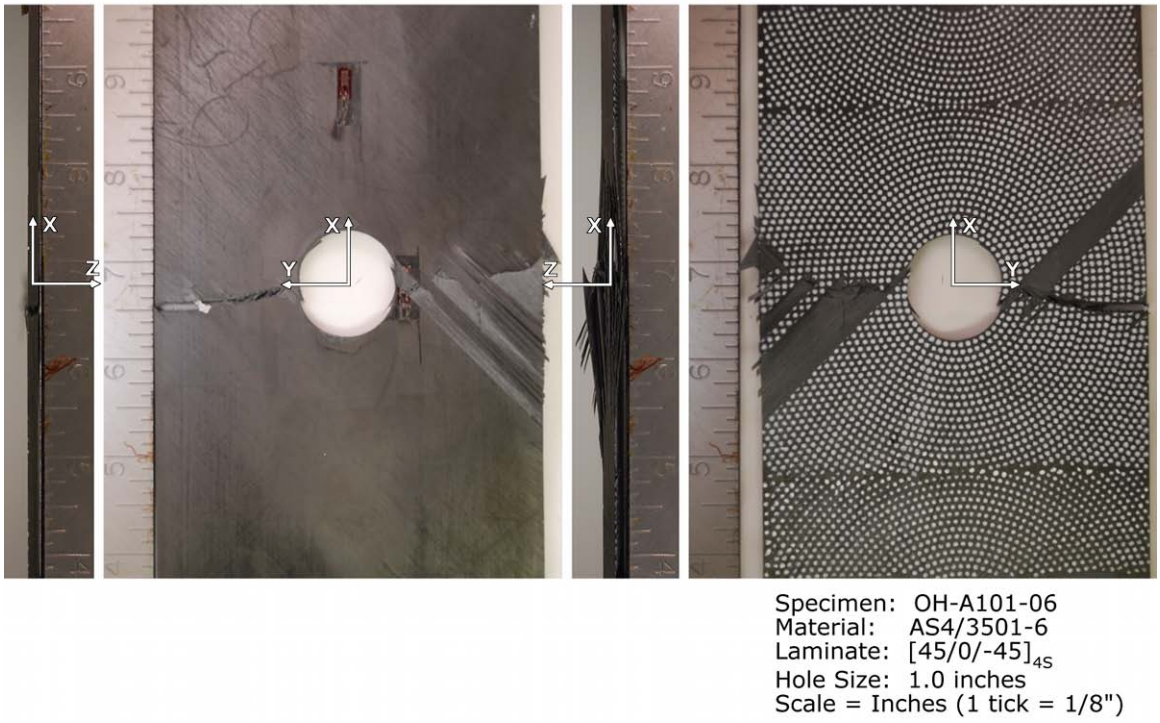

Figure 6.54 Documentation photograph and axes layer of an OHT specimen (OH-A101-06).

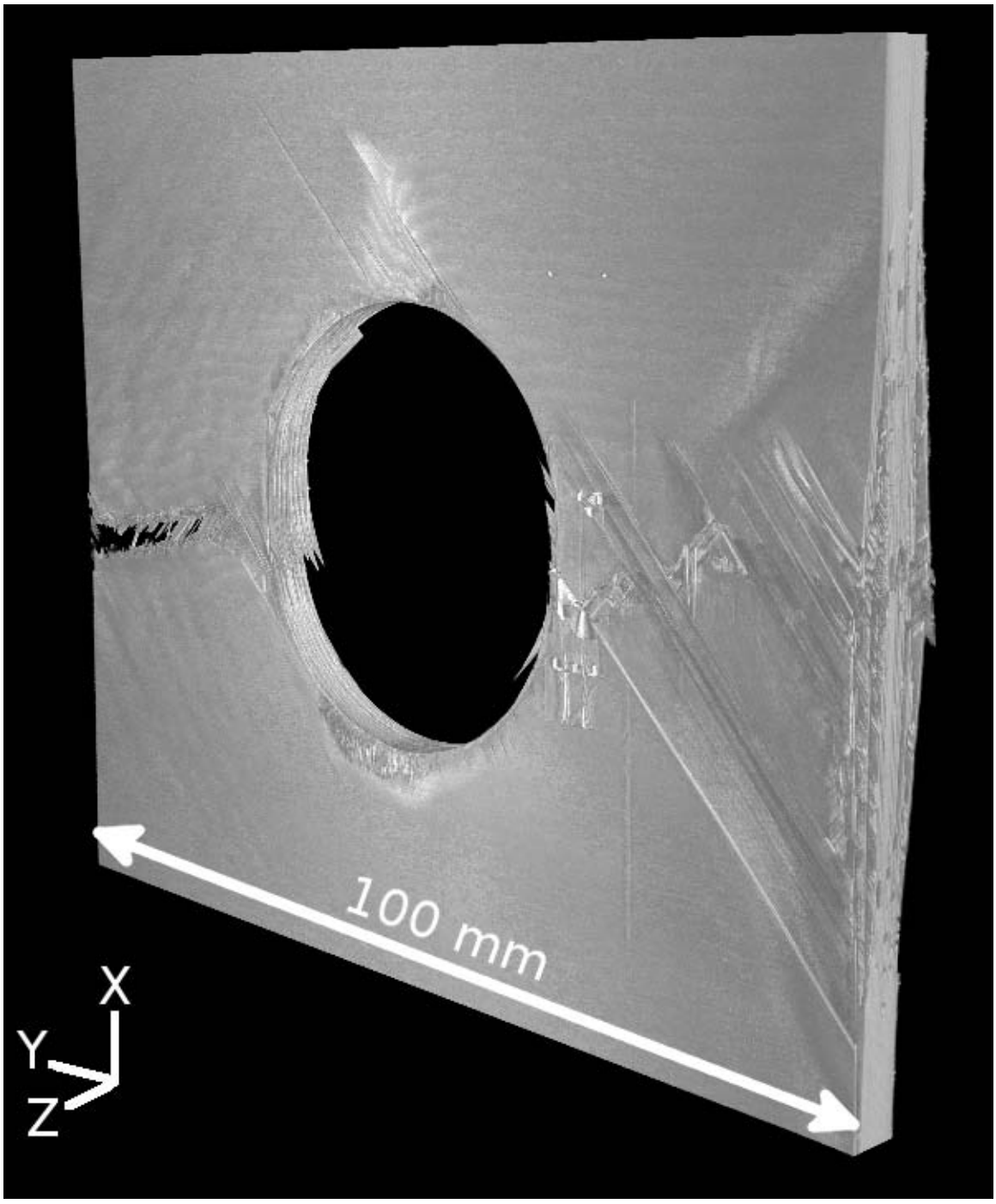

Figure 6.55 Three-dimensional view of an OHT specimen (OH-A101-06).

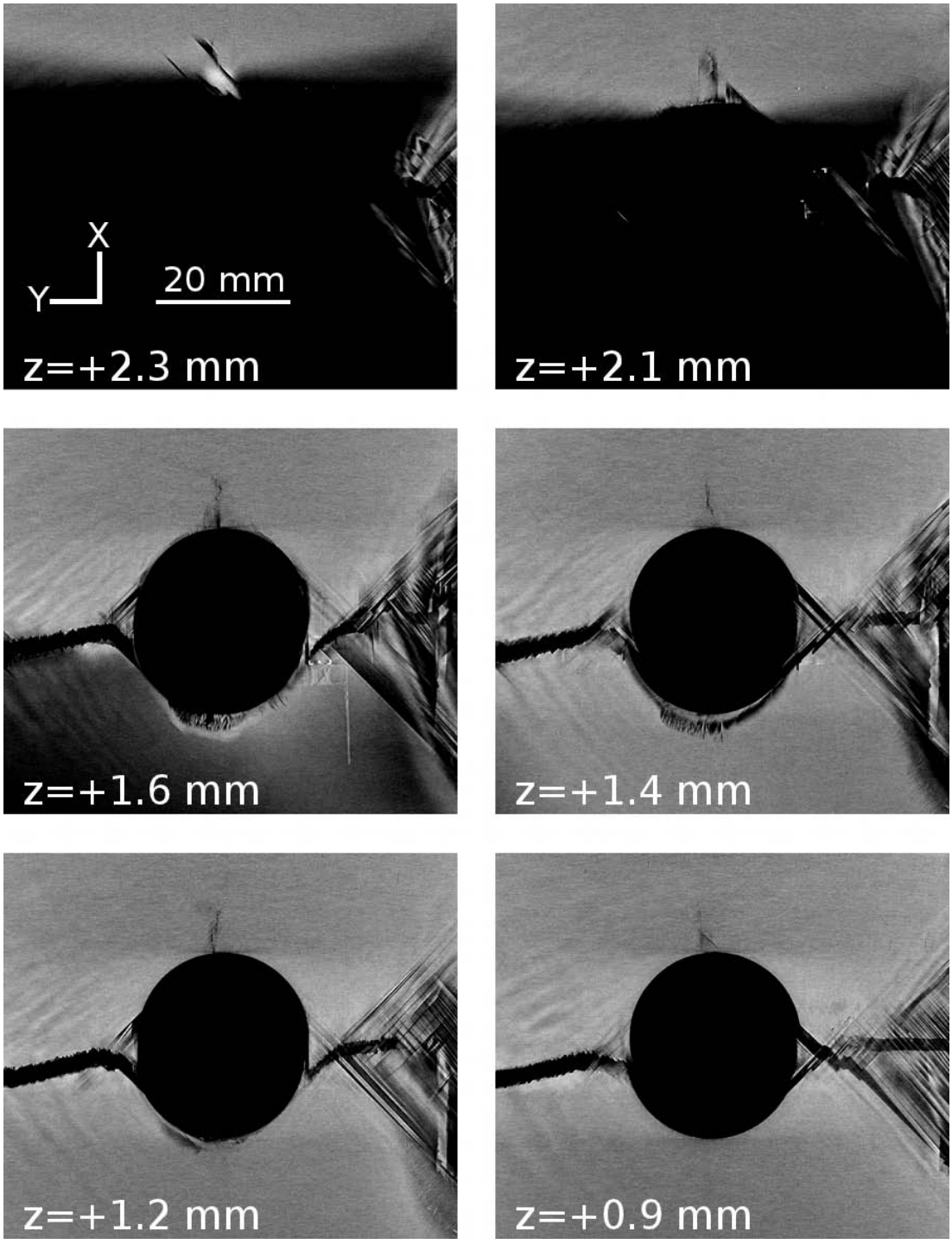

Figure 6.56 Virtually sectioned views of an OHT specimen (OH-A101-06), shown in Figure 6.54, with the views shown being from the 'front', with material virtually removed (sectioned) through the thickness from the outermost surface down (additional cuts continued in Figure 6.57).

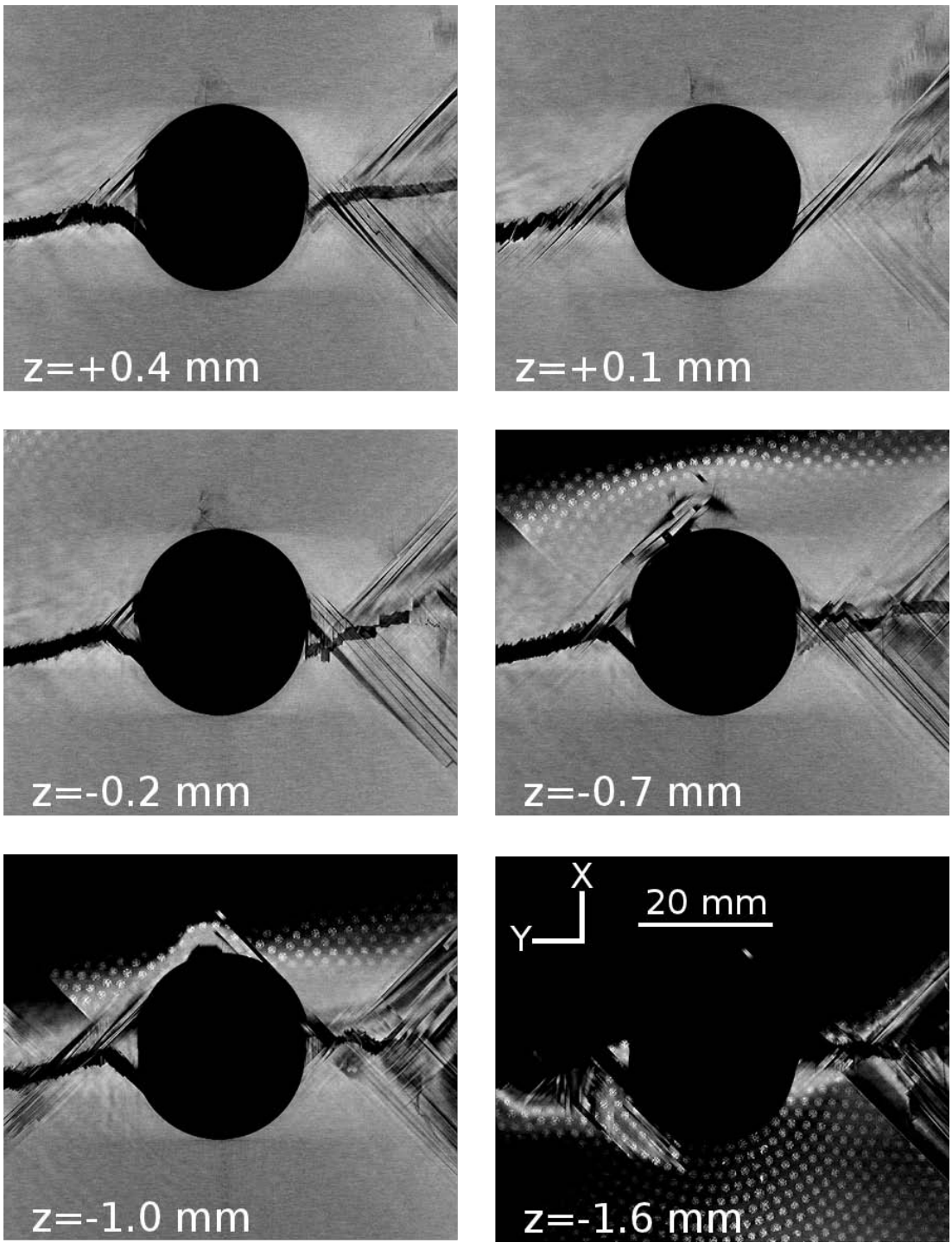

Figure 6.57 Virtually sectioned views of an OHT specimen (OH-A101-06), shown in Figure 6.54, with the views shown being from the 'front', with material virtually removed (sectioned) through the thickness from the outermost surface down (continued from Figure 6.56).

as a distance from the midplane of the lower half of the specimen, as opposed to individual layers as done for the previous OHT specimen. The approximate layer, or interface between two layers, corresponding to these z-locations are listed in Table 6.5. The angle of the corresponding layer(s) is also listed in the table. In order to show greater detail of the damage caused by the drilling procedure, these views do not show the entire width of the specimen. The same damage type seen in these views continues from the hole to the edge of the specimen (i.e. the fiber fracture seen to the left of the hole continues to the left edge of the specimen and the matrix cracking, delamination, and fiber fracture seen to the right of the hole continues to the right edge of the specimen). The damage extent through the thickness of the laminate, as shown in these figures, is contained within the triangular region observed on the surface of the specimen. Comparing the damage extent seen in Figure 6.52 (a specimen with a four-ply effective ply thickness) with that of Figures 6.56 and 6.57 (a specimen with single-ply effective ply thickness), the damage extent in the single-ply effective ply thickness laminate stays within two triangular regions to the left and right of the hole, whereas the damage in the four-ply effective ply thickness laminate is much greater and the majority of damage is within the diagonal region described in Section 6.1.3. As observed in the OHT documentation results, the same damage trends are observed in the specimens containing a 0.5-inch diameter hole and a 1.0-inch diameter hole. Specimens with no hole (referred to as a 0.0-inch diameter hole) behave as a typical tensile test specimen.

Scans of three ply-drop specimens were conducted in order to investigate the delamination paths in the region of the ply drop. As discussed in Section 4.4, all ply-drop specimens were loaded in uniaxial tension with loading along the specimen length (x-axis). Two sublaminate stacking sequences are used in the ply-drop specimens: $[+45/0/\text{-}45]_{2S}$ and $[+45_2/0_2/\text{-}45_2]_S$. Similar damage paths are observed in specimens of both the single-ply and two-ply effective ply thickness laminates. In both laminates, the dominant damage mode is delamination between plies, localized to the region near the ply drop. Matrix cracking is also observed on the front and back surfaces of some of the specimens. In order to further investigate the delamination paths and

Table 6.5 Approximate corresponding layers or interfaces and associated ply angles for the z-locations listed in Figures 6.56 and 6.57

z [mm]	**Layer or Interface**	**Ply Angle**
+2.3	-[a]	-
+2.1	-	-
+1.6	24	+45°
+1.4	23	0°
+1.2	22/21	-45°/+45°
+0.9	19	-45°
+0.4	16/15	-45°/+45°
+0.1	13	-45°
-0.2	11	0°
-0.7	7	+45°
-1.0	5	0°
-1.6	1	+45°

[a] Corresponds to the out-of-plane deformation in the top half of the specimen.

to identify similarities and differences between the single-ply effective ply thickness and two-ply effective ply thickness laminates, virtual cuts through the width of two specimens are presented and discussed.

The documentation photograph of ply-drop specimen PD-A1-02, a specimen with a single-ply effective ply thickness laminate, is shown in Figure 6.58. Delamination and matrix cracking was observed in this specimen. The matrix cracking is visible in the front and back documentation photographs of Figure 6.58 while delaminations are visible on the left and right documentation photographs subsequently described (refer to Section 5.1.1 for face definitions). The material between the dashed lines of this figure indicates the region scanned and virtually recreated. The recreated volume of this specimen is shown in Figure 6.59. This 3-dimensional view shows the front and right faces of the specimen. The recreated volume shows matrix cracking occurring in the upper left region of the figure while delaminations can be made out (though difficult to see at the shown angle) on the right face. Shown in this figure are seven virtual "cutting planes," each corresponding to a "virtually cut" view shown in Figure 6.60. The virtual cuts are shown from the right face, with material virtually removed through the width of the specimen, until reaching the left face. The y-location of each cut is indicated in the figure, with zero being the center of the specimen width, and ± 19.05 mm corresponding to the left and right faces. The cut locations are selected at an equal spacing through the width. As seen in each of the virtual cuts, the delamination path in the undropped region remains relatively consistent through the width of the specimen. The matrix cracking seen on the front and back faces of Figure 6.58 is also visible in the right half of each of the virtual cuts (Figure 6.60). The dropped region exhibits a large extent of damage, with many delamination paths and a large amount of matrix cracking occurring through ply thicknesses.

The damage observed in the single-ply effective ply thickness laminate is compared to the damage observed in a two-ply effective ply thickness laminate specimen. The documentation photograph of ply-drop specimen PD-B2-03, a specimen with a two-ply effective ply thickness laminate, is shown in Figure 6.61. Delaminations are visible

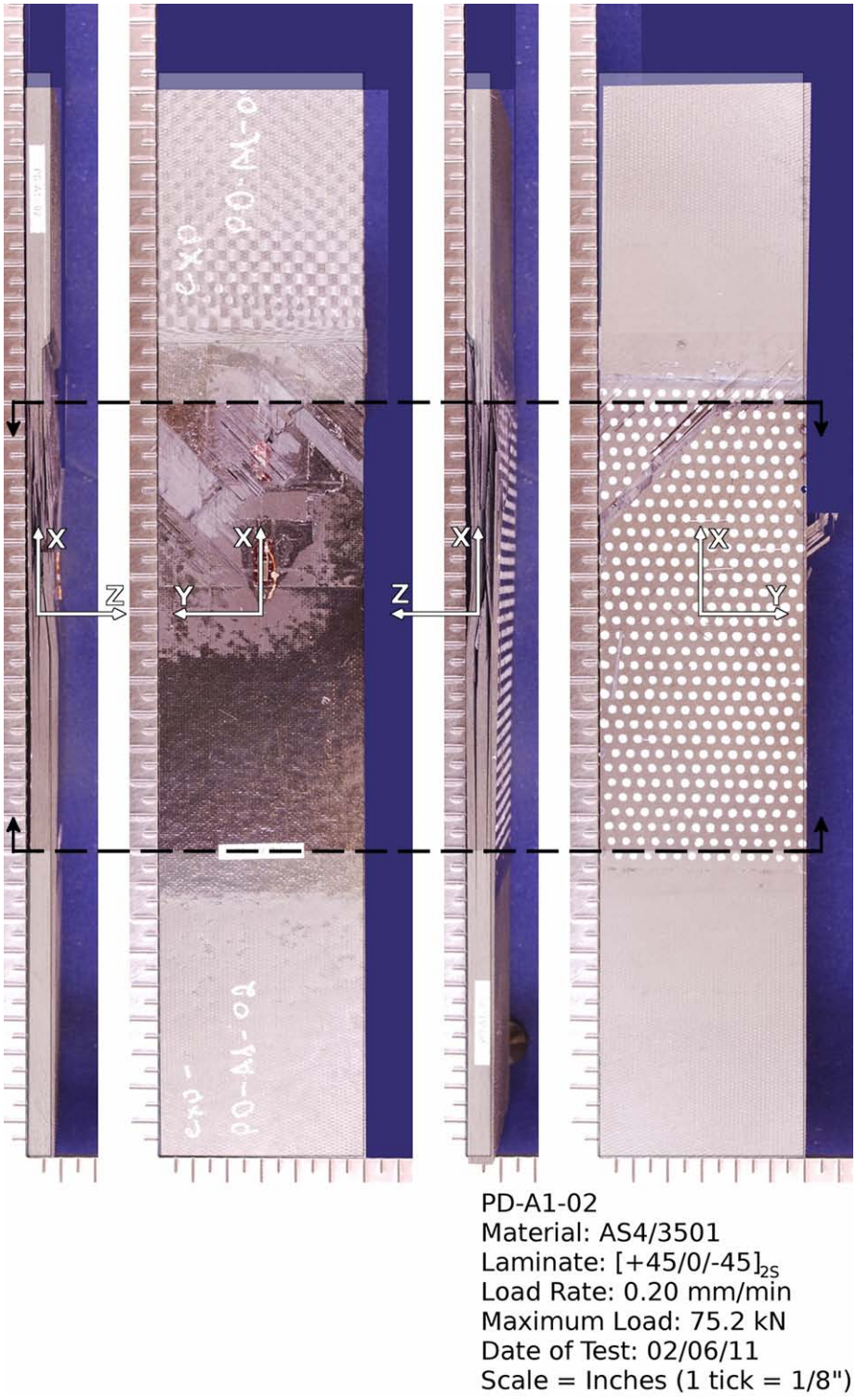

Figure 6.58 Documentation photograph and axes layer of a ply-drop specimen (PD-A1-02) with single-ply effective ply thickness laminate. (Note: Region between dashed lines represents material volume scanned and depicted in Figure 6.59)

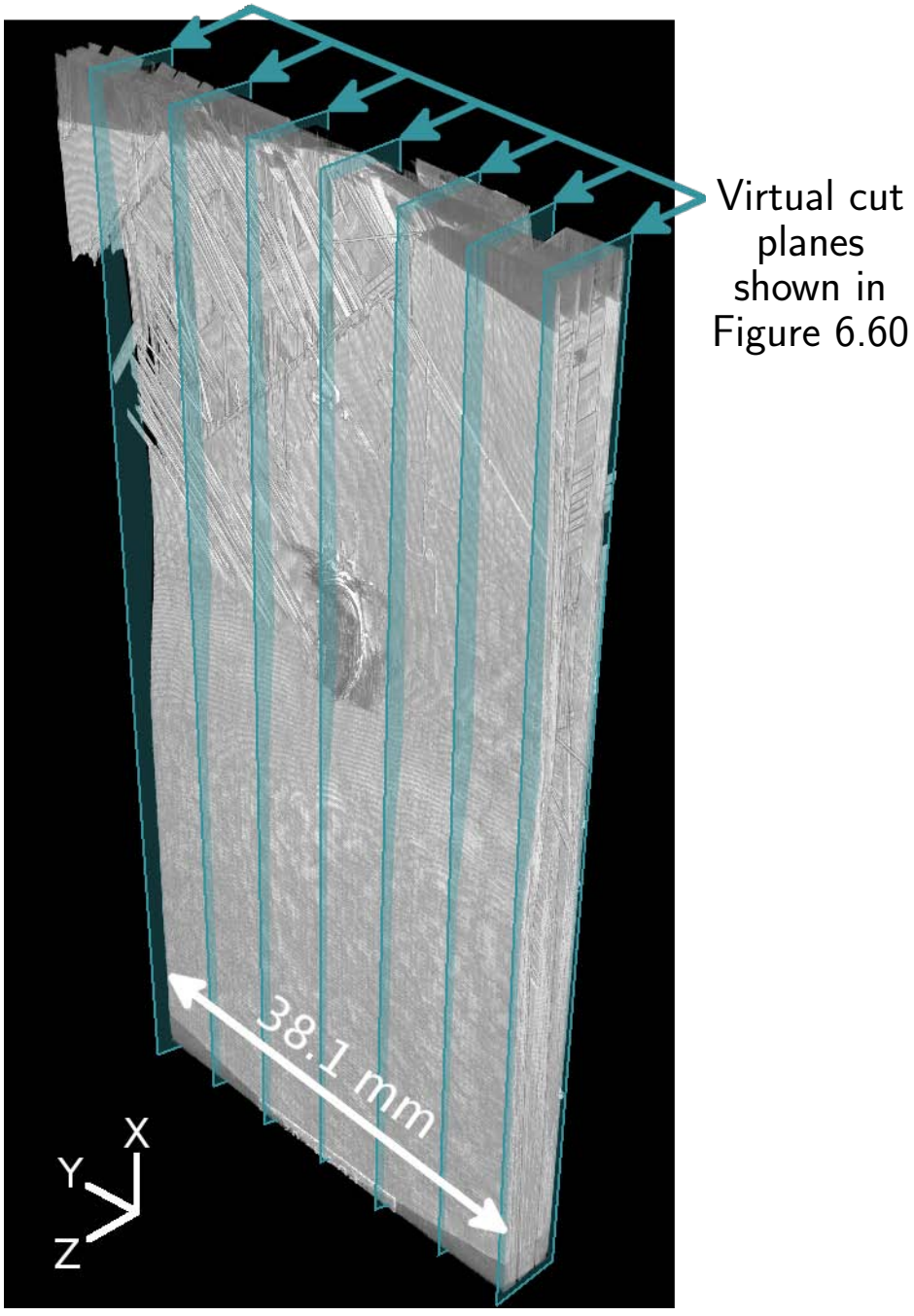

Figure 6.59 Virtual 3-D volume of a ply-drop specimen (PD-A1-02) with single-ply effective ply thickness laminate, showing a view of the front surface. (Note: Multiple virtual cut planes shown in Figure 6.60)

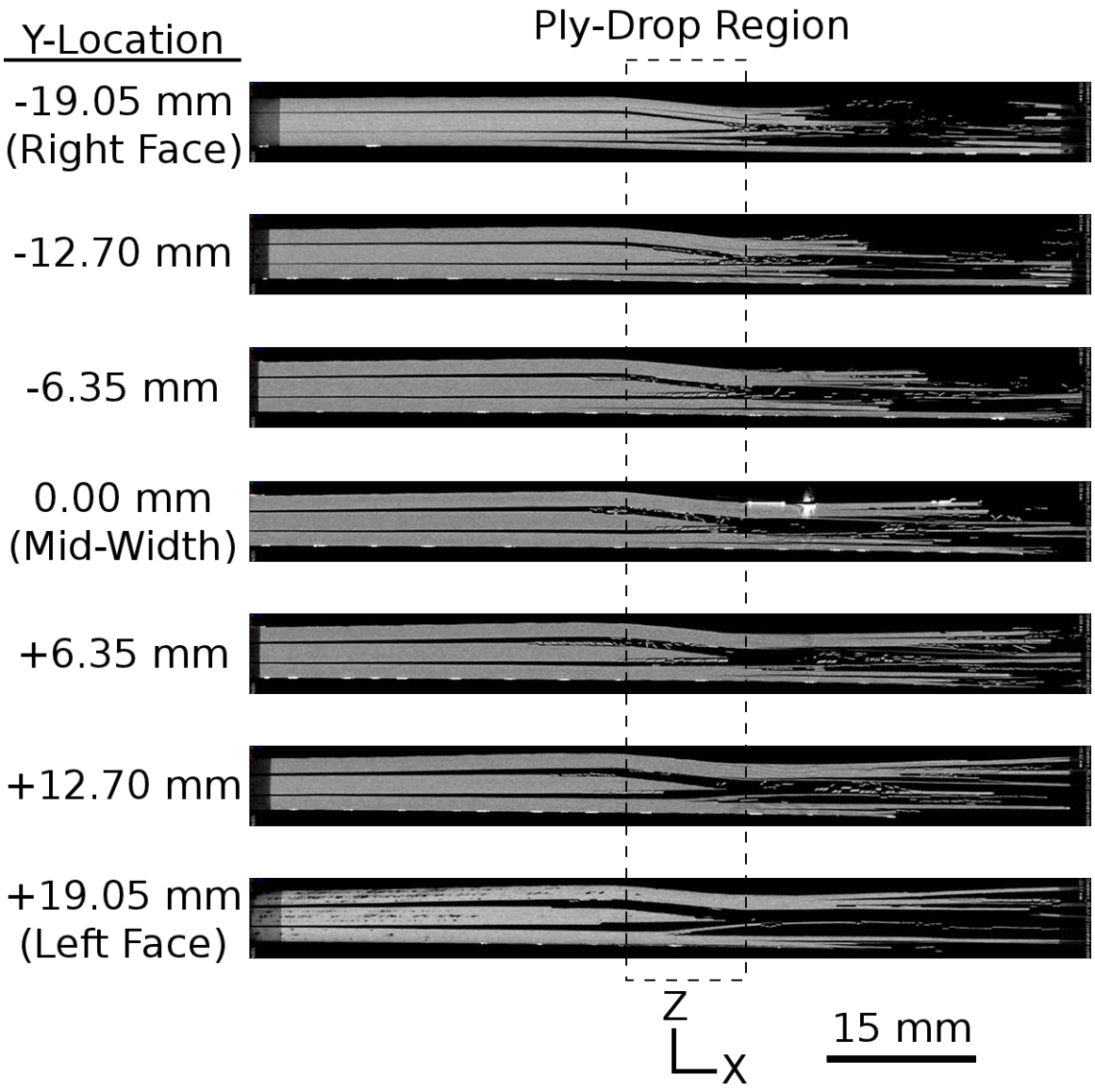

Figure 6.60 Multiple virtual cuts of a ply-drop specimen (PD-A1-02) with single-ply effective ply thickness laminate, shown in Figure 6.58, with the views being from the 'right', with material virtually removed (sectioned) through the width from the right face to the left face.

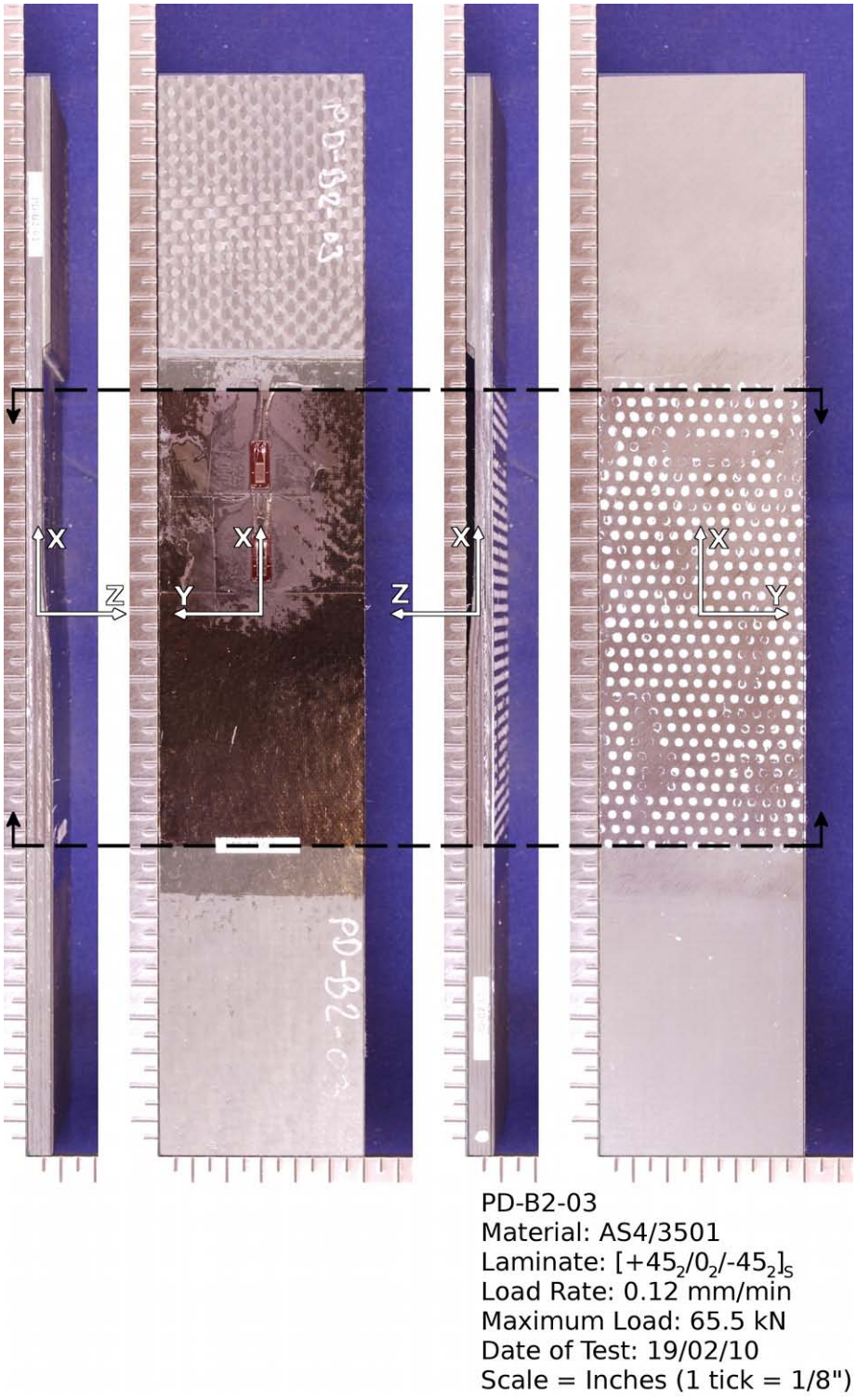

Figure 6.61 Documentation photograph and axes layer of a ply-drop specimen (PD-B2-03) with two-ply effective ply thickness laminate. (Note: Region between dashed lines represents material volume scanned and depicted in Figure 6.62)

on the left and right documentation photographs of Figure 6.61. However, matrix cracking is not visible on the front or rear faces, or on the left or right faces. The material between the dashed lines of this figure indicates the region scanned. The recreated volume of this specimen is shown in Figure 6.62. This three-dimensional view shows the front and right faces of the specimen. Delaminations can be made out (though difficult to see at the shown angle) on the right face. As with the previous specimen, seven virtual cuts are taken at the indicated cutting planes. The virtual cuts of this specimen are shown in Figure 6.63. The view of the virtual cuts is from the right face. Material is removed (virtually cut) through the width of the specimen until reaching the left face. The y-location of each cut is indicated in the figure, with zero being the center of the specimen width, and ± 19.05 mm corresponding to the left and right faces. The cut locations are selected at an equal spacing through the width. The damage observed from these virtual cuts show a similar trend in the undropped region, where delaminations run along the sublaminates. However, the extent of delamination is greater when closer to the right face than to the left face.

The delamination paths also jump interfaces in both the undropped and dropped regions of this specimen. These jumps are observed in the ply-drop region and extend along the fiber angles within the angle plies. Two such paths are highlighted by circles shown in Figure 6.63. One of the jumps in this specimen is observed to extend from the left face, within the ply-drop region, all the way to the right face (although the delamination jump at the right face is difficult to see). Another delamination jump is observed extending from the ply-drop region. However, this path terminates before reaching either the left or right face. The circles in the figure are spaced in the x-direction by approximately 6 mm with the virtual cuts spaced in the y-direction by 6.35 mm. This indicates that these jumps occur via matrix cracks at an angle through the thickness running along the angle of the ply in-plane: $+45^\circ$ for the first case and -45° for the second case. For the first case, the jump appears to occur across the four $+45^\circ$ plies of the dropped and base sublaminates (approximate ply locations determined via optical measurement of the specimen thickness). This corresponds to the delamination jumping between the interfaces of the $+45^\circ$ plies and the 0° plies,

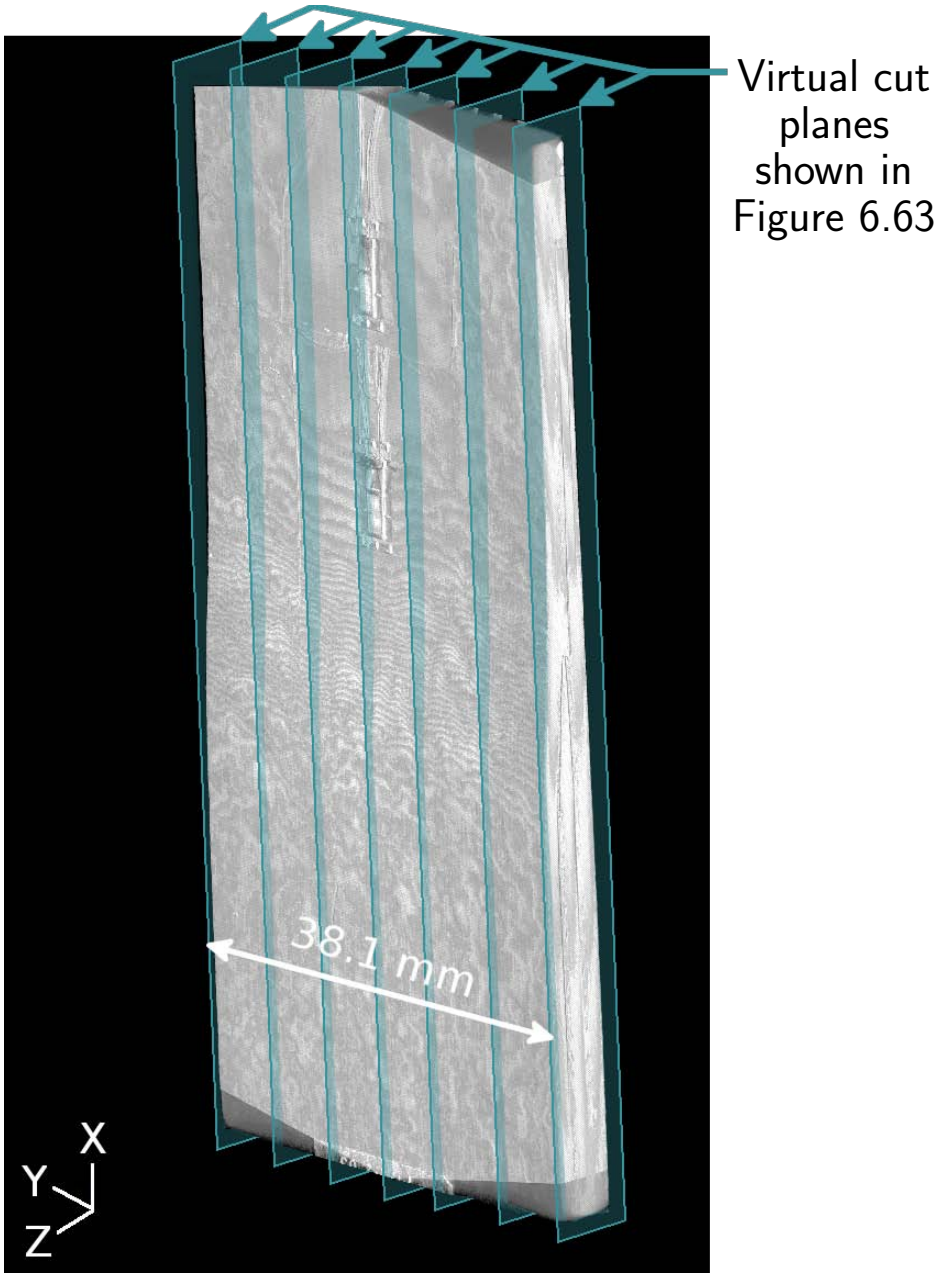

Figure 6.62 Virtual 3-D volume of a ply-drop specimen (PD-B2-03) with two-ply effective ply thickness laminate, showing a view of the front surface. (Note: Multiple virtual cut planes shown in Figure 6.63)

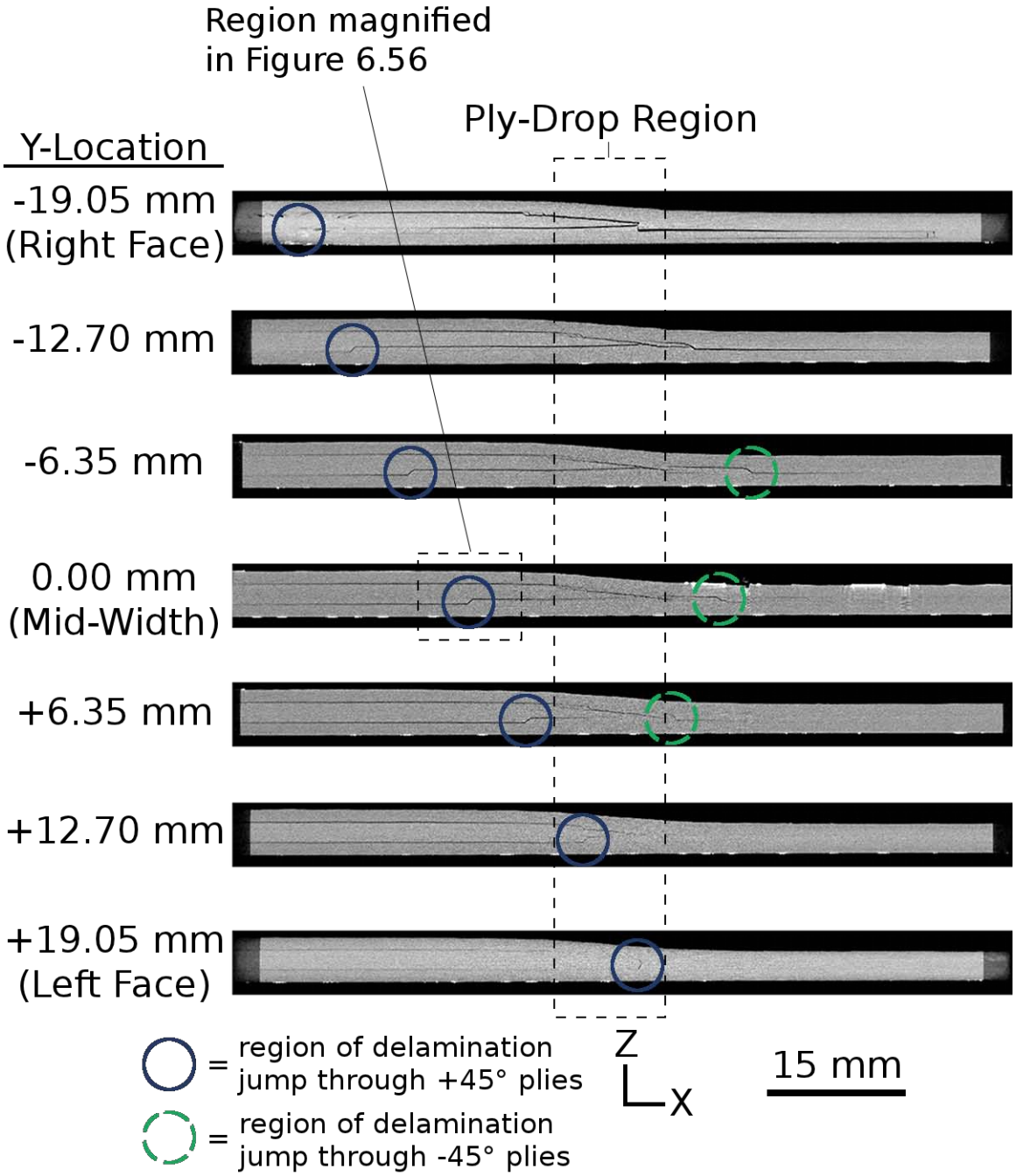

Figure 6.63 Multiple virtual cuts of a ply-drop specimen (PD-B2-03) with two-ply effective ply thickness laminate, shown in Figure 6.61, with the views being from the 'right', with material virtually removed (sectioned) through the width from the right face to the left face.

with the jump occurring through the thickness of the four +45° plies. A magnified view of the right face virtual cut at the y-location of 0.00 mm is shown in Figure 6.64, with the region shown indicated by the small dashed box of the 0.00 mm (y-location) virtual cut shown in Figure 6.63. The other delamination observed in Figure 6.64 appears to occur at one of the interfaces of the 0° plies and the +45° plies in the top sublaminate (approximate ply locations determined via optical measurement of the specimen thickness).

The delamination jump behavior was not observed in the specimen with single-ply effective ply thickness laminate. Only delamination is observed in the dropped region of the two-ply effective ply thickness laminate specimen, compared to the specimen with a single-ply effective ply thickness laminate that exhibited multiple matrix cracks through the thickness of multiple plies. The observed damage extent of this two-ply effective ply thickness specimen is much less than the damage extent of the single-ply effective ply thickness specimen, as can be seen comparing Figures 6.60 and 6.63.

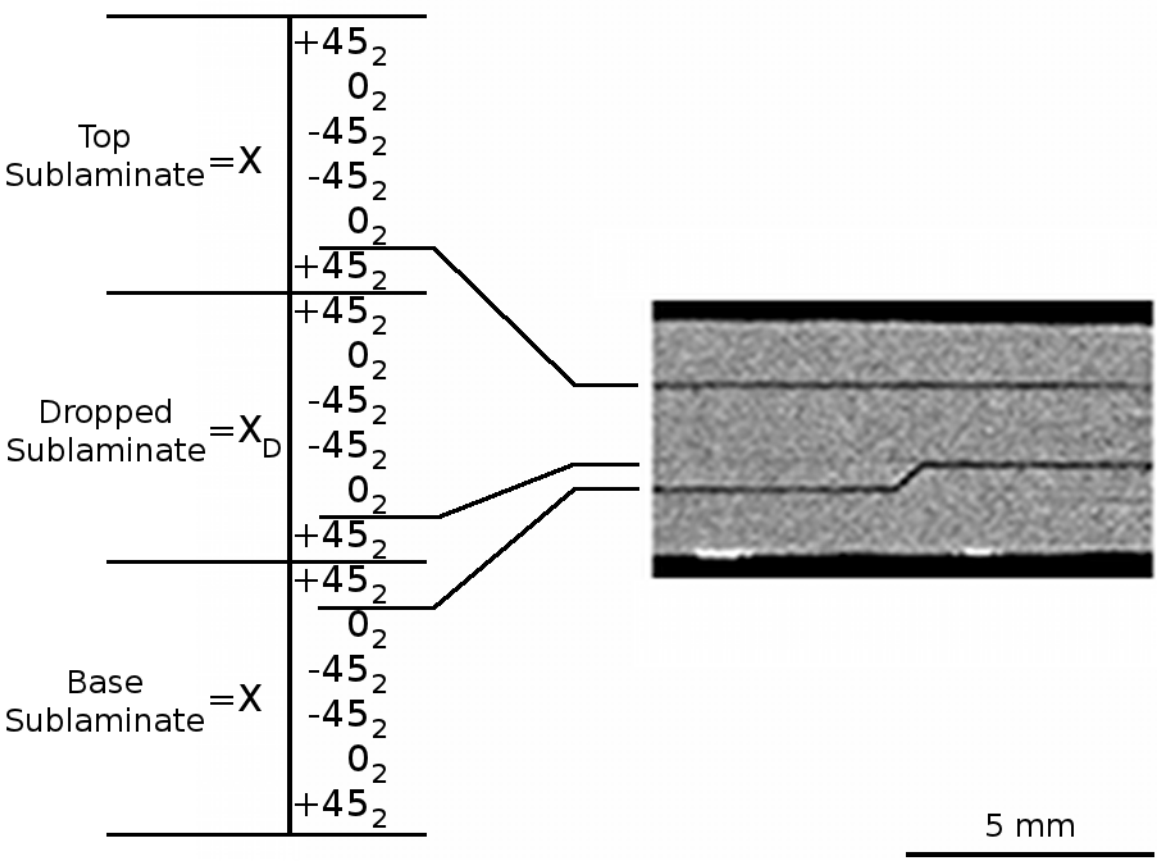

Figure 6.64 Magnified view, of the region indicated in Figure 6.63, of the virtual cut at y-location of 0.00 mm of a ply-drop specimen (PD-B2-03) with two-ply effective ply thickness laminate.

Chapter 7

Modeling

Lengthscale effects associated with gradients in the stress and strain fields are determined and discussed in this chapter. In order to investigate these fields and associated gradients, numerical models are developed in ABAQUS® (v6.11) [126], a commercially available finite element program. A study is presented where several structural parameters that affect overall stress and strain fields are considered. Varied parameters include the specimen geometry and the composite stacking sequence. The single-edge-notched specimen, double-edge-notched specimen, open-hole tension specimen, and ply-drop specimen geometries, and the laminates included in the experimental study are modeled. This allows the influences of geometric features, as well as laminate layups (including effective ply thicknesses and different ply angles) on the lengthscales associated with stress and strain fields to be investigated, and to help identify general trends and gain insight to key mechanisms controlling damage. In addition to the models of the four specimen types, the stress and strain field gradients created by selected damage modes, selected based on common damage modes observed in the experimental specimens, are investigated by modeling the damage mode in an infinite plate without structural features.

7.1 Objectives

The objective of the modeling is to investigate lengthscales associated with gradients in stress and strain fields. The potential is that lengthscales associated with stress and strain gradients exist such that once a critical length is reached and there is a sufficient magnitude of stress or strain, the mechanisms controlling the damage process may change. The idea of a lengthscale associated with gradients in the stress and strain field is similar to the principle of characteristic distances for the failure of specimens containing through the thickness discontinuities as defined by Whitney and Nuismer [127]. They define two characteristic distances: one assumes failure will occur if a critical magnitude of stress is reached at a characteristic distance away from the discontinuity, and the other assumes failure will occur if the averaged stress over a characteristic distance from the discontinuity reaches a critical value. However, Whitney and Nuismer do not explicitly account for the gradient of the field.

The goal of the models considered herein is to identify relations between the observed damage behavior and gradients and magnitudes in the stress and strain fields. The models allow characteristic lengths over which the magnitudes of the stress or strain fields vary to be investigated and defined. Unlike the characteristic length of Whitney and Nuismer, the general characteristic lengths in the gradient fields considered here do not necessarily occur at a structural feature. Instead, these lengths may occur at any point within the composite material where the fields exhibit a change in magnitude over some characteristic length (e.g., $\Delta\sigma/l_{characteristic}$ or $\Delta\epsilon/l_{characteristic}$). The models of the virgin (undamaged) specimens enable trends in the magnitudes and gradient fields, as determined by the models, to be related to the type and extent of 'active' damage observed in the experimental specimens, where the type and extent of damage in the experimental specimens are documented in the comparison database described in Section 5.2. In addition to investigating the magnitudes and gradients in the stress and strain fields formed due to the structural features (i.e., geometric features such as a hole) of a specimen, models of selected damage modes enable lengthscales associated with these modes to be identified based on the magni-

tudes and gradients in the stress and strain fields formed around such damage. For both the specimen models and damage mode models, lengthscales associated with the gradients in the strain fields are identified. Comparing these lengthscales and the magnitudes of stress or strain created by both the structural features and the damage modes allows the critical, or 'driving', mechanism(s) to be identified.

In order to investigate the gradients in stress and strain fields resulting from structural features, numerical models were created for the specimen types described in Chapter 4: the single-edge-notched specimen, the double-edge-notched specimen, the open-hole tension specimen, and the ply-drop specimen. The geometries for each specimen are shown in Figures 4.1, 4.4, 4.5, and 4.6. Within each of the models, parameters are controlled to match those of the experimental specimens. These parameters include the nominal geometry, ply angles, and the stacking sequences used in the specimens. Loading is taken to be in-plane, uniaxial displacement for all cases, as this loading is common among all specimens included in the experimental investigation. This loading is one of the fifteen experimental load cases of the single-edge-notched specimens, is one of the seventy-two experimental load cases of the double-edge-notched specimens, and is the only experimental load case for the open-hole tension and ply-drop specimens. The gradients of the stress and strain field are investigated for the virgin (undamaged) specimen models, as well as the general models containing damage, described next. The numerical strain fields determined from the models are verified using the experimental strain gradients measured and reported (using optical strain measuring techniques) for the double-edge-notched, open-hole tension, and ply-drop specimens [128, 129]. Optical strain mapping was not performed on the single-edge-notched specimens (for reasons described in Chapter 4).

In order to investigate the gradients in stress and strain fields resulting from damage modes, numerical models were created for an infinite rectangular plate containing damage. While a truly infinite plate is not modeled, the length and width of the plate are 30 times greater than the length of damage. This is done to remove the influences of edges on the resulting stress and strain resulting from the damage modes (i.e., the variation in stress and strain near the edges do not intersect with the variation due

to the damage). Two damage modes were investigated: stitch cracking, as described in Section 2.2, and delamination. These modes were selected for investigation based on observations made on the experimental specimens, as discussed in Chapter 6. As illustrated in Figures 6.25 through 6.28, there is an observed relationship between the load path, the laminate, and the presence of transverse zigzag damage for the single-edge-notched and double-edge-notched experimental specimens. In each case of transverse zigzag damage, stitch cracking and delamination are observed. Hence, these two modes are selected for investigation. The procedure discussed herein can be expanded to other damage modes, but is outside the scope of this work. While multiple approaches exist to model the initiation and/or propagation of damage using finite element methods [e.g., 130–132], the intention of the models herein is to investigate lengthscales associated with the two selected damage modes. Therefore, the geometry resulting from the damage modes are modeled and the gradient fields are investigated. This approach can be thought of as a specimen containing unique, ply-specific structural features, where these features are the modeled damage.

In all the models, the stress response at traction-free surfaces are modeled with the default ABAQUS settings. These settings satisfy the zero net traction over laminate thickness in an averaged sense. Therefore, the integration of normal stress through the thickness of a laminate at a free surface results in zero traction. However, the zero traction condition is not explicitly applied at the ply level (i.e., plies may have non-zero tractions). This influences the stress equilibrium equation and will result in inaccurate stress fields near these free surfaces [133–136]. Pagano and Pipes [137–139] provide approximate solutions to the stress fields at the free edges based on algebraic and ordinary differential equations. Their finds show a 'boundary layer' at free edges. Within this boundary layer, the stress solutions diverge from the predictions of classical laminate theory. Pagano and Pipes found the boundary layer to have a length of approximately one laminate thickness. For the models considered in this chapter, these free-edge effects are not captured. Previous studies have shown that delaminations initiate within these free edge 'boundary layers.' Therefore, the current models do not explicitly address delamination initiation at any such locations

(e.g., specimen boundaries, notch edges, open hole edge, and edges created for the damage inclusion models).

The results from the models are used to investigate lengthscales associated with gradients in the stress and strain fields. Comparing lengths associated with gradient fields (e.g., $l_{characteristic}$), the magnitude of stress or strain, and the damage exhibited in the experimental specimens, critical lengthscales associated with these gradients are defined. Interactions between critical lengthscales, such as between lengthscales associated with structural features and lengthscales associated with gradient fields, can begin to be ascertained.

7.2 Setups

The finite element (FE) analysis in the current work is preformed in ABAQUS (v6.11). The general approach used for all models is first described and then details of each model follow in separate subsections. A macroscopic approach modeling an individual ply as a homogeneous, transversely orthotropic continuum is used for all the models. The solid (continuum) element (C3D8R), a three-dimensional 8-node hexahedron with reduced integration and hourglass control, is used in the models. This element type enables the through-thickness response of a laminate to be determined [126]. The in-plane stress and strain results of all the models are resolved into and presented in ply axes in order to assess the effects of loading on the response of individual plies. Material properties of a generic AS4/3501-6 glass/epoxy ply, shown in Table 7.1, are defined for the models using the elastic engineering constants type in ABAQUS. The stacking sequences and ply orientations are input through the composite layup editor, and are listed in Table 7.2. This editor provides a convenient, table-based interface for defining laminates. First, the number of plies is specified. Then the details of each ply are defined. These details are the name, material, thickness, and orientation of the ply, as well as the number of integration points and the region of the model to which the ply is assigned [141]. The alternative to using the composite layup editor requires the model geometry to be sectioned for each ply and

Table 7.1 Generic properties of a AS4/3501-6 composite ply

Property	**AS4/3501-6***
E_L	142 GPa
E_T	10.3 GPa
E_Z	10.3 GPa
G_{LT}	7.2 GPa
G_{LZ}	7.2 GPa
G_{TZ}	3.7 GPa
ν_{LT}	0.27
ν_{LZ}	0.27
ν_{TZ}	0.40

* Values taken from references [10, 13, 140].

Table 7.2 Stacking sequences and ply orientations used in finite element models

Specimen Type	**Laminate**
Single-Edge-Notched	$[(-\theta/+\theta_2/-\theta_2/+\theta)_S]_S$ where $\theta = 15°$, $30°$, $60°$, or $75°$
Double-Edge-Notched	$[+\theta/-\theta]_{16T}$ $[+\theta_4/-\theta_4]_{4T}$ where $\theta = 15°$, $30°$, $60°$, or $75°$
Open-Hole Tension	$[+45°/0°/-45°]_{4S}$ $[+45°_4/0°_4/-45°_4]_S$
Ply-Drop	$[X, X_D, X]_T$ where $X = (+45°/0°/-45°)_{2S}$ or $(+45°_2/0°_2/-45°_2)_S$

individual section properties and material orientations to be defined. These steps are automated using the laminate toolbox.

The laminates shown in Table 7.2 are those used in the experimental tests, as described in Chapter 4. In order to investigate lengthscale effects associated with the effective ply thickness of a laminate, two of these laminate configurations are modeled for the double-edge-notched, open-hole tension, and ply-drop specimens. For the double-edge-notched and open-hole tension specimens, these are a single-ply effective ply thickness laminate and a four-ply effective ply thickness laminate. For the ply-drop specimen, these are a single-ply effective ply thickness laminate and a two-ply effective ply thickness laminate. Details on the reasons for the selection of these laminate configurations are described in Sections 4.2, 4.3, and 4.4. The experimental testing of the single-edge-notched specimens did not include laminates with different effective ply thicknesses, so such are not modeled here.

The loading for all specimens is modeled as a specified displacement. Displacement boundary conditions are defined for the top and bottom surfaces (positive and negative x-faces). A total displacement of 1% of the specimen gage length is applied. The specimen gage length is modeled as the length between the grips, as discussed in Chapter 4. The 1% strain is split equally between the top and bottom displacements, as shown in Figure 7.1, yeilding a far-field strain level of 10,000 μstrain. The specimen gage lengths and the associated applied boundary displacements are shown in Table 7.3.

The automated mesh feature within ABAQUS is used to generate the model meshes. As described in the following subsections, the models are partitioned to create regions of finer meshes near structural features (i.e., regions containing higher gradient fields). In ABAQUS, users can specify the density of a mesh by creating seeds, markers placed along the edges of a region, to specify the target mesh density in that region [126]. The mesh seeding is adjusted to create meshes with converging solutions. In order to produce a finer mesh near regions containing higher gradient fields, 'biased' seeding is used. Biased seeding allows the spacing between seeds to vary linearly along an edge. ABAQUS has the option for single-bias spacing, where

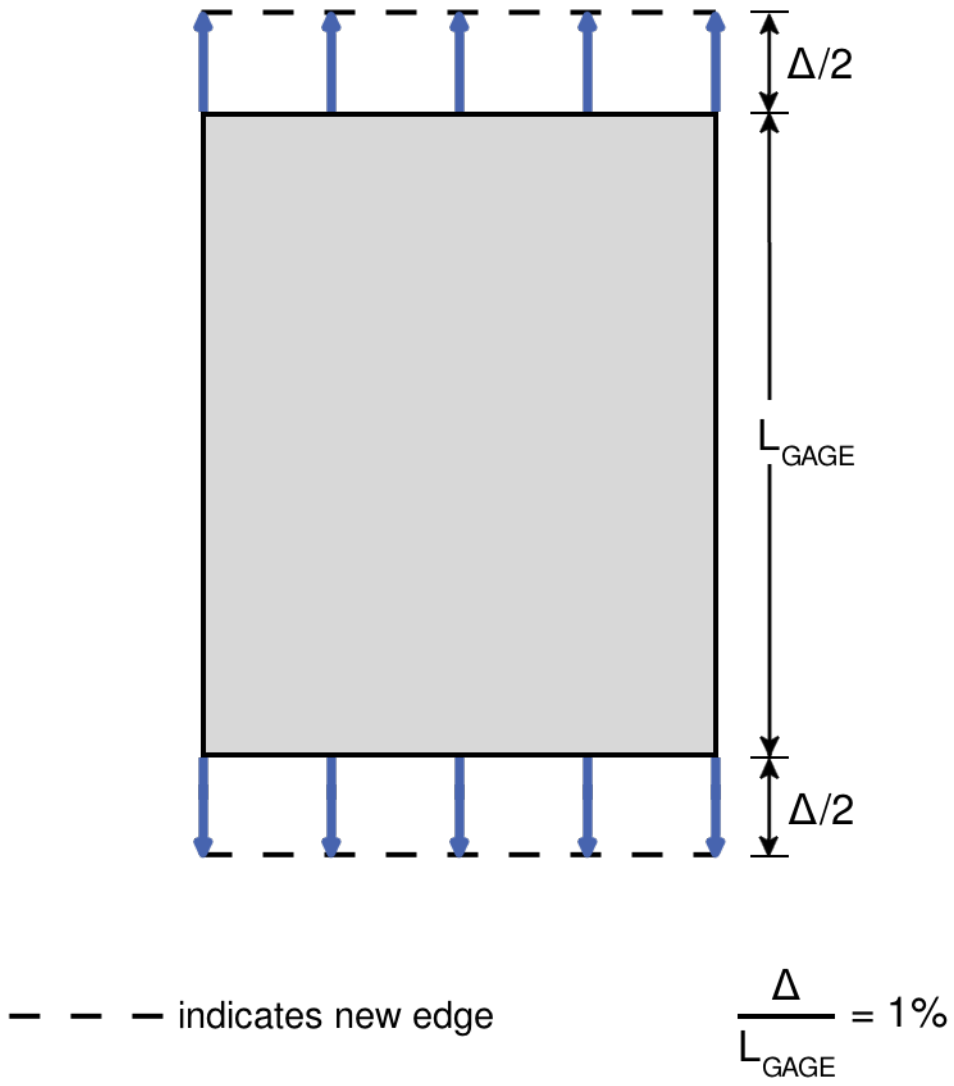

Figure 7.1 Generic applied displacement boundary conditions.

Table 7.3 Specimen gage lengths and applied displacement boundary conditions used in finite element models

Specimen Type	**Gage Length,** L_{GAGE} **[mm]**	**Applied Displacement,** $\Delta/2$ **[mm]**
Single-Edge-Notched	12.7	0.0635
Double-Edge-Notched	25	0.125
Open-Hole Tension (1/2" dia. hole)[a]	170	0.85
Open-Hole Tension (1" dia. hole)[a]	370	1.85
Ply-Drop	100	0.5
Damage Inclusion	1400	7.0

[a] Second round specimen dimensions, as described in Section 4.3.

the seed spacing varies between a specified maximum spacing at one end of the edge, and a specified minimum spacing at the other end of the edge, or double-bias spacing, where the seed spacing is specified for the ends of the edge and a different spacing is specified at the center of the edge. Once the seeding is specified, the automated mesh feature generates the mesh. Where possible, structured (hexahedral) meshes are used. As defined in the ABAQUS theory manual [126], structured meshing is a top-down technique that gives the most control over a mesh because it applies preestablished mesh patterns to particular model topologies. In regions near non-patternable structural features (i.e., regions with edges that are not straight), a swept mesh is used. The swept mesh results in non-structured hexahedral elements (i.e., the resulting elements are not square in-plane). ABAQUS creates swept meshes by internally generating the mesh on an edge or face and then sweeping that mesh along a sweep path (see Section 17 of [126] for further details on meshing techniques). As described in the following subsections, structured or swept meshes are applied to the partitioned regions of the models. The geometric dimensions of the models are the same as the nominal specimen dimensions described in Chapter 4. SI (International System) units are used for all the parameters of the FE models. The thickness of the individual plies is calculated within ABAQUS by dividing the element thickness by the total number of plies defined within that element.

7.2.1 Single-Edge-Notched Specimen Model

The single-edge-notched specimen model is based on the nominal dimensions of the experimental specimen described in Section 4.1. The planar dimensions of the model are shown in Figure 7.2. The specimen has a thickness of 3.556 mm. The specimen is partitioned along twenty-three planes parallel to plies and the x-y plane, each equally spaced, resulting in twenty-four layers through the thickness (corresponding to one layer per ply). These partitions are added in order to produce mesh elements with an average aspect ratio (longest edge compared to shortest edge) of 2.66, with the largest element aspect ratio of 8.01 occurring away from the notch tip. The model also

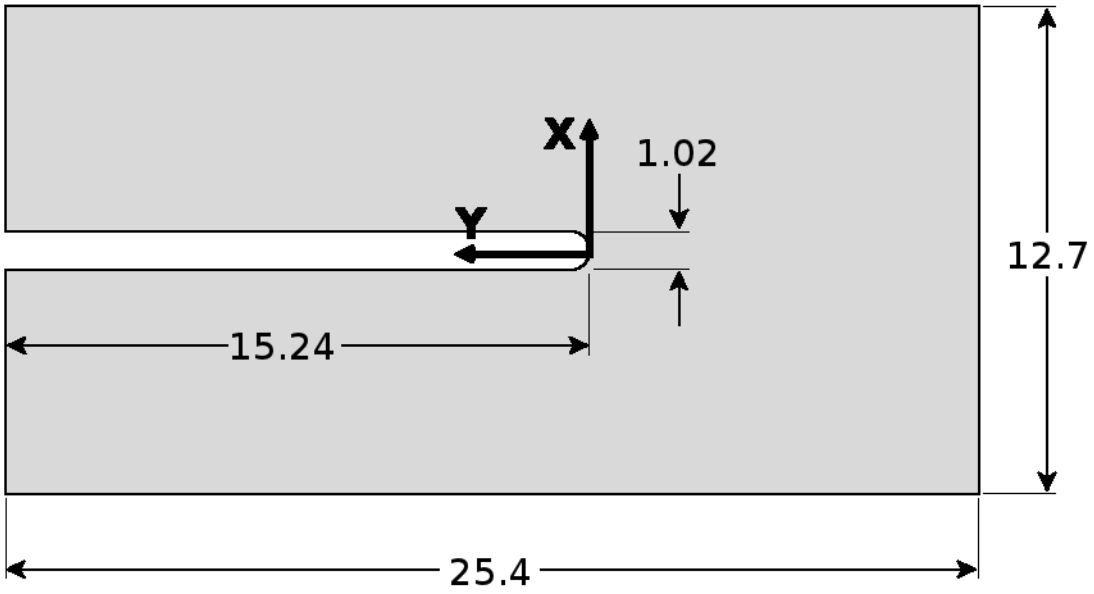

Figure 7.2 Dimensions of the single-edge-notched specimen model.

contains four partitions running through the thickness. Two are in the x-direction, and two are in the y-direction. This results in ten in-plane sections. These partitions are added to the model to permit increased mesh seeding near the notch tip.

A planar (x-y plane) view of the partitions running through the thickness is shown in Figure 7.3, where the ten in-plane sections are identified. One partition is located at the tangent points of the half-circle of the notch and is along the x-direction. Another partition along the x-direction is offset a distance of 3 notch radii (1.53 mm) to the right (toward the negative y-face of the specimen) of the previous partition. The two other partitions running through the thickness run along the y-direction. Both are located at a distance of 3 notch radii from the centerline of the notch, with one partition on the positive x side of the notch and the other on the negative x side of the notch.

Using the ABAQUS composite layup editor, twenty-four layups are specified, one for each layer of the model. Each layup contains one ply corresponding to the stacking sequence of $[(-\theta/+\theta_2/-\theta_2/+\theta)_S]_S$ where θ is equal to 15°, 30°, 60°, or 75° for the various cases considered. In order to attain and post-process the results of individual plies, every ply in the model requires a unique name specified in the composite layup editor.

The next step in the model setup is specifying the mesh seeding. For the single-edge-notched specimen model, a single-bias seeding is used along the x-faces of sections 1, 2, 3, and 4, with the bias spacing ranging from 0.50 mm at the left (positive y) end down to 0.19 mm at the right end (where sections 1 and 4 meet sections 5 and 7, respectively, and sections 2 and 3 meet section 6). A single-bias seeding is used along the y-faces of sections 1, 4, 5, 7, 8, and 10. The bias spacing ranges from 0.28 mm farthest from the notch, down to 0.12 mm nearest the center of the specimen. The x-faces of sections 8, 9, and 10 have a single-bias seed spacing ranging from 0.28 mm at the right (negative y) end down to 0.19 mm at the left end (where sections 8, 9, and 10 meet sections 5, 6, and 7, respectively). The positive y-faces of sections 2 and 3 have an unbiased (i.e., constant spacing) seeding where the number of elements is specified to be 16, equivalent to a spacing size of 0.06 mm. The negative y-faces of

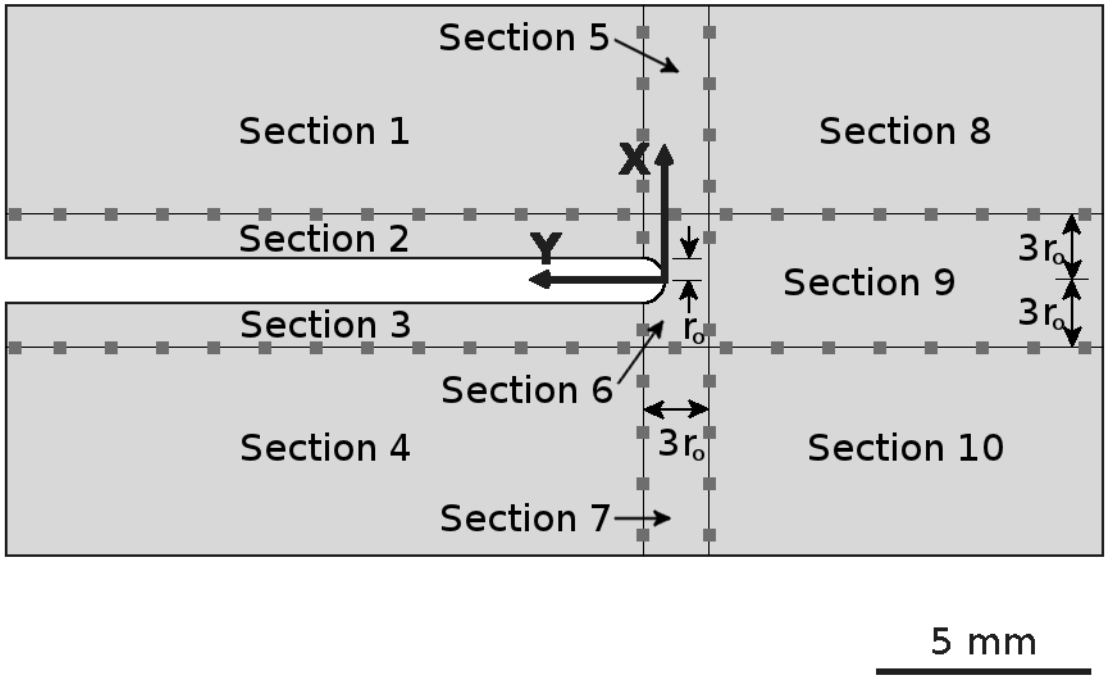

Figure 7.3 Planar (x-y) view of the partitioned single-edge-notched specimen model.

sections 2 and 3 have a single bias seeding where the number of elements is specified to be 16 with a bias ratio of 5, equivalent to a linearly varying spacing size from 0.13 mm away from the notch down to 0.03 mm at the notch edge. The bias ratio is included to decrease the element size near the curved, free-edge of the notch, where there are large gradients. The y-faces of section 9 have an unbiased seeding with the number of elements specified to be 24, equivalent to a seed spacing of 0.13 mm. The x-faces of sections 5, 6, and 7 have an unbiased seeding with the number of elements specified to be 8, equivalent to a seed spacing of 0.19 mm. The curved face of section 6 (i.e., the notch tip) has an unbiased seeding where the number of elements is specified to be 36, equivalent to a seed spacing of 0.04 mm. There is a single seed through the thickness of each layer.

Once the seeding is complete, the automatic mesh parameters are set. With the specimen geometry and selected seeding, a structured mesh can be applied to all the sections of the model. An in-plane view of the resulting mesh is shown in Figure 7.4, where this mesh is repeated through the thickness for each of the twenty-four layers. The mesh in sections 2, 3, 6 are dense, with 16 elements along the x-direction in sections 2 and 3, and 16 elements in the radial direction of section 6, resulting in what appears to be dark regions in Figure 7.4. A total of 183,264 elements are created with the set seeding. The longest element edge is 0.50 mm and the shortest element edge is 0.025 mm (roughly 3.6 times the diameter of an AS4 fiber). Applying the smeared property assumption (a macromechanical assumption) at scales on the order of a fiber diameter may yield erroneous solutions as micromechanical effects become important at these lengthscales. In this model, 96 elements have edges of length 0.025 mm. These elements are located along the free-edge of the notch, where sections 2 and 3 meet section 6. As these elements are not located in the region of interest (i.e., the high gradient region at the tip of the notch), it is assumed the model solution is valid.

Boundary conditions are specified for the C3D8R elements. This element has three translational degrees-of-freedom (DoF) and no rotational DoF. For the single-edge-notched specimen model, displacement boundary conditions in the x-direction

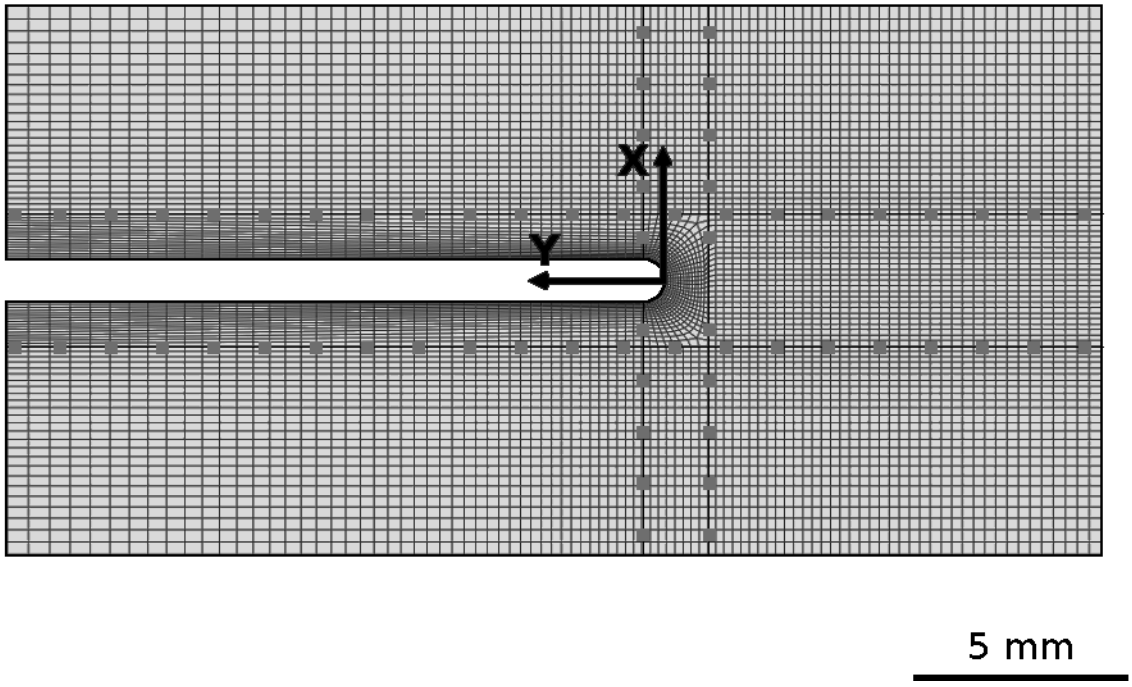

Figure 7.4 Planar (x-y) view of the mesh for the single-edge-notched specimen model.

are specified on the positive and negative x-faces. This boundary condition simulates uniaxial tension on the specimen. The gage length of the single-edge-notched specimen is 12.7 mm. A total overall strain of 1% is applied to the specimen, split equally between the upper and lower faces (i.e., that is 0.5% for each face). The resulting x-direction displacement boundary condition is 0.0635 mm. The other DoF are left free. An illustration of the applied boundary conditions is shown in Figure 7.5.

The final step in the model setup is specifying the field outputs. For the C3D8R elements used in this model, the three-dimensional strain and stress values are requested in ply axes on a ply-by-ply basis. This is done by specifying field outputs for each of the six layups defined in the composite layup editor. The results of the single-edge-notched specimen model are presented and discussed in Section 7.3.1.

7.2.2 Double-Edge-Notched Specimen Model

The double-edge-notched specimen model is based on the nominal dimensions of the experimental specimen described in Section 4.2. The planar dimensions of the model are shown in Figure 7.6. The specimen has a thickness of 4.20 mm. The specimen is partitioned along seven planes parallel to plies and the x-y plane, each equally spaced, resulting in eight layers through the thickness (not to be confused with plies). These partitions are added in order to produce mesh elements with an average aspect ratio (longest edge compared to shortest edge) of 1.34, with the largest element aspect ratio being 3.60. The model also contains six partitions running through the thickness. Four are in the x-direction and two are in the y-direction. This results in seventeen in-plane sections. These partitions are added to the model to permit increased mesh seeding near the notch tips.

A planar (x-y plane) view of the partitions running through the thickness is shown in Figure 7.7, where the seventeen in-plane sections are identified. Two partitions are located at the tangent points of the half-circle of the notches and are along the x-direction. Another two partitions are located at a distance of 3 notch radii (4.2 mm) toward the center of the specimen and are also along the x-direction. The other partitions running through the thickness are along the y-direction. Both are located

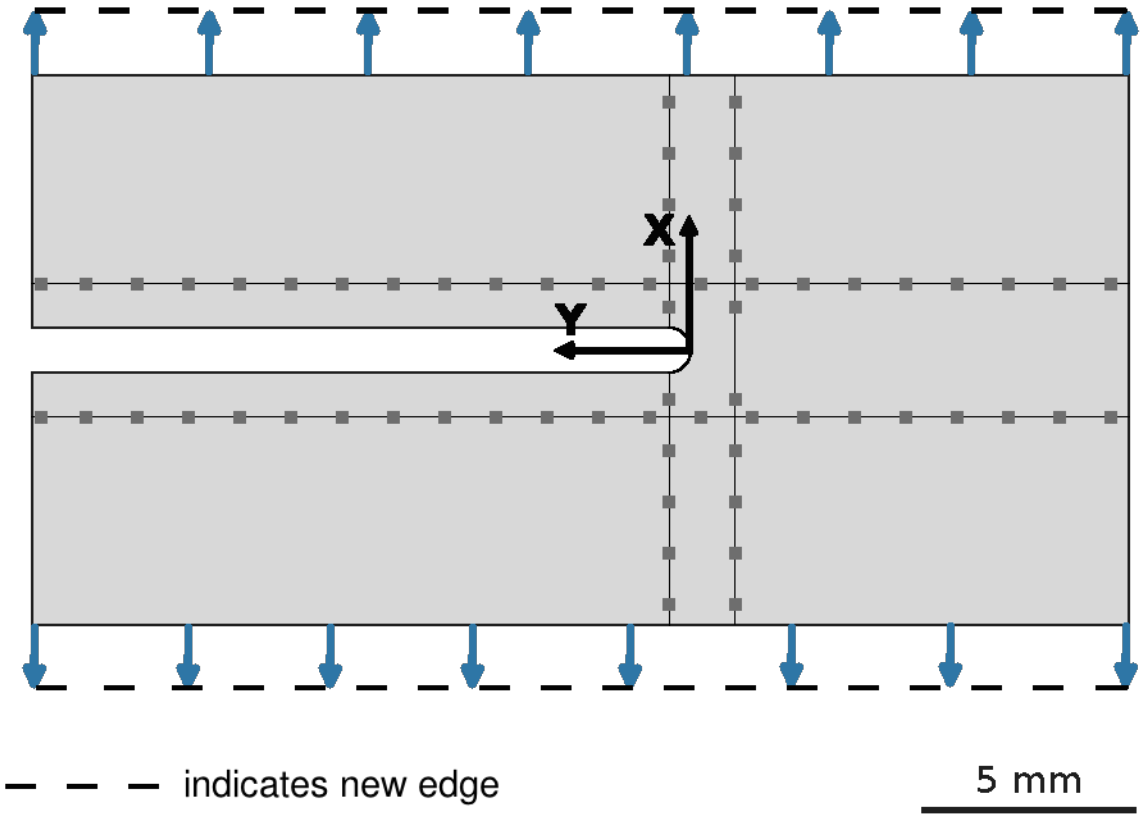

Figure 7.5 Planar (x-y) view of the boundary conditions for the single-edge-notched specimen model.

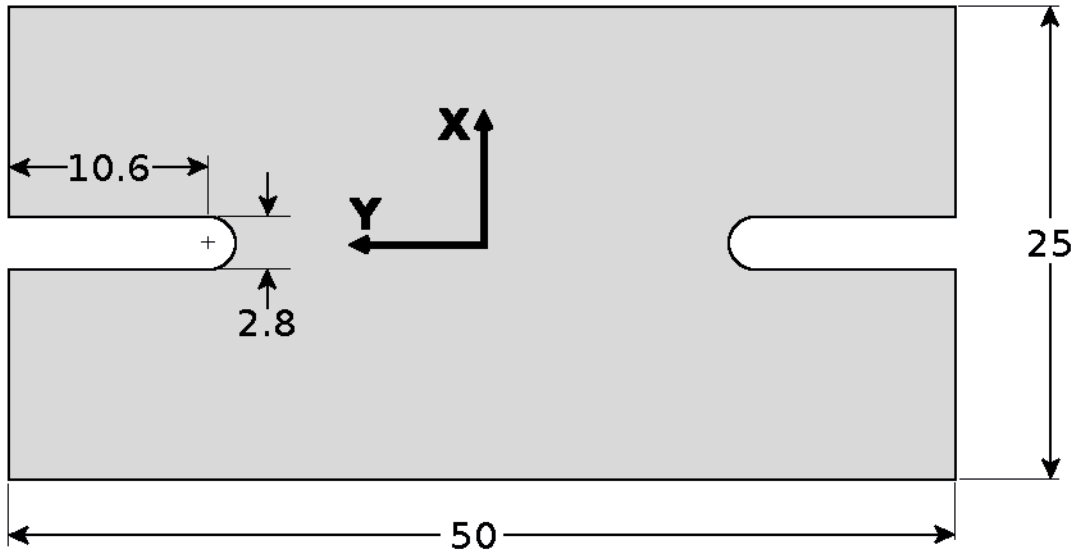

Figure 7.6 Dimensions of the double-edge-notched specimen model.

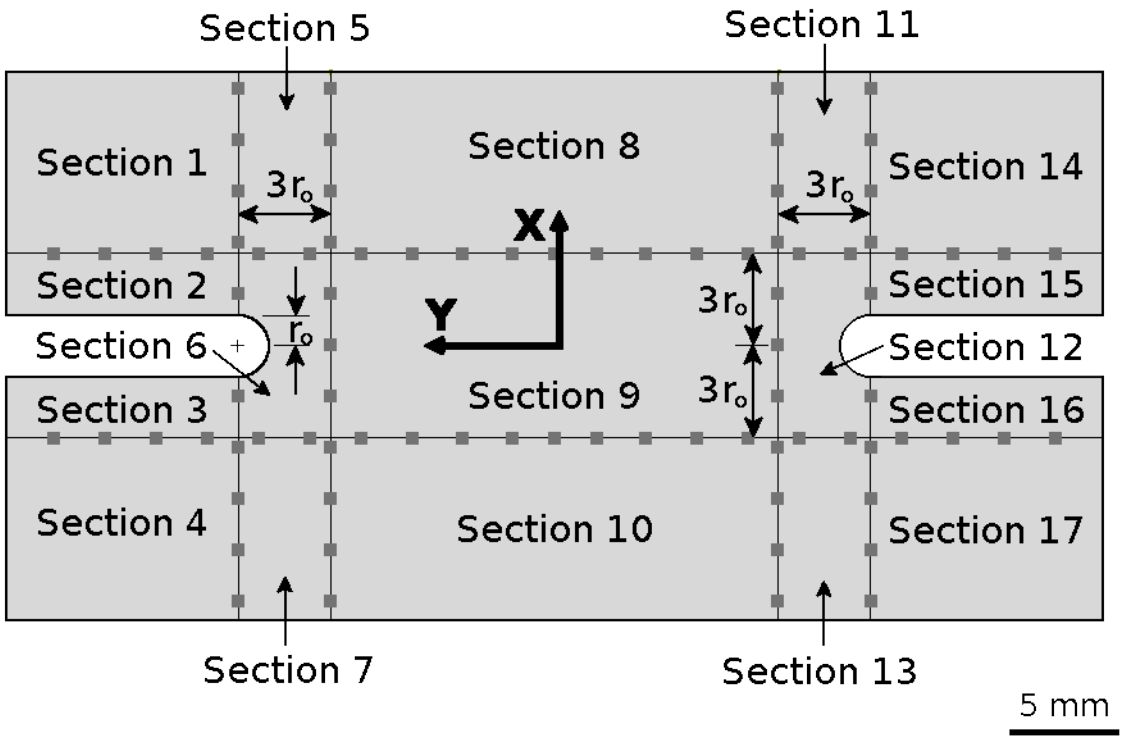

Figure 7.7 Planar (x-y) view of the partitioned double-edge-notched specimen model.

at a distance of 3 notch radii from the centerline of the notches, with one partition on the positive x side of the notch and the other on the negative x side of the notch.

Using the ABAQUS composite layup editor, eight layups are specified, one for each layer of the model. Each layup contains four plies. The model is run using two different stacking sequences of the layup, corresponding to either the single-ply effective ply thickness laminate or the four-ply effective ply thickness laminate, as described in Section 4.2. The laminates analyzed with the models are $[+\theta/-\theta]_{16T}$ and $[+\theta_4/-\theta_4]_{4T}$ where θ is equal to 15°, 30°, 60°, or 75° for the various cases considered. As with the single-edge-notched specimen model, in order to attain and post-process the results of individual plies, every ply in the model requires a unique name specified in the composite layup editor.

The next step in the model setup is specifying the mesh seeding. A global seed spacing of 0.525 mm is applied to the majority of the model. A single-bias seed spacing is used along the x-faces of sections 1 through 4 and 14 through 17, with the bias spacing ranging from 1.00 mm at the left and right specimen edges and decreasing down to 0.525 mm at the ends nearest the center (x equal to zero) of the specimen (see beginning of Section 7.2 for explanation of seed biasing). The y-faces of sections 2, 3, 15, and 16 have an unbiased seeding with the number of elements specified to be 8, equivalent to a seed spacing of 0.35 mm. The x-faces of sections 5, 6, 7, 11, 12, and 13 have an unbiased seeding with the number of elements specified to be 8, equivalent to a seed spacing of 0.26 mm. The y-faces nearest the center of the specimen of sections 6 and 12 have an unbiased seeding with the number of elements specified to be 16, equivalent to a seed spacing of 0.26 mm. The curved edges of sections 6 and 12 (i.e., the notch tips) have an unbiased seeding where the number of elements is specified to be 32, equivalent to a seed spacing of 0.14 mm. There is a single seed through the thickness of each layer.

Once the seeding is complete, the automatic mesh parameters are set. With the selected seeding, sections 6 and 12 have a swept mesh while all the other sections have a structured mesh. The resulting mesh is shown in Figure 7.8. A total of 33,440 elements are created with the set seeding. The longest element edge is 1.04 mm and

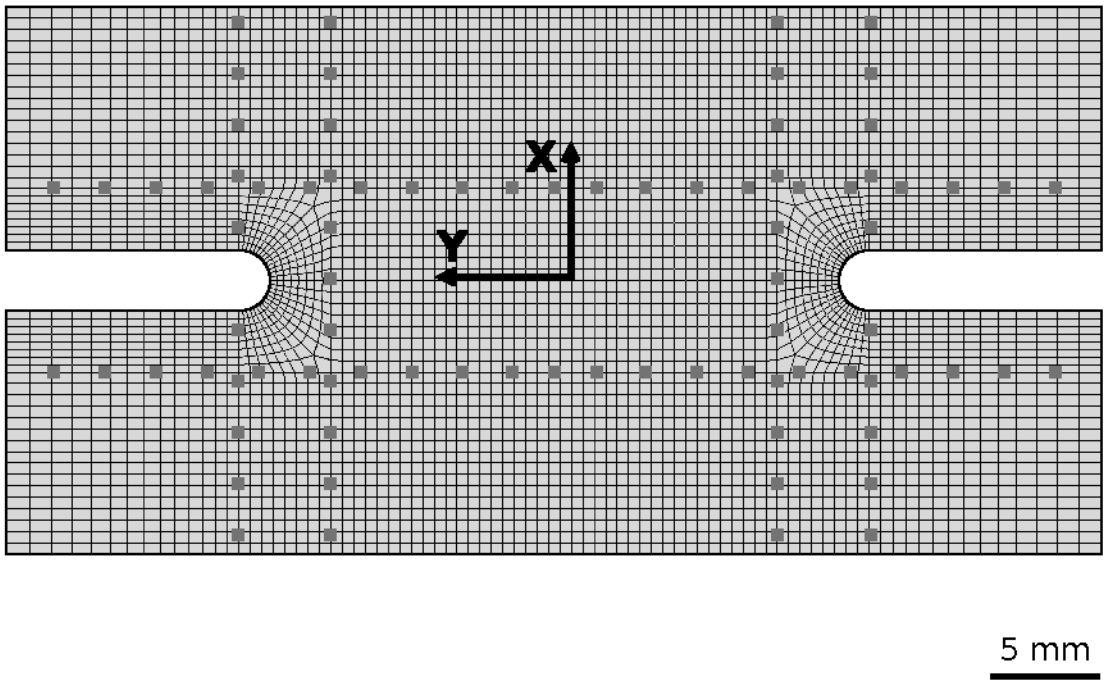

Figure 7.8 Planar (x-y) view of the mesh for the double-edge-notched specimen model.

the shortest element edge is 0.15 mm.

For the double-edge-notched specimen model, displacement boundary conditions in the x-direction are specified on the positive and negative x-faces. This boundary condition simulates uniaxial tension on the specimen. The gage length of the double-edge-notched specimen is 25 mm. A total strain of 1% is applied to the specimen, split equally between the upper and lower faces, that is 0.5% for each face. The resulting x-direction displacement boundary condition applied to each face is 0.125 mm. The other DoF are left free. An illustration of the applied boundary conditions is shown in Figure 7.9.

The final step in the model setup is specifying the field outputs. As with the single-edge-notched specimen model, the three-dimensional strain and stress values are requested in ply axes on a ply-by-ply basis. This is done by specifying field outputs for each of the six layups defined in the composite layup editor. The results of the double-edge-notched specimen model are presented and discussed in Section 7.3.2.

7.2.3 Open-Hole Tension Specimen Model

Two open-hole tension specimen models are based on the nominal dimensions of the 0.5 inch diameter hole and 1.0 inch diameter hole second round experimental specimens described in Section 4.3. The planar dimensions of the models are shown in Figure 7.10, where the diameter, D, is 25.4 mm or 50.8 mm and the width, w, is 50 mm or 100 mm, respectively, as described in Section 4.3. The gage lengths, L_{GAGE}, of the two models are listed in Table 7.3. Both specimen have a thickness of 3.2 mm. The specimen is partitioned along twenty-three planes parallel to plies and the x-y plane, each equally spaced, resulting in twenty-four layers through the thickness (corresponding to one layer per ply). The model also contains four partitions running through the thickness. A square partition, coincident with the hole, is added to each model, resulting in two in-plane sections. The square partitions have sides of length 25 mm and 50 mm for the 0.5 inch and 1.0 inch diameter hole specimen, respectively. These partitions are added in order to produce mesh elements with an average in-plane aspect ratio (longest edge compared to shortest edge) of 2.16, with the largest

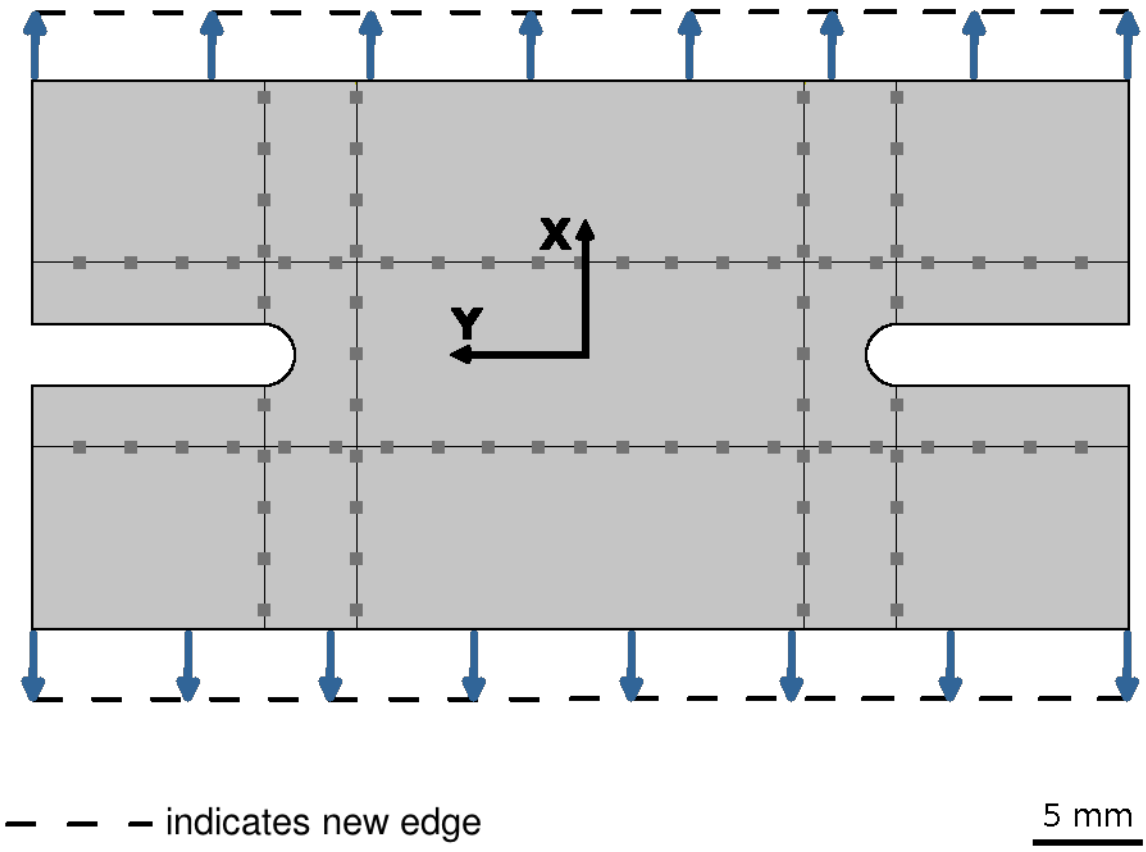

Figure 7.9 Planar (x-y) view of the boundary conditions for the double-edge-notched specimen model.

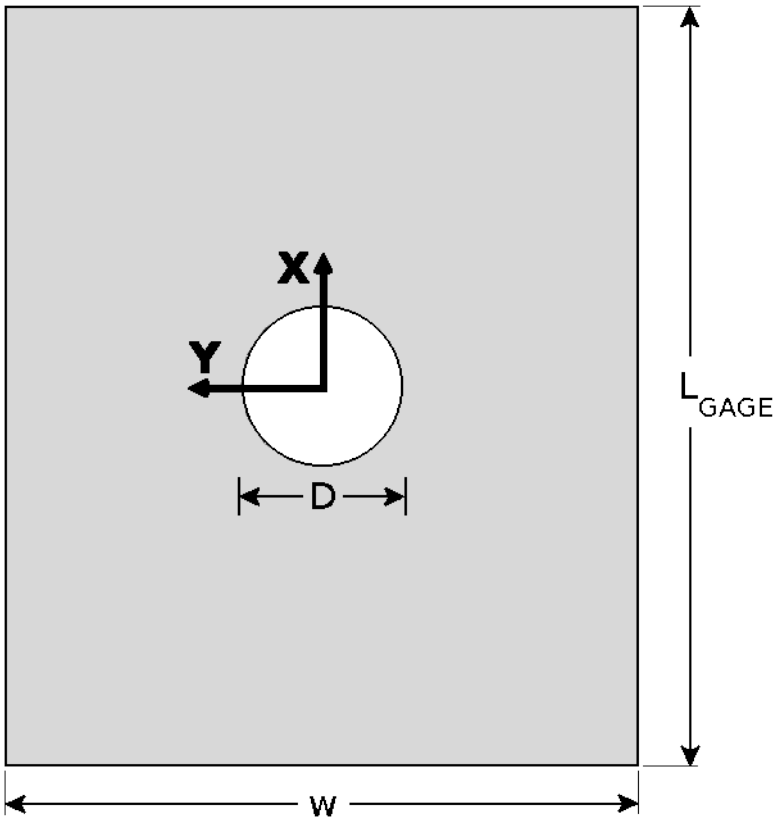

Figure 7.10 Dimensions of the open-hole tension specimen model.

in-plane element aspect ratio of 5.52. A planar (x-y plane) view of these partitions are shown in Figures 7.11 and 7.12. This partitioning allows a structured mesh to be applied in section 1 of the models and a swept mesh to be applied in section 2 (around the hole) of the models.

Using the ABAQUS composite layup editor, a single layup, containing 24 plies, is specified for the models. Each of the open-hole tension models is analyzed using two different stacking sequences of the laminate, corresponding to either the single-ply effective ply thickness laminate or the four-ply effective ply thickness laminate, as described in Section 4.3. The laminates analyzed with the models are $[+45/0/-45]_{4S}$ and $[+45_4/0_4/-45_4]_S$. In order to attain and post-process the results of individual plies, every ply in the model requires a unique name specified in the composite layup editor.

The next step in the model setup is specifying the mesh seeding. A global seed spacing of 1.56 mm is applied to the model. An unbiased seed spacing with an approximate spacing size of 0.65 mm is used around the circumference of the open hole. There is a single seed through the thickness of the model. Once the seeding is complete, the automatic mesh parameters are set. With the selected seeding, section 1 uses a structured mesh while section 2 uses a swept mesh. The resulting mesh of the 0.5 inch open-hole specimen model is shown in Figure 7.13, with a close-up view of the mesh around the hole shown in Figure 7.14. The resulting mesh for the 1.0 inch open-hole specimen model is shown in Figure 7.15, with a close-up view of the mesh around the hole shown in Figure 7.16. A total of 3,540 elements are created with the set seeding of the 0.5 inch open-hole tension specimen, and a total of 15,404 elements are created with the set seeding of the 1.0 inch open-hole tension specimen. For both models, the longest element edge is 3.20 mm and the shortest element edge is 0.58 mm.

For the open-hole tension specimen model, displacement boundary conditions in the x-direction are specified on the positive and negative x-faces. This boundary condition simulates uniaxial tension on the specimen. The gage lengths for the two open-hole tension specimens are listed in Table 7.3. A total strain of 1% is applied to

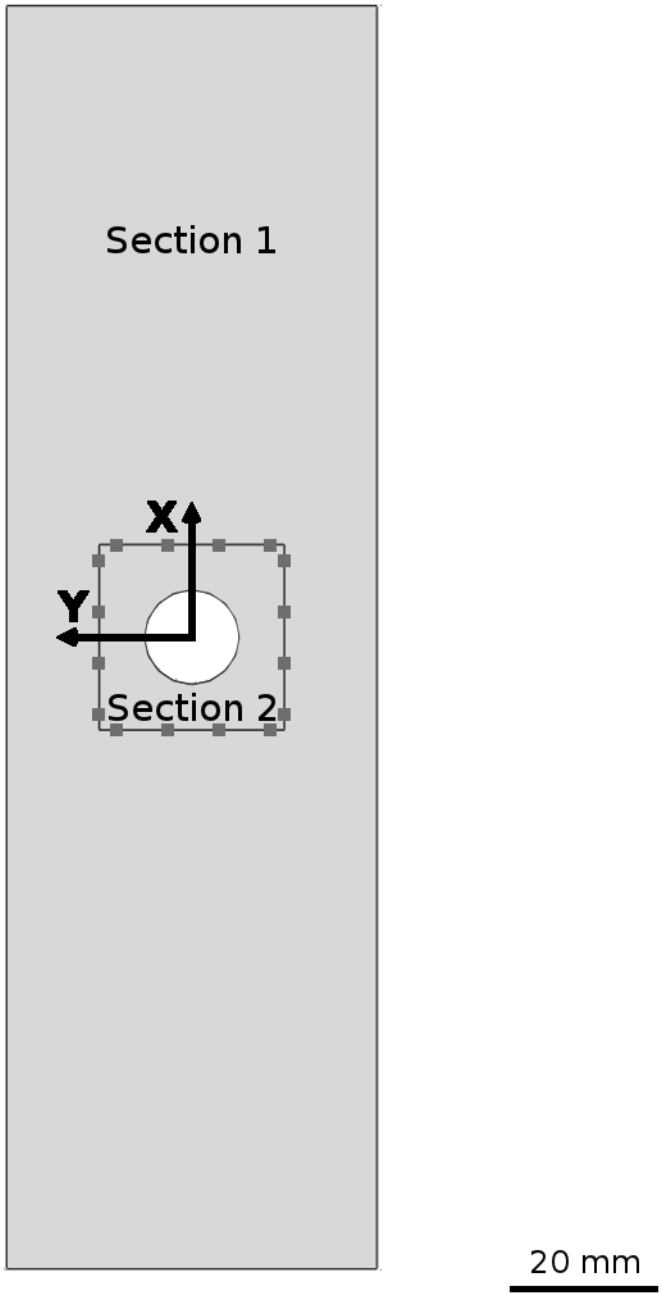

Figure 7.11 Planar (x-y) view of the partitioned open-hole tension specimen model for case of a 0.5 inch diameter hole.

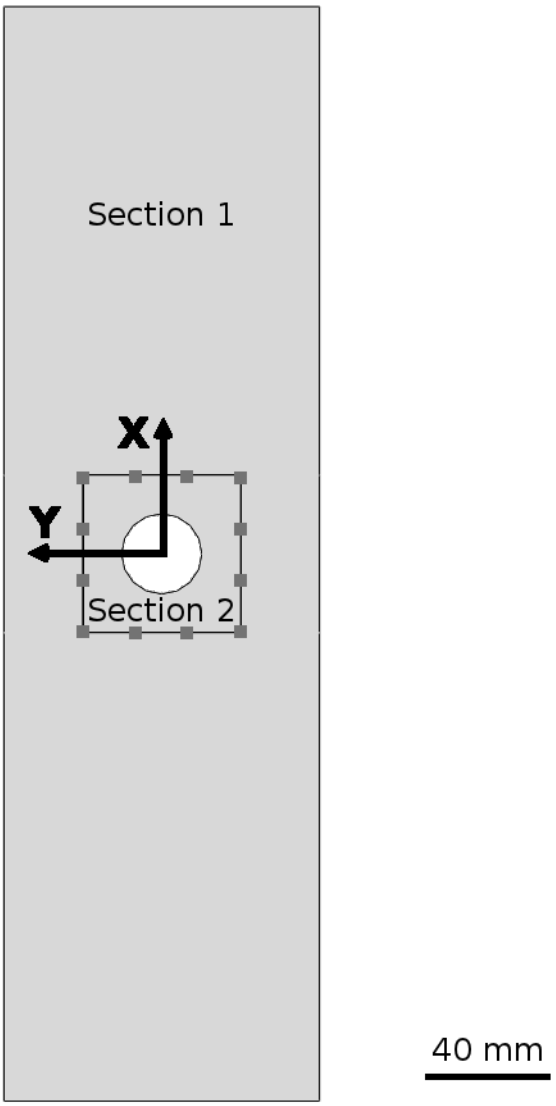

Figure 7.12 Planar (x-y) view of the partitioned open-hole tension specimen model for case of a 1.0 inch diameter hole.

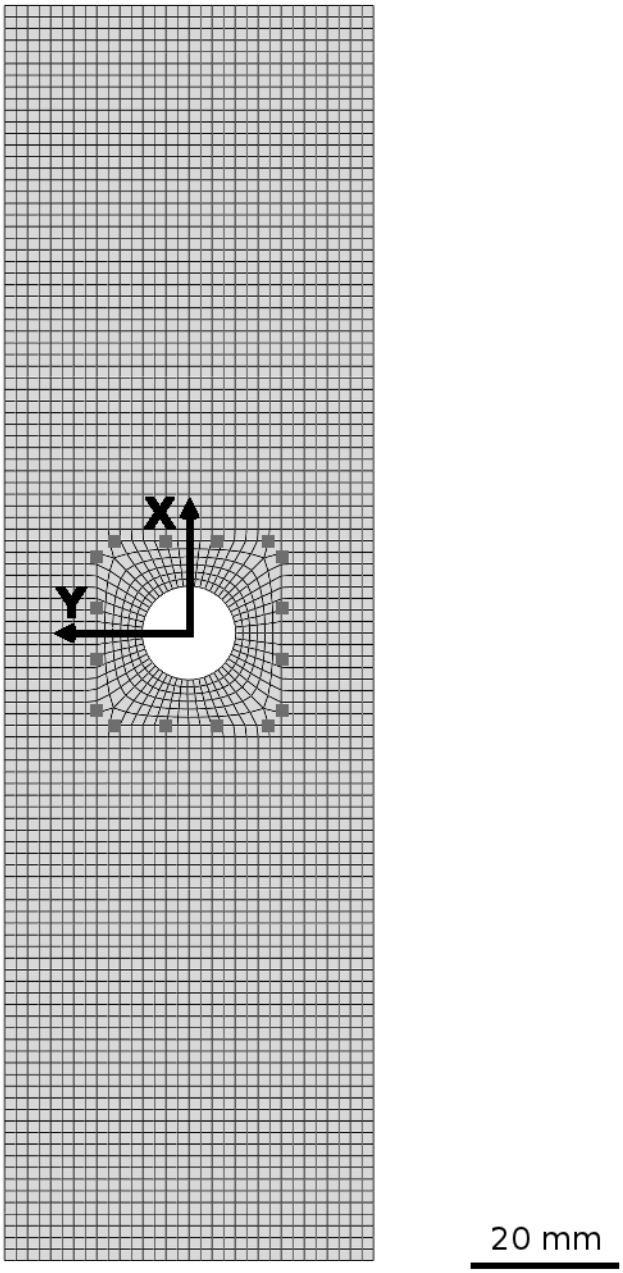

Figure 7.13 Planar (x-y) view of the mesh for the open-hole tension specimen model for the case of a 0.5 inch diameter hole.

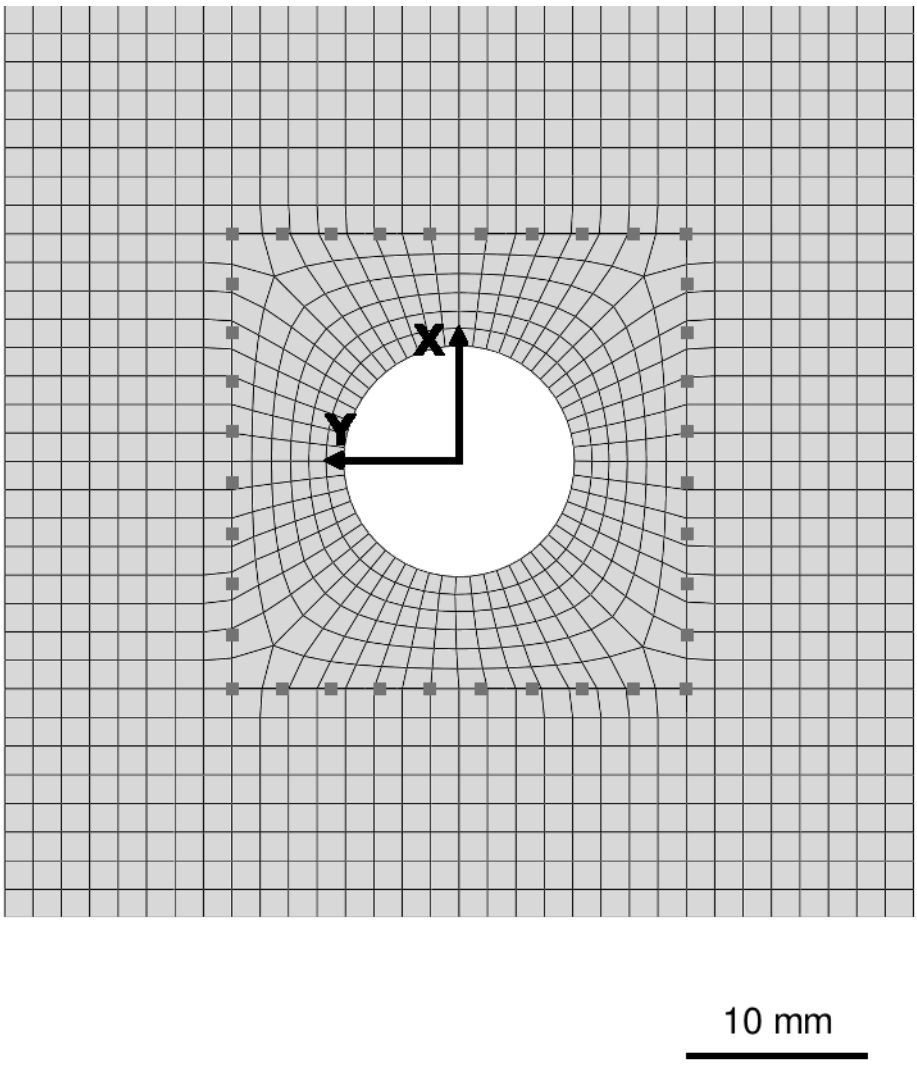

Figure 7.14 Close-up planar (x-y) view of the mesh around the hole for the open-hole tension specimen model for the case of a 0.5 inch diameter hole.

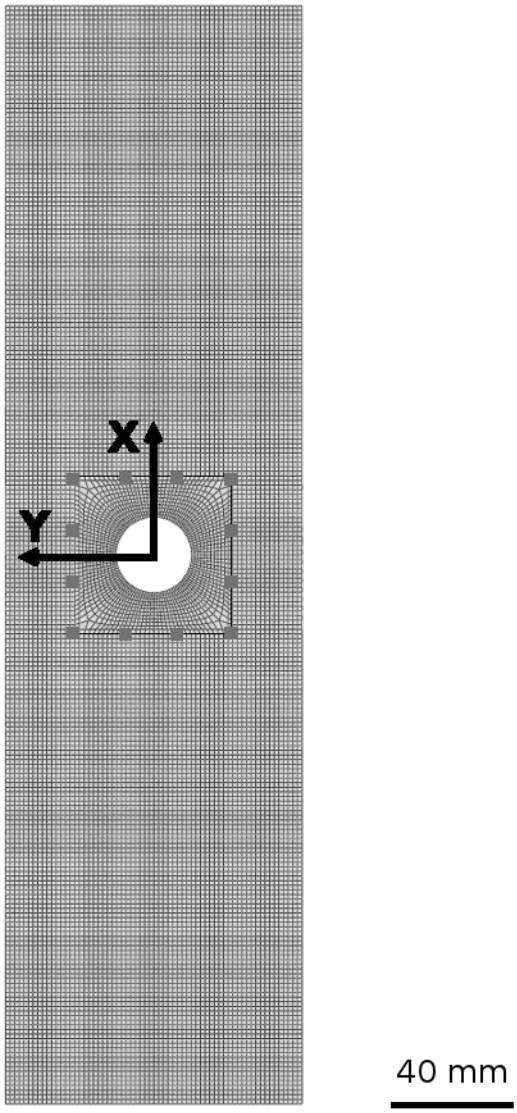

Figure 7.15 Planar (x-y) view of the mesh for the open-hole tension specimen model for the case of a 1.0 inch diameter hole.

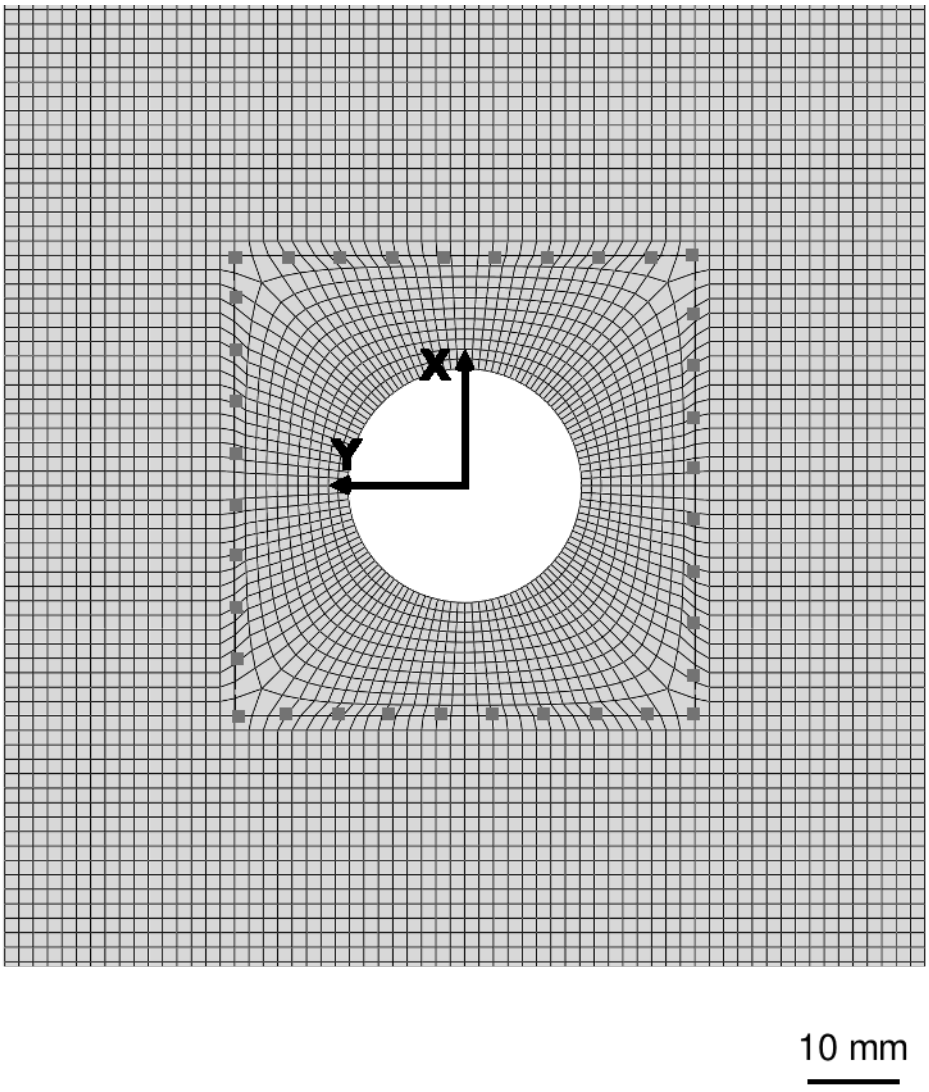

Figure 7.16 Close-up planar (x-y) view of the mesh around the hole for the open-hole tension specimen model for the case of a 1.0 inch diameter hole.

the specimen, split equally between the upper and lower faces, that is 0.5% for each face. The resulting x-direction displacement boundary condition applied to each face is listed in the last column of Table 7.3. The other DoF are left free. An illustration of the applied boundary conditions is shown in Figure 7.17.

The final step in the model setup is specifying the field outputs. As with the single-edge-notched specimen model, the three-dimensional strain and stress values are requested in ply axes on a ply-by-ply basis. This is done by specifying field outputs for the laminates defined in the composite layup editor. The results of the open-hole tension specimen models are presented and discussed in Section 7.3.3.

7.2.4 Ply-Drop Specimen Model

The ply-drop specimen model is based on the nominal dimensions of the experimental specimen described in Section 4.4. The planar dimensions of the model are shown in Figure 7.18. The specimen has a width (in the y-direction) of 38.1 mm and a thickness (in the z-direction) of 4.75 mm in the undropped region and 3.17 mm in the dropped region. The specimen contains two partitions running through the thickness, resulting in three in-plane sections. These two partitions are located at the boundaries of the ply-drop region, as discussed in Section 4.4, and are shown in Figure 7.19. In this figure, sections 1, 2, and 3 correspond to the dropped, ply-drop, and undropped regions of the specimen, respectively. In addition to these partitions, the specimen is also partitioned along planes parallel to plies. In order to model the dropped plies in the center sublaminate, X_D, as described in Section 4.4, the center sublaminate is partitioned at each ply. The top and base sublaminates are each partitioned once in order to to produce mesh elements with aspect ratios (longest edge compared to shortest edge) below 15. These partitions are seen in a close-up view of the right side of the specimen, shown in Figure 7.20, with the view centered on section 2. In order to show the details of the individual ply partitions in the dropped region, the entire specimen length is not shown (i.e., sections 1 and 3 are not shown in full). In section 1, three partitions are added parallel to the x-y plane,

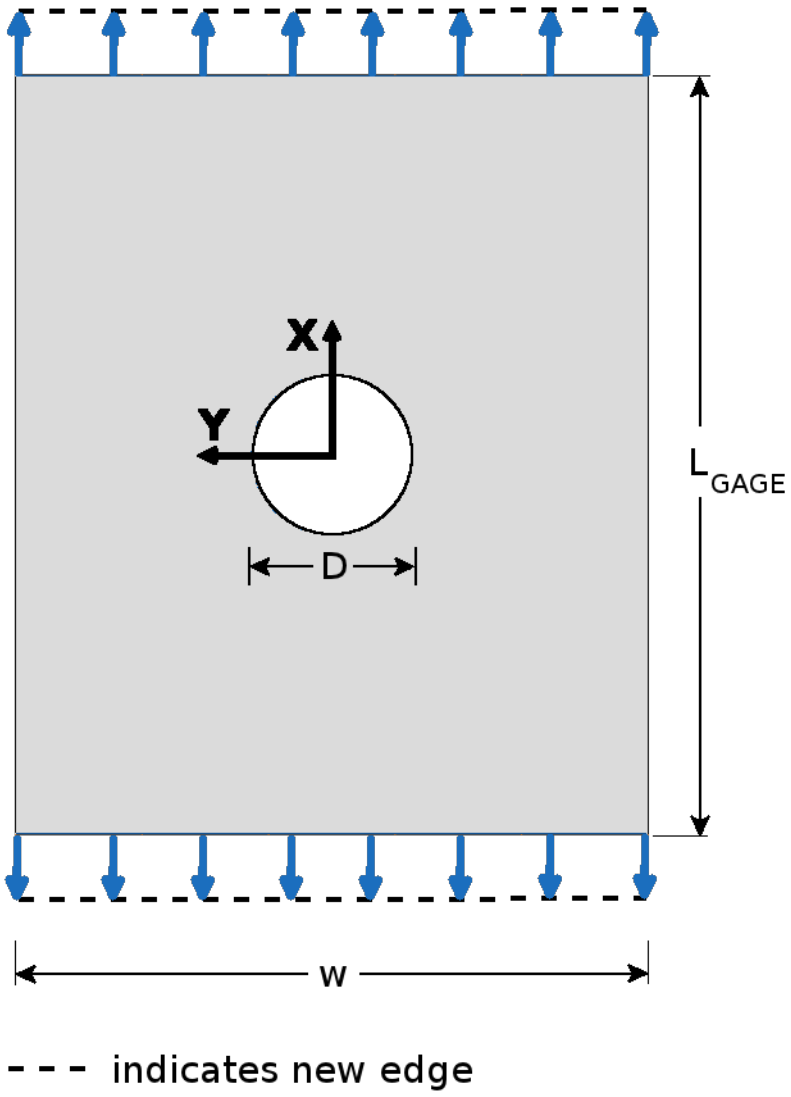

Figure 7.17 Planar (x-y) view of the boundary conditions for the open-hole tension specimen model.

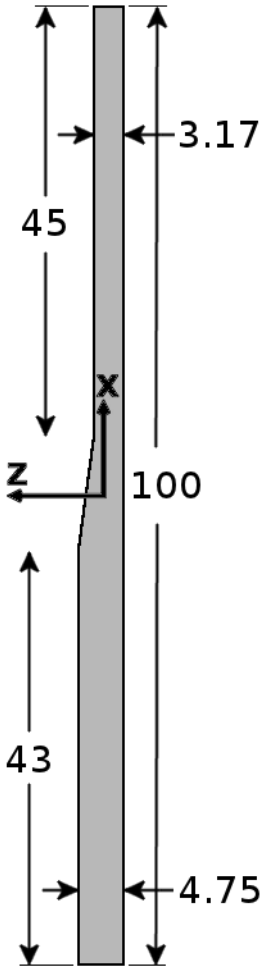

Figure 7.18 Dimensions of the ply-drop specimen model.

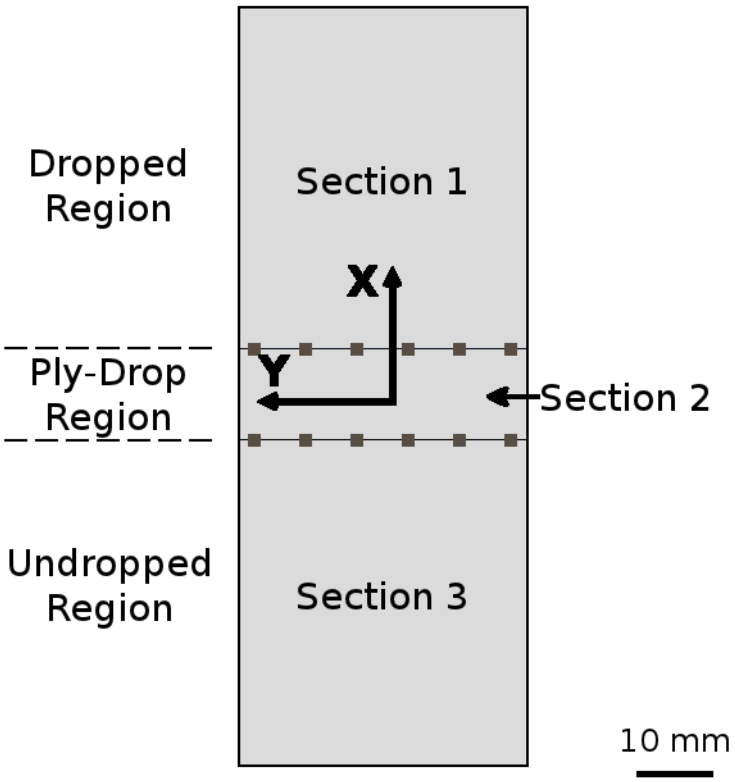

Figure 7.19 Planar (x-y) view of the partitioned ply-drop specimen model.

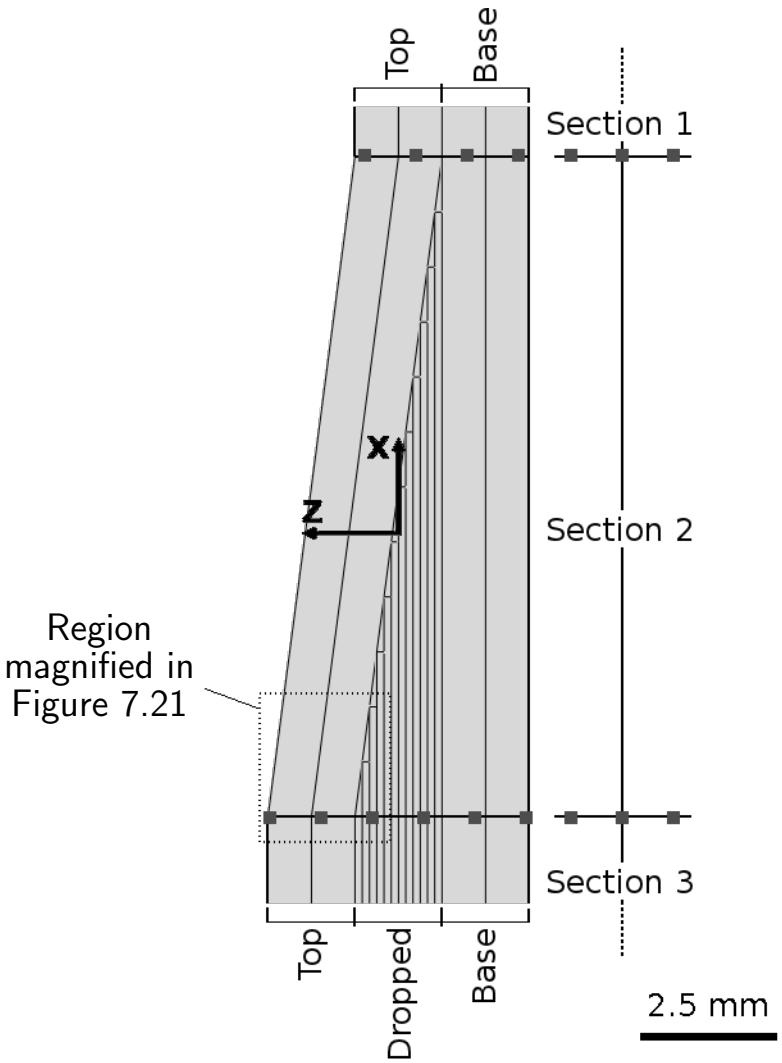

Figure 7.20 Close-up planar (x-z) view of the partitioned ply-drop specimen model in the region of the ply drops.

each equally spaced, resulting in four layers through the thickness (not to be confused with plies). In section 3, fifteen partitions are added parallel to the x-y plane. First, a partition is added at each sublaminate interface (i.e., at the top-dropped sublaminate and dropped-base sublaminate interfaces). The top and base sublaminates are then each partitioned once, creating two equally spaced layers through the thickness of each sublaminate. The dropped (middle) sublaminate is then partitioned along eleven planes, each equally spaced, resulting in twelve layers through the thickness of the sublaminate. In this case, each layer of the dropped sublaminate represents a single ply. A similar procedure is used to create partitions through the thickness of section 2. However, in this section, the plies in the top sublaminate are not parallel to the x-y plane. The resulting two partitions are determined from the specimen geometry, assuming that the plies are parallel to the top surface in that section. The through-thickness partition locations in the base laminate are the same as those in sections 1 and 3. The through-thickness partition locations in the dropped sublaminate are the same as those in section 3. However, these partitions are extended along the x-direction until they intersect with the partition of the top sublaminate. At this location, the individual ply is dropped. This partition method used results in triangular partitions between the end of a dropped ply and the angled partition of the top sublaminate, as seen in Figure 7.20. These triangular partitions represent the resin-rich region of the ply-drop.

Using the ABAQUS composite layup editor, 18 layups are defined and applied to the layers and sections of the model. Unlike the previous models, the number of plies vary between layups. For the top and base sublaminates, each layup contains six plies. For the dropped plies, each 'layup' is a single ply. In addition to defining the ply properties, wedge elements were used in the resulting triangular partitions shown in Figure 7.21. The wedge element is triangular in shape in the x-z plane, containing three nodes on the plane. The wedge element is a three-dimensional element, with the thickness of the element extending along the y-direction. The wedge element is used to represent the resin-rich region immediately following a dropped ply. For these elements, an additional, isotropic material property, representative of the 3501-6

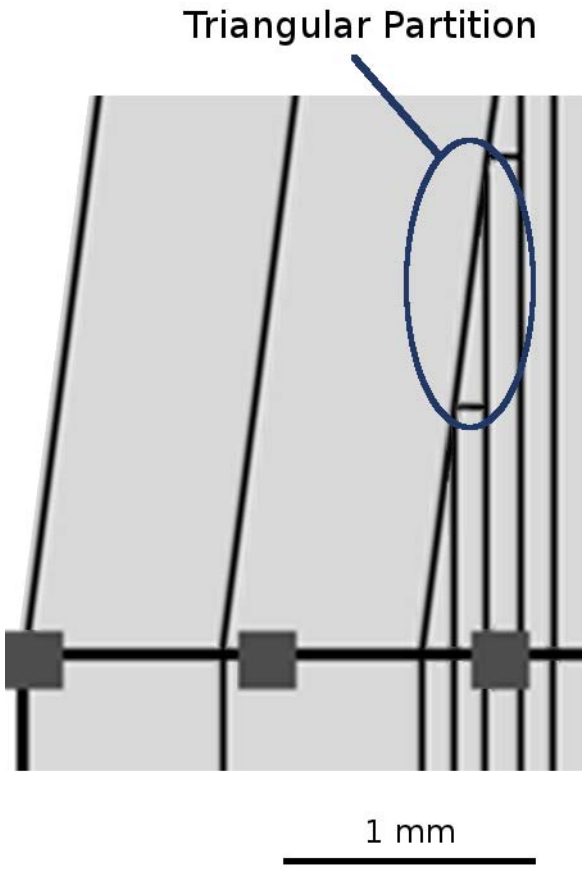

Figure 7.21 Close-up planar (x-z) view of a triangular partition in the ply-drop specimen model, region as indicated in Figure 7.20.

resin, was defined. A Young's modulus of 4.24 MPa and a Poisson's ratio of 0.36 was used [142]. In order to attain and post-process the results of individual plies, every ply in the model requires a unique name specified in the composite layup editor.

The next step in the model setup is specifying the mesh seeding. A global seeding value of approximately 1.6 mm is applied to the entire model. There is a single seed through the thickness of each layer (i.e., there is one element through the thickness of each layer). Once the seeding is complete, the automatic mesh parameters are set. With the specified seeding, a structured mesh can be applied to all the layers of the model. The resulting mesh contains 13,818 elements, shown in Figure 7.22, with a close-up x-z view of the mesh in the ply-drop region shown in Figure 7.23. The longest element edge is 1.81 mm and the shortest element edge is 0.13 mm.

Boundary conditions are specified for the C3D8R elements. For the ply-drop specimen model, displacement boundary conditions in the x-direction are specified on the positive and negative x-faces. This boundary condition simulates uniaxial tension on the specimen. The gage length of the ply-drop specimen is 100 mm. A total overall strain of 1% is applied to the specimen, split equally between the upper and lower faces, that is 0.5% for each face. The resulting x-direction displacement boundary condition is 0.5 mm applied to each face. The other DoF are left free. An illustration of the applied boundary conditions is shown in Figure 7.24.

The final step in the model setup is specifying the field outputs. As with the other models, the three-dimensional strain and stress values are requested in ply axes on a ply-by-ply basis. This is done by specifying field outputs for each of the 18 sublaminates defined in the composite layup editor. The results of the ply-drop specimen model are presented and discussed in Section 7.3.4.

7.2.5 Damage Inclusion Models

An effective 'infinite' rectangular specimen is used in the damage inclusion models. While a truly infinite plate is not modeled, the length and width of the model are over 30 times greater than the length of the damage. This is done to isolate the influences (i.e., stress and strain fields) of the free edges from the gradient fields

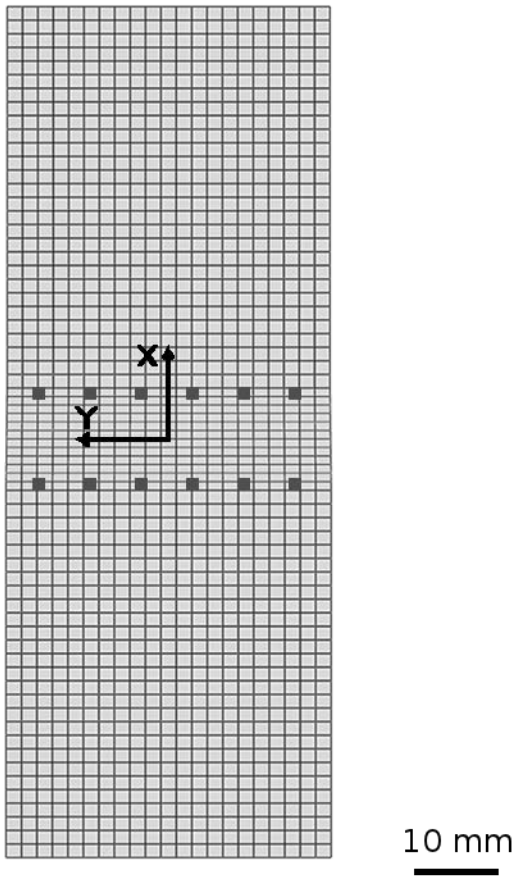

Figure 7.22 Planar (x-y) view of the mesh for the ply-drop specimen model.

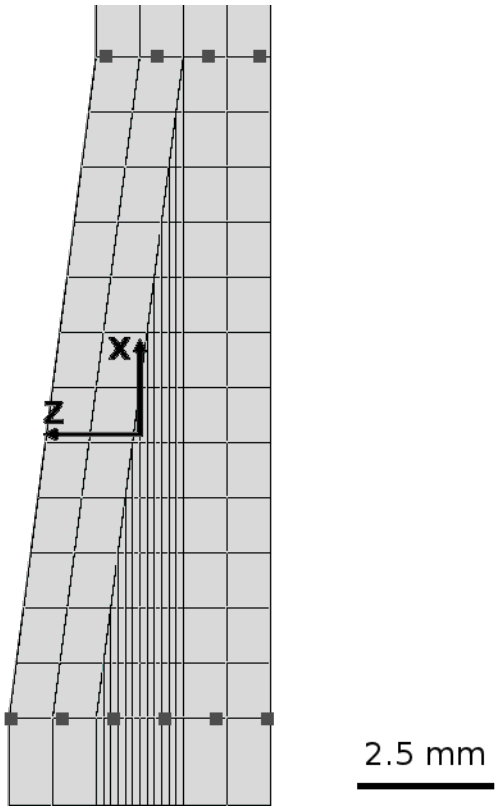

Figure 7.23 Close-up planar (x-z) view of the mesh for the ply-drop specimen model in the ply-drop region.

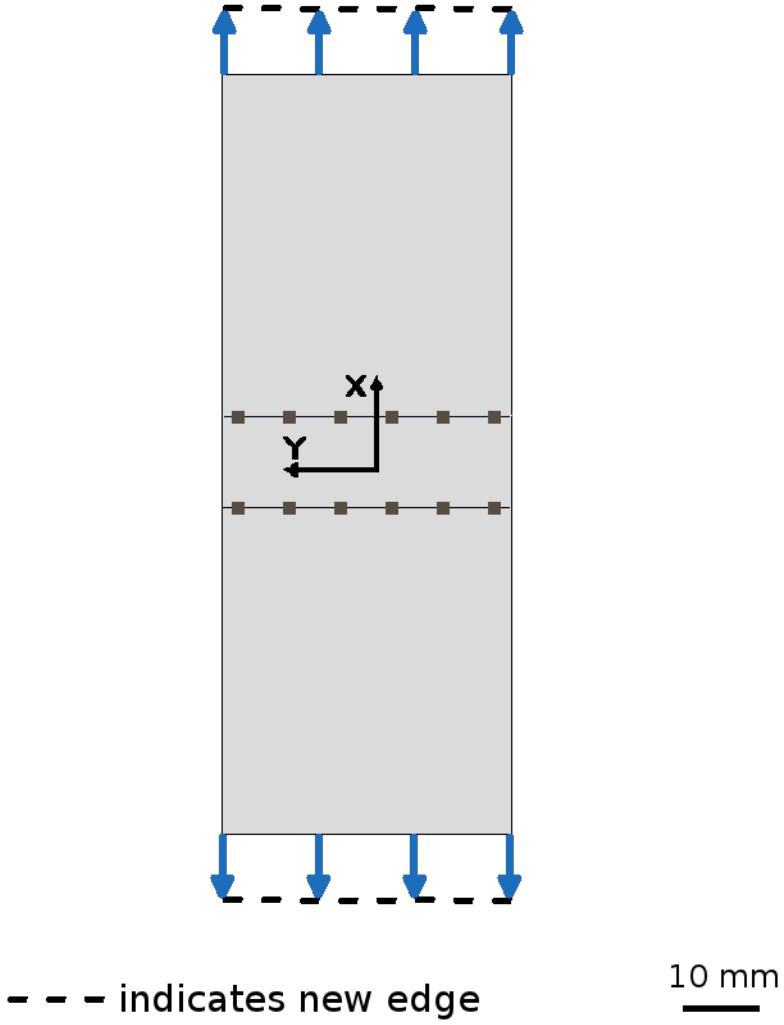

Figure 7.24 Planar (x-y) view of the boundary conditions for the ply-drop specimen model.

resulting due to the modeled damage. The planar dimensions of the model are shown in Figure 7.25. The model thickness is taken to be 4.20 mm, the same thickness as the double-edge-notched specimen. This thickness was selected based on the fact that the number of double-edge-notched experimental specimens tested was far greater than the other specimen types. Among these double-edge-notched specimens, a large number exhibited stitch cracking and/or delamination damage modes. Therefore, the double-edge-notched specimen laminate offers the most experimental data to compare with the finite element results. The model contains partitions, each equally spaced, along thirty-one planes parallel to the plies and the x-y plane. This results in thirty-two layers through the thickness. Each layer represents a single ply. These partitions are necessary to model the damage, described later.

The model also contains two partitions running through the thickness. This results in three in-plane sections. These partitions are added to the model to permit increased mesh seeding in the region of the damage. A planar (x-y plane) view of these partitions is shown in Figure 7.26, where the three in-plane sections are identified. An enlarged view of sections 2 and 3 is shown in Figure 7.27. Section 2 is a square with edges of length 200 mm. Section 3 is a rhombus with edges of length 50 mm. The shape (interior angles) of section 3 is dependent on the laminate. This is necessary to align the mesh along the fiber directions of the plies of a laminate. Sections 2 and 3 are concentric with section 1.

In addition to the partitions necessary to define the three sections, section 3 contains fourteen additional partitions. These are shown in Figure 7.28. Three of the fourteen partitions define the orientation and length of the traditional matrix crack. One of these partitions runs at $-\theta$ through the origin, defining the orientation of the traditional matrix crack, while the other two partitions run at $+\theta$ defining the ends of the matrix crack. Eleven of the fourteen partitions define the orientations and lengths of the stitch cracks. Nine of these partitions, defining the orientations of the stitch cracks, are closely spaced (modeled with a spacing of 0.254 mm) and appear as a thicker partition line running at $+\theta$ through the origin. The resolution of the experimentally measured spacing is equal to ± 0.002 in (± 0.05 mm), with the

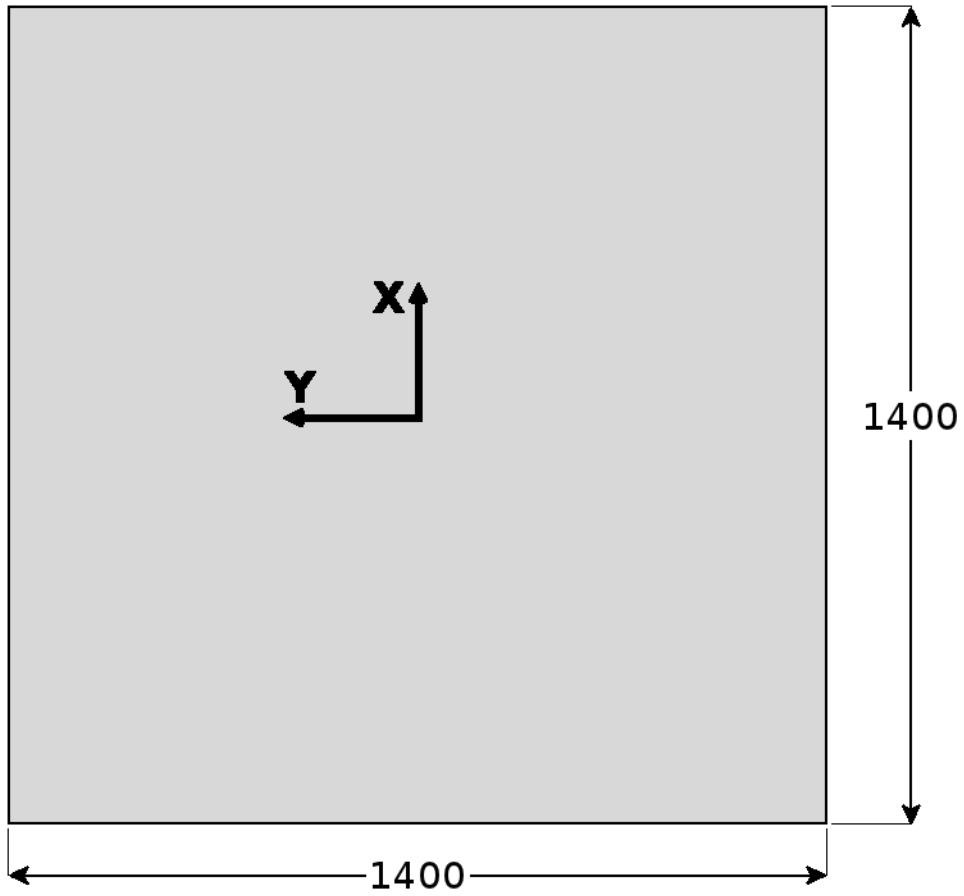

Figure 7.25 Dimensions of the damage inclusion model.

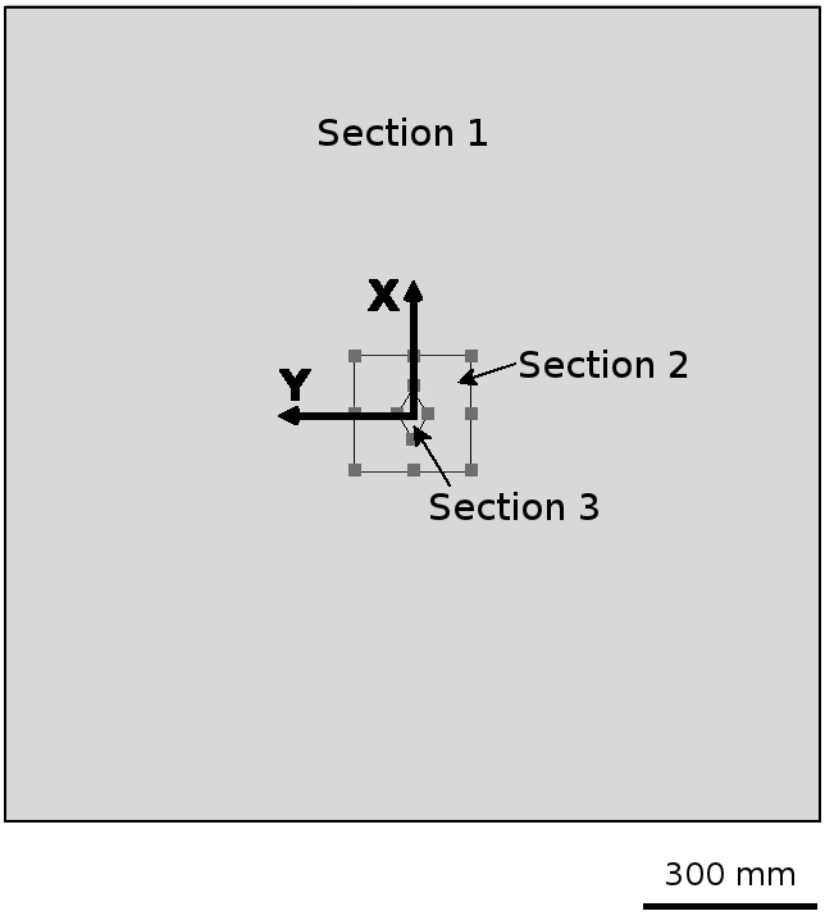

Figure 7.26 Planar (x-y) view of the partitioned damage inclusion model.

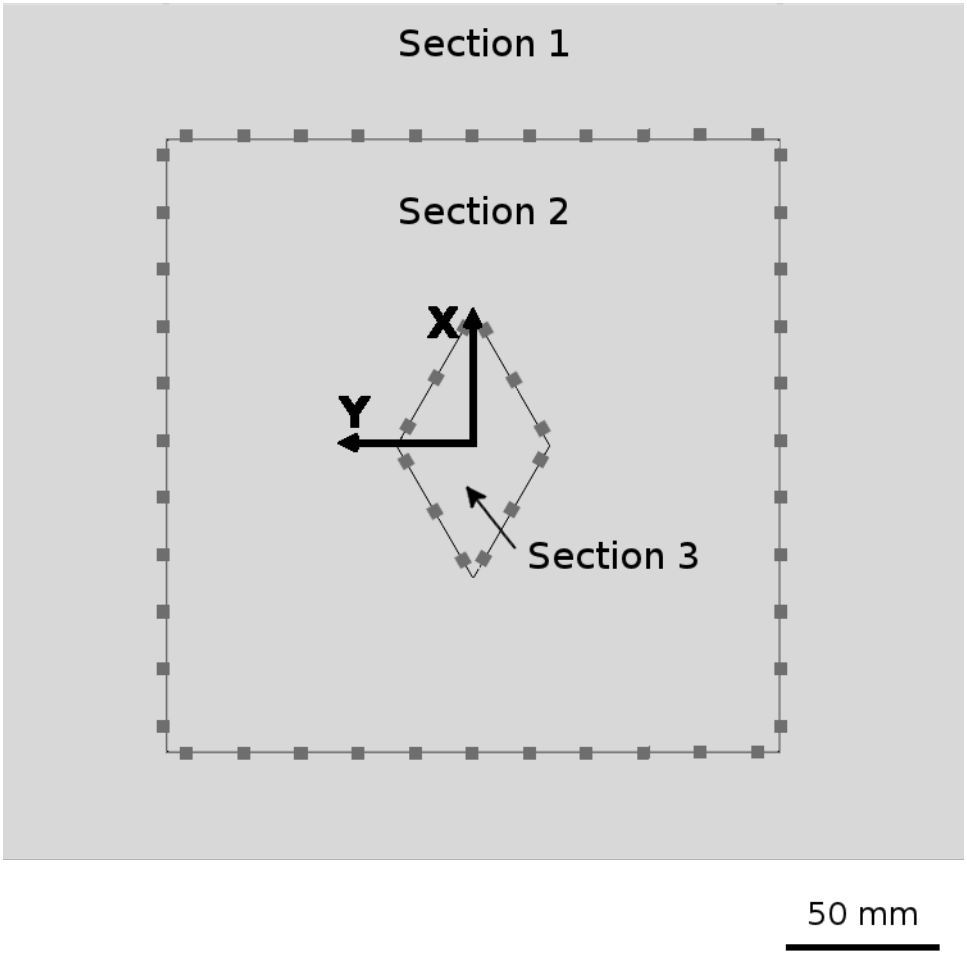

Figure 7.27 Close-up planar (x-y) view of the partitioned damage inclusion model of a laminate with θ equal to 30°.

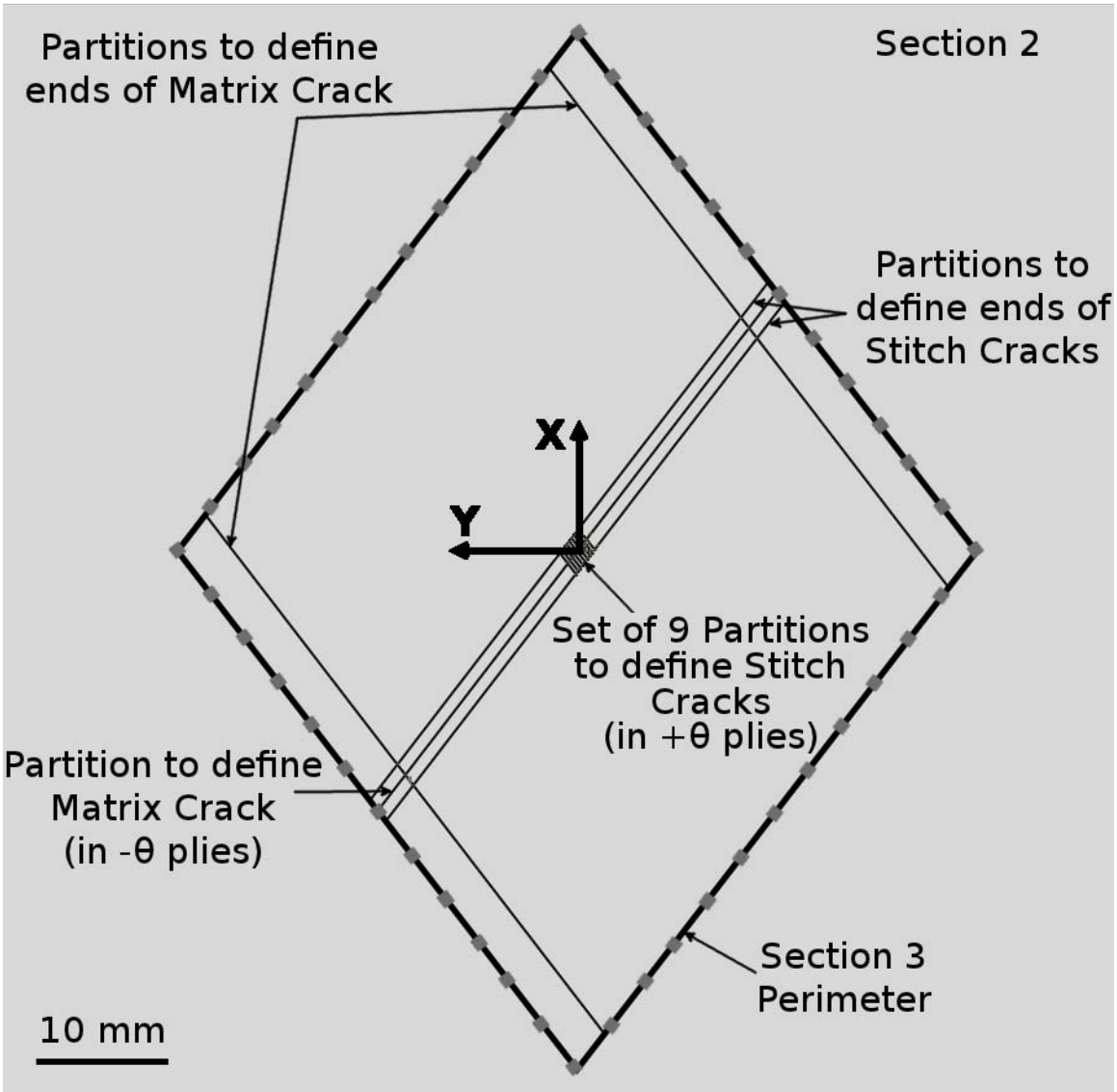

Figure 7.28 Close-up planar (x-y) view of the additional partitions in section 3 of the damage inclusion model of a laminate with θ equal to 30°.

average spacing between stitch cracks of the experimental specimens measured to be 0.010 in. This was therefore chosen as the spacing between stitch cracks of the model, as discussed in Section 7.3.5, although there was variation in the measured spacing from 2 to 10 ply thicknesses in length. The other two partitions run at $-\theta$ defining the ends of the stitch cracks. These additional partitions in section 3 allow seams, described later, to be defined at specific locations within the model. The partitions run through the laminate thickness and are at the same location in each layer.

A limited number of stitch cracks are included in the damage inclusion model. This is different from what is observed experimentally, where stitch cracks are observed along the entire length of a damage path, as described in Sections 6.1.2 and 6.3. The damage path of the stitch cracks follows the fiber angle of a ply, extending from an initiation point (e.g., the notch tip of the single- and double-edge-notched specimens) to a free edge of the specimen. In order to recreate the stress and strain fields around a single stitch crack, the influence of neighboring stitch cracks on the stress and strain fields around a "central" stitch crack is investigated in a stepwise manner. The resulting stress and strain fields around the "central" stitch crack for the stepwise study are discussed in Section 7.3.5.

The stepwise investigation increases the number of neighboring stitch cracks, beginning with no neighboring stitch cracks, until the stress and strain fields within 0.127 mm, corresponding to half the distance between the modeled stitch cracks, of the "central" stitch crack change by less than 1% when adding the additional neighboring stitch cracks. First, a traditional matrix crack of length 44 mm is incorporated within each of the negative angle plies of the model. This is calculated from the geometry of the double-edge-notched specimen as the geometrically longest possible traditional matrix crack to initiate at the notch tip and propagate along a fiber direction until intercepting an edge of the specimen. These matrix cracks are modeled as described later, and exist within each of the stepwise investigations. During each step, the number of stitch cracks neighboring the "central" stitch crack is increased in order to determine the minimum number of neighboring stitch cracks required to model the strain field at the central stitch crack. In order to reduce computation

time, the minimum number of stitch cracks required to reproduce the representative strain fields at a central stitch crack is modeled. An illustration comparing the experimentally observed stitch cracking versus the modeled stitch cracking is shown in Figure 7.29.

Using the ABAQUS composite layup editor, thirty-two 'layups' are specified, one for each layer of the model. Each layup contains a single ply, resulting in an overall model laminate stacking sequence of $[+\theta/-\theta]_{16T}$ or $[+\theta_4/-\theta_4]_{4T}$ where θ is equal to 15°, 30°, 60°, or 75° for the various cases considered. In order to attain and post-process the results of individual plies, every ply in the model requires a unique name specified in the composite layup editor.

In order to model the damage, an additional step, not implemented in the previously discussed models, is required. This step involves modifying the meshing parameters in order to simulate the damage. For both damage models, the seam command in ABAQUS is used to create the damage feature. This command modifies the mesh parameters by creating overlapping nodes along specified partitions. The seam command controls the association of the overlapping nodes of the elements along these partitions. The result is an internal surface (i.e., the elements on each side of the seam do not share nodes at the common face) that is closed in the unloaded state but can open during the analysis (i.e., application of load). Modeling of damage propagation is not included, as the objective of this model is to predict stress and strain fields after damage has initiated.

The next step in the model setup is specifying the mesh seeding. For the damage inclusion models, a global seed spacing of approximately 100 mm is used along the edges of sections 1 and 2. A double-bias seeding is used along the fourteen partitions in section 3, shown in Figure 7.28, with the minimum seed spacing of 0.1 mm at the midlength of the partitions and the maximum seed spacing of 5 mm at the ends of the partitions (i.e., where the partitions intercept the perimeter of section 3). This spacing is linked to the method used to model the damage, as described later. There is a single seed through the thickness of each layer (i.e., there is a single element through the thickness of each ply). Once the seeding is complete, the automatic

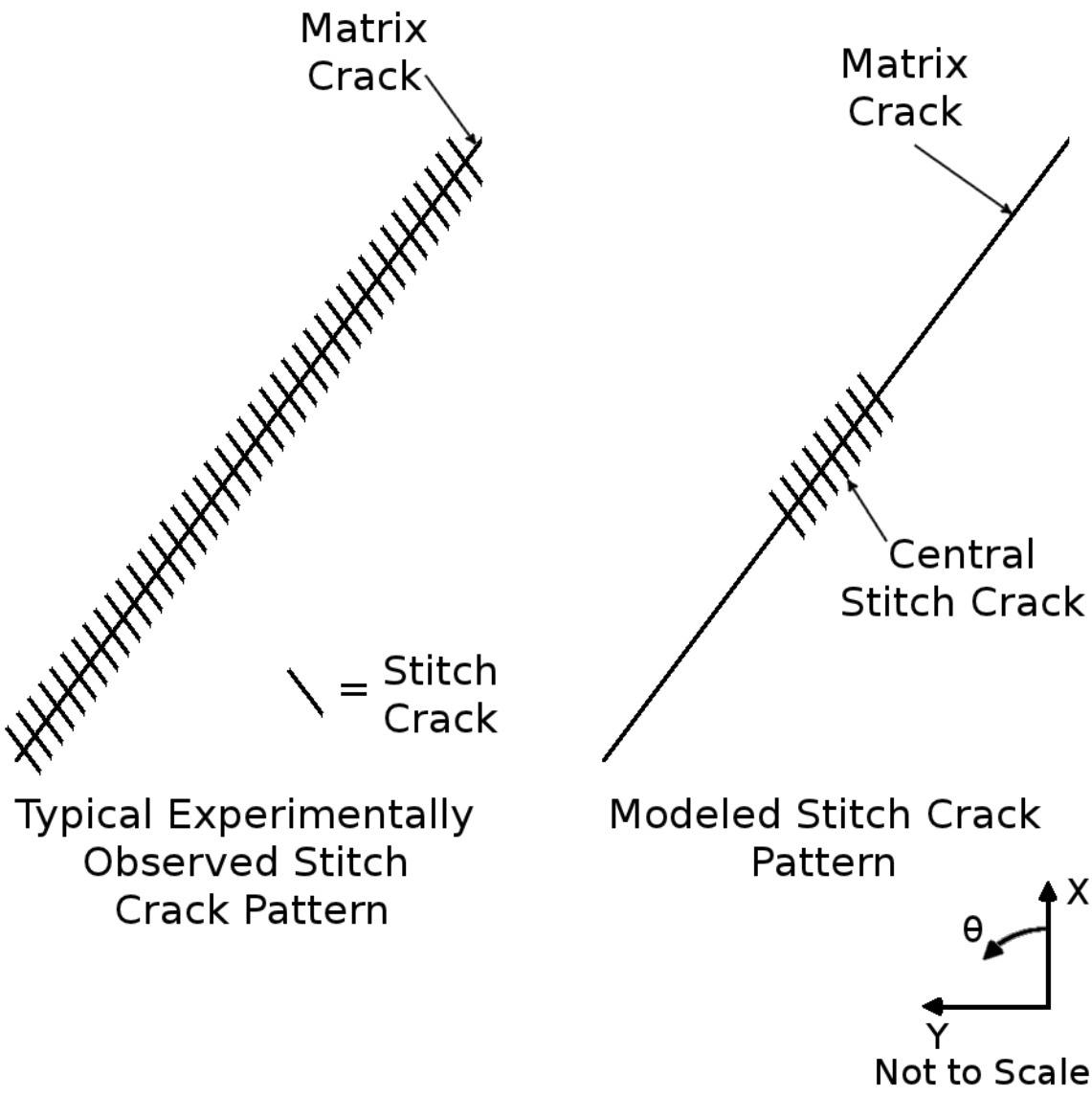

Figure 7.29 Illustration of experimentally observed stitch cracking versus modeled stitch cracking.

mesh parameters are set. With the model geometry and selected seeding, a structured mesh is applied to sections 1 and 3 of the model. Section 2 requires a swept mesh in order to transition from the finer mesh in section 3 to the coarser mesh in section 1. An in-plane view of the resulting mesh is shown in Figure 7.30, where this mesh is repeated through the thickness for each of the thirty-two layers. The total number of elements is on the order of 140,000 for each of the angle-ply laminates. The exact number of elements within section 2 varies by a few thousand elements between the different angle-ply laminates due to the varying geometry and the automated swept mesh technique used to merge the structured meshes of regions 1 and 3 (where the number of elements is constant between each of the angle-ply laminates). A close-up view of the mesh in the region of section 2 and 3 for a laminate with θ equal to 30° is shown in Figure 7.31. The longest element edge is 100 mm, occurring in section 1, and the shortest element edge is 0.098 mm, occurring at the center of section 3, with all elements having an edge length of 0.131 mm in the through-thickness direction (i.e., the thickness of each ply).

For the model containing stitch cracks, seams are created within the layers (plies) of section 3, corresponding to either stitch cracking or a matrix crack, in order to simulate the damage mode. The orientations of these seams are based on the experimentally observed damage found in the double-edge-notched specimens and are along sections of the partitions shown in Figure 7.28. As described in Section 6.3, an alternating pattern of stitch cracking (microcracks) in positive or negative angle plies and a traditional matrix crack in negative or positive angle plies, respectively, was observed, via computed microtomography, in specimens exhibiting such stitch cracking. An example of the alternating pattern observed experimentally for the single-edge-notched specimen is shown in Figures 6.41 and 6.42. For this specimen, two damage paths are observed to propagate, along the ply angles, from the notch tip to the right edge. For each layer shown in Figures 6.41 and 6.42, there exists a traditional matrix crack along one path and a series of stitch cracks along the second path. The simulated damage follows this alternating pattern for the case of stitch cracks in positive angle plies and a traditional matrix crack in negative angle plies.

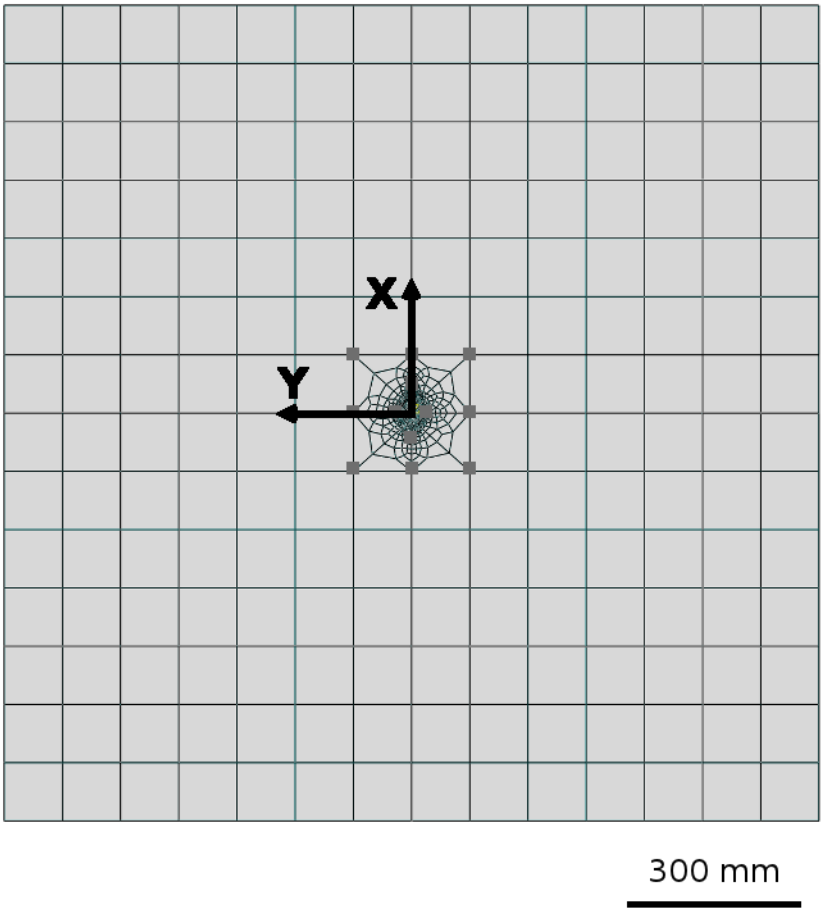

Figure 7.30 Planar (x-y) view of the mesh for the damage inclusion model.

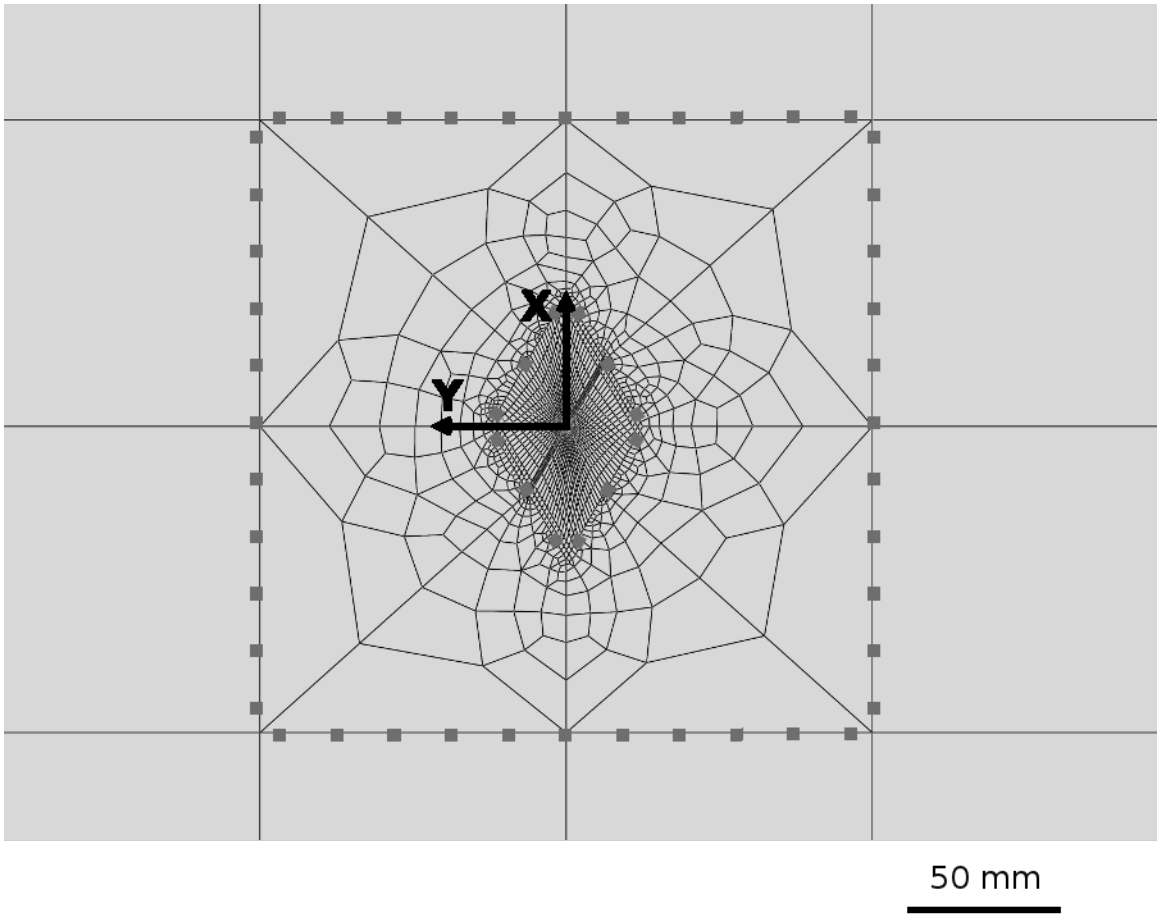

Figure 7.31 Close-up planar (x-y) view of the mesh for the damage inclusion model of a laminate with θ equal to 30°.

Due to symmetry, the resulting stress and strain fields would be observed in a symmetric fashion in the associated plies for the case of stitch cracks in negative angle plies and a traditional matrix crack in positive angle plies. Both cases are observed experimentally. The stitch cracks are a form of high density matrix microcracks that develop in layers above or below a traditional matrix crack. This is fully described in Section 2.2.

A single traditional matrix crack is created via the addition of a seam in each of the negative angle ($-\theta$) plies of a laminate. In each case, the seam is defined along the partition aligned with the fiber direction of the ply. Thus, there is a necessity to have the additional partitions in section 3, as previously described, aligned with the fiber directions of the laminate. As previously noted, the length of the traditional matrix crack is taken to be 44 mm. The in-plane location of the traditional matrix crack is the same for each negative angle ply of the laminate. An example of the orientation of the traditional matrix crack and the elements that are separated via a seam for a laminate with θ equal to 30° is shown in Figure 7.32. The elements along the partition oriented at $-\theta$ (labeled as 'matrix crack') have been split, via the seam command, between the two partition lines oriented at $+\theta$. This allows the element nodes along this seam to move independently from the previously shared node. The shaded region running along both sides of the matrix crack is the result of a dense mesh, necessary for modeling the stitch cracks, with a close-up view shown in Figure 7.33.

The stitch cracks (high density matrix microcracks) are created via the addition of three seams in each of the positive angle ($+\theta$) plies of the laminate. In each case, the seams are defined along the partitions aligned with the fiber direction of the ply, with an equal offset of 0.254 mm between each seam. The in-plane orientation of the microcracks is centered along the path of the traditional matrix crack, as this was observed in the experimental specimens exhibiting stitch cracking. The spacing between microcracks is taken to be 0.254 mm, with each microcrack having a length of 2.0 mm. The stitch crack length and the spacing between stitch cracks are based on the experimentally observed results, as described in Section 6.1.2. An example of these stitch cracks, i.e. matrix microcracks, and the elements separated via seams for

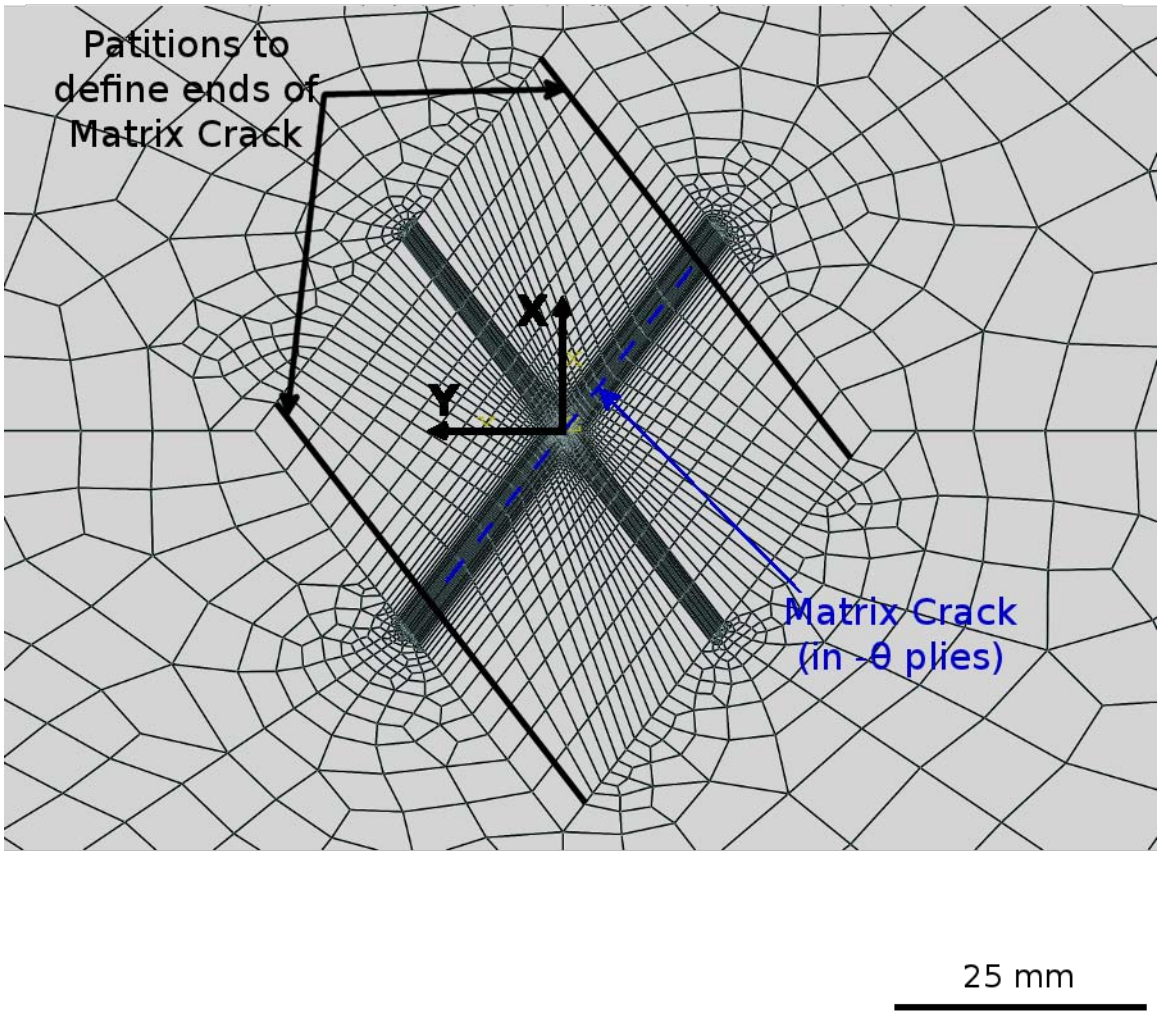

Figure 7.32 Close-up planar (x-y) view of the seam line used to create a matrix crack in a model of a laminate with θ equal to 30°.

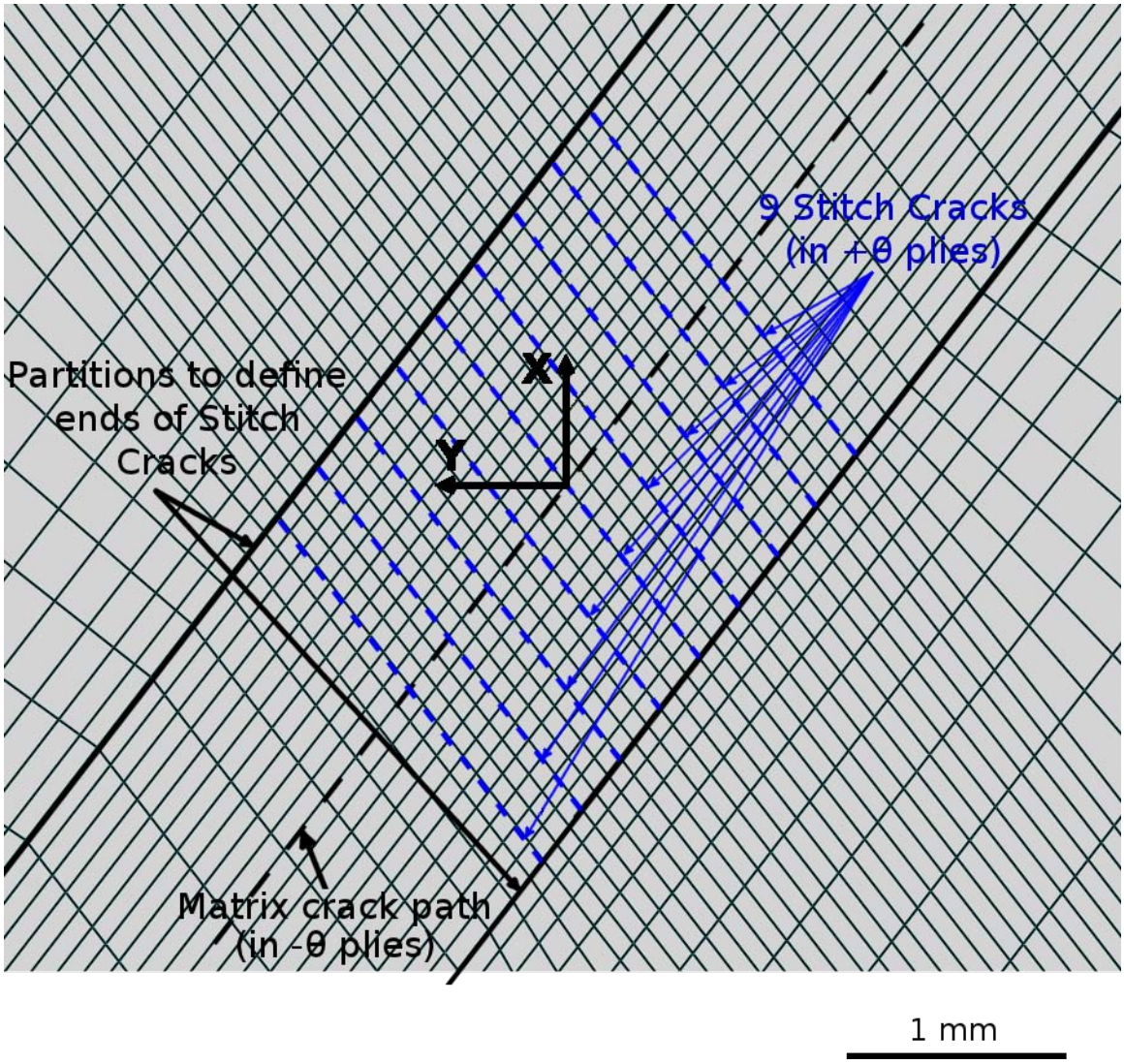

Figure 7.33 Close-up planar (x-y) view of the seam lines used to create stitch cracks in a model of a laminate with θ equal to 30°.

a laminate with θ equal to 30° is shown in Figure 7.33. The stitch cracks run between the two partitions parallel to the traditional matrix crack in the negative angle ($-\theta$) plies.

For the model containing a delamination, a similar technique involving a seam is applied. However, for the delamination, a seam is used to separate elements between two plies, with the seam parallel to the x-y plane. A single delamination occurring at the interface between the central two plies is defined. The two plies neighboring the central plane of the model have alternating angles (i.e. one at $+\theta$ and the other at $-\theta$). In the experimental specimens, delamination is typically observed between such alternating angle plies. The additional partitions used in section 3 for the stitch cracking model are not used for the model of the delamination. Instead, a partition is created offset from the perimeter of section 3, creating the edge necessary to define the delamination seam. The shape of the partition and the separated elements for a laminate with θ equal to 30° is shown in Figure 7.34. As a manifestation of the modeling technique, the delamination front is required to be a straight line. This manifestation results in the fronts coming together at points where these fronts intercept (i.e., in the shape of the rhombus). However, delamination fronts of the experimental specimens were not observed to occur along straight lines or to have sharp "corners." The effects of this modeling artifact thus create improper simulated results in the fields near these "corners." In order to avoid these issues, the results presented in Section 7.3.5 focus on the through-thickness stress and strain solutions at the center of the damage region, at lengthscales sufficiently distant from the edges such that the results are not influenced. This distance is determined by investigating the stress and strain variations along the length of the delamination front, such as the results for the single-ply effective ply thickness laminate for θ equal to 15° shown in Figure 7.35. The distance along the delamination front, where the delamination front corresponds to a value of S equal to 15 mm, is measured relative to the $\hat{S}$-axis. The upper corner (i.e., y-distance equal to zero and the most positive x-distance of the delamination) of the delamination front located at a value of $\hat{S}$ equal to 15 mm and the left-most corner (i.e., x-distance equal to zero and the most positive y-distance of

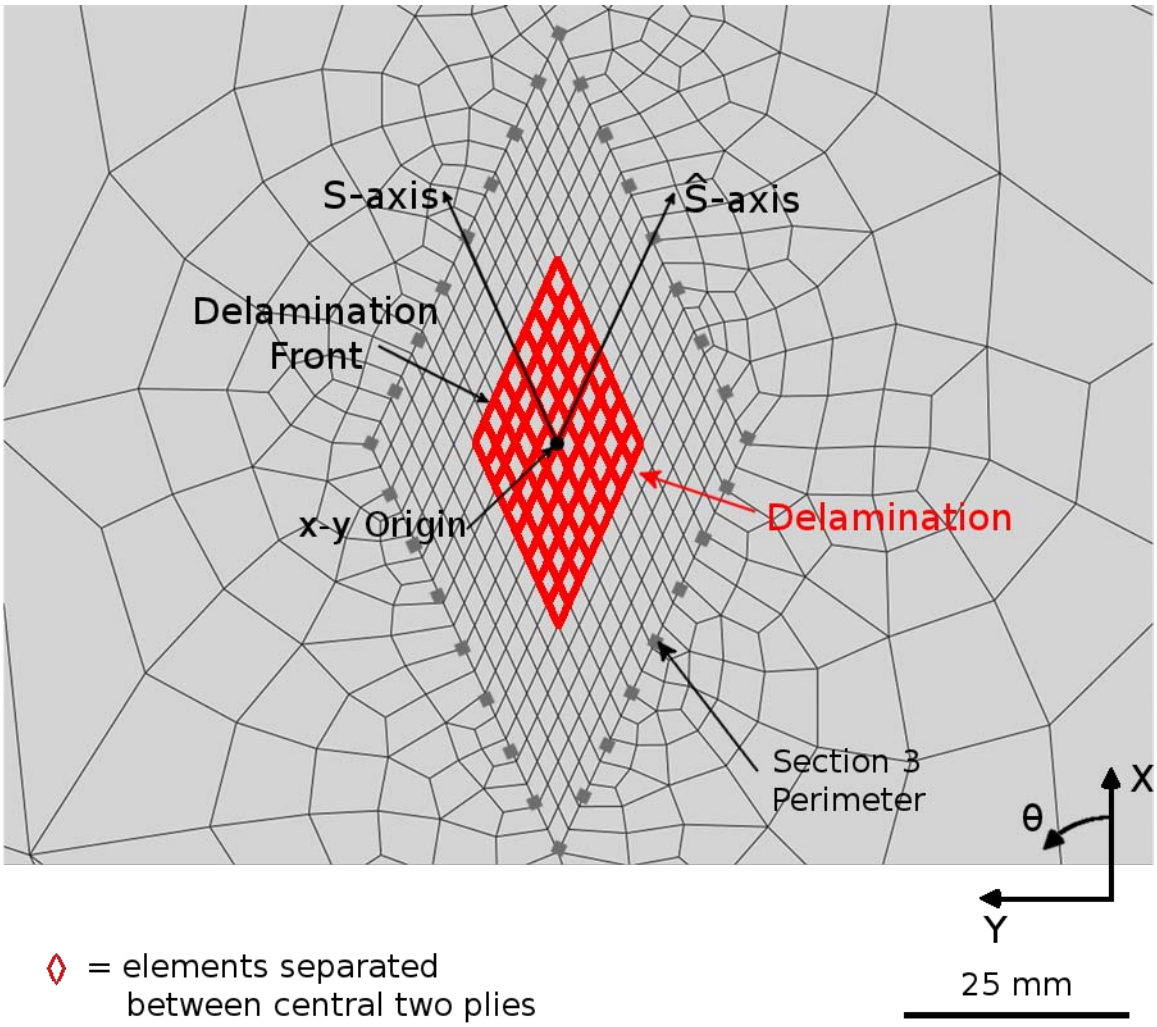

Figure 7.34 Close-up planar (x-y) view of the elements used to create a delamination between the central plies in a model of a laminate with θ equal to 30°.

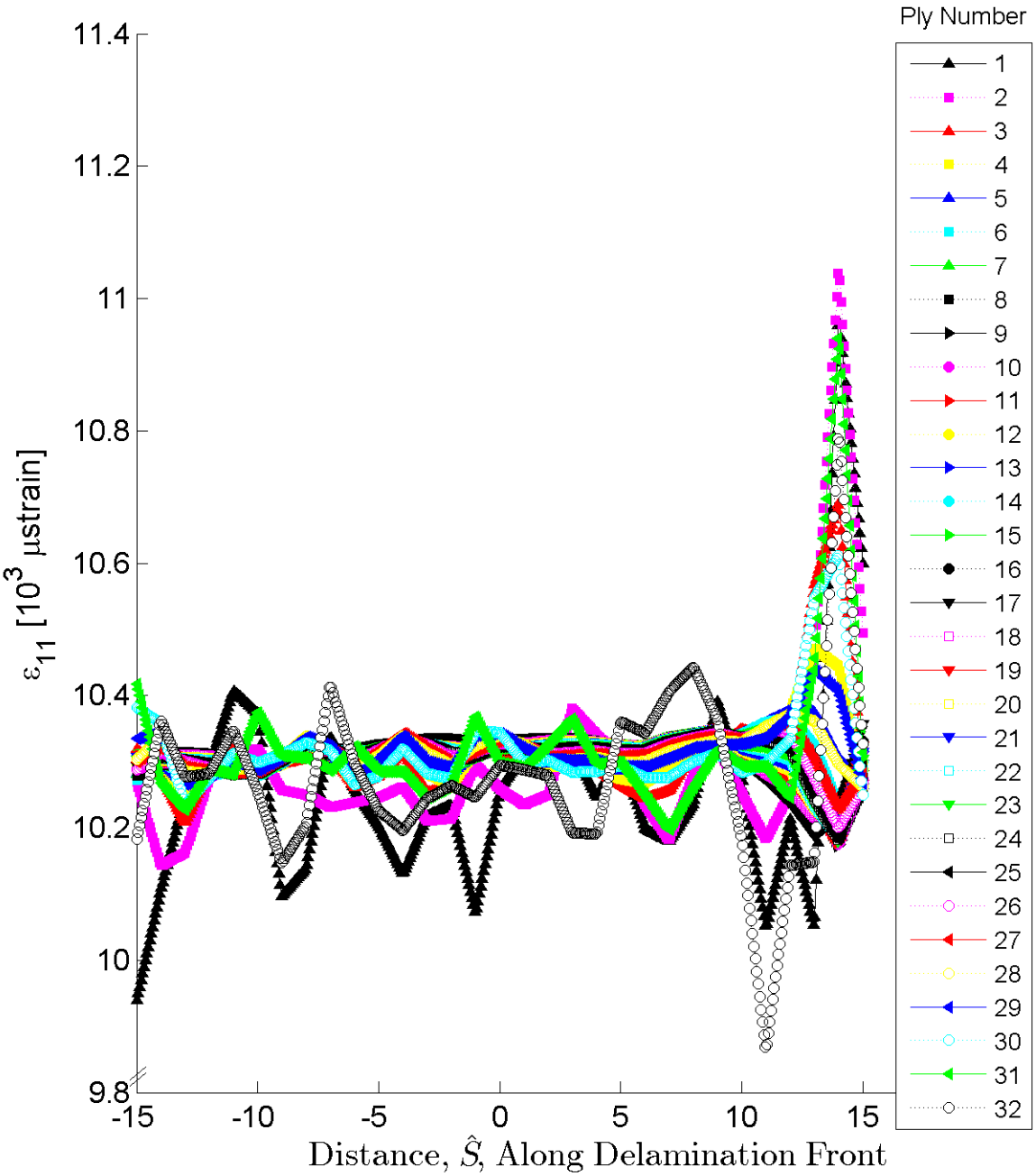

Figure 7.35 Plot of ϵ_{11}, in laminate axes, along the delamination front at the midplane of each ply for the delamination model with laminate of $[+15/-15]_{16T}$.

the delamination) of the delamination front located at a value of $\hat{S}$ equal to -15 mm. The geometry of the delamination is shown in Figure 7.34. The results illustrated in Figure 7.35, where the 1-direction is aligned with the x-axis, show the distance over which the corners influence the results, and that at the midlength of the delamination front, the results are free of corner influences. Variations of a few hundred μstrain are observed at the midlength of the delamination front throughout the results of all strain components. The effects of the corners are observed to have a maximum influence within the regions of $\hat{S}$ from -15 mm to -10 mm and from 10 mm to 15 mm. The latter region contains a peak approximately 1000 μstrain greater than the averaged value observed at the center of the delamination front (i.e., $\hat{S}$ equal to zero). All other cases considered have a smaller length of influence of the corners.

Boundary conditions are specified for the C3D8R elements. This element has three translational degrees-of-freedom (DoF) and no rotational DoF. For the damage inclusion model, displacement boundary conditions in the x-direction are specified on the positive and negative x-faces. This boundary condition simulates uniaxial tension on the model. The gage length of the damage inclusion model is 1400 mm. A total overall strain of 1% is applied to the model, split equally between the upper and lower faces (i.e., that is 0.5% for each face). The resulting x-direction displacement boundary condition is 7.0 mm. The other DoF are left free. An illustration of the applied boundary conditions is shown in Figure 7.36.

The final step in the model setup is specifying the field outputs. For the C3D8R elements used in this model, the three-dimensional strain and stress values are requested in ply axes on a ply-by-ply basis. This is done by specifying field outputs for each of the thirty-two layups defined in the composite layup editor. The results of the damage inclusion models are presented and discussed in Section 7.3.5.

7.3 Results

The use of the finite element models results in numerically calculated stress and strain fields for the modeled specimens. The C3D8R element type used throughout

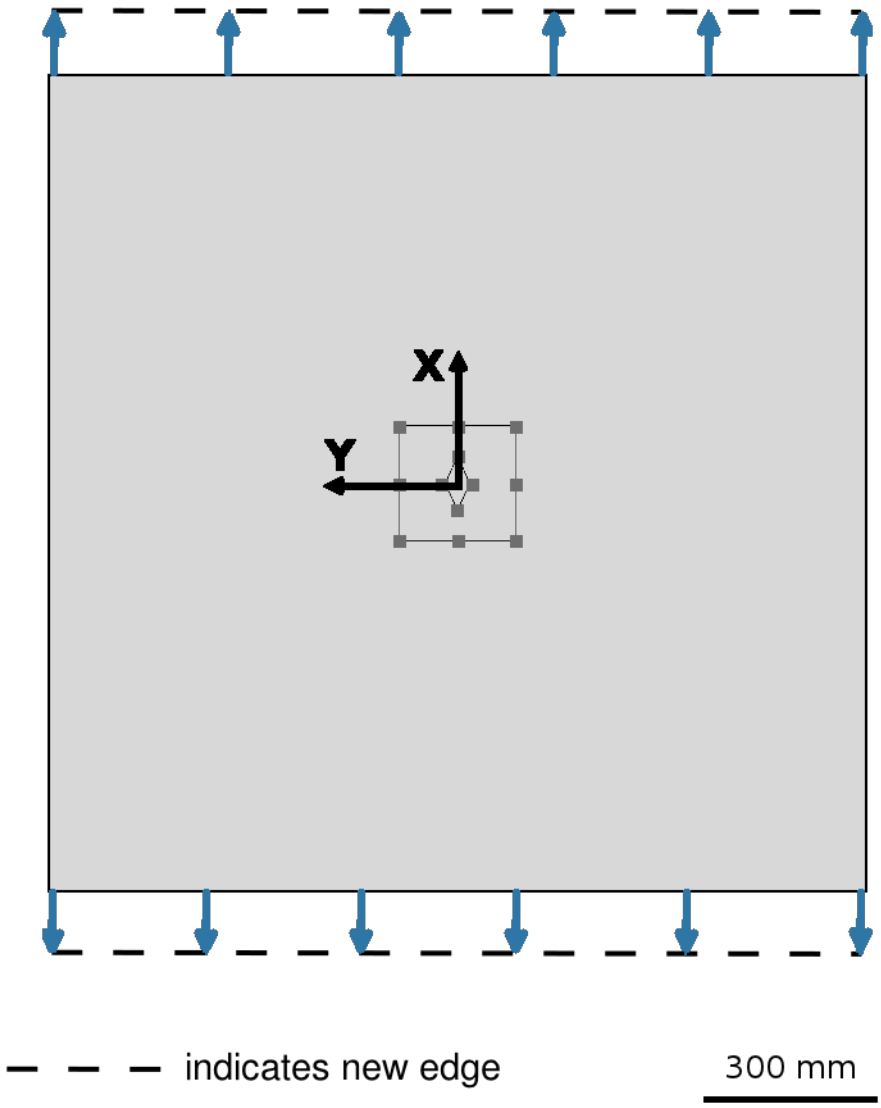

Figure 7.36 Planar (x-y) view of the boundary conditions for the damage inclusion model.

the models provides the three-dimensional stress and strain fields on a ply-by-ply basis. The models used are linear and result in a linear relationship between the magnitude of strain and the applied boundary condition strain. As described in Section 7.2, a uniaxial displacement of 1% of the gage length of the specimen is applied in each model. These results are presented, and can be scaled with far-field displacement due to the linearity of the models. Throughout the results of the models presented herein, index notation is used. The 1-direction aligns with the laminate x-axis, the 2-direction aligns with the laminate y-axis, and the 3-direction aligns with the laminate z-axis. From each of the models, the strain results are presented. The choice to consider the results in terms of strains was made because strain fields satisfy compatibility and are thus continuous through the thickness of the laminates. In order to compare lengthscales, independent of through-thickness location, strains were selected to be discussed herein.

As a result of the linear finite-element analysis combined with the in-plane loading (i.e., no bending or out-of-plane loading), the models with symmetric laminates (i.e., the single-edge-notched and open-hole tension specimens) result in nearly identical in-plane strain field predictions for plies of the same angle irrespective of location through the thickness of the laminate. The models of the double-edge-notched specimens and the damage inclusion models have balanced but unsymmetric laminates. This causes a slight change in the predicted strain fields depending on the through-thickness (along the z-axis) location of the ply. The models of the ply-drop specimens have symmetric laminates, but due to the geometry of the ply-drop, the strain fields vary through the thickness (along the z-axis) near the ply-drop region.

For all the models considered in this work, the calculated fields are shown in laminate axes. Display of the results in laminate axes allows direct comparison to the optically measured strain fields of the experimental specimens (excluding the single-edge-notched specimen in which optical strain measurements were not taken, for reasons described in Chapter 4). The experimental strain fields are reported by Michopoulos and Iliopoulos [129]. These fields are used to verify the models. Included in each of these figures are the maximum and minimum calculated strains, ϵ_T and

ϵ_C, respectively. In cases where the maximum and/or minimum calculated strain occurs along an edge of the specimen, excluding the free surfaces of the structural feature, a 'global' maximum and/or minimum are presented with an asterisk, ϵ_T^* and ϵ_C^*, respectively. For shear strains, a single value, ϵ_S, is reported. This corresponds to the maximum magnitude of the shear strain.

The resulting strains for the far-field displacement are shown and discussed in this section. These results illustrate the characteristic, or typically observed, strain fields for each of the four different specimen geometries and the damage inclusion models. The key characteristics noted for each model are illustrated via plots, representative of the strain field of each model. Additional plots of the strain fields for each laminate are included in Appendix B to illustrate variations observed between laminates of each model. From the results of the strain fields, gradients resulting from specimen geometry or included damage are observed. The representative gradients are illustrated via plots of the strain magnitudes at characteristic distances away from the structural feature. These characteristic distances, or lengthscales, are defined and established as part of the current work. Additional plots of the gradients are included for each laminate in Appendix B to illustrate variations observed between laminates of each model.

The Poisson's ratios and coefficients of mutual influence for the laminates of each specimen type are given in Table 7.4. These values are determined from Laminated Plate Theory (LPT) [143, 144] and are used in discussing the results presented in this section. The Poisson's ratios, ν_{XY} and ν_{XZ}, characterize the transverse to axial strain and the through-thickness to axial strain, respectively, for the case of applied axial stress. The coefficient of mutual influence, $\eta_{XY,X}$, $\eta_{XZ,X}$, and $\eta_{YZ,X}$, are of the second kind, as defined by Lekhnitskii [145] and Jones [146], characterizing shear strain in the plane specified by the first two subscripts to extensional strain in the direction specified by the third subscript for the case of applied stress in the direction specified by the third subscript. The contracted notation of these coefficients are η_{16}, η_{15}, and η_{14}, respectively. For the models considered, displacement boundary conditions are only specified on positive and negative x-faces. Therefore, only the Poisson's

Table 7.4 Poisson's ratios and coefficients of mutual influence for the laminates used

Laminate	**Laminate Angle, θ**	**Property**				
		ν_{XY}	ν_{XZ}	$\eta_{XY,X}$	$\eta_{XZ,X}$	$\eta_{YZ,X}$
$[(-\theta/+\theta_2/-\theta_2/+\theta)_S]_S$	15°	0.86	0.03	0.00	0.00	0.00
	30°	1.18	-0.08	0.00	0.00	0.00
	60°	0.29	0.29	0.00	0.00	0.00
	75°	0.08	0.37	0.00	0.00	0.00
$[+\theta/-\theta]_{16T}$	15°	0.86	0.03	0.00	0.00	0.00
	30°	1.18	-0.08	0.00	0.00	0.00
	60°	0.29	0.29	0.00	0.00	0.00
	75°	0.08	0.37	0.00	0.00	0.00
$[+\theta_4/-\theta_4]_{4T}$	15°	0.86	0.03	0.00	0.00	0.00
	30°	1.18	-0.08	0.00	0.00	0.00
	60°	0.29	0.29	0.00	0.00	0.00
	75°	0.08	0.37	0.00	0.00	0.00
$[+45°/0°/-45°]_{4S}$	-	0.65	0.13	0.00	0.00	0.00
$[+45°_4/0°_4/-45°_4]_S$	-	0.65	0.13	0.00	0.00	0.00
$[+45°/0°/-45°]_{2S}$	-	0.65	0.13	0.00	0.00	0.00
$[+45°_2/0°_2/-45°_2]_S$	-	0.65	0.13	0.00	0.00	0.00

ratios and coefficients of mutual influence relating the behavior of the material due to applied stress in the x-direction are included in Table 7.4.

7.3.1 Single-Edge-Notched Specimen Model

The characteristic strain fields for each of the four laminates of the single-edge-notched specimen model are illustrated via the results in this subsection and Appendix B.1. Nearly identical in-plane strain field (i.e., ϵ_{11}, ϵ_{22}, and ϵ_{12}) predictions for plies of the same angle, regardless of the through-thickness location of the ply, occur for the single-edge-notched specimens. However, the out-of-plane strain fields (i.e., ϵ_{33}, ϵ_{13}, and ϵ_{23}) depend on the through-thickness (along the z-axis) location of the ply. For each of the four laminates (θ equal to 15°, 30°, 60°, or 75°), the results are grouped together based on the in-plane and out-of-plane strain field results.

A common feature exhibited in all the strain field results is free-edge effects. These effects are observed as discontinuities in the slopes of the isostrain lines (i.e., the isoline is not smooth) near the edges of the specimen. In some results, such as the strain field of ϵ_{11} for the laminate of θ equal to 15° shown in Figure 7.37, the free-edge effects are easily identified. In this case, the isostrain lines near the positive and negative x-faces of the specimen, excluding the faces of the notch, clearly exhibit discontinuities at a distance of approximately four ply thicknesses normal to the specimen edge. In other cases, such as the strain field of ϵ_{11} for the laminate with θ equal to 75° shown in Figure 7.38, the free-edge effects are more subtle. For the in-plane results, the distance at which the effect is observed, approximately four ply thicknesses, is consistent across the results of all the strain fields. The free-edge effects near the edges of the notch are not observed in the in-plane strain results due to the modeling lengths. However, these effects are observed in the out-of-plane strain results near the edges of the notch. These would have an effect on the in-plane strain response. As shown in Figure 7.39, the isolines for the value of ϵ_{33} equal to +1250 μstrain for the laminate of θ equal to 75°, a slope discontinuity occurs along the x-faces of the notch. The discontinuities associated with the notch act at a distance of approximately two ply thicknesses normal to the notch edge. The free-edge effects along the specimen

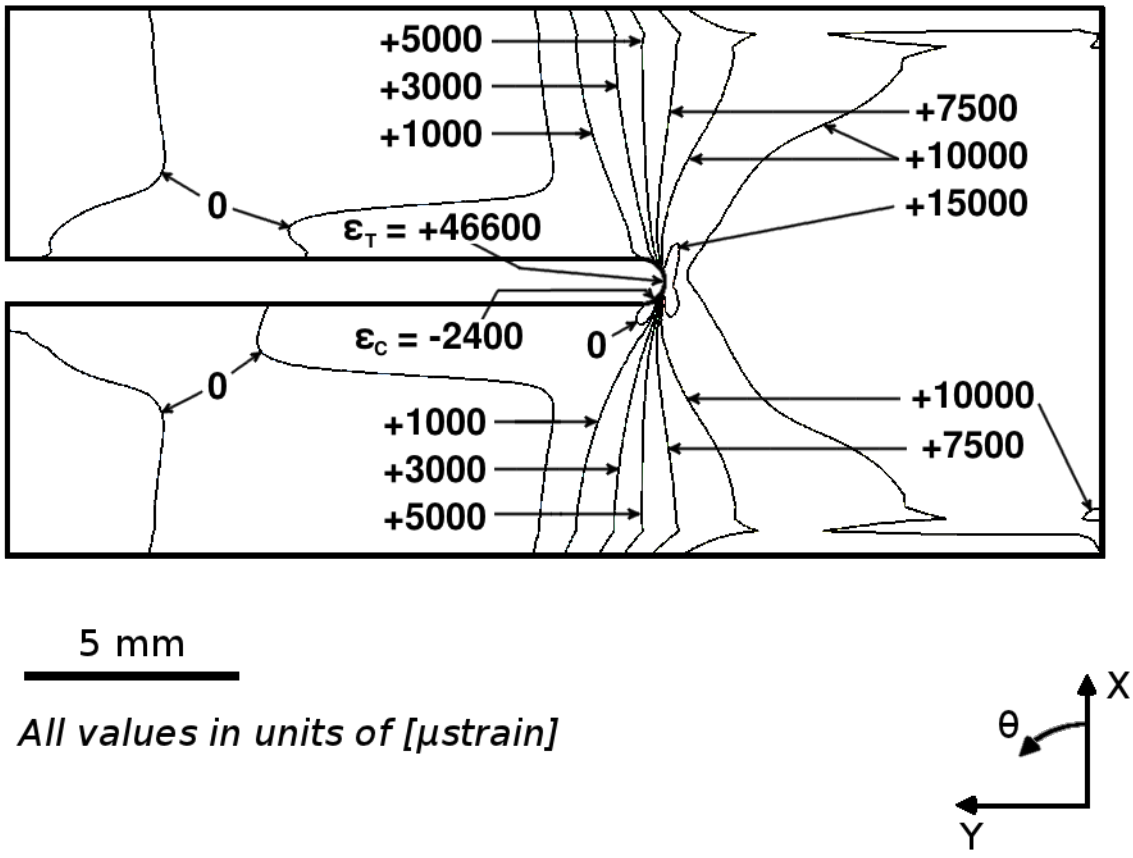

Figure 7.37 Isostrain plot of strain field of ϵ_{11}, in laminate axes, at the midplane of ply 1 (a -15° ply) of the single-edge-notched specimen model for the laminate of $[(-15/+15_2/-15_2/+15)_S]_S$.

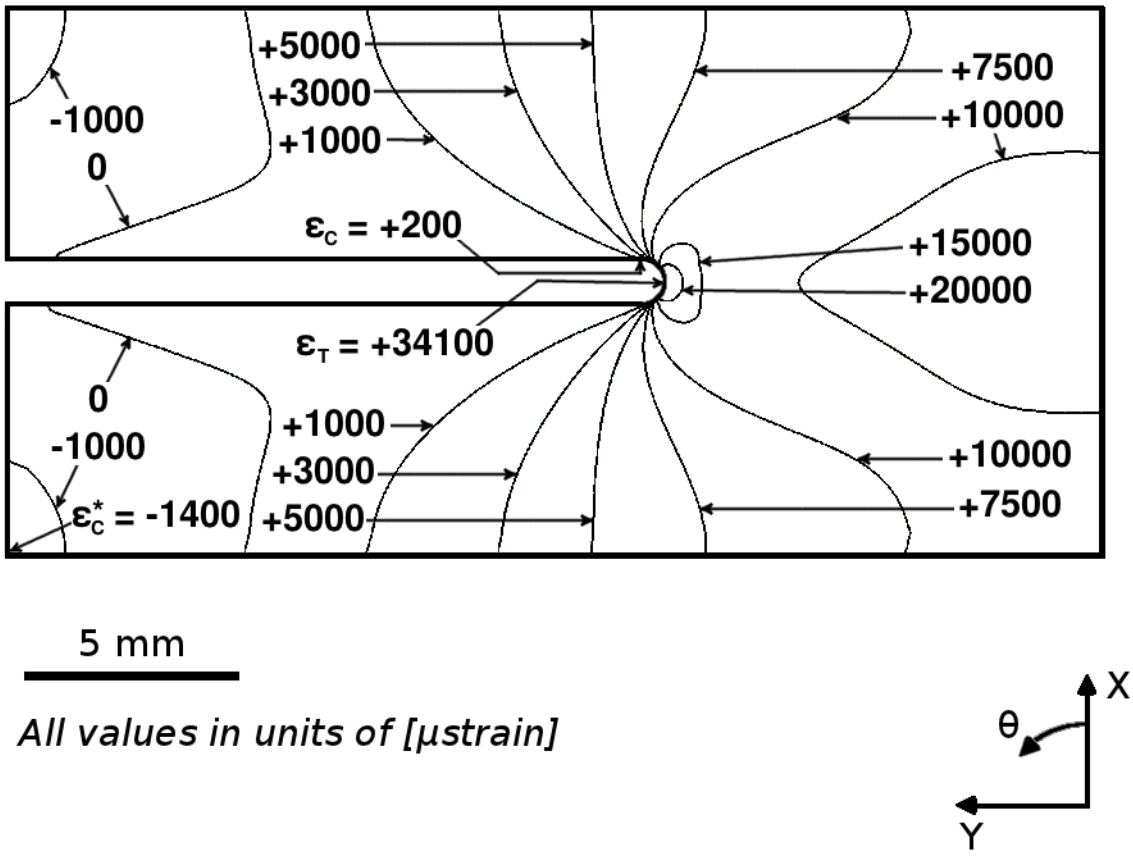

Figure 7.38 Isostrain plot of strain field of ϵ_{11}, in laminate axes, at the midplane of ply 1 (a $-75°$ ply) of the single-edge-notched specimen model for the laminate of $[(-75/+75_2/-75_2/+75)_S]_S$.

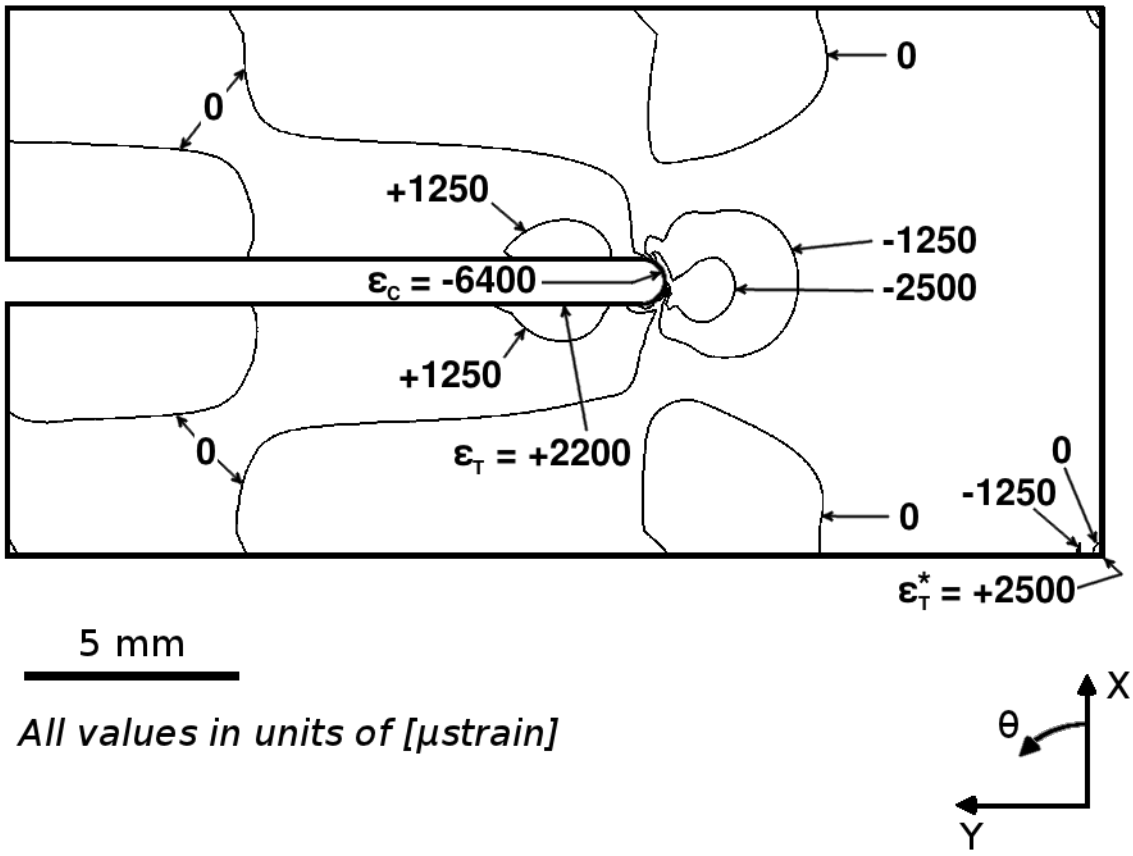

Figure 7.39 Isostrain plot of strain field of ϵ_{33}, in laminate axes, at the midplane of ply 12 (a $-15°$ ply) of the single-edge-notched specimen model for the laminate $[(-15/+15_2/-15_2/+15)_S]_S$.

edges, excluding the notch edges, of the out-of-plane strain results are exhibited at a distance of approximately four ply thicknesses, the same as observed for the in-plane strain results. Beyond these observations of the free-edge effects, these effects are not further discussed.

The results for the in-plane strain fields are considered first. This is followed by the results for the out-of-plane strain fields. The in-plane strain fields are observed to be relatively uniform through the thickness of each laminate, as is predicted via LPT. Variations from LPT exist in the model results due to free-edge effects at the notch. These variations are observed in pairs, with the exact in-plane strain fields observed in plies symmetric about the midplane of the specimen. The results for the first ply of the laminate with θ equal to 15° is shown to represent the typical in-plane strain fields of all the plies in the laminates. The strain field of ϵ_{11} from the second ply of the laminate with θ equal to 15° is included in Figure 7.40 in order to illustrate the common (i.e., across the four laminates) changes observed between positive and negative plies of a laminate.

The in-plane strain fields exhibit nearly symmetric results about the notch (y-axis) in all the plies, both positive and negative, of a laminate. Slight variations (less than 1%) are observed in the location of the isostrain lines as the results of different plies are compared. Thus, each in-plane strain field exhibits the same general fields throughout the plies of each laminate, as predicted by the LPT solution.

The majority of the strain fields of ϵ_{11} for the laminates considered have positive values, as shown in the results for ϵ_{11} for the laminate of θ equal to 15° shown in Figure 7.37. All the laminates, except the laminate with θ equal to 75°, have a small region (less than 1 mm in length and 0.5 mm wide) near the notch tip with a negative value. The peak minimum value in Figure 7.38 (θ equal to 75°) contains a 'global' ϵ_C^* and a 'local' ϵ_C. Thus, for the laminate of θ equal to 75°, the 'local' minimum of the strain, indicated as ϵ_C in Figures 7.38, is not always negative. The location of the peak 'local' minimum value is dependent on the laminate. The locations and values of the peak maximum (ϵ_T) and minimum (ϵ_C) 'local' in-plane strains for each laminate are listed in Table 7.5. The locations are given in polar coordinates, with the origin

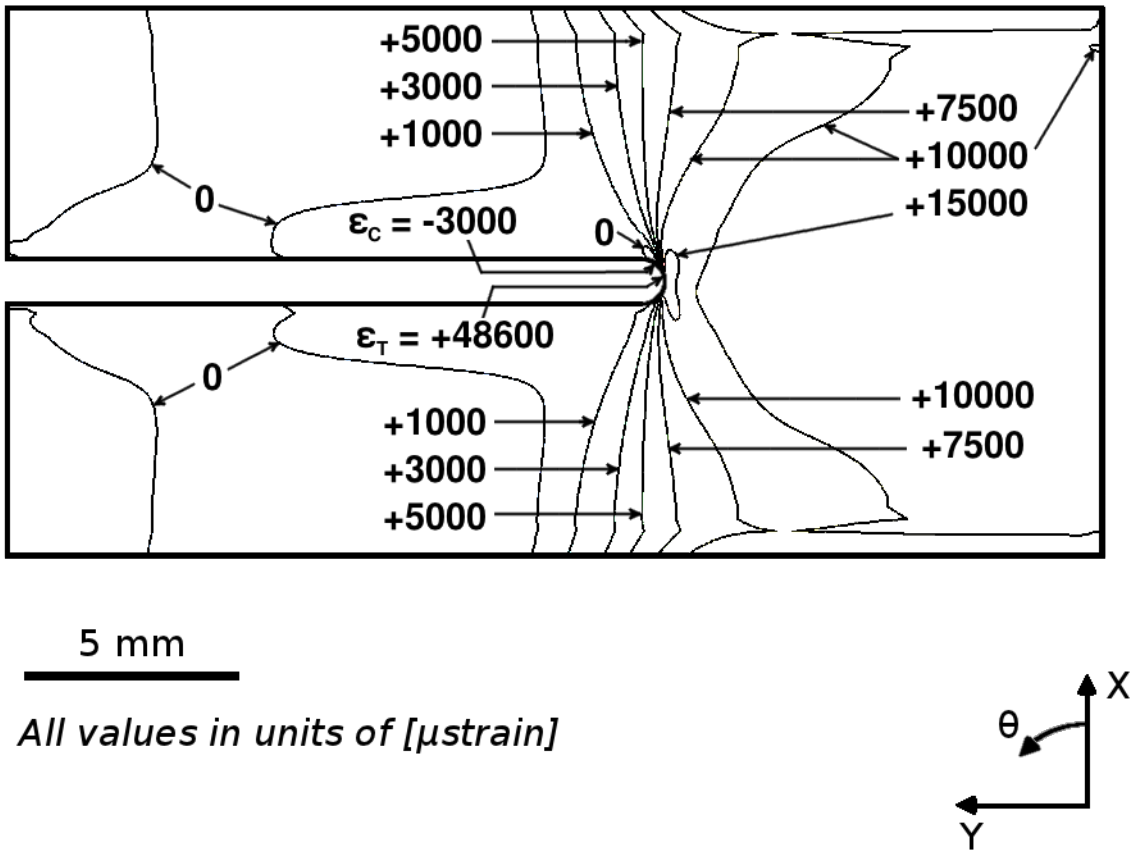

Figure 7.40 Isostrain plot of strain field of ϵ_{11}, in laminate axes, at the midplane of ply 2 (a $+15^\circ$ ply) of the single-edge-notched specimen model for the laminate of $[(-15/+15_2/-15_2/+15)_S]_S$.

Table 7.5 Locations and values of maximum and minimum in-plane strains for the single-edge-notched specimens (laminates of $[(-\theta/+\theta_2/-\theta_2/+\theta)_S]_S$)

Strain Component	**Value Considered**[a]	**Laminate Angle, θ**	**Value [μstrain]**	$\frac{\mathbf{r}}{\mathbf{r_o}}$	ϕ **[degrees]**
ϵ_{11}	ϵ_T	15°	+46600	1	-94
		30°	+44900	1	-98
		60°	+34100	1	-103
		75°	+34100	1	-94
	ϵ_C	15°	-2400	1	-142
		30°	-3000	1	-151
		60°	-1800	1	-167
		75°	+200	1	0
ϵ_{22}	ϵ_T	15°	+21900	1	-129
		30°	+15300	1	-137
		60°	+6600	1	-161
		75°	+6600	1	-31
	ϵ_C	15°	-12600	1	-89
		30°	-25700	1	-94
		60°	-11000	1	-116
		75°	-8500	1	-121
ϵ_{12}	ϵ_S	15°	+61900	1	-79
		30°	+29900	1	-79
		60°	-18800	1	-133
		75°	-24900	1	-137

[a] ϵ_T = Maximum
ϵ_C = Minimum
ϵ_S = Maximum Magnitude

concentric with the center of the semi-circular notch tip, as shown in Figure 7.41. The origin of the x-y coordinate system, defined in previous chapters, is located at the notch tip. Thus, the origin of the polar coordinate system is at the coordinates of x equal to 0 and y equal to r_o. The radial distance, r, is normalized by the notch tip radius r_o, and thus is expressed in the number of notch radii from the origin. This gives the boundary of the notch as r/r_o equal to 1. The angle, ϕ, is measured positive counterclockwise from the positive x-axis and expressed in degrees. In all cases, the local maximum (ϵ_T) and local minimum (ϵ_C) always occur at the notch boundary (i.e., r/r_o equal to 1).

The regions of negative strain at the notch tip are also observed to flip about the notch (y-axis) for positive and negative plies, with an example shown in Figures 7.37 and 7.40, illustrating the results from a negative and positive ply, respectively, for the laminate of θ equal to 15°. This trend of flipping about the y-axis when comparing results for the positive and negative plies is observed in all the laminates, except the laminate with θ equal to 75°, where negative strain is not observed at the notch tip. However, the local minimum value for the laminate with θ equal to 75° is observed to flip about the y-axis when comparing the results for the positive and negative plies.

Another observation of the strain fields of ϵ_{11} is that the value of strain in the "unnotched" (i.e., in the negative y-direction from the notch tip) section is roughly +1% strain (+10,000 μstrain), a value consistent with the applied displacement boundary condition, at a distance away from the notch tip. This distance is used to define a characteristic length associated with the structural feature. The values of strain along a path, aligned with the y-axis (i.e., ϕ equal to −90°), from the notch tip (r_o) to the right edge ($20r_o$) of the specimen is measured for each laminate. The characteristic length is defined as the number of notch radii away from the notch tip (not the origin) that the strain field returns to within a certain percentage of the "unnotched" (i.e., far field) solution. Two percentages, 10% and 5%, are selected in order to develop the process. This may require refinement as additional analyses are conducted beyond this work. Associated with these percentages are two characteristic lengths, l_{10} and l_5, defined as the distance from the notch tip (i.e., the point $(r_o, -90°)$ in the polar

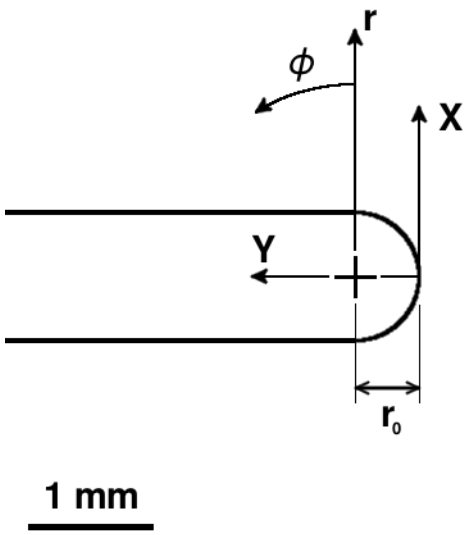

Figure 7.41 Illustration of the polar coordinate used for the results in Table 7.5.

coordinate system of Figure 7.41) to the point along ϕ equal to $-90°$ where the strain field returns to within 10% and 5%, respectively, of the "unnotched" solution.

These characteristic lengths allow measurement of the influence of the structural feature as a function of the laminate. The characteristic lengths resulting from this definition for the in-plane strain components are listed in Table 7.6. It is observed that the path along ϕ equal to $-90°$ is the minimum length of influence, as will be further discussed. The material in the "notched" (i.e., in the positive y-direction from the notch tip) section has values of ϵ_{11} near zero, as would be expected since load cannot be transmitted across the free edges of the notch. There exists a transition area between the "unnotched" and "notched" sections of the specimen. Within this region, the strain transitions from the 1% strain of the "unnotched" region to the near zero strain of the "notched" region. The extent of this region is influenced by the laminate. In laminates with smaller ply angles (i.e., 15° and 30°), the transition region is located in a narrow band above and below the notch tip. In laminates with larger ply angles (i.e., 60° and 75°), the transition is stretched over a larger region.

Gradients in the strain fields of ϵ_{11} are observed to be dependent on the laminate, as observed in the strain fields of ϵ_{11} shown in Figures 7.37, 7.38, B.1, and B.2. In order to quantify these gradients, values of the strain fields along "arc paths" defined in the polar coordinate system are plotted. The arc paths are defined as the number, n, of radii away from the free edge of the notch tip:

$$n = \frac{r - r_o}{r_o}$$

The arc paths for n equal to 1 through 12 are illustrated in Figure 7.42. In addition to the arc paths shown in this figure, paths are also defined for n equal to 0, 0.125, 0.25, and 0.5, but are not shown due to the figure scale. Note that the path for n equal to 12 extends beyond the boundaries of the specimen. This maintains a consistent polar angle sweep (i.e., ϕ goes from 0° to $-180°$) for each path. However, there are no stress or strain results beyond the specimen boundary. The points beyond the specimen boundary of the arc path for n equal to 12 are ignored.

Table 7.6 Normalized characteristic lengths[a] of the in-plane strains for the single-edge-notched specimen laminates

Strain Component	**Laminate Angle, θ**	**Far-Field Strain [μstrain]**	$\frac{l_{10}}{r_o}$	$\frac{l_5}{r_o}$
ϵ_{11}	15°	+10000	4.68	8.02
	30°	+10000	8.90	11.65
	60°	+10000	b	b
	75°	+10000	b	b
ϵ_{22}	15°	-8600	10.25	12.13
	30°	-11800	9.80	11.65
	60°	-2900	b	b
	75°	-800	b	b
ϵ_{12}	15°	0	0.83	1.17
	30°	0	0.85	1.35
	60°	0	1.27	3.30
	75°	0	4.28	6.46

[a] l_{10} = defined characteristic length for strain value to return to within 10% of far-field strain.
l_5 = defined characteristic length for strain value to return to within 5% of far-field strain.
[b] Far-field strain was not reached before edge of specimen.

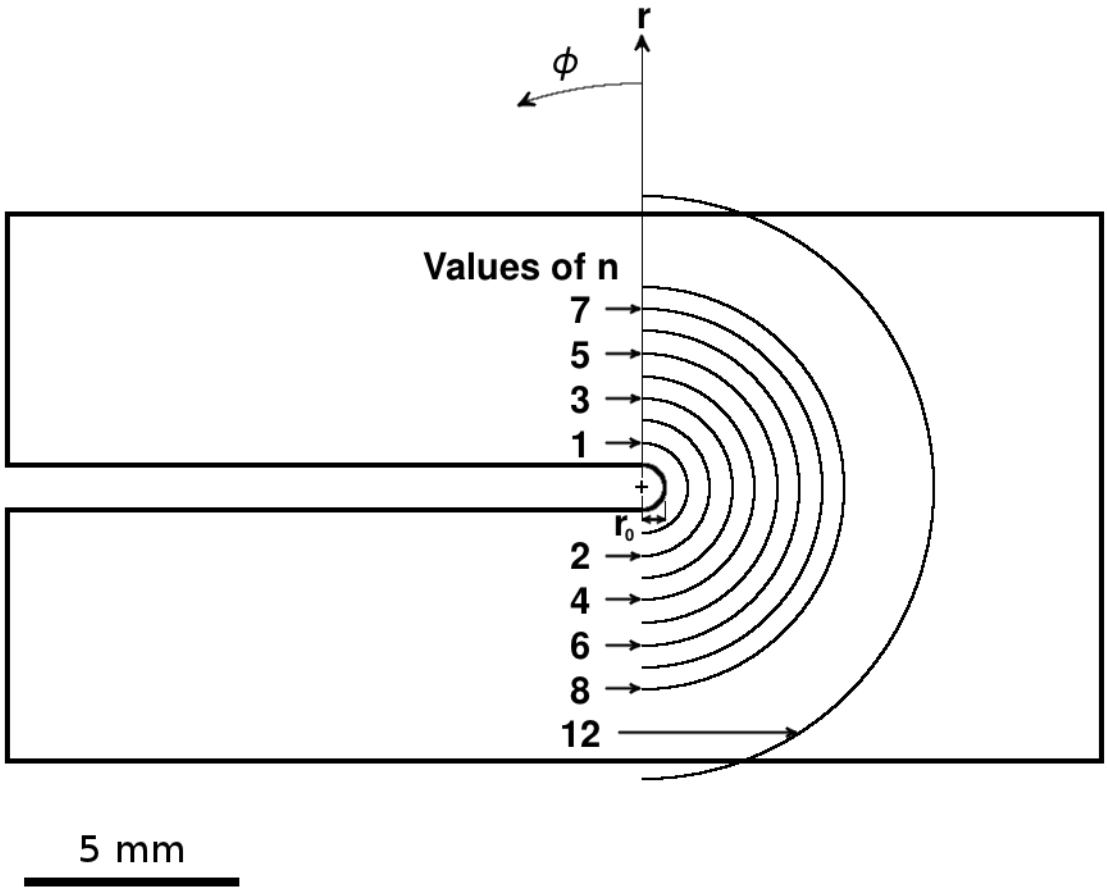

Figure 7.42 Arc path locations defined for the single-edge-notched specimen.

Values of strain are presented along these arc paths versus an angle, ψ, as defined in an offset polar coordinate system. This offset system, (r', ψ), and the original polar coordinate system, (r, ϕ), are shown in Figure 7.43. The offset system has its origin displaced a distance equal to the notch radius, r_o, along ϕ equal to $-90°$ in the original polar coordinate system. The angle ψ is thus measured from the tip of the notch. As with the angle ϕ, ψ is measured positive counterclockwise from the positive x-direction. Radial paths extending from both polar coordinate origins to an arbitrary point along an arc path are shown in the figure. In the offset polar coordinate system, the radial distance from the origin to points along the arc path is a function of the angle ψ. This is due to the arc paths being defined with a constant radius in the original polar coordinate system. In the offset system, the radial distance must vary as a function of ψ in order to remain on the arc paths. In addition, the values of the angles over which ψ varies for each arc path (i.e., starting and ending sweep angles) is a function of the distance away from the notch edge of the arc path. Transformation equations between the two polar coordinate systems are found via geometric relations. Note, due to the nature of the geometric relationship, the transformation of the data for n equal to 0 results in a discontinuity in these plots for values of ψ from $0°$ to $-180°$.

The values of ϵ_{11} along the arc paths are plotted for the laminate with θ equal to $15°$ and are shown in Figure 7.44. For the other laminates, these plots are shown in Figures B.3 through B.5, included in Appendix B.1. The plots show the value of the strain fields of ϵ_{11} versus the angle, ψ, as defined in the offset polar coordinate system. The peak strain is observed along the path of n equal to 0 in all cases, along with the peak strain decreasing as the distance from the notch tip (i.e., value of n) increases. The peak values along each path are seen to be associated with the laminate fiber angle, θ. Furthermore, two peaks are observed to form as the distance from the notch tip increases, with the distance at which this first occurs depending on the laminate angle θ. In the laminate with θ equal to $15°$, these peaks are first observed in the path for n equal to 0.25. As the laminate angle increases, the radial distance away from the notch tip at which these peaks are first observed also increase. In each of

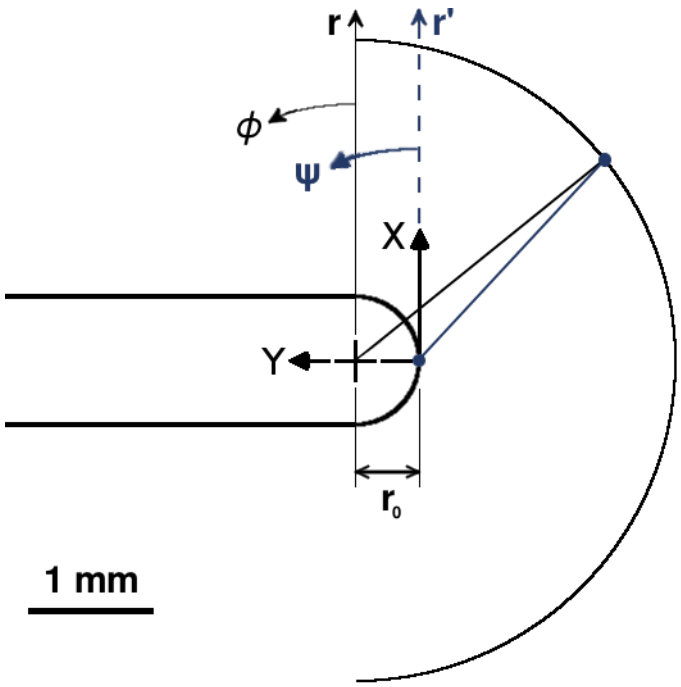

Figure 7.43 Illustration of the offset polar coordinate used for the plots of strain values along arc paths for the single-edge-notched specimens.

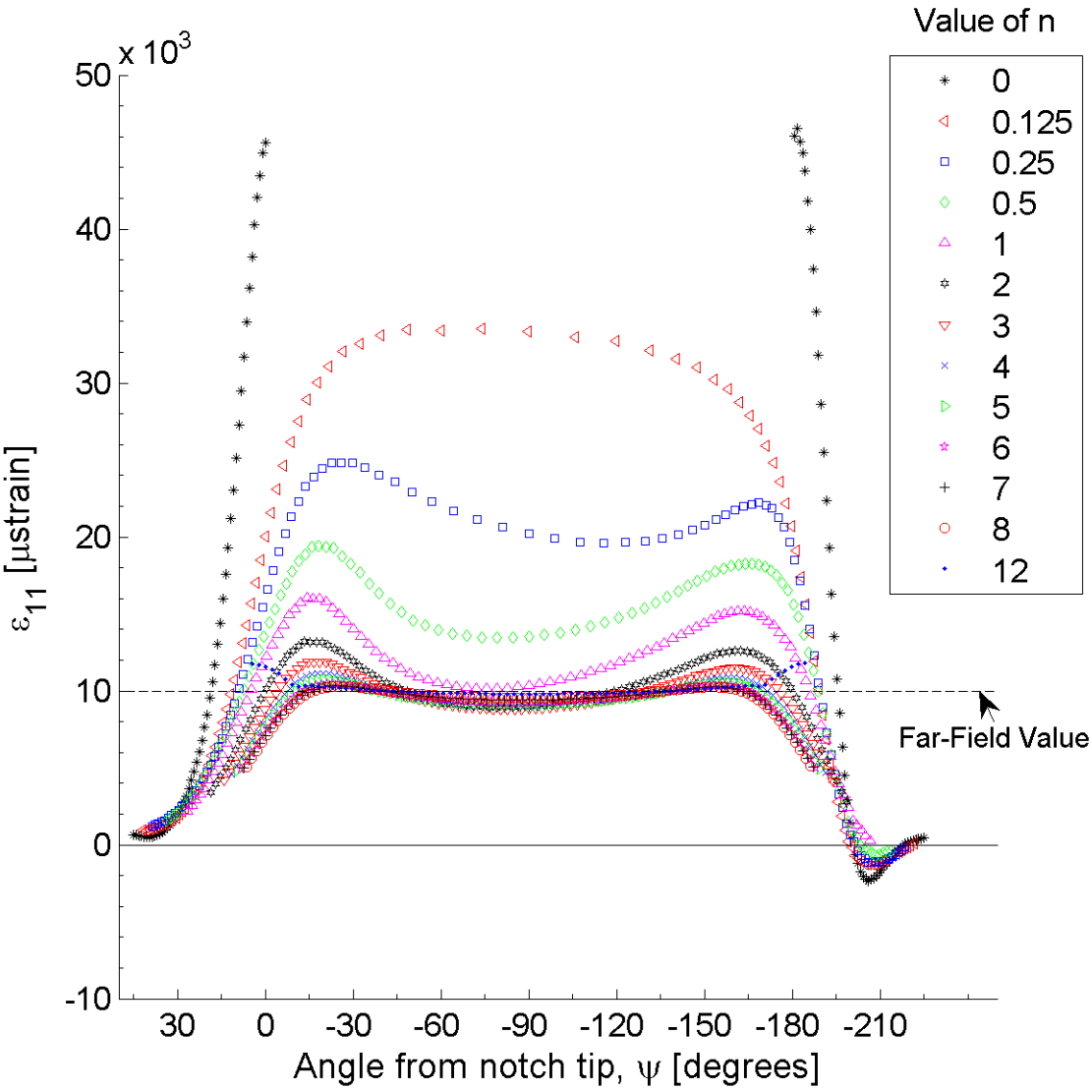

Figure 7.44 Plot of ϵ_{11}, in laminate axes, along arc paths at the midplane of ply 1 (a $-15°$ ply) of the single-edge-notched specimen model for the laminate of $[(-15/+15_2/-15_2/+15)_S]_S$.

the laminates, these peaks occur close to the fiber angles, i.e., ψ close to θ. Also observed in these figures is a slight skewness of the plots. This skewness is observed to flip about ψ equal to -90° in positive angle plies, as shown in Figure 7.45.

An advantage to plotting the values of the strain fields in such plots is that multiple gradients are observable in a single graph. The gradient of the strain fields along each arc path is the slope of the strain line for that path. The largest gradients are observed along the path for n equal to 0, with the gradients decreasing and leveling off farther away from the notch tip, as the value of n increases. Furthermore, as this radial distance away from the notch increases, the strain fields of ϵ_{11} approach the "unnotched" solution of 1% for the strain. Another advantage of these plots is that the defined characteristic lengths, l_{10} and l_5, for the specimen can be visualized at discrete distances from the notch (i.e., between arc paths for various values of the angle ψ). For example, the values of strain along ψ equal to -90° are observed to approach the far-field strain as the radial distance increases. The approximate characteristic length can be determined based on the arc path that first exhibits a value of strain equal to the value of far-field strain at ψ equal to -90°. The exact characteristic lengths, as previously determined, are listed in Table 7.6. These plots also allow other visualization of the trends in the strain fields, such as whether the strain values approach the far-field value along other values of the angle ψ. Such information may be useful in the future in identifying additional characteristic lengths associated with the geometry.

Gradients of strain in the radial direction are represented by the difference in the value of strain between arc paths at a given value of ψ in these plots divided by the distance between these arc paths. As previously noted, the radial distance between paths is a function of the offset angle ψ in the offset polar coordinate system. In order to compare the gradients in general radial directions, the radial distance between arc paths, as a function of ψ, must be calculated. This calculation is based on geometric relations. The gradients of the values of ϵ_{11} between neighboring arc paths are given in Table 7.7 for ψ equal to -90°, the same angle used to define the characteristic lengths, l_{10} and l_5. The gradients could be calculated for all angles of ψ in the future. For ψ

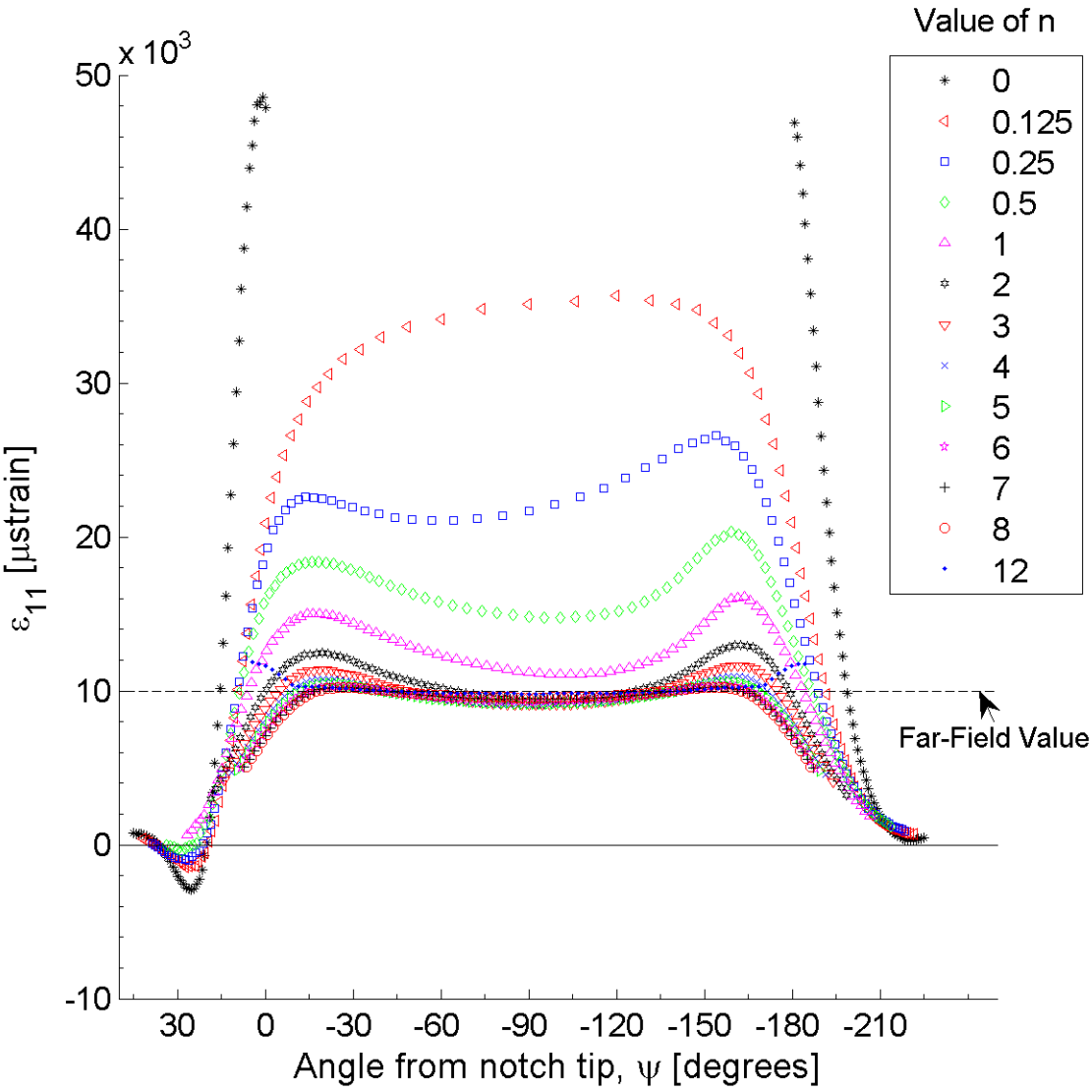

Figure 7.45 Plot of ϵ_{11}, in laminate axes, along arc paths at the midplane of ply 2 (a $+15^\circ$ ply) of the single-edge-notched specimen model for the laminate of $[(-15/+15_2/-15_2/+15)_S]_S$.

Table 7.7 Gradients of the values of ϵ_{11} between 'arc paths' for ψ equal to $-90°$ for the single-edge-notched specimen laminates

Arc Paths (n values)	**Gradient** $[\mu\epsilon/mm]$			
	Laminate Angle, θ			
	15°	**30°**	**60°**	**75°**
0 - 0.125	-192900	-83700	-29600	-38600
0.125 - 0.25	-205500	-151200	-43500	-54500
0.25 - 0.5	-52500	-91500	-33500	-35000
0.5 - 1	-12500	-18400	-27400	-19300
1 - 2	-2600	-3400	-11600	-9500
2 - 3	-300	-600	-3000	-3600
3 - 4	+200	+10	-1300	-2000
4 - 5	+300	+300	-600	-1100
5 - 6	+300	+400	-300	-600
6 - 7	+300	+400	-100	-400
7 - 8	+200	+400	-50	-300
8 - 12	+200	+400	+400	+200

equal to $-90°$, the distance between arc paths is equal to the radial distance between the paths. It is observed that these gradients are dependent on the laminate angle, θ. For the lower angle laminates of θ equal to 15° and 30°, the value of ϵ_{11} is observed to have a positive gradient beyond the arc path for n equal to 3. This indicates that the field of ϵ_{11} goes from a high strain value near the notch, then drops below the far-field solution before finally approaching the far-field solution. This trend is observed in Figure 7.44. In the higher angle laminates of θ equal to 60° and 75°, the value of ϵ_{11} monotonically decreases to the far-field solution. In these higher angle laminates, the gradients near the notch, for values of n less than 0.5, are observed to be an order of magnitude smaller than those observed in the lower angle laminates.

The majority of the strain fields of ϵ_{22} for the laminates considered have negative values, as shown in the results for ϵ_{22} for the laminate with θ equal to 15° in Figure 7.46. For the laminates with θ equal to 30°, 60°, and 75°, the strain fields of ϵ_{22} are shown in Figures B.6 through B.8, included in Appendix B.1. The peak maximum and minimum values are indicated in these figures, with the values and locations for each laminate listed in Table 7.5. As in the case of the strain fields of ϵ_{11}, these peak maximum and minimum values occur along the notch edge, at values of r/r_o equal to 1. The locations of these peak values in the polar coordinate angle ϕ are observed to be dependent on the laminate fiber angle, as indicated by the results in Table 7.5. These locations do not match the corresponding peak maximum and minimum locations for ϵ_{11}.

The strain fields of ϵ_{22} exhibit a slight asymmetry about the notch (y-axis) within each ply, similar to the asymmetry observed in the strain fields of ϵ_{11}. This asymmetry becomes more noticeable in the region near the notch tip as the laminate angle increases. For example, the upper (positive x-direction from the notch) -9000 μstrain isoline in Figure 7.46 comes to a sharper 'point' nearest the notch tip compared to the lower isoline of the same value. This trend is observed throughout the laminate thickness and for all laminates for isolines near the notch tip.

Very little change is exhibited in the strain fields of ϵ_{22} when varying between positive and negative plies. Generally, the 'far-field' (at a distance greater than 1

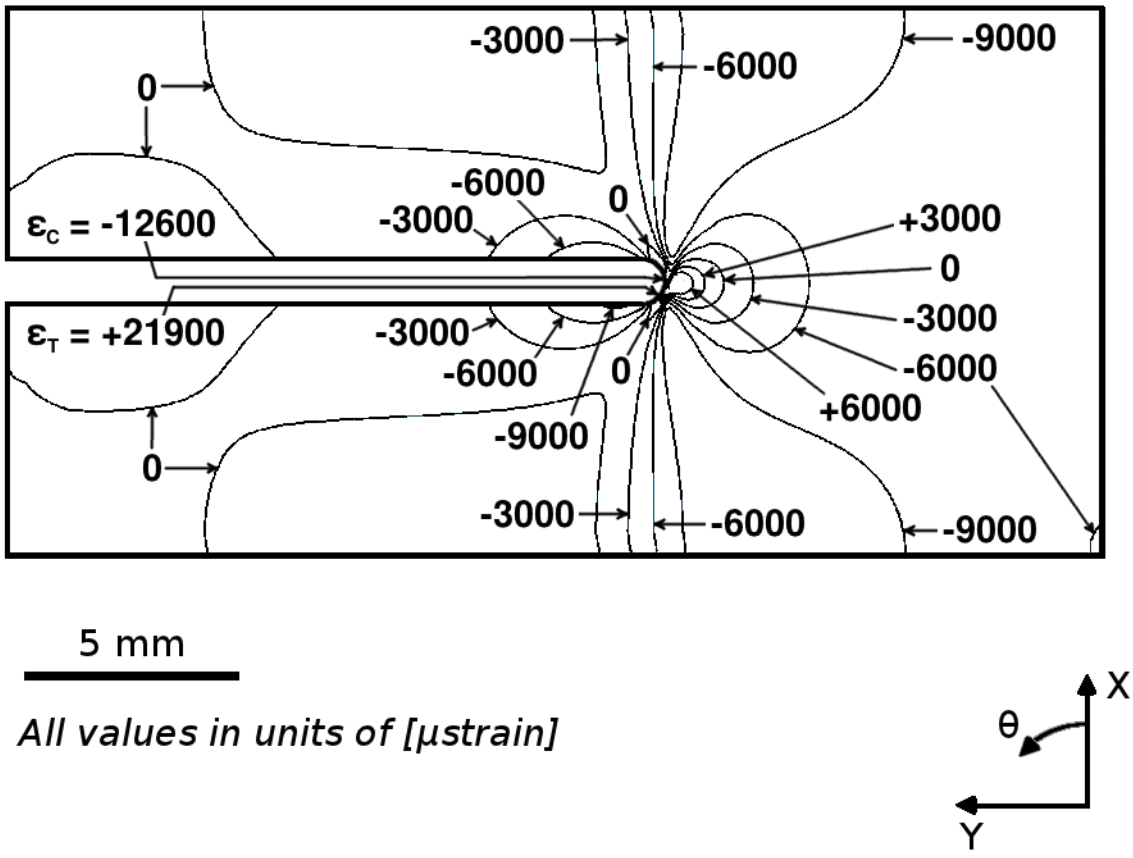

Figure 7.46 Isostrain plot of strain field of ϵ_{22}, in laminate axes, at the midplane of ply 1 (a $-15°$ ply) of the single-edge-notched specimen model for the laminate of $[(-15/+15_2/-15_2/+15)_S]_S$.

notch radius from the notch tip) isostrain lines are consistent for both positive and negative plies of a laminate, as would be predicted from LPT. In the 'near-field' (at a distance less than 1 notch radius from the notch tip), a slight variation occurs. These variations are likely due to free-edge effects, as discussed at the beginning of this section. As in the case of the strain fields of ϵ_{11}, the direction of the skewing of isolines flips for positive and negative plies. Similarly, the locations of the maximum and minimum peak strains flip about the y-axis between the positive and negative plies.

In the "unnotched" region of all the laminates, the observed values of the strain fields for ϵ_{22} are on the order of the expected Poisson's effect. For example, the Poisson's ratio for the laminate with θ equal to 15°, given in Table 7.4, is 0.86. The majority of the "unnotched" region of the laminate, shown in Figure 7.46, has a value between -9000 μstrain and -6000 μstrain. Had the specimen been featureless (i.e., without a notch), the expected value of ϵ_{22} would be -8600 μstrain due to Poisson's effects. However, the effect of the notch and the given loading creates gradients within the "unnotched" region near the notch tip. As with the results for ϵ_{11}, the characteristic lengths, l_{10} and l_5, are measured for the ϵ_{22} results and given in Table 7.6. In the higher angle laminates of θ equal to 60° and 75°, the far-field solution is not observed before reaching the right edge of the specimen.

The results for ϵ_{22} exhibit a transition region, located above and below the notch tip, similar to the transition region observed in the results for ϵ_{11}. The transition region for ϵ_{22} is clearly seen in Figure 7.46 for the laminate of θ equal to 15°. The largest gradient (i.e., isostrain lines closest together) observed in this transition region occurs for this laminate with θ equal to 15°. As the ply angle of the laminate increases, the gradients in the transition region decrease (i.e., the isostrain lines become spaced farther apart). This is the same trend observed in the results for ϵ_{11}.

As with the gradients for ϵ_{11}, gradients in the strain fields of ϵ_{22} are observed to be dependent on the laminate. The values of ϵ_{22} along the arc paths versus the polar coordinate angle, ψ, are plotted for the laminate of θ equal to 15° in Figure 7.47. For the other laminates, these plots are shown in Figures B.9 through B.11, included

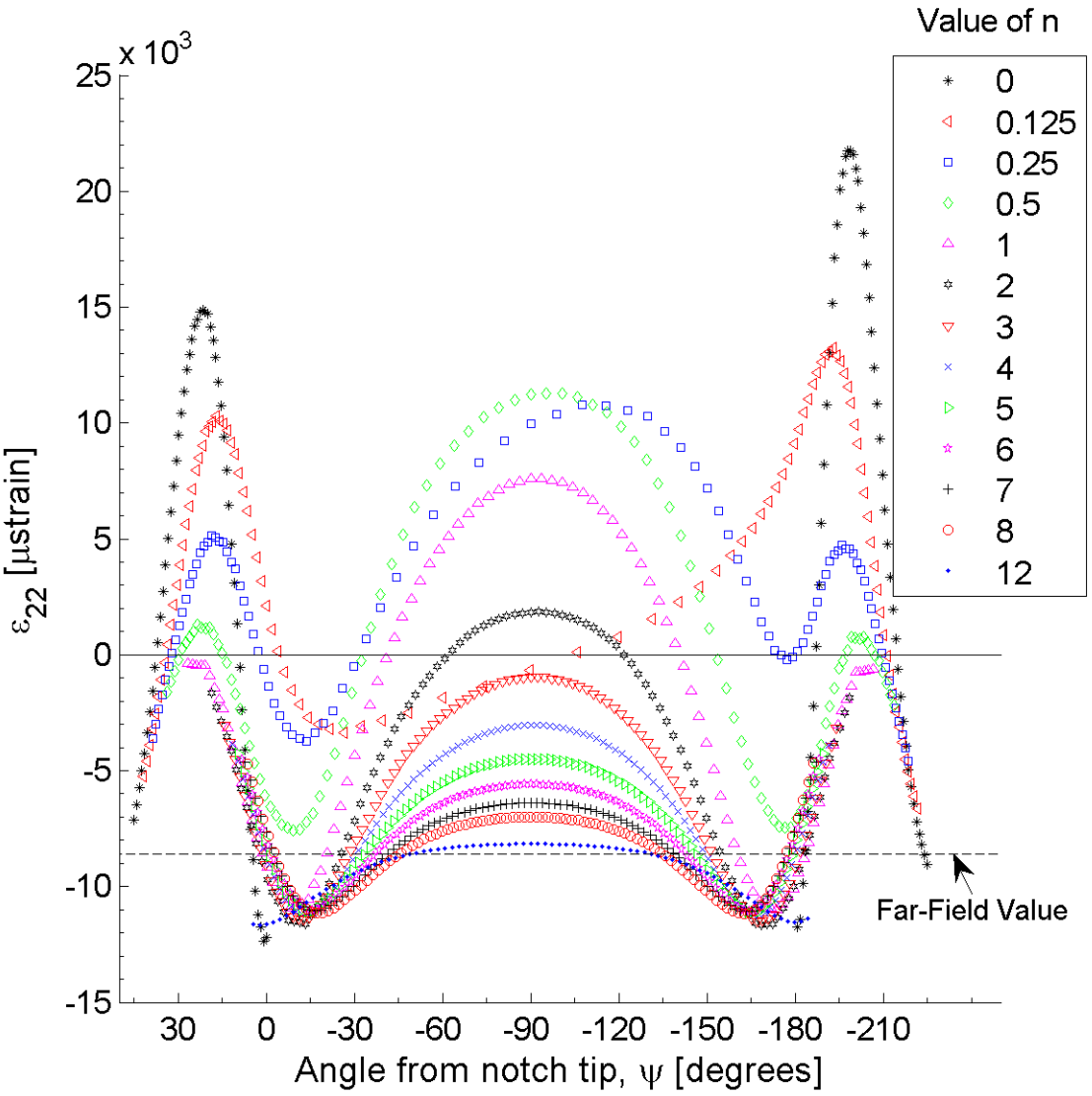

Figure 7.47 Plot of ϵ_{22}, in laminate axes, along arc paths at the midplane of ply 1 (a $-15°$ ply) of the single-edge-notched specimen model for the laminate of $[(-15/+15_2/-15_2/+15)_S]_S$.

in Appendix B.1. The peak values along each path are associated with the laminate fiber angle, θ, as observed for ϵ_{11}. For ϵ_{22}, the values of strain plotted against ψ eventually form three 'peaks' and two 'valleys' as the distance from the notch tip increases. In the laminate with θ equal to 15°, the trend is first observed in the plot for values along the arc path for n equal to 0.25. As the laminate angle increases, the trend develops farther from the notch. For the lower angle laminates of θ equal to 15° and 30°, as listed via the characteristic lengths in Table 7.6, the value of ϵ_{22}, along ψ equal to −90°, approaches the far-field solution as the distance from the notch tip increases. For the higher angle laminates of θ equal to 60° and 75°, this gradient decreases as the value of θ increases. In addition, the results for ϵ_{22} does not reach the far-field solution before the right edge of the specimen is reached for the higher angle laminates. As with the gradients of ϵ_{11}, the gradients of ϵ_{22} exhibit a skewness that is dependent on the ply angle. The values of ϵ_{22} for the positive plies of the laminates are observed to flip about ψ equal to −90° as compared to those for the negative plies. This skewness is dependent on the laminate.

As was done in Table 7.7 for ϵ_{11}, the gradients of the values of ϵ_{22} between neighboring arc paths are given in Table 7.8 for ψ equal to −90°, the same angle used to characterize the characteristic lengths, l_{10} and l_5. It is observed that these gradients are dependent on the laminate angle, θ, as for the values of ϵ_{11}. For the lower angle laminates of θ equal to 15° and 30°, the value of ϵ_{22} is observed to have a negative gradient beyond the arc path of n equal to 0.5 for θ equal to 15° and beyond the arc path of n equal to 1 for θ equal to 30°. This indicates that the strain field of ϵ_{22} first increases before decreasing toward the far-field solution. This trend is observed in Figure 7.47. The higher angle laminates of θ equal to 60° and 75° also show this trend. However, the magnitudes of the gradients are several magnitudes of order smaller for ϵ_{22} than those for the lower angle laminates. The higher angle laminates also exhibit a much smaller gradient approaching the far-field solution.

The strain fields of ϵ_{12} for the single-edge-notched specimen are observed to be uniform for each laminate, regardless of the location through the thickness (z-direction) of the laminate, as shown in the results for ϵ_{12} for the laminate with θ equal to 15° in

Table 7.8 Gradients of the values of ϵ_{22} between 'arc paths' for ψ equal to $-90°$ for the single-edge-notched specimen laminates

Arc Paths (n values)	**Gradient** $[\mu\epsilon/mm]$			
	Laminate Angle, θ			
	15°	**30°**	**60°**	**75°**
0 - 0.125	+181200	+80500	-2700	+2300
0.125 - 0.25	+166400	+143200	+100	+3700
0.25 - 0.5	+10200	+73700	+8600	+3700
0.5 - 1	-14300	+1600	+12200	+3200
1 - 2	-11300	-5500	+3000	+1500
2 - 3	-5500	-3400	-200	+100
3 - 4	-4100	-2800	-500	-200
4 - 5	-2900	-2200	-500	-300
5 - 6	-2100	-1800	-400	-300
6 - 7	-1600	-1500	-400	-200
7 - 8	-1200	-1300	-300	-200
8 - 12	-600	-800	-400	-300

Figure 7.48. For the laminates with θ equal to 30°, 60°, and 75°, the strain fields of ϵ_{12} are shown in Figures B.12 through B.14, included in Appendix B.1. In each of the four laminates modeled, the strain fields of ϵ_{12} observed in the positive plies is nearly identical to those fields in the negative plies, with one exception occurring in the boundary elements of the "unnotched" section. Here, the values of the strains switch sign between positive and negative plies. However, the solutions in these boundary regions is unimportant as the focus is on the solution in the vicinity of the notch tip.

As for the other in-plane strains, the strain fields of ϵ_{12} at the notch tip are consistent through the plies of each laminate, with small variations in shape occurring between positive and negative plies. The results for ϵ_{12} also exhibit a transition region above and below the notch tip. Similar to the transition region in the results for ϵ_{11} and ϵ_{22}, this transition region is observed to be dependent on the laminate. The transition region is clearly seen in Figure 7.48 and shows a transition from the "unnotched" strain field with a value of 0 to a far-field strain field with a value of 0, since the value of the mutual coefficient of influence for a balanced laminate is equal to 0. The largest gradient (i.e., isostrain lines closest together) observed in this transition region occurs for this laminate with θ equal to 15°. As the ply angle of the laminate increases, the gradients in the transition region decrease, as is the trend observed in the results for ϵ_{11} and ϵ_{22}.

As with the gradients for ϵ_{11} and ϵ_{22}, gradients in the strain fields of ϵ_{12} are observed to be dependent on the laminate. The values of ϵ_{12} along the arc paths versus the polar coordinate angle, ψ, are plotted for the laminate with θ equal to 15° in Figure 7.49. For the other laminates, these plots are shown in Figures B.15 through B.17, included in Appendix B.1. The peak values along each path are associated with the laminate fiber angle, as observed for ϵ_{11} and ϵ_{22}. For ϵ_{12}, the values of strain plotted against ψ eventually form two 'peaks' and two 'valleys' as the distance from the notch tip increases. In the laminate with θ equal to 15°, the trend is first observed in the arc path for n equal to 0.5. As the laminate angle increases, the trend develops farther from the notch. As with the gradients for ϵ_{11} and ϵ_{22}, the gradients observed in these figures are slightly skewed in the plots for n less than 2. Another trend,

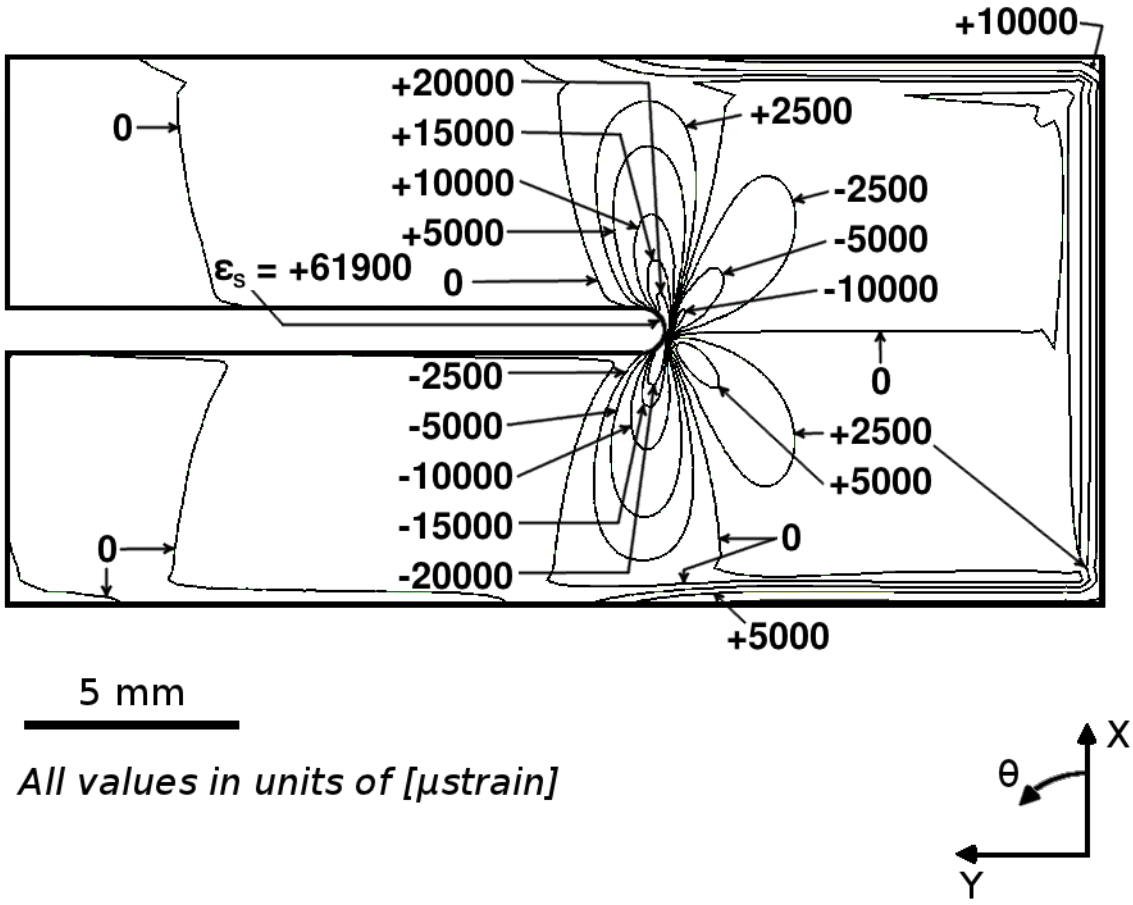

Figure 7.48 Isostrain plot of strain field of ϵ_{12}, in laminate axes, at the midplane of ply 1 (a -15° ply) of the single-edge-notched specimen model for the laminate of $[(-15/+15_2/-15_2/+15)_S]_S$.

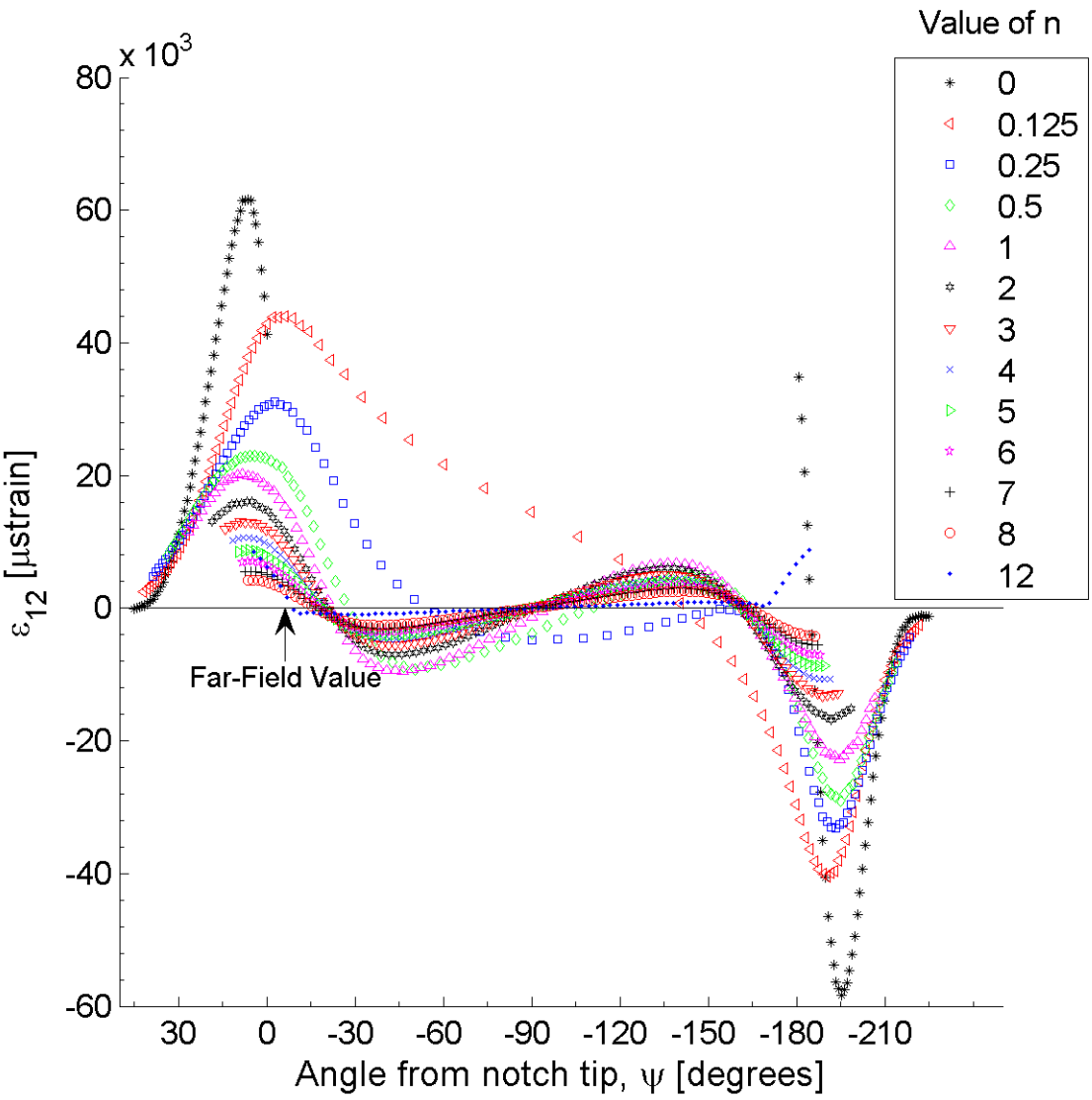

Figure 7.49 Plot of ϵ_{12}, in laminate axes, along arc paths at the midplane of ply 1 (a -15° ply) of the single-edge-notched specimen model for the laminate of $[(-15/+15_2/-15_2/+15)_S]_S$.

similar to that observed in the gradients of the other strain fields, is a symmetry in the gradient plots for positive and negative plies of the same angle. The plots of ϵ_{12} along the arc paths for positive and negative angle plies exhibit symmetry about the point ($-90°$,0). This symmetry is visualized as a rotation of 180° about the point ($-90°$,0) of the values of ϵ_{12} for each arc path.

As was done in Table 7.7 for ϵ_{11} and in Table 7.8 for ϵ_{22}, the gradients of the values of ϵ_{12} between neighboring arc paths are given in Table 7.9 for ψ equal to $-90°$, the same angle used to characterize the characteristic lengths, l_{10} and l_5. It is observed that these gradients are dependent on the laminate angle, θ, as for the values of ϵ_{11} and ϵ_{22}. For all the laminates, the gradients nearly approach zero beyond the arc path of n equal to 2, with the exception of the gradient between the last two arc paths. In all the laminates, a positive gradient is observed between the last two arc paths (n equal to 8 and 12). However, the values of these gradients are relatively small compared to the gradients near the notch tip. As with the gradients of ϵ_{11} and ϵ_{22}, the gradient near the notch (for n equal to 0 to 0.25) in the lower angle laminates of θ equal to 15° and 30° is an order of magnitude larger compared to the gradients in the higher angle laminates of θ equal to 60° and 75°. In the lower angle laminates, the values of the gradients near ψ equal to θ are observed to be inflection points, as seen in Figure 7.49. In the higher angle laminates, the inflection points do not appear to correspond to the region of ψ equal to θ but are instead located at approximately ψ equal to $-45°$ and $-135°$.

The out-of-plane strain results are considered subsequently. These strain fields are observed to have variations through the thickness of each laminate. Variations from LPT exist in the model results due to free-edge effects at the notch. Due to the mesh density used near free edges of the model, free-edge effects such as those discussed in [58, 60, 74, 76, 139] are not captured. The free-edge effects in these regions result in large gradients in the interlaminar stresses. For the single-edge-notched specimen, this boundary layer is approximately one laminate thickness, corresponding to approximately 7 notch radii. Because the models do not capture the out-of-plane gradients near the free edges, which are expected to be greater than

Table 7.9 Gradients of the values of ϵ_{12} between 'arc paths' for ψ equal to $-90°$ for the single-edge-notched specimen laminates

Arc Paths (n values)	**Gradient** $[\mu\epsilon/mm]$			
	Laminate Angle, θ			
	15°	**30°**	**60°**	**75°**
0 - 0.125	-420300	-157200	-36600	-16600
0.125 - 0.25	-301400	-194200	-47200	-22200
0.25 - 0.5	+7900	-44300	-20100	-9200
0.5 - 1	+9300	+3400	+100	-400
1 - 2	+2300	+1600	+2200	+1500
2 - 3	+200	+300	0	+400
3 - 4	+100	+100	-100	0
4 - 5	0	0	-100	-100
5 - 6	0	0	-100	-100
6 - 7	0	0	0	-100
7 - 8	0	0	0	0
8 - 12	+200	+200	+500	+700

the gradients within the specimen, little discussion is included on the out-of-plane results.

The strain fields of ϵ_{33} exhibit consistent shape through the thickness for each laminate considered. Variations in the isostrain lines are observed to be dependent on the through-thickness location and occur within the region influenced by the free edge of the notch. Thus, these are not further discussed. The strain fields of ϵ_{33} for the single-ply effective ply thickness laminate with θ equal to 15° is shown in Figure 7.50. The results for ϵ_{33} strain fields for the other laminates are shown in Figures B.18 through B.20, included in Appendix B.1. For all cases, the far-field strain fields for ϵ_{33} are on the order of the expected Poisson's effect. For example, the Poisson's ratio for laminates with θ equal to 15°, given in Table 7.4, is 0.03. The majority of the specimen, beyond the region influenced by the hole, has strain values between -1250 μstrain and 0 μstrain. Had the specimen been featureless (i.e, without a notch), the expected value of ϵ_{33} for the case of θ equal to 15° would be -300 μstrain due to Poisson's effects. Because the model does not capture the large interlaminar gradients at the free edges of the notches, the out-of-plane results offer limited insight of the lengthscales associated with the out-of-plane gradients. Therefore, further out-of-plane results are not useful.

7.3.2 Double-Edge-Notched Specimen Model

The characteristic strain fields for each of the eight laminates of the double-edge-notched specimen model are illustrated via the results in this subsection and Appendix B.2. The double-edge-notched specimen allows investigation of the influence of the effective ply thickness, as discussed in Section 4.2. The effective ply thickness is observed to influence the strain fields and the lengthscales associated with the gradients of the strain fields. For all the laminates of the double-edge-notched specimen, the results for each ply possess central symmetry (also referred to as a point reflection) about the origin of the x-y axes (i.e., strain results are reflected through the x-y

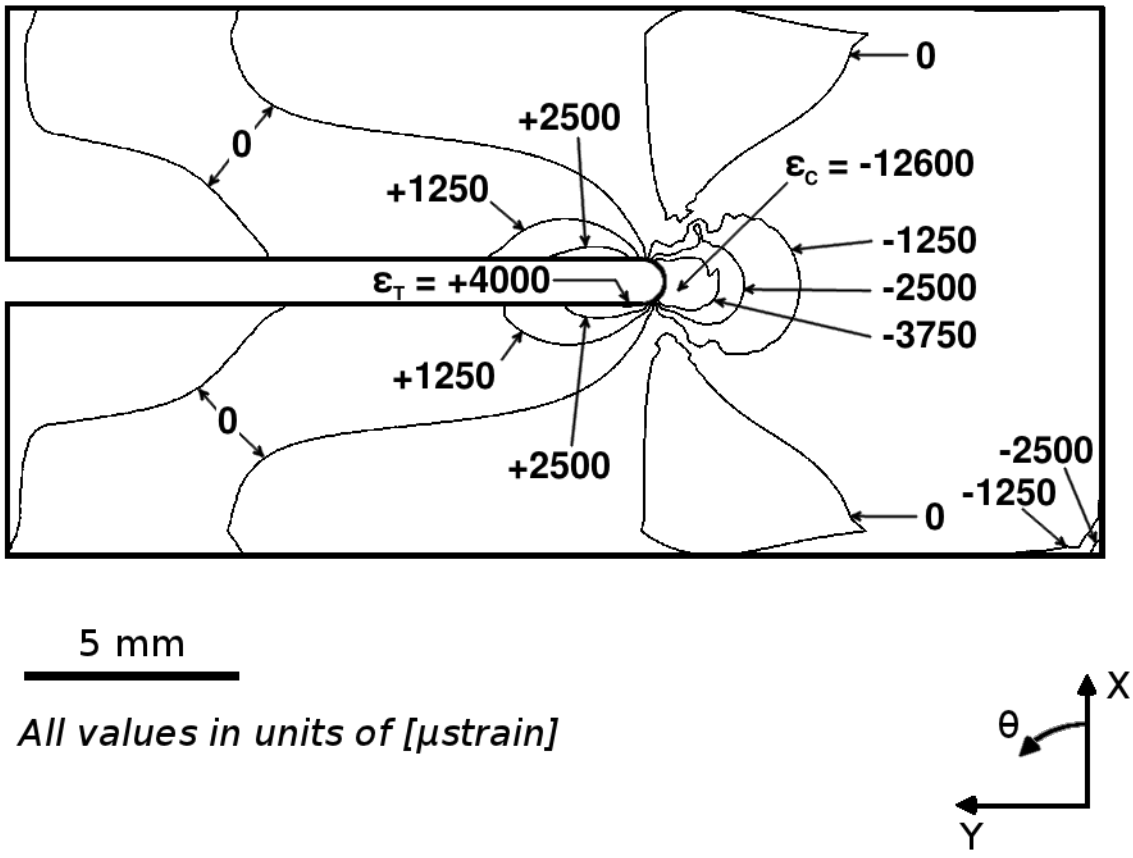

Figure 7.50 Isostrain plot of strain field of ϵ_{33}, at the midplane of ply 1 (a $-15°$ ply) of the single-edge-notched specimen model for the laminate of $[(-15/+15_2/-15_2/+15)_S]_S$.

origin). This symmetry can also be stated as:

$$\epsilon_{\alpha\beta}(x^*, y^*) = \epsilon_{\alpha\beta}(-x^*, -y^*) \tag{7.1}$$

where the point (x^*, y^*) is any point within the specimen boundaries. An illustration of central symmetry is shown in Figure 7.51, where the MIT logo and an artificial isostrain path, including a point (x^*, y^*), are both shown to posses central symmetry about the x-y origin. Due to this central symmetry, only results from the left half (positive y values) of the specimens are directly discussed as these results pertain to the other results via the central symmetry. In addition, only the strain fields about the left notch are labeled in the strain field figures and the values along the arc paths are plotted about the left notch tip. The results of the full cross-section of the specimen are plotted in the figures of the strain fields in order to illustrate the central symmetry observed throughout the results of the double-edge-notched specimen. For each of the eight laminates, the results are grouped together based on the in-plane and out-of-plane strain field results.

The results from the double-edge-notched specimen model exhibit through-thickness variations due to coupling that exists for the laminates. The laminates of the double-edge-notched specimen are of a class of laminates called regular antisymmetric angle-ply laminates. This class of laminates is balanced and unsymmetric. The regular antisymmetric laminate has plies at $+\theta$ on one side of the midplane of the laminate, and corresponding equal thickness plies at $-\theta$ on the other side of the midplane at the same distance from such [146].

An analytical investigation of representative laminates, with the same layups of the double-edge-notched specimen, but without structural features (i.e., without notches), is first presented in order to investigate the overall responses of the laminates subjected to extensional loading. The subsequent equations of this section are presented for such a representative laminate. The stiffness matrices for the eight antisymmetric angle-ply laminates ($[+\theta/-\theta]_{16T}$ and $[+\theta_4/-\theta_4]_{4T}$ where θ equals 15°, 30°, 60°, or 75°) of the double-edge-notched specimen are determined via CLPT. Each of the

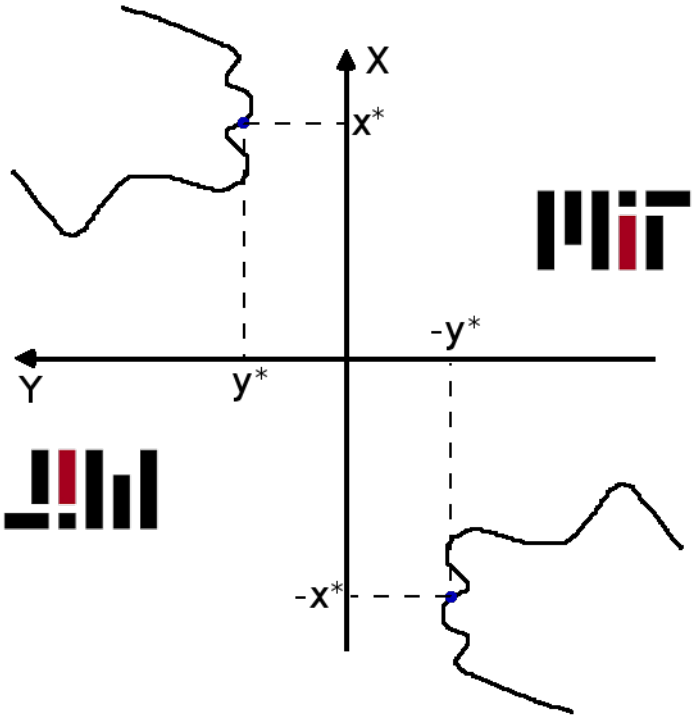

Figure 7.51 Illustration of central symmetry.

laminates exhibit non-zero extension-twisting terms, B_{16} and B_{26}. All other terms in the **B** matrix are zero for regular antisymmetric angle-ply laminates. In addition, the shear-coupling terms in the **A** and **D** matrices (i.e., A_{16}, A_{26}, D_{16}, and A_{26}) are zero. All other terms in the **A** and **D** matrices are non-zero [146]. The non-zero shear-coupling terms in the **B** matrix influence the strain response of the laminate via the relation:

$$\begin{Bmatrix} \boldsymbol{\epsilon^o} \\ \boldsymbol{\kappa} \end{Bmatrix} = \begin{bmatrix} [\mathbf{A}] & [\mathbf{B}] \\ [\mathbf{B}] & [\mathbf{D}] \end{bmatrix}^{-1} \begin{Bmatrix} \mathbf{N} \\ \mathbf{M} \end{Bmatrix} = \begin{bmatrix} [\mathbf{a}] & [\mathbf{b}] \\ [\mathbf{b}] & [\mathbf{d}] \end{bmatrix} \begin{Bmatrix} \mathbf{N} \\ \mathbf{M} \end{Bmatrix} \tag{7.2}$$

where $\boldsymbol{\epsilon^o}$ is the vector of in-plane strains (i.e., ϵ^o_{xx}, ϵ^o_{yy}, and ϵ^o_{xy}) at the midplane of the laminate, and $\boldsymbol{\kappa}$ is the vector of in-plane curvatures (i.e., κ_{xx}, κ_{yy}, and κ_{xy}). The terms of the **A**, **B**, and **D** matrices for each laminate are determined via CLPT and are grouped into a single matrix referred to as the stiffness matrix (**ABD** matrix). The compliance matrix (**abd** matrix) is then determined from the inverse of the stiffness matrix, with the constitutive relation shown in compliance form in Equation 7.2. Expanding Equation 7.2 results in six equations:

$$\begin{Bmatrix} \epsilon^o_{xx} \\ \epsilon^o_{yy} \\ \epsilon^o_{xy} \\ \kappa_{xx} \\ \kappa_{yy} \\ \kappa_{xy} \end{Bmatrix} = \begin{bmatrix} a_{11} & a_{12} & 0 & 0 & 0 & b_{16} \\ a_{12} & a_{22} & 0 & 0 & 0 & b_{26} \\ 0 & 0 & a_{66} & b_{16} & b_{26} & 0 \\ 0 & 0 & b_{16} & d_{11} & d_{12} & 0 \\ 0 & 0 & b_{26} & d_{12} & d_{22} & 0 \\ b_{16} & b_{26} & 0 & 0 & 0 & d_{66} \end{bmatrix} \begin{Bmatrix} N_{xx} \\ N_{yy} \\ N_{xy} \\ M_{xx} \\ M_{yy} \\ M_{xy} \end{Bmatrix} \tag{7.3}$$

For each of the laminates of the double-edge-notched specimen, the non-zero components of the compliance matrix are given in Tables 7.10, 7.11, and 7.12.

The terms of $\boldsymbol{A}$ are dependent on the angle and thickness of each ply, and are independent of the through-thickness location of the plies, as shown in:

$$A_{ij} = \sum_{k=1}^{N} \left[\bar{Q}_{ij}\right]_k t_k \tag{7.4}$$

Table 7.10 Compliance terms of $\boldsymbol{a}$ for the double-edge-notched specimens (laminates of $[\theta/-\theta]_{16T}$ or $[\theta_4/-\theta_4]_{4T}$)

Laminate Angle, θ	**Normalized Effective Ply Thickness**	$\mathbf{a_{11}}$ $\left[10^{-12}\frac{m}{N}\right]$	$\mathbf{a_{22}}$ $\left[10^{-12}\frac{m}{N}\right]$	$\mathbf{a_{66}}$ $\left[10^{-12}\frac{m}{N}\right]$	$\mathbf{a_{12}}$ $\left[10^{-12}\frac{m}{N}\right]$
15°	1	2.03	21.69	16.31	-1.75
	4	2.06	21.70	16.66	-1.73
30°	1	4.12	16.99	8.10	-4.87
	4	4.18	17.02	8.36	-4.83
60°	1	16.99	4.12	8.10	-4.87
	4	17.00	4.18	8.36	-4.83
75°	1	21.69	2.03	16.31	-1.75
	4	21.70	2.06	16.66	-1.73

Table 7.11 Compliance terms of $\boldsymbol{b}$ for the double-edge-notched specimens (laminates of $[\theta/-\theta]_{16T}$ or $[\theta_4/-\theta_4]_{4T}$)

Laminate Angle, θ	**Normalized Effective Ply Thickness**	**Effective Number of Plies**	$\mathbf{b_{16}}$ $\left[10^{-12}\frac{m}{N\cdot m}\right]$	$\mathbf{b_{26}}$ $\left[10^{-12}\frac{m}{N\cdot m}\right]$
15°	1	32	0.16	0.09
	4	8	0.66	0.36
30°	1	32	0.14	0.10
	4	8	0.59	0.42
60°	1	32	0.10	0.14
	4	8	0.42	0.59
75°	1	32	0.09	0.16
	4	8	0.36	0.66

Table 7.12 Compliance terms of $\boldsymbol{d}$ for the double-edge-notched specimens (laminates of $[\theta/-\theta]_{16T}$ or $[\theta_4/-\theta_4]_{4T}$)

Laminate Angle, θ	**Normalized Effective Ply Thickness**	$\mathbf{d_{11}}$ $\left[10^{-12}\frac{m}{N\cdot m^2}\right]$	$\mathbf{d_{22}}$ $\left[10^{-12}\frac{m}{N\cdot m^2}\right]$	$\mathbf{d_{66}}$ $\left[10^{-12}\frac{m}{N\cdot m^2}\right]$	$\mathbf{d_{12}}$ $\left[10^{-12}\frac{m}{N\cdot m^2}\right]$
15°	1	1.38	14.75	11.10	-1.19
	4	1.40	14.76	11.33	-1.18
30°	1	2.81	11.56	5.51	-3.31
	4	2.84	11.58	5.69	-3.28
60°	1	11.56	2.81	5.51	-3.31
	4	11.58	2.84	5.69	-3.28
75°	1	14.75	1.38	11.10	-1.19
	4	14.76	1.40	11.33	-1.18

In this expression, $\bar{Q}_{ij}$ are the transformed reduced stiffnesses for the kth ply for a plane stress state in the x-y plane, with the transformed coordinates aligned with the laminate axes. In addition, t_k is the thickness of the kth ply [146]. The terms of $\bar{Q}_{ij}$ are determined from the following equations [146]:

$$\bar{Q}_{11} = \left[Q_{11}cos^4\theta + (2Q_{12} + 4Q_{66})sin^2\theta cos^2\theta + Q_{22}sin^4\theta\right] \tag{7.5a}$$

$$\bar{Q}_{12} = \left[(Q_{11} + Q_{22} - 4Q_{66})sin^2\theta cos^2\theta + Q_{12}(sin^4\theta + cos^4\theta)\right] \tag{7.5b}$$

$$\bar{Q}_{22} = \left[Q_{11}sin^4\theta + (2Q_{12} + 4Q_{66})sin^2\theta cos^2\theta + Q_{22}cos^4\theta\right] \tag{7.5c}$$

$$\bar{Q}_{16} = \left[(Q_{11} - Q_{12} - 2Q_{66})sin\theta cos^3\theta + (Q_{12} - Q_{22} + 2Q_{66})sin^3\theta cos\theta\right] \tag{7.5d}$$

$$\bar{Q}_{26} = \left[(Q_{11} - Q_{12} - 2Q_{66})sin^3\theta cos\theta + (Q_{12} - Q_{22} + 2Q_{66})sin\theta cos^3\theta\right] \tag{7.5e}$$

$$\bar{Q}_{66} = \left[(Q_{11} + Q_{22} - 2Q_{12} - 2Q_{66})sin^2\theta cos^2\theta + Q_{66}(sin^4\theta + cos^4\theta)\right] \tag{7.5f}$$

Here, the Q_{ij} are the reduced stiffnesses for each ply for a plane stress state in the x-y plane, with the coordinates aligned with the ply axes. These reduced stiffnesses are material constants of a ply. The sine and cosine terms in the transformed reduced stiffness equations are even functions for $\bar{Q}_{11}$, $\bar{Q}_{12}$, $\bar{Q}_{22}$, and $\bar{Q}_{66}$, and are odd functions for $\bar{Q}_{16}$ and $\bar{Q}_{26}$. The evenness or oddness of these terms effect the values of the terms of $\boldsymbol{A}$, $\boldsymbol{B}$, and $\boldsymbol{D}$.

The non-zero terms of $\boldsymbol{A}$ for regular antisymmetric angle-ply laminates have the relation:

$$(A_{11}, A_{22}, A_{12}, A_{66}) = (t)\left(\bar{Q}_{11}, \bar{Q}_{22}, \bar{Q}_{12}, \bar{Q}_{66}\right) \tag{7.6}$$

Here, t is the total laminate thickness which is the same for both laminate configurations. Thus, as indicated in Equation 7.6, the terms of $\boldsymbol{A}$ are independent of the normalized effective-ply thickness, and are thus the same for the single-ply and four-ply effective ply thickness laminates for a given laminate angle. The differences observed for a given laminate angle in Table 7.10 are attributed to computer round-off

error.

For a general laminate, the terms of $\boldsymbol{D}$ are dependent on the angle, thickness, and through-thickness location of each ply, as shown in:

$$D_{ij} = \sum_{k=1}^{N} \left[\bar{Q}_{ij}\right]_k \left(t_k \bar{z}_k^2 + \frac{t_k^3}{12}\right) \tag{7.7}$$

Here, $\bar{z}_k$ is the distance from the midplane of the laminate to the centroid of the kth ply [146]. For balanced angle-ply laminates, such as those of the double-edge-notched specimen, the terms of $\boldsymbol{D}$ become independent of the thickness and through-thickness location of each ply (i.e., only dependent on the laminate thickness). Both the ply thickness, t_k, and the distance from the midplane to the centroid of the ply, $\bar{z}_k$, can be related to the total laminate thickness, t. Each ply has the same thickness, equal to the total laminate thickness divided by the total number of plies, t/N. The equation for $\bar{z}_k$ becomes:

$$\bar{z}_k = \frac{t}{N}\left[k - \left(\frac{N+1}{2}\right)\right] \tag{7.8}$$

The non-zero terms of $\boldsymbol{D}$ for regular antisymmetric angle-ply laminates thus have the relation:

$$(D_{11}, D_{22}, D_{12}, D_{66}) = \left(\frac{t^3}{12}\right)\left(\bar{Q}_{11}, \bar{Q}_{22}, \bar{Q}_{12}, \bar{Q}_{66}\right) \tag{7.9}$$

As with the terms of $\boldsymbol{A}$, the terms of $\boldsymbol{D}$ are independent of the normalized effective-ply thickness. They are the same for the single-ply and four-ply effective ply thickness laminates. The variations observed in Table 7.12 are attributed to computer round-off error.

The terms of $\boldsymbol{B}$ are dependent on the angle, thickness, and through-thickness location of each ply via the relation [146]:

$$B_{ij} = \sum_{k=1}^{N} \left[\bar{Q}_{ij}\right]_k t_k \bar{z}_k \tag{7.10}$$

As is done to determine the relations of $\boldsymbol{A}$ and $\boldsymbol{D}$ to laminate terms, the equations relating t_k and $\bar{z}_k$ to the laminate thickness, t, are substituted into Equation 7.10.

In addition, the sign of the term $\left[\bar{Q}_{ij}\right]_k$ matches the sign of the kth ply angle (i.e., the term is positive for plies of positive angles, and negative for plies of negative ply angles). Accounting for this sign change in the summation introduces an inverse dependence of B_{16} and B_{26} on the effective number of plies of the laminate, $\hat{n}$ [147]. This parameter, $\hat{n}$, is equal to 32 for the single-ply effective ply thickness laminate, and to 8 for the four-ply effective ply thickness laminate. The non-zero terms of $\boldsymbol{B}$ for regular antisymmetric angle-ply laminates thus have the relation:

$$(B_{16}, B_{26}) = -\left(\frac{t^2}{2\hat{n}}\right)\left(\bar{Q}_{16}, \bar{Q}_{26}\right) \tag{7.11}$$

As the effective number of plies increases, these terms approach zero. This trend is exhibited in the results of Table 7.11. As indicated, the effective number of plies, $\hat{n}$, is four times greater in the single-ply effective ply thickness laminate than in the four-ply effective ply thickness laminate.

The boundary conditions of the double-edge-notched specimen are specified in Section 7.2.2 as displacement in the x-direction of the positive and negative x-faces, with an enforced zero displacement in the y- and z-directions on these faces. Two cases with different boundary conditions are investigated via the representative laminates in order to assess the overall response. The first case has the same boundary conditions as used in the finite element model of the double-edge-notched specimen. The second case has relaxed boundary conditions that allow displacements in the y- and z-directions of the x-faces. These two cases are investigated analytically via the developed equations in order to validate the results of the finite element model. The geometry of the double-edge-notched specimen introduces effects that cannot be captured via CLPT. These are captured in the finite element model. The actual boundary condition of the region of interest (i.e., the material near the notch tips) falls between the non-relaxed and relaxed boundary conditions of the two cases. This should be shown via the two cases considered.

From plate theory, the tensor of bending moment is defined as:

$$M_{\alpha\beta} = \int_{-\frac{t}{2}}^{\frac{t}{2}} \sigma_{\alpha\beta}(z) z dz \tag{7.12}$$

and the tensor of axial force (membrane force) is defined as:

$$N_{\alpha\beta} = \int_{-\frac{t}{2}}^{\frac{t}{2}} \sigma_{\alpha\beta}(z) dz \tag{7.13}$$

where α and β take values of 1 (x-direction) or 2 (y-direction), t is the thickness of the laminate, and z is the distance in the through-thickness direction from the midplane of the laminate. Given the boundary conditions for both cases, the load N_{yy} and moment M_{yy} are equal to zero, as the y-faces are free edges (i.e., σ_{yy} is equal to zero on these y-faces). Additionally, the bending curvatures, κ_{xx} and κ_{yy}, for both cases are specified as zero in order to match the constraints of the finite element model. This requires the load N_{xy} and moment M_{xx} to both be equal to zero in order to satisfy the bending curvature equations of Equation 7.3. Solving Equation 7.3 for M_{xy} results in a non-zero twisting moment for the first case, due to the enforced zero displacement in the y- and z-directions on the x-faces (i.e., κ_{xy} is specified to be equal to zero). For the second case, M_{xy} is specified as zero. Thus, a non-zero twist (i.e., κ_{xy} is non-zero) develops as the specimen is extended. The midplane strain in the x-direction, ϵ^o_{xx}, for both cases is equal to the applied displacement, Δ, divided by the gage length of the specimen, L_{GAGE}. The applied displacement and gage length is taken to be the same as for the double-edge-notched specimen, listed in Table 7.3. The resulting midplane strain in the x-direction is:

$$\epsilon^o_{xx} = \frac{\Delta}{L_{GAGE}} = 0.01 \tag{7.14}$$

For the two cases, the axial force, N_{xx}, can be determined via the equations contained in Equation 7.3.

Solving for the loading terms of Equation 7.3 in terms of the components of the compliance matrix yields the following relationships. For the first case, enforcing zero

twist (i.e., κ_{xy} equal to zero), a non-zero twisting moment, M_{xy}, is present:

$$N_{xx} = \frac{\Delta}{L_{GAGE}} \frac{d_{66}}{a_{11}d_{66} - b_{16}^2} \tag{7.15a}$$

$$M_{xy} = -\frac{\Delta}{L_{GAGE}} \frac{b_{16}}{a_{11}d_{66} - b_{16}^2} \tag{7.15b}$$

where the calculated values of the compliance terms are listed in Tables 7.10, 7.11, and 7.12. The denominator of both terms has a dependency on the extension-shear term b_{16}, while M_{xy} also has a dependency on b_{16} in the numerator. For the second case, enforcing zero twisting moment, a non-zero twist curvature, κ_{xy}, is present. The axial force and twisting moment are thus:

$$N_{xx} = \frac{\Delta}{L_{GAGE}} \frac{1}{a_{11}} \tag{7.16a}$$

$$M_{xy} = 0 \tag{7.16b}$$

The antisymmetric angle-ply laminates of the double-edge-notched specimen have a non-zero extension-twist term relating the twist curvature, κ_{xy}, to the extensional load, N_{xx}. The twist curvature is also influenced by the resulting twisting moment, M_{xy}, if present. The twist curvature influences the shear strain results via the relation:

$$\epsilon_{xy} = \epsilon_{xy}^{o} + z\kappa_{xy} \tag{7.17}$$

where ϵ_{xy}^{o} is equal to zero and z is the distance in the through-thickness direction from the midplane of the laminate. Therefore, the in-plane shear strain can be calculated as a function of the compliance components and has a linear dependence on the through-thickness location. For the first case, both the midplane shear strain, ϵ_{xy}^{o}, and the twist curvature, κ_{xy}, are zero. This boundary condition develops a twisting moment, M_{xy}, in order to offset the extension-twist coupling of the laminate. For the second case, the twist curvature is non-zero. Substituting κ_{xy} from Equation 7.3, with the loading terms from Equations 7.16a and 7.16b, into Equation 7.17, the analytical in-

plane shear strain, ϵ_{xy}, of a featureless specimen (i.e., without notches) is calculated as a function of the through-thickness location:

$$\epsilon_{xy} = z \frac{\Delta}{L_{GAGE}} \frac{b_{16}}{a_{11}} \tag{7.18}$$

The relations of Equations 7.6, 7.9, and 7.11 are substituted into the **ABD** matrix of Equation 7.2 and the terms of the compliance matrix (**abd** matrix) are determined. Substituting b_{16} and a_{11} into Equation 7.18, the dependence of the shear strain on the effective number of plies is found to be:

$$\epsilon_{xy} = z \frac{\Delta}{L_{GAGE}} \frac{-6\hat{n}\left(\bar{Q}_{12}\bar{Q}_{26} - \bar{Q}_{16}\bar{Q}_{22}\right)}{t\left(\hat{n}^2\bar{Q}_{22}\bar{Q}_{66} - 3\bar{Q}_{26}^2\right)} \tag{7.19}$$

As indicated from Equation 7.17, there is a linear variation of the shear strain through the thickness (z-direction) of the laminate if the twisting curvature is non-zero. In addition, the b_{16}/a_{11} term exhibits two behaviors, depending on the relative values of the $\bar{Q}_{\alpha\beta}$ terms, as indicated in Equation 7.19. When the term $\bar{Q}_{22}\bar{Q}_{66}$ is large compared to the term $\bar{Q}_{26}^2$, the b_{16}/a_{11} term exhibits an inverse relationship with the effective number of plies. When the term $\bar{Q}_{26}^2$ is large compared to $\bar{Q}_{22}\bar{Q}_{66}$, the b_{16}/a_{11} term exhibits a linear relationship with the effective number of plies. The ratio $\bar{Q}_{22}\bar{Q}_{66}/\bar{Q}_{26}^2$ is 12.6, 2.5, 1.5, and 2.1 for the laminates with θ equal to 15°, 30°, 60°, and 75°, respectively. Thus, the b_{16}/a_{11} terms for the laminates considered generally exhibit an inverse relationship with the effective number of plies. These ratios are the same for both the single-ply and four-ply effective ply thickness laminates of a given laminate angle. The other terms of Equation 7.19 are independent of the effective number of plies.

The analytical shear strain, ϵ_{xy}, subjected to the boundary conditions for the second case (i.e., relaxed boundary conditions), at the lower surface (i.e., z equal to $-t/2$) of the eight laminates used in the double-edge-notched specimen are listed in Table 7.13. The variations in the calculated analytical shear strain for a given laminate angle, listed in Table 7.13, exhibit an inverse relation with the effective number of plies, which is equivalent to a linear relation with the normalized effective

Table 7.13 Analytical shear strain at the outer surface of ply 1 for the laminates of the double-edge-notched specimens (laminates of $[\theta/-\theta]_{16T}$ or $[\theta_4/-\theta_4]_{4T}$) for the second case of boundary conditions

Laminate Angle, θ	**Normalized Effective Ply Thickness**	**Effective Number of Plies**	$\epsilon_{\mathbf{xy}}$ $[\mu strain]$
15°	1	32	168
	4	8	675
30°	1	32	73
	4	8	296
60°	1	32	12
	4	8	51
75°	1	32	8
	4	8	35

ply thickness. The analytical results indicate that the extension-twisting terms of the double-edge-notched laminates create a non-zero far-field shear strain if the twisting moment is zero (i.e., the second case), whereas a twisting moment, equal to that given in Equation 7.15b (i.e., the first case), will react the twisting curvature of the laminate and create a zero far-field shear strain. These effects are discussed in the subsequent results.

As with the model of the single-edge-notched specimen, a common feature exhibited in all the strain field results of the double-edge-notched specimen model are the effects of free edges. These effects are observed as discontinuities in the slopes of the isostrain lines (i.e., the isoline is not smooth) near the edges of the specimen. In some results, such as the strain field of ϵ_{11} in the first ply of the laminate with θ equal to 15° shown in Figure 7.52, the free-edge effects are easily identified. In this case, the isostrain lines near the positive and negative x-faces of the specimen, excluding the faces of the notch, clearly exhibit discontinuities at a distance of approximately four ply thicknesses away from the specimen edge. These discontinuities are more distinct in the outer plies of the laminates, becoming more subtle in plies toward the center of the laminate, such as the strain field of ϵ_{11} in the sixteenth ply of the laminate with θ equal to 15° shown in Figure 7.53. For the in-plane results, the distance at which the effect is observed, approximately four ply thicknesses, is consistent across the results of all the strain fields, as well as consistent with the results for the single-edge-notched specimen. The free-edge effects near the edges of the notch are not observed in the in-plane strain results due to the in-plane element lengths at the notch boundaries. Beyond these observations of the free-edge effects, these effects are not further discussed.

The majority of the strain fields of ϵ_{11} for the laminates considered have positive values, as seen in the results for ϵ_{11} for the single-ply effective ply thickness laminate with θ equal to 15° shown in Figure 7.54. As with the in-plane results for the single-edge-notched specimen, the "far-field" (i.e., away from the notch tips) strain fields are independent of the location through the thickness of the laminate for the single-ply effective ply thickness laminates, as shown in the results at plies 1 and 16 for the

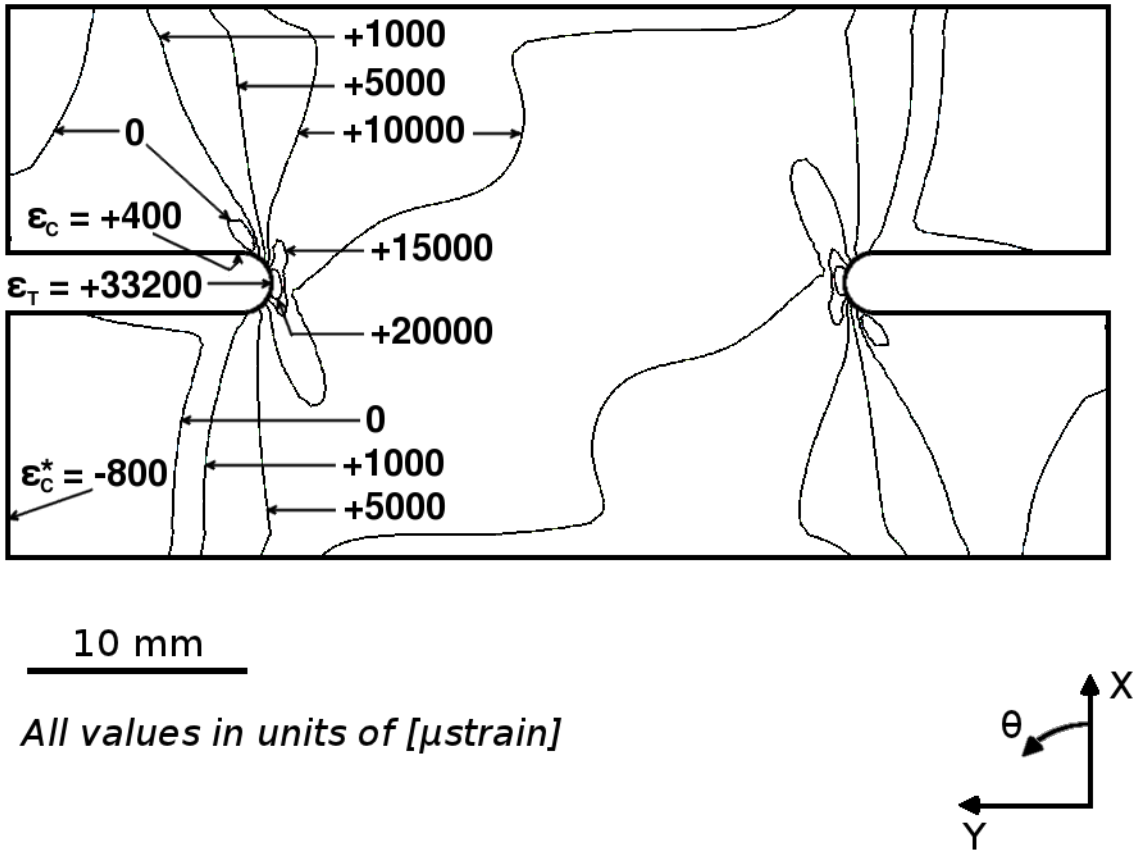

Figure 7.52 Isostrain plot of strain field of ϵ_{11}, in laminate axes, at the midplane of ply 1 (a $+15^\circ$ ply) of the double-edge-notched specimen model for the four-ply effective ply thickness laminate of $[+15_4/-15_4]_{4T}$.

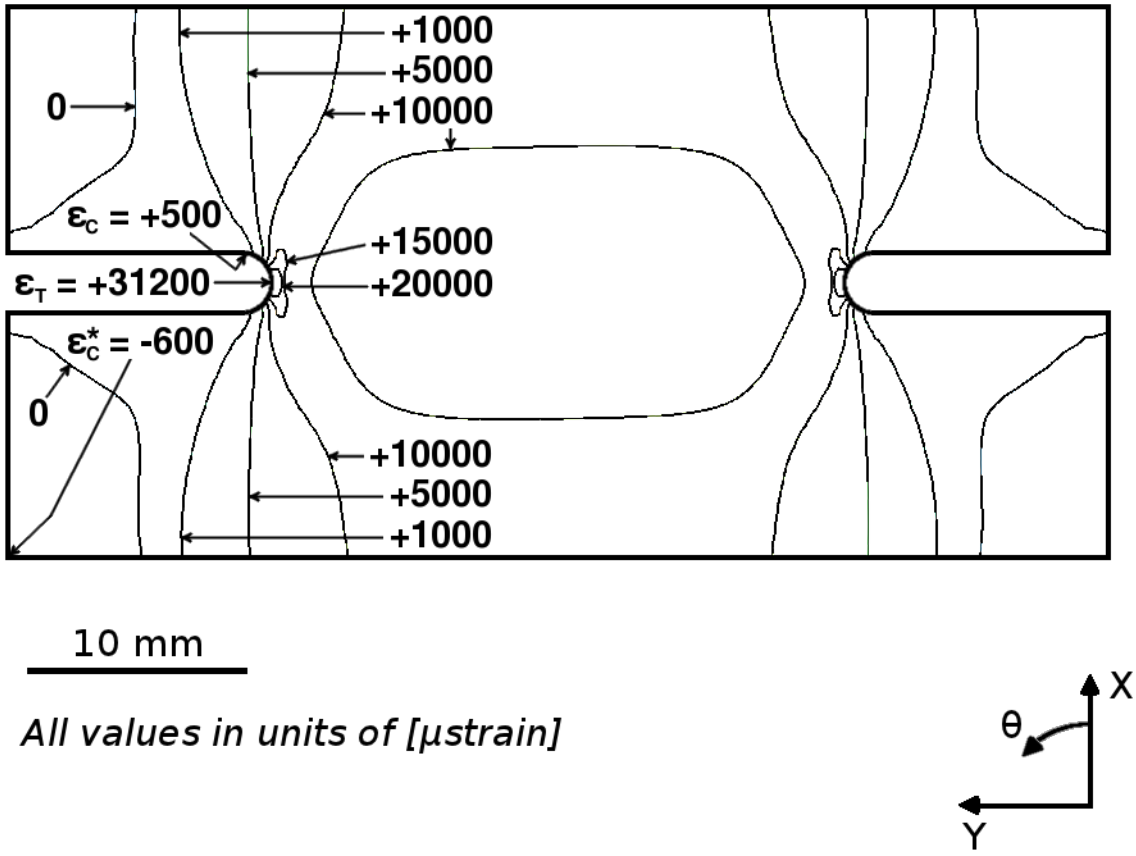

Figure 7.53 Isostrain plot of strain field of ϵ_{11}, in laminate axes, at the midplane of ply 16 (a $-15°$ ply) of the double-edge-notched specimen model for the four-ply effective ply thickness laminate of $[+15_4/-15_4]_{4T}$.

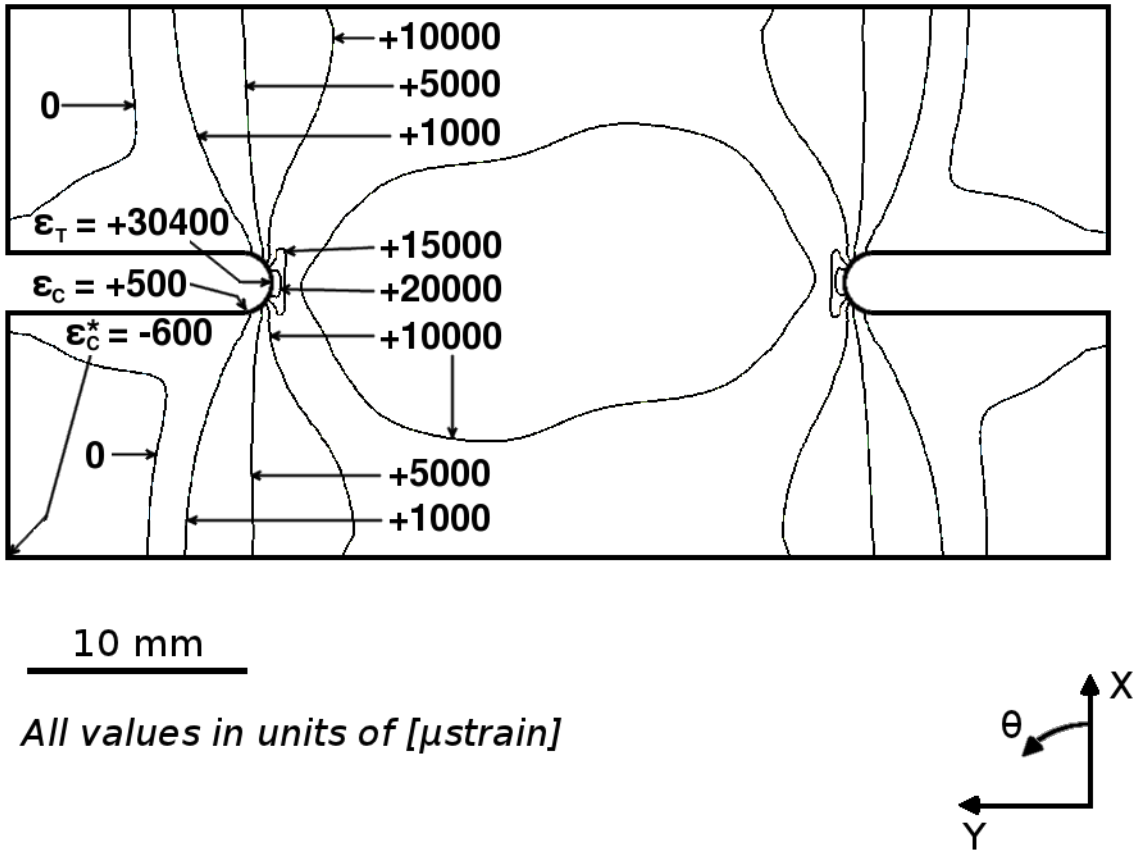

Figure 7.54 Isostrain plot of strain field of ϵ_{11}, in laminate axes, at the midplane of ply 1 (a $+15^\circ$ ply) of the double-edge-notched specimen model for the single-ply effective ply thickness laminate of $[+15/-15]_{16T}$.

single-ply effective ply thickness laminate with θ equal to 15° shown in Figures 7.54 and 7.55. The laminates with four-ply effective ply thickness exhibit greater through-thickness dependency of the "local" (i.e., near the notch tips) strain fields, as shown in the results for the four-ply effective ply thickness laminate with θ equal to 15° shown in Figures 7.52 and 7.53. The strain results at the midplane of ply 16 of the single- and four-ply effective ply thickness laminates are identical, with the exception of the peak values which can also be considered identical given model error. The differences in the results at the midplane of ply 1 indicate a dependency on the effective ply thickness of the laminate. These effects are related to the non-zero extension-twist terms of the antisymmetric laminate of the double-edge-notched specimens. As indicated in Table 7.13, the analytical shear strain at ply 1 is four times greater in the single-ply effective ply thickness laminate than in the four-ply effective ply thickness laminate. The non-zero extension-twist coupling results in asymmetric strain fields about the y-z plane (with the axes positioned as shown in Figure 7.6). The magnitude of asymmetry is observed to be dependent on the distance of a ply from the midplane of the laminate, with no asymmetry (i.e., symmetric isolines) observed in the results of the center ply, as shown in Figure 7.53. As indicated in Equation 7.18, there is no influence of the extension-twist coupling at the midplane (i.e., z equal to zero) of the laminate. In addition to these effects, only slight changes in the strain fields are observed at the notch tips between positive and negative angle plies for both the single-ply and four-ply effective ply thickness laminates. The results for ϵ_{11} strain fields for the other laminates are shown in Figures B.21 through B.26, included in Appendix B.2.

The locations and values of the peak maximum (ϵ_T) and minimum (ϵ_C) 'local' in-plane strains for each laminate are listed in Tables 7.14. The locations are given in polar coordinates, with the origin concentric with the center of the left semi-circular notch tip, as shown in Figure 7.56. The origin of the x-y coordinate system, defined in previous chapters, is located at the midpoint between the two notch tips. Thus, the origin of the polar coordinate system is at the coordinates of x equal to 0 and y equal to $10.3r_o$ (equal to 14.4 mm). The radial distance, r, is normalized by the notch tip

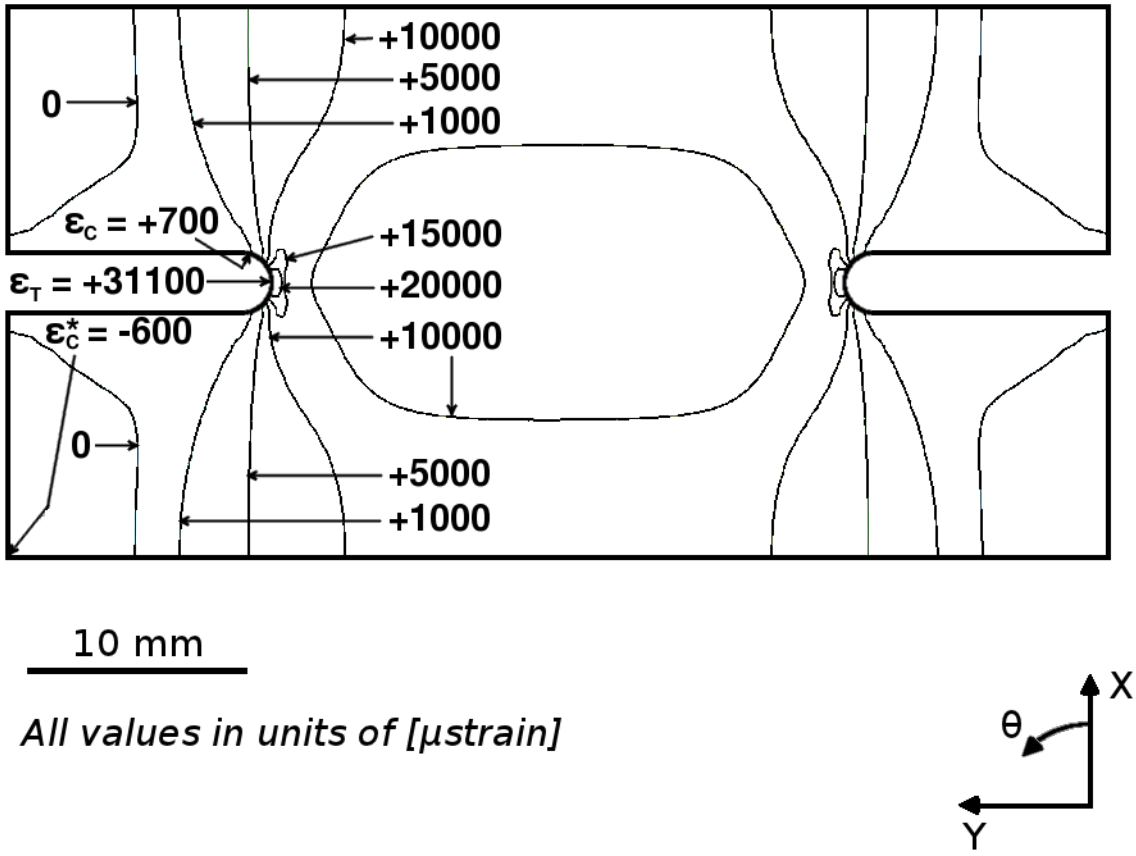

Figure 7.55 Isostrain plot of strain field of ϵ_{11}, in laminate axes, at the midplane of ply 16 (a $-15°$ ply) of the double-edge-notched specimen model for the single-ply effective ply thickness laminate of $[+15/-15]_{16T}$.

Table 7.14 Locations and values of maximum and minimum ϵ_{11} for the double-edge-notched specimens (laminates of $[\theta/-\theta]_{16T}$ or $[\theta_4/-\theta_4]_{4T}$)

Strain Component	**Value Considered**[a]	**Laminate Angle, θ**	**Nominal Effective Ply Thickness**	**Value [μstrain]**	$\frac{\mathbf{r}}{\mathbf{r_o}}$	ϕ **[degrees]**
ϵ_{11}	ϵ_T	15°	1	+30400	1	-90
			4	+33200	1	-90
		30°	1	+30200	1	-90
			4	+32300	1	-83
		60°	1	+26600	1	-83
			4	+27400	1	-76
		75°	1	+26500	1	-90
			4	+26900	1	-83
	ϵ_C	15°	1	+500	1	-173
			4	-700	1.5	-7
		30°	1	+800	1	-173
			4	-100	1.5	0
		60°	1	-700	1	-180
			4	-200	1	0
		75°	1	-200	1.1	+159
			4	+100	1.3	+38

[a] ϵ_T = Maximum
ϵ_C = Minimum

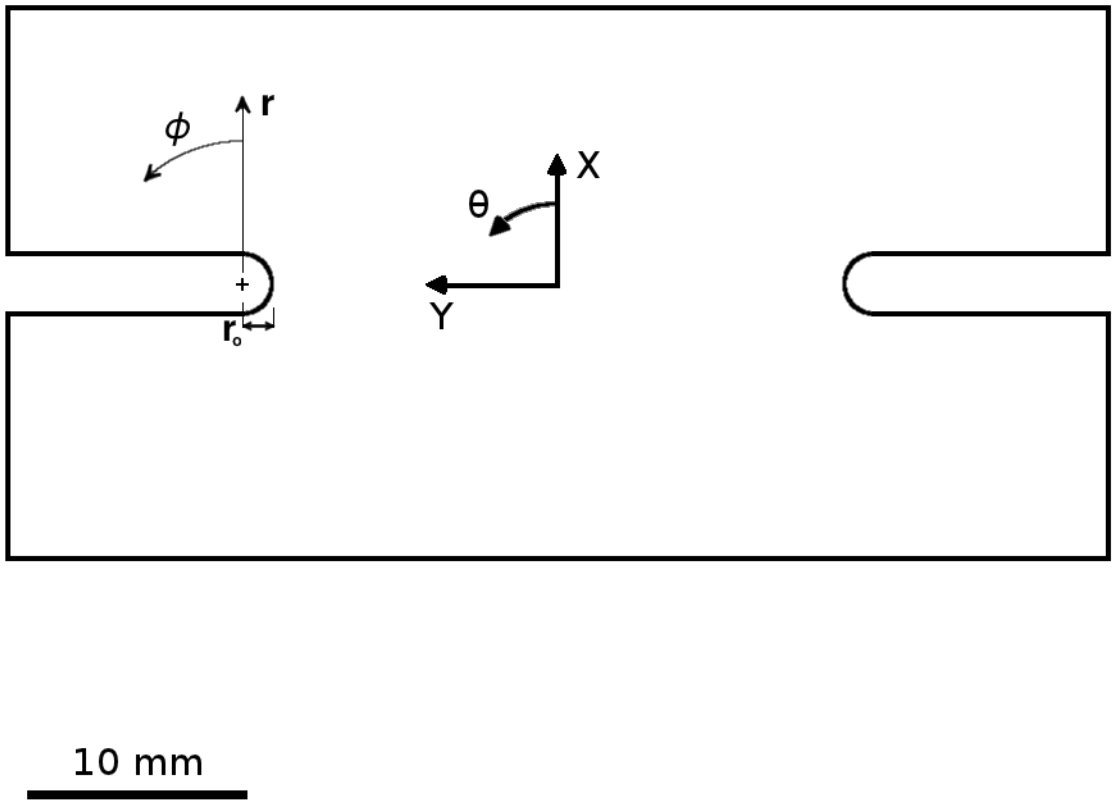

Figure 7.56 Illustration of the polar coordinate used for the results in Tables 7.14 through 7.21.

radius, r_o, and thus is expressed in the number of notch radii from the origin. This gives the boundary of the left notch as r/r_o equal to 1. The angle, ϕ, is measured positive counterclockwise from the positive x direction and expressed in degrees. In all but six cases, the local maximum (ϵ_T) and local minimum (ϵ_C) occur at the notch boundary (i.e., r/r_o equal to 1).

The results for ϵ_{11} exhibit a transition region, located above and below the notch tips, similar to the transition region observed in the results for the single-edge-notched specimen. The transition region for ϵ_{11} is clearly seen in Figure 7.54 for the single-ply effective ply thickness laminate with θ equal to 15°. Within this region, the strain transitions from the 1% strain of the "unnotched" region to the near zero strain of the "notched" region. The largest gradient (i.e., isostrain lines closest together) observed in this transition region occurs for the single-ply effective ply thickness laminate with θ equal to 15°. As the ply angle of the laminate increases, the gradients in the transition region decrease (i.e., the isostrain lines become spaced farther apart). This is the same trend observed in the results for the single-edge-notched specimen, which has a symmetric laminate with no extension-twist coupling. The gradients of the four-ply effective ply thickness laminates follow the same trend (i.e., decreasing gradients with increasing ply angle) and are only slightly less than the gradients observed in the single-ply effective ply thickness laminates, for cases of the same laminate angles.

As with the single-edge-notched specimen, the value of ϵ_{11} in the "unnotched" (i.e., in the section between the notch tips) section is roughly +1% strain (+10,000 μstrain), a value consistent with the applied displacement boundary condition, at a distance away from each notch tip. This distance is used to define a characteristic length associated with the structural feature. The values of strain along a path, aligned with the y-axis (i.e., ϕ equal to $-90°$), from the left notch tip (r_o) to the right notch tip ($18.6r_o$) of the specimen is measured for each laminate. The characteristic length is defined as the number of notch radii away from the left notch tip (not the origin) that the strain field returns to within a certain percentage of the "unnotched" (i.e., far field) solution. As with the single-edge-notched specimen, two percentages, 10% and 5%, are selected in order to develop the process. This may require refinement as additional

analyses are conducted beyond this work. Associated with these percentages are two characteristic lengths, l_{10} and l_5, defined as the distance from the notch tip (i.e., the point $(r_o, -90°)$ in the polar coordinate system of Figure 7.56) to the point along ϕ equal to $-90°$ where the strain field returns to within 10% and 5%, respectively, of the "unnotched" solution.

These characteristic lengths allow measurement of the influence of the structural feature as a function of the laminate, and hence the extension-twist coupling of the laminate, including influences of the effective ply thickness. The characteristic lengths resulting from this definition for the in-plane strain components are listed in Table 7.15. It is observed that the effective ply thickness has negligible effect for the laminates with θ equal to 15° and 30°. In these laminates, the l_5 characteristic length is a tenth of a radius larger for the four-ply effective ply thickness laminate. The characteristic lengths for the laminate with θ equal to 30° are much larger than those for the laminate with θ equal to 15°. For the higher angle laminates with θ equal to 60° and 75°, the far-field strain was not observed before reaching the centerline $(9.3r_o)$ of the specimen characteristic and no characteristic length is defined.

As was done for the single-edge-notched specimen, values of the strain fields along "arc paths" defined in the polar coordinate system are plotted. The arc paths are defined as the number, n, of radii away from the free edge of the notch tip:

$$n = \frac{r - r_o}{r_o}$$

The arc paths for n equal to 1 through 12 are illustrated in Figure 7.57. In addition to the arc paths shown in this figure, paths are also defined for n equal to 0, 0.125, 0.25, and 0.5, but are not shown due to the figure scale. Note that the path for n equal to 12 extends beyond the boundaries of the specimen. This maintains a consistent polar angle sweep (i.e., ϕ goes from 0° to $-180°$) for each path. However, there are no stress or strain results beyond the specimen boundary. The points beyond the specimen boundary of the arc path for n equal to 12 are ignored.

Values of strain are presented along these arc paths versus an angle, ψ, as de-

Table 7.15 Normalized characteristic lengths[a] of the in-plane strains for the double-edge-notched specimen laminates

Strain Component	**Laminate Angle, θ**	**Normalized Effective Ply Thickness**	**Far-Field Strain [μstrain]**	$\frac{l_{10}}{r_o}$	$\frac{l_5}{r_o}$
ϵ_{11}	15°	1	+10000	0.7	4.8
		4		0.7	4.9
	30°	1	+10000	5.4	7.3
		4		5.4	7.4
	60°	1	+10000	b	b
		4		b	b
	75°	1	+10000	b	b
		4		b	b
ϵ_{22}	15°	1	-8600	6.8	8.8
		4		7.4	b
	30°	1	-11800	6.2	7.1
		4		6.6	7.6
	60°	1	-2900	b	b
		4		b	b
	75°	1	-800	b	b
		4		b	b
ϵ_{12}	15°	1	0	0.4	1.3
		4		4.5	b
	30°	1	0	0.8	1.8
		4		b	b
	60°	1	0	2.1	5.4
		4		b	b
	75°	1	0	b	b
		4		b	b

[a] l_{10} = defined characteristic length for strain value to return to within 10% of far-field strain.
l_5 = defined characteristic length for strain value to return to within 5% of far-field strain.
[b] Far-field strain was not reached before centerline of specimen.

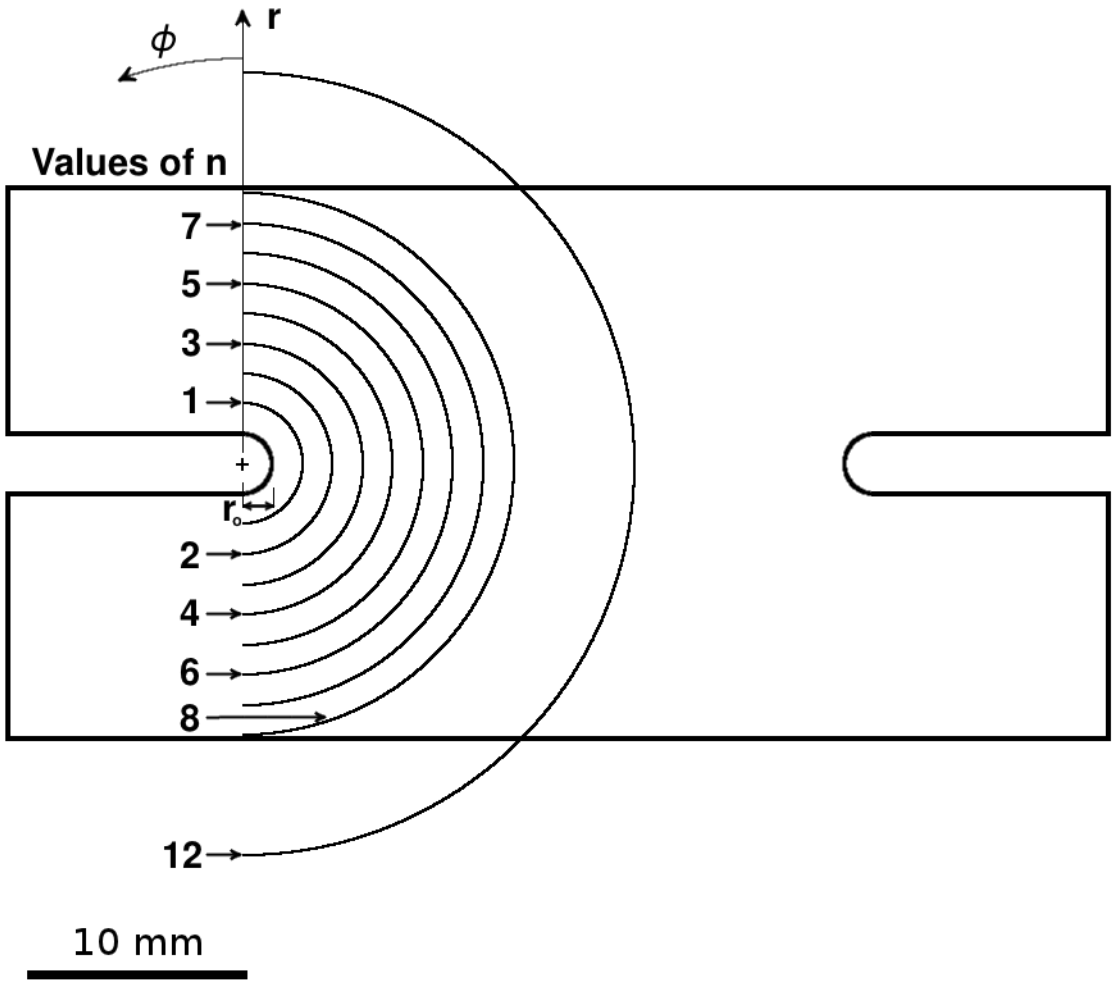

Figure 7.57 Arc path locations defined for the double-edge-notched specimen.

fined in an offset polar coordinate system, as is done in Section 7.3.1 for the single-edge-notched specimen. This offset system, (r', ψ), and the original polar coordinate system, (r, ϕ), are shown in Figure 7.58. The offset system has its origin displaced a distance equal to the notch radius, r_o, along ϕ equal to $-90°$ in the original polar coordinate system. The angle ψ is thus measured from the tip of the notch. As with the angle ϕ, ψ is measured positive counterclockwise from the positive x-direction. Radial paths extending from both polar coordinate origins to an arbitrary point along an arc path are shown in the figure. In the offset polar coordinate system, the radial distance from the origin to points along the arc path is a function of the angle ψ. This is due to the arc paths being defined with a constant radius in the original polar coordinate system. In the offset system, the radial distance must vary as a function of ψ in order to remain on the arc paths. In addition, the values of the angles over which ψ varies for each arc path (i.e., starting and ending sweep angles) are a function of the distance away from the notch edge of the arc path. Transformation equations between the two polar coordinate systems are found via geometric relations. Note, due to the nature of the geometric relationship, the transformation of the data for n equal to 0 results in a discontinuity in these plots for values of ψ from $0°$ to $-180°$.

The values of ϵ_{11} along the arc paths versus the polar coordinate angle, ψ, are plotted for the single-ply and four-ply effective ply thickness laminates with θ equal to $15°$ in Figures 7.59 and 7.60. For the other laminates, these plots are shown in Figures B.27 through B.32, included in Appendix B.2. The peak values along each path are associated with the laminate fiber angle, θ, as observed in the single-edge-notched specimen. As with the results of the single-edge-notched specimen, two peaks are observed to form as the distance from the notch tip increases, with the distance at which this first occurs depending on the laminate angle θ. In the laminate with θ equal to $15°$, these peaks are first observed in the path for n equal to 0.5. As the laminate angle increases, the radial distance away from the notch tip at which these peaks are first observed also increase. In each of the laminates, these peaks occur close to the fiber angles, i.e., ψ close to θ. Also observed in these figures is a slight skewness of the plots. This skewness is more easily observed in the higher angle laminates with

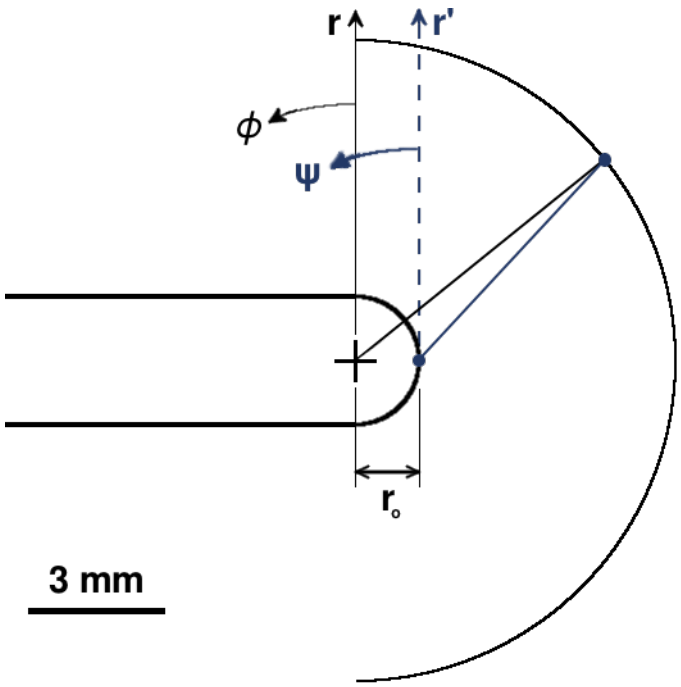

Figure 7.58 Illustration of the offset polar coordinate used for the plots of strain values along arc paths in the double-edge-notched specimens.

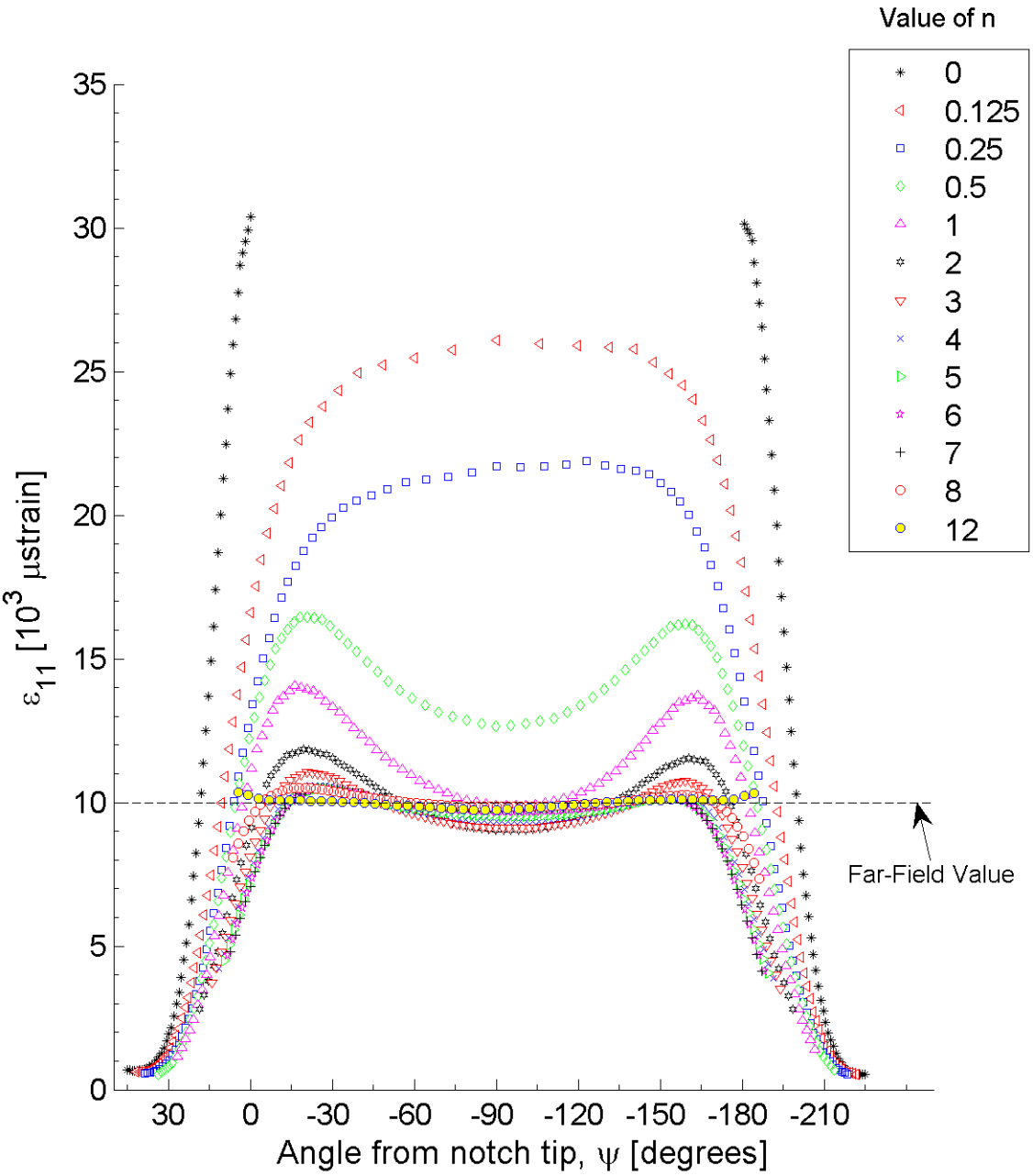

Figure 7.59 Plot of ϵ_{11}, in laminate axes, along arc paths at the midplane of ply 1 (a $+15^\circ$ ply) of the double-edge-notched specimen model for the laminate of $[+15/-15]_{16T}$.

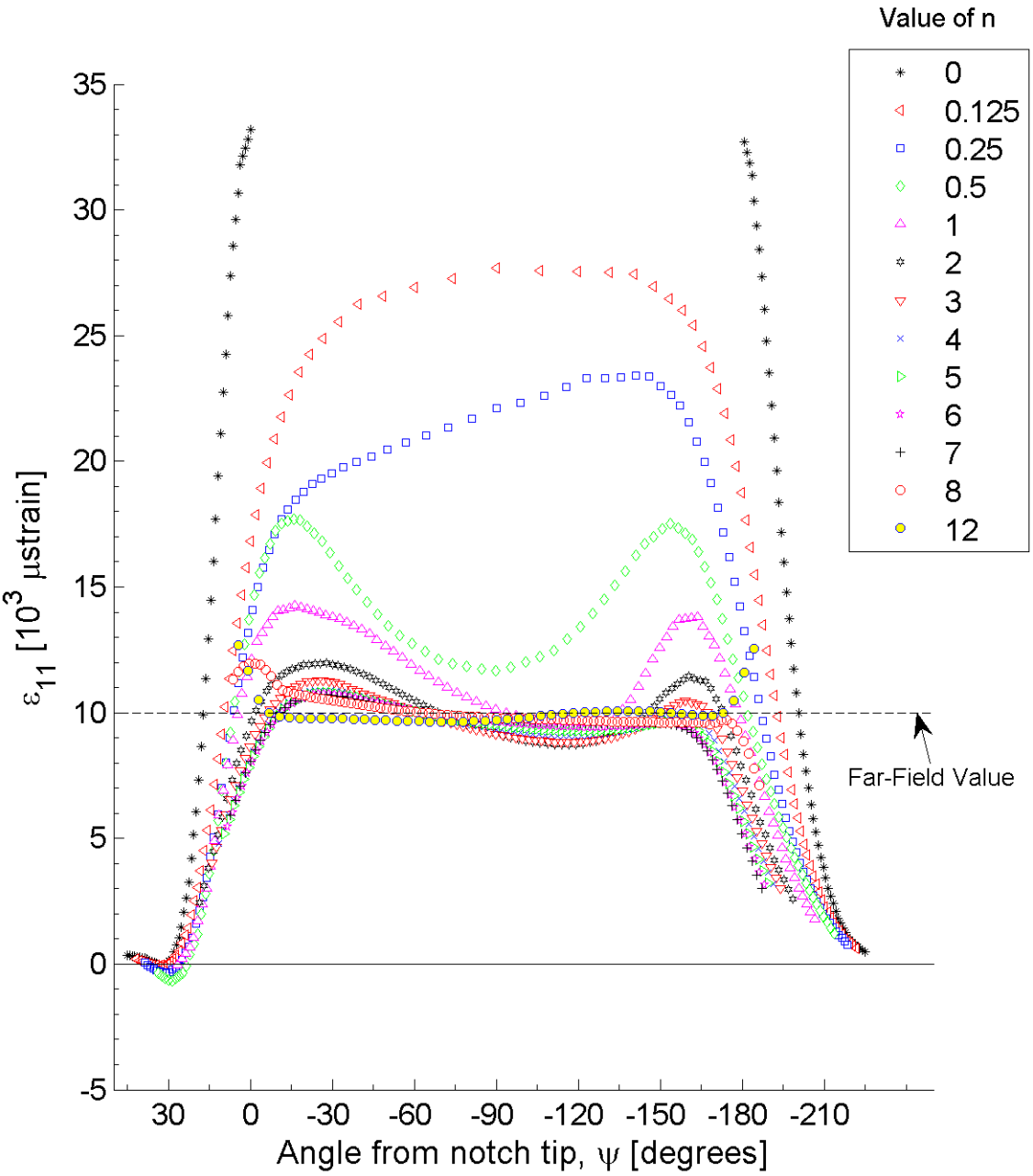

Figure 7.60 Plot of ϵ_{11}, in laminate axes, along arc paths at the midplane of ply 1 (a $+15°$ ply) of the double-edge-notched specimen model for the laminate of $[+15_4/-15_4]_{4T}$.

four-ply effective ply thickness. As with the results of the single-edge-notched, these plots flip about ψ equal to $-90°$ in negative angle plies.

As was done for the single-edge-notched specimen results, the gradients of the values of ϵ_{11} between neighboring arc paths are given in Tables 7.16 and 7.17 for ψ equal to $-90°$, the same angle used to characterize the characteristic lengths, l_{10} and l_5. It is observed that these gradients are dependent on the laminate angle, θ, as well as the effective ply thickness and hence the magnitude of the extension-twist coefficients, as listed in Table 7.11. For the lower angle laminates with θ equal to 15° and 30°, the value of ϵ_{11} is observed to have a negative gradient from the notch surface to the arc path of n equal to 2. The gradients between arc paths farther out have small positive values for both the single-ply and four-ply effective ply thickness laminates. For the higher angle laminates with θ equal to 60° and 75°, the value of ϵ_{11} is observed to have a negative gradient farther into the specimen, with negative gradients observed to the arc path of n equal to 7 for θ equal to 60° and to the arc path of n equal 8 for θ equal to 75°. The gradients between arc paths farther out are zero for both the single-ply and four-ply effective ply thickness laminates. Comparing the magnitudes of the gradients observed between the single-ply and four-ply effective ply thickness laminates, larger gradients are consistently observed in the four-ply effective ply thickness laminates, which have smaller extension-twist coupling terms than the single-ply effective ply thickness laminates, as listed in Table 7.11. In both the single-ply and four-ply effective ply thickness laminates, the maximum gradient occurs between the arc paths of n equal to 0.25-0.5, with the exception of the four-ply effective ply thickness laminate for θ equal to 15°, where the maximum gradient is observed between the arc paths of n equal to 0.125-0.25.

The majority of the strain fields of ϵ_{22} for the laminates considered have negative values, as shown in the results for ϵ_{22} for the single-ply and four-ply effective ply thickness laminates with θ equal to 15° in Figures 7.61 and 7.62. For the laminates with θ equal to 30°, 60°, and 75°, the strain fields of ϵ_{22} are shown in Figures B.33 through B.38, included in Appendix B.2. The peak maximum and minimum values are indicated in these figures, with the values and locations for each laminate listed

Table 7.16 Gradients of the values of ϵ_{11} between 'arc paths' for ψ equal to -90° for the double-edge-notched specimen with single-ply effective ply thickness laminates ($[\theta/-\theta]_{16T}$)

Arc Paths (n values)	**Gradient** $[\mu\epsilon/mm]$			
	Laminate Angle, θ			
	$\mathbf{15^\circ}$	$\mathbf{30^\circ}$	$\mathbf{60^\circ}$	$\mathbf{75^\circ}$
0 - 0.125	-24600	-17000	-4500	-5600
0.125 - 0.25	-25100	-18300	-5100	-6100
0.25 - 0.5	-25800	-26100	-10200	-10100
0.5 - 1	-3900	-7500	-8900	-6400
1 - 2	-600	-900	-3800	-3100
2 - 3	+100	0	-1000	-1200
3 - 4	+200	+200	-400	-600
4 - 5	+100	+200	-200	-300
5 - 6	+100	+200	-100	-200
6 - 7	+100	+200	-100	-100
7 - 8	0	+100	0	-100
8 - 12	0	-100	0	0

Table 7.17 Gradients of the values of ϵ_{11} between 'arc paths' for ψ equal to -90° for the double-edge-notched specimen four-ply effective ply thickness laminates ($[\theta_4/-\theta_4]_{4T}$)

Arc Paths (n values)	**Gradient** $[\mu\epsilon/mm]$			
	Laminate Angle, θ			
	15°	**30°**	**60°**	**75°**
0 - 0.125	-31400	-18000	-6300	-7300
0.125 - 0.25	-31900	-19600	-6900	-7800
0.25 - 0.5	-29800	-28300	-10800	-11200
0.5 - 1	-2200	-6100	-7300	-5700
1 - 2	-700	-1000	-3500	-2800
2 - 3	0	-100	-1000	-1200
3 - 4	+100	+100	-500	-600
4 - 5	+100	+200	-200	-400
5 - 6	+100	+200	-100	-200
6 - 7	+100	+200	-100	-100
7 - 8	0	+100	0	-100
8 - 12	0	0	0	0

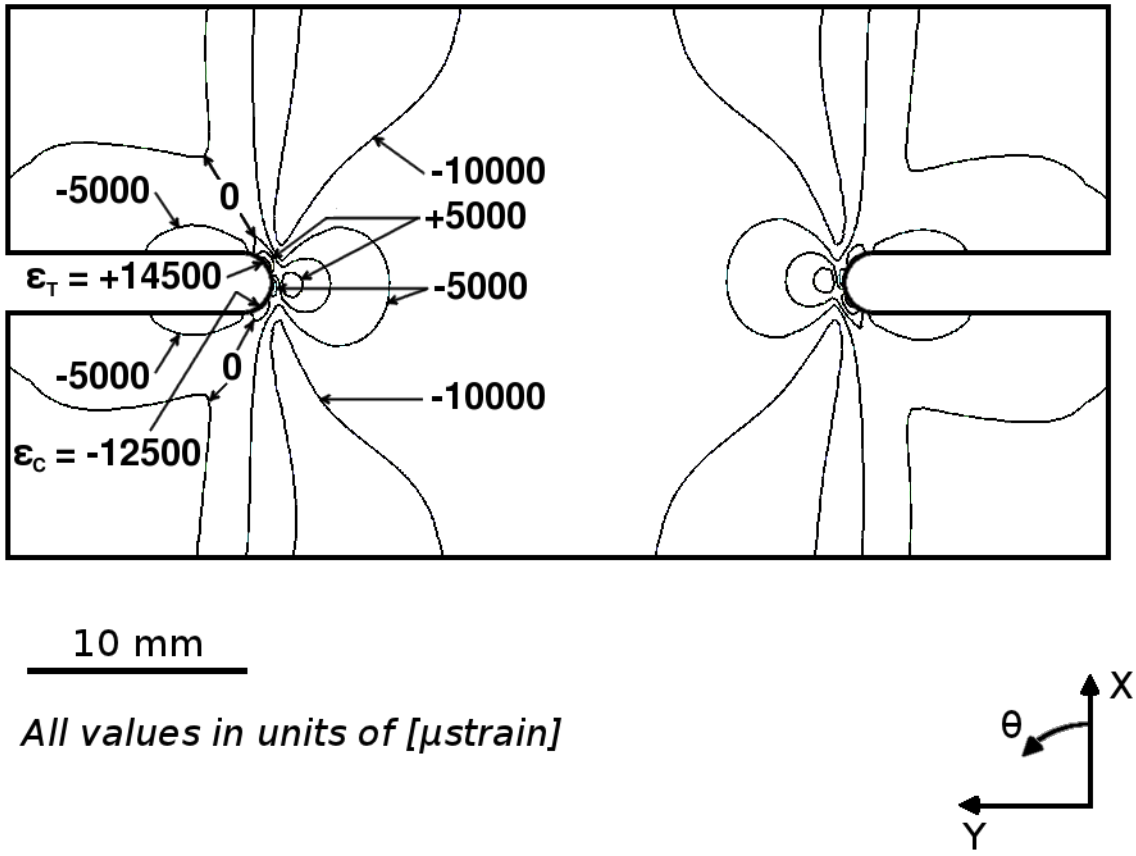

Figure 7.61 Isostrain plot of strain field of ϵ_{22}, in laminate axes, at the midplane of ply 1 (a $+15^\circ$ ply) of the double-edge-notched specimen model for the single-ply effective ply thickness laminate of $[+15/-15]_{16T}$.

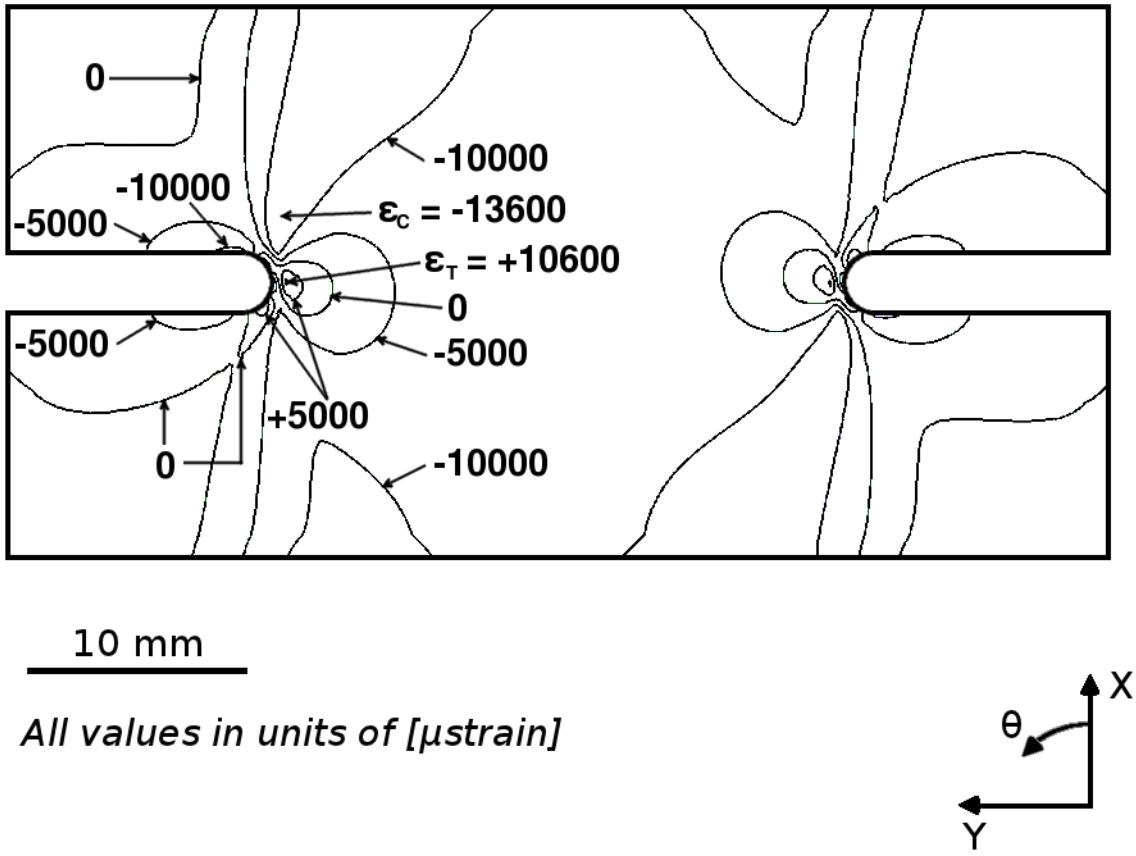

Figure 7.62 Isostrain plot of strain field of ϵ_{22}, in laminate axes, at the midplane of ply 1 (a $+15^\circ$ ply) of the double-edge-notched specimen model for the four-ply effective ply thickness laminate of $[+15_4/-15_4]_{4T}$.

in Table 7.18. As in the case of the strain fields of ϵ_{11}, these peak maximum and minimum values occur along the notch edge, at values of r/r_o equal to 1, with an exception occurring for the four-ply effective ply thickness laminate with θ equal to 15°. For this case, both the maximum and minimum values occur at 1.5 and 1.8 notch radii, respectively. The locations of these peak values in the polar coordinate angle ϕ are observed to be dependent on the laminate fiber angle, as indicated by the results in Table 7.18. These locations do not match the corresponding peak maximum and minimum locations for ϵ_{11}.

The strain fields of ϵ_{22} exhibit asymmetry about the y-z plane, similar to the asymmetry observed in the strain fields of ϵ_{11}. For example, the upper (positive x-direction from the notch) -10000 μstrain isoline in Figure 7.62 encompasses roughly twice the region compared to the lower isoline of the same value. In addition, the upper -10000 μstrain isoline comes within half a notch radii of the tip of the notch while the lower isoline is roughly 5 notch radii away from the notch at its nearest point. The asymmetry is much less obvious in the single-ply effective ply thickness laminates. However, a very slight asymmetry about the y-z plane is still observed for these laminates. This asymmetry becomes less noticeable in the region near the notch tip as the laminate angle increases. In the higher angle laminates with θ equal to 60° and 75°, the strain fields are uniform except within a notch radius of the notch, where the isolines exhibit asymmetry. As with the results of ϵ_{11}, the asymmetry is observed to be dependent on the through-thickness location of a ply.

Very little change is exhibited in the strain fields of ϵ_{22} when varying between positive and negative plies. Generally, the 'far-field' (at a distance greater than 1 notch radius from the notch tip) isostrain lines are consistent for both positive and negative plies of a laminate, as would be predicted from LPT. In the 'near-field' (at a distance less than 1 notch radius from the notch tip), a slight variation occurs. These variations are likely due to free-edge effects, as discussed at the beginning of this section. As in the case of the strain fields of ϵ_{11}, the direction of the skewing of isolines flips for positive and negative plies.

In the "unnotched" region of all the laminates, the observed values of the strain

Table 7.18 Locations and values of maximum and minimum ϵ_{22} for the double-edge-notched specimens (laminates of $[\theta/-\theta]_{16T}$ or $[\theta_4/-\theta_4]_{4T}$)

Strain Component	**Value Considered**[a]	**Laminate Angle, θ**	**Nominal Effective Ply Thickness**	**Value [μstrain]**	$\frac{\mathbf{r}}{\mathbf{r_o}}$	**ϕ [degrees]**
ϵ_{22}	ϵ_T	15°	1	+14400	1	-129
			4	+10600	1.5	-90
		30°	1	+5900	1	-39
			4	+3500	1	-147
		60°	1	+2900	1	-160
			4	+4300	1	-129
		75°	1	+2500	1	-160
			4	+3600	1	-135
	ϵ_C	15°	1	-12500	1	-83
			4	-13600	1.8	-141
		30°	1	-26800	1	-90
			4	-18400	1	-83
		60°	1	-6900	1	-83
			4	-9500	1	-63
		75°	1	-1800	1	-83
			4	-4900	1	-57

[a] ϵ_T = Maximum
ϵ_C = Minimum

fields for ϵ_{22} are on the order of the expected Poisson's effect. For example, the Poisson's ratio for the laminate with θ equal to 15°, given in Table 7.4, is 0.86. The majority of the "unnotched" region of the laminate, shown in Figure 7.61, has a value between -10000 μstrain and -5000 μstrain. Had the specimen been featureless (i.e., without a notch), the expected value of ϵ_{22} would be -8600 μstrain due to Poisson's effects. However, the effect of the notch and the given loading creates gradients within the "unnotched" region near the notch tip. As with the results for ϵ_{11}, the characteristic lengths, l_{10} and l_5, are measured for the ϵ_{22} results and given in Table 7.15. In the higher angle laminates with θ equal to 60° and 75°, the far-field solution is not observed before reaching the centerline of the specimen. In addition, the four-ply effective ply thickness laminate with θ equal to 15° does not come within the 5% bound (l_5) before the centerline of the specimen.

The results for ϵ_{22} exhibit a transition region, located above and below the notch tip, similar to the transition region observed in the results for ϵ_{11}. The transition region for ϵ_{22} is clearly seen in Figures 7.61 and 7.62 for the single-ply and four-ply effective ply thickness laminates with θ equal to 15°. The largest gradient (i.e., isostrain lines closest together) observed in this transition region occurs for this laminate with θ equal to 15°. As the ply angle of the laminate increases, the gradients in the transition region decrease (i.e., the isostrain lines become spaced farther apart). This is the same trend observed in the results for ϵ_{11} and in the results from the single-edge-notched specimen.

As with the gradients for ϵ_{11}, gradients in the strain fields of ϵ_{22} are observed to be dependent on the laminate. The values of ϵ_{22} along the arc paths versus the polar coordinate angle, ψ, are plotted for the single-ply and four-ply effective ply thickness laminates with θ equal to 15° in Figures 7.63 and 7.64. For the other laminates these plots are shown in Figures B.39 through B.44, included in Appendix B.2. The peak values along each path are associated with the laminate fiber angle, θ, as observed for ϵ_{11}. For ϵ_{22}, the values of strain plotted against ψ eventually form three 'peaks' and two 'valleys' as the distance from the notch tip increases. In the single-ply and four-ply effective ply thickness laminates with θ equal to 15°, the trend is first observed

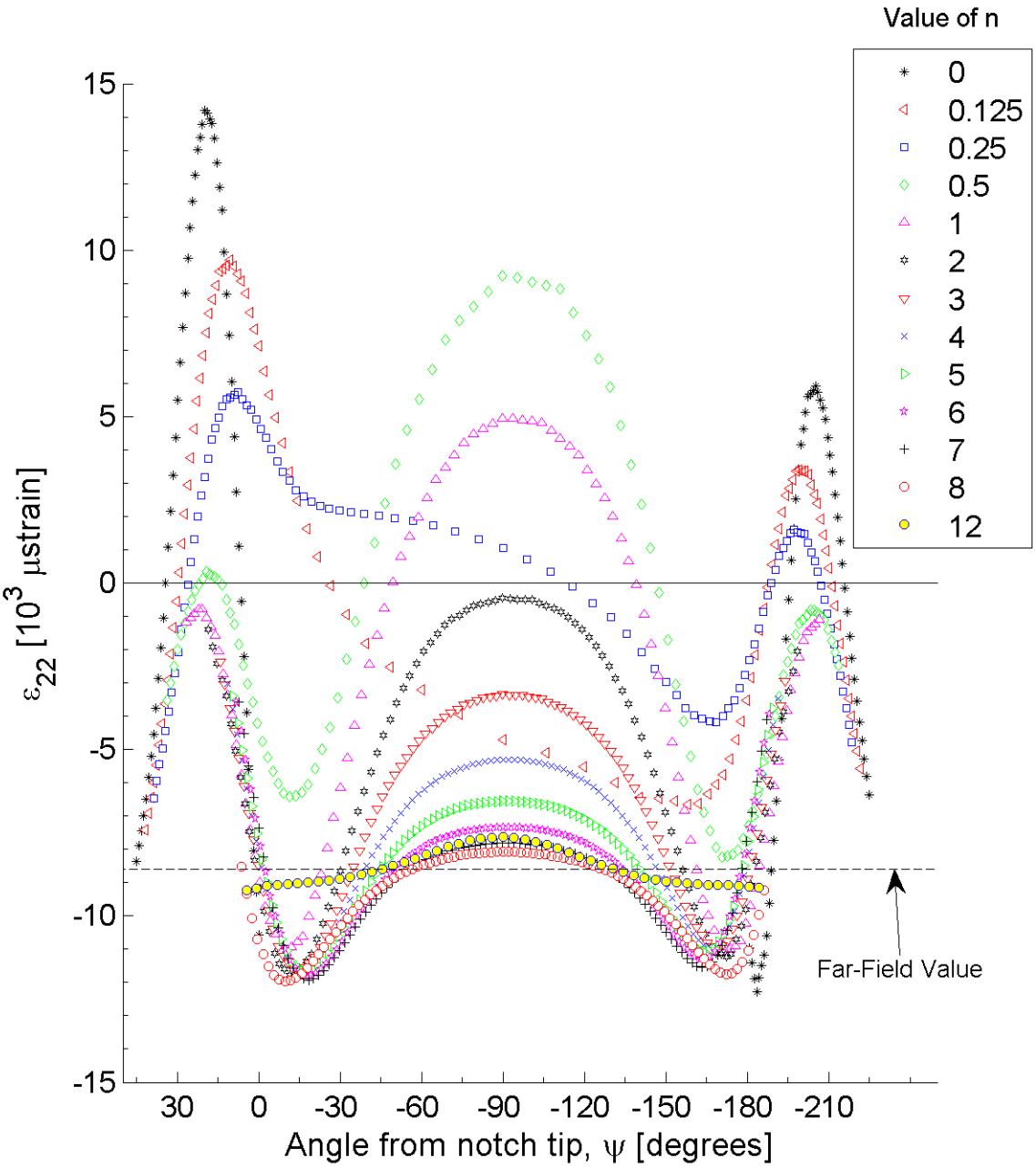

Figure 7.63 Plot of ϵ_{22}, in laminate axes, along arc paths at the midplane of ply 1 (a $+15^\circ$ ply) of the double-edge-notched specimen model for the laminate of $[(+15/-15]_{16T}$.

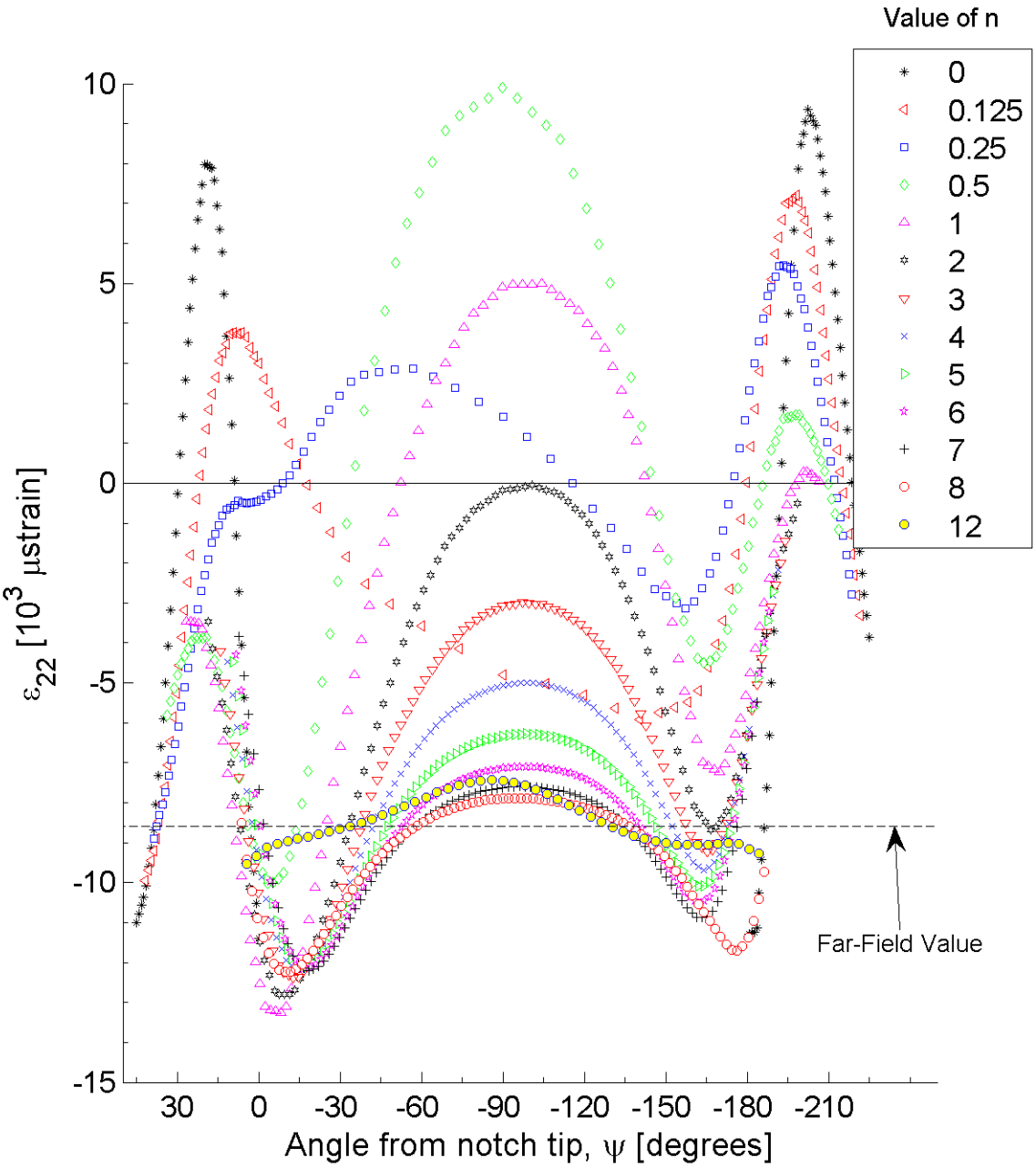

Figure 7.64 Plot of ϵ_{22}, in laminate axes, along arc paths at the midplane of ply 1 (a $+15^\circ$ ply) of the double-edge-notched specimen model for the laminate of $[(+15_4/-15_4]_{4T}$.

in the plot for values along the arc path for n equal to 0.5. As the laminate angle increases, the trend develops farther from the notch. For the lower angle laminates with θ equal to 15° and 30°, as listed via the characteristic lengths in Table 7.15, the value of ϵ_{22}, along ψ equal to $-90°$, approaches the far-field solution as the distance from the notch tip increases. The results for the arc path of n equal to 12, which is beyond the centerline of the specimen, the solution begins to diverge from the far-field solution. For the higher angle laminates with θ equal to 60° and 75°, this gradient decreases as the value with θ increases. In addition, the results for ϵ_{22} do not reach the far-field solution before the centerline of the specimen is reached for the higher angle laminates. As with the gradients of ϵ_{11}, the gradients of ϵ_{22} exhibit a skewness that is dependent on the ply angle. The values of ϵ_{22} for the positive plies of the laminates are observed to flip about ψ equal to $-90°$ as compared to those for the negative plies. This skewness is dependent on the laminate.

As was done in Tables 7.16 and 7.17 for ϵ_{11}, the gradients of the values of ϵ_{22} between neighboring arc paths are given in Tables 7.19 and 7.20 for ψ equal to $-90°$, the same angle used to characterize the characteristic lengths, l_{10} and l_5. It is observed that there is a strong relationship between the laminate angle, θ, and the magnitudes of the gradients. For both the single-ply and four-ply effective ply thickness laminates, there is greater than an order of magnitude difference in the values of the gradients near the notch between the lower angle laminates and the higher angle laminates. For the lower angle laminates with θ equal to 15° and 30°, the values of the gradients beyond the arc path of n equal to 0.5 drop in magnitude and become negative. The gradients of the lower angle laminates are relatively insensitive to the effective ply thickness. The higher angle laminates with θ equal to 60° and 75° exhibit a differences between the single-ply and four-ply effective ply thickness laminates, such as differences in the magnitudes near the notch tip. In the higher angle laminates, the gradients beyond n equal to 2 are of the same magnitude for both the single-ply and four-ply effective ply thickness laminates.

The strain fields of ϵ_{12} for the double-edge-notched specimen are observed to be dependent on the location through the thickness (z-direction) of the laminate. The

Table 7.19 Gradients of the values of ϵ_{22} between 'arc paths' for ψ equal to $-90°$ for the double-edge-notched specimen single-ply effective ply thickness laminates ($[\theta/-\theta]_{16T}$)

Arc Paths (n values)	**Gradient** $[\mu\epsilon/mm]$			
	Laminate Angle, θ			
	15°	**30°**	**60°**	**75°**
0 - 0.125	+33400	+30100	+2600	+1100
0.125 - 0.25	+32900	+31300	+2900	+1200
0.25 - 0.5	+23400	+36500	+5300	+1900
0.5 - 1	-6100	+2000	+3600	+1100
1 - 2	-3900	-2100	+800	+300
2 - 3	-2100	-1400	-100	0
3 - 4	-1400	-1100	-200	-100
4 - 5	-900	-900	-200	-100
5 - 6	-600	-700	-100	-100
6 - 7	-300	-500	-100	0
7 - 8	-200	-300	-100	0
8 - 12	+100	+100	0	0

Table 7.20 Gradients of the values of ϵ_{22} between 'arc paths' for ψ equal to $-90°$ for the double-edge-notched specimen four-ply effective ply thickness laminates ($[\theta_4/-\theta_4]_{4T}$)

Arc Paths (n values)	**Gradient** $[\mu\epsilon/mm]$			
	Laminate Angle, θ			
	15°	**30°**	**60°**	**75°**
0 - 0.125	+37700	+20900	-800	+300
0.125 - 0.25	+36900	+21900	-600	+400
0.25 - 0.5	+23600	+25000	+600	+900
0.5 - 1	-7100	-800	+2700	+900
1 - 2	-3600	-1900	+900	+400
2 - 3	-2100	-1300	-100	0
3 - 4	-1400	-1100	-200	-100
4 - 5	-900	-900	-200	-100
5 - 6	-600	-700	-100	-100
6 - 7	-300	-500	-100	0
7 - 8	-200	-300	-100	0
8 - 12	+100	+100	0	0

variation of ϵ_{12} is determined to be linearly dependent on the through-thickness (z-direction) location, as presented in Equation 7.17. The twisting curvature, κ_{xy}, related to the laminate, has the largest influence on the shear strain at the outer surfaces (farthest away from the midplane of the specimen). The influence of the extension-twist coupling of the representative laminate (i.e., without structural features) is presented in Table 7.13. The results for ϵ_{12} at the midplane of ply 1 (the outermost ply) for the single-ply and four-ply effective ply thickness laminates with θ equal to 15° are shown in Figures 7.65 and 7.65. For the laminates with θ equal to 30°, 60°, and 75°, the strain fields of ϵ_{12} are shown in Figures B.45 through B.50, included in Appendix B.2. The peak maximum and minimum values are indicated in these figures, with the values and locations for each laminate listed in Table 7.21. As in the case of the strain fields of ϵ_{11}, these peak maximum and minimum values occur along the notch edge, at values of r/r_o equal to 1. The locations of these peak values in the polar coordinate angle ϕ are observed to be dependent on the laminate fiber angle, as indicated by the results in Table 7.21. These locations do not match the corresponding peak maximum and minimum locations for ϵ_{11} or ϵ_{22}.

The strain fields of ϵ_{12} exhibit a slight asymmetry about the y-z plane within each ply, similar to the asymmetry observed in the strain fields of ϵ_{11} and ϵ_{22}. This asymmetry becomes more noticeable in the region near the notch tip as the laminate angle increases. For example, the upper (positive x-direction from the notch) -5000 μstrain isoline in Figure 7.65 encompasses a larger region compared to the lower +5000 μstrain isoline. Unlike the normal strains, the shear strain flips sign (i.e., direction) across the y-z plane. As with the results of ϵ_{11} and ϵ_{22}, the asymmetry is observed to be dependent on the through-thickness location of a ply. The results of the plies at the midplane of the laminate are symmetric.

Very little change is exhibited in the strain fields of ϵ_{12} when varying between positive and negative plies. Generally, the 'far-field' (at a distance greater than 1 notch radius from the notch tip) isostrain lines are consistent for both positive and negative plies of a laminate, as would be predicted from LPT. The influence of the extension-twist coupling of the laminates, as listed in Table 7.13, is of relatively small

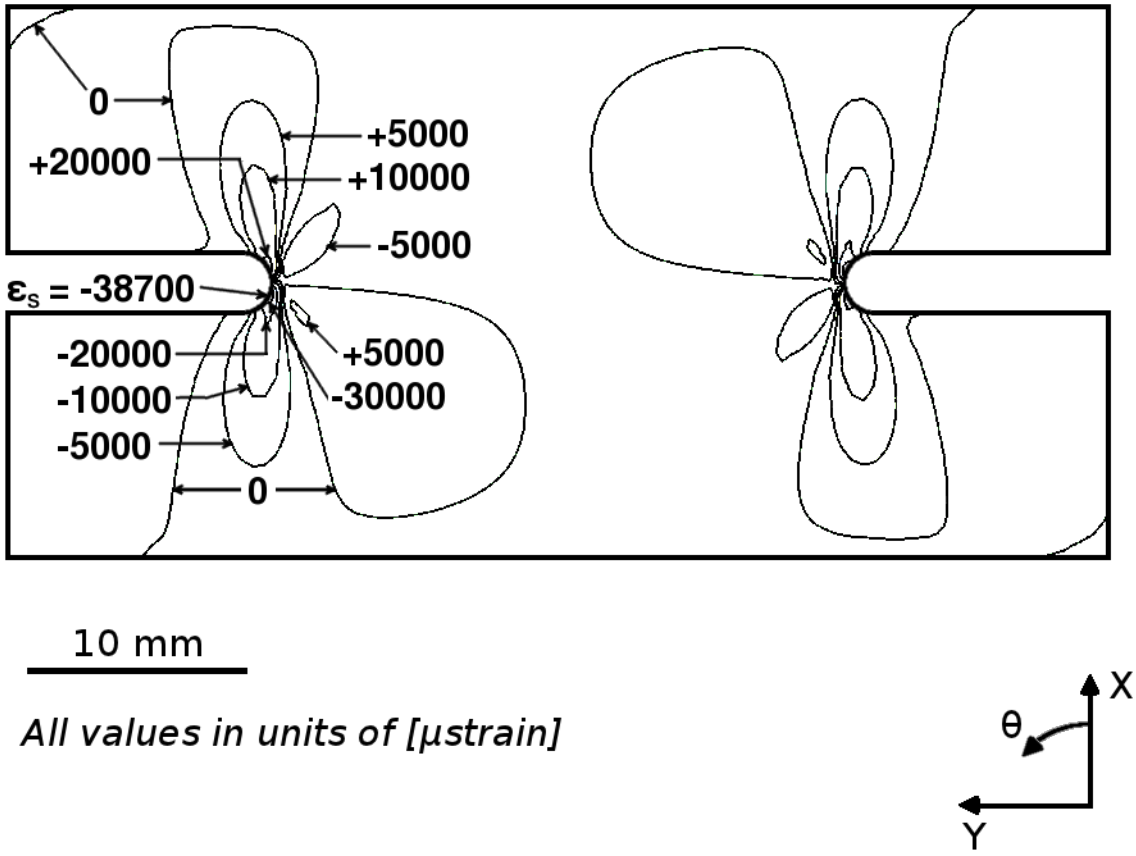

Figure 7.65 Isostrain plot of strain field of ϵ_{12}, in laminate axes, at the midplane of ply 1 (a $+15^\circ$ ply) of the double-edge-notched specimen model for the single-ply effective ply thickness laminate of $[+15/-15]_{16T}$.

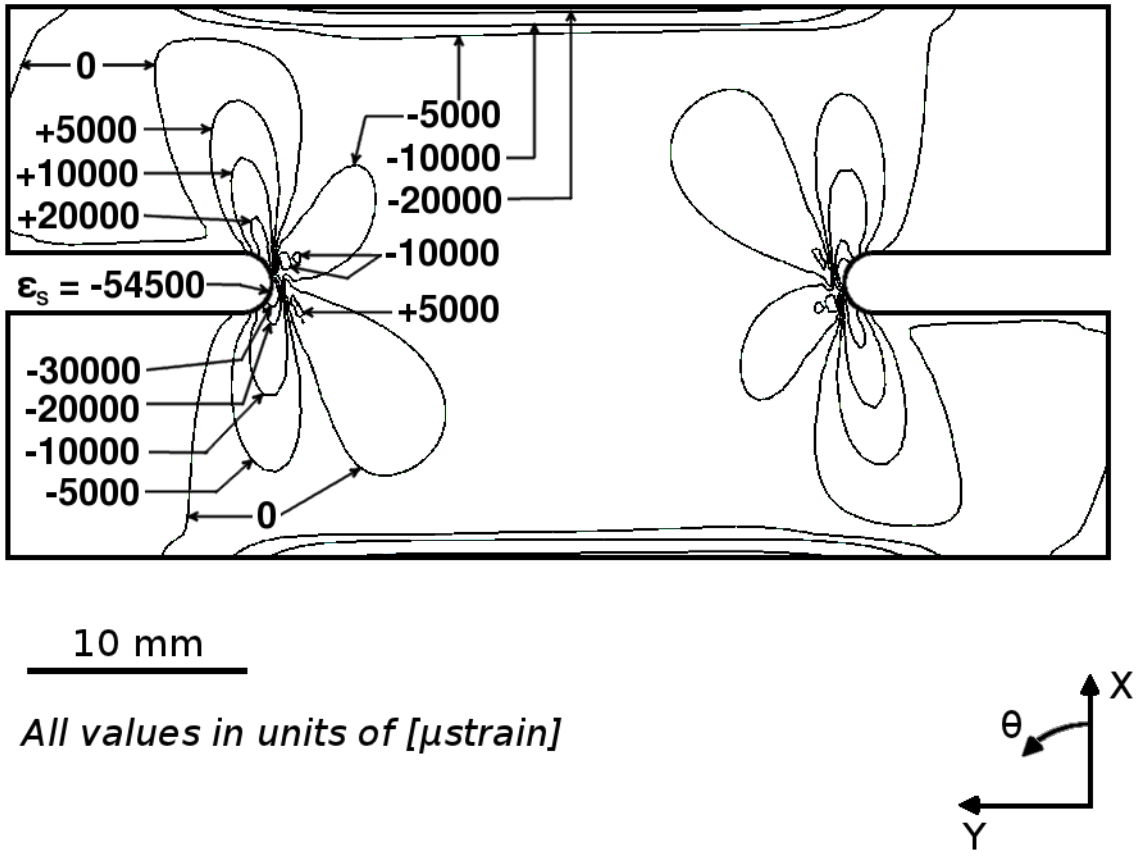

Figure 7.66 Isostrain plot of strain field of ϵ_{12}, in laminate axes, at the midplane of ply 1 (a $+15^\circ$ ply) of the double-edge-notched specimen model for the four-ply effective ply thickness laminate of $[+15_4/-15_4]_{4T}$.

Table 7.21 Locations and values of maximum magnitudes of ϵ_{12} for the double-edge-notched specimens (laminates of $[\theta/-\theta]_{16T}$ or $[\theta_4/-\theta_4]_{4T}$)

Strain Component	**Value Considered**[a]	**Laminate Angle, θ**	**Nominal Effective Ply Thickness**	**Value [μstrain]**	$\frac{\mathbf{r}}{\mathbf{r_o}}$	ϕ **[degrees]**
ϵ_{12}	ϵ_S	15°	1	-38700	1	-117
			4	-54500	1	-76
		30°	1	-19900	1	-117
			4	-32300	1	-97
		60°	1	-10200	1	-135
			4	-15100	1	-117
		75°	1	-13900	1	-141
			4	+19900	1	-45

[a] ϵ_S = Maximum Magnitude

value compared to the observed values of strain due to the notches. In the 'near-field' (at a distance less than 1 notch radius from the notch tip), a slight variation occurs. These variations are likely due to free-edge effects, as discussed at the beginning of this section. As in the case of the strain fields of ϵ_{11} and ϵ_{22}, the direction of the skewing of isolines flips for positive and negative plies.

The results for ϵ_{12} exhibit a transition region, located above and below the notch tip, similar to the transition region observed in the results for ϵ_{11} and ϵ_{22}. Unlike the single-edge-notched specimen, the expected far-field value of ϵ_{12} is non-zero and dependent on the through-thickness location, as defined in Equation 7.17, due to the extension-twist coupling discussed at the beginning of this section. The analytical far-field values for the first ply of each of the laminates of the double-edge-notched specimen are listed in Table 7.13. The transition region for ϵ_{12} is clearly seen in Figures 7.65 and 7.66 for the single-ply and four-ply effective ply thickness laminates with θ equal to 15°. The value of ϵ_{12} transitions from zero in the "notched" section to the far-field value in the "unnotched" section. The largest gradient (i.e., isostrain lines closest together) observed in this transition region occurs for this laminate with θ equal to 15°. As the ply angle of the laminate increases, the gradients in the transition region decrease (i.e., the isostrain lines become spaced farther apart). This is the same trend observed in the results for ϵ_{11} and ϵ_{22}, as well as the results from the single-edge-notched specimen.

As with the gradients for ϵ_{11} and ϵ_{22}, gradients in the strain fields of ϵ_{12} are observed to be dependent on the laminate. The values of ϵ_{12} along the arc paths versus the polar coordinate angle, ψ, are plotted for the single-ply and four-ply effective ply thickness laminates with θ equal to 15° in Figures 7.67 and 7.68. For the other laminates these plots are shown in Figures B.51 through B.56, included in Appendix B.2. The peak values along each path are associated with the laminate fiber angle, θ, as observed for ϵ_{11} and ϵ_{22}. For ϵ_{12}, the values of strain plotted against ψ form two 'peaks' and two 'valleys'. As the distance from the notch tip increases, these 'peaks' and 'valleys' flatten, as shown for the single-ply and four-ply effective ply thickness laminates with θ equal to 15° in Figures 7.67 and 7.68. Unlike the results observed

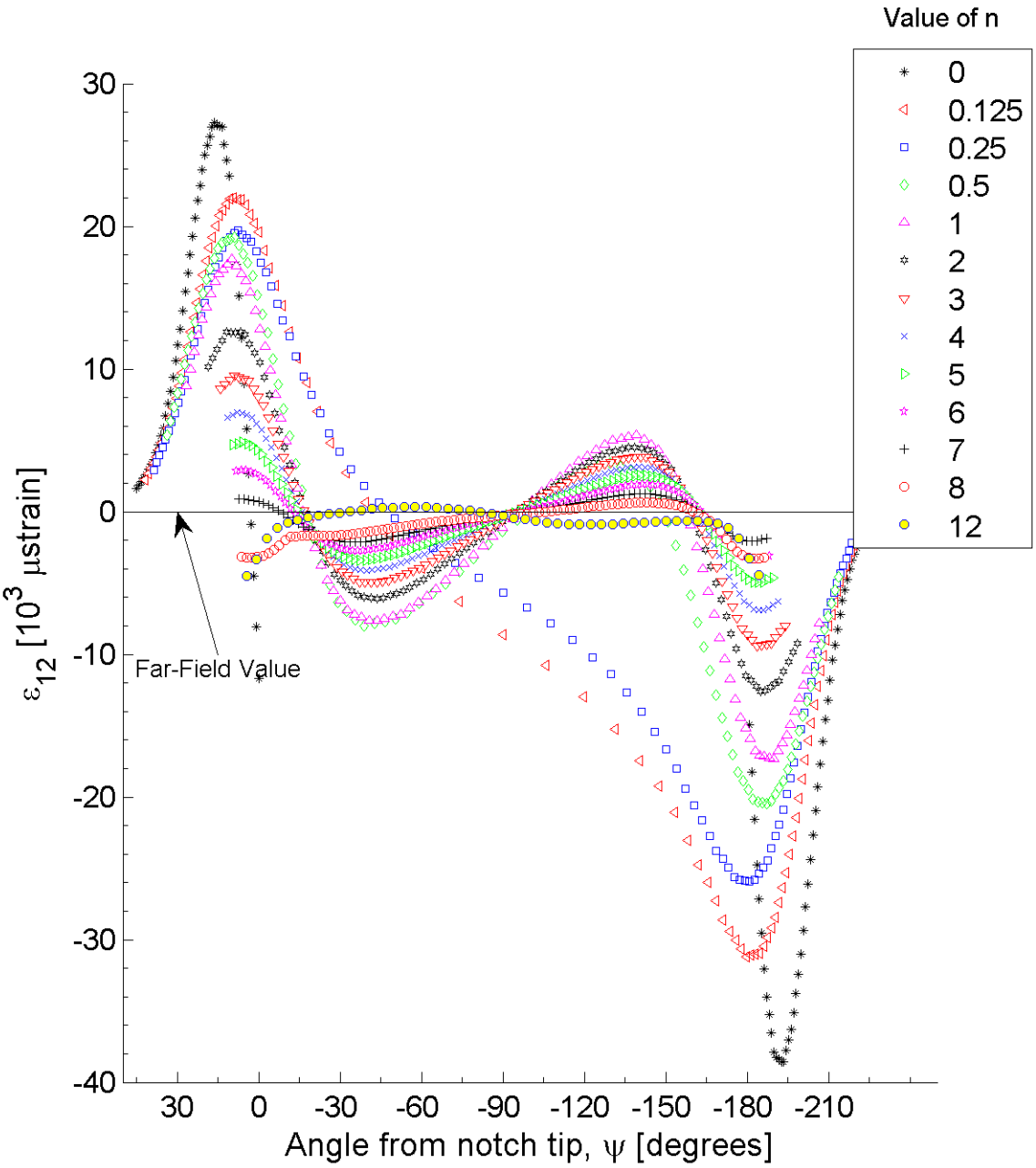

Figure 7.67 Plot of ϵ_{12}, in laminate axes, along arc paths at the midplane of ply 1 (a $+15^\circ$ ply) of the double-edge-notched specimen model for the laminate of $[(+15/-15]_{16T}$.

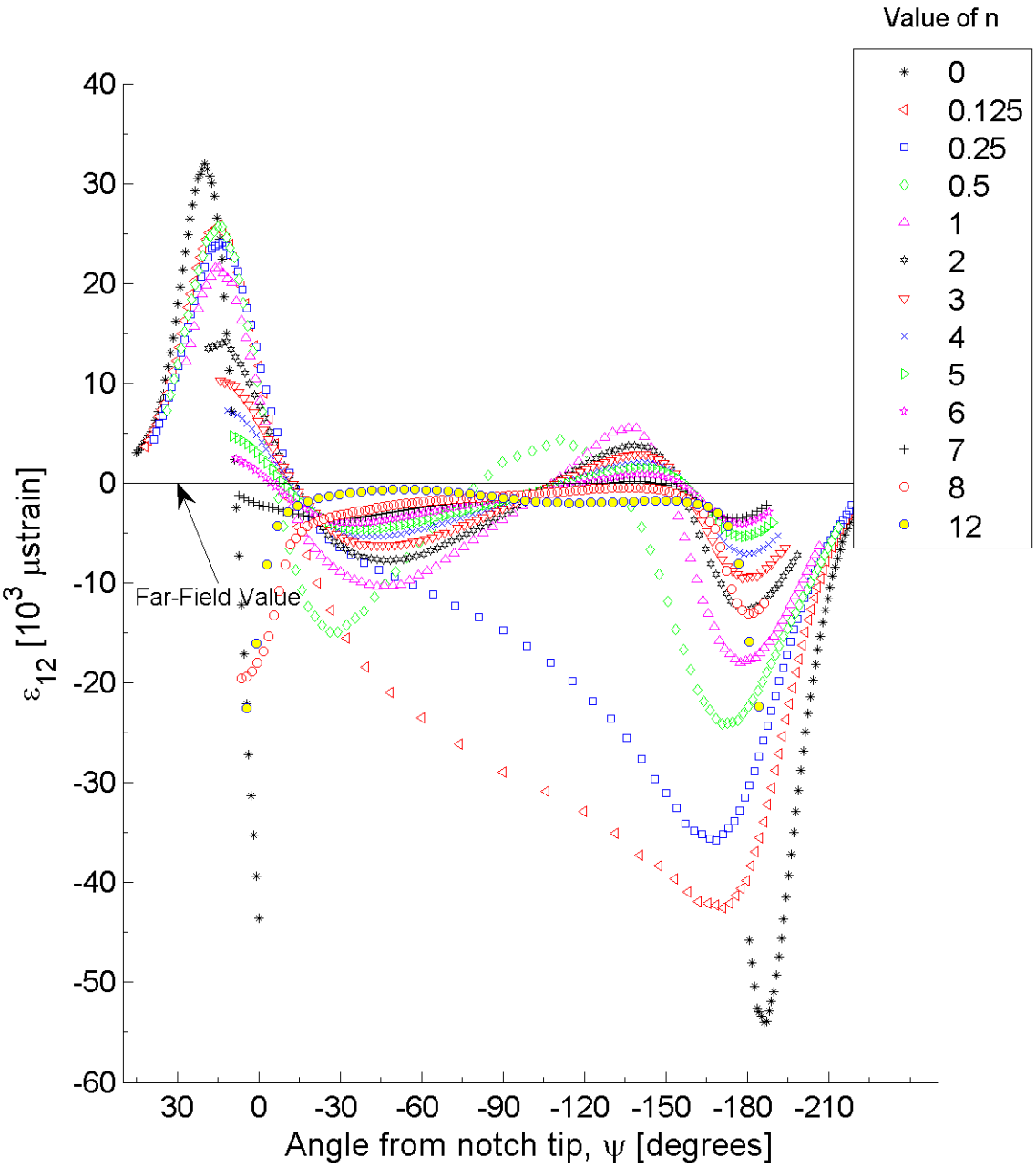

Figure 7.68 Plot of ϵ_{12}, in laminate axes, along arc paths at the midplane of ply 1 (a $+15^\circ$ ply) of the double-edge-notched specimen model for the laminate of $[(+15_4/-15_4]_{4T}$.

for ϵ_{11} and ϵ_{22}, the ϵ_{12} at ψ equal to -90° appear to hold a relatively consistent value, regardless of the distance away from the notch tip. However, the strain fields on either side of ψ equal to -90° approach the far-field solution as the distance from the notch increases.

As was done in Tables 7.16 and 7.17 for ϵ_{11} and Tables 7.22 and 7.23 for ϵ_{22}, the gradients of the values of ϵ_{12} between neighboring arc paths are given in Tables 7.22 and 7.23 for ψ equal to -90°, the same angle used to characterize the characteristic lengths, l_{10} and l_5. As with the results for ϵ_{22}, it is observed that there is a strong relationship between the laminate angle, θ, and the magnitudes of the gradients. For both the single-ply and four-ply effective ply thickness laminates, there is greater than an order of magnitude difference in the values of the gradients near the notch between the lower angle laminates and the higher angle laminates. For the lower angle laminates with θ equal to 15° and 30°, the values of the gradients beyond the arc path of n equal to 0.5 drop in magnitude. Unlike the results for ϵ_{22}, the gradients of the lower angle laminates are sensitive to the extension-twist coupling of the laminate, with the magnitudes of the gradients near the notch tip in the four-ply effective ply thickness laminate four times larger than those observed in the single-ply effective ply thickness laminate. This factor of four is directly seen in the analytical shear strain values calculated in Table 7.13. The higher angle laminates with θ equal to 60° and 75° exhibit a differences between the single-ply and four-ply effective ply thickness laminates, such as differences in the magnitudes near the notch tip. In the higher angle laminates, the gradients beyond n equal to 0.5 are of the same magnitude for both the single-ply and four-ply effective ply thickness laminates.

The out-of-plane strain results are considered subsequently. These strain fields are observed to have variations through the thickness of each laminate. Variations from LPT exist in the model results due to free-edge effects at the notch. Due to the mesh density used near free edges of the model, free-edge effects such as those discussed in [58, 60, 74, 76, 139] are not captured. The free-edge effects in these regions result in large gradients in the interlaminar stresses. Therefore, the out-of-plane results are not valid in the boundary layer [148–150] of the free edge. For the

Table 7.22 Gradients of the values of ϵ_{12} between 'arc paths' for ψ equal to -90° for the double-edge-notched specimen single-ply effective ply thickness laminates ($[\theta/-\theta]_{16T}$)

Arc Paths (n values)	**Gradient** $[\mu\epsilon/mm]$			
	Laminate Angle, θ			
	15°	**30°**	**60°**	**75°**
0 - 0.125	+17600	+6400	+500	+300
0.125 - 0.25	+16800	+6400	+600	+300
0.25 - 0.5	+12200	+6800	+800	+500
0.5 - 1	+400	+1200	+400	+300
1 - 2	+300	+300	+100	+100
2 - 3	+100	+100	+100	0
3 - 4	+100	+100	0	0
4 - 5	+100	0	0	0
5 - 6	0	0	0	0
6 - 7	0	0	0	0
7 - 8	0	0	0	0
8 - 12	0	0	0	0

Table 7.23 Gradients of the values of ϵ_{12} between 'arc paths' for ψ equal to $-90°$ for the double-edge-notched specimen four-ply effective ply thickness laminates ($[\theta_4/-\theta_4]_{4T}$)

Arc Paths (n values)	**Gradient** $[\mu\epsilon/mm]$			
	Laminate Angle, θ			
	15°	**30°**	**60°**	**75°**
0 - 0.125	+83700	+37300	+9400	+4600
0.125 - 0.25	+80900	+38300	+9800	+4700
0.25 - 0.5	+48000	+39900	+11700	+5500
0.5 - 1	-8200	0	+1100	+700
1 - 2	+400	+700	-900	-600
2 - 3	+400	+300	+100	-200
3 - 4	+300	+200	+100	0
4 - 5	+200	+100	+100	0
5 - 6	+200	+100	+100	0
6 - 7	+100	+100	0	0
7 - 8	0	0	0	0
8 - 12	0	0	0	0

double-edge-notched specimen, this boundary layer is approximately one laminate thickness, corresponding to 3 notch radii. Because the models do not capture the out-of-plane gradients near the free edges, which are expected to be greater than the gradients within the specimen, little discussion is included on the out-of-plane results.

The strain fields of ϵ_{33} exhibit consistent shape through the thickness for each laminate considered. Variations in the isostrain lines are observed to be dependent on the through-thickness location and occur within the region influenced by the free edge of the notch. Thus, these are not further discussed. The strain fields of ϵ_{33} for the single-ply effective ply thickness laminate with θ equal to 15° is shown in Figure 7.69. The results for ϵ_{33} strain fields for the other laminates are shown in Figures B.57 through B.63, included in Appendix B.2. As with the in-plane results, the out-of-plane results exhibit central symmetry. For all cases, the far-field strain fields for ϵ_{33} are on the order of the expected Poisson's effect. For example, the Poisson's ratio for both the single-ply and four-ply effective ply thickness laminates with θ equal to 15°, given in Table 7.4, is 0.03. The majority of the specimen, beyond the regions influenced by the notches, has strain values between -2000 μstrain and 0 μstrain. Had the specimen been featureless (i.e, without a notch), the expected value of ϵ_{33} for the case with θ equal to 15° would be -300 μstrain due to Poisson's effects. Because the model does not capture the large interlaminar gradients at the free edges of the notches, the out-of-plane results offer limited insight of the lengthscales associated with the out-of-plane gradients. Therefore, further out-of-plane results are not useful.

7.3.3 Open-Hole Tension Specimen Model

The characteristic strain fields for each of the open-hole tension specimen models are illustrated via the results presented in this subsection and in Appendix B.3. For these cases of the open-hole tension specimens, nearly identical in-plane strain fields (i.e., ϵ_{11}, ϵ_{22}, and ϵ_{12}) are predicted, regardless of the through-thickness location as well as the effective ply thickness. This is due to the laminates possessing the same in-plane moduli.

As with the single-edge-notched and double-edge-notched specimen models, a

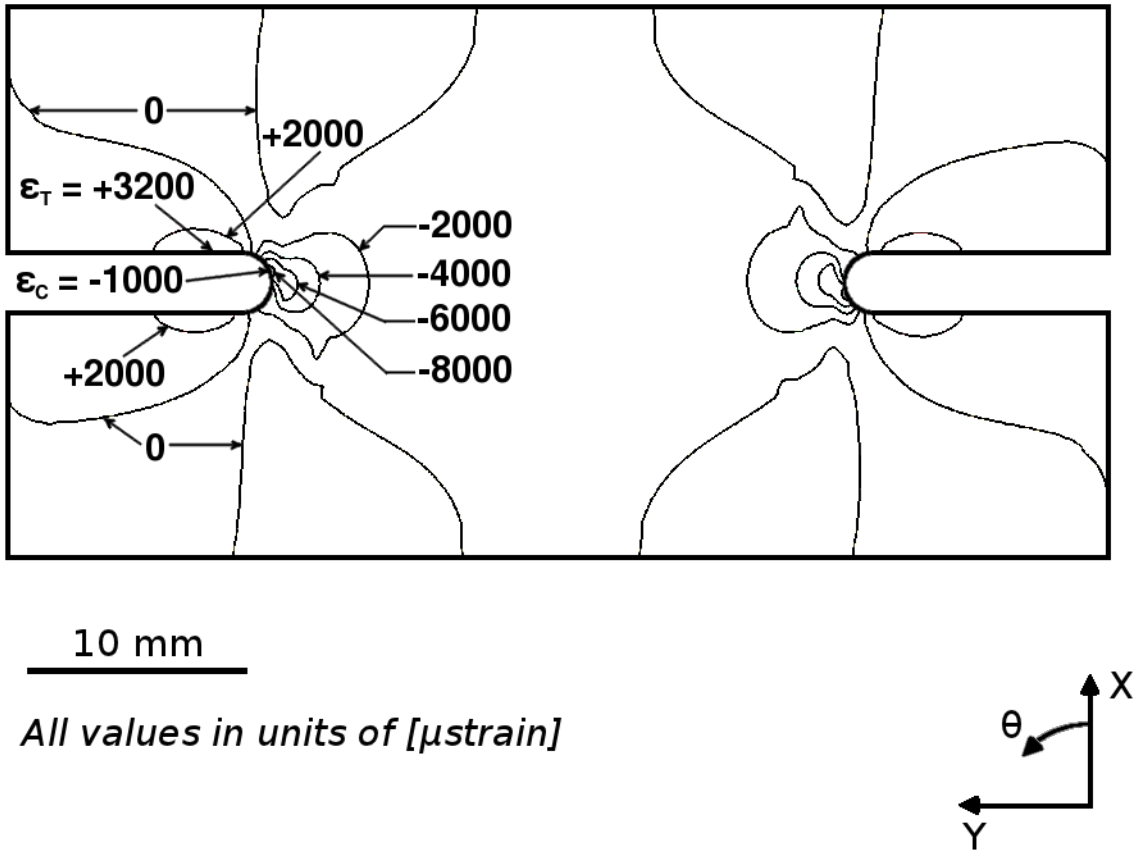

Figure 7.69 Isostrain plot of strain field of ϵ_{33}, at the midplane of ply 1 (a $+15^\circ$ ply) of the double-edge-notched specimen model for the single-ply effective ply thickness laminate of $[15/-15]_{16T}$.

common feature exhibited in all the strain field results is free-edge effects. These effects are observed as discontinuities in the slopes of the isostrain lines (i.e., the isoline is not smooth) near the edges of the specimen. For the in-plane results, the distance at which the effect is observed, approximately one laminate thickness, is consistent across the results of all the strain fields. This is shown in the strain field of ϵ_{12} for the first ply of the single-ply effective ply thickness laminate for the case of a 0.5 inch diameter hole as presented in Figure 7.70. The free-edge effects near the edges of the hole are not observed in the in-plane or out-of-plane strain results due to the modeling lengths. At the free edge of the hole, an increased mesh density, as described in Section 7.2.3, is used in order to better resolve the free-edge effects. Beyond these observations of the free-edge effects, these effects are not further discussed.

The results for the in-plane strain fields are considered first. This is followed by the results for the out-of-plane strain fields. As previously noted, the in-plane strain fields are observed to be uniform in regions beyond the influence of free-edge effects, regardless of the through-thickness location as well as the effective ply thickness, as is predicted via LPT. Variations from LPT exist in the model results due to free-edge effects at the hole and the specimen boundaries, with the region influenced by these effects observed at a distance approximately equal to 1 to 1.5 laminate thicknesses. As previously noted, the models of this chapter do not capture the free-edge effects. The in-plane strain field results possess central symmetry (also referred to as a point reflection), as first described in Section 7.3.2, about the center of the open hole. An example of central symmetry in the open-hole tension specimen is shown in Figure 7.71 for the strain field of ϵ_{11} of the first ply of the four-ply effective ply thickness laminate for the case of a 0.5 inch diameter hole specimen. Rotating the results from the top half (positive x direction) of the specimen by 180° about the center of the open hole yields the exact strain results from the bottom half of the specimen. This central symmetry is exhibited throughout the results for the open-hole tension specimen. For this reason, only half of the isostrain lines are labeled and discussed. In addition, the maximum and minimum strain locations (i.e., ϵ_T, ϵ_C, ϵ_S, as defined in Section 7.3.1) also exhibit central symmetry and are only labeled once for each figure.

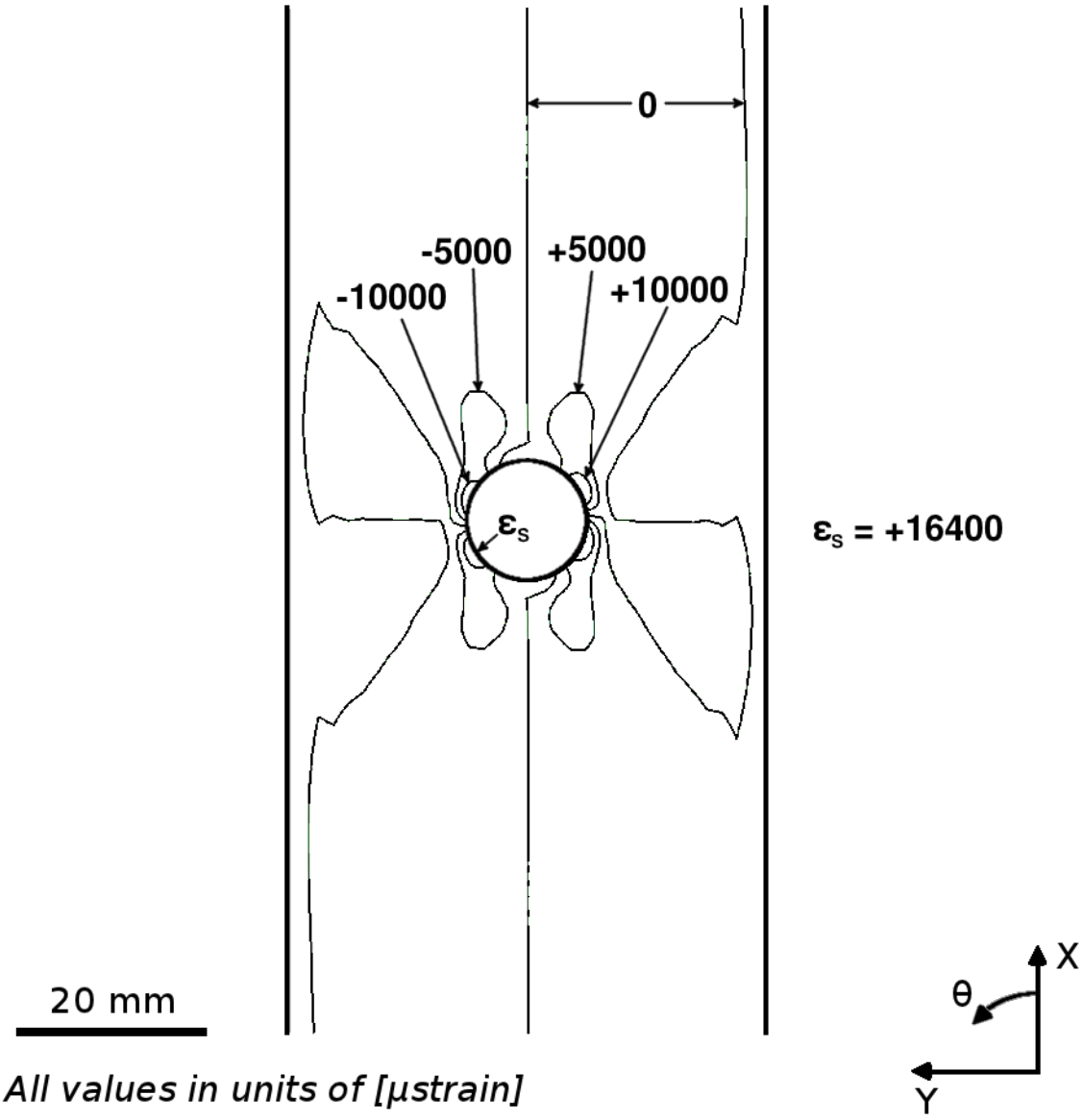

Figure 7.70 Isostrain plot of strain field of ϵ_{12}, in laminate axes, at the midplane of ply 1 (a +45° ply) of the open-hole tension specimen model for case of a 0.5 inch diameter hole for the single-ply effective ply thickness laminate of $[+45/0/-45]_{4S}$.

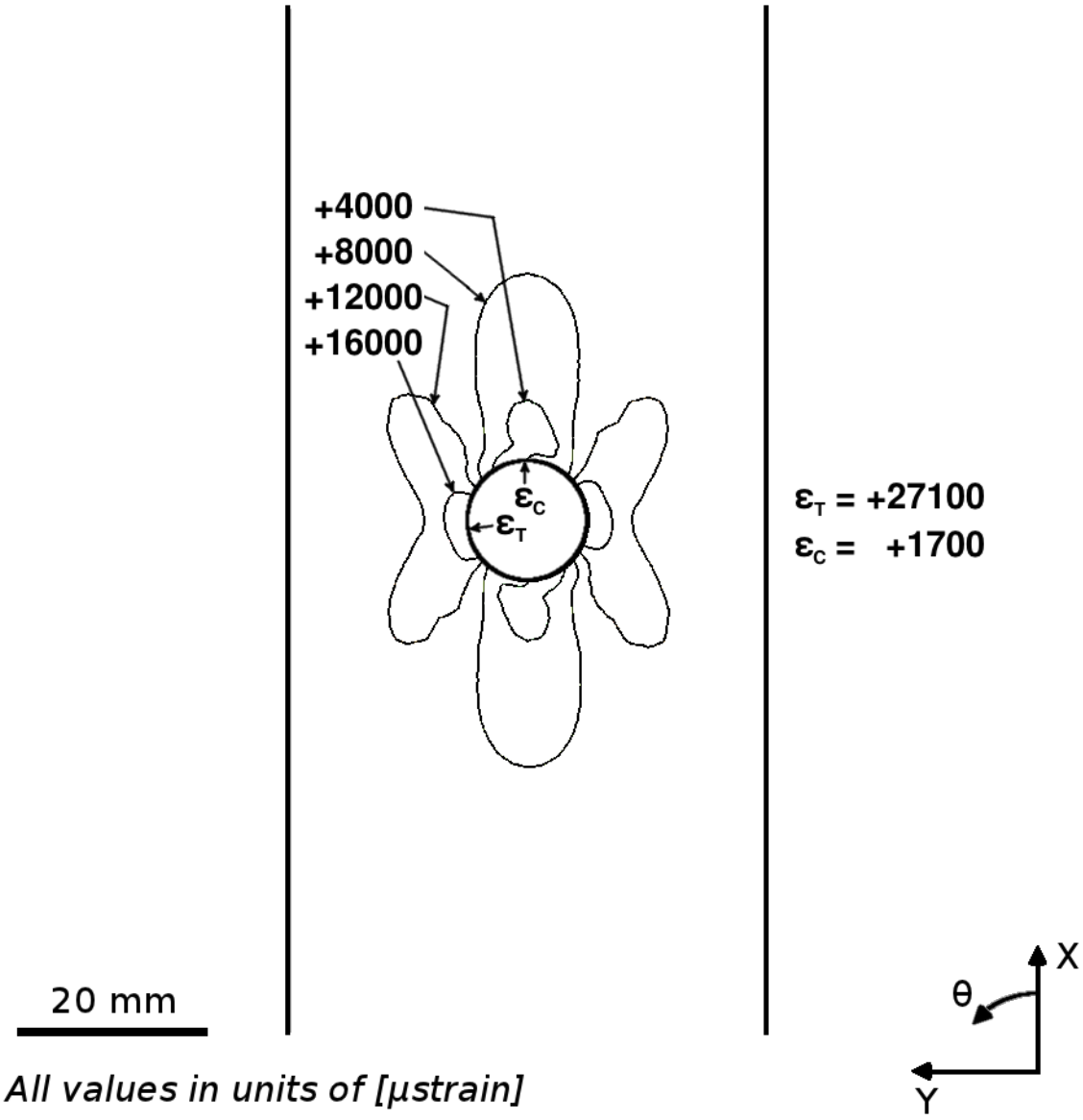

Figure 7.71 Isostrain plot of strain field of ϵ_{11}, in laminate axes, at the midplane of ply 1 (a $+45°$ ply) of the open-hole tension specimen model for case of a 0.5 inch diameter hole for the four-ply effective ply thickness laminate of $[+45_4/0_4/-45_4]_S$.

The strain fields of ϵ_{11} for the laminates considered have positive values, as shown in the results for ϵ_{11} for the single-ply effective ply thickness laminate for the cases of a 0.5 inch and a 1.0 inch diameter hole shown in Figures 7.72 and 7.73, respectively. The strain fields of ϵ_{11} for the open-hole tension specimens do not exhibit negative values. Overlaying the strain fields for the single-ply effective ply thickness laminate for the cases of a 0.5 inch and 1.0 inch diameter hole, shown in Figures 7.72 and 7.73, show that the fields are normalized via hole diameter (i.e., the distance from the hole edge for each isoline is scaled via the hole diameter size). The fields for the cases of the 0.5 inch and 1.0 inch diameter hole specimens overlay exactly.

The effective ply thickness is observed to have minimum influence on the strain fields of ϵ_{11}. Comparing the isostrain lines of +8000 μstrain, above and below the hole (i.e., along the positive and negative x-axis from the center of the hole), for the single-ply and four-ply effective ply thickness results, shown in Figures 7.73 and 7.74, the isostrain lines of the four-ply effective ply thickness laminate are observed to extend slightly farther from the edge of the hole than is observed in the case of the single-ply effective ply thickness laminate. The distance is observed to be dependent on the geometry of the specimen. For the case of the 0.5 inch diameter hole specimen, the isostrain line of the four-ply effective ply thickness extends a distance equal to 0.10 hole diameters farther than the single-ply effective ply thickness laminate. For the case of the 1.0 inch diameter hole specimen, the +8000 μstrain isostrain line of the four-ply effective ply thickness extends a distance equal to 0.05 hole diameters farther than the +8000 μstrain isostrain line of the single-ply effective ply thickness laminate. For both specimen geometries, these variations occur at a x-distance equal to approximately 1.5 hole diameters from the edge of the hole. This is well beyond the influence of the free-edges. The other isostrain lines (i.e., other values of strain) are consistently observed to be slightly farther from the edge of the hole for the four-ply effective ply thickness laminate than the respective isostrain lines of the single-ply effective laminate. The largest distance between isostrain lines occurs for the +8000 μstrain isoline, with all other distances between isolines being a fraction thereof.

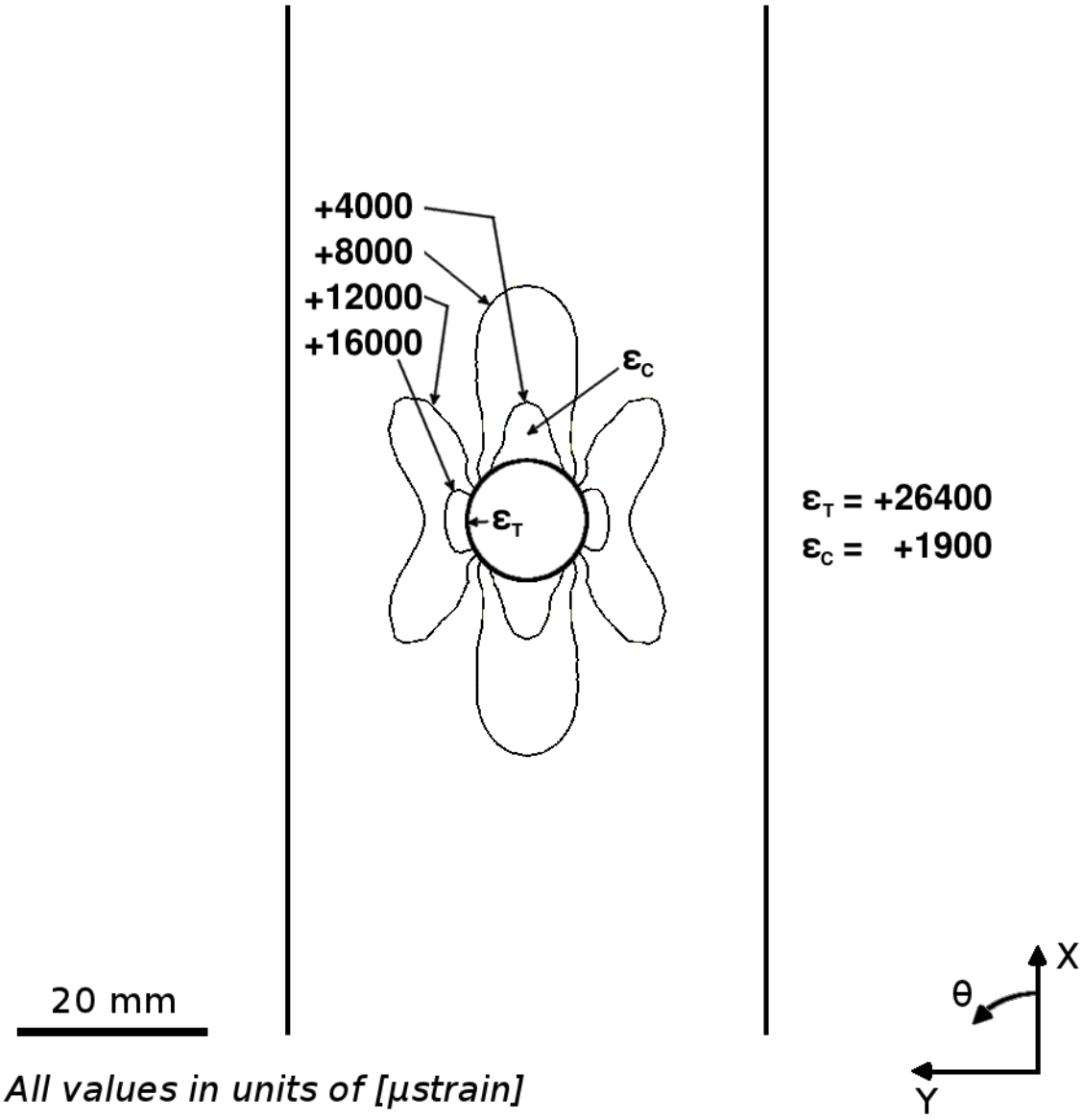

Figure 7.72 Isostrain plot of strain field of ϵ_{11}, in laminate axes, at the midplane of ply 1 (a $+45°$ ply) of the open-hole tension specimen model for case of a 0.5 inch diameter hole for the single-ply effective ply thickness laminate of $[+45/0/-45]_{4S}$.

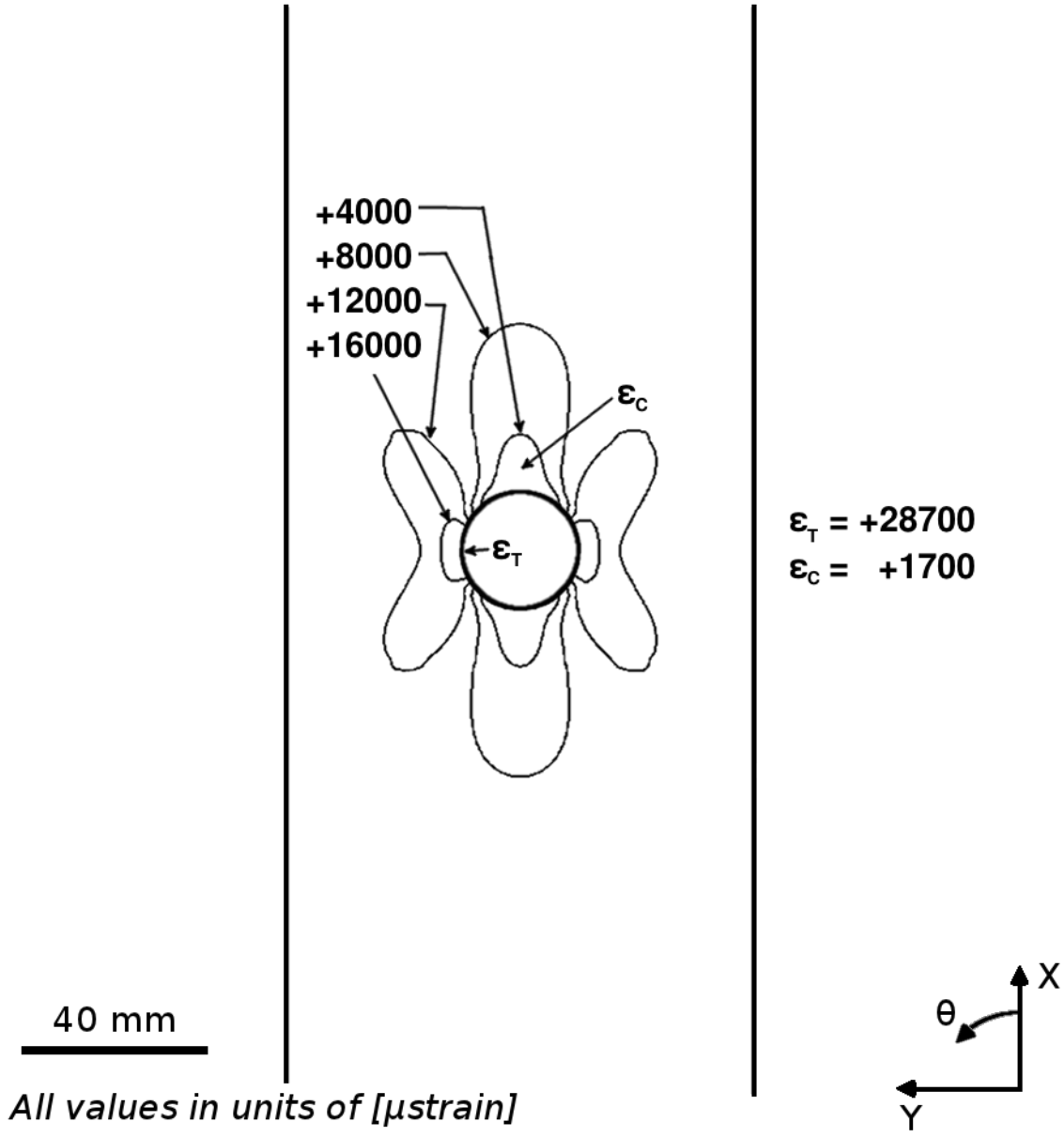

Figure 7.73 Isostrain plot of strain field of ϵ_{11}, in laminate axes, at the midplane of ply 1 (a $+45°$ ply) of the open-hole tension specimen model for case of a 1.0 inch diameter hole for the single-ply effective ply thickness laminate of $[+45/0/-45]_{4S}$.

In addition to variations in the distance between the free edge of the hole and the isostrain lines, variations between the results for the single-ply and four-ply effective ply thickness laminates are observed in an annular region extending from the free edge of the hole to a radial distance equal to one-half the diameter of the hole. The solution within this annular region is uncertain due to free-edge effects, as previously discussed. However, the strain contours are observed to vary between the results of the single-ply and four-ply effective ply thickness laminates. This variation is observed for specimens both with a 0.5 inch diameter hole, as shown in Figures 7.72 and 7.71, and a 1.0 inch diameter hole, as shown in Figures 7.73 and 7.74. For the single-ply effective ply thickness laminate, the strain fields are symmetric about both the x- and y-axis. For the four-ply effective ply thickness laminate, the strain fields are dependent on the ply angle, with a slight skewness developing within the annular region. Thus, the isostrains within the annular region of the four-ply effective ply thickness laminate are not symmetric about the x- and y-axis.

The locations and values of the peak maximum (ϵ_T) and minimum (ϵ_C) 'local' in-plane strains for each laminate are listed in Table 7.24. The locations are given in polar coordinates, with the origin concentric with the center of the open hole, as shown in Figure 7.75. The origin of the x-y coordinate system, defined in previous chapters, is also located at the center of the open hole. Thus, the origin of the polar coordinate system is at the coordinates of x equal to 0 and y equal to 0. The radial distance, r, is normalized by the hole radius, r_o, and thus is expressed in the number of hole radii from the origin. This gives the boundary of the hole as r/r_o equal to 1. The angle, ϕ, is measured positive counterclockwise from the positive x-axis and expressed in degrees. In all cases, the local maximum (ϵ_T) always occurs at the edge of the hole (i.e., r/r_o equal to 1). The local minimum (ϵ_C) occurs at the edge of the hole for the four-ply effective ply thickness laminate while occurring at a distance of approximately 0.25 hole diameters away from the edge of the hole for the single-ply effective ply thickness laminate. Free-edge effects may contribute to the variation of location of ϵ_C between the single-ply and four-ply effective ply thickness laminates.

The strain fields are independent of the angle of the ply, with slight variations

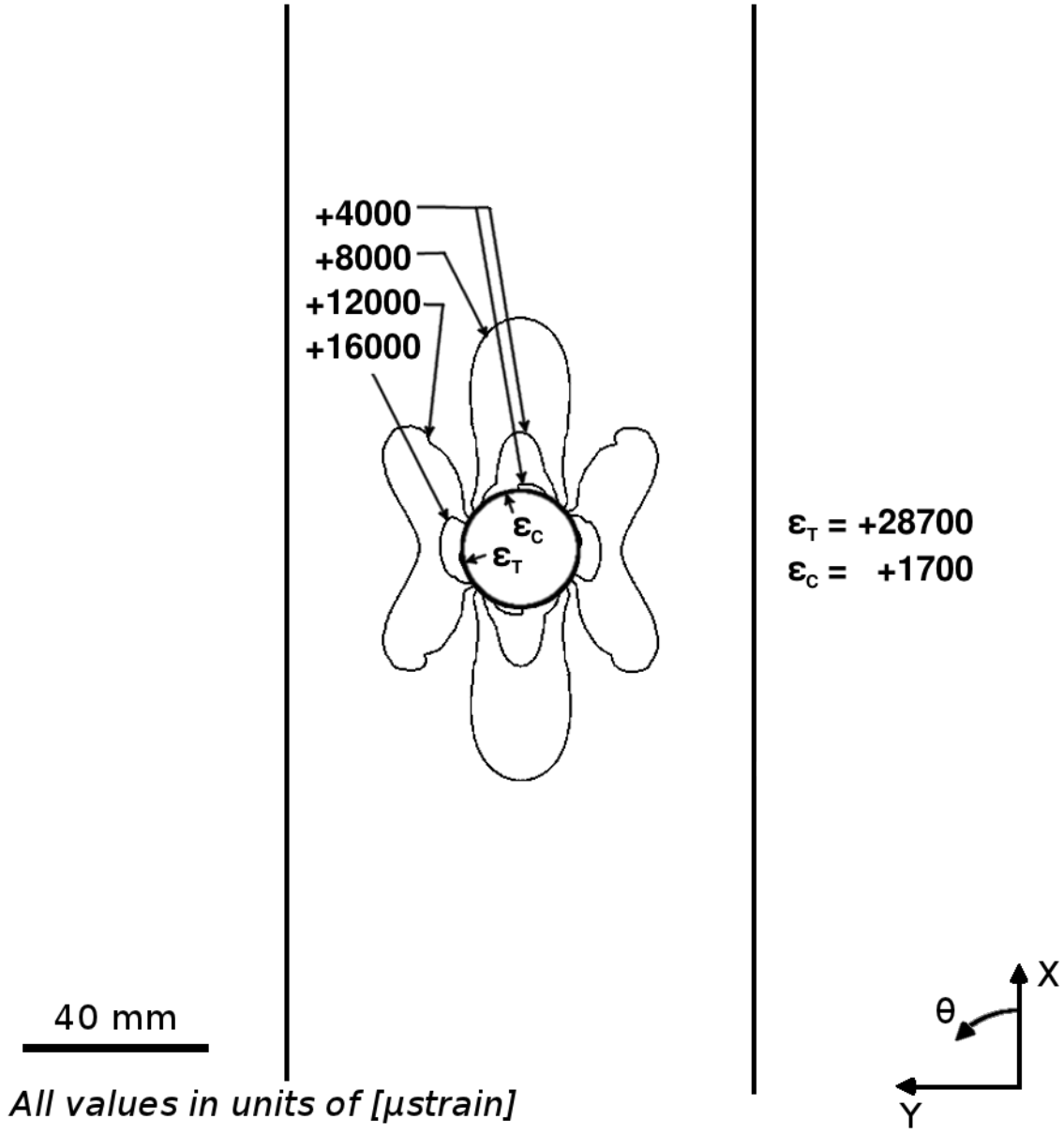

Figure 7.74 Isostrain plot of strain field of ϵ_{11}, in laminate axes, at the midplane of ply 1 (a $+45°$ ply) of the open-hole tension specimen model for case of a 1.0 inch diameter hole for the four-ply effective ply thickness laminate of $[+45_4/0_4/-45_4]_S$.

Table 7.24 Locations and values of maximum and minimum in-plane strains for the open-hole tension specimens (laminates of $[+45/0/-45]_{4S}$ and $[+45_4/0_4/-45_4]_S$)

Strain Component	**Value Considered**[a]	**Hole Diameter [in]**	**Nominal Effective Ply Thickness**	**Value [μstrain]**	$\frac{\mathbf{r}}{\mathbf{r_o}}$	ϕ **[degrees]**
ϵ_{11}	ϵ_T	0.5	1	+26400	1	95
			4	+27100	1	102
		1.0	1	+28700	1	93
			4	+29300	1	100
	ϵ_C	0.5	1	+1900	1.46	0
			4	+1700	1.46	0
		1.0	1	+1700	1.34	0
			4	+1500	1	23
ϵ_{22}	ϵ_T	0.5	1	0	1	56
			4	+2100	1	57
		1.0	1	+1600	1	56
			4	+3400	1	61
	ϵ_C	0.5	1	-15400	1	104
			4	-14200	1	173
		1.0	1	-19400	1	103
			4	-16200	1	173
ϵ_{12}	ϵ_S	0.5	1	+16400	1	117
			4	-17000	1	70
		1.0	1	+19800	1	116
			4	-20200	1	73

[a] ϵ_T = Maximum
ϵ_C = Minimum
ϵ_S = Maximum Magnitude

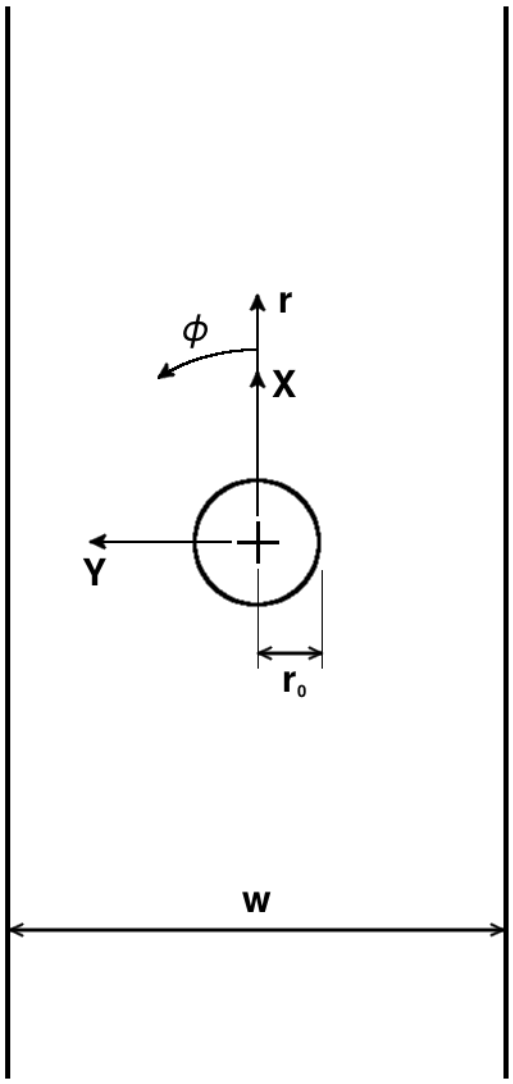

Figure 7.75 Illustration of the polar coordinate used for the results in Table 7.24.

occurring near the edge of the hole of the four-ply effective ply thickness laminate. These variations in the strain fields due to different ply angles within a laminate are observed to be limited to a region extending from the hole edge to a distance of approximately twenty ply thicknesses (equivalent to 0.85 laminate thicknesses) normal to the hole edge. Within this region, the strain fields are observed to be dependent on the ply angle. This variation is observed to have stronger influence in the four-ply effective ply thickness laminates. The strain fields of ϵ_{11} in the $+45°$, $0°$, and $-45°$ plies for the case of a 0.5 inch diameter hole is shown in Figures 7.71, 7.76, and 7.77, respectively, for the case of the $[+45_4/0_4/-45_4]_S$ laminate. In all cases, there is symmetry about the x-z plane between the strain fields of $+45°$ plies and $-45°$, as seen in Figures 7.71 and 7.77. The strain fields in the angle plies (i.e., $+45°$ and $-45°$ plies) neighboring $0°$ plies transition to the strain fields observed in the $0°$ plies. The strain fields of the fourth ply, a $+45°$ ply neighboring a $0°$ ply, of a four-ply effective ply thickness laminate is shown in Figure 7.78. This strain field is nearly identical to the strain fields observed in all the $0°$ plies of this laminate. These variations in the region neighboring the edge of the hole is not observed in the results of the single-ply effective ply thickness laminate.

Another observation of the strain fields of ϵ_{11} is that the value of strain approaches roughly +1% strain (+10,000 μstrain), a value consistent with the applied displacement boundary condition, at a distance away from the hole. The distance normal to the hole surface to reach this value is dependent on the orientation relative to the applied loading. In order to be consistent with the defined characteristic lengths of the single-edge-notched and double-edge-notched specimens, the characteristic lengths associated with the structural feature of an open hole are defined normal to the direction of loading, and thus, along the y-axis. The values of strain along a path, aligned with the y-axis (i.e., ϕ equal to $-90°$), from the edge of the hole (r_o) to the right edge ($2.94r_o$) of the specimen is measured for each laminate of the 0.5 inch diameter hole specimen and 1.0 inch diameter hole specimen. The characteristic length is defined as the number of hole radii away from the edge of the hole (not the origin) that the strain field returns to within a certain percentage of the "unnotched" (i.e., a

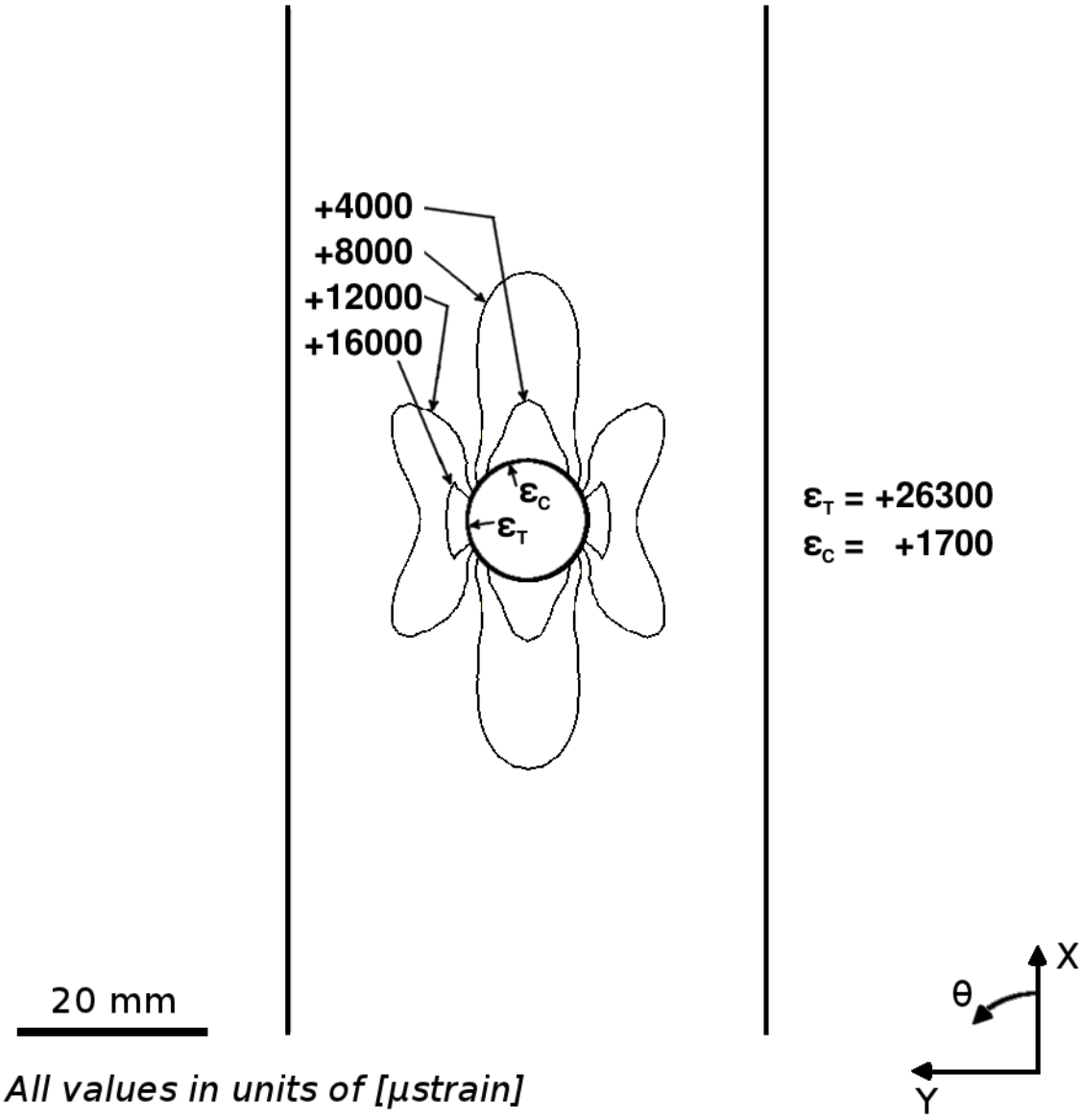

Figure 7.76 Isostrain plot of strain field of ϵ_{11}, in laminate axes, at the midplane of ply 6 (a 0° ply) of the open-hole tension specimen model for case of a 0.5 inch diameter hole for the four-ply effective ply thickness laminate of $[+45_4/0_4/-45_4]_S$.

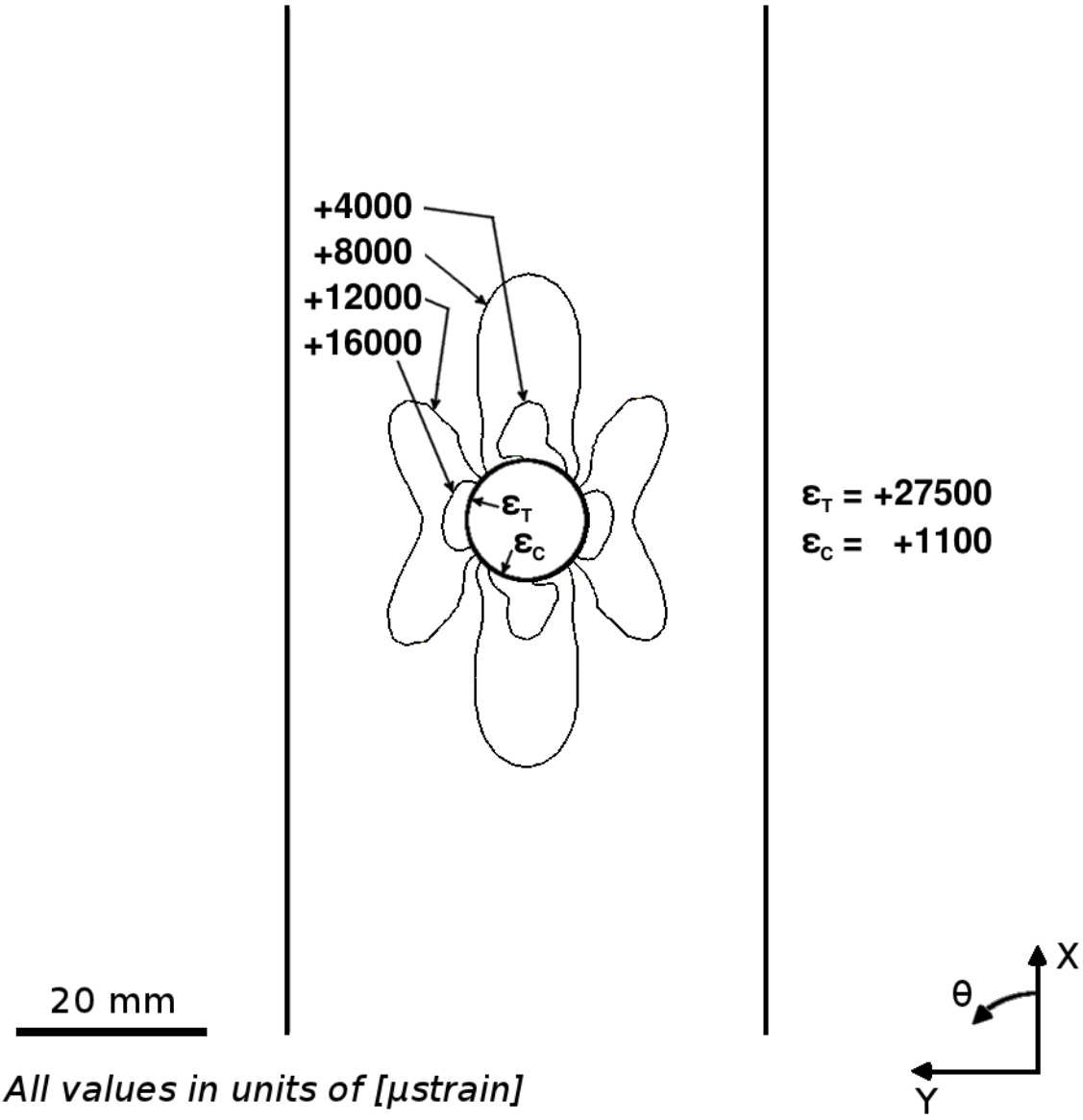

Figure 7.77 Isostrain plot of strain field of ϵ_{11}, in laminate axes, at the midplane of ply 12 (a $-45°$ ply) of the open-hole tension specimen model for case of a 0.5 inch diameter hole for the four-ply effective ply thickness laminate of $[+45_4/0_4/-45_4]_S$.

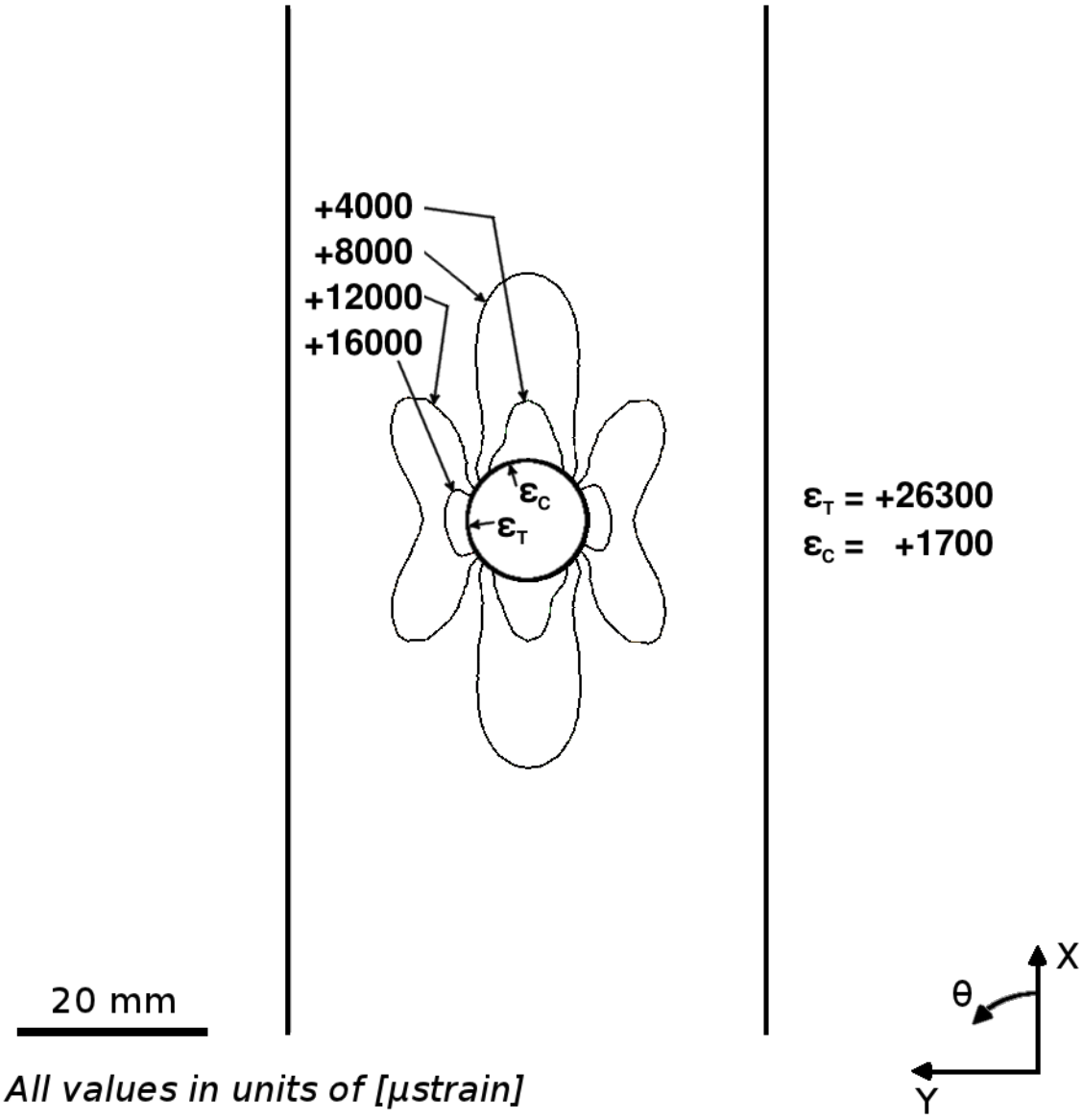

Figure 7.78 Isostrain plot of strain field of ϵ_{11}, in laminate axes, at the midplane of ply 4 (a +45° ply) of the open-hole tension specimen model for case of a 0.5 inch diameter hole for the four-ply effective ply thickness laminate of $[+45_4/0_4/-45_4]_S$.

rectangular specimen with no hole) solution. As defined for the single-edge-notched and double-edge-notched specimens, two percentages, 10% and 5%, are selected in order to develop the process. This may require refinement as additional analyses are conducted beyond this work. Associated with these percentages are two characteristic lengths, l_{10} and l_5, defined as the distance from the edge of the hole (i.e., the point $(r_o, -90°)$ in the polar coordinate system of Figure 7.75) to the point along ϕ equal to $-90°$ where the strain field returns to within 10% and 5%, respectively, of the "unnotched" solution.

These characteristic lengths allow measurement of the influence of the structural feature as a function of the laminate. The characteristic lengths resulting from this definition for the in-plane strain components are listed in Table 7.25. It is observed that the path along ϕ equal to $-90°$ is the minimum length of influence, as will be further discussed. In addition, these results match the analytical solution presented by Lekhnitskii for an open hole plate [145]. Unlike the single-edge-notched and double-edge-notched specimens, the results from the open-hole tension specimen do not exhibit a transition region. Instead, the structural feature creates a region of influence that extends radially from the surface of the hole.

The region influenced by the open hole is investigated via the strain gradients captured along "arc paths," as was done for the single-edge-notched and double-edge-notched specimens. In order to quantify the gradients, values of the strain fields along "arc paths" defined in the polar coordinate system are plotted, as is done for the single-edge-notched and double-edge-notched specimens. The arc paths are defined as the number, n, of radii away from the free edge of the hole:

$$n = \frac{r - r_o}{r_o}$$

The arc paths for n equal to 0.5 through 2.9 are illustrated in Figure 7.79. In addition to the arc paths shown in this figure, paths are also defined for n equal to 0, 0.125, and 0.25, but are not shown due to the figure scale. Each path has a consistent polar angle sweep (i.e., ϕ goes from $0°$ to $-180°$).

Table 7.25 Normalized characteristic lengths[a] of the in-plane strains for the open-hole tension specimen laminates

Strain Component	**Hole Diameter [in]**	**Nominal Effective Ply Thickness**	**Far-Field Strain [μstrain]**	$\frac{l_{10}}{r_o}$	$\frac{l_5}{r_o}$
ϵ_{11}	0.5	1	+10000	0.97	1.45
		4	+10000	1.02	1.46
	1.0	1	+10000	1.03	1.49
		4	+10000	1.06	1.51
ϵ_{22}	0.5	1	-6500	1.93	b
		4	-6500	b	b
	1.0	1	-6500	1.93	b
		4	-6500	1.96	b
ϵ_{12}	0.5	1	0	0.32	0.39
		4	0	0.55	1.08
	1.0	1	0	0.13	0.19
		4	0	0.38	0.47

[a] l_{10} = defined characteristic length for strain value to return to within 10% of far-field strain.
l_5 = defined characteristic length for strain value to return to within 5% of far-field strain.
[b] Far-field strain was not reached before edge of specimen.

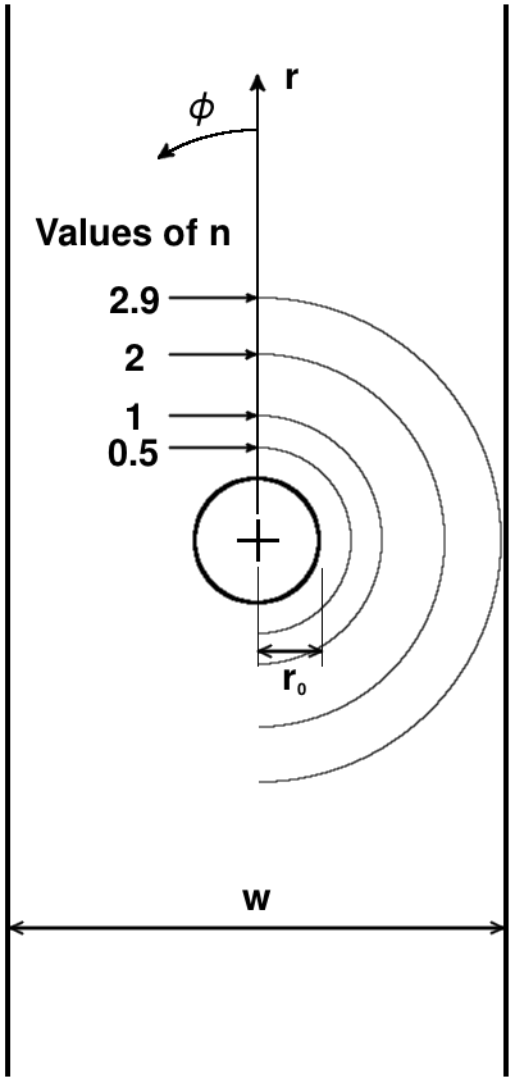

Figure 7.79 Arc path locations defined for the open-hole tension specimen.

Values of strain are presented along these arc paths versus an angle, ψ, as defined in an offset polar coordinate system, similar in definition to that for the single-edge-notched and double-edge-notched specimens. This offset system, (r', ψ), and the original polar coordinate system, (r, ϕ), are shown in Figure 7.80. The offset system has its origin displaced a distance equal to the hole radius, r_o, along ϕ equal to $-90°$ in the original polar coordinate system. In order to maintain consistent terminology with the strain graphs of the single- and double-edge-notched specimens, the origin of the offset polar coordinate system is herein referred to as the 'notch tip' of the open hole although there is no actual 'notch tip' for an open hole. The angle ψ is thus measured from this edge (i.e., 'notch tip') of the open hole. As with the angle ϕ, ψ is measured positive counterclockwise from the positive x-direction. Radial paths extending from both polar coordinate origins to an arbitrary point along an arc path are shown in the figure. In the offset polar coordinate system, the radial distance from the origin to points along the arc path is a function of the angle ψ. This is due to the arc paths being defined with a constant radius in the original polar coordinate system. In the offset system, the radial distance must vary as a function of ψ in order to remain on the arc paths. In addition, the values of the angles over which ψ varies for each arc path (i.e., starting and ending sweep angles) is a function of the distance away from the edge of the hole of the arc path. Transformation equations between the two polar coordinate systems are found via geometric relations. Due to the nature of the geometric relationship, the transformation of the data for n equal to 0 results in a discontinuity in these plots for values of ψ from $0°$ to $-180°$.

The values of ϵ_{11} along the arc paths are plotted at the midplane of ply 1 (a $+45°$ ply) for the single-ply effective ply thickness laminate and are shown in Figure 7.81. The plot shows the value of the strain fields of ϵ_{11} versus the angle, ψ, as defined in the offset polar coordinate system. The peak strain is observed along the path of n equal to 0 (i.e., along the free edge of the hole) in all cases, along with the peak strain decreasing as the distance from the notch tip (i.e., value of n) increases. Furthermore, two peaks are observed to form as the distance from the edge of the hole increases, with the distance at which this first occurs independent of the effective ply thickness

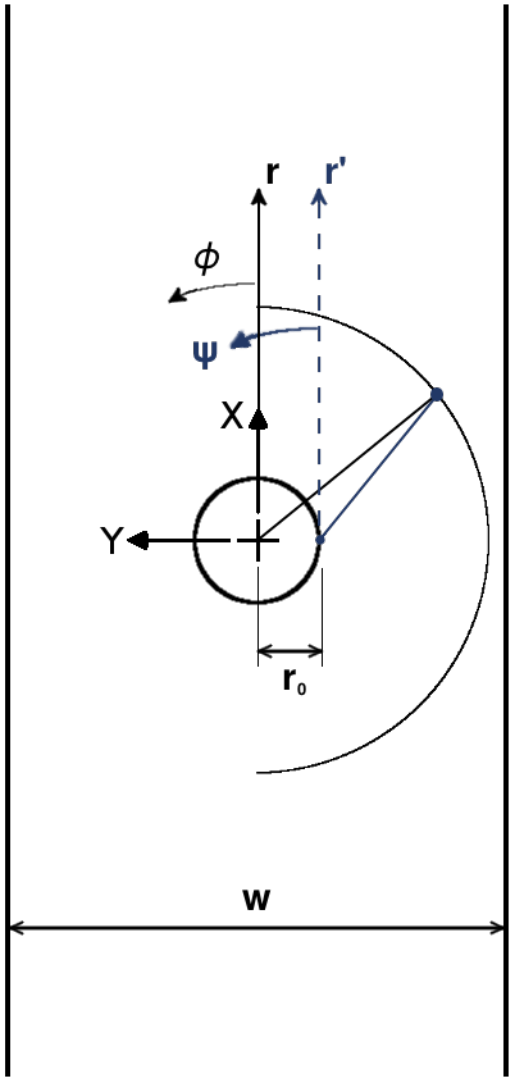

Figure 7.80 Illustration of the offset polar coordinate used for the plots of strain values along arc paths in the open-hole tension specimens.

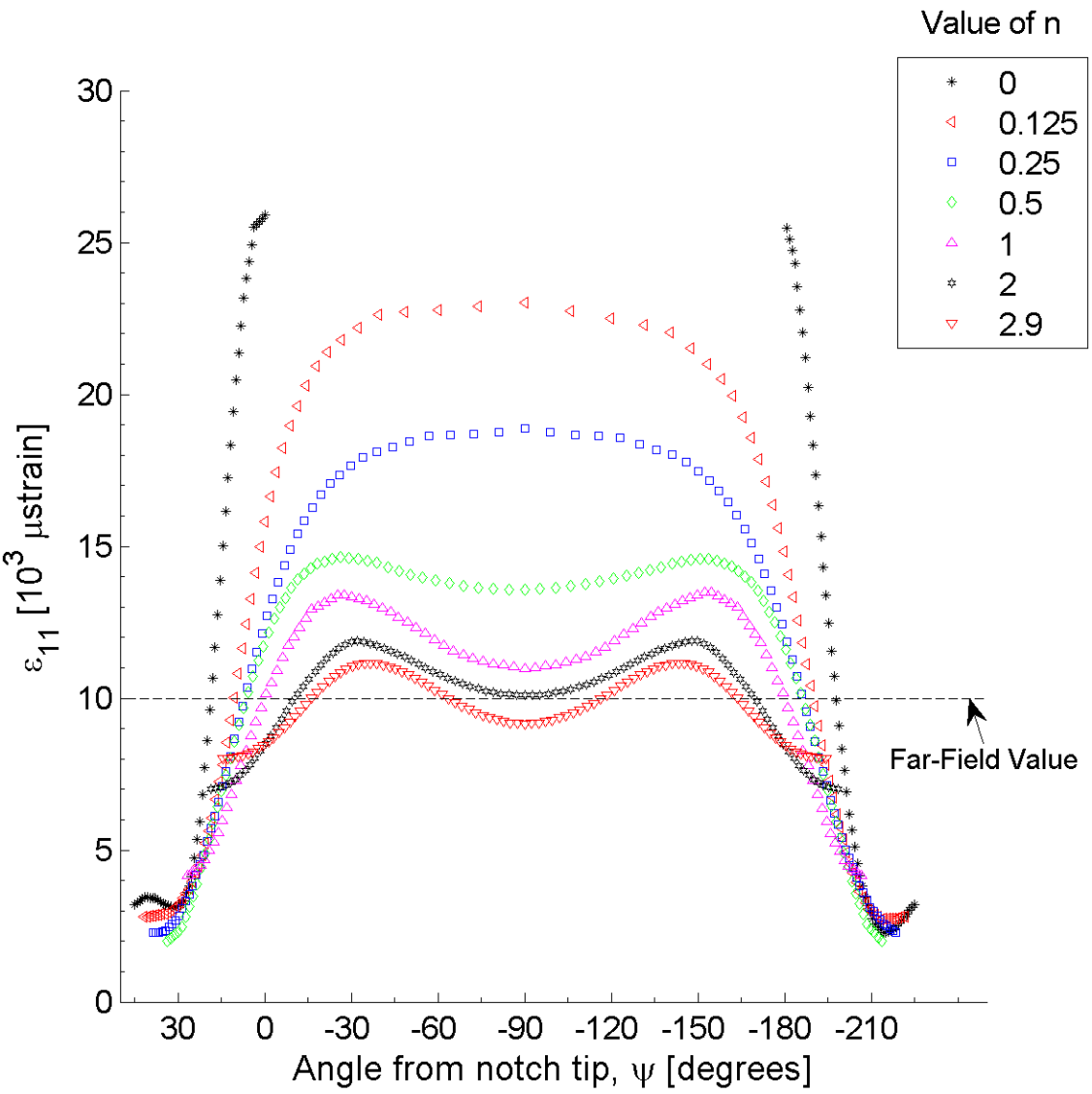

Figure 7.81 Plot of ϵ_{11}, in laminate axes, along arc paths at the midplane of ply 1 (a $+45°$ ply) of the open-hole tension specimen model for case of a 0.5 inch diameter hole for the single-ply effective ply thickness laminate of $[+45/0/-45]_{4S}$.

and geometry. In all cases, these peaks are first observed in the path for n equal to 0.5, as can be seen in Figures 7.81, B.64, B.67, and 7.82. In each of the laminates, these peaks occur close to the fiber angles of the angle plies, i.e., ψ close to $\pm 45°$. Also observed in these figures is a slight skewness of the plots. The skewness is observed in the arc paths where n is equal to 0, 0.125, and 0.25, which are within the edge effect region of the edge of the hole, for the four-ply effective ply thickness laminates, and not observed for the single-ply effective ply thickness laminates. This skewness is observed to vary through the thickness (z-direction) of the four-ply effective ply thickness laminates, as shown in Figures 7.82, 7.83, and 7.84. The skewness is not observed in arc paths with values of n greater than 0.25. The graphs of the gradients of the single-ply effective ply thickness laminates are independent of location through the thickness. For the other laminates these plots are shown in Figures B.64 through B.67, included in Appendix B.3.

As discussed in Section 7.3.1, an advantage to plotting the values of the strain fields in such plots is that multiple gradients are observable in a single graph. The gradient of the strain fields along each arc path is the slope of the strain line for that path. The largest gradients are observed along the path for n equal to 0, with the gradients decreasing and leveling off farther from the edge of the hole, that is as the value of n increases. Unlike the single-edge-notched and double-edge-notched specimens, the gradient along the farthest arc path, n equal to 2.9, is observed to increase compared to the gradient along the neighboring arc path, n equal to 2, in the region between ψ equal to $-50°$ to $-130°$. The corresponding region of the arc path of n equal to 2.9 is near the right edge. Thus, these results may be attributed to free-edge effects. Furthermore, as this radial distance away from the edge of the hole increases, the strain fields of ϵ_{11} approach the "unnotched" solution of 1% for the strain. Another advantage of these plots is that the defined characteristic lengths for the specimen, l_{10} and l_5, can be visualized at discrete distances from the edge of the hole (i.e., between arc paths for various values of the angle ψ). For example, the values of strain along ψ equal to $-90°$ are observed to approach the far-field strain as the radial distance increases. The approximate characteristic length can be

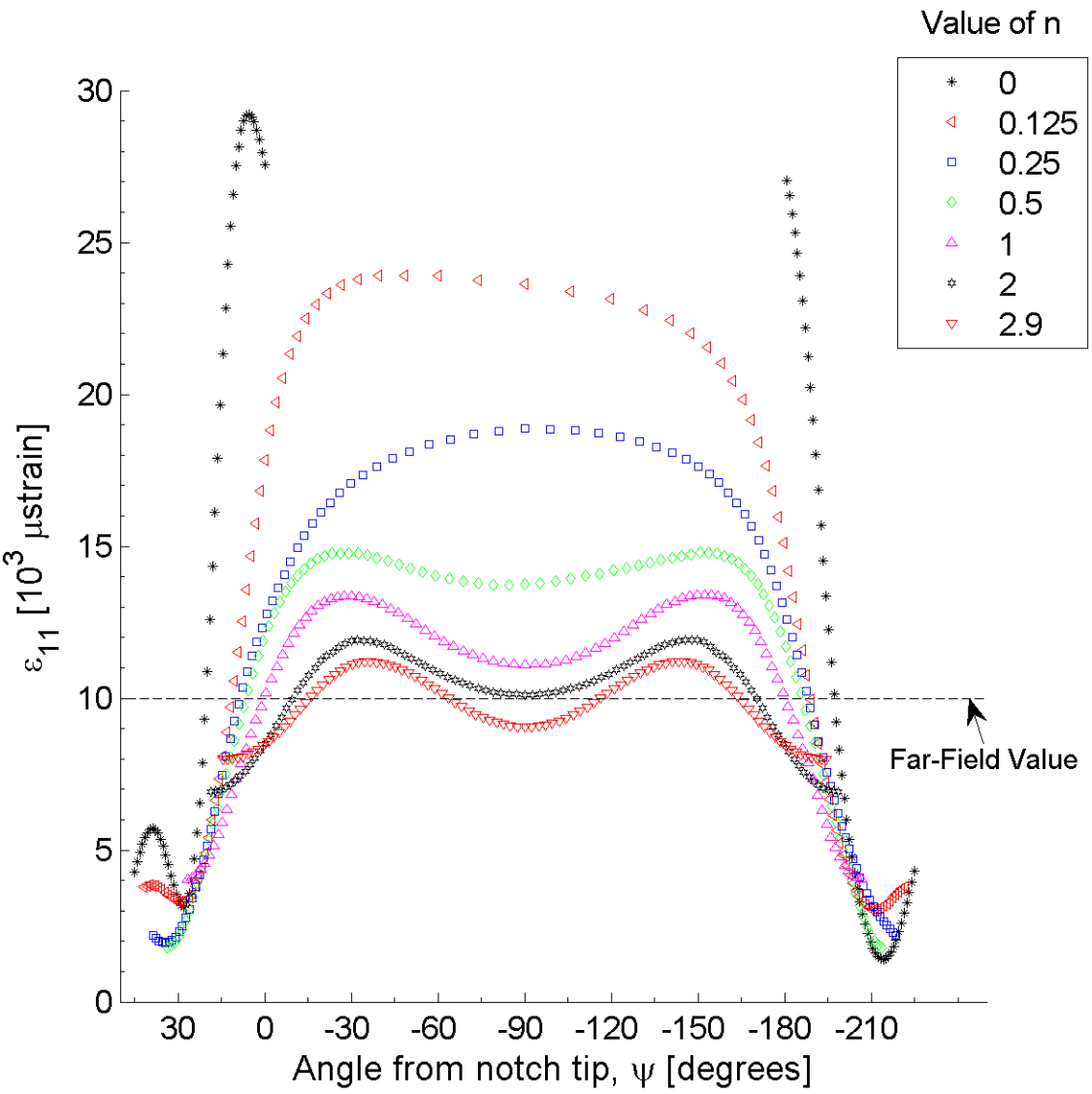

Figure 7.82 Plot of ϵ_{11}, in laminate axes, along arc paths at the midplane of ply 1 (a $+45°$ ply) of the open-hole tension specimen model for case of a 1.0 inch diameter hole for the four-ply effective ply thickness laminate of $[+45_4/0_4/-45_4]_S$.

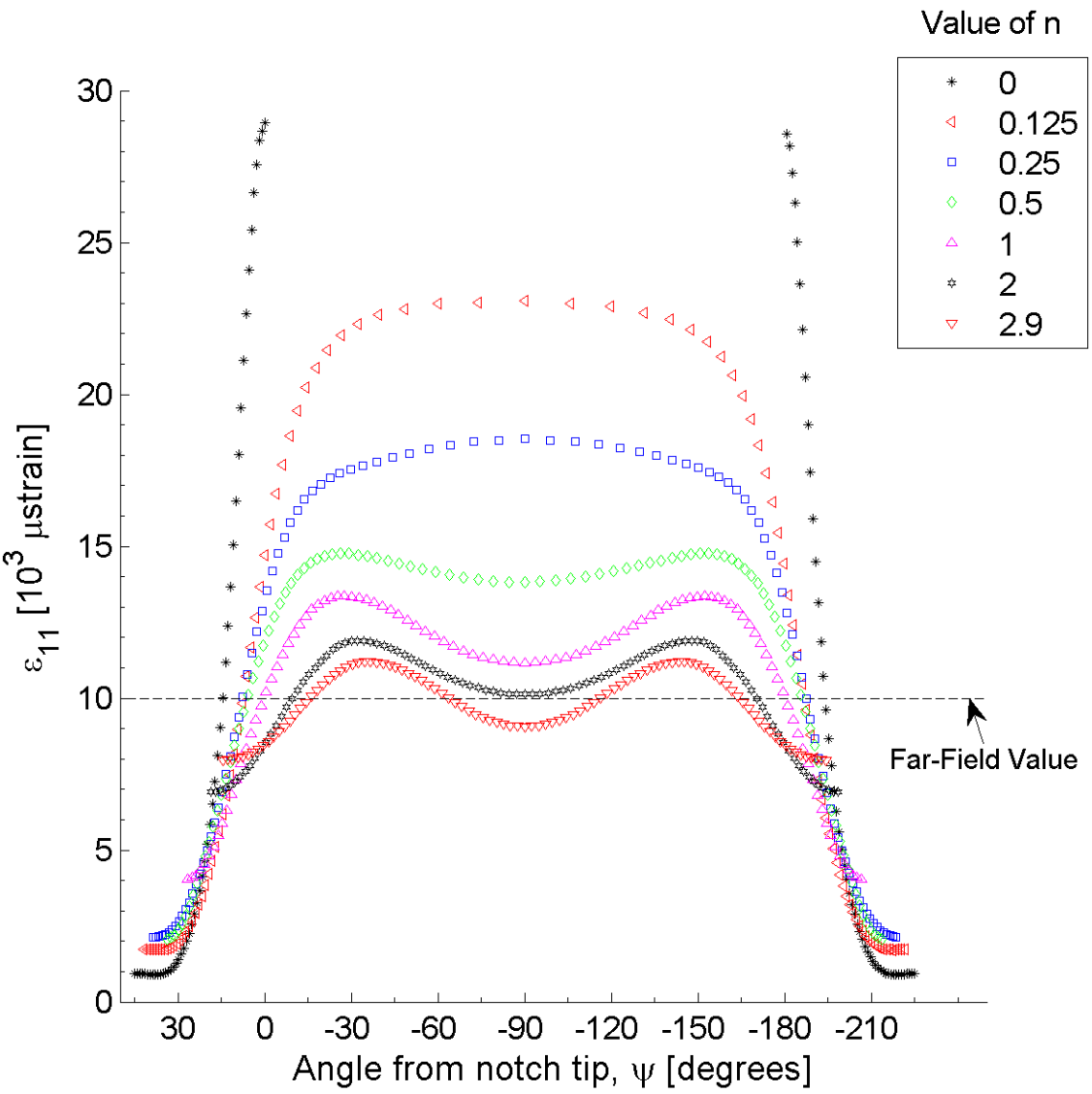

Figure 7.83 Plot of ϵ_{11}, in laminate axes, along arc paths at the midplane of ply 6 (a 0° ply) of the open-hole tension specimen model for case of a 1.0 inch diameter hole for the four-ply effective ply thickness laminate of $[+45_4/0_4/-45_4]_S$.

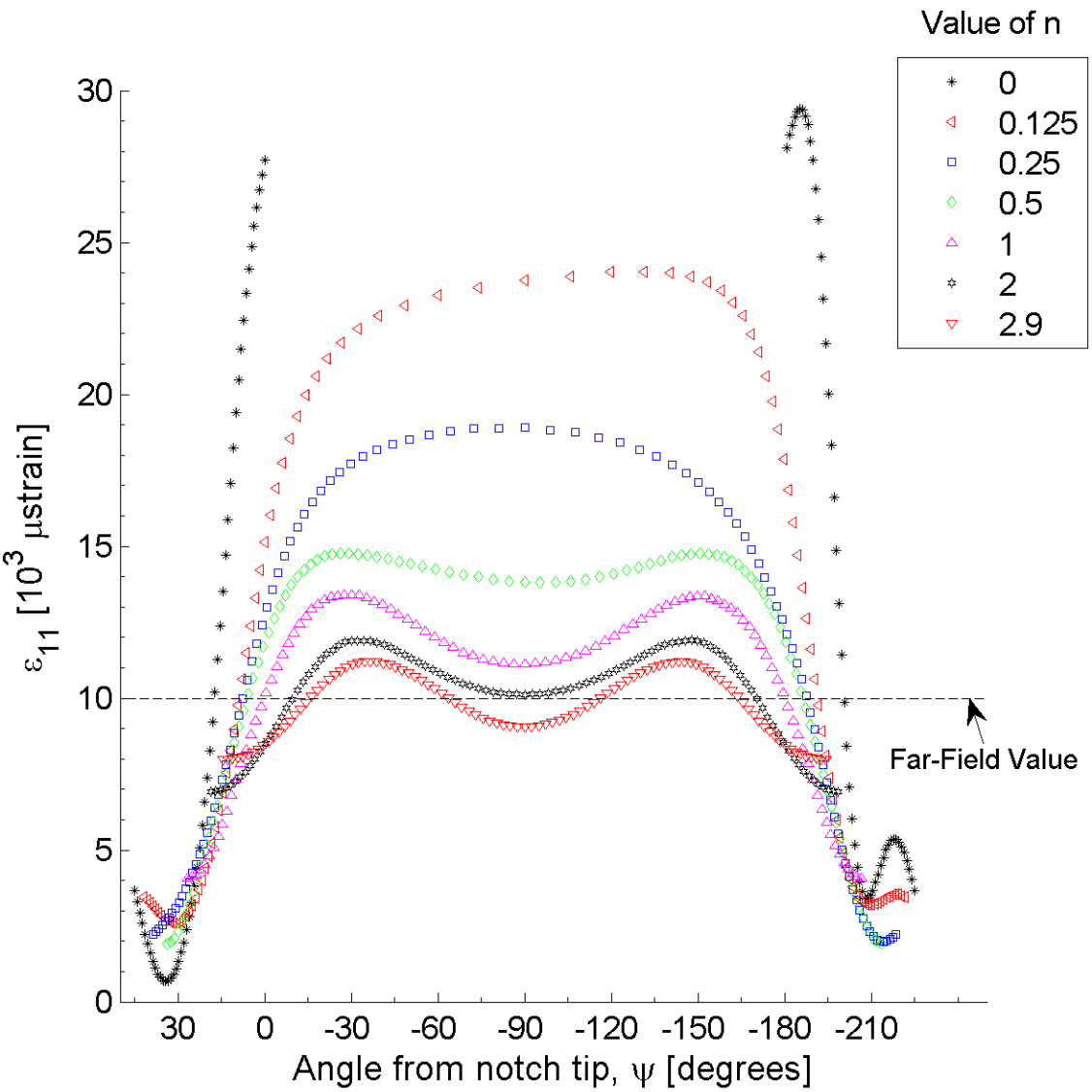

Figure 7.84 Plot of ϵ_{11}, in laminate axes, along arc paths at the midplane of ply 12 (a $-45°$ ply) of the open-hole tension specimen model for case of a 1.0 inch diameter hole for the four-ply effective ply thickness laminate of $[+45_4/0_4/-45_4]_S$.

determined based on the arc path that first exhibits a value of strain equal to the value of far-field strain at ψ equal to $-90°$. The exact characteristic lengths, as previously determined, are listed in Table 7.25. These plots also allow other visualizations of the trends in the strain fields, such as whether the strain values approach the far-field value along other values of the angle ψ. Such information may be useful in the future in identifying additional characteristic lengths associated with the geometry.

Gradients of strain in the radial direction are represented by the difference in the value of strain between arc paths at a given value of ψ in these plots divided by the distance between these arc paths. As previously noted, the radial distance between paths is a function of the offset angle ψ in the offset polar coordinate system. In order to compare the gradients in general radial directions, the radial distance between arc paths, as a function of ψ, must be calculated. This calculation is based on geometric relations. The gradients of the values of ϵ_{11} between neighboring arc paths are given in Table 7.26 for ψ equal to $-90°$, the same angle used to define the characteristic lengths, l_{10} and l_5. The gradients could be calculated for all angles of ψ in the future. For ψ equal to $-90°$, the distance between arc paths is equal to the radial distance between the paths. It is observed that there are slightly higher gradients near the edge of the hole for the single-ply effective ply thickness laminates. Both laminates, as well as both geometries (i.e., in-plane specimen dimensions), exhibit large gradients between the arc paths of n less than 0.5. Between the arc paths of n equal to 0.5 and 1, the gradients decrease by a factor of approximately four. Beyond the arc path of n equal to 1, the gradients are relatively small.

The strain fields of ϵ_{22} for the laminates considered have negative values, as shown in the results for ϵ_{22} for the single-ply effective ply thickness laminate for the case of a 0.5 inch diameter hole shown in Figure 7.85. The strain fields of ϵ_{22} for the four-ply effective ply thickness laminate as well as the single-ply and four-ply effective laminates for the case of a 1.0 inch diameter hole are shown in Figures B.68 through B.70, included in Appendix B.3. The peak maximum and minimum values are indicated in these figures, with the values and locations for each laminate listed in Table 7.24. The peak maximum and minimum values occur along the edge of the hole, at values

Table 7.26 Gradients of the values of ϵ_{11} between 'arc paths' for ψ equal to $-90°$ for the open-hole tension specimen laminates

Hole Diameter, r_o [in]	**Normalized Effective Ply Thickness**	**Arc Paths (n values)**	**Gradient** $[\mu\epsilon/mm]$
0.5	1	0 - 0.125	-3600
		0.125 - 0.25	-5200
		0.25 - 0.5	-3300
		0.5 - 1	-800
		1 - 2	-100
		2 - 2.9	-200
	4	0 - 0.125	-2800
		0.125 - 0.25	-4600
		0.25 - 0.5	-3500
		0.5 - 1	-900
		1 - 2	-200
		2 - 2.9	-200
1.0	1	0 - 0.125	-2900
		0.125 - 0.25	-3300
		0.25 - 0.5	-1600
		0.5 - 1	-400
		1 - 2	-100
		2 - 2.9	-100
	4	0 - 0.125	-2500
		0.125 - 0.25	-3000
		0.25 - 0.5	-1600
		0.5 - 1	-400
		1 - 2	-100
		2 - 2.9	-100

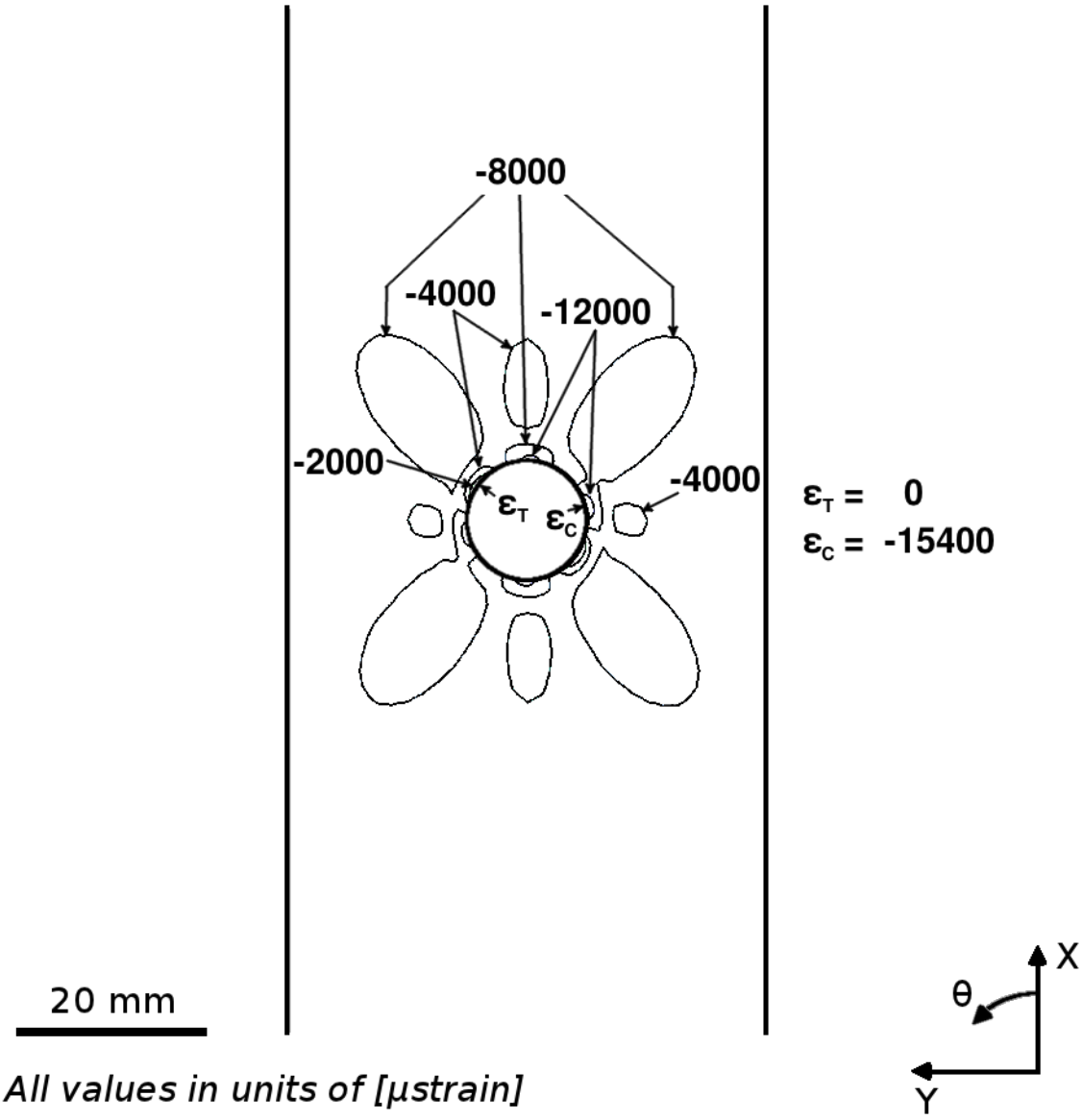

Figure 7.85 Isostrain plot of strain field of ϵ_{22}, in laminate axes, at the midplane of ply 1 (a $+45°$ ply) of the open-hole tension specimen model for case of a 0.5 inch diameter hole for the single-ply effective ply thickness laminate of $[+45/0/-45]_{4S}$.

of r/r_o equal to 1. The locations of these peak values in the polar coordinate angle ϕ are observed to be independent of the effective ply thickness and geometric size of the specimen, as indicated by the results in Table 7.24. These locations do not match the corresponding peak maximum and minimum locations for ϵ_{11}. Overlaying the strain fields for the single-ply effective ply thickness laminate for the cases of a 0.5 inch and 1.0 inch diameter hole, shown in Figures 7.85 and B.69, shows that the fields are normalized via hole diameter (i.e., the distance from the hole edge for each isoline is scaled via the hole diameter size). The fields for the cases of the 0.5 inch and 1.0 inch diameter hole specimens overlay exactly for both the single-ply and four-ply effective ply thickness laminates.

The strain fields of ϵ_{22} exhibit central symmetry about the center of the hole (x-y origin). These strain fields exhibit slight asymmetries in the angle plies (i.e., $+45°$ and $-45°$ plies) when comparing symmetry about the x-z plane and the y-z plane, as seen in Figure 7.85. These asymmetries are located in an annular region contained within a distance of approximately one-half the diameter of the hole from the edge of the hole, as was the size of the region observed to exhibit differences in the strain fields of ϵ_{11} for the single-ply and four-ply effective ply thickness laminates. This region is influenced by the free edge of the hole. Beyond this region, the results are symmetric about the x-z and y-z planes. This trend is observed throughout the laminate thickness and for the laminates and geometric sizes considered.

The strain fields of ϵ_{22} in the 'far-field' are identical between the angle plies and the $0°$ plies, as seen in Figures 7.85 and B.71. The 'far-field' (at a distance greater than 1 hole radii from the edge of the hole) isostrain lines are consistent for all plies of a laminate, as would be predicted from LPT. In the 'near-field' (at a distance less than 1 hole radii from the edge of the hole and within the influence of the free-edge effects), a slight variation occurs, as for the results of ϵ_{11}. These variations are more noticeable in the four-ply effective ply thickness laminates, such as the strain fields shown in Figure B.68. The strain fields of the negative plies are mirrored about the y-z place from the fields shown in this figure. As with ϵ_{11}, the strain fields of the angle plies neighboring $0°$ plies transition to the symmetric strain fields of the $0°$ plies, as

shown in Figure B.72.

In the "unnotched" region of all the laminates, the observed values of the strain fields for ϵ_{22} are on the order of the expected Poisson's effect. For example, the Poisson's ratio for the single-ply and four-ply effective ply thickness laminates, given in Table 7.4, is 0.65. The majority of the "unnotched" region of the laminate, shown in Figure 7.85, has a value between -8000 μstrain and -4000 μstrain. Had the specimen been featureless (i.e., without a hole), the expected value of ϵ_{22} would be -6500 μstrain due to Poisson's effects, excluding the regions within the free edge zone. However, the effect of the hole and the given loading creates gradients within the region near the hole. As with the results for ϵ_{11}, the characteristic lengths, l_{10} and l_5, are measured for the ϵ_{22} results and given in Table 7.25. The l_{10} characteristic length is constant across the specimens, with the exception of the four-ply effective ply thickness laminate for the case of the 0.5 inch diameter hole specimen, where a far-field strain is not reached before the edge of the specimen. In all specimens, ϵ_{22} does not reach within 5% of the far-field strain before the specimen edge.

As with the gradients for ϵ_{11}, gradients in the strain fields of ϵ_{22} are observed to be relatively independent of the angle of a ply and dependent on the through-thickness location of a ply. The values of ϵ_{22} along the arc paths versus the polar coordinate angle, ψ, are plotted for the single-ply effective ply thickness laminate for the case of a 0.5 inch diameter hole in Figure 7.86. The respective plot for the single-ply effective ply thickness laminate for the case of a 1.0 inch diameter hole is shown in Figure B.73, and the plots for the four-ply effective ply thickness laminate for the cases of a 0.5 and 1.0 inch diameter hole are shown in Figures B.74 and B.75, included in Appendix B. For the arc paths with n equal to 0, 0.125, and 0.25, which are within the region influenced by the free-edge of the hole, the values are skewed toward the right side of the plot. Unlike the previous models, this skewness does not exhibit a dependence on the ply angle, instead there is a dependence on the through-thickness location of the ply, as seen in Figure 7.87. The magnitudes along these arc paths slowly transition from those in Figure 7.86 to those in Figure 7.87, with the magnitudes fairly symmetric about ψ equal to -90° in the sixth ply. The

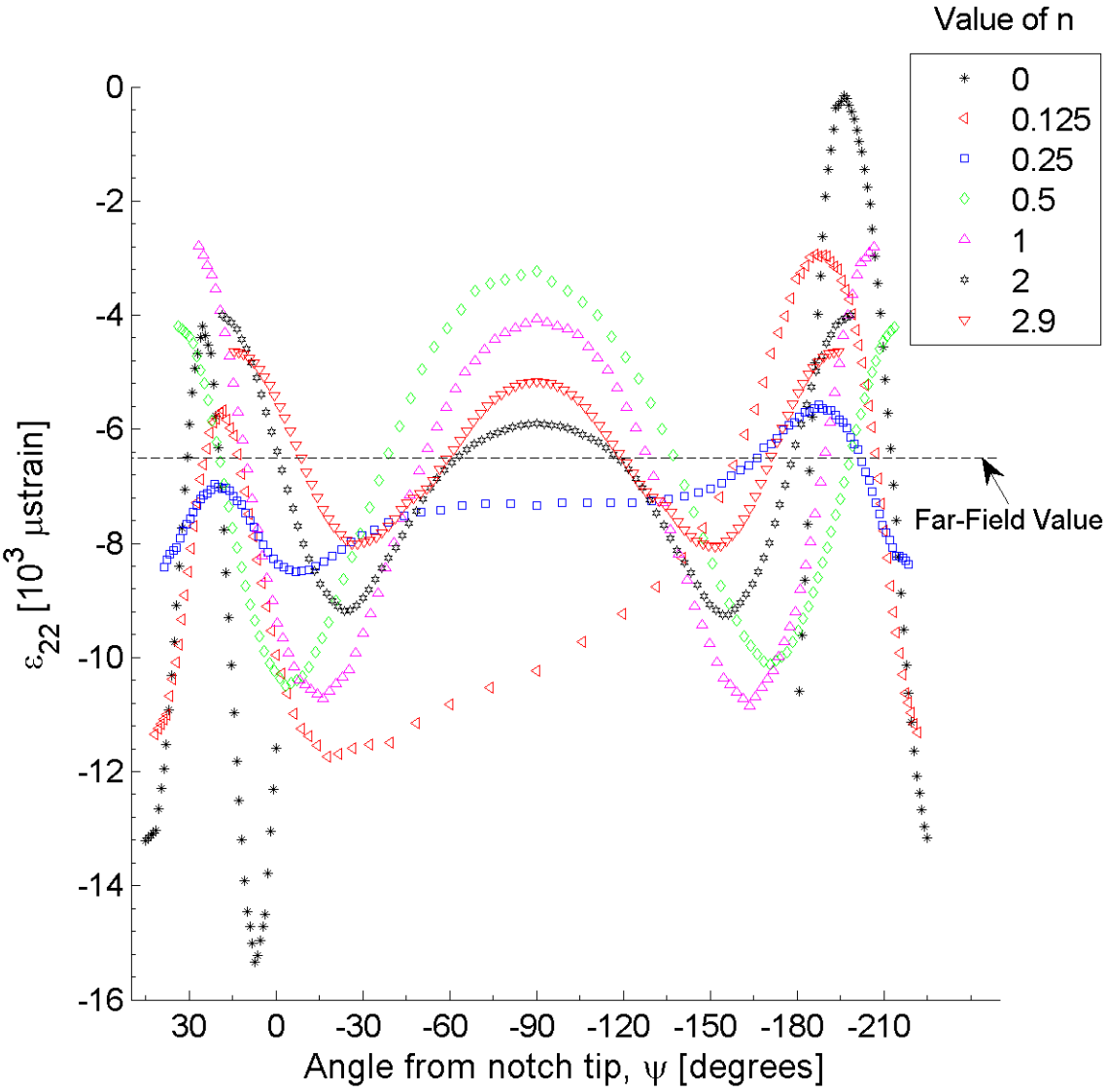

Figure 7.86 Plot of ϵ_{22}, in laminate axes, along arc paths at the midplane of ply 1 (a $+45°$ ply) of the open-hole tension specimen model for case of a 0.5 inch diameter hole for the single-ply effective ply thickness laminate of $[+45/0/-45]_{4S}$.

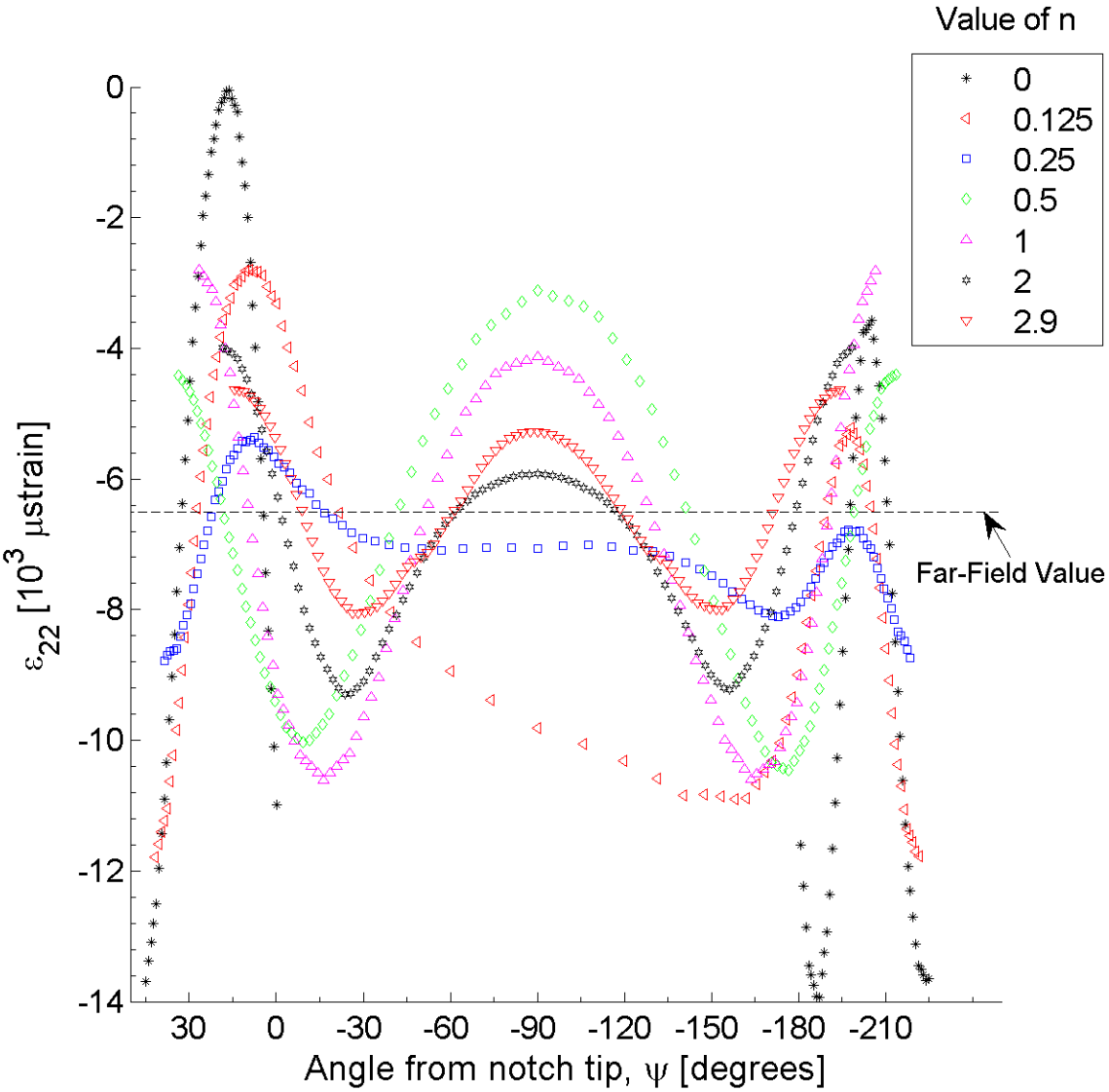

Figure 7.87 Plot of ϵ_{22}, in laminate axes, along arc paths at the midplane of ply 12 (a $-45°$ ply) of the open-hole tension specimen model for case of a 0.5 inch diameter hole for the four-ply effective ply thickness laminate of $[+45/0/-45]_{4S}$.

values of strain plotted against ψ eventually form one 'peak' and two 'valleys' as the distance from the hole edge increases. For the two geometric sizes of the specimen, these 'peaks' and 'valleys' are first observed for the arc path with n equal to 0.5. A 'far-field' values of ϵ_{22} is not established within the distances of the arc paths. The 'peak' established in the arc path of n equal to 0.5 trends toward the far-field solution up to the arc path of n equal to 2. For the arc path of n equal to 2.9, the results diverge from the far-field solution, likely due to free-edge effects.

As was done in Table 7.26 for ϵ_{11}, the gradients of the values of ϵ_{22} between neighboring arc paths are given in Table 7.27 for ψ equal to $-90°$, the same angle used to characterize the characteristic lengths, l_{10} and l_5. It is observed that these gradients are dependent on the effective ply thickness. For the single-ply effective ply thickness laminate, the value of ϵ_{22} is observed to have a positive gradient between the hole edge and the arc path of n equal to 0.5. However, the results in this region are uncertain due to the free-edge effects discussed in Section 7.1. Beyond the arc path of n equal to 0.5, the gradient magnitude is only a couple hundred μstrain per millimeter. For the four-ply effective ply thickness laminate, there is a slightly negative gradient between the hole edge and the arc path with n equal to 0.125. The gradient then become positive between the arc paths of n equal to 0.125 and 0.5. Again, the results in this region are uncertain due to free-edge effects. The magnitudes of the gradients in this region are smaller than those observed in the single-ply effective ply thickness laminate, with the exception of the gradient between the arc paths of n equal 0.25 to 0.5 for the case of the 1.0 inch diameter hole specimen. As with the single-ply effective ply thickness laminate, beyond the arc path of n equal to 0.5, the gradient magnitude is only a couple hundred μstrain per millimeter.

The strain fields of ϵ_{12} for the open-hole tension specimen, as shown for the single-ply effective ply thickness laminate for the case of a 0.5 inch diameter hole in Figure 7.70, are observed to be uniform for each laminate, regardless of the location through the thickness (z-direction) of the laminate, as observed for ϵ_{11} and ϵ_{22}. The strain fields of ϵ_{12} for the four-ply effective ply thickness laminate as well as the single-ply and four-ply effective laminates for the case of a 1.0 inch diameter hole are shown

Table 7.27 Gradients of the values of ϵ_{22} between 'arc paths' for ψ equal to $-90°$ for the open-hole tension specimen laminates

Hole Diameter, r_o [in]	**Normalized Effective Ply Thickness**	**Arc Paths (n values)**	**Gradient** $[\mu\epsilon/mm]$
0.5	1	0 - 0.125	+1700
		0.125 - 0.25	+3600
		0.25 - 0.5	+2600
		0.5 - 1	-300
		1 - 2	-300
		2 - 2.9	+100
	4	0 - 0.125	-200
		0.125 - 0.25	+1100
		0.25 - 0.5	+1900
		0.5 - 1	0
		1 - 2	-300
		2 - 2.9	+400
1.0	1	0 - 0.125	+1400
		0.125 - 0.25	+3300
		0.25 - 0.5	+900
		0.5 - 1	-200
		1 - 2	-100
		2 - 2.9	+100
	4	0 - 0.125	-600
		0.125 - 0.25	+1500
		0.25 - 0.5	+1200
		0.5 - 1	-100
		1 - 2	-100
		2 - 2.9	+200

in Figures B.76 through B.78, included in Appendix B.3. In each case, the strain fields of ϵ_{12} observed are identical regardless of the angle of the ply or the through thickness location of the ply, excluding the annular regions effected by free edges discussed later. As is the case for the results of ϵ_{11} and ϵ_{22}, overlaying the strain fields for the single-ply effective ply thickness laminate for the cases of a 0.5 inch and 1.0 inch diameter hole, shown in Figures 7.70 and B.77, shows that the fields are normalized via hole diameter. The fields for the cases of the 0.5 inch and 1.0 inch diameter hole specimens overlay exactly for both the single-ply and four-ply effective ply thickness laminates.

As for the other in-plane strains, the strain fields of ϵ_{12} at the edge of the hole are consistent through the plies of each laminate, with small variations between positive and negative plies occurring within the annular region near the edge of the hole where free-edge effects exist. These effects are more easily seen in the four-ply effective ply thickness laminate. As with the results for ϵ_{11} and ϵ_{22}, the results of ϵ_{12} approach the predicted LPT solution as the distance from the edge of the hole increases. For example, the coefficient of mutual influence for the single-ply and four-ply effective ply thickness laminates, given in Table 7.4, is 0. The majority of the "unnotched" region of the laminate, shown in Figure 7.70, has a value between -5000 μstrain and +5000 μstrain. Had the specimen been featureless (i.e., without a hole), the expected value of ϵ_{12} would be 0 μstrain due to the balanced laminate, excluding the regions within the free edge zone. However, the effect of the hole and the given loading creates gradients within the region near the hole, and extending beyond the region influenced by the free-edge effects.

The gradients in the strain fields of ϵ_{12} are observed to be dependent on the effective ply thickness of the laminate. The values of ϵ_{12} along the arc paths versus the polar coordinate angle, ψ, are plotted for the single-ply effective ply thickness laminate for the case of a 0.5 inch diameter hole in Figure 7.88. For the four-ply effective ply thickness laminate and the single-ply and four-ply effective ply thickness laminate for the case of a 1.0 inch diameter hole these plots are shown in Figures B.79 through B.81, included in Appendix B.3. As for ϵ_{22}, the values of ϵ_{12} plotted against

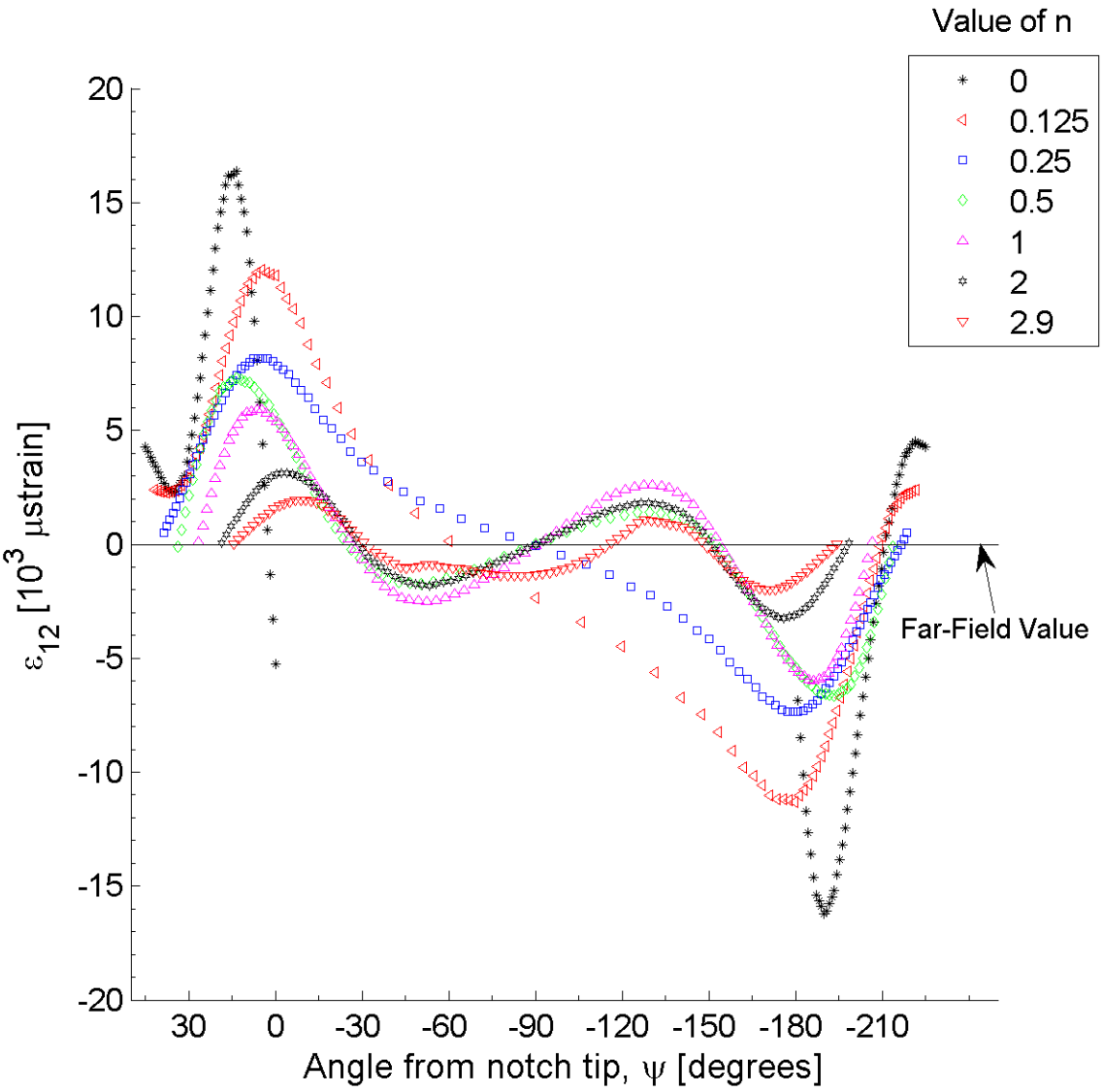

Figure 7.88 Plot of ϵ_{12}, in laminate axes, along arc paths at the midplane of ply 1 (a $+45°$ ply) of the open-hole tension specimen model for case of a 0.5 inch diameter hole for the single-ply effective ply thickness laminate of $[+45/0/-45]_{4S}$.

ψ eventually form two 'peaks' and two 'valleys' as the distance from the edge of the hole increases. In both the single-ply and four-ply effective ply thickness laminates, the trend is first observed in the arc path for n equal to 0.5, as seen in Figure 7.88. As with the gradients for ϵ_{22}, the gradients observed in these figures are slightly skewed in the plots for n less than 0.5, which corresponds with the region of uncertain solution due to free-edge effects. This trend remains consistent through the thickness of the laminate, with variations only in the relative magnitudes of the plots. The same basic trend is observed throughout the thickness of both laminates and both specimen geometries.

As with the results for ϵ_{11} and ϵ_{22}, the characteristic lengths, l_{10} and l_5, are measured for the ϵ_{12} results and given in Table 7.25. Unlike the characteristic lengths of the other in-plane results, the characteristic lengths of ϵ_{12} have a large variation. The variation in characteristic lengths of ϵ_{11} and ϵ_{22} was only a few hundredths of a hole radius, the variation in characteristic lengths of ϵ_{12} was on order of a few tenths of a hole radius, with the largest variation being 0.89 radii between the l_5 for the four-ply effective ply thickness laminate for the case of the 0.5 inch diameter hole and the single-ply effective ply thickness laminate for the case of the 1.0 inch diameter hole.

As was done in Table 7.26 for ϵ_{11} and in Table 7.27 for ϵ_{22}, the gradients of the values of ϵ_{12} between neighboring arc paths are given in Table 7.28 for ψ equal to $-90°$, the same angle used to characterize the characteristic lengths, l_{10} and l_5. It is observed that these gradients are relatively independent of the geometric size of the specimen. Both the single-ply and four-ply effective ply thickness laminate specimens exhibit a large gradient between the edge of the hole and the arc path with n equal to 0.25, which is within the region effected by the free-edge of the hole. Beyond the arc path with n equal to 0.25 the magnitudes of the gradients becomes relatively small compared to those near the hole. It is observed that the gradients in the four-ply effective ply thickness laminate specimens are approximately 50% larger than those of the single-ply effective ply thickness laminate specimen.

The out-of-plane strain results are considered subsequently. These strain fields

Table 7.28 Gradients of the values of ϵ_{12} between 'arc paths' for ψ equal to $-90°$ for the open-hole tension specimen laminates

Hole Diameter, r_o [in]	**Normalized Effective Ply Thickness**	**Arc Paths (n values)**	**Gradient** $[\mu\epsilon/mm]$
0.5	1	0 - 0.125	+3700
		0.125 - 0.25	+2900
		0.25 - 0.5	0
		0.5 - 1	0
		1 - 2	0
		2 - 2.9	-200
	4	0 - 0.125	+5500
		0.125 - 0.25	+6700
		0.25 - 0.5	+2000
		0.5 - 1	-400
		1 - 2	0
		2 - 2.9	-600
1.0	1	0 - 0.125	+3300
		0.125 - 0.25	+500
		0.25 - 0.5	0
		0.5 - 1	0
		1 - 2	0
		2 - 2.9	-100
	4	0 - 0.125	+5700
		0.125 - 0.25	+3400
		0.25 - 0.5	-200
		0.5 - 1	-100
		1 - 2	0
		2 - 2.9	-300

are observed to have variations through the thickness of each laminate. Variations from LPT exist in the model results due to free-edge effects at the edge of the hole. Due to the mesh density used near free edges of the model, free-edge effects such as those discussed in [58, 60, 74, 76, 139] are not captured. The free-edge effects in these regions result in large gradients in the interlaminar stresses. Therefore, the out-of-plane results are not valid in the boundary layer [148–150] of the free edge. For the open-hole tensions specimen, this boundary layer is approximately one laminate thickness, corresponding to 0.25 and 0.13 hole radii for the 0.5 inch diameter and 1.0 inch diameter hole specimens, respectively. Because the models do not capture the out-of-plane gradients near the free edges, which are expected to be greater than the gradients within the specimen, little discussion will be included on the out-of-plane results.

The strain fields of ϵ_{33} exhibit consistent shape through the thickness for each laminate considered. Variations in the isostrain lines are observed to be dependent on the through-thickness location and occur within the region influenced by the free edge of the hole. Thus, these are not further discussed. The strain fields of ϵ_{33} for the single-ply effective ply thickness laminate for the case of the 0.5 inch diameter hole specimen is shown in Figure 7.89. The strain fields of the four-ply effective ply thickness laminate as well as the single-ply and four-ply effective ply thickness laminates for the case of a 1.0 inch diameter hole specimen are shown in Figures B.82 through B.83, included in Appendix B.84. As with the in-plane results, the out-of-plane results exhibit central symmetry. For all cases, the far-field strain fields for ϵ_{33} are on the order of the expected Poisson's effect. For example, the Poisson's ratio for both the single-ply and four-ply effective ply thickness laminates, given in Table 7.4, is 0.13. The majority of the specimen, beyond the region influenced by the hole, has strain values between -1000 μstrain and -2000 μstrain. Had the specimen been featureless (i.e, without a hole), the expected value of ϵ_{33} would be -1300 μstrain due to Poisson's effects.

The locations and values of the peak maximum (ϵ_T) and minimum (ϵ_C) 'local' out-of-plane strains for each laminate are listed in Table 7.29. The locations of the

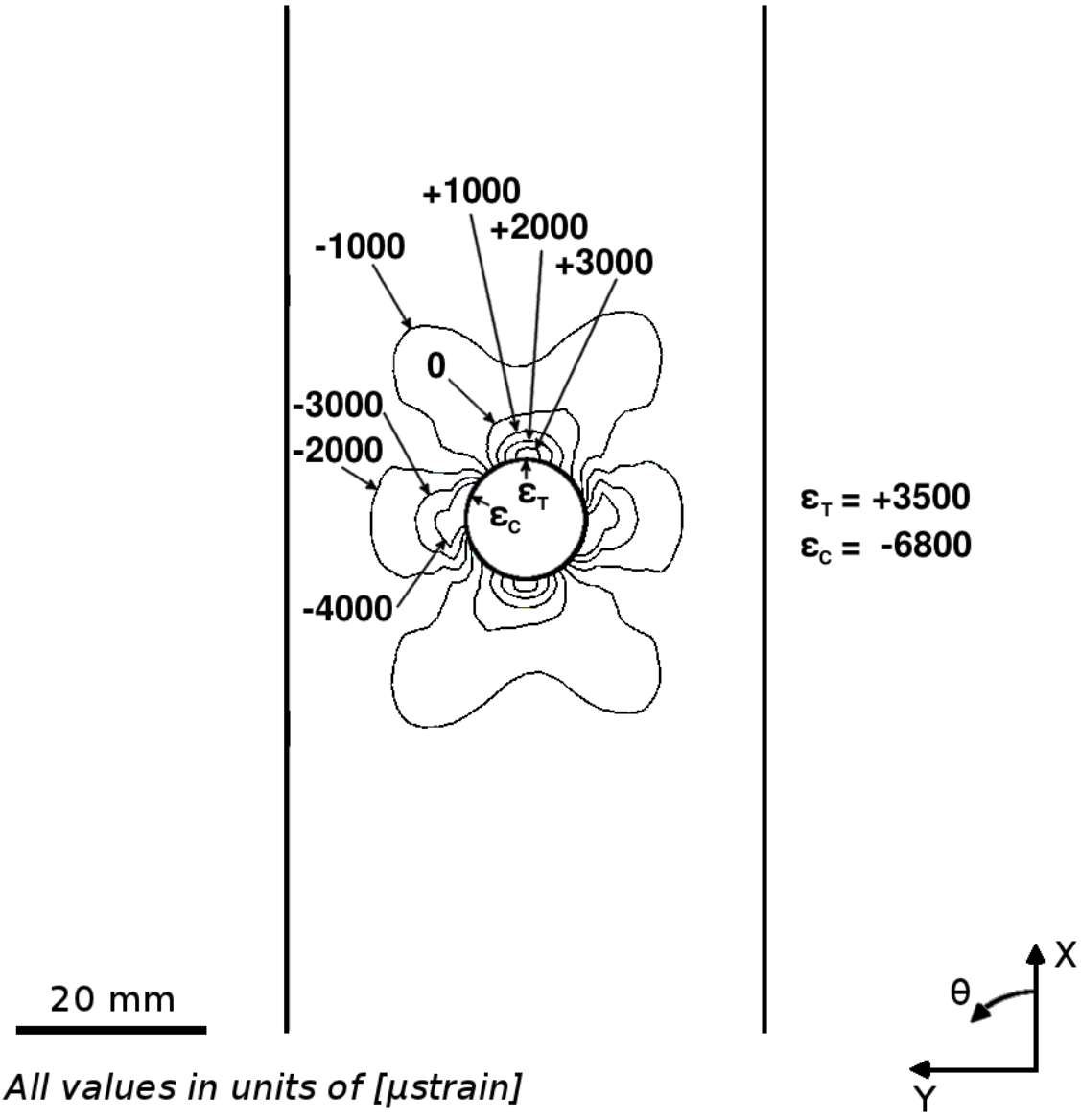

Figure 7.89 Isostrain plot of strain field of ϵ_{33}, at the midplane of ply 1 (a $+45°$ ply) of the open-hole tension specimen model for case of a 0.5 inch diameter hole for the single-ply effective ply thickness laminate of $[+45/0/-45]_{4S}$.

Table 7.29 Locations and values of maximum and minimum out-of-plane strains for the open-hole tension specimens (laminates of $[+45/0/-45]_{4S}$ and $[+45_4/0_4/-45_4]_S$)

Strain Component	**Value Considered**[a]	**Hole Diameter [in]**	**Nominal Effective Ply Thickness**	**Value [μstrain]**	$\frac{\mathbf{r}}{\mathbf{r_o}}$	ϕ **[degrees]**
ϵ_{33}	ϵ_T	0.5	1	+3500	1	0
			4	+3800	1	0
		1.0	1	+4100	1	0
			4	+4400	1	0
	ϵ_C	0.5	1	-6800	1	75
			4	-7400	1	75
		1.0	1	-7600	1	77
			4	-8700	1	77
ϵ_{13}	ϵ_S	0.5	1	$\pm$5700	1	109
			4	$\pm$2100	1	128
		1.0	1	$\pm$6700	1	107
			4	$\pm$3000	1	110
ϵ_{23}	ϵ_S	0.5	1	$\pm$2600	1	0
			4	$\pm$1100	1	0
		1.0	1	$\pm$3000	1	0
			4	$\pm$1100	1	170

[a] ϵ_T = Maximum
ϵ_C = Minimum
ϵ_S = Maximum Magnitude

peak maximum and minimum out-of-plane shear results (ϵ_{13} and ϵ_{23}) are included for comparison purpose, although these strain fields are not further discussed. As with the results for ϵ_{33}, it is expected that the largest gradients occur in the boundary layer of the free edges. In order to define characteristic lengths and accurately capture the large gradient fields near free edges, additional models are needed. This is beyond the scope of the current work.

7.3.4 Ply-Drop Specimen Model

The characteristic strain fields for each of the ply-drop specimen models are illustrated via the results in this subsection. Unlike the other single-edge-notch, double-edge-notch, and open-hole tension specimen models, the in-plane strain field (i.e., ϵ_{11}, ϵ_{22}, and ϵ_{12}) predictions of the ply-drop specimen model are dependent on the through-thickness location. Unique to the ply-drop specimens, the geometry is designed to allow results to be analyzed in the x-z plane. This plane cuts the specimen perpendicular to the y-direction, shown in Figures 4.6 and 7.19. Results presented in this subsection are from the midplane (through-thickness direction) of each ply. The paths from which result are taken correspond to one-dimensional (1-D) paths contained within the x-z plane, as shown in Figure 7.90. The z-location of the paths in the top sublaminate (i.e., plies 25 through 36) changes along the x-direction within the ply-drop region.

As with the models for the single-edge-notched, double-edge-notched, and open-hole tension specimens, a common feature exhibited in all the strain field results is the effects of free edges. These effects are observed as discontinuities in the slopes of the isostrain lines (i.e., the isoline is not smooth) near the edges of the specimen. For the in-plane results, the distance at which the effect is observed, approximately one laminate thickness, is consistent across the results for all the strain fields. Free-edge effects are not observed to influence the region within the x-z plane of the specimen as long as this plane is away from these effects. All results presented for the ply-drop specimens are on this plane, outside the influence of the free-edge effects. Beyond

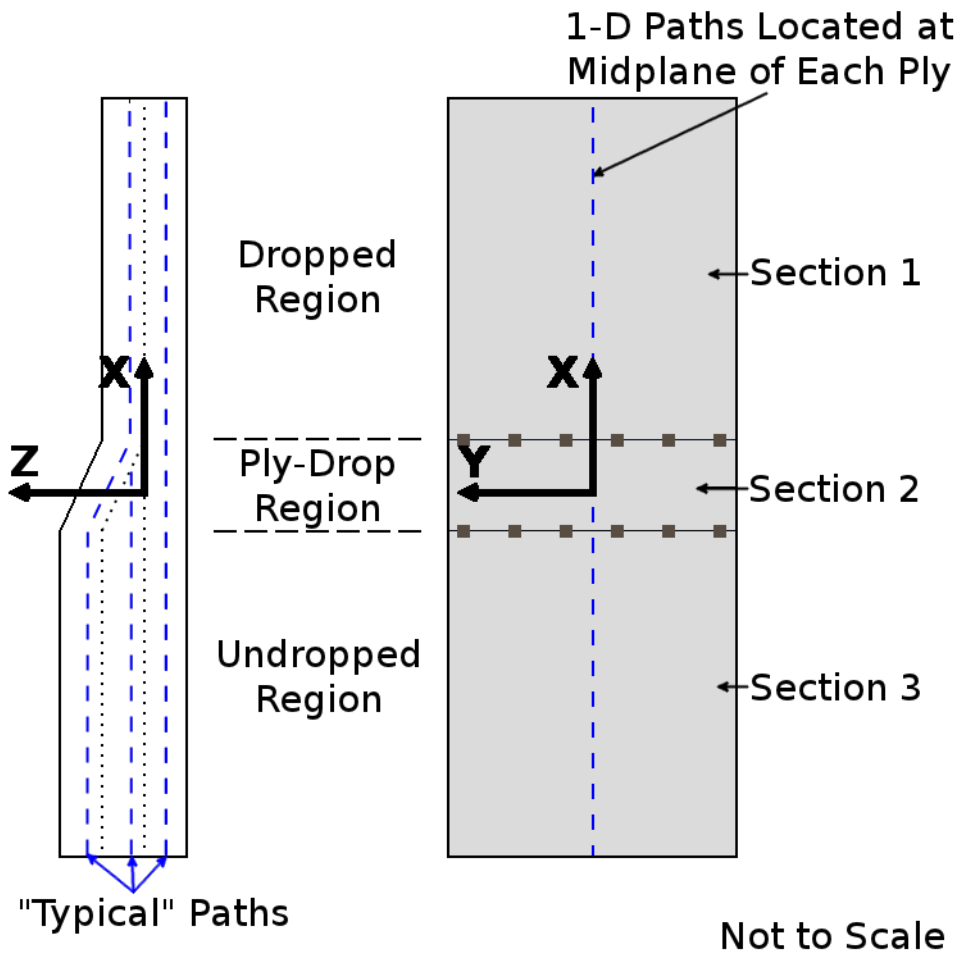

Figure 7.90 Planar (x-y) view of the paths along which strain results are analyzed for the ply-drop specimen model.

these observations of the free-edge effects, these effects are not further discussed.

The results for the in-plane strain fields are considered first. This is followed by the results for the out-of-plane strain fields. As previously noted, the in-plane strain fields are dependent on the through-thickness location of each ply. In order to fully investigate the through-thickness effects, a mechanics of materials approach is first investigated to understand the through-thickness variations of stress and strain. As described in Section 7.2.4, the displacement of the positive and negative x-faces of the specimen are specified via the boundary conditions of the model. These boundary conditions enforce a normal displacement that is proportional to the gage length of the specimen, as shown in Figure 7.24, while enforcing zero displacement in the plane of the x-faces. All other faces are stress free.

In the following mechanics of materials approach, the specimen is first modeled as a series of elastic springs in order to determine effective far-field strains of the specimen. The stress distributions on the two x-faces required to satisfy overall equilibrium are then determined in order to discuss the variation in moment along the length of the ply-drop specimen. This variation in moment is observed in the results of the ply-drop specimen.

The far-field strain of the ply-drop specimen requires calculation based on mechanics of materials relations. Unlike the other specimen geometries considered, the geometry of the ply-drop specimen has varying thickness along the length of the specimen. As discussed in Section 4.4 and shown in Figure 4.6, the ply-drop specimen consists of three regions: undropped, ply-drop, and dropped. The thickness of the specimen is constant in the undropped and dropped regions, while there is a linear variation in thickness, connecting the thickness of the undropped to dropped regions, within the ply-drop region.

In order to calculate the far-field strain in the undropped and dropped regions, the axial force in the x-direction is required. The concept of a far-field strain is not applicable within the ply-drop region due to the limitations of CLPT, which require a constant thickness. The axial force required to achieve the applied displacement, Δ, is calculated by approximating the specimen as three springs in series, with each spring

corresponding to the three regions of the specimen. The effective spring constant of the specimen, k_{eff}, is calculated via the formula for springs in series:

$$\frac{1}{k_{eff}} = \frac{1}{k_{UD}} + \frac{1}{k_{PD}(x)} + \frac{1}{k_D} \tag{7.20}$$

where k_{UD} is the stiffness of the undropped region, k_D is the stiffness of the dropped region, and $k_{PD}(x)$ is the varying stiffness of the ply-drop region.

Beginning with Hooke's Law, the axial force, F, is related to an effective spring constant multiplied by the applied displacement, Δ:

$$F = k_{eff}\Delta \tag{7.21a}$$

$$\sigma_x = E_L\epsilon_x \tag{7.21b}$$

$$\frac{F}{A} = E_L\frac{\Delta}{L} \tag{7.21c}$$

$$F = \frac{E_L A}{L}\Delta \tag{7.21d}$$

This is connected to axial stresses and strains, σ_x and ϵ_x, via length, L, cross-section, A, and the average modulus in the direction aligned with the force and the displacement, E_L. The specimen is assumed to have unit width and an averaged, constant Young's modulus throughout each of the three regions.

The assumption of constant modulus is consistent with CLPT within the undropped and dropped regions. However, this assumption does not accurately capture variations of modulus within the ply-drop region due to the geometry associated with each ply drop. The Young's modulus is underestimated in the region beyond (positive x-direction) the dropped angle plies, while it is overestimated in the region beyond a dropped zero-degree ply. The resulting laminate in the region beyond a dropped angle ply effectively has more plies oriented in the zero direction, thus resulting in a laminate with a larger modulus than the averaged Young's modulus from the laminate of the undropped or dropped regions. By the same method, the resulting laminate

following a dropped zero-degree ply will have a lower modulus than the averaged Young's modulus of the laminate of the undropped or dropped regions because the effective laminate will have a larger ratio of angle plies than zero-degree plies. The assumption also does not account for the modulus of the resin rich triangular regions, as seen in Figure 7.21, following each ply drop. In addition, the assumption overestimates the contribution of Young's modulus from the plies of the top sublaminate in the ply-drop region. The plies of the top sublaminate are rotated about the y-axis in the ply-drop region, as shown in Figure 7.20, and are thus not fully aligned with the x-direction. Armanios and Parnas [151] provide the three-dimensional transformation of stiffness for the plies of the top sublaminate within the ply-drop region. All these effects are captured within the models of the ply-drop specimen. For the analytical calculations herein, the modulus within the ply-drop region is assumed constant and equal to the longitudinal modulus, E_L, of the laminate of the undropped and dropped regions. The ratio of angle plies to zero-degree plies is the same for the laminates of the undropped and dropped regions, resulting in the same longitudinal modulus as calculated via CLPT.

Equation 7.21a relates the axial force required to stretch the ply-drop specimen by the specified displacement given an effective specimen spring constant. Each region of the specimen will experience the same axial force, but each region will have a different strain response due to the change in thickness and hence a change in axial stiffness. The spring constants for each region are dependent on the Young's modulus, E_L, the cross-sectional area, A, and the length, L, of the region, as seen in Equation 7.21d.

In order to determine the spring constant of each region, Equation 7.21d is applied to each region, with the resulting spring constants:

$$k_{UD} = \frac{E * 3t}{L_{UD}} \tag{7.22a}$$

$$k_{PD} = \frac{E * h_{PD}(x)}{L_{PD}} \tag{7.22b}$$

$$k_{D} = \frac{E * 2t}{L_{D}} \tag{7.22c}$$

where the thickness, t, is equal to the thickness of a sublaminate, as described in Section 4.4. Thus, $3t$ is the thickness of the undropped region and $2t$ is the thickness of the dropped region. The lengths, L_{UD} (43 mm), L_{PD} (12 mm), and L_D (45 mm), are the x-direction lengths of the undropped, ply-drop, and dropped regions, respectively, as shown in Figure 4.6. The specimen contains three sublaminates in the undropped region, two sublaminates in the dropped region, and has one sublaminate dropped over the length of the ply-drop region.

In the ply-drop region, the thickness, h_{PD}, of the specimen is a function of the x-position:

$$h_{PD}(x) = 3t - \frac{t}{L_{PD}}\left(x - L_{UD}\right) \tag{7.23}$$

where x varies from L_{UD} to $(L_{UD} + L_{PD})$. The effective spring constant of the ply-drop region, $k_{PD_{eff}}$, is determined from integration of the inverse of Equation 7.22b over the length of the ply-drop region:

$$\frac{1}{k_{PD_{eff}}} = \int_{L_{UD}}^{L_{UD}+L_{PD}} \frac{dx}{Eh_{PD}(x)} \tag{7.24}$$

Solving the definite integral yields the effective spring stiffness of the ply-drop region.

$$k_{PD_{eff}} = \frac{Et}{ln\left(\frac{3}{2}\right)L_{PD}} \tag{7.25}$$

With the spring constants determined for each region, the effective spring constant of the specimen is determined by use of Equation 7.20 to be:

$$k_{eff} = \frac{Et}{\frac{1}{3}L_{UD} + ln(\frac{3}{2})L_{PD} + \frac{1}{2}L_D} \tag{7.26}$$

Substituting this into Equation 7.21a, the required force to impose the applied displacement on the ply-drop specimen is determined to be:

$$F = \frac{Et\Delta}{\frac{1}{3}L_{UD} + ln(\frac{3}{2})L_{PD} + \frac{1}{2}L_D} \tag{7.27}$$

With the extensional force known, the far-field strains for the undropped and dropped

regions can be solved via:

$$\epsilon_{UD}^{far-field} = \frac{\delta_{UD}}{L_{UD}} = \frac{F}{k_{UD}L_{UD}} = \frac{\Delta}{3(\frac{1}{3}L_{UD} + ln(\frac{3}{2})L_{PD} + \frac{1}{2}L_D)} \tag{7.28a}$$

$$\epsilon_{D}^{far-field} = \frac{\delta_{D}}{L_{D}} = \frac{F}{k_{D}L_{D}} = \frac{\Delta}{2(\frac{1}{3}L_{UD} + ln(\frac{3}{2})L_{PD} + \frac{1}{2}L_D)} \tag{7.28b}$$

where δ_{UD} and δ_D are the local extensional displacements of the undropped and dropped regions, respectively. Substituting values for the lengths of each region, from Figure 4.6, and the applied displacement, from Table 7.3, into Equations 7.28a and 7.28b, the analytical far-field strain of ϵ_{11} for the undropped and dropped regions are determined to be:

$$\epsilon_{UD}^{far-field} = 0.008 = \ 8000 \ \mu strain \tag{7.29a}$$

$$\epsilon_{D}^{far-field} = 0.012 = 12000 \ \mu strain \tag{7.29b}$$

Due to the geometry of the ply-drop specimen, a moment is induced when the specimen is loaded. The axial force, as calculated in Equation 7.27, is applied across the x-faces of the specimen as a distribution of stress. The stress on the x-faces is assumed to be composed of both a constant component and a gradient component that varies linearly through the thickness (consistent with the effect of a bending moment). Generic equations of the stress on the x-faces are given with unknown constants:

$$\sigma_A(z) = \sigma_{A_o} + \alpha z \tag{7.30a}$$

$$\sigma_B(z) = \sigma_{B_o} + \beta z \tag{7.30b}$$

The stresses acting on the overall ply-drop specimen are illustrated in a free-body diagram shown in Figure 7.91. The constants of the stress equations are determined

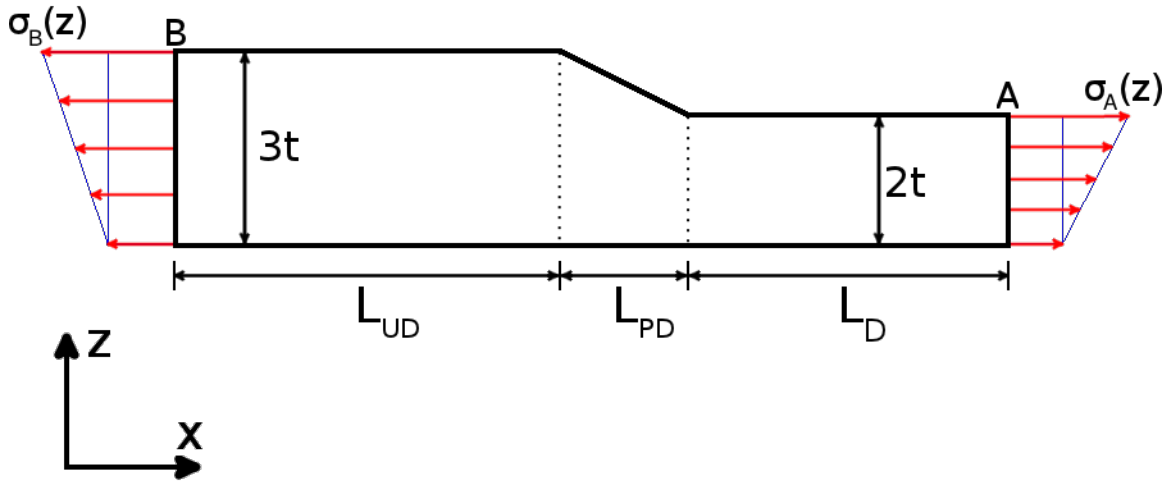

Figure 7.91 Free-body diagram of the ply-drop specimen indicating positive axial force and negative moment on x-faces.

via the overall force and moment equilibrium equations:

$$\int_0^{2t} \sigma_A(z)dz = \int_0^{3t} \sigma_B(z)dz \tag{7.31a}$$

$$\int_0^{2t} \sigma_A(z)zdz = \int_0^{3t} \sigma_B(z)zdz \tag{7.31b}$$

Relations between the four unknown constants of Equations 7.30a and 7.30b are determined from these equilibrium equations. These relations are substituted back into Equation 7.30a resulting in the equation having only one unknown. The integration of the stress over the x-face must equal the axial force previously determined from Equation 7.27.

$$\int_0^{2t} \sigma_A(z)dz = F \tag{7.32}$$

From the relations of Equations 7.30a, 7.30b, and 7.32, the constants of the stress equations are determined to be:

$$\sigma_{A_o} = \frac{2E\Delta}{\left(\frac{1}{3}L_{UD} + ln(\frac{3}{2})L_{PD} + \frac{1}{2}L_D\right)} \tag{7.33a}$$

$$\alpha = \frac{-3E\Delta}{2t\left(\frac{1}{3}L_{UD} + ln(\frac{3}{2})L_{PD} + \frac{1}{2}L_D\right)} \tag{7.33b}$$

$$\sigma_{B_o} = \frac{4E\Delta}{3\left(\frac{1}{3}L_{UD} + ln(\frac{3}{2})L_{PD} + \frac{1}{2}L_D\right)} \tag{7.33c}$$

$$\beta = \frac{-2E\Delta}{3t\left(\frac{1}{3}L_{UD} + ln(\frac{3}{2})L_{PD} + \frac{1}{2}L_D\right)} \tag{7.33d}$$

Therefore, the stress profiles on the x-faces are:

$$\sigma_A(z) = \frac{E\Delta}{\left(\frac{1}{3}L_{UD} + ln(\frac{3}{2})L_{PD} + \frac{1}{2}L_D\right)}\left(2 - \frac{3}{2}\frac{z}{t}\right) \tag{7.34a}$$

$$\sigma_B(z) = \frac{E\Delta}{\left(\frac{1}{3}L_{UD} + ln(\frac{3}{2})L_{PD} + \frac{1}{2}L_D\right)}\left(\frac{4}{3} - \frac{2}{3}\frac{z}{t}\right) \tag{7.34b}$$

where z is measured from the bottom face of the specimen. The resulting moments

within the three regions are calculated by taking section cuts and solving the resulting free-body diagrams.

$$M_D(x) = \frac{Et^2\Delta}{\left(\frac{1}{3}L_{UD} + ln(\frac{3}{2})L_{PD} + \frac{1}{2}L_D\right)} \tag{7.35a}$$

$$M_{PD}(x) = \left(\frac{3}{2} - \frac{x - L_{UD}}{L_{PD}}\right) \frac{Et^2\Delta}{\left(\frac{1}{3}L_{UD} + ln(\frac{3}{2})L_{PD} + \frac{1}{2}L_D\right)} \tag{7.35b}$$

$$M_{UD}(x) = \frac{3}{2} \frac{Et^2\Delta}{\left(\frac{1}{3}L_{UD} + ln(\frac{3}{2})L_{PD} + \frac{1}{2}L_D\right)} \tag{7.35c}$$

The moment in the undropped and dropped regions are constant, while the moment in the ply-drop region is linear in x. The subsequent results from the finite element model are discussed in the context of the stress, moment, and force relations developed.

As discussed in Section 7.2.4 and shown in Figure 7.21, each ply is dropped as a unit. In the finite element model, the resulting wedge regions are given the properties of neat resin (i.e., isotropic material properties, representative of 3501-6 resin). An illustration of the ply drop region, including the x-locations of each dropped ply, is shown in Figure 7.92. The results from the finite element model presented herein do not show the results for the regions of the neat resin wedges. The results indicate that the peak strains occur at a distance of approximately 0.25 ply thicknesses before the end of a dropped ply (i.e., the strains exhibited within the neat resin wedges exhibit lower strains than observed within the ply regions). Therefore, the results in the neat resin triangular regions are not discussed.

The values of ϵ_{11} at the midplane of each ply in the x-direction are plotted for the single-ply and two-ply effective ply thickness laminates and are shown in Figures 7.93 and 7.94. The results exhibit similar trends for both effective ply thickness laminates. In the undropped region (i.e., $-50\ mm \leq x \leq -7\ mm$), the bottom ply, ply 1, exhibits the greatest strain of all the plies, whereas the top ply, ply 36, exhibits the lowest strain. The plies are observed to have decreasing strain as the through-thickness location increases. This result is consistent with the presence of a positive bending moment acting within the region. The "far-field" bending moment within the

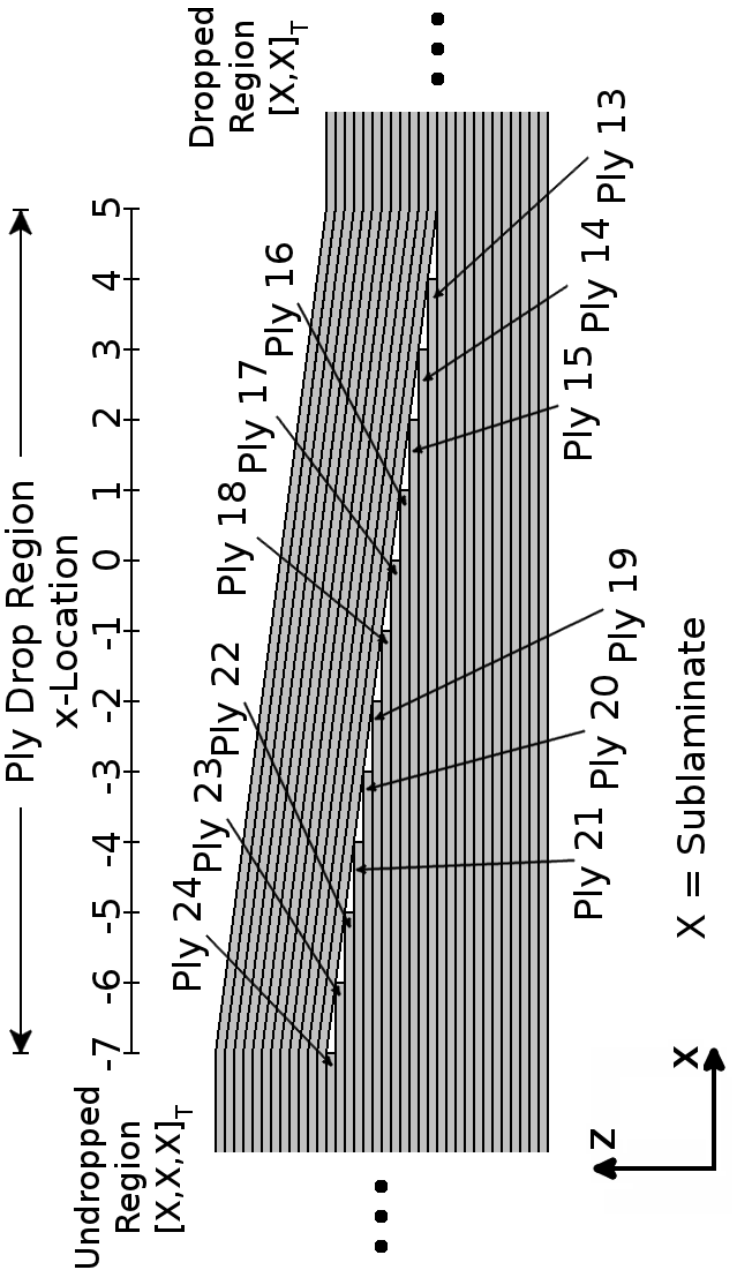

Figure 7.92 Illustration of ply drop region, with x-locations and dropped ply numbering, for $[X, X_D, X]_T$ configuration with X being sublaminate $[+45/0/-45]_{2S}$ or $[+45_2/0_2/-45_2]_S$.

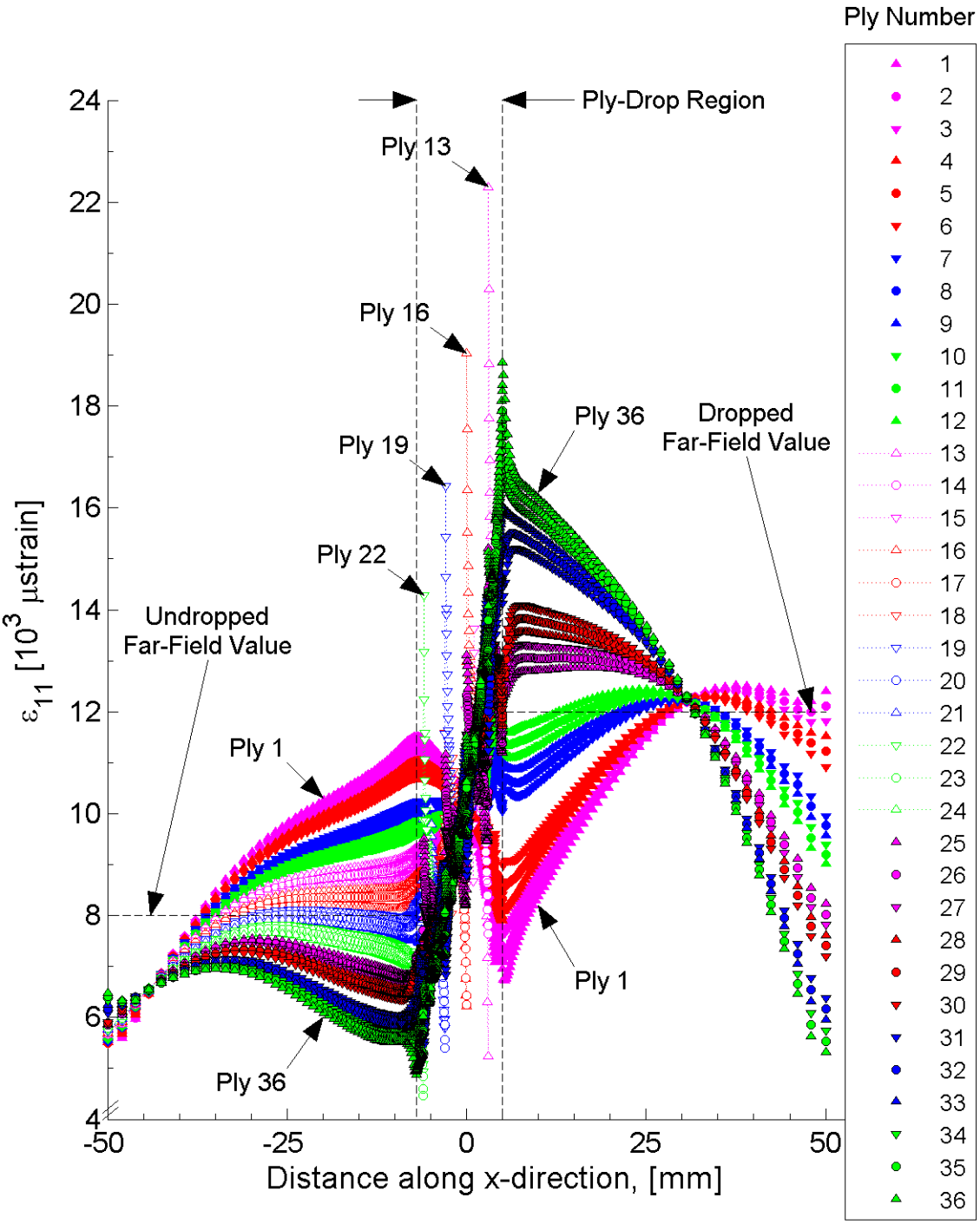

Figure 7.93 Plot of ϵ_{11}, in laminate axes, at the midplane of each ply within the x-z plane of the ply-drop specimen model for the single-ply effective ply thickness sublaminate of $[+45/0/-45]_{2S}$.

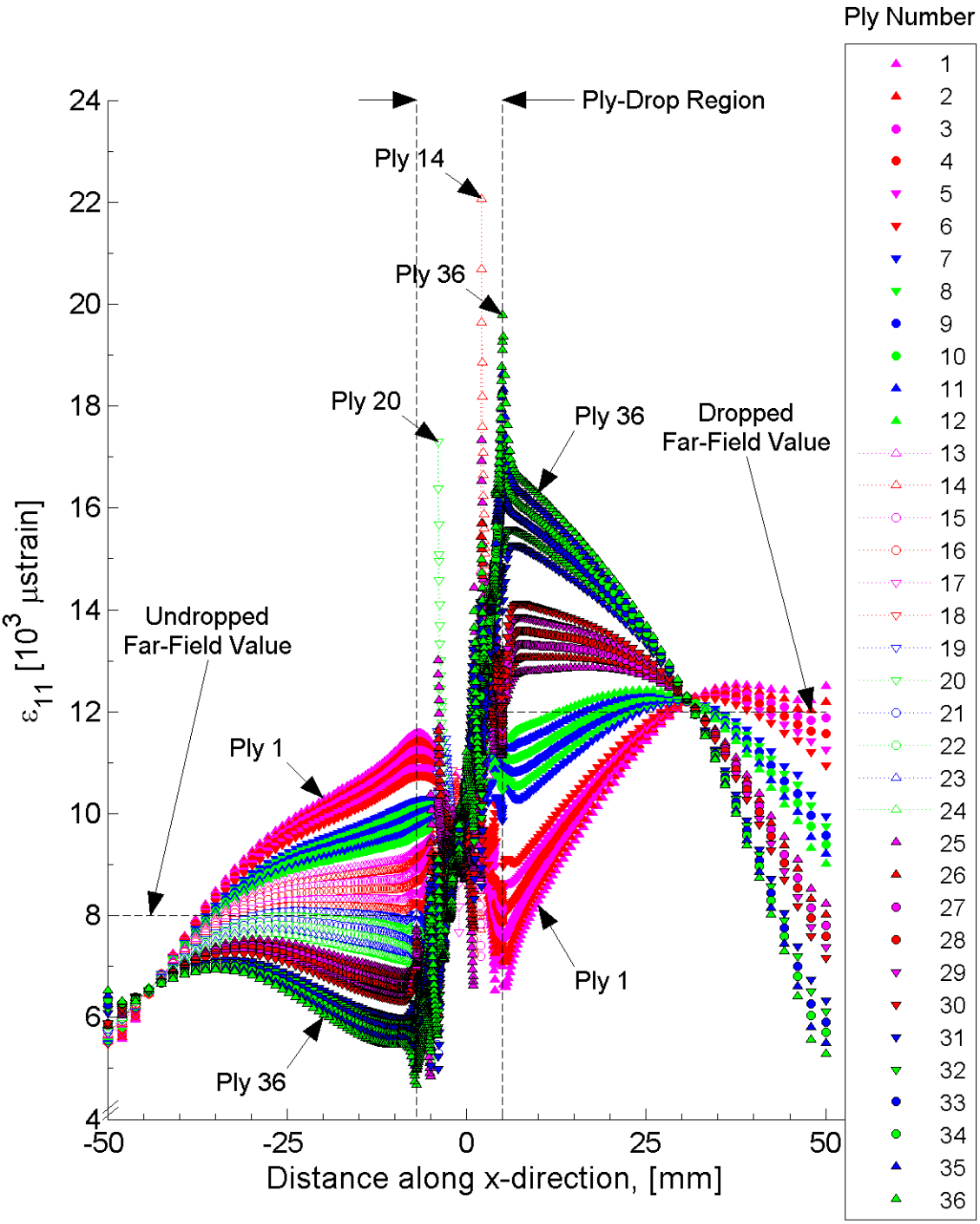

Figure 7.94 Plot of ϵ_{11}, in laminate axes, at the midplane of each ply within the x-z plane of the ply-drop specimen model for the two-ply effective ply thickness sublaminate of $[+45_2/0_2/-45_2]_S$.

undropped and dropped regions is constant, as indicated in Equation 7.35c and 7.35a, where "far-field" in this context indicates a region uninfluenced by the boundary conditions and local effects of the ply-drop region. With a constant moment, there should be no gradient of the strain values within each ply of the undropped and dropped region. The only gradient should be a through-thickness gradient associated with the linear relation between ϵ_{11} and the curvature linked to the bending moment. The specified boundary conditions are that the nodes on the x-faces of the specimen have zero displacement in the y- and z-directions and an applied displacement in the x-direction, as described in Section 7.2.4. This influences the results over a distance approximately equal to the lengths of the undropped and dropped regions.

A case was analyzed with relaxed boundary conditions, where only the x-displacement was specified on the two x-faces and all other degrees of freedom were free, and the results showed near zero slopes in the undropped and dropped regions for each individual ply (i.e., through-thickness gradients remained). The values of ϵ_{11} at the midplane of each ply within the x-z plane are plotted for the single-ply effective ply thickness laminates with the relaxed boundary conditions and are shown in Figure 7.95. Comparing the results from the two boundary conditions, shown in Figures 7.93 and 7.95, the case of the relaxed boundary condition does not exhibit influences from the boundary conditions (i.e., the strain in the undropped and dropped regions are independent of x-location, with the exception of a small region bordering the ply-drop region). This observation indicates that the non-relaxed boundary conditions have a region of influence approximately equal to the length of the undropped and dropped regions. However, the non-relaxed boundary conditions (i.e., the two x-faces have zero y- and z-displacements and the x-displacement is equal to the applied displacement listed in Table 7.3) better simulate the experimental testing and are thus discussed.

In addition to the influence of the boundaries, the structural feature of the ply-drop is observed to have a small region of influence within both the undropped and dropped regions. A transition region approximately 2 mm in length is observed to neighbor the boundaries of the ply-drop region (i.e., $-9\ mm \leq x \leq -7\ mm$ for

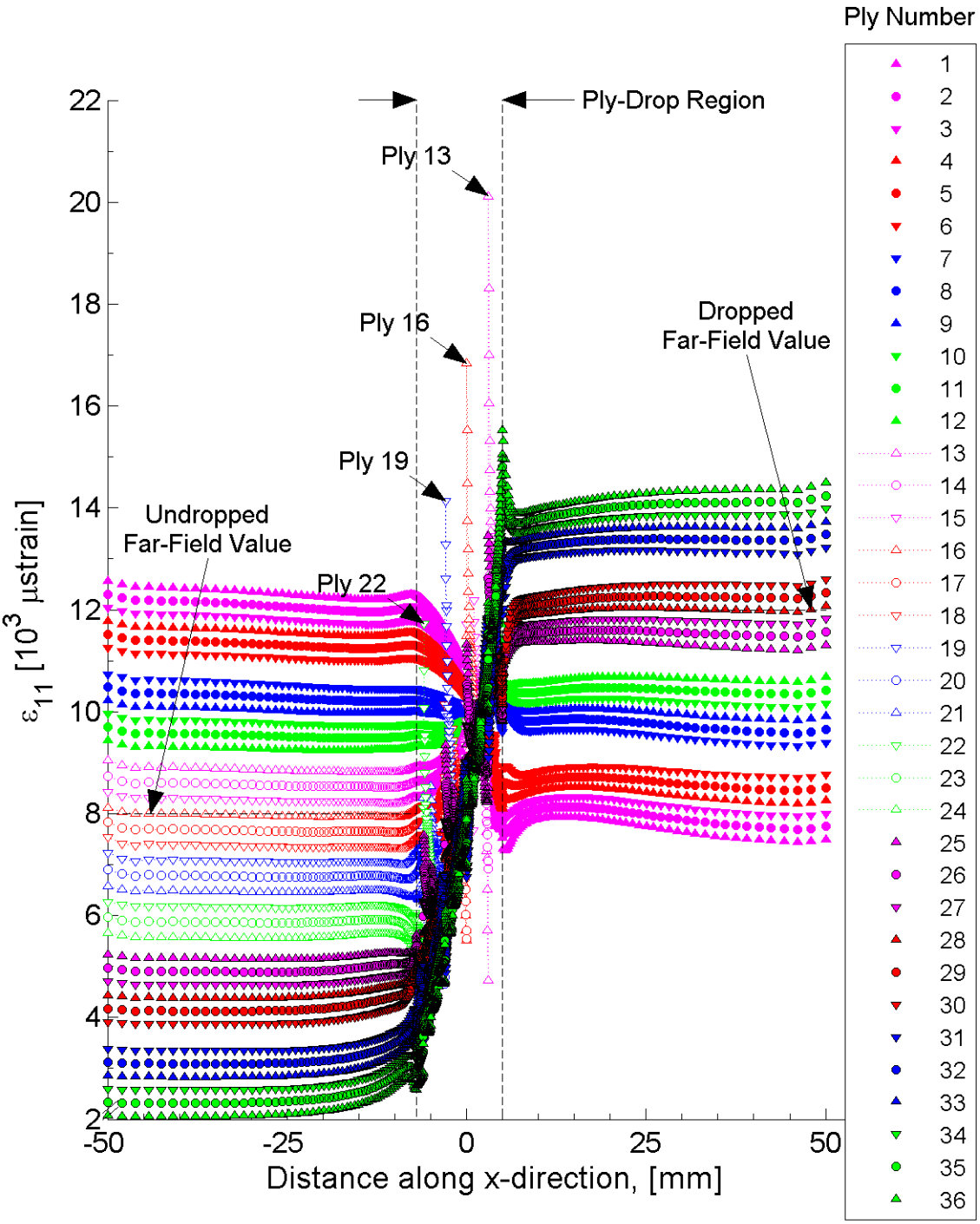

Figure 7.95 Plot of ϵ_{11}, in laminate axes, at the midplane of each ply within the x-z plane of the ply-drop specimen model with relaxed boundary conditions for the single-ply effective ply thickness sublaminate of $[+45/0/-45]_{2S}$.

the undropped region, and 5 $mm \leq x \leq 7$ mm for the dropped region). Within this region, the rate of change of the gradient is greater than observed throughout the rest of the respective regions, such as seen for ply 1 in the results shown in Figure 7.93.

The largest gradients observed in the ply-drop specimen occur within the ply-drop region. The values of ϵ_{11} at the midplane of each ply within the ply-drop region are plotted for the single-ply and two-ply effective ply thickness laminates and are shown in Figures 7.96 and 7.97, with the x-direction expanded from Figures 7.93 and 7.94. Large peaks in strain are observed to occur within the ply-drop region. These peaks occur within plies 13, 16, 19, and 22 for the single-ply effective ply thickness laminate, and within plies 14 and 20 for the two-ply effective ply thickness laminate, with the value and x-location of each peak listed in Table 7.30. In both the single-ply and two-ply effective ply thickness laminates, these peaks occur at x-locations just beyond a dropped zero-degree ply, within the neighboring angle ply. In both laminates, the x-location of the peak is 0.04 mm beyond (in the positive x-direction) the dropping of a zero-degree ply. The distance of 0.04 mm corresponds to the sampling distance of the strain fields (i.e., the peak values are measured one unit measure from the end of the dropped ply). In addition, a peak is not observed when a zero-degree ply is dropped and the ply neighboring this drop (i.e., the ply below the drop) is another zero-degree ply. This is observed in the results of the two-ply effective ply thickness laminate when plies 22 and 16, both zero-degree plies, are dropped and the neighboring plies 21 and 15, respectively, are also zero-degree plies.

Another observation is that plies 1 through 12 (continuous plies) exhibit a smooth transition from the undropped to ply-drop region and rough transition (almost discontinuous) from the dropped to the ply-drop region. The rough transitions are observed to occur at the locations of the three ply drops neighboring the dropped region (i.e., at x locations of 3 mm, 4 mm, and 5 mm). Unlike the first 12 plies, the top 12 plies (plies 25 through 36) exhibit changes in gradients at the locations of each ply drop. Within the plies exhibiting the rough transition, the change in magnitude at each ply-drop location is observed to be greater for the two-ply effective ply thickness laminate.

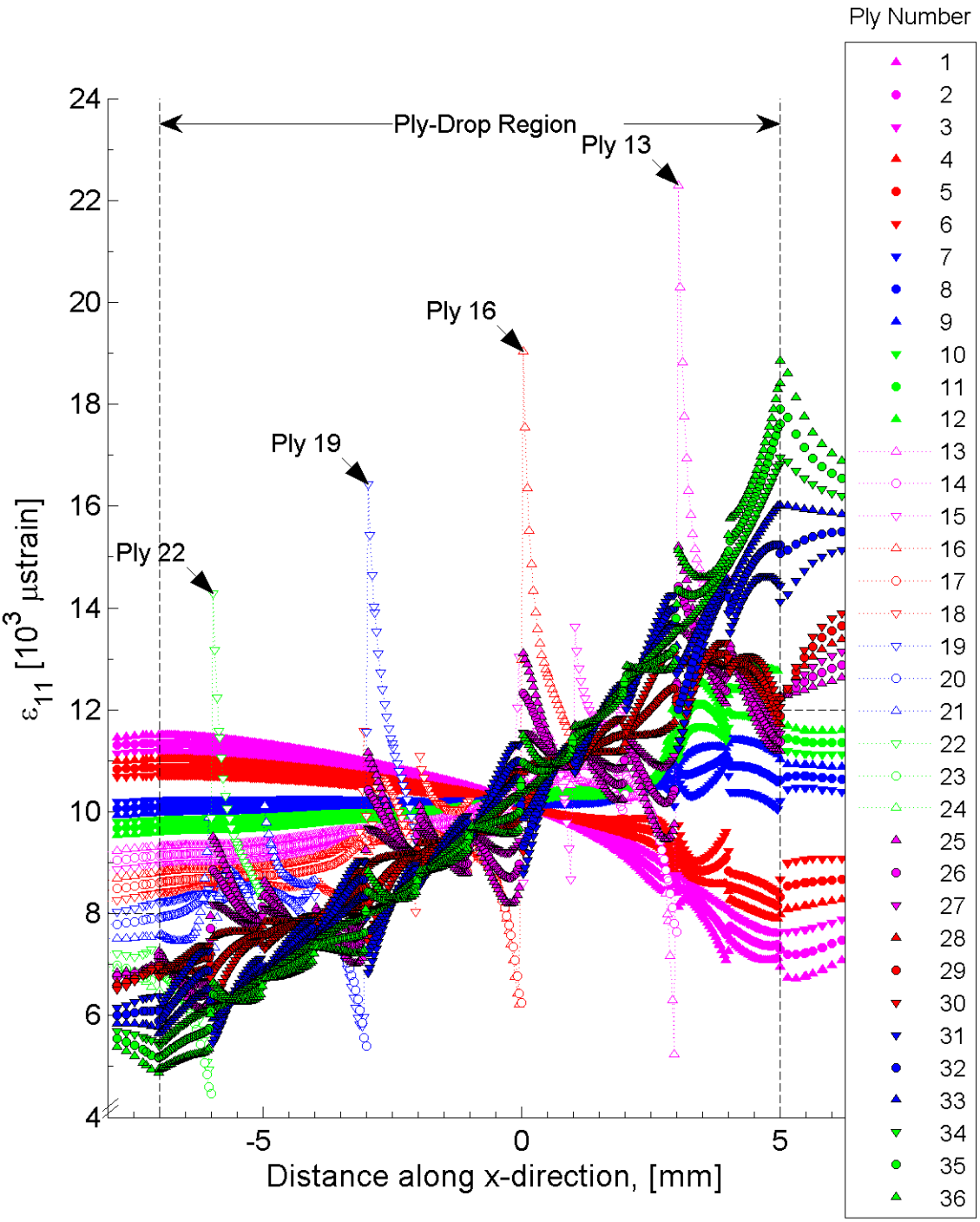

Figure 7.96 Plot of ϵ_{11}, in laminate axes, at the midplane of each ply within the x-z plane within the ply-drop region of the ply-drop specimen model for the single-ply effective ply thickness sublaminate of $[+45/0/-45]_{2S}$.

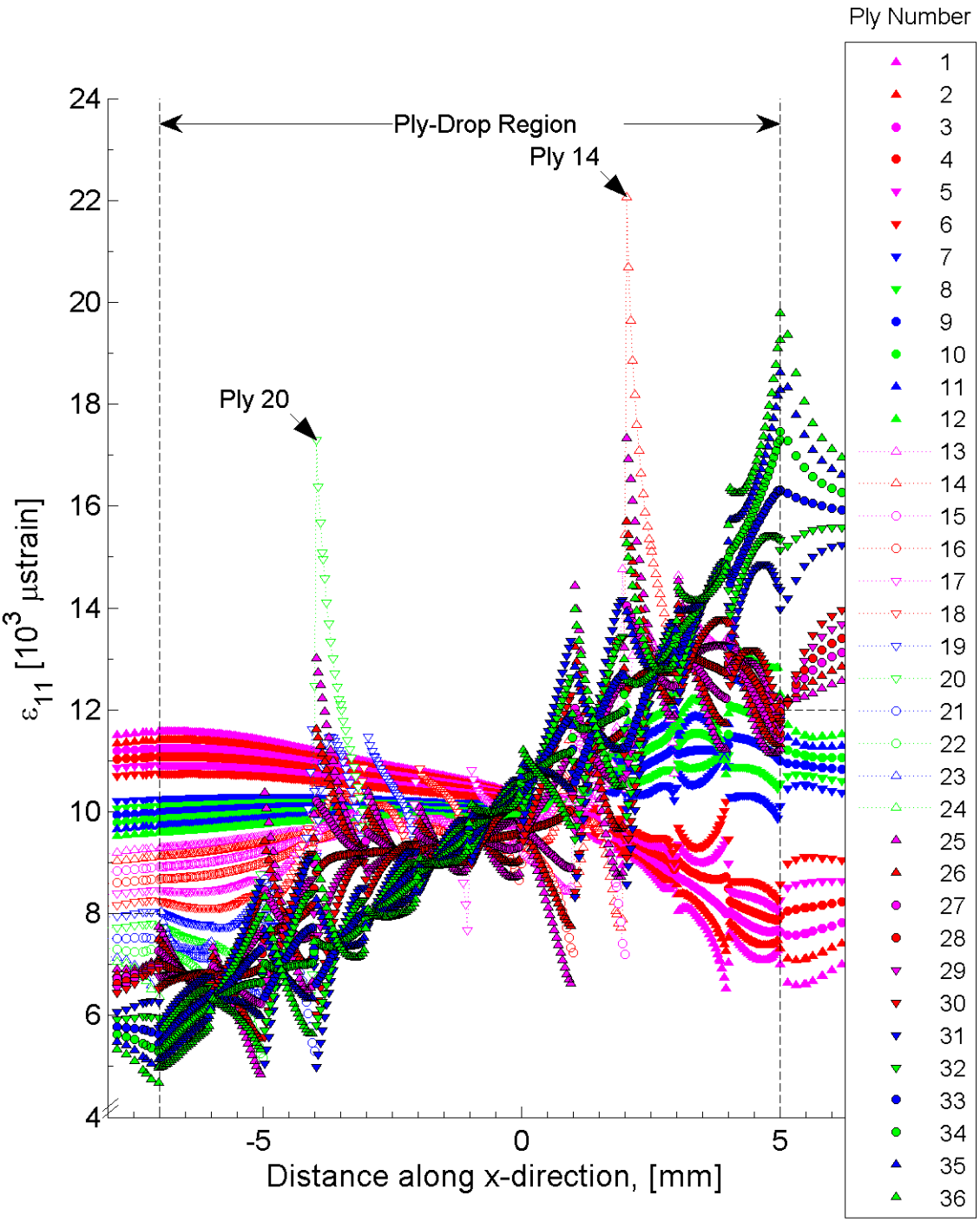

Figure 7.97 Plot of ϵ_{11}, in laminate axes, at the midplane of each ply within the x-z plane within the ply-drop region of the ply-drop specimen model for the two-ply effective ply thickness sublaminate of $[+45_2/0_2/-45_2]_S$.

Table 7.30 Locations and values of large peaks in in-plane strains within the ply-drop region for the ply-drop specimens (sublaminates of $[+45/0/-45]_{2S}$ and $[+45_2/0_2/-45_2]_S$)

Strain Component	**Nominal Effective Ply Thickness**	**Through-Thickness Location [ply number]**	**Value [μstrain]**	**$x-$ Location [mm]**
ϵ_{11}	1	13	+22300	3.04
		16	+19000	0.04
		19	+16400	-2.96
		22	+14300	-5.96
	2	14	+22100	2.04
		20	+17300	-3.96
ϵ_{22}	1	25	-8300	3.04
		25	-7900	0.04
		25	-7400	-2.96
		25	-6900	-5.96
	2	25	-9200	2.04
		25	-8500	1.04
		25	-8100	-3.96
		25	-7400	-4.96
ϵ_{12}	1	13	-7200	3.04
		13	4200	2.96
		16	-6700	0.04
		16	3800	-0.04
		19	5000	-2.96
		19	-2000	-3.04
		22	4800	-5.96
		22	-2800	-6.04
	2	14	-7000	2.04
		14	2500	1.96
		20	5900	-3.96
		21	-1800	-4.00

The locations and values of the peak maximum (ϵ_T) and minimum (ϵ_C) in-plane strains for each laminate are listed in Table 7.31. The peak maximum values of ϵ_{11} occur within positive angle plies near the boundary of the ply-drop and dropped regions for both the single-ply and two-ply effective ply thickness laminates. In both cases, the x-location of the peak maximum value corresponds to the dropping of a neighboring 0° ply (i.e., the peak value is observed to occur 1 mm from the dropped end of the positive angle ply, as indicated in Figure 4.7). The peak minimum values of ϵ_{11} occur near the boundary of the ply-drop and undropped regions. The peak values of the single-ply and two-ply effective ply thickness laminates are basically the same, although the x-locations of the peaks are dependent on the effective ply thickness of the laminate.

The values of ϵ_{22} at the midplane of each ply within the x-z plane are plotted for the single-ply and two-ply effective ply thickness laminates and are shown in Figures 7.98 and 7.99. The results have a skewness that appear to approach the far-field values. The boundary condition applied to the nodes of the x-faces (i.e., at x-locations of -50 mm and +50 mm) enforce zero displacement in the y- (2) direction. From the strain-displacement relation, this causes ϵ_{22} to go to a value of zero at these faces. This boundary condition is observed to have an influence on the results over a length of approximately 35 mm, measured from the point where the results of ϵ_{22} diverge from the general slope observed near transition regions of the ply drop. This influence length is consistent with the length observed in the results of ϵ_{11}. In the small area of the undropped and dropped regions beyond the influence of the boundaries, the results are observed to be trending toward the respective far-field values.

The largest gradients observed in the values of ϵ_{22} occur within the ply-drop region as for those of ϵ_{11}. The values of ϵ_{22} in the ply-drop region are plotted for the single-ply and two-ply effective ply thickness laminates, and are shown in Figures 7.100 and 7.101, with the x-direction expanded from Figures 7.98 and 7.99, as is done for ϵ_{11}. As with the results of ϵ_{11}, the gradients of the bottom sublaminate, plies 1 through 12, are slowly changing at the transition between the undropped and ply-drop regions while they become fast changing (i.e., derivative of the gradient increases) at the transition

Table 7.31 Locations and values of maximum and minimum in-plane strains for the ply-drop specimens (sublaminates of $[+45/0/-45]_{2S}$ and $[+45_2/0_2/-45_2]_S$)

Strain Component	**Value Considered**[a]	**Nominal Effective Ply Thickness**	**Value [μstrain]**	**Through-Thickness Location [ply number]**	**$x-$ Location [mm]**
ϵ_{11}	ϵ_T	1	+22300	13	3.04
		2	+22100	14	2.04
	ϵ_C	1	+4500	23	-6.00
		2	+4700	36	-7.00
ϵ_{22}	ϵ_T	1	0	6	50.00
		2	0	6	50.00
	ϵ_C	1	-8300	25[b]	3.04
		2	-9200	25	2.04
ϵ_{12}	ϵ_S	1	-7200	13	3.04
		2	-7000	14	2.04

[a] ϵ_T = Maximum
ϵ_C = Minimum
ϵ_S = Maximum Magnitude
[b] Ply 36 exhibits a value of -8400 μstrain at x-location 5.00 mm

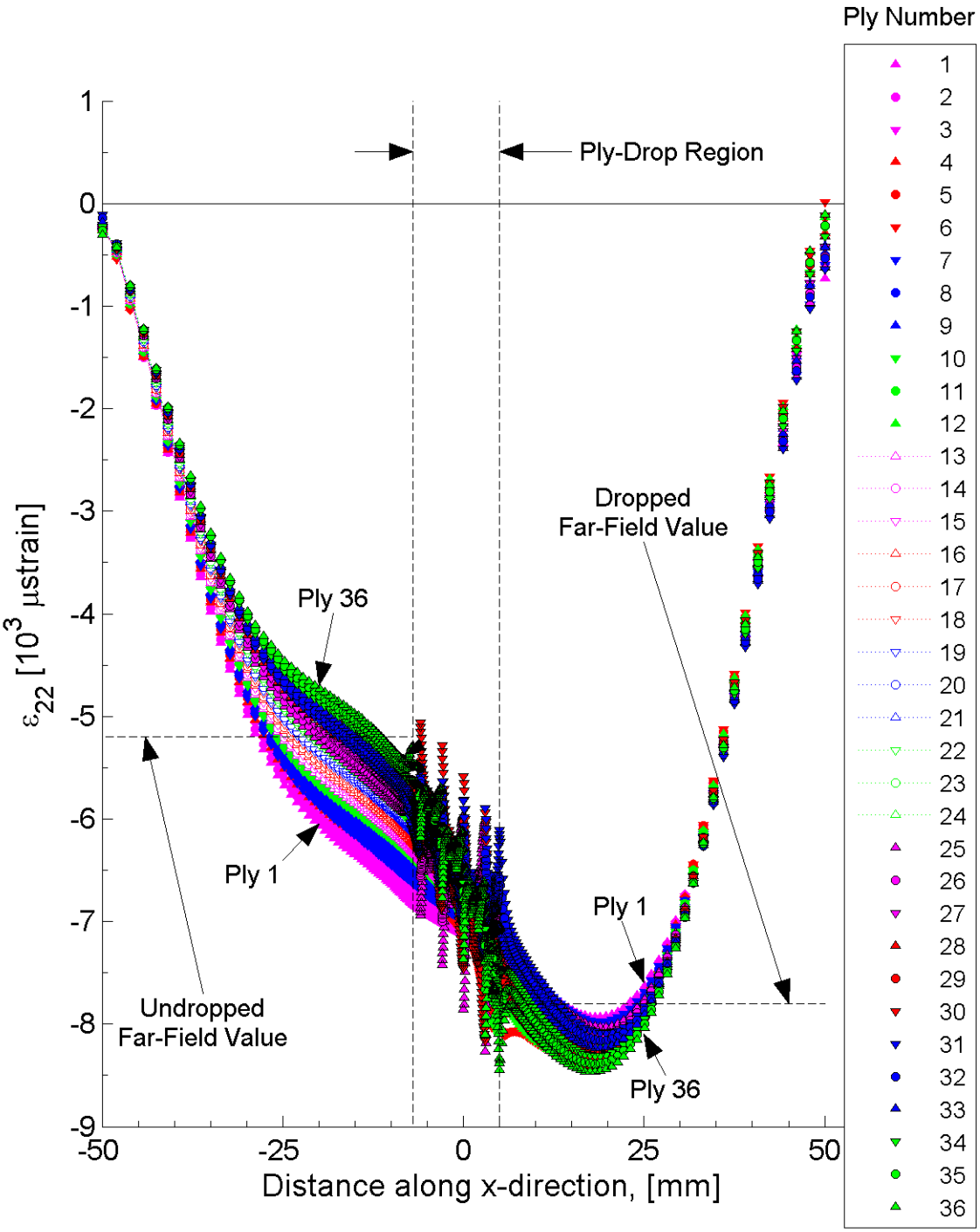

Figure 7.98 Plot of ϵ_{22}, in laminate axes, at the midplane of each ply within the x-z plane of the ply-drop specimen model for the single-ply effective ply thickness sublaminate of $[+45/0/-45]_{2S}$.

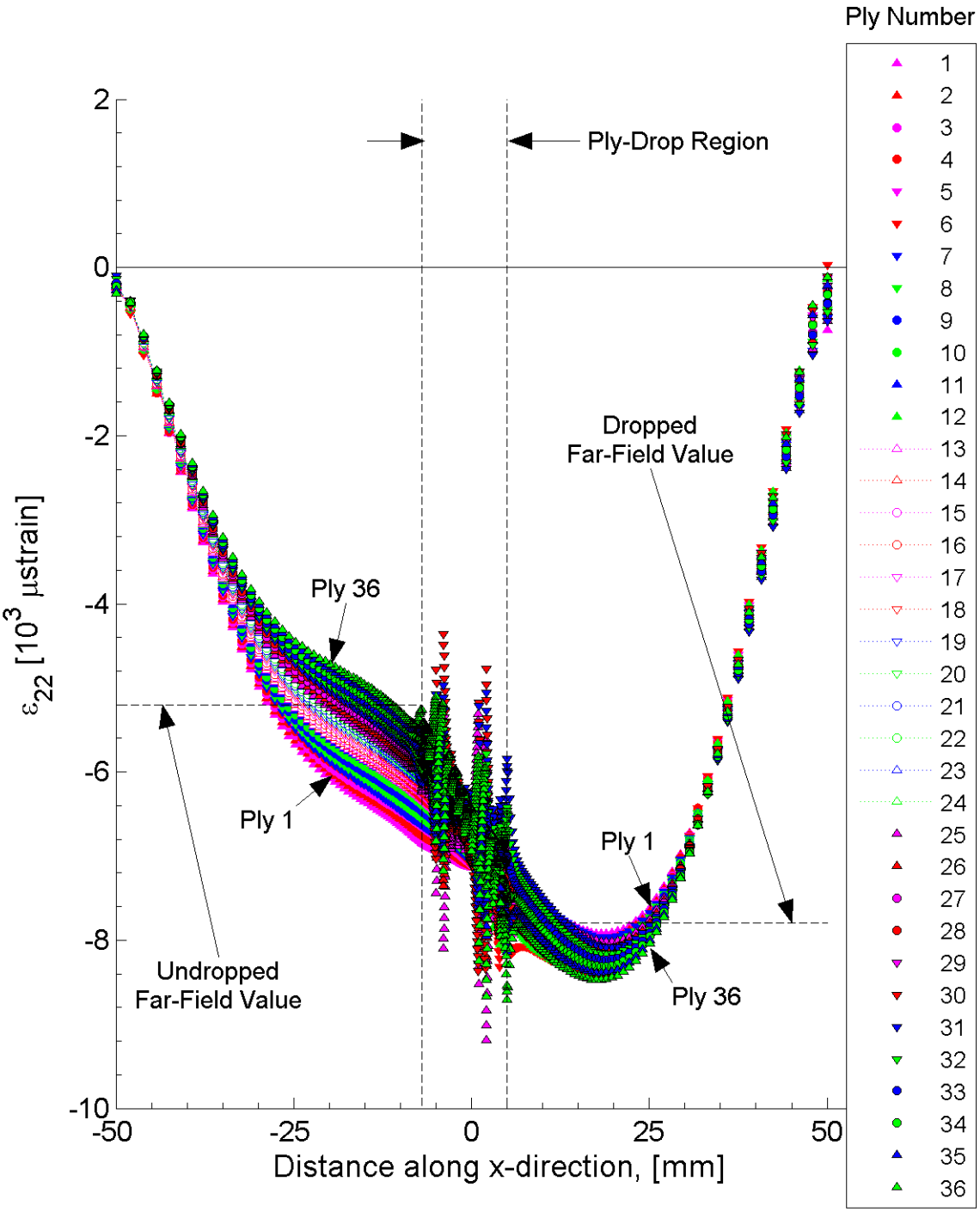

Figure 7.99 Plot of ϵ_{22}, in laminate axes, at the midplane of each ply within the x-z plane of the ply-drop specimen model for the two-ply effective ply thickness sublaminate of $[+45_2/0_2/-45_2]_S$.

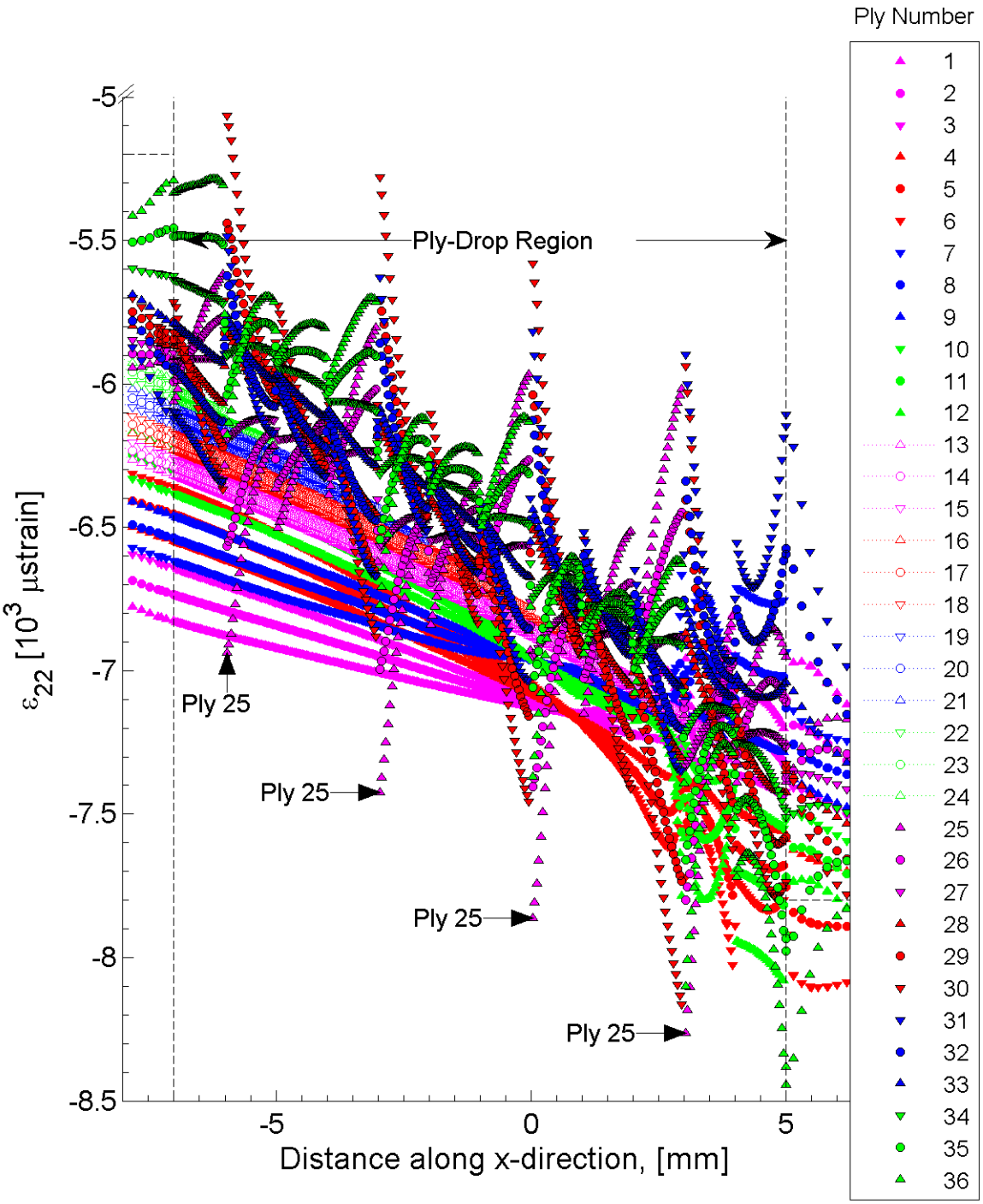

Figure 7.100 Plot of ϵ_{22}, in laminate axes, at the midplane of each ply within the x-z plane within the ply-drop region of the ply-drop specimen model for the single-ply effective ply thickness sublaminate of $[+45/0/-45]_{2S}$.

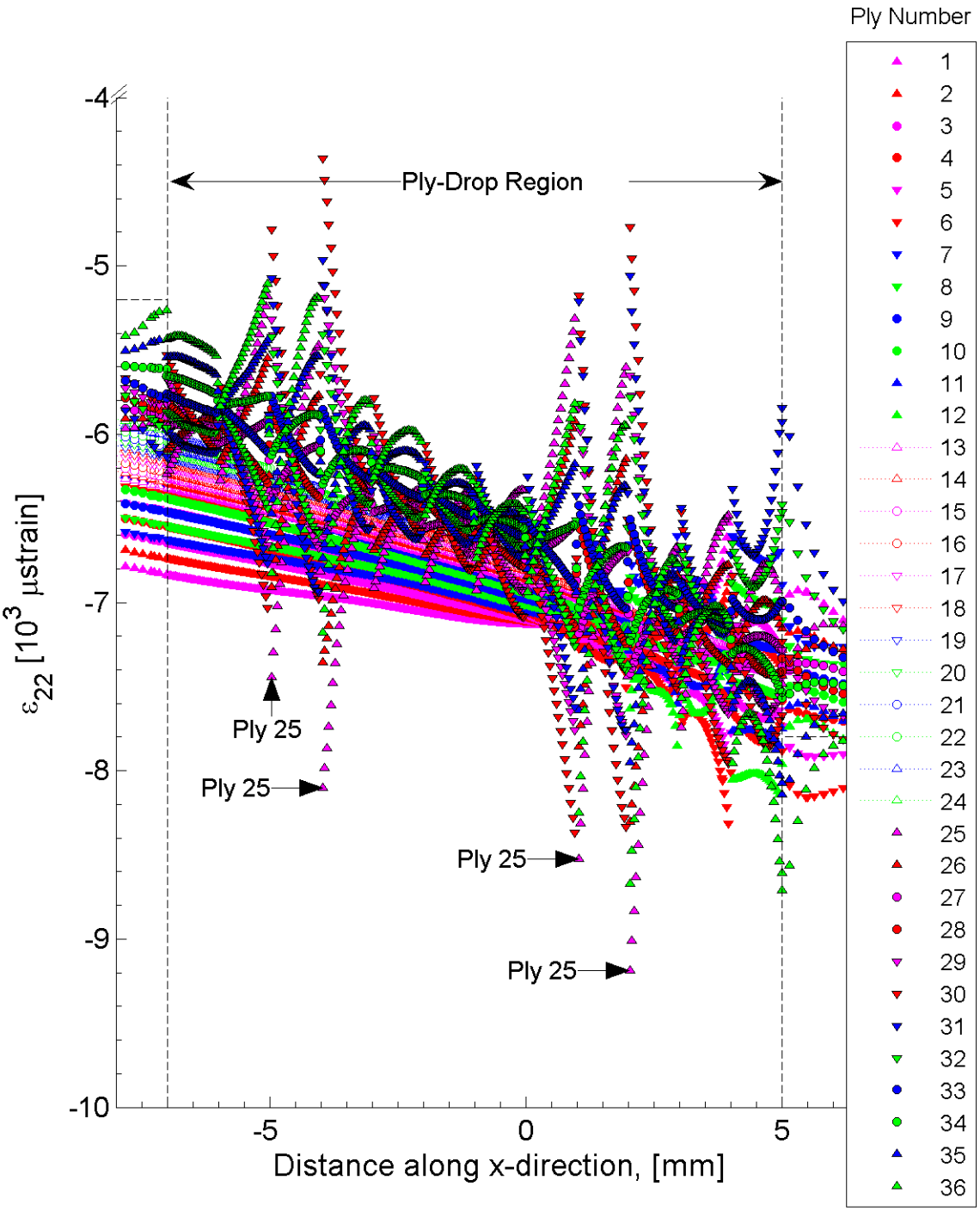

Figure 7.101 Plot of ϵ_{22}, in laminate axes, at the midplane of each ply within the x-z plane within the ply-drop region of the ply-drop specimen model for the two-ply effective ply thickness sublaminate of $[+45_2/0_2/-45_2]_S$.

between the ply-drop and dropped regions. In addition, the gradients of ϵ_{22} within the plies of the dropped sublaminate are slowly changing throughout the entire ply-drop region. However, the plies of the upper sublaminate, plies 25 through 36, exhibit large gradient changes at x-locations corresponding to ply drops. The largest variation in the value of ϵ_{22} of a single ply occurs in ply 25, the first ply neighboring the dropped sublaminate. The locations and values of the large peak values of ϵ_{22} within the ply-drop region are listed in Table 7.30. A variation within ply 25 of over 2000 μstrain is observed across the x-location of 3.04 mm to 2.96 mm for both the single-ply and two-ply effective ply thickness laminates, as seen in Figures 7.100 and 7.101. Additional large gradients within ply 25, for both laminates, are observed to repeat every 3 mm (decreasing along the x-direction) contained in the ply-drop region. This corresponds to the locations in the model where ply 25 shares a corner node with a 0° dropped ply. In reality, ply 25 and the dropped 0° plies will not be fixed together, but will rather have a matrix rich region. This will relax the large strain gradients in the region. However, these results indicate a possible region for delamination initiation.

Peaks in the value of ϵ_{22} are not observed to occur in the dropped plies. Unlike the results for ϵ_{11}, the gradients of these plies are constant and equal for all plies of the middle sublaminate (i.e., plies 13 through 24). The strain values of ϵ_{22} are the only strain fields of the ply-drop specimen to exhibit this behavior. In investigating the finite element model, it is observed that peaks in the value of ϵ_{22} occur only at the finite elements adjacent to the locations of ply drops. The elements neighboring these elements have a constant value.

The peak maximum and minimum values of ϵ_{22} are listed in Table 7.31. The peak maximum values occur within ply 6 within the dropped region, at the x-location where the boundary conditions are applied. The boundary conditions have a direct effect at this location. Therefore these values are not valid. The peak minimum values occur away from the boundaries. Two minimum values of ϵ_{22} of the single-ply effective ply thickness laminate occur near the transition from the ply-drop to dropped regions. The first occurs in the top ply, ply 36, at the boundary of the ply-drop region and the dropped region (i.e., x-location equal to 5.0 mm). The second occurs in ply 25

at the x-location of 3.04 mm. This location corresponds to the maximum value of ϵ_{11}, as indicated in Table 7.31, although being in a different ply. In addition to these minimums, the results for the plies in the dropped region reach a global minimum near the x-location of 17.54 mm. Unlike the peak minimums observed in the ply-drop region, the upper plies of the dropped region smoothly approach a minimum at the x-location equal to 17.54 mm. The minimum value at the x-location of 17.54 mm for ply 36 is of near equal value to the peak minimums observed at the x-locations of 3.04 mm and 5.0 mm. For the two-ply effective ply thickness laminate, the minimum value occurs in ply 25 and within the ply-drop region, near the transition to the dropped region. The x-location of this minimum corresponds to the maximum value of ϵ_{11}, as listed in Table 7.31, although being in a different ply.

The values of ϵ_{12} at the midplane of each ply within the x-z plane are plotted for the single-ply and two-ply effective ply thickness laminates and are shown in Figures 7.102 and 7.103. The results approach the far-field value of zero away from the ply-drop region. The results of the single-ply and two-ply effective ply thickness laminate exhibit a through-thickness variation in strain in the undropped and dropped regions, as seen in Figures 7.102 and 7.103. The variation is more pronounced in the dropped region near the transition to the ply-drop region of the two-ply effective ply thickness laminate. The variation of the single-ply effective ply thickness laminate is observed to be half the variation observed in the two-ply effective ply thickness laminate.

As with ϵ_{11} and ϵ_{22}, the largest gradients observed in the values of ϵ_{12} occur within the ply-drop region. The values of ϵ_{12} at the midplane of each ply within the x-z plane within the ply-drop region are plotted for the single-ply and two-ply effective ply thickness laminates, and are shown in Figures 7.104 and 7.104, with the x-direction expanded from Figures 7.102 and 7.103, as is done for ϵ_{11} and ϵ_{22}. Four large peaks are observed in the ply-drop region of the single-ply effective ply thickness laminate, with the magnitudes and x-locations of the peaks listed in Table 7.30. These peaks occur in plies 13, 16, 19, and 22, the same as the results for ϵ_{11}. In addition, these peaks occur at the same x-location as the peaks in the results of ϵ_{11}. Plies 13 and

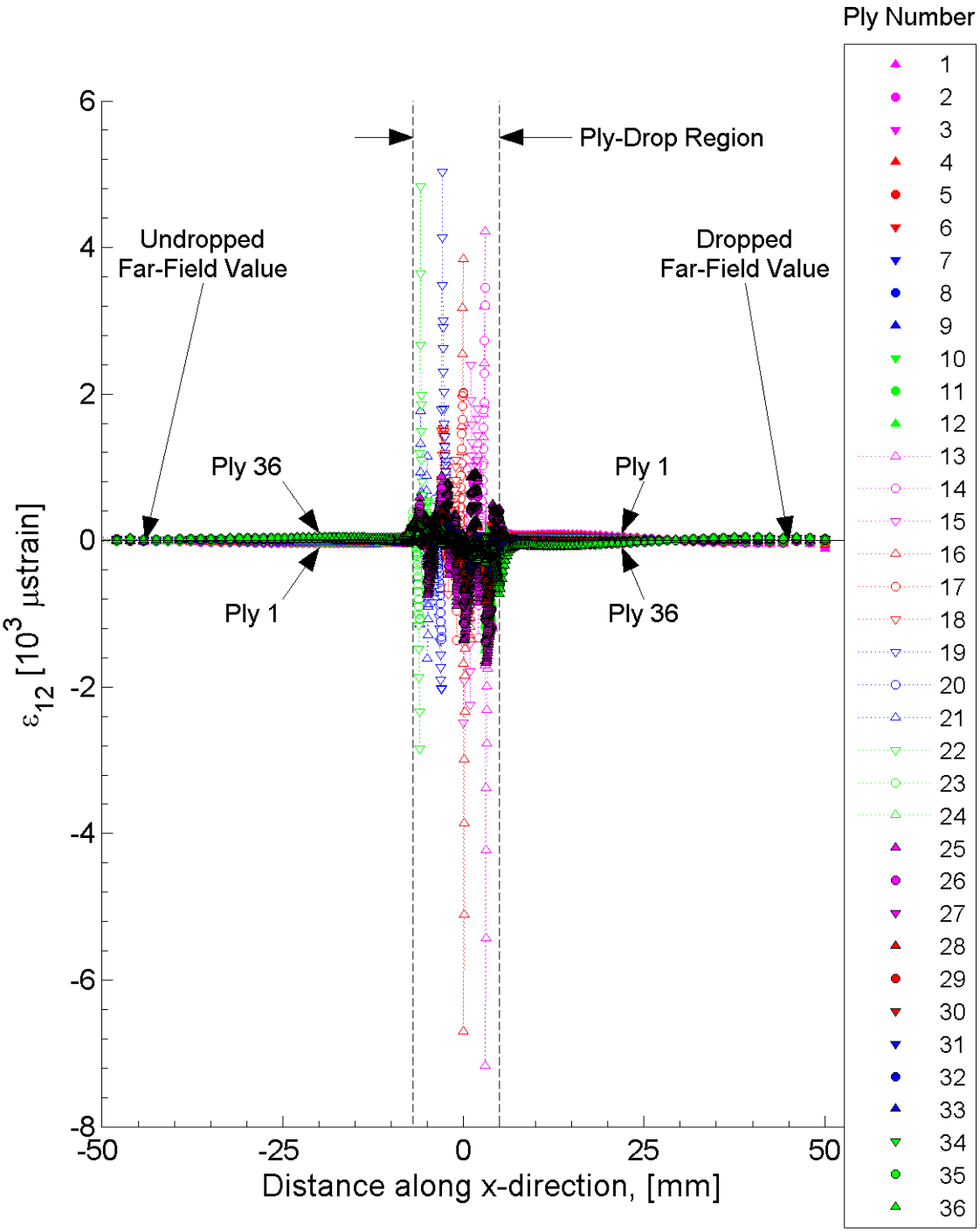

Figure 7.102 Plot of ϵ_{12}, in laminate axes, at the midplane of each ply within the x-z plane of the ply-drop specimen model for the single-ply effective ply thickness sublaminate of $[+45/0/-45]_{2S}$.

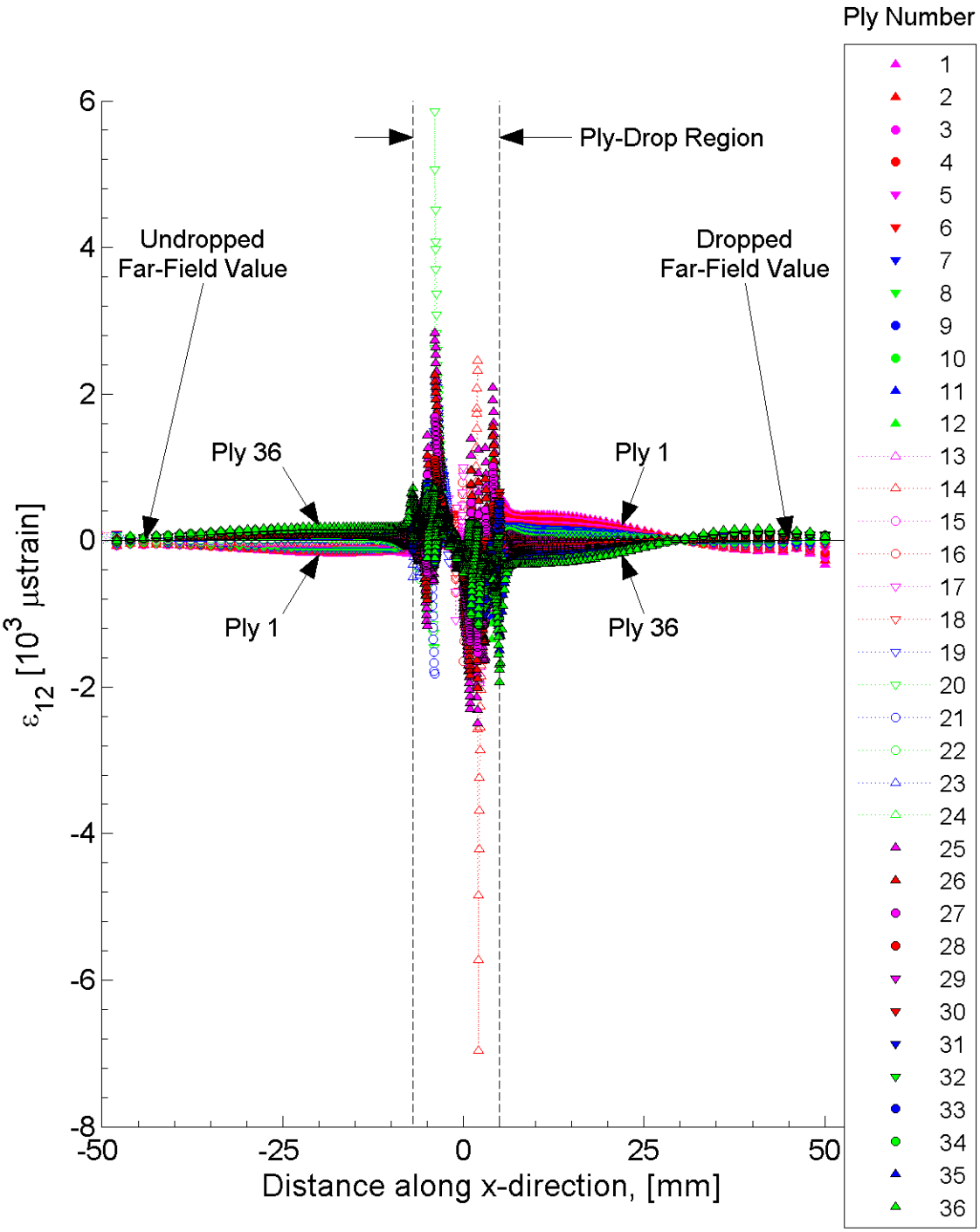

Figure 7.103 Plot of ϵ_{12}, in laminate axes, at the midplane of each ply within the x-z plane of the ply-drop specimen model for the two-ply effective ply thickness sublaminate of $[+45_2/0_2/-45_2]_S$.

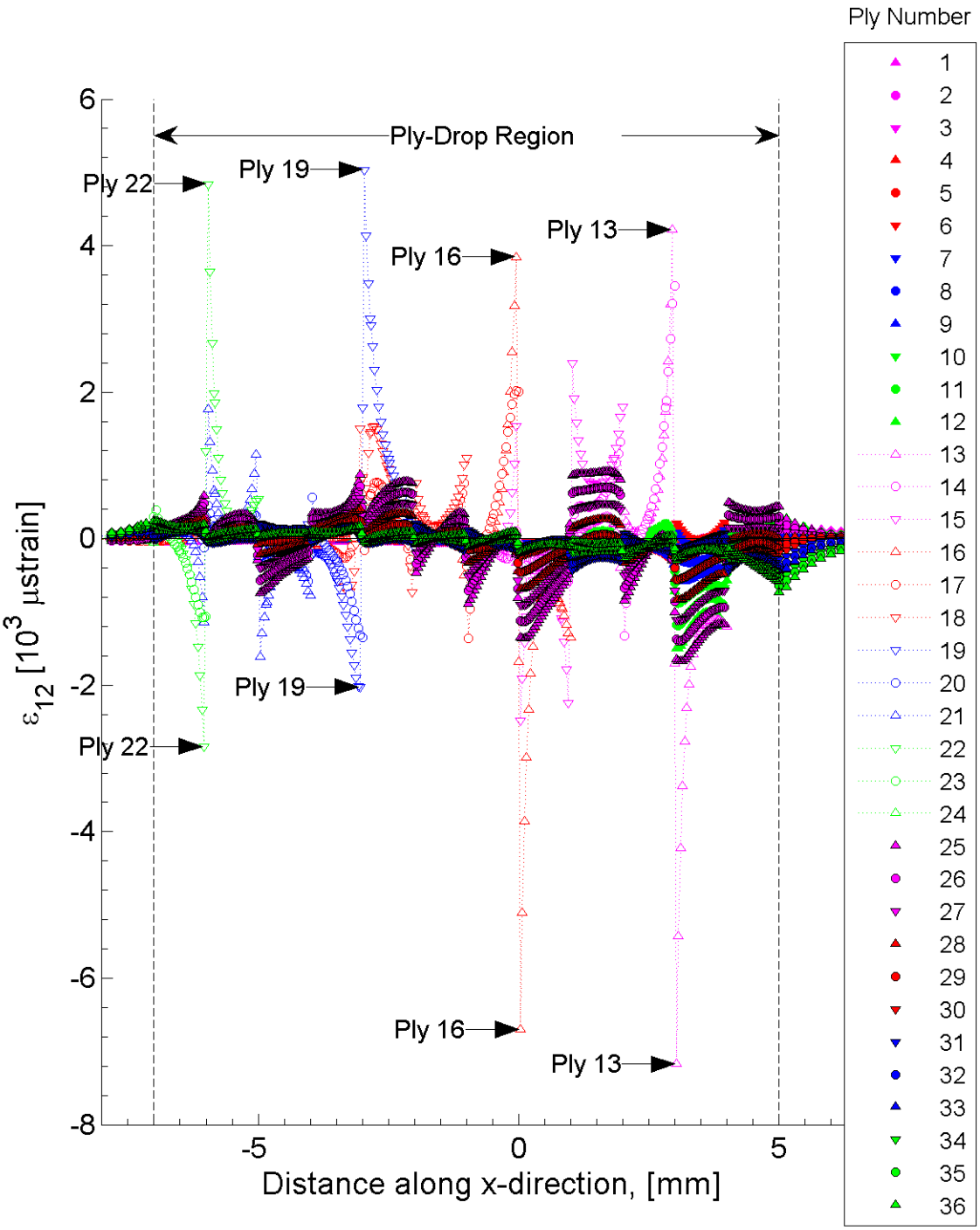

Figure 7.104 Plot of ϵ_{12}, in laminate axes, at the midplane of each ply within the x-z plane within the ply-drop region of the ply-drop specimen model for the single-ply effective ply thickness sublaminate of $[+45/0/-45]_{2S}$.

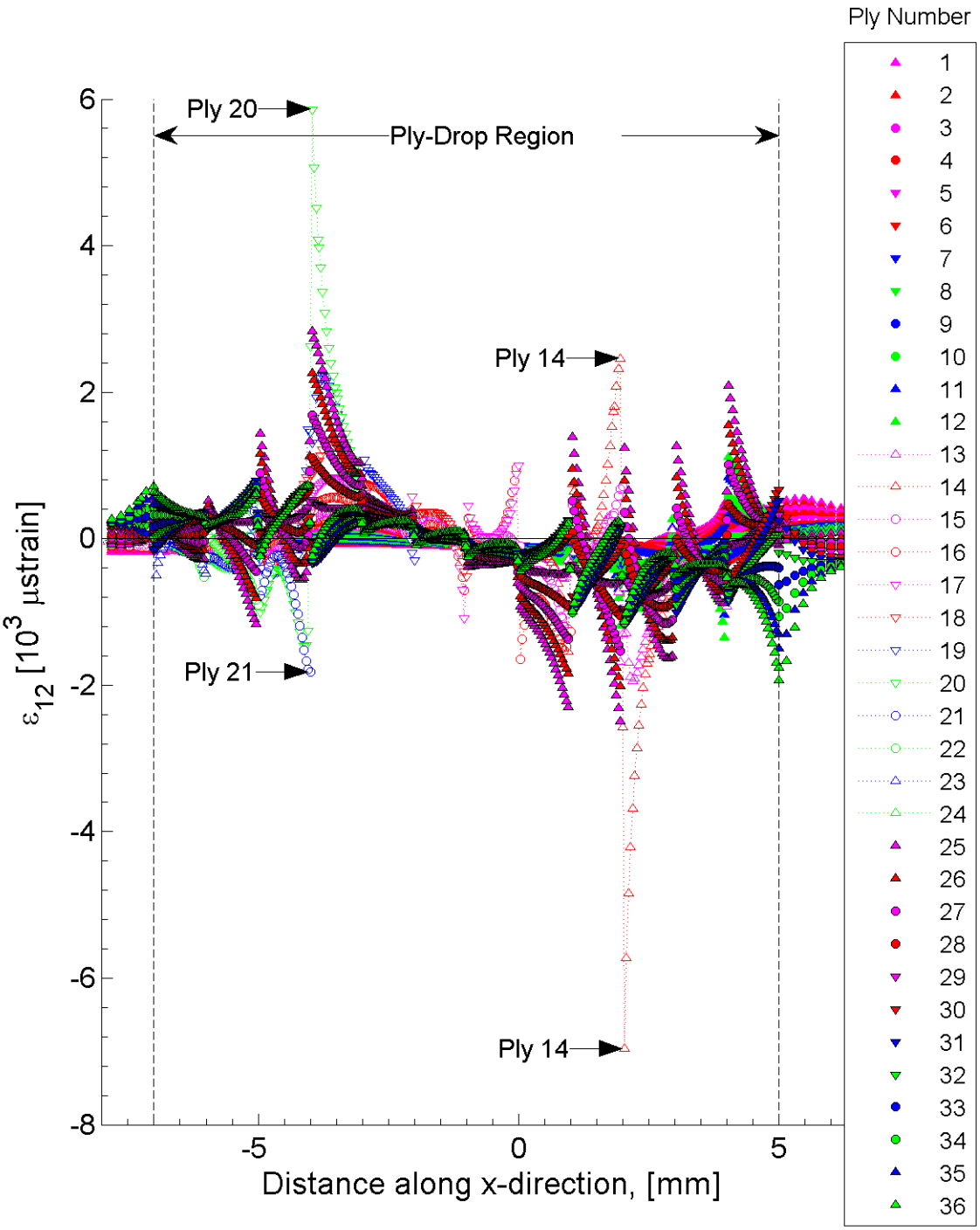

Figure 7.105 Plot of ϵ_{12}, in laminate axes, at the midplane of each ply within the x-z plane within the ply-drop region of the ply-drop specimen model for the two-ply effective ply thickness sublaminate of $[+45_2/0_2/-45_2]_S$.

16 have a ply angle of $+45°$, and plies 19 and 22 have a ply angle of $-45°$. Within each ply, the peaks of ϵ_{12} are observed to change sign and magnitude on each side of the ply-drop (e.g., the peaks in ply 13 jump from -7200 μstrain at the x-location of 3.04 mm to +4200 μstrain at the x-location 2.96 mm). This change in sign across a dropped ply is not observed in the results of ϵ_{11}. Two large peaks are observed in the ply-drop region of the two-ply effective ply thickness laminate. These peaks occur in plies 14 and 20, a $+45°$ and $-45°$ ply, respectively. As with the peaks of the single-ply effective ply thickness laminate, the x-locations of these peaks are the same as the peaks observed in the results of ϵ_{11} for the two-ply effective ply thickness laminate. In both laminates, these peaks occur in plies neighboring a $0°$ ply. As with the results for ϵ_{11} and ϵ_{22}, additional smaller peaks are observed at every x-location corresponding to a ply drop.

The peak magnitude of ϵ_{12} for the single-ply and two-ply effective ply thickness laminates are listed in Table 7.31. The peak magnitudes are effectively the same for the two laminates. The x-locations of the peaks for the single-ply and two-ply effective ply thickness laminates vary by a distance equal to the spacing between ply drops. These x-locations correspond to the x-locations of the maximum values of ϵ_{11}. As stated for the peak maximum values of ϵ_{11}, these locations correspond to the x-locations where a neighboring $0°$ ply is dropped.

The out-of-plane strain results are considered subsequently. These strain fields are observed to have variations through the thickness of each laminate. Variations from LPT exist in the model results due to free-edge effects. Due to the mesh density used near free edges of the model, free-edge effects such as those discussed in [58, 60, 74, 76, 139] are not captured. The free-edge effects in these regions result in large gradients in the interlaminar stresses. Therefore, the out-of-plane results are not valid in the boundary layer [148–150] of the free edge. For the ply-drop specimen, this boundary layer is approximately one laminate thickness. Because the results at the midplane of each ply within the x-z plane of the ply-drop model are outside of this region, the out-of-plane results are valid, unlike the previous models that contain a structural feature involving a free edge.

The strain fields of ϵ_{33} exhibit a consistent trend in shape through the thickness for both effective ply thickness laminates considered. Variations in ϵ_{33} are observed to be dependent on the through-thickness location as well as the proximity to the ply-drop region. The values of ϵ_{33} at the midplane of each ply are plotted for the single-ply and two-ply effective ply thickness laminate and are shown in Figures 7.106 and 7.107. For both cases, the far-field strain fields for ϵ_{33} in the undropped and dropped regions are on the order of the expected Poisson's effect. For example, the Poisson's ratio, ν_{xz}, for both the single-ply and two-ply effective ply thickness laminates, given in Table 7.4, is 0.13. Had the undropped and dropped regions been loaded individually (i.e., each region was an independent specimen loaded with the equivalent load), the expected value of ϵ_{33} due to Poisson's effects would be -1040 μstrain for the undropped region and -1560 μstrain for the dropped region. The majority of the plies of the ply-drop specimen have strain values greater than the expected Poisson's effect. As with the in-plane results, a through-thickness trend is observed. For the majority of the undropped region, the largest magnitudes of ϵ_{33} are observed in the bottom ply (ply number 1). In the portion of the dropped region from x equal to 5 mm to approximately 30 mm, the largest magnitudes are observed in the top ply (ply number 36). The values of ϵ_{33} at each through-thickness location in the undropped and dropped regions are observed to be nearly identical for the single-ply and two-ply effective ply thickness laminates.

The gradient of ϵ_{33} along the length of the specimen is dependent on both through-thickness location and proximity to the ply-drop region. In the undropped region, there is a positive gradient in ϵ_{33} as one approaches the ply-drop, with the exception of a region, roughly 5 mm in length, at the boundary between the undropped and ply-drop regions, where the gradients change sign, as observed in Figure 7.106. In the dropped region, the sign and magnitude of the gradient are observed to be dependent on the through-thickness location.

The values of ϵ_{33} are observed to have large variations within the ply-drop region. The values of ϵ_{33} at the midplane of each ply within the ply-drop region are plotted for the single-ply and two-ply effective ply thickness laminates and are shown in

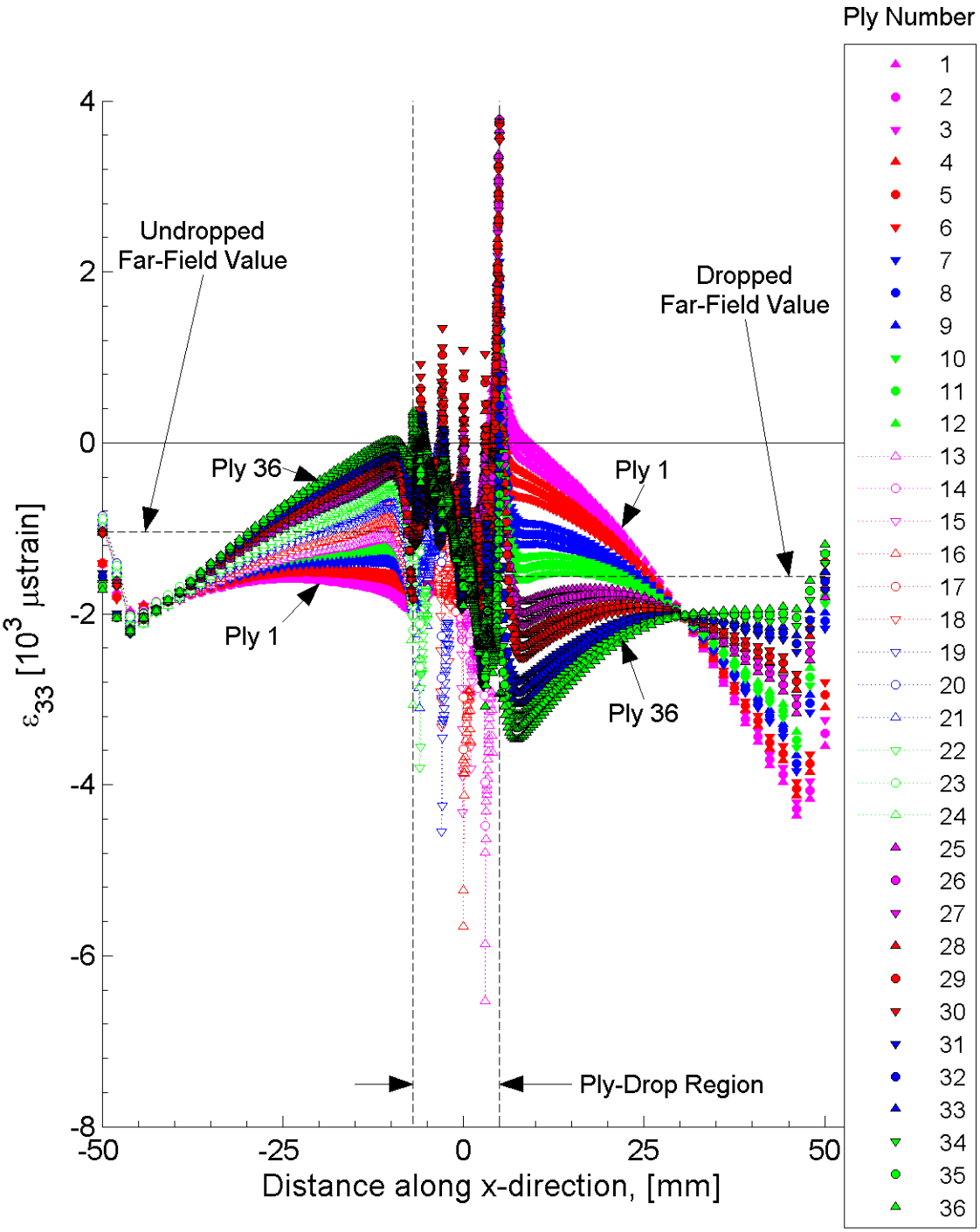

Figure 7.106 Plot of ϵ_{33}, in laminate axes, at the midplane of each ply within the x-z plane of the ply-drop specimen model for the single-ply effective ply thickness sublaminate of $[+45/0/-45]_{2S}$.

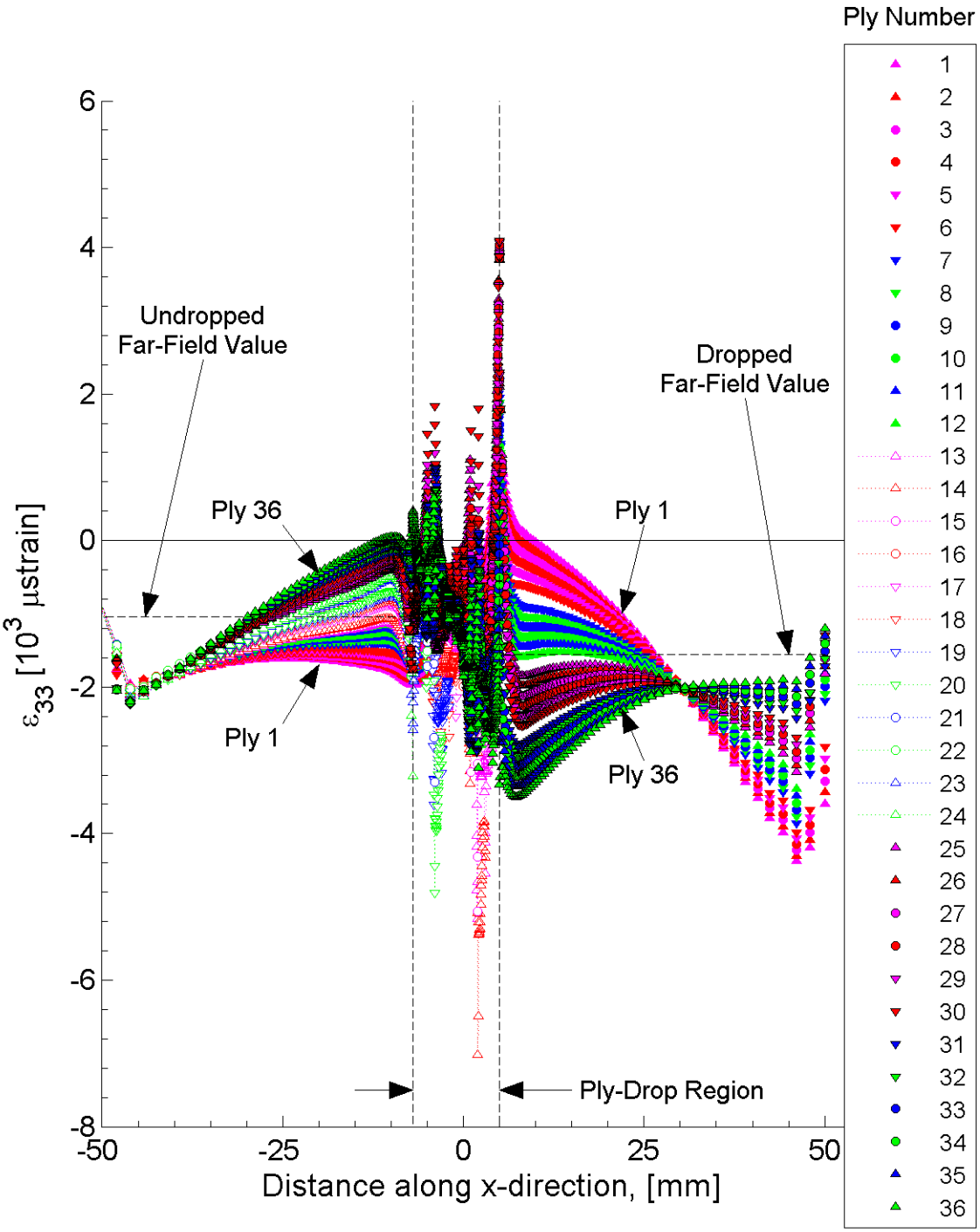

Figure 7.107 Plot of ϵ_{33}, in laminate axes, at the midplane of each ply within the x-z plane of the ply-drop specimen model for the two-ply effective ply thickness sublaminate of $[+45_2/0_2/-45_2]_S$.

Figure 7.108 and 7.109, with the x-direction expanded from Figures 7.106 and 7.107. Large peaks in magnitude are observed within plies that are dropped, with the largest peaks and the x-locations listed in Table 7.32. Unlike the in-plane peak locations, the x-locations of the peaks of ϵ_{33} occur at the exact location of ply drops. However, these locations are at a distance equal to the resolution of the finite element results (i.e., 0.04 mm). Every peak listed in Table 7.32 has a corresponding peak in ϵ_{11}, as listed in Table 7.30. The peak values of ϵ_{33} are greater than the Poisson effects corresponding to the peak values of ϵ_{11}. For example, the peak value of ϵ_{11} in ply 13 of the single-ply effective ply thickness laminate is +22300 μstrain, occurring at an x-distance of 3.04 mm, and is +22100 μstrain within ply 14 of the two-ply effective ply thickness laminate, occurring at an x-distance of 2.04 mm, as listed in Table 7.30. The Poisson's ratio, ν_{xz}, for both laminates, listed in Table 7.4, is 0.13. The expected value of ϵ_{33} due to only Poisson effects would be approximately -2900 μstrain for both laminates. In addition to the large peaks within plies that are dropped, smaller peaks are observed within the ply-drop region in the plies of the top sublaminate (plies 25 through 36). In contrast, the gradients in the plies of the bottom sublaminate (plies 1 through 12) are relatively constant, with the strain values observed to be relatively smooth through the ply-drop region.

The locations and values of the peak maximum (ϵ_T) and minimum (ϵ_C) out-of-plane strains for each laminate are listed in Table 7.33. The peaks of all the out-of-plane strains occur within the ply-drop region. The maximum value (ϵ_T) of ϵ_{33} occurs at the boundary of the ply-drop and dropped regions. For both the single-ply and two-ply effective ply thickness laminates, the peak minimum strain is approximately four times the expected Poisson effect. Consistent with the in-plane results, the peak minimum strains occur in an angle ply that neighbors a 0° ply. The x-locations and the through-thickness locations directly correspond to the in-plane peak locations. With the exception of the maximum value (ϵ_T) of ϵ_{33}, the peak out-of-plane strains (i.e., ϵ_{33}, ϵ_{13}, and ϵ_{23}) occur at the same x-location as the maximum value (ϵ_T) of ϵ_{11}, as listed in Table 7.31.

The strain fields of ϵ_{13} exhibit a consistent trend in shape through the thickness for

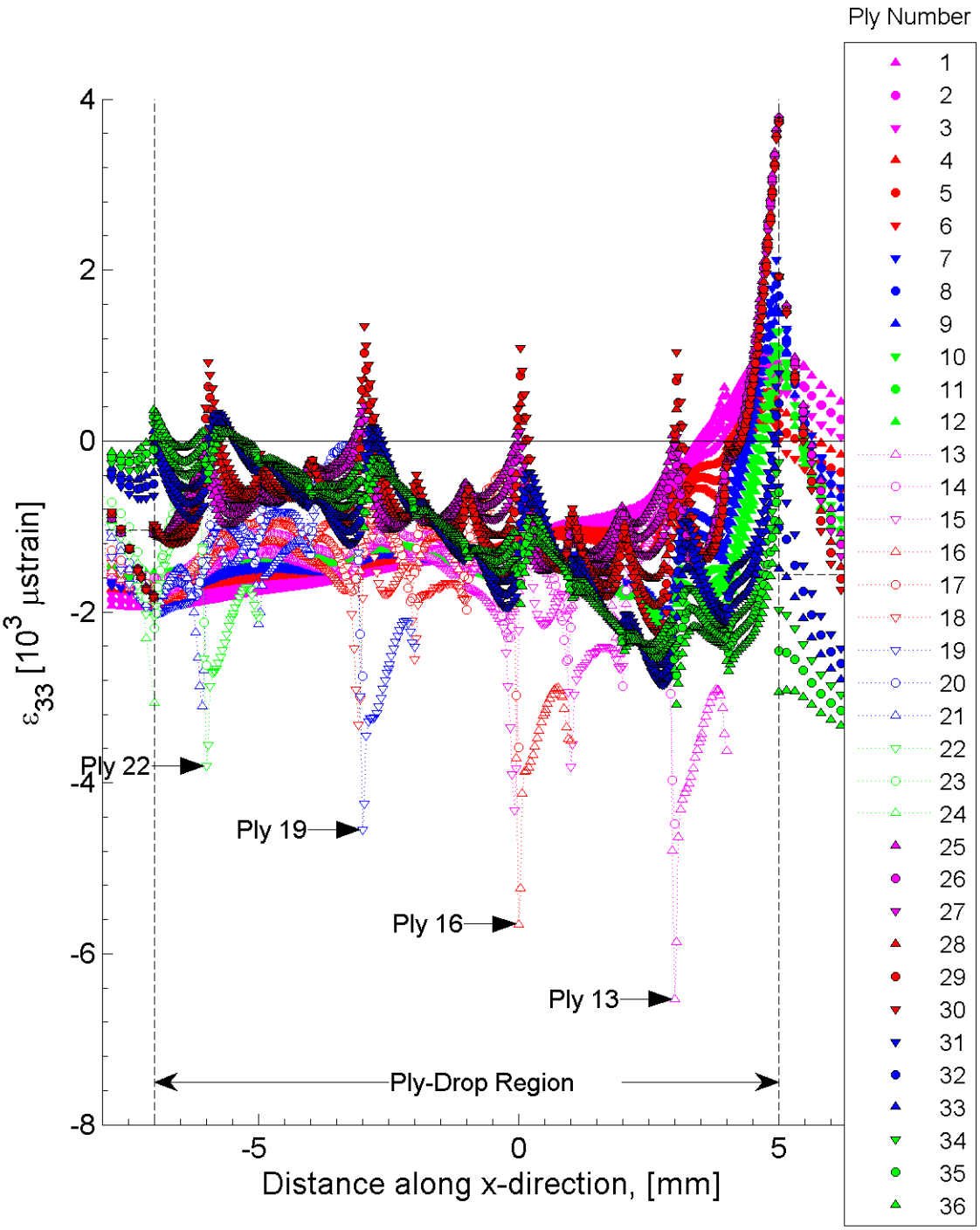

Figure 7.108 Plot of ϵ_{33}, in laminate axes, at the midplane of each ply within the x-z plane within the ply-drop region of the ply-drop specimen model for the single-ply effective ply thickness sublaminate of $[+45/0/-45]_{2S}$.

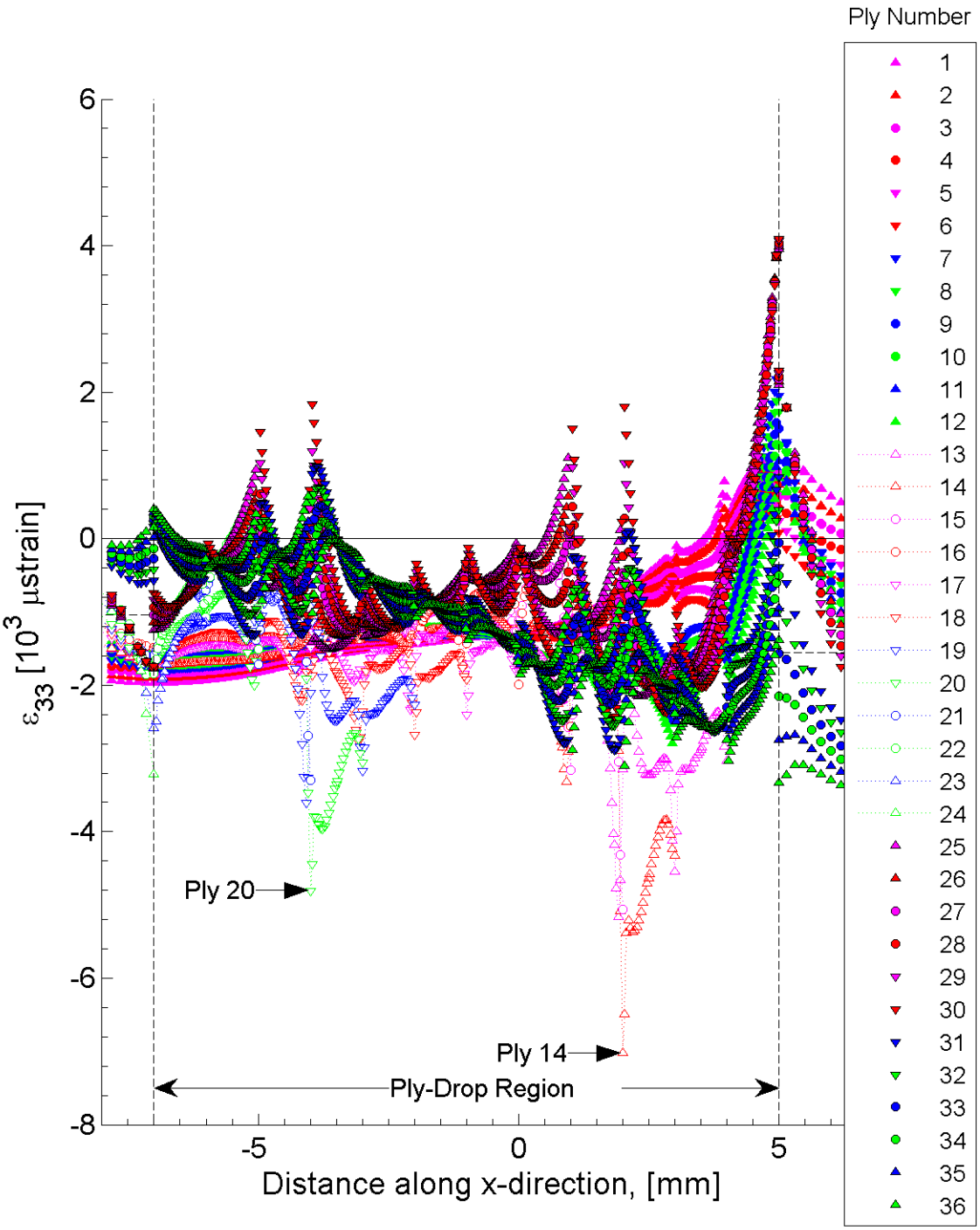

Figure 7.109 Plot of ϵ_{33}, in laminate axes, at the midplane of each ply within the x-z plane within the ply-drop region of the ply-drop specimen model for the two-ply effective ply thickness sublaminate of $[+45_2/0_2/-45_2]_S$.

Table 7.32 Locations and values of large peaks of ϵ_{33} strains within the ply-drop region for the ply-drop specimens (sublaminates of $[+45/0/-45]_{2S}$ and $[+45_2/0_2/-45_2]_S$)

Strain Component	**Nominal Effective Ply Thickness**	**Through-Thickness Location [ply number]**	**Value [μstrain]**	**$x-$ Location [mm]**
ϵ_{33}	1	13	-6500	3.00
		16	-5700	0.00
		19	-4500	-3.00
		22	-3800	-6.00
	2	14	-7000	2.00
		20	-4800	-4.00

Table 7.33 Locations and values of maximum and minimum out-of-plane strains for the ply-drop specimens (sublaminates of $[+45/0/-45]_{2S}$ and $[+45_2/0_2/-45_2]_S$)

Strain Component	**Value Considered**[a]	**Nominal Effective Ply Thickness**	**Value [μstrain]**	**Through-Thickness Location [ply number]**	**$x-$ Location [mm]**
ϵ_{33}	ϵ_T	1	+3800	25	5.00
		2	+4100	30	5.00
	ϵ_C	1	-6500	13	3.00
		2	-7000	14	2.00
ϵ_{13}	ϵ_S	1	+21800	14	3.00
		2	+21100	25	2.08
ϵ_{23}	ϵ_S	1	+9500	20	3.00
		2	-15600	15	2.00

[a] ϵ_T = Maximum
ϵ_C = Minimum
ϵ_S = Maximum Magnitude

both effective ply thickness laminates considered. Variations in ϵ_{13} are observed to be dependent on the through-thickness location as well as the proximity to the ply-drop region. The values of ϵ_{13} at the midplane of each ply are plotted for the single-ply and two-ply effective ply thickness laminate and are shown in Figures 7.110 and 7.111. For both cases, the far-field strain fields for ϵ_{13} in the undropped and dropped regions are -100 to -2500 μstrain below the expected value predicted from the coefficient of mutual influence, listed in Table 7.4 as equal to zero for both laminates. As with the in-plane results, a through-thickness trend is observed for both laminates. For the majority of the undropped region, the largest magnitudes of ϵ_{13} are observed in the bottom ply (ply number 1). In the dropped region, the largest magnitudes are observed in the top ply (ply number 36). In the dropped region, the through-thickness variation is limited to two distinct values, as seen in Figures 7.110 and 7.111. The values of ϵ_{13} at each through-thickness location in the undropped and dropped regions are observed to be nearly identical for the single-ply and two-ply effective ply thickness laminates.

The gradient of ϵ_{13} along the length of the specimen is nearly zero for the majority of the undropped and dropped regions, with exceptions near the applied boundary conditions and near the ply drop region. Near the ply-drop region, the sign and magnitude of the gradients are observed to be dependent on through-thickness location. The sign of the gradient in this region reverses at outer plies (e.g., the sign of the gradient is positive on the bottom ply and negative on the top ply for a given x-location).

The values of ϵ_{13} are observed to have large variations within the ply-drop region. The values of ϵ_{13} at the midplane of each ply within the ply-drop region are plotted for the single-ply and two-ply effective ply thickness laminate, and are shown in Figure 7.112 and 7.113, with the x-direction expanded from Figures 7.110 and 7.111. As with the results for ϵ_{33} in the ply-drop region, large peaks in magnitude are observed within plies that are dropped. The largest peaks are observed to occur within plies of the dropped sublaminate and are listed in Table 7.34. Unlike the results for ϵ_{33}, peaks are observed in the same plies and locations as the peaks of ϵ_{11}. The single-ply effective ply thickness laminate also exhibits peaks that are not seen

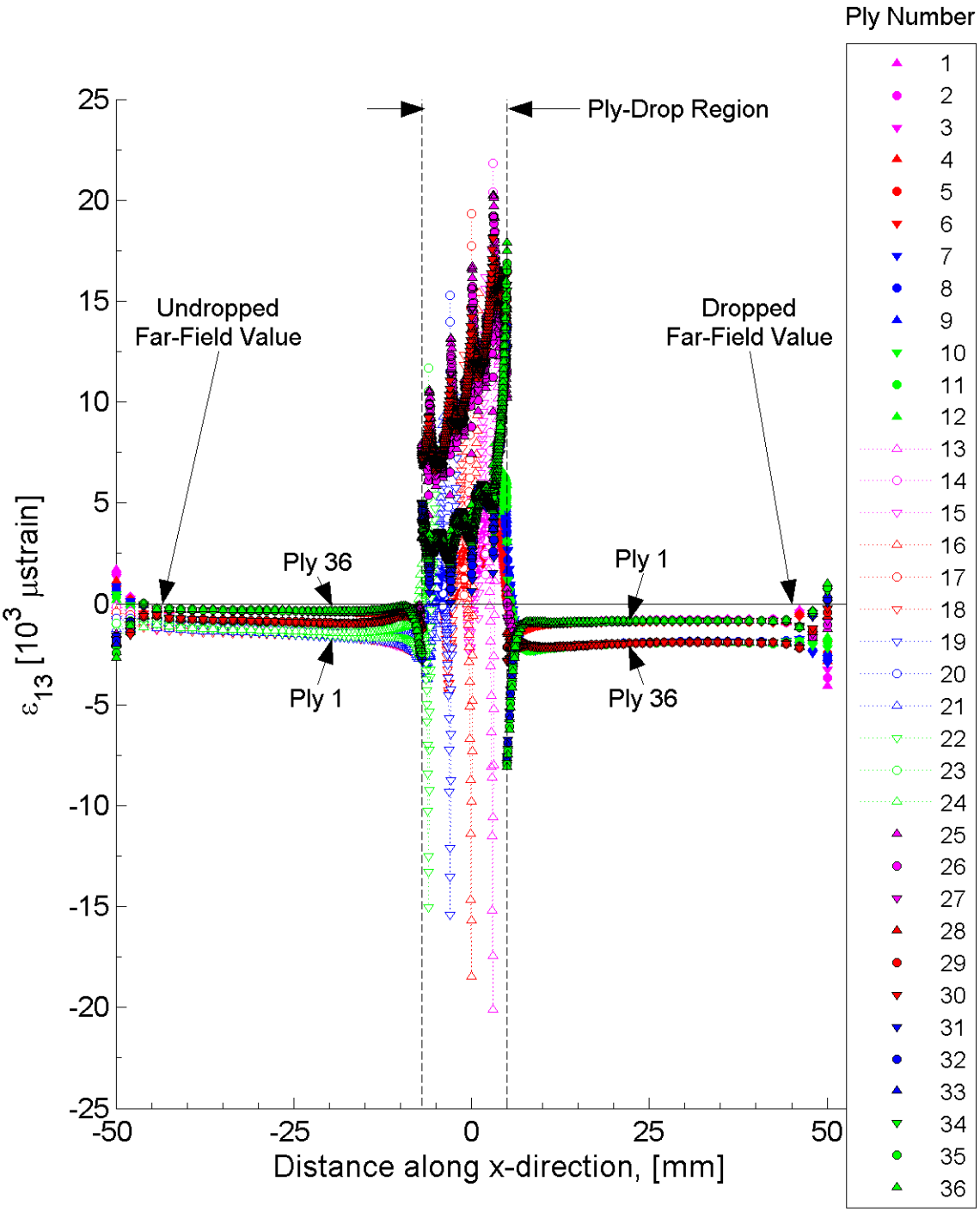

Figure 7.110 Plot of ϵ_{13}, in laminate axes, at the midplane of each ply within the x-z plane of the ply-drop specimen model for the single-ply effective ply thickness sublaminate of $[+45/0/-45]_{2S}$.

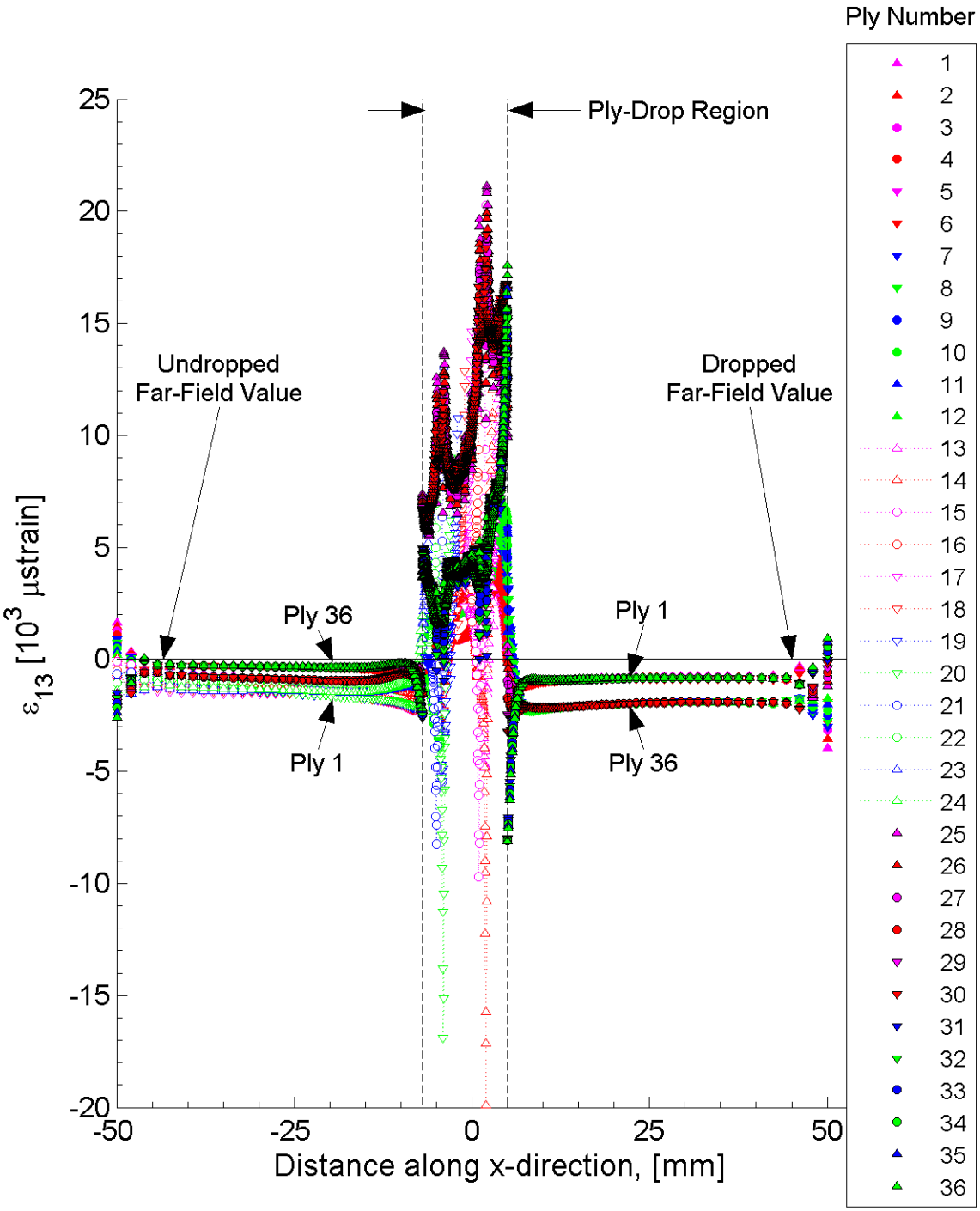

Figure 7.111 Plot of ϵ_{13}, in laminate axes, at the midplane of each ply within the x-z plane of the ply-drop specimen model for the two-ply effective ply thickness sublaminate of $[+45_2/0_2/-45_2]_S$.

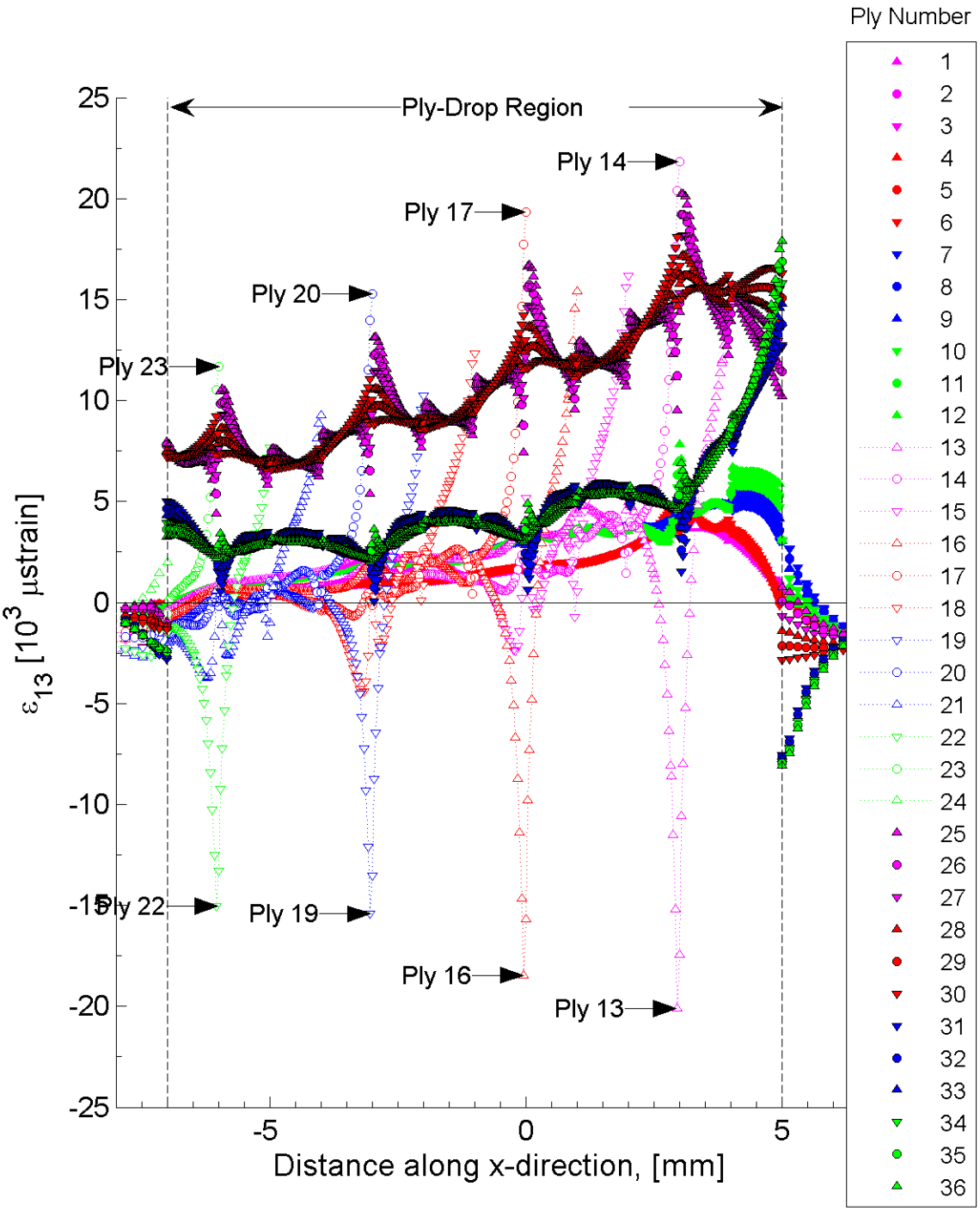

Figure 7.112 Plot of ϵ_{13}, in laminate axes, at the midplane of each ply within the x-z plane within the ply-drop region of the ply-drop specimen model for the single-ply effective ply thickness sublaminate of $[+45/0/-45]_{2S}$.

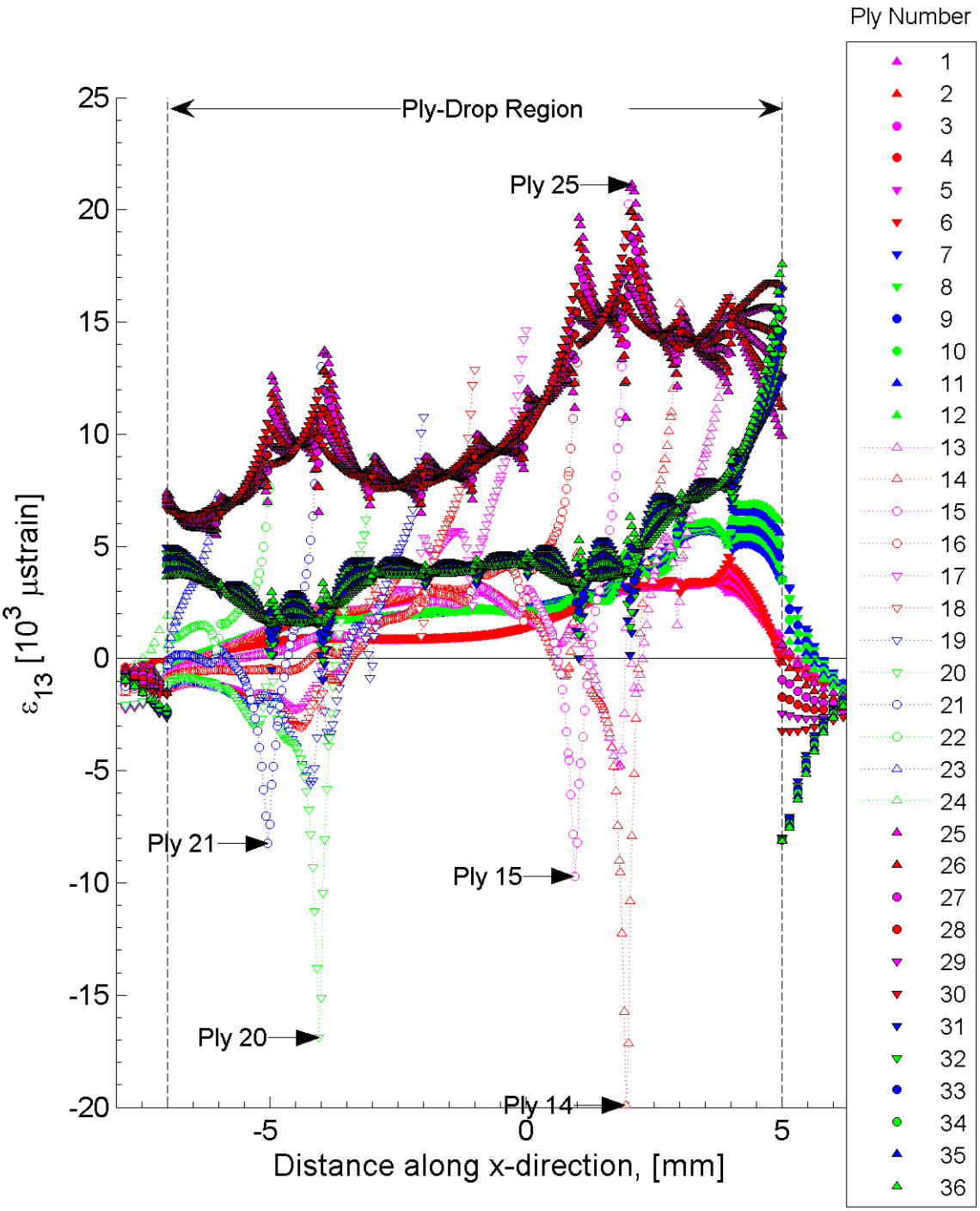

Figure 7.113 Plot of ϵ_{13}, in laminate axes, at the midplane of each ply within the x-z plane within the ply-drop region of the ply-drop specimen model for the two-ply effective ply thickness sublaminate of $[+45_2/0_2/-45_2]_S$.

Table 7.34 Locations and values of large peaks of ϵ_{13} strains within the ply-drop region for the ply-drop specimens (sublaminates of $[+45/0/-45]_{2S}$ and $[+45_2/0_2/-45_2]_S$)

Strain Component	**Nominal Effective Ply Thickness**	**Through-Thickness Location [ply number]**	**Value [μstrain]**	**$x-$ Location [mm]**
ϵ_{13}	1	13	-20100	2.96
		14	21800	3.00
		16	-18500	-0.04
		17	19300	0.00
		19	-15400	-3.04
		20	15300	-3.00
		22	-15000	-6.04
		23	11700	-6.00
	2	14	-19900	1.96
		15	-9700	0.96
		20	-16900	-4.04
		21	-8200	-5.04

in the results of ϵ_{11}. Whereas the peaks of ϵ_{11} occur in plies 13, 16, 19, and 22, the results of ϵ_{13} exhibit these peaks as well as additional peaks in plies 14, 17, 20, and 23. These additional peaks have the opposite sign as the peaks in plies 13, 16, 19, and 22, but have magnitudes on the order of the neighboring peak value (i.e., the peak in ply 14 is on the order of the peak in ply 13). The two-ply effective ply thickness laminate exhibits a somewhat different behavior. For this laminate, peaks are again observed at the same location and within the same plies, plies 14 and 20, as the results for ϵ_{11}. Additional peaks are observed in plies 15 and 21, but the behavior is different from that of the single-ply effective ply thickness laminate. For the two-ply effective ply thickness laminate, the magnitudes of the peaks in plies 15 and 21 are roughly half that of plies 14 and 20, respectively, and of the same sign. For both the single-ply and two-ply effective laminates, peaks of positive magnitude are observed in ply 25 at the x-locations corresponding to the large peaks of ϵ_{13} in the ply-drop region. Additional smaller peaks are observed in the plies of the top sublaminate (plies 25 through 36). In contrast, the gradients in the plies of the bottom sublaminate (plies 1 through 12) are relatively constant, with the strain values observed to be relatively smooth through the ply-drop region. This was also observed for the results of ϵ_{33}.

The locations and values of the peak (ϵ_S) out-of-plane strains for each laminate are listed in Table 7.33. The peaks of ϵ_{13} occur within the ply-drop region. The maximum value (ϵ_S) of ϵ_{13} occurs at the same x-location as the peak (ϵ_T) of ϵ_{11}. Consistent with the in-plane results, the peak minimum strains occur in an angle ply that neighbors a 0° ply. The x-locations and the through-thickness locations directly correspond to the in-plane peak locations.

The strain fields of ϵ_{23} exhibit a consistent trend in shape through the thickness for both effective ply thickness laminates considered. Variations in ϵ_{23} are observed to be dependent on the through-thickness location as well as the proximity to the ply-drop region. The values of ϵ_{23} at the midplane of each ply are plotted for the single-ply and two-ply effective ply thickness laminate and are shown in Figures 7.114 and 7.115. For both cases, the far-field through-thickness strain fields for ϵ_{23} in the undropped and dropped regions are distributed symmetrically about the expected value predicted

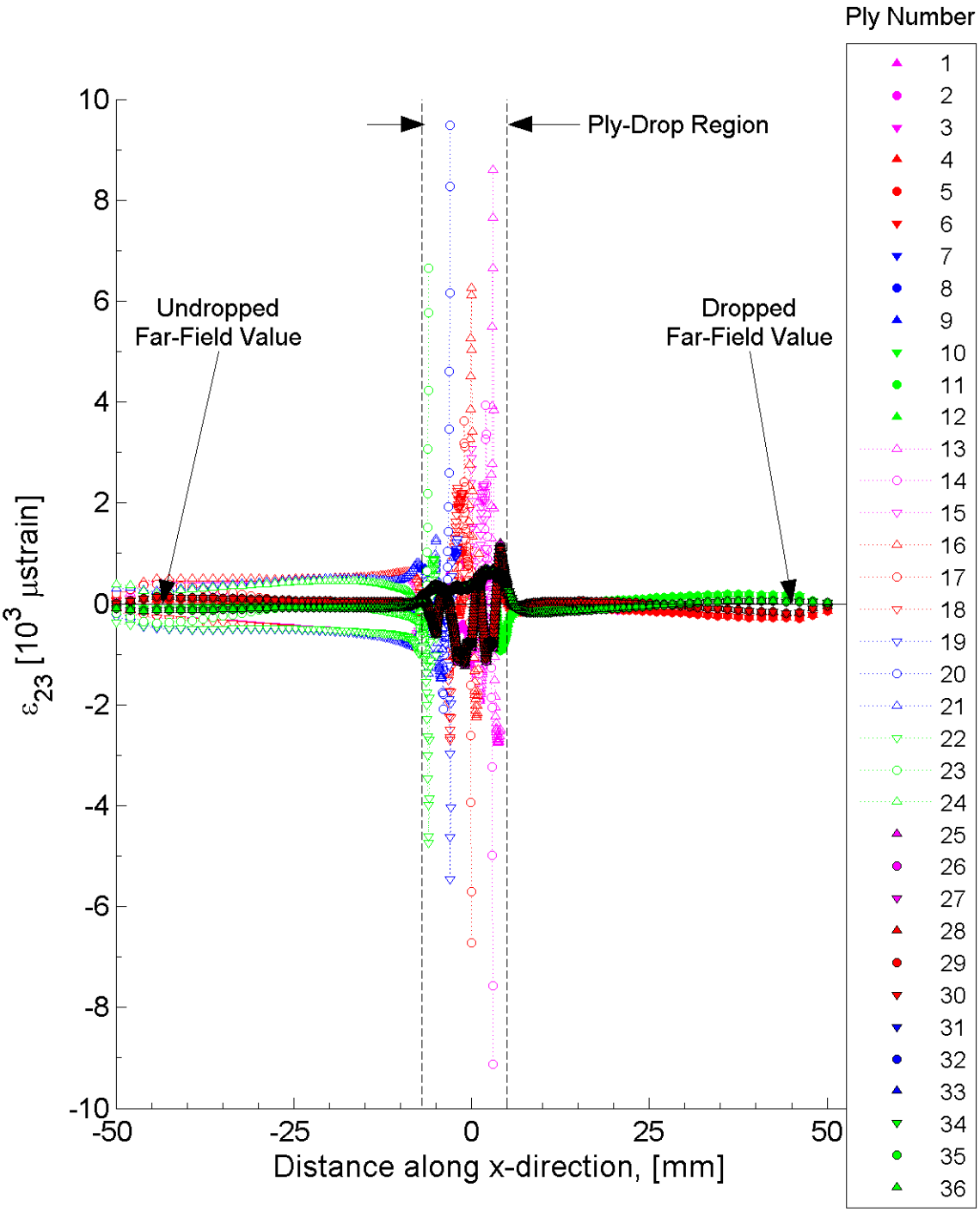

Figure 7.114 Plot of ϵ_{23}, in laminate axes, at the midplane of each ply within the x-z plane of the ply-drop specimen model for the single-ply effective ply thickness sublaminate of $[+45/0/-45]_{2S}$.

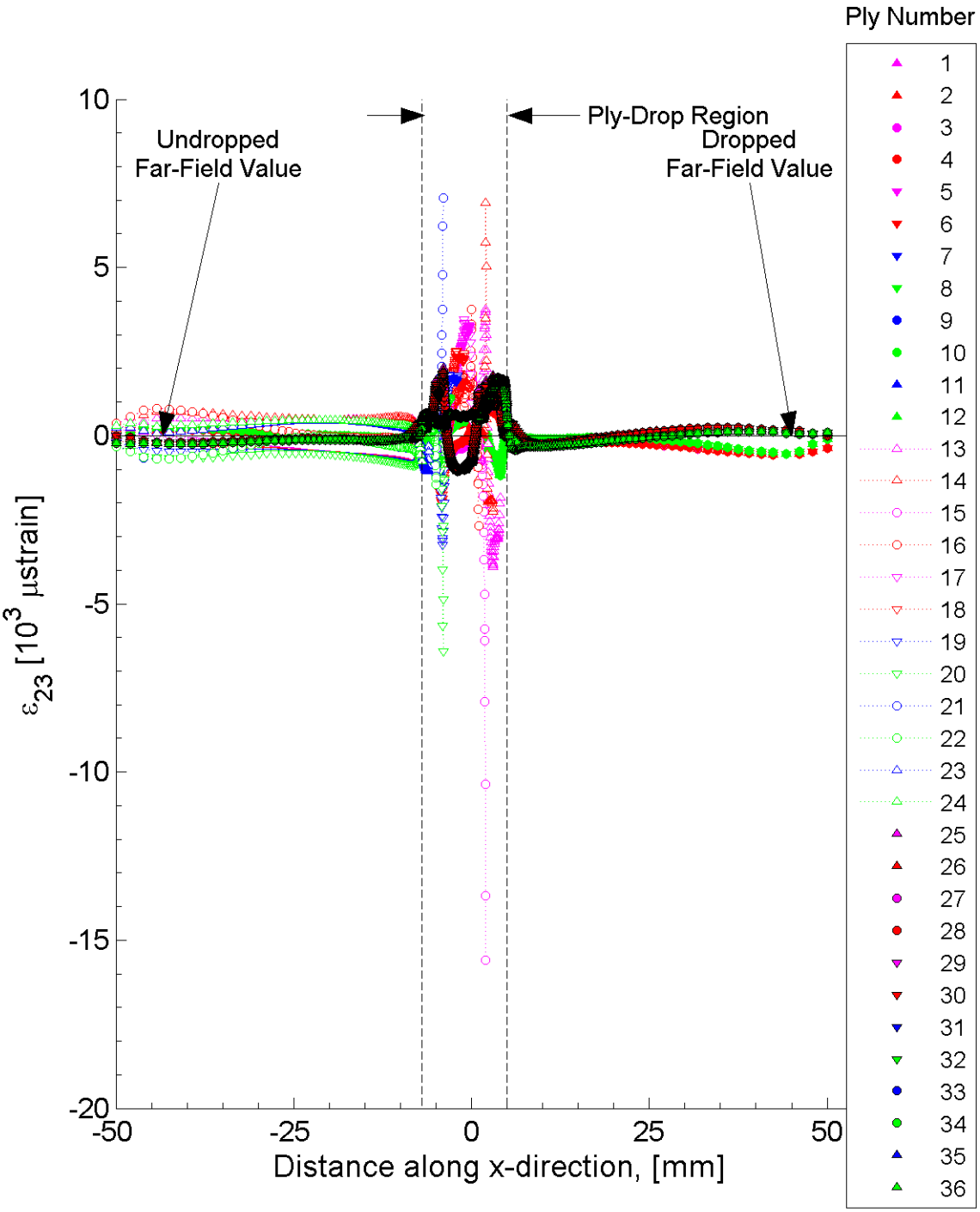

Figure 7.115 Plot of ϵ_{23}, in laminate axes, at the midplane of each ply within the x-z plane of the ply-drop specimen model for the two-ply effective ply thickness sublaminate of $[+45_2/0_2/-45_2]_S$.

from the coefficient of mutual influence, listed in Table 7.4 as equal to zero for both laminates. In both cases, this distribution is not perfectly symmetric. Unlike all the other strain cases, the bounding strains in the undropped and dropped regions are not the outer plies (i.e., plies 1 and 36), but are plies located near the midplane of the respective regions.

The gradient of ϵ_{23} along the length of the specimen is nearly zero for the majority of the undropped and dropped regions, with exceptions near the applied boundary conditions and near the ply-drop region. Near the ply-drop region, the sign and magnitude of the gradients are observed to be dependent on through-thickness location. The sign of the gradient in this region reverses at outer plies (e.g., the sign of the gradient is positive on the bottom ply and negative on the top ply for a given x-location).

The values of ϵ_{23} are observed to have large variations within the ply-drop region. The values of ϵ_{23} at the midplane of each ply within the ply-drop region are plotted for the single-ply and two-ply effective ply thickness laminates, and are shown in Figure 7.116 and 7.117, with the x-direction expanded from Figures 7.114 and 7.115. As with the results of ϵ_{33} and ϵ_{13} in the ply-drop region, large peaks in magnitude are observed within plies that are dropped. The largest peaks are observed to occur within plies of the dropped sublaminate and are listed in Table 7.35. Peaks of the results of ϵ_{23} are observed in the same plies and locations as the peaks of ϵ_{11}. The single-ply effective ply thickness laminate exhibits the additional peaks seen in the results of ϵ_{13}. As with the results of ϵ_{13}, these peaks in plies 14, 17, 20, and 23 have magnitudes on the order of the neighboring peak value, but with opposite sign. The two-ply effective ply thickness laminate also exhibit a similar behavior as observed in the results of ϵ_{13}. Unlike the results of ϵ_{13}, the peak values in plies 15 and 21 have an opposite sign as the peak values in plies 14 and 20. Similar to the results of ϵ_{13}, the magnitude of the peak of ply 14 is approximately half the magnitude of the peak of ply 15. Unlike the results of ϵ_{13}, the magnitudes of the peaks of plies 20 and 21 are approximately the same. The peaks in the results of ϵ_{23} for both the single-ply and two-ply effective ply thickness laminate are observed in the same x-locations as

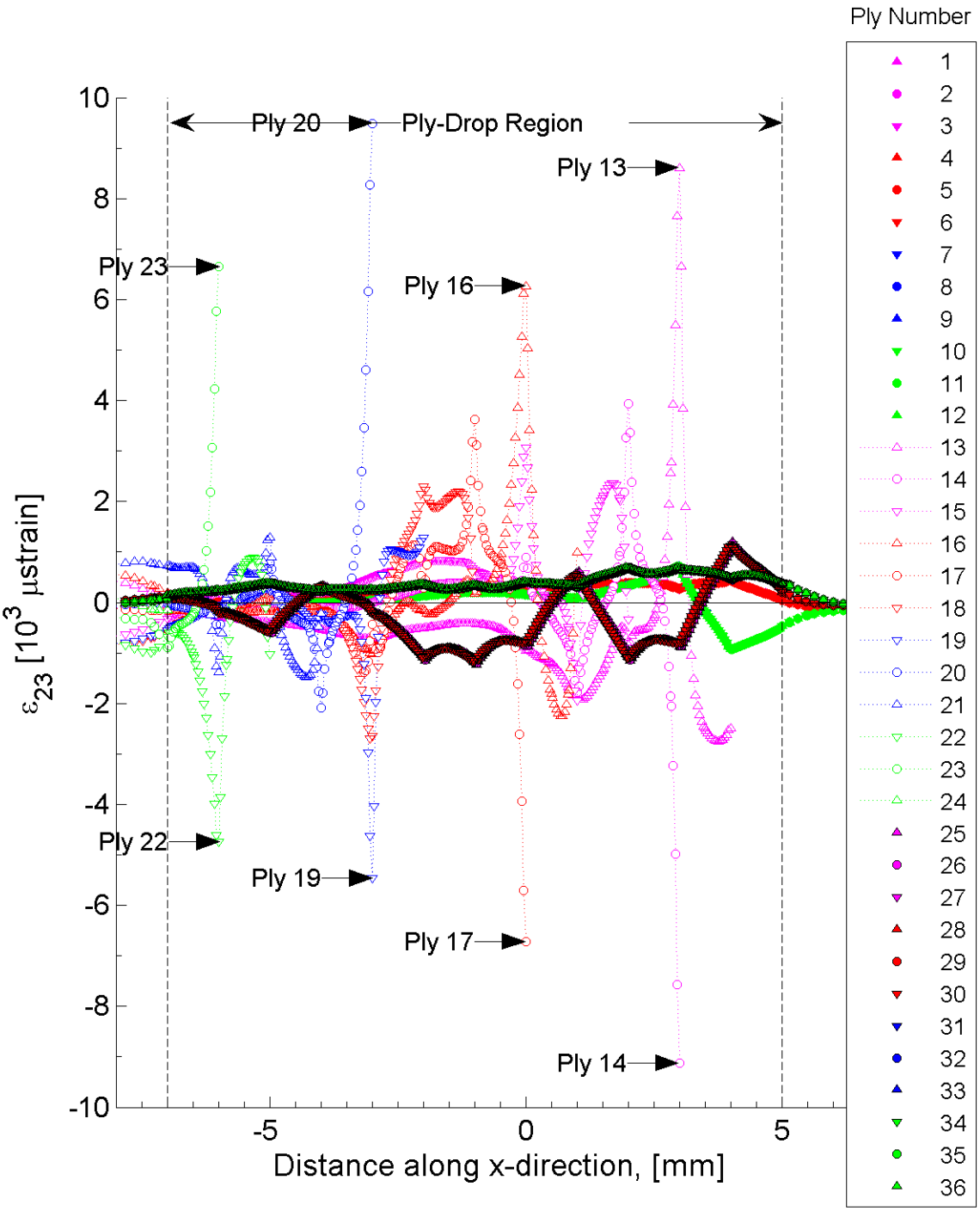

Figure 7.116 Plot of ϵ_{23}, in laminate axes, at the midplane of each ply within the x-z plane within the ply-drop region of the ply-drop specimen model for the single-ply effective ply thickness sublaminate of $[+45/0/-45]_{2S}$.

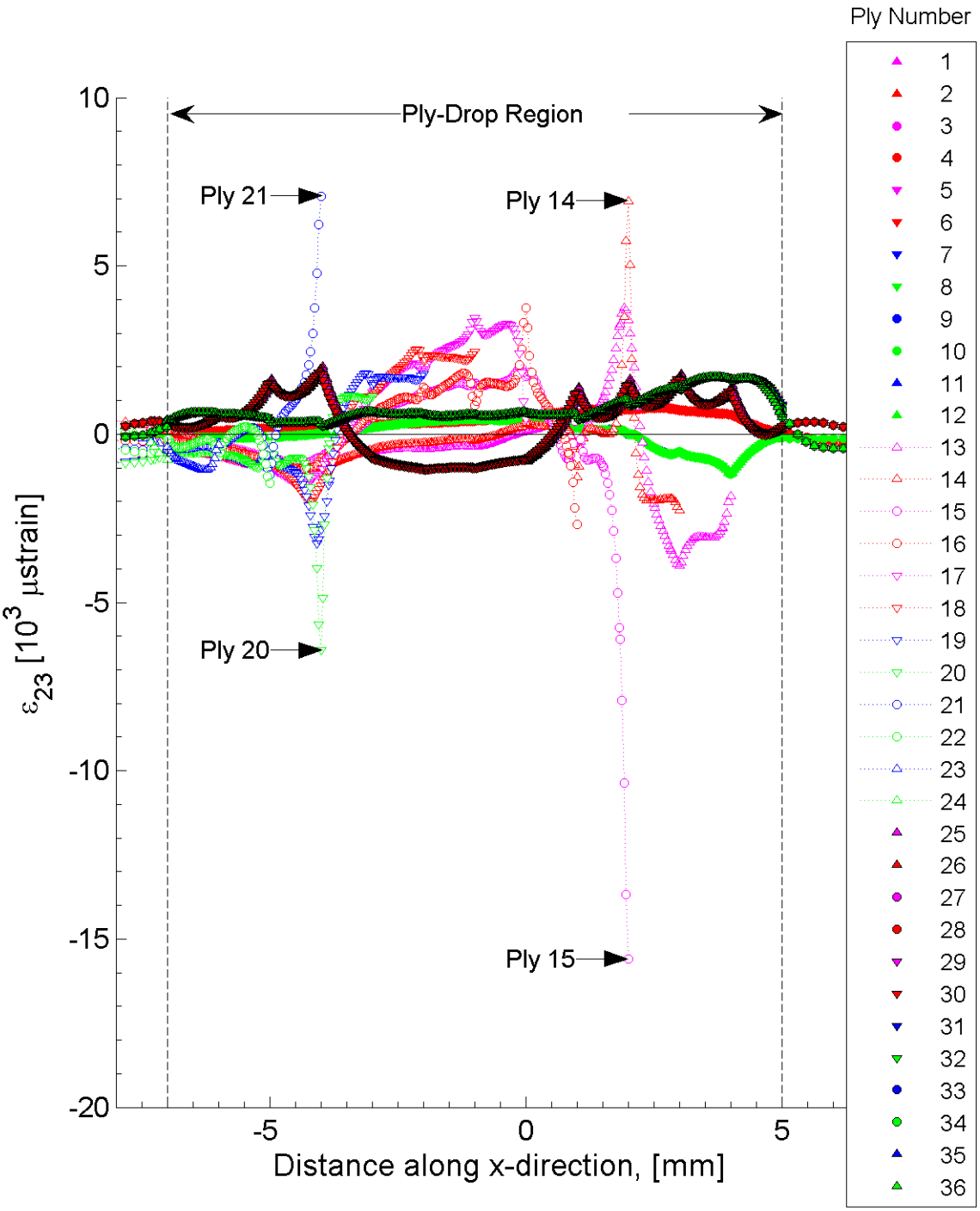

Figure 7.117 Plot of ϵ_{23}, in laminate axes, at the midplane of each ply within the x-z plane within the ply-drop region of the ply-drop specimen model for the two-ply effective ply thickness sublaminate of $[+45_2/0_2/-45_2]_S$.

Table 7.35 Locations and values of large peaks of ϵ_{23} strains within the ply-drop region for the ply-drop specimens (sublaminates of $[+45/0/-45]_{2S}$ and $[+45_2/0_2/-45_2]_S$)

Strain Component	**Nominal Effective Ply Thickness**	**Through-Thickness Location [ply number]**	**Value [μstrain]**	**$x-$ Location [mm]**
ϵ_{13}	1	13	8600	3.00
		14	-9100	3.00
		16	6300	0.00
		17	-6700	0.00
		19	-5500	-3.00
		20	9500	-3.00
		22	-4700	-6.00
		23	6600	-6.00
	2	14	6900	2.00
		15	-15600	2.00
		20	7100	-4.00
		21	-6400	-4.00

the peaks observed in the results of ϵ_{11}. Additional smaller peaks are observed in the plies of the top sublaminate (plies 25 through 36). In contrast, the gradients in the plies of the bottom sublaminate (plies 1 through 12) are relatively constant, with the strain values observed to be relatively smooth through the ply-drop region. This is also observed for the results of ϵ_{33} and ϵ_{13}.

The locations and values of the peak (ϵ_S) out-of-plane strains for each laminate are listed in Table 7.33. The peaks of ϵ_{23} occur within the ply-drop region. The maximum value (ϵ_S) of ϵ_{23} occurs at the same x-location as the peaks (ϵ_S) of ϵ_{11}. Consistent with the in-plane results, the peak minimum strains occur in an angle ply that neighbors a 0° ply. The x-locations and the through-thickness locations directly correspond to the in-plane peak locations.

7.3.5 Damage Inclusion Models

The characteristic strain fields for the two damage inclusion models are illustrated via the results in this subsection and Appendix B.4. Unlike the single-edge-notch, double-edge-notch, open-hole tension, and ply-drop specimen models, where lengthscales associated with geometric features are investigated, the results of the damage inclusion models are used to investigate lengthscales associated with damage features. Two damage modes commonly observed within the experimental specimens, stitch cracking and delamination, are modeled, as described in Section 7.2.5, and the resulting strain fields are discussed. The results of the stitch crack model are presented first, followed by the results of the delamination model.

As with the single-edge-notched, double-edge-notched, open-hole tension, and ply-drop specimen models, a common feature exhibited in all the strain field results is free-edge effects. These effects are observed as discontinuities in the slopes of the isostrain lines (i.e., the isoline is not smooth) near the edges of the model. These free-edge effects do not influence the region of interest (i.e., near the modeled damage) due to the use of a quasi-infinite plate, as described in Section 7.2.5. Beyond these observations of the free-edge effects, these effects are not further discussed.

The results for the in-plane strain fields of the stitch crack damage inclusion model

are considered first. This is followed by the results for the out-of-plane strain fields, and subsequently the results for the delamination damage inclusion model.

The spacing "between stitch cracks" and the length of the stitch cracks is observed, in the experimental specimens, to be approximately constant for the single-ply effective ply thickness laminates while being dependent on the angle of the four-ply effective ply thickness angle-ply laminates, as presented in Section 6.1.2. The results of the model presented herein are based on the spacing and stitch crack length observed throughout the single-ply effective ply thickness laminates. These lengths, taken from the experimental results of the single-ply effective ply thickness laminates, define the representative stitch crack modeled, as described in Section 7.2.5. Although the experimental results of the four-ply effective ply thickness laminates do not have constant lengths, the stitch crack length and spacing are modeled with constant lengths for both the single-ply and four-ply effective ply thickness laminates. Further modeling is required to investigate the effects of the varying spacing and stitch crack length of the four-ply effective ply thickness laminates.

The results of the stitch crack model are illustrated along one of two paths. These paths are located at the midplane of each ply and are oriented parallel to the stitch cracks, as shown in Figure 7.118. The path labeled "along stitch crack" lies within the x-y plane, begins at the tip of the central stitch crack, and extends colinearly with the central stitch crack (i.e., along the $+\theta$ direction). The central stitch crack is fixed in space, with neighboring stitch cracks added symmetrically about the 'central' stitch crack. The path labeled "between stitch cracks" is defined to lie within the x-y plane, parallel to the S-axis (i.e., parallel to the stitch cracks), located halfway between the "central" stitch crack and the stitch crack located in the $+\hat{S}$-direction neighboring this central stitch crack, and beginning at the intercept with the path of the matrix crack (i.e., S equal to zero). The $\hat{S}$-distance between stitch cracks is dependent on θ, such that:

$$|\hat{S}| = \frac{0.254\ mm}{sin(2\theta)} \tag{7.36}$$

This gives values of $\hat{S}$ for this spacing of 0.508 mm, 0.293 mm, 0.293 mm, and

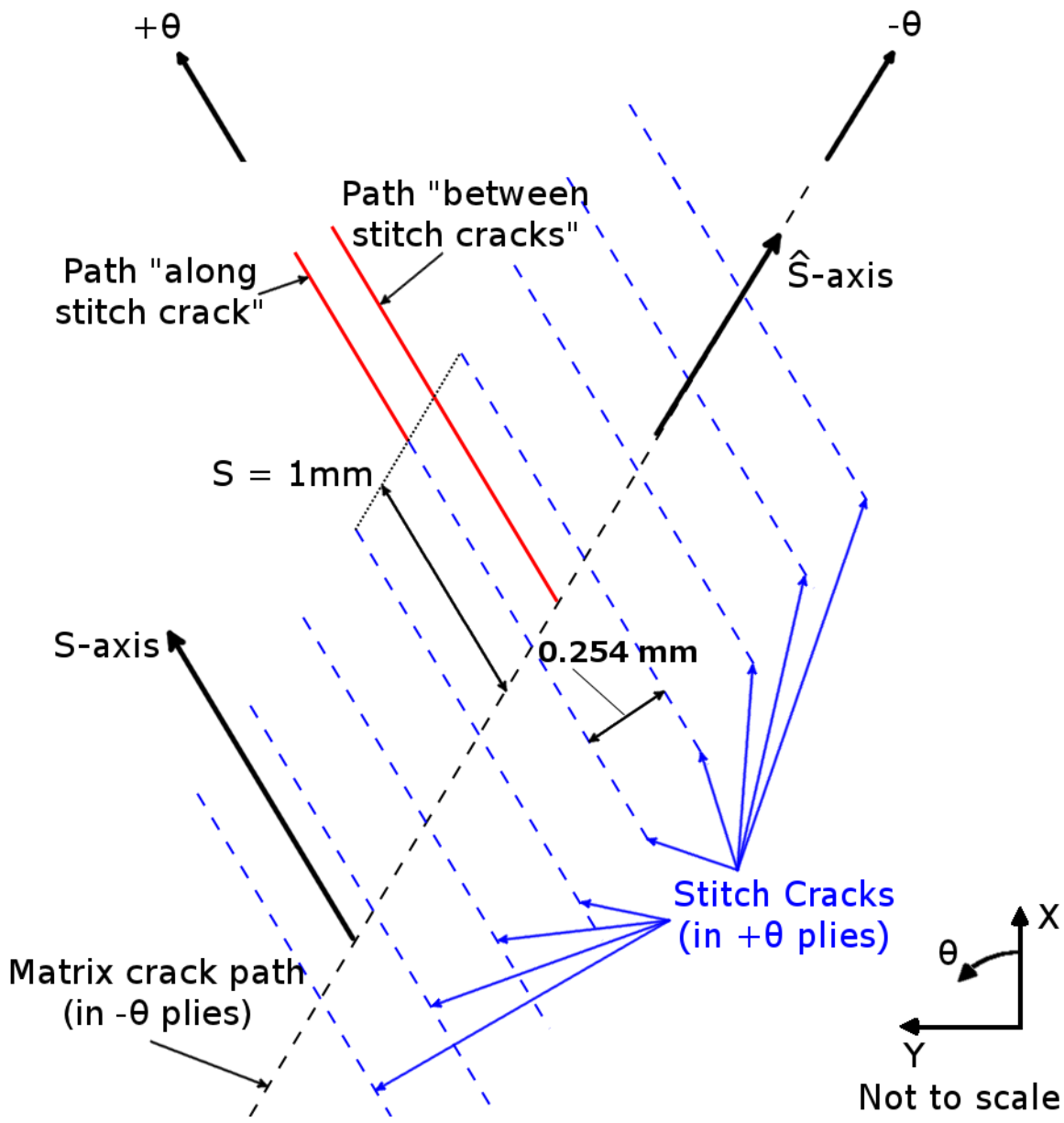

Figure 7.118 Illustration of the two paths from which results for the stitch crack damage model are taken.

0.508 mm for values of θ of 15°, 30°, 60°, and 75°, respectively. Comparing the results from the "along" path and "between" path provides gradient information along the $\hat{S}$-direction (i.e., along the direction of the negative ply angle for a given value of S). The S- and $\hat{S}$-axes are non-orthogonal. The distance along each path is measured along the S-axis, with the origin at the matrix crack path. The tip of the "central" stitch crack is located at a S-distance equal to 1 mm for each of the laminates. The relative orientation of both the paths as well as the S- and $\hat{S}$-axes changes for each angle-ply laminate. The results presented herein are taken at the midplane of each ply along these paths. The paths could also be oriented along the negative S-direction and would exhibit the same results due to the symmetry of the model. In addition, the symmetry of the model gives the same results if the path "between stitch cracks" were oriented in the negative $\hat{S}$-direction relative to the "central" stitch crack.

The resulting strain field of ϵ_{11} along the path "between stitch cracks" (i.e., if there were a neighboring stitch crack) for the model containing a single stitch crack with a laminate of $[+30/-30]_{16T}$ is shown in Figure 7.119. The effects of adding neighboring stitch cracks, in pairs, about the central stitch crack on the resulting strain field of ϵ_{11} are shown in Figures 7.120, 7.121, 7.122, and 7.123. These figures correspond to the model containing three, five, seven, and nine stitch cracks, respectively. The strain fields of ϵ_{11} for the top and the bottom two plies (1, 31, and 32) exhibit the largest gradients through the thickness of the laminate and along the S-direction. The distribution of strains is observed to vary as the number of stitch cracks increases. In order to determine the minimum number of stitch cracks required to model the behavior at the "central" stitch crack, the change in strain fields as the number of stitch cracks increases is investigated. It is observed that the strain fields of ϵ_{11} become stable after five stitch cracks are modeled (i.e., two stitch cracks are present on each side of the central stitch crack), with variations of less then 0.7% of the far-field value (i.e., 10,000 μstrain) when seven stitch cracks are modeled. In addition to the results for ϵ_{11}, the other strain fields of the model are investigated for each step. It is found that the shear strain components exhibit changes on the order of 3% between the models of five and seven stitch cracks. Adding an additional neighboring

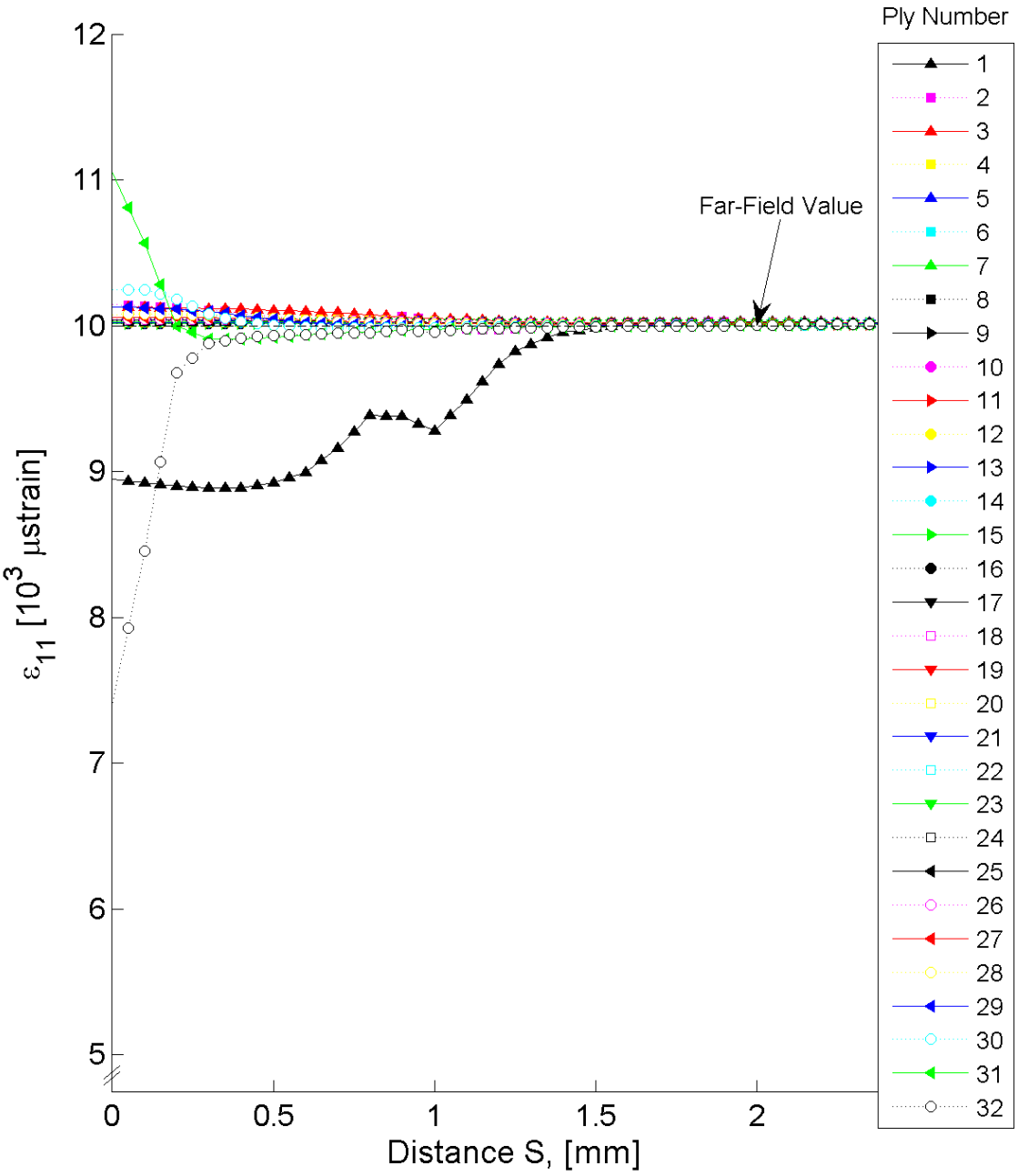

Figure 7.119 Plot of ϵ_{11}, in laminate axes, along the path located at a $\hat{S}$-distance of 0.1465 mm from the central stitch crack at the midplane of each ply for the stitch crack model containing one stitch crack with laminate of $[+30/-30]_{16T}$.

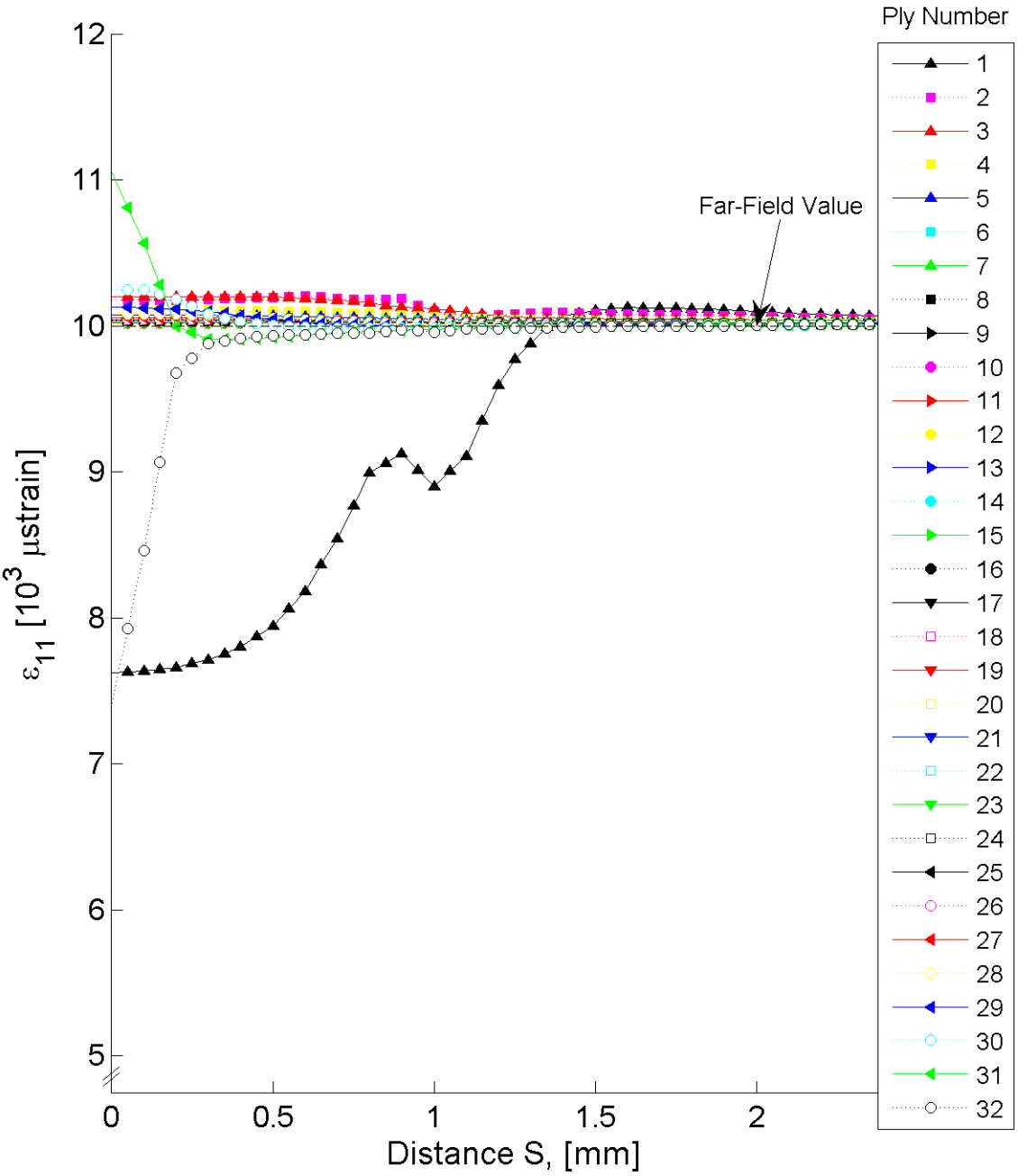

Figure 7.120 Plot of ϵ_{11}, in laminate axes, along the path "between stitch cracks" at the midplane of each ply for the stitch crack model containing three stitch cracks with laminate of $[+30/-30]_{16T}$.

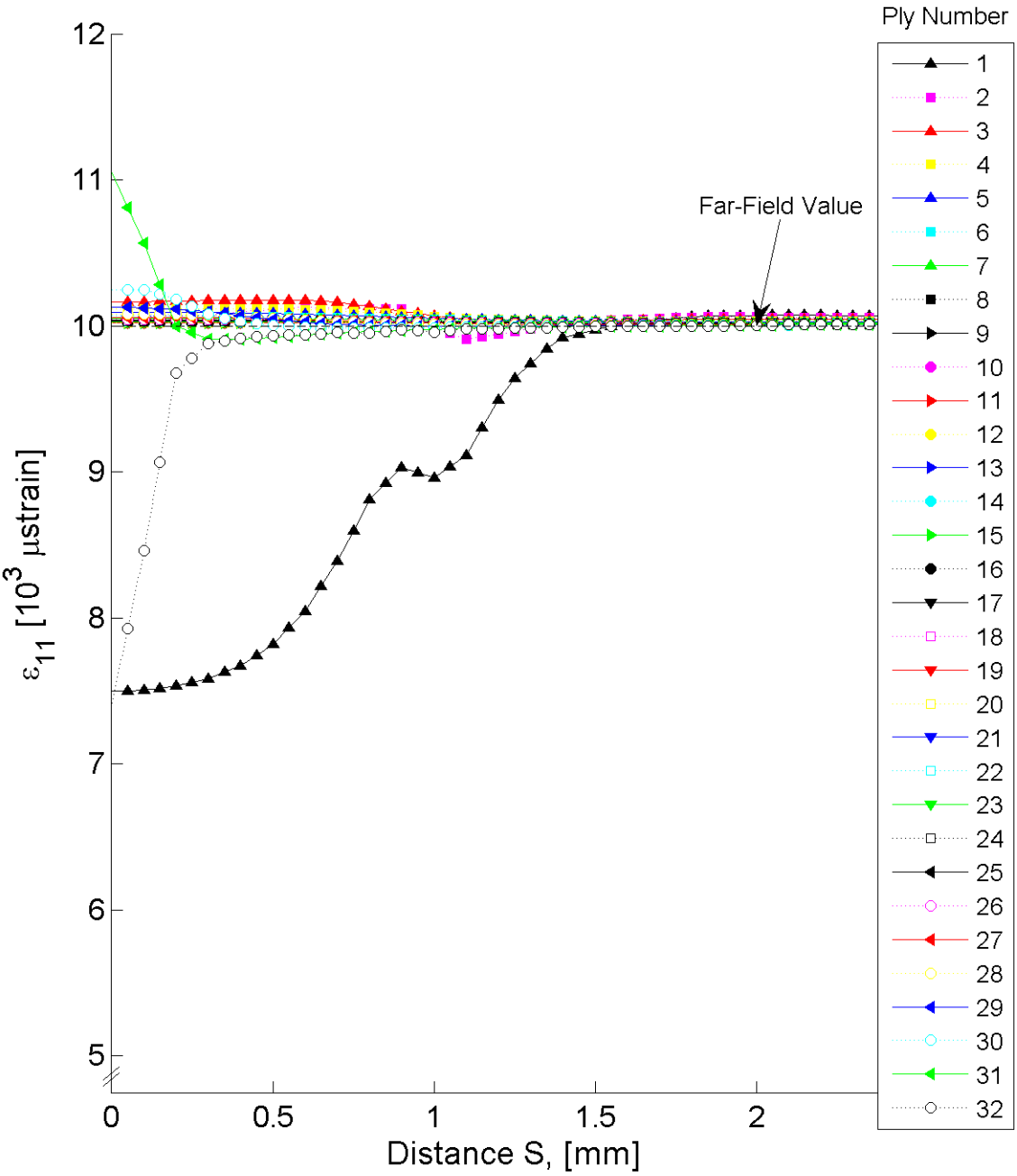

Figure 7.121 Plot of ϵ_{11}, in laminate axes, along the path "between stitch cracks" at the midplane of each ply for the stitch crack model containing five stitch cracks with laminate of $[+30/-30]_{16T}$.

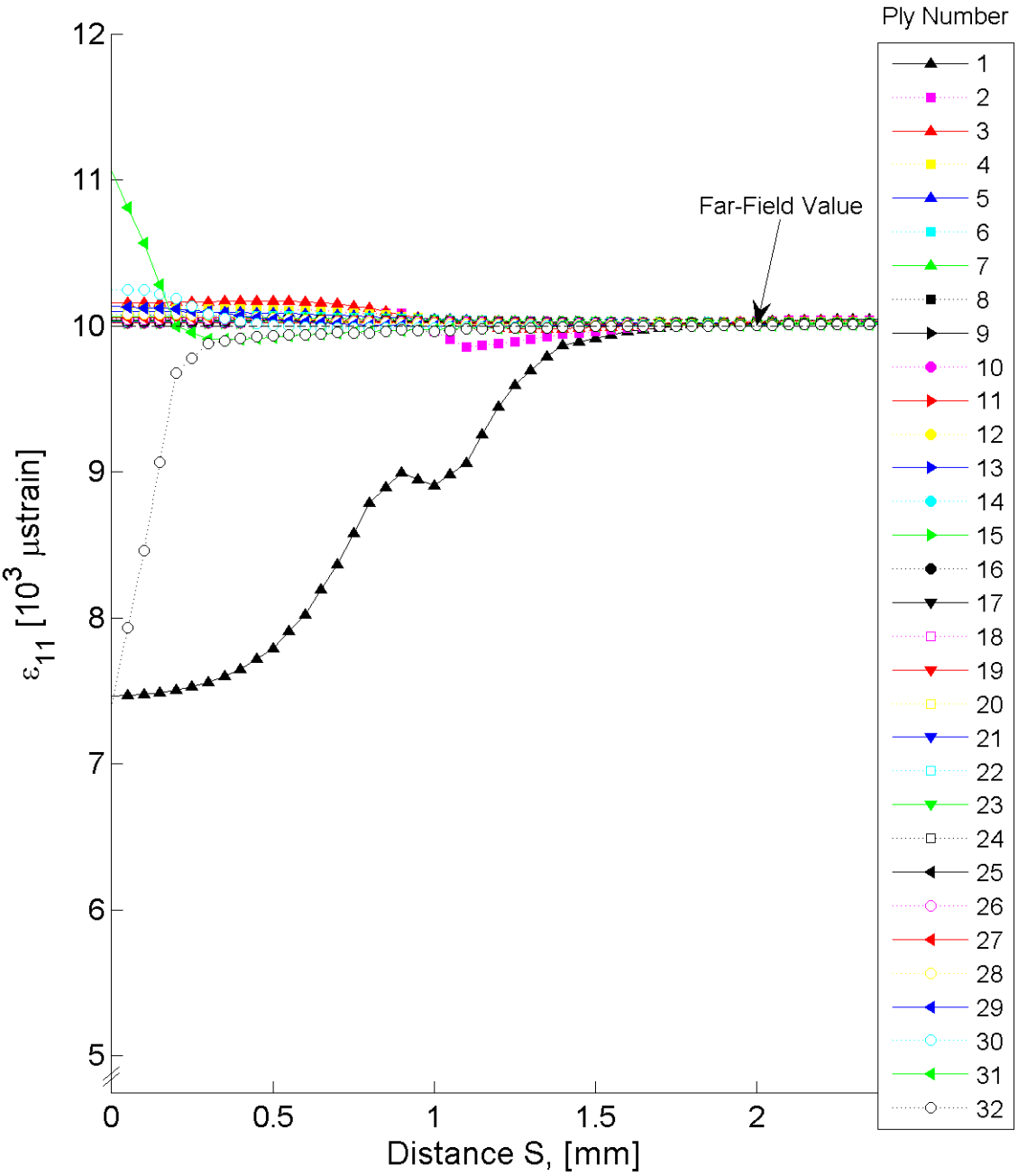

Figure 7.122 Plot of ϵ_{11}, in laminate axes, along the path "between stitch cracks" at the midplane of each ply for the stitch crack model containing seven stitch cracks with laminate of $[+30/-30]_{16T}$.

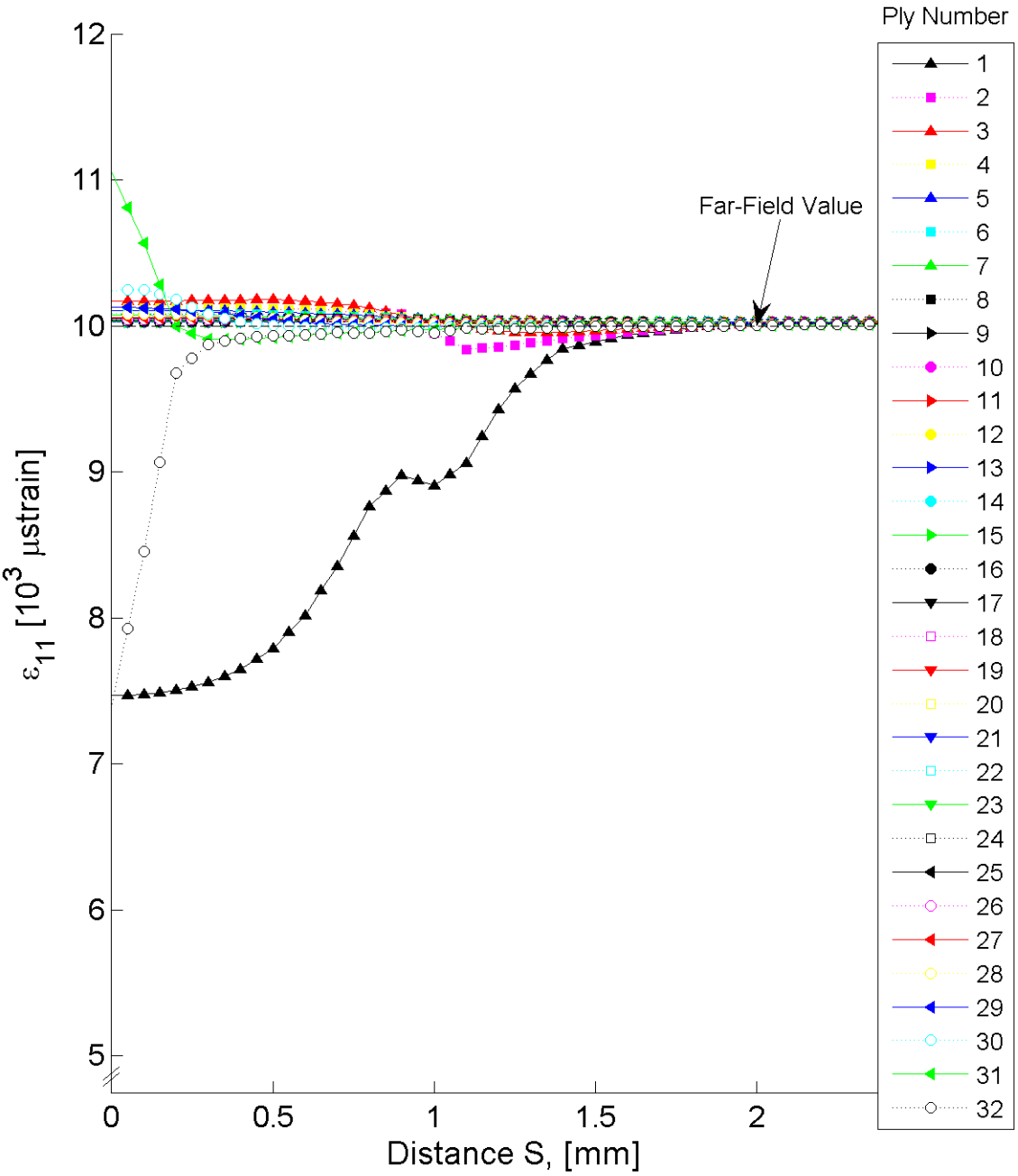

Figure 7.123 Plot of ϵ_{11}, in laminate axes, along the path "between stitch cracks" at the midplane of each ply for the stitch crack model containing nine stitch cracks with laminate of $[+30/-30]_{16T}$.

stitch crack to both ends of the model (i.e., a total of nine stitch cracks) causes the strain fields at the "central" stitch crack to vary by less than 1.0%. This same trend is observed for the laminates at the other angles for both the single-ply and four-ply effective ply thickness laminates. Therefore, the influence of the number of neighboring stitch cracks indicates nine total stitch cracks are required in order to reach a "steady-state" solution at the central stitch crack. Additional stitch cracks beyond this number extend the overall effected strain zone, but do not change the fields at the "central" stitch crack. Thus, the subsequent results are based on a model containing nine stitch cracks.

The strain fields of ϵ_{11} for the laminates considered have positive values near the tip of the stitch cracks, as shown in the plots for the path "along" the stitch crack for the single-ply and four-ply effective ply thickness laminates with θ equal to 15° in Figures 7.124 and 7.125. For the other laminates, these plots are shown in Figures B.85 through B.90, included in Appendix B.4. In addition to the plots of ϵ_{11} along the path of the stitch crack, the results of the strain fields "between stitch cracks" is investigated. The plots of the strain fields of ϵ_{11} for the path "between stitch cracks" for the single-ply and four-ply effective ply thickness laminates with θ equal to 15° are shown in Figures 7.126 and 7.127. For the other laminates, these plots are shown in Figures B.91 through B.96, included in Appendix B.4.

The gradient in the $\hat{S}$-direction is determined by comparing the results of the paths "along the stitch crack" and "between the stitch cracks." The distance along the $\hat{S}$-direction between the paths is 0.254 mm, 0.146 mm, 0.146 mm, and 0.254 mm for values of θ of 15°, 30°, 60°, and 75°, respectively. These distances are used to calculate the gradients in the $\hat{S}$-direction for each laminate. The perpendicular distance between the two paths is independent of the laminate angle and is equal to 0.127 mm. The perpendicular distance between the paths is not used for calculating gradients. The gradients for the results of ϵ_{11} of the single-ply and four-ply effective ply thickness laminates with θ equal to 15° are plotted and shown in Figures 7.128 and 7.129. For the other laminates, these plots are shown in Figures B.97 through B.102, included in Appendix B.4. The largest gradient in the $\hat{S}$-direction is always observed

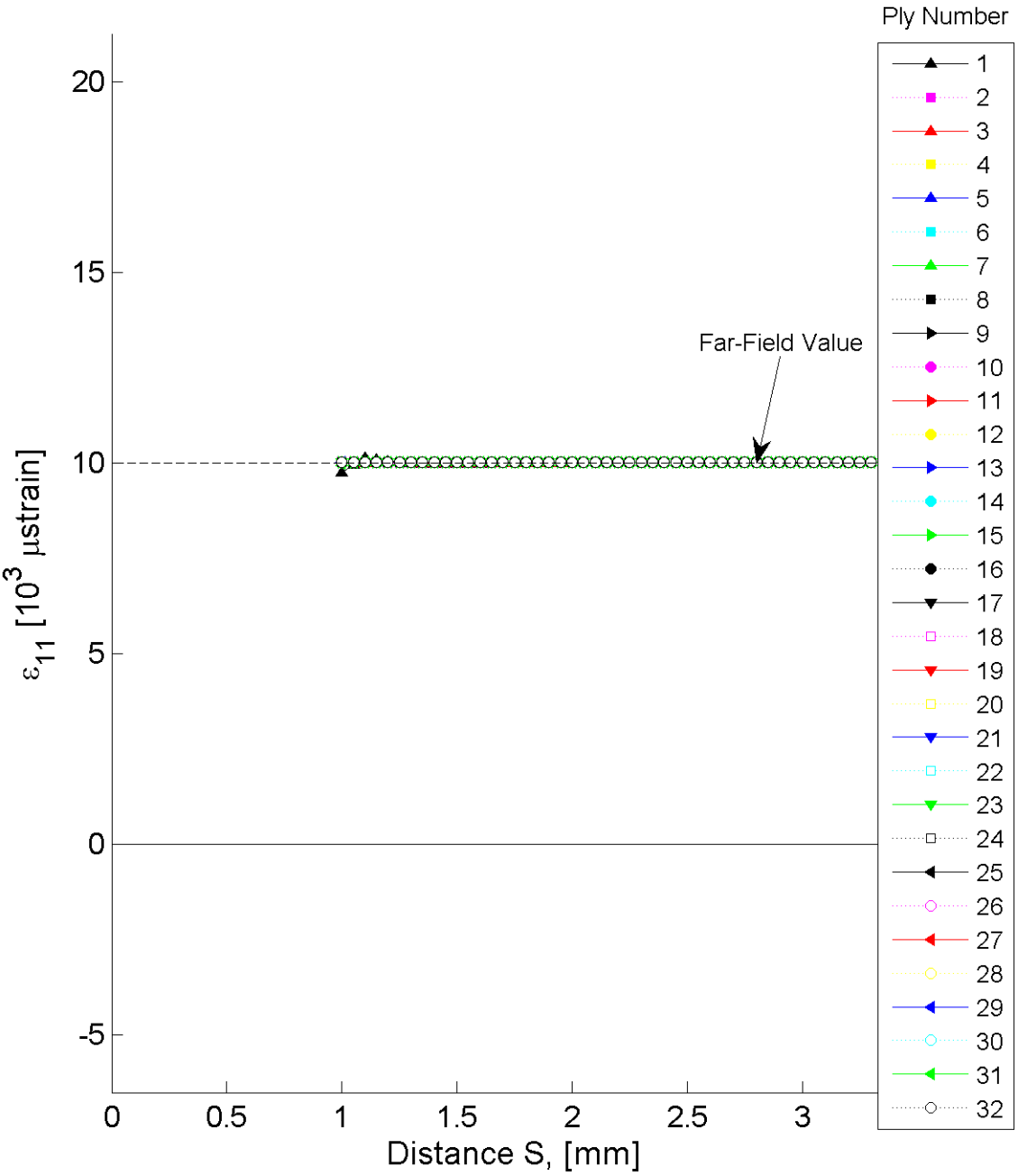

Figure 7.124 Plot of ϵ_{11}, in laminate axes, along the path of the stitch crack at the midplane of each ply for the stitch crack model with laminate of $[+15/-15]_{16T}$.

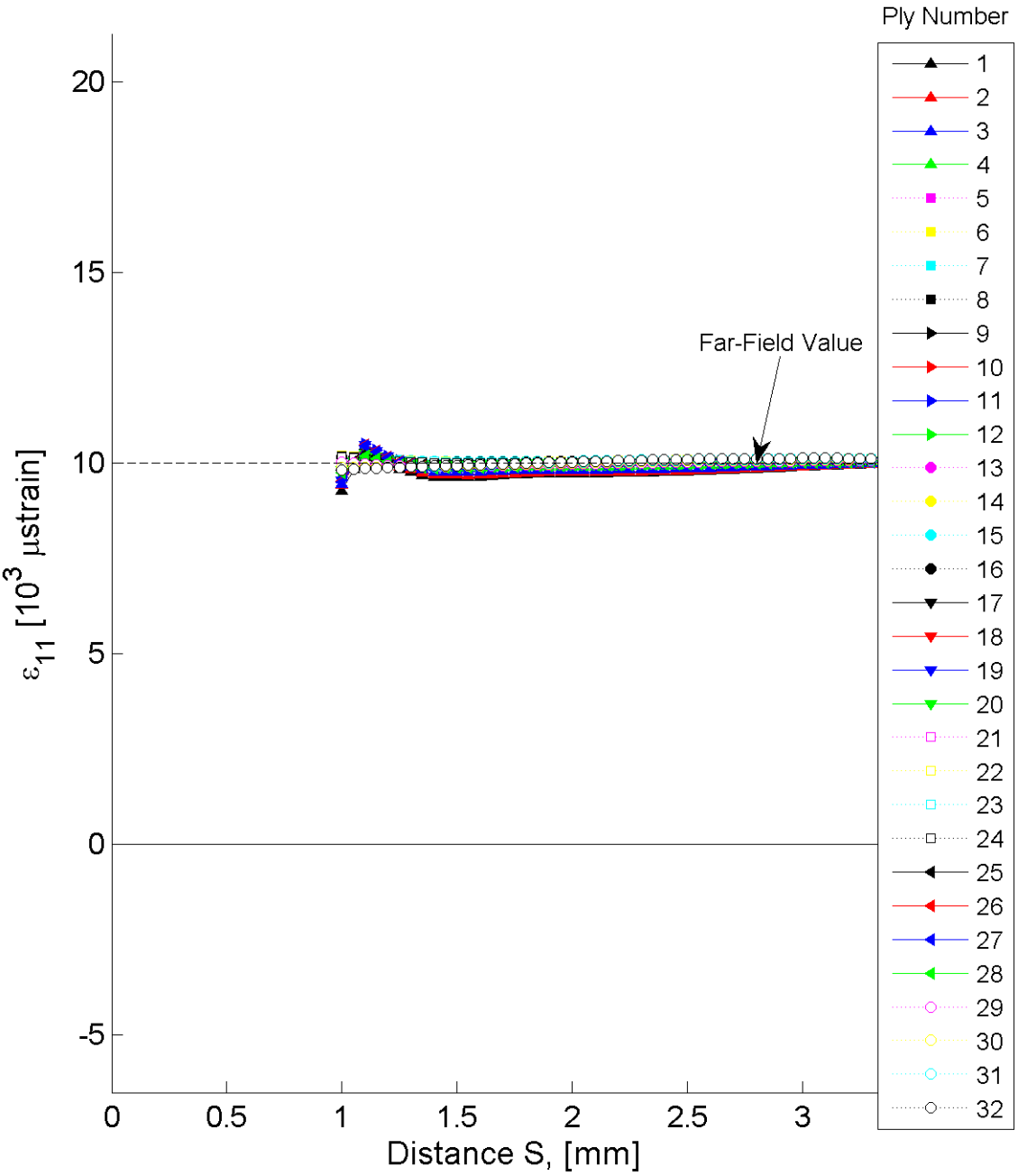

Figure 7.125 Plot of ϵ_{11}, in laminate axes, along the path of the stitch crack at the midplane of each ply for the stitch crack model with laminate of $[+15_4/-15_4]_{4T}$.

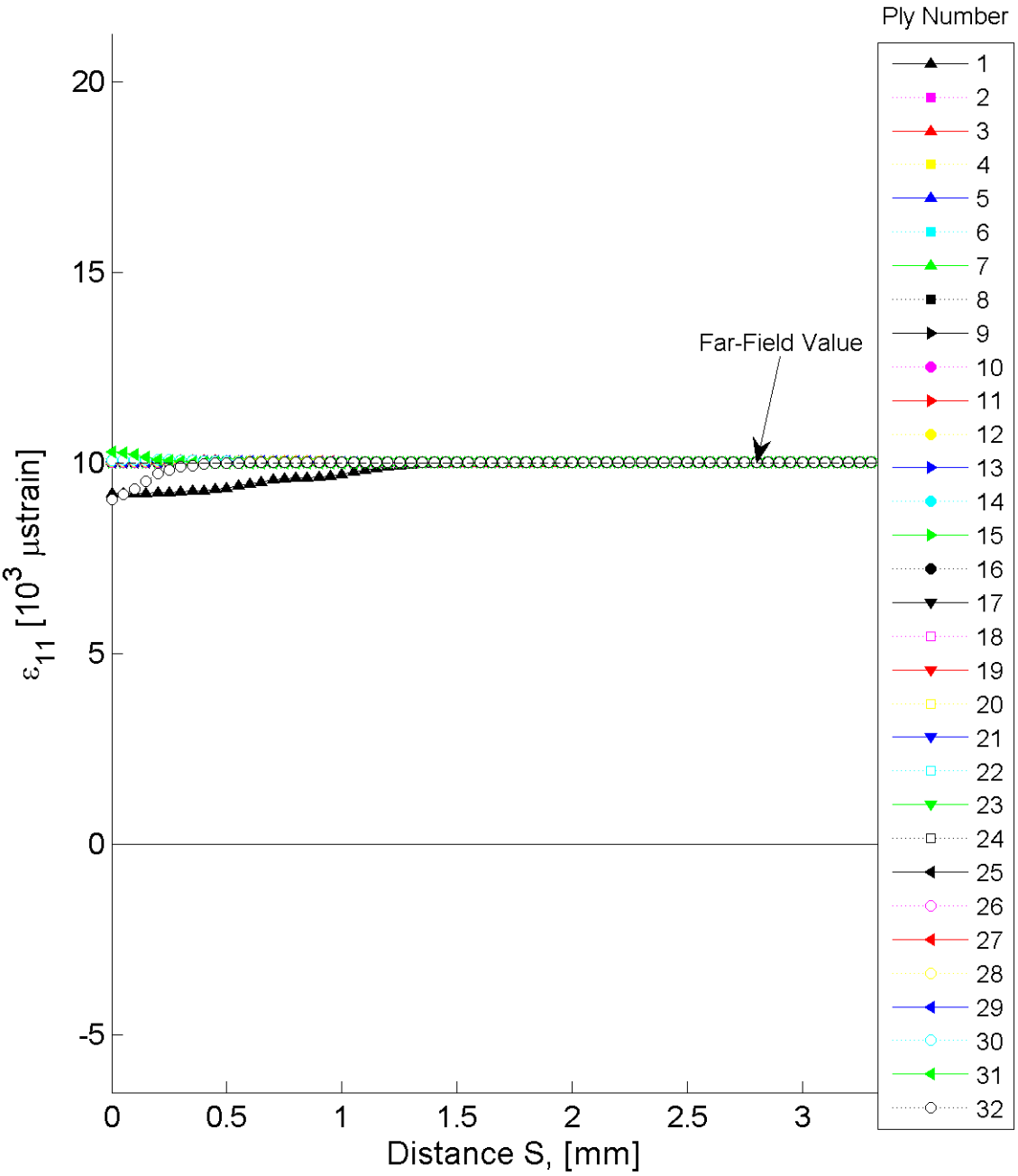

Figure 7.126 Plot of ϵ_{11}, in laminate axes, along the path "between stitch cracks" at the midplane of each ply for the stitch crack model with laminate of $[+15/-15]_{16T}$.

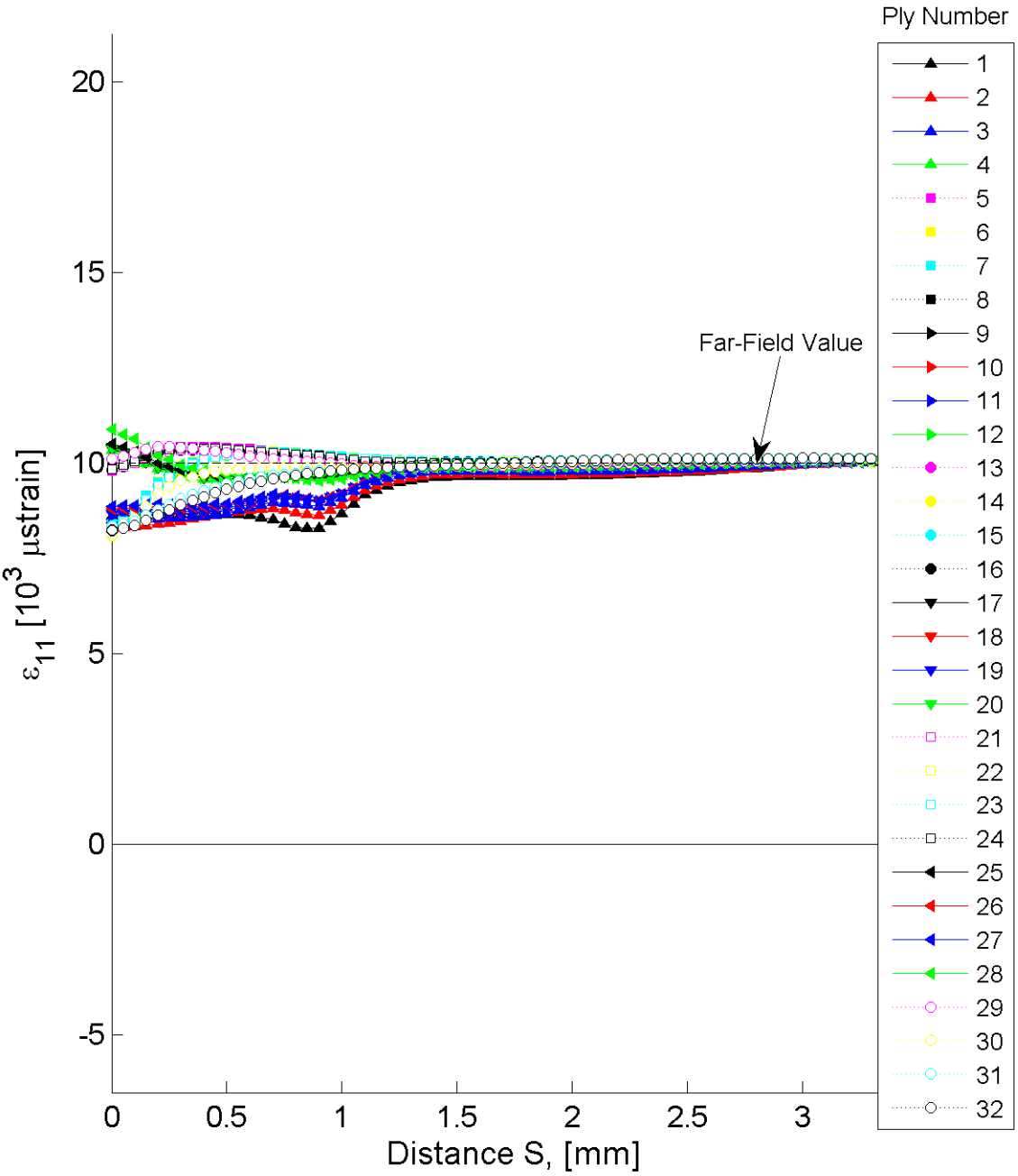

Figure 7.127 Plot of ϵ_{11}, in laminate axes, along the path "between stitch cracks" at the midplane of each ply for the stitch crack model with laminate of $[+15_4/-15_4]_{4T}$.

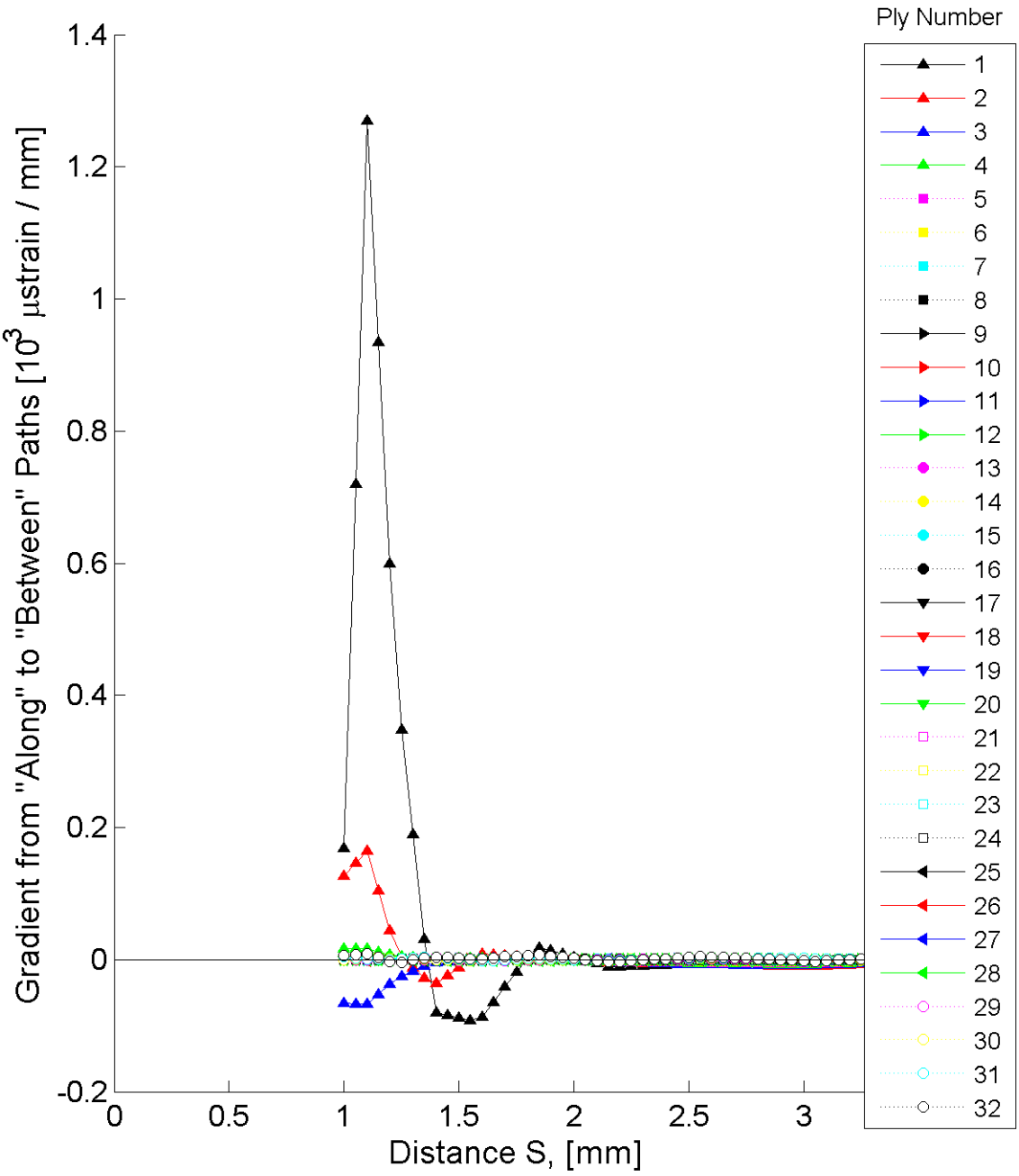

Figure 7.128 Plot of the gradient of ϵ_{11}, in laminate axes, in the $\hat{S}$-direction at the midplane of each ply for the stitch crack model with laminate of $[+15/-15]_{16T}$.

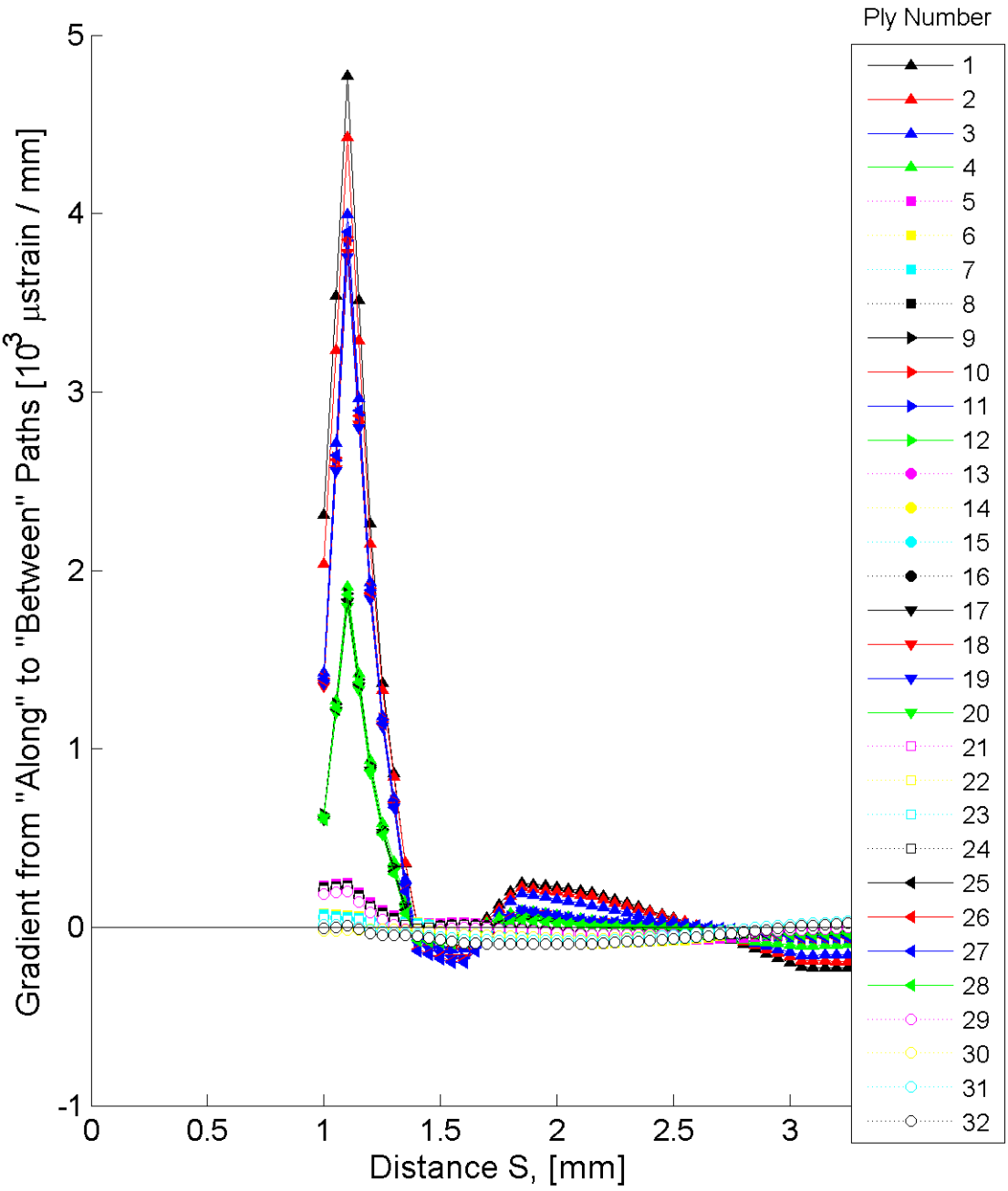

Figure 7.129 Plot of the gradient of ϵ_{11}, in laminate axes, in the $\hat{S}$-direction at the midplane of each ply for the stitch crack model with laminate of $[+15_4/-15_4]_{4T}$.

within ply 1 of each of the laminates at an S-distance equal to approximately 1.1 mm (i.e., approximately 0.1 mm from the tip of the stitch crack) with the majority of plies in this region having relatively small gradients (i.e., near zero). The magnitude of variation between the two paths was taken at the S-distance equal to 1.1 mm for the single-ply effective ply thickness laminates and is 1250 μstrain, 8100 μstrain, 8000 μstrain, and 3400 μstrain for values of θ of 15°, 30°, 60°, and 75°, respectively. For the four-ply effective ply thickness laminates, these variations are 4800 μstrain, 26500 μstrain, 20500 μstrain, and 9000 μstrain, respectively.

For each of the laminates, three distinct regions of strain and associated gradient behavior are observed. The first region is defined as the "detailed effects" region. Within this region, the strain fields are influenced by the details of the individual stitch cracks. Large gradients and stress/strain concentrations are observed within this region. The strain field of ϵ_{11} in this "detailed effects" region of the first ply of the four-ply effective ply thickness laminates with θ equal to 30° is shown in Figure 7.130 as an example. This shows the typical planar distribution of the strain concentrations observed in the first ply of each of the laminates. Large gradients surrounding the tips of each stitch crack are observed. A strain concentration, located at an S-distance of approximately 1.1 mm on the path "along the stitch crack" (i.e., approximately 0.1 mm from the tip of the stitch crack), is observed in this figure. Variation between the strain fields at the tips of the two neighboring stitch cracks (i.e., the tip of the neighboring stitch crack in the $+\hat{S}$-direction is visible in Figure 7.130 while only the strain concentration of the neighboring stitch crack in the $-\hat{S}$-direction is visible) is due to the modeling of a finite number of neighboring stitch cracks, as described in Section 7.2.5. Including additional stitch cracks (i.e., more than nine stitch cracks) would make these concentrations uniform, but would not change the trends of the gradient fields. The concentrations observed at the tip of each stitch crack have an associated strain field variation in the x-y plane that takes a skewed elliptical shape, with the major and minor axes of the ellipse oriented along and normal to the S-axis, respectively. However, the ellipse is not symmetric about the concentration point. The major and minor radius of the ellipse are biased, with shorter radii in

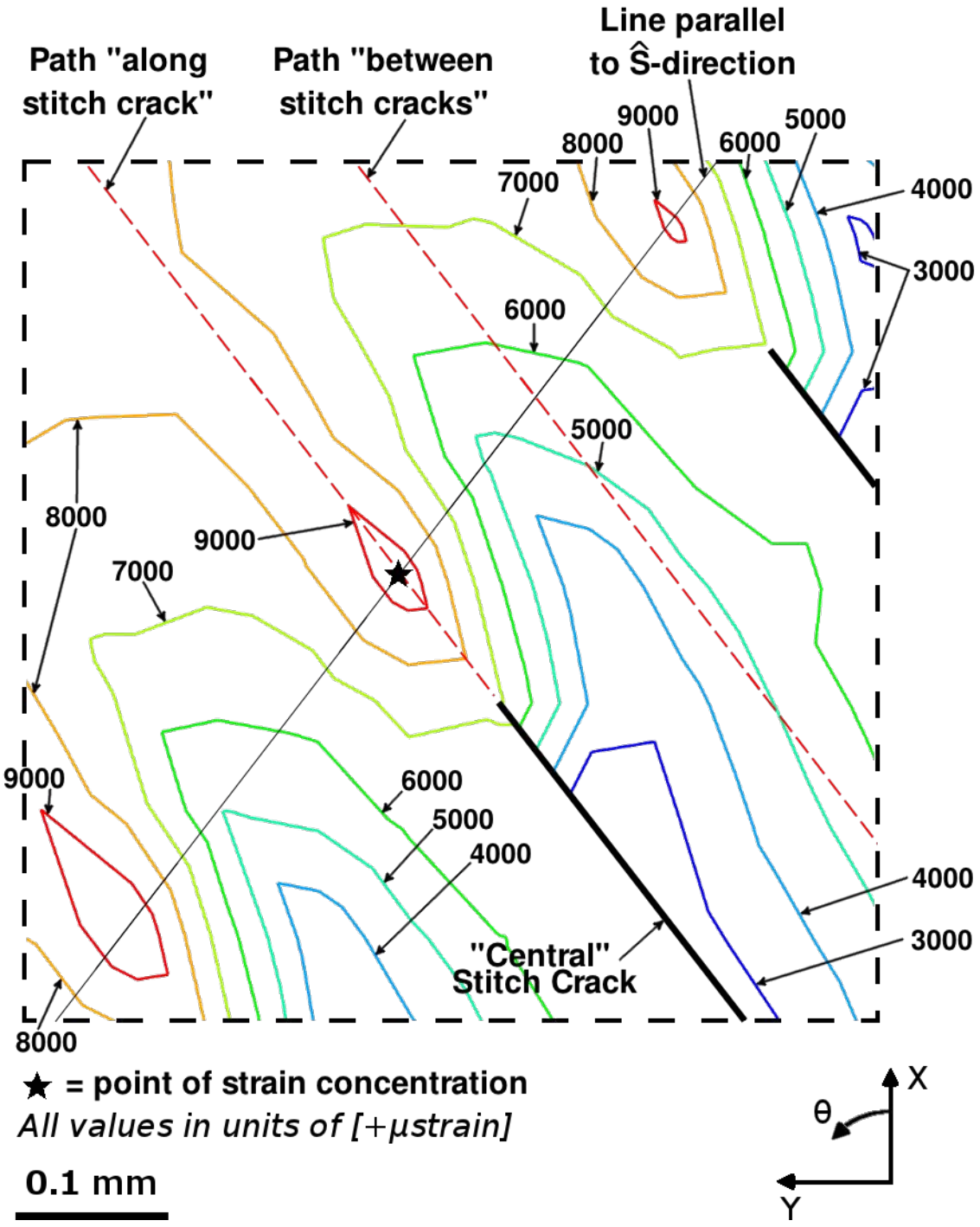

Figure 7.130 Isostrain plot of strain field of ϵ_{11}, in laminate axes, in the "detailed effects" region of the tip of the "central" stitch crack, at the midplane of ply 1 (a +30° ply) of the stitch crack model for the laminate of $[+30_4/-30_4]_{4T}$.

both the negative S-direction and the direction normal to the S-direction, oriented in the positive $\hat{S}$-direction (although not aligned with the $\hat{S}$-direction since the S- and $\hat{S}$-directions are not orthogonal). The bias ratio is on the order of 1.4 to 2.0 for the strain fields shown in Figure 7.130. In addition, the gradients in the region of the concentration are different in the S- and $\hat{S}$-directions.

The second region of strain and associated gradient behavior is defined as the "averaged effects" region. Within this region, the 'local' effects of the details of the damage are not observed, as only the overall effect of the presence of the damage is observed with the loading and resulting strains being redistributed in an 'averaged' sense. This region is characterized as surrounding the region of damage, with strain magnitudes having fairly uniform in-plane gradients, and transitioning to the far-field strain value as the distance from the region of damage increases. The strain fields of ϵ_{11} in the "averaged effects" region of the first ply of the single-ply and four-ply effective ply thickness laminates with θ equal to 30° are shown, as examples, in Figures 7.131 and 7.132, respectively. The local strain concentration in the "averaged effects" region is not observable in these figures. A plot of ϵ_{11} for the path "along stitch crack" of the strain fields of Figure 7.132 is shown in Figure 7.133. The sharp peak of the strain magnitude at S equal to 1.1 mm corresponds to the strain concentration in the "detailed effects" region shown in Figure 7.130. Beyond the concentration in the "detailed effects" region, the strain magnitude is observed to first decrease (i.e., between S from 1.1 mm to 1.4 mm) before beginning to increase. The S-distance where the strain fields transition to the "averaged effects" region is determined via the plots of the gradients in the $\hat{S}$-direction, shown in Figures 7.128, 7.129, and B.97 through B.102. The transition is defined at the point where the gradient in the $\hat{S}$-direction of the first ply drops below 100 μstrain per millimeter. The transition from the "detailed effects" region to the "averaged effects" region occurs at an S-distance of approximately 1.8 mm, 1.7 mm, 2.6 mm, and 4.6 mm for the single-ply effective ply thickness laminates with θ equal to 15°, 30°, 60°, and 75°, respectively. For the four-ply effective ply thickness laminates, the transition occurs at an S-distance of approximately 4.9 mm, 2.6 mm, 8.0 mm, and 10.5 mm, respectively. Within the

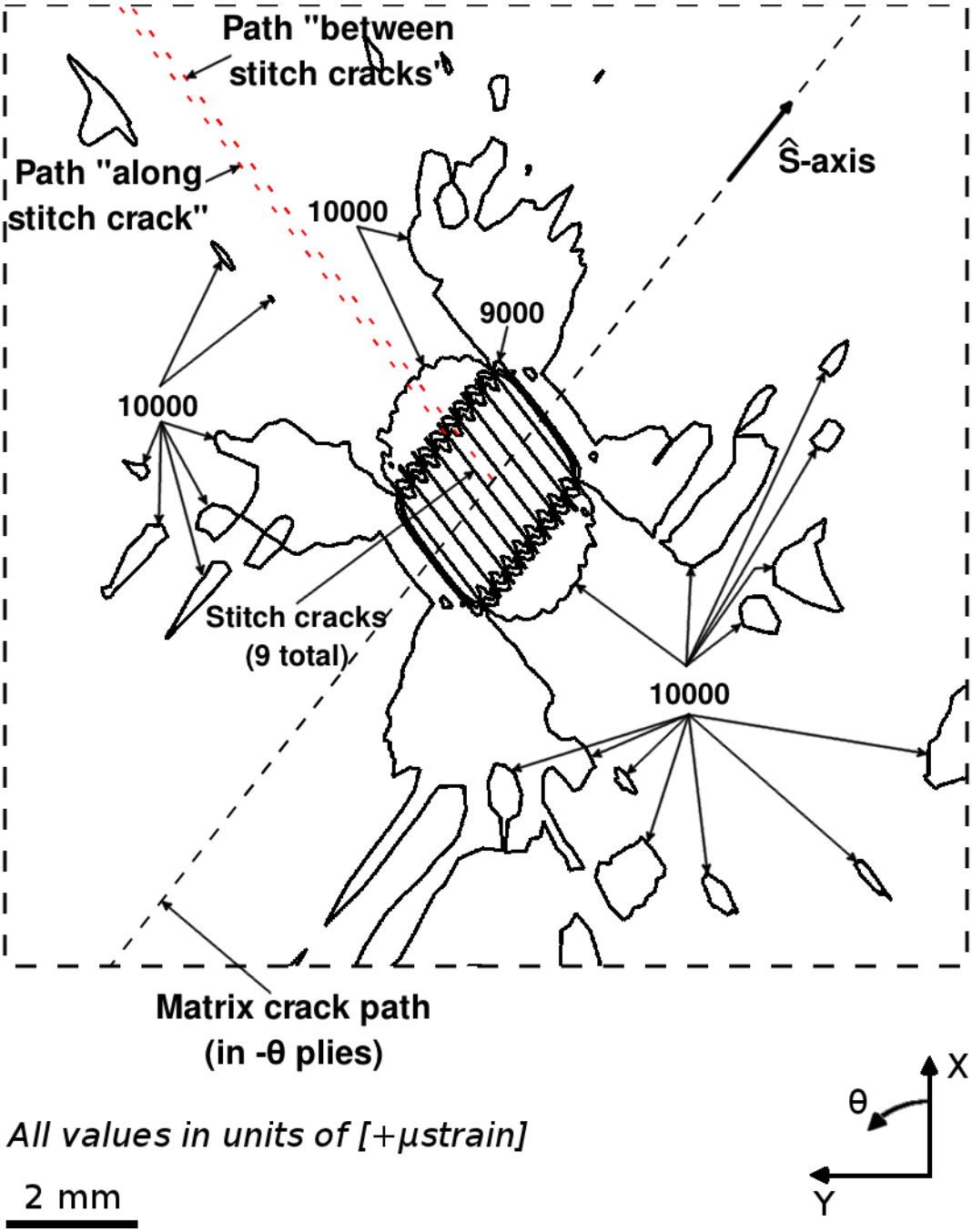

Figure 7.131 Isostrain plot of strain field of ϵ_{11}, in laminate axes, in the "averaged effects" region, at the midplane of ply 1 (a +30° ply) of the stitch crack model for the laminate of $[+30/-30]_{16T}$.

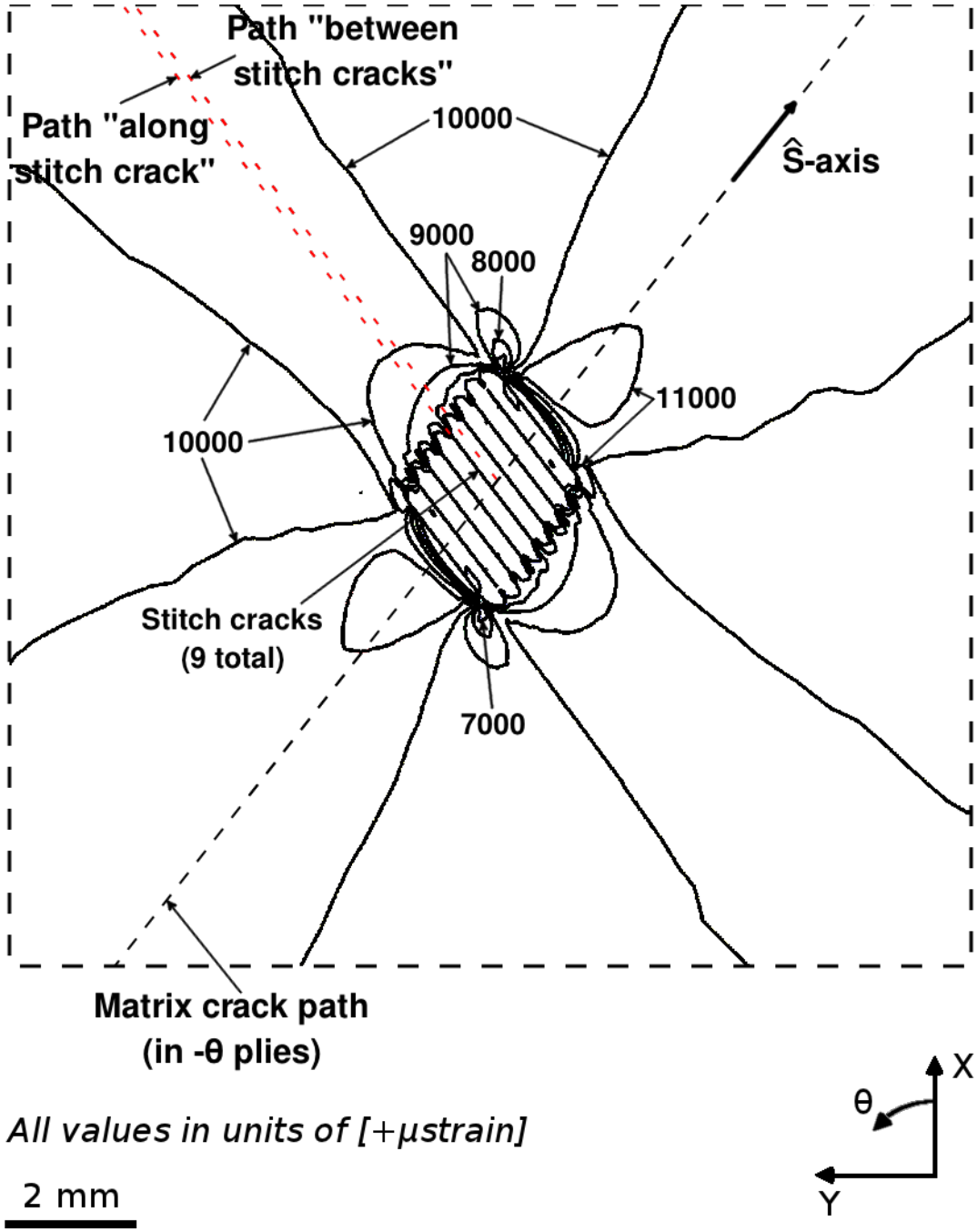

Figure 7.132 Isostrain plot of strain field of ϵ_{11}, in laminate axes, in the "averaged effects" region, at the midplane of ply 1 (a +30° ply) of the stitch crack model for the laminate of $[+30_4/-30_4]_{4T}$.

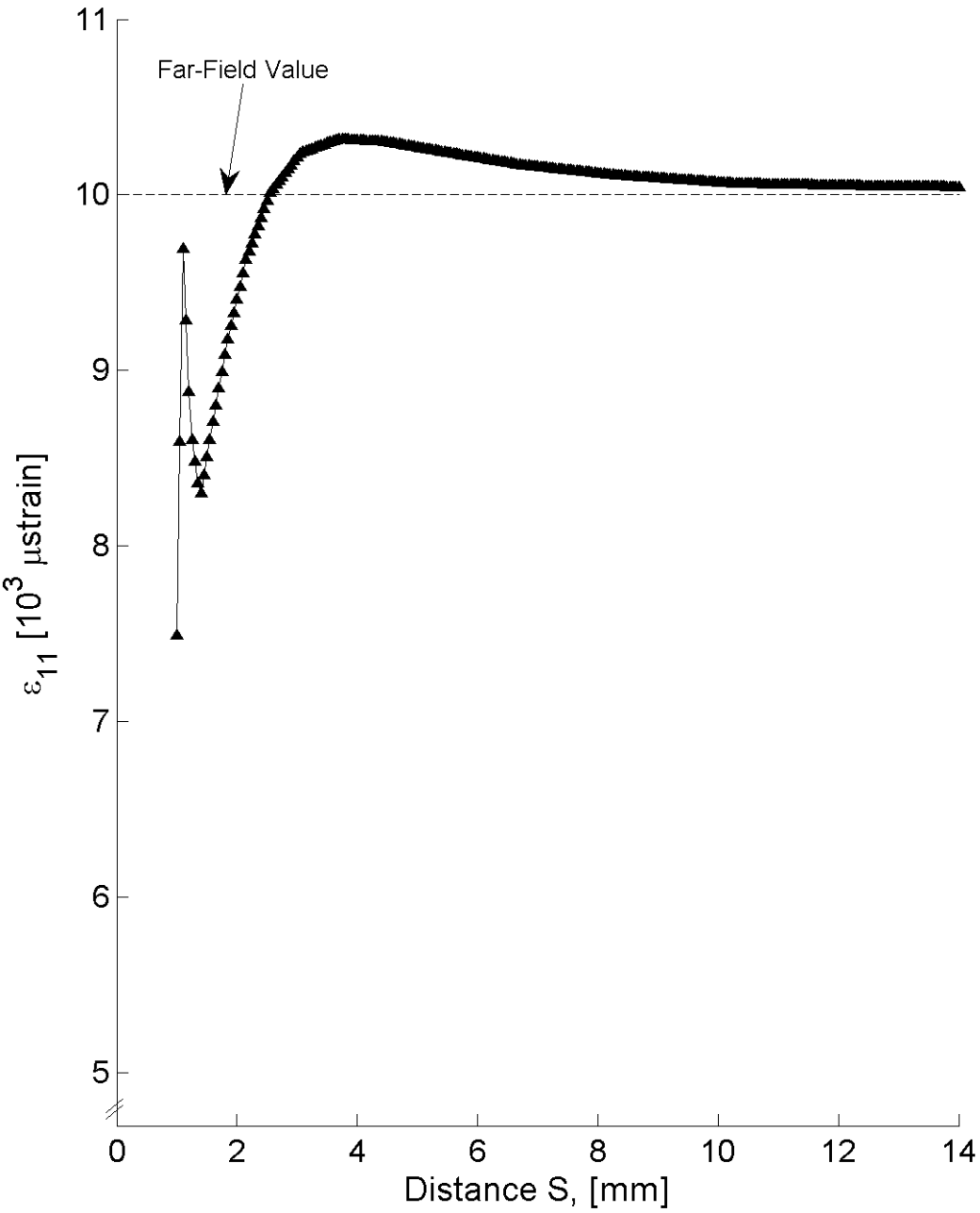

Figure 7.133 Plot of ϵ_{11}, in laminate axes, along the path "along stitch crack" at the midplane of ply 1 for the stitch crack model containing nine stitch cracks with laminate of $[+30_4/-30_4]_{4T}$.

"averaged effects" region, the strain fields first increase above the far-field level, to a maximum value of 10030 μstrain, 10040 μstrain, 10010 μstrain, and 10010 μstrain for the single-ply effective ply thickness laminates with θ equal to 15°, 30°, 60°, and 75°, respectively, and 10160 μstrain, 10300 μstrain, 10320 μstrain, and 10530 μstrain for the four-ply effective ply thickness laminates, respectively. The S-distance where these maximum values occur is equal to 3.05 mm, 3.05 mm, 3.70 mm, and 5.50 mm for the single-ply effective ply thickness laminates, respectively, and 4.50 mm, 3.70 mm, 3.70 mm, and 4.5 mm for the four-ply effective ply thickness laminates, respectively. At S-distances greater than those at which the maximum value of strain is observed, the strain fields are observed to asymptotically decrease until reaching the far-field value.

The third region of strain and gradient behavior is defined as the "far-field" region, where the gradient of strain is zero throughout. The strain fields within this region are equal to the far-field value of 10000 μ-strain, as the effects due to the presence of the damage are not exhibited within the region. For the four-ply effective ply thickness laminate with θ equal to 30°, the far-field value is recovered at an S-distance approximately equal to 13 mm, as shown in Figure 7.133. For the single-ply effective ply thickness laminates, the transition point from the "averaged effects" region to the "far-field" region takes place at an S-distance approximately equal to 8.3 mm, 6.0 mm, 5.8 mm, and 9.8 mm for θ equal to 15°, 30°, 60°, and 75°, respectively. For the four-ply effective ply thickness laminates, the transition occurs at an S-distance approximately equal to 12.0 mm, 13.0 mm, 20.0 mm, and 24.0 mm, respectively.

The effect of modeling a finite number of stitch cracks is exhibited in the strain fields of the "averaged effects" region, shown in Figures 7.131 and 7.132 as an example. Two main effects are present due to the finite number of stitch cracks. The first effect is that the strain fields surrounding the outer stitch cracks exhibit significant gradients due to a portion of the applied load bypassing the region of damage. The specifics concerning the strain magnitudes and associated gradients from the region surrounding the outer stitch cracks are not discussed herein because the experimental specimens that exhibited stitch cracking had an 'infinite' number of cracks at final

failure (i.e., stitch cracks are present along the path from the structural feature up to the edge of the specimen, as presented in Section 6.3, with an example shown in Figure 6.10). However, discussion of the importance of the lengthscale associated with these finite effects are presented in Chapter 8, particularly in considering damage progression. The second effect is on the distribution of stress and strain in the $\hat{S}$-direction. As the S-distance increases from the tips of the stitch cracks, the gradient in the $\hat{S}$-direction is observed to approach a near zero value. Due to the finite number of stitch cracks modeled, the gradient in the $\hat{S}$-direction does not reach zero, as seen in the 9000 μstrain and 10000 μstrain isostrain lines near the tip of the 'central' stitch crack, shown in Figure 7.132. Increasing the number of modeled stitch cracks would result in these isostrain lines becoming 'flat' in the $\hat{S}$-direction (i.e., the gradient in the $\hat{S}$-direction reaching zero until the region where the effect of the finite number of stitch cracks is manifested. This is associated with the effect on the uniformity of the local strain fields in the "detailed effects" region). Further models are suggested in order to confirm the finite number of stitch cracks required for the flattening of the isostrain lines (i.e., gradient in the $\hat{S}$-direction equal to zero) to be manifested within this region. The plot of ϵ_{11} for the path "along stitch crack" for the first ply of the four-ply effective ply thickness laminate is shown in Figure 7.133. The results along similar paths for stitch cracks other than the 'central' stitch crack are strongly influenced by the finite number of stitch cracks and cannot be used to determine the limits of the three regions. Therefore, the strain fields shown in Figures 7.131 and 7.132 should only be considered in the regions along the paths "along stitch crack" and "between stitch cracks." The strain fields beyond these regions are influenced by the finite number of modeled stitch cracks.

The loading applied to the model redistributes differently within each of the three distinct regions via two particular effects that are observed. Within the "averaged effects" region, a "global bypass" effect is observed via strain values above the far-field strain. This corresponds to a portion of the applied load 'bypassing' the region of damage, resulting in an increased loading of the material within the "averaged effects" region. The amount of load that must bypass the region of damage is dependent

on a particular phenomenon of this damage scenario observed in the strain field results of the "detailed effects" region. This is defined as the "carry-through" effect. This results in a "carry-through" load which is the amount of load that is carried through the region with the stitch cracks. Within the "detailed effects" region, "carry-through" load is observed via strain values occurring between stitch cracks, that are lower than the far-field strain but larger than zero. The strain values corresponding to the "carry-through" load is illustrated at S equal to zero in Figures 7.126, 7.127, and B.91 through B.96. The strain values corresponding to the "carry-through" load of the single-ply effective ply thickness laminate with θ equal to 15°, 30°, 60°, and 75° are 9200 μstrain, 7500 μstrain, 5400 μstrain, and 5300 μstrain, respectively. For the four-ply effective ply thickness laminate, these values are 8600 μstrain, 5500 μstrain, 1800 μstrain, and 1000 μstrain, respectively. As the amount of "carry-through" load increases, the "global bypass" load decreases. Within the "far-field" region, the loads are unaffected by the region of damage.

The "carry-through" load is dependent on the orientation of the damage relative to the applied loading as well as on the laminate angle (i.e., the laminate angle influences the geometry of the damage details). However, the ability to "carry-through" load is independent of the actual load passing through the region. Unlike a traditional slit-like crack that is oriented through the thickness of the region of damage and is unable to carry loads through the region of damage, the plies of the laminate containing stitch cracks (i.e., the positive plies for the models considered herein) have capability to carry loads through the region of damage. The plies of the laminate with traditional matrix cracks (i.e., the negative plies for the models considered herein) behave similar to a slit-like crack in that loads cannot be carried across the damage. However, because loads "carry-through" the region of damage via the plies with stitch cracks, the "carry-through" load redistributes into the plies with matrix cracks across a shorter distance than for a traditional slit-like crack. Further discussion on the lengthscales associated with the orientation of the damage relative to the applied loading are presented in Chapter 8.

In considering the strain fields and various regions and effects, it is important to

identify the specific gradients and lengthscales associated with the strain fields. Both the "detailed effects" and "averaged effects" regions are observed in the plots of the strain distribution in the S-direction and the plots of the gradients in the $\hat{S}$-direction. The spikes at S approximately equal to 1.1 mm in the graphs of the gradients in the $\hat{S}$-direction show the concentrations and redistribution as the distance along the S-direction increases. The peak gradients in the $\hat{S}$-direction are approximately three and a half times larger for the four-ply effective ply thickness laminate than for the single-ply effective ply thickness laminate for the lower angle laminates, and approximately two and a half times larger for the higher angle laminates. The gradients in the $\hat{S}$-direction of the laminates indicate that the lengthscale associated with this gradient in the region of the tip of the stitch crack is on the order of half the distance "between stitch cracks." For the region beyond S equal to 2.6 mm of the four-ply effective ply thickness laminate with θ equal to 30°, the gradient in the $\hat{S}$-direction becomes negligible (i.e., the details of the stitch cracks effect the local gradient in the $\hat{S}$-direction only for S from 0 to 2.6 mm). As compared to the gradient in the $\hat{S}$-direction, the gradients of the strain fields in the S-direction redistribute over a greater distance, with slight gradients existing until the "far-field" region.

The results for the gradients in the $\hat{S}$-direction present in the stitch crack model are somewhat higher than, but still on the same order of magnitude as, those in the S-direction (i.e., oriented along the stitch crack). The peak gradients in the through-thickness direction (i.e., in the z-direction) of the laminates are orders of magnitude larger than those in the S- and $\hat{S}$-directions. That is:

$$\frac{\partial \epsilon_{11}}{\partial z} \gg \frac{\partial \epsilon_{11}}{\partial \hat{S}} \approx \frac{\partial \epsilon_{11}}{\partial S} \tag{7.37}$$

The remainder of the in-plane results presented for the stitch crack model are from the path "between stitch cracks" since this path contains the strain fields between the stitch cracks (i.e., S from 0.0 mm to 1.0 mm), as well as the strain fields beyond the tip of the stitch crack (i.e., S greater then 1.0 mm). The path "along the stitch crack" only contains strain fields for S greater than 1.0 mm. With the exception of

the strain concentration observed at S equal to 1.1 mm of the path "along the stitch crack," similar trends are observed in the two paths for the region of S greater then 1.0 mm.

For all laminates, the largest gradients in the S-direction occur within the region of S from 0.0 mm to 1.5 mm. In this region, gradients are observed to be dependent on the through-thickness location and the effective ply thickness of the laminate. For all the laminates, the strain of the first ply has an overall positive gradient, with strain values increasing from a value lower than the far-field strain (i.e., less then 10000 μstrain) to a value that asymptotically approaches the far-field strain. Local exceptions occur within this region where the gradient in the first ply takes small negative values. Within the region of S from 0.0 mm to 0.7 mm, the gradient is small and constant (i.e., the strain exhibits a linear change) within ply 1 for all the single-ply and four-ply effective ply thickness laminates. Within the region of S from 0.0 mm to 0.5 mm, the bottom two effective plies (i.e., plies 31 and 32 of the single-ply effective ply thickness laminates and plies 25 through 32 of the four-ply effective ply thickness laminates) exhibit their largest gradients. As the distance from the tip of the stitch crack increases, the gradient decreases in magnitude and eventually becomes zero. In addition, the maximum variation in magnitude from the far-field value occurs at S equal to 0.0 mm, with the variation approximately two times greater for the four-ply effective ply thickness laminates compared to the single-ply effective ply thickness laminates for a given laminate angle. This trend is more clearly seen in the results of the laminates with θ greater than 15°, shown in Figures B.91 through B.96, although the trend is observed in the results of the laminates with θ equal to 15°, shown in Figures 7.126 and 7.127.

The gradients of the single-ply and four-ply effective ply thickness laminates exhibit different through-thickness behavior. The single-ply effective ply thickness laminates exhibit a fairly uniform through-thickness behavior, with the exception of the top and two bottom plies (i.e., plies 1, 31, and 32). All other plies exhibit a near zero gradient in the S-direction. The top and two bottom plies of each of the single-ply effective ply thickness laminates exhibit larger gradients, compared to the gradients of

the inner plies. At distances greater than S equal to 2.5 mm (1.5 mm farther from the tip of the stitch crack), the through-thickness behavior is relatively uniform, although the four-ply effective ply thickness laminates exhibit greater through-thickness dependency. Unlike the results of the single-ply effective ply thickness laminates, there is a through-thickness distribution of strains at the tip of the stitch crack. While the results of the single-ply effective ply thickness laminates have slight (i.e., less than 100 μstrain) through-thickness variation, excluding the top and the two bottom plies, the four-ply effective ply thickness laminates clearly have variations on the order of hundreds of μstrain between neighboring plies. Within an effective ply of the four-ply effective ply thickness laminates, through-thickness variations are observed between the central plies and the plies that neighbor plies of different angles. This behavior of the two central plies, as well as plies 1 and 32 (which have a free surface), of an effective ply is to be expected as the four-ply effective ply thickness laminate should behave as a "single ply" with an effective ply thickness equal to four normalized ply thicknesses. This trend is observed throughout the thickness of the four-ply effective ply thickness laminate. In addition, the trends of the gradients vary between the single-ply and four-ply effective ply thickness laminates, suggesting that the observed differences are more than just amplification in the magnitudes of the through-thickness variations for the four-ply effective ply thickness laminate cases. Comparing the region near S equal to 1.0 mm in Figures 7.126 and 7.127, gradients are observed to be dependent on both the through-thickness location as well as on the distance from the tip of the stitch crack of the four-ply effective ply thickness laminates, while the gradients of the central plies (i.e., plies 5 through 28) of the single-ply effective ply thickness laminates are independent of both the through-thickness location and the distance from the tip of the stitch crack.

The modeling techniques used for the single-ply and four-ply effective ply thickness laminates influence the ability to capture through-ply gradients. In analyzing the results of the models, it is observed that the effective plies of the four-ply effective ply thickness laminates behave as a single ply. The strain values of the effective plies, each composed of four individual plies, exhibit the same trends along the S-direction.

However, gradients in the through-thickness direction are typically observed in a ply neighboring a ply of a different angle. Unlike the single-ply effective ply thickness laminate, the four-ply effective ply thickness laminate exhibits through-thickness gradients within effective plies. This through-thickness behavior is not exhibited in the results of the single-ply effective ply thickness laminate. This behavior is likely attributed to the setup of each of the models. The single-ply effective ply thickness laminate has a single element through each ply, while the four-ply effective ply thickness laminate has four elements through each effective ply (corresponding to one element per ply composing the four-ply effective ply thickness laminate). It is likely that through-thickness gradients exist within the plies of the single-ply effective ply thickness laminate, but are not observable as there is only a single element through the thickness.

The strain fields of ϵ_{22} for the laminates considered have negative values near the tip of the stitch cracks, as shown in the plots for the single-ply and four-ply effective ply thickness laminates with θ equal to 15° in Figures 7.134 and 7.135. For the other laminates, these plots are shown in Figures B.103 through B.108, included in Appendix B.4. As was the case for ϵ_{11}, the largest gradient along the S-direction of ϵ_{22} occurs within the last ply of the single-ply effective ply thickness laminates in the region of S from 0.0 mm to 0.5 mm. In this region, the strain of the last ply has a smaller magnitude (i.e., less negative) than the far-field strain. The four-ply effective ply thickness laminates exhibit gradients along the S-direction that are dependent on the through-thickness ply location, whereas the single-ply effective ply thickness laminates exhibit relatively small gradients through the thickness compared to the gradients of the four-ply effective ply thickness laminates. The largest through-thickness gradients in the single-ply effective ply thickness laminates occur in the outer two plies (i.e., plies 1, 2, 31, and 32). For the four-ply effective ply thickness laminates, the largest gradients along the S-direction occur within the region of S from 0.0 mm to 0.5 mm, the same region where the largest gradient of the single-ply effective ply is observed. However, for the four-ply effective ply thickness laminate, multiple plies exhibit a steep gradient within this region, with some gradients being

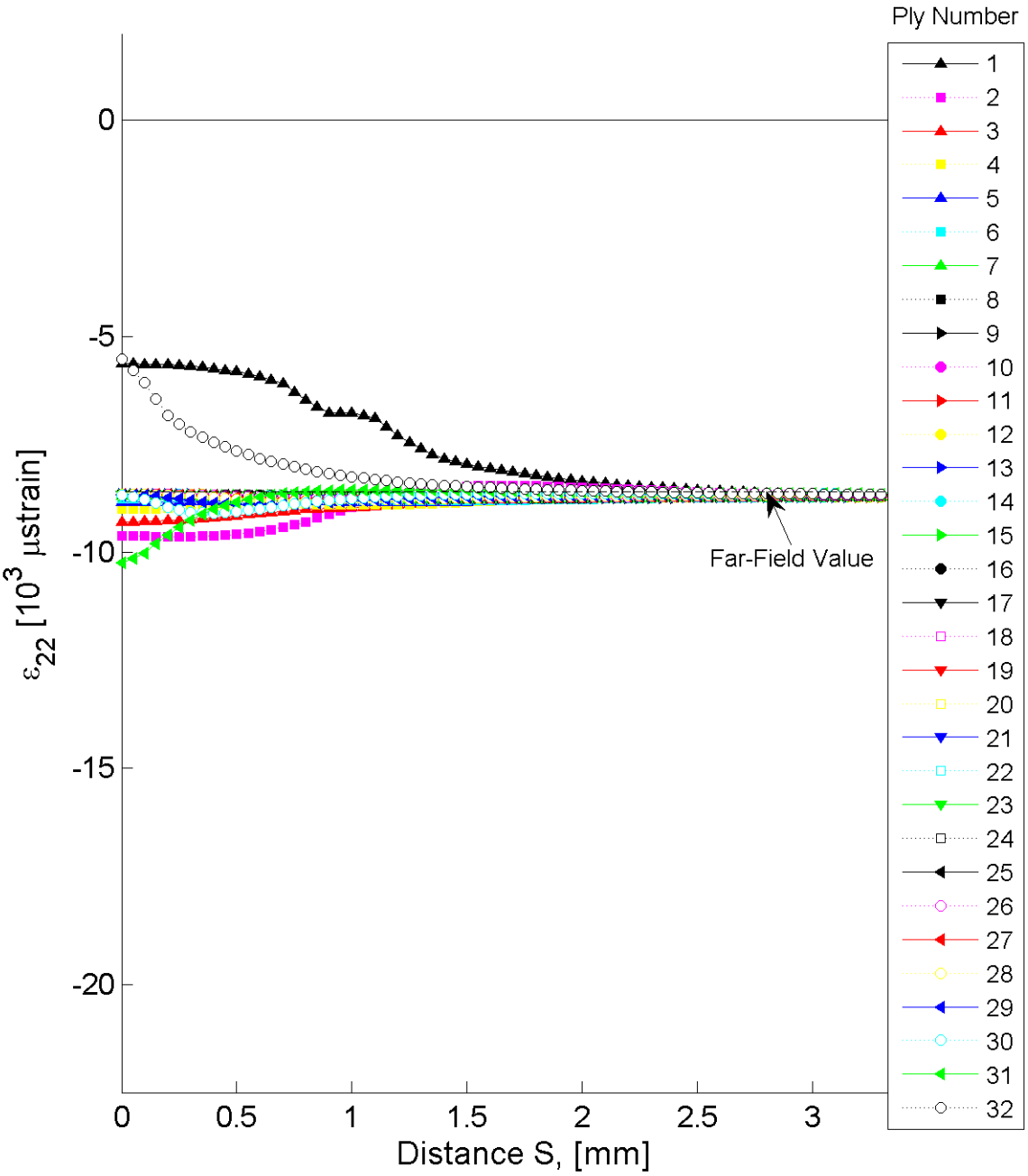

Figure 7.134 Plot of ϵ_{22}, in laminate axes, along the path "between stitch cracks" at the midplane of each ply for the stitch crack model with laminate of $[+15/-15]_{16T}$.

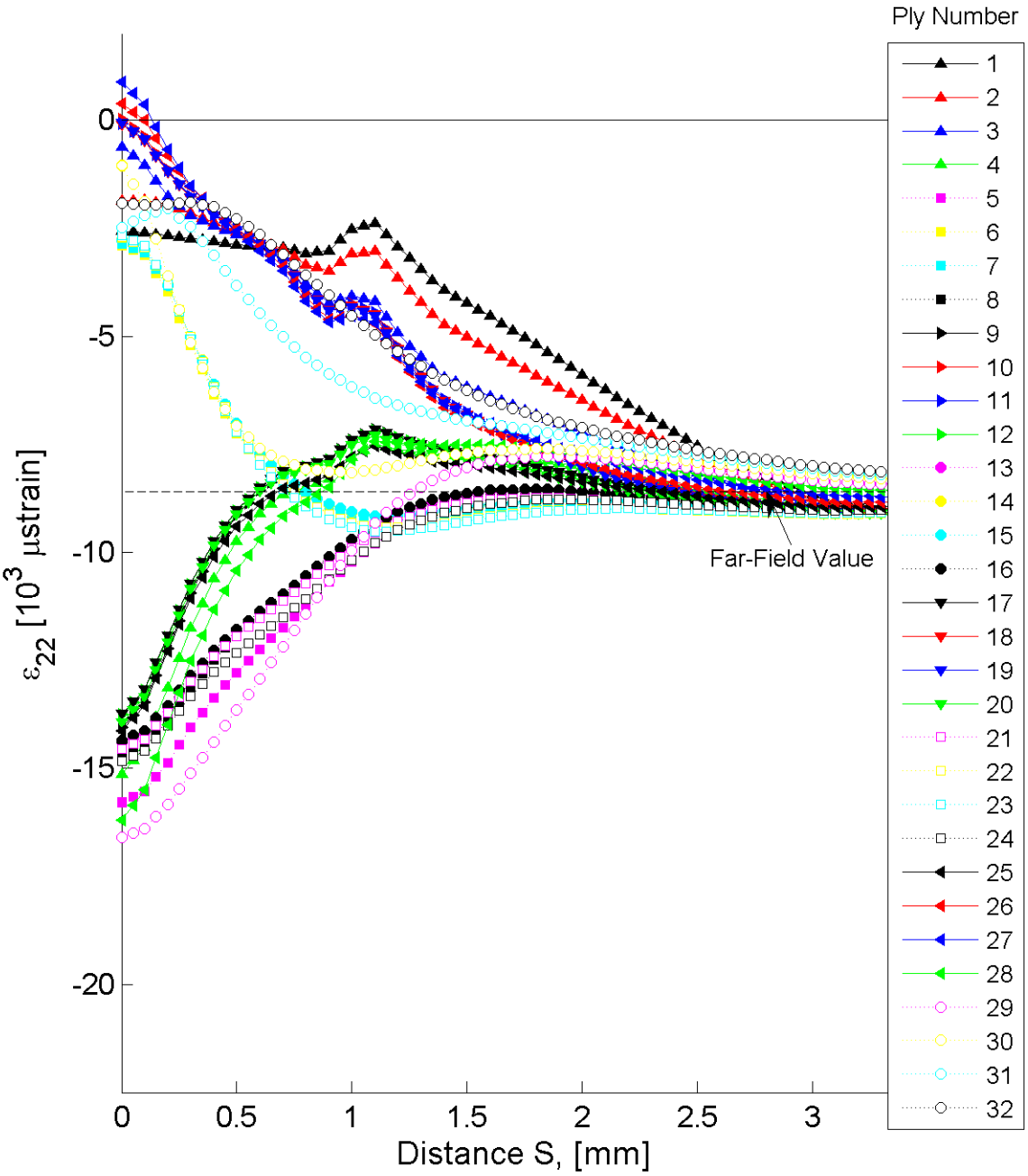

Figure 7.135 Plot of ϵ_{22}, in laminate axes, along the path "between stitch cracks" at the midplane of each ply for the stitch crack model with laminate of $[+15_4/-15_4]_{4T}$.

positive and others being negative. In addition, for the case of the four-ply effective ply thickness laminate with θ equal to 75°, the strain value of the first and second plies is positive around the tip of the stitch crack (i.e., S from 0.8 mm to 1.2 mm).

The strain values of ϵ_{22} approach the analytical far-field values, as determined from Poisson's effects, within the lengthscale of observation. The Poisson's ratio for the single-ply and four-ply effective ply thickness laminate with θ equal to 15°, 30°, 60°, and 75° is 0.86, 1.18, 0.29, and 0.08, respectively, as listed in Table 7.4. The resulting far-field values are plotted in Figures 7.134, 7.135, and B.103 through B.108. The distance along the path "between stitch cracks" that it takes to reach the far-field values is independent of both the effective ply thickness and the laminate angle.

The setup of the stitch crack models results in geometric relations between the S-direction (i.e., the path upon which results are taken) and the geometry of the damage. For larger values of θ, the damage is closer to being perpendicular to the load path, while the S-direction also runs more parallel to the damage. For the lower values of θ, the damage is closer to being parallel with the load path. Therefore, for lower values of θ, the stress is able to "flow" around the damaged region.

As the distance from the tip of the stitch crack increases, the gradient within a ply, as well as the gradient through the thickness, decreases until reaching a near zero value. The distance is observed to be dependent on the angle of the plies and the effective ply thickness. For the single-ply effective ply thickness laminates, the distance from the tip of the stitch crack is approximately 1.6 mm, 1.0 mm, 0.7 mm, and 0.5 mm (i.e., S equal to 2.6 mm, 2.0 mm, 1.7 mm, and 1.5 mm) for the laminate with θ equal to 15°, 30°, 60°, and 75°, respectively. For the four-ply effective ply thickness laminates, this distance is approximately 2.5 mm, 1.5 mm, 1.7 mm, 2.2 mm (i.e., S equal to 3.5 mm, 2.5 mm, 2.7 mm, and 3.2 mm), respectively. As is observed in the results of ϵ_{11}, the four-ply effective ply thickness laminates exhibit a greater variation, compared to the results of the single-ply effective ply thickness laminates, in gradient through the thickness within the region of S from 0.0 mm to 2.5 mm. This is observed in Figure 7.135, where plies through the thickness of the laminate exhibit one of five gradient trends. These trends are observed to be related to the

through-thickness location and ply angle of each ply. For example, plies 3, 10, 11, 18, 19, 26, and 27, shown in Figure 7.135, exhibit similar gradients as the distance along S is increased. As with ϵ_{11}, ply 4, a positive angle ply which neighbors a negative angle ply (i.e., ply 5), exhibits a through-thickness gradient compared to plies 1, 2, and 3, which exhibit minimum through-thickness gradient. These through-thickness gradients within an effective ply are consistent with the results observed for ϵ_{11}.

The strain fields of ϵ_{12} for the laminates considered have both negative values and positive values near the tip of the stitch cracks, as shown in the plots for the single-ply and four-ply effective ply thickness laminates with θ equal to 15° in Figures 7.136 and 7.137. For the other laminates, these plots are shown in Figures B.109 through B.114, included in Appendix B.4. The same trends observed in the results of ϵ_{11} and ϵ_{22} are observed and are therefore not readdressed. From the calculated coefficients of mutual influence, listed in Table 7.4, the expected far-field value of ϵ_{12} is zero for all the laminates. The results of the single-ply effective ply thickness laminate approach this value at a distance from the tip of the stitch crack of approximately 0.5 mm (i.e., S equal to 1.5 mm). The results of the four-ply effective ply thickness laminate approach this value at a distance from the tip of the stitch crack of approximately 1.5 mm (i.e., S equal to 2.5 mm), with the exception of the laminate with θ equal to 75° which does not reach the far-field value within the observed region of S. The four-ply effective ply thickness laminate with θ equal to 75° reaches the far-field value at a distance from the stitch crack of approximately 7.0 mm (i.e., S equal to 8.0 mm).

The out-of-plane strain results are considered subsequently. For the stitch crack model, each stitch crack and matrix crack are modeled via a seam, as described in Section 7.2.5. The free edges of the plate are sufficiently distant, as described in the model setup. As with the ply-drop specimen, the out-of-plane results are valid within the region of interest (i.e., in the vicinity of the "central" stitch crack) for the stitch crack model.

The strain fields of ϵ_{33} for the laminates considered have both positive and negative values near the tip of the stitch cracks, as shown in the plots for the single-ply and four-ply effective ply thickness laminates with θ equal to 15° in Figures 7.138 and

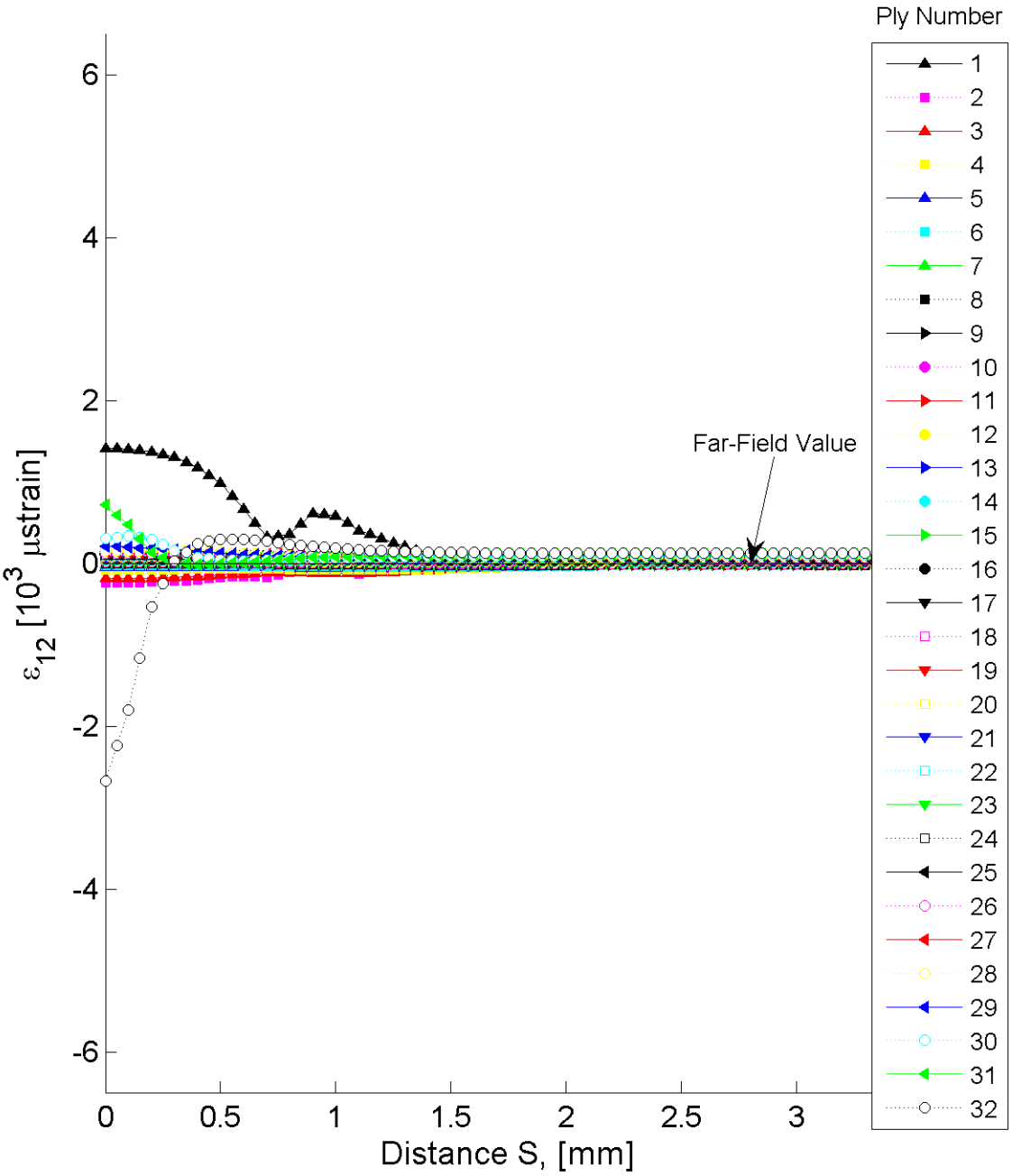

Figure 7.136 Plot of ϵ_{12}, in laminate axes, at the intersection of the midplane of each ply and the plane of the stitch crack for the stitch crack model with laminate of $[+15/-15]_{16T}$.

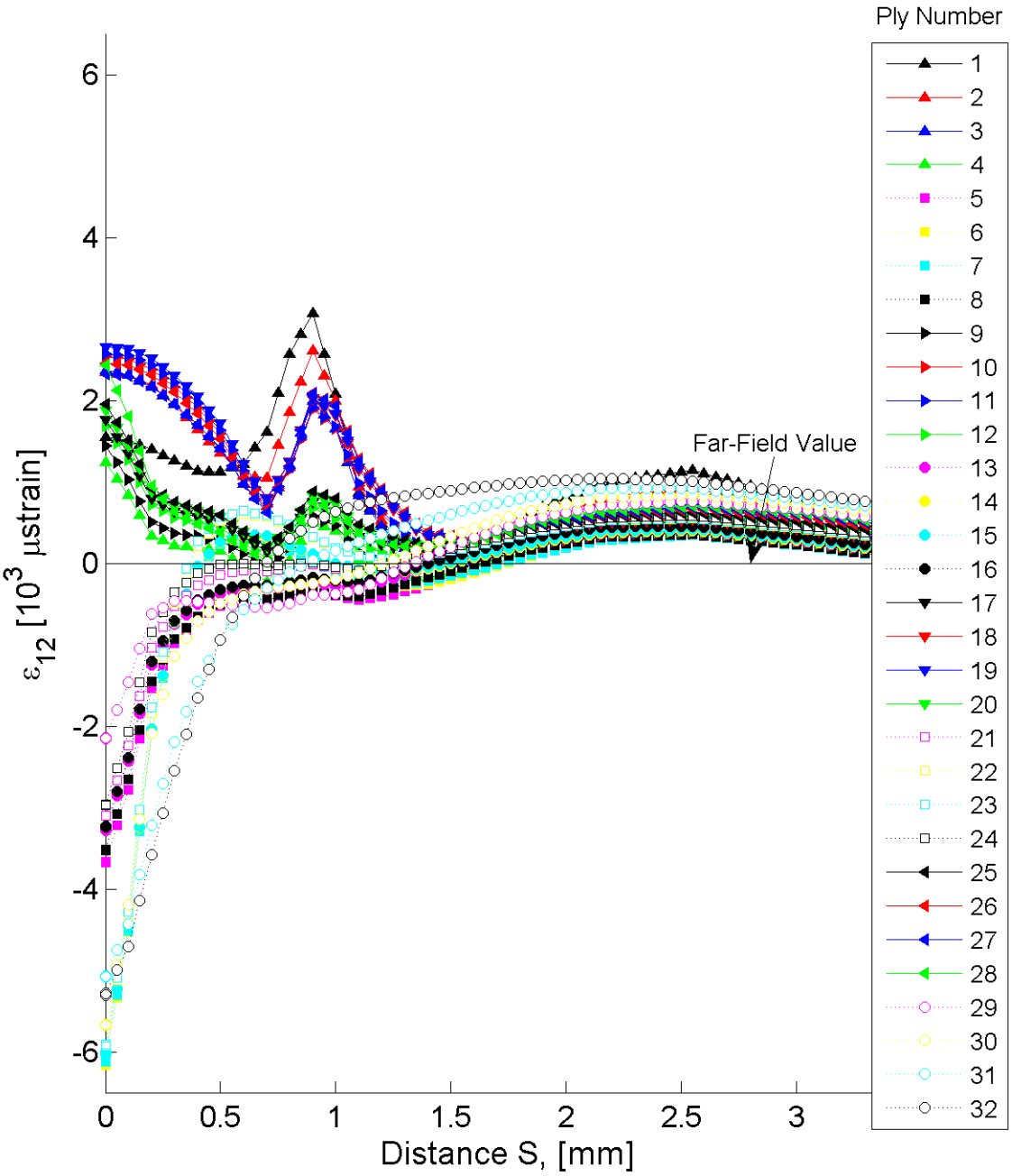

Figure 7.137 Plot of ϵ_{12}, in laminate axes, at the intersection of the midplane of each ply and the plane of the stitch crack for the stitch crack model with laminate of $[+15_4/-15_4]_{4T}$.

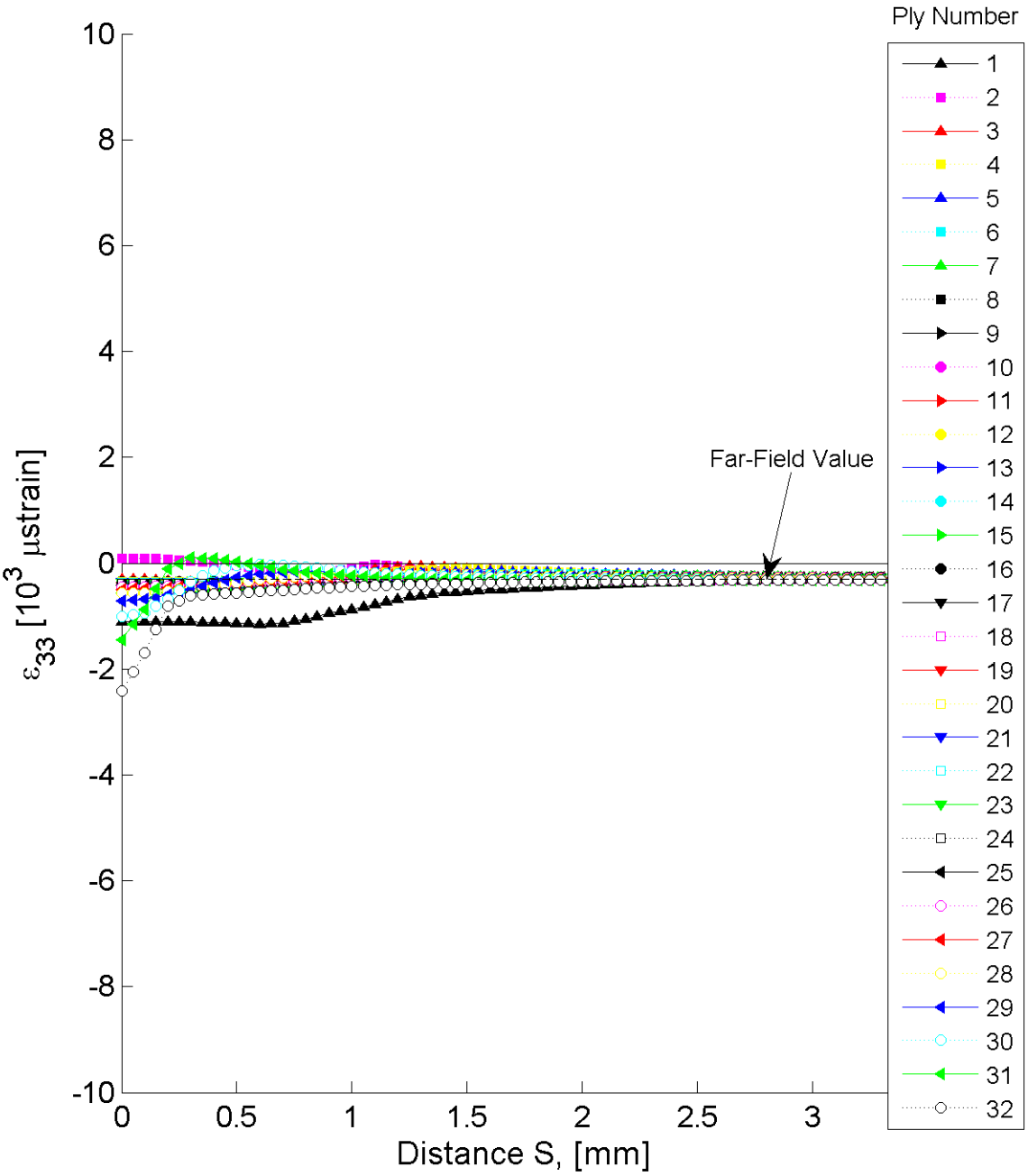

Figure 7.138 Plot of ϵ_{33}, in laminate axes, at the intersection of the midplane of each ply and the plane of the stitch crack for the stitch crack model with laminate of $[+15/-15]_{16T}$.

7.139. For the other laminates, these plots are shown in Figures B.115 through B.120, included in Appendix B.4. Like the in-plane results, in the region of S from 0.0 mm to 0.5 mm, the largest gradient in the S-direction of ϵ_{33} occurs within the last two plies (i.e., plies 31 and 32) of the single-ply effective ply thickness laminates. Unlike the in-plane results, within this region, a large gradient exists between the mismatch angle plies of the four-ply effective ply thickness laminate.

As with the in-plane results, the results of ϵ_{33} approach the analytical far-field values, as determined from Poisson's effects, within the lengthscale of observation. The Poisson's ratio, ν_{xz}, for the single-ply and four-ply effective ply thickness laminate with θ equal to 15°, 30°, 60°, and 75° is 0.03, -0.08, 0.29, and 0.37, respectively, as listed in Table 7.4. The far-field solution of the laminates is recovered at, or before, S equal to 2.7 mm, with the exception of the four-ply effective ply thickness laminate with θ equal to 75° which does not reach the far-field value within the observed region of S. As with the results of ϵ_{12}, the four-ply effective ply thickness laminate with θ equal to 75° reaches the far-field value at a distance from the stitch crack of approximately 7.0 mm (i.e., S equal to 8.0 mm). The same trends in gradient are observed along the S-direction for the single-ply and four-ply effective ply thickness laminates of a given ply angle. However, the maximum variation of the magnitude of ϵ_{33} compared to the far-field value is amplified by a factor of four or greater for the four-ply effective ply thickness laminate as compared to the single-ply effective ply thickness laminate.

As with the results for ϵ_{11}, the gradient in the $\hat{S}$-direction is determined by comparing the results of the paths "along the stitch crack" and "between the stitch cracks." The gradients for the results of ϵ_{33} for the single-ply and four-ply effective ply thickness laminates with θ equal to 15° are plotted and shown in Figures 7.140 and 7.141. For the other laminates, these plots are shown in Figures B.121 through B.126, included in Appendix B.4. Unlike the results of ϵ_{11}, the largest gradient in the $\hat{S}$-direction is dependent on the effective ply thickness. For the single-ply effective ply thickness laminates, the largest gradient is observed in ply 2. An exception occurs for the single-ply effective ply thickness laminate with θ equal to 60°, where the largest

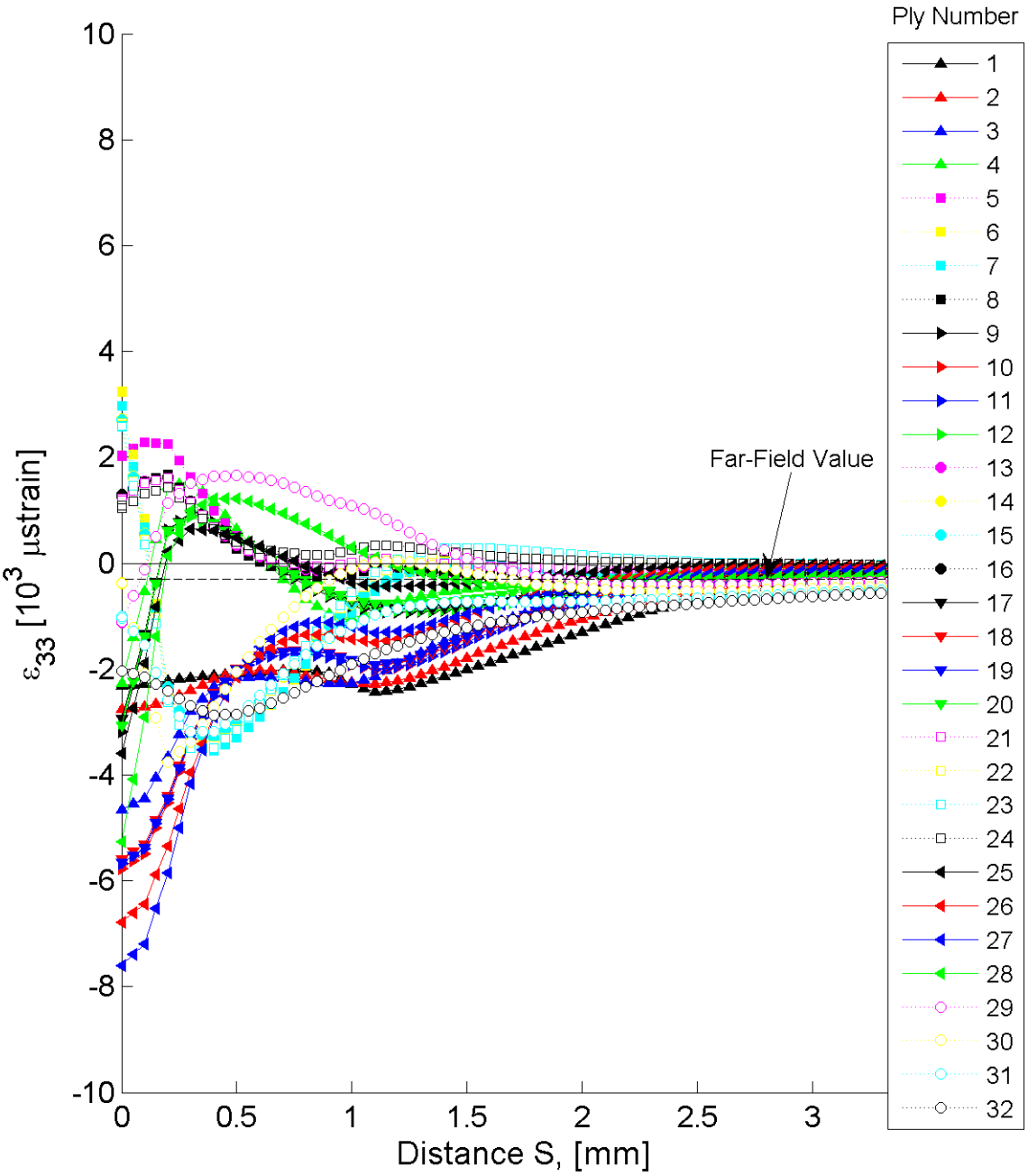

Figure 7.139 Plot of ϵ_{33}, in laminate axes, at the intersection of the midplane of each ply and the plane of the stitch crack for the stitch crack model with laminate of $[+15_4/-15_4]_{4T}$.

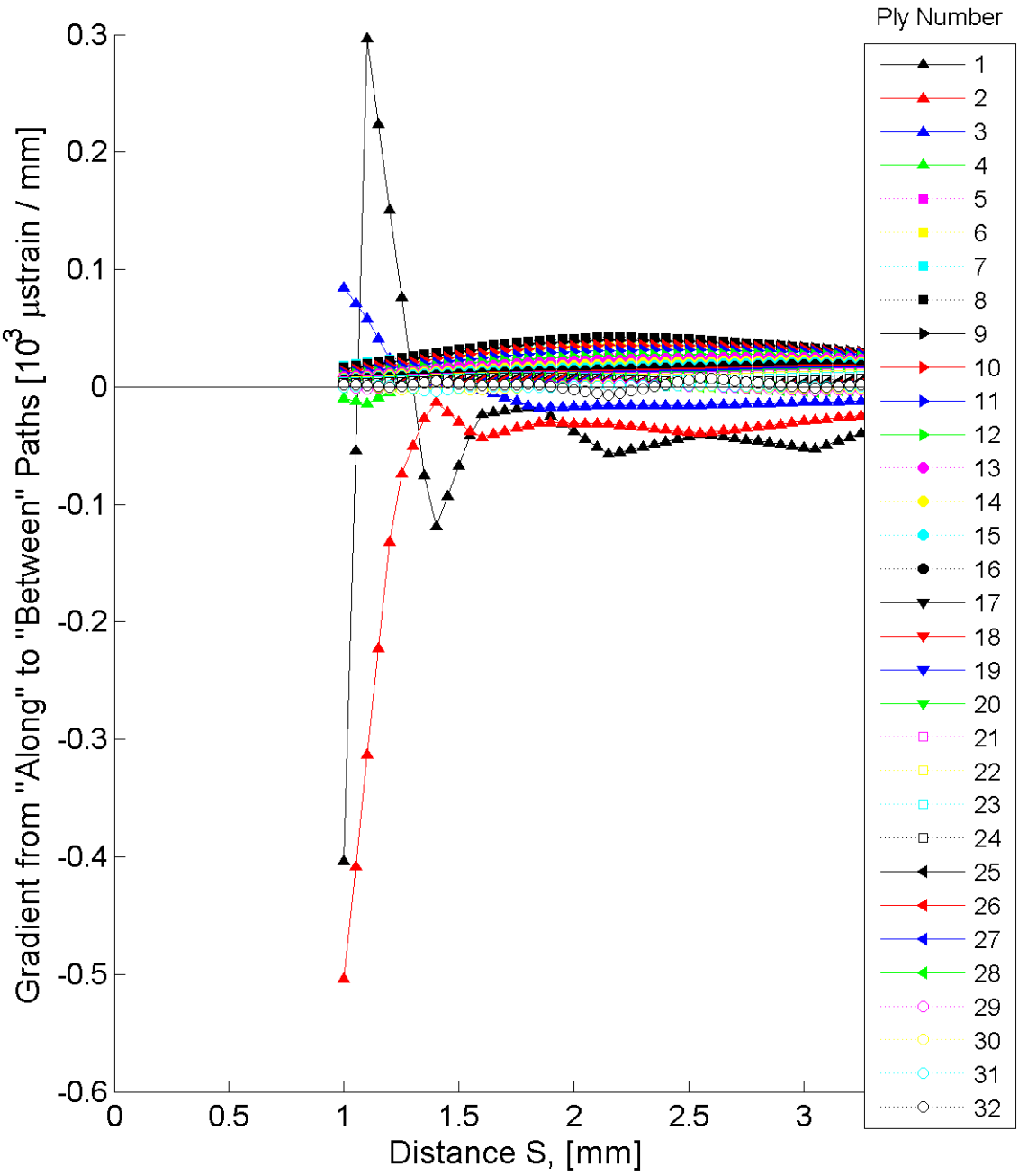

Figure 7.140 Plot of the gradient of ϵ_{33} in the $\hat{S}$-direction at the midplane of each ply for the stitch crack model with laminate of $[+15/-15]_{16T}$.

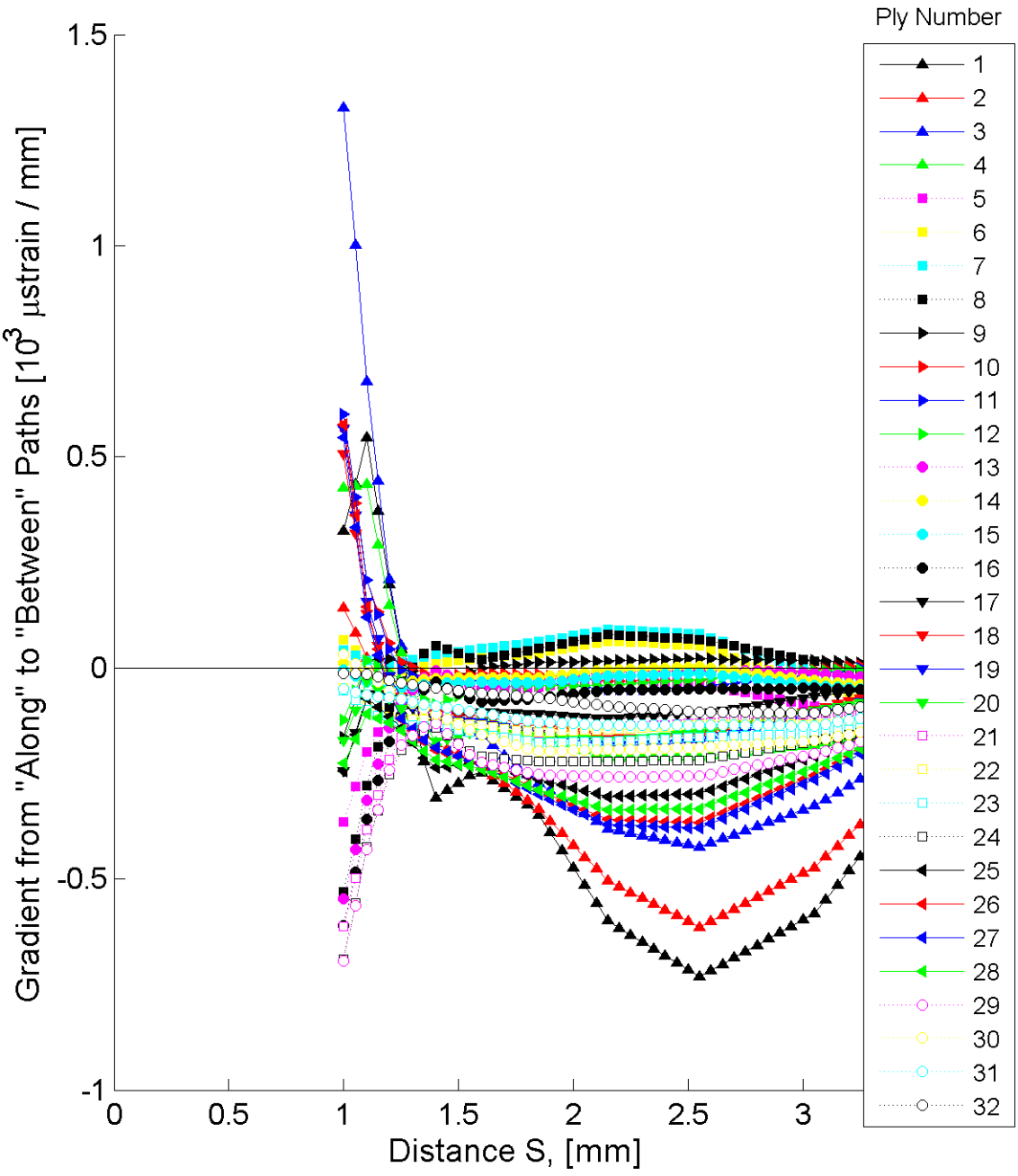

Figure 7.141 Plot of the gradient of ϵ_{33} in the $\hat{S}$-direction at the midplane of each ply for the stitch crack model with laminate of $[+15_4/-15_4]_{4T}$.

gradient is observed in ply 1. For the four-ply effective ply thickness laminates, the largest gradient is observed in ply 3. The peak gradients in the $\hat{S}$-direction are four or more times larger in magnitude for the four-ply effective ply thickness laminates than for the single-ply effective ply thickness laminates. The gradients of the laminates with θ equal to 30° are negative while the other laminates have positive gradients. As with the results for ϵ_{11}, the results of ϵ_{33} indicate that the lengthscale associated with this gradient in the region of the tip of the stitch crack is on the order of half the distance between stitch cracks.

The through-thickness gradients of the out-of-plane results dissipate at the same rate as the in-plane results. For the single-ply and four-ply effective ply thickness laminates, the through-thickness variation of gradient dissipates such that the gradients along the direction of the stitch crack is independent of through-thickness location at a S-distance of approximately 2.0 mm. As discussed for the in-plane results, the modeling techniques used for the single-ply and four-ply effective ply thickness laminates influence the ability to capture through-ply gradients. The effective plies of the four-ply effective ply thickness laminates have additional degrees of freedom within the effective ply that allows through-thickness effects to be captured. These effects are exhibited as gradients in the through-thickness direction are observed in the mismatch angle plies. Unlike the single-ply effective ply thickness laminate, the four-ply effective ply thickness laminate exhibits through-thickness gradients within effective plies. This through-thickness behavior is not exhibited in the results of the single-ply effective ply thickness laminate. It is likely that through-thickness out-of-plane gradients exist within the plies of the single-ply effective ply thickness laminate, but are not observable as there is only a single element through the thickness.

The out-of-plane trends discussed for ϵ_{33} are also observed in the results for ϵ_{13} and ϵ_{23}. The plots of the gradients for these are shown in Figures B.127 through B.142, included in Appendix B.4.

The results for the in-plane strain fields of the delamination damage inclusion model are considered subsequently. This is followed by the results for the out-of-plane strain fields. As described in Section 7.2.5, the delamination damage model

allows investigation of the lengthscales associated with delamination fronts. The resulting stress and strain fields in the vicinity of a delamination are investigated. As a manifestation of the modeling technique, the delamination front is required to be a straight line. This is different from what is observed experimentally, where delaminations are observed to have smooth fronts with rounded corners, as described in Section 6.3. The results for the delamination model are taken along a path normal to the delamination front, with the path intersecting the $x-y$ coordinates of the midspan of the delamination front. This is subsequently described. The size of the delamination model was selected in order for the results along this path to be outside the region influenced by the delamination "corners," as described in Section 7.2.5. The maximum distance influenced by these corners is observed to be 5 mm. Thus, based on the criteria used for the model size selection, there are effectively no gradients in the model results normal to this path in its vicinity.

As indicated, the results of the delamination model are illustrated along one path. This path is located at the midplane of each ply and is oriented normal to the delamination front, as shown in Figure 7.142. The path lies within the x-y plane, begins at the $x-y$ origin of the model, and extends through the midspan of the delamination front in the positive $x-y$ quadrant. The distance along each path is measured along the S-axis. The delamination front is located at a S-distance equal to 15 mm for each of the laminates. The relative orientation of the path as well as the S-axis changes for each angle-ply laminate. The results presented herein are taken from the positive $x-y$ quadrant. The paths could also be oriented along any of the other quadrants and would exhibit the same results due to the symmetry of the model.

The strain fields of ϵ_{11} for the laminates considered have positive values throughout the delamination model, as shown in the plots for the single-ply and four-ply effective ply thickness laminates with θ equal to 15° in Figures 7.143 and 7.144. For the other laminates, these plots are shown in Figures B.143 through B.148, included in Appendix B.4. In all cases, the results exhibit an "interior far-field" value. This is a value determined from the models that is approximately constant within the region of delamination (e.g., for a value of S less than 12 mm for the laminates with θ

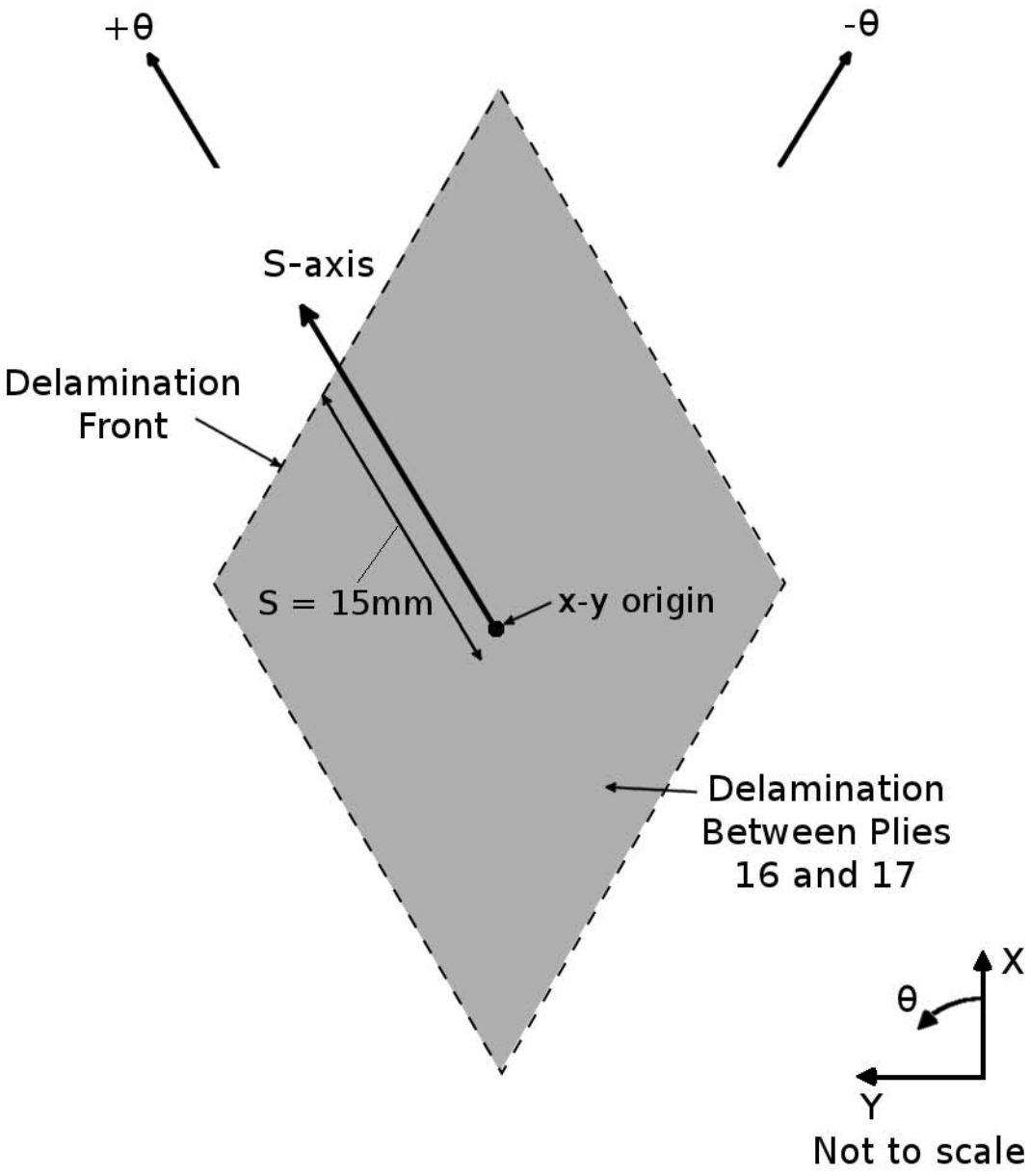

Figure 7.142 Illustration of the path from which results for the delamination damage model are taken.

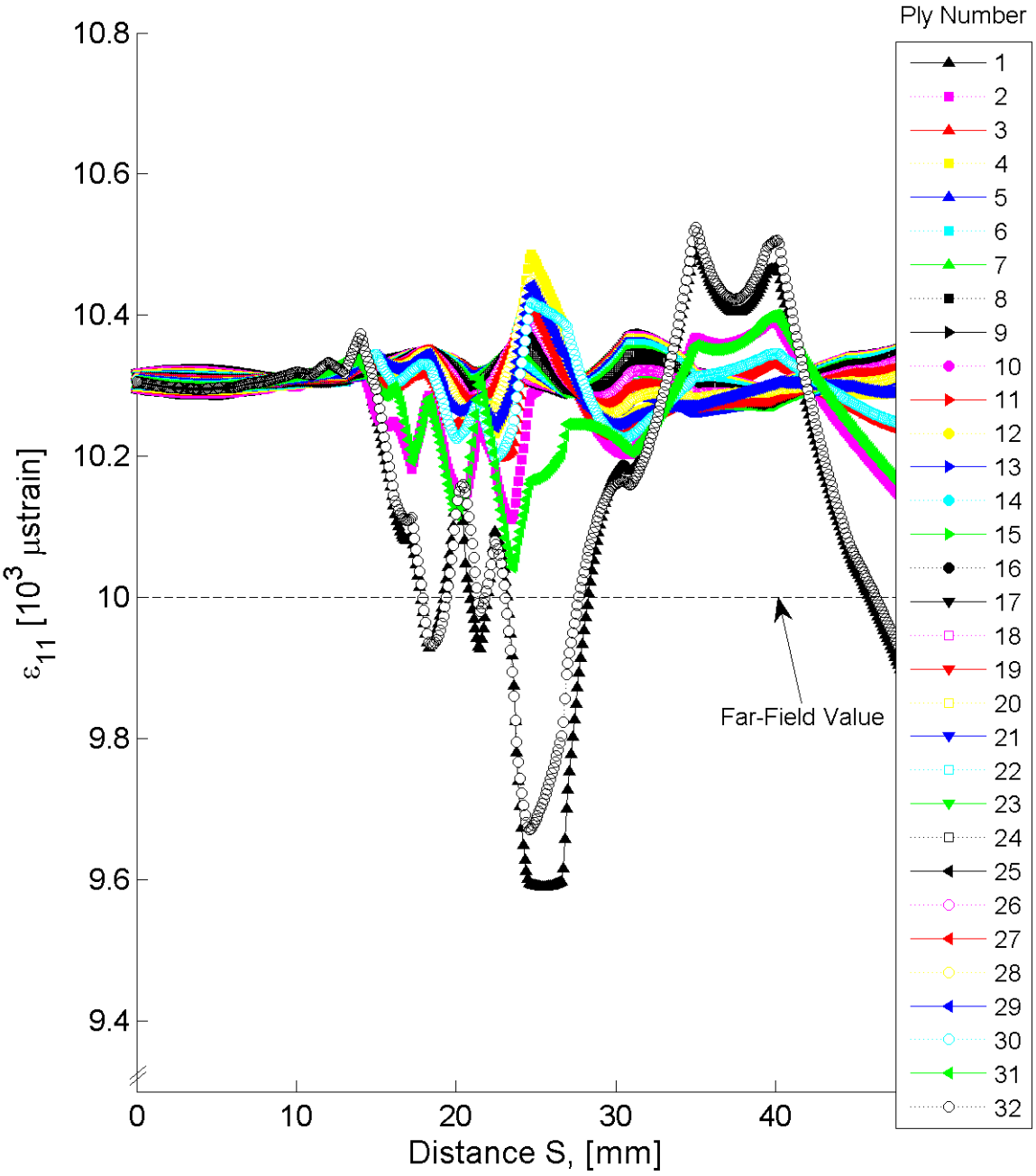

Figure 7.143 Plot of ϵ_{11}, in laminate axes, along the path at the midplane of each ply for the delamination model with laminate of $[+15/-15]_{16T}$.

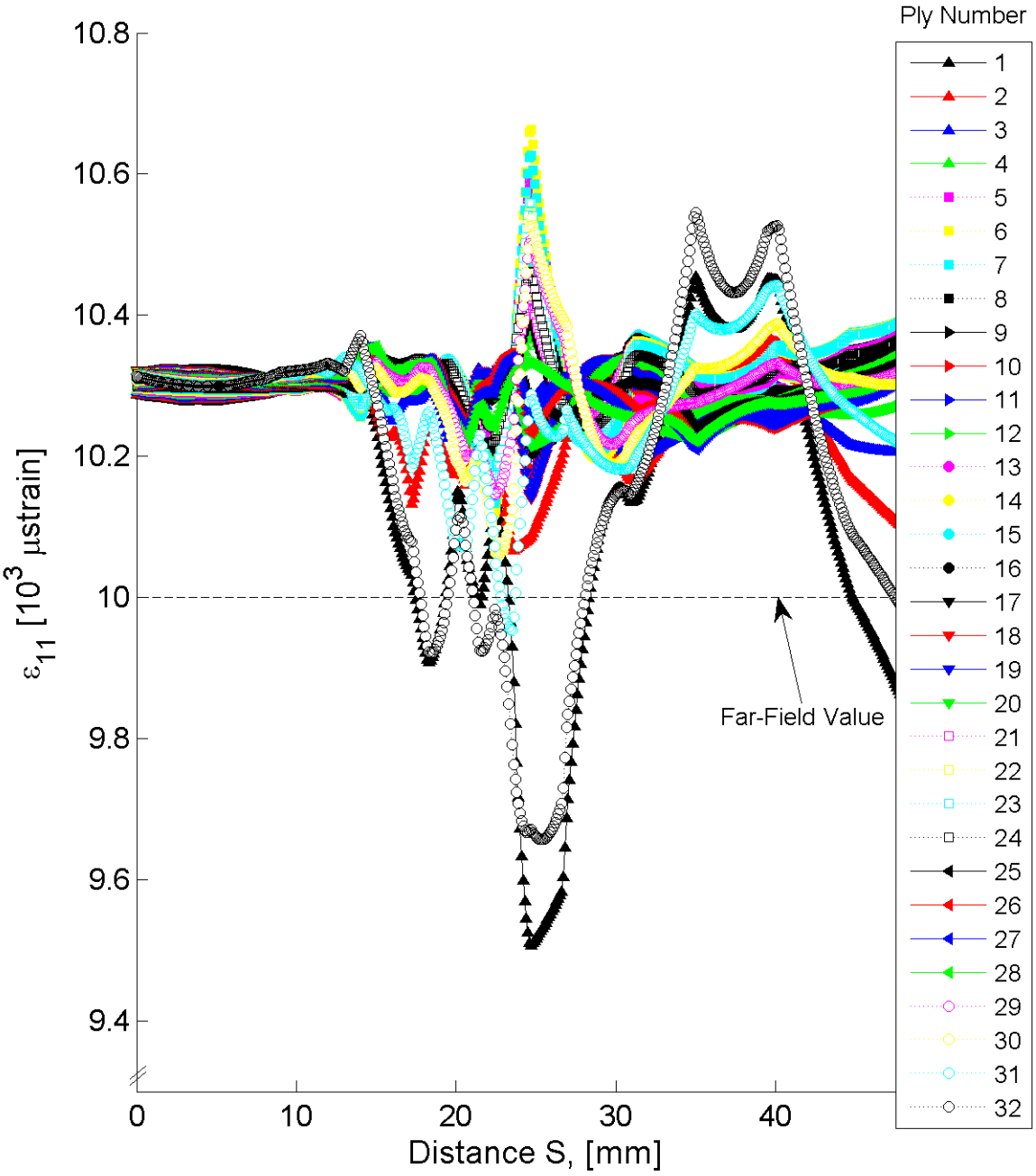

Figure 7.144 Plot of ϵ_{11}, in laminate axes, along the path at the midplane of each ply for the delamination model with laminate of $[+15_4/-15_4]_{4T}$.

equal to 15°). The term "interior far-field" refers to the localized change in laminate due to the delamination. For each of the laminates, the "interior far-field" value is determined by visual inspection of the results for the single-ply and four-ply effective ply thickness laminates. For the laminates of θ equal to 15°, this "interior far-field" value is approximately 10300 μstrain and does not change with effective ply thickness. For the laminates of θ equal to 30°, 60°, and 75°, the "interior far-field" values are approximately 11400 μstrain, 12700 μstrain, and 10300 μstrain, respectively, and do not change with effective ply thickness. The values of strain within the region of S from 0 mm to 40 mm vary about this "interior far-field" value for each of the laminates.

For all laminates, the largest gradients in the S-direction occur within the region of S from 12 mm to 40 mm. For a given angle ply, regardless of effective ply thickness, the strain behavior through the thickness follows the same trend. For the case of the four-ply effective ply thickness laminate, the extrema of strain values, compared relative to the "interior far-field" value, are a few hundred μstrain greater than the case of the single-ply effective ply thickness laminate. Overall, the behavior of the single-ply and four-ply effective ply thickness laminates are very similar. Unlike the gradients observed in the stitch crack model, which are typically on the order of thousands of μstrain, the variations in strain observed in the delamination model are on the order of hundreds of μstrain. In both the single-ply and four-ply effective ply thickness laminates, the largest gradients of ϵ_{11} are observed in the outer plies. The region of S from 0 mm to 12 mm (i.e., from the center of the of the delamination region outward to 3 mm before the delamination front) exhibits uniform strains, approximately equal to the "interior far-field values," for all the laminates of the single-ply and four-ply effective ply thickness laminates. Beyond values of S of 12 mm, the strain fields exhibit gradients that vary along S. The results begin to diverge near S equal to 50 mm, which corresponds to the change in the modeled mesh density, as described in Section 7.2.5. Thus, results for values of S greater than 40 mm are not considered.

The strain fields of ϵ_{22} for the laminates considered have negative values throughout the delamination model, as shown in the plots for the single-ply and four-ply

effective ply thickness laminates with θ equal to 15° in Figures 7.145 and 7.146. For the other laminates, these plots are shown in Figures B.149 through B.154, included in Appendix B.4. As with the results for ϵ_{11}, the values of ϵ_{22} are observed to vary about an "interior far-field" value, determined by the average of the strain fields in the region S equal from 0 mm to 12 mm. For the laminates with θ equal to 15°, 30°, 60°, and 75°, the "interior far-field" values are approximately -4200 μstrain, -5600 μstrain, -3800 μstrain, and -900 μstrain, respectively, and do not change with effective ply thickness. As with ϵ_{11}, the results of ϵ_{22} exhibit the same gradient trends in the single-ply and four-ply effective ply thickness laminates. Unlike the results of ϵ_{11}, the extrema of ϵ_{22} for the four-ply effective ply thickness laminate are not always greater than those of the single-ply effective ply thickness laminate. There is only slight (i.e., tens of μstrain) difference when comparing the through-thickness values of strain between the two effective ply thickness laminates. For all laminates, the largest gradients in the S-direction occur within the region of S from 20 mm to 30 mm. The largest gradient is on the order of one thousand μstrain for both the single-ply and four-ply effective ply thickness laminates. As with the results for ϵ_{11}, the largest gradients of ϵ_{22} are observed in the top and bottom plies (i.e., plies 1 and 32). The region of S from 0 mm to 12 mm exhibits relatively uniform strains for all the laminates of the single-ply and four-ply effective ply thickness laminates. The laminates with θ equal to 60° exhibit the smallest gradients of the laminates considered.

The strain fields of ϵ_{12} for the laminates considered have both positive and negative values throughout the delamination model, as shown in the plots for the single-ply and four-ply effective ply thickness laminates with θ equal to 15° in Figures 7.147 and 7.148. For the other laminates, these plots are shown in Figures B.155 through B.160, included in Appendix B.4. As with the results for ϵ_{11} and ϵ_{22}, the values of ϵ_{12} are observed to vary about an "interior far-field" value, determined by the average of the strain fields in the region S equal from 0 mm to 12 mm. For the laminates with θ equal to 15°, 30°, 60°, and 75°, the "interior far-field" values are approximately 0 μstrain, which is equal to the analytical far-field value. The "interior far-field" values are

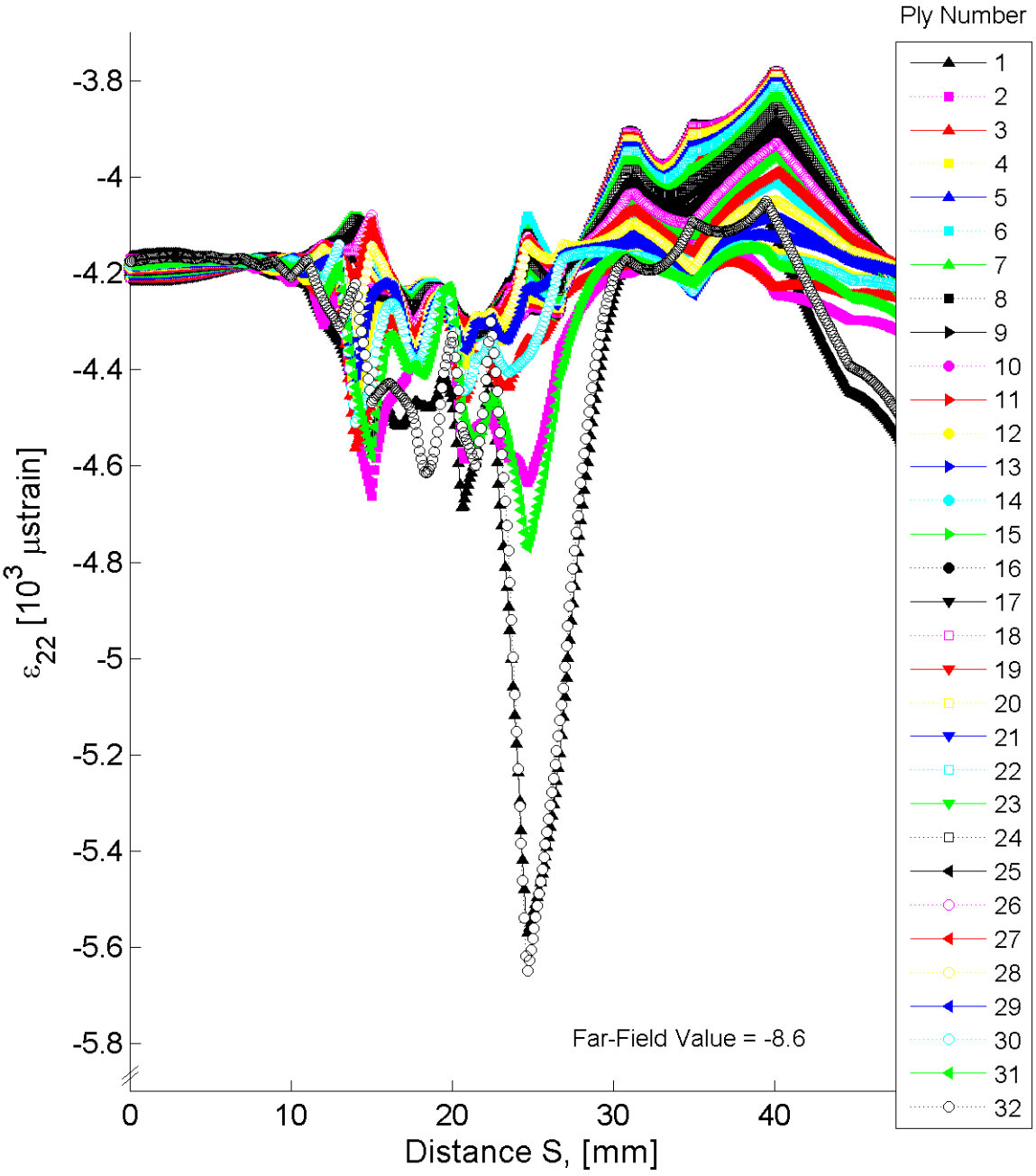

Figure 7.145 Plot of ϵ_{22}, in laminate axes, along the path at the midplane of each ply for the delamination model with laminate of $[+15/-15]_{16T}$.

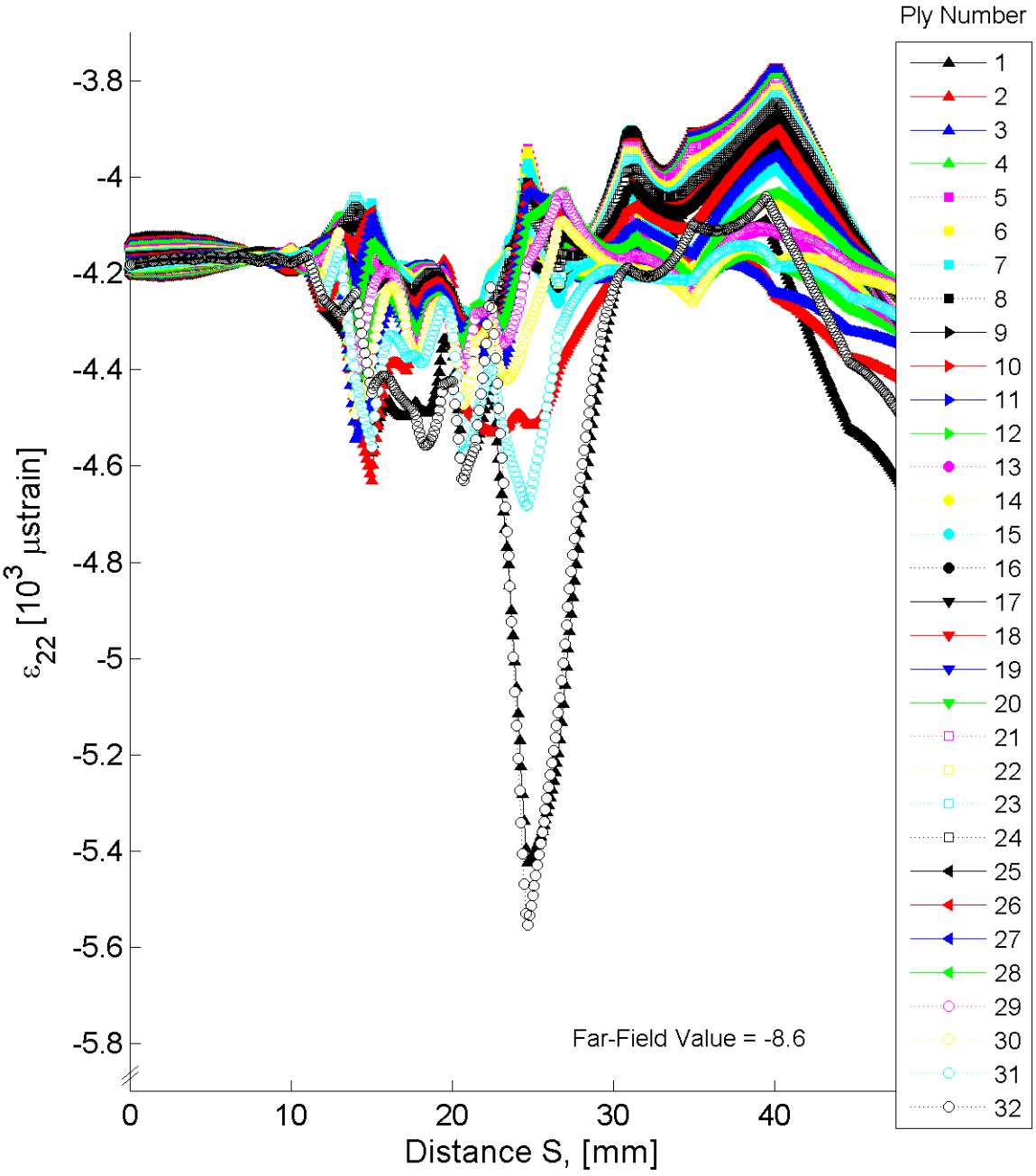

Figure 7.146 Plot of ϵ_{22}, in laminate axes, along the path at the midplane of each ply for the delamination model with laminate of $[+15_4/-15_4]_{4T}$.

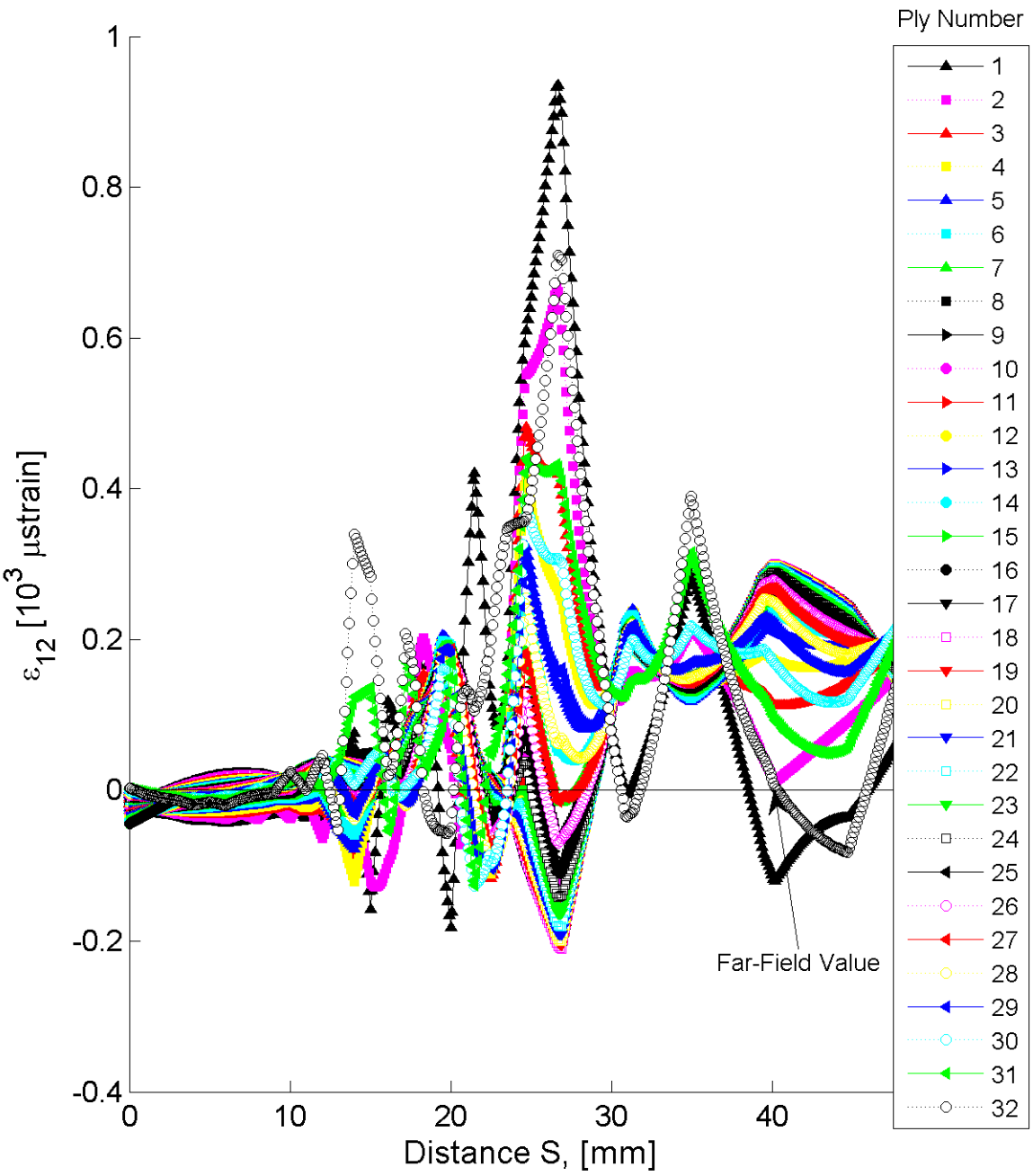

Figure 7.147 Plot of ϵ_{12}, in laminate axes, along the path at the midplane of each ply for the delamination model with laminate of $[+15/-15]_{16T}$.

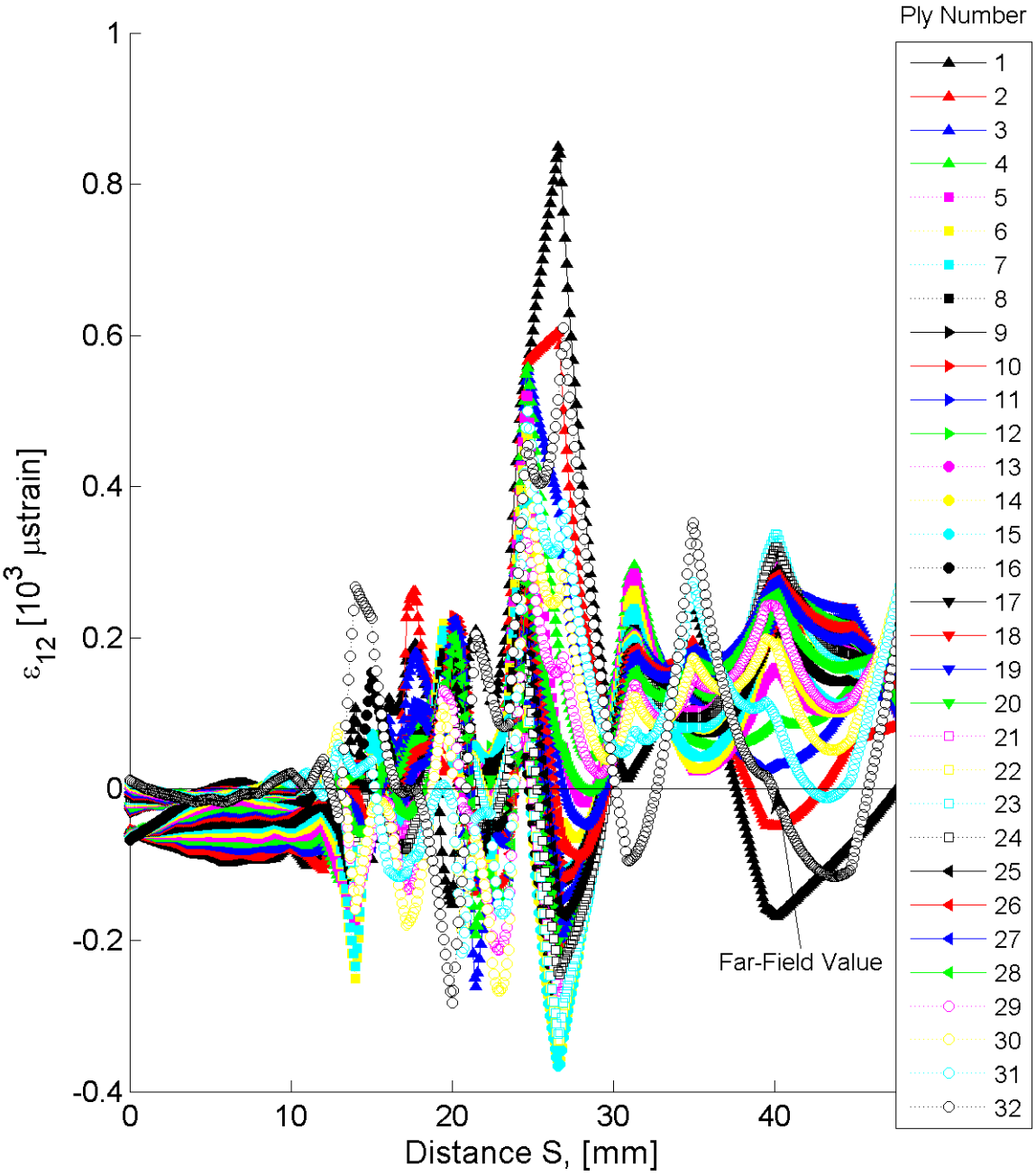

Figure 7.148 Plot of ϵ_{12}, in laminate axes, along the path at the midplane of each ply for the delamination model with laminate of $[+15_4/-15_4]_{4T}$.

approximately equal to the analytical far-field value for all the laminates, regardless of effective ply thickness. For all laminates, the largest gradients in the S-direction occur within the region of S from 20 mm to 30 mm. The largest gradient is on the order of hundreds of μstrain for both the single-ply and four-ply effective ply thickness laminates. As with the results for ϵ_{11}, the largest gradients of ϵ_{12} are observed in the top and bottom plies (i.e., plies 1 and 32). The values of ϵ_{12} begin to exhibit gradients in the wake (i.e., for values of S less than 15 mm) of the delamination front. The distance 'behind' (i.e., the distance less than S equal to 15 mm) the delamination front where the gradients begin becoming active is approximately 3 mm for each of the laminates, consistent with the results for ϵ_{11} and ϵ_{22} (i.e., these results were relatively constant over the region of S from 0 mm to 12 mm). This length is consistent for both the single-ply and four-ply effective ply thickness laminates. A through-thickness variation is observed in the length associated with gradient activity. The gradients in the outer plies become active closer to the delamination front while the gradient of the inner plies take up to 5 mm beyond the delamination front (i.e., S equal to 20 mm) to become active.

The out-of-plane strain results are considered subsequently. For the delamination model, the delamination is modeled via a seam, as described in Section 7.2.5. Free edge effects from the edges of the plate are sufficiently distant from the region of interest, as described in the model setup. Unlike the stitch crack model, the seam of the delamination model are between plies, as opposed to through the thickness of plies. Therefore, the orientation of the seam defining the delamination does not create the free-edge effects previously described. The out-of-plane results are valid within the region of interest (i.e., in the vicinity of the delamination front) for the delamination model.

The strain fields of ϵ_{33} for the laminates considered have negative values throughout the delamination model, as shown in the plots for the single-ply and four-ply effective ply thickness laminates with θ equal to 15° in Figures 7.149 and 7.150. For the other laminates, these plots are shown in Figures B.161 through B.166, included in Appendix B.4. As with the in-plane results, the values of ϵ_{33} are observed to vary

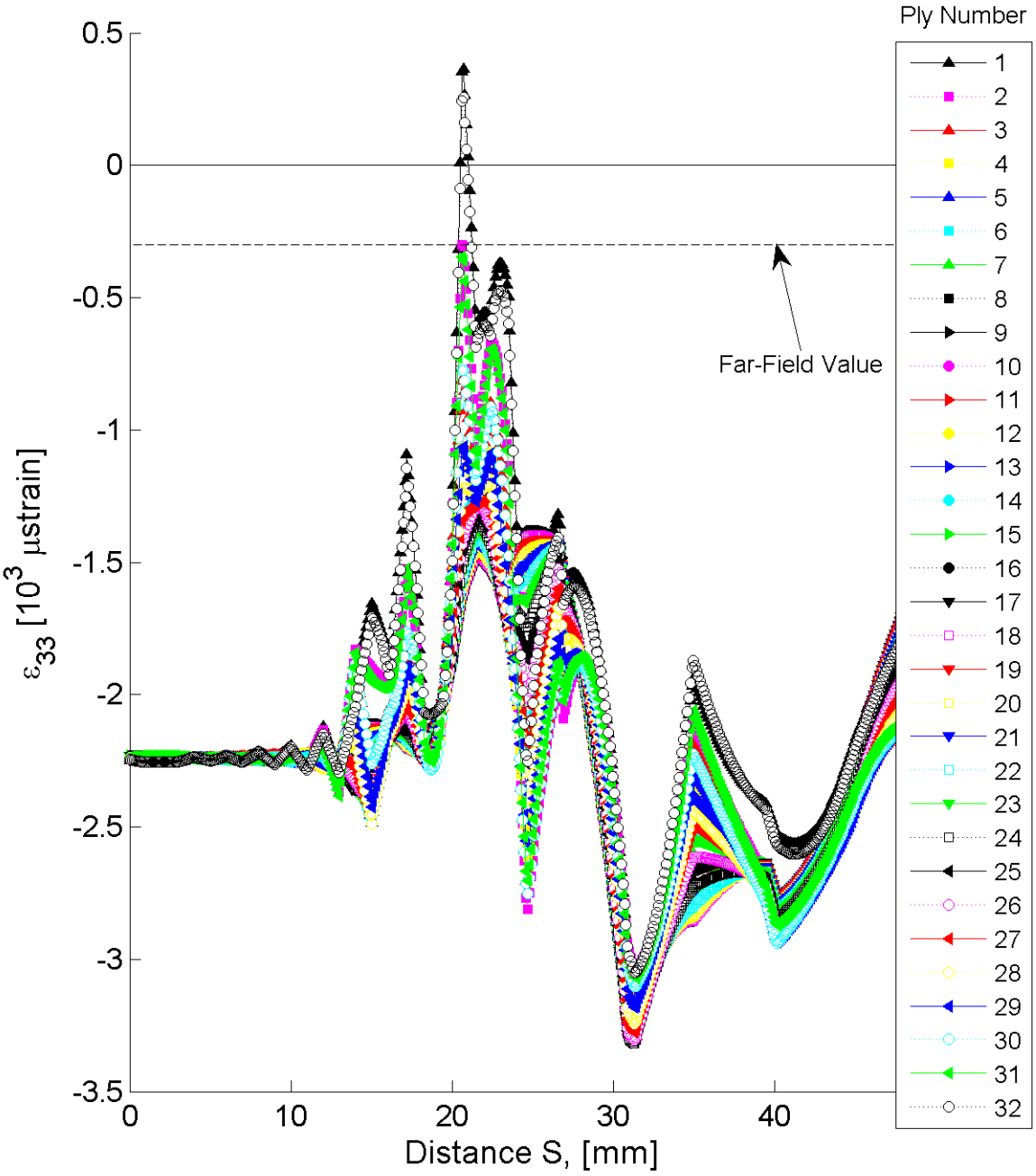

Figure 7.149 Plot of ϵ_{33}, in laminate axes, along the path at the midplane of each ply for the delamination model with laminate of $[+15/-15]_{16T}$.

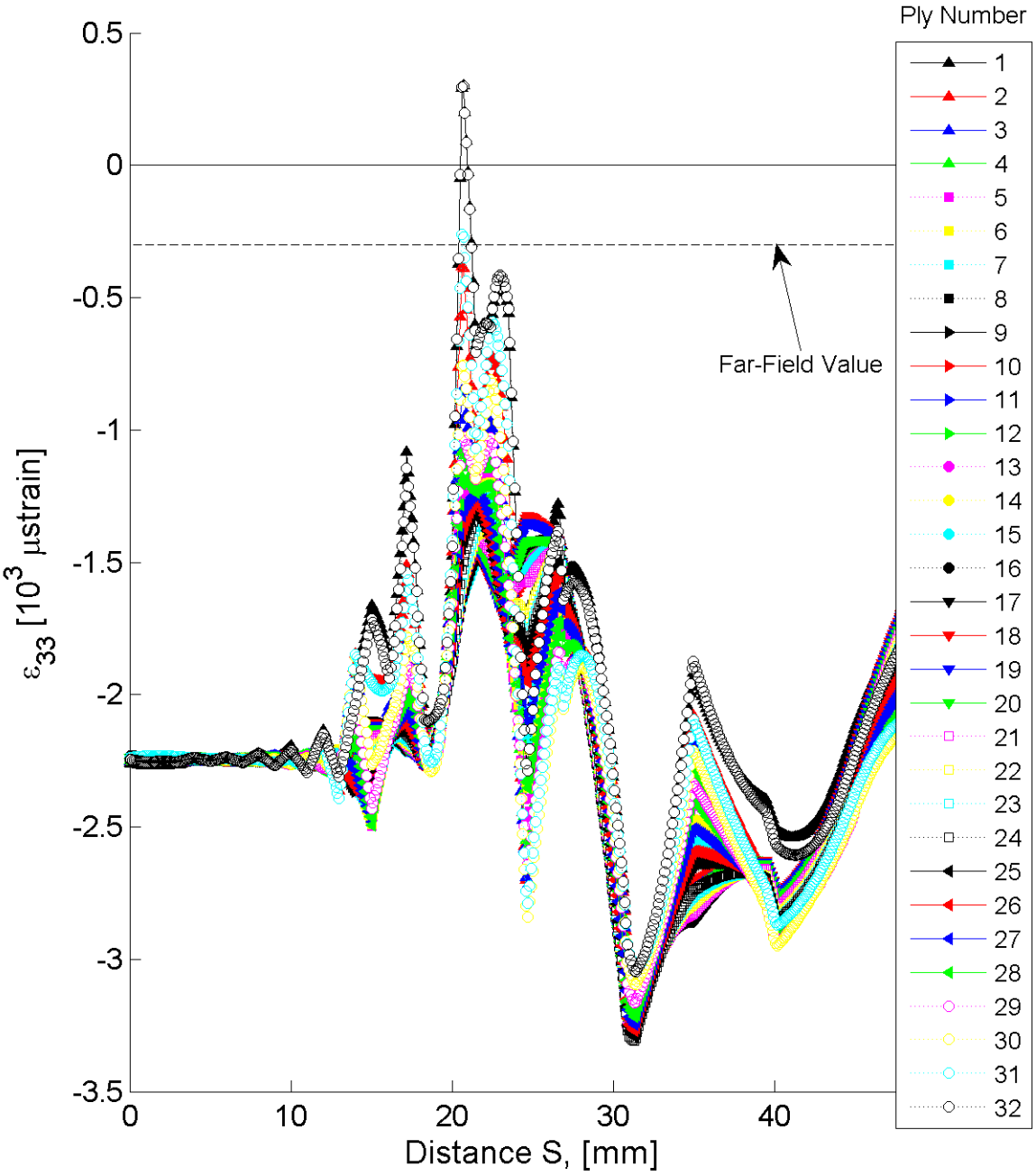

Figure 7.150 Plot of ϵ_{33}, in laminate axes, along the path at the midplane of each ply for the delamination model with laminate of $[+15_4/-15_4]_{4T}$.

about an "interior far-field" value, determined by the average of the strain fields in the region S equal from 0 mm to 12 mm. The "interior far-field" value is approximately -2250 μstrain for the laminates with θ equal to 15° and 30°, -3600 μstrain for the laminates with θ equal to 60°, and -3850 μstrain for the laminates with θ equal to 75°. These values do not vary with effective ply thickness. For all laminates, the largest gradients in the S-direction occur within the region of S from 15 mm to 40 mm. The largest gradient is on the order of a thousand μstrain per millimeter for both the single-ply and four-ply effective ply thickness laminates with θ equal to 15° and 30°. The gradients of the laminates with θ equal to 60° and 75° are on the order of a few hundred μstrain per millimeter. As with the results for the in-plane strain, the extrema of ϵ_{33} are observed in the top and bottom plies (i.e., plies 1 and 32). Overall, the results for ϵ_{33} of the delamination model exhibit the same gradient trends through the thickness of a laminate with a given ply angle, with the magnitude of the gradients changing for each ply. This is observed as the relative change in magnitude from the "interior far-field" value through the thickness of the laminate. This relative change is observed to be fairly independent of effective ply thickness, with the extrema of each ply having approximately the same magnitude for the single-ply and four-ply effective ply thickness laminates.

The strain fields of ϵ_{13} for the laminates considered have values throughout the delamination model such that half are positive and half are negative. This is shown in the plots for the single-ply and four-ply effective ply thickness laminates with θ equal to 15° in Figures 7.151 and 7.152. For the other laminates, these plots are shown in Figures B.167 through B.172, included in Appendix B.4. Unlike the in-plane results and the results for ϵ_{33}, the values of ϵ_{13} are observed to vary about the analytical far-field value, equal to zero for all laminates. As with the results for ϵ_{33}, the results of ϵ_{13} exhibit large gradients that begin immediately at the delamination front (i.e., S equal to 15 mm). These gradients are exhibited through the thickness of the laminate. As with the results for ϵ_{33}, there are no effects of the effective ply thickness. The region of S from 15 mm to 30 mm exhibits the largest gradients in the S-direction, observed by the narrow peaks of strain. Beyond this region (i.e., for S greater than 30 mm)

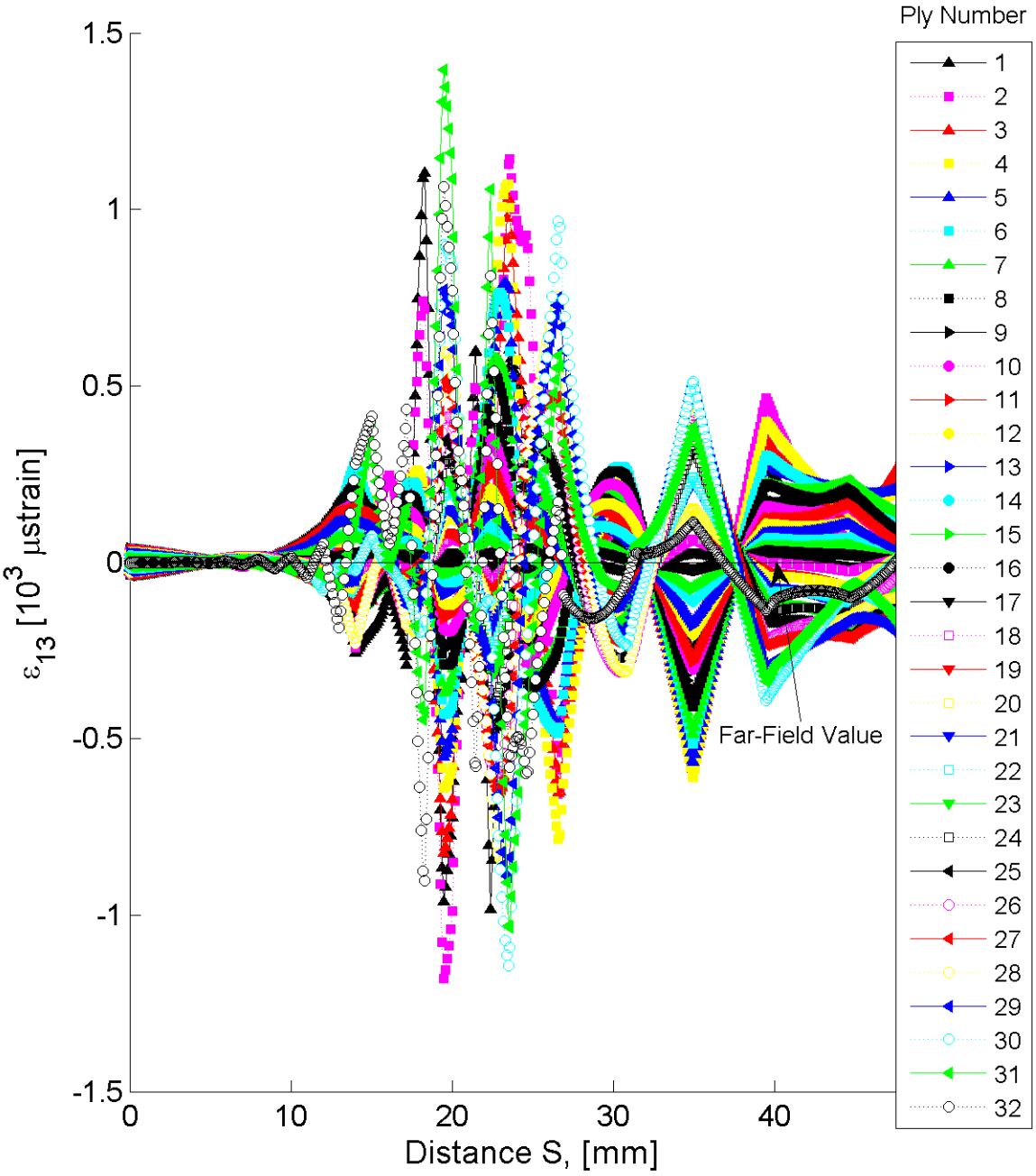

Figure 7.151 Plot of ϵ_{13}, in laminate axes, along the path at the midplane of each ply for the delamination model with laminate of $[+15/-15]_{16T}$.

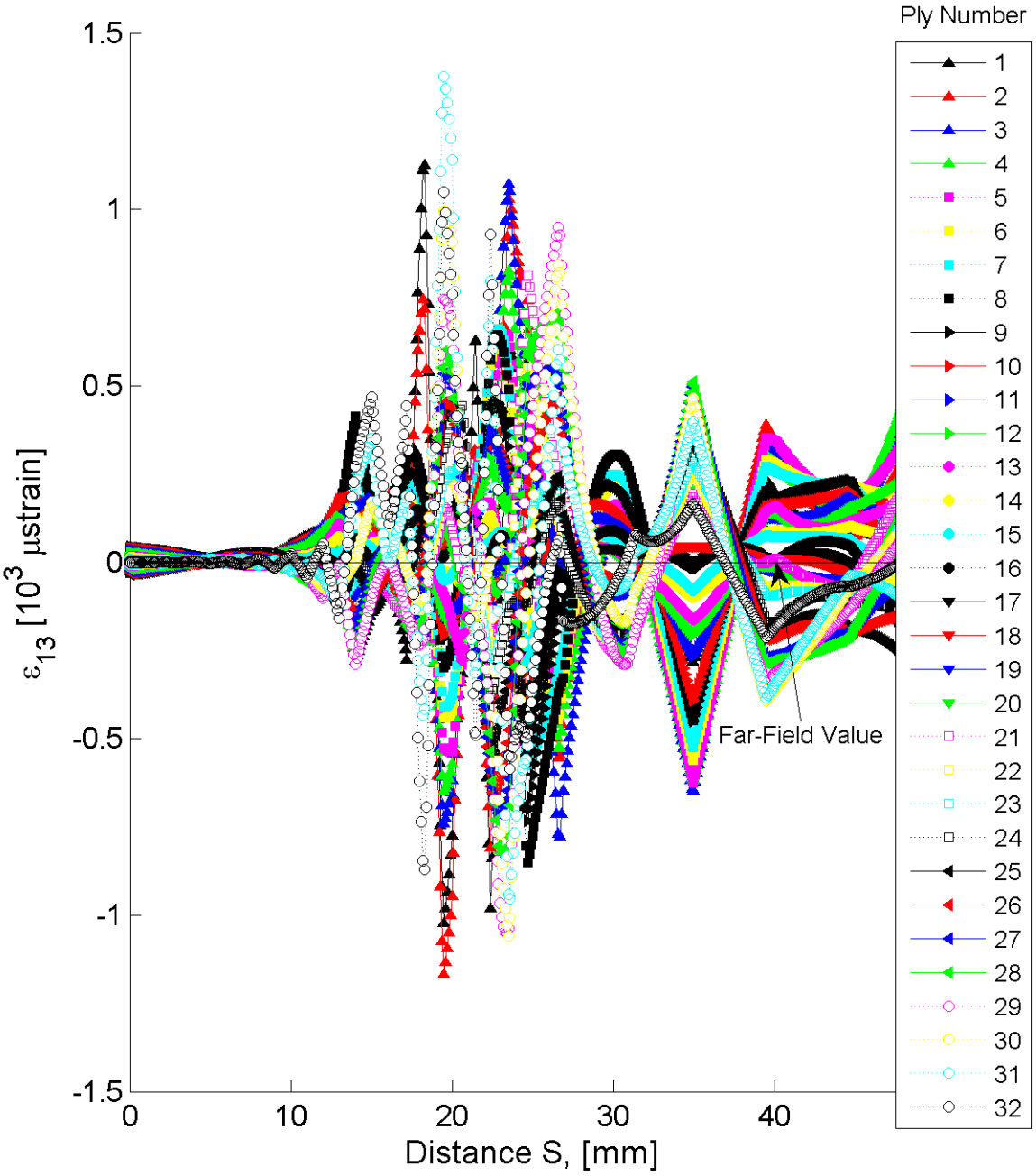

Figure 7.152 Plot of ϵ_{13}, in laminate axes, along the path at the midplane of each ply for the delamination model with laminate of $[+15_4/-15_4]_{4T}$.

gradients become uniform through the thickness and are more slowly changing. In this region, the through-thickness behavior is observed to be fairly symmetric about the far-field value (i.e. zero μstrain).

The strain fields of ϵ_{23} for the laminates considered have values throughout the delamination model such that half are positive and half are negative. This is shown in the plots for the single-ply and four-ply effective ply thickness laminates with θ equal to 15° in Figures 7.153 and 7.154. For the other laminates, these plots are shown in Figures B.173 through B.178, included in Appendix B.4. As with the results for ϵ_{13}, the values of ϵ_{23} are observed to vary about the analytical far-field value, equal to zero for all laminates. As with the results for ϵ_{33} and ϵ_{13}, the results of ϵ_{23} exhibit large gradients that begin immediately at the delamination front (i.e., S equal to 15 mm). The magnitudes of ϵ_{23} exhibit peaks at S-locations that are dependent on the laminate angle, with the exception of the results for the laminate with θ equal to 75° which does not exhibit a single peak of significant magnitude (i.e., the variation of ϵ_{23} is on the order of tens of μstrain). Overall, the through-thickness behavior is observed to be mostly symmetric about the far-field value (i.e. zero μstrain). As with the results of ϵ_{13}, the largest gradients are observed along the S-direction. As with the results for ϵ_{33} and ϵ_{13}, there are no effects of the effective ply thickness.

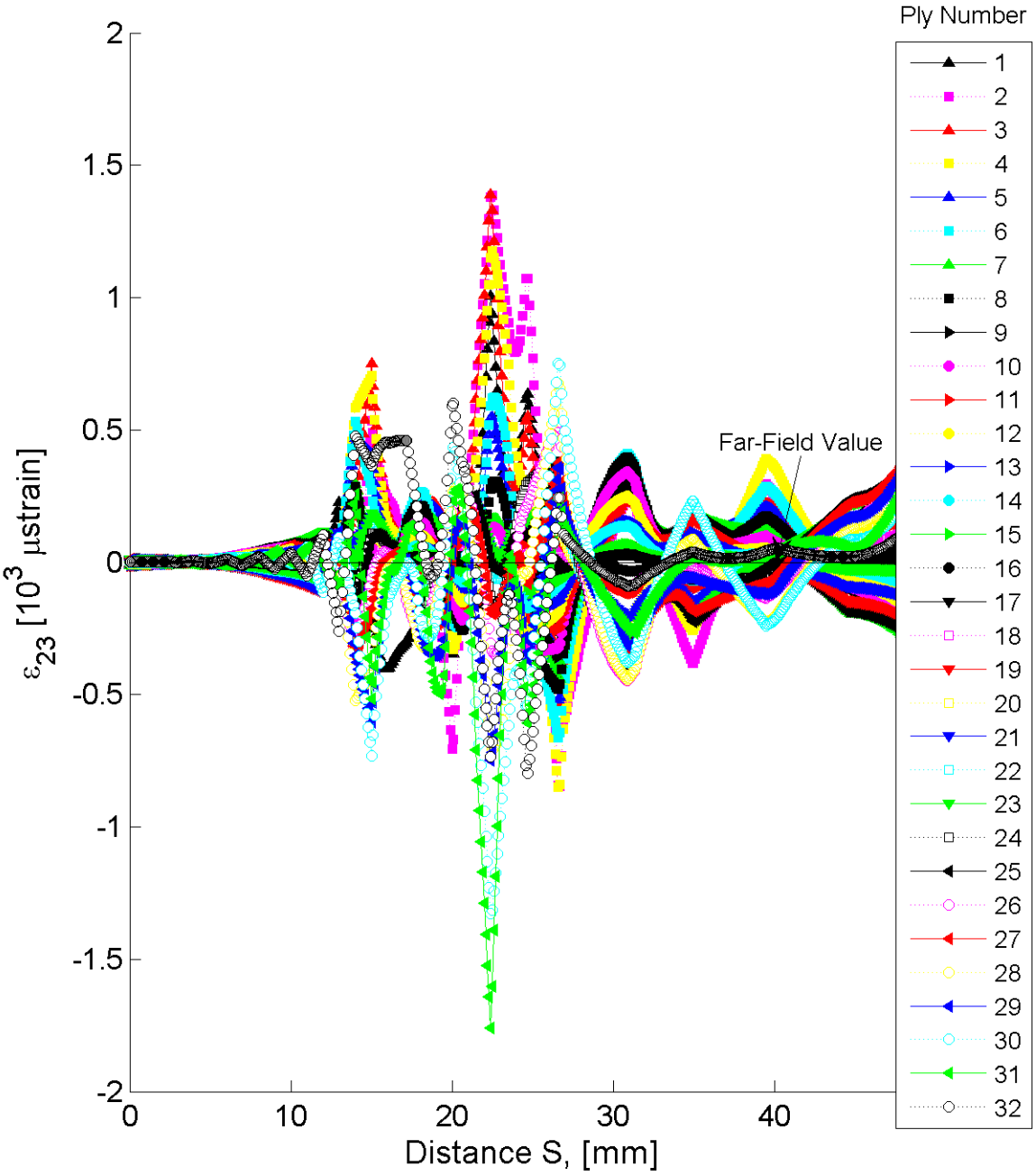

Figure 7.153 Plot of ϵ_{23}, in laminate axes, along the path at the midplane of each ply for the delamination model with laminate of $[+15/-15]_{16T}$.

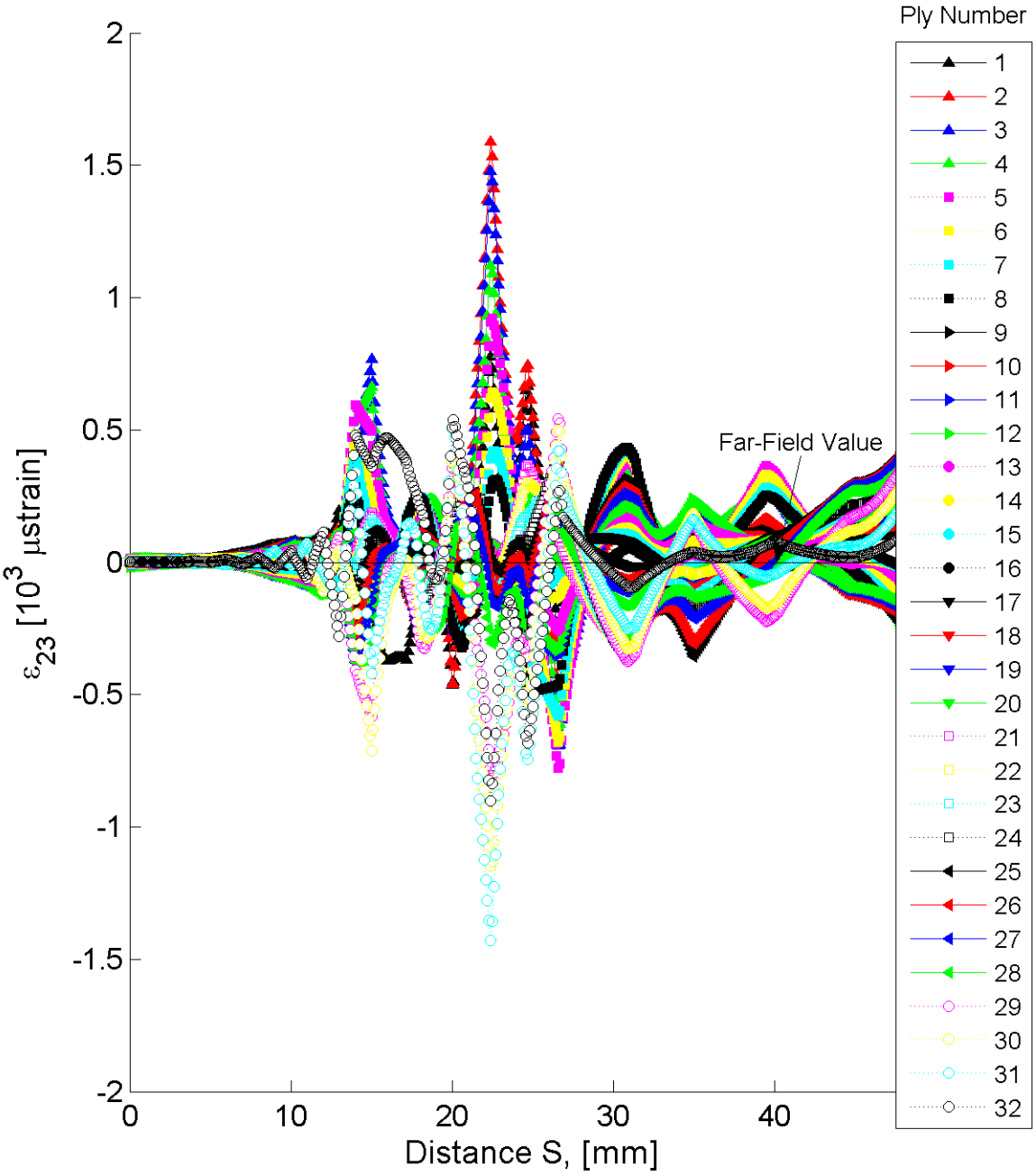

Figure 7.154 Plot of ϵ_{23}, in laminate axes, along the path at the midplane of each ply for the delamination model with laminate of $[+15_4/-15_4]_{4T}$.

[THIS PAGE INTENTIONALLY LEFT BLANK]

Chapter 8

Discussion

The objective of this work is to investigate and identify lengthscale effects associated with damage in composite materials and their structures, to investigate their interactions, and to determine how these lengthscales vary across levels of composites in order to assess the overall response of composite structures. As discussed in Chapter 3, this objective is an advancement in a much larger pursuit towards developing a new methodology that utilizes composite failure and material data collected across all levels in order to predict the occurrence of damage and its effects at any operative level of composite structures. Lengthscales associated with each damage mode, as well as the structural features included within this investigation, and their interactions and importance, are discussed within this chapter based on observations of the experimental and numerical results presented in Chapters 6 and 7. Additional work required to further investigate open issues identified during this work is suggested.

8.1 Lengthscales of Composite Damage

Identifying the lengthscales involved in composites is an important step in advancing the understanding of damage and failure of composites and structures made from such. Many lengthscales exist in the context of composites, from the micro-scale (or even the nano-scale in such systems), to the meso-scale, up to the macro-scale. As the scale of interest changes, so do the critical lengthscales that influence the behavior of

the overall composite structural system. The critical lengthscales for each of the five individual damage modes are presented and discussed in Section 8.1.1. These lengthscales are linked to the constituents of the composite material. When multiple modes of damage interact, the critical lengthscale(s) change. Two lengthscale interactions are presented and discussed in Section 8.1.2.

8.1.1 Lengthscales of Individual Damage Modes

Critical lengthscales for each of the five individual damage modes of the composite material, as identified in Section 2.1, are presented herein. These five individual damage modes are fiber fracture, matrix cracking, fiber microbuckling, interfacial debonding, and delamination. The critical lengthscales are identified from the literature review (Chapter 2), experimental observations (Chapter 6), and/or results of the finite element models (Chapter 7). A new lengthscale is defined for the damage modes of matrix cracking and delamination. The critical lengthscale for each of the five damage modes is presented in the same presentation order as in Section 2.1. As presented in Section 3.1, the necessity of recognizing two damage regimes is important for characterizing lengthscales associated with each of the damage modes. The first regime involves the initiation of damage, where there are no interactions between damage modes. The second regime involves damage propagation and may include interaction of damage modes. Lengthscales associated with individual damage modes were identified for both regimes, and lengthscales associated with the general propagation of damage were identified for the second regime, thereby allowing investigation of how the critical lengthscale(s) controlling the damage mode(s) change(s) (if they do) across regimes. The lengthscales of the individual damage modes discussed in this section focus on the critical lengthscales of the initiation regime.

The critical lengthscale of the initiation of the fiber fracture damage mode is the fiber diameter [e.g., 5, 13, 15, 17, 18, 20]. This critical lengthscale is identified in Section 2.5.1 of the literature review, with additional lengthscales associated with fiber fracture discussed in Section 2.1.1. The additional lengthscales, fiber length

and inter-fiber spacing, are identified to have less effect on the fiber fracture damage mode than the critical lengthscale. The additional lengthscales become important as the damage mode propagates. As identified in the literature, the strength of fibers increases as the fiber diameter decreases. This increase in strength is attributed to the probability of fewer flaws being present in fibers of smaller diameter.

For the initiation of the damage mode of matrix cracking, no single lengthscale is identified as "critical." Multiple lengthscales of the matrix cracking damage mode are identified in the literature [e.g., 2, 6, 24–26, 30, 109]. These include the void/nucleation size for the initiation of microcracks, ply thickness, spacing between cracks, and the length of the matrix crack. The latter two lengthscales are associated with the general propagation of matrix cracking, not the initiation regime. The lengthscales associated with matrix cracking are discussed in Section 2.1.2.

One of the outcomes drawn from the literature review was the need to define a "length" associated with the mismatch angle between plies. In order to allow an investigation of the influence of the mismatch angle between plies via a database, a new parameter is proposed herein:

$$L_\gamma \equiv 1 \cdot \gamma \tag{8.1}$$

where L_γ is herein defined as a normalized length associated with the mismatch angle between plies, with the mismatch angle expressed in radians. This normalized length is thus equivalent to the arc length swept by a unit radius over the angle γ, with γ defined as the absolute value of mismatch angle between plies. This mismatch angle ranges from 0° to 90° initially and is then expressed in radians using a value times π. This proposed definition allows the mismatch angle to be written in a similar manner as a laminate stacking sequence. As an example, a laminate with a stacking sequence of $[30/-30/0/90]_{2S}$ has normalized mismatch lengths written as: $L_\gamma = \pi[1/3, 1/6, 1/2, 1/3, 1/3, 1/6, 1/2, \bar{0}]_S$. The importance of the normalized mismatch lengthscale in the initiation and propagation regimes requires further investigation. In addition, investigation is required in order to determine the influence of the effective

ply thickness on this lengthscale.

For the damage mode of microbuckling, two critical lengthscales exist for the initiation regime. As identified in Section 2.1.3, two different theories on microbuckling have emerged in the literature. These two theories are referred to as elastic microbuckling and plastic microbuckling. There is a corresponding critical lengthscale for each of the theories, as identified from the literature and discussed in Section 2.5.1. For elastic microbuckling, the critical lengthscale for initiation is on the order of a fiber diameter or smaller [e.g., 3]. For plastic microbuckling, the critical lengthscale for initiation is on the order of ten to twenty fiber diameters [e.g., 19, 31, 33, 35, 36, 42]. Microbuckling was not observed experimentally in this work, nor were analytical models of the modes analyzed during this work.

For the damage mode of interfacial debonding, the critical lengthscale for initiation is on the order of tens of fiber diameters [e.g., 24, 43–49, 51–53]. This critical lengthscale is identified in Section 2.5.1 of the literature review, with additional lengthscales associated with interfacial debonding discussed in Section 2.1.4. Lengthscales associated with the stress state acting at the interface of the fiber and matrix are not identifiable from the data available in the literature. Additional work is required in order to investigate the influence of these lengthscales. Interfacial debonding was not observed experimentally in this work, nor were analytical models of the mode analyzed during this work.

For the damage mode of delamination, two critical lengthscales influence the initiation behavior of the mode. These critical lengthscales are the laminate thickness and the ply thickness [e.g., 4, 6, 30, 55–65], as identified in Section 2.5.1. Additional lengthscales associated with delamination are discussed in Section 2.1.5. As with matrix cracking, one of the outcomes drawn from the literature was the need to define a "length" associated with the mismatch angle between plies. The mismatch angle between plies was identified in the literature to influence the behavior of delamination, as presented in Section 2.1.5 [e.g., 4]. The same definition of the mismatch lengthscale presented in Equation 8.1 is used for investigating delamination. While the current lengthscales for delamination are defined, one consideration for the future is

that changes in the constituents may change the critical lengthscales associated with delamination. For example, current research is investigating strengthening inter-ply strength by adding carbon nano-tubes between plies [e.g., 152]. The introduction of a new constituent also introduces new lengthscales, which may change the critical lengthscales associated with the damage mode.

8.1.2 Lengthscale Interactions

Once damage modes have initiated, the critical lengthscales discussed in Section 8.1.1 rarely occur in isolation, but instead interact with critical and non-critical lengthscales of other damage modes, damage types, and structural features. This is the regime of damage propagation. Interactions with lengthscales associated with other damage modes and structural features occur in general situations of the regime of propagation. Most generally, only in the case of controlled coupon-level specimens is it possible to isolate the influence of the lengthscales of the initiation regime from those of the propagation regime. The interactive issues of lengthscales of the propagation regime, for each of the damage modes discussed in Section 8.1.1, are discussed in this section. In addition, a unique damage type that demonstrates mode interaction of damage modes is presented.

The majority of experimental specimens exhibiting fiber fracture reveal the interactive nature of the mode as it propagates. The experimental results, as presented in Section 6.2, indicate that this damage mode is independent of effective ply thickness. The comparison database, presented and discussed in Section 6.2, enabled lengthscale effects associated with fiber fracture to be investigated for each of the four specimen types. For the single-edge-notched specimens, no conclusions can be made, as there are no trends observed in the results. As discussed in Section 4.1, some items of the single-edge-notched specimen set were missing, creating a sparsely filled database.

Within the double-edge-notched specimens, the effective ply thickness has no influence on the presence, or lack thereof, of fiber fracture for angle-ply laminates with low fiber angles (i.e., θ equal to 15° and 30°). The damage database presented in Chapter 6 reveals that the same load paths, without considering load magnitude (specimens

were tested until a drop in load-carrying capability was observed, indicating damage had initiated and propagated), initiate fiber fracture for both the single-ply and four-ply effective ply thickness laminates, as indicated in the graphs shown in Figures 6.29, 6.30, 6.31, and 6.32. The angle-ply laminates with θ equal to 60° do not exhibit clear dependency on the effective ply thickness, but are not independent thereof as are the laminates with values of θ of 15° and 30°. The load paths that 'activate' fiber fracture in the single-ply and four-ply effective ply thickness laminates with θ equal to 60° are shown in Figures 6.33 and 6.34. Increasing the fiber angle to θ equal to 75°, a clear dependency on the effective ply thickness and load path is exhibited as the load paths that 'activate' fiber fracture are different for single-ply and four-ply effective ply thickness as shown in Figures 6.35 and 6.36. Across all the laminates, load paths with a component in compression and another component in either bending, twisting, or rotation (as described in Section 4.2) are present in the majority of specimens with 'active' fiber fracture. In order to determine if the trend in the higher angle laminates is a direct observation of a change in fiber fracture critical lengthscale or if the observation is a result in a changed interaction, finite element models for each load path (only the results of uniaxial tension are considered in Chapter 7), as described in Section 4.2, would need to be worked in order to investigate structural lengthscale and identify if an interaction is occurring. In addition, the experimental testing should be repeated, with testing stopped at incremental loading levels in order to allow the lengthscales of the initiation and propagation regimes to be investigated (i.e., stopping loading at incremental levels in order to conduct damage inquiries), as well as testing a statistically significant number of specimens.

Within the results for the open-hole tension specimens, a conclusion cannot be made regarding the influence of the effective ply thickness on the presence of fiber fracture. Fiber fracture is observed in 14 of the 26 specimens with the single-ply effective ply thickness laminate of $[+45/0/\text{-}45]_{4S}$, and in 15 of the 25 specimens with the four-ply effective ply thickness laminate of $[+45_4/0_4/\text{-}45_4]_S$. Investigating the results from the two hole sizes indicates that there may be interaction between the geometric lengthscales of the hole diameter and the constituent lengthscales of the effective ply

thickness on the presence of fiber fracture. Fiber fracture is observed in 2 of the 9 specimens of the single-ply effective ply thickness laminate with a hole diameter of 0.5 in, whereas 4 of the 8 specimens of the four-ply effective ply thickness laminate with a hole diameter of 0.5 in exhibit fiber fracture. For the specimens with a hole diameter of 1.0 in, 7 of the 9 specimens of the single-ply effective ply thickness laminate, and 5 of the 9 specimens of the four-ply effective ply thickness laminate exhibit fiber fracture. However, a statistically significant number of specimens were not tested and the maximum loading level varied between specimens. For each combination of laminates and load paths, only two repetitive specimens were tested. Additional testing is required to further investigate if there is an actual interaction between the lengthscales of the geometry and constituents. Such testing should include incremental loading levels to allow the lengthscales of the initiation and propagation regimes to be investigated (i.e., stopping loading at incremental levels in order to conduct damage inquiries), as well as testing a statistically significant number of specimens.

As with the results of the open-hole tension specimens, conclusions cannot be made from the database results regarding the presence of fiber fracture for the two laminates of the ply-drop specimens. The laminate configuration of the ply-drop specimens is [X, X_D, X]$_T$ where 'X' is a sublaminate and the subscript 'D' indicates the dropped sublaminate. The technique used for dropping the center sublaminate, X_D, is to have each successive ply shorter in length by 1.0 mm within the ply drop region. This results in twelve 'steps' to go from the [X, X_D, X]$_T$ laminate to the [X, X]$_T$ laminate as illustrated in Figure 4.7. The two sublaminates, X, used in the specimens are $[+45/0/\text{-}45]_{2S}$ and $[+45_2/0_2/\text{-}45_2]_S$. The database indicates that fiber fracture is observed in 2 of the 9 ply-drop specimens. One of the specimens has a single-ply effective ply thickness sublaminate while the other specimen has a two-ply effective ply thickness sublaminate. These two specimens were taken to the largest axial load of all the ply-drop specimens. Additional experimental testing is required to further investigate if there is an interaction between the lengthscales of the geometry and constituents. Such testing should include incremental loading levels to allow the lengthscales of the initiation and propagation regimes to be investigated

(i.e., stopping loading at incremental levels in order to conduct damage inquiries) as well as testing a statistically significant number of specimens.

Experimental observations across all the specimen types and laminates indicate that fiber fracture propagates in a ragged manner. The fiber fracture damage mode was observed to propagate along a jagged 'front,' as seen in the upper left portion of the specimen shown in Figure 6.15. The lengthscale associated with the geometry of the propagation path of fiber fracture is on the order of tens of fiber diameters. Other damage modes are also typically observed near the propagation path of fiber fracture. The proximity of these other modes to that of fiber fracture indicates that the critical lengthscale of fiber fracture interacts with these other modes within the propagation regime. Analytical models of fiber fracture were not a part of this work, and thus the interaction of the stress and strain fields associated with fiber fracture and their interaction with other fields were not specifically investigated. As indicated for each of the specimen types, additional experimental testing and analytical modeling is required in order to identify the lengthscales interacting during the propagation of the fiber fracture damage mode.

After initiating the matrix cracking damage mode, the propagation regime is entered. The comparison database, presented and discussed in Section 6.2, enabled lengthscale effects associated with matrix cracking to be investigated for each of the four specimen types. As was the case for the fiber fracture damage mode, no conclusions can be made for matrix cracking within the single-edge-notched specimens as there are no trends observed in the results.

For the double-edge-notched specimens, the propagation of matrix cracking in the single-ply effective ply thickness laminates is more dependent on load path than in the four-ply effective ply thickness laminates. This is clearly exhibited for the laminates with θ equal to 15°. As an example, specimens for a single load case, that of the tensile load path (load path #4 from Table 4.5), reveal dependence on the effective ply thickness. The single-ply effective ply thickness laminates have a strong dependence on the ply angle, with neither of the two specimens with θ equal to 15° exhibiting matrix cracking and one of the two specimens with θ equal to 30° exhibiting matrix

cracking. The single-ply effective ply thickness laminates with higher ply angles (i.e., θ equal to 60° and 75°) exhibit matrix cracking in all the specimens (i.e., 4 of the 4 specimens). For the four-ply effective ply thickness laminates for this load path, all the specimens exhibit matrix cracking, with the exception of 1 of the 2 specimens with θ equal to 30°. Therefore, as the effective ply thickness increases, the importance of the ply angle on the presence of matrix cracks decreases. This dependence is also exhibited within the specimens for other load paths. The presence of matrix cracking is more dependent on the load path for the single-effective ply thickness laminates with lower angle plies, with the influence of the angle ply decreasing as the effective ply thickness increases. For these results, the presence of matrix cracking does not explicitly exclude the presence of other damage modes. Additional specimens tested for each of the load paths is required in order to have statistically significant results. Such testing should include incremental loading levels to allow the lengthscales of the initiation and propagation regimes to be investigated (i.e., stopping loading at incremental levels in order to conduct damage inquiries).

For the open-hole tension specimens, the lengthscale of the structural feature dominates the ply mismatch length of the two effective ply thickness laminates investigated during this work. The trend of matrix cracking running along the outer ply angle, within a triangular region for the single-ply effective ply-thickness laminate and within a diagonal region for the four-ply effective ply thickness laminate, as presented in Section 6.1.3, are observed within most of the specimens, indicating that any influence of the effective ply thickness on the behavior of matrix cracking is overshadowed by the geometric lengthscales. This is also true for the ply-drop specimens. Additional open-hole tension specimen testing should be conducted with laminates containing varying ply angles in order to investigate the influence of the ply mismatch angles. The two laminates (i.e., $[+45/0/\text{-}45]_{4S}$ and $[+45_4/0_4/\text{-}45_4]_S$) investigated during this work do not provide data on such influences. As with the suggestions for additional testing of the other specimens, testing should include incremental loading levels to allow the lengthscales of the initiation and propagation regimes to be investigated.

For the ply-drop specimens, the geometric lengthscales again have a greater influence on the presence of matrix cracking than the influence of the effective ply thickness for the two laminates investigated. Both effective ply thickness laminates, [X, X_D, X]$_T$ where 'X' is a sublaminate of either [+45/0/-45]$_{2S}$ or [+45$_2$/0$_2$/-45$_2$]$_S$, exhibit the same damage trends. Matrix cracking within the ply-drop specimens is observed in the top and bottom plies, as well as through the thickness, in the region of the transition from the ply-drop region to the dropped region. In these specimens, 4 of the 5 single-ply effective ply thickness laminates, and 2 of the 4 two-ply effective ply thickness laminates exhibit matrix cracking. The three ply-drop specimens without matrix cracking exhibit no visual damage (i.e., the specimens were not damaged). Therefore, all ply-drop specimens that exhibit damage have matrix cracking present. As with the open-hole tension specimens, the influence of ply mismatch angles could not be investigated from the specimens tested during this work since ply angles were not altered. Multiple laminates with different angle plies are suggested for future study in order to allow investigation into these influences. In addition, laminates with effective ply thicknesses greater than two are suggested. This will increase the lengthscales associated with the effective ply thickness in order to investigate influences of such. The additional testing should include incremental loading levels to allow the lengthscales of the initiation and propagation regimes to be investigated.

Lengthscales associated with gradients in the strain fields near matrix cracks are dependent on the orientation of the crack relative to the loading direction. For the special case of stitch cracking, a form of matrix cracking described in Section 2.2, finite element models were analyzed in order to investigate lengthscales associated with the stress and strain fields near the damage. For each of the models, with the model setup described in Section 7.2.5, load was observed to "bypass" and "carry-through" the damaged region, as presented in Section 7.3.5. This "bypass" of load corresponds to the reduced capability of load paths through the region of damage, requiring some load to pass around the region while some load is carried across the intact portion of the damaged region. The amount of load "bypass" varies for each laminate angle due to the details of the geometry of the stitch cracks. The geometry

formed by the combination of stitch cracks and traditional matrix cracks in laminates with θ equal to 15° and 75° nearly form a traditional fracture mechanics sharp crack (i.e., 'slit'). For laminates with θ equal to 15°, the 'slit' crack is nearly parallel to the loading direction, and the region that has reduced load-carrying capability is relatively small. For laminates with θ equal to 75°, the 'slit' crack is nearly perpendicular to the loading direction, and the region that has reduced load-carrying capability is relatively large. In general, as the laminate angle increases, the region of damage becomes more perpendicular to the original load direction. Thus, as the laminate angle increases, the region of damage causes greater reduction of load-carrying capability. However, the ability of the damaged region to carry load must also be considered.

The results of the analytical models, presented in Section 7.3.5, allow quantification of the load carried through the damaged region versus that which must be carried around the region, referred to as "bypass." The strain value for the stress carried through the damaged region, as defined and described in Section 7.3.5, is dependent on both the laminate angle and the effective ply thickness. This "carry-through" strain value for the single-ply effective ply thickness laminates of 15°, 30°, 60°, and 75° is 7000 μstrain, 4000 μstrain, 2000 μstrain, and 1200 μstrain, respectively. For the four-ply effective ply thickness laminates, these values are 9000 μstrain, 6000 μstrain, 2500 μstrain, and 1800 μstrain, respectively. The far-field strain in each case is 10000 μstrain. The four-ply effective ply thickness laminates exhibit higher "carry-through" capability compared to the single-ply effective ply thickness laminates of the same angle. Single-ply effective ply thickness laminates have a shorter through-thickness distance to redistribute the "carry-through" load into neighboring plies with matrix cracks, resulting in fairly uniform strain fields through the thickness of the laminates. Four-ply effective ply thickness laminates have a greater through-thickness distance to redistribute the "carry-through" loads, with the results exhibiting a magnification of stress/load in the mismatch angle plies at the corners of the stitch cracks. As previously noted, the orientation of the stitch cracks relative to the loading direction also has a strong influence on the amount of load that must bypass the region of damage. The laminate with θ equal to 15° has a smaller region

of damage that is perpendicular to the loading (i.e., the projection of the damaged area to a plane normal to the direction of loading). It also has the greatest capability to carry the load through the region of damage as the intact material of the stitch crack plies is most parallel, compared to the other laminates, to the loading direction. The combination of a smaller projected damage area and fibers that are more closely aligned with the loading direction results in a decrease in the amount of load that needs to "bypass" the damage for smaller laminate angles. In contrast, the amount of "carry-through" capability decreases as the laminate angle increases (i.e., as the stitch cracks become more perpendicular to the applied loading), and the amount of "bypass" load increases as the laminate angle increases.

Within the experimental specimens, delamination was influenced by the effective ply thickness of a laminate for cases when applied loading contained compressive and/or shear components. In the case of the open-hole tension specimens, no difference in the occurrence of delamination was exhibited between the single-ply and four-ply effective ply thickness laminates, as both exhibited delamination occurring at the interface between mismatch ply angles within the regions described in Section 6.1.3. However, for the single-edge-notched specimens, uniaxial compression caused delamination in all specimens, with the exception of the laminates with θ equal to 30°. For the single-edge-notched specimens, delamination typically initiated near the notch tip and propagated to the edge of the specimen. As the extent of delamination increased, the delamination front would propagate to the grip boundaries and the delamination front would advance back toward the notch. Within the single-edge-notched specimens, the load paths with compressive and/or shear components increased the presence of delamination, but only in the uniaxial compression case was delamination present in all but one specimen. For the double-edge-notched specimens, delamination typically initiated from a matrix crack near one of the two notch tips and propagated to the grip boundary before the propagation front began to grow toward the centerline of the specimen. Increased effective ply thickness increased the number of specimens exhibiting delamination for the lower angle laminates (i.e., θ equal to 15° and 30°). The presence of delamination in the higher angle laminates

(i.e., θ equal to 60° and 75°) were not influenced by the change in effective ply thickness, as the single-ply and four-ply effective ply thickness laminates exhibited roughly the same number of specimens exhibiting the damage mode.

The open-hole tension and ply-drop specimens were loaded only in uniaxial tension. However, the structural features of the open-hole and the ply-drop created complex through-thickness loading. Delamination was observed in every ply-drop specimen that exhibited damage, regardless of the effective ply thickness. In order to draw further conclusions on the influence of the effective ply thickness on the damage behavior within open-hole tension and ply-drop specimens, as well as the lengthscale interactions occurring within these specimens, additional experimental and analytical research is required. Detailed stress and strain fields surrounding the open hole and throughout the ply drop region should be investigated and related to the initiation and propagation of damage within experimental specimens. The additional experimental testing should include incremental loading levels to allow the lengthscales of the initiation and propagation regimes to be investigated. As suggested earlier, additional laminates should be considered for the experimental testing of the open-hole tension and ply-drop specimens in order to investigate the effects on the delamination initiation and propagation.

Lengthscales associated with gradients in the strain fields near a delamination considered in isolation are dependent on the location relative to the delamination front. Finite element models were analyzed for different laminates, as described in Section 7.2.5 with the results of the models discussed in Section 7.3.5, in order to investigate lengthscales associated with the stress and strain fields associated with the damage mode. For the cases analyzed, the strain fields in the "wake" (i.e., trailing the delamination front) are uniform (i.e., there are relatively no gradients). The strain fields in the "wake" of the delamination front were observed to reach an "interior far-field value," different from the far-field value predicted from CLPT. The "interior far-field values" are independent of the effective ply thickness. Prior to the delamination front, the strain fields do not approach the analytical far-field results within the observable lengthscale of the models, as discussed in Section 7.3.5, which is a distance

of 30 mm beyond the delamination front. The largest gradients of the strain fields are observed between the delamination front and a distance of approximately 6 laminate thicknesses. This distance is observed to be independent of the effective ply thickness.

A unique damage type and associated lengthscale interaction discovered during this work involves the "transverse zigzag" damage type. "Transverse zigzag" is a combination of matrix cracking, stitch cracking (i.e., a type of matrix cracking, as described in Section 2.2), and delamination damage modes. These three modes interact to form the "transverse zigzag" damage type. The through-ply matrix cracks (of both the stitch cracks and the traditional matrix cracks) connect via delaminations between mismatch angle plies. In all experimental specimens exhibiting "transverse zigzag," stitch cracking is present and was observed in the results of the computed microtomography (CμT) investigations of the single-edge-notched and double-edge-notched specimens. The "transverse zigzag" damage type is not found reported in previous literature. Literature on stitch cracking is very limited and fails to identify delaminations between ply interfaces. The previous studies that identify stitch cracking failed to look at damage in the through-thickness plane (i.e., x-z or y-z plane), so it is possible that "transverse zigzag" could have gone unnoticed. A similar damage type found in the literature is "delamination switching," described in Section 2.2. The delamination switching damage type could also be characterized with a zigzag shape, where a delamination propagates along a ply interface and a matrix crack through a ply allows the delamination to switch to a neighboring interface. The delamination continues propagating along its original direction, but at a "switched" interface. There are cases where the delamination will "switch" back to the original ply interface, creating a zigzag shape between ply interfaces as opposed to "transverse zigzag" damage where the zigzag shape is observed to occur in a relatively narrow band and occurs through the entire thickness of the laminate, with an example shown in Figure 6.1.

This damage type of "transverse zigzag" is observed in the experimental specimens of the single-edge-notched, double-edge-notched, and open-hole tension specimen types. Within the open-hole tensions specimens, "transverse zigzag" is not

as 'clean' (i.e., the zigzag does not have the exact repetitive geometry as observed in those of the single-edge-notched and double-edge-notched specimens) as in the single-edge-notched and double-edge-notched specimens due to the presence of 0° plies (open-hole tension specimens have laminates with +45°, −45°, and 0° plies, while the single- and double-edge-notched specimens are angle-ply laminates having no 0° plies). The presence of the 0° plies requires additional damage modes and/or interactions in order to propagate the damage in the transverse direction.

The lengthscales involved with the interactions of damage modes involved in the "transverse zigzag" damage type include the laminate thickness, the normalized ply mismatch length, L_γ, and the lengthscales associated with matrix cracking (as described in Section 8.1.1). In addition, new lengthscales are introduced from transverse zigzag: the "width" of the zig-zag pattern (i.e., in-plane length), the angle relative to loading, and the length of the propagation of the damage type. The results from the CμT scans, presented in Section 6.3, reveal that the "transverse zigzag" damage type propagates along fiber angles, maintaining the same zigzag shape, as shown in Figure 6.1, along the entire propagation path. Therefore, the lengthscales influencing the damage type propagate with the type, but do not change as the type propagates.

Another interaction commonly observed in the experimental specimens was mode "switching." This interaction involves a change to another damage mode along the propagation of a different damage mode. This interaction is found to be influenced by the effective ply thickness, with mode switching occurring more frequently in single-ply effective ply thickness laminates. Within larger effective ply thickness laminates, the damage maintains the initiated mode. The in-plane locations of the mode "switch" always occurred near a free edge or centered between a structural feature and a free edge. Mode switching was not observed 'close' (i.e., within 10 laminate thicknesses) to structural features, wherein a free-edge is not considered a structural feature. This suggests a change in the stress/strain fields outside the region influenced by the structural feature. Further discussion on the influence of structural features is presented in Section 8.2.

8.2 Effect of Structural Details

Structural features introduce additional lengthscales beyond those of the basic damage modes. These lengthscales are manifested via the interaction and influence of the stress and strain fields that control the initiation and propagation of the basic damage modes. As the geometric shape and size of a structural feature changes, so do the associated lengthscales in the stress and strain fields. The interaction of lengthscales associated with the basic damage modes and the structural features are presented in Section 8.3.

Strain gradients resulting from geometric features allow key lengthscales to be identified and investigated. The finite element models of the experimental specimens developed in Chapter 7 permit the gradients of each of the features to be investigated. For the single-edge-notched and double-edge-notched specimens, the lengthscales associated with the structural feature include the notch radius, notch length, specimen width, and specimen gage length. The geometry of these specimens is given in Section 4.1 and 4.2. A normalized characteristic length is defined in Section 7.3.1 which allows measurement of the influence of the notches (i.e., the structural features for these two specimen types) as a function of the laminate. The characteristic length is defined as the distance, perpendicular to the loading direction, from the tip of the notch to the point that the strain returns to within a designated percentage of the far-field value. This length is normalized by the radius of the notch. Two percentages, 10% and 5%, were selected in order to develop the characteristic length concept.

These normalized characteristic lengths for the in-plane results of the single-edge-notched specimen are given in Table 7.6. These lengths show a dependence on the laminate angle, with laminates with larger laminate angles failing to reach the selected percentage of the far-field value before the edge of the specimen. In addition, each component of strain for a given laminate exhibits a different normalized characteristic length (i.e., the characteristic length for ϵ_{11} is not necessarily equal to that for ϵ_{22}).

The normalized characteristic lengths for the in-plane results of the double-edge-notched specimen are given in Table 7.15. As for the single-edge-notched results, each

component of strain for a given laminate exhibits a different characteristic length. These characteristic lengths of the double-edge-notched specimen again show a dependence on the laminate angles with those for larger laminate angles, laminates with θ equal to 60° and 75°, being greater in length than the distance to reach the centerline of the specimen. Therefore, the two notches within the lower angle laminates act independently, while the two notches of the higher angle laminates have influence on the stress and strain field of the other. Thus, for the higher angle laminates of the double-edge-notched specimen, consideration needs to be taken on the influence between the two notches, while for the lower angle laminates, each notch can be analyzed independently. With the laminates used for the double-edge-notched specimens, this also allows for the influence of effective ply thickness to be investigated. For each of the in-plane results, the normalized characteristic length for a given component is independent of the effective ply thickness.

As with the double-edge-notched specimen, the characteristic length of the open-hole tension specimen is dependent on the angle of the laminate and independent of the effective ply thickness. The characteristic length of the open-hole tension specimen is defined as the distance, perpendicular to the loading direction, from the edge of the hole to the point that the strain returns to within a designated percentage of the far-field value. This length is normalized by the radius of the hole. The normalized characteristic lengths for the in-plane results of the open-hole tension specimens are given in Table 7.25. As with the single-edge-notched and double-edge-notched specimens, each component of strain has a different normalized characteristic length for a given laminate. As for the double-edge-notched specimen, the effective ply thickness is not observed to influence these lengths. In addition, the open-hole tension specimens allow investigation of the in-plane scaling of the structural feature. The normalized characteristic length of the open-hole specimen is found to be independent of the scaled in-plane dimensions of the specimen, indicating that additional information is not gained from two sizes of open-hole tension specimens.

A normalized characteristic length for the ply-drop specimens was not defined. Unlike the other specimen types, which have an obvious structural lengthscale (i.e.,

the radius of the feature), the ply-drop specimens have five fundamental lengthscales; the undropped laminate thickness, the dropped laminate thickness, the sublaminate thickness, the length of the ply-drop region, and the pitch (i.e., distance between) of the ply drops. Additional experimental testing to establish a statistically significant number of tested ply-drop specimens is required in order to determine an appropriate characteristic length for these specimens.

It is suggested to expand the concept of the normalized characteristic length in order to create in-plane 'maps' of the region of influence of the structural feature. In order to accomplish this, the definition of the characteristic length, as defined in Section 7.3.1, would be modified to look at the characteristic length surrounding the structural feature. This would involve evaluating the characteristic length at a full range of angles of ϕ, the angle measured counterclockwise from a point located at the tip of the notch, from 0° to 360°. The characteristic length defined within this work for the single-edge-notched, double-edge-notched, and open-hole tension specimens results in a length along the direction normal to the loading (i.e., ϕ equals $-90°$ for each of the specimens). Defining the characteristic length at a single angle relative to the loading allowed the concept to be developed and to assess its ability to characterize structural features. As demonstrated within this work, the characteristic length defines a measure of the influence of the structural feature on the resulting strain field. Additional information on the influence of the structural feature can be collected by extending the concept of the characteristic length into characteristic 'maps' of influence. The information captured by these 'maps' could be input into the damage documentation database, similar to the illustrations of the damage grids and damage sketches discussed in Sections 5.1.2 and 5.1.3.

Additional effects of the single-edge-notched and double-edge-notched specimens are characterized based on the results of the finite element modeling. Both of these specimens exhibit a "transition" area between the "notched" and "unnotched" sections of the specimens. Within this region, the strain transitions from the far-field strain level in the unnotched region to the near-zero strain of the notched region. The extent of these regions is influenced by the laminate. In laminates with smaller ply

angles (i.e., θ equal to 15° and 30°), the transition region is located in a narrow band above and below the notch tip. In laminates with larger ply angles (i.e., θ equal to 60° and 75°), the transition is stretched over a larger region. For the single-edge-notched specimen, the width of the transition band (i.e., the y-distance from the 0 μstrain isoline to the far-field strain isoline of 10000 μstrain) at an x-distance of 6.7 notch radii from the center of the notch, equivalent to the midlength of the notched section, is 7.1, 10.2, 14.3, and 16.3 notch radii in length for the laminates with θ equal to 15°, 30°, 60°, and 75°, respectively. For the double-edge-notched specimen, the width of the transition band at an x-distance of 5.0 notch radii from the center of the notch, equivalent to the midlength of the notched section, is 5.6, 7.1, 9.8, and 11.8 notch radii for the single-ply effective ply thickness laminates with θ equal to 15°, 30°, 60°, and 75°, respectively, and 8.1, 7.8, 9.6, and 11.5 notch radii for the four-ply effective ply thickness laminates with θ equal to 15°, 30°, 60°, and 75°, respectively. The effective ply thickness has minimum influence on the width of the transition region, with the exception of the double-edge-notched specimen laminate with θ equal to 15°. The largest gradients are observed within the transition regions of these specimens. For the double-edge-notched specimens, the finite element analysis results indicate that the left and right notches have slight influence on each other (i.e., far-field results are not recovered at the centerline of the specimen, which is halfway between the left and right notch tips).

The influence of boundaries was observed throughout the experimental specimens of this work. While each of the experimental specimens had structural features with associated lengthscales, the boundaries used to test these specimens contributed an additional lengthscale. The influence of the boundaries is clearly observed in the single-edge-notched and double-edge-notched specimens. In these specimens, the grips used to impart loading within the specimen were relatively close to the structural feature, where the distance between the notch and the grip line is 12.4 notch radii (r_0) for the single-edge-notched specimen, and 8.9 notch radii for the double-edge-notched specimens, as described in Sections 4.1 and 4.2. As a result, there were a number of cases where damage would propagate from the structural feature and

eventually intercept the grip boundaries. Of the single-edge-notched specimens, 29 of 182 have damage propagation paths that intercept the grip boundary. Of the double-edge-notched specimens, 104 of 1152 have damage propagation paths that intercept the grip boundary.

In 12 of these 29 single-edge-notched specimens and 43 of these 104 double-edge-notched specimens, the damage mode and propagation path were unaffected (i.e., path progresses along original vector with same damage type) by the boundary as the damage propagates 'under' the grips. In all these cases, the damage mode was the "transverse zigzag" damage mode, with a matrix crack propagating along the ply angle, θ, from the notch tip to the edge of the specimen. An example is shown in Figure 6.3. The specimen shown in this figure was the only single-edge-notched specimen to exhibit two "transverse zigzag" damage modes, with one propagation path visible as a matrix crack on the front and back surfaces, and the other propagation path visible as fiber fracture. The majority (7 of the 12) of these single-edge-notched specimens have θ equal to 30°, while 4 have θ equal to 15°, and 1 has θ equal to 60°. Within the double-edge-notched specimens, the damage mode visible on the faces was matrix cracking and stitch cracking. The majority (35 of the 43) of these double-edge-notched specimens have a single-ply effective ply thickness with θ equal to 60°. The other 8 double-edge-notched specimens have θ equal to 30°, with equal numbers having singe-ply and four-ply effective ply thicknesses.

For a minority of the specimens (7 of the 29 single-edge-notched specimens, and 24 of the 104 double-edge-notched specimens) containing damage paths that intercept the grip boundaries, the damage propagation path 'reflects' at the boundary. In all the cases with 'reflections', the damage mode that reflects from the grip boundary is different than the damage mode that propagates to the boundary from the notch tip. The two damage modes involved in all cases with 'reflections' are matrix cracking and fiber fracture. In all the cases with 'reflections', either fiber fracture or a matrix crack propagates along either the positive or negative ply angle, θ, of the angle-ply laminates, from a notch tip to the grip line, where the damage propagation path 'reflects.' The reflecting damage mode switches to matrix cracking or fiber fracture

(i.e., the damage mode switches from that which propagates to the grip line from the notch tip), and then continues to propagate along the changed sense of the reflective ply angle. One such case is illustrated in Figure 6.4, where fiber fracture is observed to propagate along the positive ply angle, $+\theta$, from the notch tip toward the lower grip boundary, then to reflect at the grip line and switch the propagation direction to the negative ply angle, $-\theta$, and switch the damage mode to a matrix crack. Reflections always occur right at the grip line, indicating the lengthscale associated with the boundary grips does not extend beyond the grip in the in-plane direction. Of the single-edge-notched specimens exhibiting a 'reflection', 1 of these 7 have θ equal to 15° while the other 6 have θ equal to 30°. Of the 24 double-edge-notched specimens exhibiting a 'reflection', 9 are single-ply effective ply thickness laminates and 15 are four-ply effective ply thickness laminates. Of these specimens with single-ply effective ply thickness laminates, 2 have θ equal to 15°, 6 have θ equal to 30°, and 1 has θ equal to 60°. Of those specimens with four-ply effective ply thickness laminates, 14 have θ equal to 30° and 1 has θ equal to 60°. The majority (26 of 31) of specimens that exhibit a 'reflection' had θ equal to 30°, indicating that the incident angle of the propagation path to the grip line influences the interaction between the grip and the propagating damage. As presented in Section 6.1.2, the path along the ply angle from the tip of the notch to the edge of the specimen for the laminates with θ equal to 75° does not intercept the grip boundaries. The damage modes of matrix cracking and fiber fracture were observed to propagate along this path. For this reason, the damage modes of matrix cracking and fiber fracture exhibited within laminates with θ equal to 75° are not observed to intercept the boundaries, nor are influences from the boundaries observed in these specimens.

Besides 'reflections', other interactions at the grip boundary were observed. These other interactions include changes in damage mode and/or a change in the propagation path, or arresting of the damage mode at the grip boundary. Such interactions were observed in 10 of the 29 single-edge-notched specimens, and 37 of the 104 double-edge-notched specimens. Within these single-edge-notched specimens, 2 specimens with θ equal to 30° exhibited a change in the propagation path of a matrix crack

after passing the grip boundary. In these 2 cases, the matrix crack propagation path before the grip line was along θ, but after the grip line the propagation path was approximately 8° greater than θ, with the matrix crack arrested approximately 1.5 laminate thicknesses beyond the grip line. There were 3 specimens with θ equal to 30° that had matrix cracks propagating along θ from the notch tip that arrested at the grip boundary. Finally, 5 specimens (3 with θ equal to 15° and 2 with θ equal to 75°) had delamination initiate near one of the notch tips and propagate, primarily along the θ direction, to the grip line, where the propagation changed paths and became parallel to the grip boundary.

Although delamination was observed to primarily propagate along the θ direction, the exact progression of delamination propagation was not identifiable from the postmortem specimens due to the total amount of delamination and how it extended through the specimen (i.e., postmortem inspection was not able to identify the exact propagation path of the delamination). Despite some observed differences, it can be clearly stated that in all cases exhibiting delaminations, the damage never propagated into the gripped regions. The influence of the grips on the delamination propagation indicates that the compressive action of the grips changed the interply stress and strain field such that the driving forces to continue delamination propagation were affected.

Within the 37 double-edge-notched specimens with interaction at the grip boundary besides 'reflections,' damage was only observed to either arrest or to propagate parallel to the grip boundary. No damage paths were observed to change propagation angle past the grip line. Of these 37 specimens, 27 had single-ply effective ply thickness laminates. Of these 27 cases, 4 specimens had θ equal to 15° and all these had delamination propagate, primarily along θ, to and then along the grip boundary. There were 12 specimens with θ equal to 30° that had the damage, where matrix cracking was always present and fiber fracture and/or delamination was present in approximately 75%, propagate primarily along θ and arrest at the grip. There was 1 specimen with θ equal to 30° that had delamination propagate, primarily along θ, to and then along the grip boundary. The remaining 10 specimens had θ equal to

60°, with 8 having matrix cracking and fiber fracture or delamination present and 2 having only matrix cracking, propagate along θ and arrest at the grip. The other 10 of the 37 specimens had four-ply effective ply thickness laminates. Of these cases, 4 specimens had θ equal to 15°, with 2 of the 4 having matrix cracking, fiber fracture, and delamination propagate along θ and arrest at the grip, and the other 2 of the 4 specimens having matrix cracking and delamination propagate along θ to the grip boundary, with delamination then propagating along the grip boundary. There were 4 specimens with θ equal to 60° that had the matrix cracking and delamination propagate along θ and arrest at the grip, and 2 specimens with θ equal to 60° that had matrix cracking and delamination propagate along θ to the grip boundary, and then had delamination propagate along the grip boundary.

The influence of the grip boundaries is thus dependent on both the ply angle of the angle-ply laminates, and the effective ply thickness of the laminate. Within the single-edge-notched specimens, the specimens with θ equal to 30° exhibit the most reflections and other interactions, the specimens with θ equal to 15° exhibit the second most reflections and other interactions, and the specimens with θ equal to 60° and 75° exhibit no affect. Among the double-edge-notched specimens, as with the single-edge-notched specimens, the specimens with θ equal to 30° exhibit the most reflections and other interactions, with more than twice as many four-ply effective ply thickness laminates exhibiting such behavior as compared to the single-ply effective ply thickness laminates for the given ply angle. The double-edge-notched specimens with θ equal to 60° generally exhibit no affect, with a small number of the four-ply effective ply thickness laminates exhibiting delaminations that either arrest at the boundary or propagate up to and then along the grip boundary. It is further noted that the interaction of the grip boundaries are more likely to arrest propagating damage within single-ply than four-ply effective ply thickness laminates.

Not all specimens types exhibited damage that interacted with the grip boundaries of the specimens. Within the open-hole tension specimens, grip boundaries are not observed to influence the damage. For these specimens, the geometric length-scale associated with hole diameter (based on the finite element analysis results of

Section 7.3.3) is small compared to the in-plane geometry of the specimens. The distance between the upper and lower gripped boundaries and the open-hole is sufficiently large such that these boundaries do not influence damage results. Within the ply-drop specimens, the boundaries are observed to be of secondary importance. The finite element results, presented in Section 7.3.4, indicate that the boundary conditions of the ply-drop specimen have influence up to the ply-drop region. However, the majority of the experimental observations of damage have initiation and propagation located within the transition between the ply-drop region and the dropped region, as discussed in Section 6.1.4. In very few cases is the experimental damage observed to propagate within the dropped region up to the grip boundary.

8.3 Importance of Lengthscales

The investigation and identification of the effects of lengthscales associated with damage in composite materials and their structures, and the determination of how these lengthscales vary across levels in composites provide an important tool that can be used to assess the overall response of composite structures. In undamaged structures, the lengthscales associated with structural details are present in terms of stress and strain gradients, and the lengthscales associated with the initiation of damage modes are present in terms of the key lengths of each of the five basic damage modes, discussed in Section 8.1.1. When damage initiates, the key lengthscale(s) change due to the increased influence of interactions in the damage propagation regime, as discussed in Section 8.1.2. In damaged structures, additional stress and strain gradients, beyond those of the structural details, are created within regions around the initiated damage. These additional gradients have associated lengthscales that interact with both the structural lengthscales and the lengthscales associated with the propagation of the damage mode(s) present within the structure. Thus, the interactive behavior between lengthscales associated with damage modes and lengthscales associated with structural details changes from the initiation regime to the propagation regime. The additional interactions must be considered when identifying key lengthscales of

the propagation regime. Within this section, the interaction of lengthscales associated with different damage modes and with particular structural details, and the importance of the lengthscale concept are presented.

The "observable lengthscale" is an important consideration when investigating lengthscales in experimental specimens and structures. The observable lengthscale, presented in Section 2.5.2, is dependent on the resolution of the inspection technique. In order to observe and study damage in composites, the damage must be resolvable via the inspection technique. An example is the observation of stitch cracks, as described in Section 2.2, which had previously been undetected. Prior to the higher resolution X-ray technique, researchers had not been able to observe this damage type. As inspection methods for composite materials and structures continue to improve, damage modes and damage types previously unknown are being, and may continue to be, identified. As the ability to resolve damage at smaller scales continues to improve, interactions occurring at smaller scales can be studied. As inspection techniques continue to improve, lengthscales not yet identied may be discovered. The new inspection techniques also allow the currently identied damage modes and mode interactions to be studied with greater resolution.

Key lengthscales of the basic damage modes and of four structural details are identified within this work, and can be used when choosing the scale of finite element models. The choice of the key lengthscale is important when conducting investigation via finite element models. This is analogous to the "observable lengthscale" of the experimental inspection techniques presented in Section 2.5.2. In order to conduct lengthscale studies via finite element models, the models must have a resolution at least as fine as the key lengthscale of the mode under investigation. An important point to this is that only the key lengthscale(s) for the current damage state need to be resolved. As it is currently infeasible to have resolution down to the scale of a fiber diameter while modeling large (e.g., a full wing of a commercial airliner) structures, only the scale of the key lengthscale needs to be resolved. As the lengthscale concept is further developed, the key lengthscales will drive the required finite element resolution.

The key lengthscale associated with each of the damage modes increases in size from the initiation to the propagation regime. As identified in Sections 8.1.1 and 8.1.2, the key lengthscales of the fiber fracture and matrix cracking damage modes increase once the propagation regime is reached. In contrast, the damage mode of fiber microbuckling does not exhibit a propagation regime. Instead, after fiber microbuckling initiates (typically plastic microbuckling for reasons described in Section 2.1.3), other damage modes, such as fiber fracture or matrix cracking, initiate within the region that has microbuckled. When this occurs, the key lengthscale momentarily decreases from that of the critical fiber microbuckling lengthscale (i.e., ten to twenty fiber diameters) to that of the initiation lengthscale of the other damage mode. After the initiation of the other damage mode(s) from the region that has microbuckled, the key lengthscale increases in size to that of the propagation regime of the other damage mode. This similar increase in key lengthscale of the delamination damage mode is observed within the results of Section 7.3.5. As identified in Section 8.1.1, the key lengthscales of the initiation regime of delamination are the ply thickness and the laminate thickness. Within the propagation regime of delamination, the critical lengthscale is on the order of tens of laminate thicknesses, as observed in the results presented in Section 7.3.5. As each of the damage modes enters the propagation regime, the key lengthscale increases in length. This increased length results in more possible interactions with nearby damage modes and/or nearby structural features.

The interaction of key lengthscales due to structural features (i.e., those associated with structural details resulting in stress and strain gradients), and the key lengthscales associated with damage initiation drives the damage type present within composites. It was found that the normalized characteristic lengths, l_5 and l_{10}, corresponding to the strain fields returning to within 5% and 10% of far-field strain, of the double-edge-notched specimens are related to the presence of the "transverse zigzag" damage type. The characteristic lengths of the laminates of the double-edge-notched specimen are listed in Table 7.15. These results are from the analysis of the double-edge-notched specimen loaded in pure tension. It was found that the characteristic length increases as the ply angle increases. For laminates with θ equal to 60° and

75°, the characteristic lengths are greater than the distance from the notch tip to the centerline of the specimen. The experimental results of the double-edge-notched specimen from the comparison database, presented in Section 6.2, show that the "transverse zigzag" damage type is present in exactly half of the specimens tested. The half with the "transverse zigzag" damage type present correspond to the laminates with θ equal to 60° and 75°. Thus, in order for the "transverse zigzag" damage type to develop and propagate, the gradients of the stress and strain fields must be low (i.e., slowly changing fields). Within the experimental results of the laminates with θ equal to 15° and 30°, the "transverse zigzag" damage type was not present. For these laminates, the characteristic length, l_{10}, was determined from the results of the finite element models to be 0.7 and 5.4 (measured as the number of notch radii from the edge of the notch), respectively. For these laminates, the resulting strain fields due to the structural feature create unfavorable conditions (i.e., the strain fields do not initiate the damage mode) for the development of the "transverse zigzag" damage type.

The "transverse zigzag" damage type is present in laminates other than the $[(\text{-}\theta/+\theta_2/\text{-}\theta_2/+\theta)_S]_S$ angle-ply laminates of the single-edge-notched specimen and the $[+\theta/\text{-}\theta]_{16T}$ and $[+\theta_4/\text{-}\theta_4]_{4T}$ angle-ply laminates of the double-edge-notched specimens. The "transverse zigzag" damage type was also observed in 5 of the open-hole tension specimens with a laminate of $[+45/0/\text{-}45]_{4S}$ and a hole diameter of 1.0 inches. There were a total of 8 specimens tested with this laminate and hole size, with one of these not tested to ultimate failure. The "transverse zigzag" damage mode was not observed in the other open-hole tension specimens, including all those with a smaller hole diameter of 0.5 inches, nor any of the ply-drop specimens. Within the open-hole tensions specimens that exhibited the "transverse zigzag" damage type, the uniform zigzag pattern commonly observed for the single- and double-edge-notched specimens was not exhibited. Additional discussion of the non-uniform pattern observed within the open-hole tensions specimens exhibiting "transverse zigzag" is presented in Section 8.1.2.

In order for the "transverse zigzag" damage mode to be present in the laminates

of the open-hole tension specimen, additional damage is required. This is due to the presence of the 0° plies of the laminates of the open-hole tension specimens. Additional damage, beyond the damage modes composing the damage type within the single- and double-edge-notched specimens, is needed in the 0° plies, which are not present in the other specimens, in order to propagate the damage in the transverse direction of the open-hole tension specimens. This additional damage in the 0° plies provides alternate damage paths for propagation in the in-plane direction, resulting in the non-uniform through-thickness zigzag pattern observed in the open-hole tension specimens. The experimental observations are consistent with this reasoning.

Additional damage modes, beyond those associated with the "transverse zigzag" damage type, are observed to be located in the vicinity of the propagation path of the "transverse zigzag" damage type for the open-hole tensions specimens, while the presence of the "transverse zigzag" damage type in the singe- and double-edge-notched specimens was always observed to occur unaccompanied by other damage modes. Within the postmortem experimental open-hole tension specimens, the order of damage development could not be determined (i.e., whether the "transverse zigzag" damage type developed before, after, or concurrent with the other damage in its vicinity). The interaction of the "transverse zigzag" damage type and the other damage in the vicinity, or vice-versa, needs to be investigated in order to characterize the key lengthscales of the damage type in laminates other than angle-ply laminates.

As with the double-edge-notched, the interaction of key lengthscales due to the structural feature of the open-hole and the key lengthscale associated with damage initiation drives the damage type present within the specimens. While the normalized characteristic lengths of the open-hole tension specimens, listed in Table 7.25, are approximately equal for the two hole sizes, the gradients of the stress and strain fields are lower (i.e., changing more slowly) for the specimens with the 1.0 inch diameter hole. As with the double-edge-notched specimen results, the resulting strain fields due to the structural feature of a 0.5 inch diameter hole create unfavorable conditions (i.e., the strain fields do not initiate the damage mode) for the development of the "transverse zigzag" damage type.

The ply-drop specimens had similar laminates to the open-hole tension specimens, but this specimen type did not exhibit the "transverse zigzag" damage type within any of the experimental specimens. The structural feature of the ply-drop exhibited the initiation of delaminations near the locations of dropped plies. However, the gradients due to this structural feature were not favorable for the "transverse zigzag" damage type to initiate.

The "transverse zigzag" damage type was determined via the results of the computed microtomography to be linked to the stitch crack damage type. The "transverse zigzag" damage type was first observed via application of the damage documentation procedures, presented in Section 5.1. From the damage sketches, it was found that stitch cracks are always observed on either the front or back face of specimens exhibiting the zigzag damage type. From the ply-by-ply damage results provided by the computed microtomography scans of specimens with the "transverse zigzag" damage type, it was discovered that stitch cracking was present throughout the thickness of the specimen, as presented in Section 6.3. Therefore, it is concluded that in order for the zigzag damage type to propagate, stitch cracking must be present.

Further investigation of the "transverse zigzag" damage type is required in order to identify the key lengthscales associated with the initiation and propagation of the damage type. These investigations should identify the key lengthscales associated with each of the damage constituents of the "transverse zigzag" damage type, as well as identifying the interactions between these constituent modes. Experimental work should include repeating those double-edge-notched tests that exhibited the "transverse zigzag" damage type, but at incremental loading steps in order to allow the initiation and propagation regimes to be investigated. Additional experimental testing should include angle-ply laminates with θ incremented every 5° from 15° to 75°, including both single-ply and four-ply effective ply thickness laminates in order to investigate the influence of ply angle and effective ply thickness at a finer ply angle resolution, thus permitting trends related to the ply angle to be further developed. Finite element analysis should accompany the experimental testing. The analysis done within this work identified lengthscales associated with the strain gradients of

the specimens in the undamaged state, and identified lengthscales associated with the stress and strain gradients of the resulting geometry of the postmortem stitch cracks. Additional models are required in order to study the initiation and propagation of this damage type. The development of the initiation and propagation models should be aided by the experimental findings of these two regimes. The key lengthscales of the initiation and propagation regimes for the "transverse zigzag" damage type are required in order to further investigate the interaction between structural details and the damage type. Once established, the key lengthscales associated with the initiation and propagation of the "transverse zigzag" damage type should be compared to the lengthscales of the undamaged double-edge-notched specimen.

Lengthscales associated with the delamination damage mode were not defined during this investigation. Further studies are required in order to determine the key interaction lengthscales of the delamination damage mode. The second damage inclusion model, presented in Section 7.3.5, allowed lengthscales associated with the strain gradients at the delamination front to be identified. The results of this model indicate that there is a near zero strain gradient in the 'wake' (i.e., behind the advancing delamination front) region of the delamination. A relatively short region (on the order of 3 mm for the models investigated) of the delamination 'wake' has non-zero strain gradients, occurring right at the delamination front. Beyond the delamination front, the gradients in strain are dependent on through-thickness location, ply angle, and effective ply-thickness. Of the experimental specimens included in this work, the ply-drop specimen was most suited for investigating delamination. The structural feature of the dropped plies initiated multiple delamination fronts occurring throughout the ply-drop region. The structural features of the other specimens included in this work typically initiated damage modes other than delamination. Thus, the experimental and analytical results from the ply-drop specimen require further investigation in order to define the key interaction lengthscales associated with delamination. Additional ply-drop specimens with a single dropped ply are suggested. In addition to the laminates of the ply-drop specimens of this work, ply-drop specimens should include angle-ply laminates with different effective ply thicknesses in order to compare the

damage results to those of the single- and double-edge-notched specimens. The overall dimension of the ply-drop specimen tested in this work should be maintained in order to compare additional results with additional testing results.

In order to continue the development of the lengthscale concept, further work is required to better assess the key lengthscales of damage modes, damage types, and structural features, and how such lengthscales interact in the initiation and propagation regimes. A first step would be to implement the damage documentation procedures, presented in Chapter 5, on additional specimens. These could include previously tested specimens, as was the case here for the single-edge-notched specimens, and should include future experimental testing.

Future experimental specimens should include the recommendations made throughout Section 8.1 involving additional testing of the specimen types investigated herein, with additional laminates and effective ply thicknesses included. A specific recommendation is related to the "transverse zigzag" damage type observed in the double-edge-notched specimens. Increasing the width of the specimen will allow the characteristic lengths of the laminates with θ equal to 60° and 75° to be determined as the increased width will separate the influence of the notches on the strain fields of the other notch. This will allow better investigation of the influence of this interaction on the initiation and propagation of the "transverse zigzag" damage type. An additional specific recommendation for further experimental testing is varying the laminates of the open-hole tensions specimens. These tests should include the angle-ply laminates used in the double-edge-notched specimens in order to allow a more direct comparison between the resulting damage from each structural detail. It is not recommended to include open-hole tension specimens containing a hole with 0 inch diameter (i.e., no hole) as these specimens lacked the structural detail of the open-hole. It is recommended to scale the planar dimensions of the open-hole tension specimen to include two additional hole diameters: one with a 0.25 inch hole diameter and the second with a 1.5 inch hole diameter. These two additional sizes will allow the influence of the strain gradient on the presence of the "transverse zigzag" damage type to be further studied. Laminates for these additional tests should include those of the open-hole

tension specimen included within this work, with the expectation that the "transverse zigzag" damage type will be present in the specimen with the larger diameter hole, but not in the smaller diameter hole. Another specific recommendation for further experimental testing is specimens with a single ply dropped. The ply-drop specimens investigated during this work contained multiple ply-drops located within a relatively close proximity. This resulted in overlapping interactions from multiple ply-drops, preventing identification of the influence(s) of each ply-drop. In addition to experimental testing of a single ply-drop, high fidelity analytical models of the geometry of the single ply-drop specimen should be conducted in order to investigate the lengthscales associated with the gradients of the stress and strain fields. Surface strain mapping, such as the technique used in the experimental specimens of this work, should be included as a means to validate the results of the finite element models to the experimental results.

In order to allow better investigations of lengthscale effects, the information collected on these specimens via the damage documentation procedures should be stored in an accessible, central database. Such a database should be accessible via the internet and should provide means for investigators to input their collected data. The database should be searchable in order to allow easy investigation of the damage trends. The database created for this work, presented in Section 6.2, was implemented in Microsoft Excel. The use of Excel for the database becomes impractical as the number of specimens grows. In addition, the ability to search the data within the Excel spreadsheets is limited. For these reasons, it is advised that a better database be established. This work has suggested initial capabilities required by such a database, and has identified data fields that should be included within the database. As the database is populated by additional investigators, further data fields may be identified and added to the database.

Including three-dimensional damage documentation should be considered when establishing the database. The information gained for tools such as computed microtomography allow details of damage within composites to be investigated in a spatial manner. As these tools improve, spatial mapping of damage may provide useful in-

formation related to the lengthscales of damage. The quantification of damage extent could be extended beyond the surface quantification specified in Section 5.1.2. Using a tool such as computed microtomography to document damage in three dimensions would allow the procedures of Section 5.1 to be applied ply-by-ply through the thickness of the laminate as well as investigating damage in the regions of ply interfaces that involve through-thickness damage propagation. In addition, the propagation of damage modes and damage types could be captured. For example, in order to better assess the "transverse zigzag" damage type, computed microtomography could be used to map the propagation of the damage within experimental specimens that are loaded to incremental load levels. This will allow investigators to establish whether the matrix cracks propagate to the edge of the specimen before stitch cracks initiate, or if stitch cracks and the matrix cracks propagate from the structural feature to the edge of the specimen concurrently, as well as documenting the through thickness "history" of damage (i.e., which plies and/or interfaces develop damage first and how the damage propagates throughout the volume of the specimen). Such information is required in order to characterize the critical lengthscales influencing the damage type. The same three-dimensional damage documentation data is recommended to be collected on experimental specimens where damage may be present within the specimen volume.

[THIS PAGE INTENTIONALLY LEFT BLANK]

Chapter 9

Conclusions and Recommendations

In this work, the lengthscale effects associated with damage in composite materials and their structures were investigated with the objective of determining how these lengthscales vary across levels of composite in order to be used in assessing the overall response of composite structures. To this end, documentation procedures were developed to capture qualitative and quantitative information of experimental specimens; experimental specimens containing structural details were investigated postmortem to identify lengthscales associated with damage modes; and detailed finite element models were developed in order to investigate the interaction of lengthscales associated with structural details with those associated with the basic damage modes. In this section, the conclusions, as drawn from the overall results and discussions, are presented, and recommendations for further investigations are proposed based on the understanding of the role of lengthscales in the damage and failure of composites acquired from this work, and the identified needs to further this understanding.

The following conclusions can be drawn from the current investigation of lengthscales associated with composite damage:

1. The concept of lengthscales is a viable tool to characterize the overall response of composite structures, particularly involving damage initiation, propagation, and failure. The determination of how these lengthscales vary across levels in composites provides an important tool that can be used to assess this overall response of composite structures.

2. The "observable lengthscale" is an important consideration when investigating lengthscales in experimental specimens and structures. As inspection methods for composite materials and structures continue to improve, damage modes and damage types previously unknown are being, and may continue to be, identified. As the ability to resolve damage at smaller scales continues to improve, interactions occurring at smaller scales can be studied.

3. Key lengthscales of basic damage modes and of structural details need to be used when choosing the scale of finite element models as this is analogous to the "observable lengthscale" of the experimental inspection techniques in that models must have a resolution at least as fine as the key lengthscale of the mode under investigation.

4. Recognizing two damage regimes, the damage initiation regime and the damage propagation regime, is important for characterizing lengthscales associated with damage modes. Within the damage initiation regime, there are no interactions between damage modes, while within the damage propagation regime, the key lengthscales increase in size and interactions between damage modes may be present. Identifying key lengthscales within each regime allows investigation of how the critical lengthscale(s) controlling the damage mode(s) change(s) across regimes.

5. The documentation procedures developed during this work enable damage to be documented in both quantitative and qualitative bases, thus allowing the damage data to be entered into a database. The documentation procedures were developed such that any researcher should be able to document experimental specimens via basic camera and image processing software.

6. The fiber fracture damage mode is independent of the effective ply thickness of a laminate for angle-ply laminates with lower angles while becoming dependent on the effective ply thickness of a laminate for higher angles. The lengthscale associated with the geometry of the propagation path of fiber fracture is deter-

mined to be on the order of tens of fiber diameters. Other damage modes were typically observed near the propagation path of fiber fracture indicating that the lengthscales of the modes interact within the propagation regime.

7. The importance of ply angle in angle-ply laminates on the presence and propagation of matrix cracking decreases as the effective ply thickness increases, as does the dependence on the load path.

8. Lengthscales associated with gradients in the strain fields near matrix cracks are dependent on the orientation of the crack relative to the loading direction. For the specific case of the stitch crack damage type, load was observed to "bypass" and "carry-through" the damaged region. The "bypass" of load corresponds to the reduced capability of load paths through the region of damage, requiring load to pass around the region while some load is carried across the intact portion of the damaged region. The amount of load "bypass" increases with laminate angle due to the details of the geometry of the stitch cracks with the region of damage causing greater reduction of load-carrying capability as the laminate angle increases. Thus, the ability to "carry-through" load is dependent on the laminate angle which influences the orientation of the details of the damage relative to the applied loading.

9. A unique damage type and associated lengthscale interaction discovered during this work involves the "transverse zigzag" damage type which is an interaction of matrix cracking, stitch cracking, and delamination. The lengthscales associated with the damage type include those of the three constituent damage modes, the width of the zigzag pattern, the angle relative to loading, and the length of the propagation of the damage type. The damage type was observed to maintain the characteristic zigzag pattern through the thickness of the specimen along the entire propagation path indicating that the lengthscales influencing the damage type do not change as the type propagates.

10. "Transverse zigzag" damage type can be present in laminates other than reg-

ular antisymmetric angle-ply laminates, e.g., $[+\theta/-\theta]_{16T}$, via interaction and propagation through the thickness with additional damage in other angles of other plies.

11. An interaction commonly observed in the experimental specimens is mode "switching," which involves a change to another damage mode along the propagation of a different damage mode. This is influenced by the effective ply thickness, with mode switching occurring more frequently in single-ply effective ply thickness laminates.

12. A normalized characteristic length is defined for the structural features investigated that allows measurement of the influence of the structural detail as a function of the laminate, as well as the interaction of the stress and strain fields, developed due to the detail, with those of the damage modes/types. The characteristic lengths involve the distance over which the structural detail influences the strain fields, and are normalized by a length associated with the structural detail. The characteristic lengths are dependent on the laminate angle, but independent of the effective ply thickness.

13. In order for the "transverse zigzag" damage type to develop and propagate within laminates, the gradients associated with the stress and strain fields due to a structural feature must be slowly changing. The normalized characteristic lengths of specimens with the "transverse zigzag" damage type present are always greater than those of specimens lacking the damage type. The resulting strain fields of structural features with relatively short normalized characteristic lengths are an indication that an unfavorable strain field is present and damage modes will not interact to initiate and propagate the "transverse zigzag" damage type.

14. The influence of grip boundaries on damage propagation is dependent on both the ply angle, since the associated damage mode/type must have a propagation path that intercepts the grip boundaries, and the effective ply thickness of the

laminate, as the grip boundaries are more likely to arrest propagating damage within single-ply thickness effective ply thickness laminates.

The following recommendations are proposed as future work based on the understanding established in the current work and in order to further explore the key findings:

1. Additional investigation should be conducted to identify the importance of the normalized mismatch lengthscale associated with the mismatch angle between plies, as herein defined, to allow investigation of the influence of the mismatch angle between plies on the characteristics of damage initiation and propagation. In particular, experimental testing of laminates with varying mismatch lengths should be conducted in order to identify trends in damage in both the initiation and propagation regimes.

2. Lengthscales associated with the stress and strain states acting at the interface of the fiber and matrix should be investigated for the damage mode of interfacial debonding via finite element modeling pertinent to geometric details of the initiation and propagation regimes of the damage mode, and the results used to investigate the influence of the damage mode on the lengthscales in the propagation regime.

3. The fiber fracture damage mode should be further investigated by both experimental and modeling work, and results compared to assess key lengthscales in both the initiation and propagation regimes. Open-hole tension and ply-drop specimen testing is recommended including incremental loading levels with damage inquiries. A model incorporating the experimental load paths that 'activate' fiber fracture in the double-edge-notched specimen should be analyzed and compared to the experimental results.

4. Additional investigation is required in order to define the key lengthscale(s) associated with the matrix cracking damage mode as no single lengthscale has been identified as "critical." In particular, additional double-edge-notched specimen

testing for each of the load paths should be conducted including incremental loading levels with damage inquiries to allow the lengthscales of the initiation and propagation regimes to be investigated and identified.

5. Additional open-hole tension and ply-drop specimen experimental testing should be conducted in order to include laminates containing different ply angles from those tested during this work in order to investigate the influence of the ply mismatch angles as the lengthscale of the structural feature dominates the ply mismatch length of the laminates investigated during this work. It is specifically suggested to test these specimen types with the angle-ply laminates of the double-edge-notched specimen, with testing including incremental loading levels with damage inquiries, in order to allow a more direct comparison of the damage results documented in the double-edge-notched specimens. In addition, laminates with effective ply thicknesses greater than two are suggested in order to investigate the influence of increasing the lengthscale associated with the effective ply thickness.

6. Further experimental work and modeling should be conducted in order to better identify the key interaction lengthscales of the delamination damage mode for the propagation regime from amongst lengthscales identified herein. The influence of the mismatch angle and the effective ply thickness on delamination should be investigated in additional open-hole tension and ply-drop specimens, as these specimens most frequently exhibited delamination, with a ply-drop specimen created with a single ply drop in order to investigate the individual effects of the ply drop, including incremental loading levels with damage inquiries. Detailed stress and strain fields should be attained through models and related to the initiation and propagation of damage within experimental specimens. A characteristic length associated with the ply-drop structural detail should be established.

7. The concept of the normalized characteristic length should be expanded by creating in-plane 'maps' of the region of influence of the structural features in

order to provide additional information on the spatial influence surrounding the structural feature.

8. Additional studies to identify the key lengthscales associated with the "transverse zigzag" damage type for the initiation and propagation regimes need to be conducted and compared with the structural lengthscales of the undamaged specimens containing structural details. In particular, incremental load tests with damage inquiries of the double-edge-notched cases that exhibited the "transverse zigzag" damage type should be conducted along with angle-ply laminates with θ incremented every 5° from 15° to 75°, including both single-ply and four-ply effective ply thickness laminates, thus permitting trends related to the ply angle to be further developed. Finite element analysis should accompany the experimental testing.

9. The initiation and propagation of the "transverse zigzag" damage type should be further explored via additional double-edge-notched and open-hole tension specimen testing. This includes increasing the width of the double-edge-notched specimen in order to separate the influence of one notch on the strain fields of the other notch. Testing should include angle-ply laminates for the open-hole tension specimens to allow a more direct comparison of the damage development, along with open-hole tension specimens with in-plane dimensions scaled to create geometries with a 0.25 inch diameter hole and a 1.5 inch diameter hole in order to explore the effects of the structural feature on this damage type.

10. Finite element models should be developed in order to investigate in greater detail how the gradients and lengthscales change with the length and spacing parameters of stitch cracks, which were observed in the experimental work to vary with ply angle and effective ply thickness. This includes extension to include all the load paths used for the single- and double-edge-notched experimental specimens.

11. Finite element models of the single-edge-notched and double-edge-notched spec-

imens should be expanded to include all the experimental load paths utilized, beyond that of uniaxial tension, in order to investigate how the lengthscales are affected by the loading, including the lengthscales associated with these structural details.

12. The damage documentation procedures should be expanded to more specimens and three dimensions, and a standardized code be developed in order to implement damage documentation procedures more consistently.

13. A damage documentation database that is structured to allow lengthscale investigations should be implemented and built on the concepts of the database created during this work in order to allow researchers to contribute their experimental results into the database and others to access this information.

14. As the introduction of new constituents to a composite can introduce new lengthscales, experimental and modeling work should take place to study such issues and such cases.

References

[1] The Boeing Company, "AERO, QTR_04." World Wide Web, http://www.boeing.com/commercial/aeromagazine/articles/qtr_4_06/article_04_2.html, 2006. Accessed July 27, 2011.

[2] D. L. Flaggs and M. H. Kural, "Experimental Determination of the In Situ Transverse Lamina Strength in Graphite/Epoxy Laminates," *Journal of Composite Materials*, Vol. 16, pp. 103–115, Mar. 1982.

[3] B. W. Rosen, "Mechanics of Composite Strengthening," *Fiber Composite Materials*, pp. 37–75, American Society of Metals, Metals Park, Ohio, 1965.

[4] N. J. Pagano and R. B. Pipes, "The Influence of Stacking Sequence on Laminate Strength," *Journal of Composite Materials*, Vol. 5, pp. 50–57, Jan. 1971.

[5] S. L. Phoenix, "Statistical Analysis of Flaw Strength Spectra of High-Modulus Fibers," *Composite Reliability, ASTM STP 580*, pp. 77–89, 1975.

[6] T. K. O'Brien, "Characterization of Delamination Onset and Growth in a Composite Laminate," *Damage in Composite Materials, ASTM STP 775*, pp. 140–167, 1982.

[7] M. J. Hinton, A. S. Kaddour, and P. D. Soden, "A Comparison of the Predictive Capabilities of Current Failure Theories for Composite Laminates, Judged Against Experimental Evidence," *Composites Science and Technology*, Vol. 62, pp. 1725–1797, 2002.

[8] S. M. Spearing, P. A. Lagacé, and H. L. N. McManus, "On the Role of Length-scale in the Prediction of Failure of Composite Structures: Assessment and Needs," *Applied Composite Materials*, Vol. 5, pp. 139–149, 1998.

[9] P. Beaumont, ed., *Proceedings of the Conference on Advances in Multi-Scale Modelling of Composite Material Systems of Components*, (Monterey, CA), 2005.

[10] Composite Materials Handbook 17 (CMH-17-3F), *Polymer Matrix Composites: Materials Usage, Design, and Analysis*. Volume 3F, Chapter 4, June 2002.

[11] R. S. Whitehead and R. B. Deo, "A Building Block Approach to Design Verification Testing of Primary Composite Structure," *in Proceedings of the 24th AIAA/ASME/ASCE/AHS Structures, Structural Dynamics, and Materials Conference*, (Lake Tahoe, NV), pp. 473–477, AIAA 83–0947, 1983.

[12] R. Pyrz and J. Schjødt-Thomsen, "Bridging the Length-Scale Gap — Short Fibre Composite Material as an Example," *Journal of Materials Science*, Vol. 41, pp. 6737–6750, 2006.

[13] I. M. Daniel and O. Ishai, *Engineering Mechanics of Composite Materials*. New York: Oxford University Press, 1994.

[14] B. D. Coleman, "On the Strength of Classical Fibres and Fibre Bundles," *Journal of the Mechanics and Physics of Solids*, Vol. 7, No. 1, pp. 60–70, 1958.

[15] S. L. Phoenix and H. M. Taylor, "The Asymptotic Strength Distribution of a General Fiber Bundle," *Advances in Applied Probability*, Vol. 5, No. 2, pp. 200–216, 1973.

[16] W. A. Weibull, "A Statistical Theory of the Strength of Materials," *Ingvetensk. Akad. Handl.*, Vol. 151, pp. 5–45, 1939.

[17] S. L. Phoenix, "Stochastic Strength and Fatigue of Fiber Bundles," *International Journal of Fracture*, Vol. 14, pp. 327–344, June 1978.

[18] D. G. Harlow and S. L. Phoenix, "The Chain-of-Bundles Probability Model for the Strength of Fibrous Materials I: Analysis and Conjectures," *Journal of Composite Materials*, Vol. 12, No. 2, pp. 195–214, 1978.

[19] H. T. Hahn and J. G. Williams, "Compression Failure Mechanisms in Unidirectional Composites," NASA-TM-85834, NASA, Aug. 1984.

[20] B. W. Rosen, "Tensile Failure of Fibrous Composites," *AIAA Journal*, Vol. 2, No. 11, pp. 1985–1991, 1964.

[21] M. H. R. Jen, Y. S. Kau, and J. M. Hsu, "Initiation and Propagation of Delamination in a Centrally Notched Composite Laminate," *Journal of Composite Materials*, Vol. 27, No. 3, pp. 272–302, 1993.

[22] R. Y. Kim and H. T. Hahn, "Effect of Curing Stresses on the First Ply-failure in Composite Laminates," *Journal of Composite Materials*, Vol. 13, pp. 2–16, 1979.

[23] S. L. Phoenix, "Probabilistic Strength Analysis of Fibre Bundle Structures," *Fibre Science and Technology*, Vol. 7, pp. 15–31, 1974.

[24] P. S. Theocaris and C. A. Stassinakis, "Crack Propagation in Fibrous Composite Materials Studied by SEM," *Journal of Composite Materials*, Vol. 15, pp. 133–141, 1981.

[25] E. Altus and O. Ishai, "Transverse Cracking and Delamination Interaction in the Failure Process of Composite Laminates," *Composites Science and Technology*, Vol. 26, No. 1, pp. 59–77, 1986.

[26] C. E. Harris, D. H. Allen, and E. W. Nottorf, "Predictions of Poisson's Ratio in Cross-Ply Laminates Containing Matrix Cracks and Delaminations," *Journal of Composite Technology and Research*, Vol. 11, No. 2, pp. 53–58, 1989.

[27] H. T. Hahn and S. W. Tsai, "On the Behavior of Composite Laminates After Initial Failures," *Journal of Composite Materials*, Vol. 8, pp. 288–305, 1974.

[28] A. K. Ditcher and J. P. H. Webber, "Edge Effects in Uniaxial Compression Testing of Cross-Ply Carbon-Fiber Laminates," *Journal of Composite Materials*, Vol. 16, pp. 228–243, May 1982.

[29] D. W. Wilson, "Evaluation of the V-Notched Beam Shear Test Through an Interlaboratory Study," *Journal of Composite Technology and Research*, Vol. 12, No. 3, pp. 131–138, 1990.

[30] S. A. Salpekar and T. K. O'Brien, "Analysis of Matrix Cracking and Local Delamination in $(0/+\theta/-\theta)_s$ Graphite Epoxy Laminates Under Tension Load," *in Proceedings of the 8th International Conference on Composite Materials*, Vol. 3, (Honolulu, HI), 1991. 28-G.

[31] N. A. Fleck, L. Deng, and B. Budiansky, "Prediction of Kink Width in Compressed Fiber Composites," *Journal of Applied Mechanics*, Vol. 62, pp. 329–337, June 1995.

[32] P. M. Jelf and N. A. Fleck, "Compression Failure Mechanisms in Unidirectional Composites," *Journal of Composite Materials*, Vol. 26, No. 18, pp. 2706–2726, 1992.

[33] P. Berbinau, C. Soutis, and I. A. Guz, "Compressive Failure of 0° Unidirectional Carbon-Fibre-Reinforced Plastic (CFRP) Laminates by Fibre Microbuckling," *Composites Science and Technology*, Vol. 59, pp. 1451–1455, 1999.

[34] A. S. Argon, "Fracture of Composites," *Treatise on Materials Science and Technology*, Vol. 1, pp. 79–114, 1972.

[35] B. Budiansky and N. A. Fleck, "Compressive Failure of Fibre Composites," *Journal of the Mechanics and Physics of Solids*, Vol. 41, No. 1, pp. 183–211, 1993.

[36] A. G. Evans and W. F. Adler, "Kinking as a Mode of Structural Degradation in Carbon Fiber Composites," *Acta Metallurgica*, Vol. 26, pp. 725–738, 1978.

[37] B. Budiansky, "Micromechanics," *Computers and Structures*, Vol. 16, No. 1-4, pp. 3–12, 1983.

[38] A. Maewal, "Postbuckling Behavior of a Periodically Laminated Medium in Compression," *International Journal of Solids and Structures*, Vol. 17, pp. 335–344, 1981.

[39] C. A. Berg and M. Salama, "Fatigue of Graphite Fibre-Reinforced Epoxy in Compression," *Fibre Science and Technology*, Vol. 6, pp. 79–118, 1973.

[40] C. W. Weaver and J. G. Williams, "Deformation of a Carbon-Epoxy Composite under Hydrostatic Pressure," *Journal of Materials Science*, Vol. 10, pp. 1323–1333, 1975.

[41] C. R. Chaplin, "Compressive Fracture in Undirectional Glass-Reinforced Plastics," *Journal of Materials Science*, Vol. 12, pp. 347–352, 1977.

[42] C. Soutis, P. T. Curtis, and N. A. Fleck, "Compressive Failure of notched carbon fibre composites," *Proceedings of the Royal Society of London, Series A*, Vol. 440, pp. 241–256, 1993.

[43] A. Kelly, "Interface Effects and the Work of Fracture of a Fibrous Composite," *Proceedings of the Royal Society of London, Series A*, Vol. 319, pp. 95–116, July 1970.

[44] A. Takaku and R. G. C. Arridge, "The Effect of Interfacial Radial and Shear Stress on Fibre Pull-Out in Composite Materials," *Journal of Physics D: Applied Physics*, Vol. 6, pp. 2038–2047, 1973.

[45] J. W. Hutchinson and H. M. Jensen, "Models of Fiber Debonding and Pullout in Brittle Composites with Friction," *Mechanics of Materials*, Vol. 9, pp. 139–163, 1990.

[46] P. Lawrence, "Some Theoretical Considerations of Fibre Pull-Out from an Elastic Matrix," *Journal of Materials Science*, Vol. 7, pp. 1–6, 1972.

[47] L. S. Sigl and A. G. Evans, "Effects of Residual Stress and Frictional Sliding on Cracking and Pull-Out in Brittle Matrix Composites," *Mechanics of Materials*, Vol. 8, pp. 1–12, 1989.

[48] C. Liang and J. W. Hutchinson, "Mechanics of the Fiber Pushout Test," *Mechanics of Materials*, Vol. 14, pp. 207–221, 1993.

[49] G. Lin, P. H. Geubelle, and N. R. Sottos, "Simulation of Fiber Debonding with Friction in a Model Composite Pushout Test," *International Journal of Solids and Structures*, Vol. 38, pp. 8547–8562, 2001.

[50] A. Kelly and W. R. Tyson, "Tensile Properties of Fibre-Reinforced Metals: Copper/Tungsten and Copper/Molybdenum," *Journal of the Mechanics and Physics of Solids*, Vol. 13, pp. 329–350, 1965.

[51] P. B. Bowden, "The Effect of Hydrostatic Pressure on the Fibre-Matrix Bond in a Steel-Resin Model Composite," *Journal of Materials Science*, Vol. 5, pp. 517–520, 1970.

[52] P. W. R. Beaumont and D. C. Phillips, "Tensile Strengths of Notched Composites," *Journal of Composite Materials*, Vol. 6, pp. 32–46, 1972.

[53] M. S. El-Zein and K. L. Reifsnider, "The Strength Prediction of Composite Laminates Containing a Circular Hole," *Journal of Composites Technology and Research*, Vol. 12, No. 1, pp. 24–30, 1990.

[54] N. J. Pagano and R. B. Pipes, "Some Observation on the Interlaminar Strength of Composite Laminates," *International Journal of Mechanical Sciences*, Vol. 15, pp. 679–688, 1973.

[55] T. K. O'Brien, "Analysis of Local Delaminations and Their Influence on Composite Laminate Behavior," *Delamination and Debonding of Materials, ASTM STP 876*, pp. 282–297, 1985.

[56] T. K. O'Brien, "Interlaminar Fracture of Composites," *NASA Technical Memorandum 85768*, June 1984. N84-27835.

[57] S. R. Soni and R. Y. Kim, "Delamination of Composite Laminates Stimulated by Interlaminar Shear," *Composite Materials: Testing and Design (Seventh Conference), ASTM STP 893*, pp. 286–307, 1986.

[58] J. C. Brewer and P. A. Lagace, "Quadratic Stress Criterion for Initiation of Free Edge Delamination," *Journal of Composite Materials*, Vol. 22, pp. 1141–1155, Dec. 1988.

[59] R. Y. Kim and S. R. Soni, "Experimental and Analytical Studies on the Onset of Delamination in Laminated Composites," *Journal of Composite Materials*, Vol. 18, pp. 70–80, Jan. 1984.

[60] C. Kassapoglou and P. A. Lagace, "An Efficient Method for the Calculation of Interlaminar Stresses in Composite Materials," *Journal of Applied Mechanics*, Vol. 53, pp. 744–750, Dec. 1986.

[61] N. V. Bhat and P. A. Lagace, "An Analytical Method for the Evaluation of Interlaminar Stresses Due to Material Discontinuities," *Journal of Composite Materials*, Vol. 28, No. 3, pp. 190–210, 1994.

[62] K. J. Saeger, P. A. Lagace, and D. J. Shim, "Interlaminar Stresses Due to In-Plane Gradient Stress Fields," *Journal of Composite Materials*, Vol. 36, No. 2, pp. 211–227, 2002.

[63] T. K. O'Brien and S. J. Hooper, "Local Delamination in Laminates with Angle Ply Matrix Crack, Part II: Delamination Fracture Analysis and Fatigue Characterization," *Composite Materials: Fatigue and Fracture, ASTM STP 1156*, Vol. 4, pp. 507–538, 1993.

[64] S. S. Wang, "Fracture Mechanics for Delamination Problems in Materials," *Journal of Composite Materials*, Vol. 17, pp. 210–223, May 1983.

[65] P. A. Lagace and N. V. Bhat, "Efficient Use of Film Adhesive Interlayers to Suppress Delamination," *Composite Materials: Testing and Design, ASTM STP 1120*, Vol. 10, pp. 384–396, 1992.

[66] E. A. Armanios, L. W. Rehfield, and F. Weinstein, "Understanding and Predicting Sublaminate Damage Mechanisms in Composite Structures," *Composite Materials: Testing and Design, ASTM STP 1059*, Vol. 9, pp. 231–249, 1990.

[67] T. K. O'Brien and S. J. Hooper, "Local Delamination in Laminates with Angle Ply Matrix Crack, Part I: Tension Tests and Stress Analysis," *Composite Materials: Fatigue and Fracture, ASTM STP 1156*, Vol. 4, pp. 491–506, 1993.

[68] R. A. Kline and F. H. Chang, "Composite Failure Surface Analysis," *Journal of Composite Materials*, Vol. 14, pp. 315–324, Oct. 1980.

[69] J. D. Whitcomb, "Predicted and Observed Effects of Stacking Sequence and Delamination Size on Instability Related Delamination Growth," *Journal of Composite Technology and Research*, Vol. 11, No. 3, pp. 94–98, 1989.

[70] I. M. Daniel, R. E. Rowlands, and J. B. Whiteside, "Effects of Material and Stacking Sequence on Behavior of Composite Plates with Holes," *Experimental Mechanics*, Vol. 14, pp. 1–9, Jan. 1974.

[71] J. M. Whitney and C. E. Browning, "Free-Edge Delamination of Tensile Coupons," *Journal of Composite Materials*, Vol. 6, pp. 300–303, 1972.

[72] K. E. Jackson, "Scaling Effects in the Flexural Response and Failure of Composite Beams," *AIAA Journal*, Vol. 30, pp. 2099–2105, Aug. 1992.

[73] D. P. Johnson, J. Morton, S. Kellas, and K. E. Jackson, "Scaling Effect in Sublaminate-Level Scaled Composite Laminates," *AIAA Journal*, Vol. 36, pp. 441–447, Mar. 1998.

[74] C. T. Herakovich, "Influence of Layer Thickness on the Strength of Angle-Ply Laminates," *Journal of Composite Materials*, Vol. 16, pp. 216–227, May 1982.

[75] S. Kellas and J. Morton, "Strength Scaling in Fiber Composites," AIAA-91-1144-CP, NASA Contract Report 4335, Nov. 1990.

[76] P. A. Lagace, J. C. Brewer, and C. Kassapoglou, "The Effect of Thickness on Interlaminar Stresses and Delamination in Straight-Edged Laminates," *Journal of Composite Technology and Research*, Vol. 9, No. 3, pp. 81–87, 1987.

[77] K. E. Jackson, "Analytical and Experimental Evaluation of the Strength Scale Effect in the Flexural Response of Graphite-Epoxy Composite Beams," *in Proceedings of the AIAA/ASME/ASCE/AHS/ASC Structures, Structural Dynamics, and Materials Conference*, (Baltimore, MD), AIAA-91-1025-CP, 1991.

[78] M. R. Wisnom, "Size Effects in the Testing of Fibre-Composite Materials," *Composites Science and Technology*, Vol. 59, pp. 1937–1957, 1999.

[79] T. K. O'Brien and S. A. Salpekar, "Scale Effects on the Transverse Tensile Strength of Graphite Epoxy Composites," US Army Aviation Systems Command, Aviation R&T Activity, National Aeronautics and Space Administration, Langley Research Center, 1992.

[80] R. H. Martin, "Incorporating Interlaminar Fracture Mechanics into Design," *Proceedings of the Institution of Mechanical Engineers, Part L: Journal of Materials: Design and Applications*, Vol. 214, No. 2, pp. 91–97, 2000.

[81] R. D. Jamison, K. Schulte, K. L. Reifsnider, and W. W. Stinchcomb, "Characterization and Analysis of Damage Mechanisms in Tension-Tension Fatigue of Graphite/Epoxy Laminates," *Effects of Defects in Composite Materials, ASTM STP 836*, pp. 21–55, 1984.

[82] J. A. Lavoie and E. Adolfsson, "Stitch Cracks in Constraint Plies Adjacent to Cracked Plies," *Journal of Composite Materials*, Vol. 35, No. 23, pp. 2077–2097, 2001.

[83] P. R. Guyett and A. W. Cardrick, "The Certification of Composite Airframe Structures," *Aeronautical Journal*, Vol. 84, pp. 188–203, July 1980.

[84] C. E. Harris, J. H. Starnes, Jr., and M. J. Shuart, "Design and Manufacturing of Aerospace Composite Structures, State-of-the-Art Assessment," *Journal of Aircraft*, Vol. 39, No. 4, pp. 545–560, 2002.

[85] A. Fawcett, J. Trostle, and S.Ward, "777 Empennage Certification Approach," *in Proceedings of the 11th International Conference on Composite Materials*, (Gold Coast, Australia), July 1997.

[86] M. J. Hinton and P. D. Soden, "Predicting Failure in Composite Laminates: The Background to the Exercise," *Composites Science and Technology*, Vol. 58, pp. 1001–1010, 1998.

[87] P. D. Soden, M. J. Hinton, and A. S. Kaddour, "A Comparison of the Predictive Capabilities of Current Failure Theories for Composite Laminates," *Composites Science and Technology*, Vol. 58, pp. 1225–1254, 1998.

[88] M. J. Hinton, A. S. Kaddour, and P. D. Soden, "Evaluation of Failure Prediction in Composite Laminates: Background to Part C of the Exercise," *Composites Science and Technology*, Vol. 64, pp. 321–327, 2004.

[89] P. Soden, A. S. Kaddour, and M. Hinton, eds., *Special Issue on World Wide Failure Exercise, Composites Science and Technology.* Vol. 64, No. 3-4, pp. 319-605, March 2004.

[90] A. S. Kaddour, M. J. Hinton, and P. D. Soden, "A Comparison of the Predictive Capabilities of Current Failure Theories for Composite Laminates: Additional Contributions," *Composites Science and Technology*, Vol. 64, pp. 449–476, 2004.

[91] P. D. Soden, A. S. Kaddour, and M. J. Hinton, "Recommendations for Designers and Researchers Resulting from the World-Wide Failure Exercise," *Composites Science and Technology*, Vol. 64, pp. 589–604, 2004.

[92] C. C. Chamis, "Failure Criteria for Filamentary Composites," NASA-TN-D-5367, National Aeronautics and Space Administration, 1969.

[93] T. A. Bogetti, C. P. R. Hoppel, V. M. Harik, J. F. Newill, and B. P. Burns, "Predicting the Nonlinear Response and Progressive Failure of Composite Laminates," *Composites Science and Technology*, Vol. 64, No. 3-4, pp. 329–342, 2004.

[94] P. A. Zinoviev, S. V. Grigoriev, O. V. Lebedeva, and L. P. Tairova, "The Strength of Multilayered Composites Under a Plane-Stress State," *Composites Science and Technology*, Vol. 58, No. 7, pp. 1209–1223, 1998.

[95] S. W. Tsai and E. M. Wu, "A General Theory of Strength for Anisotropic Materials," *Journal of Composite Materials*, Vol. 5, pp. 58–80, Jan. 1971.

[96] A. Puck and H. Schürmann, "Failure Analysis of FRP Laminates by Means of Physically Based Phenomological Models," *Composites Science and Technology*, Vol. 58, pp. 1045–1067, 1998.

[97] M. E. Waddoups, "Advanced Composite Material Mechanics for the Design and Stress Analyst," FZM-4763, General Dynamics, Forth Worht Division, 1967.

[98] M. E. Waddoups, "Characterization and Design of Composite Materials," *in Proceedings of the Composite Materials Workshop* (S. Tsai, J. Halpin, and N. Pagano, eds.), (Stamford, Connecticut), pp. 254–308, Technomic Pub. Co., 1968.

[99] R. S. Sandhu, "A Survey of Failure Theories of Isotropic and Anisotropic Materials," AD-756 889, Air Force Flight Dynamics Laboratory, Wright-Patterson Air Force Base, Ohio, Jan. 1972.

[100] L. J. Hart-Smith, "Predictions of the Original and Truncated Maximum-Strain Failure Models for Certain Fibrous Composite Laminates," *Composites Science and Technology*, Vol. 58, No. 7, pp. 1151–1178, 1997.

[101] T. A. Bogetti, C. P. R. Hoppel, V. M. Harik, J. F. Newill, and B. P. Burns, "Predicting the Nonlinear Response and Failure of Composite Laminates: Correlation with Experimental Results," *Composites Science and Technology*, Vol. 64, No. 3-4, pp. 477–485, 2004.

[102] C. F. Jenkins, "Report on Materials of Construction Used in Aircraft and Aircraft Engines," Technical Report, Great Britain Aeronautical Research Committee, 1920.

[103] P. A. Zinoviev, O. V. Lebedeva, and L. P. Tairova, "A Coupled Analysis of Experimental and Theoretical Results on the Deformation and Failure of Composite Laminates Under a State of Plane Stress," *Composites Science and Technology*, Vol. 62, No. 12-13, pp. 1711–1723, 2002.

[104] A. Puck and H. Schürmann, "Failure Analysis of FRP Laminates by Means of Physically Based Phenomological Models," *Composites Science and Technology*, Vol. 62, pp. 1633–1662, 2002.

[105] P. K. Gotis, C. C. Chamis, and L. Minnetyan, "Prediction of Composite Laminate Fracture: Micromechanics and Progressive Failure," *Composites Science and Technology*, Vol. 58, pp. 1137–1149, 1998.

[106] P. K. Gotis, C. C. Chamis, and L. Minnetyan, "Application of Progressive Fracture Analysis for Predicting Failure Envelopes and Stress-Strain Behaviors of Composite Laminates: A Comparison with Experimental Results," *Composites Science and Technology*, Vol. 62, pp. 1545–1559, 2002.

[107] R. G. Cuntze and A. Freund, "The Predictive Capability of Failure Mode Concept-Based Strength Criteria for Multidirectional Laminates," *Composites Science and Technology*, Vol. 64, No. 3-4, pp. 343–377, 2004.

[108] R. G. Cuntze, "The Predictive Capability of Failure Mode Concept-Based Strength Criteria for Multidirectional Laminates - Part B," *Composites Science and Technology*, Vol. 64, No. 3-4, pp. 487–516, 2004.

[109] A. Rotem and Z. Hashin, "Failure Modes of Angle Ply Laminates," *Journal of Composite Materials*, Vol. 9, pp. 191–206, 1975.

[110] R. H. Bossi and G. E. Georgeson, "Composite Structure Development Decisions Using X-Ray CT Measurements," *Materials Evaluation*, Vol. 53, pp. 1198–1203, Oct. 1995.

[111] R. H. Bossi, "Failure Analysis Using Microfocus X-ray Imaging," *Journal of Testing and Evaluation*, Vol. 27, pp. 137–142, Mar. 1999.

[112] P. J. Schilling, B. R. Karedla, A. K. Tatiparthi, M. A. Verges, and P. D. Herrington, "X-ray Computed Microtomography of Internal Damage in Fiber Reinforced Polymer Matrix Composites," *Composites Science and Technology*, Vol. 65, pp. 2071–2078, 2005.

[113] P. Wright, X. Fu, I. Sinclair, and S. M. Spearing, "Ultra High Resolution Computed Tomography of Damage in Notched Carbon Fiber-Epoxy Composites," *Journal of Composite Materials*, Vol. 42, No. 19, pp. 1993–2002, 2008.

[114] Hexcel Corporation, *HexTow AS4 Carbon Fiber Product Data*, Mar. 2010.

[115] L. H. Peebles, *Carbon Fibers: Formation, Structure, and Properties*, p. 62. Ann Arbor: CRC Press, 1995.

[116] Composite Materials Handbook 17 (CMH-17-2F), *Polymer Matrix Composites: Material Properties*. Volume 2F, Chapter 4, June 2002.

[117] P. W. Mast, G. E. Nash, J. G. Michopoulos, R. Thomas, R. Badaliance, and I. Wolock, "Experimental Determination of Dissipated Energy Density as a Measure of Strain-Induced Damage in Composites," report 9369, Naval Research Laboratory, Apr. 1992.

[118] P. W. Mast, G. E. Nash, J. G. Michopoulos, R. Thomas, R. Badaliance, and I. Wolock, "Characterization of Strain-Induced Damage in Composites Based on the Dissipated Energy Density Part I. Basic Scheme and Formulation," *Theoretical and Applied Fracture Mechanics*, Vol. 22, pp. 71–96, 1995.

[119] J. G. Michopoulos, J. C. Hermanson, and T. Furukawa, "Towards the robotic characterization of the constitutive response of composite materials," *Composite Structures*, Vol. 86, pp. 154–164, 2008.

[120] M. R. Wisnom, M. I. Jones, and W. Cui, "Failure of Tapered Composites Under Static and Fatigue Tension Loading," *AIAA Journal*, Vol. 33, No. 5, pp. 911–918, 1995.

[121] M. R. Wisnom, R. Dixon, and G. Hill, "Delamination in Asymmetrically Tapered Composites Loaded in Tension," *Composite Structures*, Vol. 35, pp. 309–322, 1996.

[122] K. He, S. V. Hoa, and R. Ganesan, "The Study of Tapered Laminated Composite Structures: A Review," *Composites Science and Technology*, Vol. 60, pp. 2643–2657, 2000.

[123] J. Chambers, "Documentation Images of Tested Composite Specimens Investigated During Chambers' Ph.D. Studies," Technical Report, Technology Laboratory of Advanced Materials and Structures, Dept. of Aeronautics and Astronautics, Massachusetts Institute of Technology, TELAMS Report 2012-1, volumes A through C, 2012.

[124] H. Chai, "The Characterization of Mode I Delamination Failure in Non-Woven, Multidirectional Laminates," *Composites*, Vol. 15, No. 4, pp. 277–290, 1984.

[125] M. Kashtalyan and C. Soutis, "Analysis of Composite Laminates with Intra- and Interlaminar Damage," *Progress in Aerospace Sciences*, Vol. 41, pp. 152–173, 2005.

[126] Dassault Systemes, *ABAQUS Theory Manual (v6.11)*.

[127] J. M. Whitney and R. J. Nuismer, "Stress Fracture Criteria for Laminated Composites Containing Stress Concentrations," *Journal of Composite Materials*, Vol. 8, pp. 253–265, July 1974.

[128] J. G. Michopoulos and A. Iliopoulos, "A computational workbench for remote full field 3d displacement and strain measurements," *in Proceedings of the ASME 2011 International Design Engineering Technical Conferences & Computers and Information in Engineering Conference IDETC/CIE*, (Washington, DC, USA), Aug. 2011.

[129] J. C. H. John G. Michopoulos, A. Iliopoulos and A. C. Orifici, "Preliminary Validation of Composite Material Constitutive Characterization," *in Proceedings of the ASME 2012 International Design Engineering Technical Conferences & Computers and Information in Engineering Conference IDETC/CIE*, (Chicago, IL, USA), Aug. 2012.

[130] T. W. Coats and C. E. Harris, "A Progressive Damage Methodology for Residual Strength Predictions of Notched Composite Panels," Technical Report, National Aeronautics and Space Administration Technical Memorandum 207646, Apr. 1998.

[131] J. Chen, M. Crisfield, A. Kinloch, E. Busso, F. Matthews, and Y. Qiu, "Predicting Progressive Delamination of Composite Material Specimens via Interface Elements," *Mechanics of Composite Materials and Structures*, Vol. 6, No. 4, pp. 301–317, 1999.

[132] V. Laš and R. Zemčík, "Progressive Damage of Unidirectional Composite Panels," *Journal of Composite Materials*, Vol. 42, No. 1, pp. 25–44, 2008.

[133] A. H. Puppo and H. A. Evensen, "Interlaminar Shear in Laminated Composites," *Journal of Composite Materials*, Vol. 4, pp. 204–220, 1970.

[134] P. L. N. Murthy and C. C. Chamis, "A Study of Interply Layer Effects on the Free Edge Stress Field of Angleplied Laminates," *Computers & Structures*, Vol. 20, No. 1-3, pp. 431–441, 1985.

[135] C. T. Sun, "Intelligent Tailoring of Composite Laminates," *Carbon*, Vol. 27, No. 5, pp. 679–687, 1989.

[136] M. Tahani and A. Nosier, "Free Edge Stress Analysis of General Cross-Ply Composite Laminates Under Extension and Thermal Loading," *Composites Structures*, Vol. 60, pp. 91–103, 2003.

[137] R. B. Pipes and N. J. Pagano, "Interlaminar Stresses in Composite Laminates Under Uniform Axial Extension," *Journal of Composite Materials*, Vol. 4, pp. 538–548, Oct. 1970.

[138] N. J. Pagano, "Stress Fields in Composite Laminates," *International Journal of Solids and Structures*, Vol. 14, pp. 385–400, 1978.

[139] N. J. Pagano, "Free Edge Stress Fields in Composite Laminates," *International Journal of Solids and Structures*, Vol. 14, pp. 401–406, 1978.

[140] P. D. Soden, M. J. Hinton, and A. S. Kaddour, "Lamina Properties, Lay-Up Configurations and Loading Conditions for a Range of Fibre-Reinforced Composite Laminates," *Composites Science and Technology*, Vol. 58, pp. 1011–1022, 1998.

[141] Dassault Systemes, *ABAQUS Theory Manual (v6.11)*. Section 23.2.

[142] Hexcel Corporation, *3501-6 Epoxy Matrix Product Data*, 1998.

[143] P. C. Chou, J. Carleone, and C. M. Hsu, "Elastic Constants of Layered Media," *Journal of Composite Materials*, Vol. 6, No. 1, pp. 80–93, 1971.

[144] T. A. Bogetti, C. P. R. Hoppel, and W. H. Drysdale, "Three-Dimensional Effective Property and Strength Prediction of Thick Laminated Composite Media," Technical Report ARL-TR-911, Army Research Laboratory, 1995.

[145] S. G. Lekhnitskii, *Theory of Elasticity of an Anisotropic Elastic Body*. San Francisco: Holden-Day, Inc., 1963.

[146] R. M. Jones, *Mechanics of Composite Materials, 2nd ed.* New York: Taylor & Francis Group, 1999.

[147] G. H. Staab, *Laminar Composites*, ch. 6. Boston, Massachusetts: Butterworth Heinemann, 1999.

[148] C. Kassapoglou, "Interlaminar Stresses at Straight Free Edges of Composite Laminates," Technical Report 84-18, Massachusetts Institute of Technology, 1984.

[149] C. Kassapoglou and P. A. Lagace, "Closed Form Solutions for the Interlaminar Stress Field in Angle-Ply and Cross-Ply Laminates," *Journal of Composite Materials*, Vol. 21, pp. 292–308, 1987.

[150] S. S. Wang and I. Choi, "Boundary-Layer Effects in Composite Laminates: Part 1-Free-Edge Stress Singularities," *Journal of Applied Mechanics*, Vol. 49, pp. 541–548, Sept. 1982.

[151] E. A. Armanios and L. Parnas, "Delamination Analysis of Tapered Laminated Composites Under Tensile Loading," *Composite Materials: Fatigue and Fracture, ASTM STP 1110*, Vol. 3, pp. 340–358, 1991.

[152] S. Wicks, R. Guzman de Villoria, and B. L. Wardle, "Interlaminar and Intralaminar Reinforcement of Composite Laminates with Aligned Carbon Nanotubes," *Composites Science and Technology*, Vol. 70, pp. 20–28, 2010.

Appendices

[THIS PAGE INTENTIONALLY LEFT BLANK]

Appendix A

Question Tree

This appendix contains the detailed branches of the Question Tree, as described in Section 3.2. The high level objective of the work is broken down into two primary branches, Branch A and Branch B, as shown in Figure 3.1 in Chapter 3. The overall focus of Branch A deals with the manifestation of different damage mechanisms within a composite material, laminate, and structure, along with the lengthscales associated with such mechanisms. This branch is the main focus of the current work. The lead question of Branch B deals with ways to predict failure in composites. Thus, the overall focus of Branch B deals with the predictive capabilities to calculate stress states, to predict failure, and to assess overall structural behavior. The further breakdowns of the branches continue until "root" questions are reached, as described in Section 3.2. Such questions are those that must first be answered in order to answer higher-level questions. These are shown in the figures in this appendix.

As described in Section 3.2, branches with a shading of gray are indicative of the questions in that branch having an answer from the literature. Questions with a hatch pattern are indicative of a partial answer to the question having been reached from the literature. Questions remaining outstanding after evaluating the reviewed literature are left unshaded. The two main branches, Branch A and Branch B, of the question tree are shown in Figures A.1 and A.2. Following these figures are enlarged views of sections of the main branches, detailing the sub-branches. The details of the sub-branches of Branch A are shown in Figures A.3 through A.5. The details of the

sub-branches of Branch B are shown in Figures A.6 and A.7.

One branch remains unattached from the tree, shown in Figure A.4, located between Branches A.1.1.1.1 and A.1.1.1.2. This branch deals with "unk-unks", or unknown unknowns. As described in Section 3.2, there is always a possibility that a previously unknown damage mode is discovered and that it will be unknown how to address this mode. This branch is included in the tree (although not attached) as a reminder that such unknown modes and issues may exist.

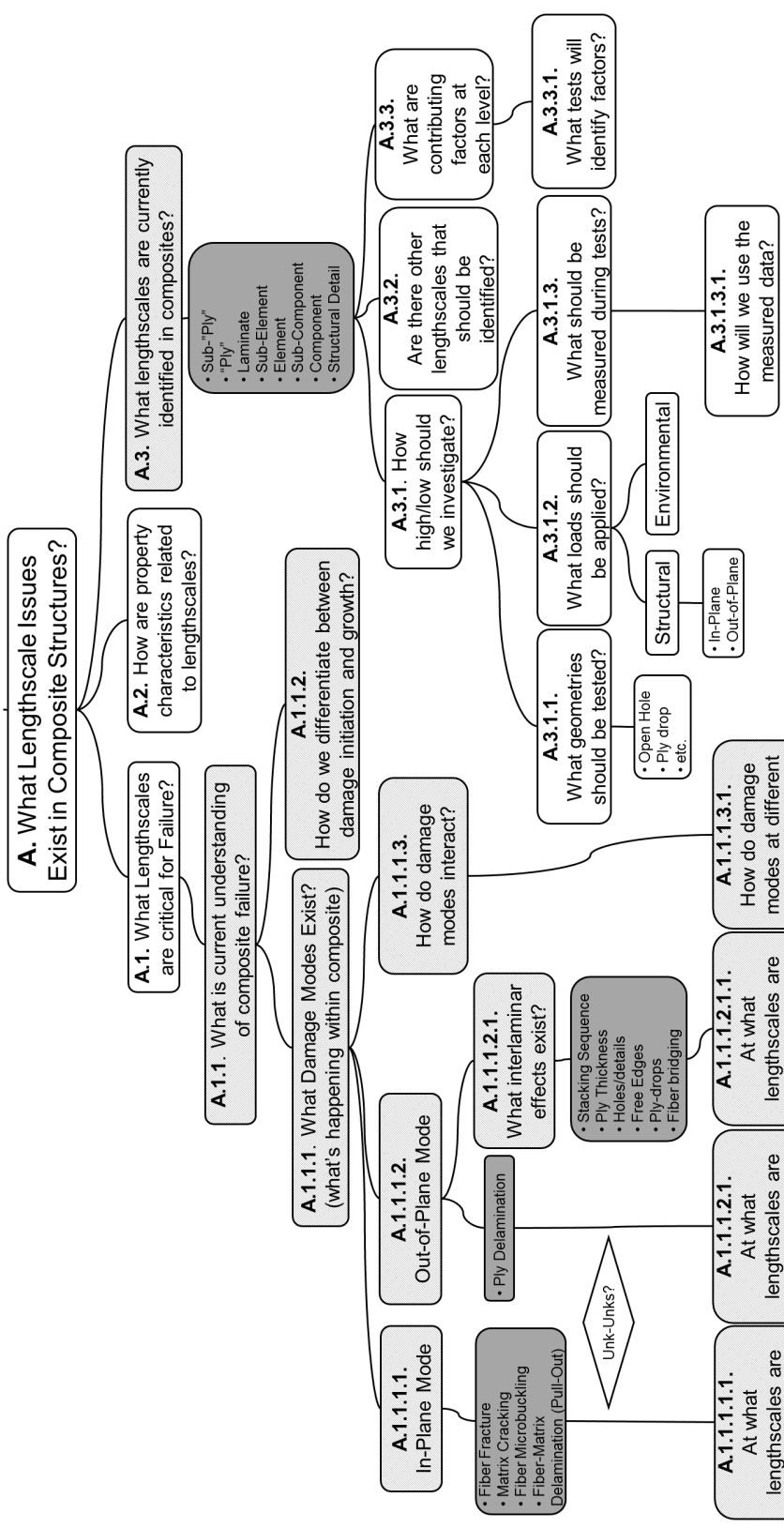

Figure A.1 Overall details of Branch A of the Question Tree.

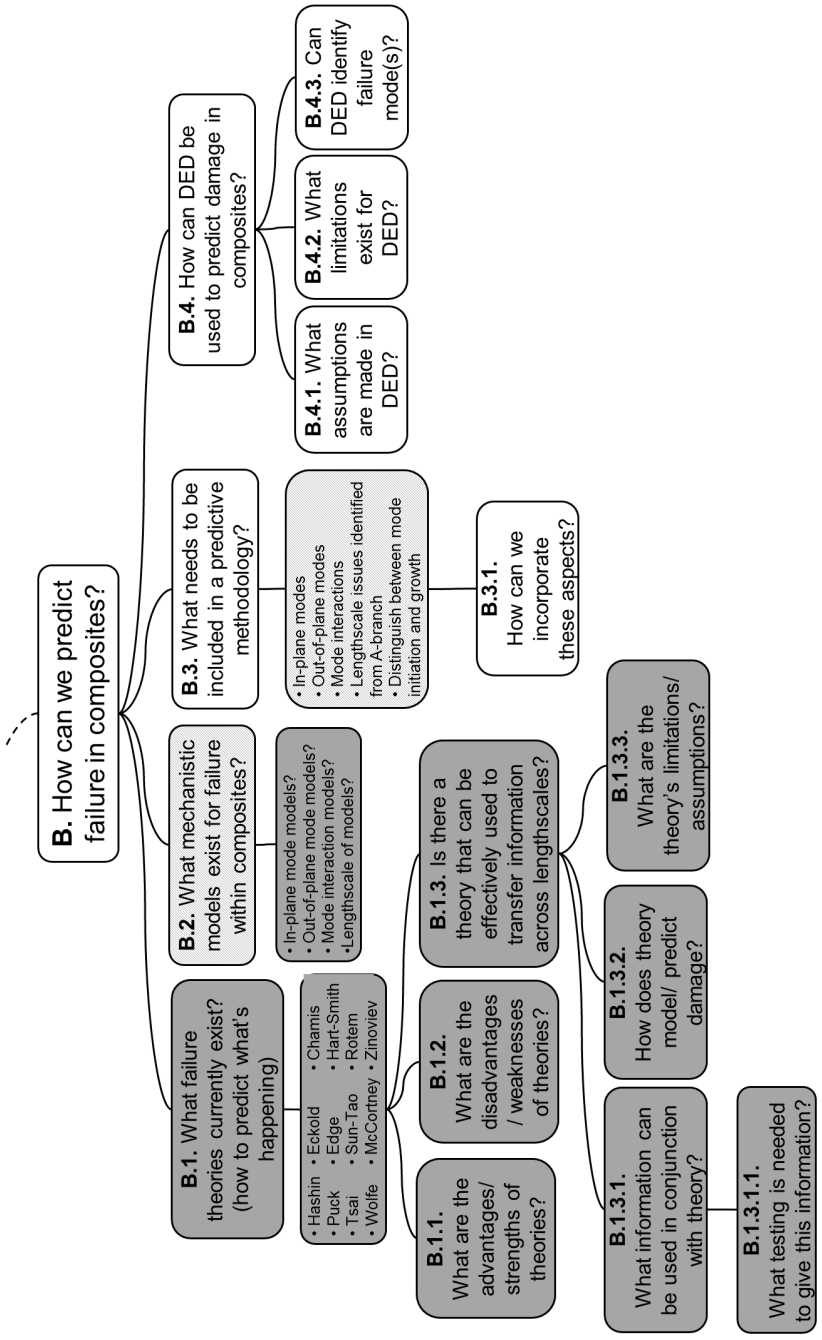

Figure A.2 Overall details of Branch B of the Question Tree.

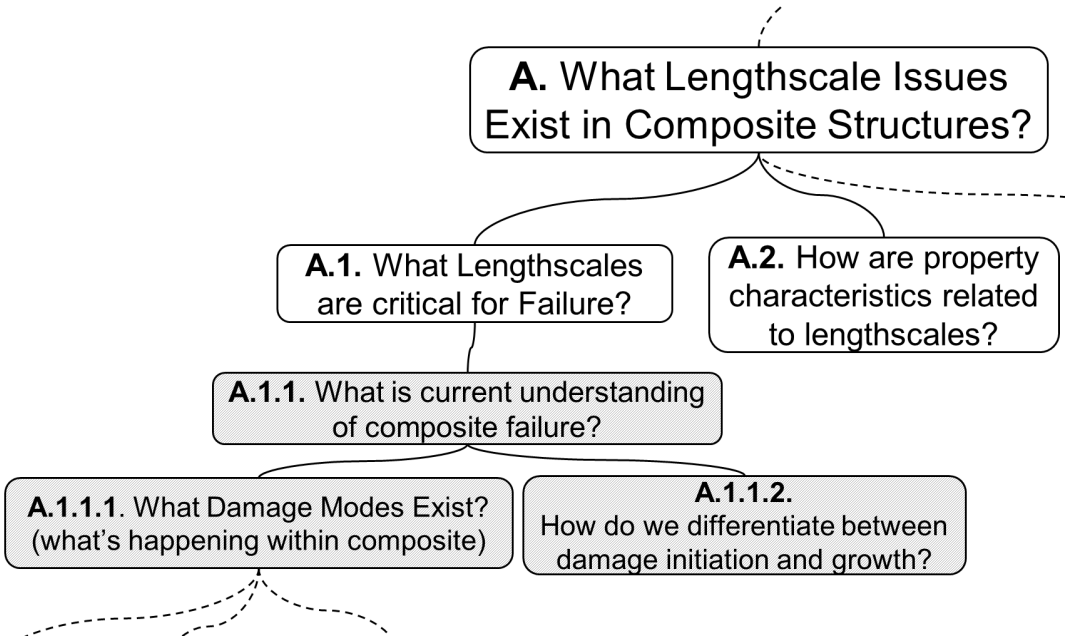

Figure A.3 Details of the first three levels of Branches A.1 and A.2 of the Question Tree.

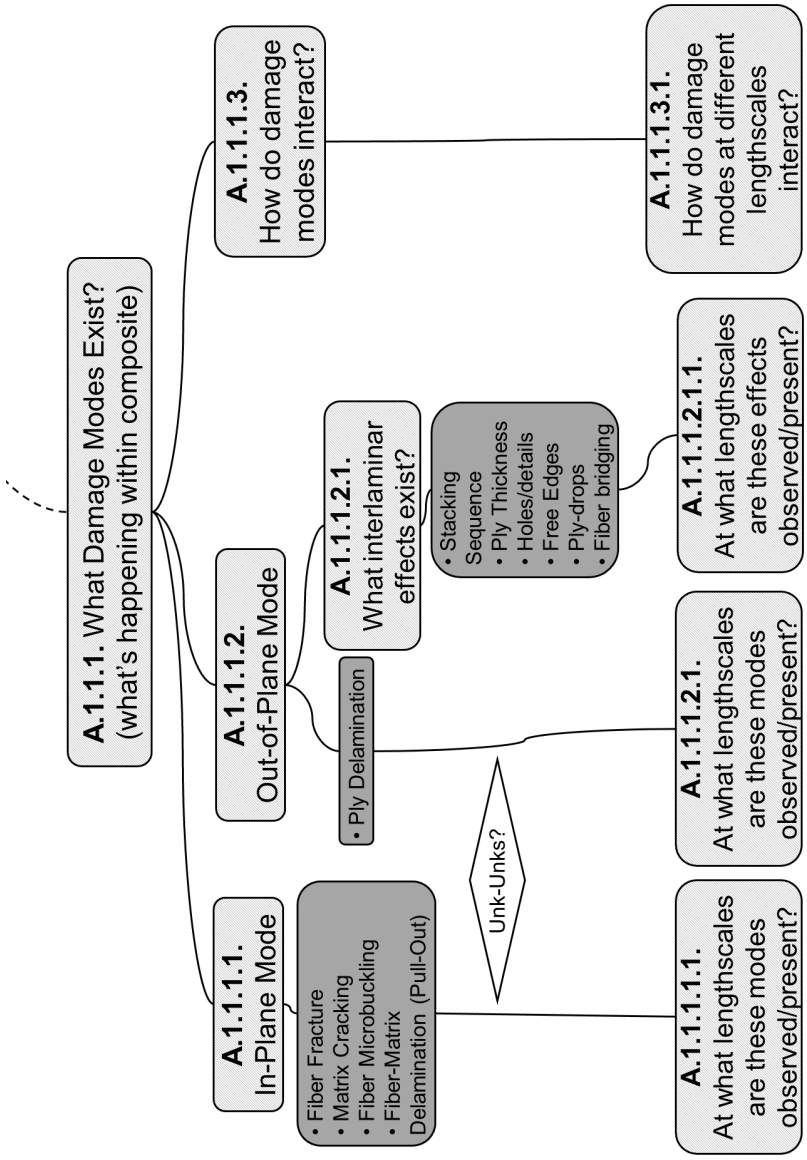

Figure A.4 Full details of Branch A.1.1.1 of the Question Tree.

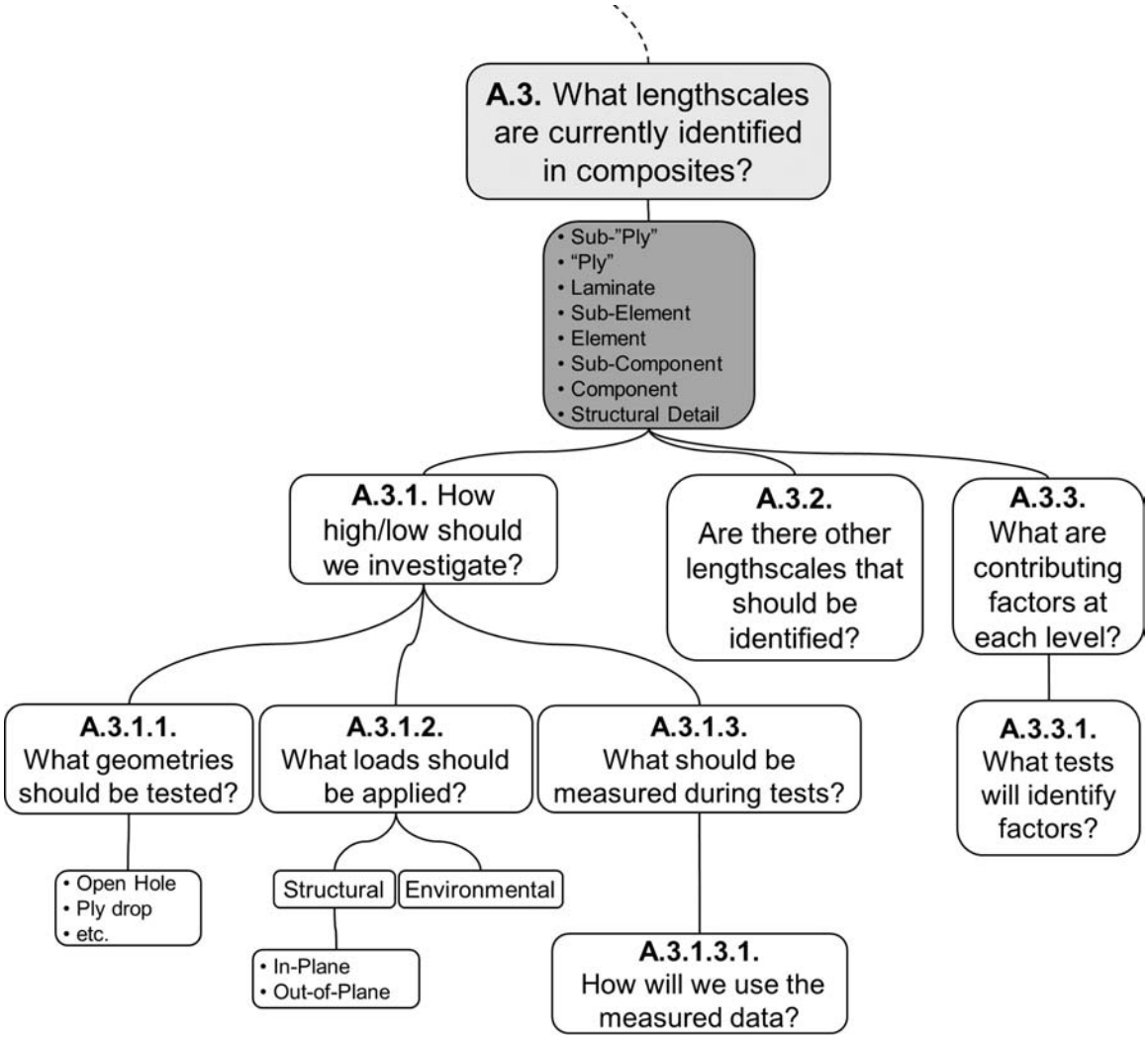

Figure A.5 Full details of Branch A.3 of the Question Tree.

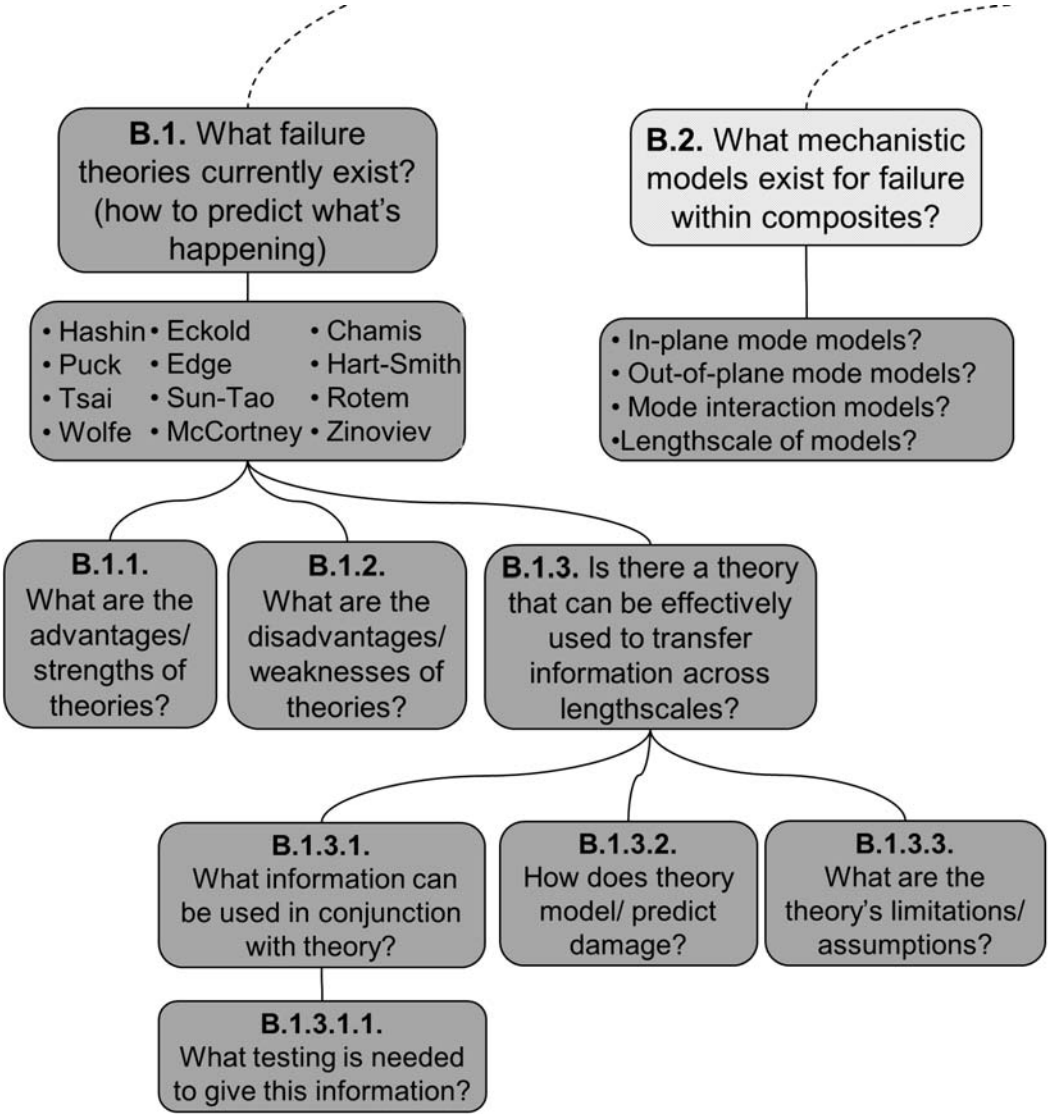

Figure A.6 Full details of Branches B.1 and B.2 of the Question Tree.

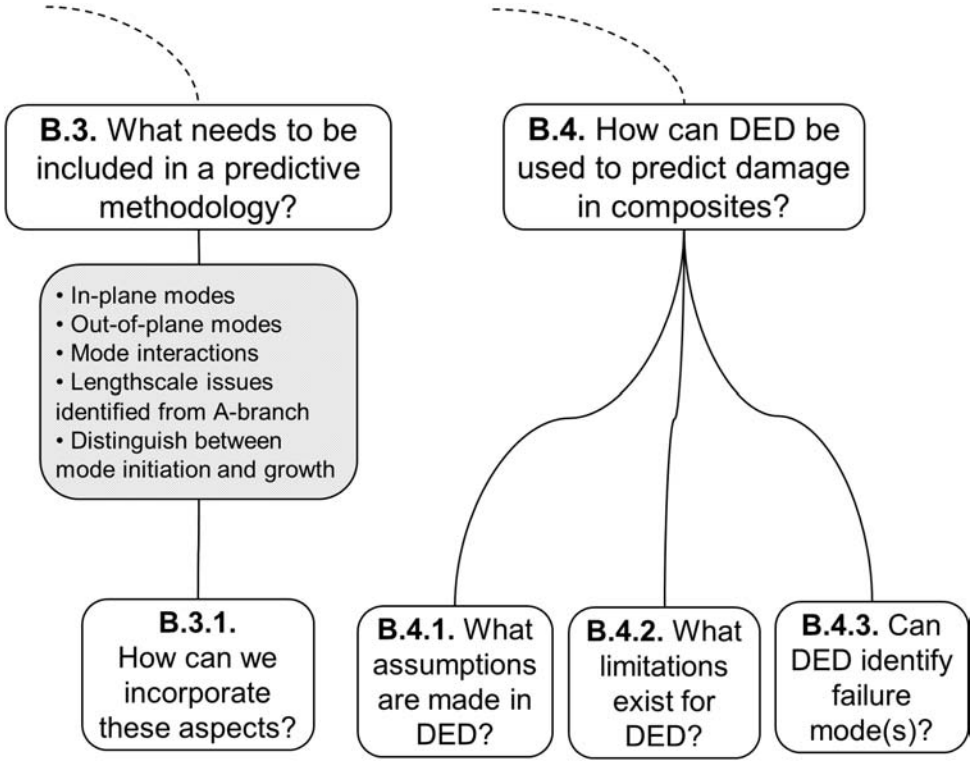

Figure A.7 Full details of Branches B.3 and B.4 of the Question Tree.

[THIS PAGE INTENTIONALLY LEFT BLANK]

Appendix B

Additional Strain Results

This appendix contains additional figures relating to the material discussed in Section 7.3. Two types of figures are included in this appendix; isostrain plots of the strain fields of specimens, and plots of strain magnitudes along arc paths for specimens, as defined in Section 7.3. The figures in this appendix illustrate the variations of the strain fields, and the plots of strain magnitudes along arc paths for laminate angles not shown in Section 7.3.

The appendix is organized by specimen type. Figures B.1 through B.20 pertain to the single-edge-notched specimen and are included in Section B.1. Figures B.21 through B.63 pertain to the double-edge-notched specimen and are included in Section B.2. Figures B.64 through B.84 pertain to the open-hole tension specimen and are included in Section B.3. Finally, Figures B.85 through B.178 pertain to the damage inclusion specimens and are included in Section B.4.

B.1 Strain Plots for Single-Edge-Notched Specimen

This section contains additional figures relating to the results of the single-edge-notched specimen discussed in Section 7.3.1. Two types of figures are included in this section: isostrain plots of the strain fields of the single-edge-notched specimens, and plots of strain magnitudes along arc paths for the single-edge-notched specimens, as defined in Section 7.3.1. The figures in this section of the appendix illustrate the variations of the strain fields, and the plots of strain magnitudes along arc paths for laminate angles not shown in Section 7.3.1.

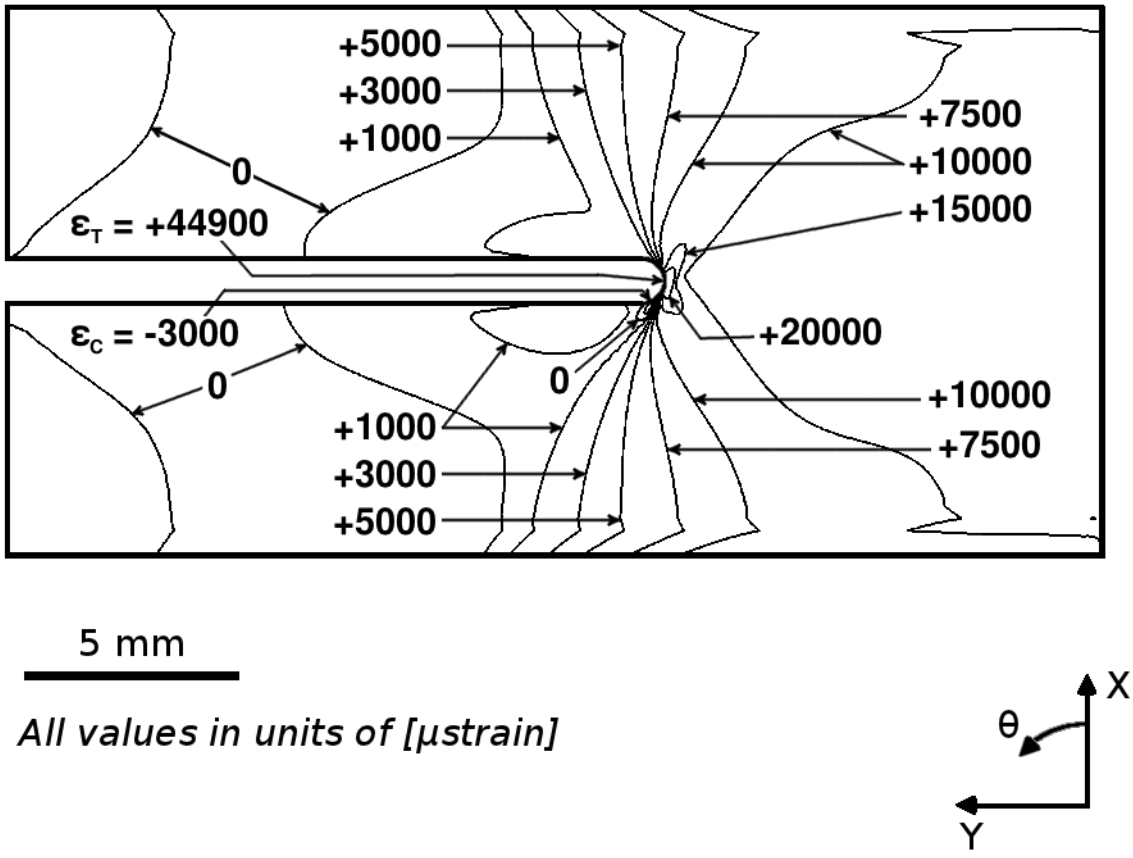

Figure B.1 Isostrain plot of strain field of ϵ_{11}, in laminate axes, at the midplane of ply 1 (a $-30°$ ply) of the single-edge-notched specimen model for the laminate of $[(-30/+30_2/-30_2/+30)_S]_S$.

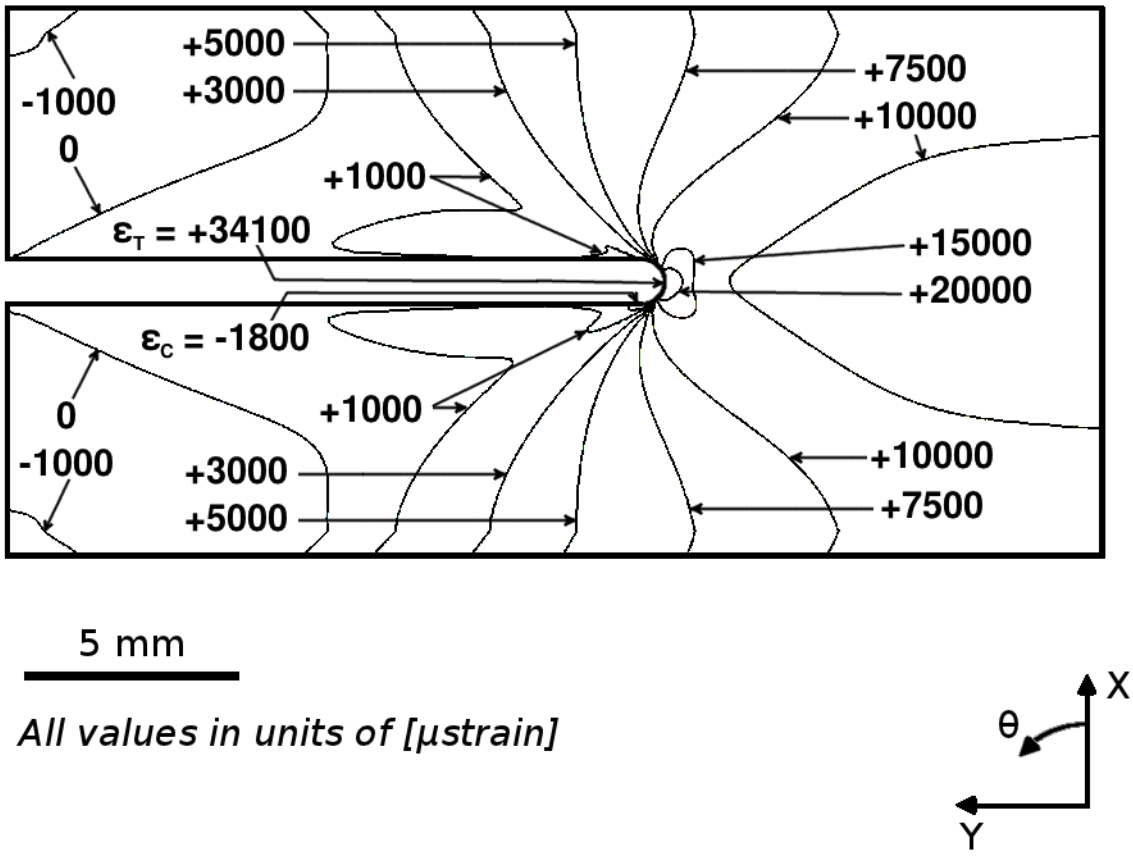

Figure B.2 Isostrain plot of strain field of ϵ_{11}, in laminate axes, at the midplane of ply 1 (a -60° ply) of the single-edge-notched specimen model for the laminate of $[(-60/+60_2/-60_2/+60)_S]_S$.

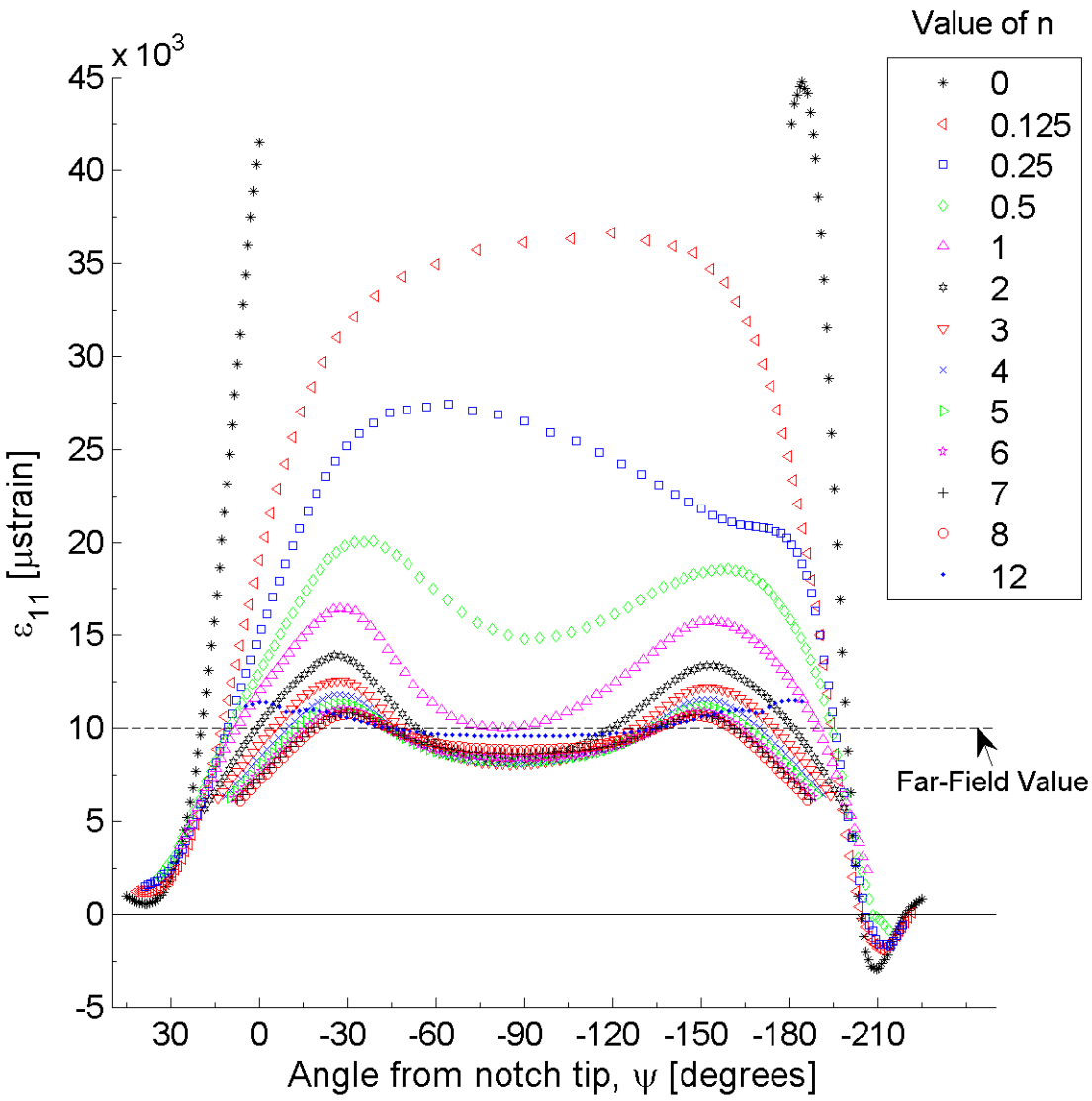

Figure B.3 Plot of ϵ_{11}, in laminate axes, along arc paths at the midplane of ply 1 (a $-30°$ ply) of the single-edge-notched specimen model for the laminate of $[(-30/+30_2/-30_2/+30)_S]_S$.

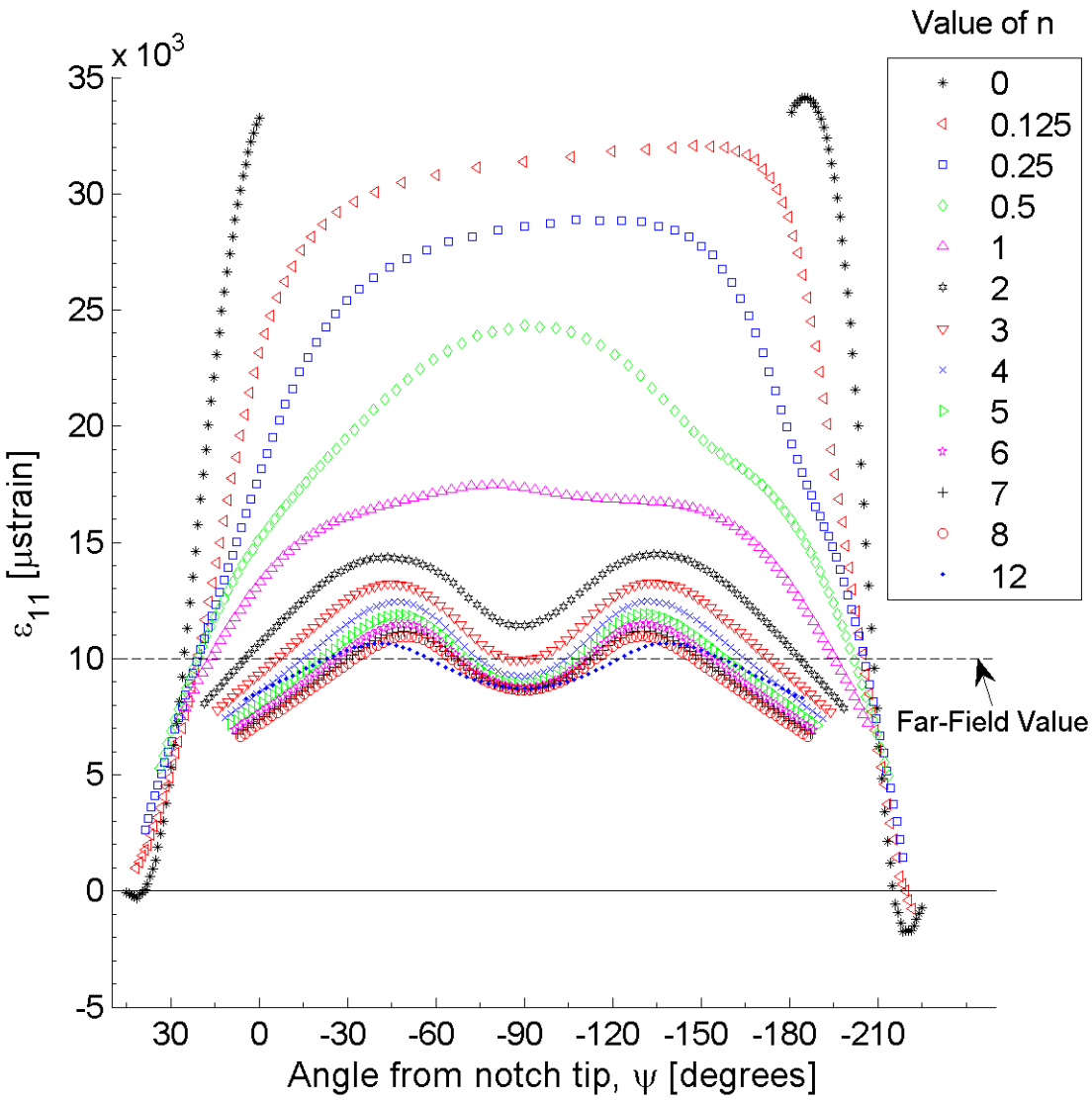

Figure B.4 Plot of ϵ_{11}, in laminate axes, along arc paths at the midplane of ply 1 (a $-60°$ ply) of the single-edge-notched specimen model for the laminate of $[(-60/+60_2/-60_2/+60)_S]_S$.

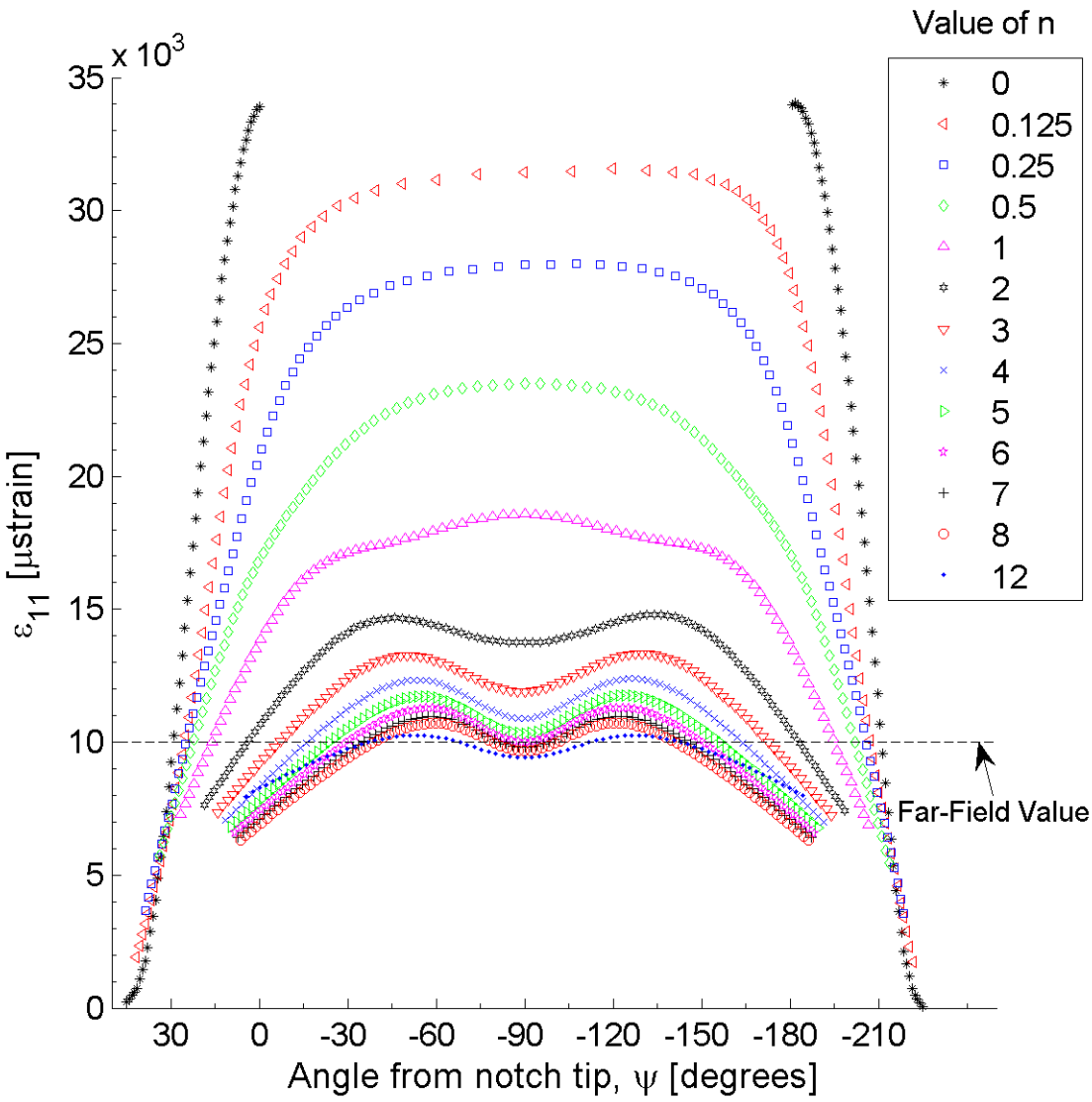

Figure B.5 Plot of ϵ_{11}, in laminate axes, along arc paths at the midplane of ply 1 (a $-75°$ ply) of the single-edge-notched specimen model for the laminate of $[(-75/+75_2/-75_2/+75)_S]_S$.

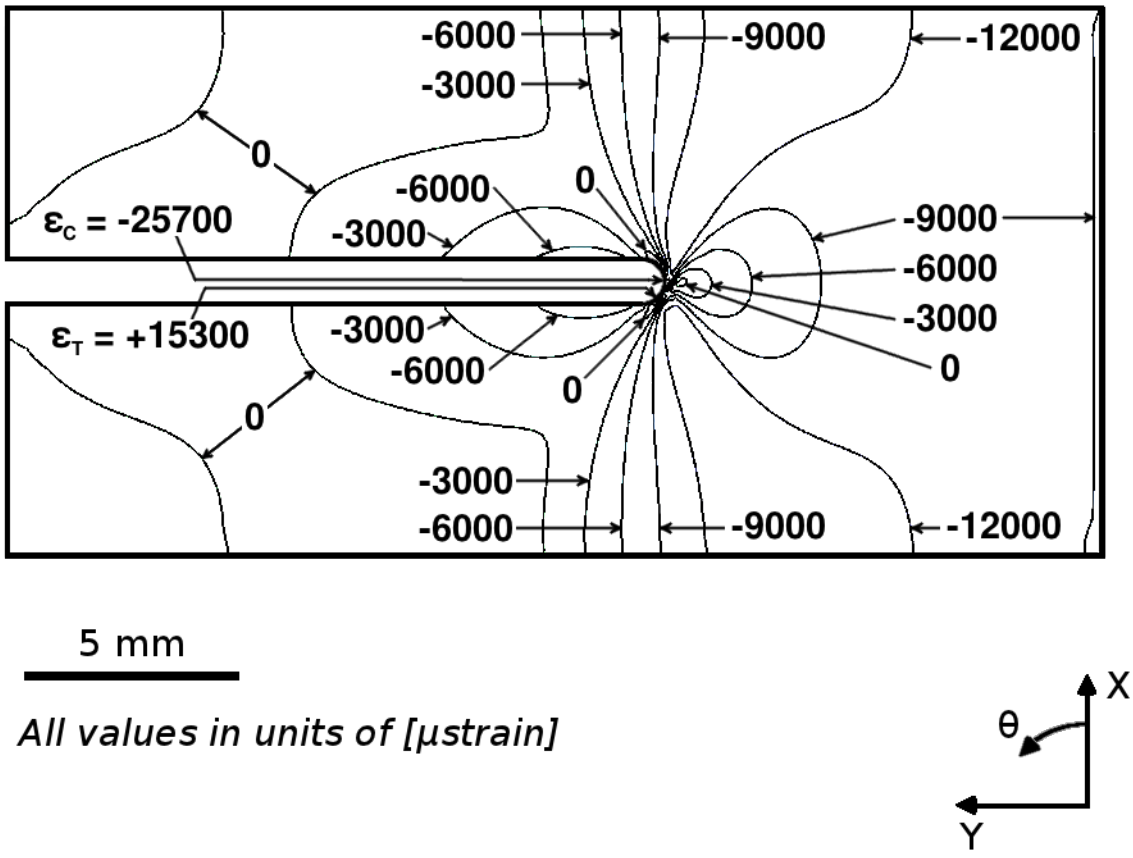

Figure B.6 Isostrain plot of strain field of ϵ_{22}, in laminate axes, at the midplane of ply 1 (a $-30°$ ply) of the single-edge-notched specimen model for the laminate of $[(-30/+30_2/-30_2/+30)_S]_S$.

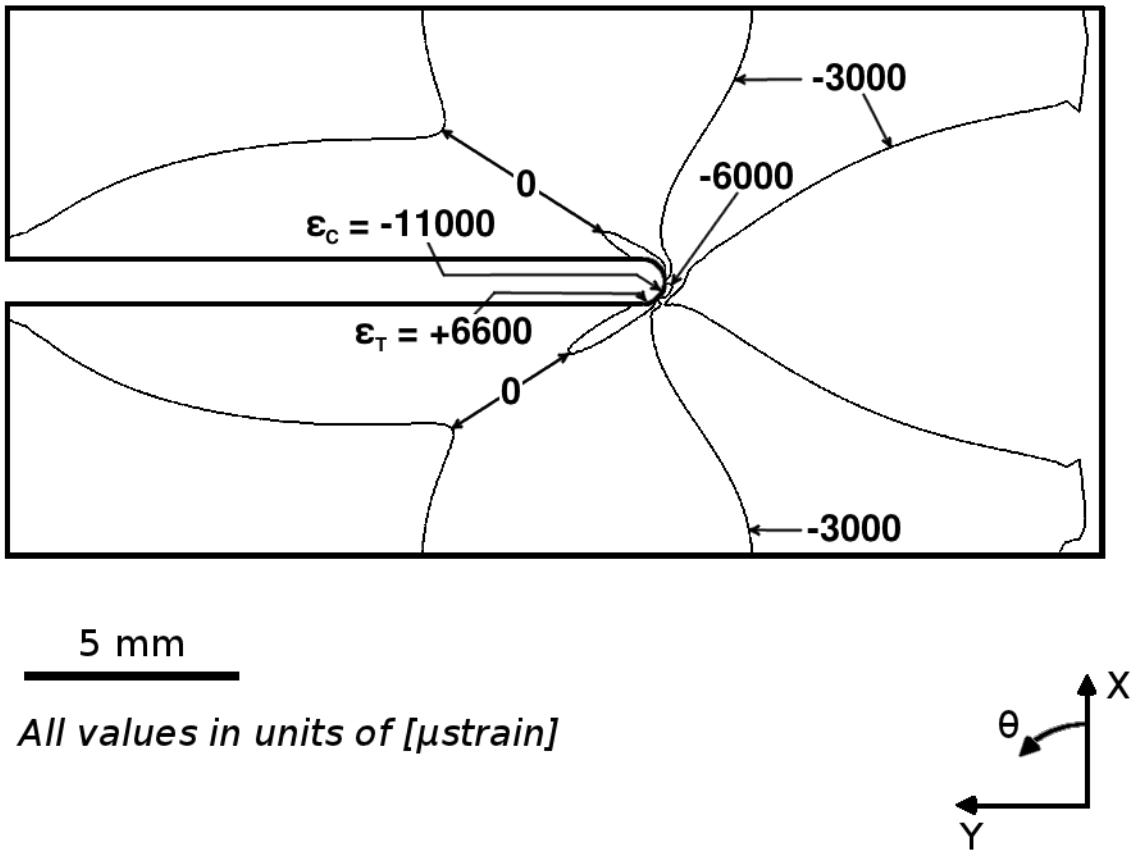

Figure B.7 Isostrain plot of strain field of ϵ_{22}, in laminate axes, at the midplane of ply 1 (a -60° ply) of the single-edge-notched specimen model for the laminate of $[(-60/+60_2/-60_2/+60)_S]_S$.

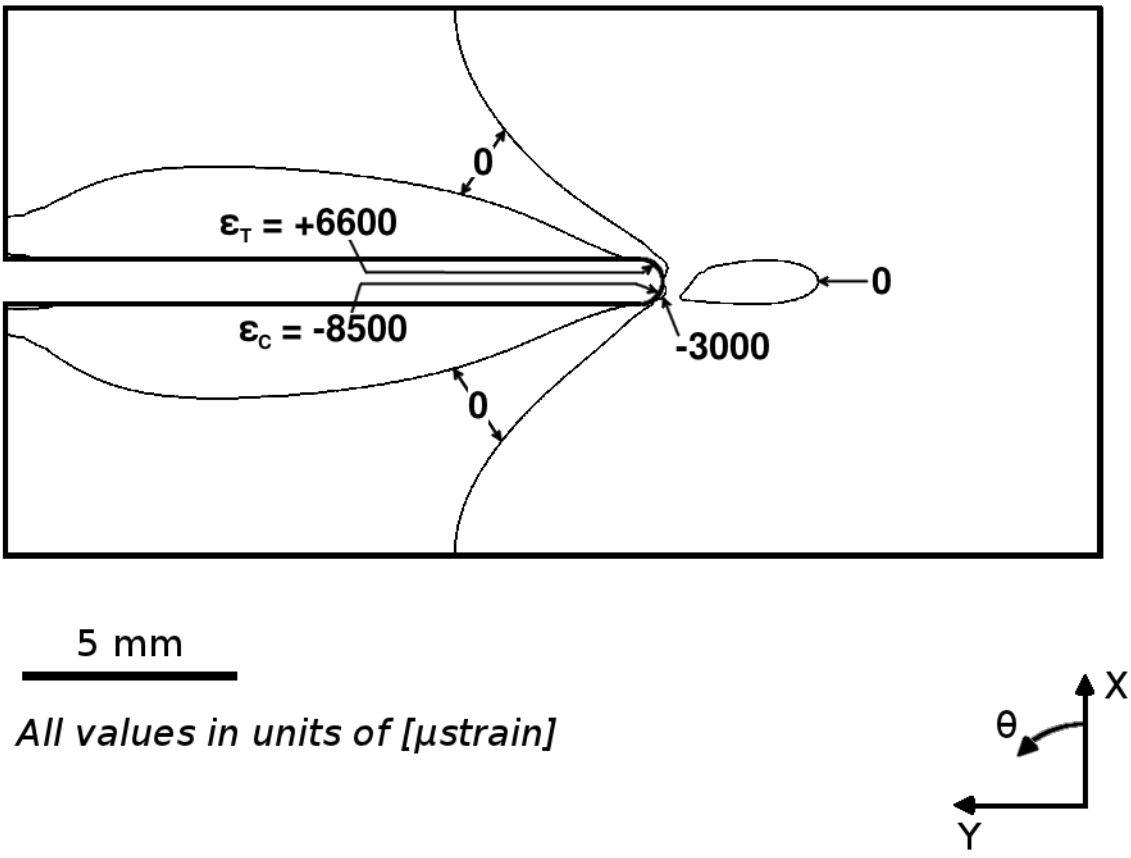

Figure B.8 Isostrain plot of strain field of ϵ_{22}, in laminate axes, at the midplane of ply 1 (a -75° ply) of the single-edge-notched specimen model for the laminate of $[(-75/+75_2/-75_2/+75)_S]_S$.

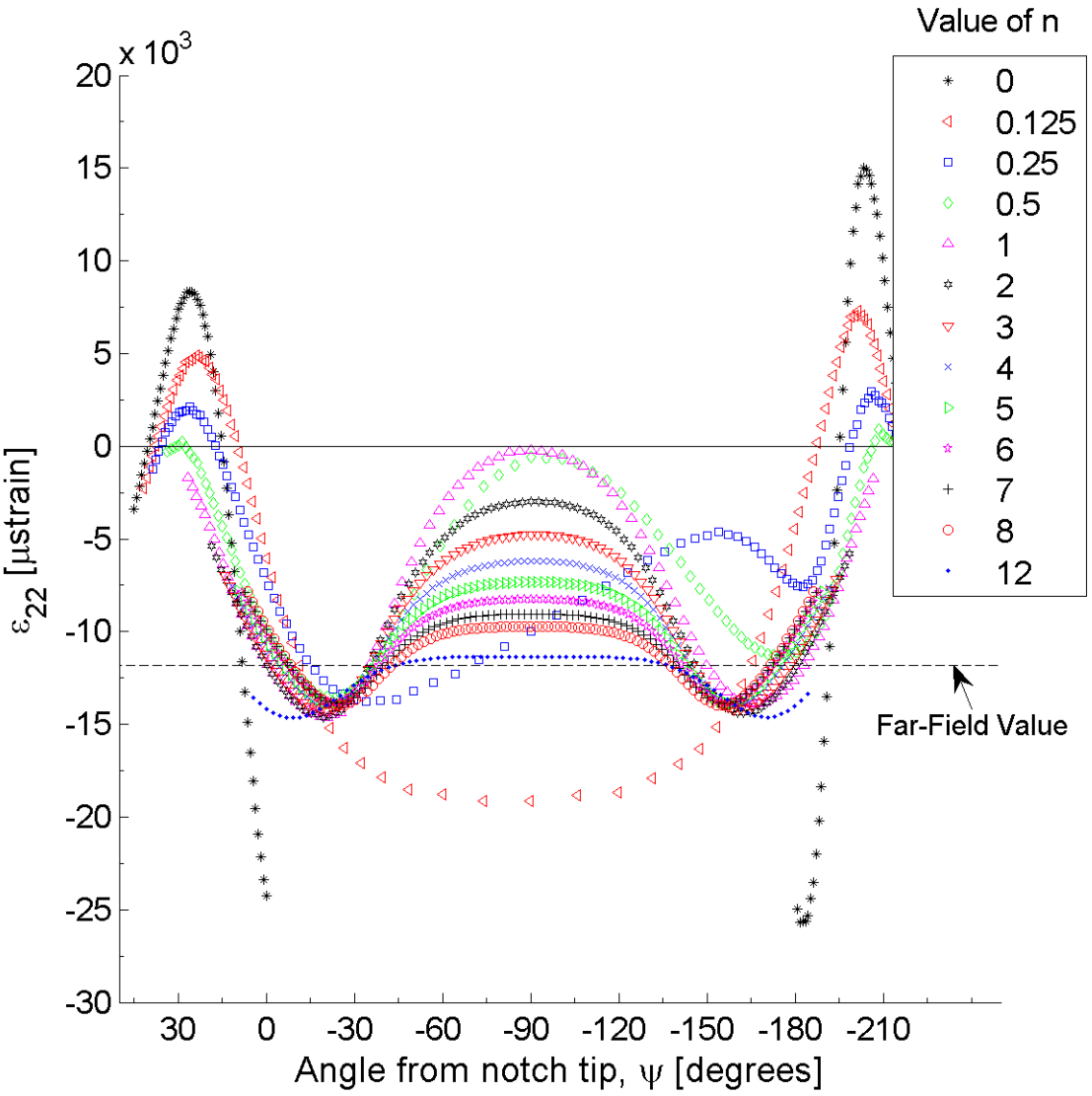

Figure B.9 Plot of ϵ_{22}, in laminate axes, along arc paths at the midplane of ply 1 (a -30° ply) of the single-edge-notched specimen model for the laminate of $[(-30/+30_2/-30_2/+30)_S]_S$.

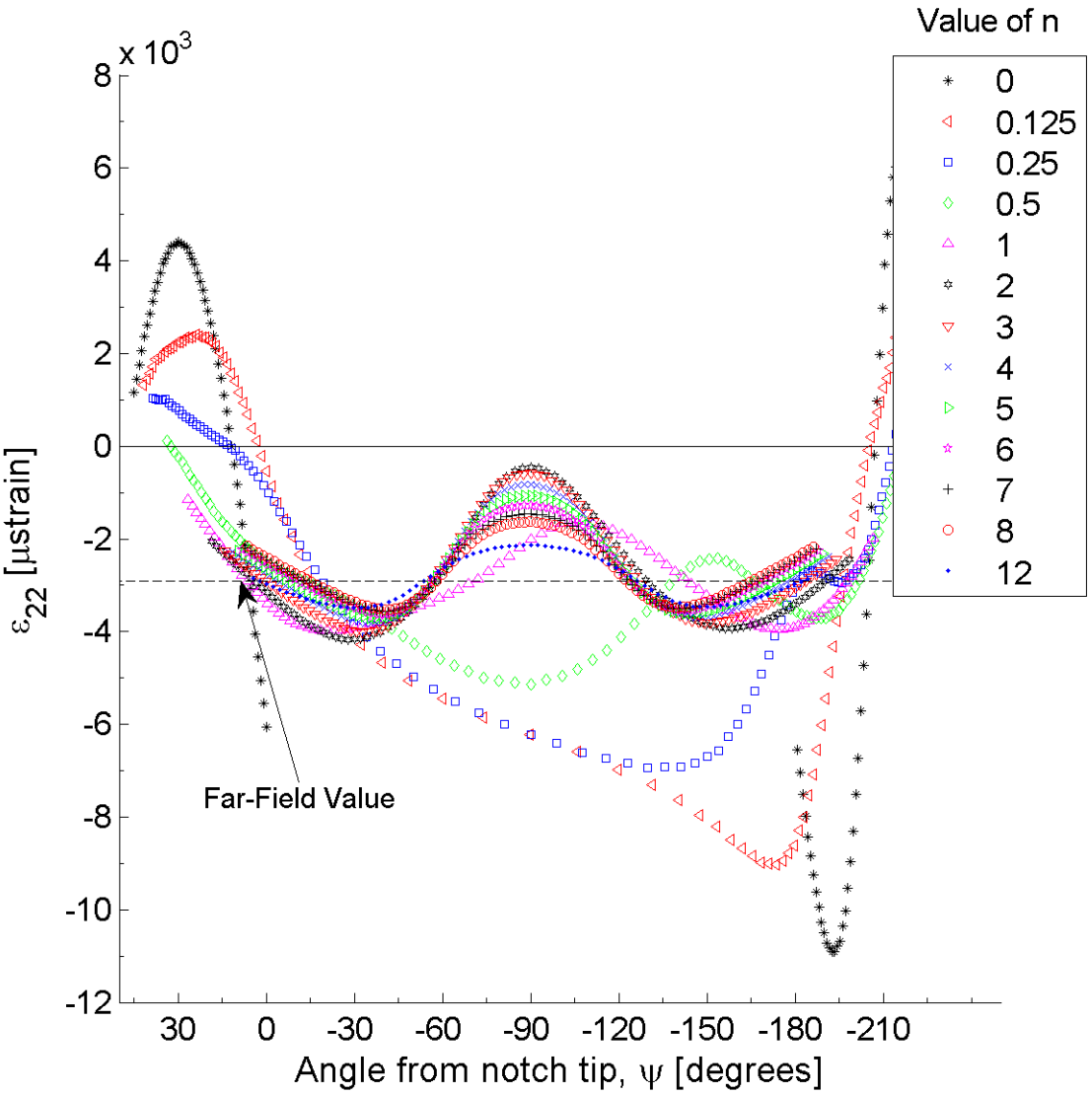

Figure B.10 Plot of ϵ_{22}, in laminate axes, along arc paths at the midplane of ply 1 (a -60° ply) of the single-edge-notched specimen model for the laminate of $[(-60/+60_2/-60_2/+60)_S]_S$.

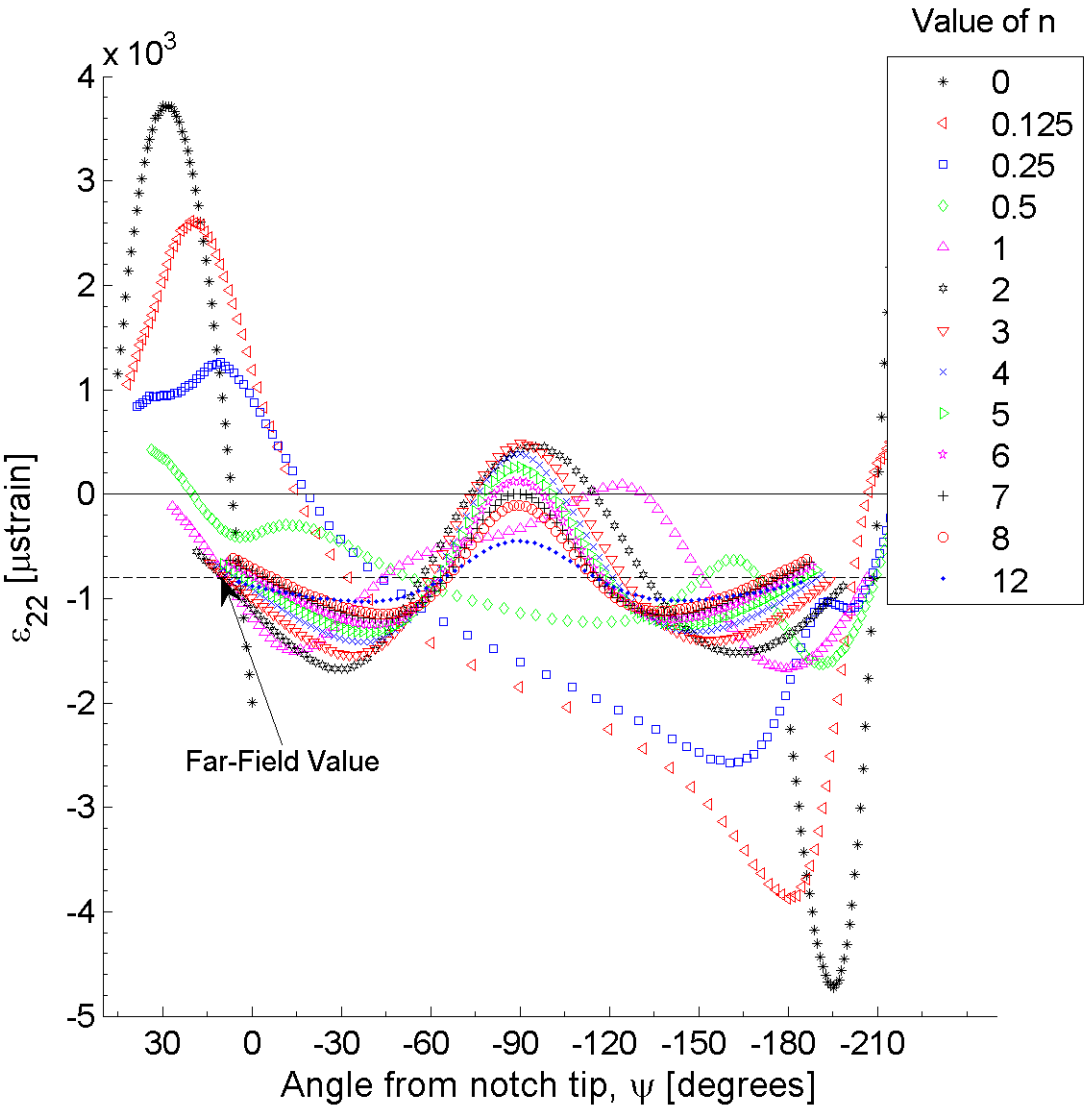

Figure B.11 Plot of ϵ_{22}, in laminate axes, along arc paths at the midplane of ply 1 (a -75° ply) of the single-edge-notched specimen model for the laminate of $[(-75/+75_2/-75_2/+75)_S]_S$.

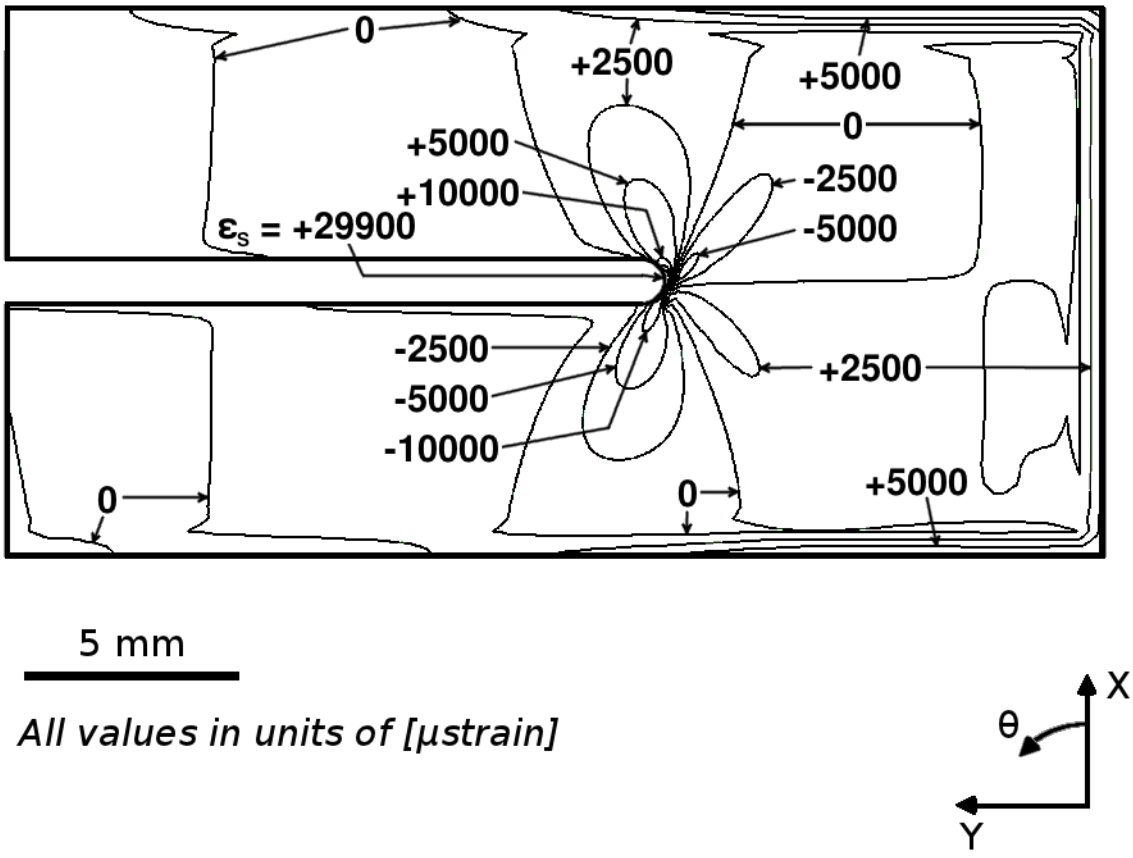

Figure B.12 Isostrain plot of strain field of ϵ_{12}, in laminate axes, at the midplane of ply 1 (a $-30°$ ply) of the single-edge-notched specimen model for the laminate of $[(-30/+30_2/-30_2/+30)_S]_S$.

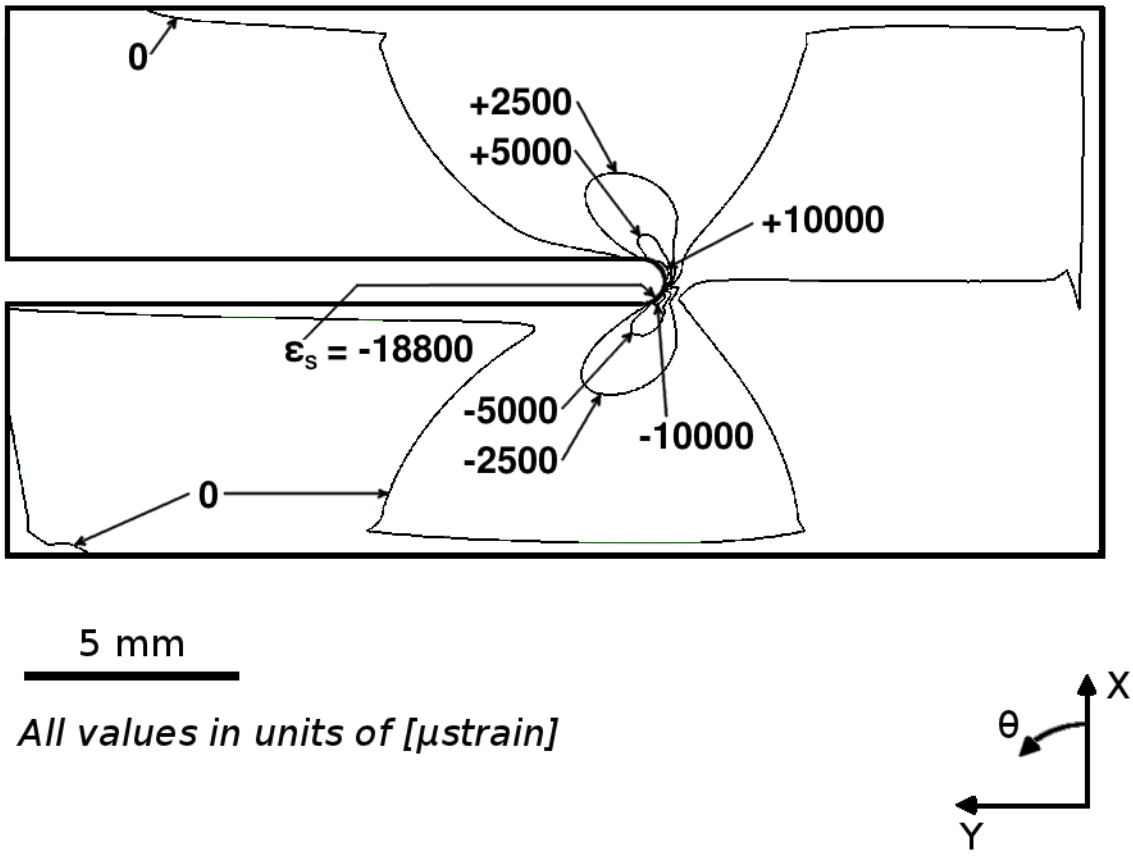

Figure B.13 Isostrain plot of strain field of ϵ_{12}, in laminate axes, at the midplane of ply 1 (a $-60°$ ply) of the single-edge-notched specimen model for the laminate of $[(-60/+60_2/-60_2/+60)_S]_S$.

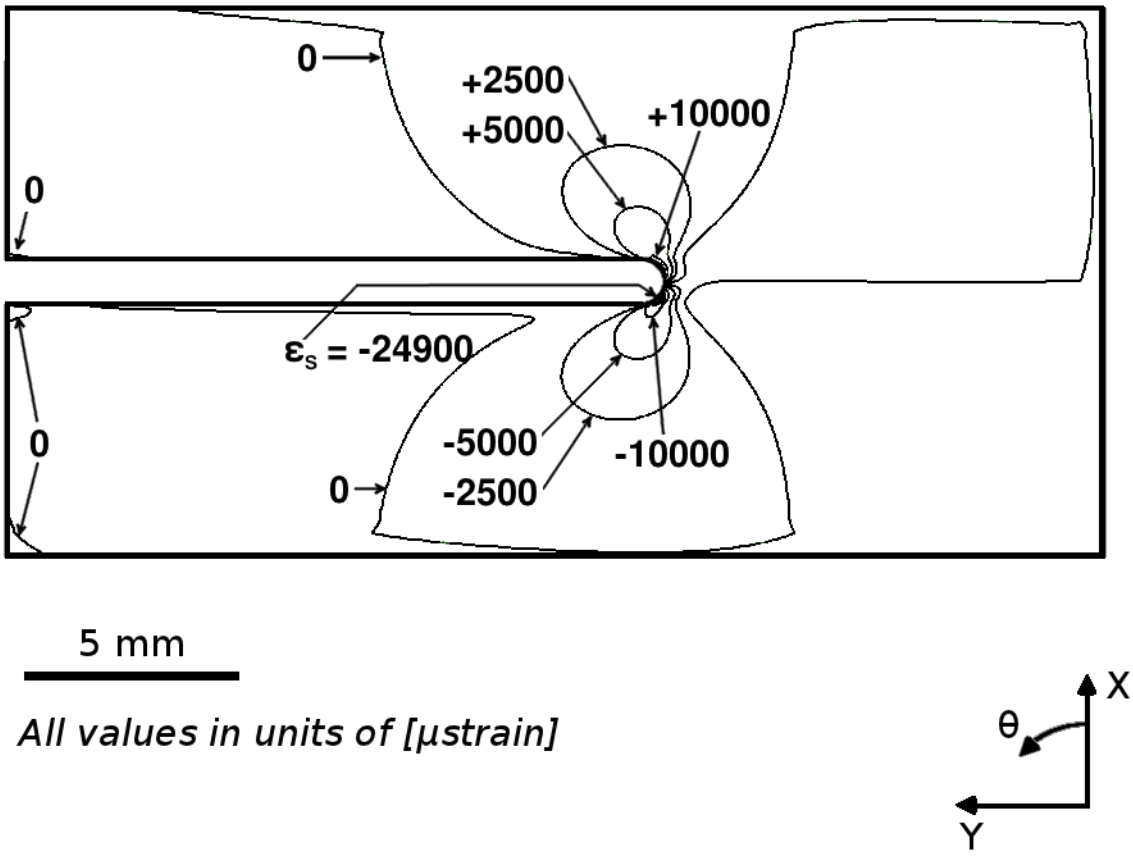

Figure B.14 Isostrain plot of strain field of ϵ_{12}, in laminate axes, at the midplane of ply 1 (a -75° ply) of the single-edge-notched specimen model for the laminate of $[(-75/+75_2/-75_2/+75)_S]_S$.

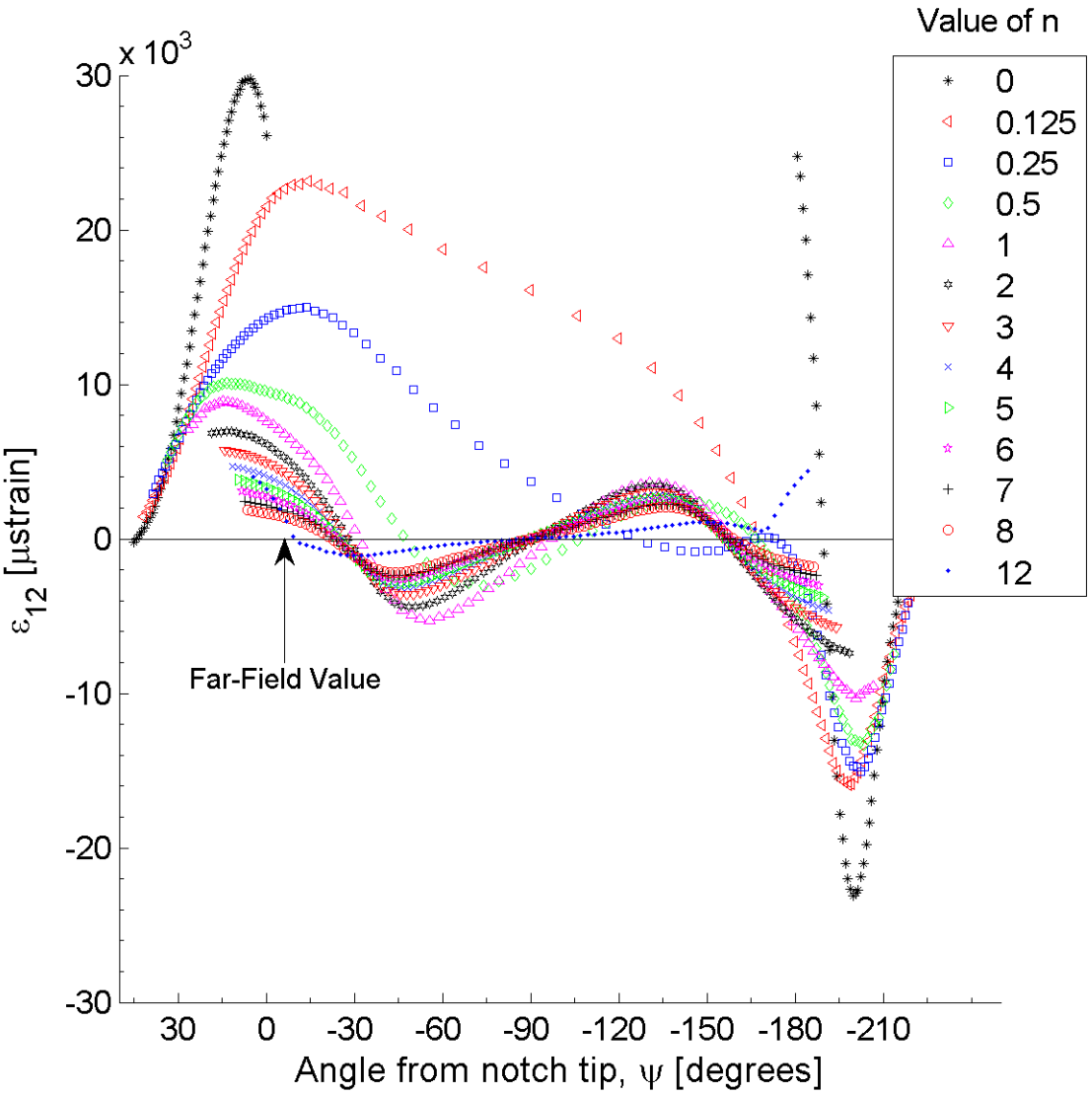

Figure B.15 Plot of ϵ_{12}, in laminate axes, along arc paths at the midplane of ply 1 (a -30° ply) of the single-edge-notched specimen model for the laminate of $[(-30/+30_2/-30_2/+30)_S]_S$.

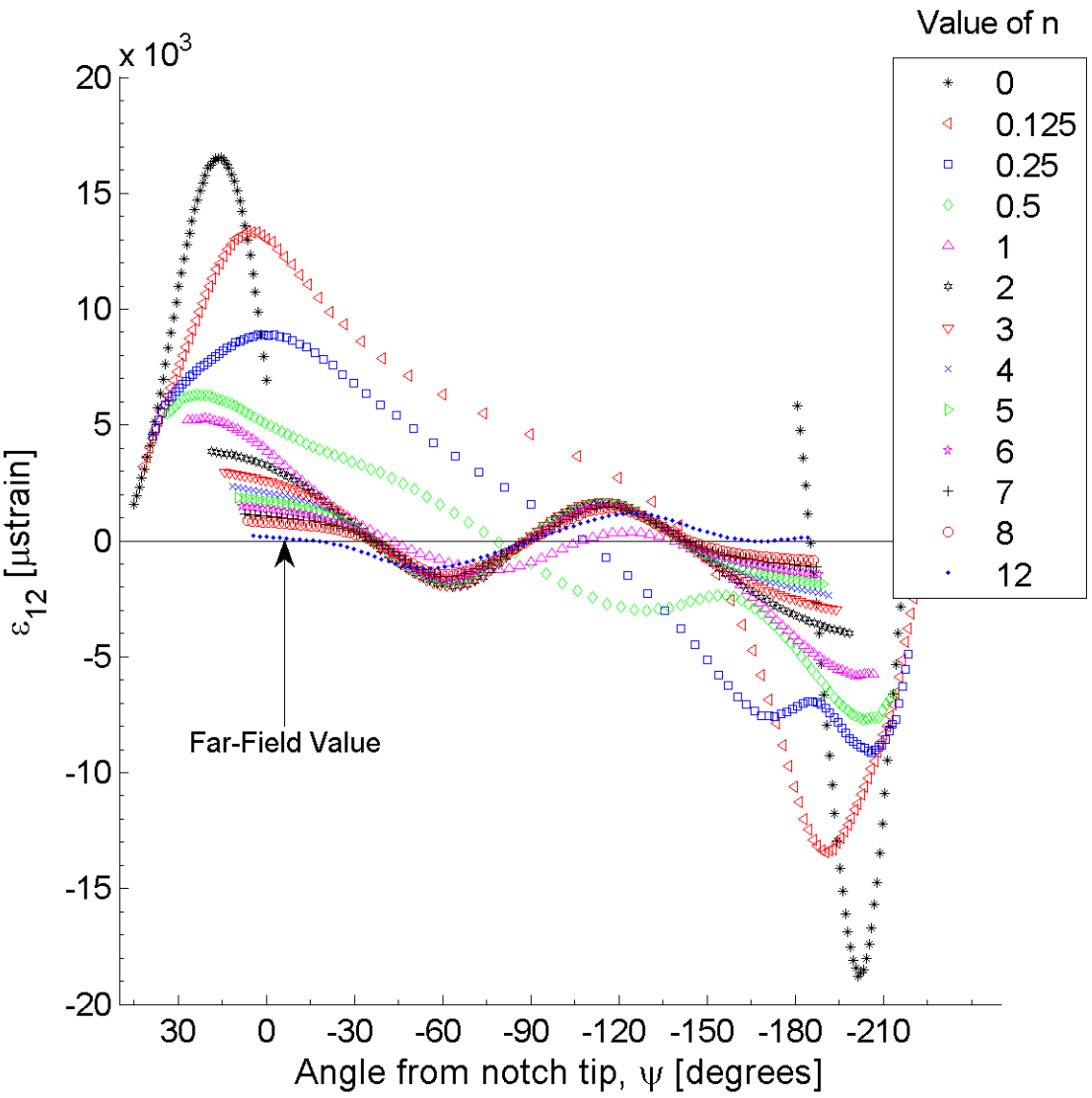

Figure B.16 Plot of ϵ_{12}, in laminate axes, along arc paths at the midplane of ply 1 (a -60° ply) of the single-edge-notched specimen model for the laminate of $[(-60/+60_2/-60_2/+60)_S]_S$.

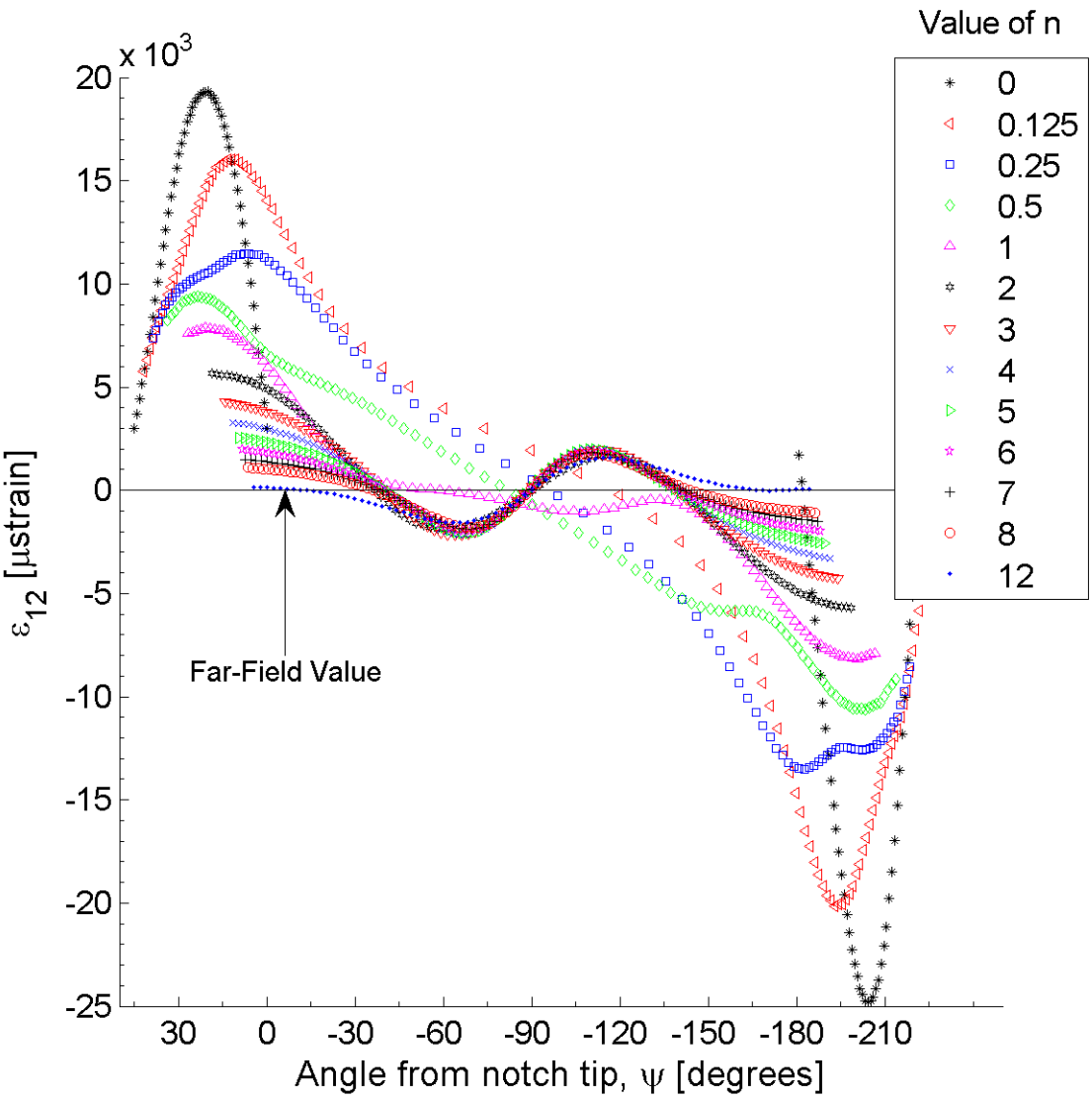

Figure B.17 Plot of ϵ_{12}, in laminate axes, along arc paths at the midplane of ply 1 (a -75° ply) of the single-edge-notched specimen model for the laminate of $[(-75/+75_2/-75_2/+75)_S]_S$.

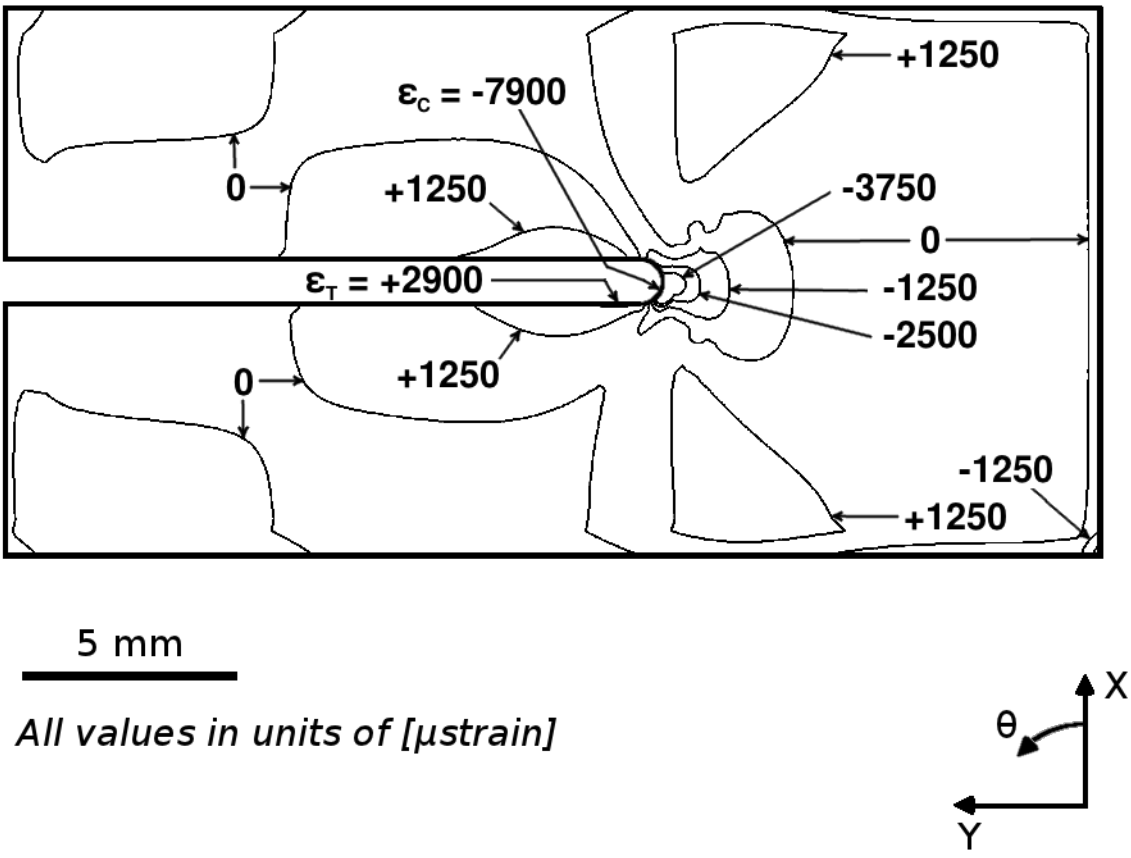

Figure B.18 Isostrain plot of strain field of ϵ_{33}, in laminate axes, at the midplane of ply 1 (a $-30°$ ply) of the single-edge-notched specimen model for the laminate $[(-30/+30_2/-30_2/+30)_S]_S$.

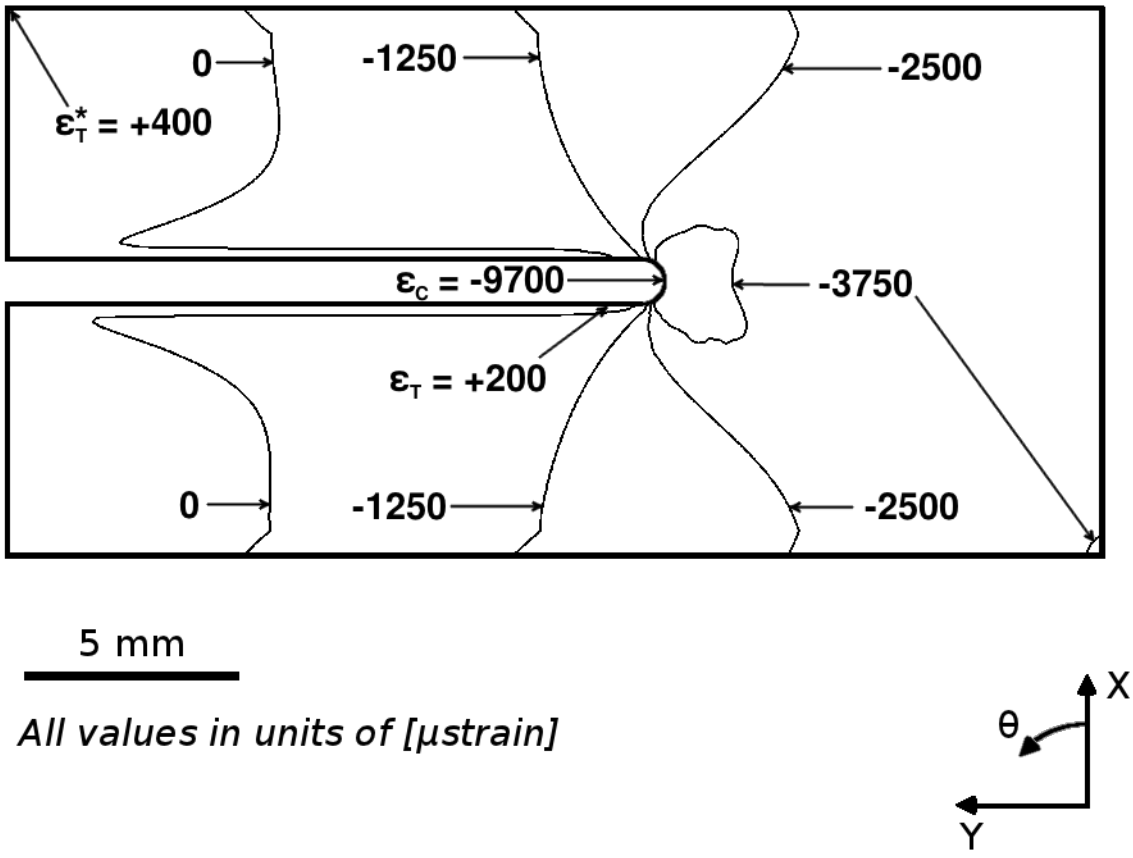

Figure B.19 Isostrain plot of strain field of ϵ_{33}, in laminate axes, at the midplane of ply 1 (a $-60°$ ply) of the single-edge-notched specimen model for the laminate $[(-60/+60_2/-60_2/+60)_S]_S$.

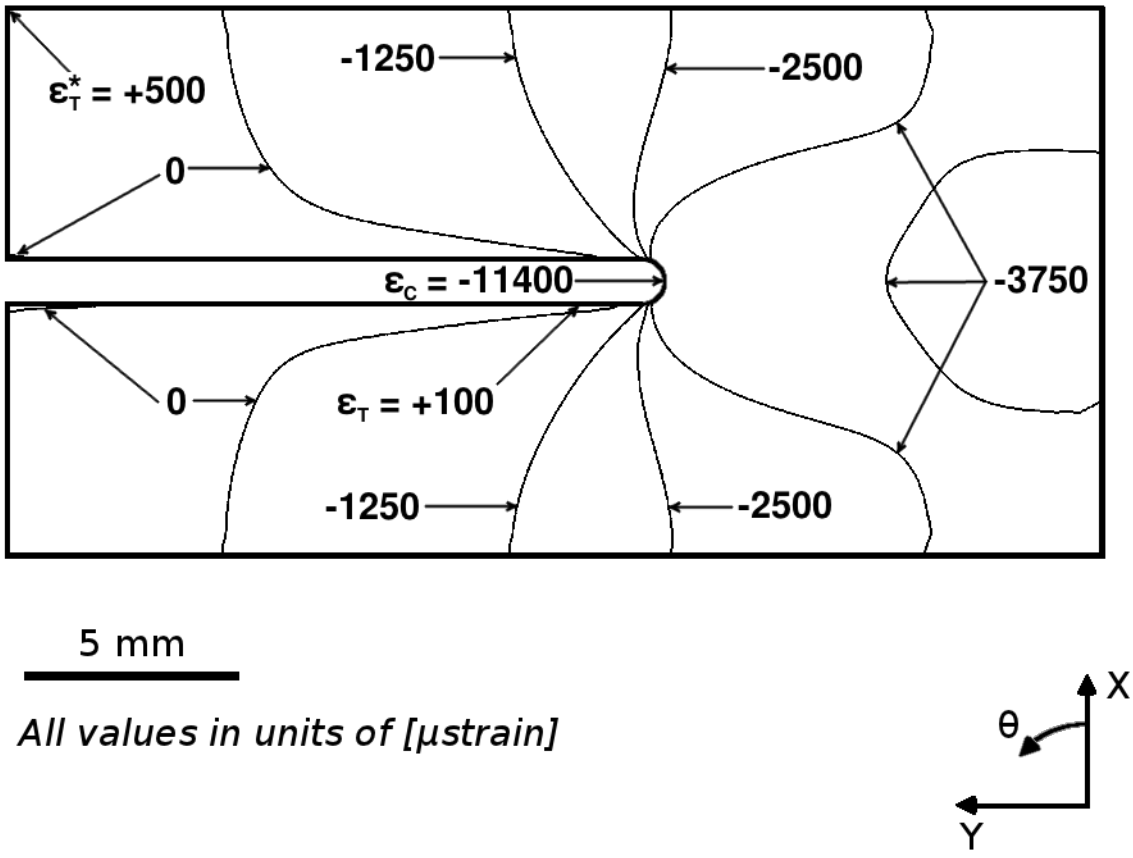

Figure B.20 Isostrain plot of strain field of ϵ_{33}, in laminate axes, at the midplane of ply 1 (a -75° ply) of the single-edge-notched specimen model for the laminate $[(-75/+75_2/-75_2/+75)_S]_S$.

B.2 Strain Plots for Double-Edge-Notched Specimen

This section contains additional figures relating to the results of the double-edge-notched specimen discussed in Section 7.3.2. Two types of figures are included in this section: isostrain plots of the strain fields of the double-edge-notched specimens, and plots of strain magnitudes along arc paths for the double-edge-notched specimens, as defined in Section 7.3.2. The figures in this section of the appendix illustrate the variations of the strain fields, and the plots of strain magnitudes along arc paths for laminate angles not shown in Section 7.3.2.

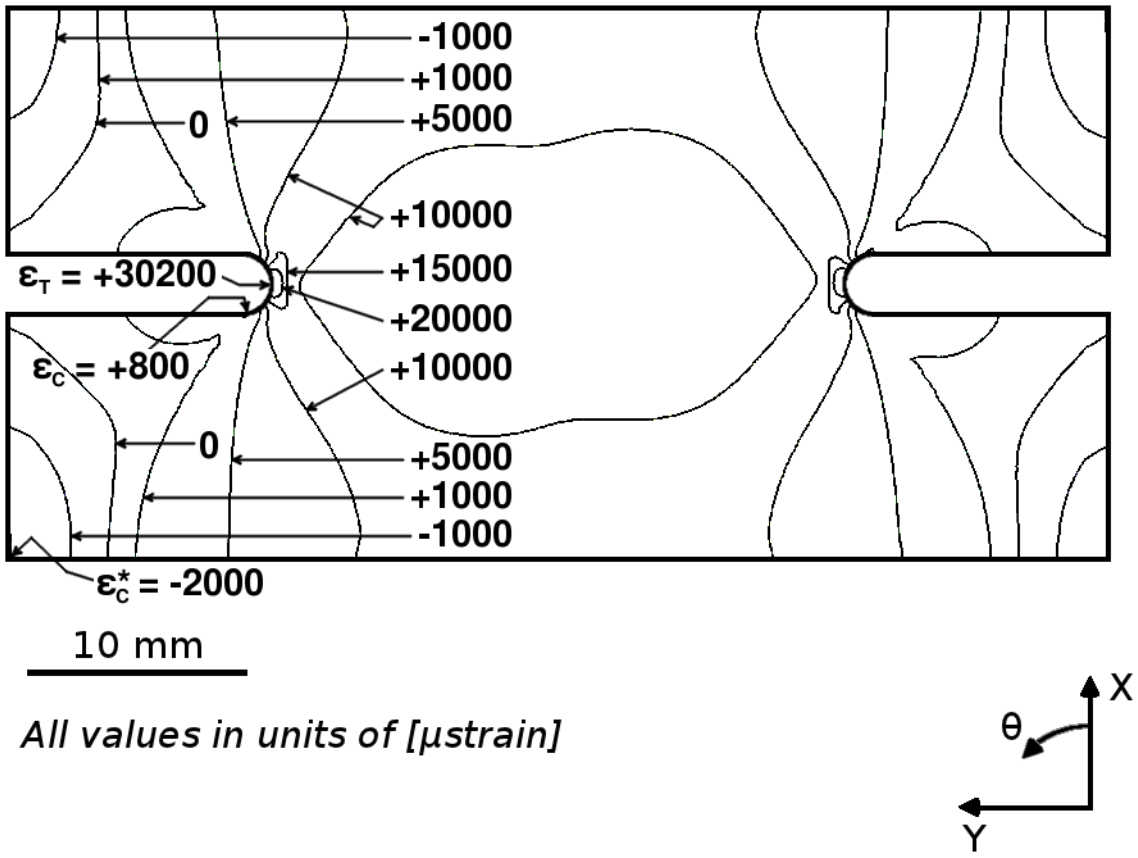

Figure B.21 Isostrain plot of strain field of ϵ_{11}, in laminate axes, at the midplane of ply 1 (a $+30°$ ply) of the double-edge-notched specimen model for the single-ply effective ply thickness laminate of $[+30/-30]_{16T}$.

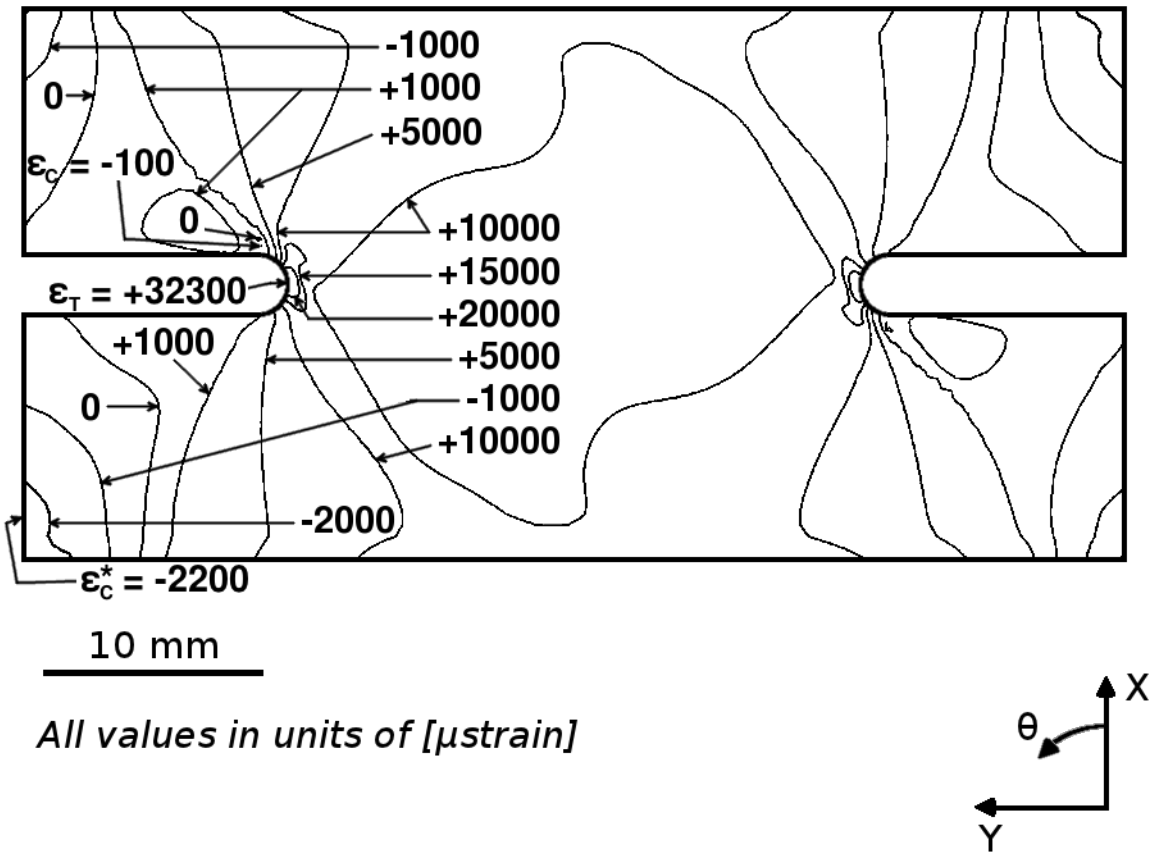

Figure B.22 Isostrain plot of strain field of ϵ_{11}, in laminate axes, at the midplane of ply 1 (a $+30^\circ$ ply) of the double-edge-notched specimen model for the four-ply effective ply thickness laminate of $[+30_4/-30_4]_{4T}$.

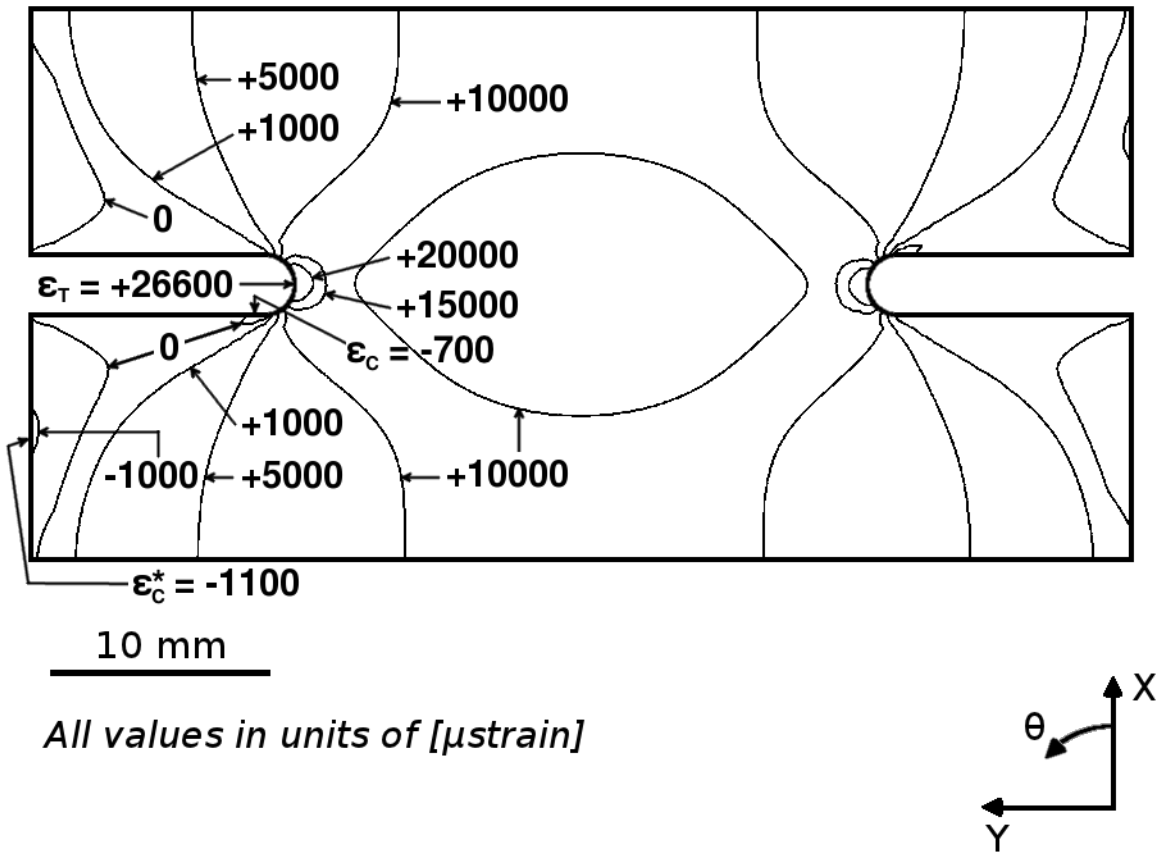

Figure B.23 Isostrain plot of strain field of ϵ_{11}, in laminate axes, at the midplane of ply 1 (a $+60^\circ$ ply) of the double-edge-notched specimen model for the single-ply effective ply thickness laminate of $[+60/-60]_{16T}$.

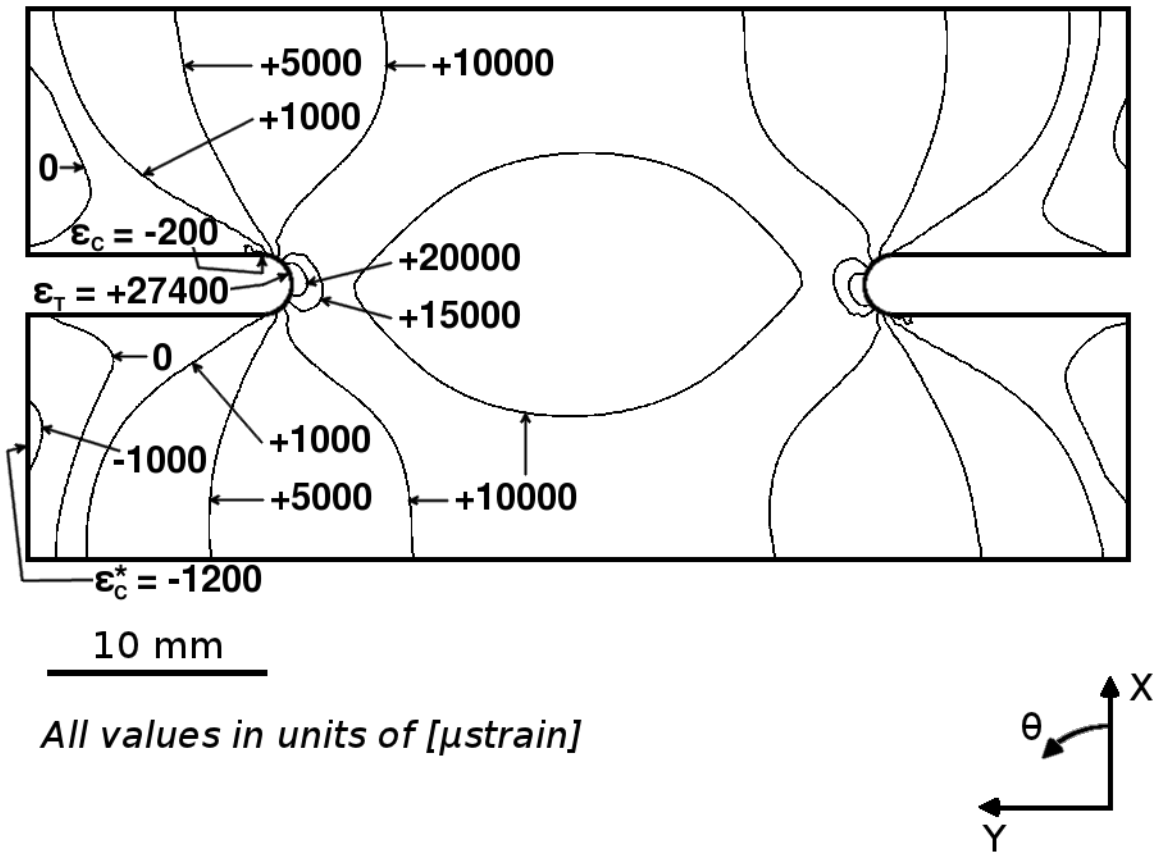

Figure B.24 Isostrain plot of strain field of ϵ_{11}, in laminate axes, at the midplane of ply 1 (a $+60^\circ$ ply) of the double-edge-notched specimen model for the four-ply effective ply thickness laminate of $[+60_4/-60_4]_{4T}$.

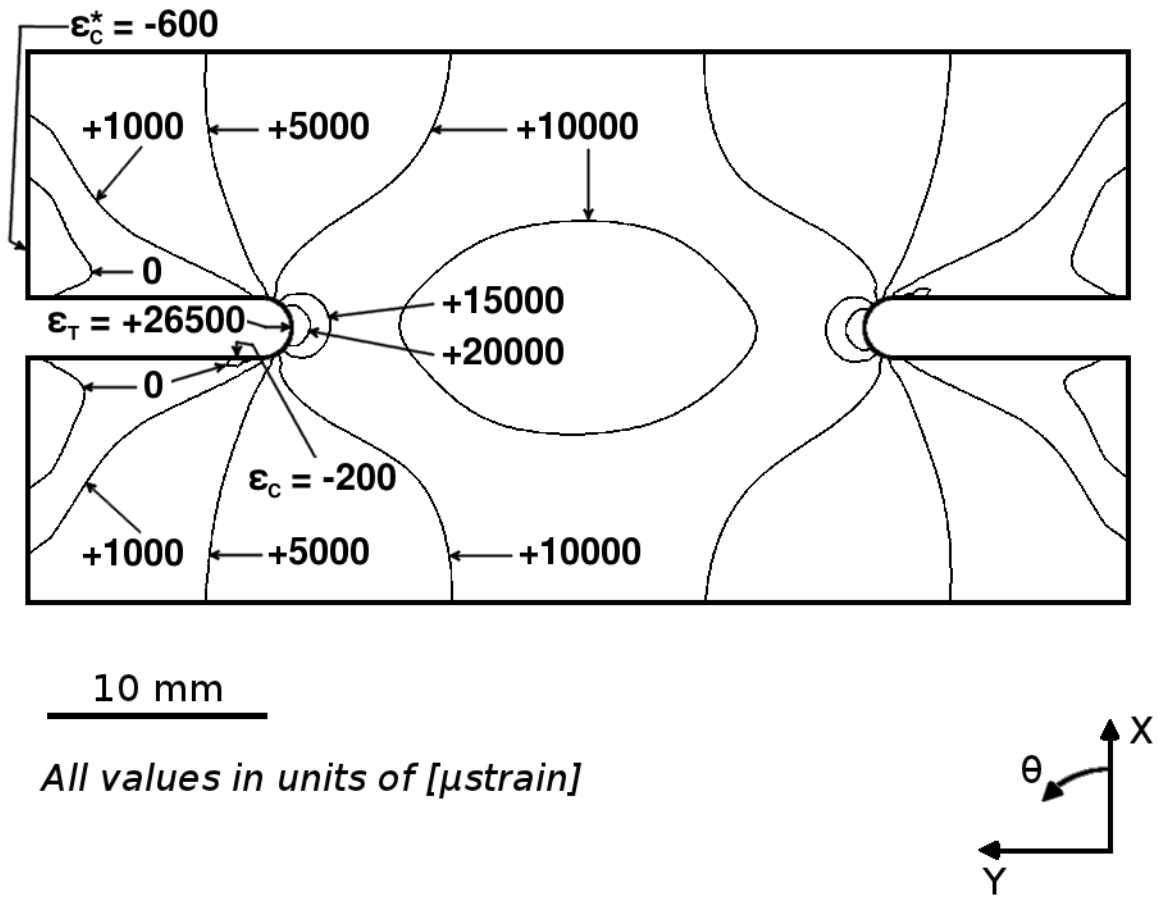

Figure B.25 Isostrain plot of strain field of ϵ_{11}, in laminate axes, at the midplane of ply 1 (a $+75^\circ$ ply) of the double-edge-notched specimen model for the single-ply effective ply thickness laminate of $[+75/-75]_{16T}$.

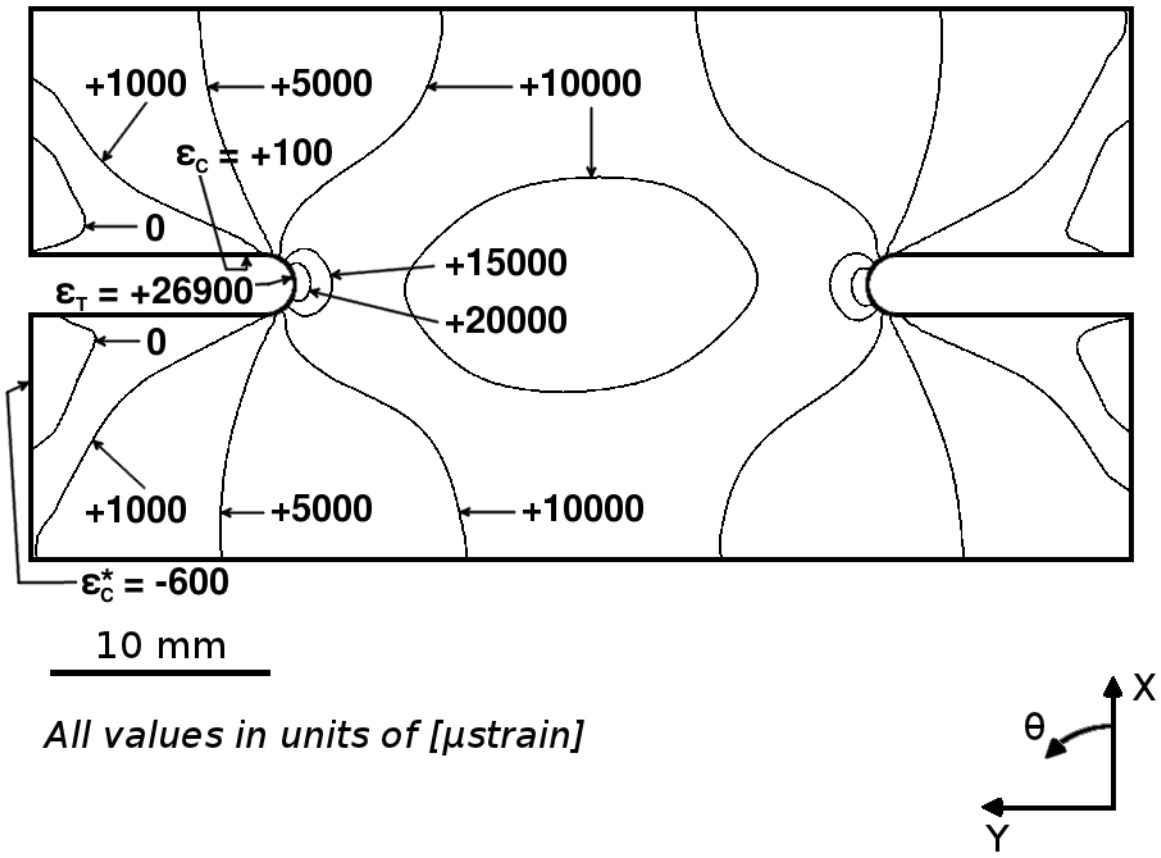

Figure B.26 Isostrain plot of strain field of ϵ_{11}, in laminate axes, at the midplane of ply 1 (a $+75^\circ$ ply) of the double-edge-notched specimen model for the four-ply effective ply thickness laminate of $[+75_4/-75_4]_{4T}$.

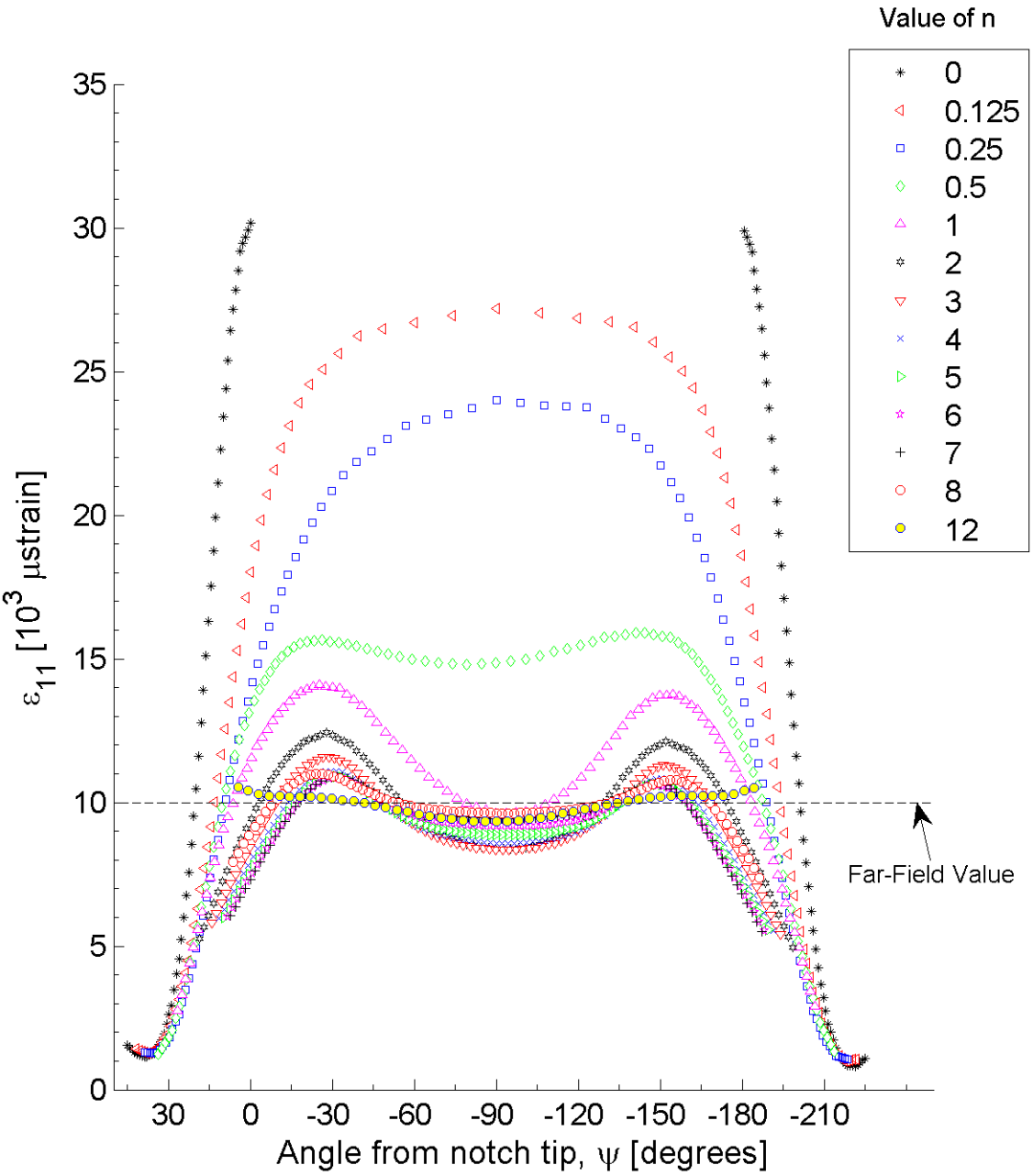

Figure B.27 Plot of ϵ_{11}, in laminate axes, along arc paths at the midplane of ply 1 (a $+30°$ ply) of the double-edge-notched specimen model for the laminate of $[+30/-30]_{16T}$.

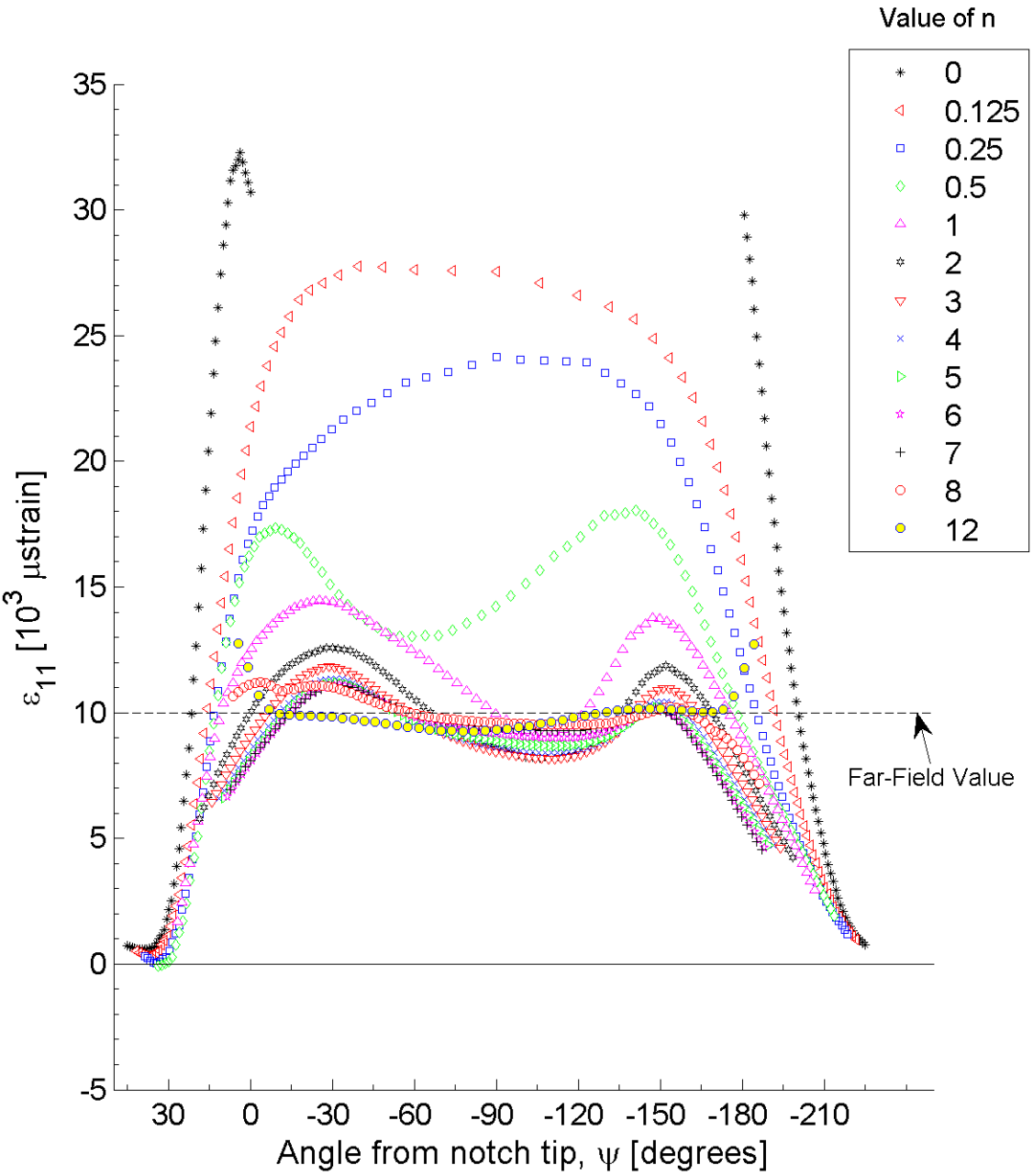

Figure B.28 Plot of ϵ_{11}, in laminate axes, along arc paths at the midplane of ply 1 (a $+30°$ ply) of the double-edge-notched specimen model for the laminate of $[+30_4/-30_4]_{4T}$.

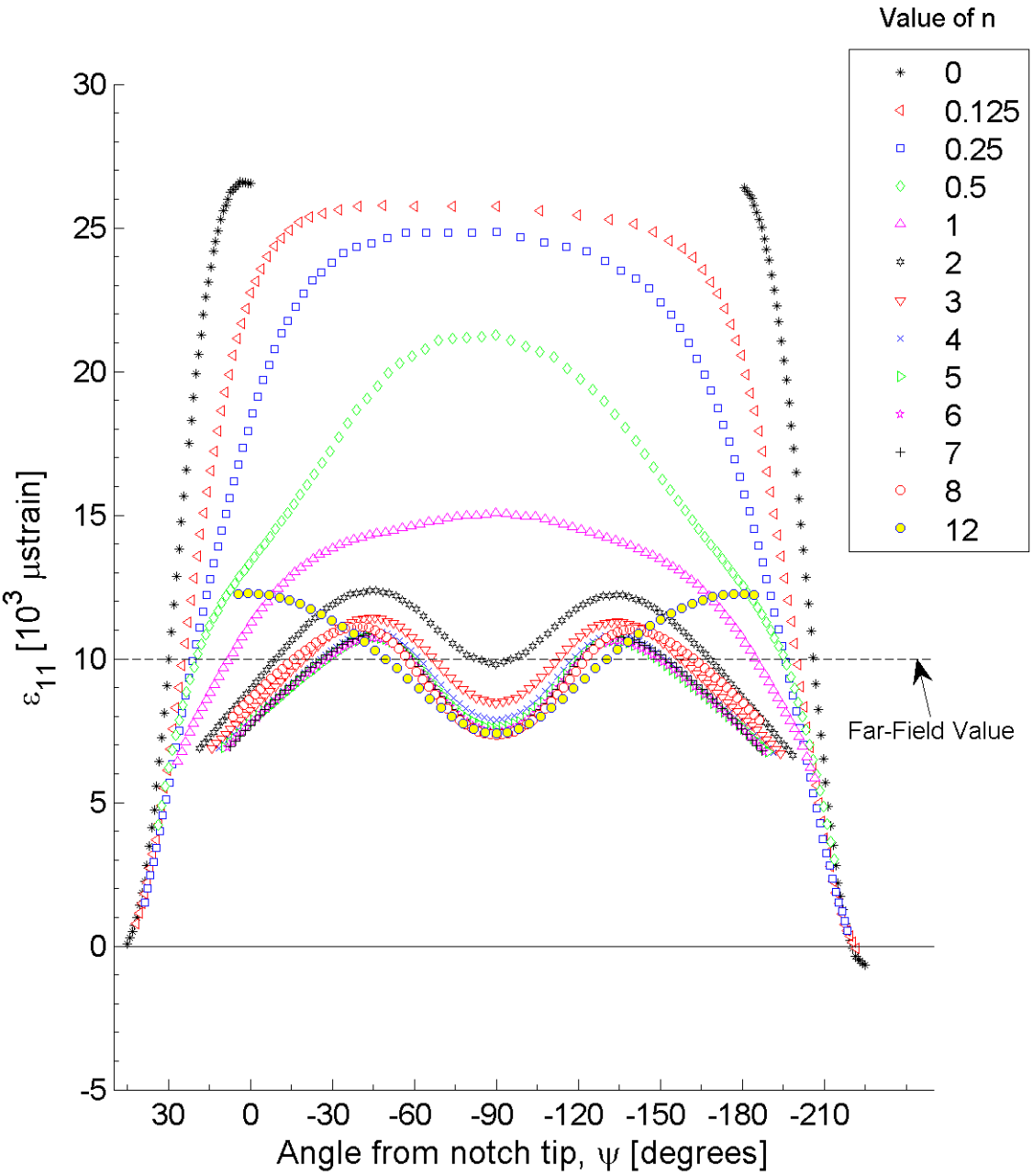

Figure B.29 Plot of ϵ_{11}, in laminate axes, along arc paths at the midplane of ply 1 (a $+60°$ ply) of the double-edge-notched specimen model for the laminate of $[+60/-60]_{16T}$.

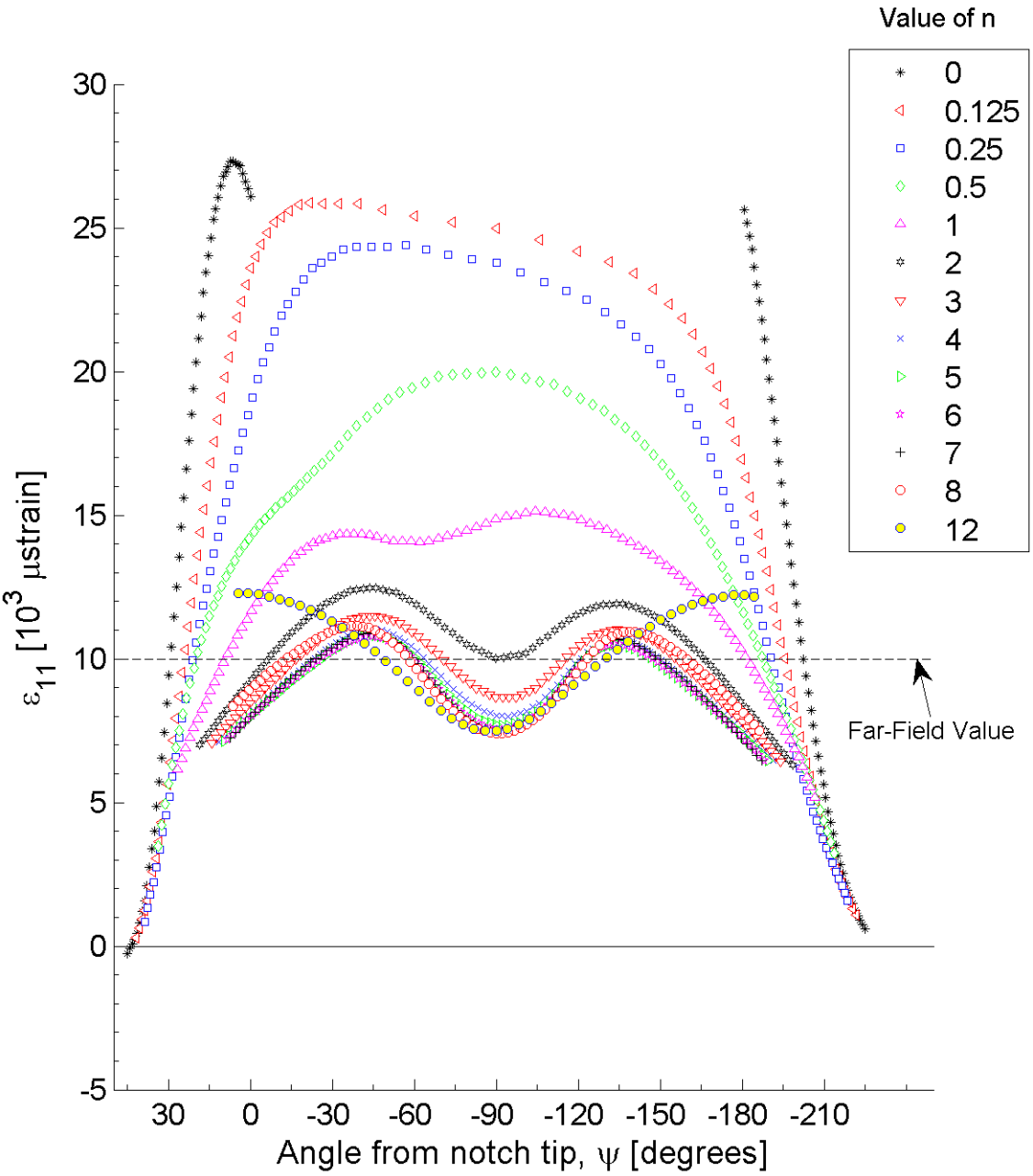

Figure B.30 Plot of ϵ_{11}, in laminate axes, along arc paths at the midplane of ply 1 (a $+60°$ ply) of the double-edge-notched specimen model for the laminate of $[+60_4/-60_4]_{4T}$.

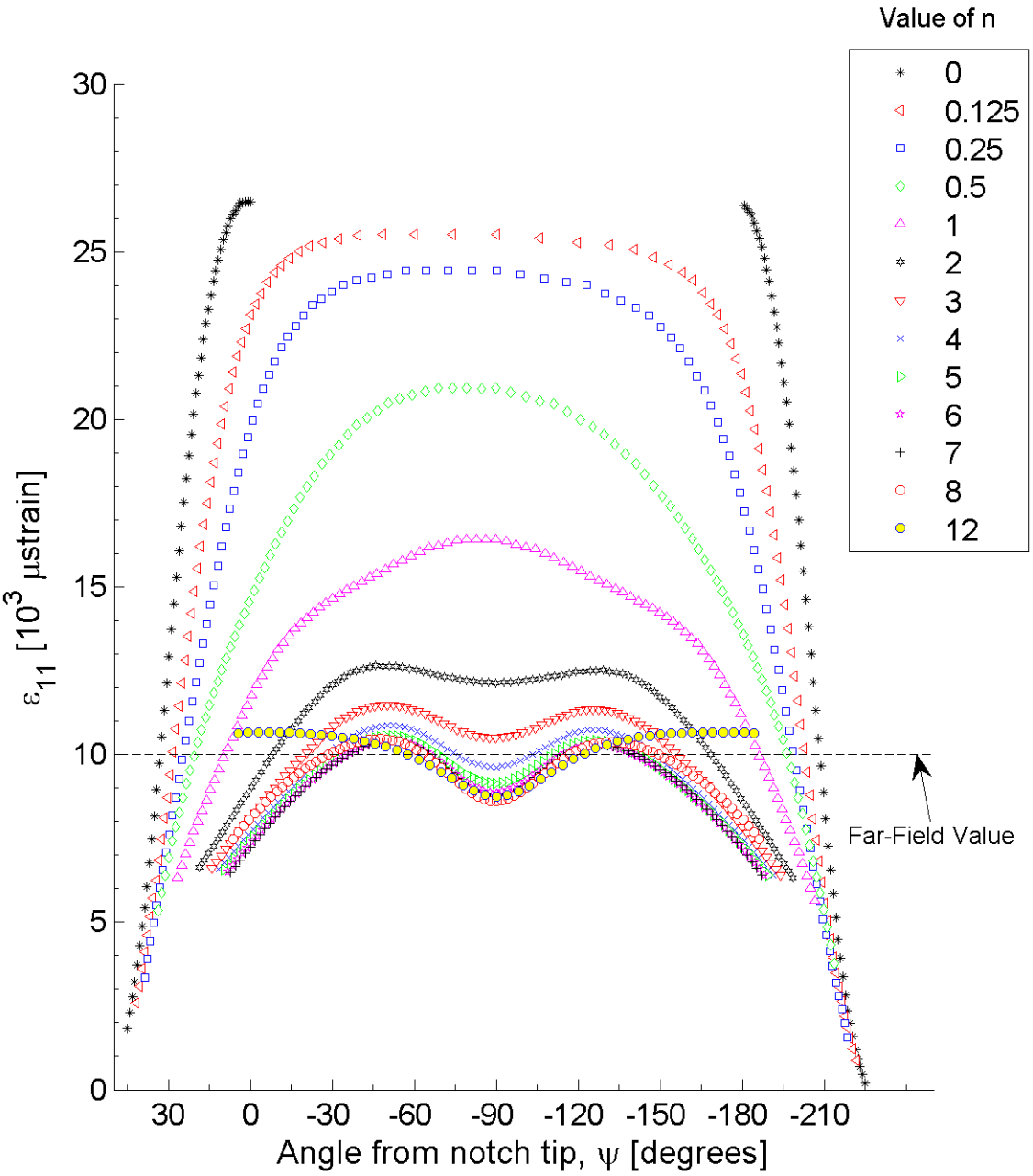

Figure B.31 Plot of ϵ_{11}, in laminate axes, along arc paths at the midplane of ply 1 (a $+75°$ ply) of the double-edge-notched specimen model for the laminate of $[+75/-75]_{16T}$.

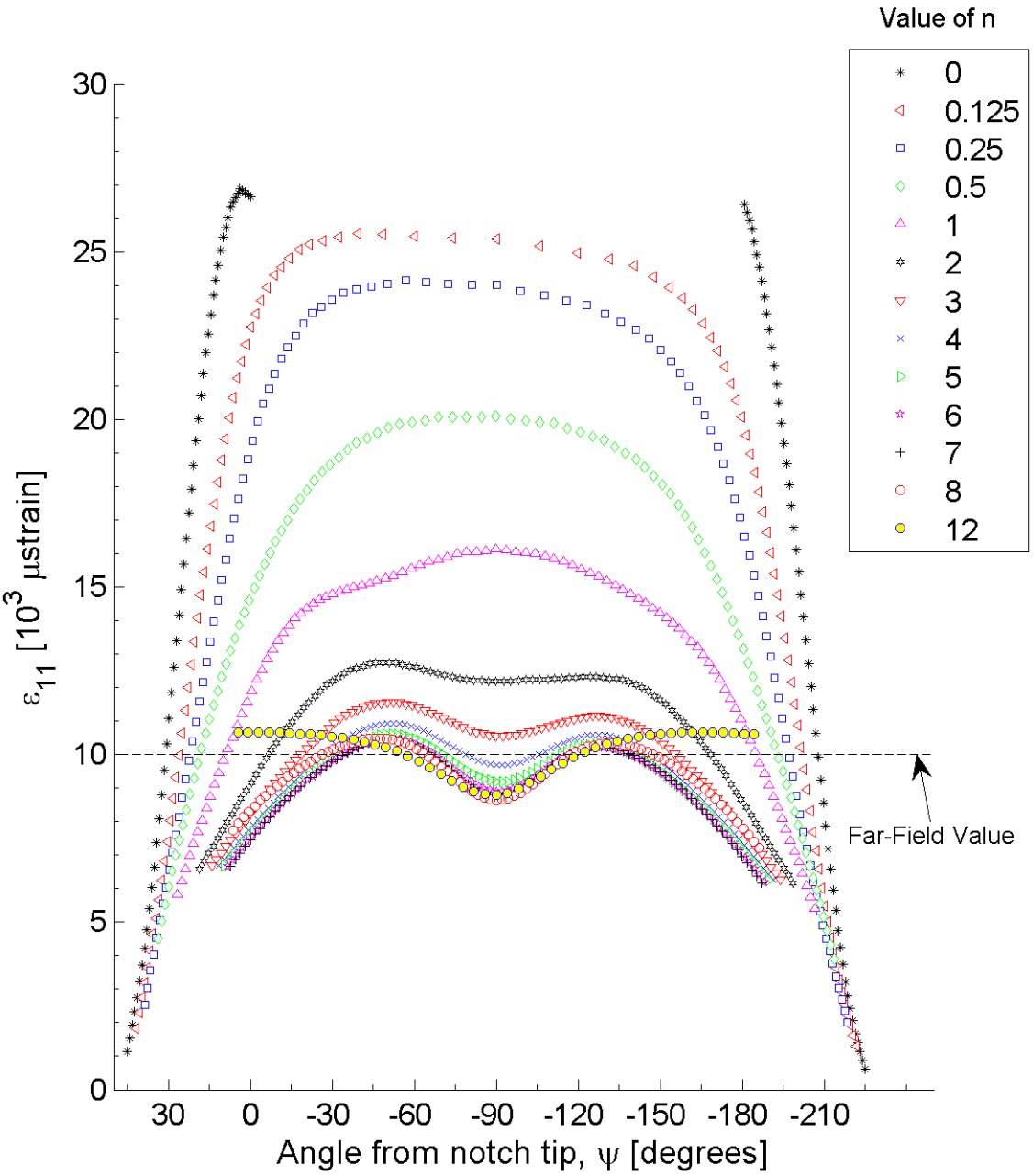

Figure B.32 Plot of ϵ_{11}, in laminate axes, along arc paths at the midplane of ply 1 (a $+75°$ ply) of the double-edge-notched specimen model for the laminate of $[+75_4/-75_4]_{4T}$.

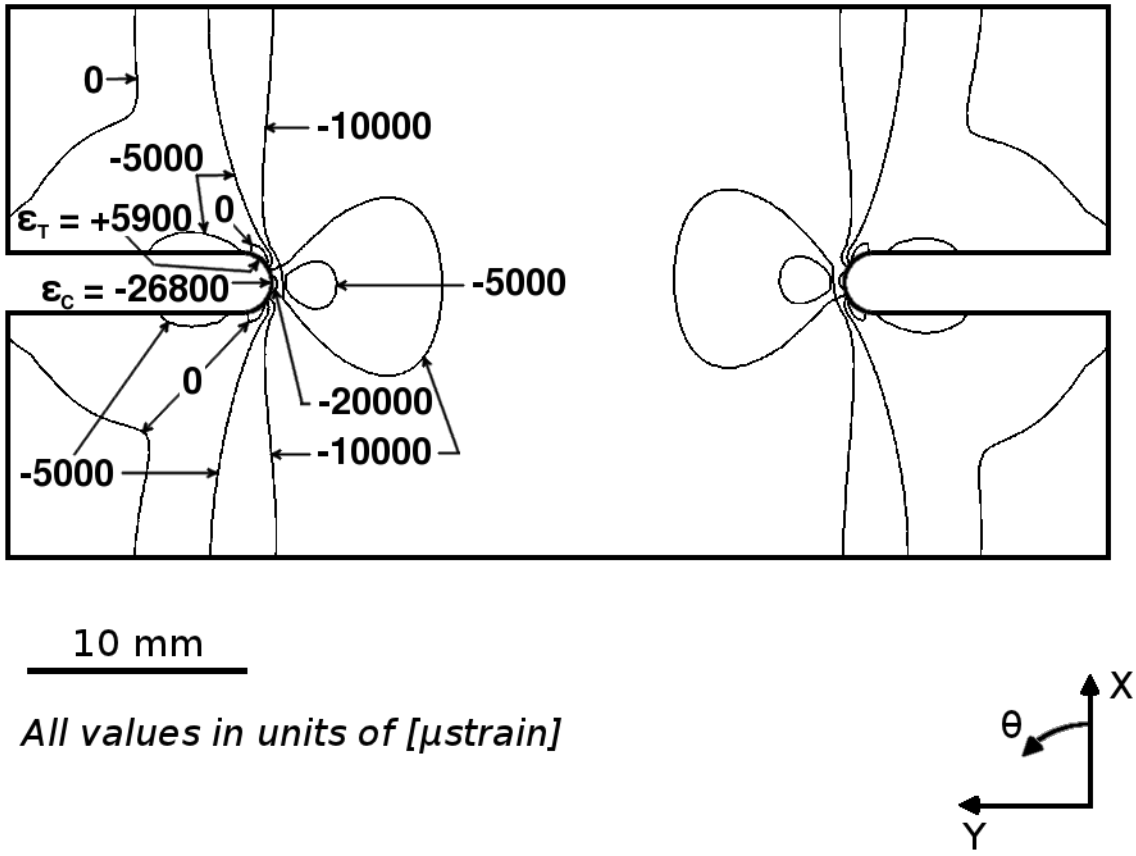

Figure B.33 Isostrain plot of strain field of ϵ_{22}, in laminate axes, at the midplane of ply 1 (a $+30^\circ$ ply) of the double-edge-notched specimen model for the single-ply effective ply thickness laminate of $[+30/-30]_{16T}$.

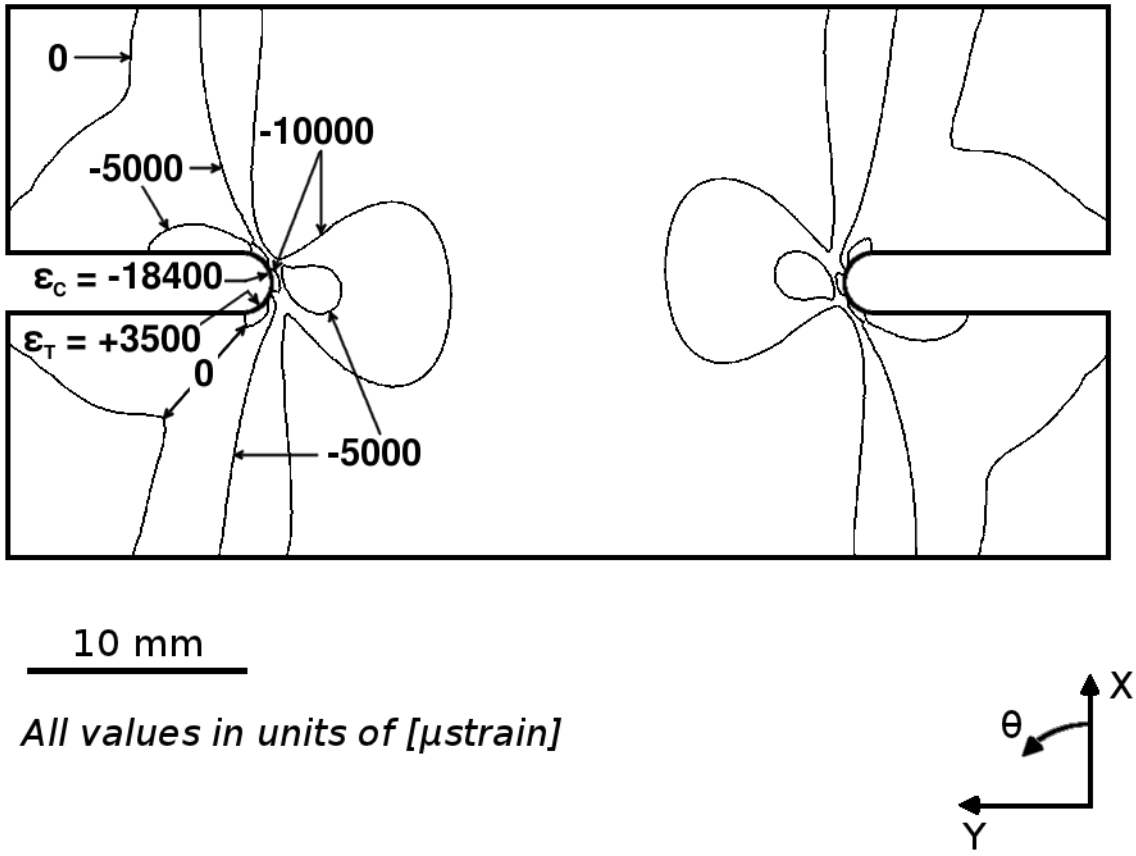

Figure B.34 Isostrain plot of strain field of ϵ_{22}, in laminate axes, at the midplane of ply 1 (a $+30^\circ$ ply) of the double-edge-notched specimen model for the four-ply effective ply thickness laminate of $[+30_4/-30_4]_{4T}$.

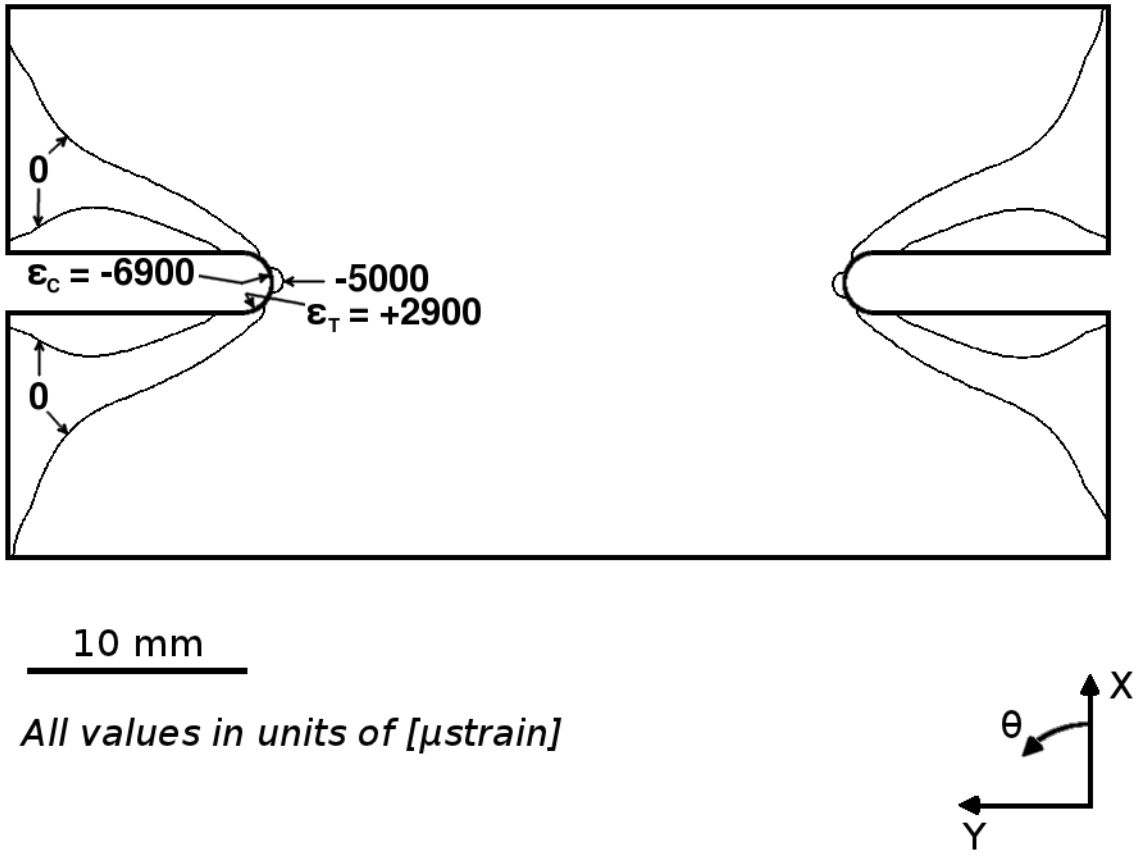

Figure B.35 Isostrain plot of strain field of ϵ_{22}, in laminate axes, at the midplane of ply 1 (a $+60^\circ$ ply) of the double-edge-notched specimen model for the single-ply effective ply thickness laminate of $[+60/-60]_{16T}$.

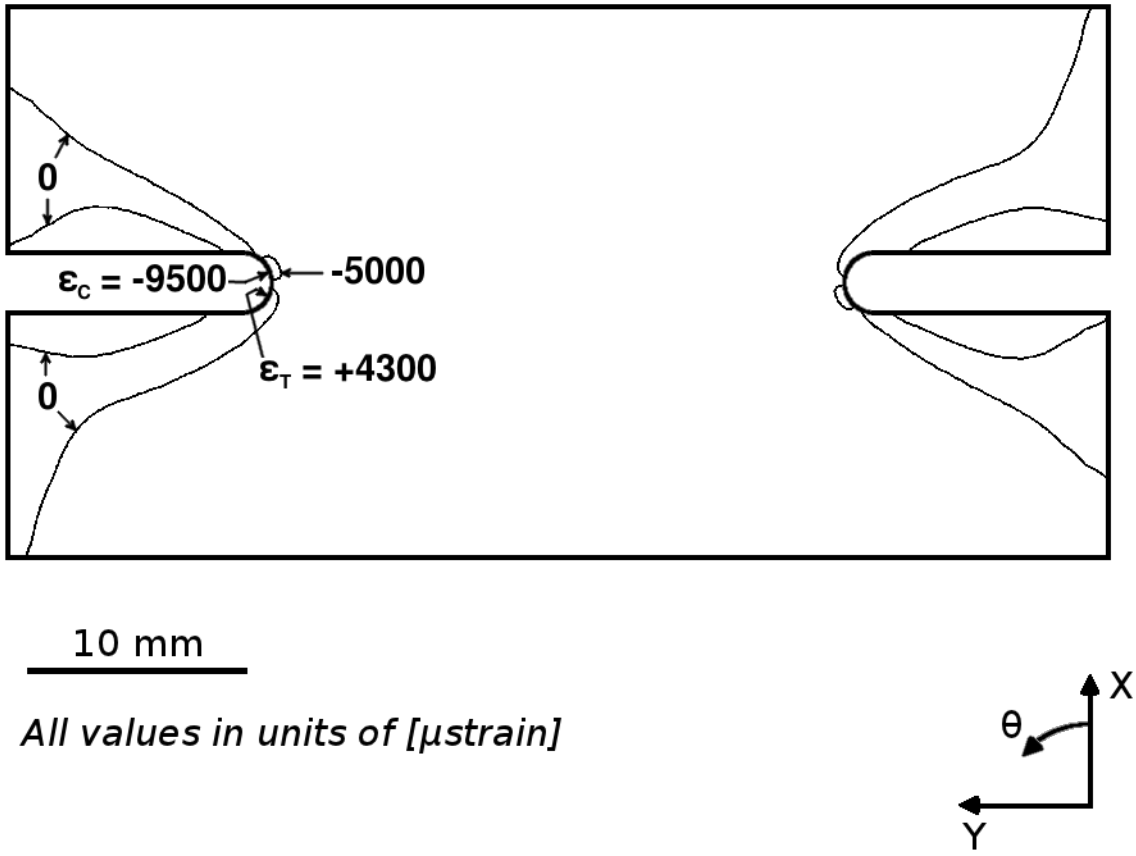

Figure B.36 Isostrain plot of strain field of ϵ_{22}, in laminate axes, at the midplane of ply 1 (a $+60^\circ$ ply) of the double-edge-notched specimen model for the four-ply effective ply thickness laminate of $[+60_4/-60_4]_{4T}$.

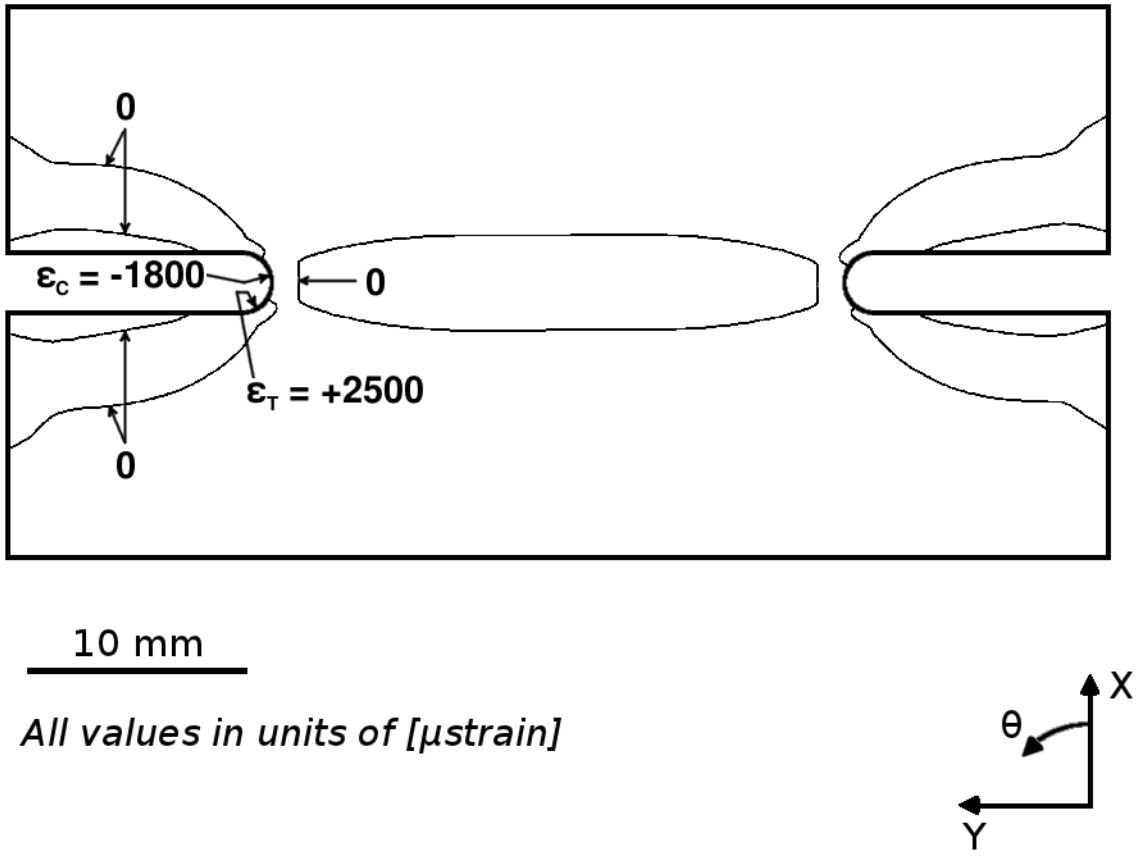

Figure B.37 Isostrain plot of strain field of ϵ_{22}, in laminate axes, at the midplane of ply 1 (a $+75^\circ$ ply) of the double-edge-notched specimen model for the single-ply effective ply thickness laminate of $[+75/-75]_{16T}$.

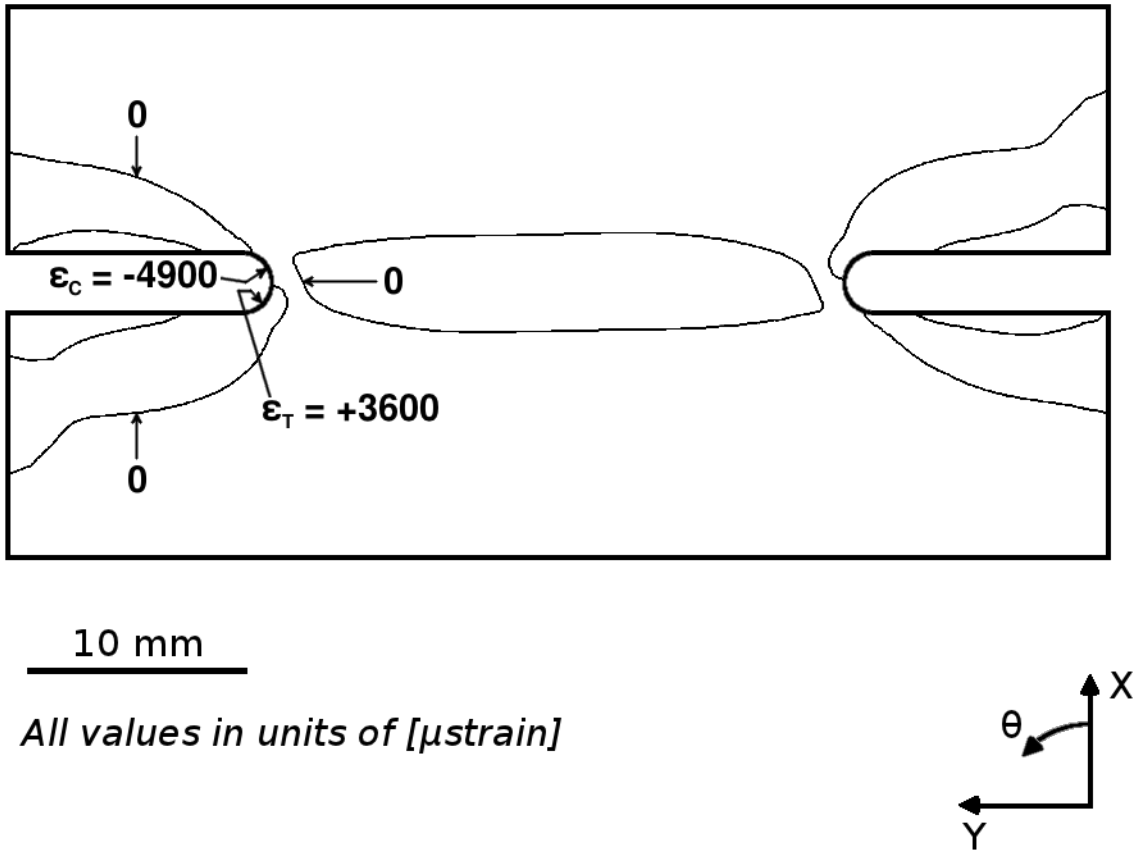

Figure B.38 Isostrain plot of strain field of ϵ_{22}, in laminate axes, at the midplane of ply 1 (a $+75^\circ$ ply) of the double-edge-notched specimen model for the four-ply effective ply thickness laminate of $[+75_4/-75_4]_{4T}$.

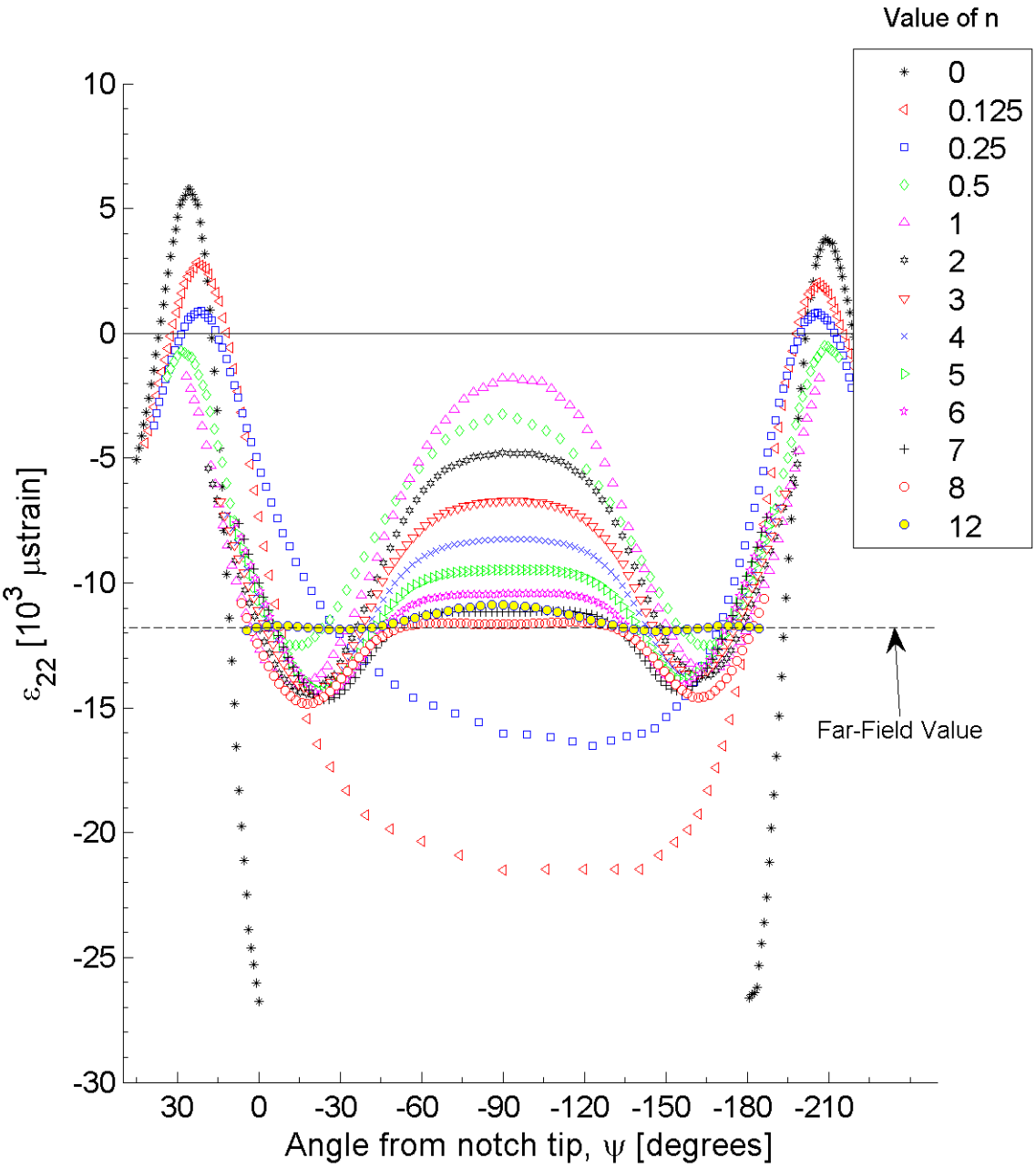

Figure B.39 Plot of ϵ_{22}, in laminate axes, along arc paths at the midplane of ply 1 (a $+30°$ ply) of the double-edge-notched specimen model for the laminate of $[(+30/-30]_{16T}$.

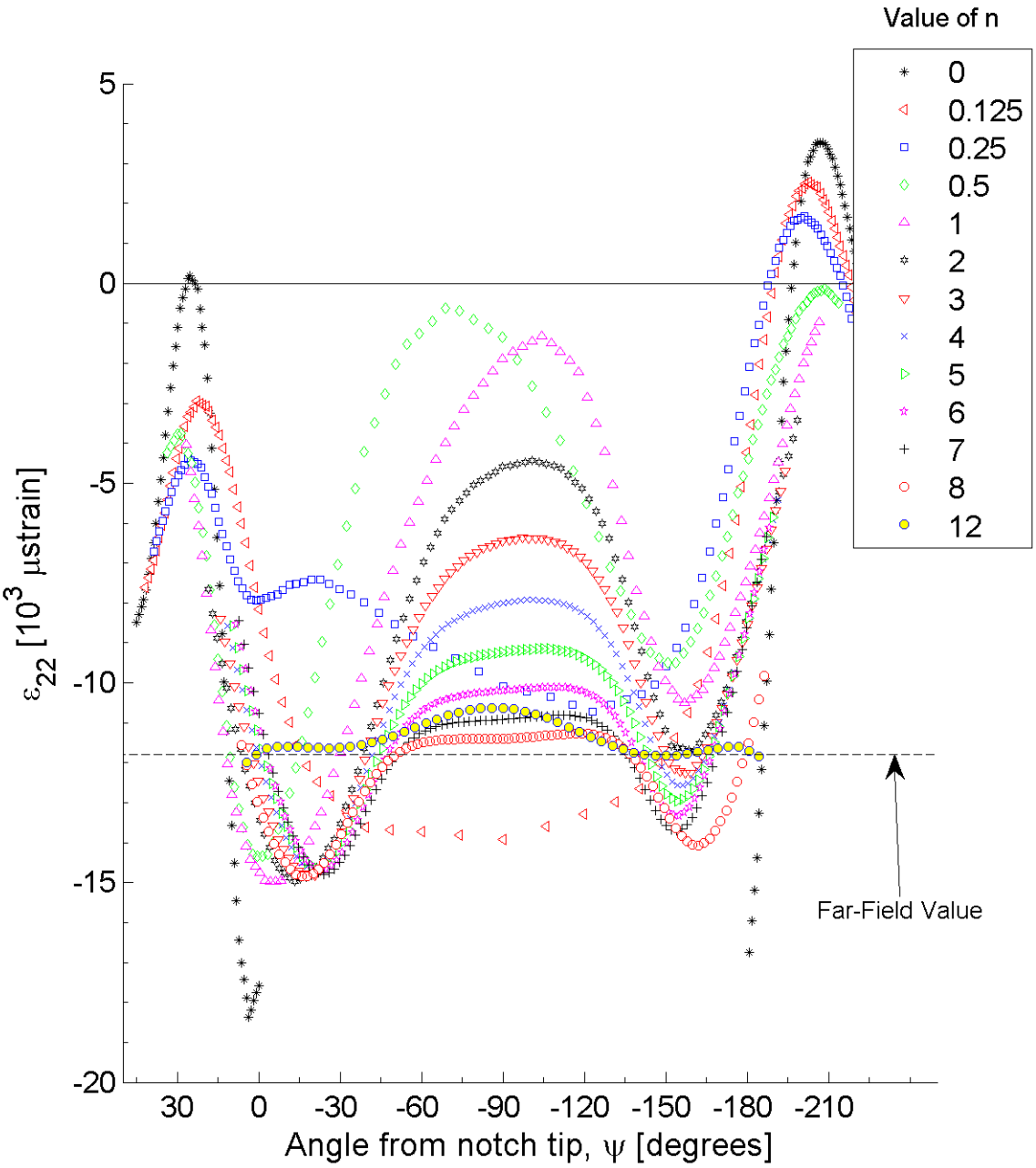

Figure B.40 Plot of ϵ_{22}, in laminate axes, along arc paths at the midplane of ply 1 (a $+30°$ ply) of the double-edge-notched specimen model for the laminate of $[(+30_4/-30_4]_{4T}$.

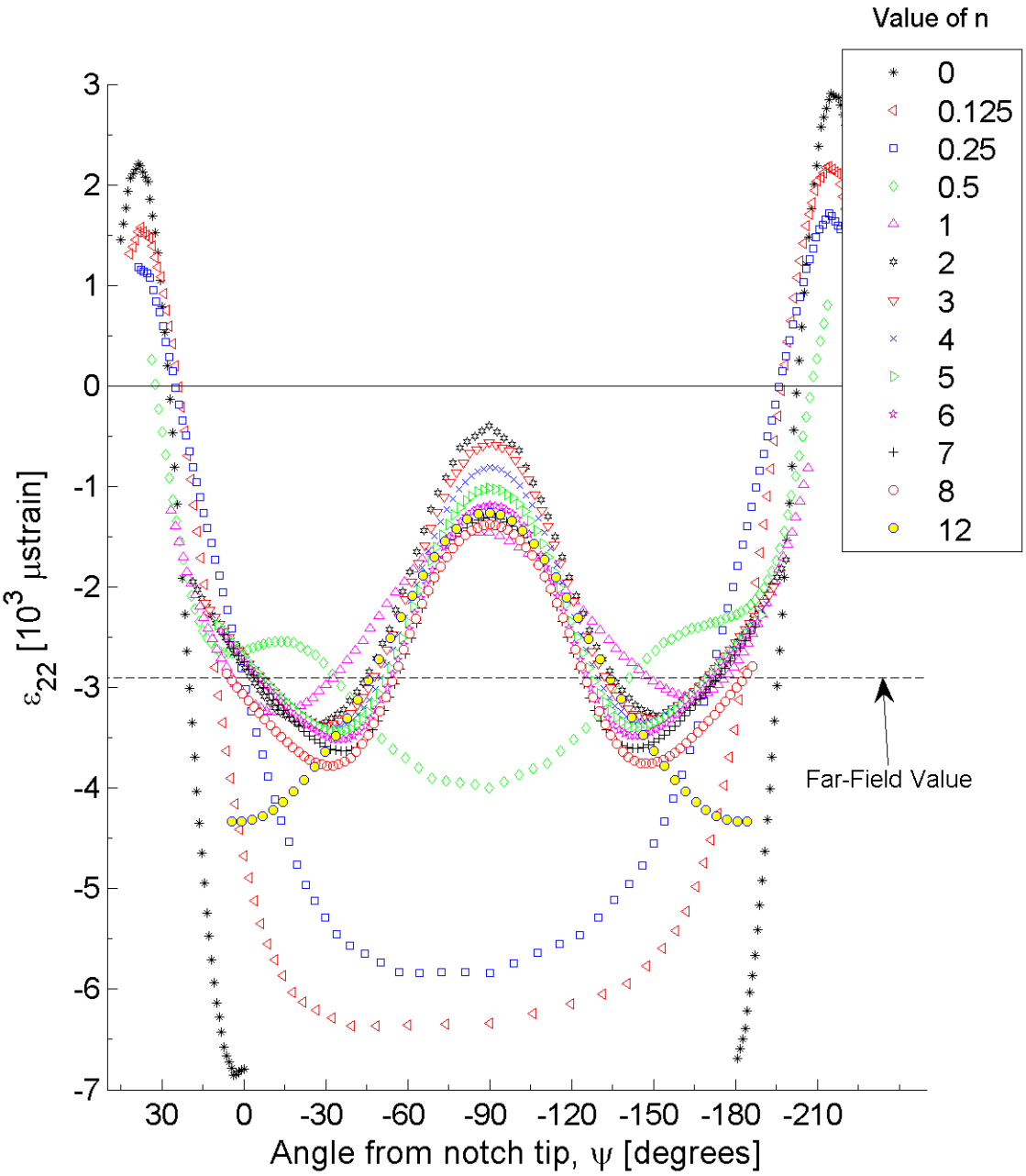

Figure B.41 Plot of ϵ_{22}, in laminate axes, along arc paths at the midplane of ply 1 (a $+60°$ ply) of the double-edge-notched specimen model for the laminate of $[(+60/-60]_{16T}$.

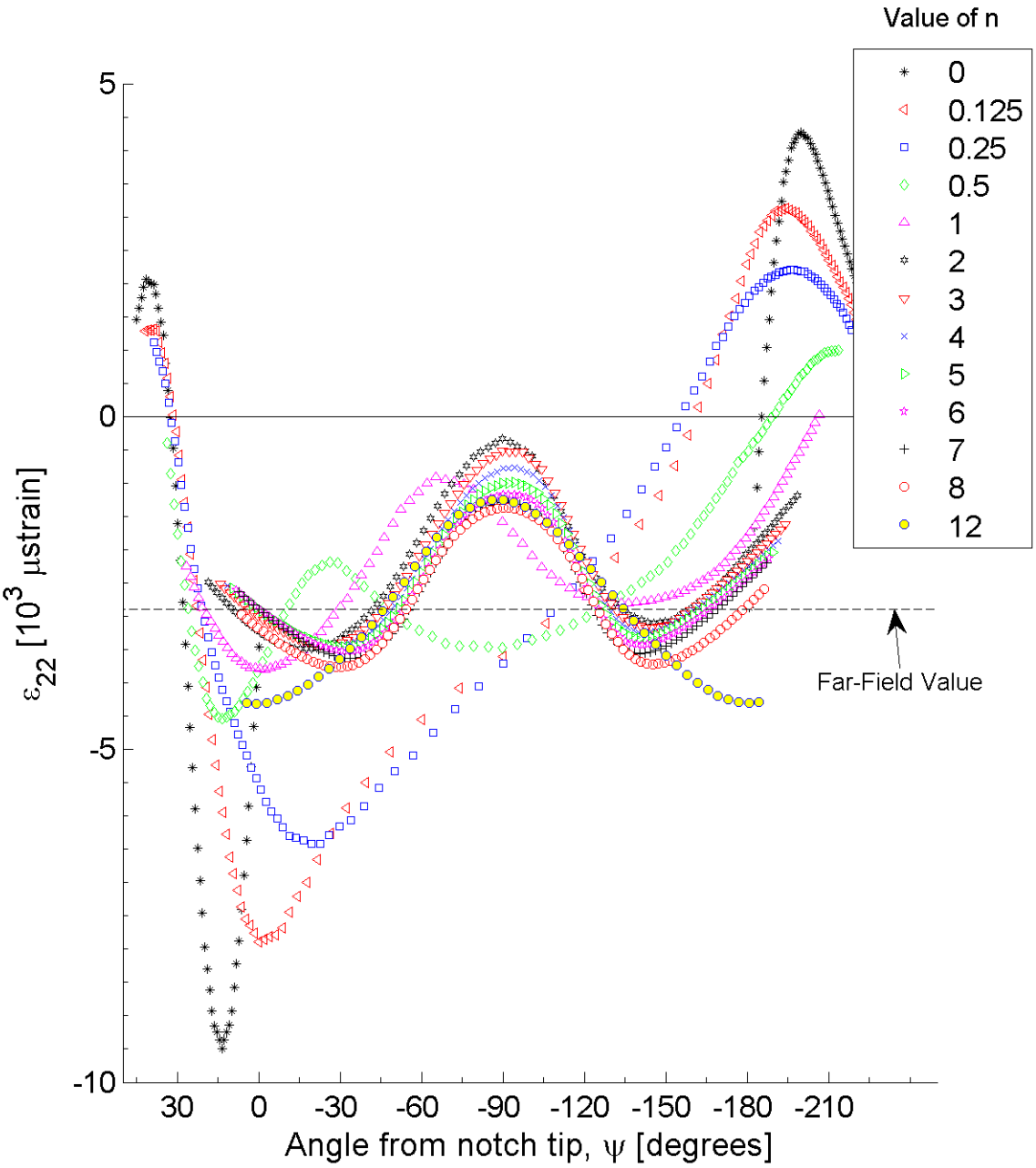

Figure B.42 Plot of ϵ_{22}, in laminate axes, along arc paths at the midplane of ply 1 (a $+60^\circ$ ply) of the double-edge-notched specimen model for the laminate of $[(+60_4/-60_4]_{4T}$.

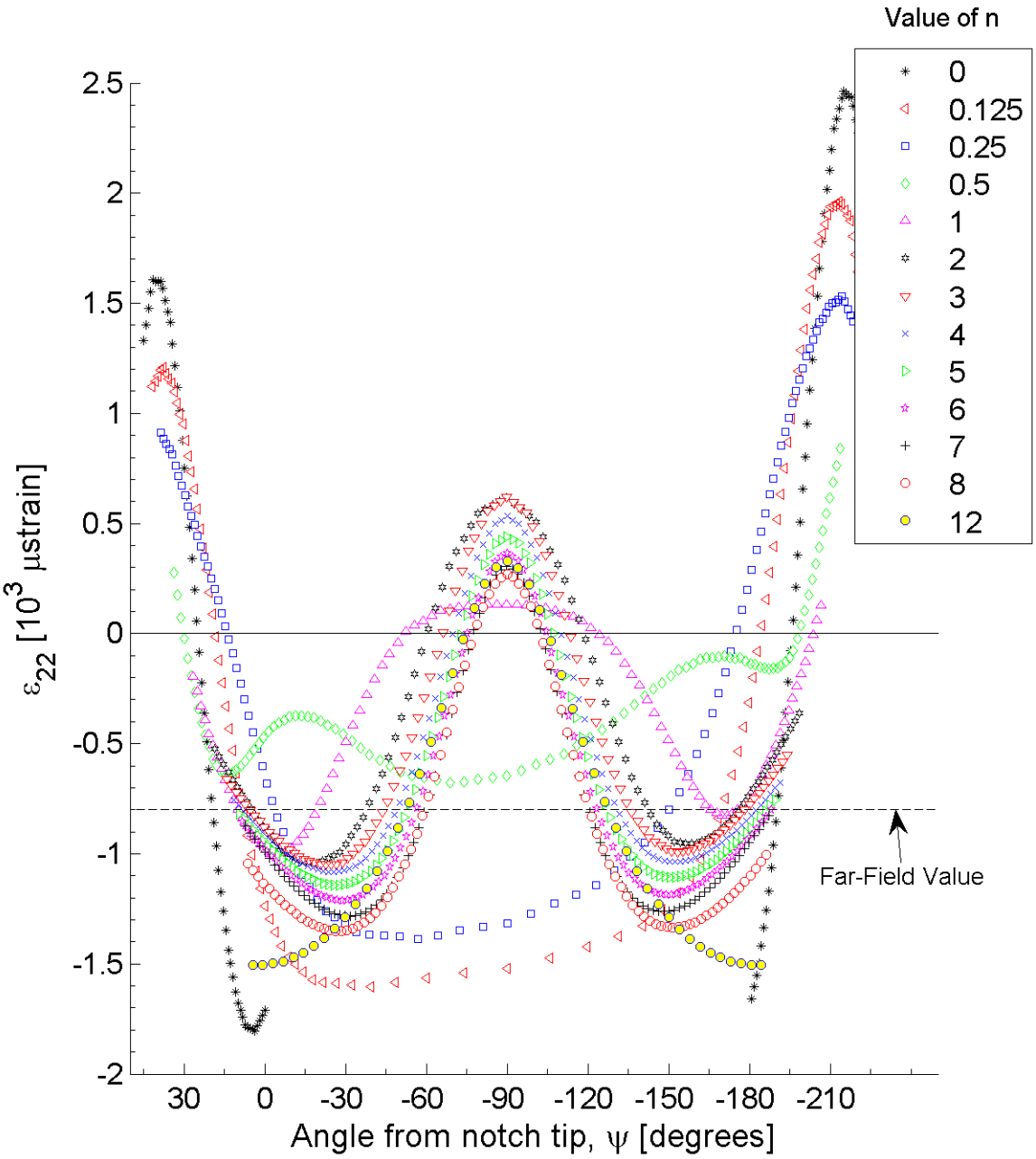

Figure B.43 Plot of ϵ_{22}, in laminate axes, along arc paths at the midplane of ply 1 (a $+75°$ ply) of the double-edge-notched specimen model for the laminate of $[(+75/-75]_{16T}$.

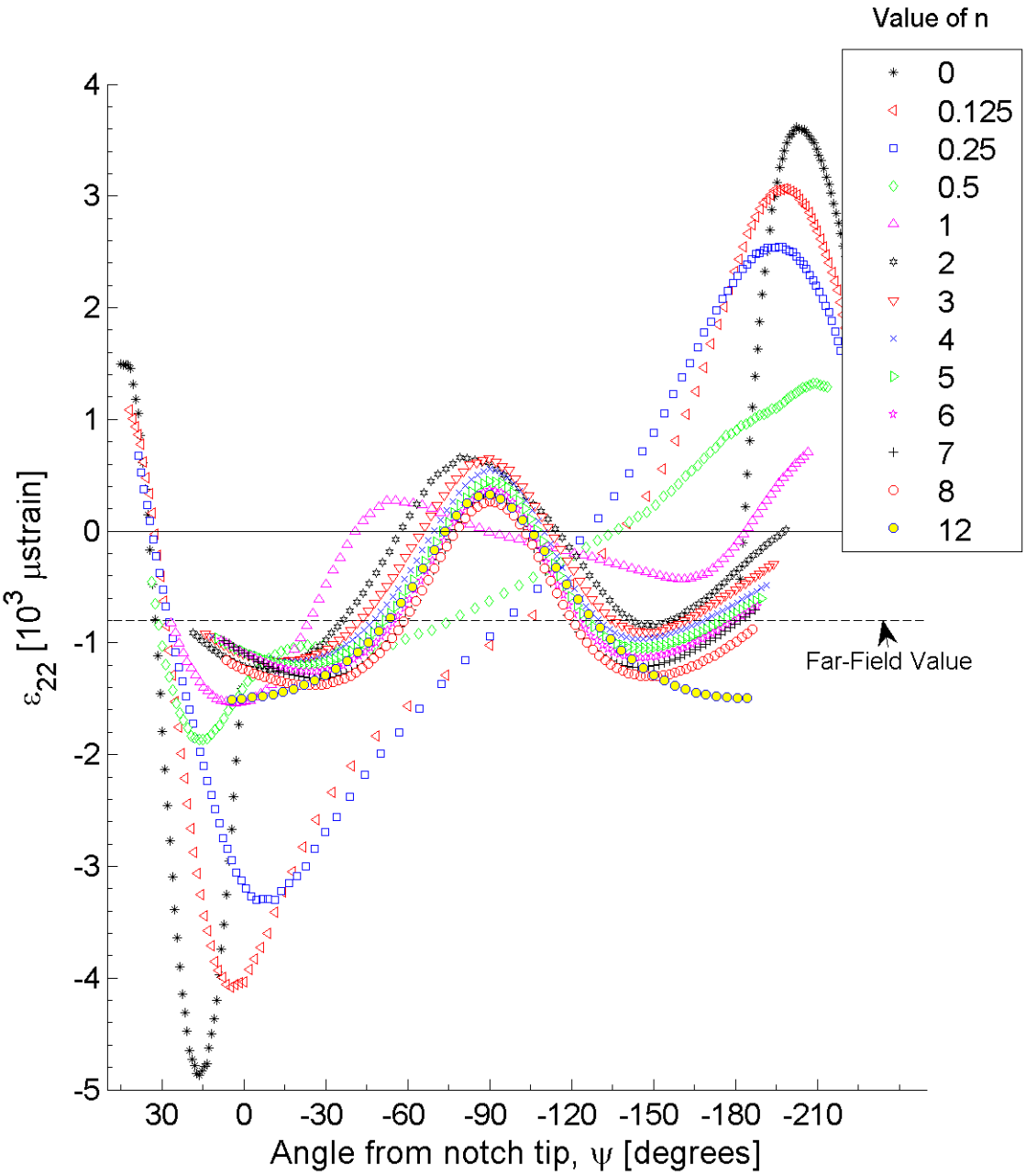

Figure B.44 Plot of ϵ_{22}, in laminate axes, along arc paths at the midplane of ply 1 (a $+75°$ ply) of the double-edge-notched specimen model for the laminate of $[(+75_4/-75_4]_{4T}$.

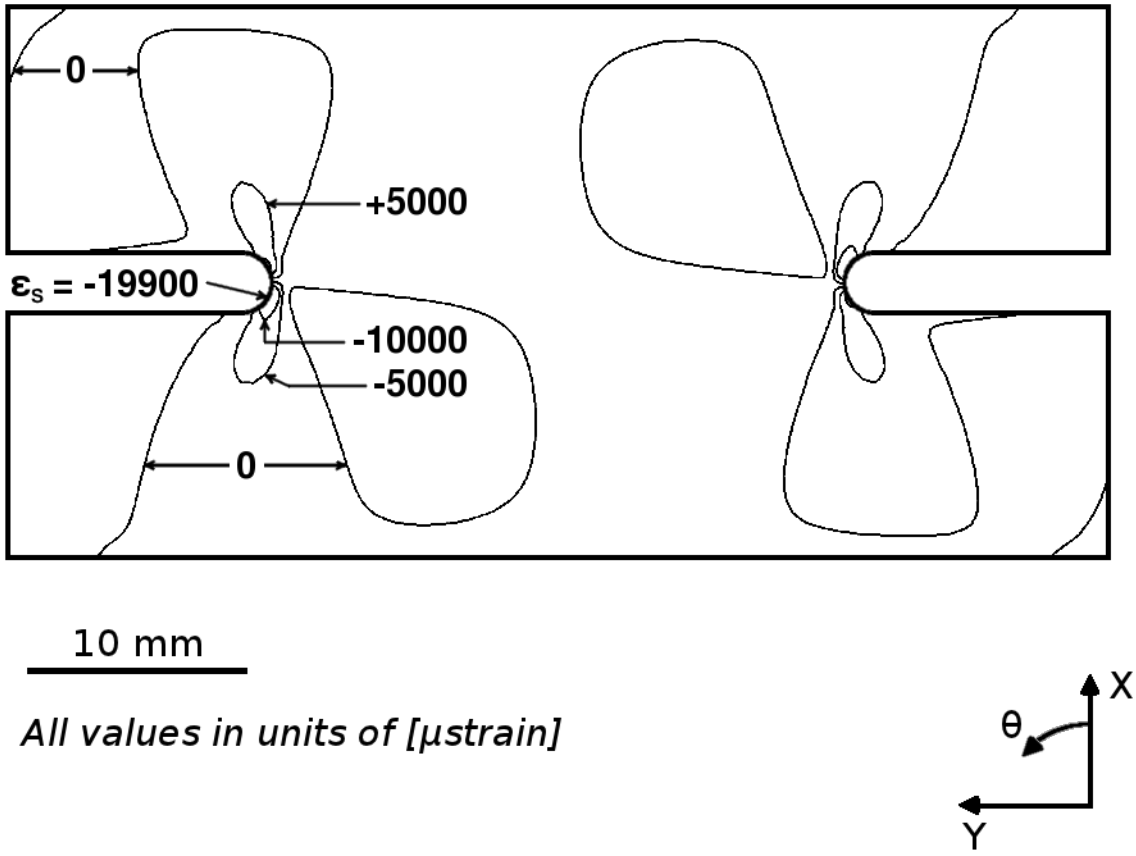

Figure B.45 Isostrain plot of strain field of ϵ_{12}, in laminate axes, at the midplane of ply 1 (a $+30^\circ$ ply) of the double-edge-notched specimen model for the single-ply effective ply thickness laminate of $[+30/-30]_{16T}$.

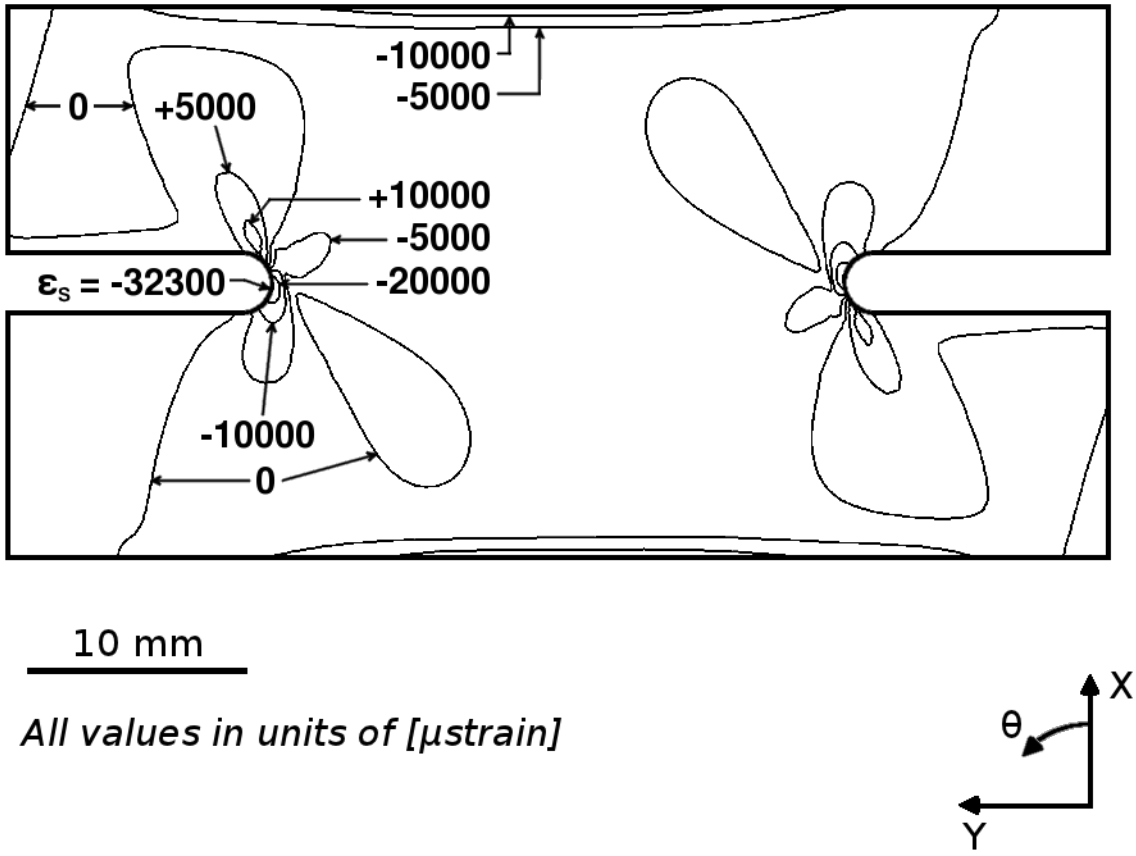

Figure B.46 Isostrain plot of strain field of ϵ_{12}, in laminate axes, at the midplane of ply 1 (a $+30^\circ$ ply) of the double-edge-notched specimen model for the four-ply effective ply thickness laminate of $[+30_4/-30_4]_{4T}$.

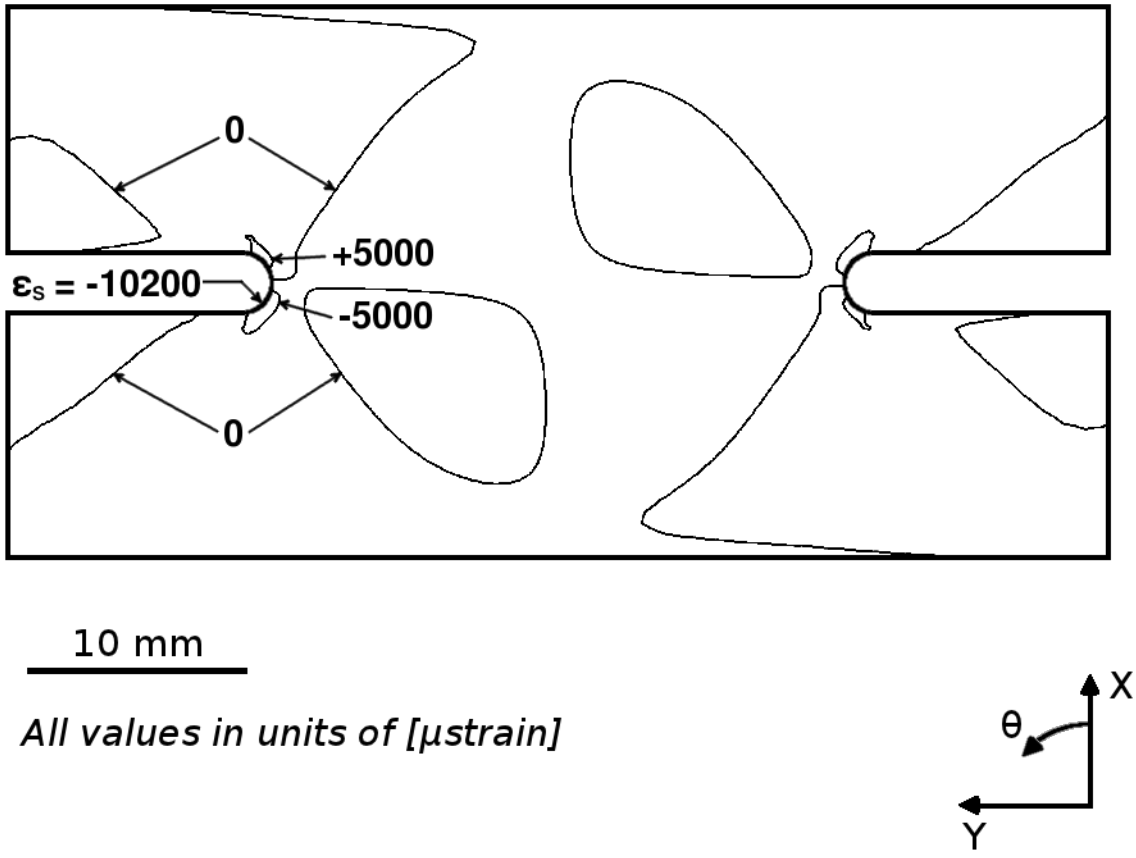

Figure B.47 Isostrain plot of strain field of ϵ_{12}, in laminate axes, at the midplane of ply 1 (a $+60^\circ$ ply) of the double-edge-notched specimen model for the single-ply effective ply thickness laminate of $[+60/-60]_{16T}$.

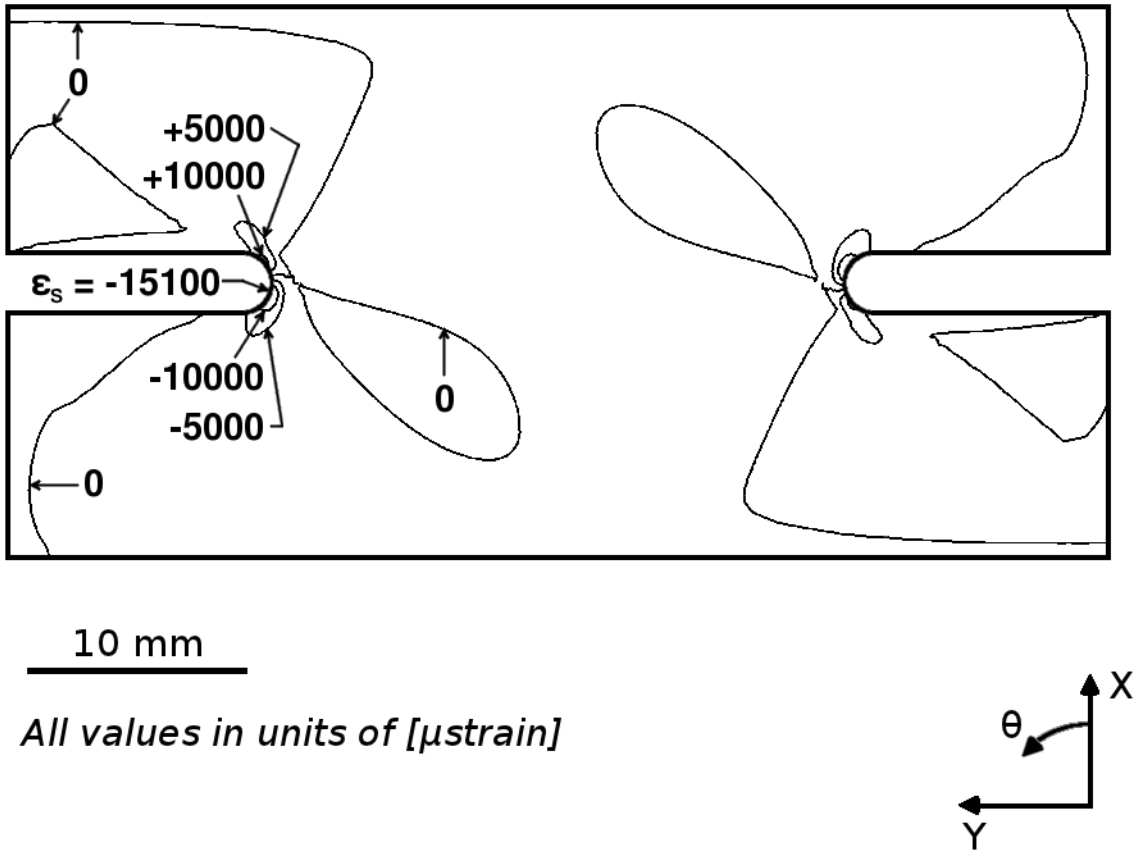

Figure B.48 Isostrain plot of strain field of ϵ_{12}, in laminate axes, at the midplane of ply 1 (a $+60^\circ$ ply) of the double-edge-notched specimen model for the four-ply effective ply thickness laminate of $[+60_4/-60_4]_{4T}$.

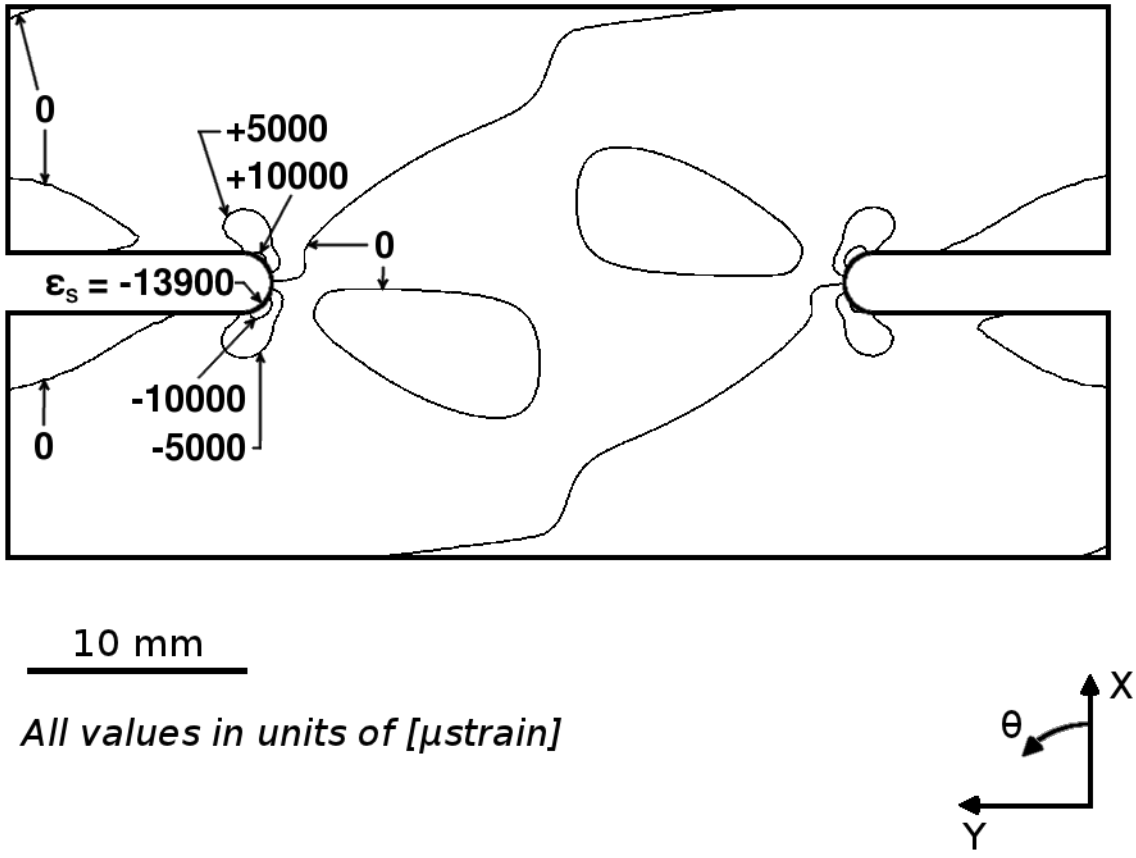

Figure B.49 Isostrain plot of strain field of ϵ_{12}, in laminate axes, at the midplane of ply 1 (a $+75°$ ply) of the double-edge-notched specimen model for the single-ply effective ply thickness laminate of $[+75/-75]_{16T}$.

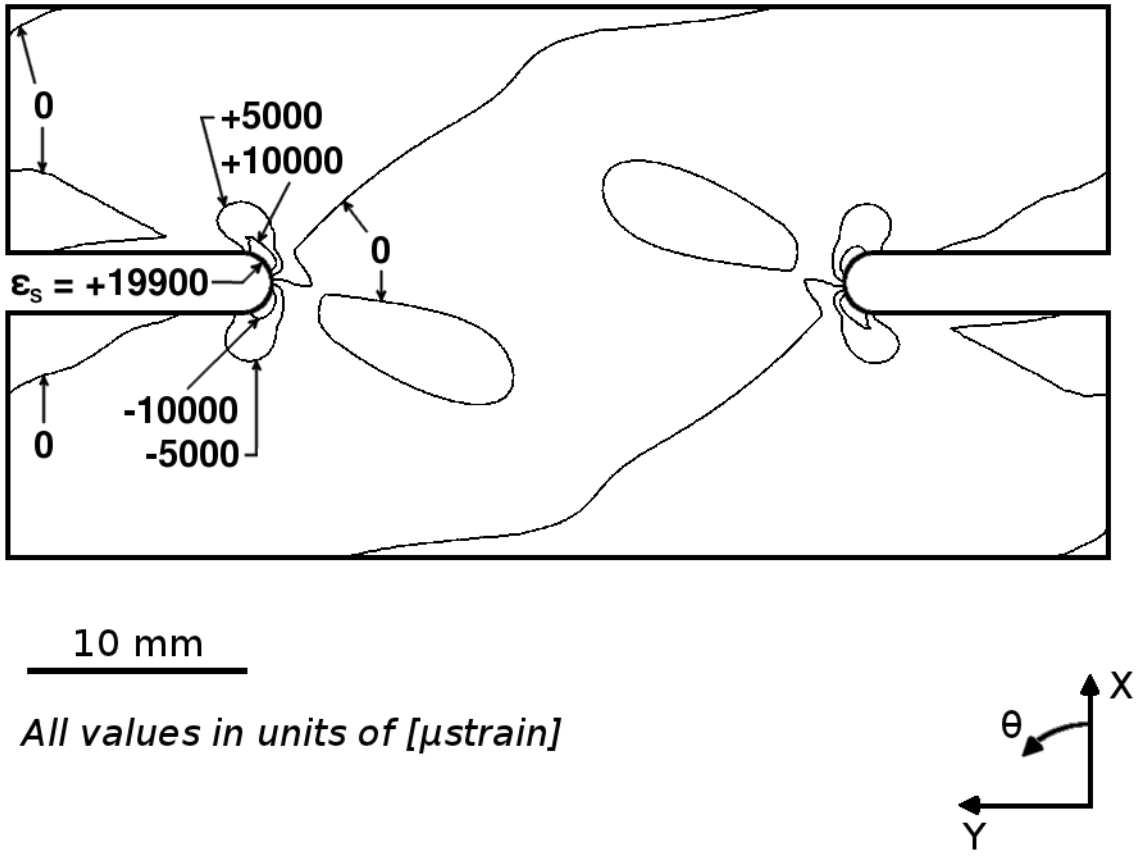

Figure B.50 Isostrain plot of strain field of ϵ_{12}, in laminate axes, at the midplane of ply 1 (a $+75^\circ$ ply) of the double-edge-notched specimen model for the four-ply effective ply thickness laminate of $[+75_4/-75_4]_{4T}$.

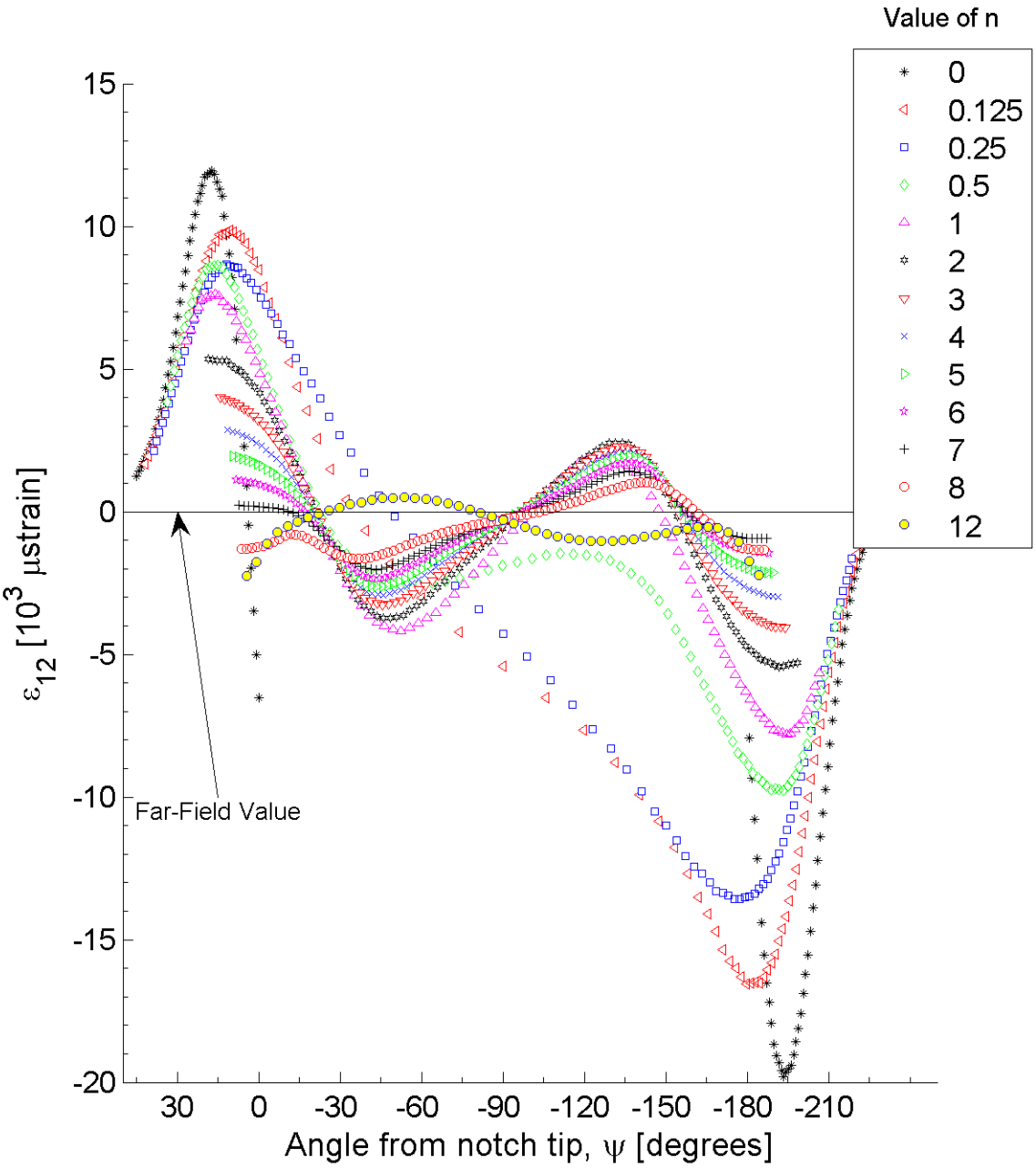

Figure B.51 Plot of ϵ_{12}, in laminate axes, along arc paths at the midplane of ply 1 (a $+30°$ ply) of the double-edge-notched specimen model for the laminate of $[(+30/-30]_{16T}$.

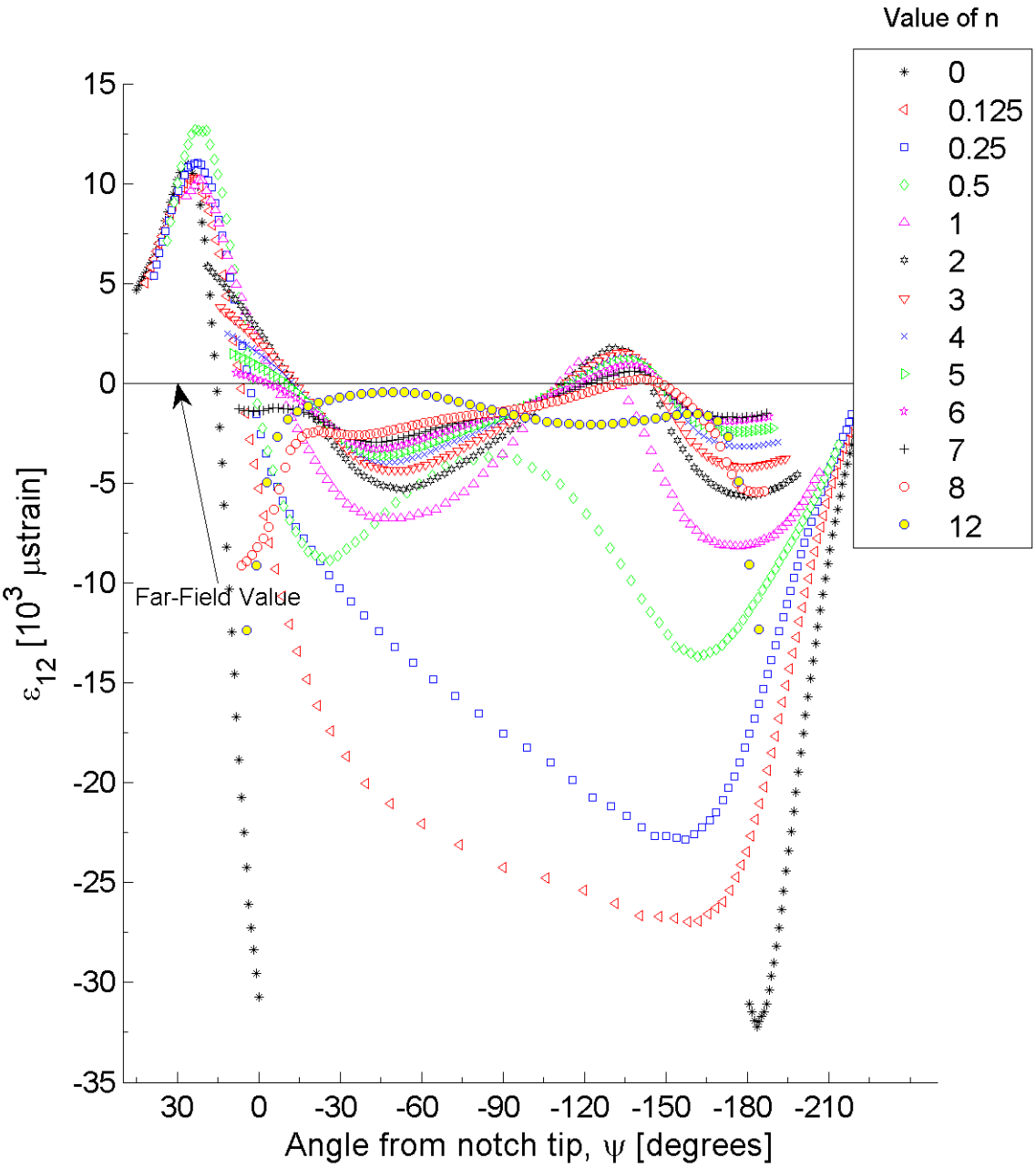

Figure B.52 Plot of ϵ_{12}, in laminate axes, along arc paths at the midplane of ply 1 (a $+30°$ ply) of the double-edge-notched specimen model for the laminate of $[(+30_4/-30_4]_{4T}$.

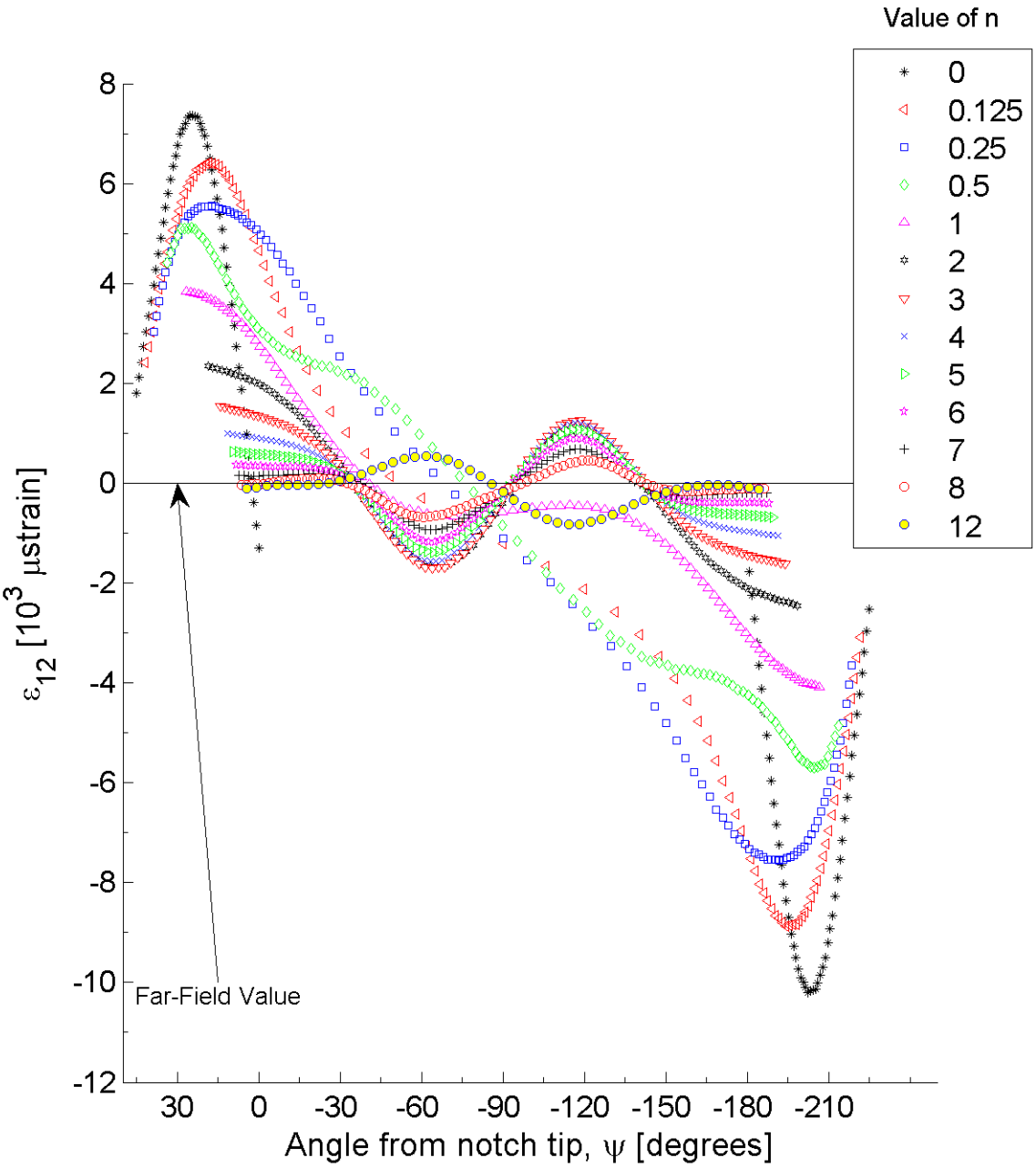

Figure B.53 Plot of ϵ_{12}, in laminate axes, along arc paths at the midplane of ply 1 (a $+60°$ ply) of the double-edge-notched specimen model for the laminate of $[(+60/-60]_{16T}$.

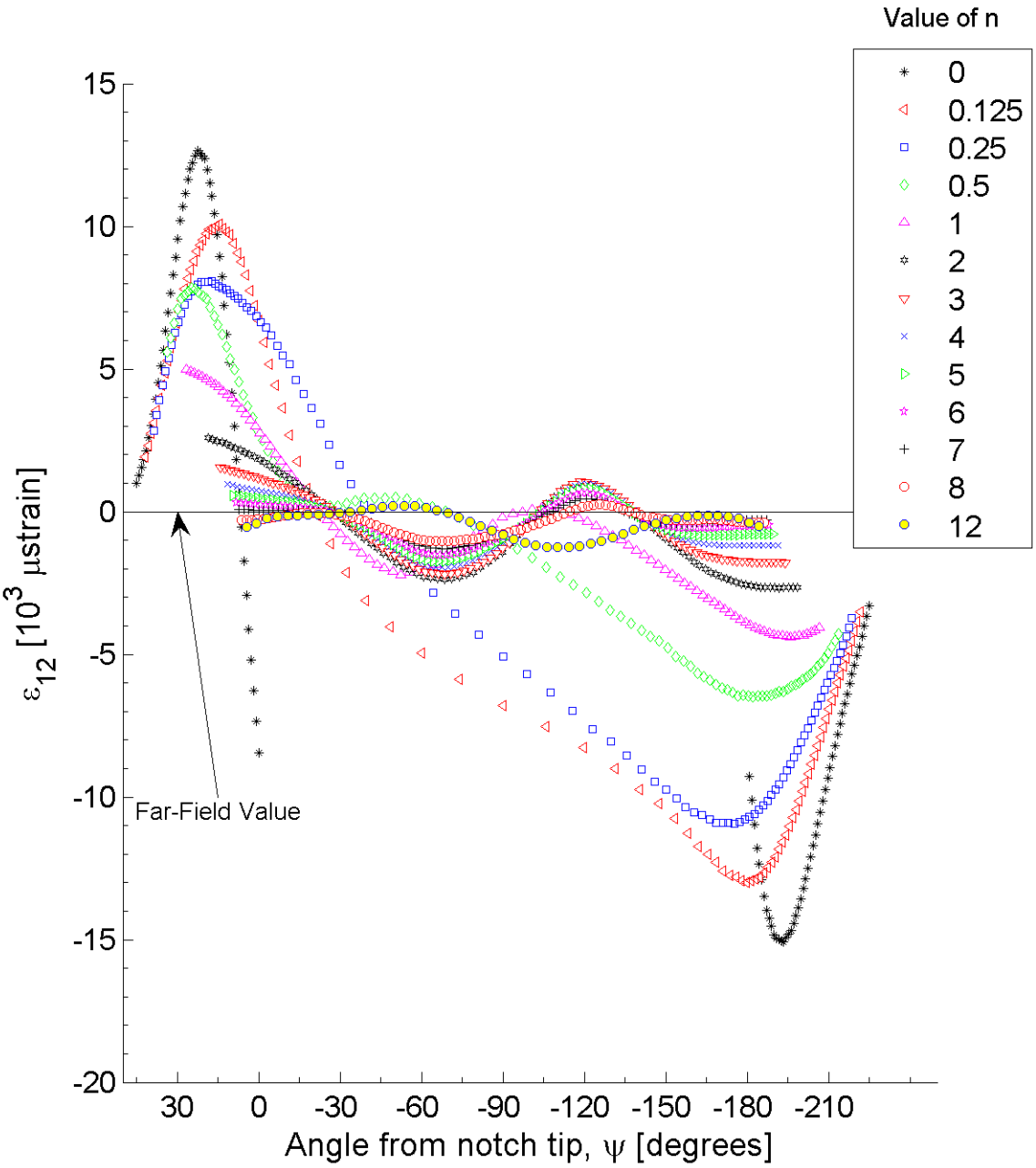

Figure B.54 Plot of ϵ_{12}, in laminate axes, along arc paths at the midplane of ply 1 (a $+60°$ ply) of the double-edge-notched specimen model for the laminate of $[(+60_4/-60_4]_{4T}$.

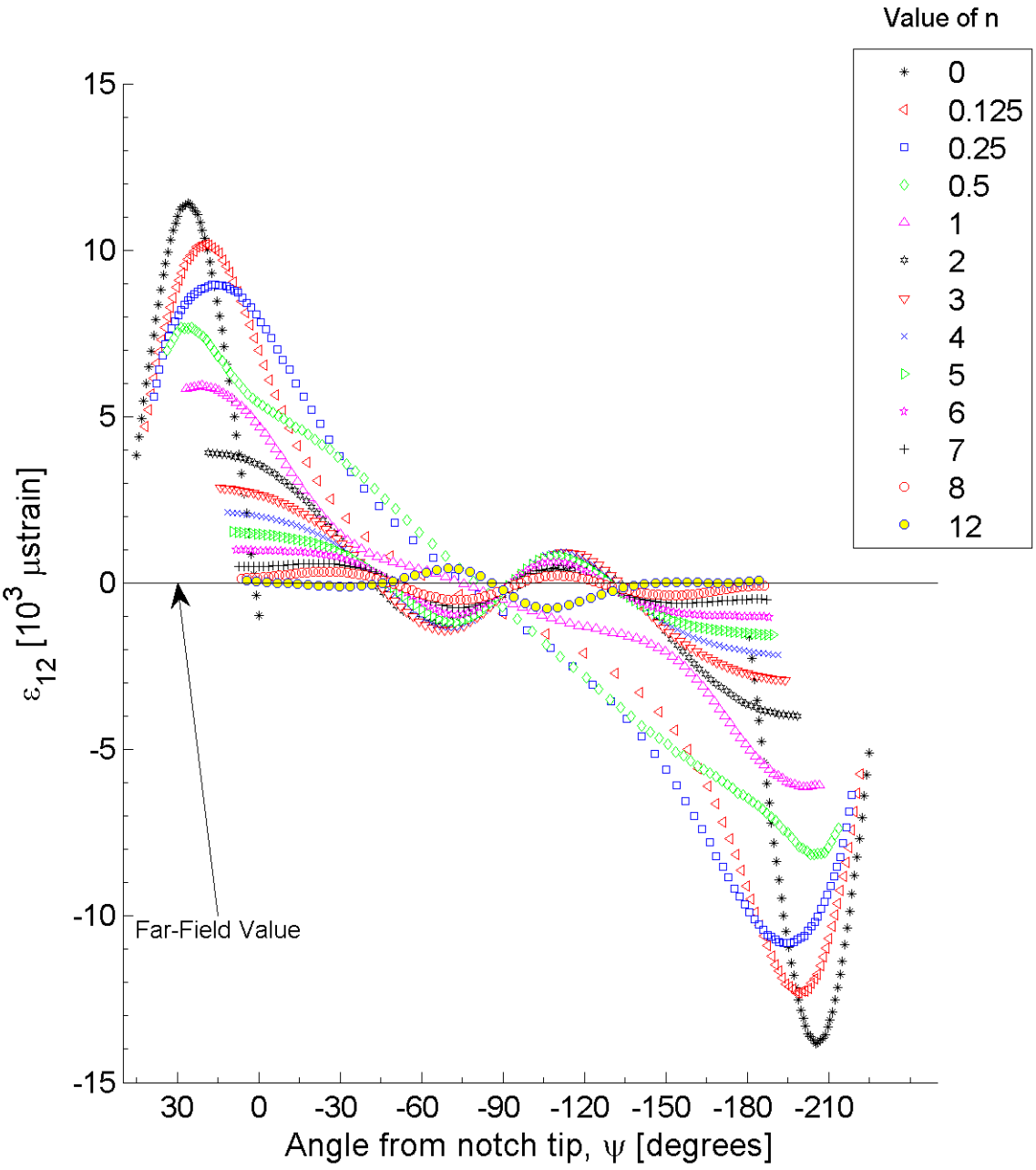

Figure B.55 Plot of ϵ_{12}, in laminate axes, along arc paths at the midplane of ply 1 (a $+75°$ ply) of the double-edge-notched specimen model for the laminate of $[(+75/-75]_{16T}$.

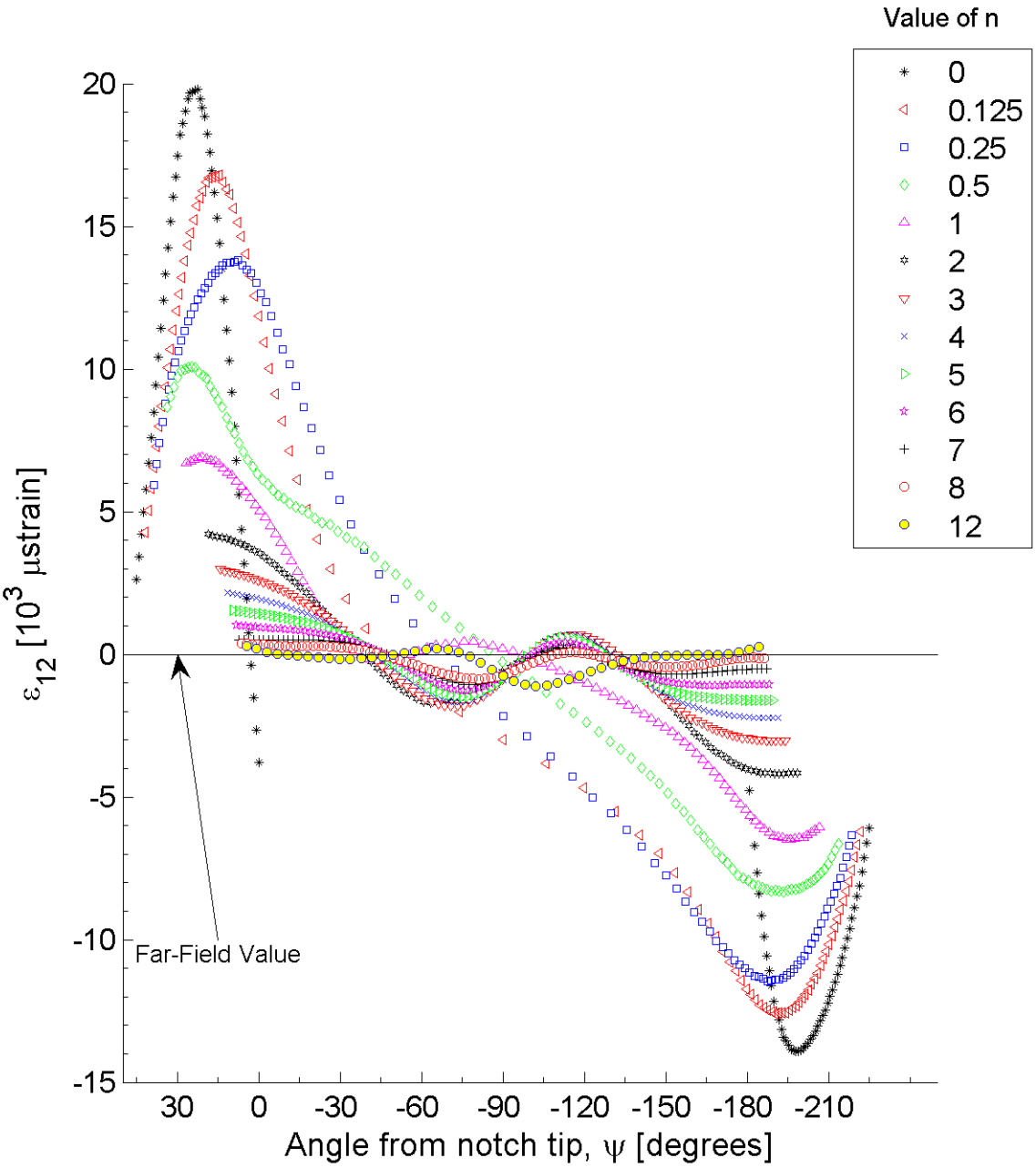

Figure B.56 Plot of ϵ_{12}, in laminate axes, along arc paths at the midplane of ply 1 (a $+75°$ ply) of the double-edge-notched specimen model for the laminate of $[(+75_4/-75_4]_{4T}$.

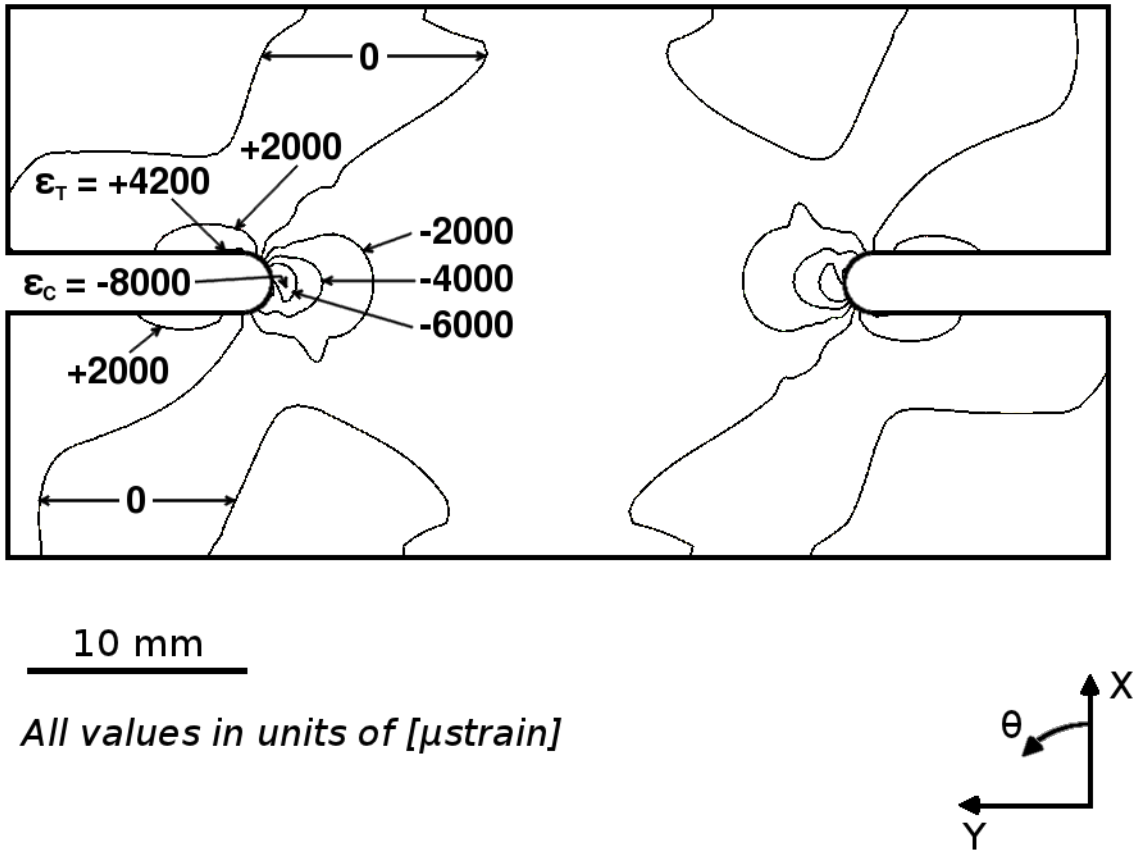

Figure B.57 Isostrain plot of strain field of ϵ_{33}, at the midplane of ply 1 (a +15° ply) of the double-edge-notched specimen model for the four-ply effective ply thickness laminate of $[15_4/-15_4]_{4T}$.

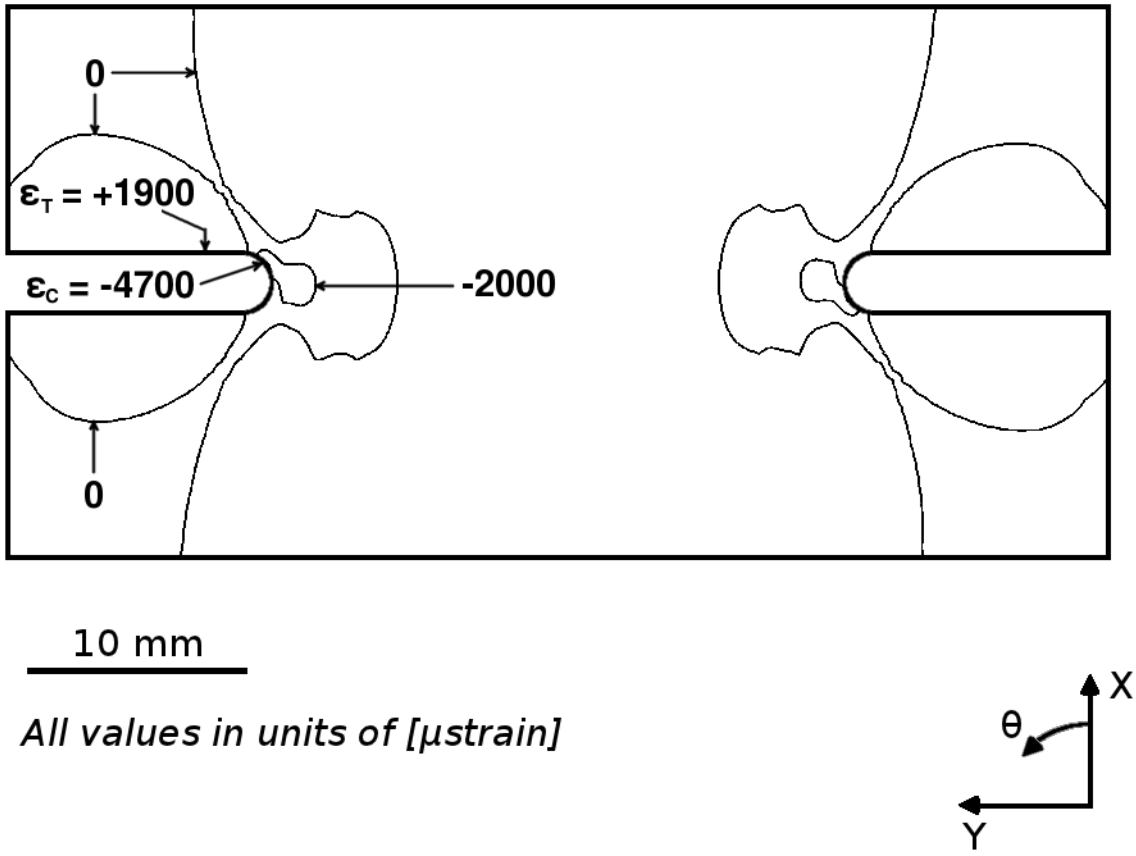

Figure B.58 Isostrain plot of strain field of ϵ_{33}, at the midplane of ply 1 (a $+30^\circ$ ply) of the double-edge-notched specimen model for the single-ply effective ply thickness laminate of $[30/-30]_{16T}$.

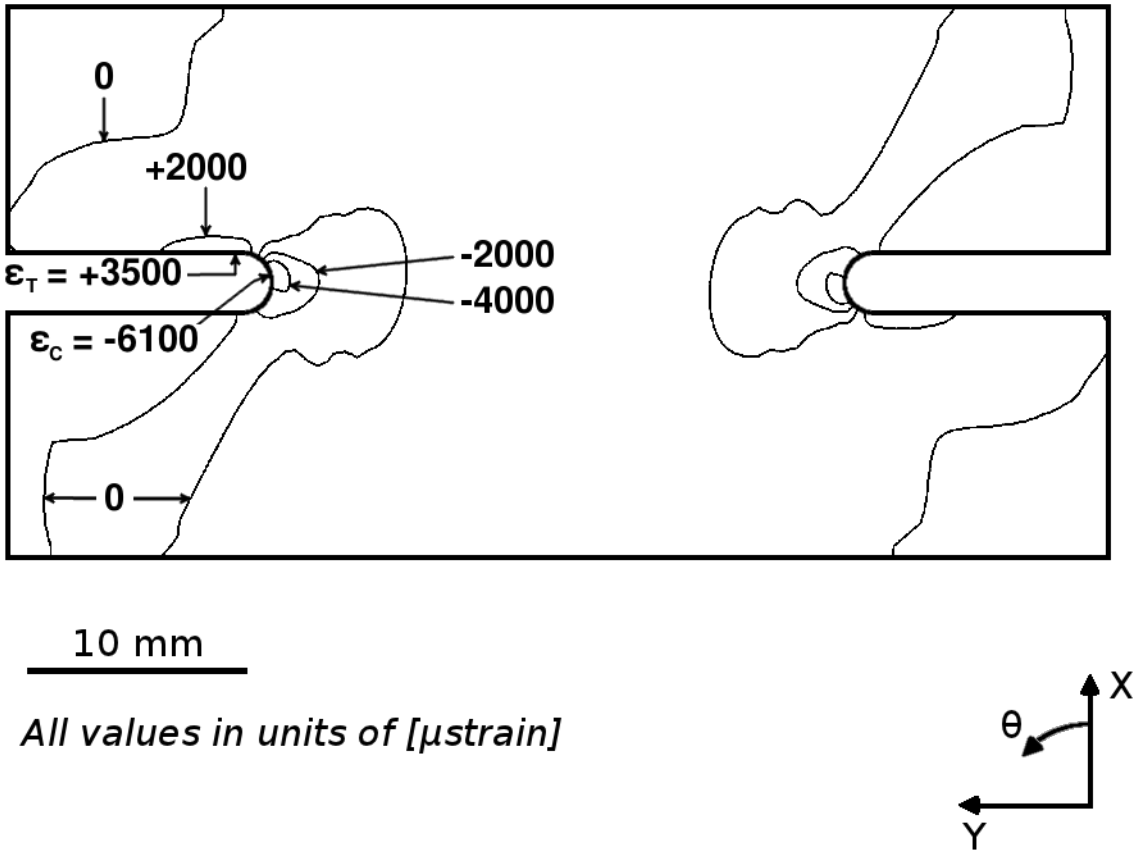

Figure B.59 Isostrain plot of strain field of ϵ_{33}, at the midplane of ply 1 (a $+30^\circ$ ply) of the double-edge-notched specimen model for the four-ply effective ply thickness laminate of $[30_4/-30_4]_{4T}$.

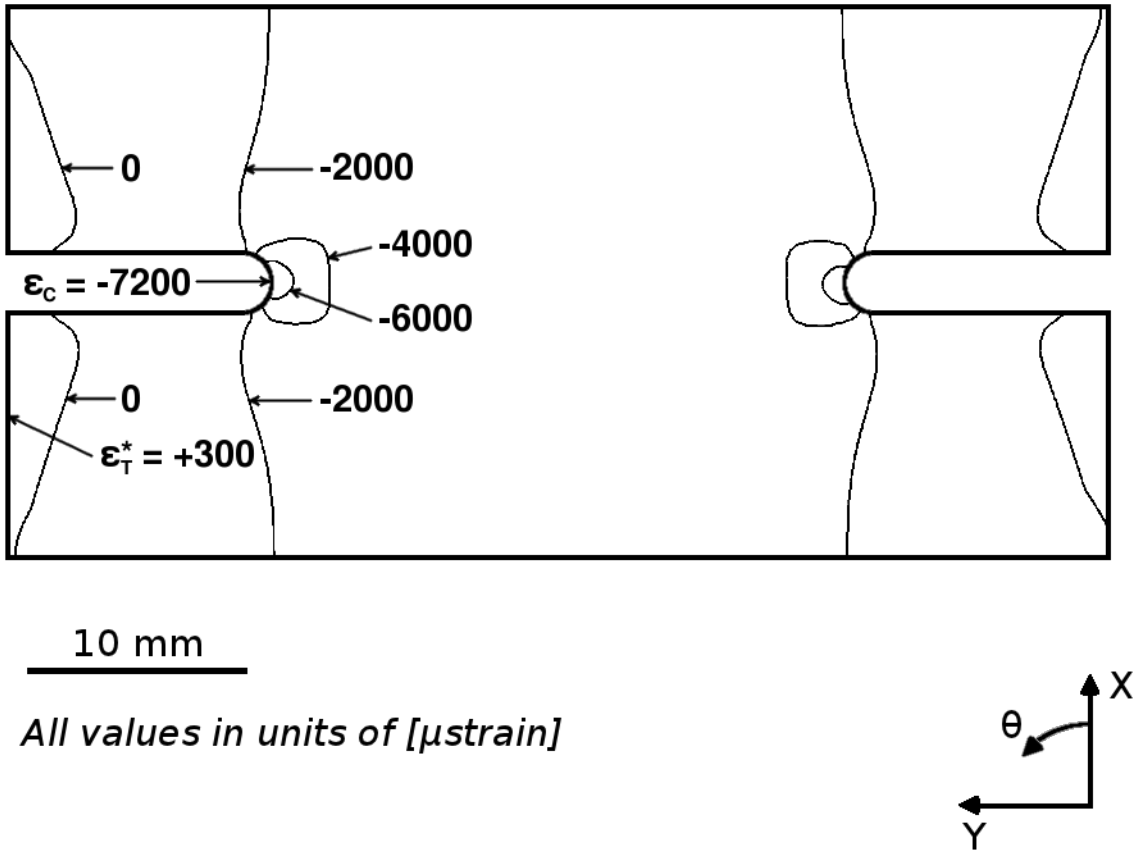

Figure B.60 Isostrain plot of strain field of ϵ_{33}, at the midplane of ply 1 (a $+60^\circ$ ply) of the double-edge-notched specimen model for the single-ply effective ply thickness laminate of $[60/-60]_{16T}$.

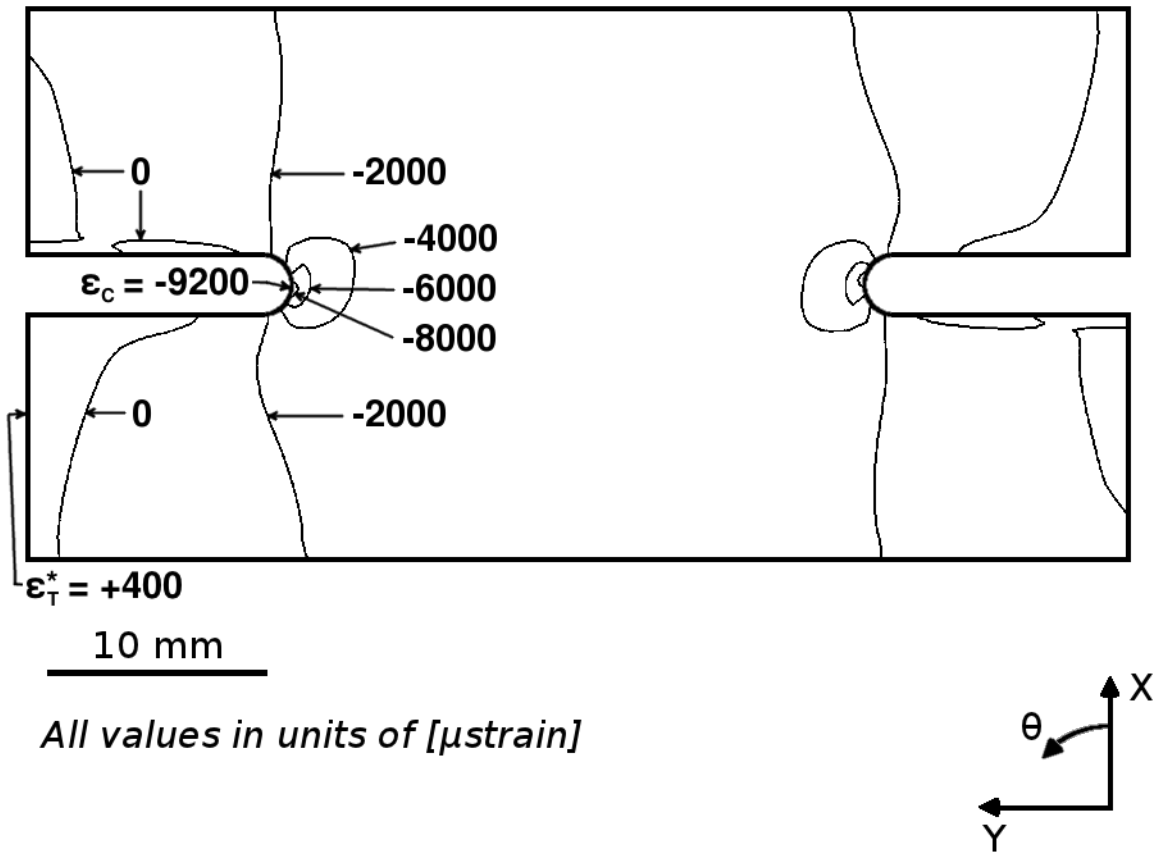

Figure B.61 Isostrain plot of strain field of ϵ_{33}, at the midplane of ply 1 (a $+60^\circ$ ply) of the double-edge-notched specimen model for the four-ply effective ply thickness laminate of $[60_4/-60_4]_{4T}$.

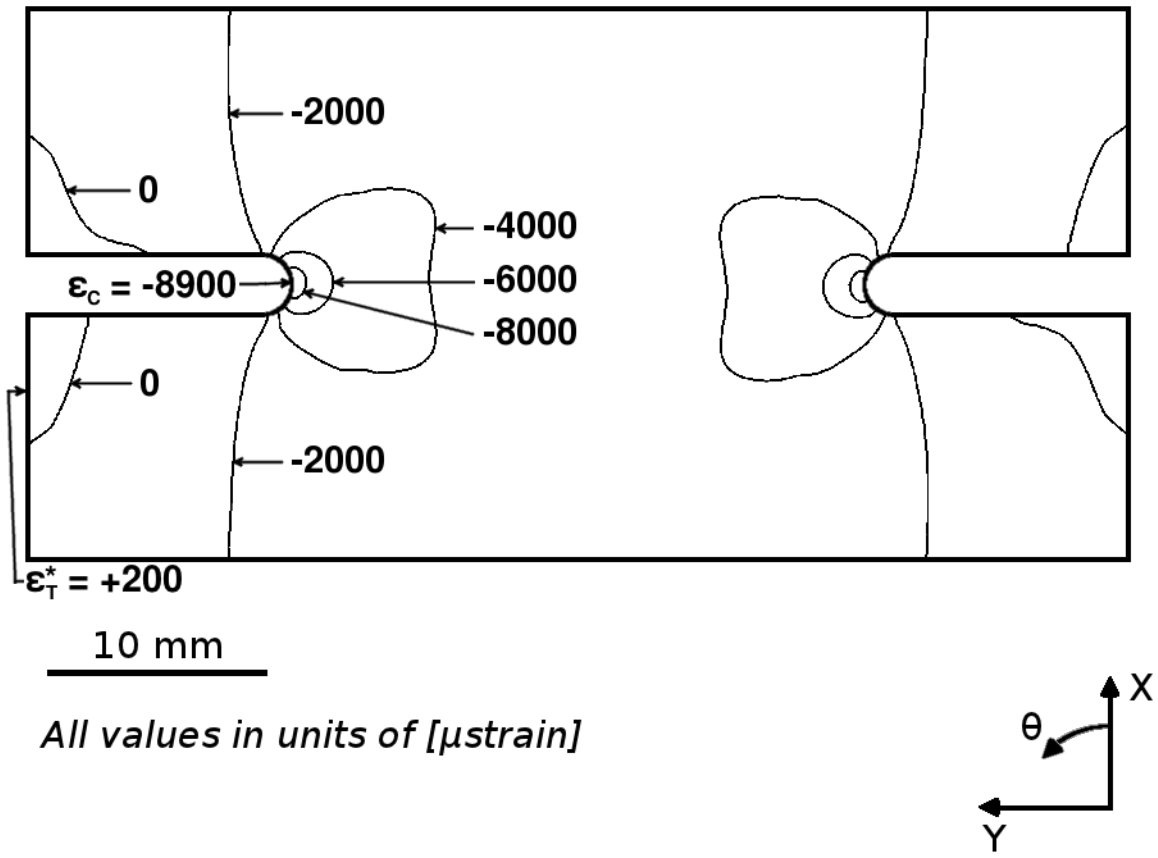

Figure B.62 Isostrain plot of strain field of ϵ_{33}, at the midplane of ply 1 (a $+75^\circ$ ply) of the double-edge-notched specimen model for the single-ply effective ply thickness laminate of $[75/-75]_{16T}$.

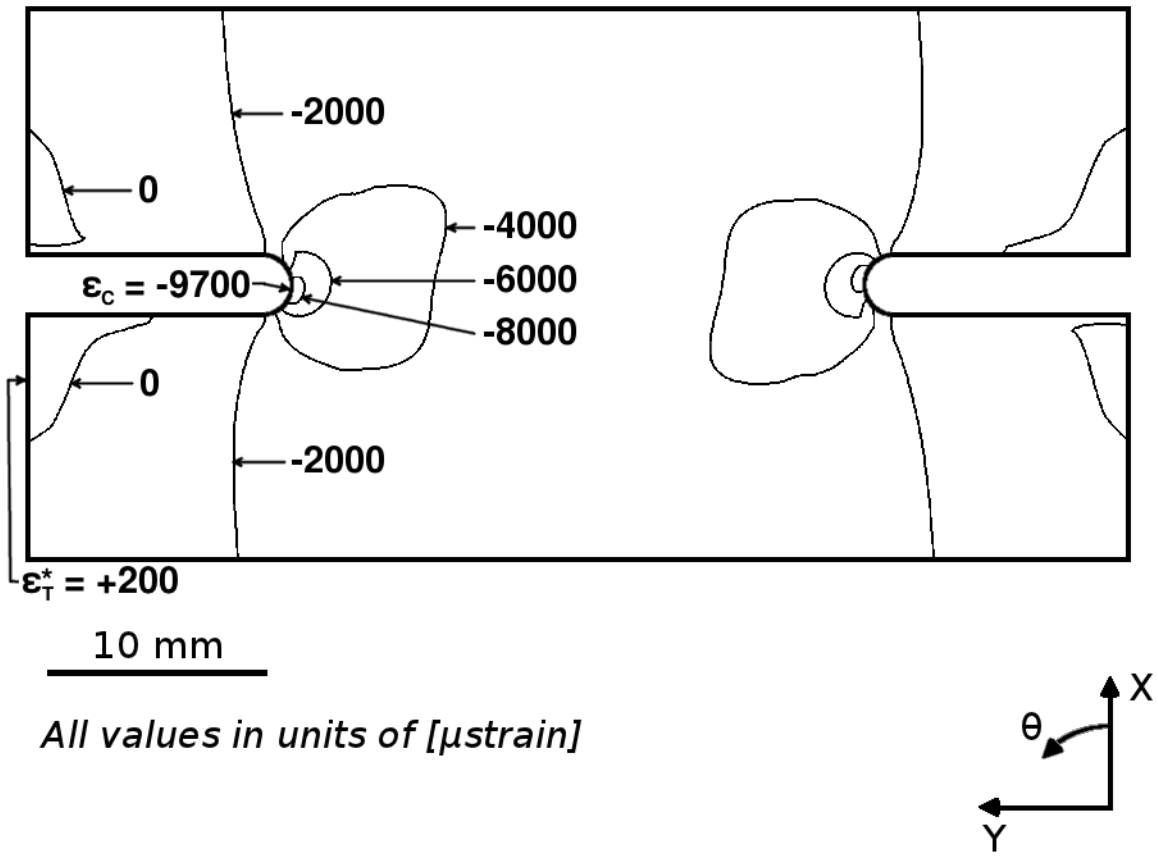

Figure B.63 Isostrain plot of strain field of ϵ_{33}, at the midplane of ply 1 (a $+75^\circ$ ply) of the double-edge-notched specimen model for the four-ply effective ply thickness laminate of $[75_4/-75_4]_{4T}$.

B.3 Strain Plots for Open-Hole Tension Specimens

This section contains additional figures relating to the results of the open-hole tension specimens discussed in Section 7.3.3. Two types of figures are included in this section: isostrain plots of the strain fields of the open-hole tension specimens, and plots of strain magnitudes along arc paths for the open-hole tension specimens, as defined in Section 7.3.3. The figures in this section of the appendix illustrate the variations of the strain fields, and the plots of strain magnitudes along arc paths for laminate angles not shown in Section 7.3.3.

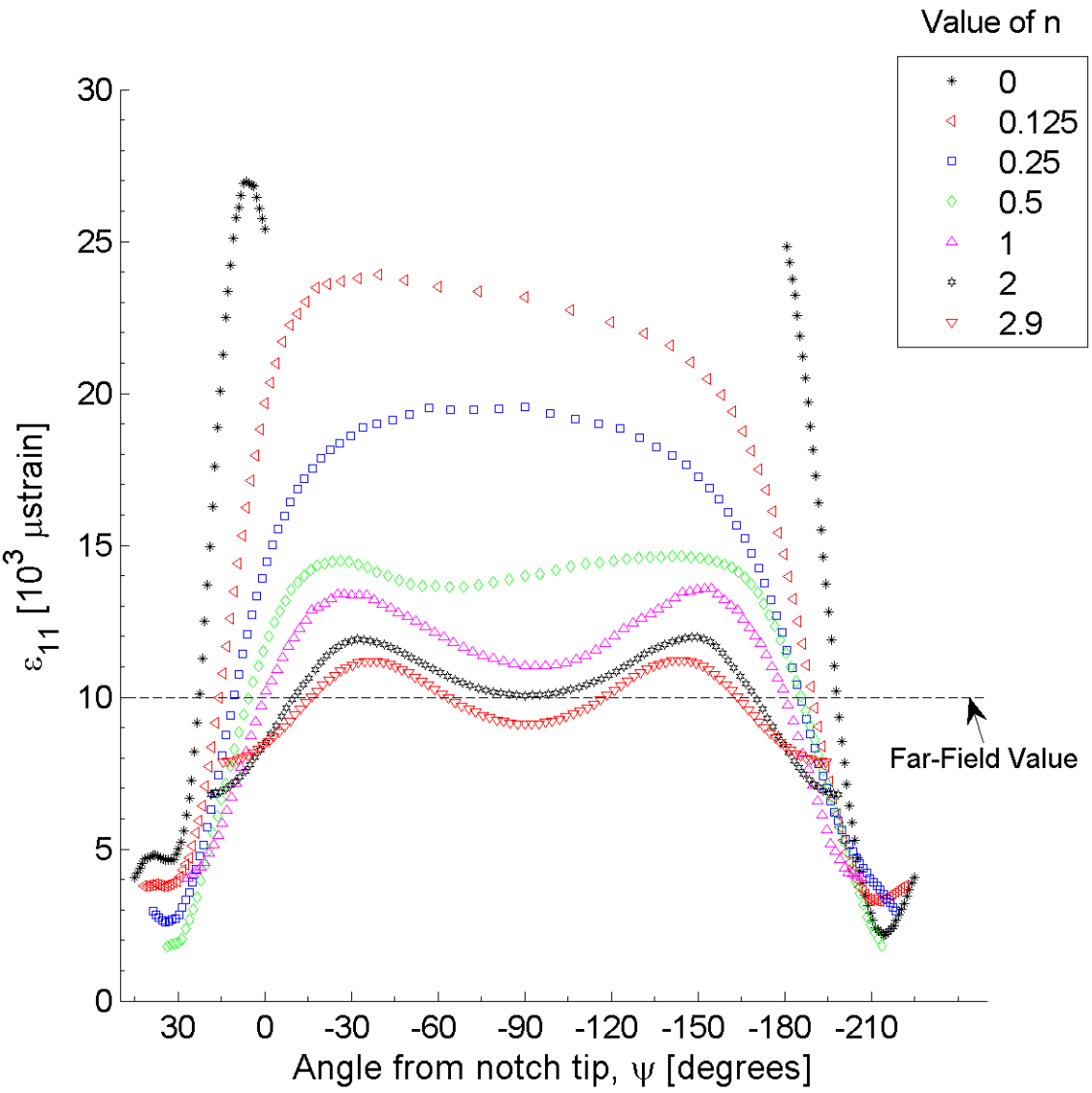

Figure B.64 Plot of ϵ_{11}, in laminate axes, along arc paths at the midplane of ply 1 (a +45° ply) of the open-hole tension specimen model for case of a 0.5 inch diameter hole for the four-ply effective ply thickness laminate of $[+45_4/0_4/-45_4]_S$.

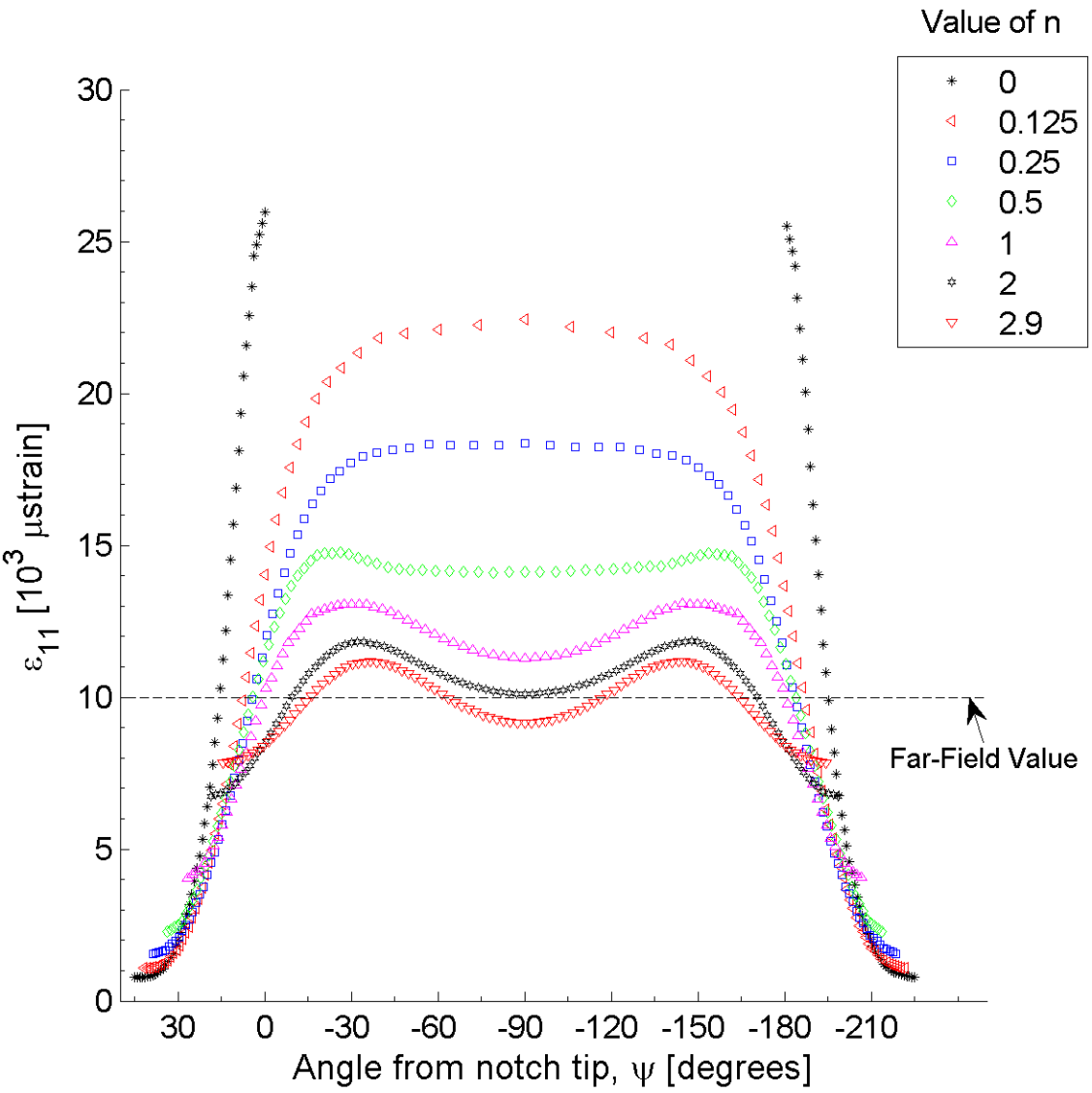

Figure B.65 Plot of ϵ_{11}, in laminate axes, along arc paths at the midplane of ply 6 (a 0° ply) of the open-hole tension specimen model for case of a 0.5 inch diameter hole for the four-ply effective ply thickness laminate of $[+45_4/0_4/-45_4]_S$.

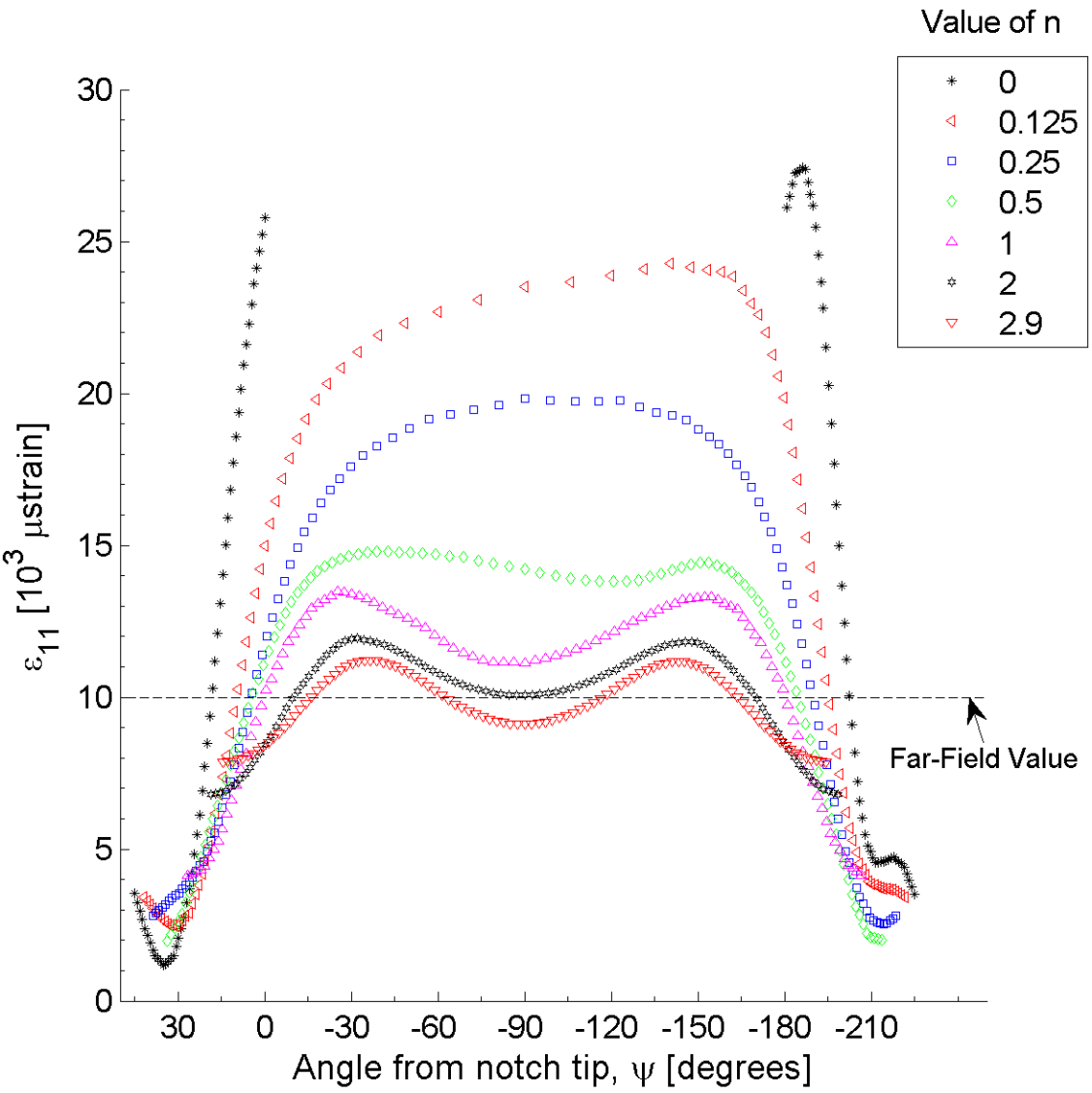

Figure B.66 Plot of ϵ_{11}, in laminate axes, along arc paths at the midplane of ply 12 (a $-45°$ ply) of the open-hole tension specimen model for case of a 0.5 inch diameter hole for the four-ply effective ply thickness laminate of $[+45_4/0_4/-45_4]_S$.

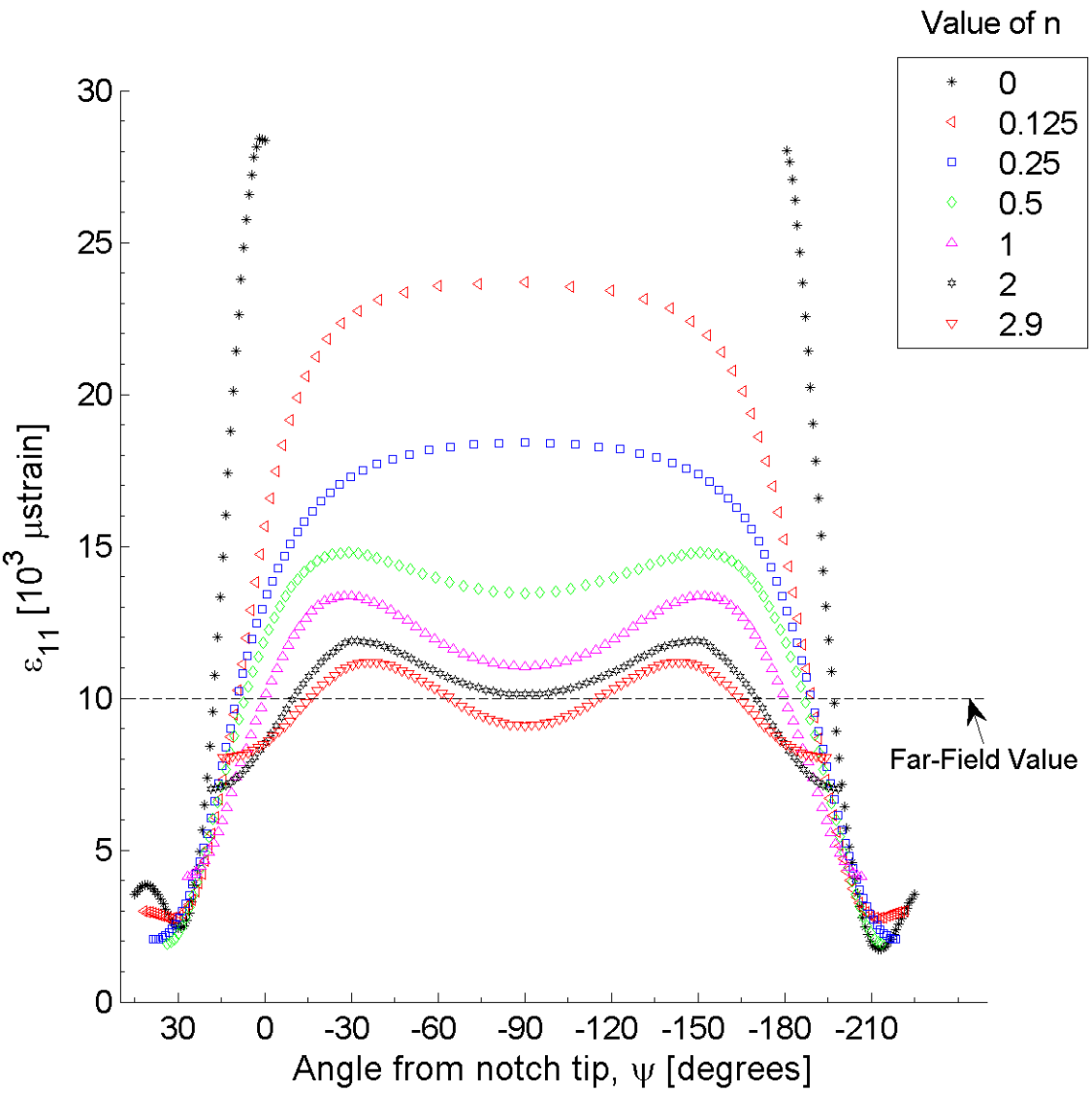

Figure B.67 Plot of ϵ_{11}, in laminate axes, along arc paths at the midplane of ply 1 (a $+45°$ ply) of the open-hole tension specimen model for case of a 1.0 inch diameter hole for the single-ply effective ply thickness laminate of $[+45/0/-45]_{4S}$.

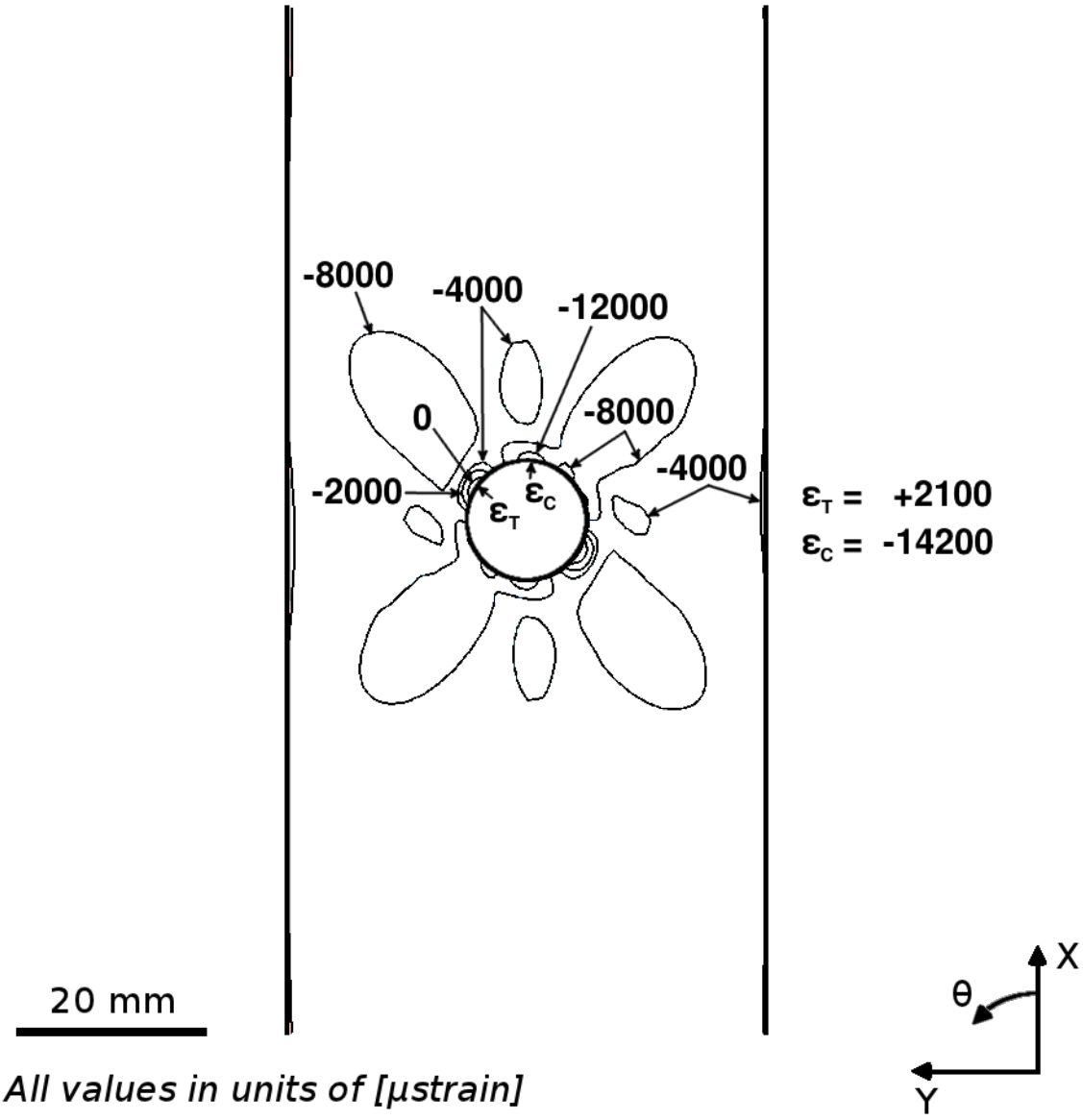

Figure B.68 Isostrain plot of strain field of ϵ_{22}, in laminate axes, at the midplane of ply 1 (a $+45^\circ$ ply) of the open-hole tension specimen model for case of a 0.5 inch diameter hole for the four-ply effective ply thickness laminate of $[+45_4/0_4/-45_4]_S$.

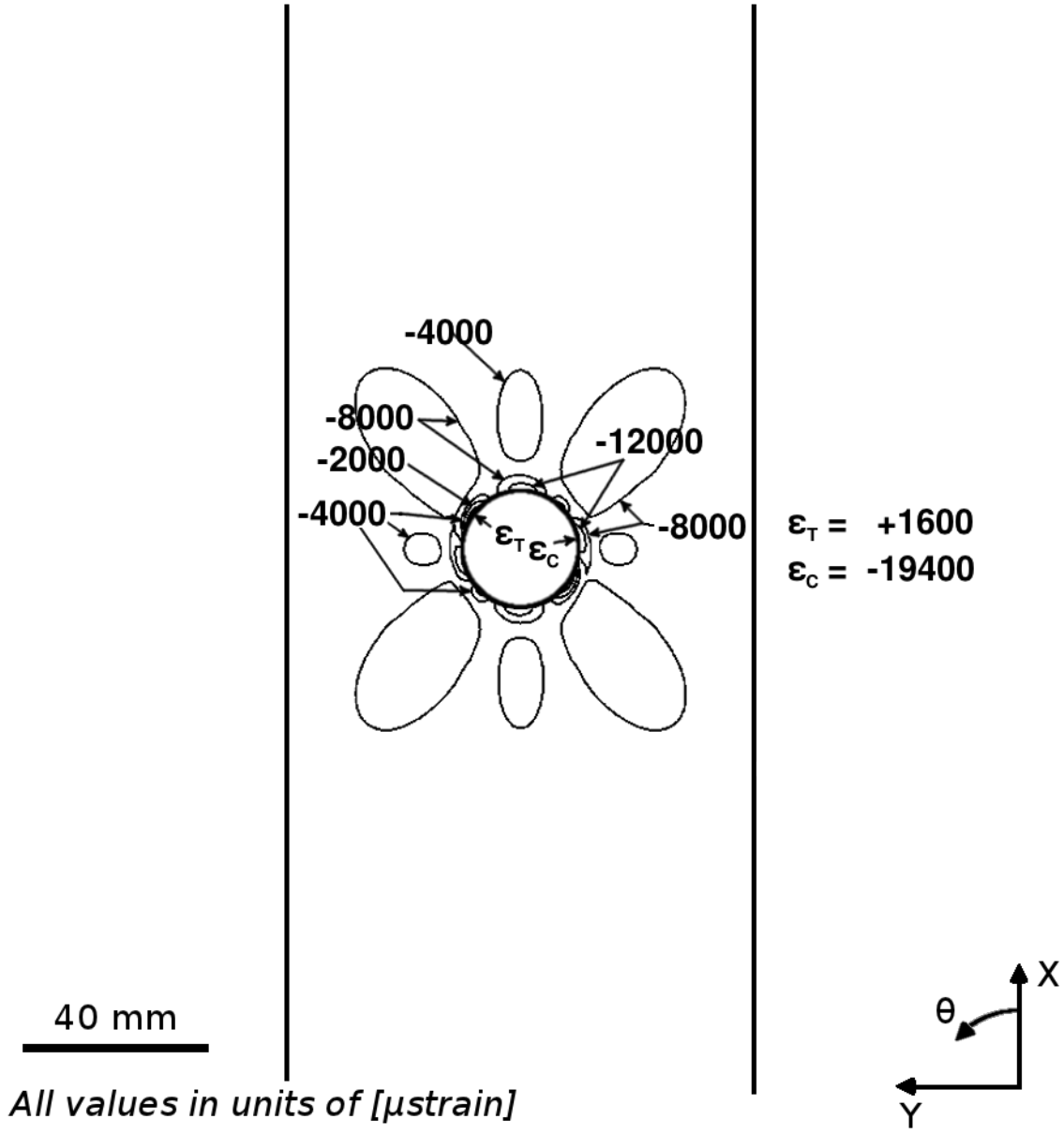

Figure B.69 Isostrain plot of strain field of ϵ_{22}, in laminate axes, at the midplane of ply 1 (a $+45^\circ$ ply) of the open-hole tension specimen model for case of a 1.0 inch diameter hole for the single-ply effective ply thickness laminate of $[+45/0/-45]_{4S}$.

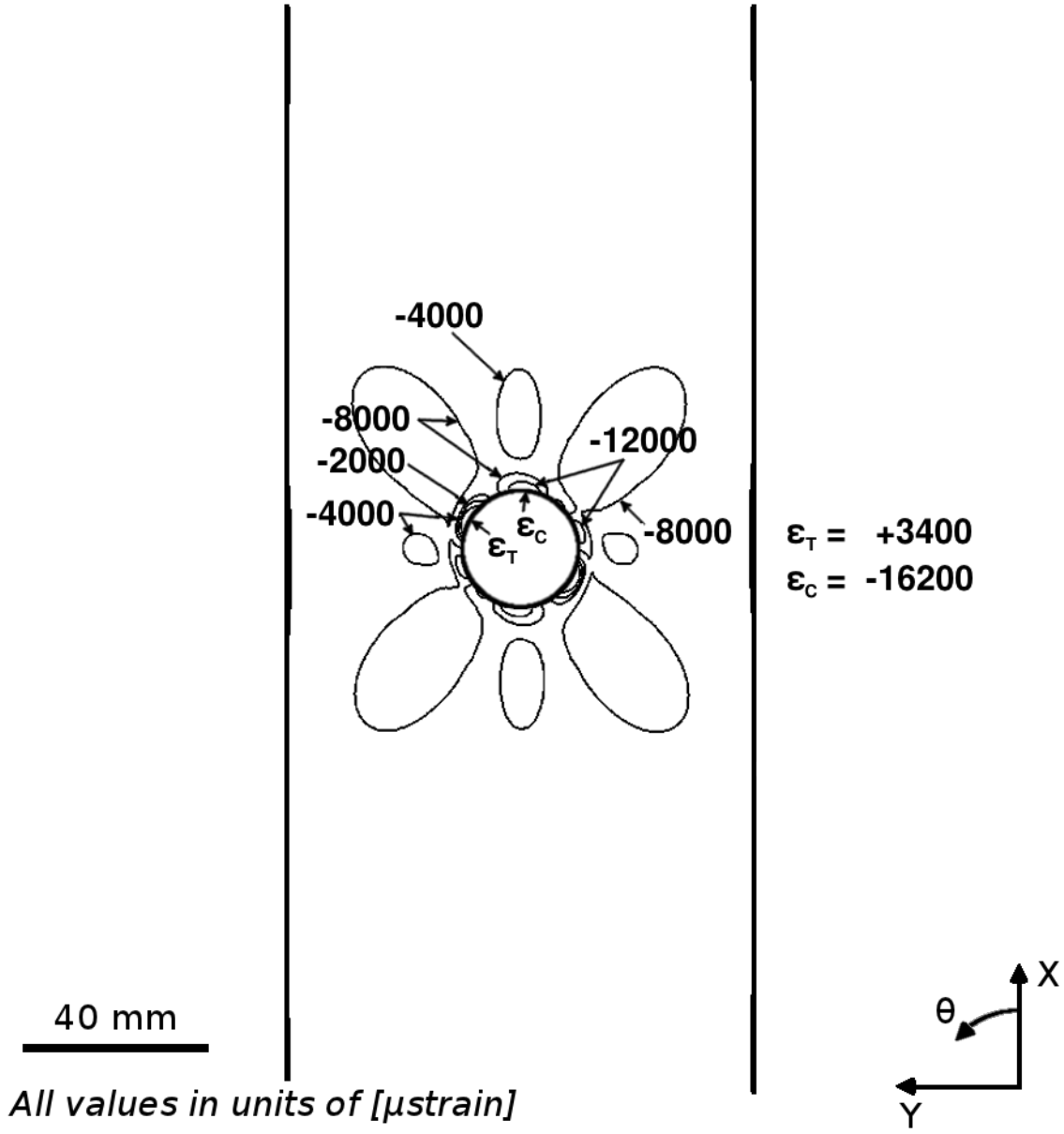

Figure B.70 Isostrain plot of strain field of ϵ_{22}, in laminate axes, at the midplane of ply 1 (a $+45^\circ$ ply) of the open-hole tension specimen model for case of a 1.0 inch diameter hole for the four-ply effective ply thickness laminate of $[+45_4/0_4/-45_4]_S$.

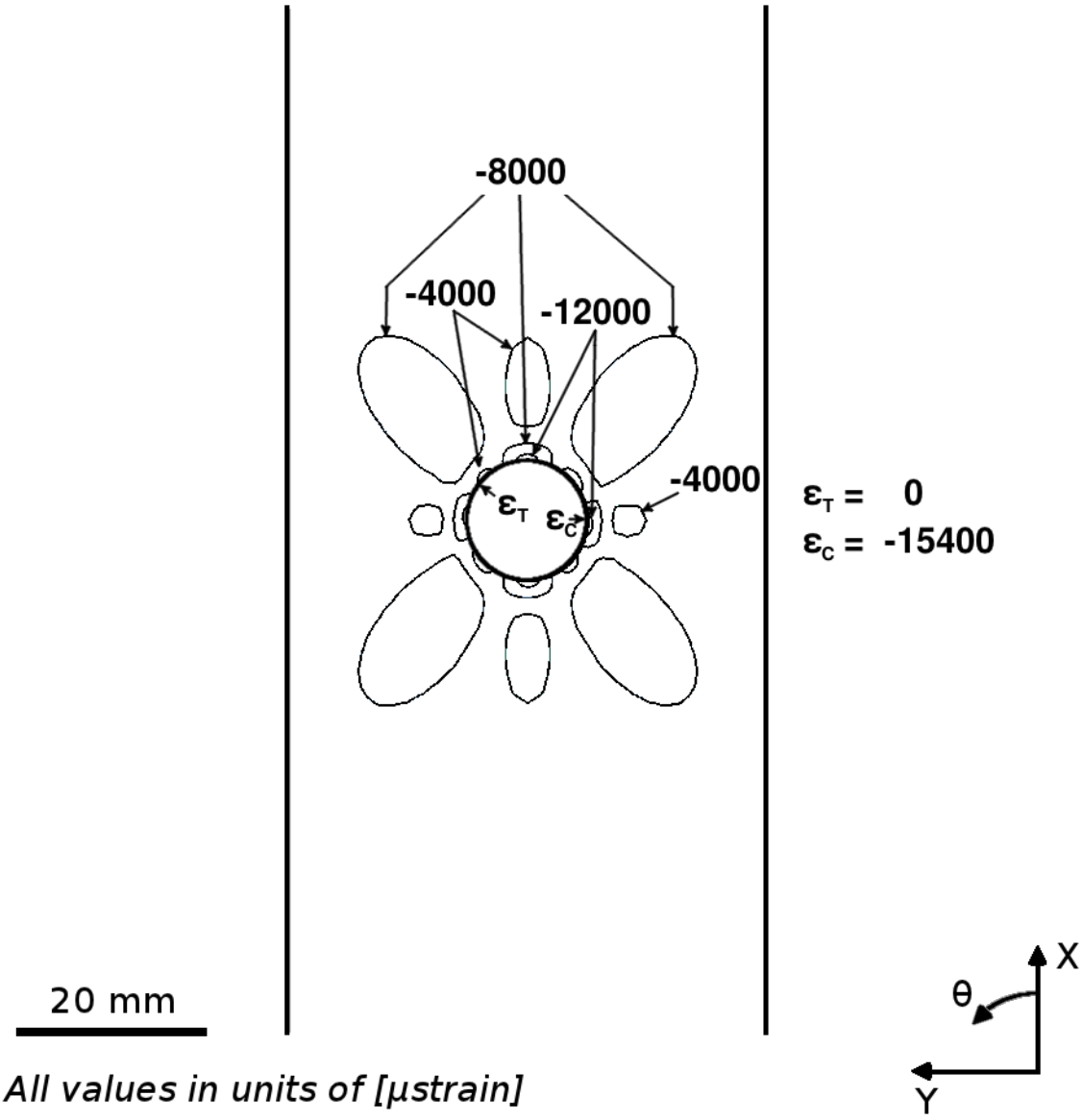

Figure B.71 Isostrain plot of strain field of ϵ_{22}, in laminate axes, at the midplane of ply 6 (a 0° ply) of the open-hole tension specimen model for case of a 0.5 inch diameter hole for the single-ply effective ply thickness laminate of $[+45/0/-45]_{4S}$.

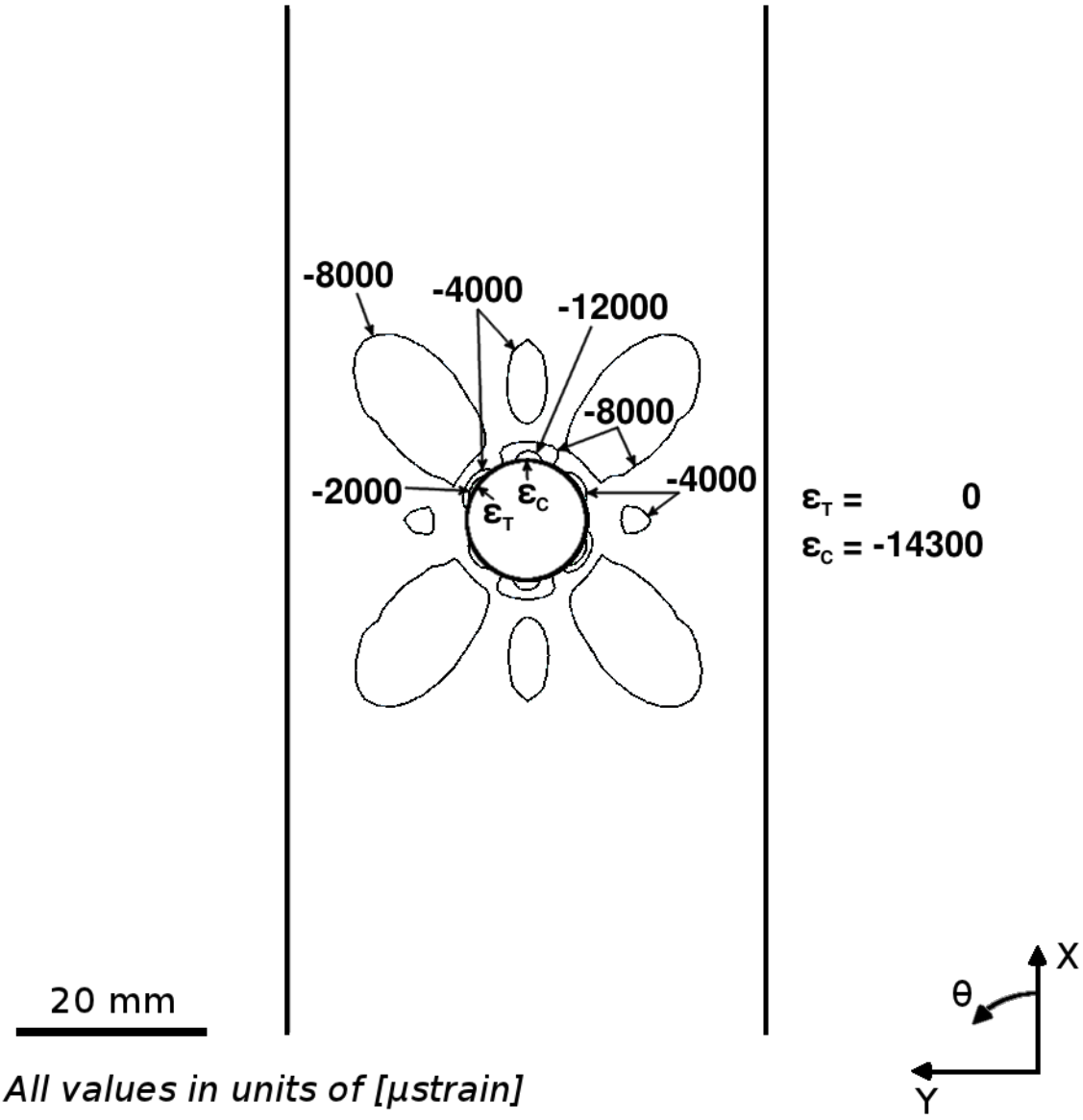

Figure B.72 Isostrain plot of strain field of ϵ_{22}, in laminate axes, at the midplane of ply 6 (a 0° ply) of the open-hole tension specimen model for case of a 0.5 inch diameter hole for the four-ply effective ply thickness laminate of $[+45_4/0_4/-45_4]_S$.

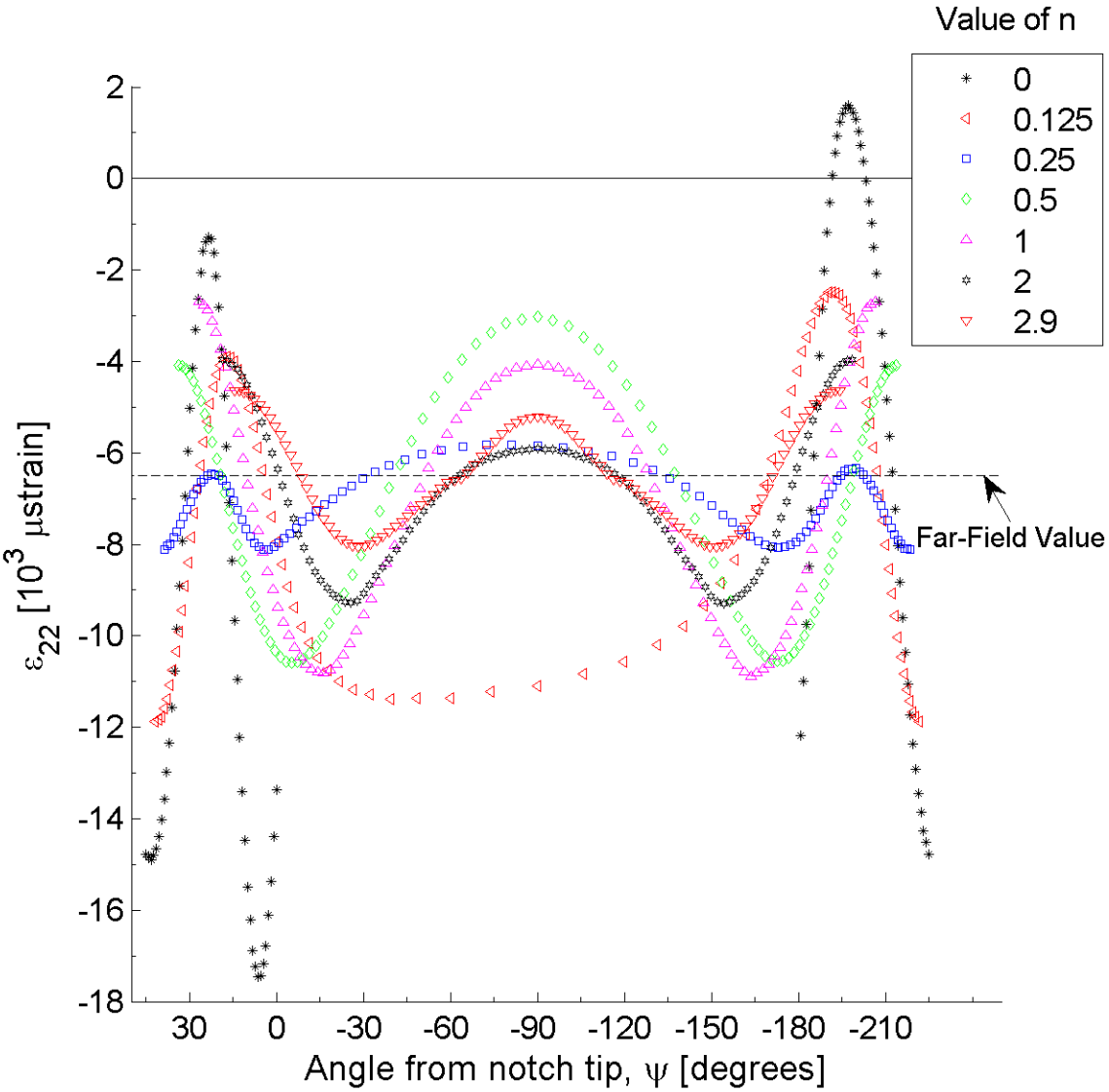

Figure B.73 Plot of ϵ_{22}, in laminate axes, along arc paths at the midplane of ply 1 (a $+45°$ ply) of the open-hole tension specimen model for case of a 1.0 inch diameter hole for the single-ply effective ply thickness laminate of $[+45/0/-45]_{4S}$.

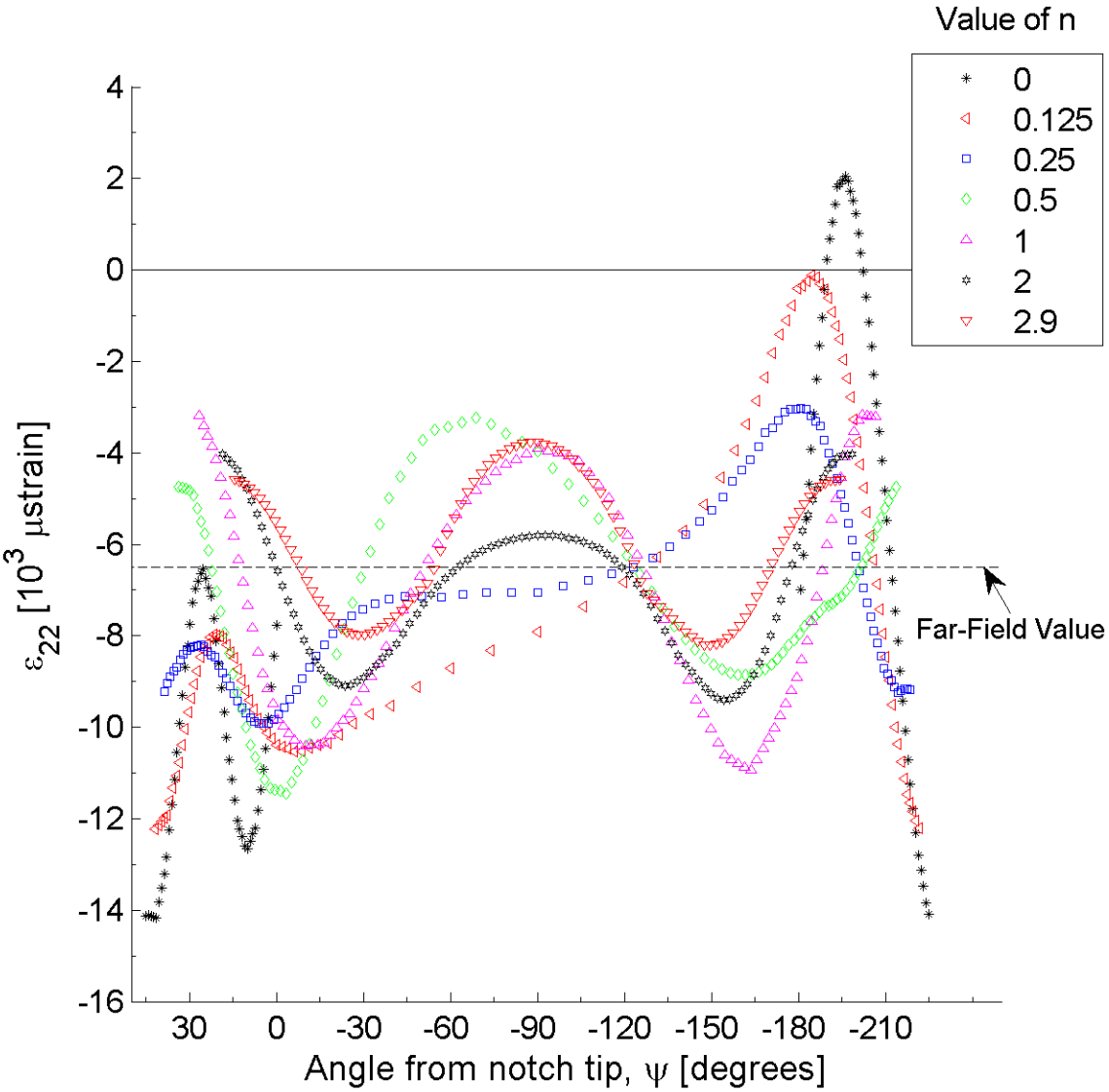

Figure B.74 Plot of ϵ_{22}, in laminate axes, along arc paths at the midplane of ply 1 (a $+45°$ ply) of the open-hole tension specimen model for case of a 0.5 inch diameter hole for the four-ply effective ply thickness laminate of $[+45_4/0_4/-45_4]_S$.

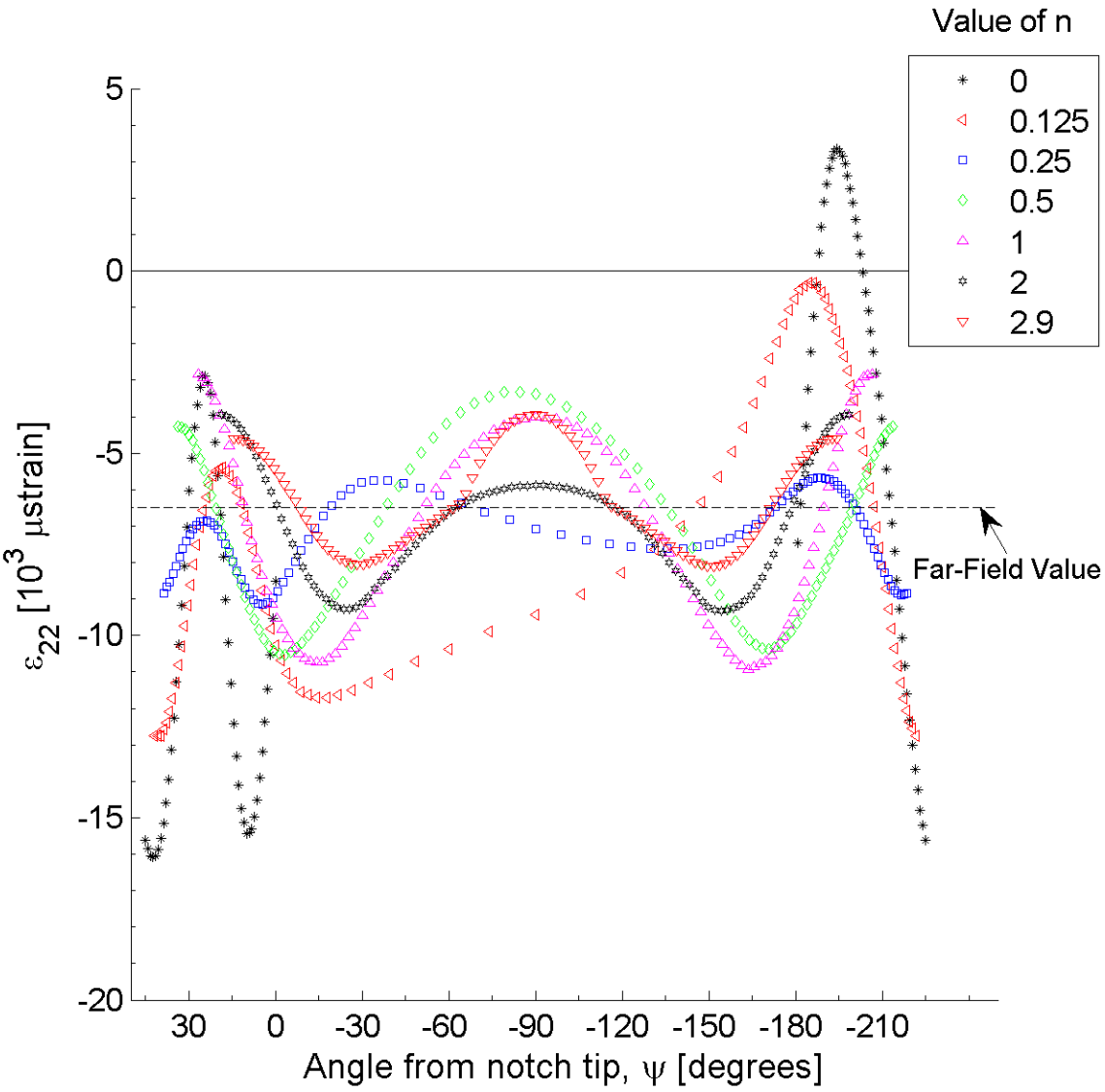

Figure B.75 Plot of ϵ_{22}, in laminate axes, along arc paths at the midplane of ply 1 (a +45° ply) of the open-hole tension specimen model for case of a 1.0 inch diameter hole for the four-ply effective ply thickness laminate of $[+45_4/0_4/-45_4]_S$.

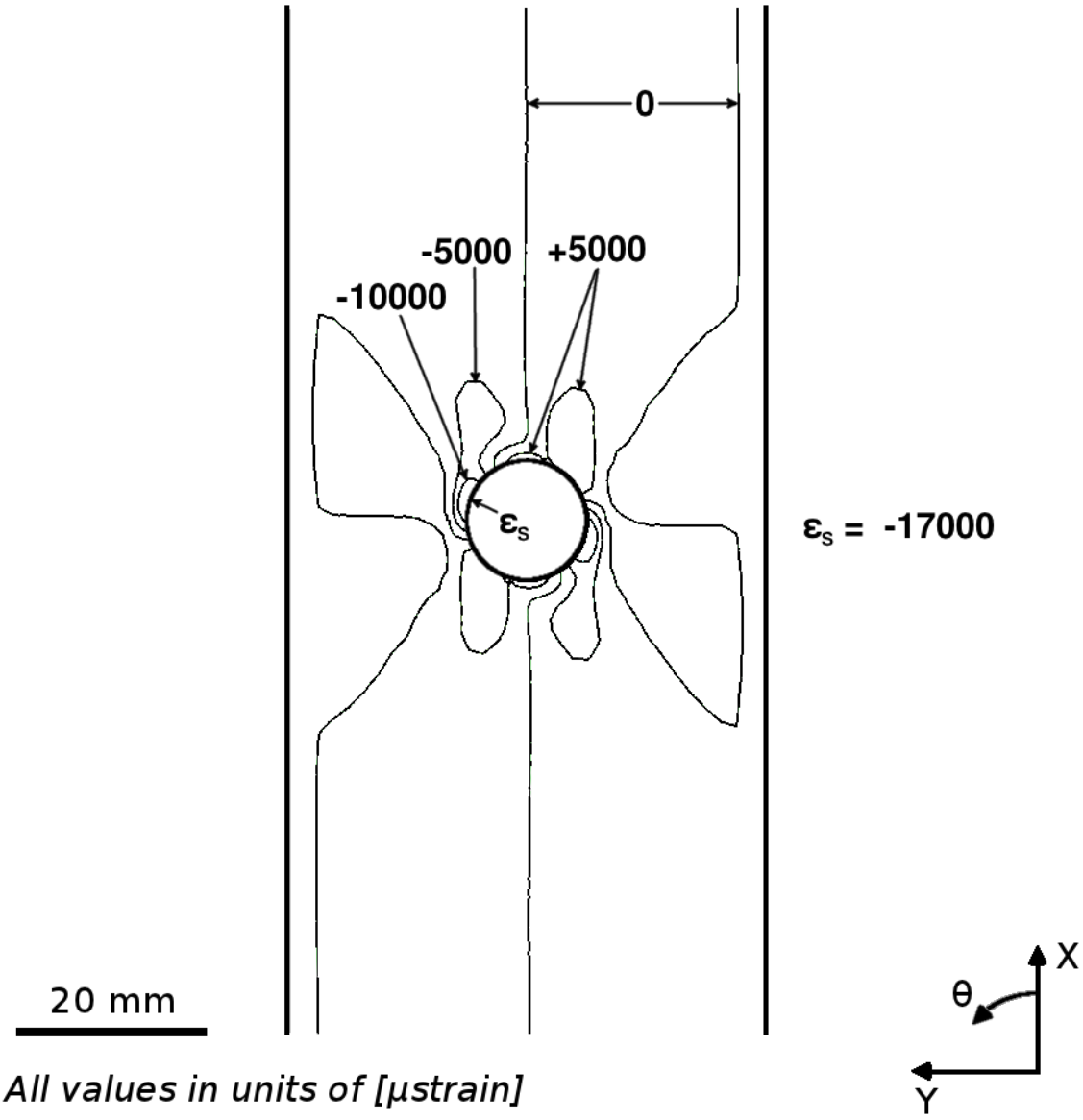

Figure B.76 Isostrain plot of strain field of ϵ_{12}, in laminate axes, at the midplane of ply 1 (a $+45^\circ$ ply) of the open-hole tension specimen model for case of a 0.5 inch diameter hole for the four-ply effective ply thickness laminate of $[+45_4/0_4/-45_4]_S$.

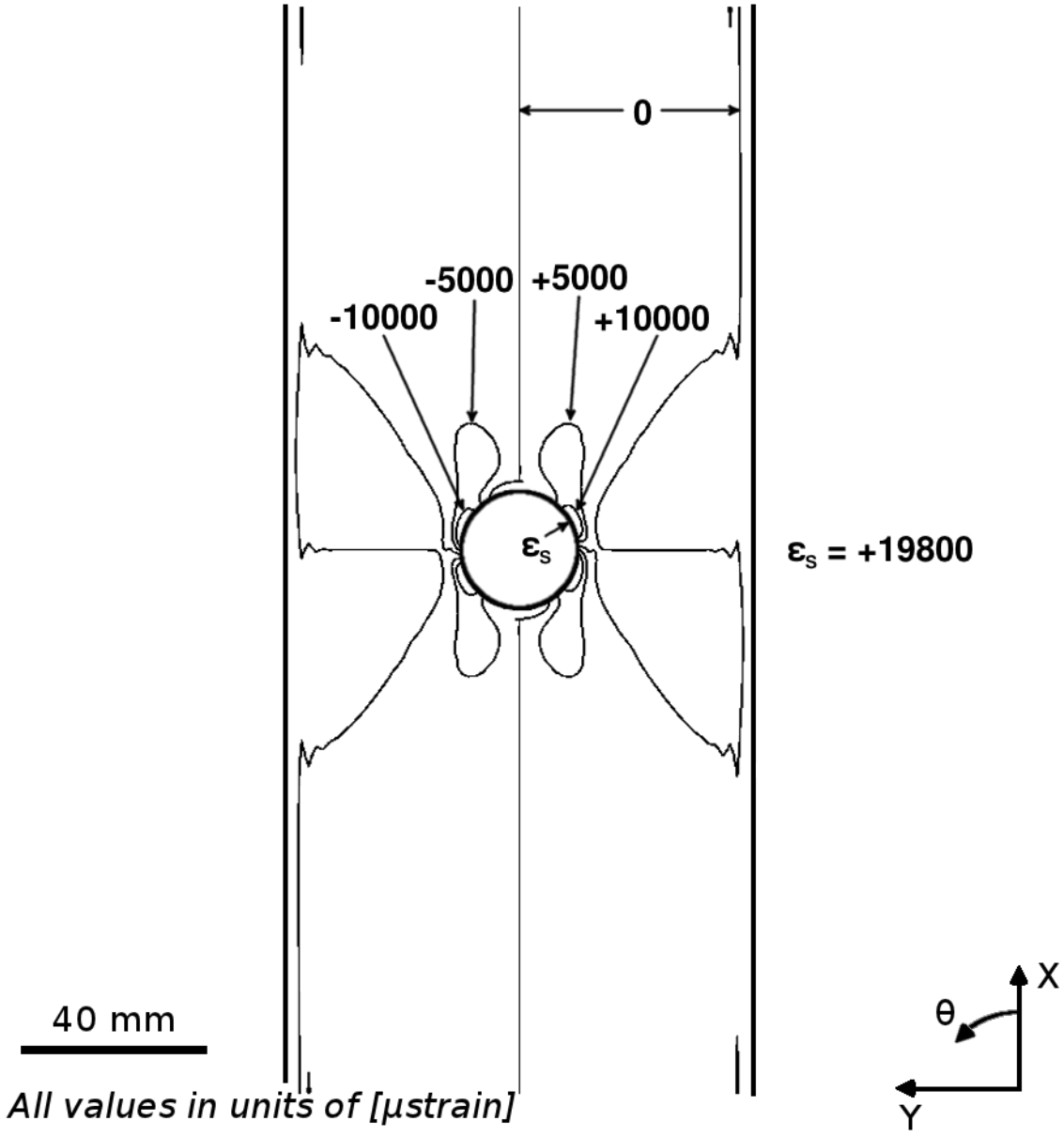

Figure B.77 Isostrain plot of strain field of ϵ_{12}, in laminate axes, at the midplane of ply 1 (a +45° ply) of the open-hole tension specimen model for case of a 1.0 inch diameter hole for the single-ply effective ply thickness laminate of $[+45/0/-45]_{4S}$.

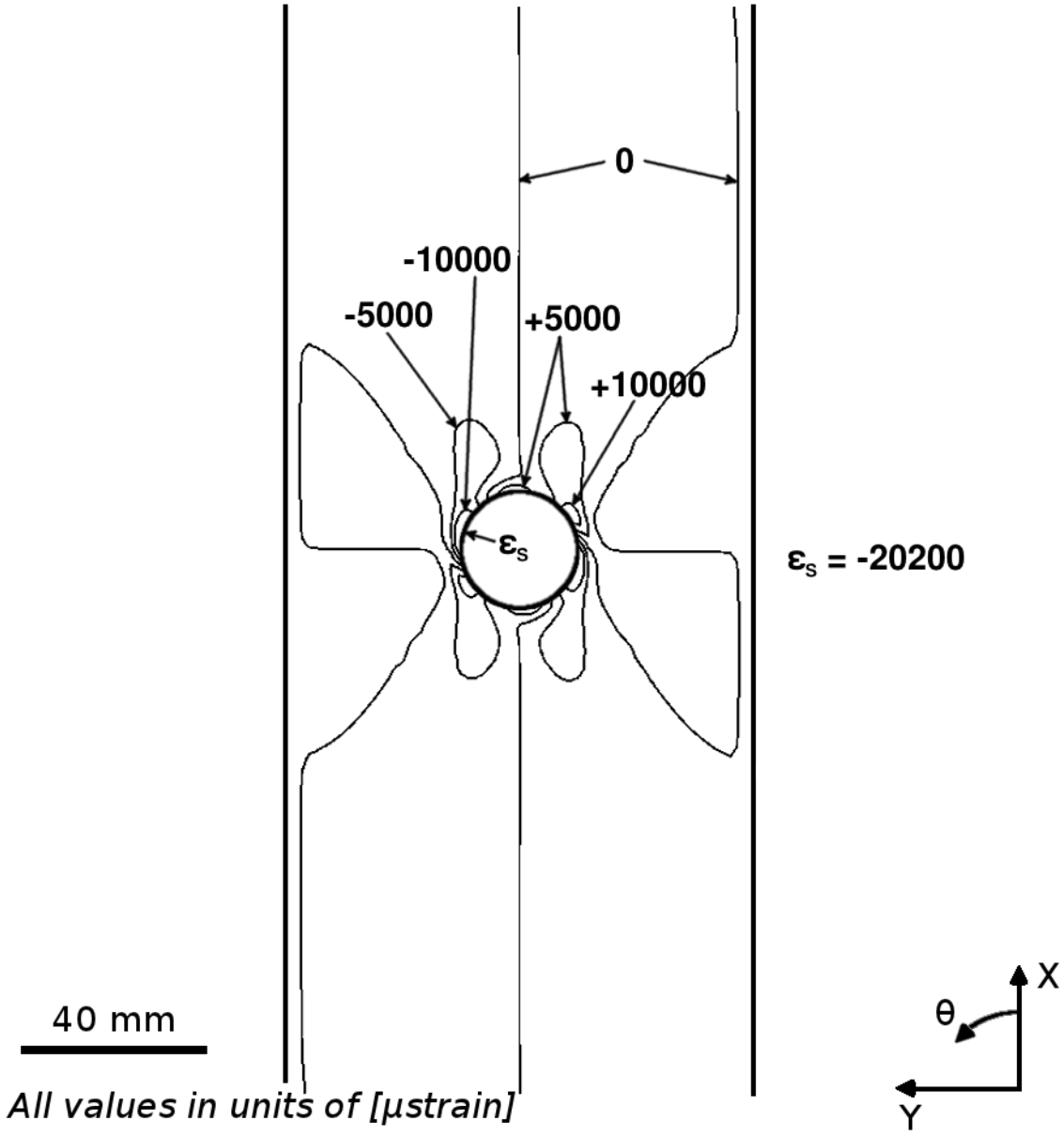

Figure B.78 Isostrain plot of strain field of ϵ_{12}, in laminate axes, at the midplane of ply 1 (a $+45^\circ$ ply) of the open-hole tension specimen model for case of a 1.0 inch diameter hole for the four-ply effective ply thickness laminate of $[+45_4/0_4/-45_4]_{4S}$.

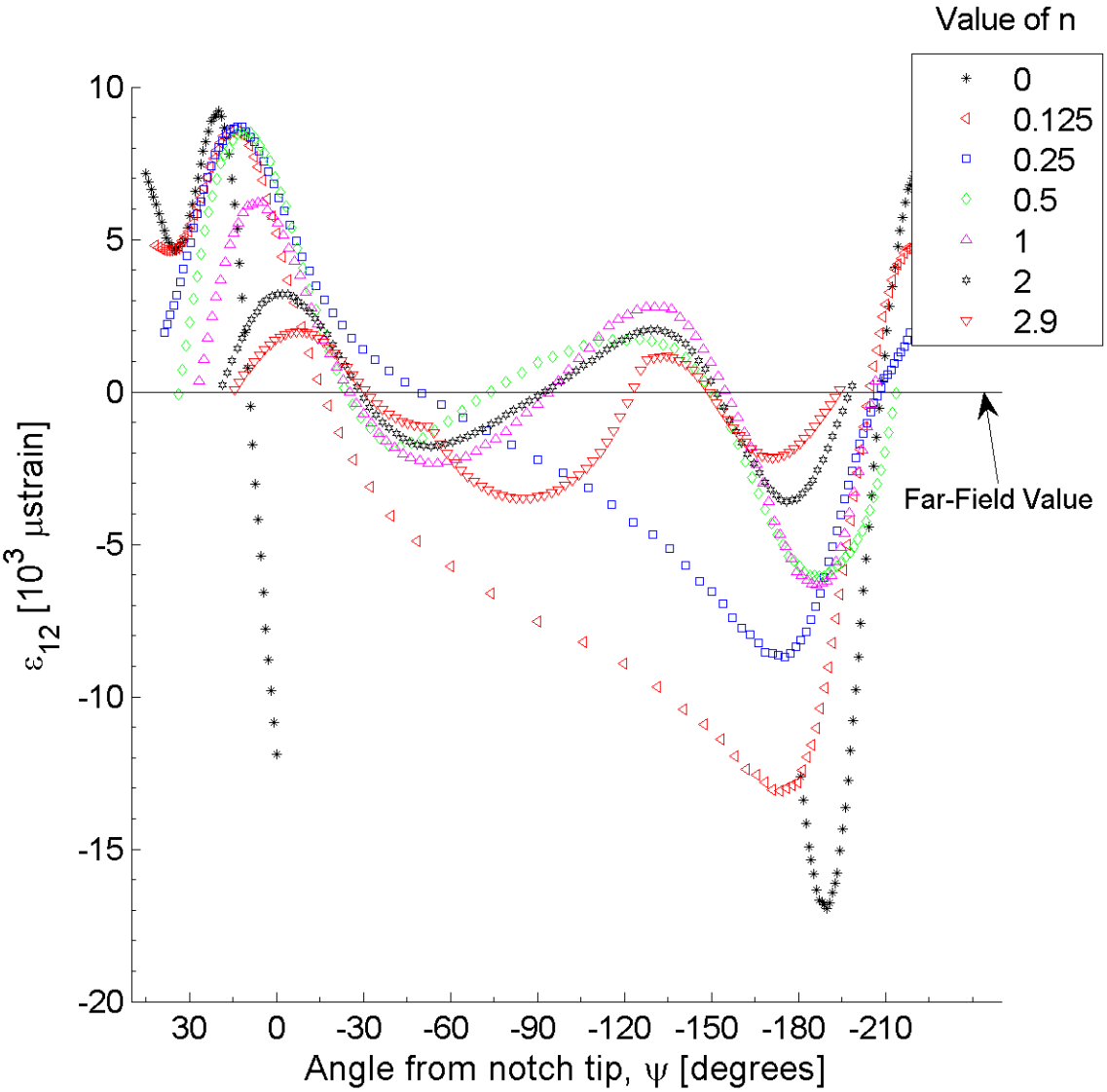

Figure B.79 Plot of ϵ_{12}, in laminate axes, along arc paths at the midplane of ply 1 (a $+45°$ ply) of the open-hole tension specimen model for case of a 0.5 inch diameter hole for the four-ply effective ply thickness laminate of $[+45_4/0_4/-45_4]_S$.

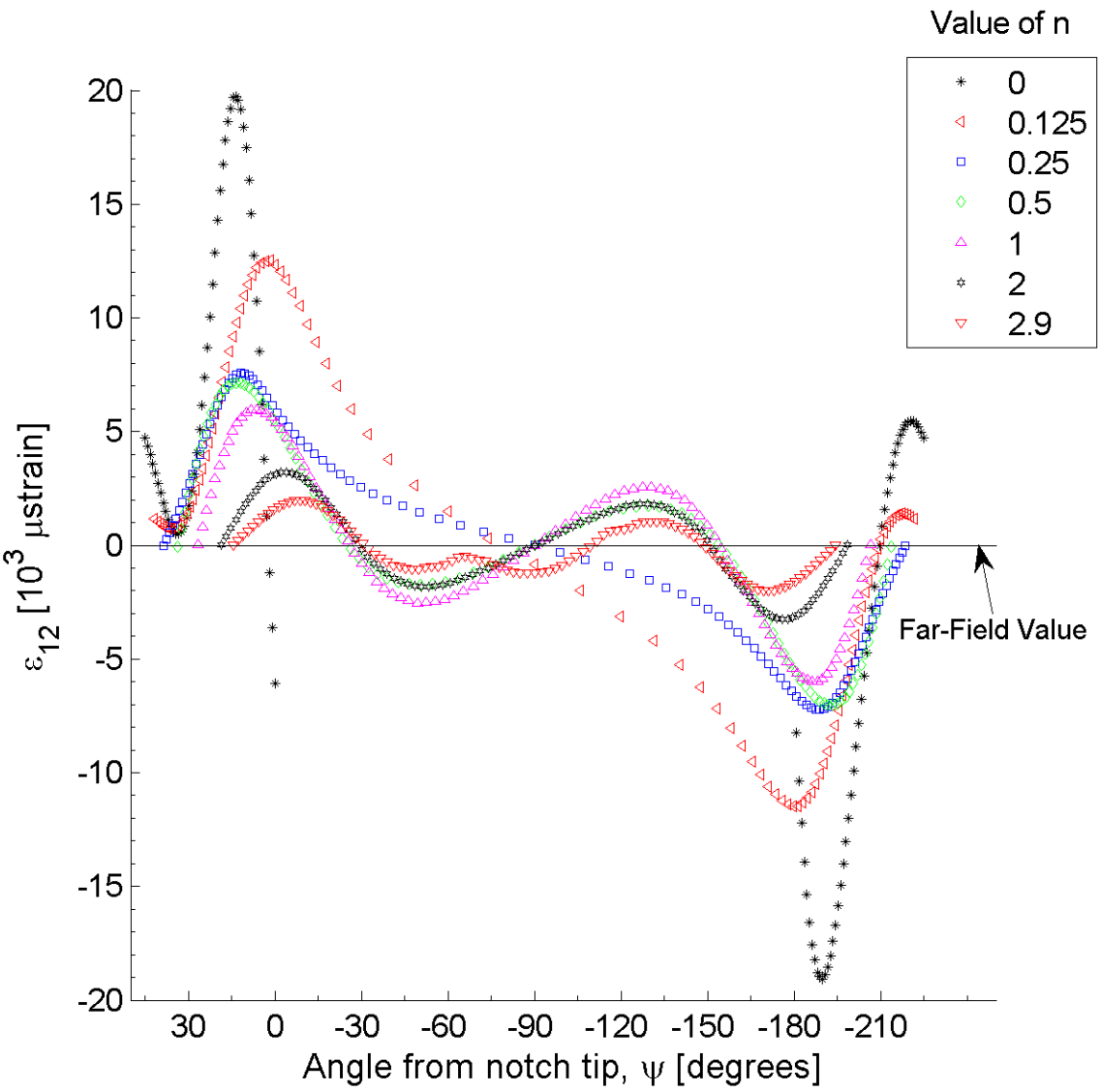

Figure B.80 Plot of ϵ_{12}, in laminate axes, along arc paths at the midplane of ply 1 (a $+45°$ ply) of the open-hole tension specimen model for case of a 1.0 inch diameter hole for the single-ply effective ply thickness laminate of $[+45/0/-45]_{4S}$.

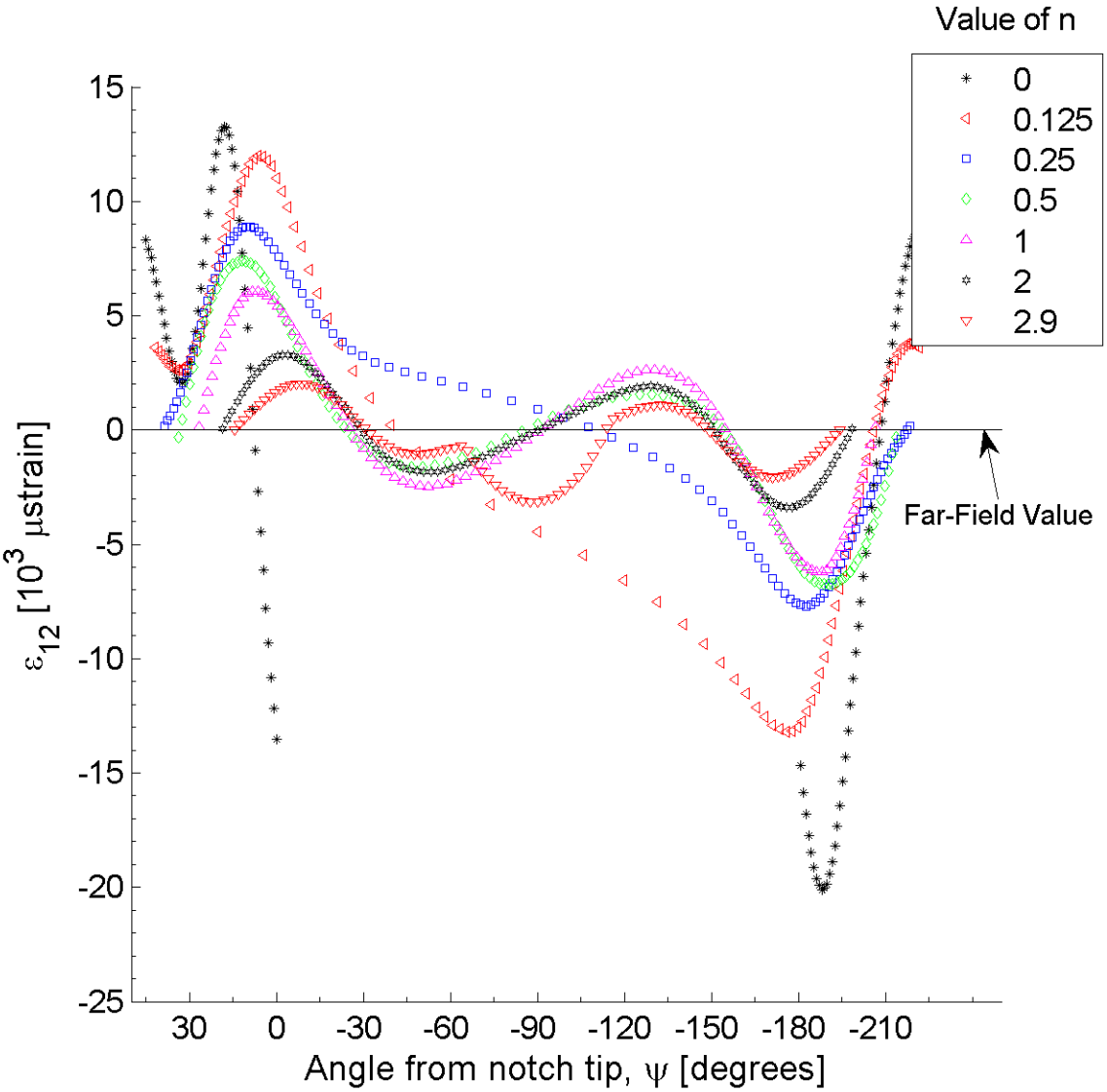

Figure B.81 Plot of ϵ_{12}, in laminate axes, along arc paths at the midplane of ply 1 (a $+45°$ ply) of the open-hole tension specimen model for case of a 1.0 inch diameter hole for the four-ply effective ply thickness laminate of $[+45_4/0_4/-45_4]_S$.

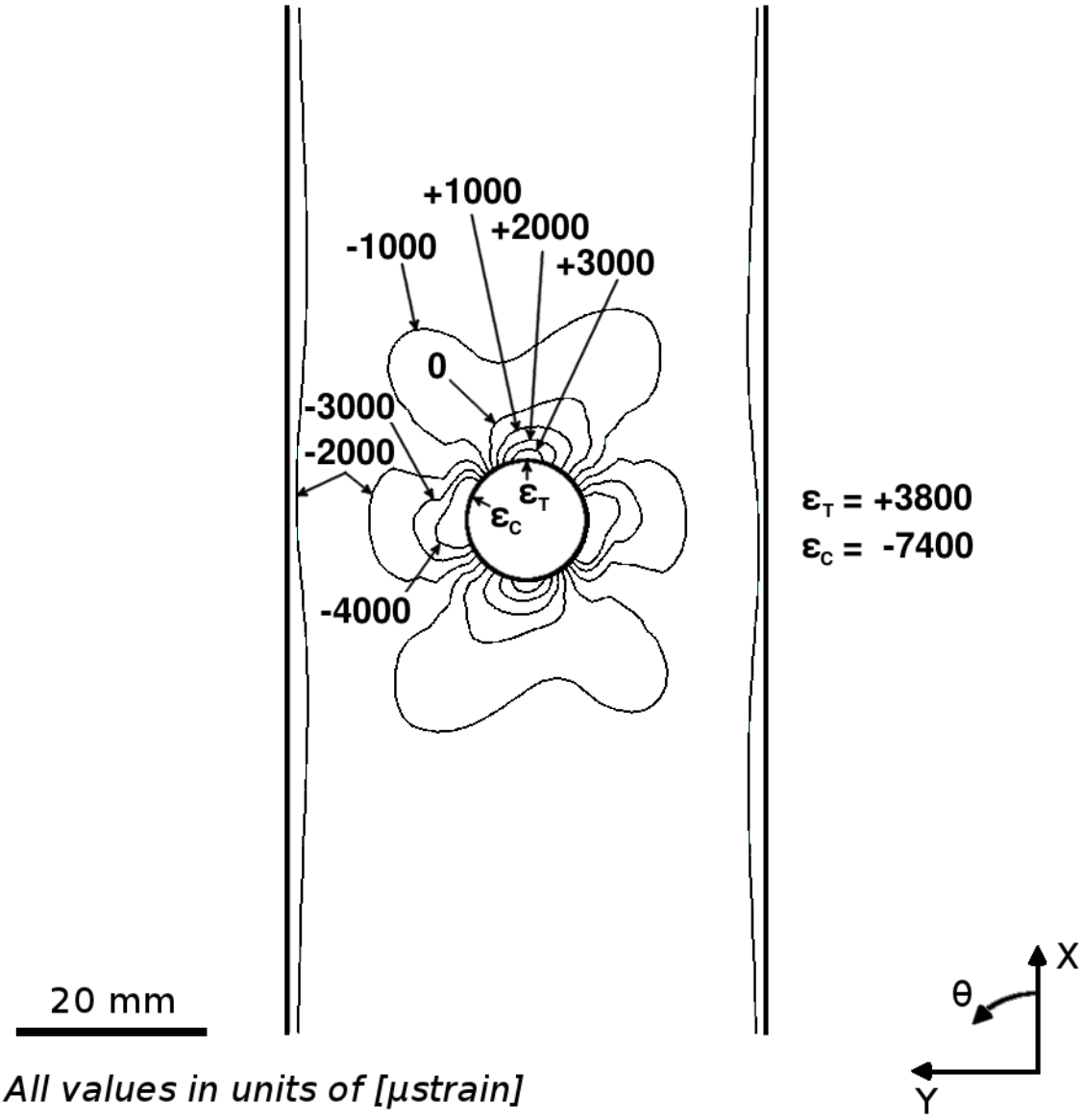

Figure B.82 Isostrain plot of strain field of ϵ_{33}, at the midplane of ply 1 (a $+45^\circ$ ply) of the open-hole tension specimen model for case of a 0.5 inch diameter hole for the four-ply effective ply thickness laminate of $[+45_4/0_4/-45_4]_S$.

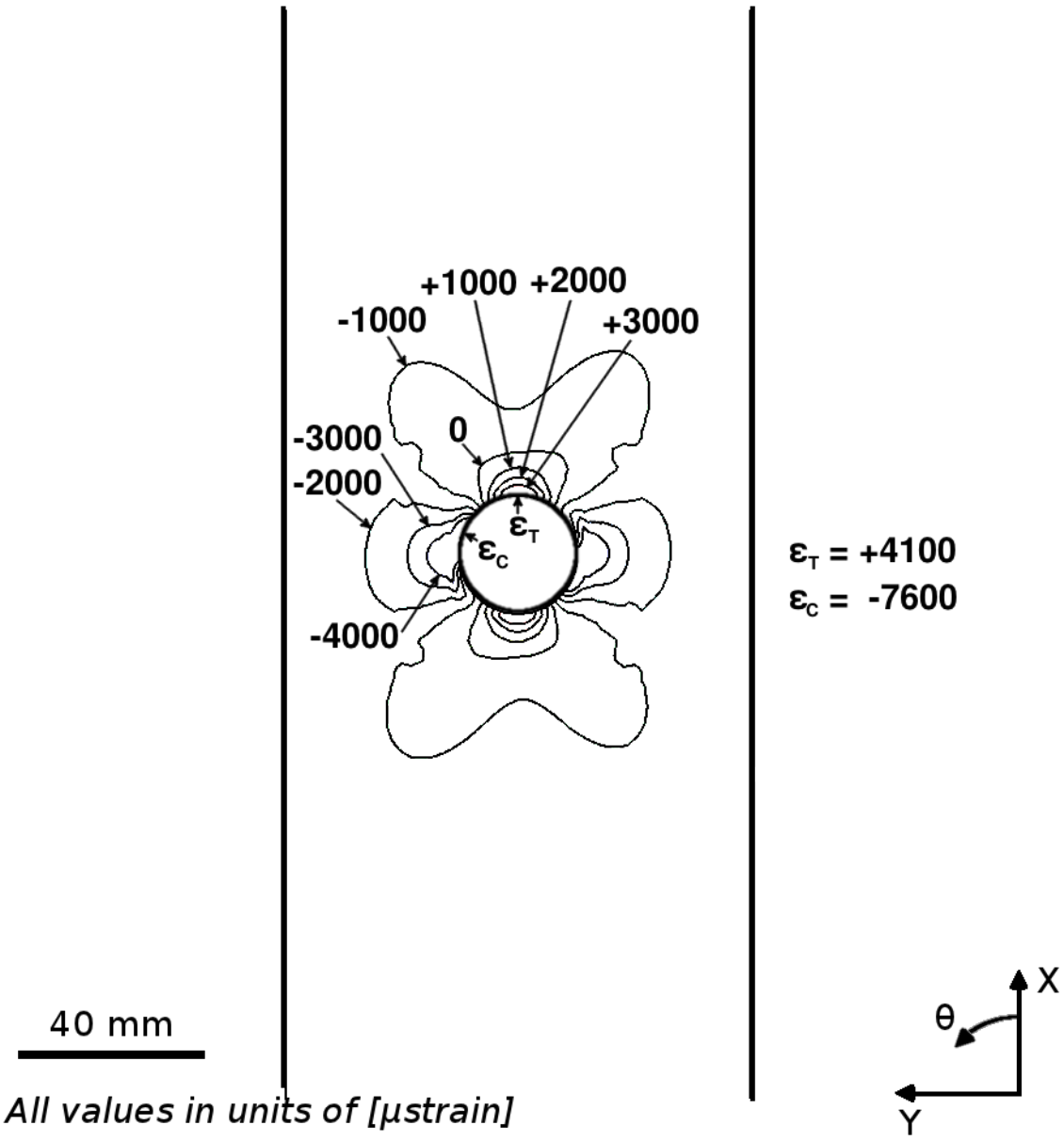

Figure B.83 Isostrain plot of strain field of ϵ_{33}, at the midplane of ply 1 (a $+45^\circ$ ply) of the open-hole tension specimen model for case of a 1.0 inch diameter hole for the single-ply effective ply thickness laminate of $[+45/0/-45]_{4S}$.

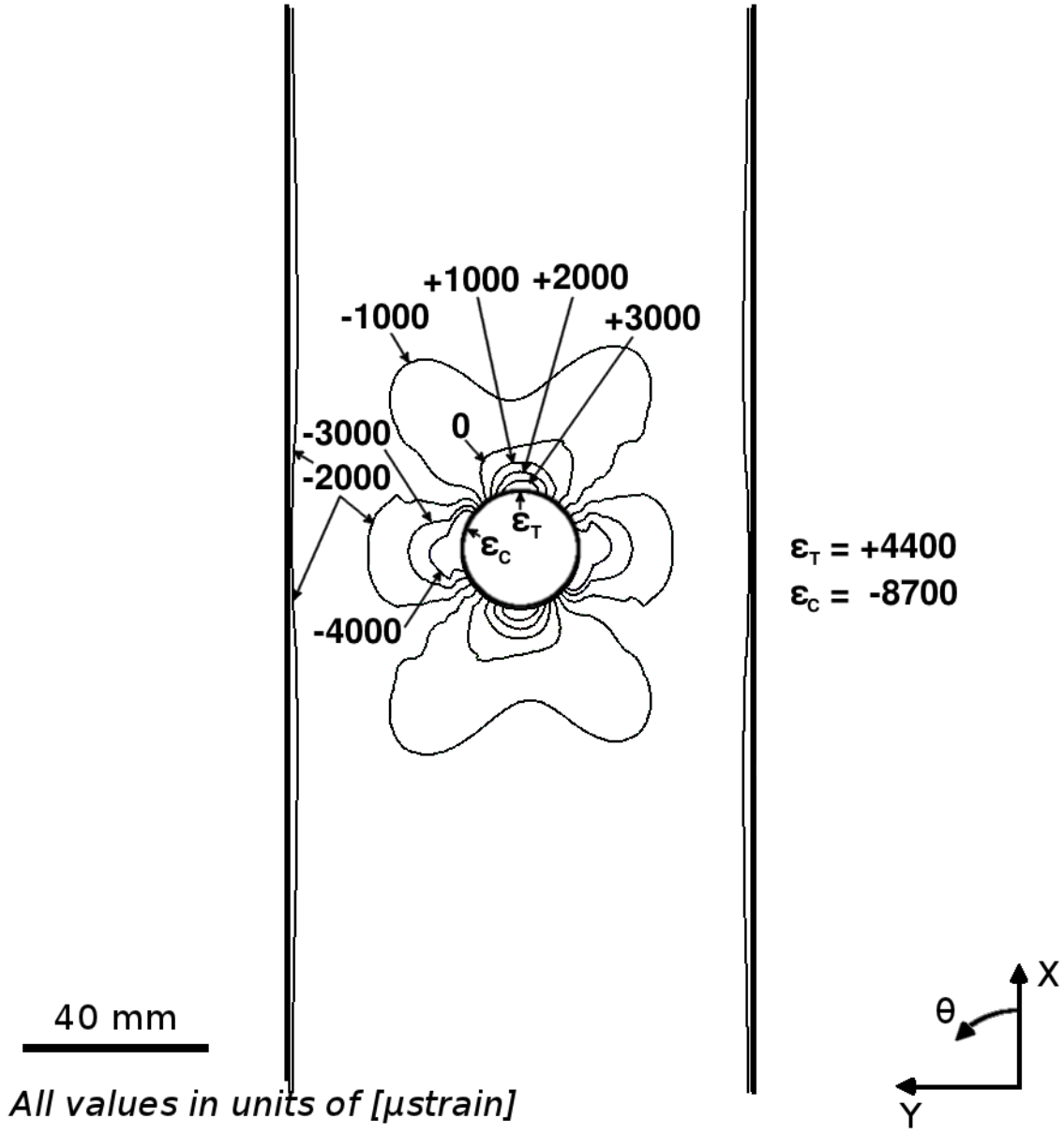

Figure B.84 Isostrain plot of strain field of ϵ_{33}, at the midplane of ply 1 (a $+45^\circ$ ply) of the open-hole tension specimen model for case of a 1.0 inch diameter hole for the four-ply effective ply thickness laminate of $[+45_4/0_4/-45_4]_S$.

B.4 Strain Plots for Damage Inclusion Models

This section contains additional figures relating to the results of the damage inclusion models discussed in Section 7.3.5. Plots of strain magnitudes along paths for the two damage inclusion models, as defined in Section 7.3.5, are included. The figures in this section of the appendix illustrate the plots of strain magnitudes along paths for laminate angles not shown in Section 7.3.5.

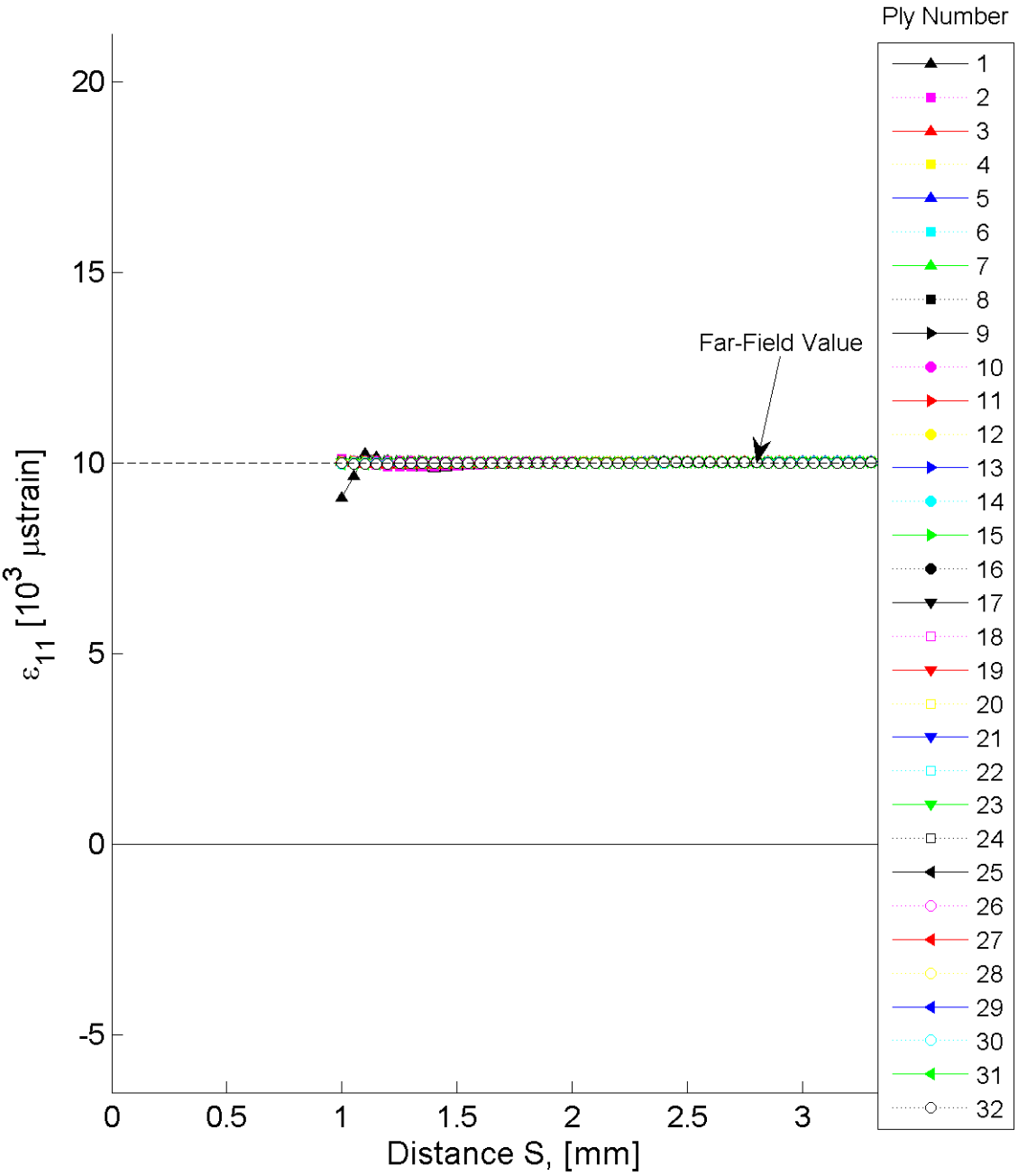

Figure B.85 Plot of ϵ_{11}, in laminate axes, along the path of the stitch crack at the midplane of each ply for the stitch crack model with laminate of $[+30/-30]_{16T}$.

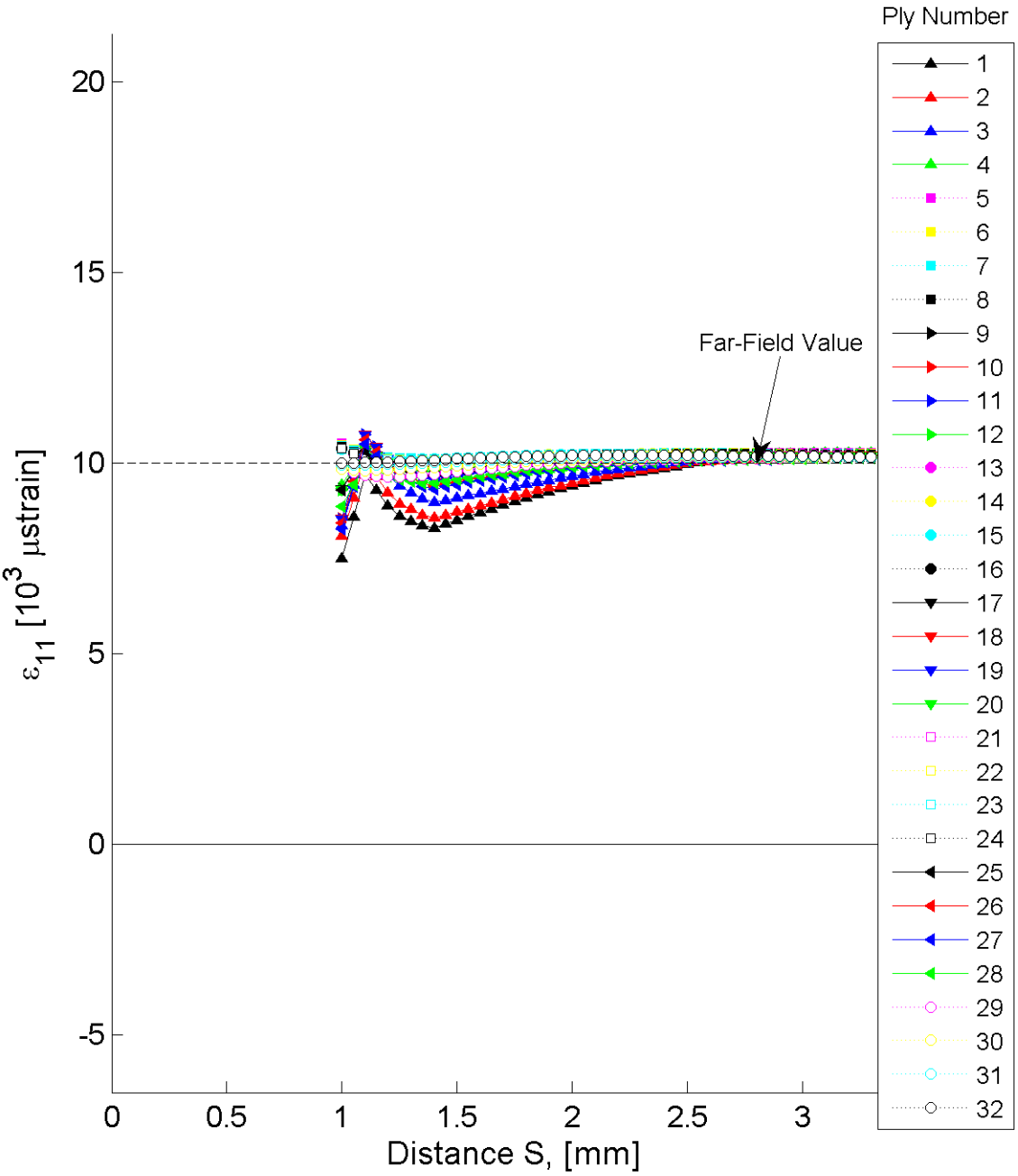

Figure B.86 Plot of ϵ_{11}, in laminate axes, along the path of the stitch crack at the midplane of each ply for the stitch crack model with laminate of $[+30_4/-30_4]_{4T}$.

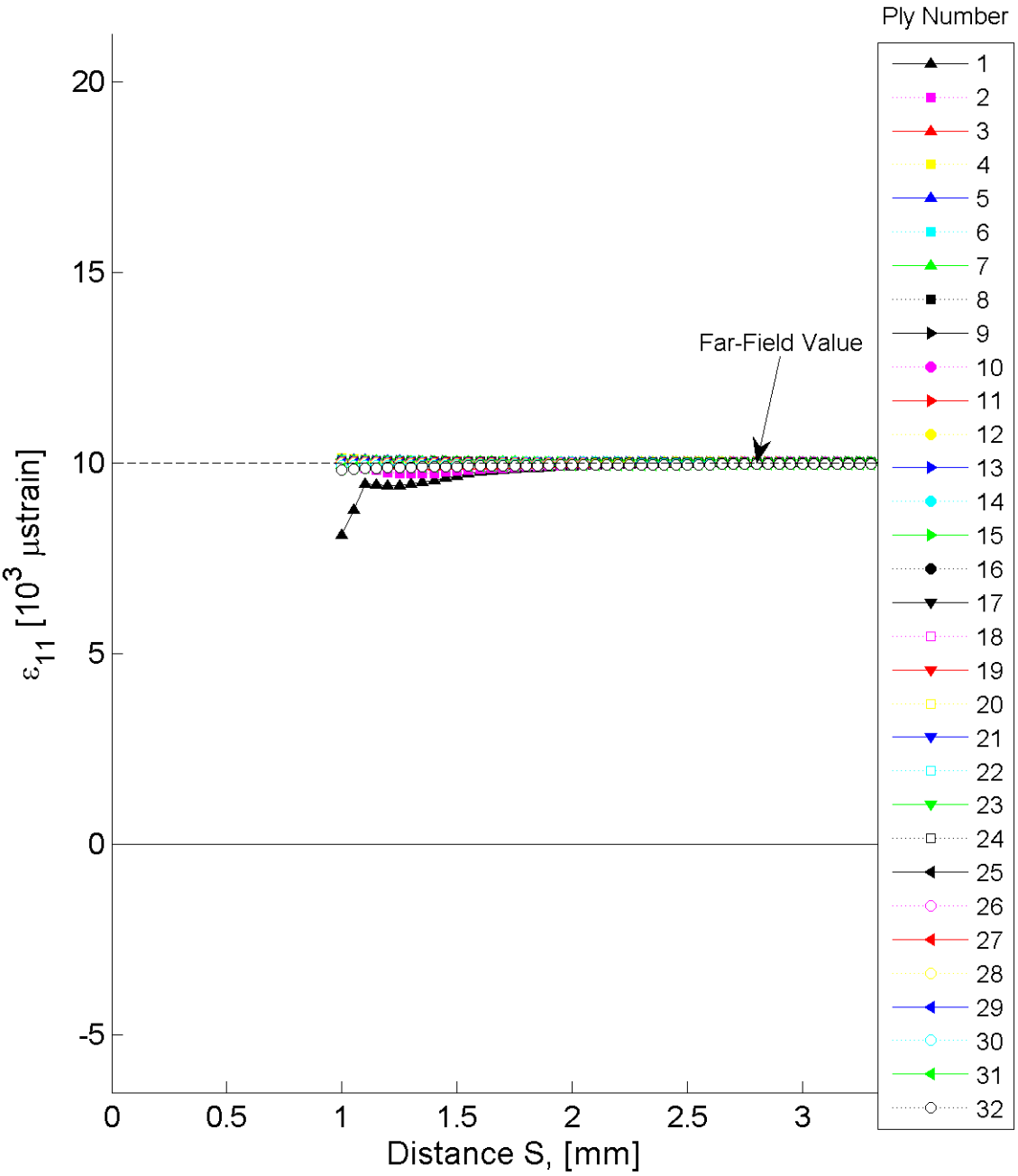

Figure B.87 Plot of ϵ_{11}, in laminate axes, along the path of the stitch crack at the midplane of each ply for the stitch crack model with laminate of $[+60/-60]_{16T}$.

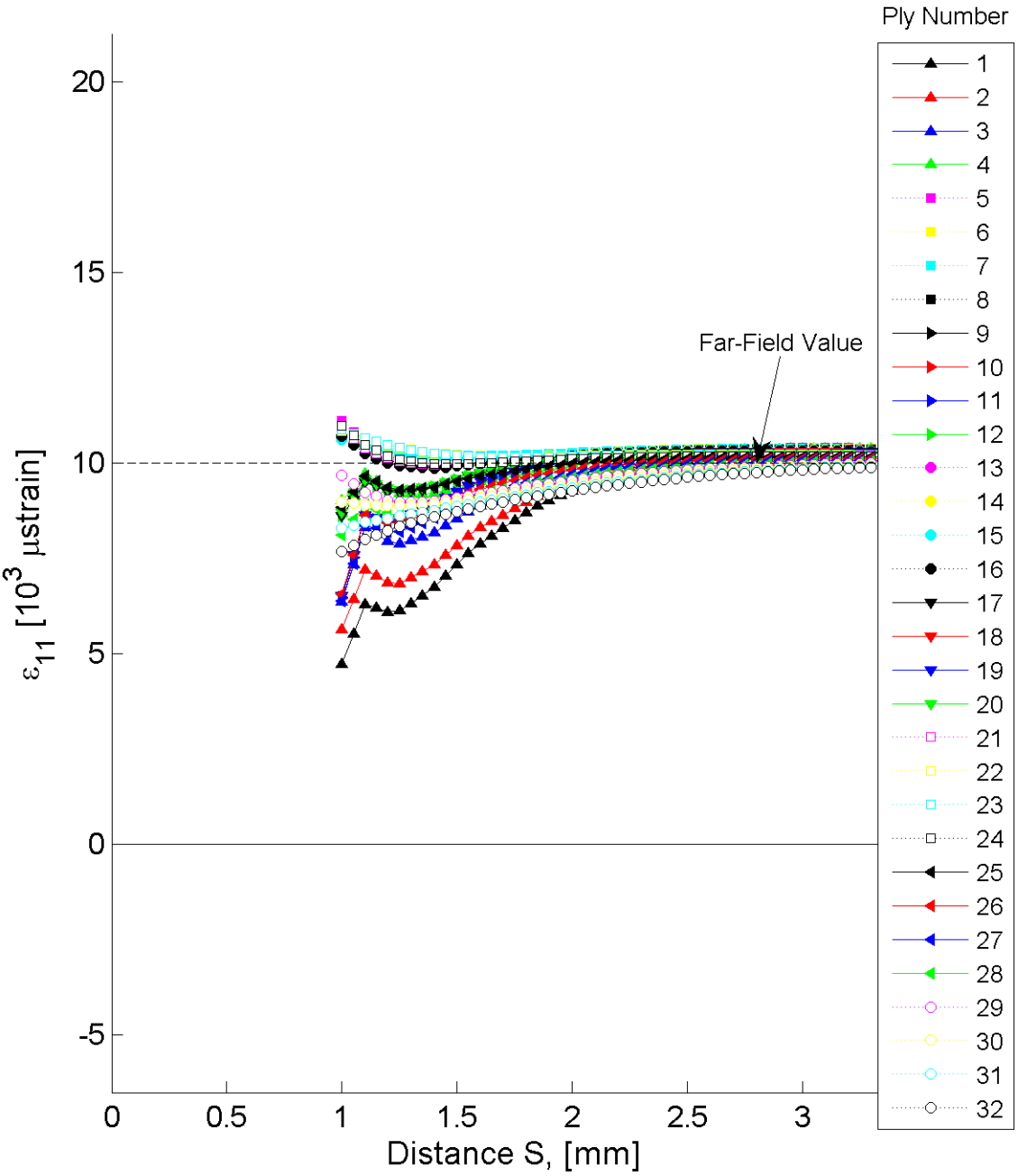

Figure B.88 Plot of ϵ_{11}, in laminate axes, along the path of the stitch crack at the midplane of each ply for the stitch crack model with laminate of $[+60_4/-60_4]_{4T}$.

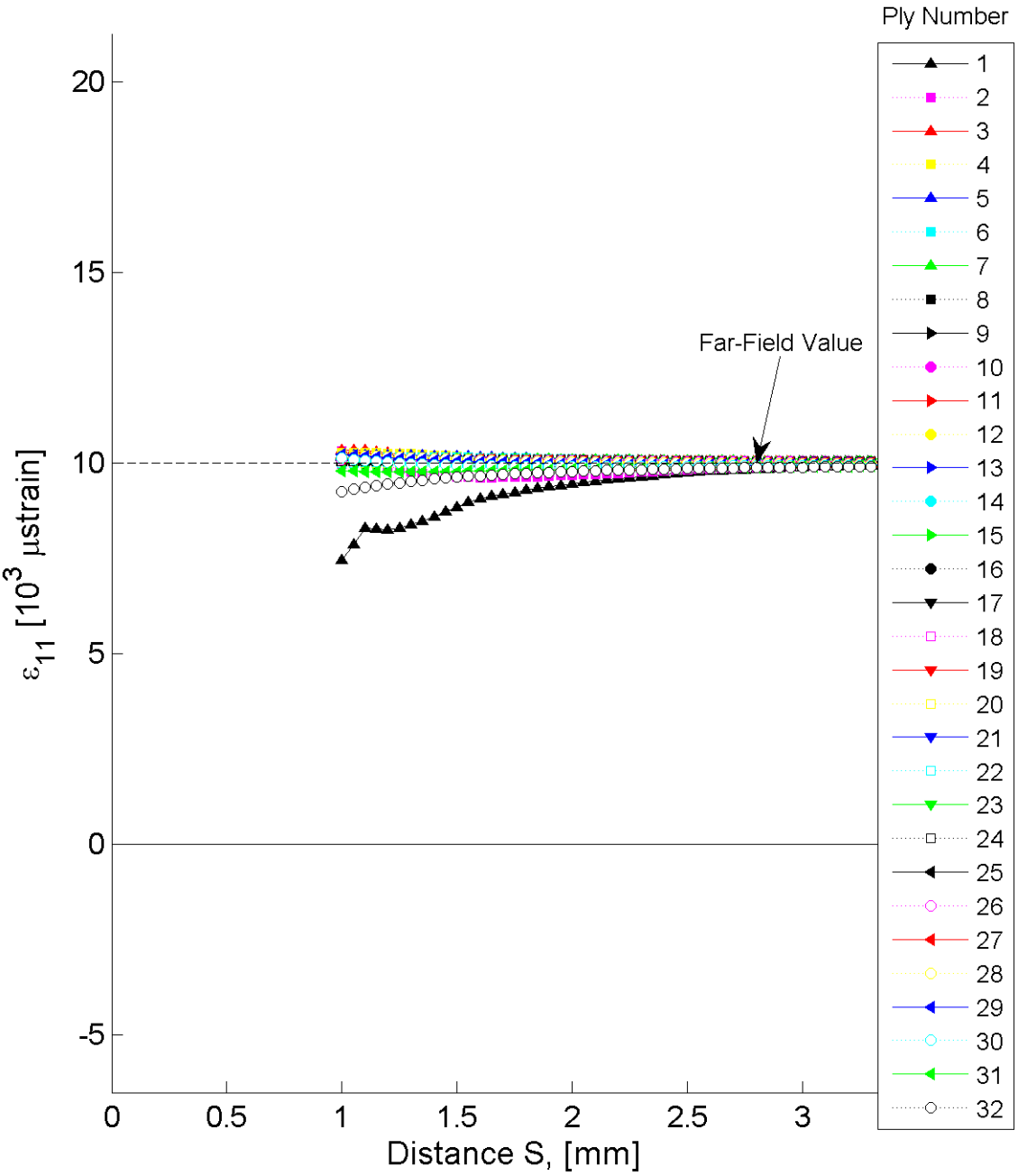

Figure B.89 Plot of ϵ_{11}, in laminate axes, along the path of the stitch crack at the midplane of each ply for the stitch crack model with laminate of $[+75/-75]_{16T}$.

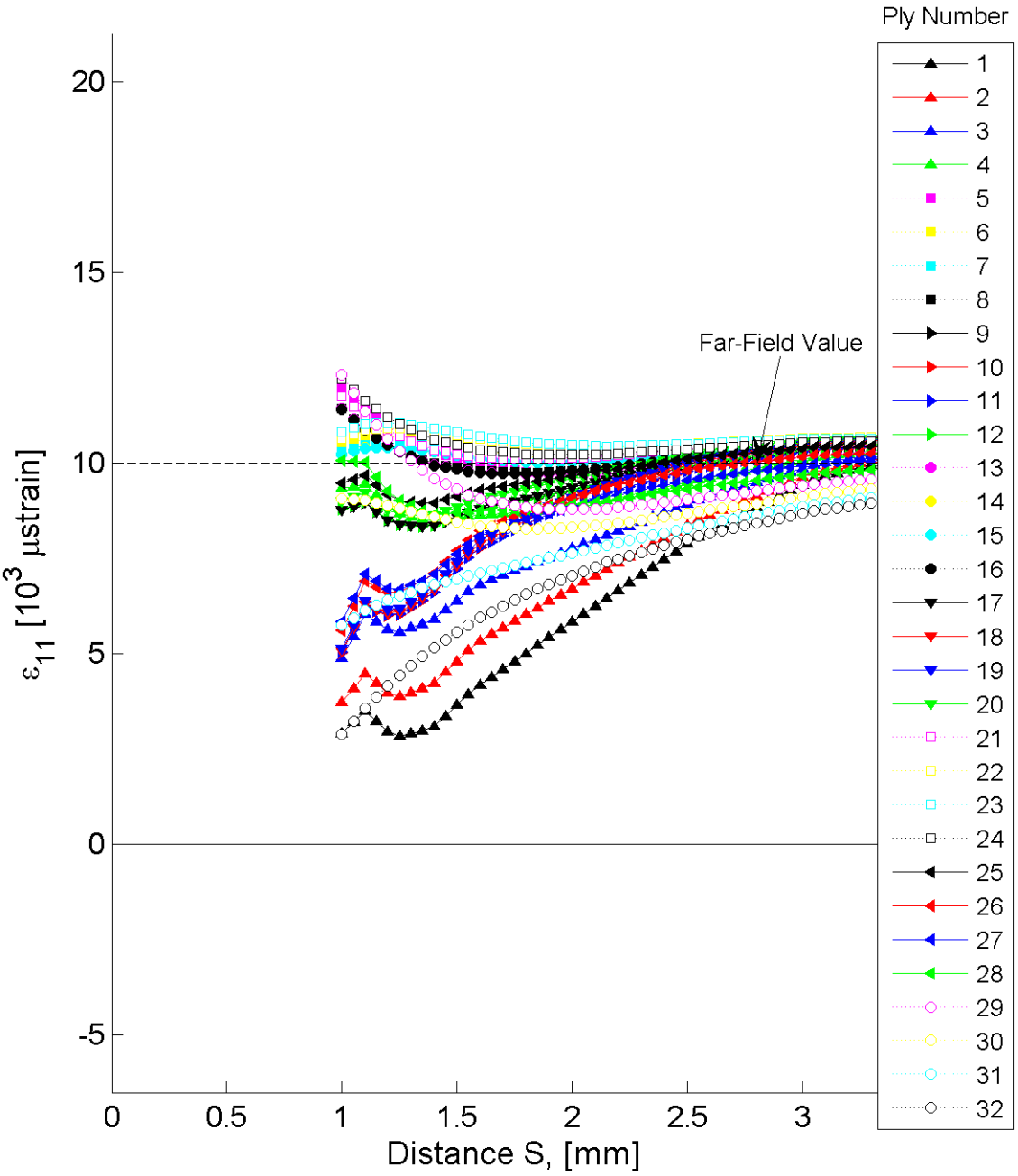

Figure B.90 Plot of ϵ_{11}, in laminate axes, along the path of the stitch crack at the midplane of each ply for the stitch crack model with laminate of $[+75_4/-75_4]_{4T}$.

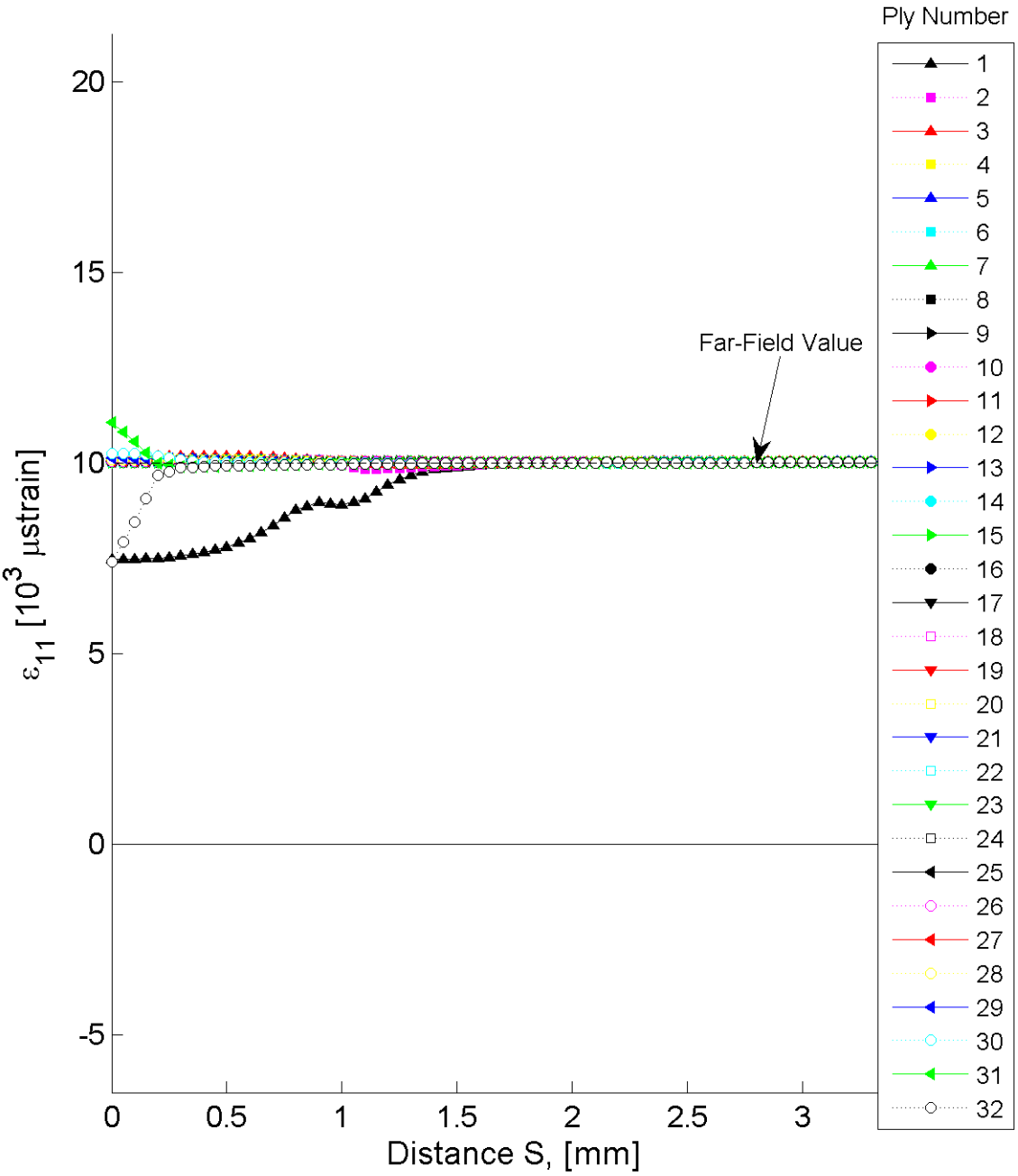

Figure B.91 Plot of ϵ_{11}, in laminate axes, along the path "between stitch cracks" at the midplane of each ply for the stitch crack model with laminate of $[+30/-30]_{16T}$.

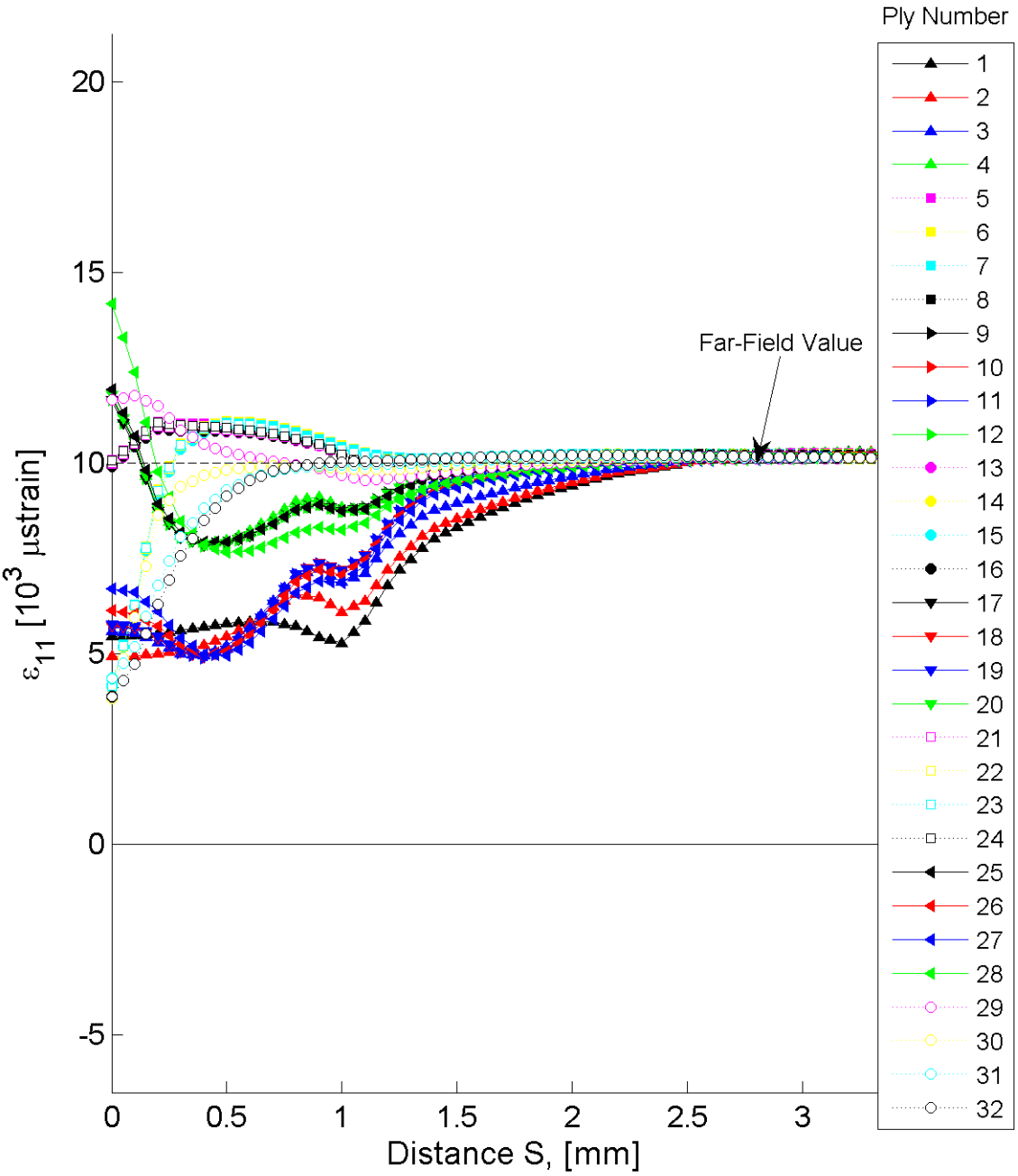

Figure B.92 Plot of ϵ_{11}, in laminate axes, along the path "between stitch cracks" at the midplane of each ply for the stitch crack model with laminate of $[+30_4/-30_4]_{4T}$.

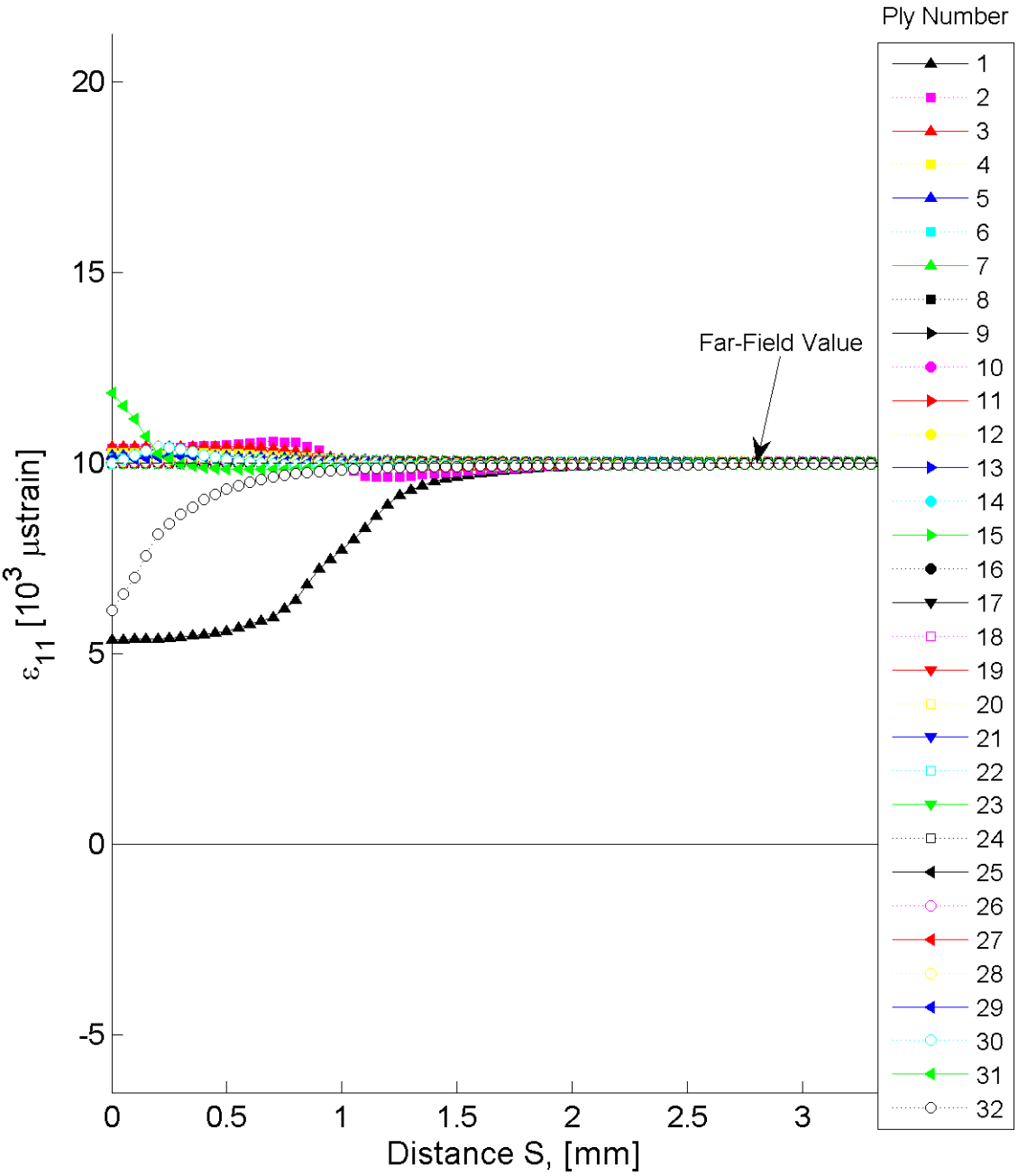

Figure B.93 Plot of ϵ_{11}, in laminate axes, along the path "between stitch cracks" at the midplane of each ply for the stitch crack model with laminate of $[+60/-60]_{16T}$.

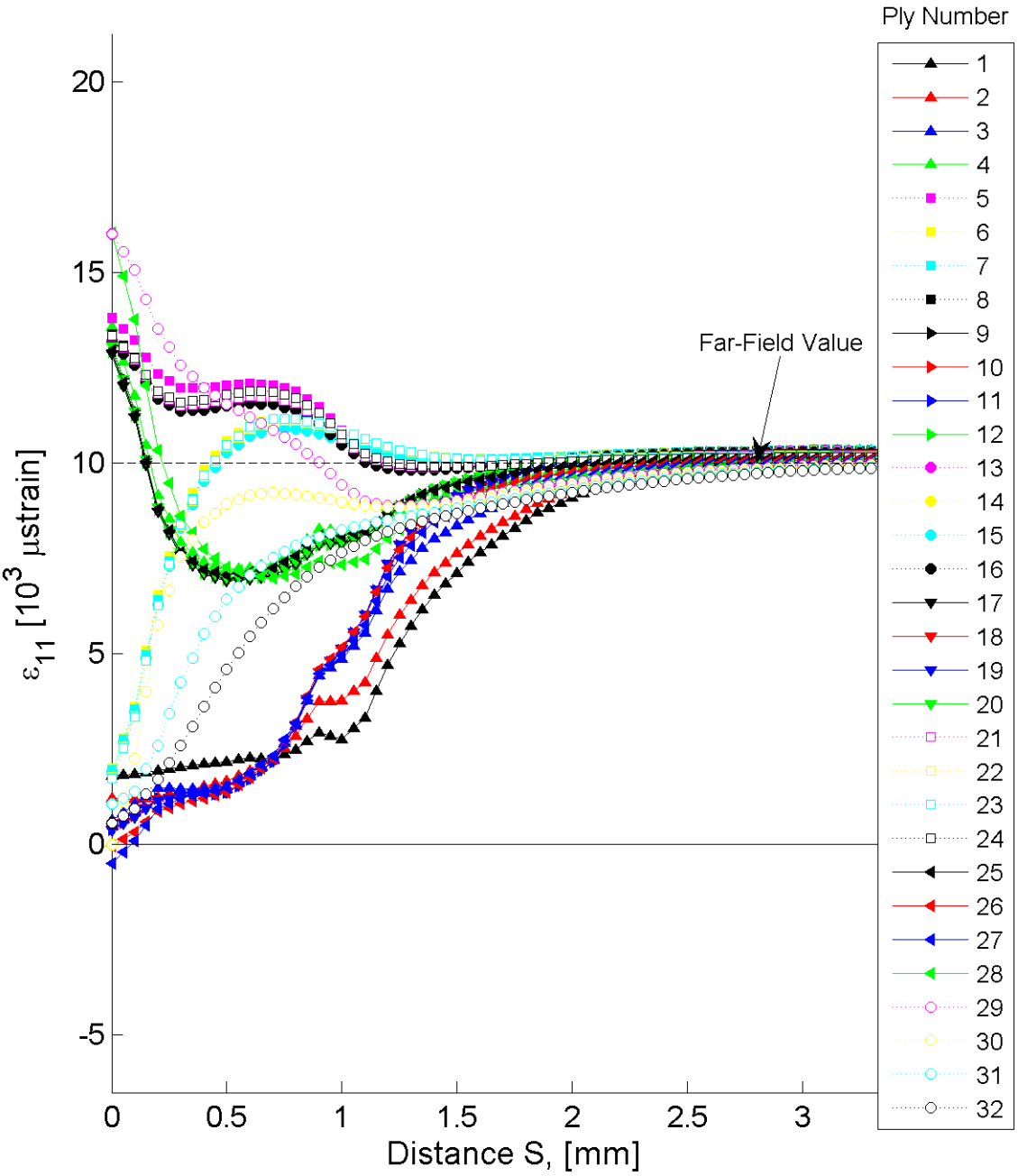

Figure B.94 Plot of ϵ_{11}, in laminate axes, along the path "between stitch cracks" at the midplane of each ply for the stitch crack model with laminate of $[+60_4/-60_4]_{4T}$.

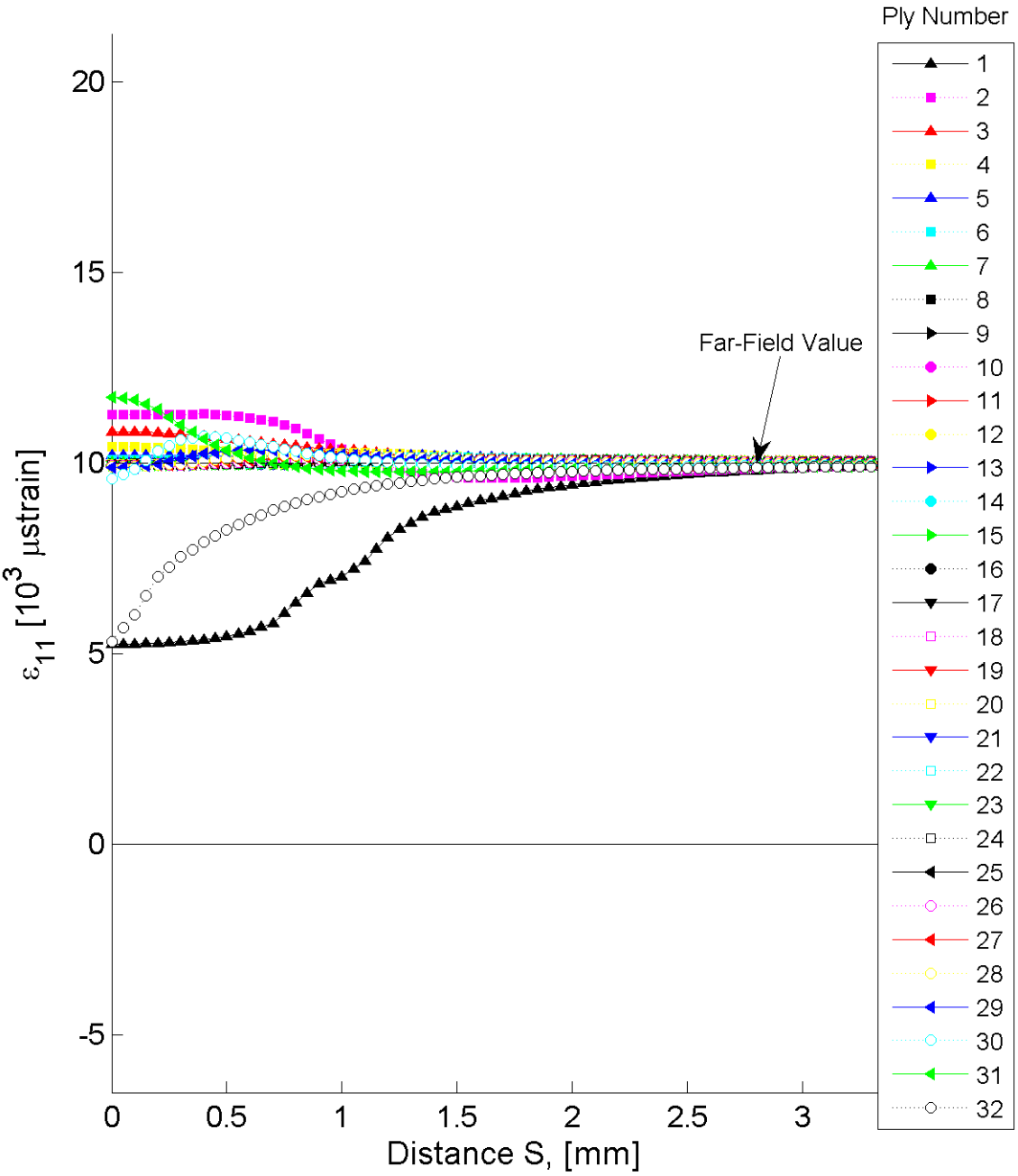

Figure B.95 Plot of ϵ_{11}, in laminate axes, along the path "between stitch cracks" at the midplane of each ply for the stitch crack model with laminate of $[+75/-75]_{16T}$.

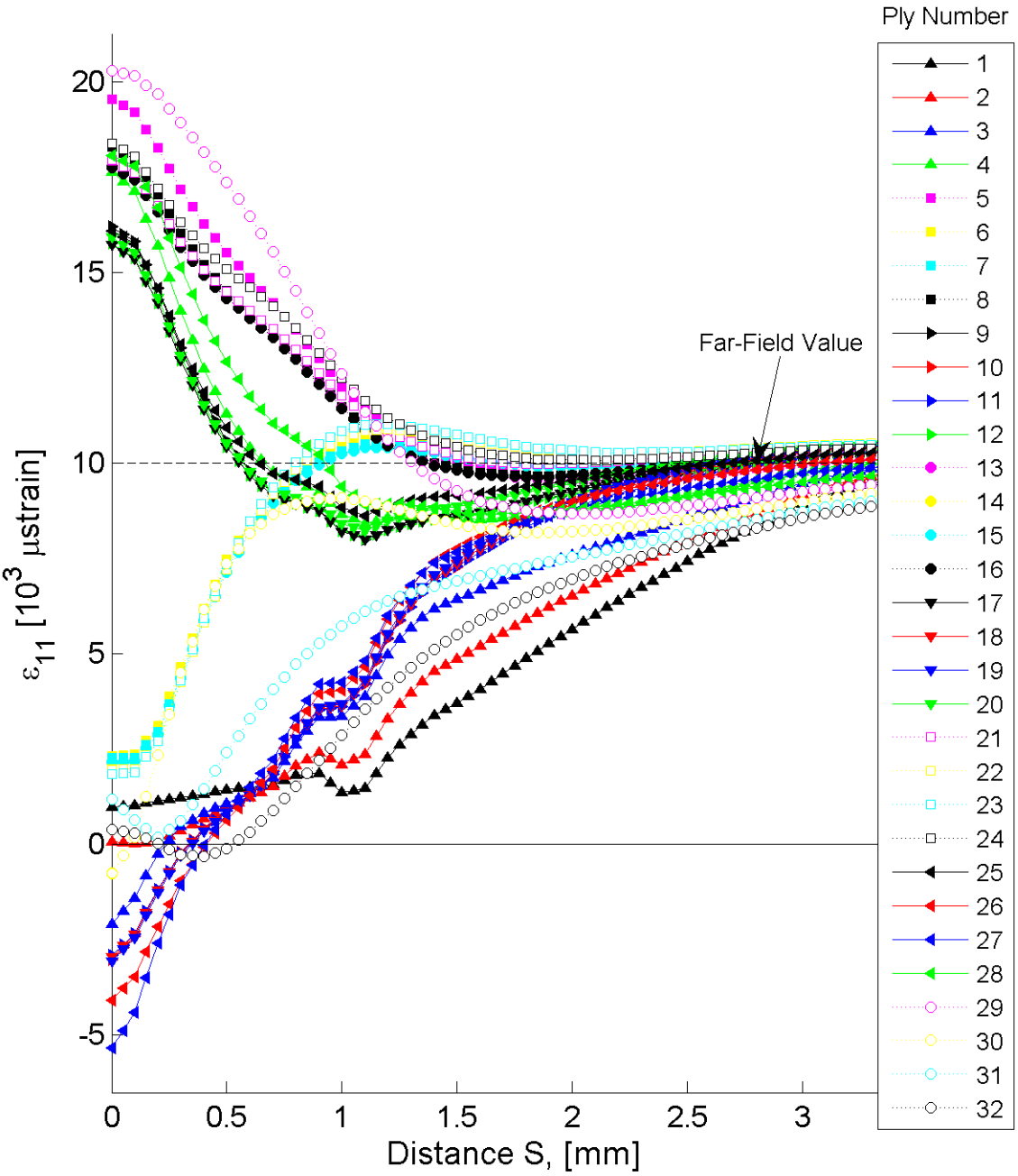

Figure B.96 Plot of ϵ_{11}, in laminate axes, along the path "between stitch cracks" at the midplane of each ply for the stitch crack model with laminate of $[+75_4/-75_4]_{4T}$.

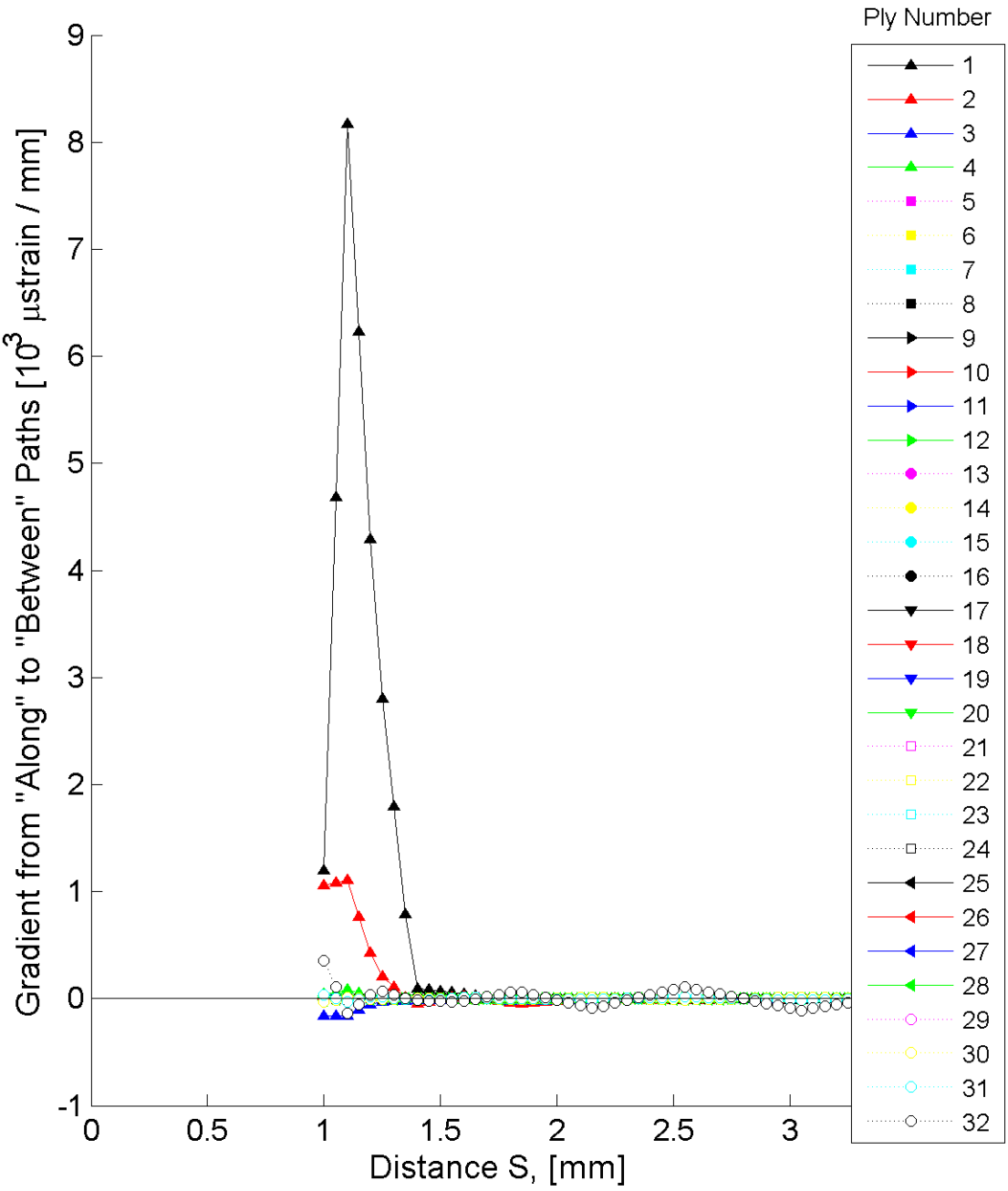

Figure B.97 Plot of the gradient of ϵ_{11}, in laminate axes, in the $\hat{S}$-direction at the midplane of each ply for the stitch crack model with laminate of $[+30/-30]_{16T}$.

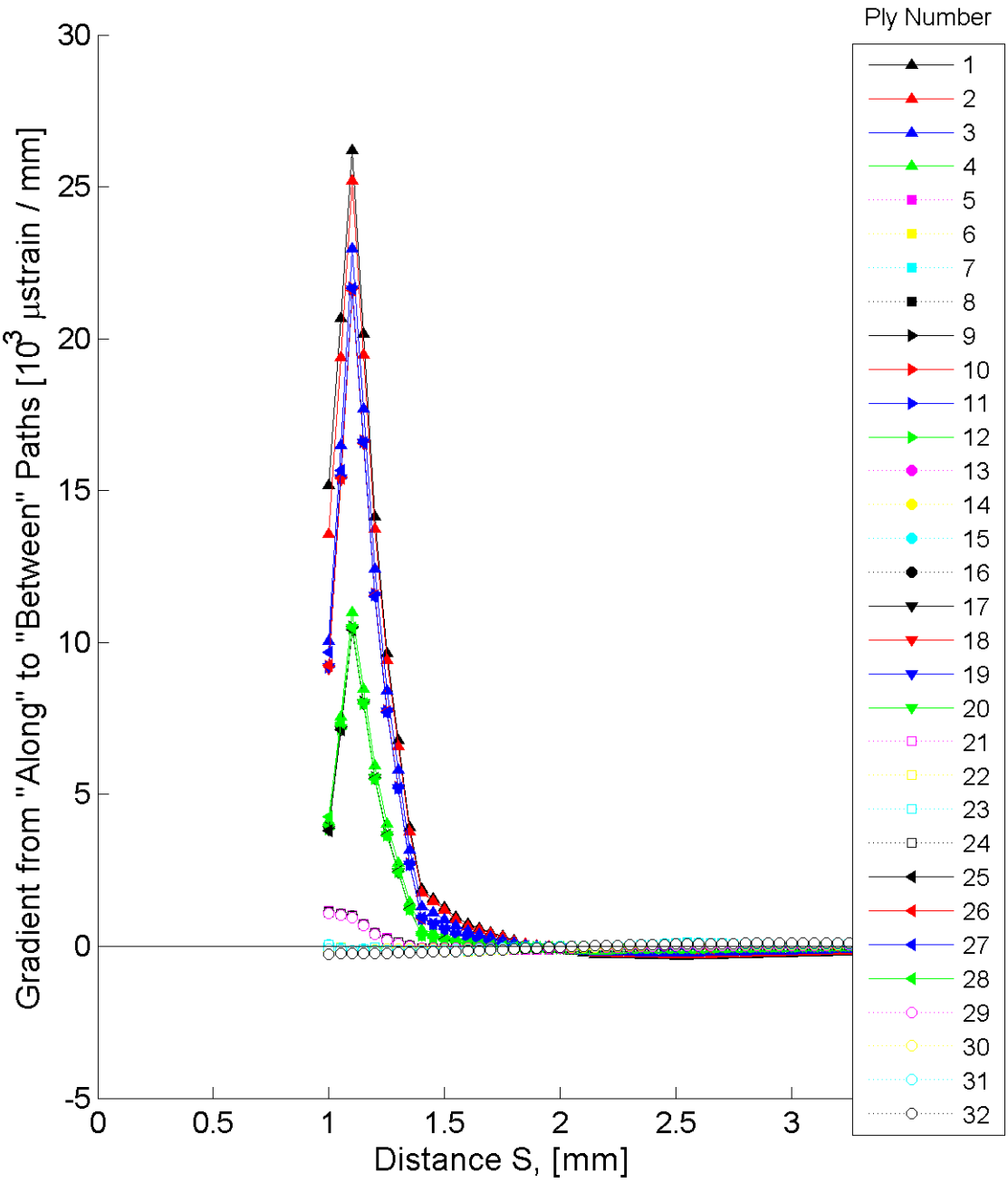

Figure B.98 Plot of the gradient of ϵ_{11}, in laminate axes, in the $\hat{S}$-direction at the midplane of each ply for the stitch crack model with laminate of $[+30_4/-30_4]_{4T}$.

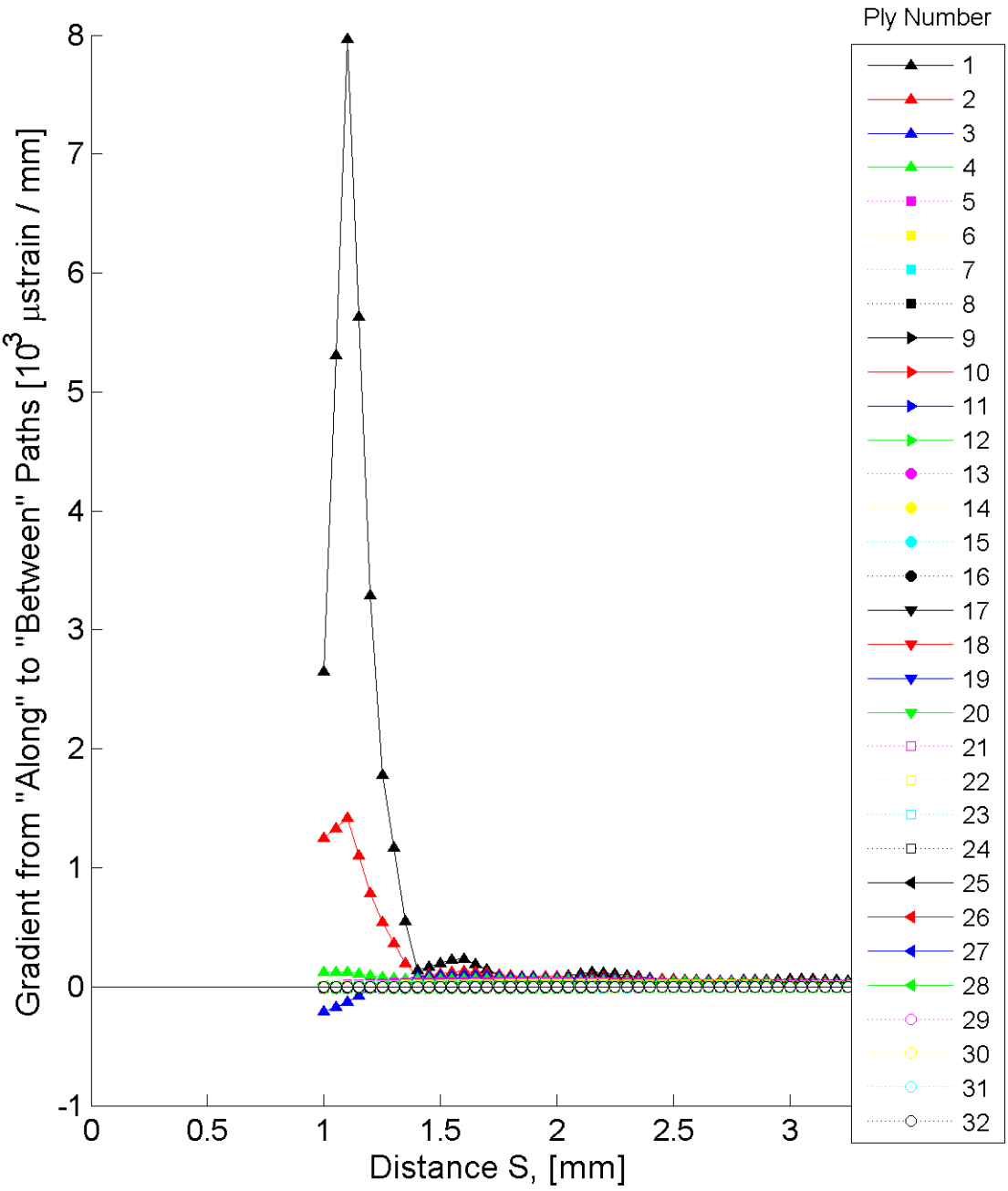

Figure B.99 Plot of the gradient of ϵ_{11}, in laminate axes, in the $\hat{S}$-direction at the midplane of each ply for the stitch crack model with laminate of $[+60/-60]_{16T}$.

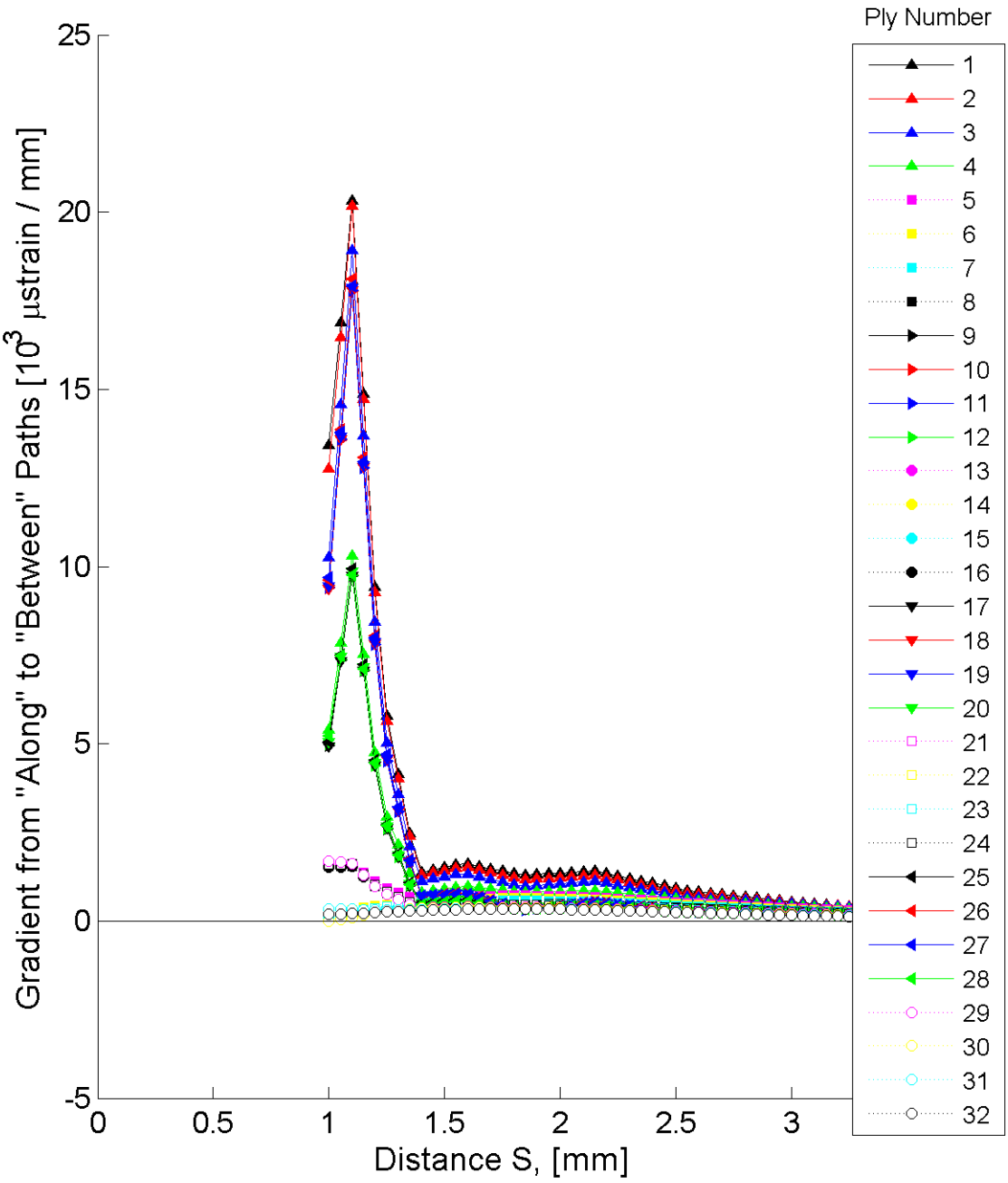

Figure B.100 Plot of the gradient of ϵ_{11}, in laminate axes, in the $\hat{S}$-direction at the midplane of each ply for the stitch crack model with laminate of $[+60_4/-60_4]_{4T}$.

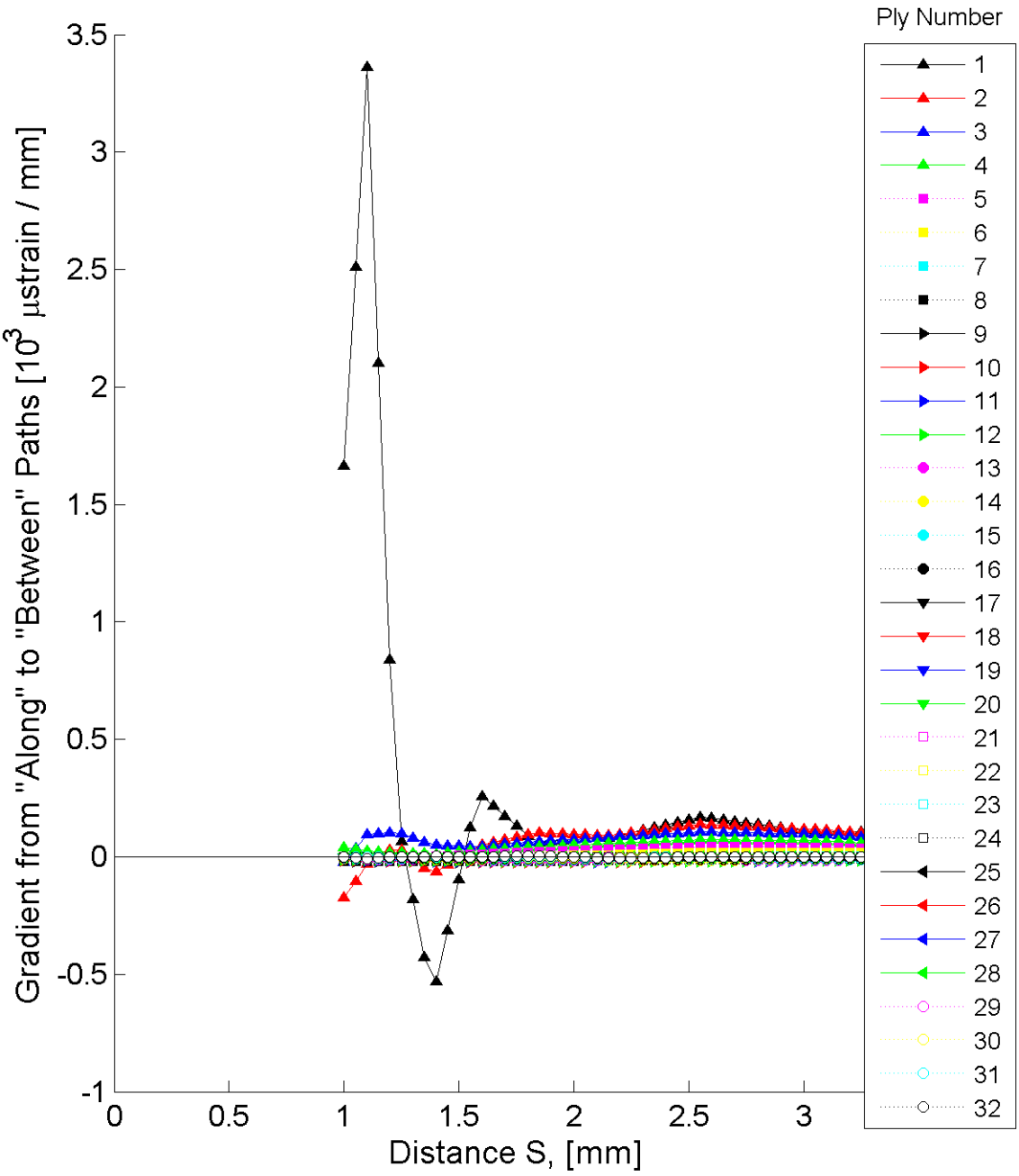

Figure B.101 Plot of the gradient of ϵ_{11}, in laminate axes, in the $\hat{S}$-direction at the midplane of each ply for the stitch crack model with laminate of $[+75/-75]_{16T}$.

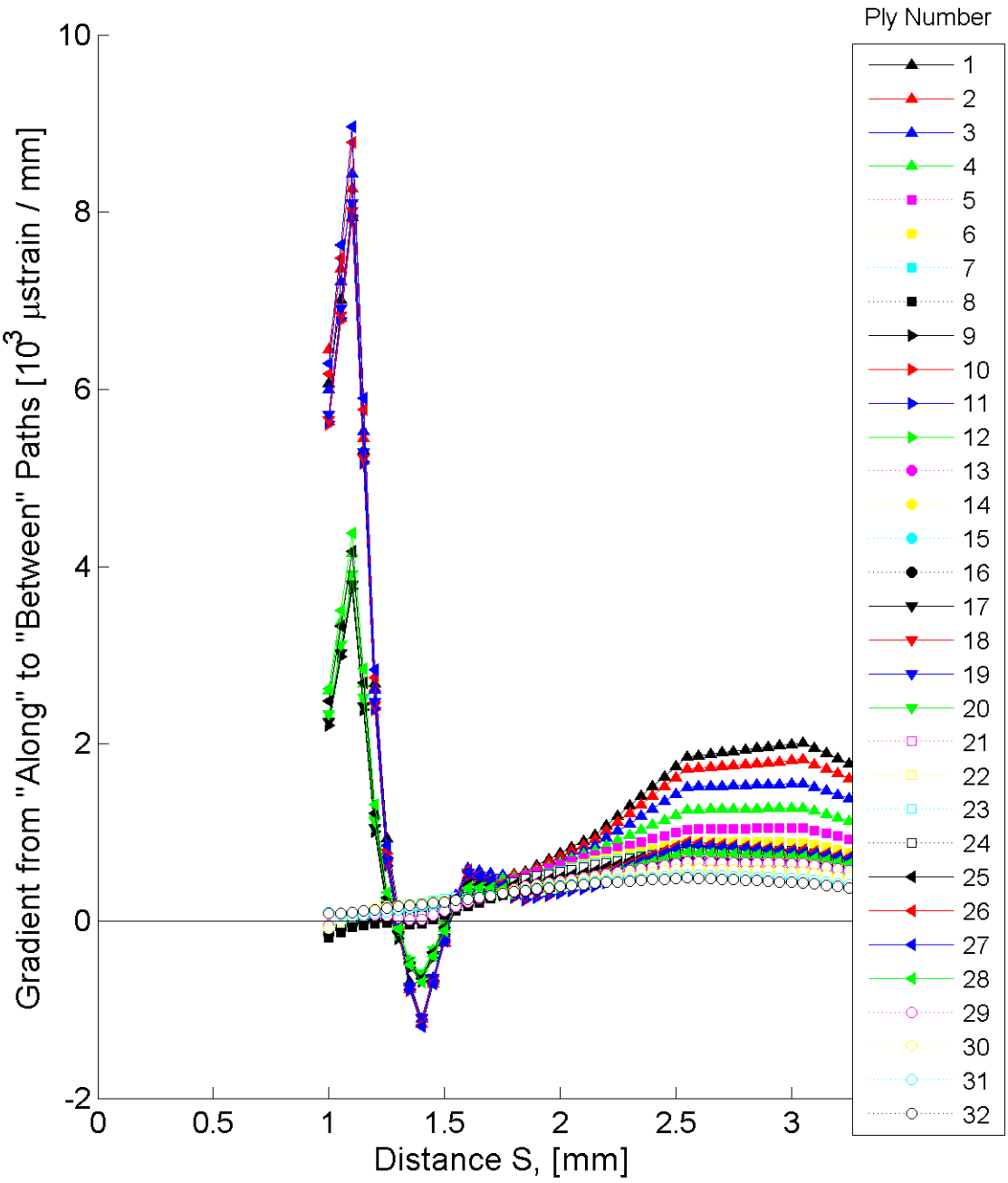

Figure B.102 Plot of the gradient of ϵ_{11}, in laminate axes, in the $\hat{S}$-direction at the midplane of each ply for the stitch crack model with laminate of $[+75_4/-75_4]_{4T}$.

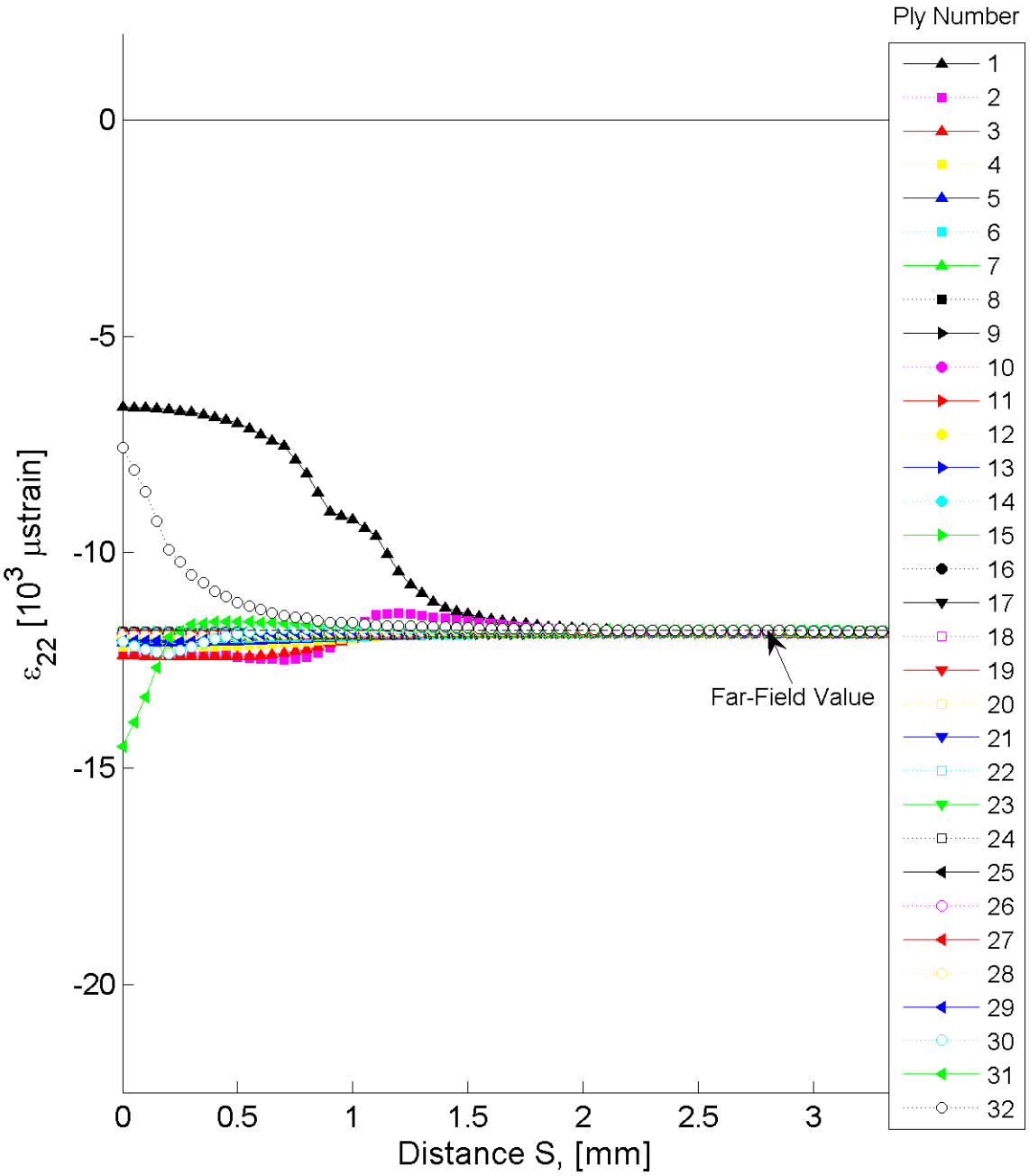

Figure B.103 Plot of ϵ_{22}, in laminate axes, along the path "between stitch cracks" at the midplane of each ply for the stitch crack model with laminate of $[+30/-30]_{16T}$.

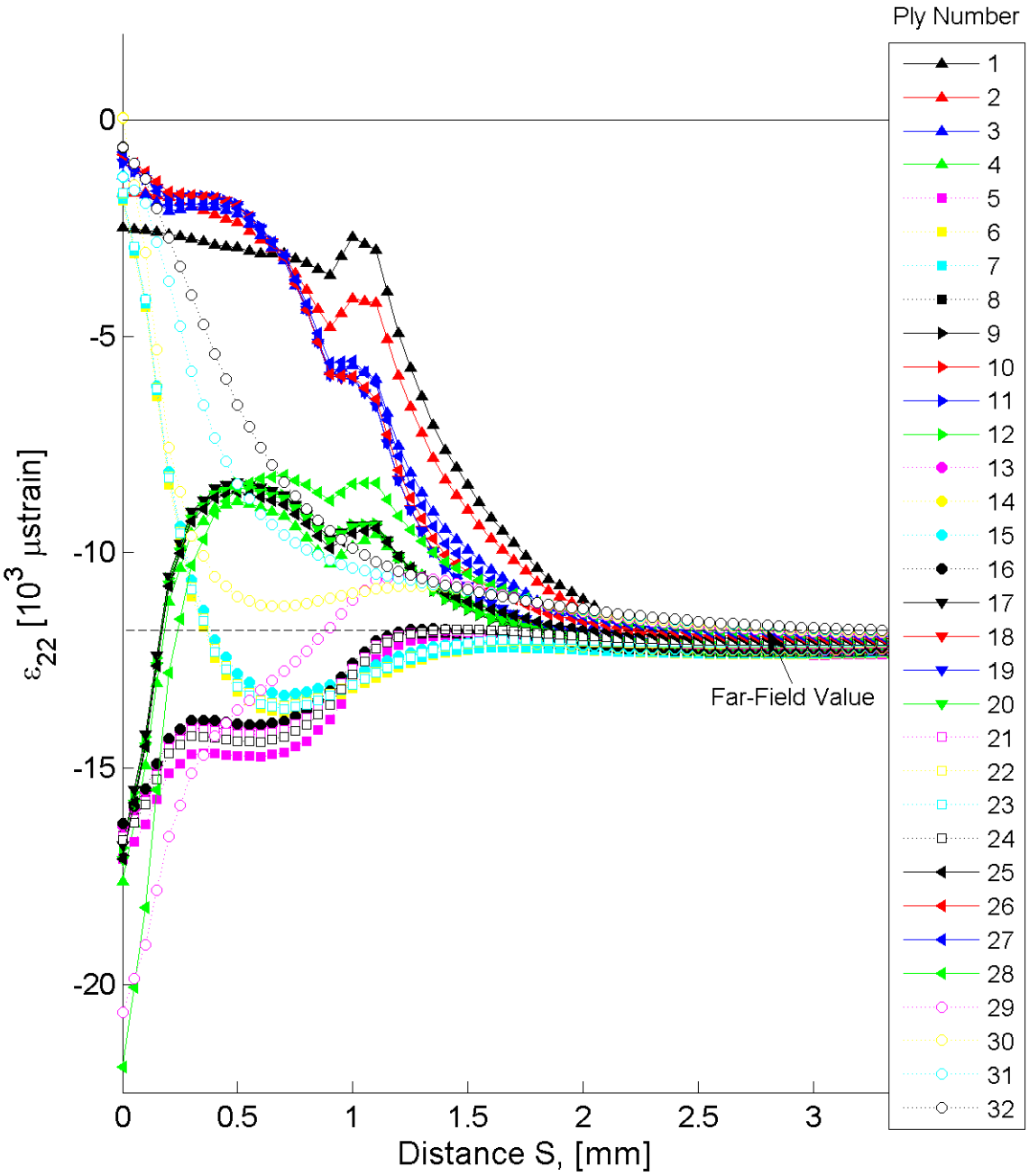

Figure B.104 Plot of ϵ_{22}, in laminate axes, along the path "between stitch cracks" at the midplane of each ply for the stitch crack model with laminate of $[+30_4/-30_4]_{4T}$.

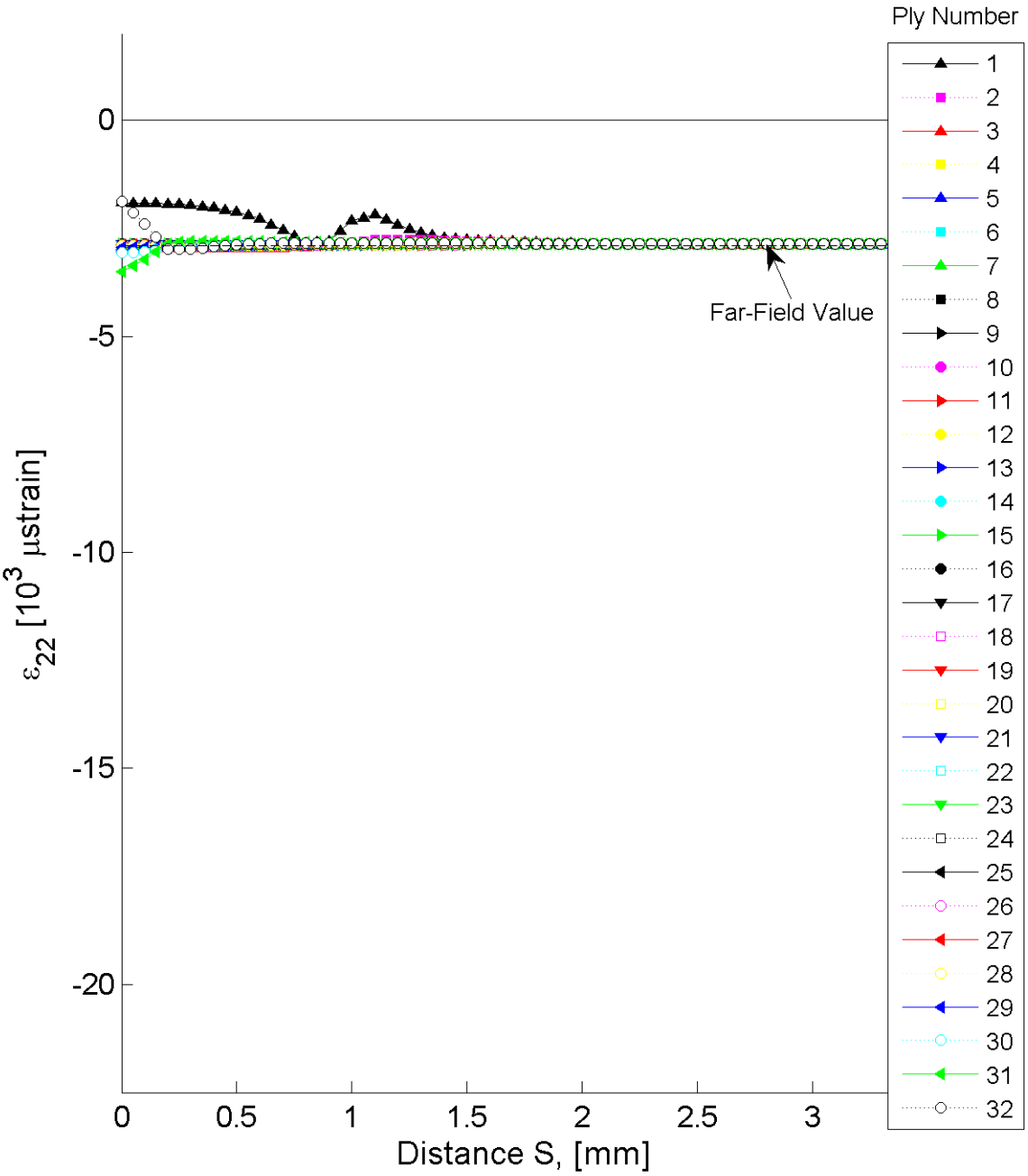

Figure B.105 Plot of ϵ_{22}, in laminate axes, along the path "between stitch cracks" at the midplane of each ply for the stitch crack model with laminate of $[+60/-60]_{16T}$.

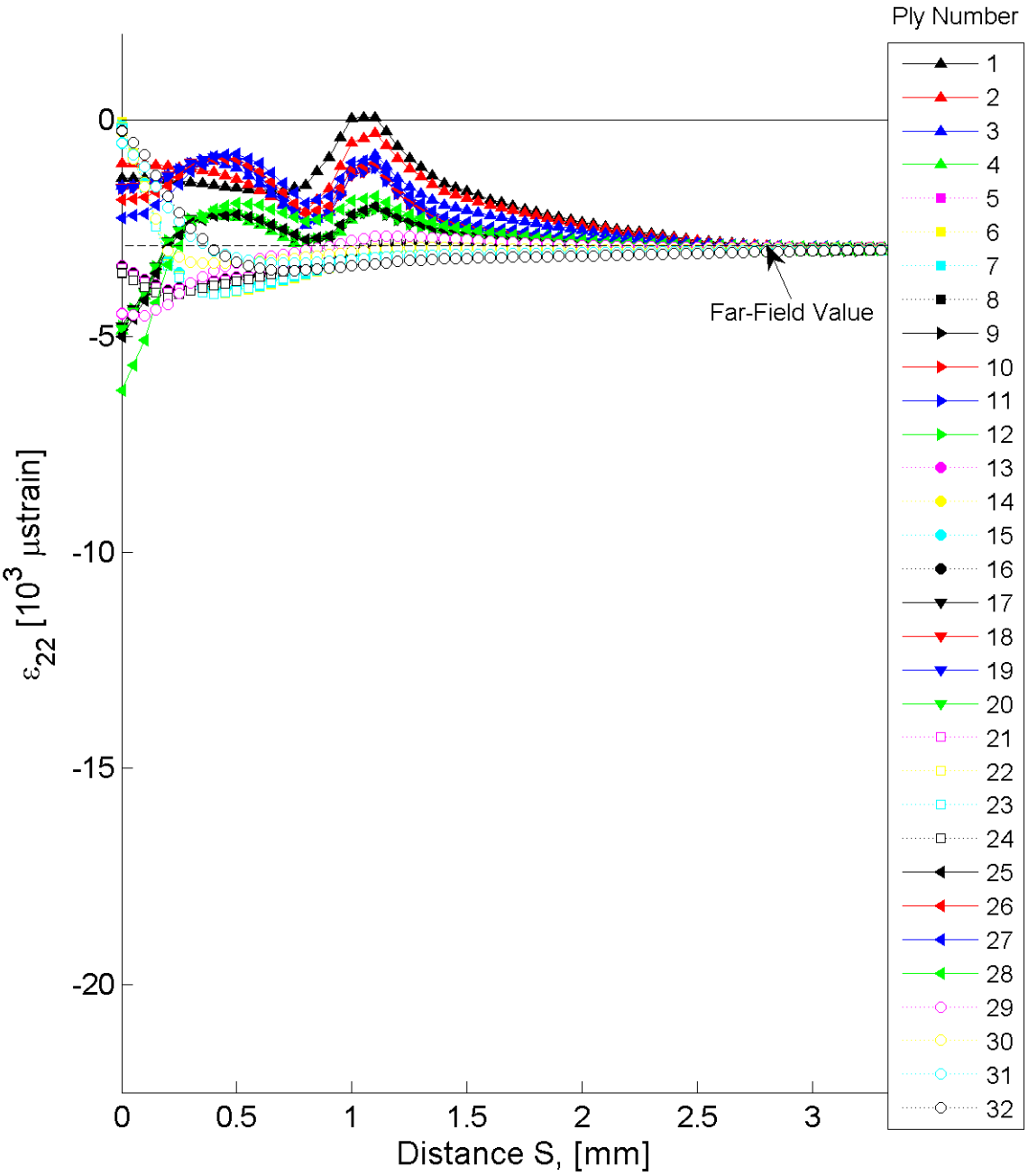

Figure B.106 Plot of ϵ_{22}, in laminate axes, along the path "between stitch cracks" at the midplane of each ply for the stitch crack model with laminate of $[+60_4/-60_4]_{4T}$.

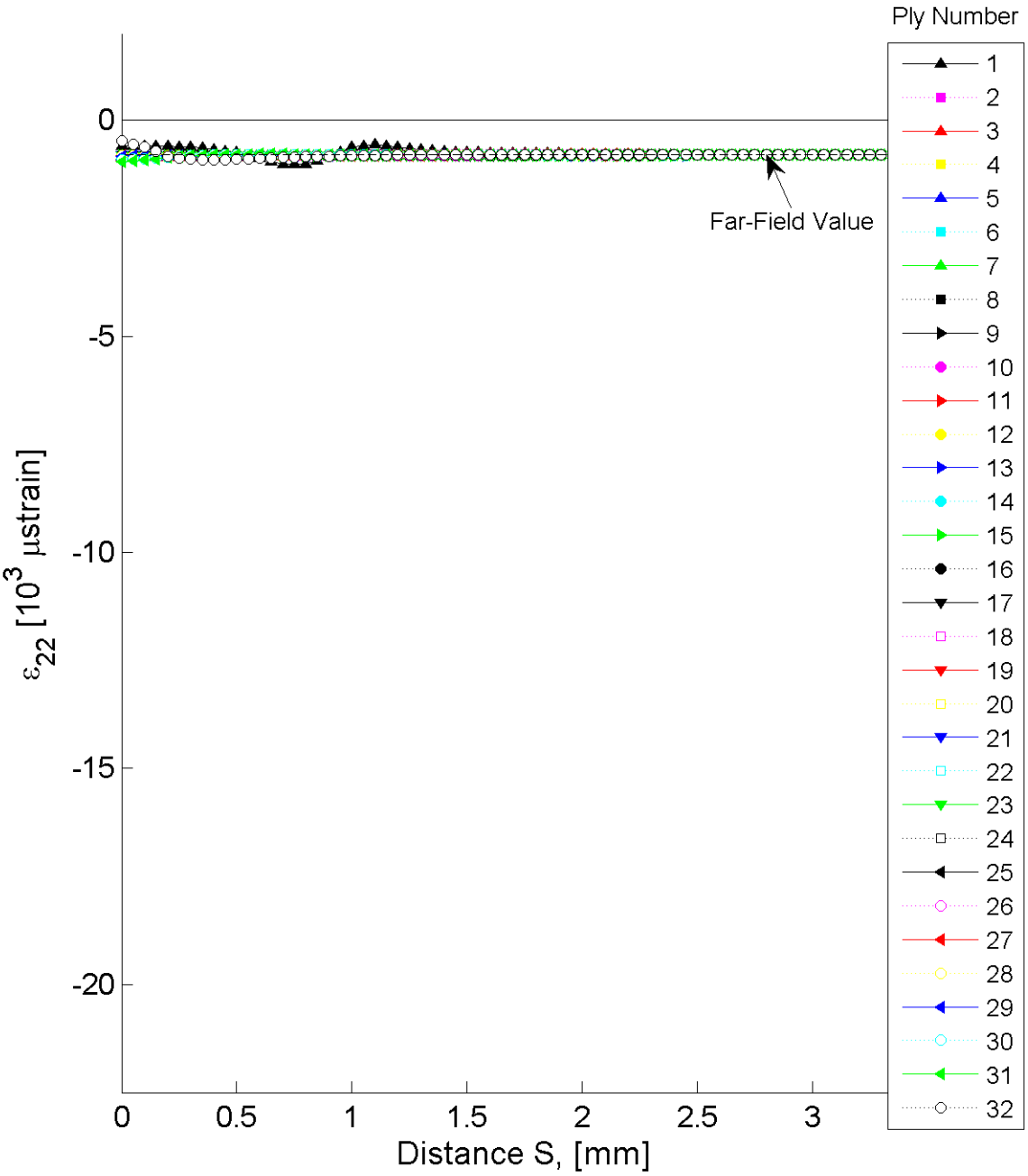

Figure B.107 Plot of ϵ_{22}, in laminate axes, along the path "between stitch cracks" at the midplane of each ply for the stitch crack model with laminate of $[+75/-75]_{16T}$.

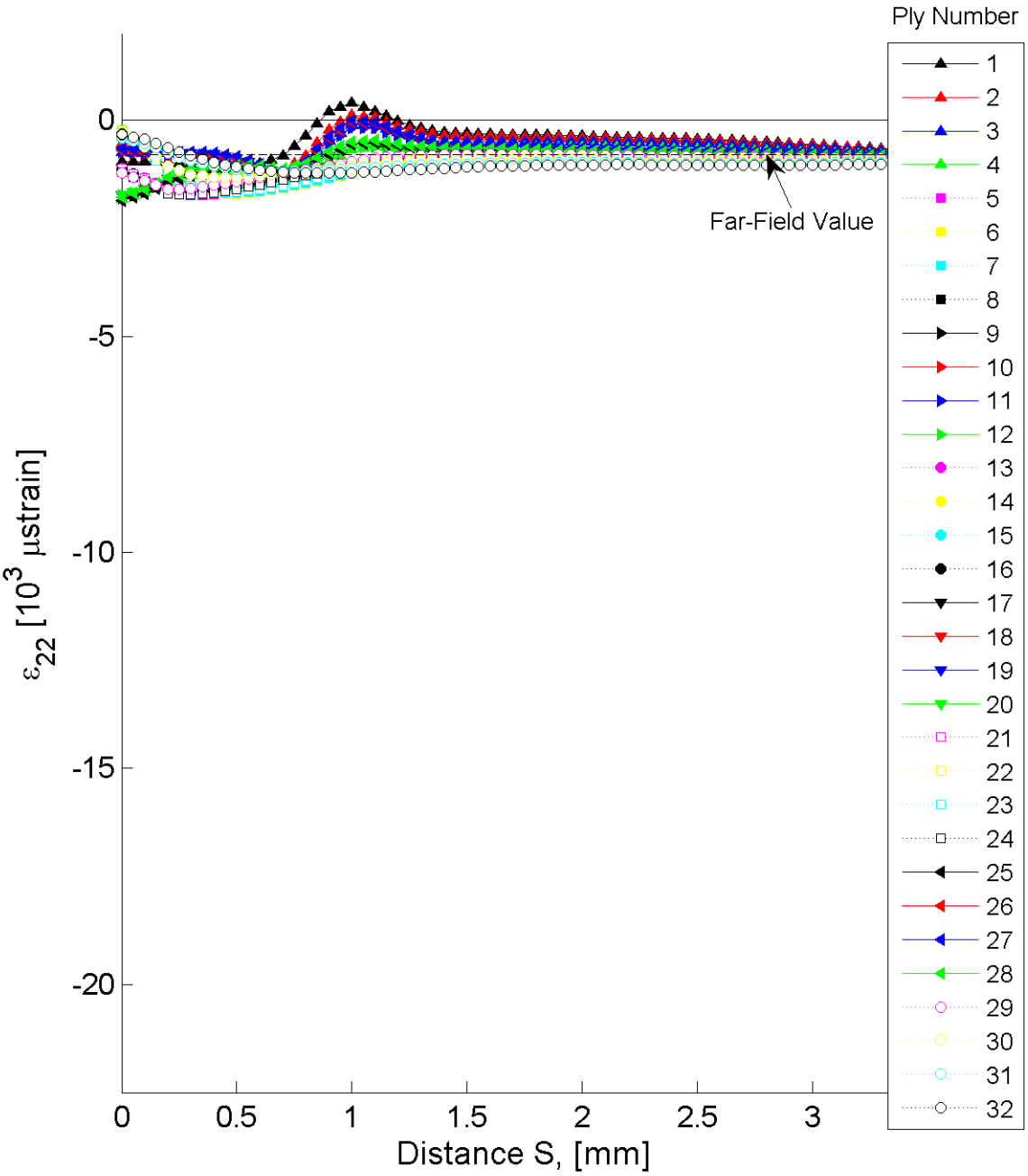

Figure B.108 Plot of ϵ_{22}, in laminate axes, along the path "between stitch cracks" at the midplane of each ply for the stitch crack model with laminate of $[+75_4/-75_4]_{4T}$.

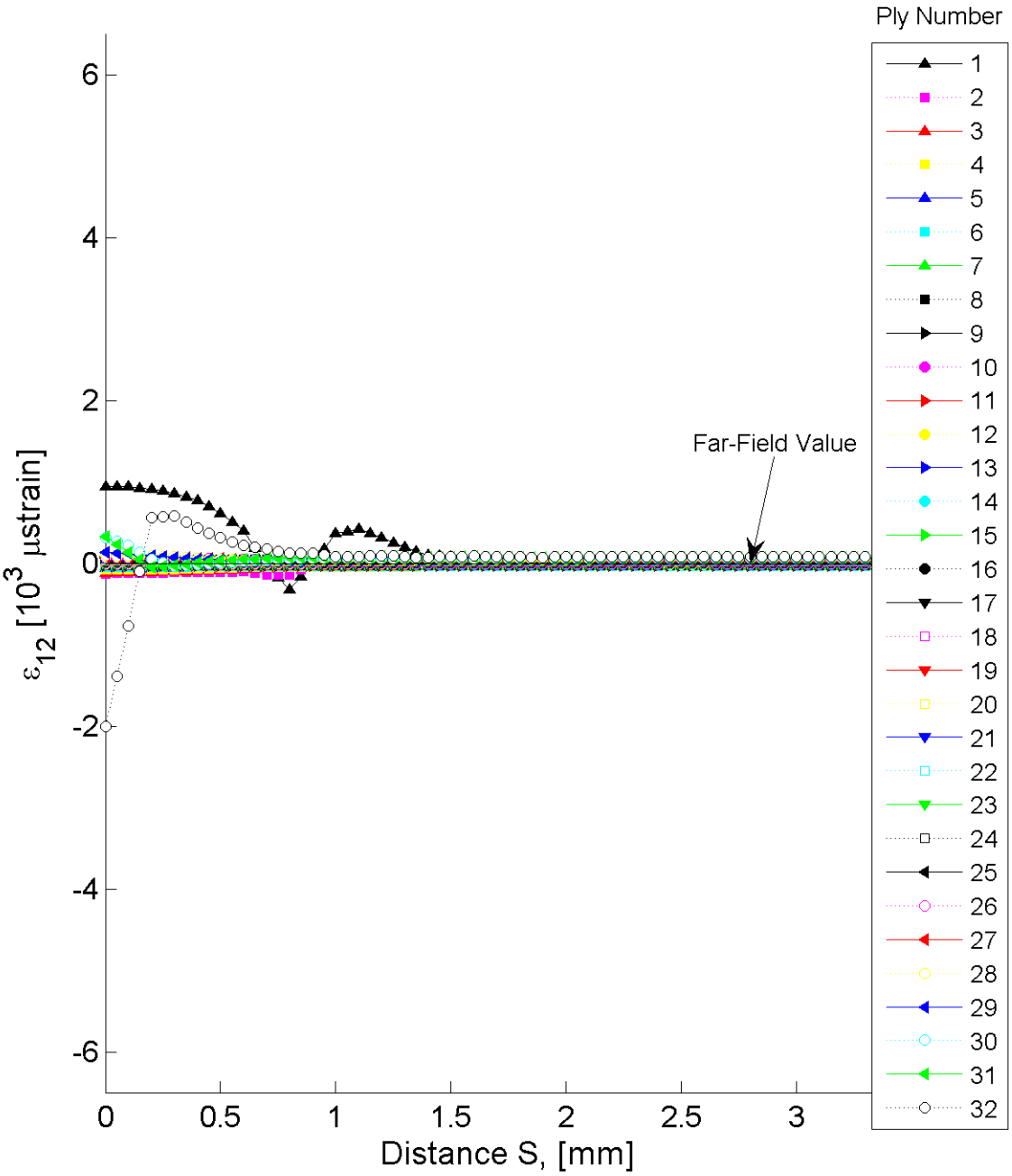

Figure B.109 Plot of ϵ_{12}, in laminate axes, along the path "between stitch cracks" at the midplane of each ply for the stitch crack model with laminate of $[+30/-30]_{16T}$.

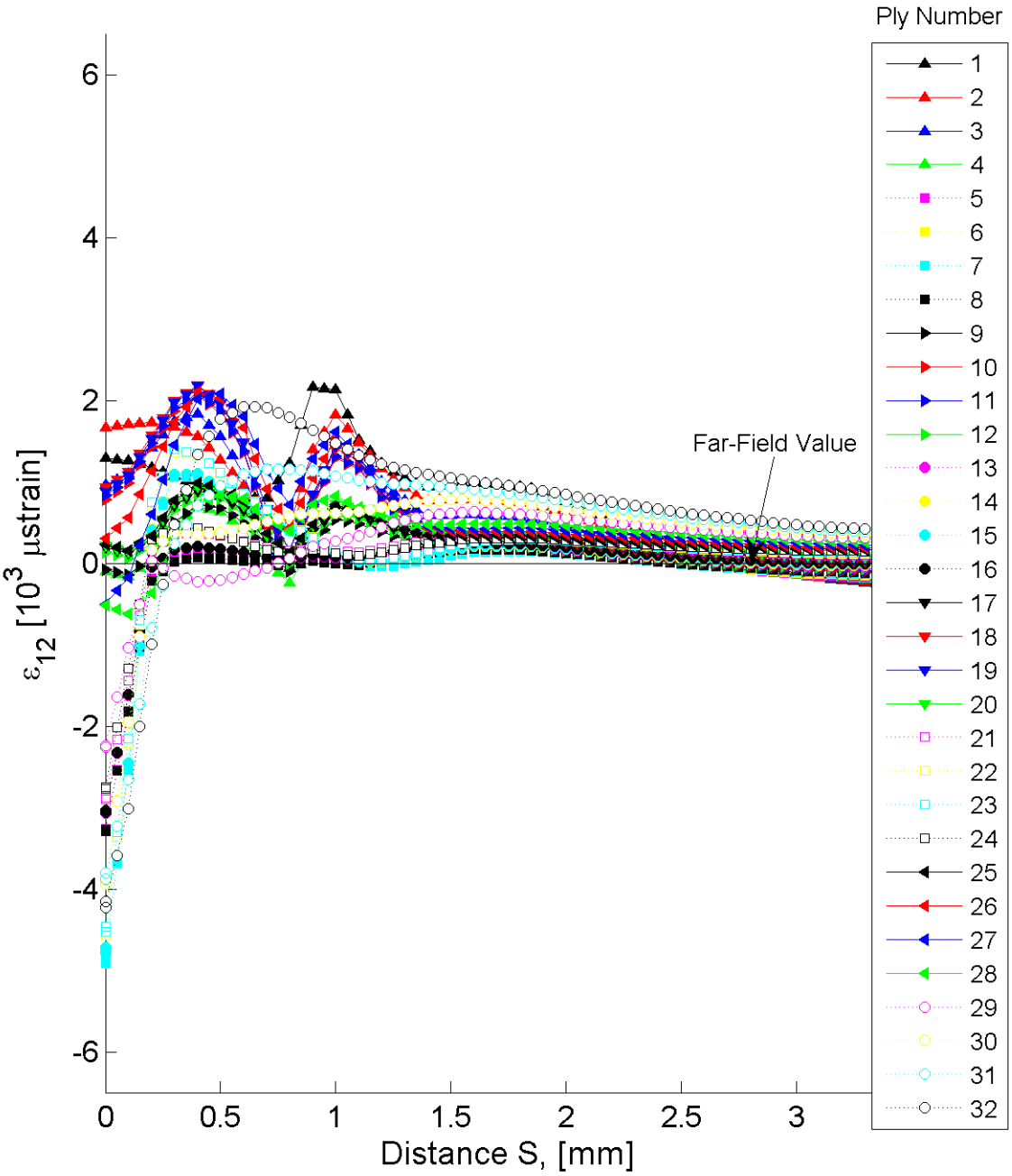

Figure B.110 Plot of ϵ_{12}, in laminate axes, along the path "between stitch cracks" at the midplane of each ply for the stitch crack model with laminate of $[+30_4/-30_4]_{4T}$.

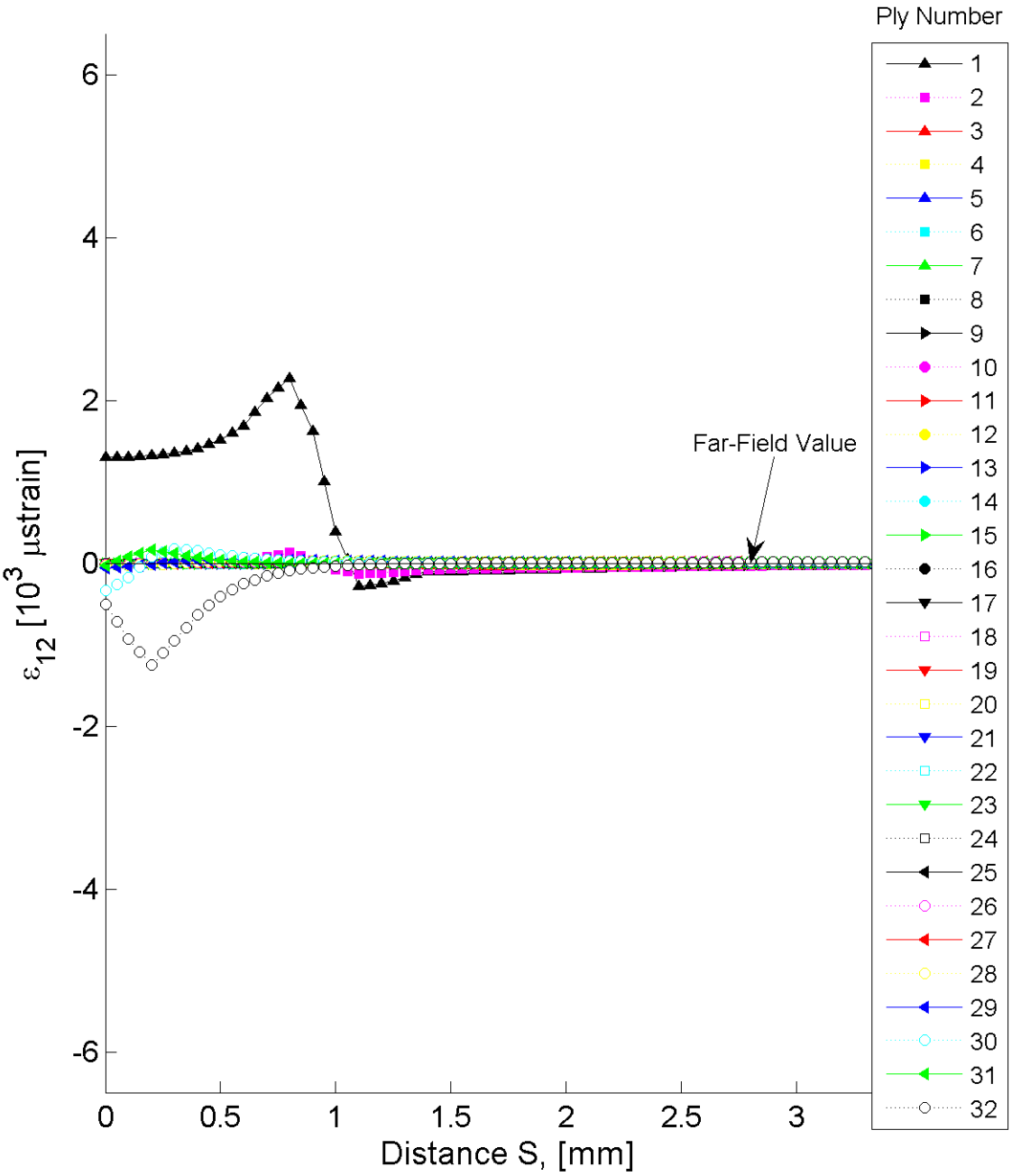

Figure B.111 Plot of ϵ_{12}, in laminate axes, along the path "between stitch cracks" at the midplane of each ply for the stitch crack model with laminate of $[+60/-60]_{16T}$.

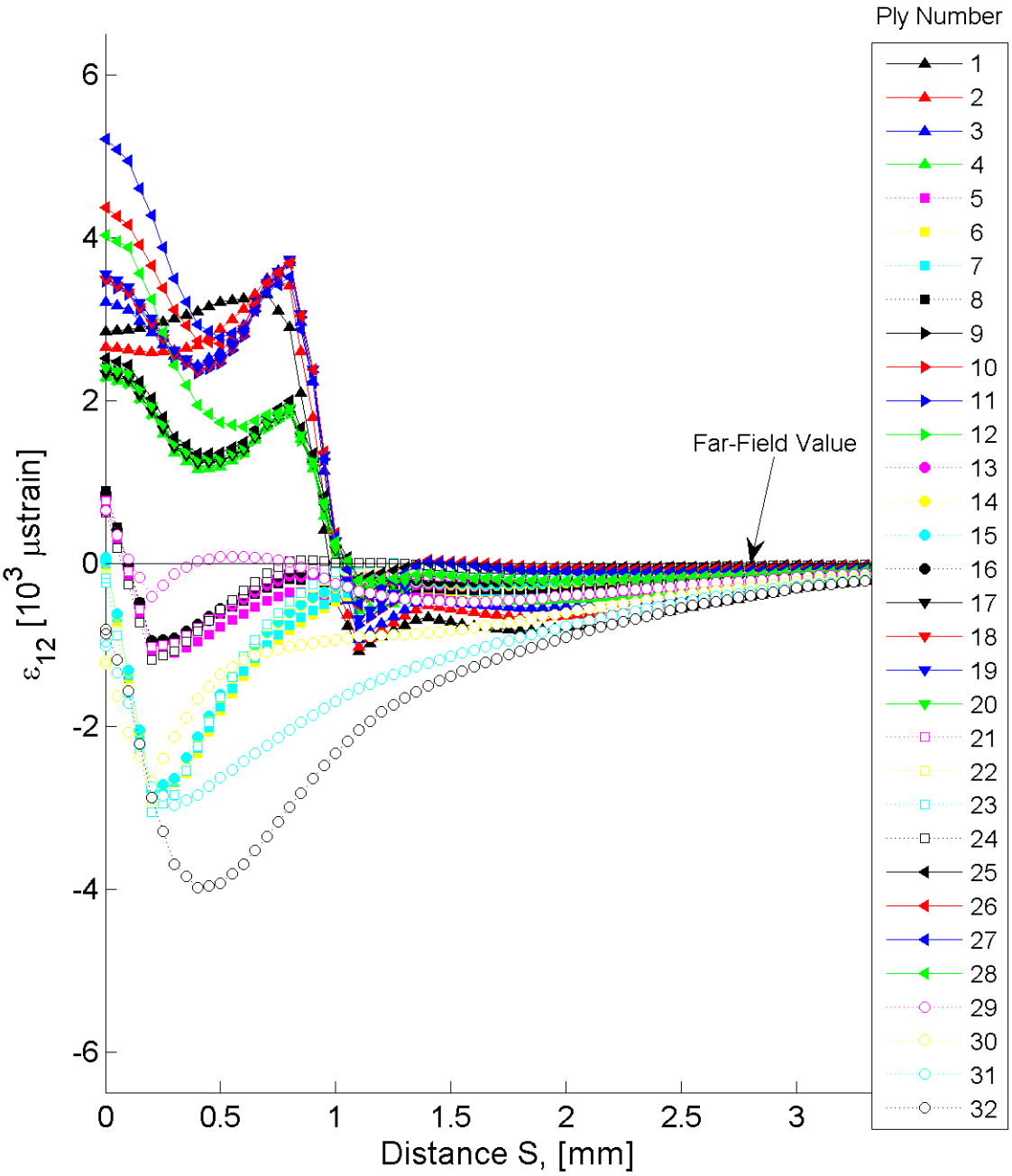

Figure B.112 Plot of ϵ_{12}, in laminate axes, along the path "between stitch cracks" at the midplane of each ply for the stitch crack model with laminate of $[+60_4/-60_4]_{4T}$.

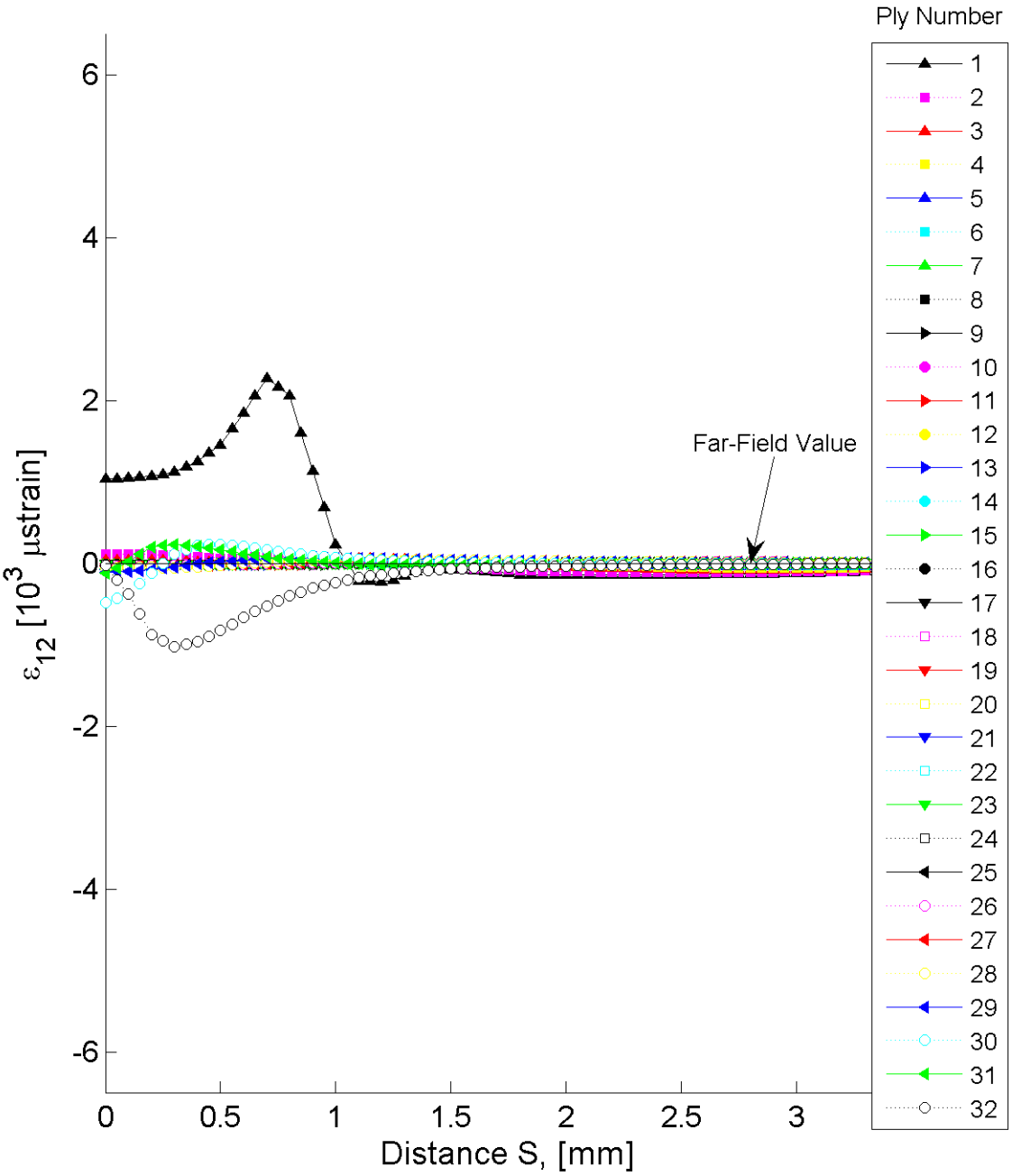

Figure B.113 Plot of ϵ_{12}, in laminate axes, along the path "between stitch cracks" at the midplane of each ply for the stitch crack model with laminate of $[+75/-75]_{16T}$.

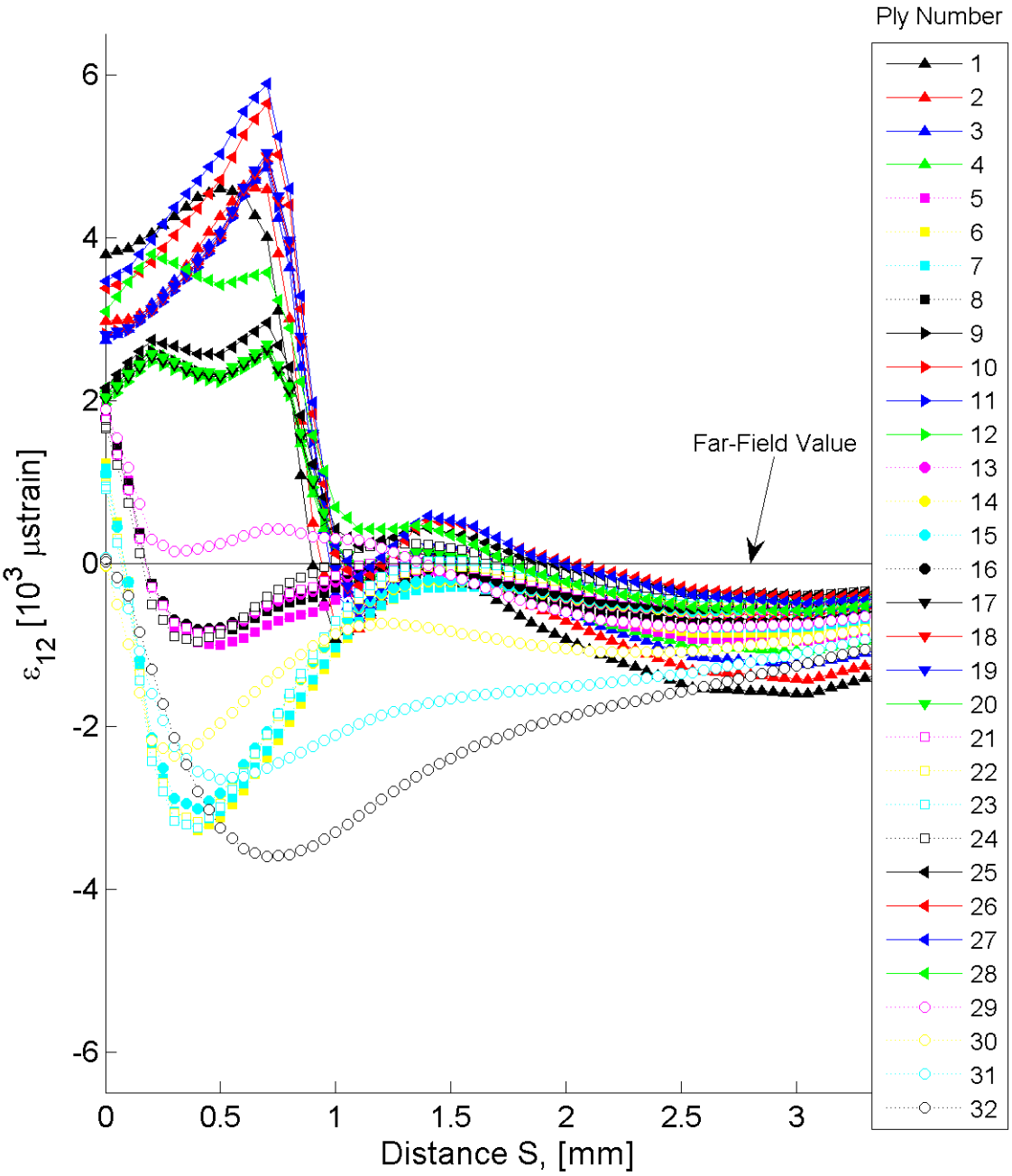

Figure B.114 Plot of ϵ_{12}, in laminate axes, along the path "between stitch cracks" at the midplane of each ply for the stitch crack model with laminate of $[+75_4/-75_4]_{4T}$.

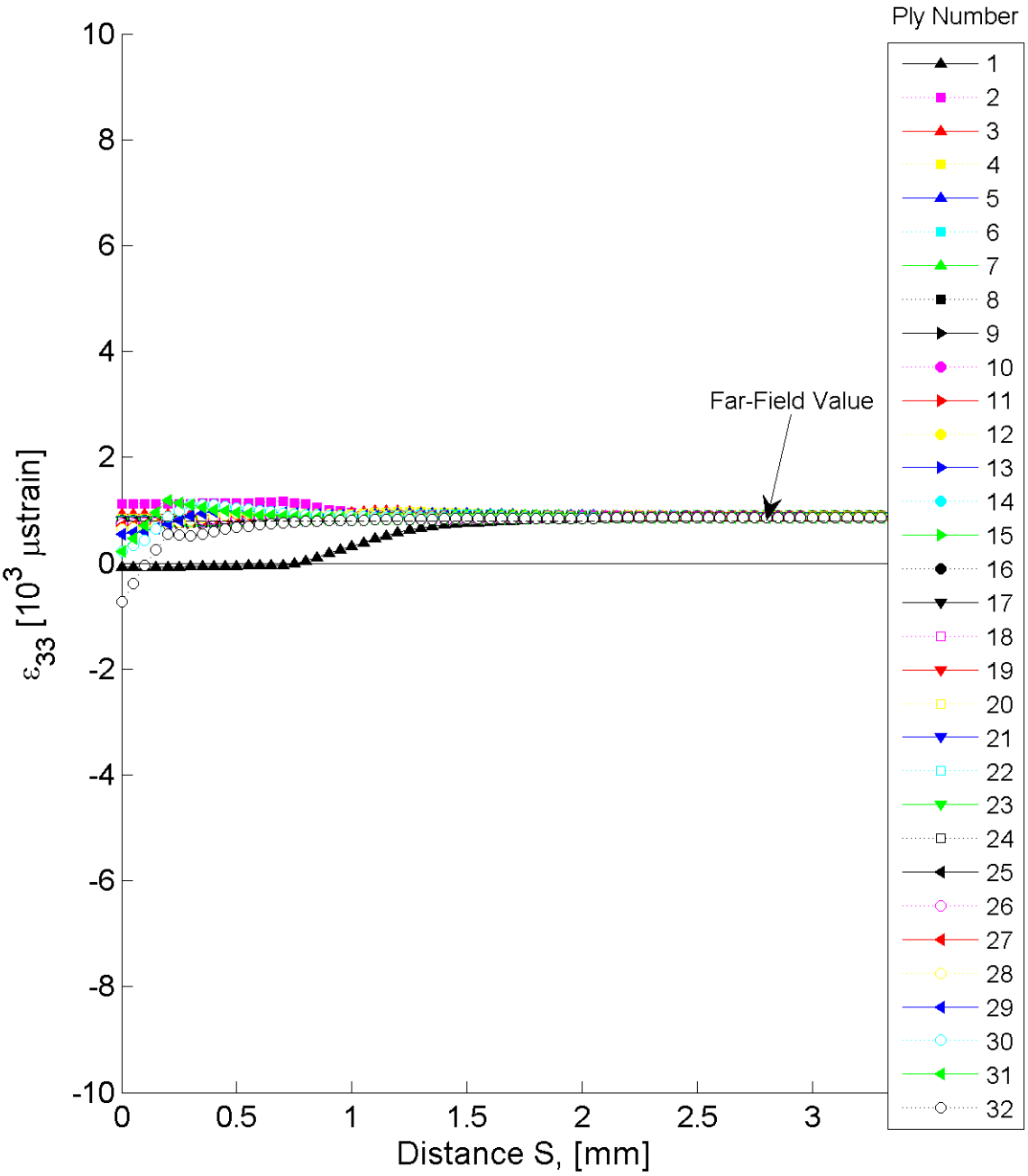

Figure B.115 Plot of ϵ_{33}, in laminate axes, along the path "between stitch cracks" at the midplane of each ply for the stitch crack model with laminate of $[+30/-30]_{16T}$.

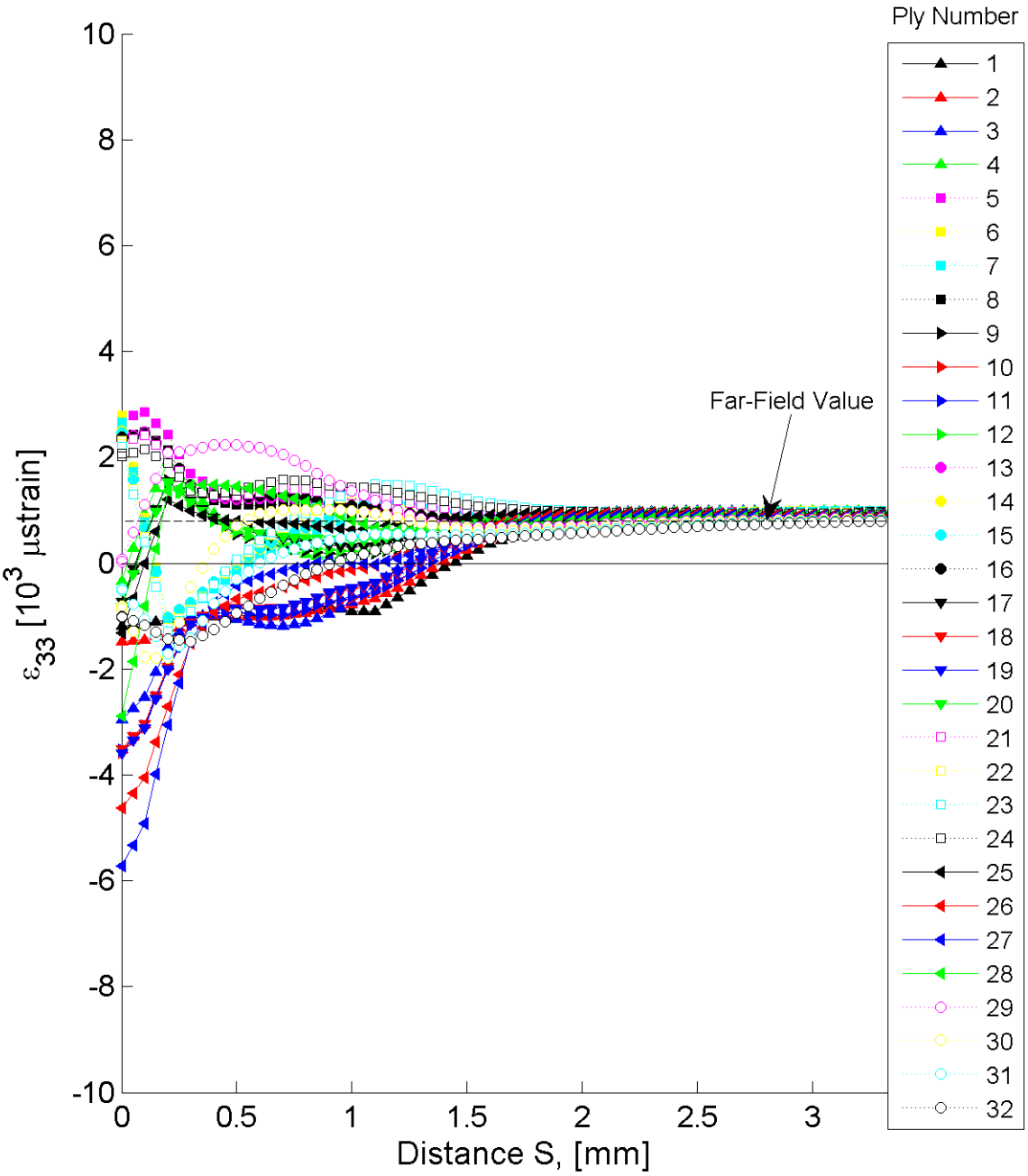

Figure B.116 Plot of ϵ_{33}, in laminate axes, along the path "between stitch cracks" at the midplane of each ply for the stitch crack model with laminate of $[+30_4/-30_4]_{4T}$.

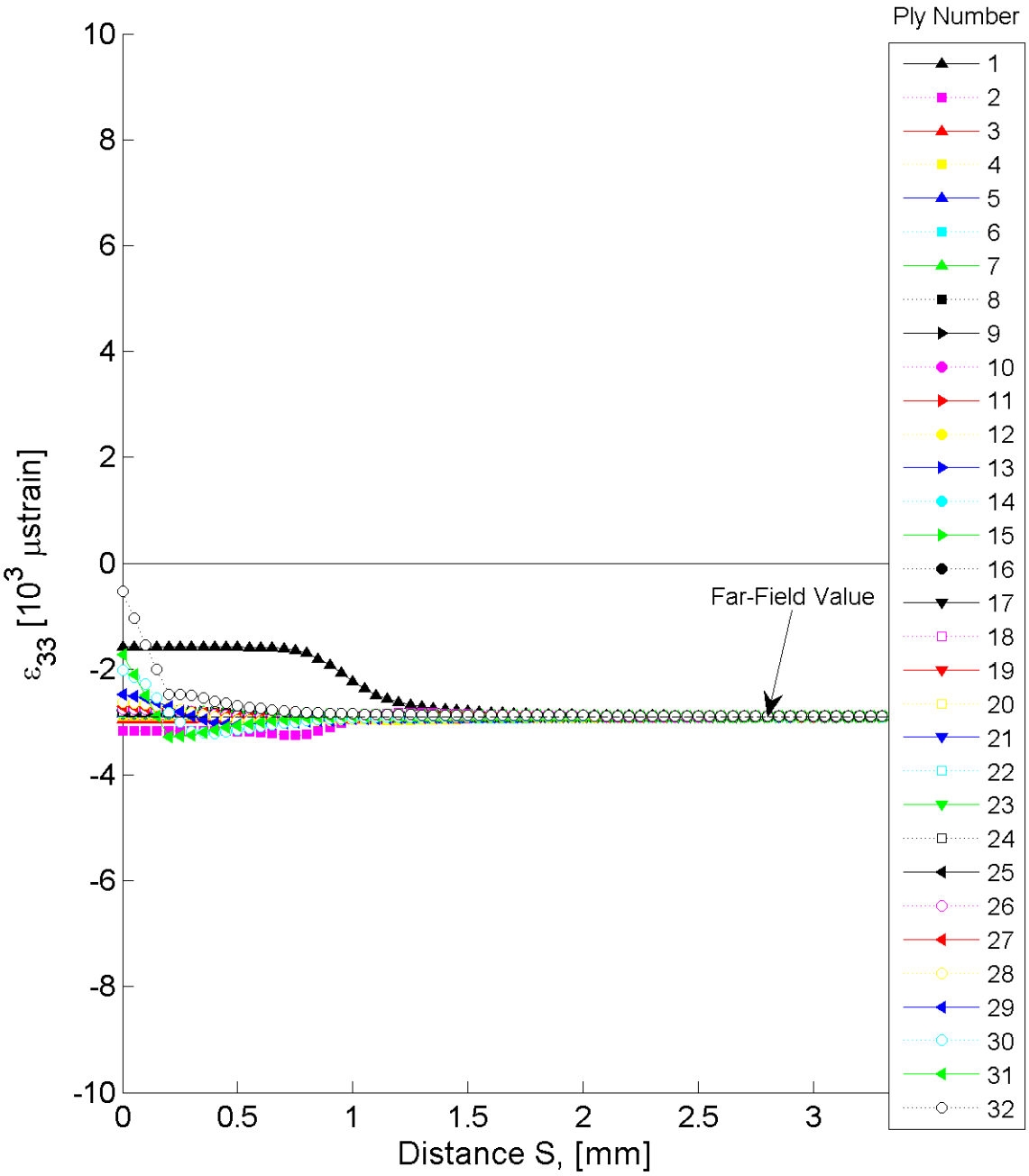

Figure B.117 Plot of ϵ_{33}, in laminate axes, along the path "between stitch cracks" at the midplane of each ply for the stitch crack model with laminate of $[+60/-60]_{16T}$.

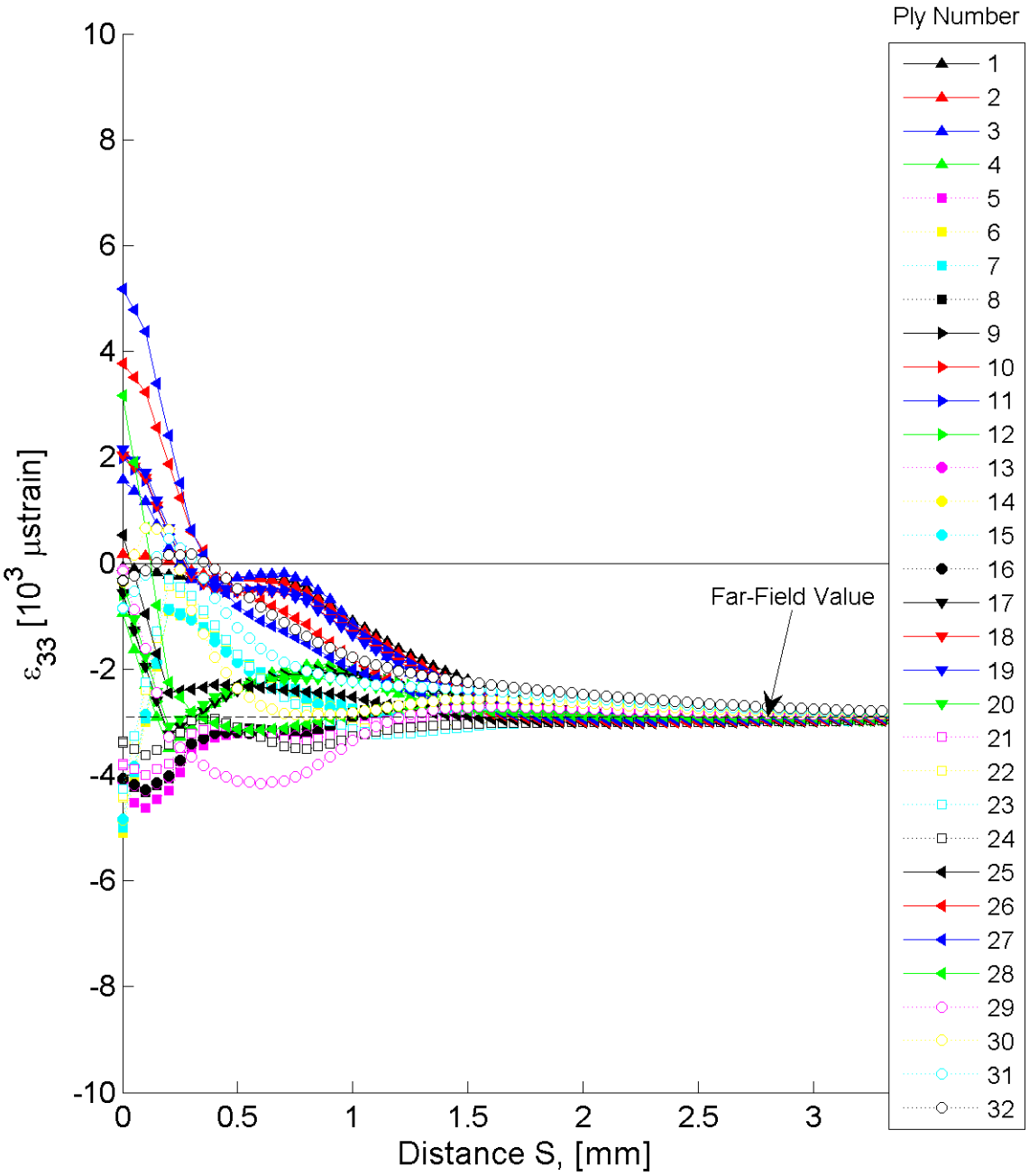

Figure B.118 Plot of ϵ_{33}, in laminate axes, along the path "between stitch cracks" at the midplane of each ply for the stitch crack model with laminate of $[+60_4/-60_4]_{4T}$.

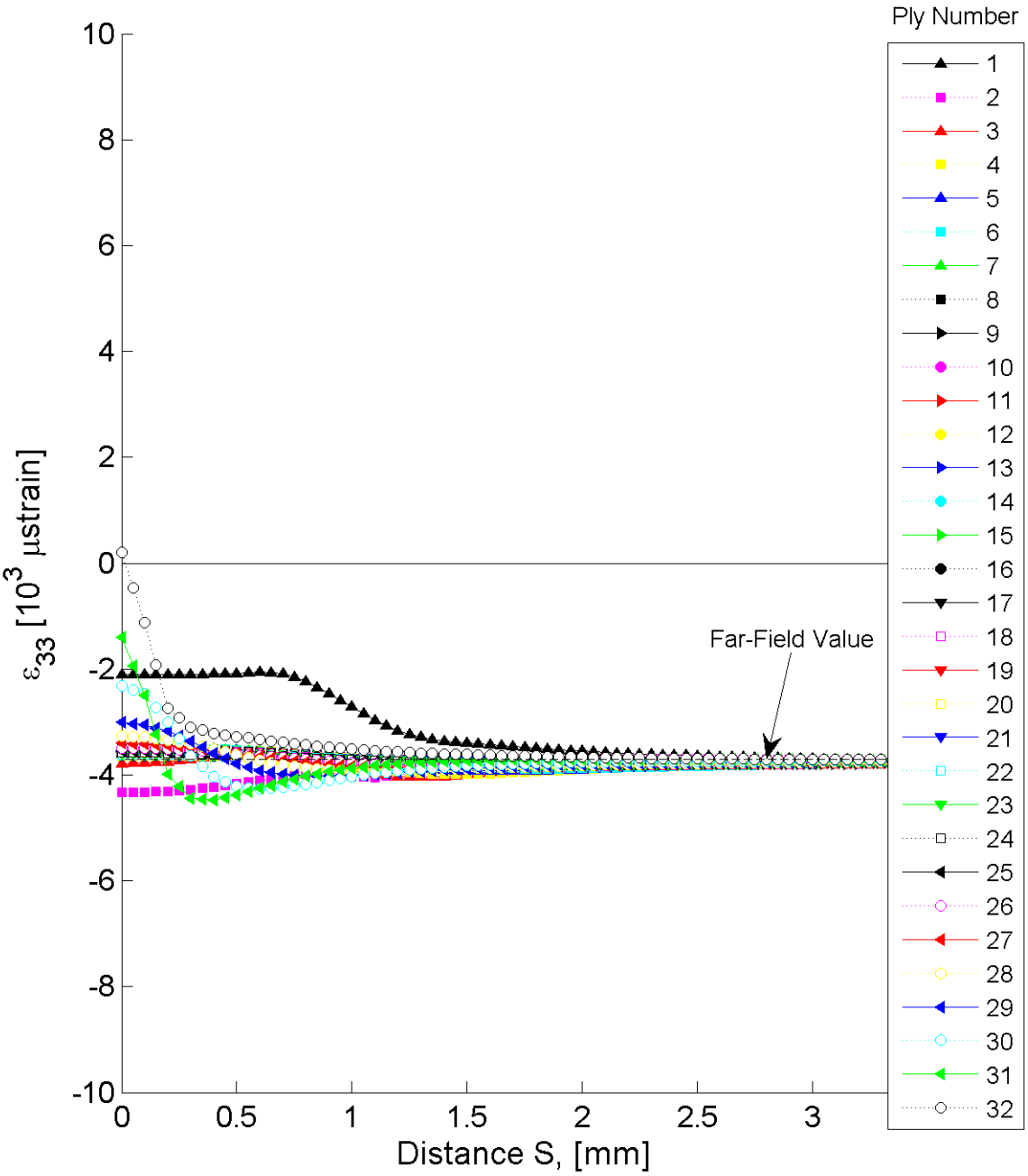

Figure B.119 Plot of ϵ_{33}, in laminate axes, along the path "between stitch cracks" at the midplane of each ply for the stitch crack model with laminate of $[+75/-75]_{16T}$.

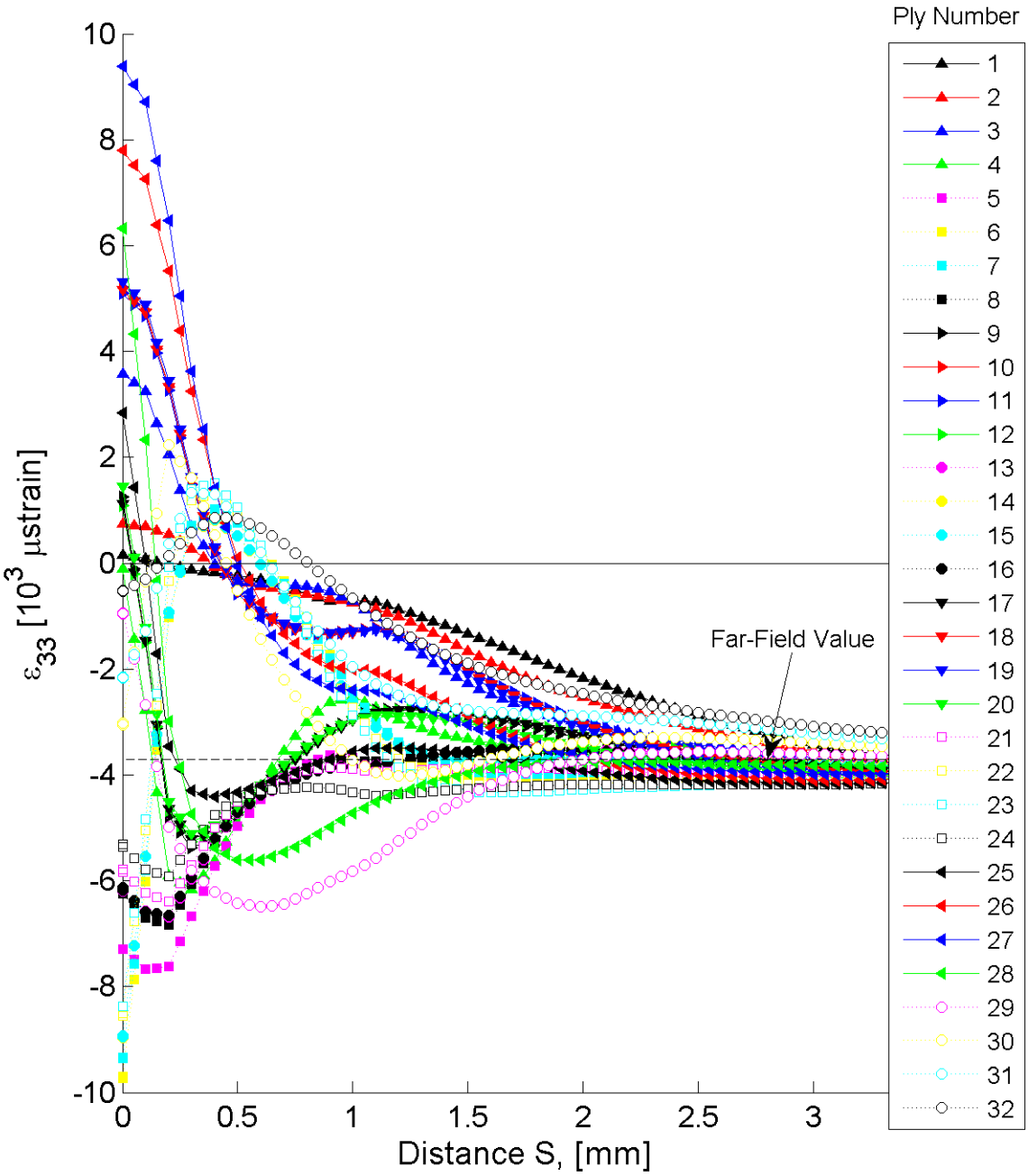

Figure B.120 Plot of ϵ_{33}, in laminate axes, along the path "between stitch cracks" at the midplane of each ply for the stitch crack model with laminate of $[+75_4/-75_4]_{4T}$.

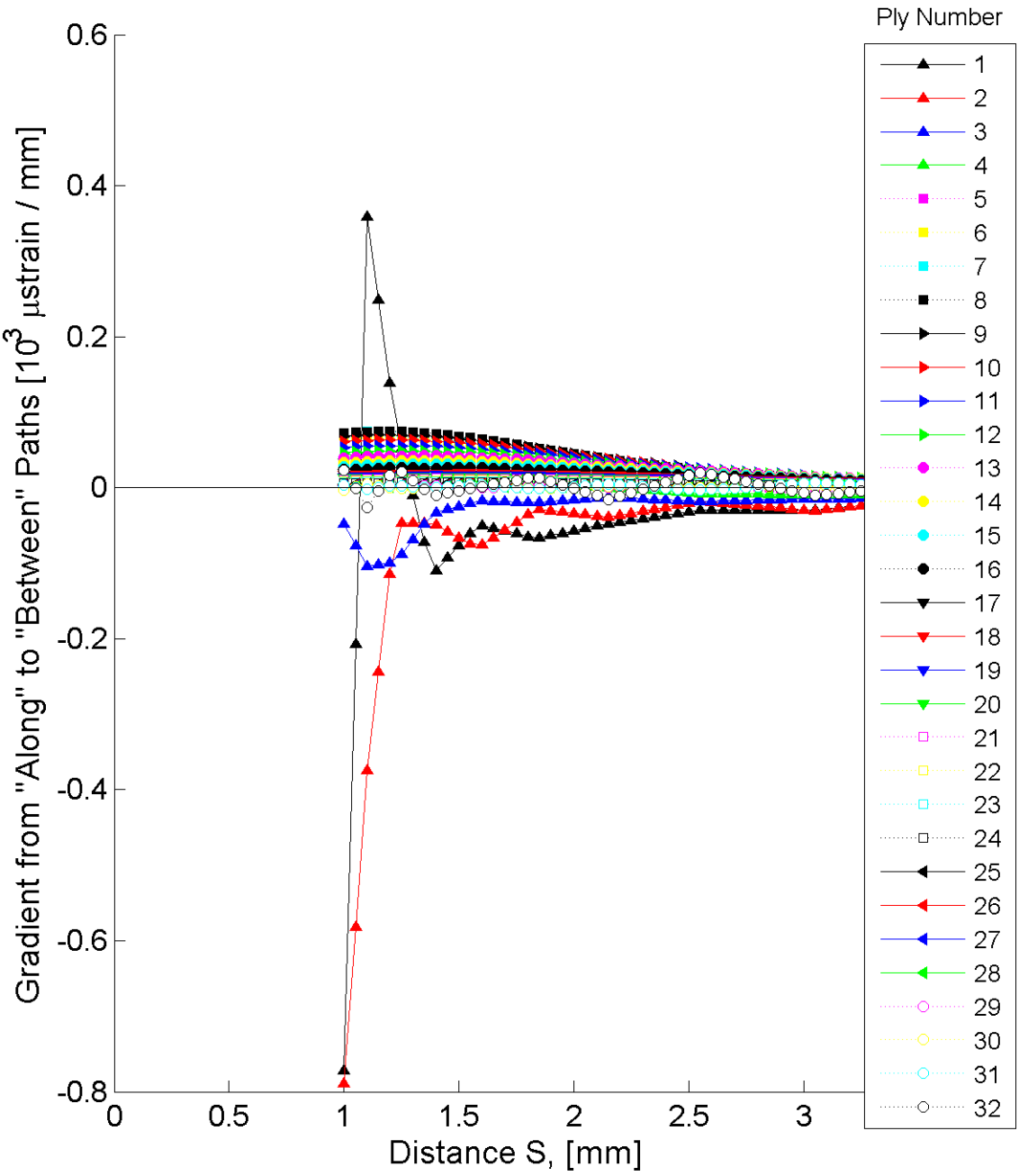

Figure B.121 Plot of the gradient of ϵ_{33} in the $\hat{S}$-direction at the midplane of each ply for the stitch crack model with laminate of $[+30/-30]_{16T}$.

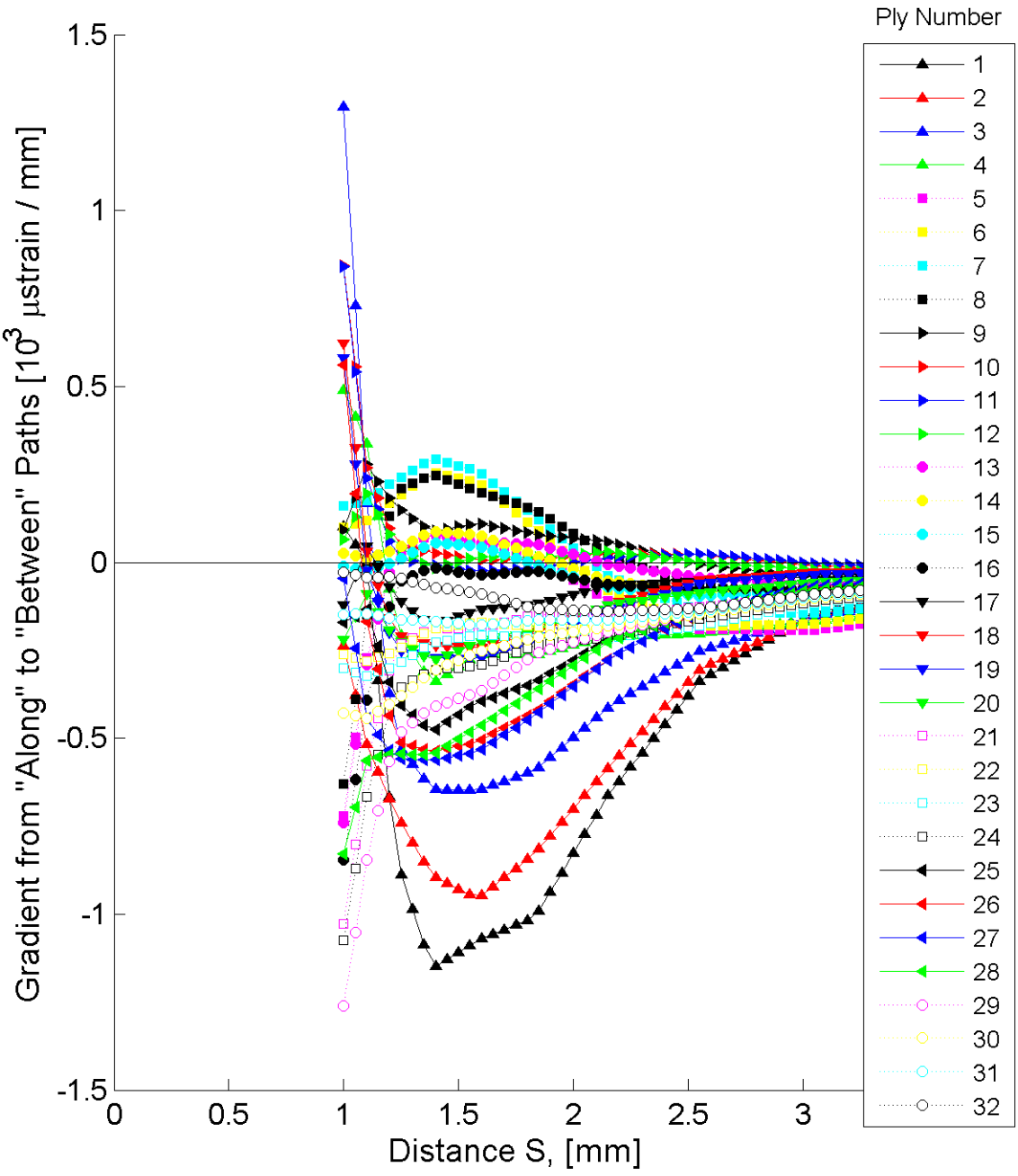

Figure B.122 Plot of the gradient of ϵ_{33} in the $\hat{S}$-direction at the midplane of each ply for the stitch crack model with laminate of $[+30_4/-30_4]_{4T}$.

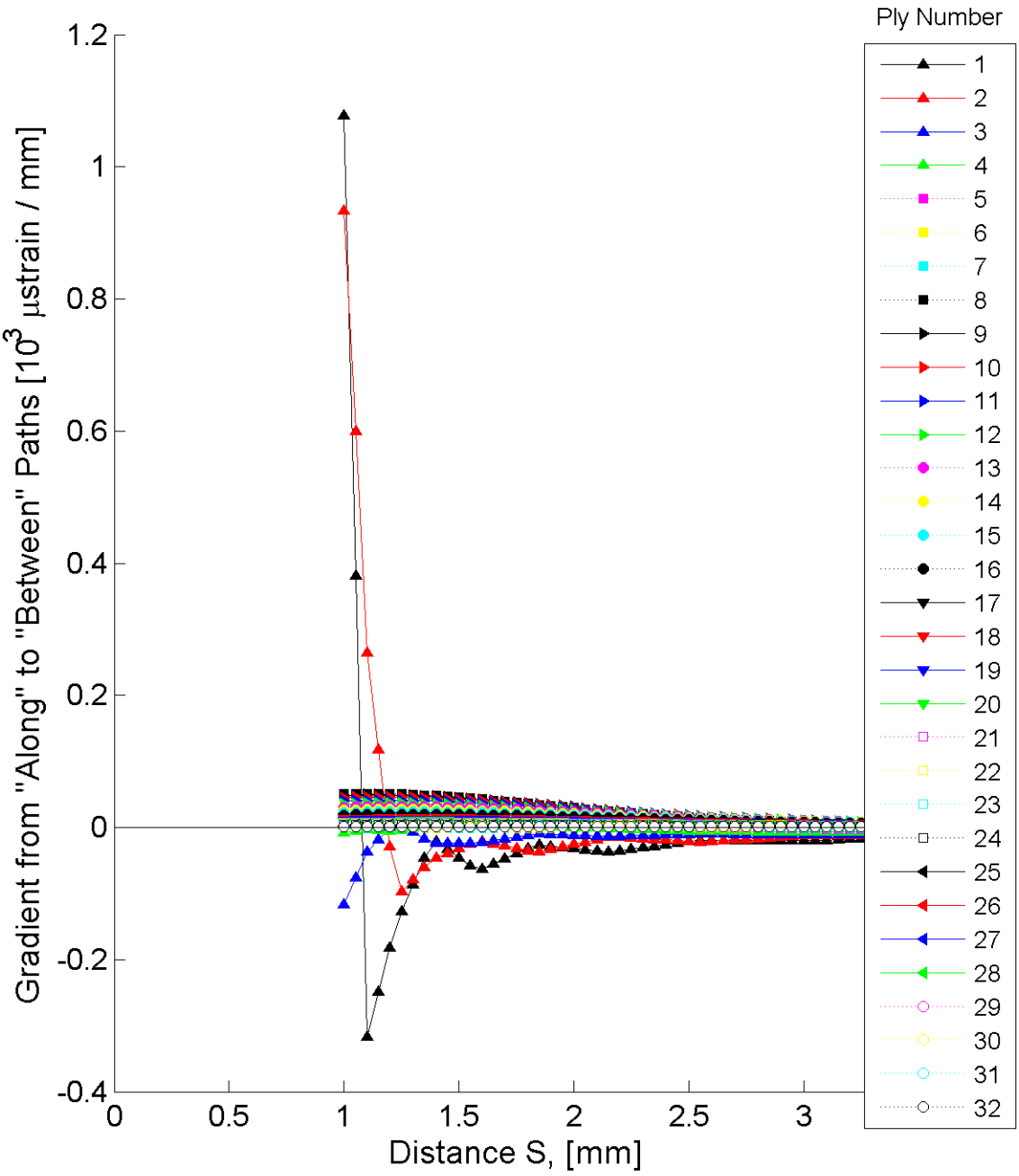

Figure B.123 Plot of the gradient of ϵ_{33} in the $\hat{S}$-direction at the midplane of each ply for the stitch crack model with laminate of $[+60/-60]_{16T}$.

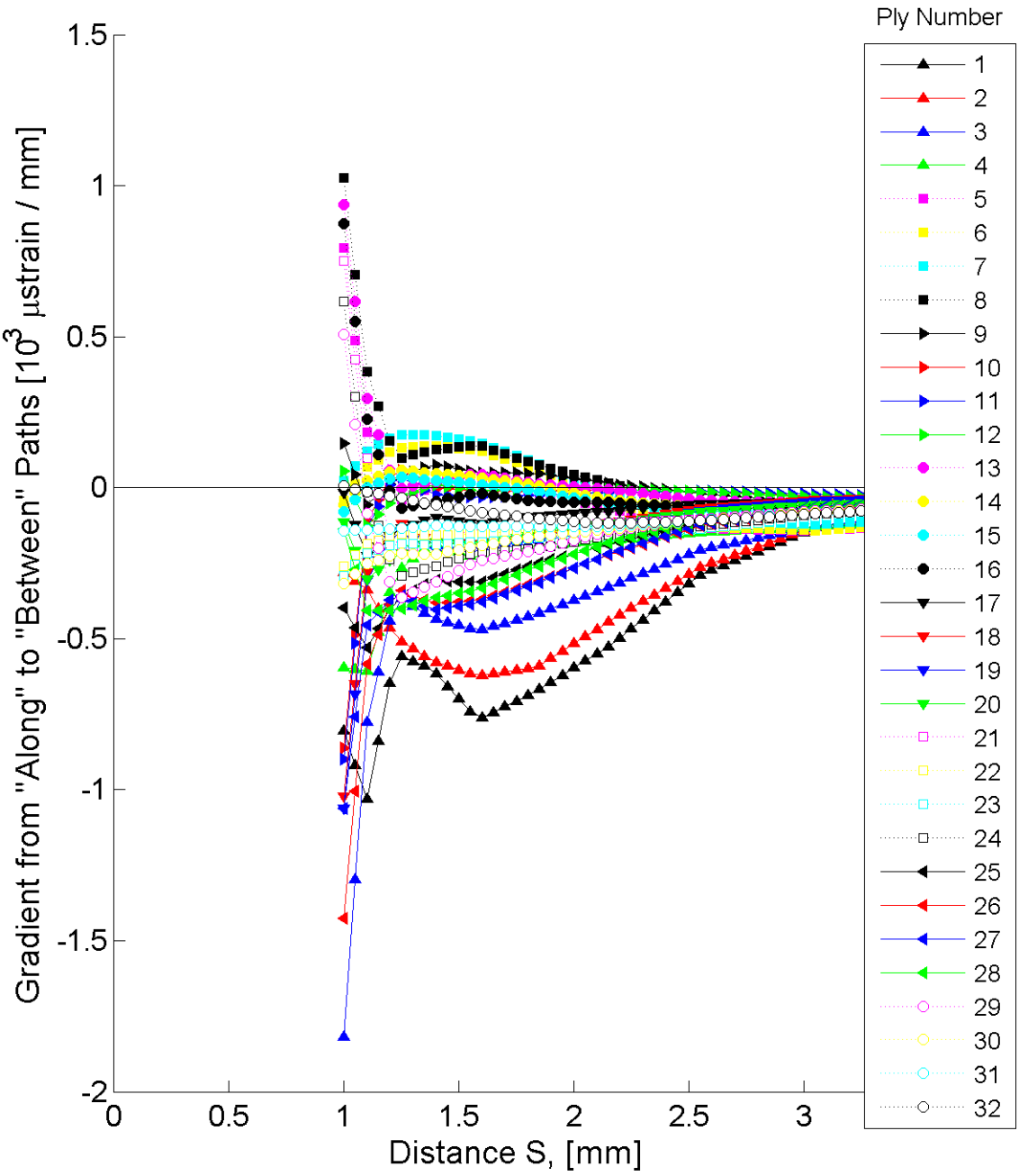

Figure B.124 Plot of the gradient of ϵ_{33} in the $\hat{S}$-direction at the midplane of each ply for the stitch crack model with laminate of $[+60_4/-60_4]_{4T}$.

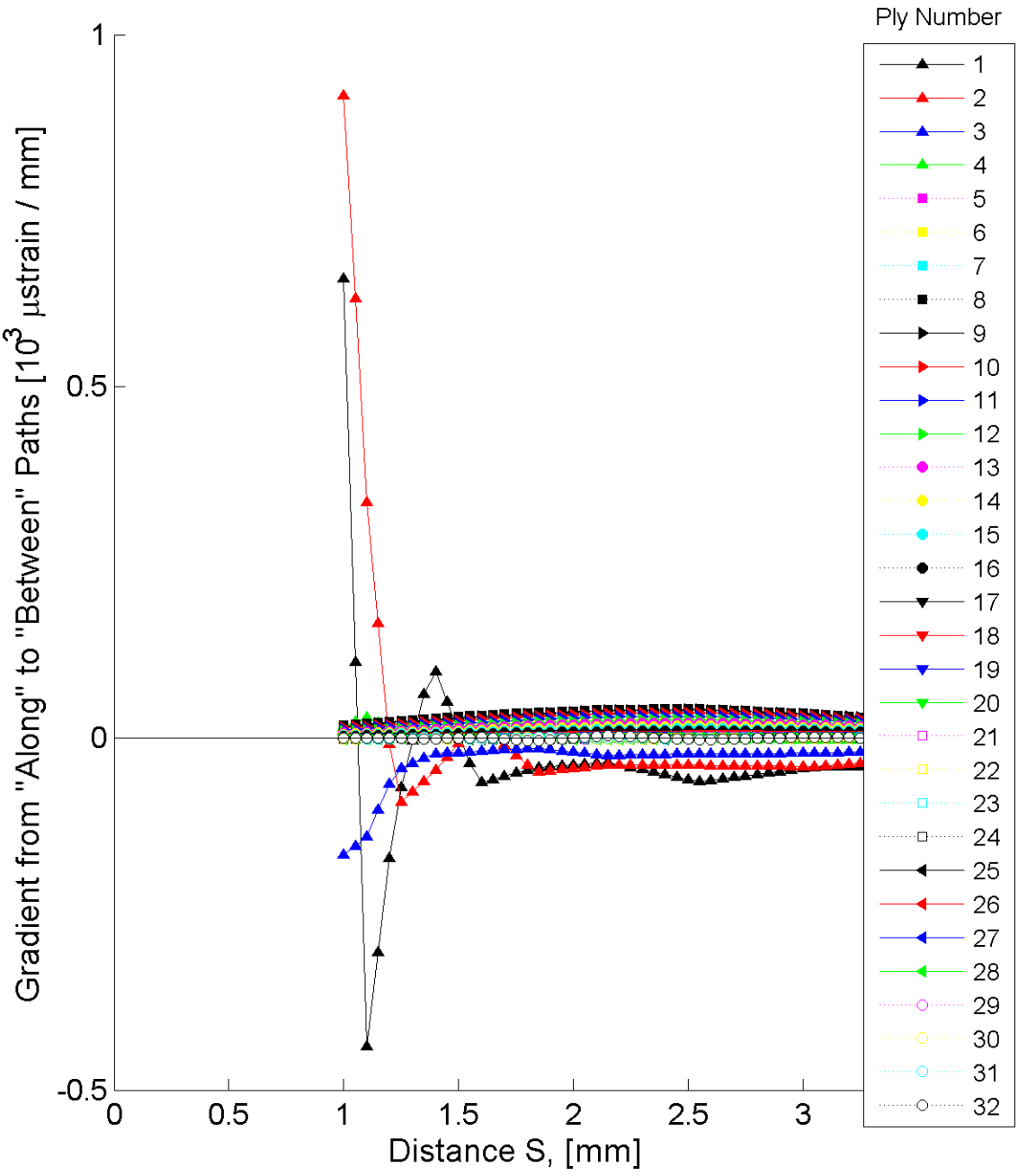

Figure B.125 Plot of the gradient of ϵ_{33} in the $\hat{S}$-direction at the midplane of each ply for the stitch crack model with laminate of $[+75/-75]_{16T}$.

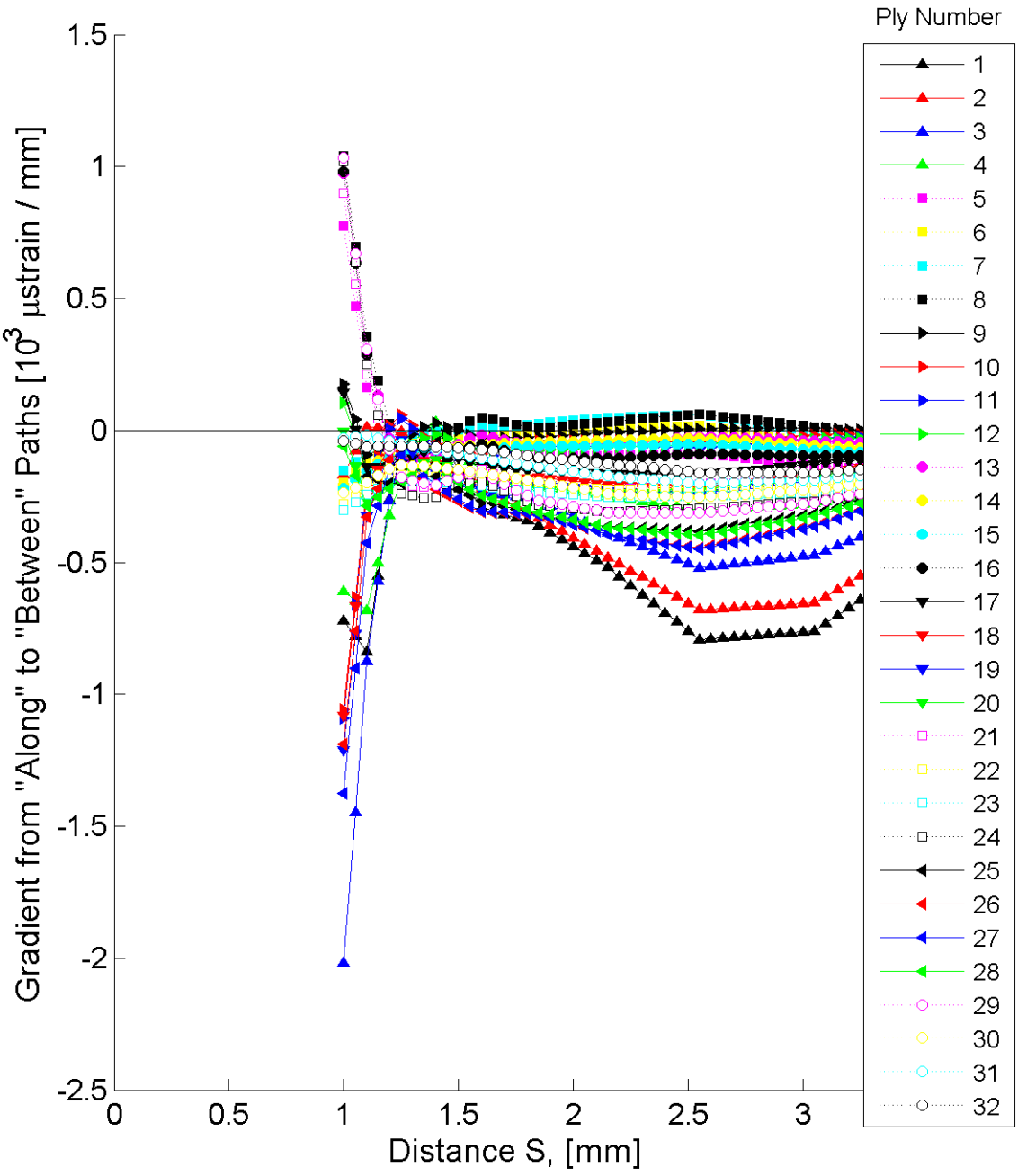

Figure B.126 Plot of the gradient of ϵ_{33} in the $\hat{S}$-direction at the midplane of each ply for the stitch crack model with laminate of $[+75_4/-75_4]_{4T}$.

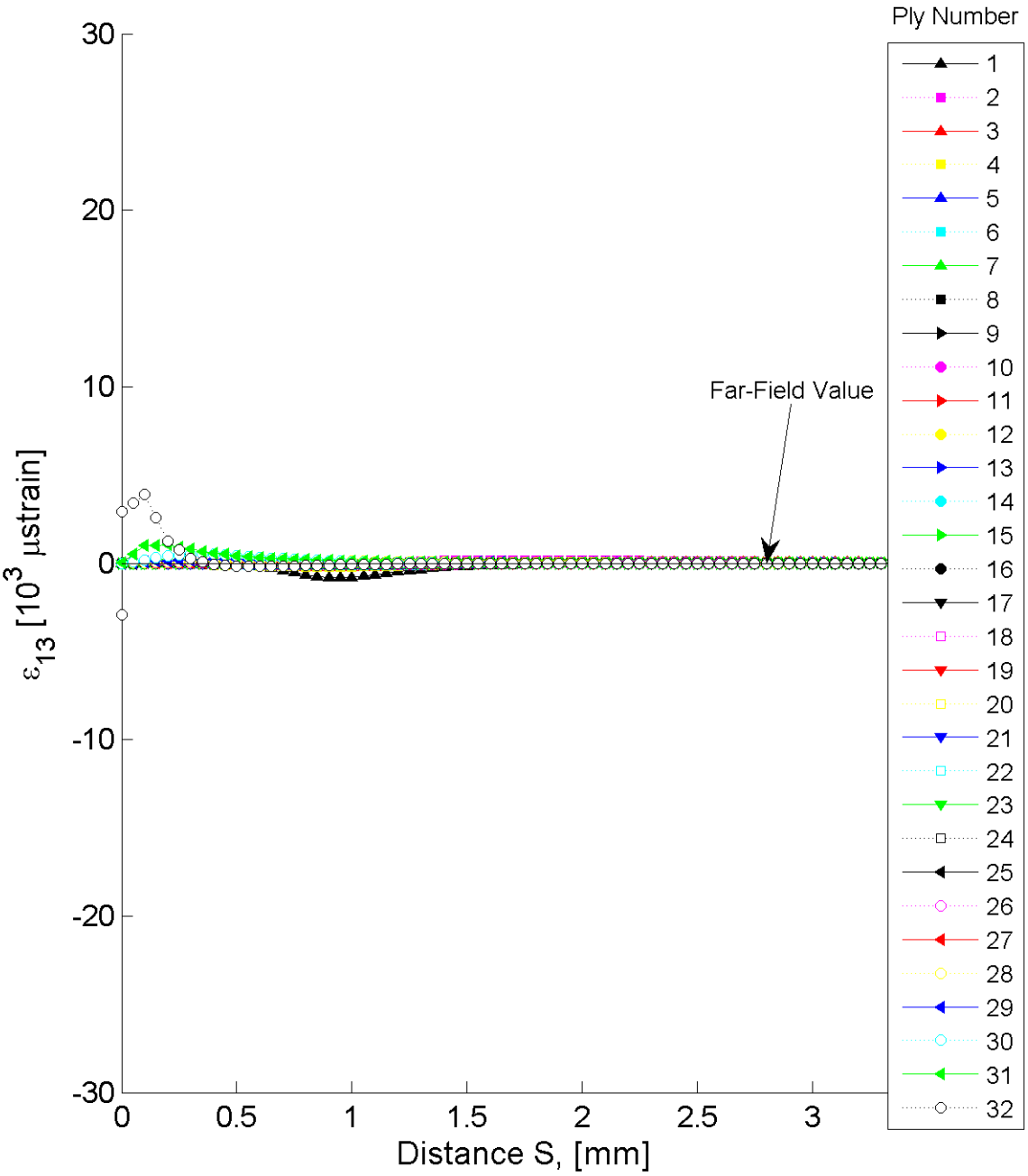

Figure B.127 Plot of ϵ_{13}, in laminate axes, along the path "between stitch cracks" at the midplane of each ply for the stitch crack model with laminate of $[+15/-15]_{16T}$.

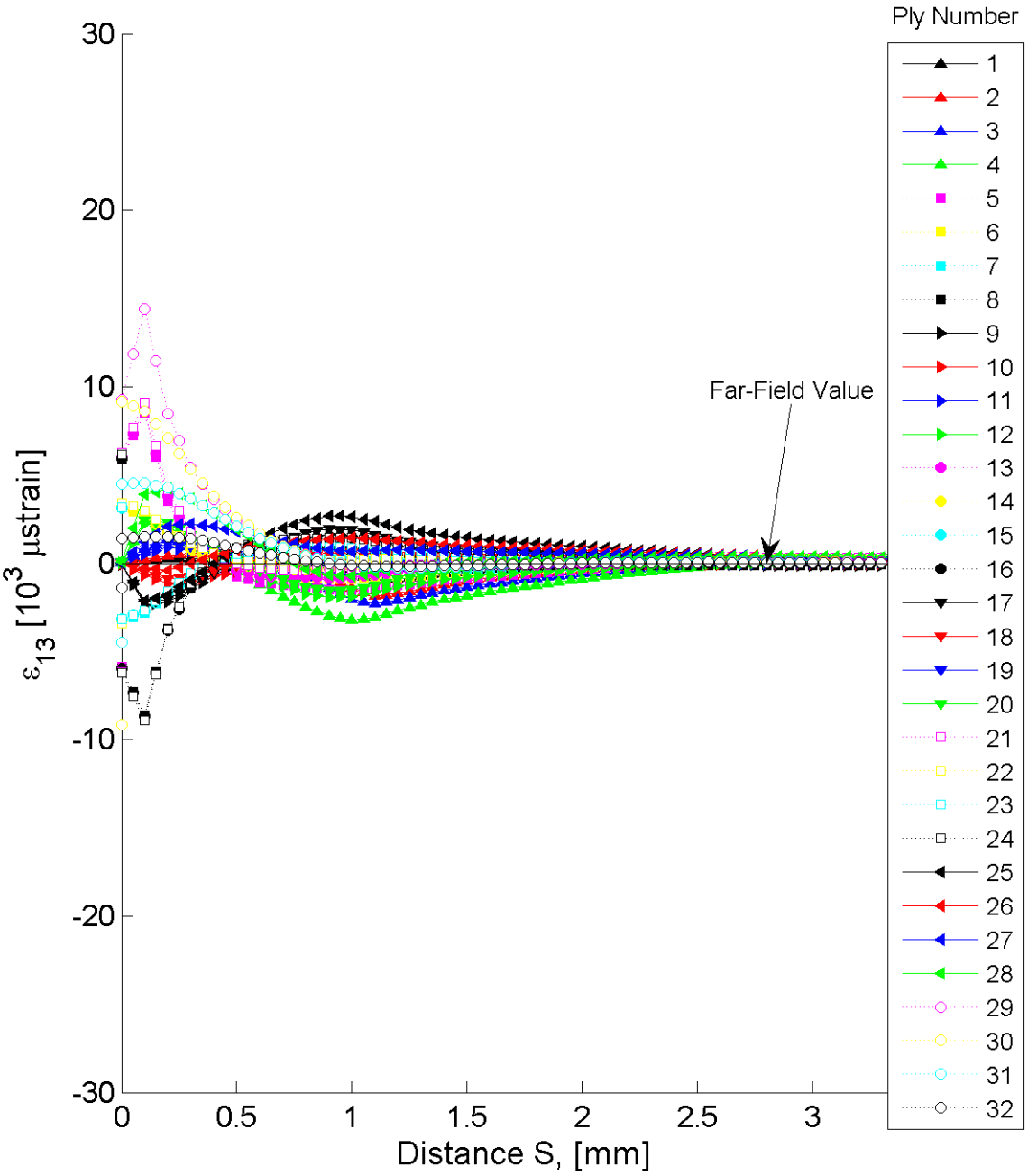

Figure B.128 Plot of ϵ_{13}, in laminate axes, along the path "between stitch cracks" at the midplane of each ply for the stitch crack model with laminate of $[+15_4/-15_4]_{4T}$.

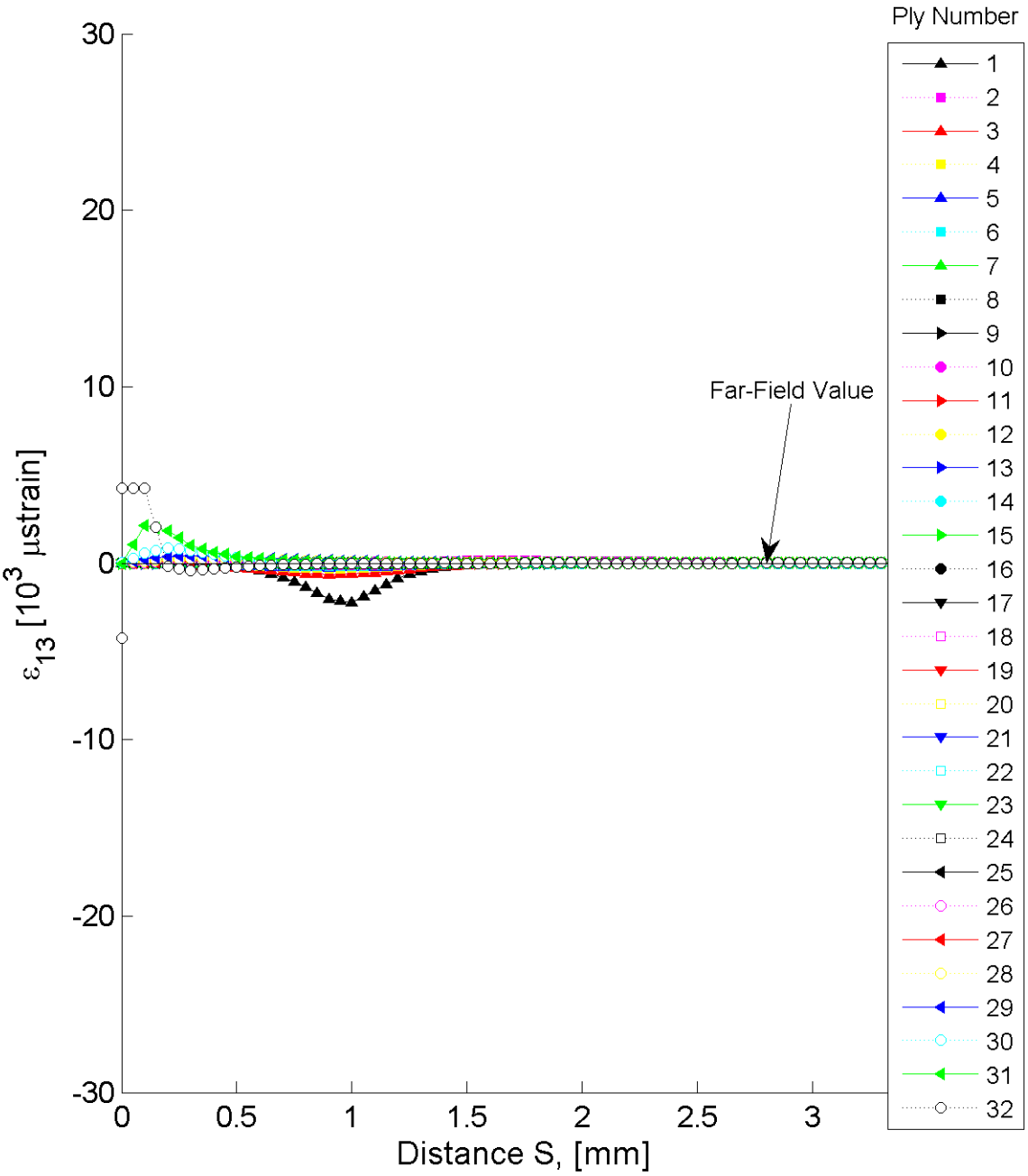

Figure B.129 Plot of ϵ_{13}, in laminate axes, along the path "between stitch cracks" at the midplane of each ply for the stitch crack model with laminate of $[+30/-30]_{16T}$.

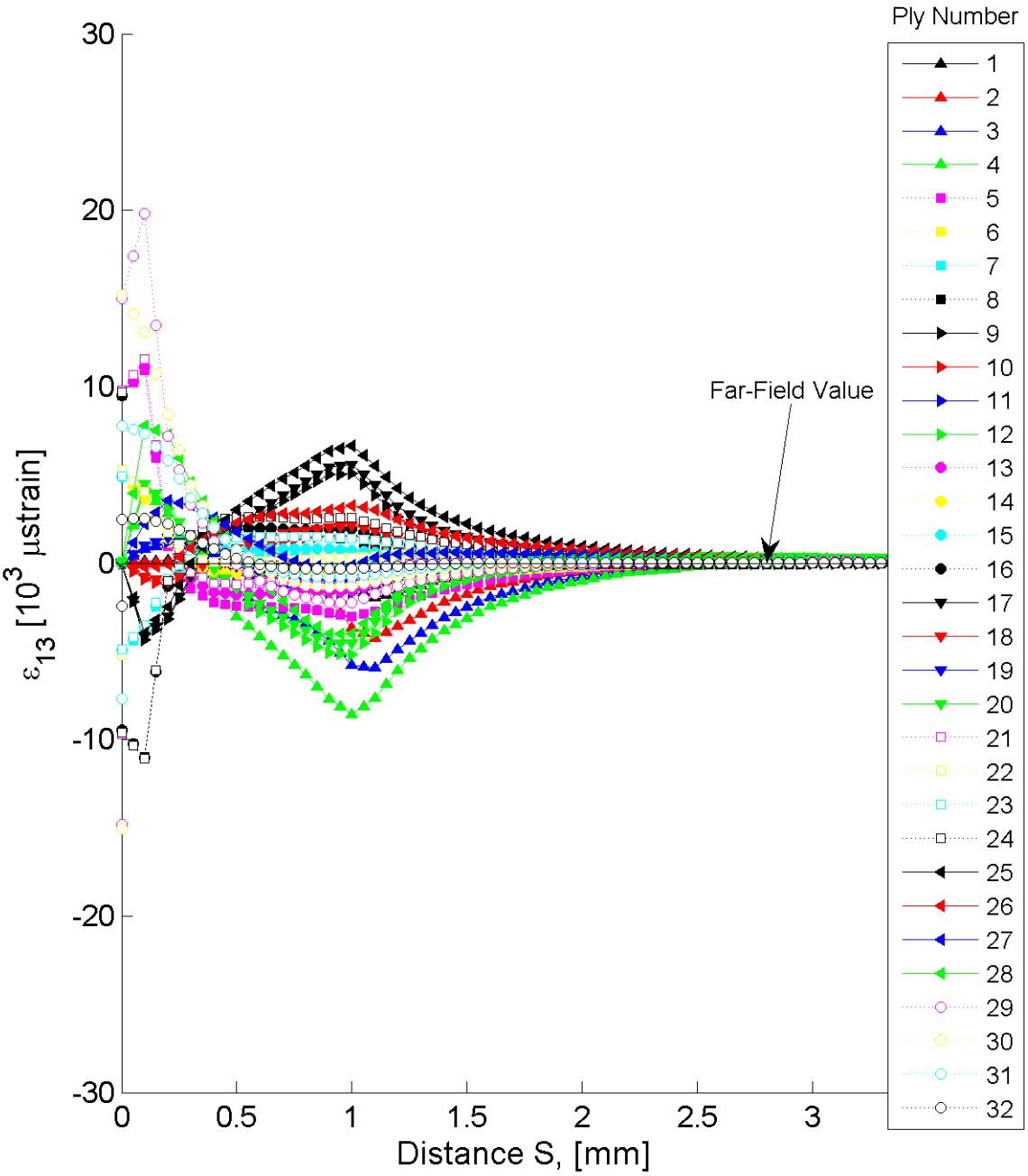

Figure B.130 Plot of ϵ_{13}, in laminate axes, along the path "between stitch cracks" at the midplane of each ply for the stitch crack model with laminate of $[+30_4/-30_4]_{4T}$.

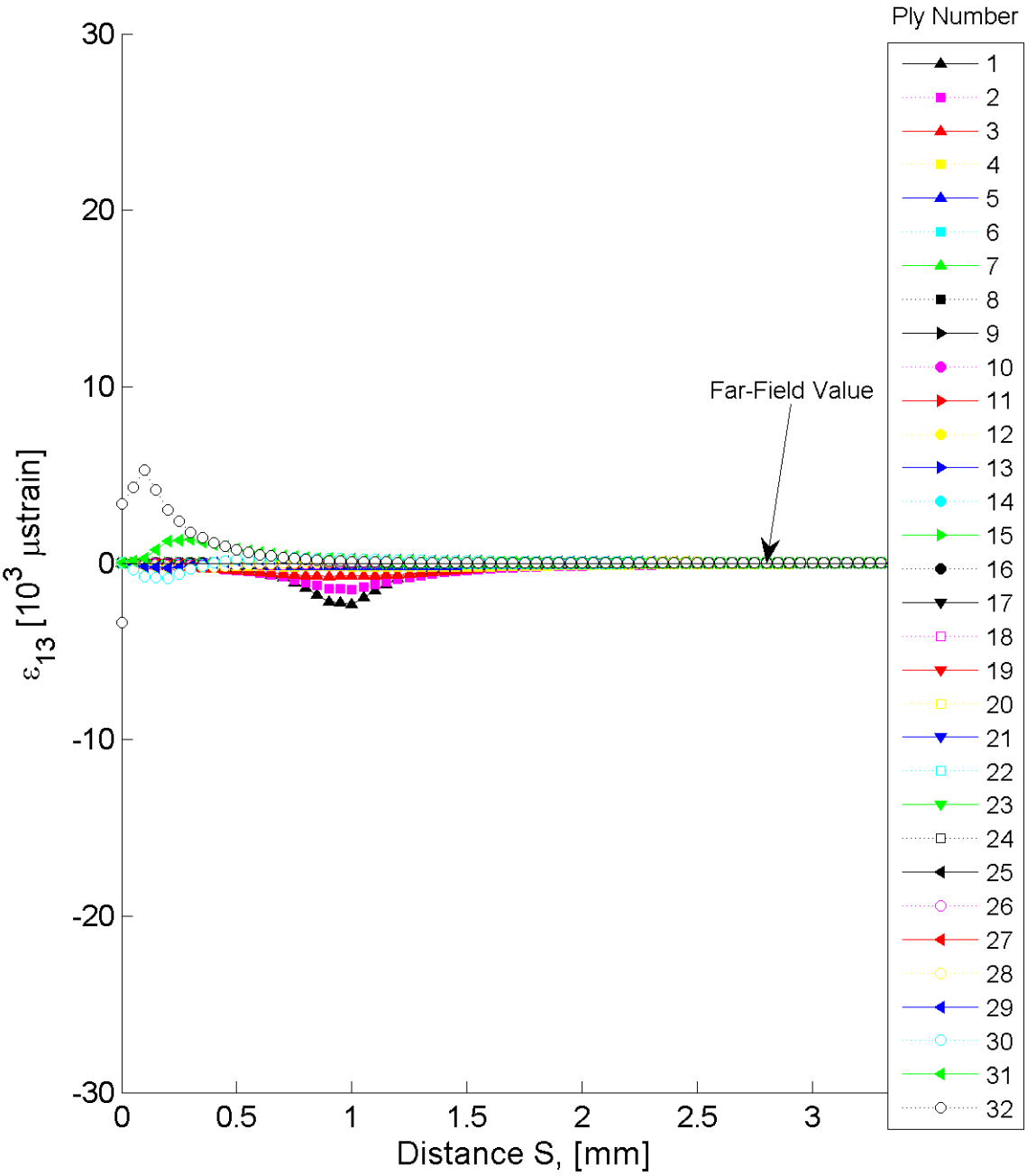

Figure B.131 Plot of ϵ_{13}, in laminate axes, along the path "between stitch cracks" at the midplane of each ply for the stitch crack model with laminate of $[+60/-60]_{16T}$.

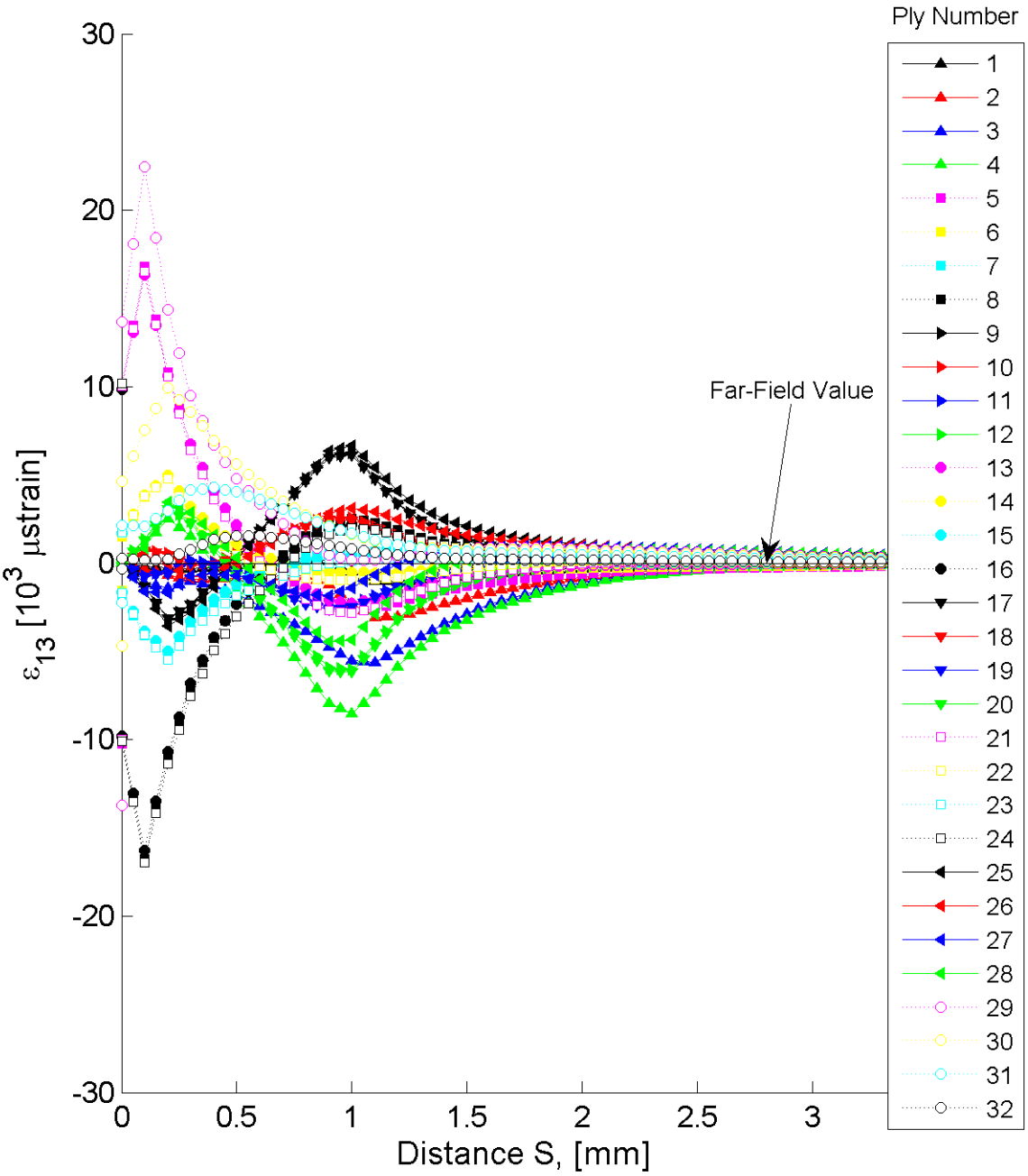

Figure B.132 Plot of ϵ_{13}, in laminate axes, along the path "between stitch cracks" at the midplane of each ply for the stitch crack model with laminate of $[+60_4/-60_4]_{4T}$.

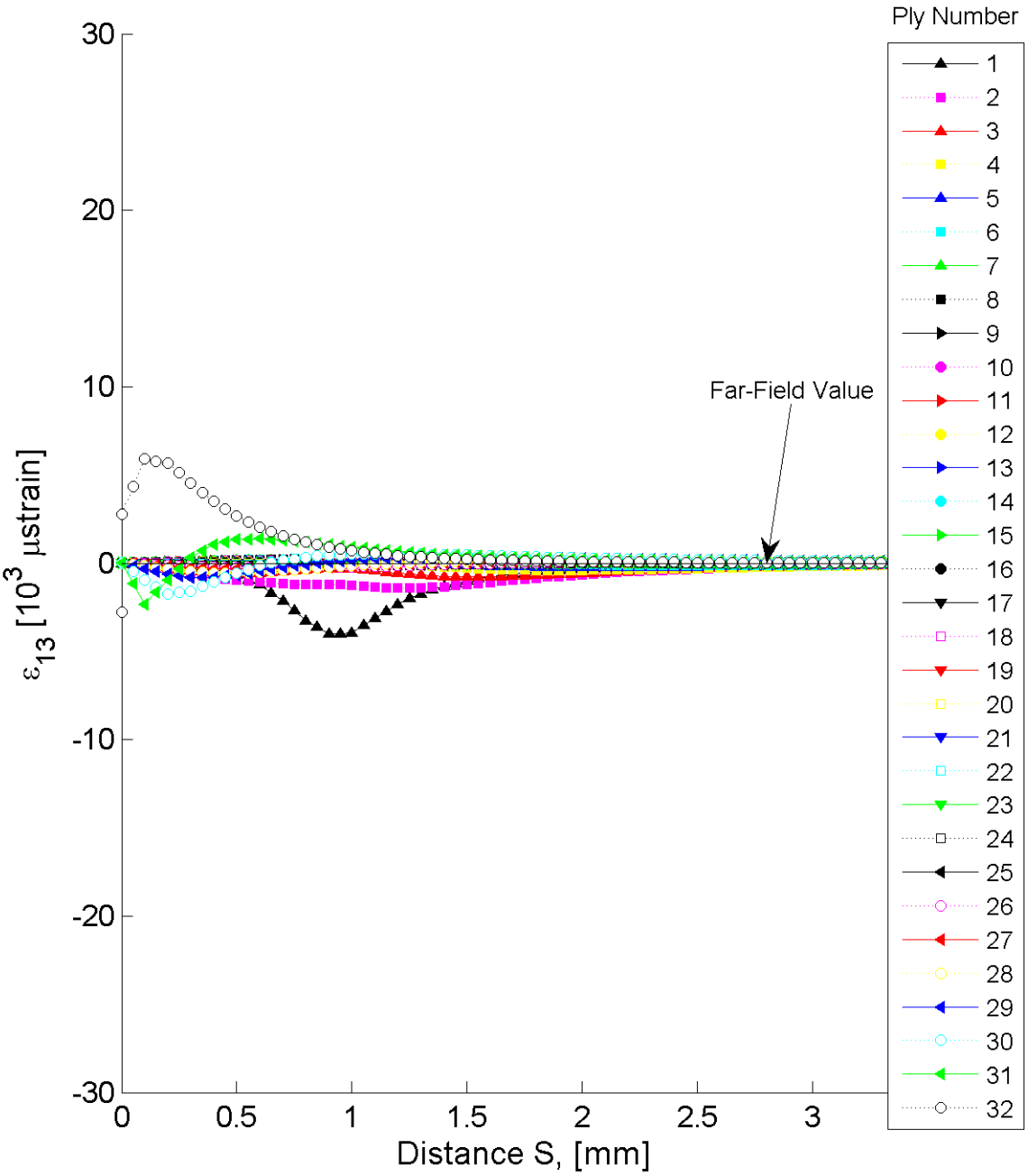

Figure B.133 Plot of ϵ_{13}, in laminate axes, along the path "between stitch cracks" at the midplane of each ply for the stitch crack model with laminate of $[+75/-75]_{16T}$.

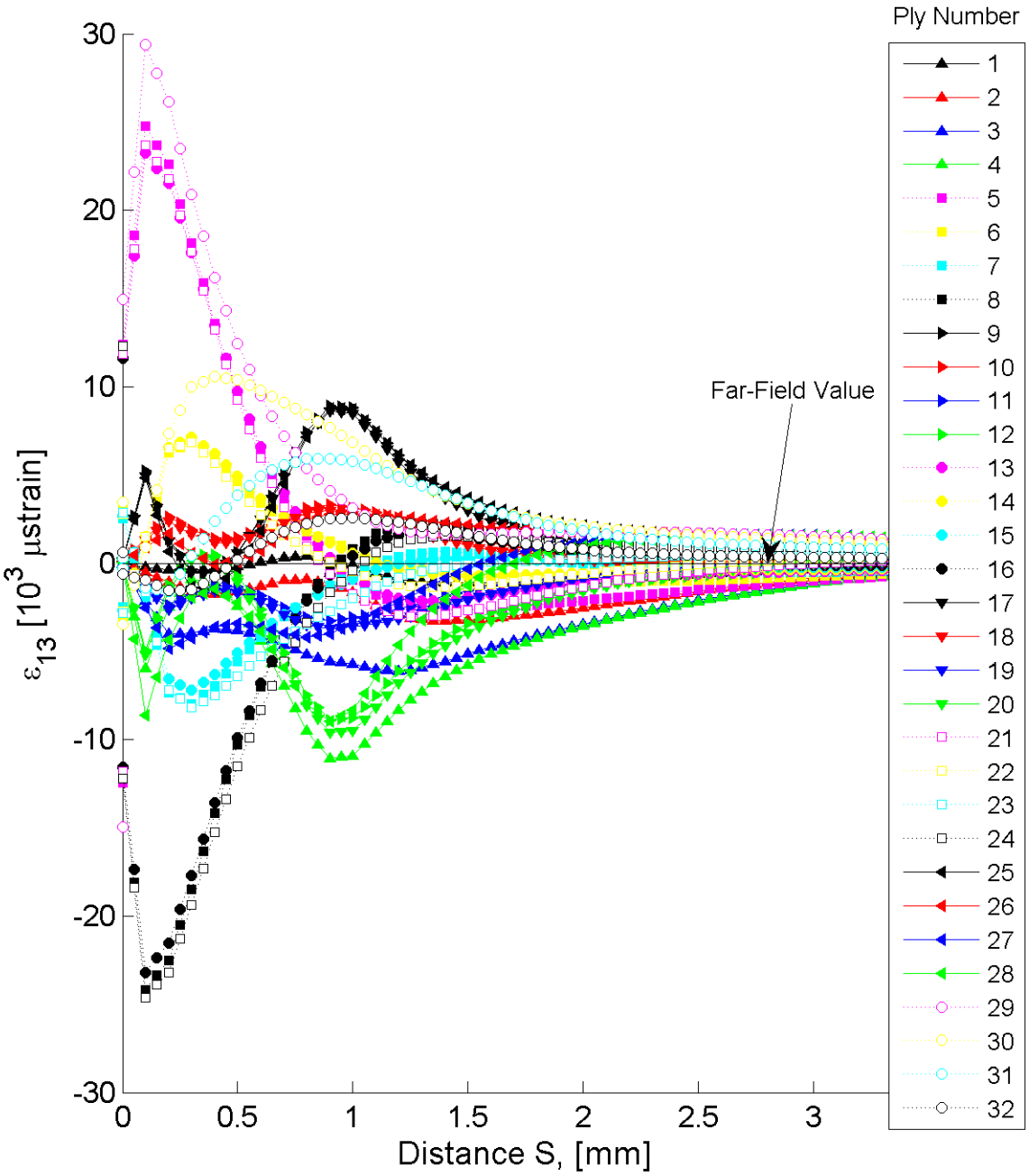

Figure B.134 Plot of ϵ_{13}, in laminate axes, along the path "between stitch cracks" at the midplane of each ply for the stitch crack model with laminate of $[+75_4/-75_4]_{4T}$.

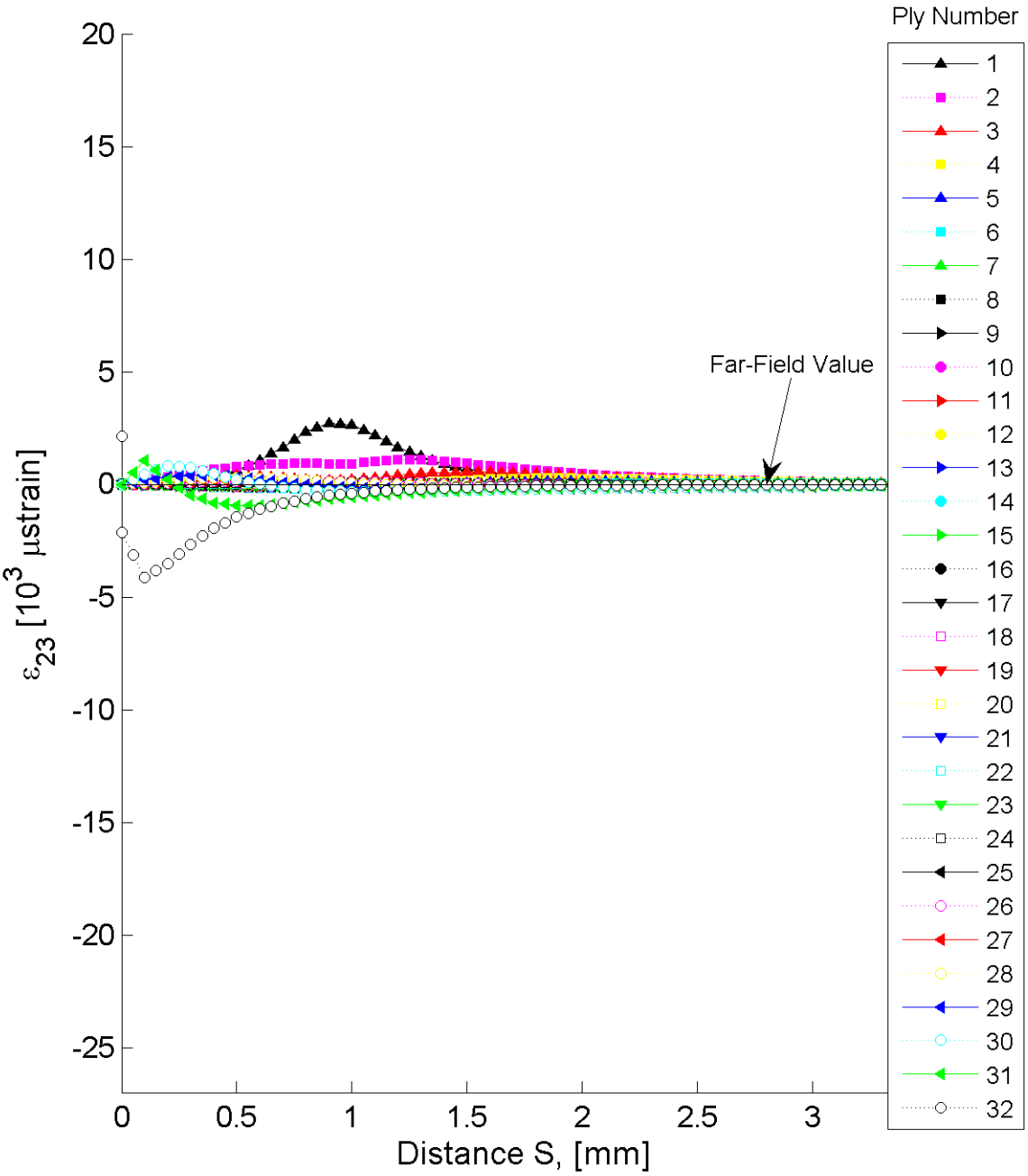

Figure B.135 Plot of ϵ_{23}, in laminate axes, along the path "between stitch cracks" at the midplane of each ply for the stitch crack model with laminate of $[+15/-15]_{16T}$.

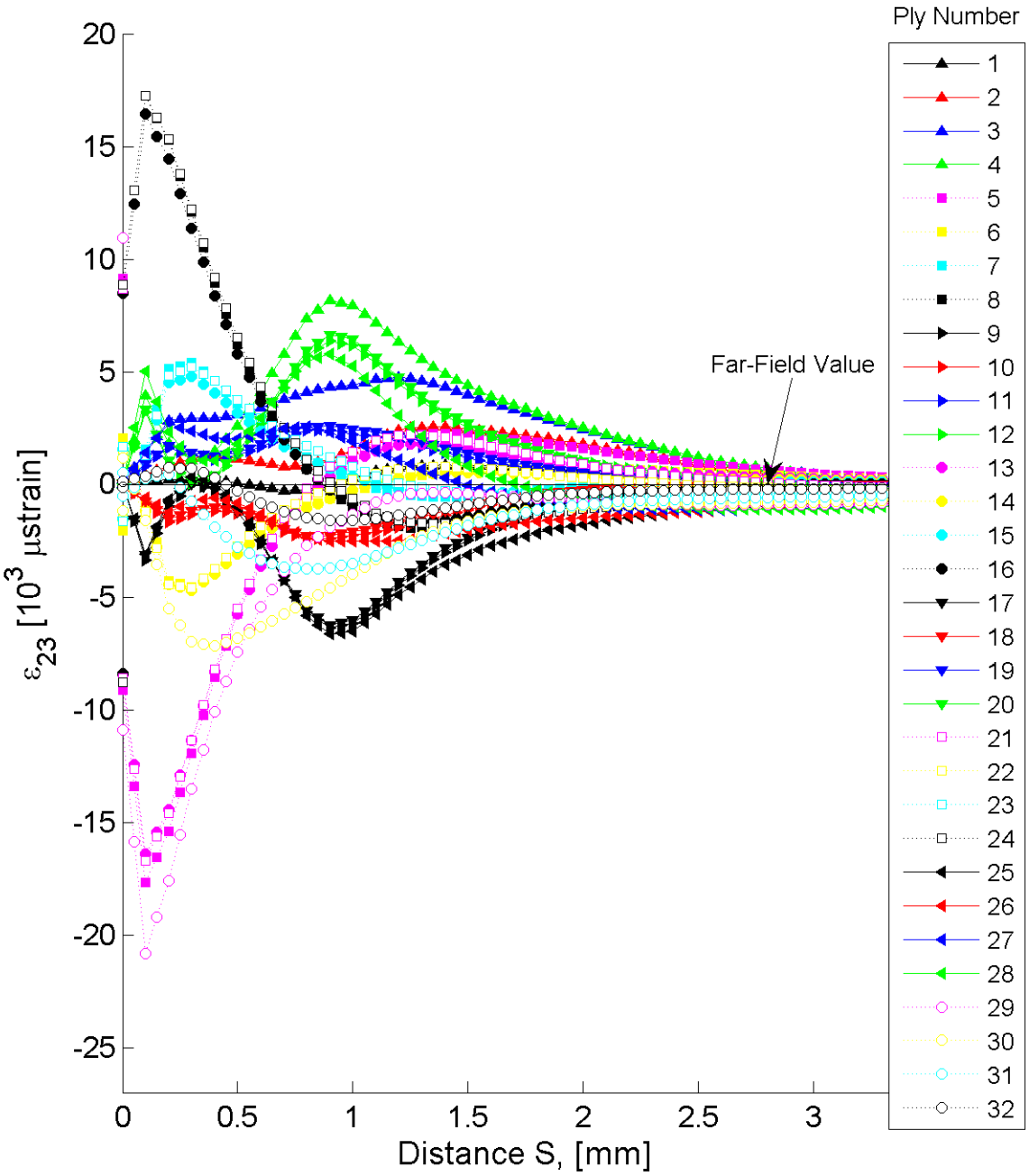

Figure B.136 Plot of ϵ_{23}, in laminate axes, along the path "between stitch cracks" at the midplane of each ply for the stitch crack model with laminate of $[+15_4/-15_4]_{4T}$.

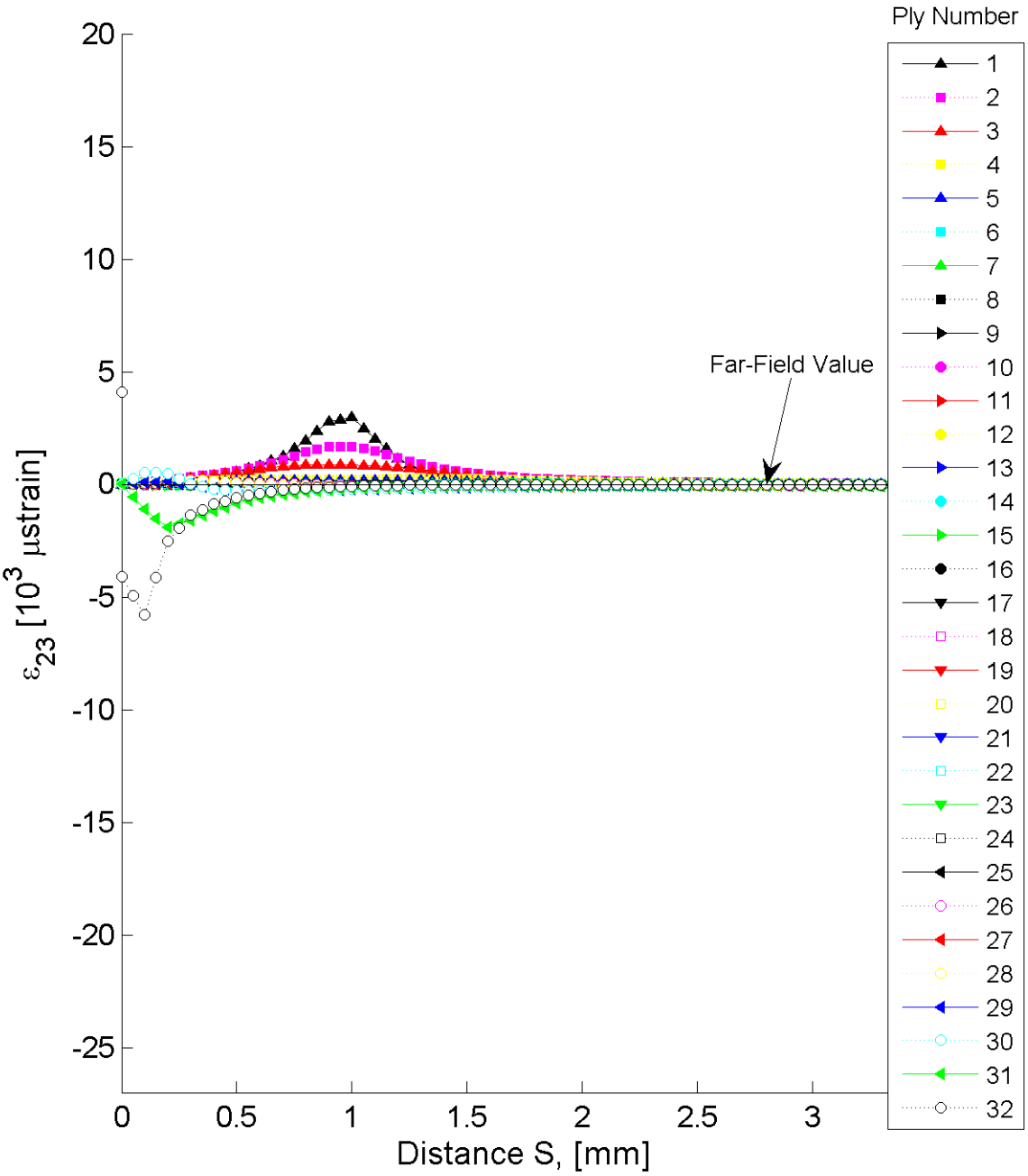

Figure B.137 Plot of ϵ_{23}, in laminate axes, along the path "between stitch cracks" at the midplane of each ply for the stitch crack model with laminate of $[+30/-30]_{16T}$.

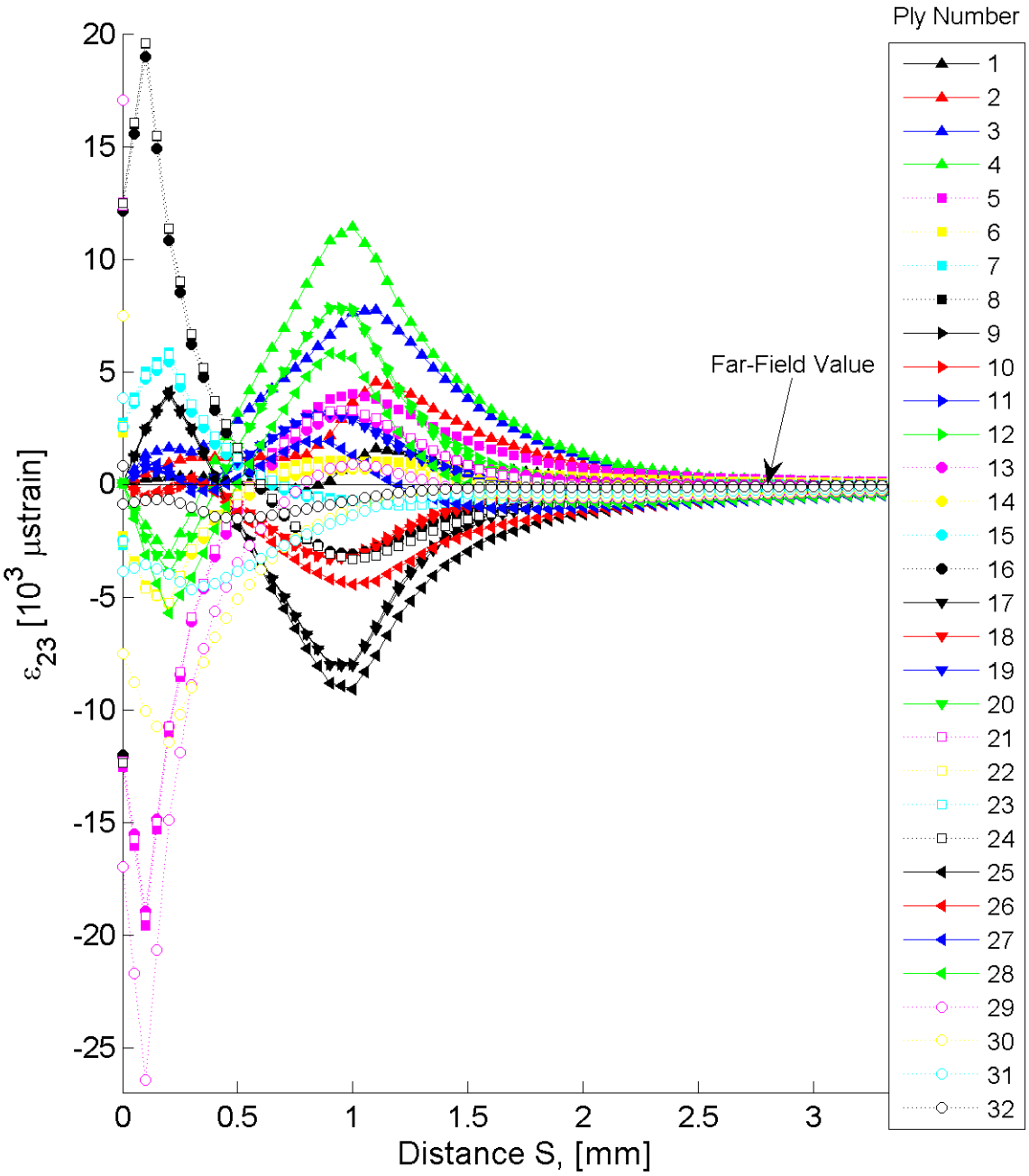

Figure B.138 Plot of ϵ_{23}, in laminate axes, along the path "between stitch cracks" at the midplane of each ply for the stitch crack model with laminate of $[+30_4/-30_4]_{4T}$.

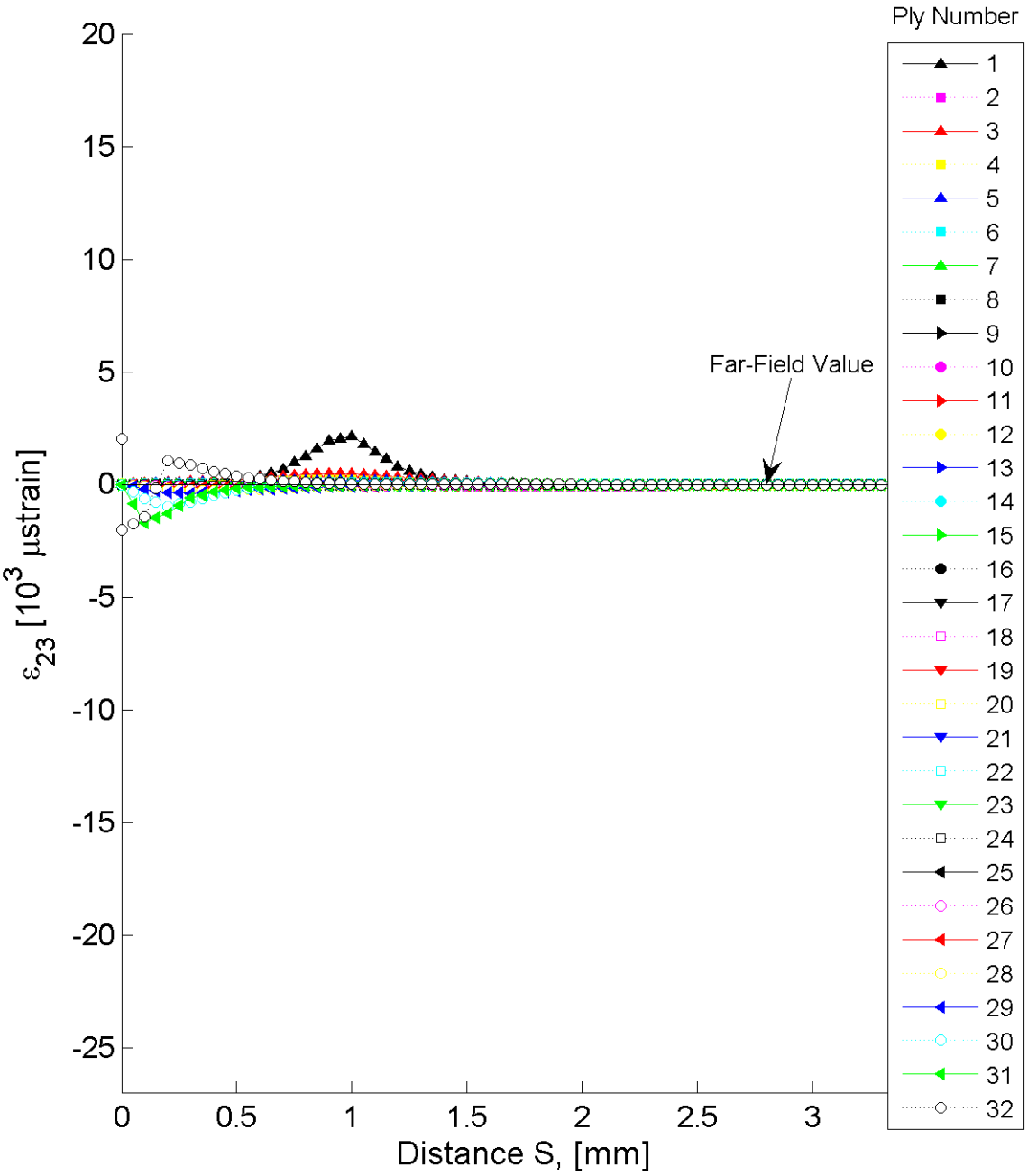

Figure B.139 Plot of ϵ_{23}, in laminate axes, along the path "between stitch cracks" at the midplane of each ply for the stitch crack model with laminate of $[+60/-60]_{16T}$.

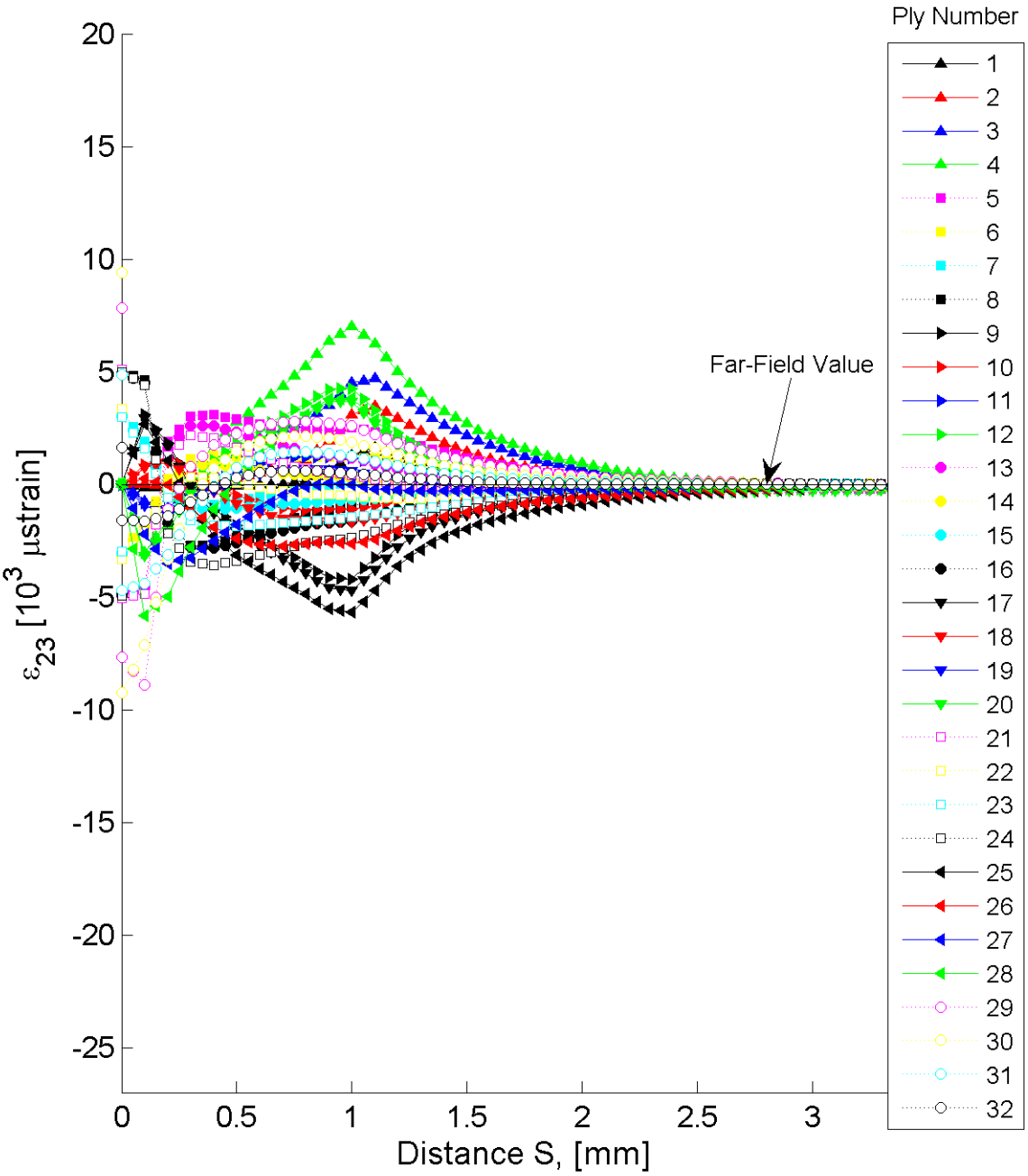

Figure B.140 Plot of ϵ_{23}, in laminate axes, along the path "between stitch cracks" at the midplane of each ply for the stitch crack model with laminate of $[+60_4/-60_4]_{4T}$.

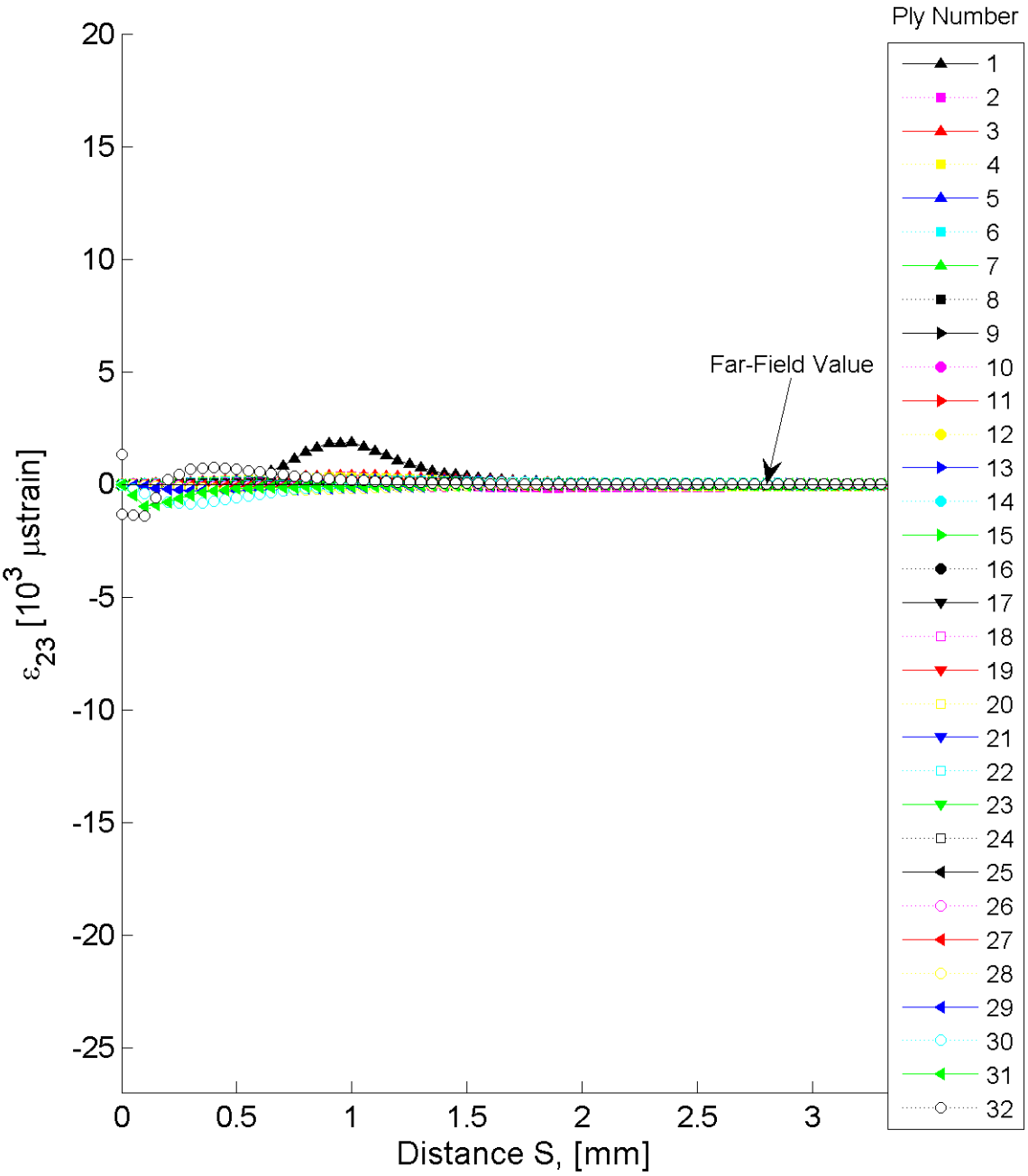

Figure B.141 Plot of ϵ_{23}, in laminate axes, along the path "between stitch cracks" at the midplane of each ply for the stitch crack model with laminate of $[+75/-75]_{16T}$.

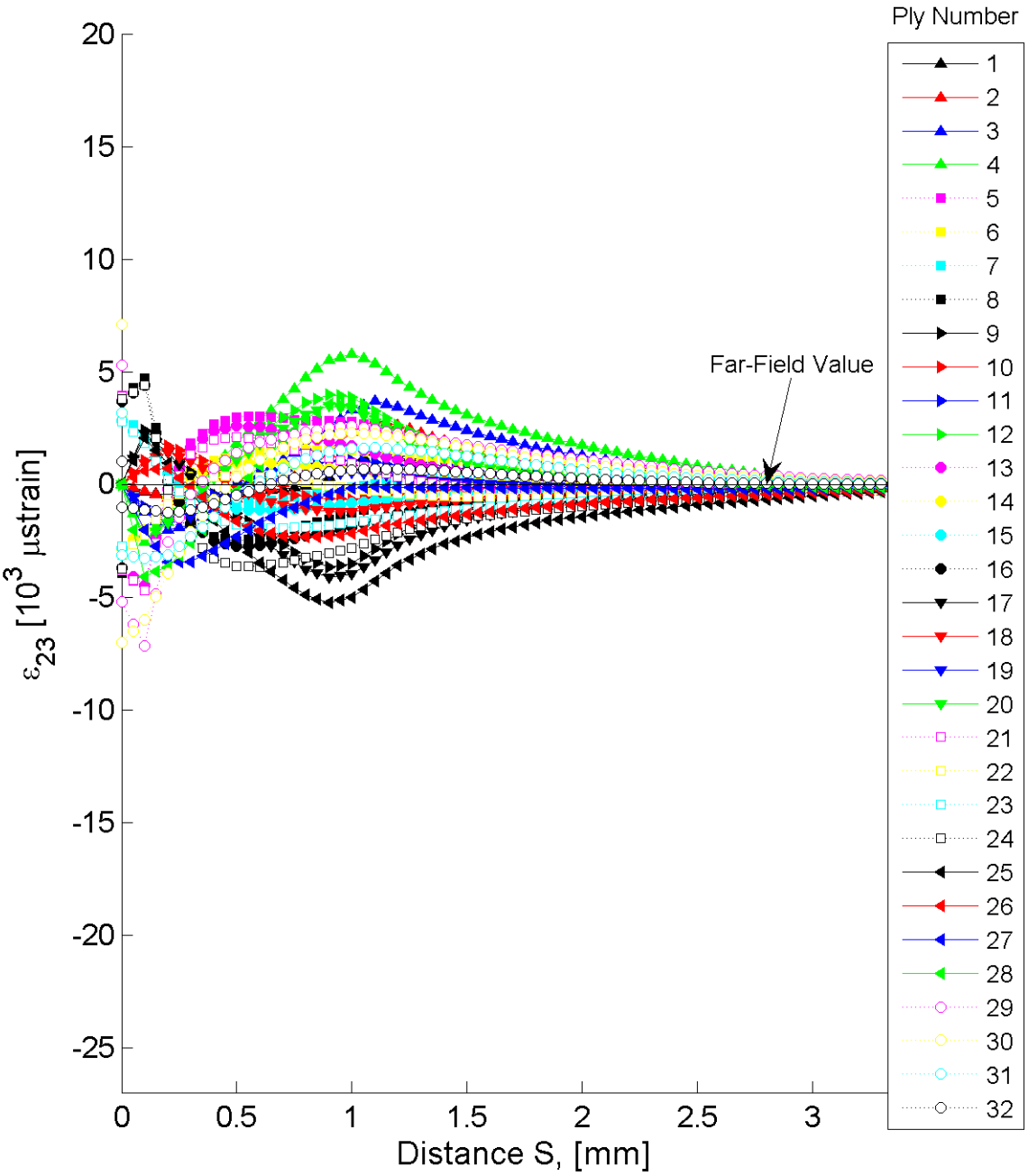

Figure B.142 Plot of ϵ_{23}, in laminate axes, along the path "between stitch cracks" at the midplane of each ply for the stitch crack model with laminate of $[+75_4/-75_4]_{4T}$.

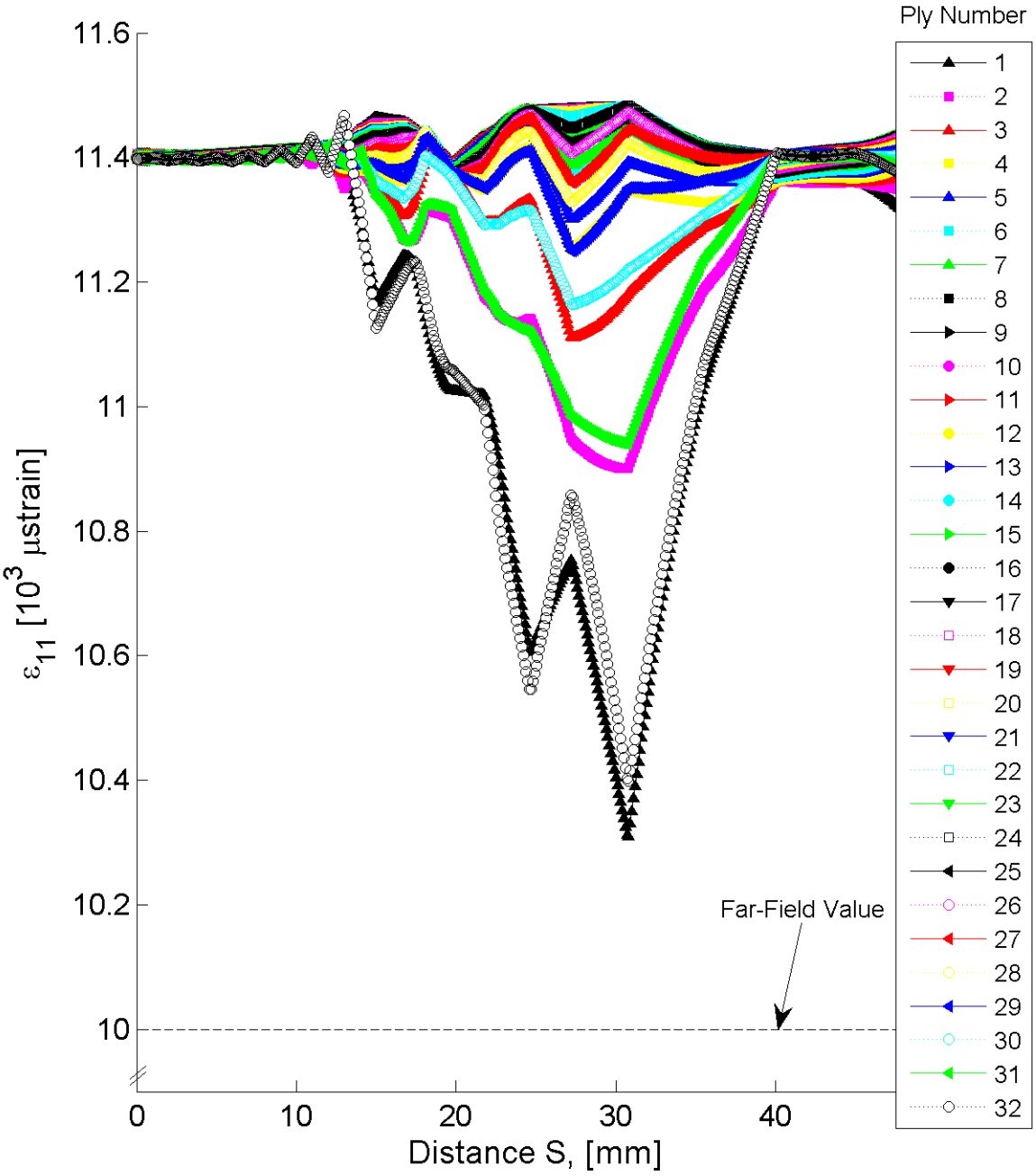

Figure B.143 Plot of ϵ_{11}, in laminate axes, along the path at the midplane of each ply for the delamination model with laminate of $[+30/-30]_{16T}$.

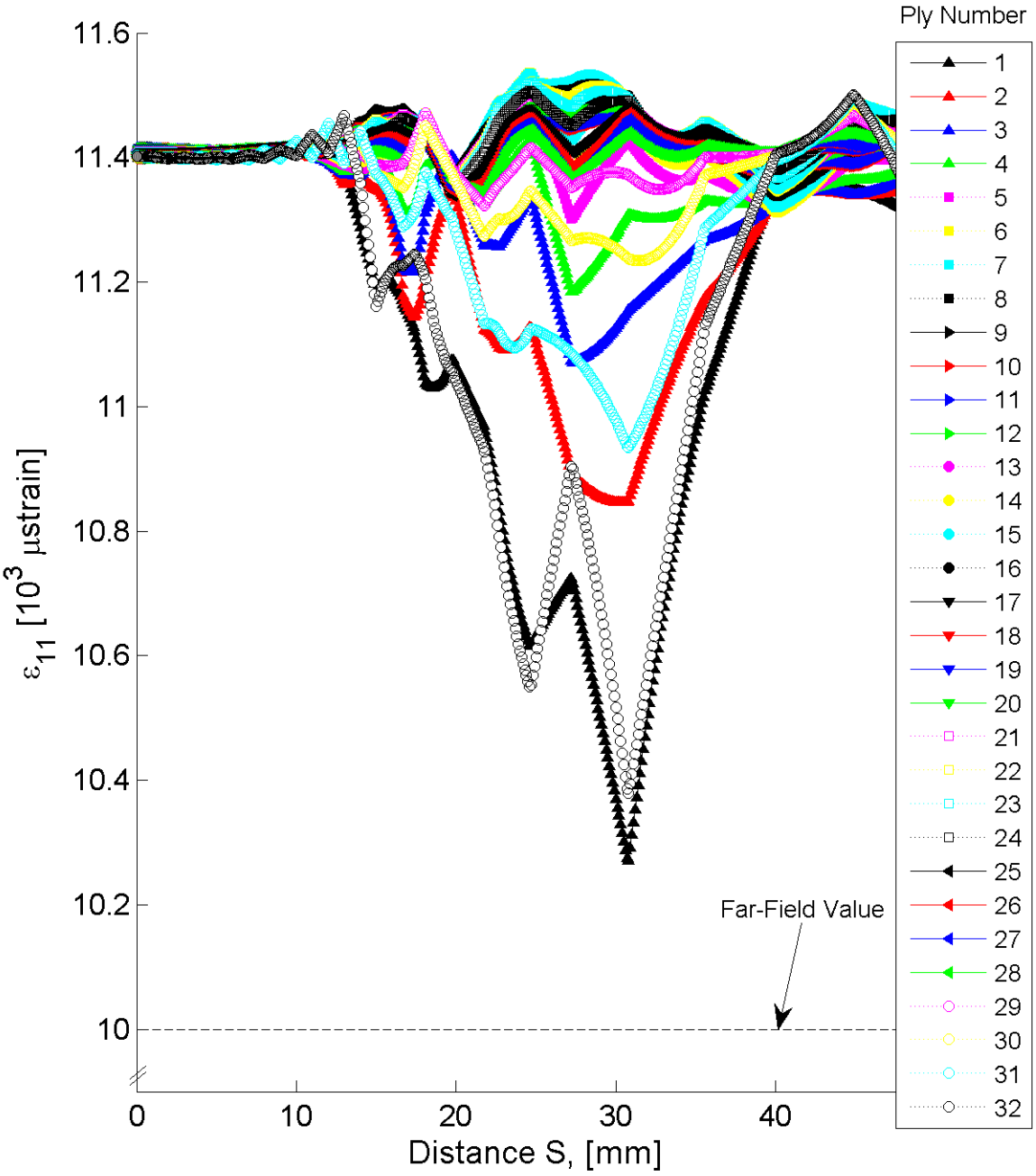

Figure B.144 Plot of ϵ_{11}, in laminate axes, along the path at the midplane of each ply for the delamination model with laminate of $[+30_4/-30_4]_{4T}$.

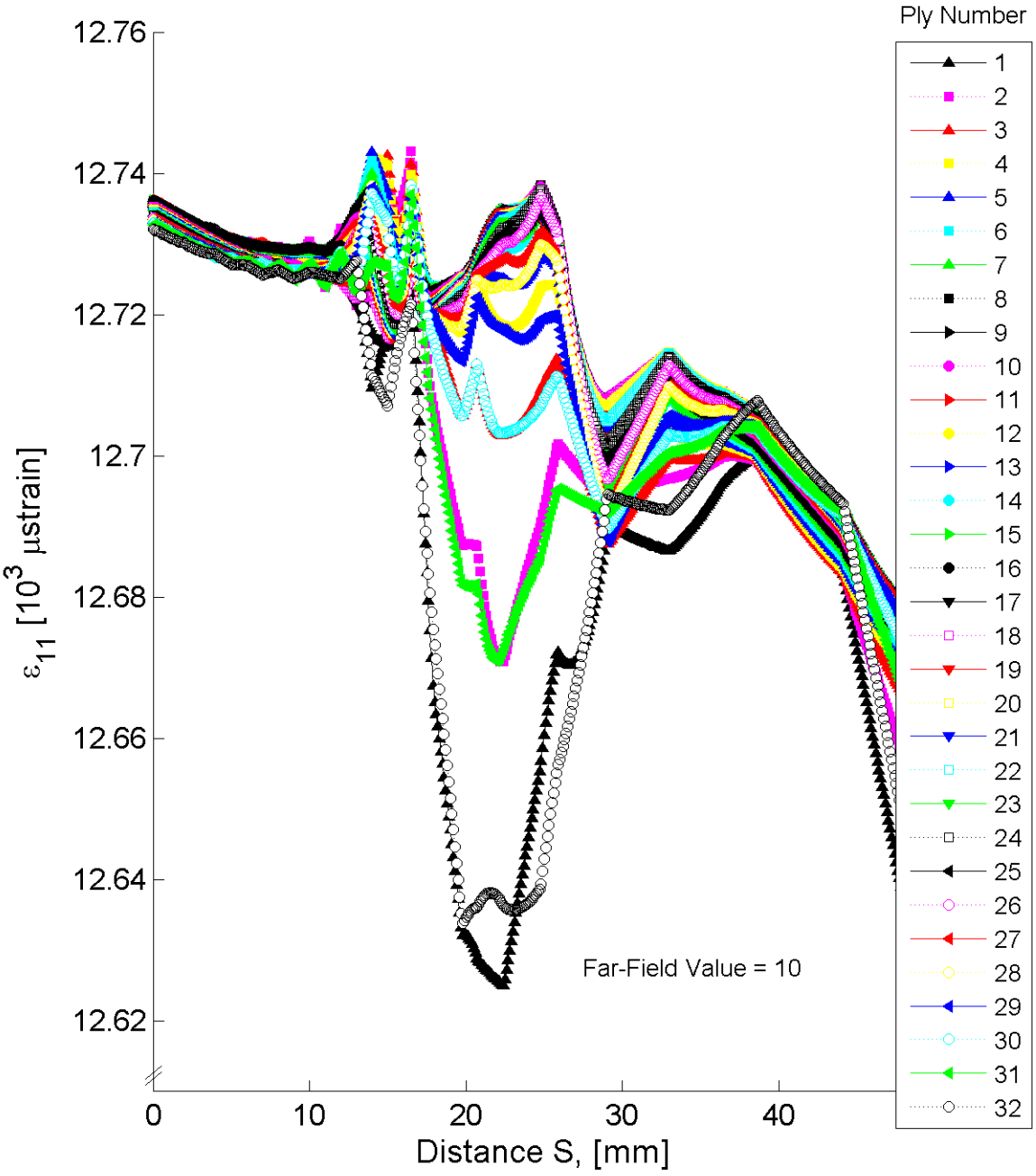

Figure B.145 Plot of ϵ_{11}, in laminate axes, along the path at the midplane of each ply for the delamination model with laminate of $[+60/-60]_{16T}$.

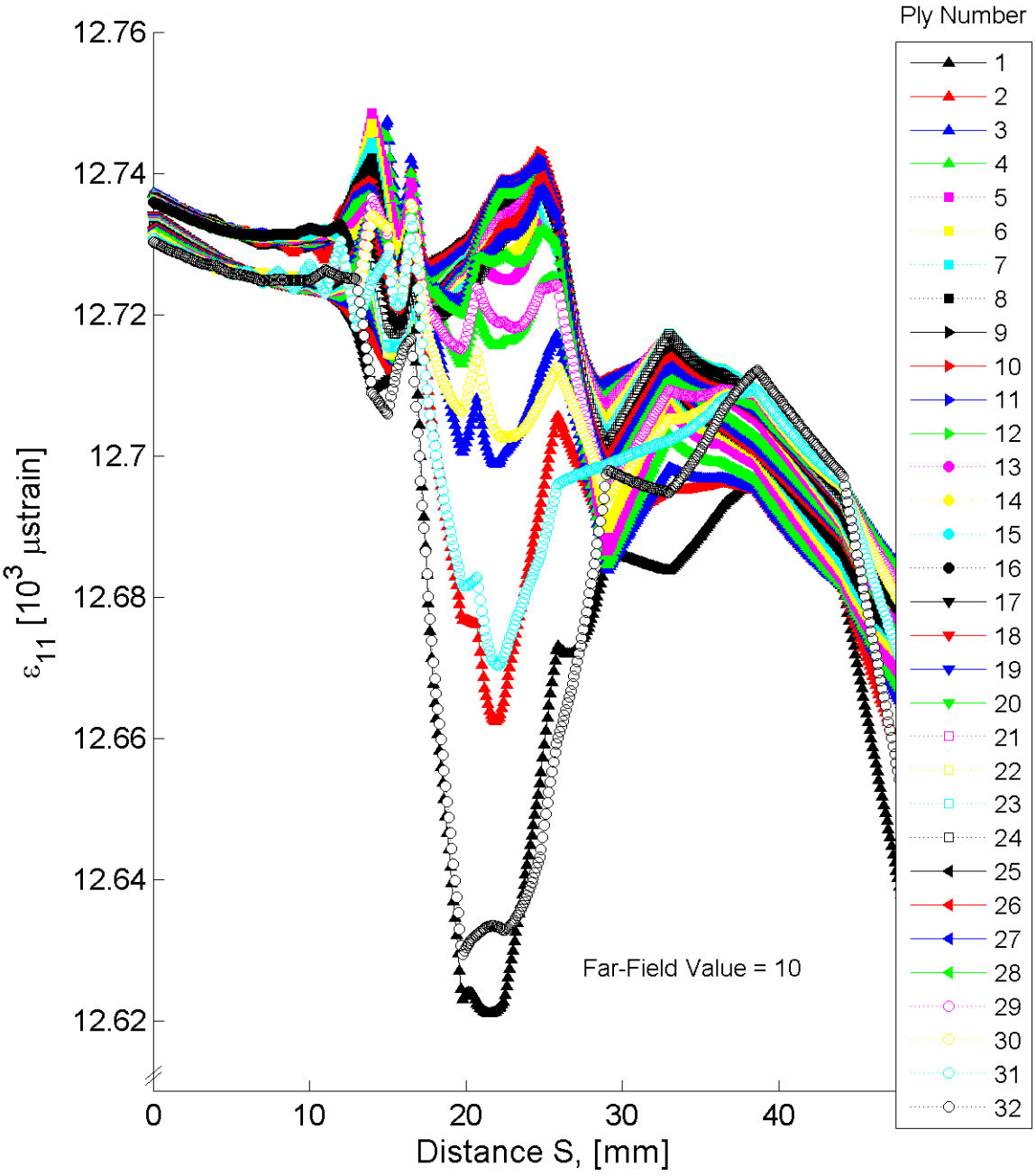

Figure B.146 Plot of ϵ_{11}, in laminate axes, along the path at the midplane of each ply for the delamination model with laminate of $[+60_4/-60_4]_{4T}$.

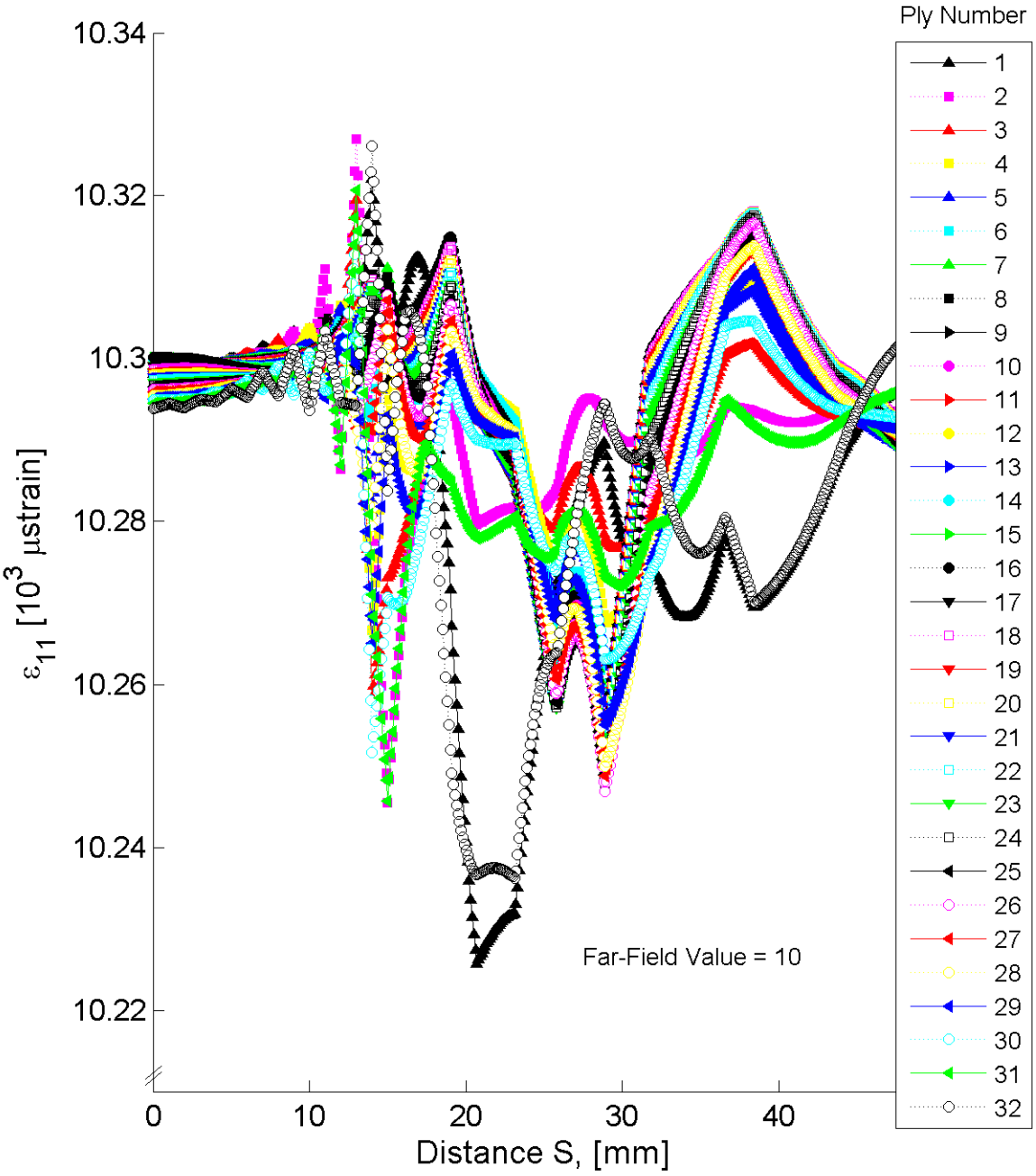

Figure B.147 Plot of ϵ_{11}, in laminate axes, along the path at the midplane of each ply for the stitch crack model with laminate of $[+75/-75]_{16T}$.

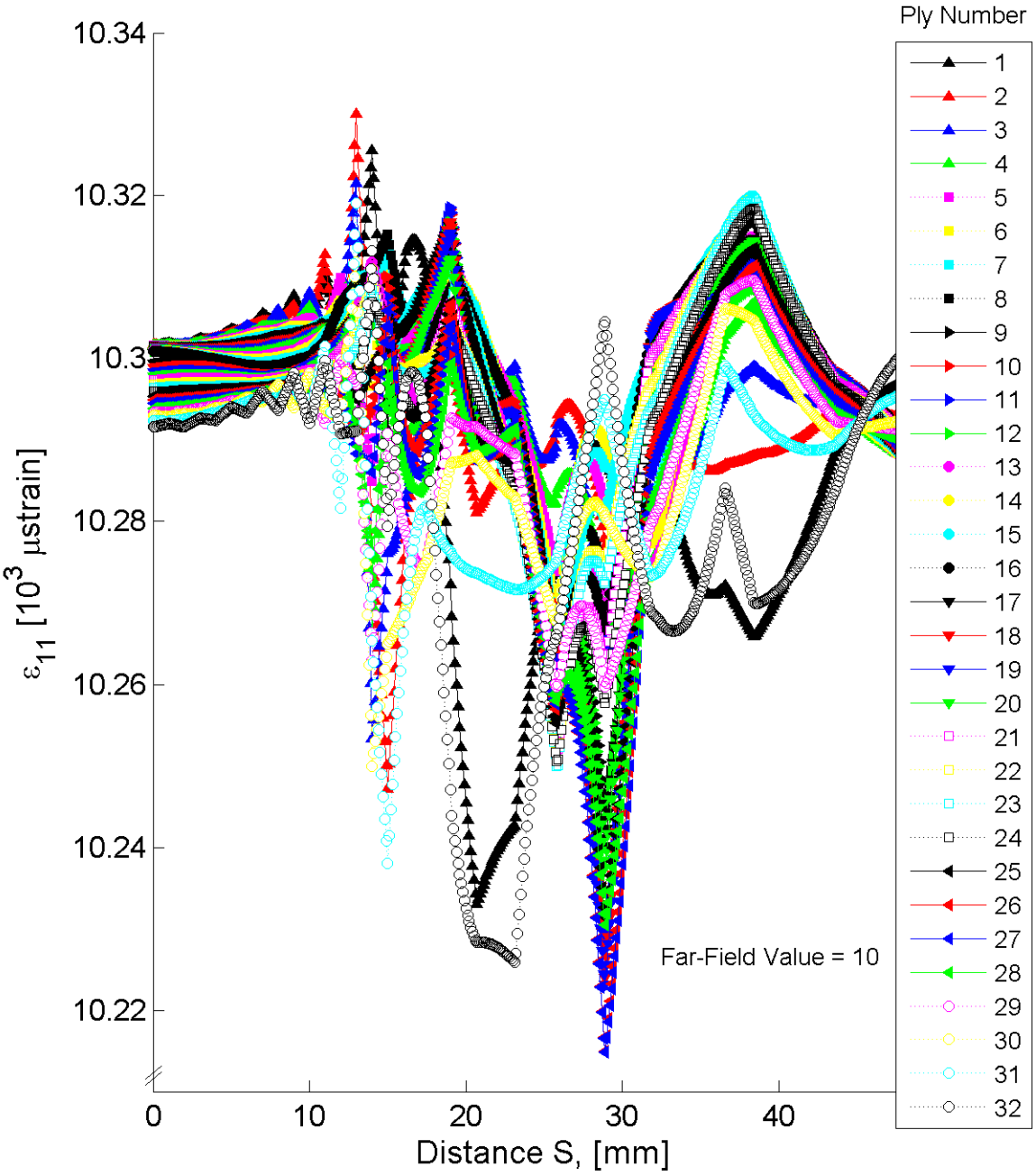

Figure B.148 Plot of ϵ_{11}, in laminate axes, along the path at the midplane of each ply for the delamination model with laminate of $[+75_4/-75_4]_{4T}$.

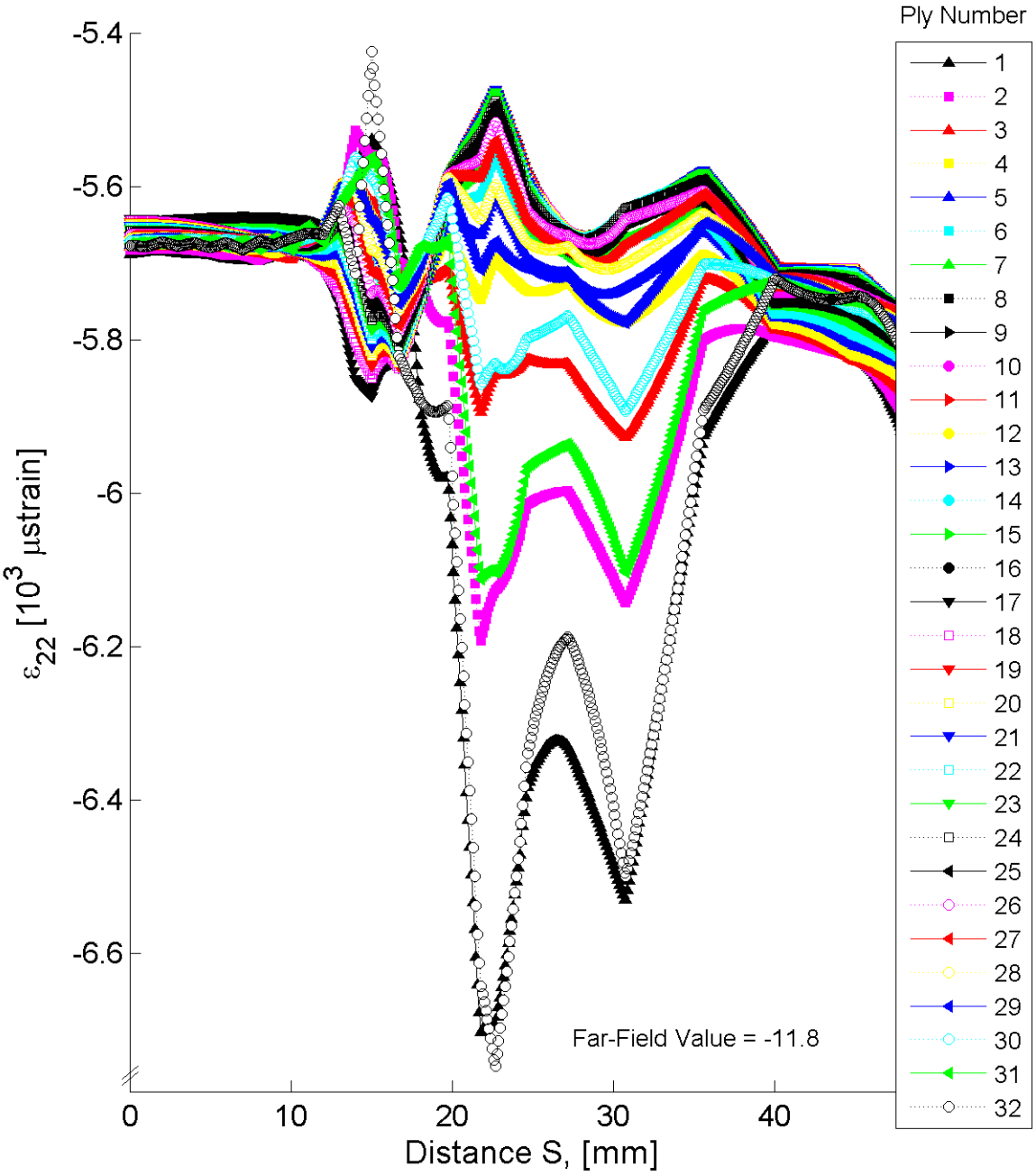

Figure B.149 Plot of ϵ_{22}, in laminate axes, along the path at the midplane of each ply for the delamination model with laminate of $[+30/-30]_{16T}$.

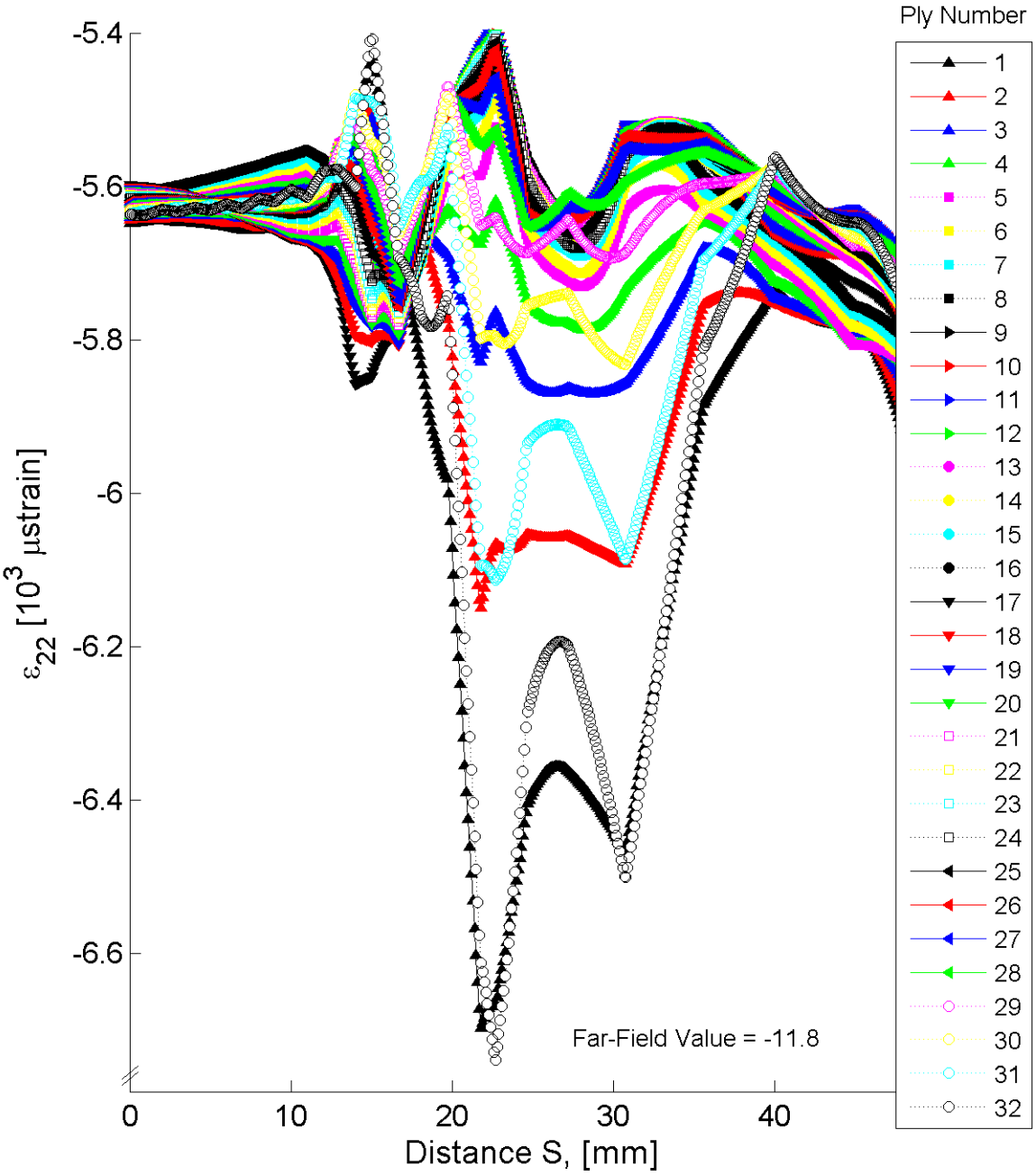

Figure B.150 Plot of ϵ_{22}, in laminate axes, along the path at the midplane of each ply for the delamination model with laminate of $[+30_4/-30_4]_{4T}$.

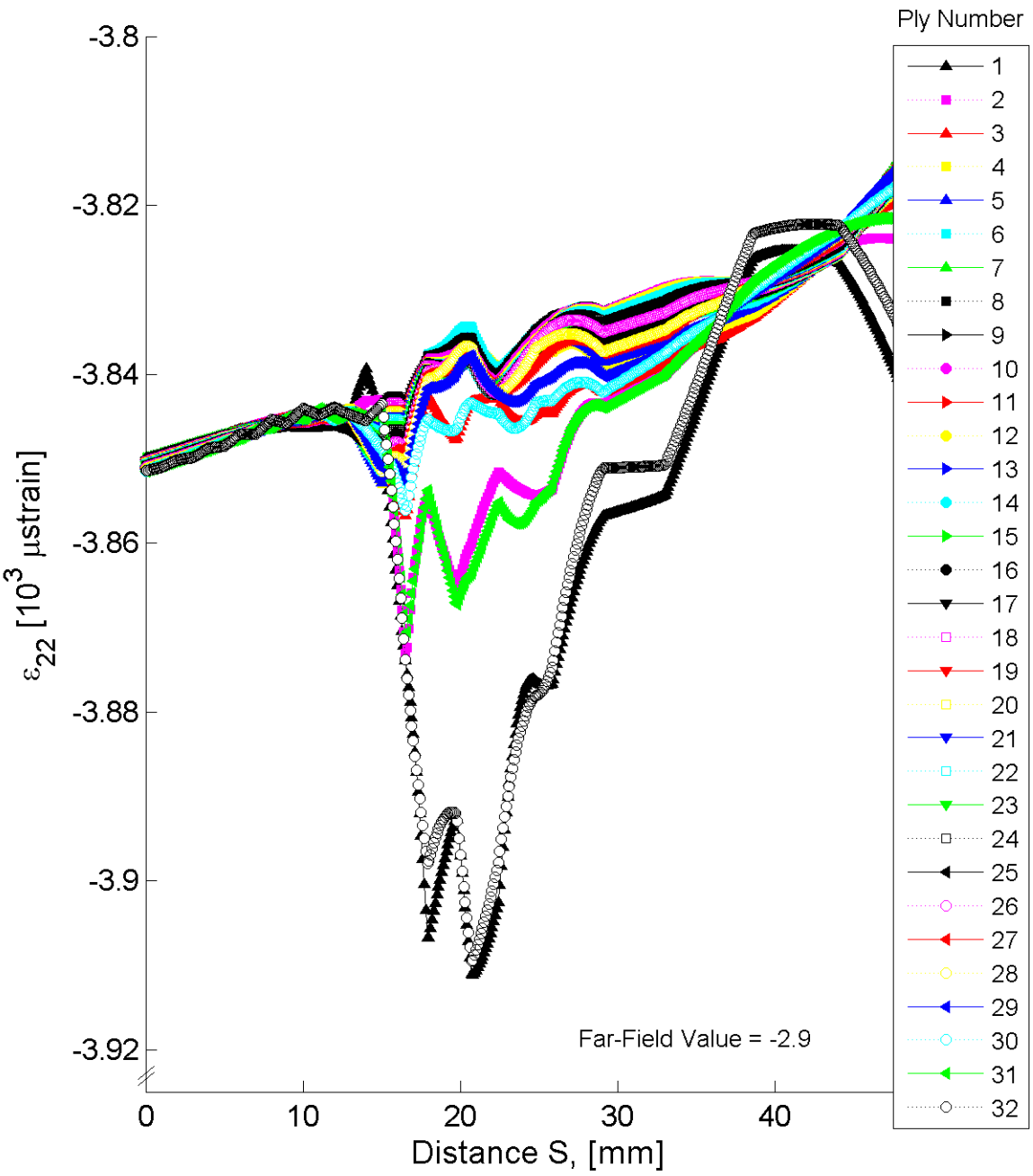

Figure B.151 Plot of ϵ_{22}, in laminate axes, along the path at the midplane of each ply for the delamination model with laminate of $[+60/-60]_{16T}$.

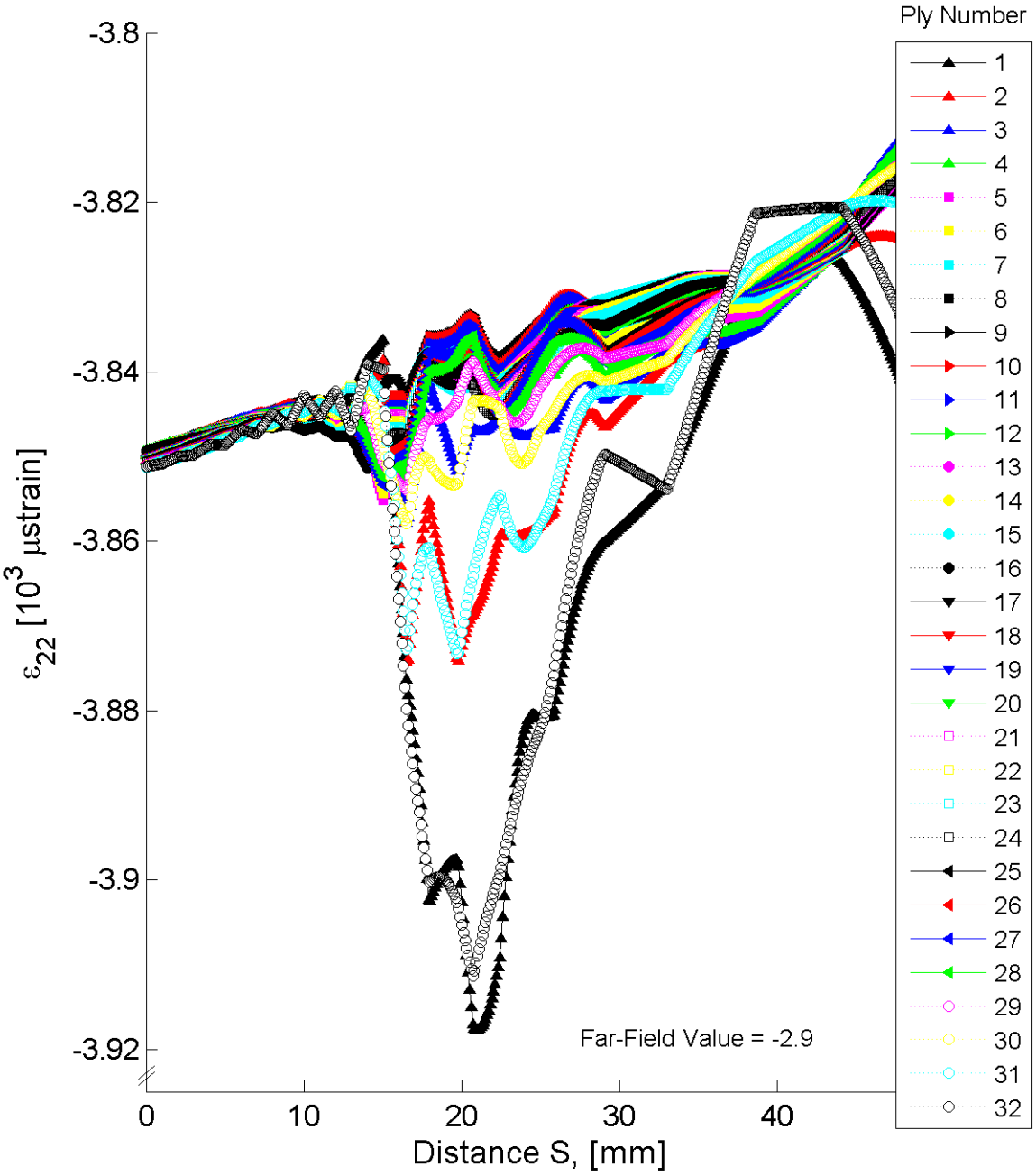

Figure B.152 Plot of ϵ_{22}, in laminate axes, along the path at the midplane of each ply for the delamination model with laminate of $[+60_4/-60_4]_{4T}$.

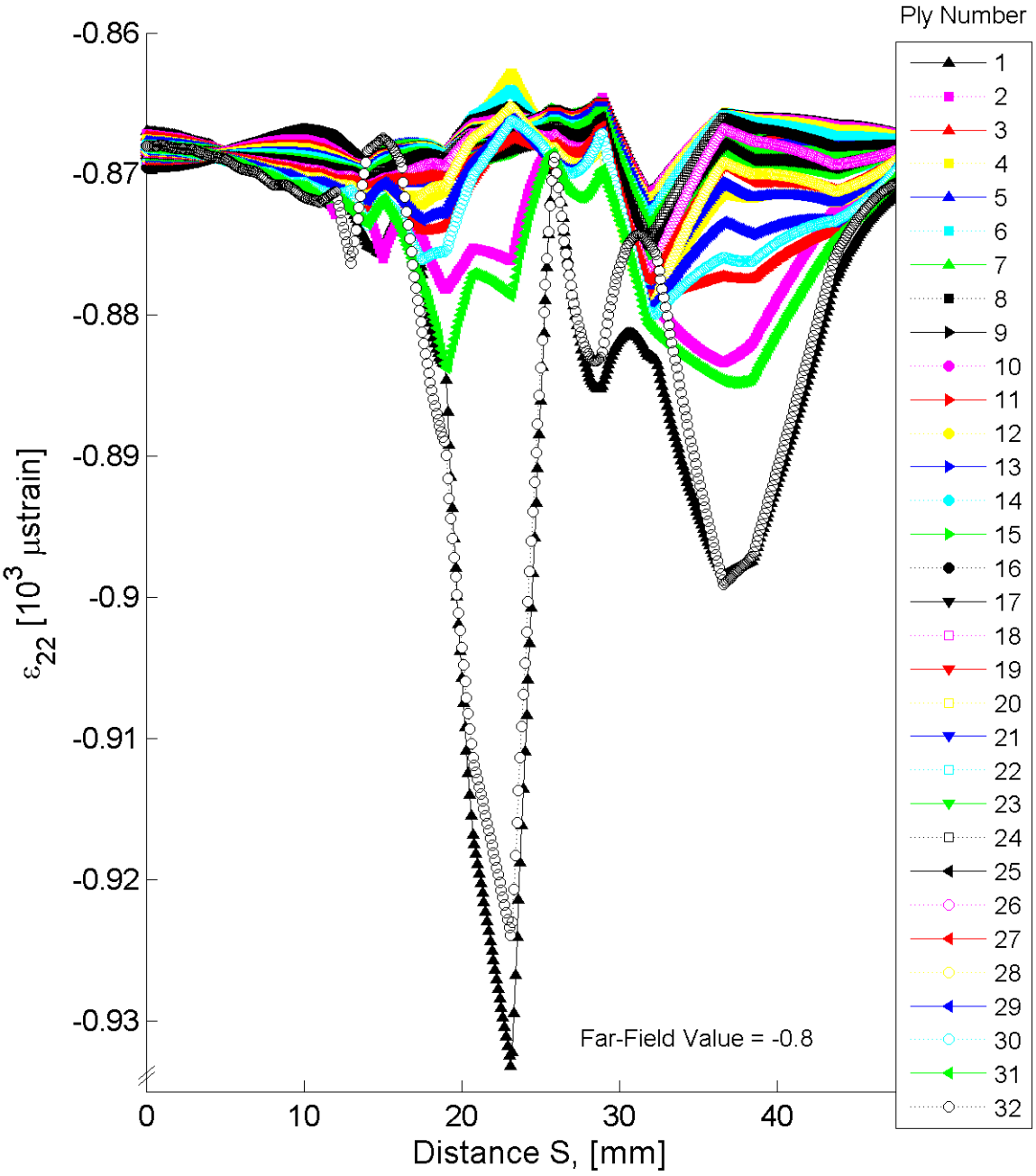

Figure B.153 Plot of ϵ_{22}, in laminate axes, along the path at the midplane of each ply for the delamination model with laminate of $[+75/-75]_{16T}$.

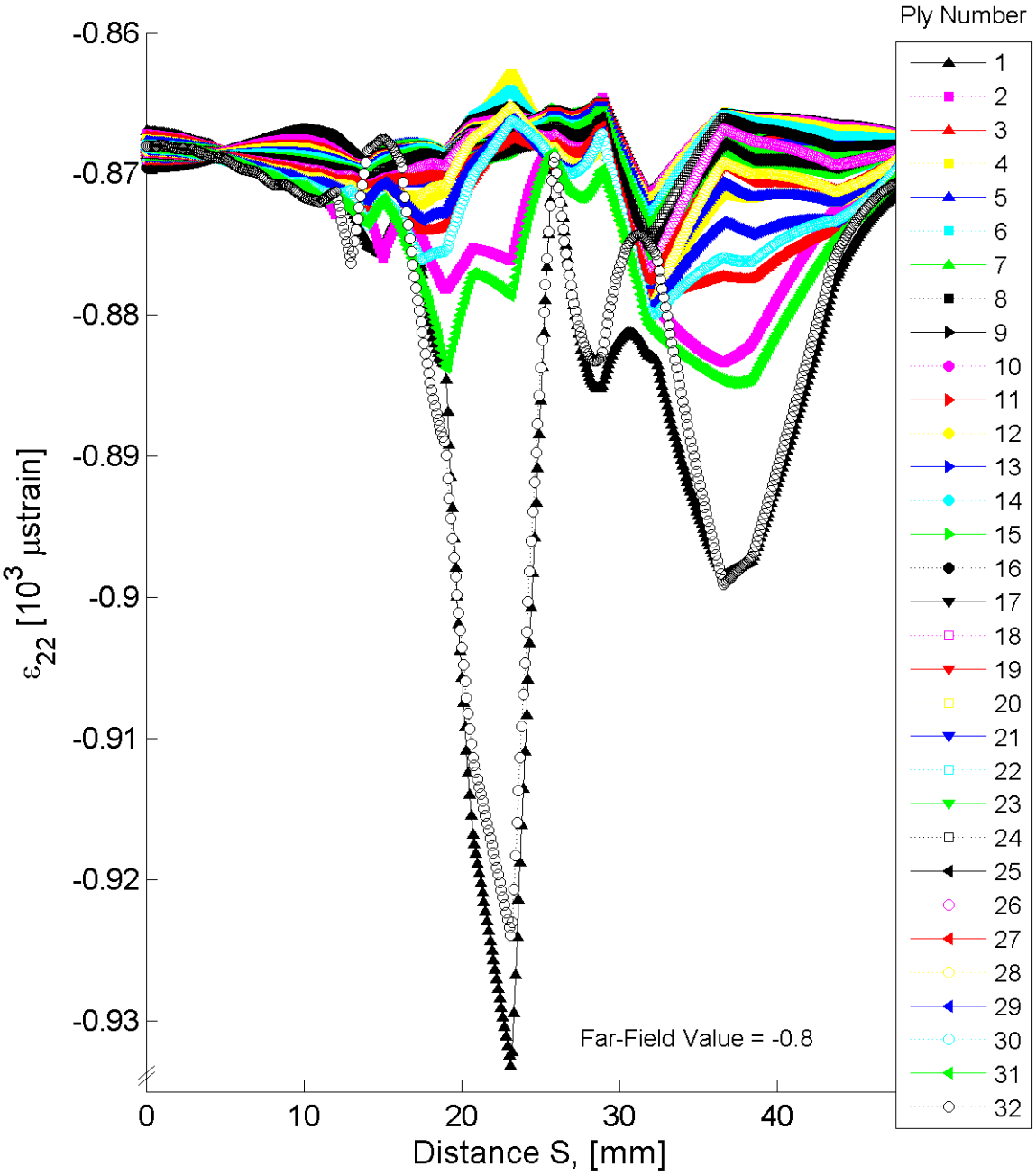

Figure B.154 Plot of ϵ_{22}, in laminate axes, along the path at the midplane of each ply for the delamination model with laminate of $[+75_4/-75_4]_{4T}$.

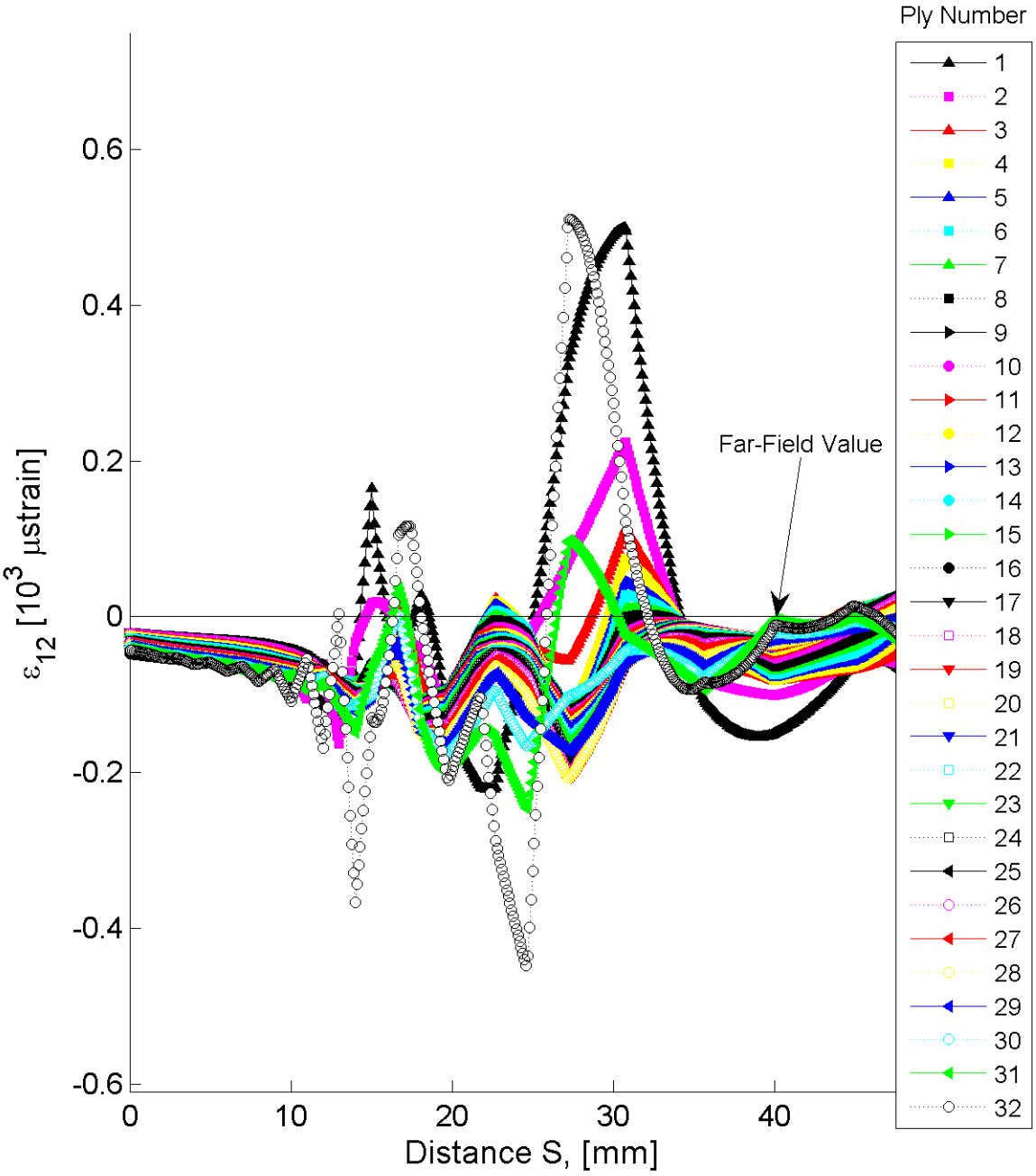

Figure B.155 Plot of ϵ_{12}, in laminate axes, along the path at the midplane of each ply for the delamination model with laminate of $[+30/-30]_{16T}$.

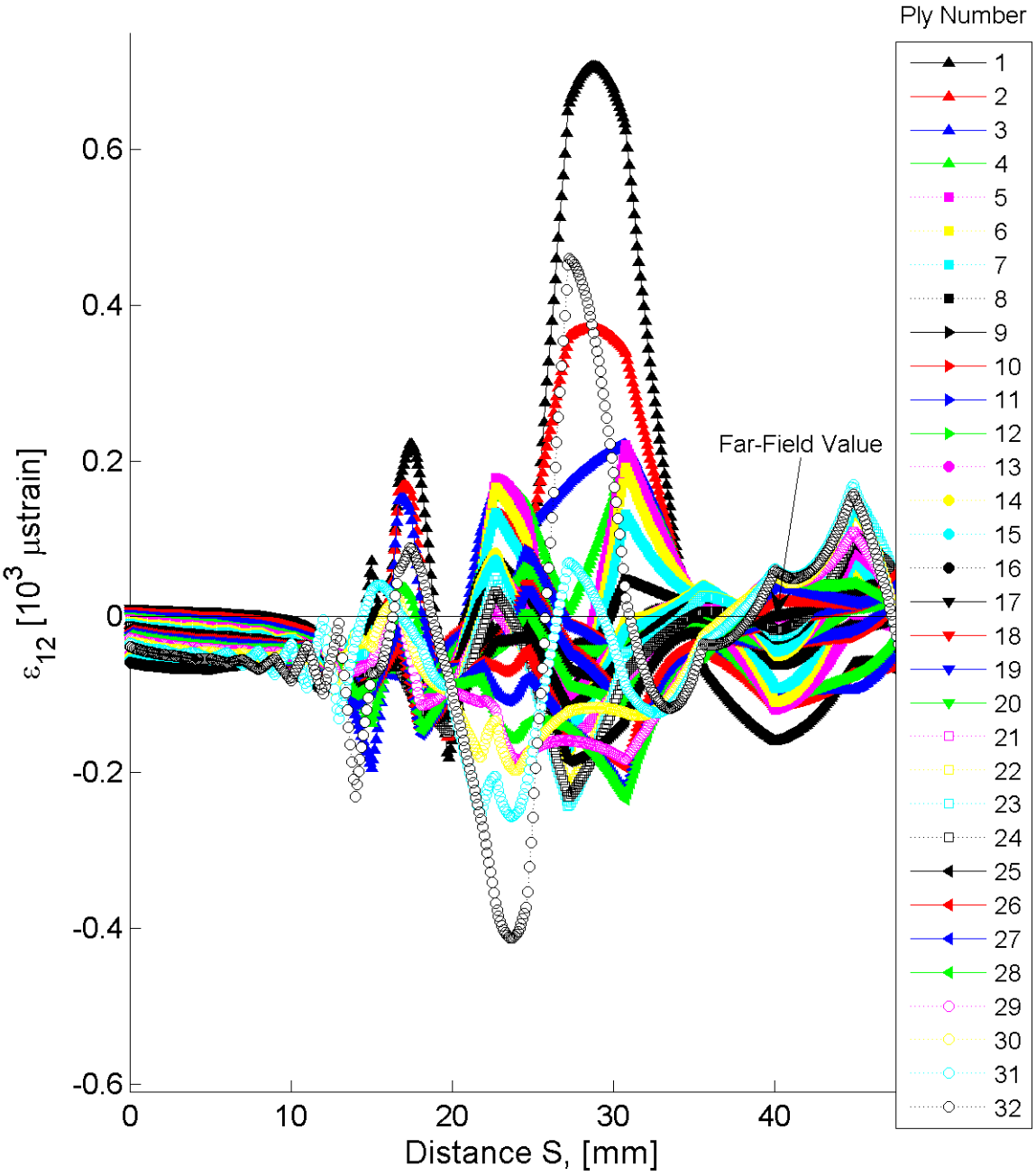

Figure B.156 Plot of ϵ_{12}, in laminate axes, along the path at the midplane of each ply for the delamination model with laminate of $[+30_4/-30_4]_{4T}$.

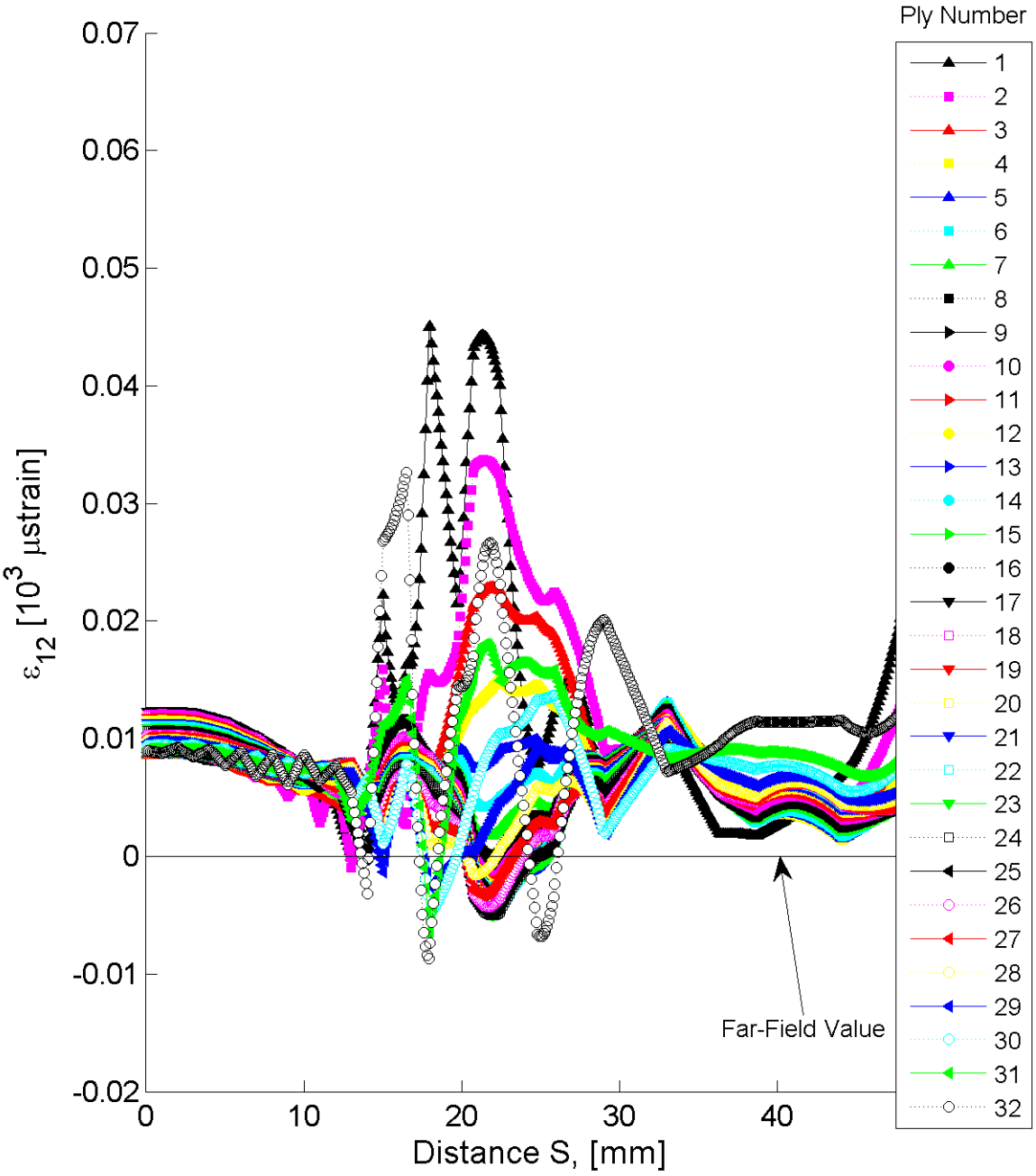

Figure B.157 Plot of ϵ_{12}, in laminate axes, along the path at the midplane of each ply for the delamination model with laminate of $[+60/-60]_{16T}$.

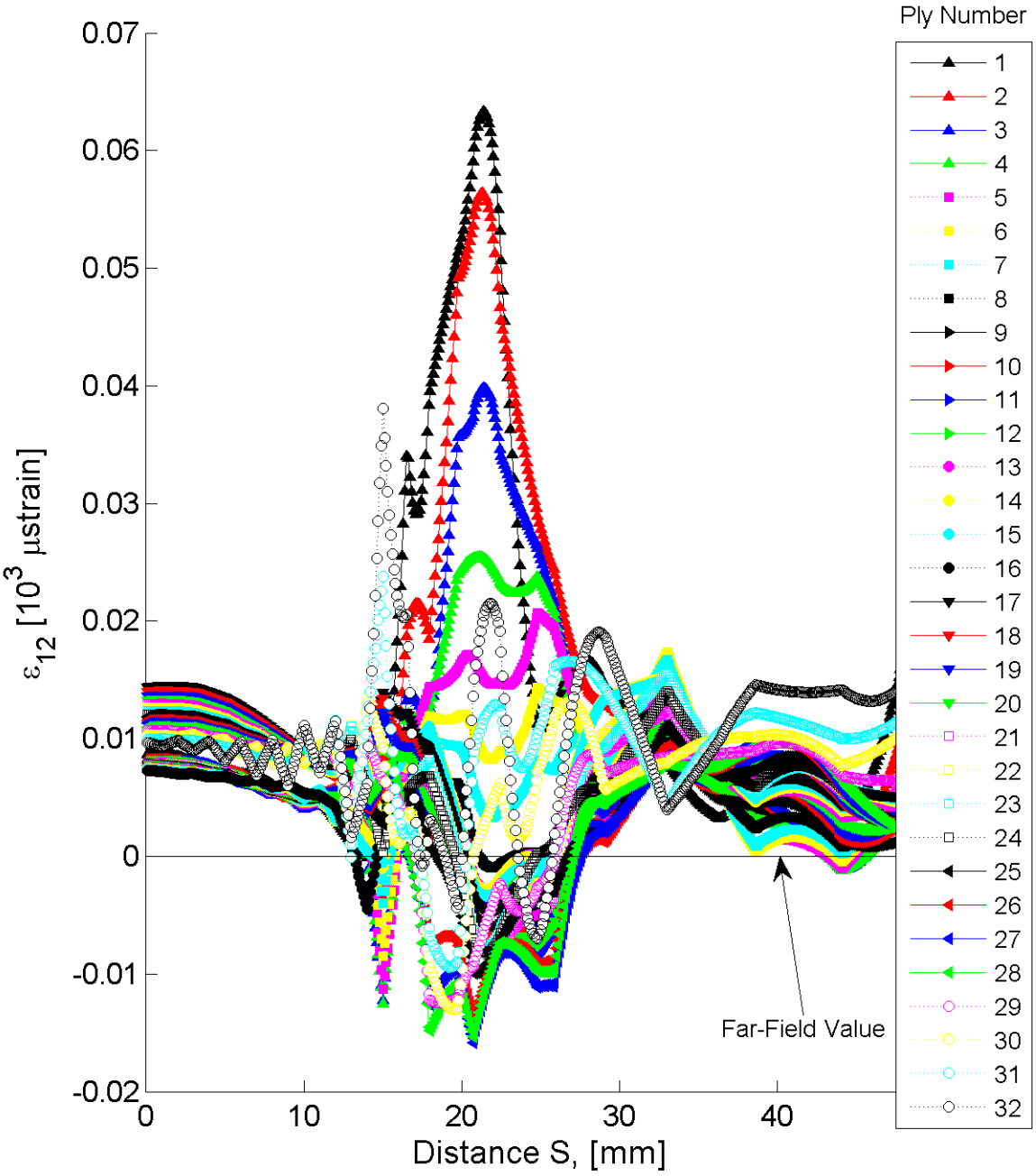

Figure B.158 Plot of ϵ_{12}, in laminate axes, along the path at the midplane of each ply for the delamination model with laminate of $[+60_4/-60_4]_{4T}$.

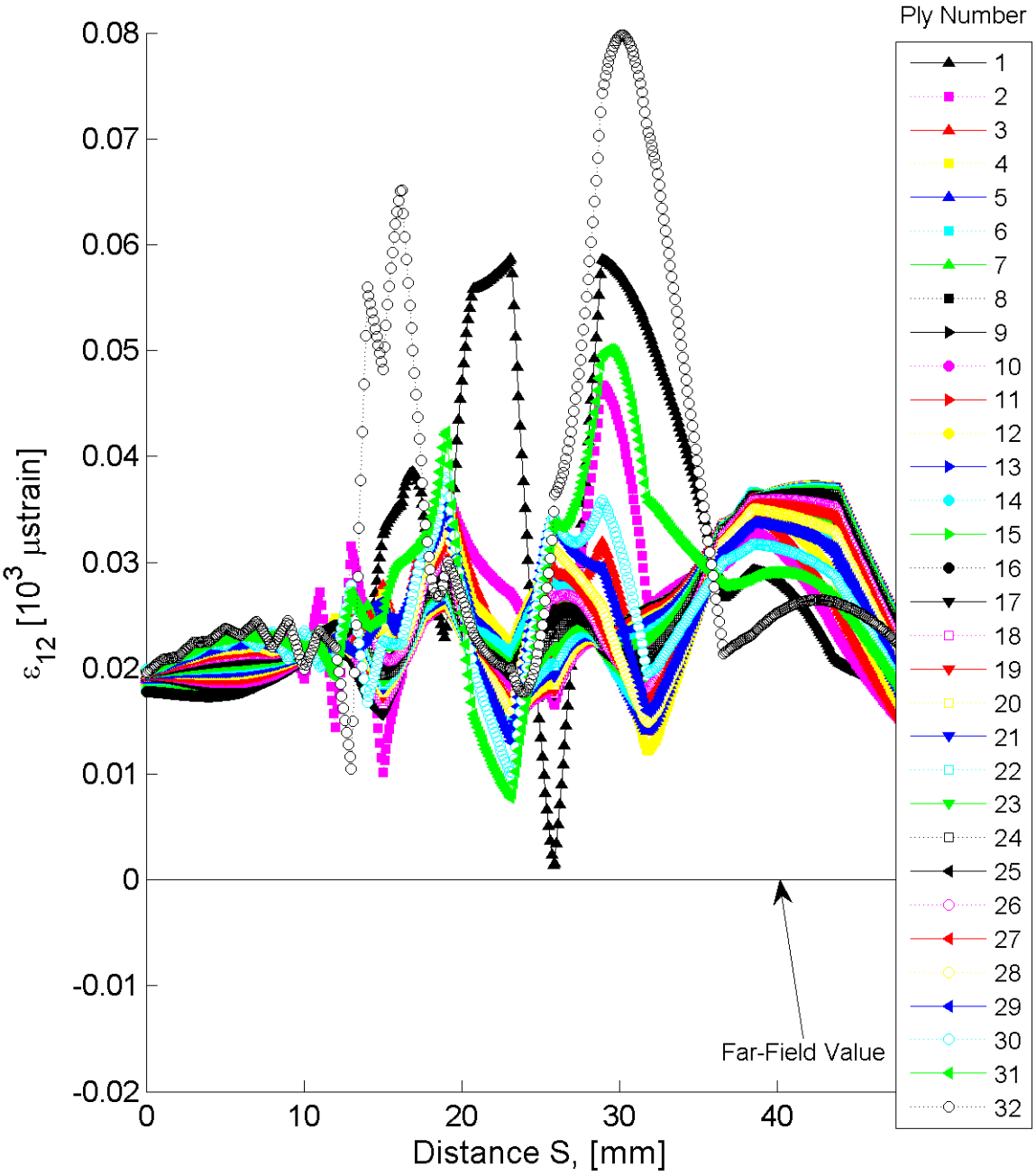

Figure B.159 Plot of ϵ_{12}, in laminate axes, along the path at the midplane of each ply for the delamination model with laminate of $[+75/-75]_{16T}$.

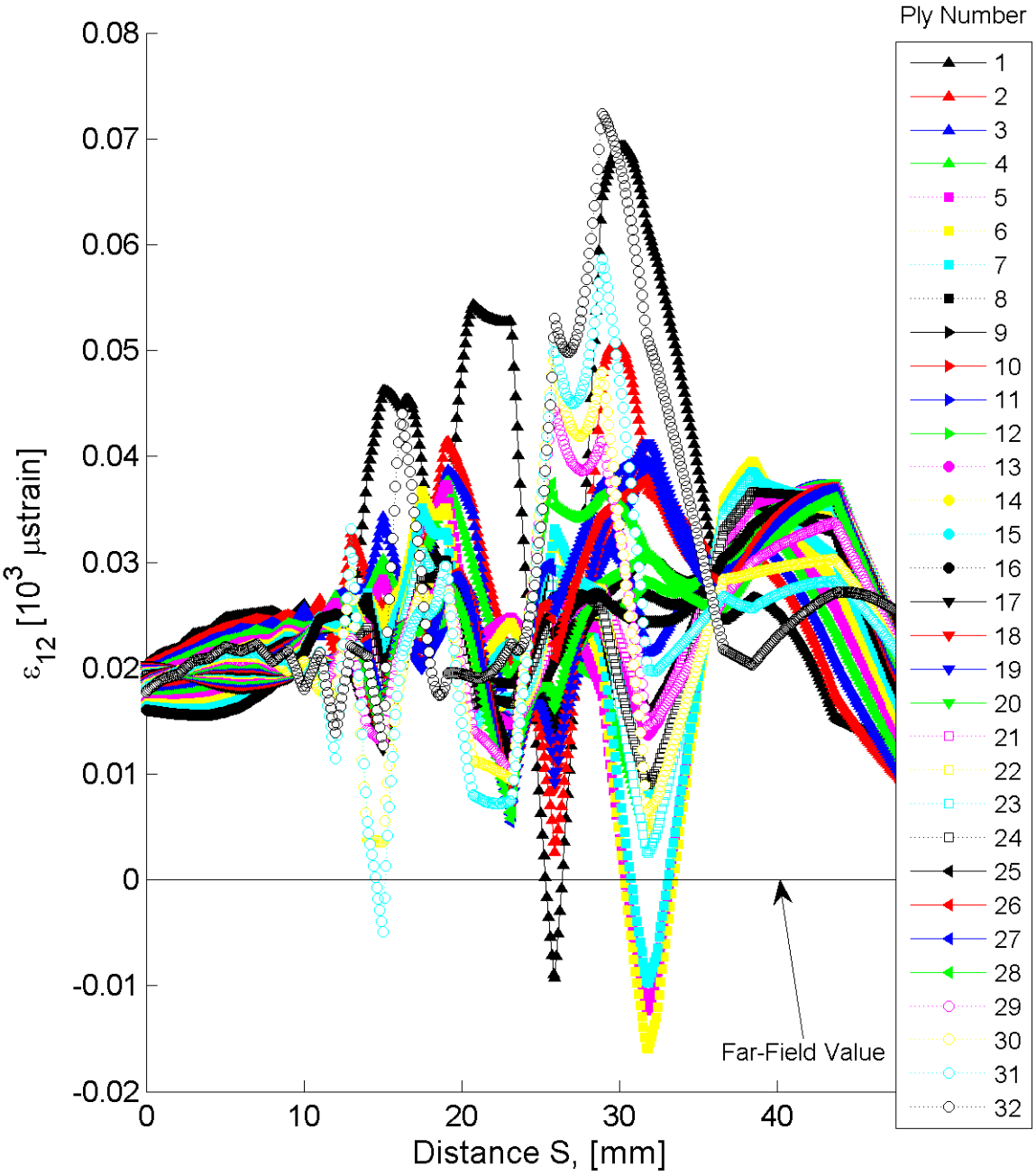

Figure B.160 Plot of ϵ_{12}, in laminate axes, along the path at the midplane of each ply for the delamination model with laminate of $[+75_4/-75_4]_{4T}$.

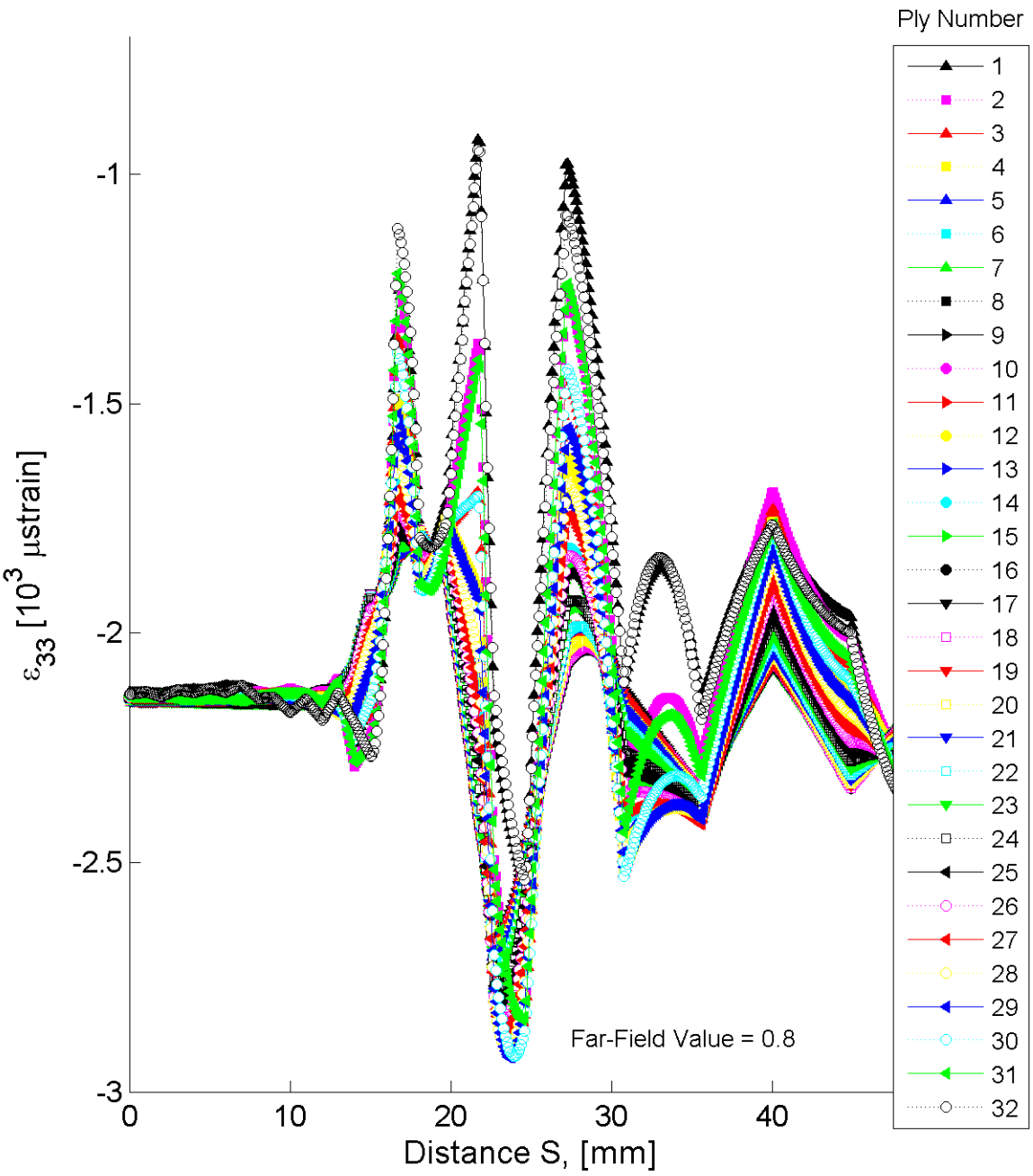

Figure B.161 Plot of ϵ_{33}, in laminate axes, along the path at the midplane of each ply for the delamination model with laminate of $[+30/-30]_{16T}$.

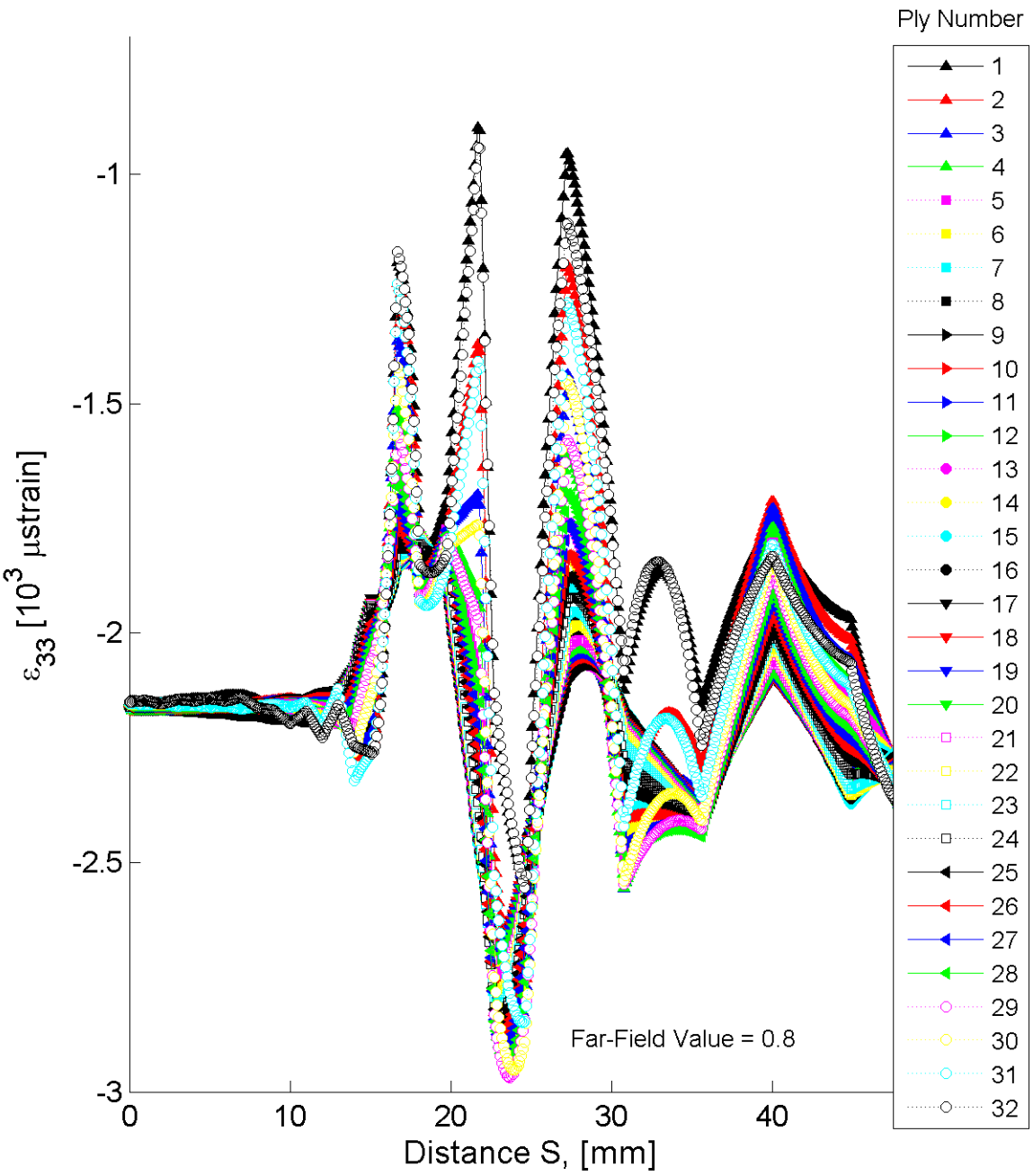

Figure B.162 Plot of ϵ_{33}, in laminate axes, along the path at the midplane of each ply for the delamination model with laminate of $[+30_4/-30_4]_{4T}$.

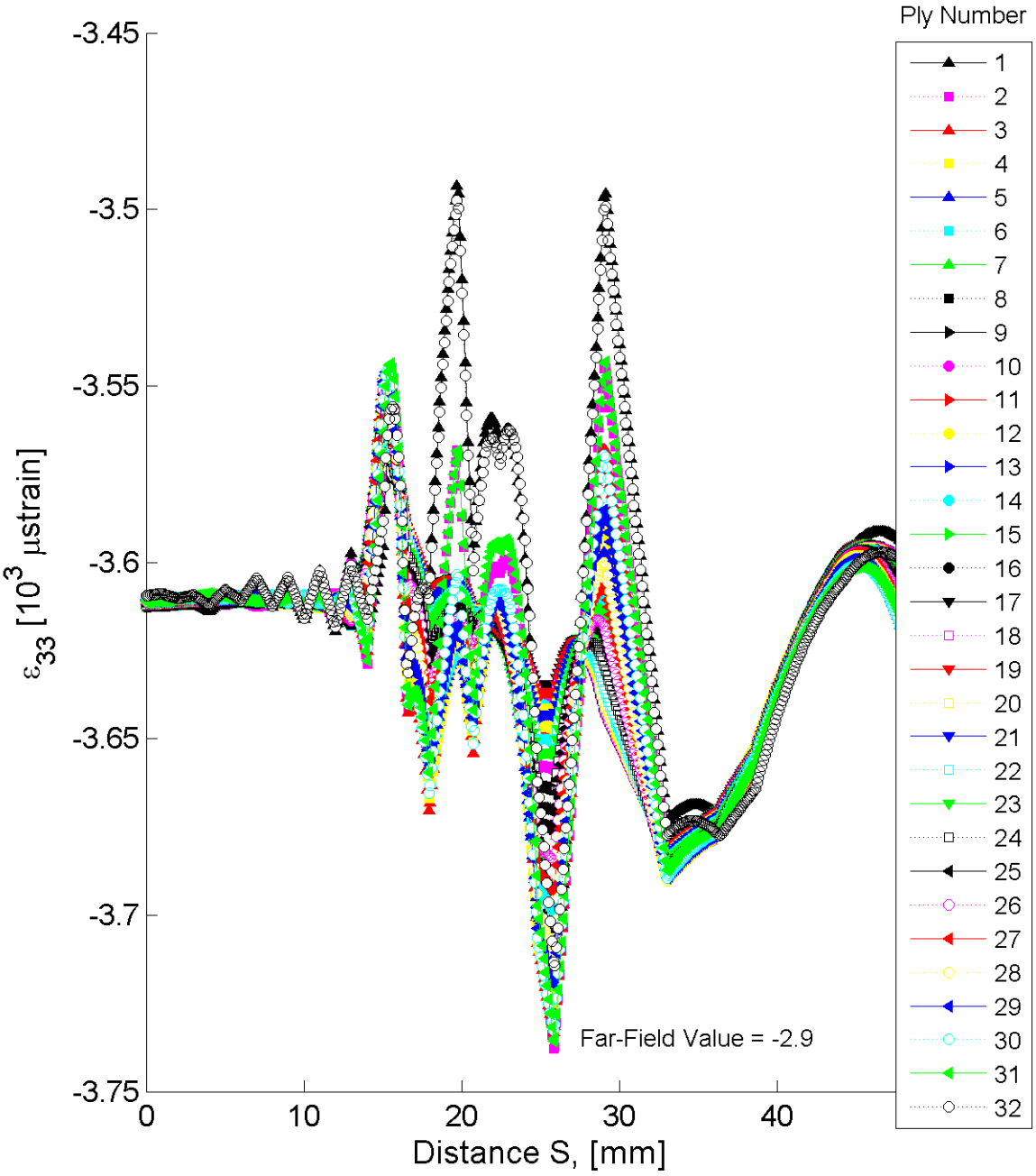

Figure B.163 Plot of ϵ_{33}, in laminate axes, along the path at the midplane of each ply for the delamination model with laminate of $[+60/-60]_{16T}$.

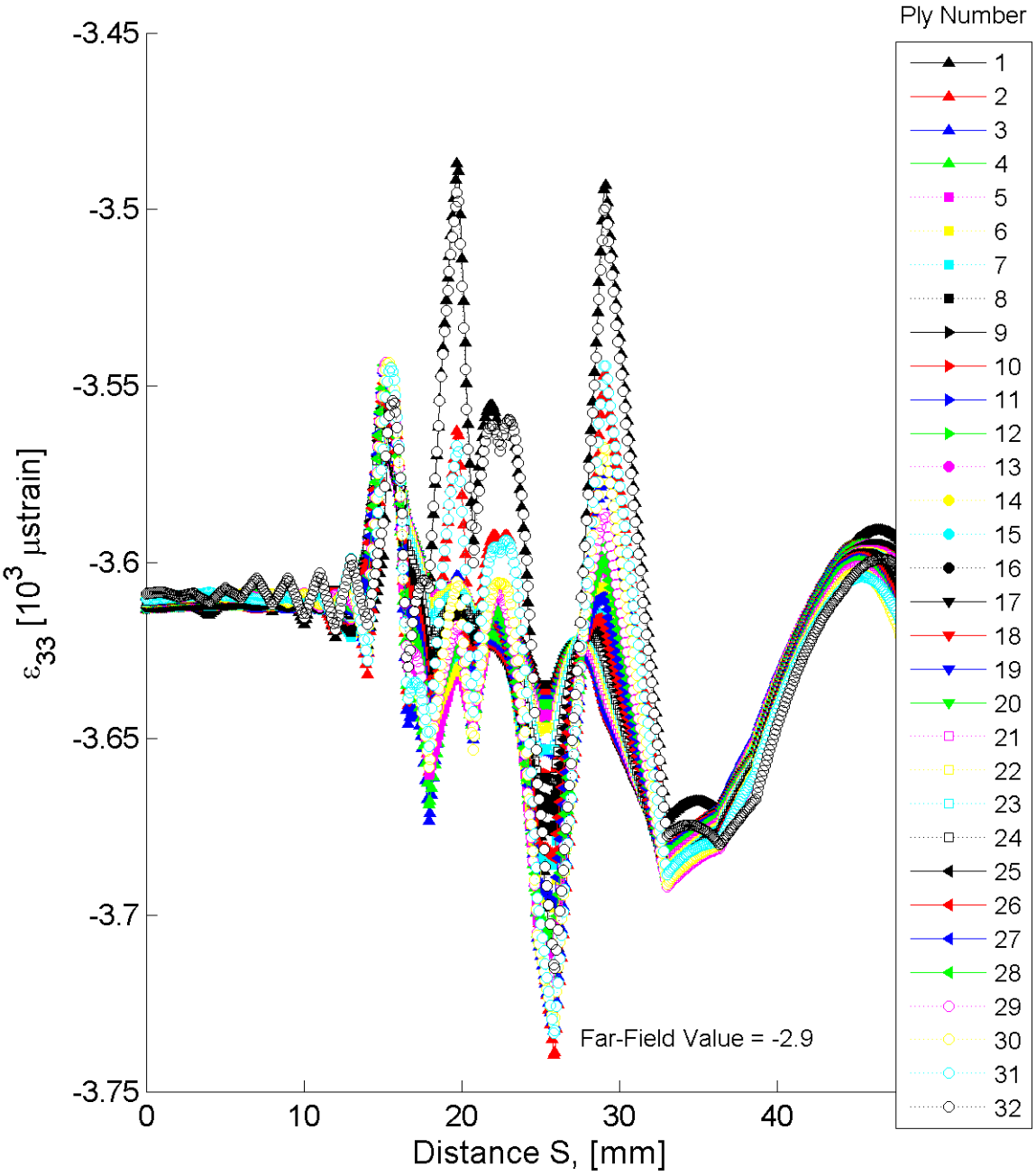

Figure B.164 Plot of ϵ_{33}, in laminate axes, along the path at the midplane of each ply for the delamination model with laminate of $[+60_4/-60_4]_{4T}$.

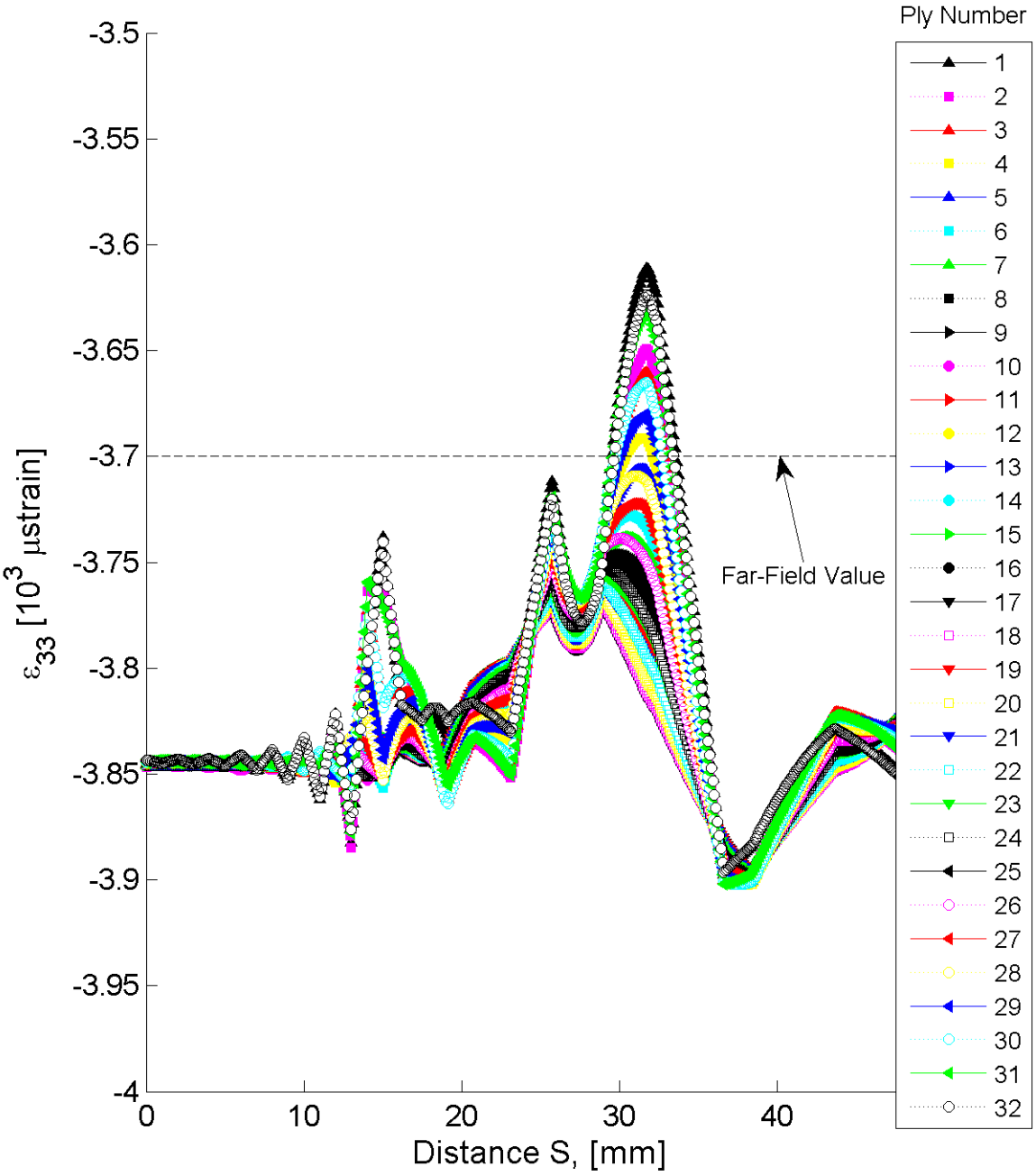

Figure B.165 Plot of ϵ_{33}, in laminate axes, along the path at the midplane of each ply for the delamination model with laminate of $[+75/-75]_{16T}$.

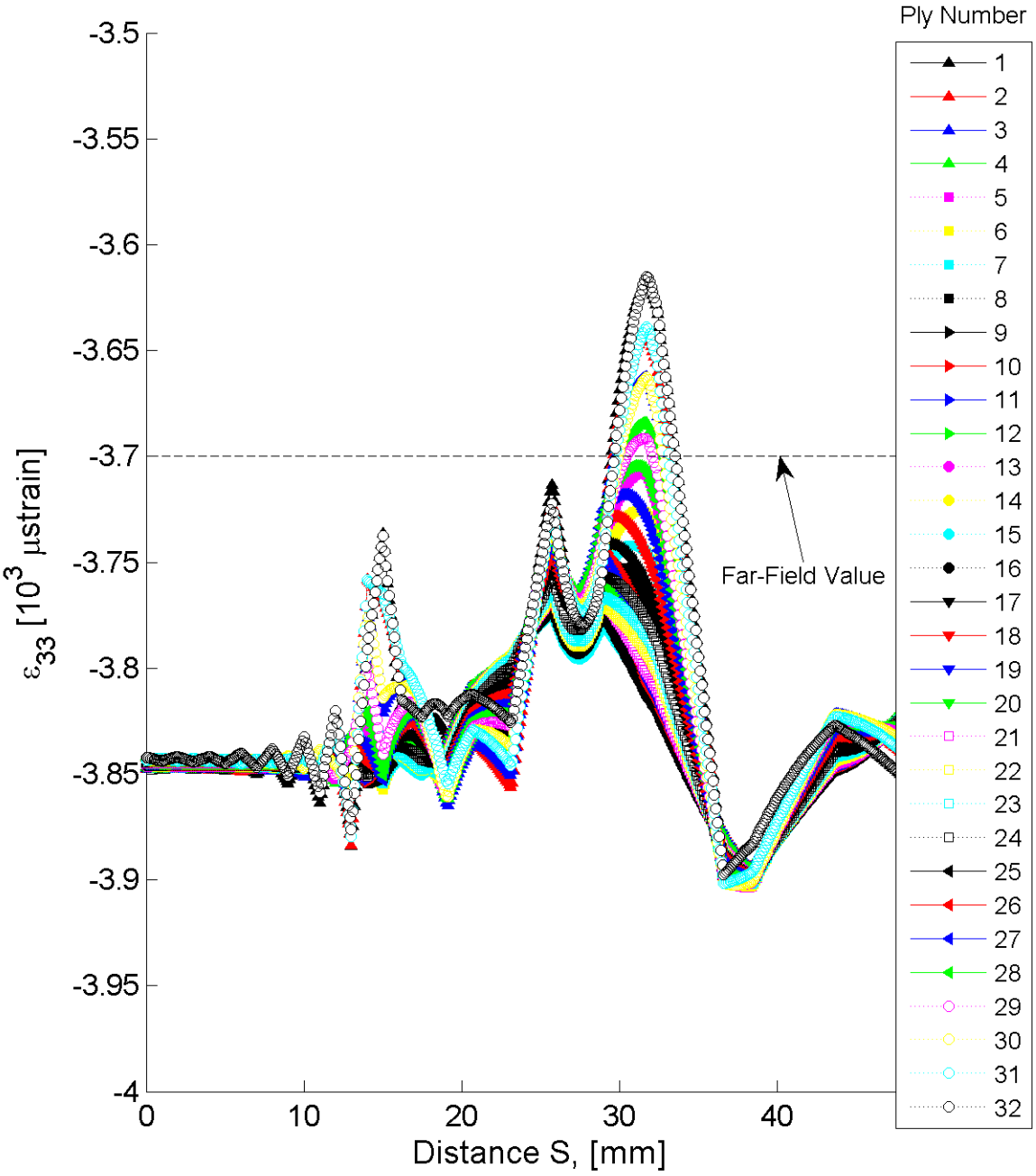

Figure B.166 Plot of ϵ_{33}, in laminate axes, along the path at the midplane of each ply for the delamination model with laminate of $[+75_4/-75_4]_{4T}$.

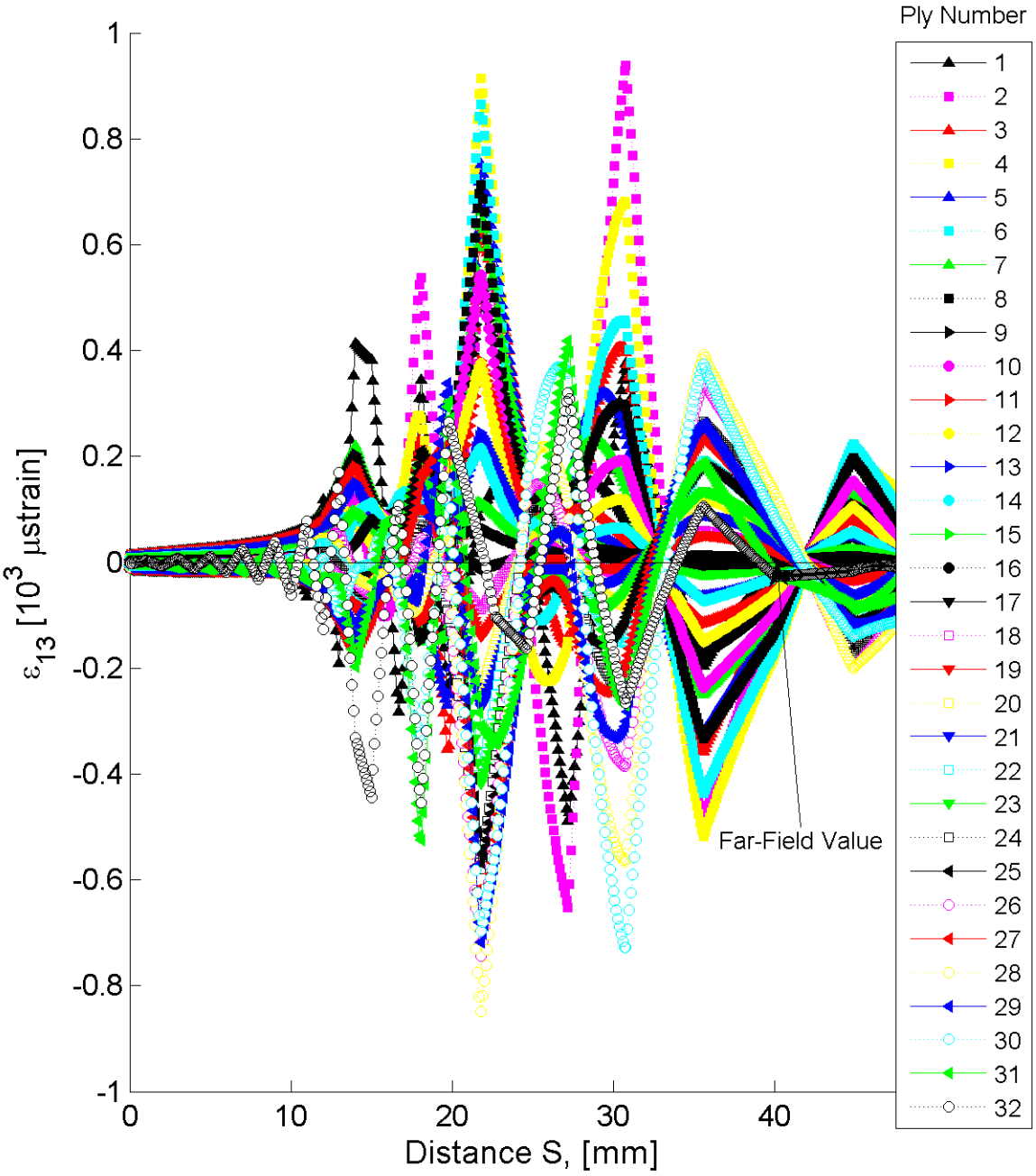

Figure B.167 Plot of ϵ_{13}, in laminate axes, along the path at the midplane of each ply for the delamination model with laminate of $[+30/-30]_{16T}$.

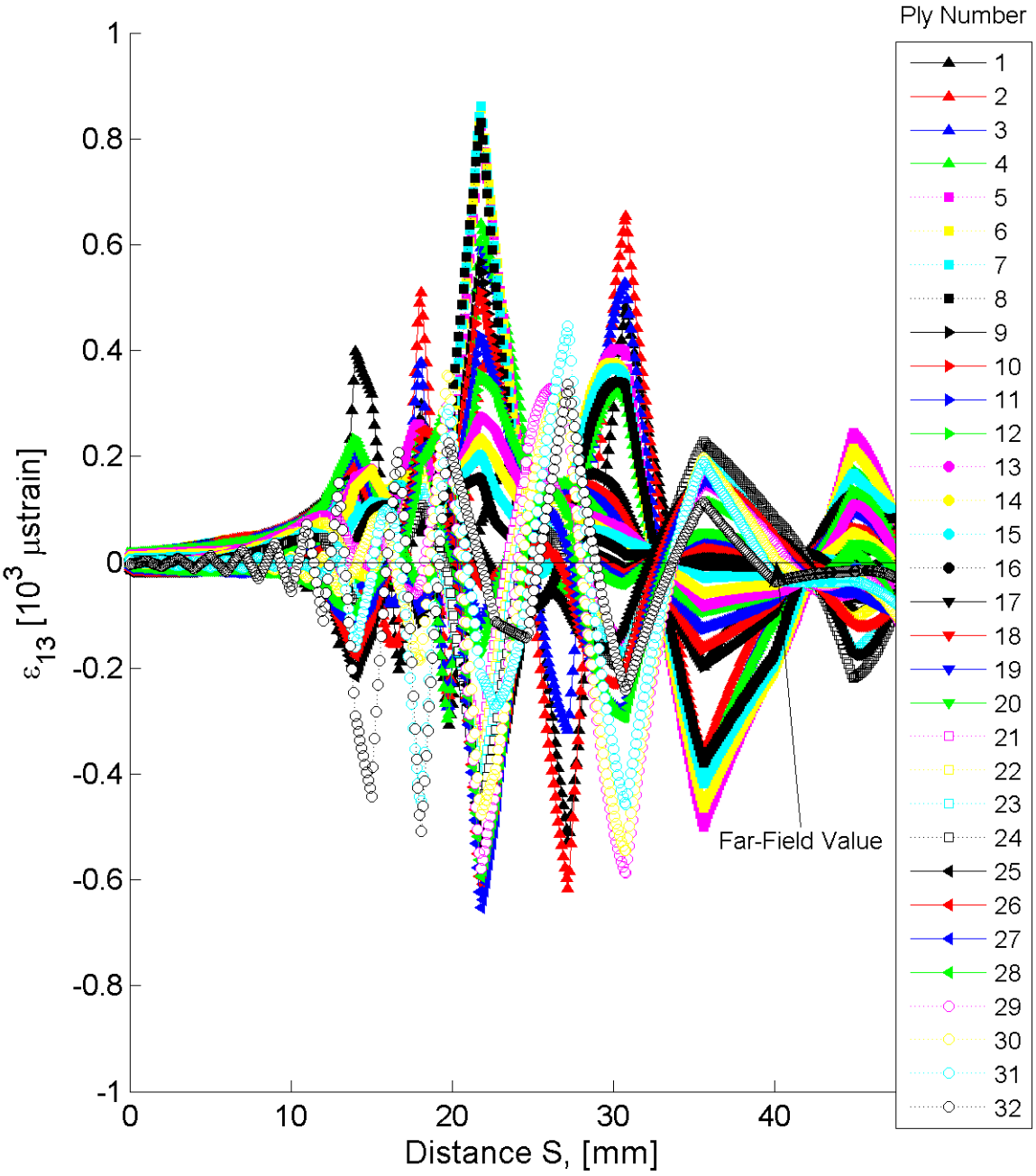

Figure B.168 Plot of ϵ_{13}, in laminate axes, along the path at the midplane of each ply for the delamination model with laminate of $[+30_4/-30_4]_{4T}$.

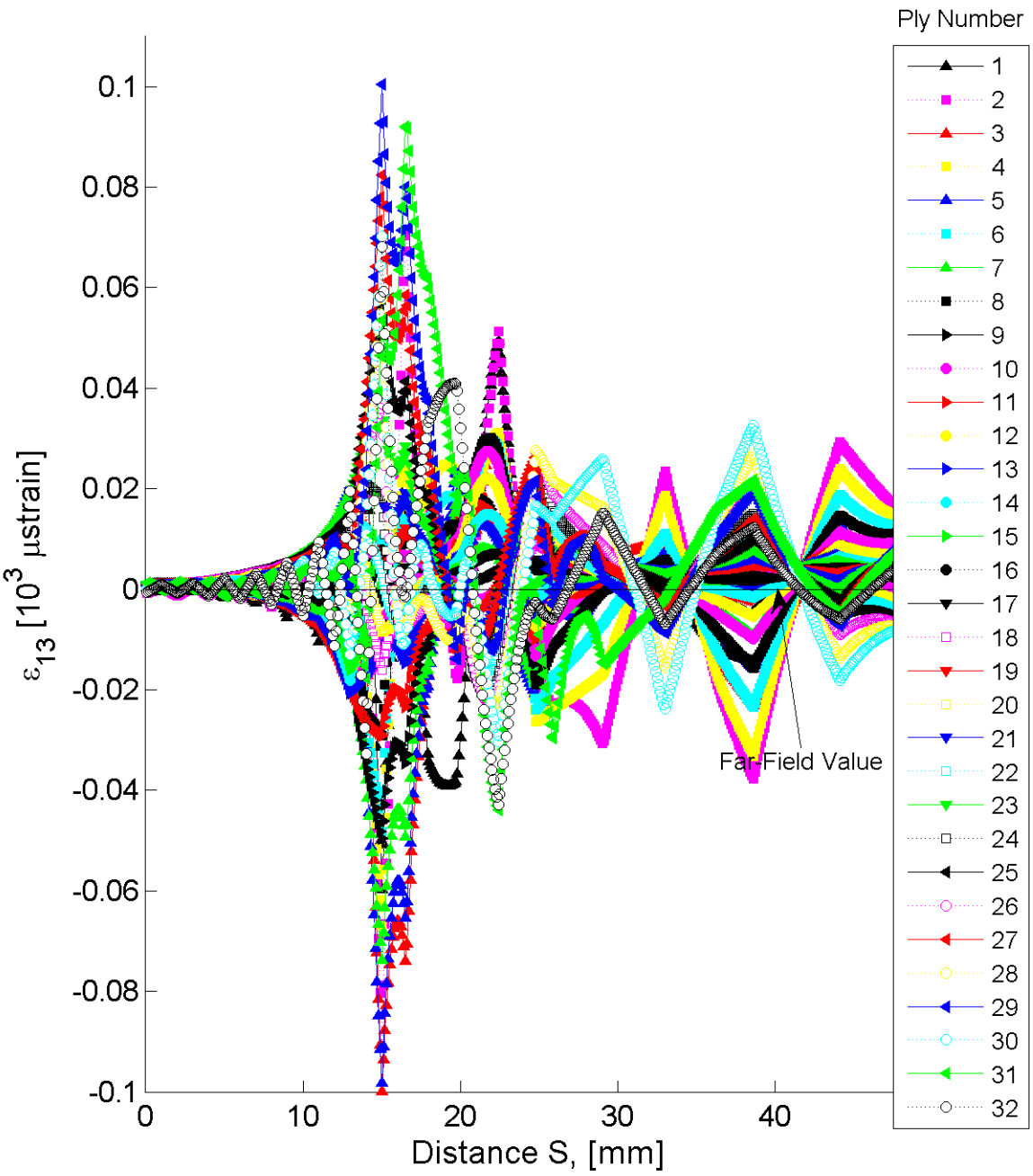

Figure B.169 Plot of ϵ_{13}, in laminate axes, along the path at the midplane of each ply for the delamination model with laminate of $[+60/-60]_{16T}$.

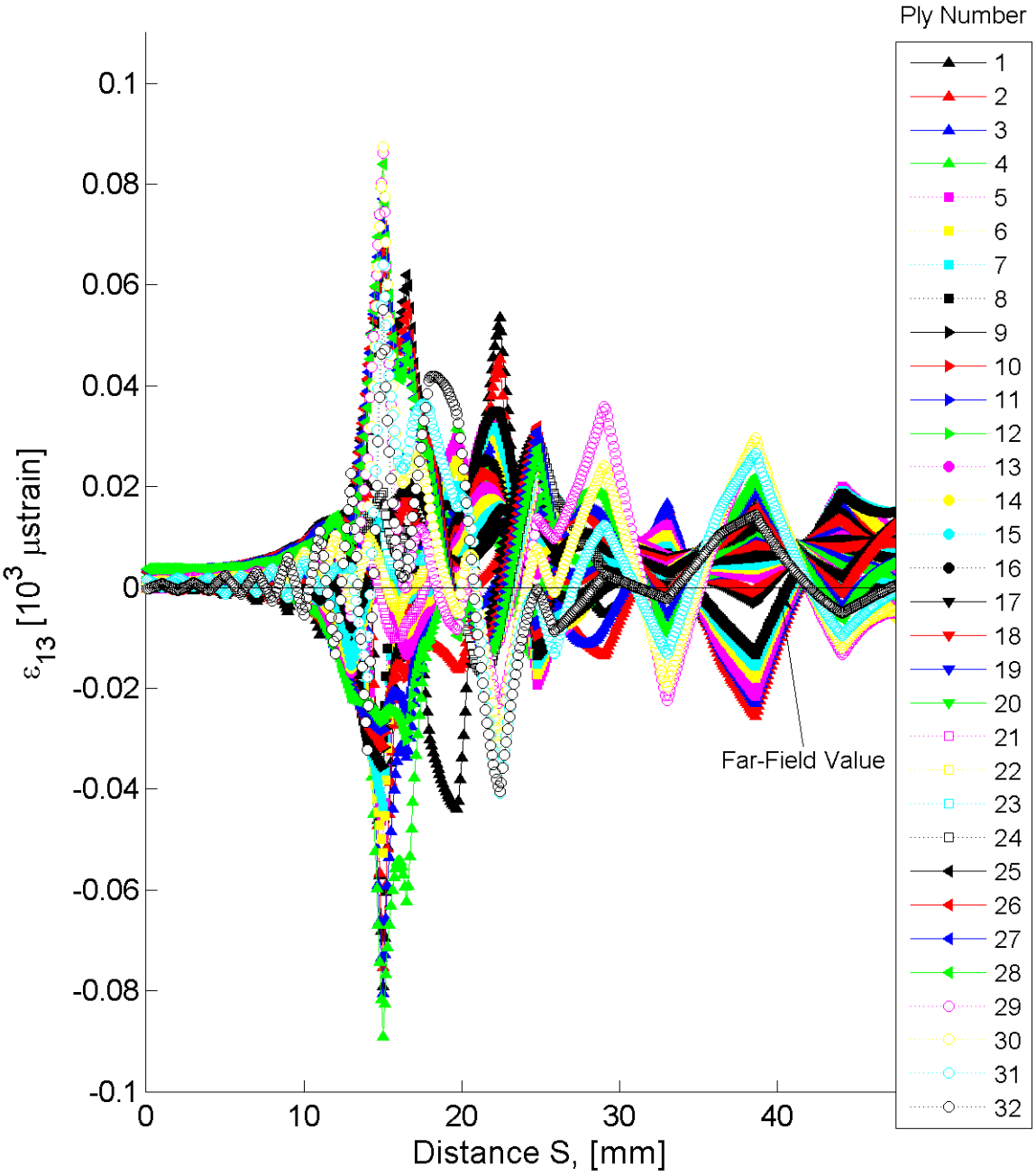

Figure B.170 Plot of ϵ_{13}, in laminate axes, along the path at the midplane of each ply for the delamination model with laminate of $[+60_4/-60_4]_{4T}$.

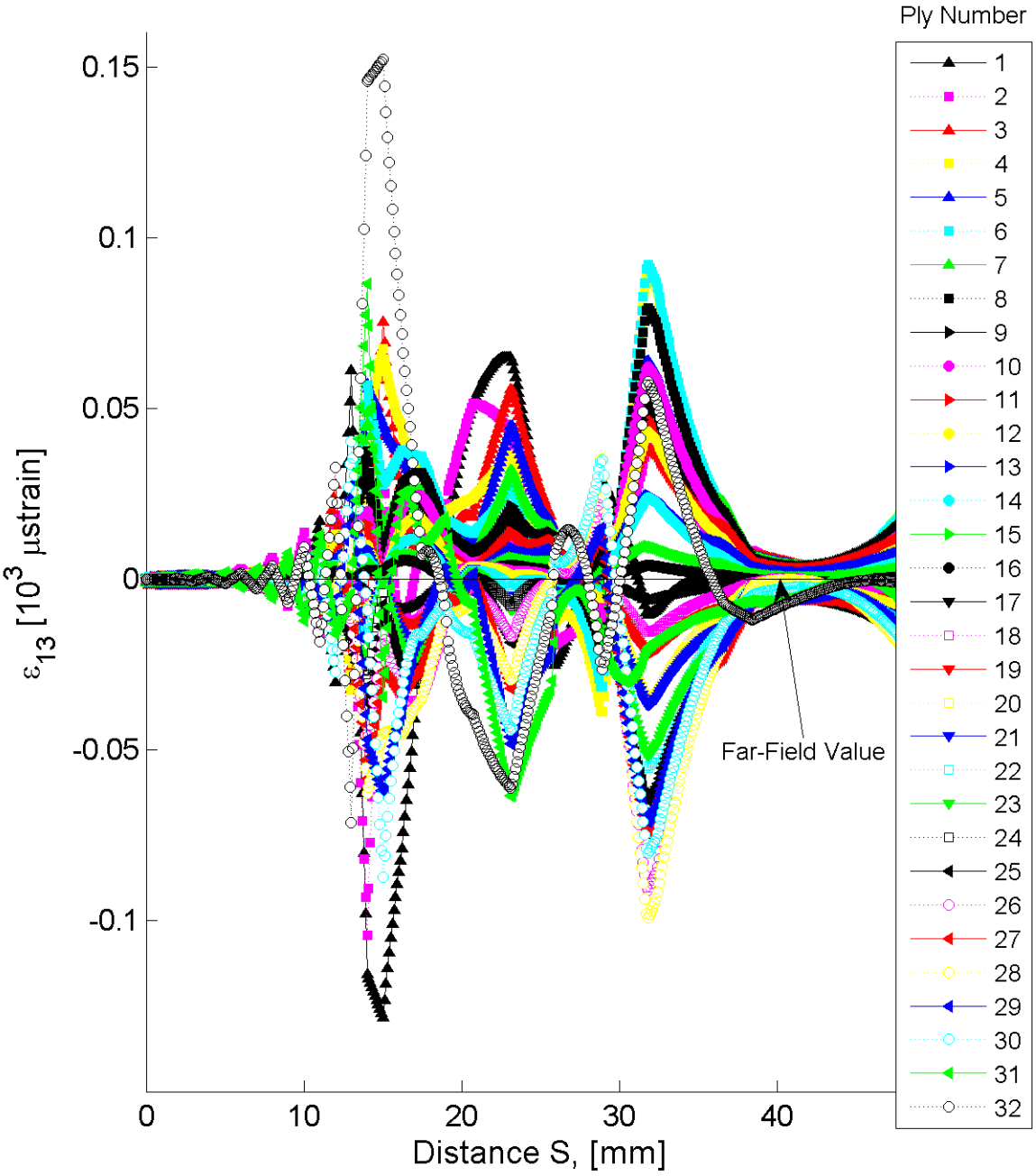

Figure B.171 Plot of ϵ_{13}, in laminate axes, along the path at the midplane of each ply for the delamination model with laminate of $[+75/-75]_{16T}$.

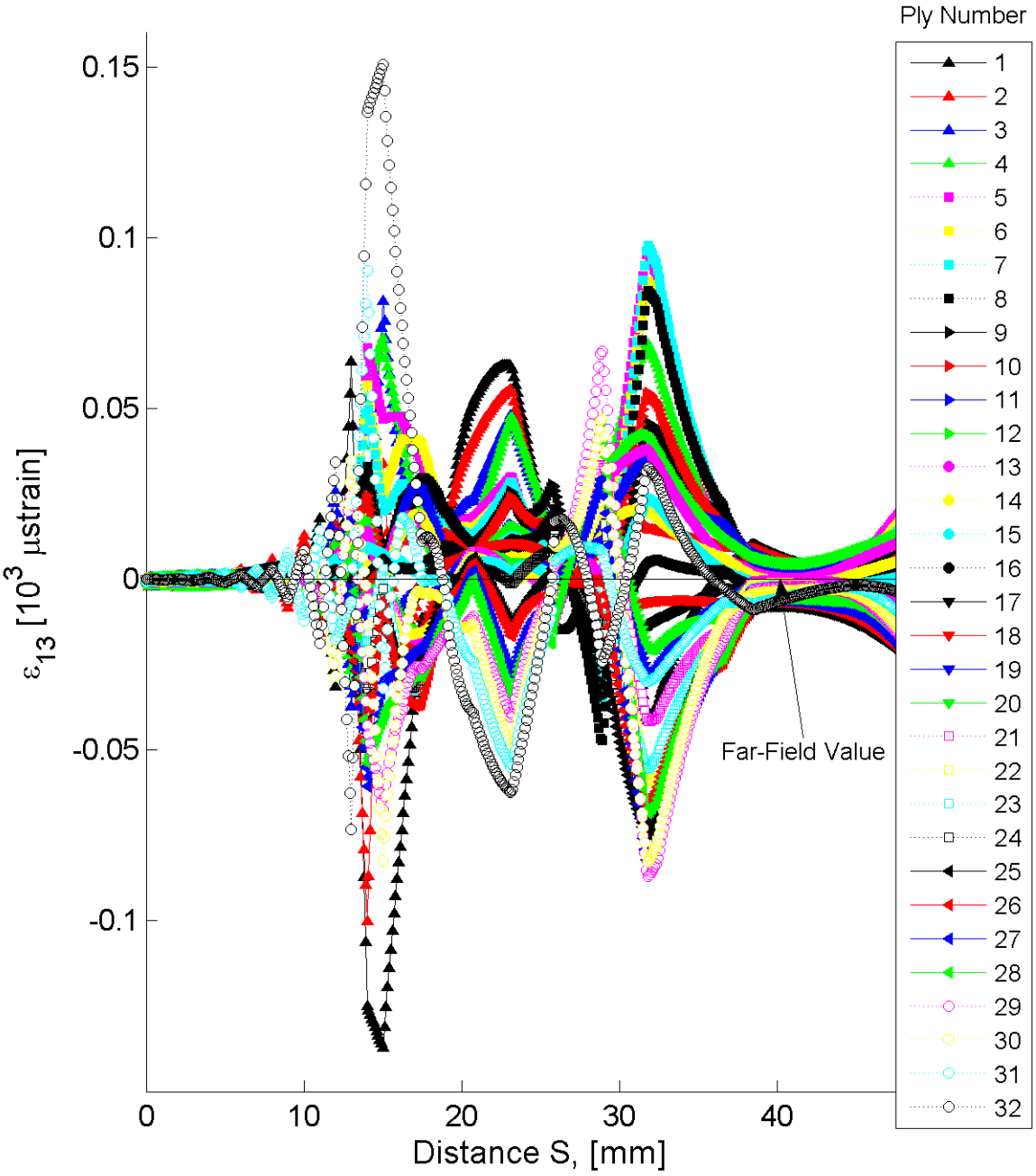

Figure B.172 Plot of ϵ_{13}, in laminate axes, along the path at the midplane of each ply for the delamination model with laminate of $[+75_4/-75_4]_{4T}$.

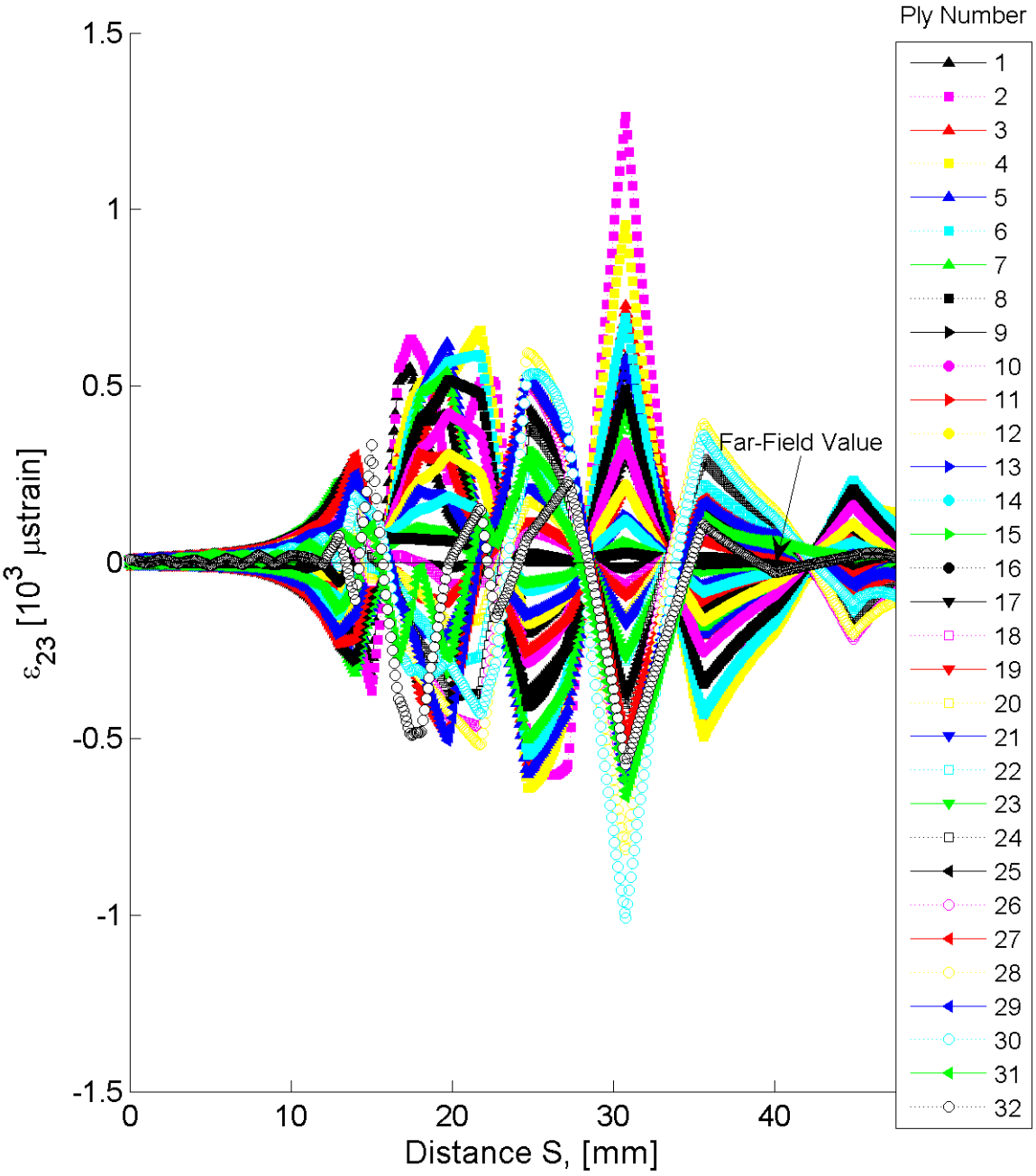

Figure B.173 Plot of ϵ_{23}, in laminate axes, along the path at the midplane of each ply for the delamination model with laminate of $[+30/-30]_{16T}$.

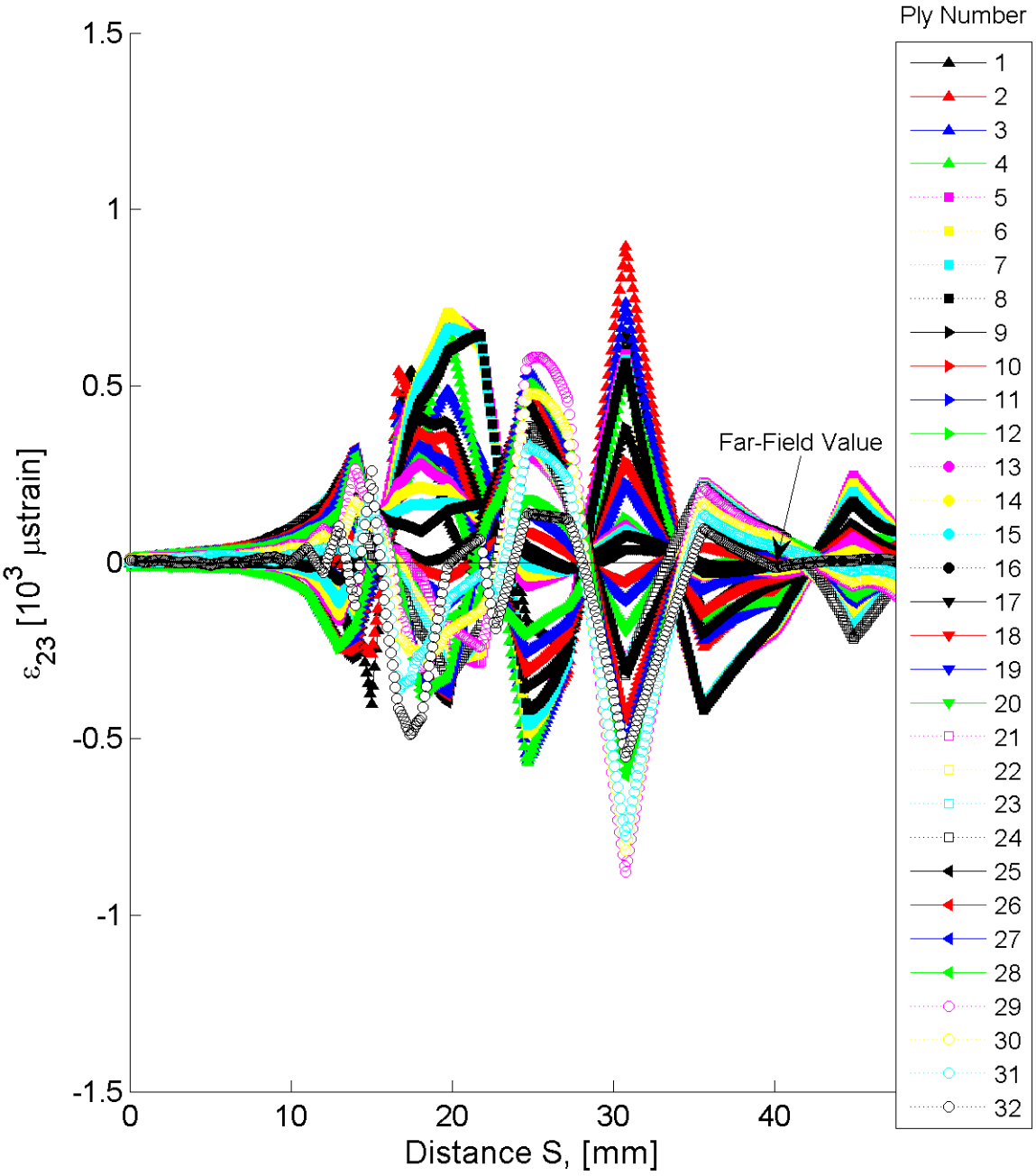

Figure B.174 Plot of ϵ_{23}, in laminate axes, along the path at the midplane of each ply for the delamination model with laminate of $[+30_4/-30_4]_{4T}$.

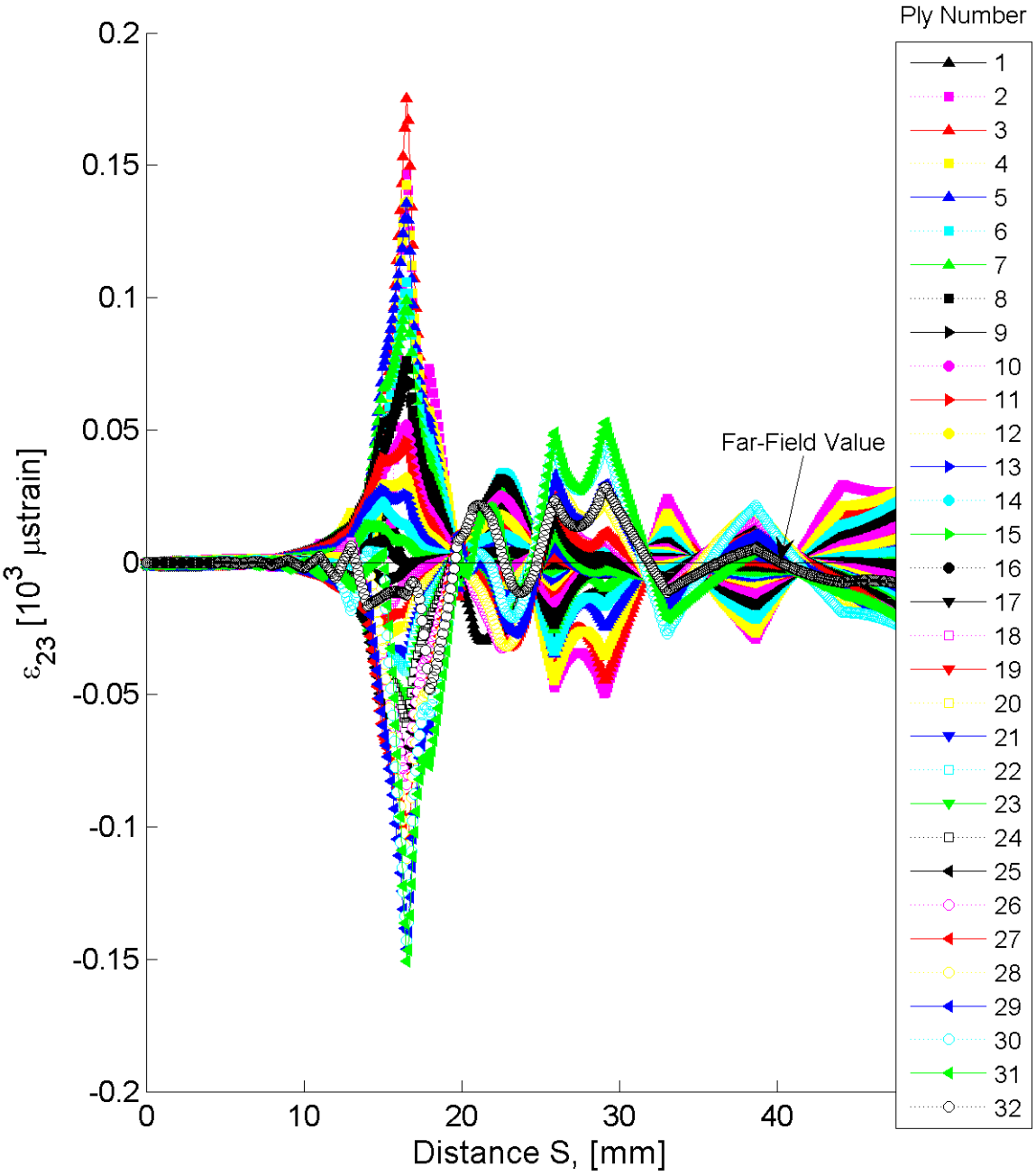

Figure B.175 Plot of ϵ_{23}, in laminate axes, along the path at the midplane of each ply for the delamination model with laminate of $[+60/-60]_{16T}$.

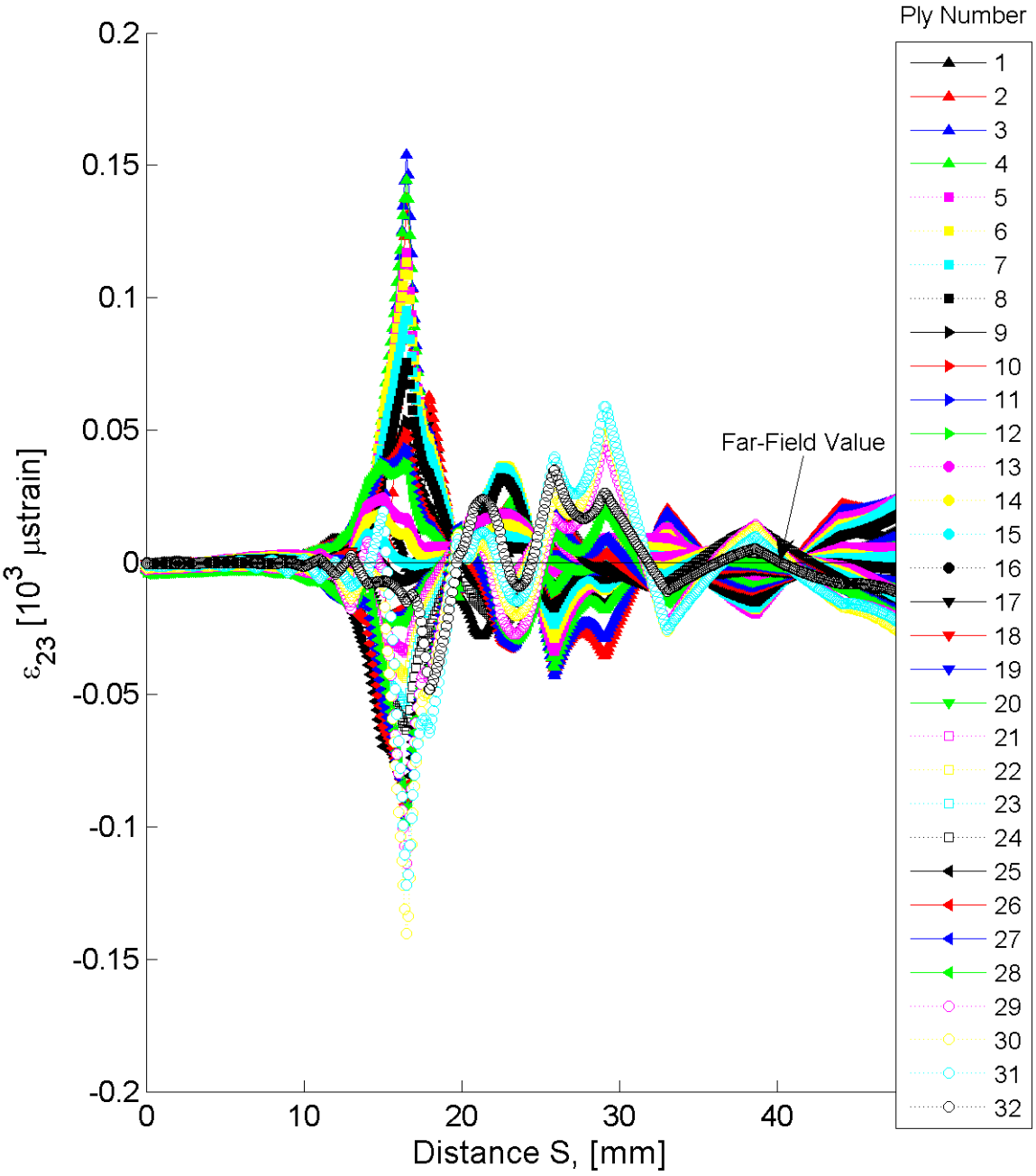

Figure B.176 Plot of ϵ_{23}, in laminate axes, along the path at the midplane of each ply for the delamination model with laminate of $[+60_4/-60_4]_{4T}$.

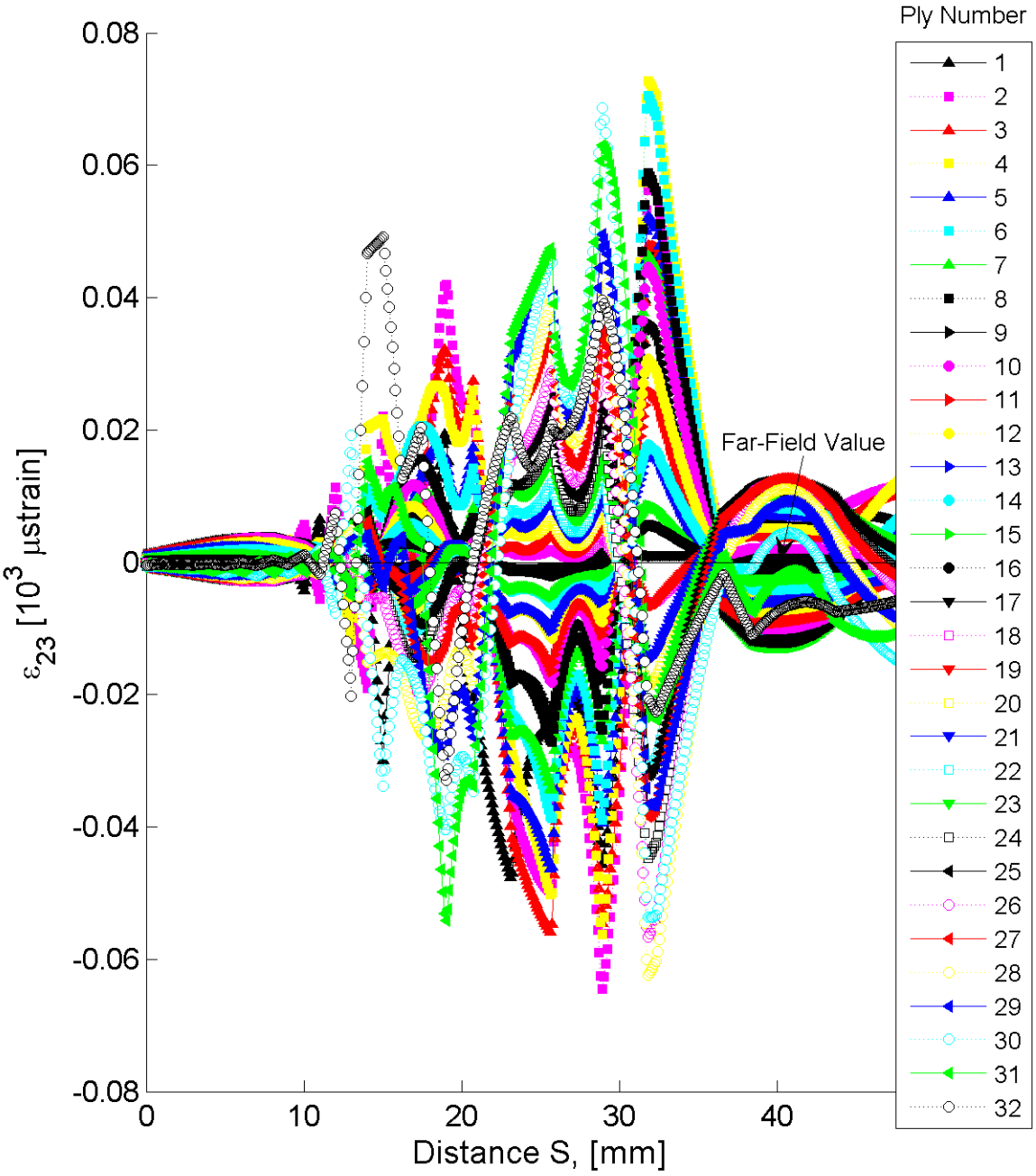

Figure B.177 Plot of ϵ_{23}, in laminate axes, along the path at the midplane of each ply for the delamination model with laminate of $[+75/-75]_{16T}$.

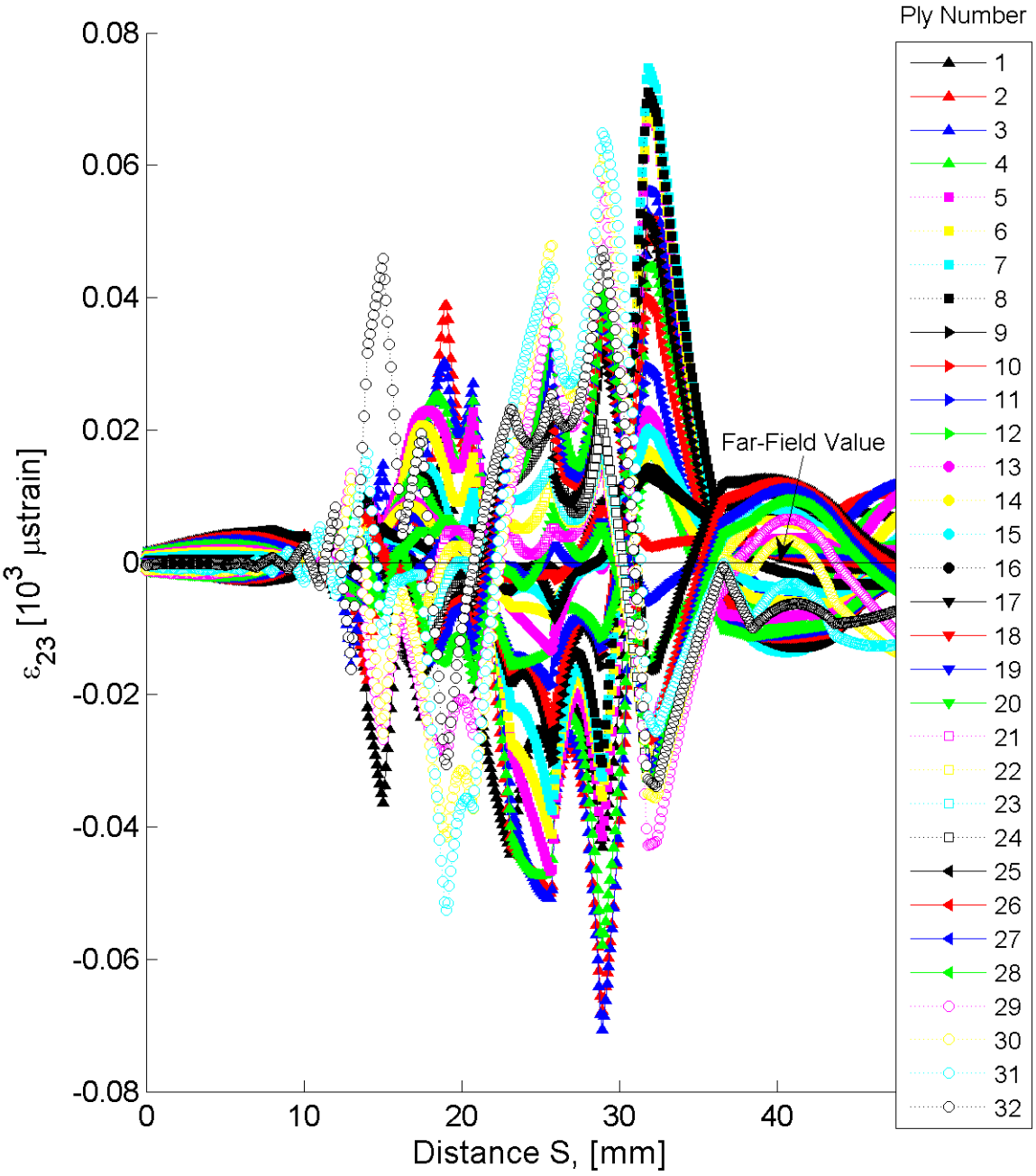

Figure B.178 Plot of ϵ_{23}, in laminate axes, along the path at the midplane of each ply for the delamination model with laminate of $[+75_4/-75_4]_{4T}$.